CODEN: JASMAN

ISSN: 0001-4966

The Journal of the Acoustical Society of America

Vol. 118, No. 6 December 2005

(Continued)

THE JOURNAL OF THE ACOUSTICAL SOCIETY OF AMERICA VOL. 118, NO. 6, DECEMBER 2005

CONTENTS—*Continued from preceding page*

(Continued)

THE JOURNAL OF THE ACOUSTICAL SOCIETY OF AMERICA VOL. 118, NO. 6, DECEMBER 2005

CONTENTS—*Continued from preceding page*

(Continued)

THE JOURNAL OF THE ACOUSTICAL SOCIETY OF AMERICA VOL. 118, NO. 6, DECEMBER 2005

CONTENTS—*Continued from preceding page*

ACOUSTICAL NEWS—USA

E. Moran
Acoustical Society of America, Suite 1NO1, 2 Huntington Quadrangle, Melville, NY 11747-4502

Editor's Note: *Readers of the journal are encouraged to submit news items on awards, appointments, and other activities about themselves or their colleagues. Deadline dates for news items and notices are 2 months prior to publication.*

New Fellows of the Acoustical Society of America

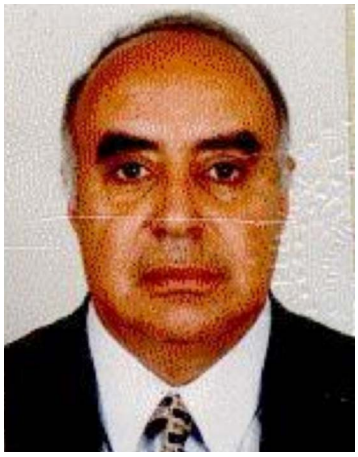

Samir N.Y. Gerges—For international service to acoustics.

Sheryl M. Gracewski—For contributions to cavitation in biomedical ultrasound.

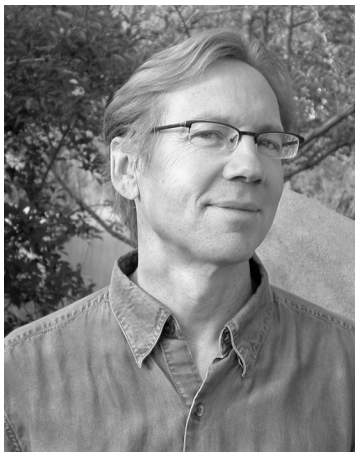

Paul Johnson—For contributions to nonlinear acoustics of rocks.

Jixun Zhou—For contributions to shallow water acoustics.

 0001-4966/2005/118(6)/3371/2/$22.50

USA Meetings Calendar

Listed below is a summary of meetings related to acoustics to be held in the U.S. in the near future. The month/year notation refers to the issue in which a complete meeting announcement appeared.

2006

9–12 Feb.	46th Annual Convention, Illinois Speech-Language-Hearing Association, Rosemont, IL [ISHA, 230 E. Ohio St., Suite 400, Chicago, IL 60611-3265; Tel.: 312-644-0828; Fax: 315-644-8557; Web: www.aishil.org].
16–18 Feb.	31st Annual Conference, National Hearing Conservation Association, Tampa, FL [NHCA, 7995 E. Prentice Ave., Suite 100 East, Greenwood Village, CO 80111-2710; Tel: 303-224-9022; Fax: 303-770-1614; E-mail: nhca@gwami.com; WWW: www.hearingconservation.org].
6–9 June	151st Meeting of the Acoustical Society of America, Providence, RI [Acoustical Society of America, Suite 1NO1, 2 Huntington Quadrangle, Melville, NY 11747-4502; Tel.: 516-576-2360; Fax: 516-576-2377; E-mail: asa@aip.org; WWW: http://asa.aip.org]. Deadline for receipt of abstracts: 23 January 2006.
17–21 Sept.	INTERSPEECH 2006 (ICSLP 2006), Pittsburgh, PA; Web: www.interspeech2006.org
28 Nov.–2 Dec.	152nd Meeting of the Acoustical Society of America joint with the Acoustical Society of Japan, Honolulu, HI [Acoustical Society of America, Suite 1NO1, 2 Huntington Quadrangle, Melville, NY 11747-4502; Tel.: 516-576-2360; Fax: 516-576-2377; E-mail: asa@aip.org; WWW: http://asa.aip.org]. Deadline for receipt of abstracts: 30 June 2006.

2007

4–8 June	153rd Meeting of the Acoustical Society of America, Salt Lake City, UT [Acoustical Society of America, Suite 1NO1, 2 Huntington Quadrangle, Melville, NY 11747-4502; Tel.: 516-576-2360; Fax: 516-576-2377; E-mail: asa@aip.org; WWW: http://asa.aip.org].
27 Nov.–2 Dec.	154th Meeting of the Acoustical Society of America, New Orleans, LA [Acoustical Society of America, Suite 1NO1, 2 Huntington Quadrangle, Melville, NY 11747-4502; Tel.: 516-576-2360; Fax: 516-576-2377; E-mail: asa@aip.org; WWW: http://asa.aip.org].

2008

28 July–1 Aug.	9th International Congress on Noise as a Public Health Problem (Quintennial meeting of ICBEN, the International Commission on Biological Effects of Noise), Foxwoods Resort, Mashantucket, CT [Jerry V. Tobias, ICBEN 9, Post Office Box 1609, Groton, CT 06340-1609; Tel. 860-572-0680; Web: www.icben.org. E-mail icben2008@att.net].

Cumulative Indexes to the Journal of the Acoustical Society of America

Ordering information: Orders must be paid by check or money order in U.S. funds drawn on a U.S. bank or by Mastercard, Visa, or American Express credit cards. Send orders to Circulation and Fulfillment Division, American Institute of Physics, Suite 1NO1, 2 Huntington Quadrangle, Melville, NY 11747-4502; Tel.: 516-576-2270. Non-U.S. orders add $11 per index.

Some indexes are out of print as noted below.

Volumes 1–10, 1929–1938: JASA and Contemporary Literature, 1937–1939. Classified by subject and indexed by author. Pp. 131. Price: ASA members $5; Nonmembers $10.

Volumes 11–20, 1939–1948: JASA, Contemporary Literature, and Patents. Classified by subject and indexed by author and inventor. Pp. 395. Out of Print.

Volumes 21–30, 1949–1958: JASA, Contemporary Literature, and Patents. Classified by subject and indexed by author and inventor. Pp. 952. Price: ASA members $20; Nonmembers $75.

Volumes 31–35, 1959–1963: JASA, Contemporary Literature, and Patents. Classified by subject and indexed by author and inventor. Pp. 1140. Price: ASA members $20; Nonmembers $90.

Volumes 36–44, 1964–1968: JASA and Patents. Classified by subject and indexed by author and inventor. Pp. 485. Out of Print.

Volumes 36–44, 1964–1968: Contemporary Literature. Classified by subject and indexed by author. Pp. 1060. Out of Print.

Volumes 45–54, 1969–1973: JASA and Patents. Classified by subject and indexed by author and inventor. Pp. 540. Price: $20 (paperbound); ASA members $25 (clothbound); Nonmembers $60 (clothbound).

Volumes 55–64, 1974–1978: JASA and Patents. Classified by subject and indexed by author and inventor. Pp. 816. Price: $20 (paperbound); ASA members $25 (clothbound); Nonmembers $60 (clothbound).

Volumes 65–74, 1979–1983: JASA and Patents. Classified by subject and indexed by author and inventor. Pp. 624. Price: ASA members $25 (paperbound); Nonmembers $75 (clothbound).

Volumes 75–84, 1984–1988: JASA and Patents. Classified by subject and indexed by author and inventor. Pp. 625. Price: ASA members $30 (paperbound); Nonmembers $80 (clothbound).

Volumes 85–94, 1989–1993: JASA and Patents. Classified by subject and indexed by author and inventor. Pp. 736. Price: ASA members $30 (paperbound); Nonmembers $80 (clothbound).

Volumes 95–104, 1994–1998: JASA and Patents. Classified by subject and indexed by author and inventor. Pp. 632. Price: ASA members $40 (paperbound); Nonmembers $90 (clothbound).

Volumes 105–114, 1999–2003: JASA and Patents. Classified by subject and indexed by author and inventor. Pp. 616. Price: ASA members $50; Nonmembers $90 (paperbound).

ACOUSTICAL NEWS—INTERNATIONAL

Walter G. Mayer
Physics Department, Georgetown University, Washington, DC 20057

International Meetings Calendar

Below are announcements of meetings and conferences to be held abroad. Entries preceded by an * are new or updated listings.

December 2005

7–9 **Symposium on the Acoustics of Poro-Elastic Materials**, Lyon, France (Fax: +33 4 72 04 70 41; Web: v0.intellagence.eu.com/sapem2005).

January 2006

5–7 **First International Conference on Marine Hydrodynamics**, Visakhapatnam, India (V. B. Rao, Naval Science & Technological Laboratory, Vigyan Nagar, Visakhapatnam-530 027, India; Web: www.mahy2006.com).

17–19 **Anglo-French Physical Acoustics Conference**, Wye College, Kent, UK (Web: www.ioa.org.uk/viewupcoming.asp).

March 2006

14–16 **Spring Meeting of the Acoustical Society of Japan**, Tokyo, Japan (Acoustical Society of Japan, Nakaura 5th-Bldg., 2-18-20 Sotokanda, Chiyoda-ku, Tokyo 101-0021, Japan; Fax: +81 3 5256 1022; Web: www.asj.gr.jp/index-en.html).

20–23 **Meeting of the German Acoustical Society (DAGA 2006)**, Braunschweig, Germany (Web: www.daga2006.de).

April 2006

24–27 **French Congress on Acoustics**, Tours, France (Web: cfa06.med.univ-tours.fr).

May 2006

2–5 **International Conference on Speech Prosody 2006**, Dresden, Germany (Web: www.ias.et.tu-dresden.de/sp2006).

5–7 *__Sixth International Conference on Auditorium Acoustics__, Copenhagen, Denmark (e-mail: t.j.cox@salford.ac.uk; Web: www.ioa.org.uk/viewupcoming.asp).

15–19 **IEEE International Conference on Acoustics, Speech, and Signal Processing**, Toulouse, France (Web: icassp2006.org).

23–26 **17th Session of the Russian Acoustical Society**, Moscow, Russia (Web: www.akin.ru).

30–1 **6th European Conference on Noise Control (EURONOISE2006)**, Tampere, Finland (Fax: +358 9 7206 4711; Web: www.euronoise2006.org).

June 2006

12–15 **8th European Conference on Underwater Acoustics**, Carvoeiro, Portugal (Web: www.ecua2006.org).

17–19 *__9th International Conference on Recent Advances in Structural Dynamics__, Southampton, UK (Web: www.isvr.soton.ac.uk/sd2006/index.htm).

26–28 **9th Western Pacific Acoustics Conference (WESPAC 9)**, Seoul, Korea (Web: wespac9.org).

26–29 *__11th International Conference on Speech and Computer__, St. Petersburg, Russia (Web: www.specom.nw.ru).

July 2006

3–7 **13th International Congress on Sound and Vibration (ICSV13)**, Vienna, Austria (Web: info.tuwienac.at/icsv13).

17–20 **International Symposium for the Advancement of Boundary Layer Remote Sensing (ISARS13)**, Garmisch-Partenkirchen, Germany (Fax: +49 8821 73 573; Web: imk-ifu.fzk.de/isars).

17–19 **9th International Conference on Recent Advances in Structural Dynamics**, Southampton, UK (Web: www.isvr.soton.ac.uk/sd2006/index.htm).

September 2006

13–15 **Autumn Meeting of the Acoustical Society of Japan**, Kanazawa, Japan (Acoustical Society of Japan, Nakaura 5th-Bldg., 2-18-20 Sotokanda, Chiyoda-ku, Tokyo 101-0021, Japan; Fax: +81 3 5256 1022; Web: www.asj.gr.jp/index-en.html).

18–20 *__Sixth International Symposium on Active Noise and Vibration Control (ACTIVE2006)__, Adelaide, Australia (Web: www.active2006.com).

18–20 **International Conference on Noise and Vibration Engineering (ISMA2006)**, Leuven, Belgium (Fax: 32 16 32 29 87; Web: www.isma-isaac.be).

October 2006

25–28 **Fifth Iberoamerican Congress on Acoustics**, Santiago, Chile (Web: www.fia2006.cl).

November 2006

20–22 **1st Joint Australian and New Zealand Acoustical Societies Conference**, Christchurch, New Zealand (Web: www.acoustics.org.nz).

July 2007

9–12 **14th International Congress on Sound and Vibration (ICSV14)**, Cairns, Australia (e-mail: n.kessissoglou@unsw.edu.au).

August 2007

26–29 *__Inter-Noise 2007__, İstanbul, Turkey (Web: www.internoise2007.org.tr).

27–31 **Interspeech 2007**, Antwerp, Belgium (e-mail: conf@isca-speech.org).

September 2007

2–7 **19th International Congress on Acoustics (ICA2007)**, Madrid, Spain (SEA, Serrano 144, 28006 Madrid, Spain; Web: www.ica2007madrid.org).

9–12 *__ICA Satellite Symposium on Musical Acoustics (ISMA2007)__, Barcelona, Spain (SEA, Serano 144, 28006 Madrid, Spain; Web: www.isma2007.org).

 0001-4966/2005/118(6)/3373/2/$22.50

June 2008

29–4 ⋆**Forum Acusticum: Joint Meeting of European Acoustical Association (EAA), Acoustical Society of America (ASA), and Acoustical Society of France (SFA)**, Paris, France (Web: www.sfa.asso.fr; e-mail: phillipe.blanc-benon@ec-lyon.fr).

July 2008

28–1 **19th International Congress on Noise as a Public Health Problem**, Mashantucket, Pequot Tribal Nation (ICBEN 9, P.O. Box 1609, Groton CT 06340-1609, USA: Web: www.icben.org).

August 2010

23–27 ⋆**20th International Congress on Acoustics (ICA2010)**, Sydney, Australia (Web: www.acoustics.asn.au).

Preliminary Announcement

October 2006

3–6 **IEEE Ultrasonics Symposium**, Vancouver, BC, Canada (TBA).

BOOK REVIEWS

P. L. Marston
Physics Department, Washington State University, Pullman, Washington 99164

These reviews of books and other forms of information express the opinions of the individual reviewers and are not necessarily endorsed by the Editorial Board of this Journal.

*Editorial Policy: If there is a negative review, the author of the book will be given a chance to respond to the review in this section of the Journal and the reviewer will be allowed to respond to the author's comments. [See "Book Reviews Editor's Note," J. Acoust. Soc. Am. **81**, 1651 (May 1987).]*

Sonoluminescence

F. Ronald Young

CRC Press, Boca Raton, FL, 2004. 227 pp. Price: $99.95 (hardcover), ISBN: 0849324394

This book summarizes, often quoting directly from journal articles, the theme(s) described in published papers relating to sonoluminescence. Indeed, it either summarizes or cites almost every single paper ever written in the field! As such, it can be considered an historical reference list.

But I believe that sonoluminescence is more than a simple collection of papers and summaries. Sonoluminescence conjures up images of magical bubbles giving off spectacular bursts of light. A lot of that magic came about after Felipe Gaitan discovered single-bubble sonoluminescence (SBSL), in which a single light-emitting bubble could be isolated and studied. It is the hydrogen atom of cavitation and its isolation sparked a decade of discoveries.

But the history of sonoluminescence does not begin there. The first period begins in 1933 with the discovery of sonoluminescence from cavitation fields (called multiple bubble sonoluminescence or MBSL) and is accurately described in the book as lasting up to 1990, when SBSL was discovered. This first period saw many experiments and discarded theories (which were later dusted off and revamped to describe SBSL!). As this book focuses on SBSL, I shall call this first period "SBSL prehistory."

The second period I call the "age of discovery" and it begins with the discovery of SBSL in 1990 and lasts until 1996. This period saw remarkable discoveries and even more remarkable theories to describe the observations coming out of various labs. I suppose one could also label this period the "age of confusion," because each discovery and theory seemed to bring about more questions than answers.

Most of those early discoveries occurred within the laboratories of Seth Putterman at UCLA. He had heard of Gaitan's magical bubble and, perhaps sensing the implications of a simple air bubble that can emit light, traveled with his graduate student Brad Barber to the lab of Larry Crum to observe Gaitan's method of isolation. Back at his own lab, Barber set out to measure the lifetime of the light flash, only to discover that the flash was too short to measure! They also measured the synchronicity of the flashes, only to find out that the bubble was much more stable than the equipment used to isolate it! They measured the radial pulsation of the bubble and used well-known and accepted equations for describing that motion, only to find out that the equations could not explain how the bubble remained stable for long periods.

Putterman's lab also measured the first spectrum from SBSL. The spectrum looked like the tail of a black body radiator, but without knowing where the peak of the spectrum lay, it was hard to get any information about the temperature. Measurements suggested that the back body temperature was about 25 000 K. But just as the sun has a cool surface temperature, and a very hot core, calculations of the core temperature within a single sonoluminescing bubble suggested that fusion may even be possible!

These early studies captivated the scientific community. Many theories were developed. The book touches on most, if not all, the theories. It would have been nice to categorize these theories in terms of their applicability. Instead, the book simply summarizes each theory, without interpretation.

In the meantime, experiments were being conducted on all sorts of liquids and gasses, in environments as varied as high magnetic fields or microgravity. The book touches on many of these studies, but, again, does so only in summary form, without interpretation.

The third period, the "age of reason," began in 1996 and lasted to 2002. In this period fundamental theories came forth that could account for most of the observations.

The transition to this age of reason began at a landmark ASA meeting held in Hawaii in 1996. At the meeting, Robert Apfel presented a list of challenges to theorists and experimentalists for advancing the science of sonoluminescence. At the same meeting, Detlef Lohse, an up-and-coming physicist, presented a hypothesis to explain how a bubble could remain stable for long periods of time. He came up with the notion that chemical reactions were occurring within the bubble, that the nitrogen and oxygen (the air) within the bubble underwent dissociation and dissolved into the liquid, leaving only argon inside (the argon concentration in air is about 1%). This remarkable hypothesis was proved true about a year later by Matula and Crum, and shortly thereafter independently by Ketterling and Apfel.

This period also saw more sophisticated techniques to accurately measure the duration of the light flash. With this information, Lohse and colleagues presented a detailed description of how light can be emitted from a collapsing bubble. By incorporating additional important physics from Willy Moss, Kyuichi Yasui, and others, they were able to describe the emission process in terms of fundamental physics—bremsstrahlung and recombination radiation. The chemical reaction and light-emitting models matched very well with many observations and laid the foundation for understanding SBSL (although some aspects have yet to be resolved).

The fourth period, which I humorously call the "atomic age," started in 2002 with the publication in *Science* magazine that sonoluminescence bubbles generate fusion. This apparent discovery has caused quite a stir. At the time of this writing, there has not been any independent confirmation of cavitation fusion (or sonofusion). This potentially explosive result is only touched on by the book. Parenthetically, Hollywood anticipated sonofusion in their movie *Chain Reaction*, produced in 1996!

It would have been nice to include some of the wonder of sonoluminescence in the book. For example, a presentation on the topic of sonoluminescence always drew big audiences. Whether it was a technical scientific conference, or in a colloquium setting, the room overflowed with people eager to hear the latest buzz. When we gave demonstrations of sonoluminescence, our labs were always filled with students, professors, artists, reporters, and even congressional representatives, crowded around a small glass of water, in the dark, peering at a small bluish light emanating from within. That magic is missing in the book. Perhaps others will disagree, and that we should leave the magic to Hollywood writers.

In any case, the book does not present the topic historically as I tried to express here, nor does it distinguish the great work from the good work from the average work. It simply presents all the work. As the author states, this book is a reference book; it does contain all relevant citations associated with sonoluminescence (even a diagram of a filing cabinet the author used to store sonoluminescence papers). It just doesn't convey the magic. *Sonoluminescence* does not meet the expectations of his previous book *Cavitation*, which has recently been reprinted by Imperial College Press.

THOMAS MATULA
University of Washington,
Applied Physics Laboratory,
Seattle, Washington 98105

 0001-4966/2005/118(6)/3375/1/$22.50

Stress, Strain, and Structural Dynamics: An Interactive Handbook of Formulas, Solutions, and MATLAB Toolboxes

Bingen Yang

Elsevier Academic Press, Burlington, MA, 2005. 942 pp. Price: $89.95 (hardcover), ISBN: 0-12-787767-3.

Less engineering is done with pencil and paper, as computers and software get more sophisticated. As this trend continues, it is very easy for the physics concepts to be replaced with black box computer programs which "plug and chug" the correct answer to problems. *Stress, Strain, and Structural Dynamics* by Bingen Yang is a combination reference text and software package. Each is designed to complement the other. The theory demystifies the "plug and chug" nature of the software, and the software allows visualization of the concepts presented in the text. The software is a set of functions, a toolbox, which must be run with the popular software package MATLAB by Mathworks, Inc. MATLAB is currently in wide use in academia, government, and industry because of its versatility and ease of use. It retains all the power of a lower level language, such as C or FORTRAN, but hides tedious bookkeeping like variable declaration.

The book generally follows the two semester undergraduate series of Statics and Dynamics. However, equations are presented, rather than derived, and there are no problems provided for student to solve, so it would be inappropriate as a primary text for these courses. It is, instead, more appropriate as a supplementary text by providing a way for students to quickly visualize solutions and to see how they evolve with parameters. For practicing engineers and scientists the book and the software's value lie in their straightforward review of basic topics in structural dynamics, again allowing quick visualization of simple situations. For the structural acoustician, about half the book is devoted to vibration and resonance of primarily straightforward shapes, and only the last two chapters are devoted to numerical solutions, using the finite element method. The book is divided into five parts, Strength of Materials, Structural Mechanics, Dynamics and Vibrations, Structural Dynamics, and Two-Dimensional Elastic Continua. More attention is given to the parts dealing with Dynamics.

The chapters start with a quick tutorial on setting up the toolbox in MATLAB and a preview of the problems that will be studied in the chapter. Each chapter's accompanying toolbox is designed to be independent from the others. The user, then, can have only one chapter's toolbox on the MATLAB path at a time or there will be functions with duplicate names. A summary of theory follows. The theory is the strongest part of the text; each section follows clearly from the one before and leads smoothly into the next. Interlaced within the theory are examples using the toolboxes, allowing the user to quickly see results. The author is careful to explain, in optional sections, the techniques used to program the toolboxes. MATLAB is designed to be straightforward when problems are formulated as matrices rather than as vector differential equations. Thus, the programming techniques differ from those presented in the main text. The chapters conclude with a Quick Solution Guide reviewing the important equations and helping to locate explanations of the functions within the text. These guides allow someone already familiar with, or not interested in, the theory to quickly obtain results.

The reviewer warns that the following paragraph contains jargon that may be familiar only to MATLAB users.

A check to see that the toolbox functions ran smoothly was straightforward due to the inclusion of functions that run all the examples in each chapter together. They all ran with only one minor glitch, which was cleared up with a prompt response from the author. Testing the validity of each function would be extremely time consuming and is beyond the scope of this review. The software supplied suffers one major drawback, the manner in which it was compiled. The strength of MATLAB is its flexibility and transparency; toolboxes offered by Mathworks are given as m-files which allows the user to view and even alter the code written by the programmer. If there is a problem with the code, the user can then see exactly what is going on and attempt to fix it. The author (or publisher) of *Stress, Strain, and Structural Dynamics* has chosen to compile the code instead as p-code, which hides the code from the user and makes viewing and modifying the code impossible. This severely limits one from incorporating these functions into their own code.

This deficiency aside, there is often a need for back of the envelope calculations and quick understanding of fundamental concepts. With *Stress, Strain, and Structural Dynamics* you can get better, faster results than utilizing even a large manila envelope. The Professional engineer or graduate student with this software and text on their shelf would be able to test a new structural idea quickly and easily. This new idea could quickly be sorted into the "What was I thinking?" or the "This might just work!" basket.

The author states in the Introduction, "With this book an undergraduate student in earlier years can solve various engineering problems without worrying about numerical algorithms. This allows the student to focus on important aspects of fundamental principles in engineering science and explore the physical insight of practical problems." As computers become more important to problem solving, fundamental principles and numerical algorithms must be taught along side each other so that students understand that the differences between them are only subtle. Even in their early years the undergraduates in engineering should be learning to translate what they learn in the classroom into code that they can run. The value of this text as a teaching tool may be in having the students try writing their own MATLAB code to solve the problems studied in class; these can then be tested against the functions given with the text. In this case, it is better that the code is hidden after all.

BENJAMIN DZIKOWICZ
Naval Surface Warfare Center, Panama City,
110 Vernon Ave.,
Panama City, Florida 32407

 0001-4966/2005/118(6)/3376/1/$22.50

OBITUARY

Arthur A. Myrberg, Jr. • 1933–2005

Arthur A. Myrberg, Jr., a long-time member of the Acoustical Society and one of the world's leading figures in the field of animal bioacoustics, died in Miami, Florida on April 8, 2005.

Professor Myrberg was born in Chicago Heights, Illinois on June 28, 1933, and was raised in the small farming town of Lulenecks, which is about six miles from Joliet, Illinois. He began his education in a one-room school house and then graduated to a large metropolitan high school. He attended Ripon College where he received a B.A. in 1954 with a major in Biology and a secondary major in Education. After graduation, Myrberg entered military service with the U.S. Army, serving as an officer in the Second Armored Division in Germany. After three years in the service, he spent one year at the University of Illinois in Champaign/Urbana where he received an M.S. degree (1958). He subsequently received his doctorate from the University of California, Los Angeles, in 1961. Myrberg immediately left for Europe where he took up a postdoc at the Max-Planck-Institute for Behavioral Physiology in Seewiesen (1961–1964), Germany, studying under the Nobel Prize-winning ethologist Konrad Lorenz.

In 1964 Myrberg assumed a position as assistant professor at the University of Miami's Institute of Marine and Atmospheric Sciences. When Warren Wisby was tapped to establish the National Aquarium in Washington, D.C., Myrberg took over the well-funded animal behavior group at the school and thus began his lifelong interest in shark biology and animal bioacoustics. He was promoted to associate professor in 1967 and was awarded tenure in 1971. He was promoted to full tenured professor in 1972 and remained at the University of Miami for the duration of his career, continuing to work past his retirement.

Myrberg's earliest published work, in 1964, "An analysis of the preferential care of eggs and young by adult brooding cichlid fishes" started him on his lifelong study of fish and other marine organisms. In 1965, the paper "Sound production by cichlid fishes" was published in *Science*. This paper was followed by subsequent papers that pioneered the study of sound production and behavior of cichlid fishes, one of the most diverse groups of freshwater fishes. The work was comparative and it looked at sound production in a number of related species. It was also one of the first studies to closely relate sound production with behavior of fishes.

While Myrberg's earlier work was on cichlids, his research extended to marine organisms in general. In the early 1970s, he and his students began research on sharks and pomacentrid fishes. Each study included laboratory and field examinations of behavior and of how sound plays a role in the lives of the subjects. This work, done in collaboration with his colleagues and students, included the study of the attraction of sharks and other fishes by low-frequency sound. Among the widely cited work carried out in Myrberg's laboratory were studies carried out by Don Nelson and Samuel Gruber that provided the first behavioral data on shark hearing.

Myberg's research led to studies on details of the response and of the stimuli that evoked it, with subsequent consideration of causal agents and the possible use of sound as a practical shark repellent. He also investigated the ethology and bioacoustics of a group of marine fishes, the Pomacentridae (damselfish), that showed similar diversity in behavior and sound production as the freshwater cichlids. One achievement was the understanding of how a number of sympatric species of pomocentrids use acoustic signals to identify conspecifics by discrimination between the temporal patterns of the sounds produced by the different species. A review, "Ocean noise and the behavior of marine animals: Relationships and implications" published in 1980 was one of the first scholarly articles to express concerns about the potential effects of human-generated sounds on marine organisms. In 1981, Myrberg proposed the idea of "interception," a behavior where one animal, the interceptor, intercepts communication signals from a sender to the intended receiver, unbeknownst to those animals. The interceptor then modifies its own behavior based on that sound. This idea is currently regarded as a critical part of our understanding of how animals communicate.

Myrberg was a fellow of the Animal Behavior Society and the American Institute of Fishery Research Biologists. He published over 90 papers, had long-term funding from the National Science Foundation, the Office of Naval Research, and other granting agencies, and supervised 28 masters and doctoral students. The importance of his work, rather than the numbers of papers published, is his real legacy.

Professor Arthur A. Myrberg, Jr., is survived by a son Arthur Junior and daughter Beverly.

ARTHUR N. POPPER
RICHARD R. FAY
SAMUEL H. GRUBER
WILLIAM N. TAVOLGA

 0001-4966/2005/118(6)/3377/1/$22.50

REVIEWS OF ACOUSTICAL PATENTS

Lloyd Rice
11222 Flatiron Drive, Lafayette, Colorado 80026

The purpose of these acoustical patent reviews is to provide enough information for a Journal reader to decide whether to seek more information from the patent itself. Any opinions expressed here are those of reviewers as individuals and are not legal opinions. Printed copies of United States Patents may be ordered at $3.00 each from the Commissioner of Patents and Trademarks, Washington, DC 20231. Patents are available via the Internet at http://www.uspto.gov.

Reviewers for this issue:

GEORGE L. AUGSPURGER, *Perception, Incorporated, Box 39536, Los Angeles, California 90039*
JOHN M. EARGLE, *JME Consulting Corporation, 7034 Macapa Drive, Los Angeles, California 90068*
SEAN A. FULOP, *California State University, Fresno, 5245 N. Backer Avenue M/S PB92, Fresno, California 93740-8001*
JEROME A. HELFFRICH, *Southwest Research Institute, San Antonio, Texas 78228*
DAVID PREVES, *Starkey Laboratories, 6600 Washington Ave. S., Eden Prarie, Minnesota 55344*
DANIEL R. RAICHEL, *2727 Moore Lane, Fort Collins, Colorado 80526*
CARL J. ROSENBERG, *Acentech Incorporated, 33 Moulton Street, Cambridge, Massachusetts 02138*
NEIL A. SHAW, *Menlo Scientific Acoustics, Inc., Post Office Box 1610, Topanga, California 90290*
ERIC E. UNGAR, *Acentech, Incorporated, 33 Moulton Street, Cambridge, Massachusetts 02138*
ROBERT C. WAAG, *University of Rochester, Department of Electrical and Computer Engineering, Rochester, New York 14627*

6,914,991

43.25.Lj PARAMETRIC AUDIO AMPLIFIER SYSTEM

Frank Joseph Pompei, Wayland, Massachusetts
5 July 2005 (Class 381/111); filed 17 April 2001

A parametric loudspeaker typically uses an array of piezoelectric transducers, requiring a high-voltage connection between the amplifier and the array. By moving the stepup transformer and bias generator from the amplifier housing to the array itself, conventional low-voltage cabling can be used. Owners of electrostatic loudspeakers may notice a faint similarity to established prior art.—GLA

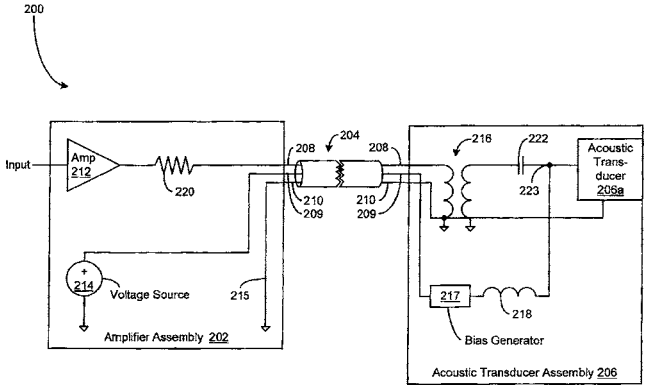

6,909,340

43.35.Pt BULK ACOUSTIC WAVE FILTER UTILIZING RESONATORS WITH DIFFERENT ASPECT RATIOS

Robert Aigner *et al.*, assignors to Infineon Technologies AG
21 June 2005 (Class 333/189); filed in Germany 24 November 2000

This patent discloses several physical arrangements of bulk acoustic wave resonators designed to smooth and control the passband response of bandpass filters in the GHz range. The devices are small thickness-mode resonators made of AlN, though the principles would seem to be generally applicable. It is curious in that there are no equations and only one or two numbers actually stated for optimum aspect ratios, so to this reviewer there does not seem to be any content to the patent other than what one might call ''rules of thumb.''—JAH

6,909,823

43.35.Sx ACOUSTO-OPTIC TUNABLE APPARATUS HAVING A FIBER BRAGG GRATING AND AN OFFSET CORE

Wayne V. Sorin and B. Yoon Kim, assignors to Novera Optics, Incorporated
21 June 2005 (Class 385/28); filed 28 December 2001

This is a device for executing one or more operations on a band of wavelengths extant within an optical signal. Use is made of the interaction between the acoustic wave and the fiber Bragg grating, which reflects one or more *n*th-order sidebands of reflection wavelengths within an optical signal in order to couple the specific band of wavelengths in one mode with a second mode.—DRR

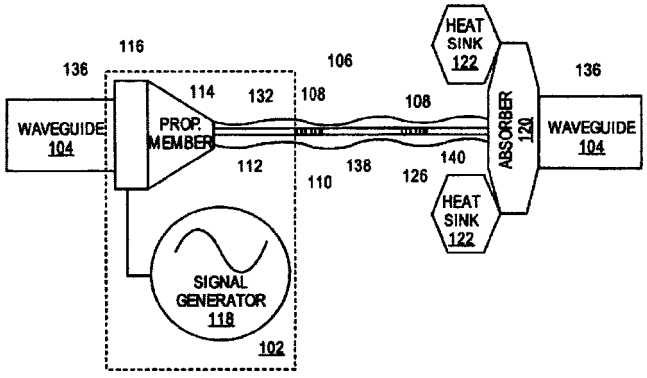

 0001-4966/2005/118(6)/3379/14/$22.50

6,912,925

43.35.Yb ACOUSTIC METER ASSEMBLY

Erik Cardelius, assignor to Maquet Critical Care AB
5 July 2005 (Class 73/866.5); filed in Sweden 5 February 2003

Gas flow meters and the like may employ one or more transducers operating in the ultrasonic range. Typically, a signal is generated, travels across a conduit, and is reflected back to a receiver. The property to be measured is then determined from differences between the transmitted and received signals. It is essential that the acoustic path length be known accurately, yet the exposed front face of the transducer assembly is subject to any pressure changes of the fluid within the conduit, causing the transducer to shift slightly in its resilient mounting. According to this patent, such a pressure differential can be reduced by providing a vent **18** into back chamber **24**, which also reduces the force required from bias spring **28**.—GLA

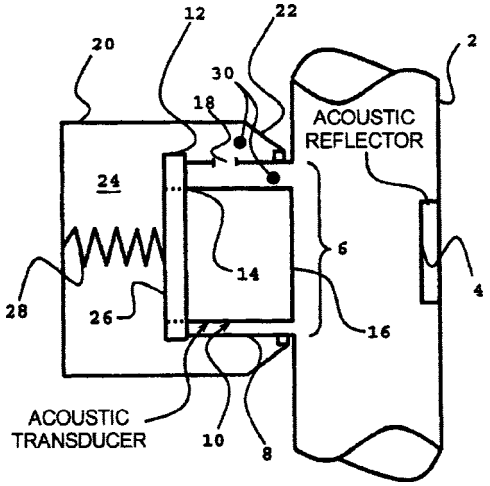

6,911,708

43.35.Zc DUPLEXER FILTER HAVING FILM BULK ACOUSTIC RESONATOR AND SEMICONDUCTOR PACKAGE THEREOF

Jae-Yeong Park, assignor to LG Electronics Incorporated
28 June 2005 (Class 257/416); filed in the Republic of Korea 21 February 2003

This patent teaches the use of bimetal bonding layers to improve adhesion of electrodes to various semiconductor substrates. Much ado is made of this and other improvisations on the basic bulk acoustic wave resonator, but really this patent tells us nothing that is not common practice in the field. The language in it is difficult to understand, so the reader is advised to browse elsewhere for information.—JAH

6,911,765

43.35.Zc QUARTZ CRYSTAL TUNING FORK RESONATOR

Hirofumi Kawashima, assignor to Piedek Technical Laboratory
28 June 2005 (Class 310/370); filed in Japan 31 October 2000

This patent tells us about a variety of tuning fork modifications that can be used to change the temperature coefficient of the ordinary cuts to be near zero. The modifications include fabricating multiple tines on a common base, cutting the tines at an angle to the crystal axis, and cutting and electroding grooves in the tines. All this seems to be a lot of cost and work to reduce a temperature coefficient, but perhaps some day one of these techniques will become standard. The patent is clear and concise in its description and claims.—JAH

6,914,992

43.38.Ar SYSTEM CONSISTING OF A MICROPHONE AND A PREAMPLIFIER

Aart Zeger van Halteren and Claus Erdmann Furst, assignors to Sonion Nederland B.V.
5 July 2005 (Class 381/113); filed in the Netherlands 2 July 1998

The patent describes structural details of an integral microphone-preamplifier design in which a rear gradient path has been designed so that its acoustical admittance is effective only at low frequencies. The result is an improvement in low-frequency noise reduction.—JME

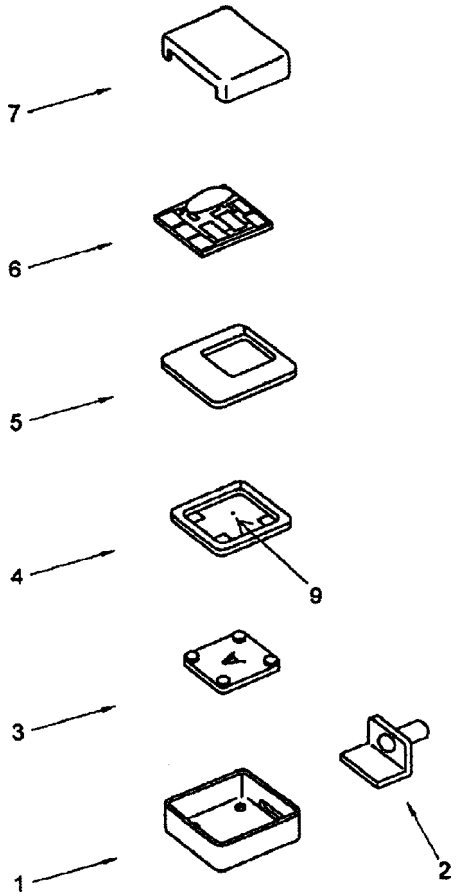

6,909,589

43.38.Bs MEMS-BASED VARIABLE CAPACITOR

Michael A. Huff, assignor to Corporation for National Research Initiatives
21 June 2005 (Class 361/281); filed 20 November 2003

This patent describes the creation of various variable, parallel-plate capacitors in low-temperature, cofired ceramics. The claims broadly cover nearly every flexible capacitor that has been made, and do not address any of the real problems of control of such a variable-separation device. The novelty of the claims appears to come solely from the use of ceramic as the structural material, but no mention is made of the processing and layer alignment steps required for success. There are a few interesting, electrode shapes depicted in the figures, but any knowledge that isn't patently obvious here (e.g., the use of physical stops to control snap-in) has been around for years.—JAH

6,888,946

43.38.Dv HIGH FREQUENCY LOUDSPEAKER

Wolfgang Bachmann *et al.*, assignors to Harman Audio Electronic Systems GmbH
3 May 2005 (Class 381/184); filed in Germany 23 May 2000

A loudspeaker is described that can be excited using either an electrodynamic or piezoeletric motor and which features a planar radiating surface that can be constructed in a fractal manner to produce a wide-range assembly. The faces of the planar structure can be glass, metal, or carbon fiber reinforced resin. The composite planar structure can have alternating rows of periodic bulges, which can be stamped knobs, pyramids, or other shapes,

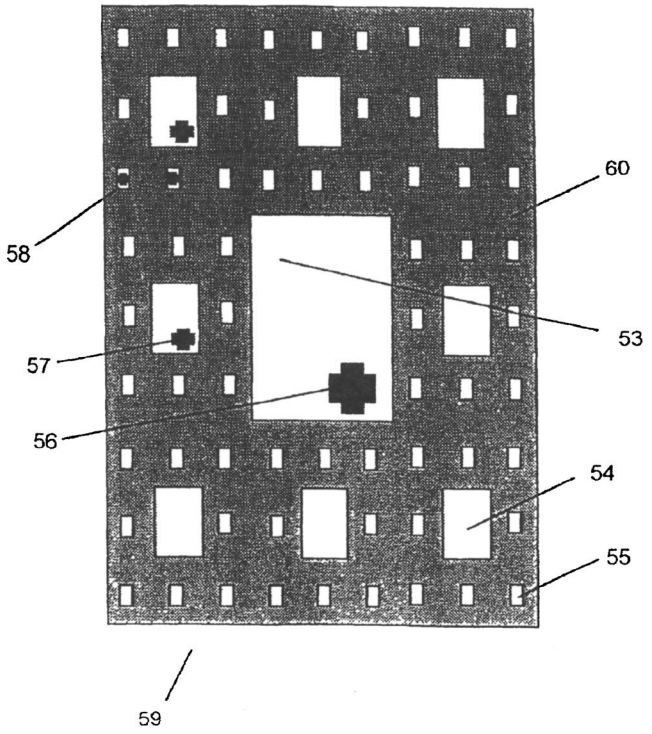

with alternating rows being stamped in opposite directions with the periodic arrangement in alternate rows offset by one-half a "knob" between rows. Assembly **59** shows a fractal pattern of structurally changed zones in a honeycomb sandwich material **60**. Large **56**, medium large **57**, and small **58** drivers can be inserted into the appropriate zone(s).—NAS

6,895,097

43.38.Dv PLANAR TYPE SPEAKER AND SYSTEM USING IT

Iwao Furuyama, assignor to Fal Company Limited
17 May 2005 (Class 381/152); filed in Japan 26 November 2002

By isolating the perimeter of a planar type loudspeaker **1** from the frame **4** using flexble edge members **3**, consisting of identical parts **3a** and **3b**, the performance of **1** is improved (or so the patent argues). The patent describes the construction and manufacture of the diaphragm in some detail,

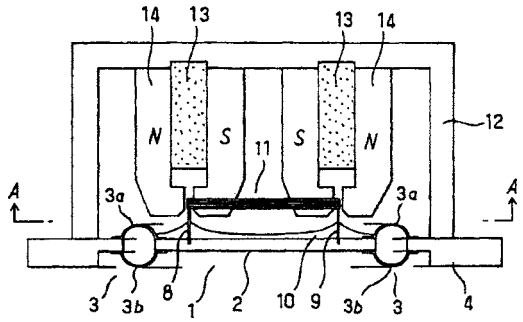

as well as the voice coil and other parts of the assembly. The planar assembly appears to be part of a larger consumer speaker assembly.—NAS

6,911,901

43.38.Dv MULTI-FUNCTIONAL VIBRO-ACOUSTIC DEVICE

Russ Bown, assignor to New Transducers Limited
28 June 2005 (Class 340/384.1); filed in the United Kingdom 20 December 2000

A panel-type loudspeaker is augmented by one or more input sensors so that it can also serve as a touch-sensitive panel. The touch-sensitive areas

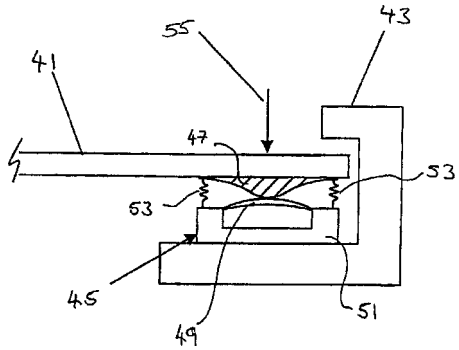

include provisions for force feedback. That pretty much sums up Claim 1 of the patent, which is the sole independent claim.—GLA

6,909,224

43.38.Fx PIEZOELECTRIC GENERATOR

Kamyar Ghandi *et al.*, assignors to Continuum Photonics, Incorporated
21 June 2005 (Class 310/339); filed 2 December 2003

This patent describes an interesting electric generator designed to take rotating input (a hand crank is shown in one figure) and convert it to dc electrical power. The inventors seem to be targeting small portable applications such as radios, computers, lights, and the like. The crank drives a circular piezo plate over ball bearings or other protrusions, creating a circulating mechanical wave in the plate. Segmented electrodes on the plate allow the deformation to be converted to electricity with "all the energy being put into the system to rotate plate...converted to electrically energy... ." The claim is that such a standing wave allows coupling coefficients approaching unity, a claim that seems unbased in fact. No design equations or supporting data are given, but numerous circuits and waveforms are shown to suggest that some such devices have been made and tested.—JAH

6,911,787

43.38.Fx DRIVING METHOD AND DRIVING CIRCUIT FOR PIEZOELECTRIC TRANSFORMER, COLD-CATHODE TUBE LIGHT-EMITTING APPARATUS, LIQUID CRYSTAL PANEL AND DEVICE WITH BUILT-IN LIQUID CRYSTAL PANEL

Katsu Takeda and Hiroshi Nakatsuka, assignors to Matsushita Electric Industrial Company, Limited
28 June 2005 (Class 315/209 PZ); filed in Japan 25 November 2002

This patent describes the application of piezoelectric transformers to the task of driving cold-cathode displays. The content of the patent is mostly how to tailor the driving waveform to reduce heating and overdriving of the piezo element. There is little here that is not known to the average engineer, and what is covered in depth is the drive circuitry for such a transformer.—JAH

6,910,548

43.38.Ja MODULAR SPEAKER CONSTRUCTION

Mark H. Powell, assignor to Gibson Guitar Corporation
28 June 2005 (Class 181/199); filed 31 March 2003

Prior art includes a number of designs for loudspeaker boxes that can be collapsed or disassembled during shipping or storage. In this case, the goal is to enable a variety of enclosures to be built from a small number of

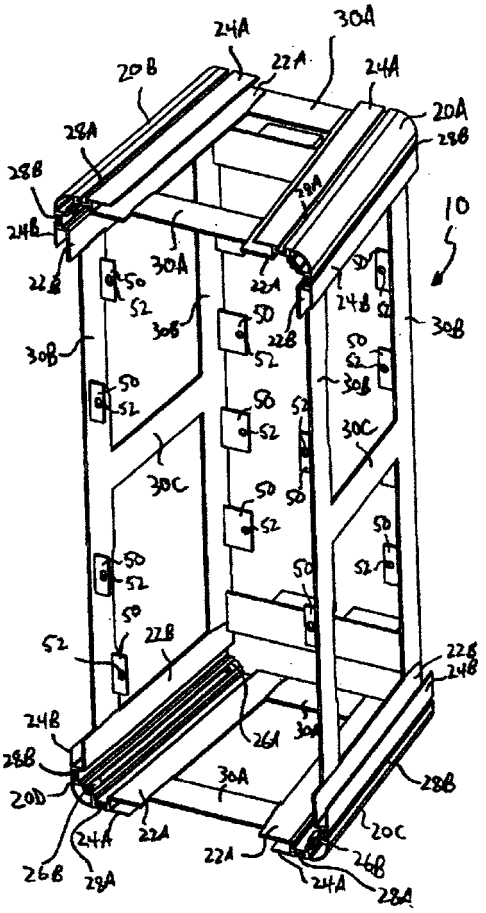

modular elements. A skeleton frame is first assembled and then individual panels are fastened in place. The novelty appears to lie in the design of corner units **20A**–**20D**.—GLA

6,912,292

43.38.Ja CONCENTRIC CO-PLANAR MULTIBAND ELECTRO-ACOUSTIC CONVERTER

Anders Sagren, Uppsala, Sweden
28 June 2005 (Class 381/421); filed 26 December 2001

Dome tweeter assembly **192** is mounted in the center of woofer assembly **181** such that "the acoustic centers of said drive units substantially coincide." Since that phrase, taken from Claim 1 of the patent, describes known prior art, any novelty must lie elsewhere. Well, Claim 1 also requires

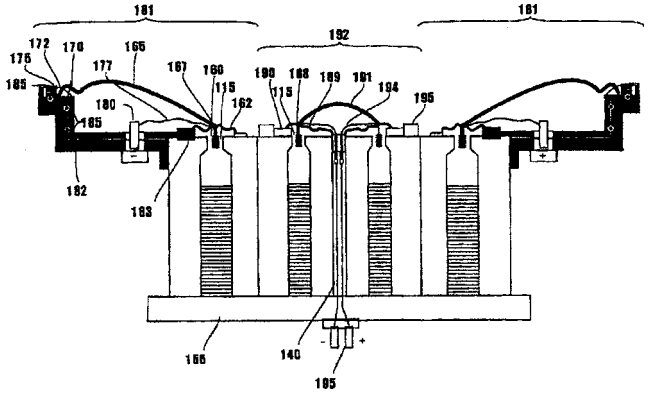

that at least one of the permanent magnets must be magnetized radially. No specific reason is given for this requirement but the patent implies that it allows a more powerful tweeter to be fitted into the limited space available.—GLA

6,914,989

43.38.Kb DEVICE AND METHOD FOR CALIBRATION OF A MICROPHONE

Cornelis Pieter Janse and Harm Jan Willem Belt, assignors to Koninklijke Philips Electronics N.V.
5 July 2005 (Class 381/92); filed in the European Patent Office 30 June 2000

This patent deals with a technique for measuring the essential performance parameters of a microphone on the production line. According to the abstract, "The calibration arrangement includes an impulse response estimating device **7** for estimating an acoustic impulse response of the microphone by correlating the microphone output signal **6** and the loudspeaker

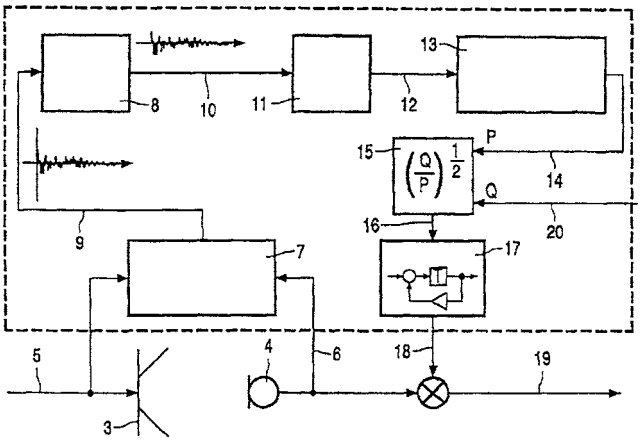

input signal **5** when the microphone **4** receives sound from the loudspeaker **3**, whereby the output power of the microphone **4** is estimated." Convoluted English aside, this patent should be read by all who are in the manufacturing sector.—JME

6,912,287

43.38.Si WEARABLE COMMUNICATION DEVICE

Masaaki Fukumoto and Yoshinobu Tonomura, assignors to Nippon Telegraph and Telephone Corporation
28 June 2005 (Class 381/151); filed in Japan 18 March 1998

Here we have another giant-size patent. It includes 52 drawing sheets and 44 claims. The invention is described as "a full-time wearable command input device in which a user can input a command by minute movements of a human body while preventing any improper input caused by bending or twisting the user's wrist from being input as a command." In the embodiment shown, the user can initiate or receive a call simply by inserting

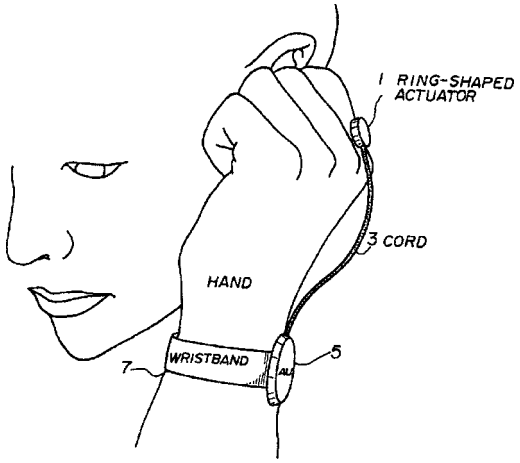

a fingertip into one ear. Voice signals are transmitted via a microphone built into wristband **7**. Audio is received via bone conduction from the fingertip, which is energized by ring-shaped actuator **1**. Although the device is described in considerable detail, there is no indication that a working model has actually been tested.—GLA

6,909,041

43.38.Vk SOUND FIELD CONTROL METHOD AND SOUND FIELD CONTROL SYSTEM

Yoshiki Ohta, assignor to Pioneer Corporation
21 June 2005 (Class 84/630); filed in Japan 28 February 2002

When multichannel reverberant sound fields are generated (or reproduced) for musical enhancement, the elements of that sound field become a part of the program that is fed directly into the listening space. What the

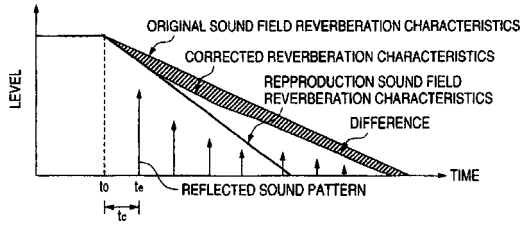

listener hears is, in effect, a combination of local room reflections and recorded reverberant information. Normally this is not a problem, insofar as the local reflections in most listening spaces are not likely to intrude on the reproduced sound field. This patent discusses means of identifying local reflections and cancelling them during the playback process, thus presenting to the listener a more natural simulation of the original recording acoustics. Music listening in the automobile is a good case in point where this could help.—JME

6,909,787

43.38.Vk METHOD AND RELATED APPARATUS FOR STEREO VOCAL CANCELLATION

Ken-Chi Chen, assignor to Mediatek Incorporation
21 June 2005 (Class 381/17); filed in Taiwan, Province of China 21 August 2003

The Karaoke craze of the 1980s brought with it a number of audio devices that removed the vocal information from a stereo program so that brave bar patrons could in effect sing along with the remaining recorded instrumental program. Since vocal information in a stereo program is essentially in-phase in the stereo channels, a simple phase inversion of the stereo

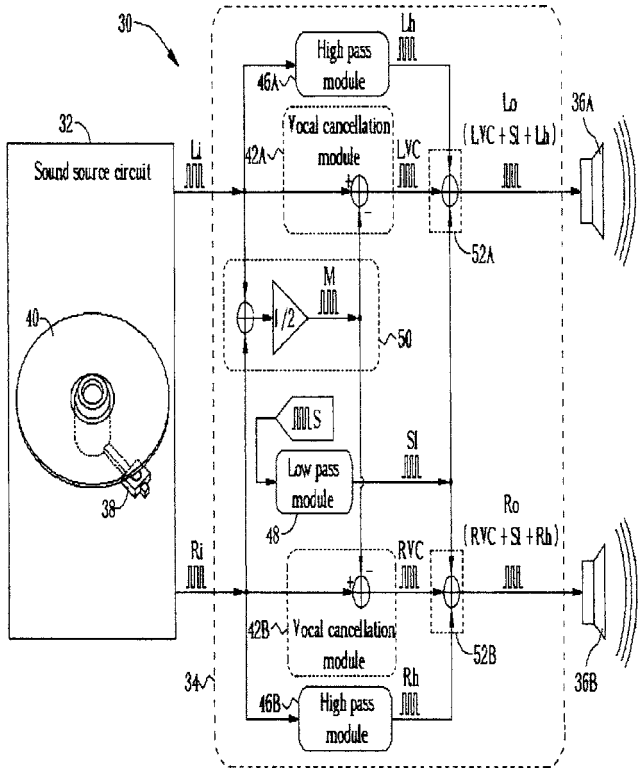

pair, when summed, will cancel the vocal portion of the program. What remains when this is done is a single anti-phase monophonic channel. This patent explores means of converting this mono channel to artificial stereo through careful reequalization, taking into account some of the original stereo content that may be out of the vocal frequency band.—JME

6,917,139

43.40.Cw FILM BULK ACOUSTIC RESONATOR

Kuk Hyun Sunwoo *et al.*, assignors to Samsung Electro-Mechanics Company, Limited
12 July 2005 (Class 310/321); filed in the Republic of Korea 5 December 2000

This is a "me-too" patent on a method for forming an effective bulk acoustic wave resonator on a silicon substrate without having all the energy of the resonant structure leak into the silicon. There is nothing novel here, just some procedures for carving out silicon in thin membranes, depositing ZnO or AlN, and getting electrical leads to the resulting structure. There are other much more interesting patents on the subject of FBARs, and the reader is advised to refer to them for information.—JAH

6,917,261

43.40.Cw COMPONENT OPERATING WITH BULK ACOUSTIC WAVES, AND HAVING ASYMMETRIC/SYMMETRICAL CIRCUITRY

Michael Unterberger, assignor to EPCOS AG
12 July 2005 (Class 333/189); filed in Germany 5 December 2002

This brief patent describes the stacking of bulk acoustic resonators in order to exploit their acoustic coupling. The parts are interposed with tungsten and silicon dioxide layers to create impedance matching structures and create splitting and broadening of the passband of the filter. It is all done for use in the 1500–1600-MHz range, for baluns in cell phone systems. The discussion is quite basic and general, with no equations and no design rules other than remarks like ''this layer should be one quarter wavelength thick,'' etc.—JAH

6,911,117

43.40.Tm METHOD AND EQUIPMENT FOR ATTENUATION OF OSCILLATION IN A PAPER MACHINE OR IN A PAPER FINISHING DEVICE

Jouko Karhunen *et al.*, assignors to Metso Paper, Incorporated
28 June 2005 (Class 162/199); filed in Finland 30 April 1997

Vibration reduction of a paper roll device is obtained by means of a dynamic absorber attached to a bearing housing. The absorber consists in essence of a spring-mass system whose natural frequency is tuned to the roll's rotational frequency or one of its harmonics. A control system changes the absorber's effective spring constant, so as to keep the absorber appropriately tuned as the rotational speed of the roll changes.—EEU

6,916,017

43.40.Tm VIBRATION DAMPER DEVICE

Mathieu Noe, assignor to Hutchinson
12 July 2005 (Class 267/161); filed in France 6 June 2001

This patent describes a vibration isolator of compact construction that includes a coil to provide electrodynamic damping, as well as centering springs to maintain axial alignment of the structural elements.—EEU

6,915,783

43.40.Vn METHOD FOR THE DAMPING OF MECHANICAL VIBRATIONS IN THE DRIVE TRAIN OF AN INTERNAL COMBUSTION ENGINE

Ralph Mader and Michael Suedholt, assignors to Siemens Dematic AG
12 July 2005 (Class 123/406.24); filed in Germany 3 December 1999

Attenuation of vibrations of the drive train of an internal combustion engine is accomplished by active adjustment of the engine's ignition angle. The control algorithm takes account of sensed vibrations of the drive train, as well as effects of imminent acceleration or load changes, as determined from the throttle valve position. It may also take account of such other parameters as temperature, vehicle speed, and transmission settings.—EEU

6,883,754

43.40.Yq REMEDIATION OF FAN SOURCE PRODUCTION OF SMOKE IN AN AIRCRAFT CABIN

Stephen D. Ehrick, assignor to Inflight Warning Systems, LLC
26 April 2005 (Class 244/118.5); filed 15 August 2002

Failure of fans used for cabin ventilation in aircraft can introduce smoke into the passenger space. The patent describes a method of detecting excessive vibration of inflight fan motors that may indicate the imminent failure of the fan, which could cause the production of smoke. The vibration

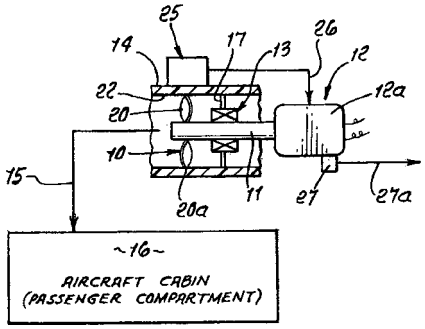

of fan housing **14** is detected by vibration detector apparatus **25**. When vibrations due to excessive bearing wear or rotor tip interference are detected, the fan is then shut down or, altenatively, the fan speed is reduced.—NAS

6,907,736

43.50.Gf GAS TURBINE COMBUSTOR HAVING AN ACOUSTIC ENERGY ABSORBING WALL

Keizo Ohnishi *et al.*, assignors to Mitsubishi Heavy Industries, Limited
21 June 2005 (Class 60/725); filed in Japan 9 January 2001

A thin corrugated plate within the combustor of a gas turbine absorbs acoustical energy by means of a perforated plate.—CJR

6,914,020

43.55.Ev SOUND AND HEAT INSULATION MATERIAL

Friedhelm Beckmann, assignor to Moeller Tech GmbH
5 July 2005 (Class 442/222); filed in Germany 9 February 1999

An otherwise normal insulation material for buildings, motor vehicles, conduits, and such is covered with an exterior wrapping material that foams up when at high temperatures and is difficult or impossible to ignite.—CJR

6,895,378

43.55.Ka SYSTEM AND METHOD FOR PRODUCING ACOUSTIC RESPONSE PREDICTIONS VIA A COMMUNICATIONS NETWORK

John D. Meyer *et al.*, assignors to Meyer Sound Laboratories, Incorporated
17 May 2005 (Class 704/270); filed 24 September 2001

There are many stand-alone computer programs that are used by audio and other designers to calculate the response of electroacoustic sytems in rooms. This patent describes a remote client version of one such program. A Java applet resides on the user's computer. The applet allows for project parameter input and communication with the processing system maintained by the assignee. Anyone who has used a resident prediction program will

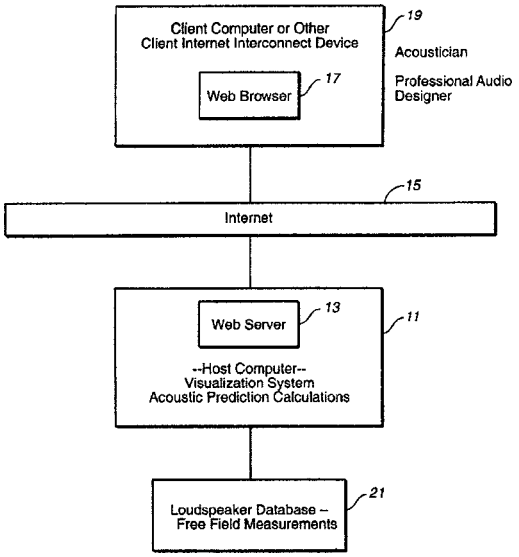

appreciate the ability to offload the computational grunt work and also in having an up-to-date database running on the latest version of the main prediction program.—NAS

6,907,784

43.58.Vb VIBRATION TYPE ANGULAR VELOCITY SENSOR

Kenji Kato, assignor to Denso Corporation
21 June 2005 (Class 73/514.15); filed in Japan 13 March 2003

The Background section of this patent explains that electrically driven tuning forks are used as angular velocity sensors in vehicular automatic braking systems and the like. One problem with this type of sensor is that a slight mechanical imbalance can create instability in the operation of the sensor. Such errors can be reduced by grinding away a small amount of material—a process somewhat similar to dynamic balancing of rotating ma-

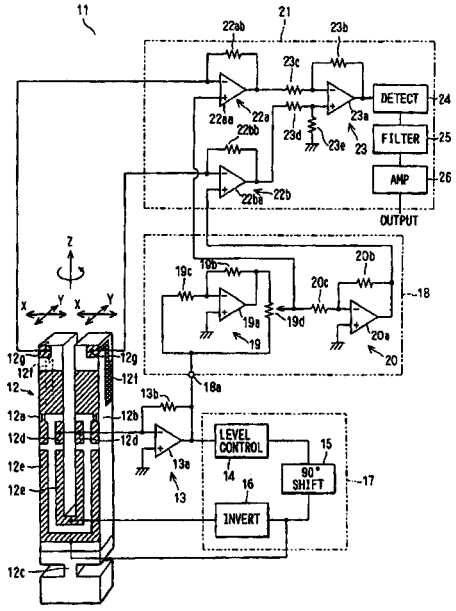

chinery. However, this calibration process not only requires a suction device to remove the grindings but is difficult to correct if too much material is removed. The patent describes a method for including the required correction in the associated electronic circuitry, requiring no mechanical calibration procedure and enabling readjustment to be performed at any time.—GLA

6,895,093

43.60.Dh ACOUSTIC ECHO-CANCELLATION SYSTEM

Murtaza Ali, assignor to Texas Instruments Incorporated
17 May 2005 (Class 381/66); filed 3 March 1999

Time-varying all-pass filters **45** and **47** are used to better decorrelate

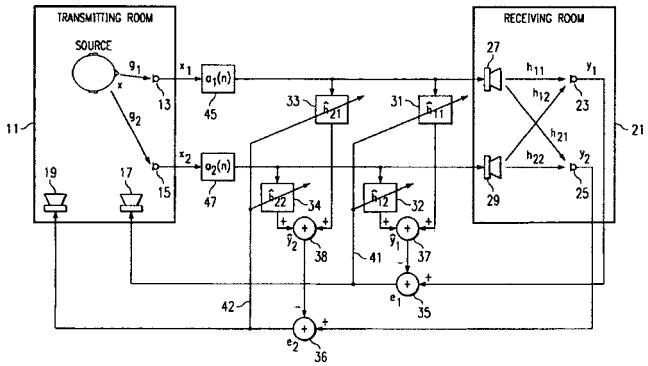

the signals in a teleconference system to improve the performance of a multichannel (in this case, a two channel) AEC system.—NAS

6,912,178

43.60.Fg SYSTEM AND METHOD FOR COMPUTING A LOCATION OF AN ACOUSTIC SOURCE

Peter L. Chu *et al.*, assignors to Polycom, Incorporated
28 June 2005 (Class 367/123); filed 15 April 2003

The patent describes techniques for precisely identifying the position of an acoustical source relative to an arbitrary microphone array. The analysis takes place in multiple frequency bands and addresses the problems of

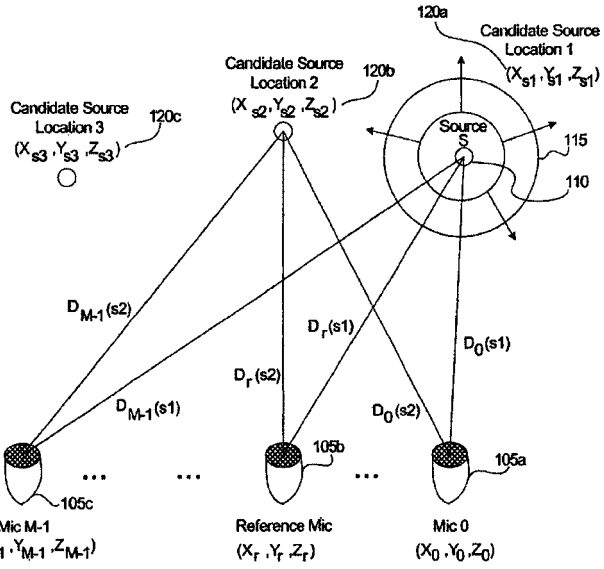

speed, accuracy, and reliability of analysis. Such systems would have use in teleconferencing and surveillance activities. The patent is well written and deserves to be read by all who work in these fields.—JME

6,914,854

43.60.Fg METHOD FOR DETECTING EXTENDED RANGE MOTION AND COUNTING MOVING OBJECTS USING AN ACOUSTICS MICROPHONE ARRAY

Jeffrey R. Heberley *et al.*, assignors to The United States of America as represented by the Secretary of the Army
5 July 2005 (Class 367/119); filed 30 June 2003

The patent addresses problems in military surveillance, and the like, where a large physical range of object movement must be assessed. According to the abstract, ''Algorithms detect and confirm the appropriate presence

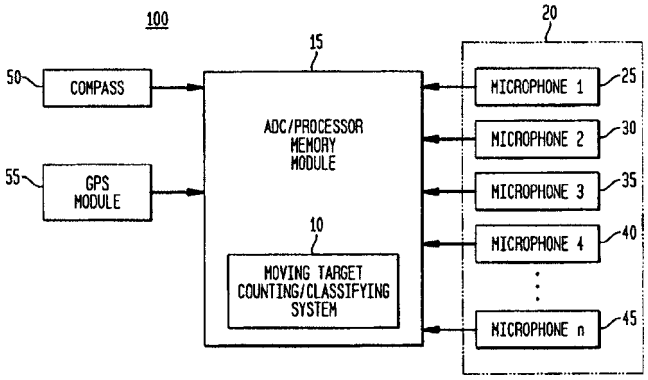

of objects moving through the beam and perform other algorithmic tests to verify that the object is a valid object to be counted.'' The patent is well supported by measurements.—JME

6,917,688

43.60.Fg ADAPTIVE NOISE CANCELLING MICROPHONE SYSTEM

Zhuliang Yu and Wee Ser, assignors to Nanyang Technological University
12 July 2005 (Class 381/94.7); filed 11 September 2002

The patent describes signal processing techniques for enhancing speech using only two fairly closely spaced (2–3 cm) microphones. The microphone outputs are added and subtracted to create an enhanced speech signal (sum) and a speech-nulled (difference) signal. Through several com-

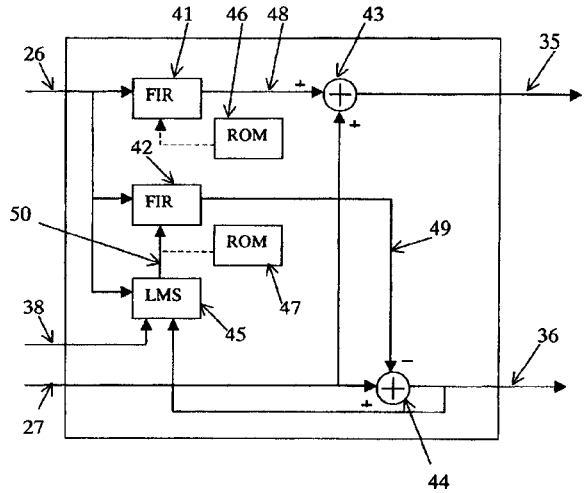

plex stages of signal-derived FIR equalization, the noise floor of the desired signal is reduced further. References are made to the DSP techniques by which these operations are carried out; regrettably, there are no measurements showing how effective the entire operation may be.—JME

6,909,819

43.60.Uv SYSTEM AND METHOD FOR CANCELING DISTURBANCE MEMS DEVICES

Brian P. Tremaine and Joseph E. Davis, assignors to Capella Photonics, Incorporated
21 June 2005 (Class 385/17); filed 16 April 2004

This patent discloses the use of feedforward techniques to cancel the mechanical cross-coupling between moving elements in a mirror array. The algorithm described is one-dimensional in that it covers only nearest-row neighbors, but one can easily imagine 2-D versions and more sophisticated adaptive versions of the model for cross-coupling. This algorithm is said to be in use in a commercial WDM optical switch.—JAH

6,915,264

43.60.Uv COCHLEAR FILTER BANK STRUCTURE FOR DETERMINING MASKED THRESHOLDS FOR USE IN PERCEPTUAL AUDIO CODING

Frank Baumgarte, assignor to Lucent Technologies Incorporated
5 July 2005 (Class 704/500); filed 22 February 2001

For compression of audio signals, as well as for automatic audio quality assessment, perceptual models are usually employed to estimate the audibility of signal distortions. The patent describes a method and apparatus for determining masked thresholds for the perceptual auditory model used, e.g., in a perceptual audio coder, which uses a filter bank structure consisting of multiple filter bank stages connected in series. Each filter bank stage, in

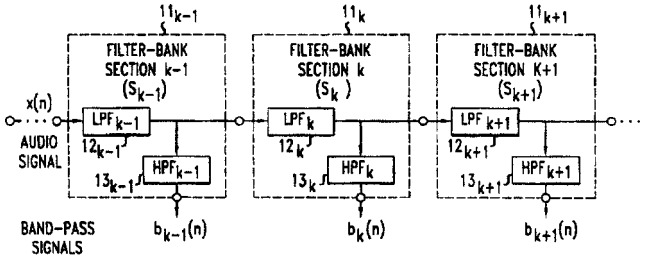

turn, comprises a number of low-pass filters connected in series and an equal number of high-pass filters. Downsampling is applied between each successive pair of filter bank stages. The filter bank coefficients may be optimized for modeling of masked threshold patterns of narrow-band maskers, and the generated thresholds may be applied in a perceptual audio coder.—DRR

6,913,578

43.64.Yp METHOD FOR CUSTOMIZING AUDIO SYSTEMS FOR HEARING IMPAIRED

Zezhang Hou, assignor to Apherma Corporation
5 July 2005 (Class 600/559); filed 24 April 2002

This apparatus provides methods for customization of personal audio systems for hearing-impaired individuals and aids for designing and producing audio products that incorporate components or software that helps to compensate for individual hearing-loss characteristics. The customization

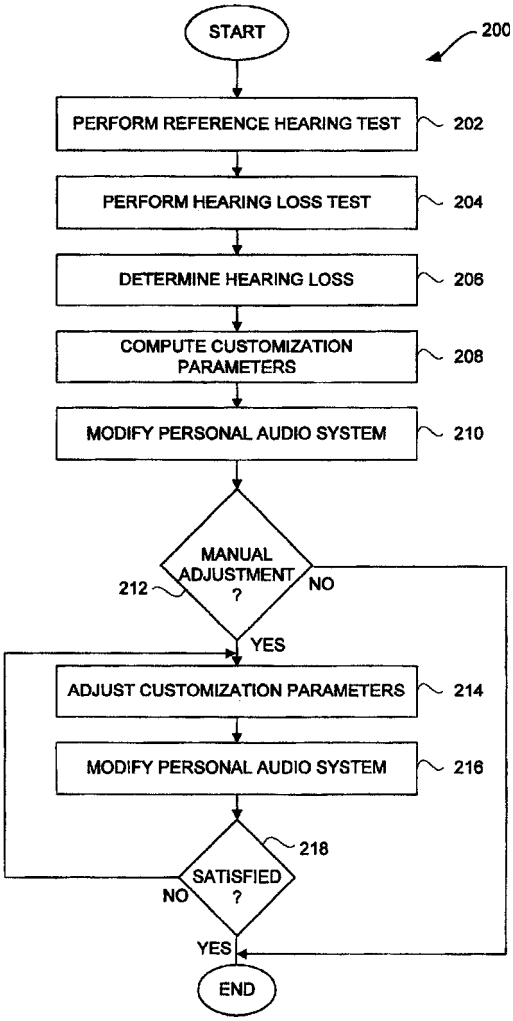

can be performed either online or offline. The customization entails the testing of the patient's hearing to obtain reference parameters such as aural frequency response, threshold of hearing, etc.—DRR

6,904,334

43.66.Qp ROBOT APPARATUS AND METHOD FOR CONTROLLING THE OPERATION THEREOF

Yasuharu Asano and Junichi Yamashita, assignors to Sony Corporation
7 June 2005 (Class 700/245); filed in Japan 18 March 2002

Mechanisms are described by which a robot would determine the direction from which a speech signal or other sound had come and orient head and then body toward that sound. The orientation is done in two steps. First, the neck is turned at rotation joint **101** in the direction of the sound, using body movements only as needed to face directly toward the sound. After a

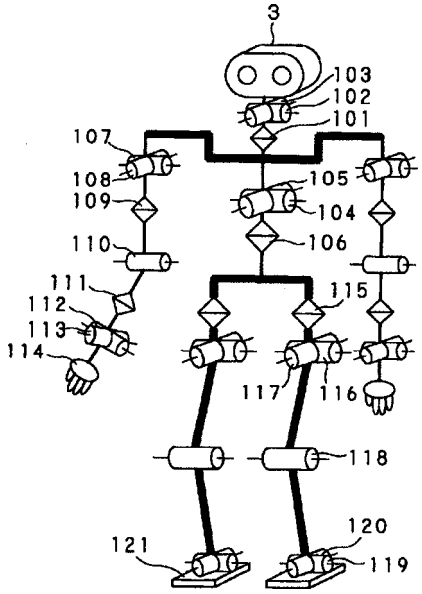

preliminary analysis of the sound, and especially if the source is deemed by prior training to be a known individual, the body movement is completed, allowing the neck position to be straightened out. These operations, from analysis of the dual-microphone pickup to descriptions of joint movements, are covered in considerable detail.—DLR

6,912,500

43.66.Qp FACILITATION OF SPEECH RECOGNITION IN USER INTERFACE

Marianne Hickey and Paul St John Brittan, assignors to Hewlett-Packard Development Company, L.P.
28 June 2005 (Class 704/270); filed in the United Kingdom 29 January 2001

This patent is extremely general in scope, and suggests various ways of connecting a 3D audio field presented to a user with computer recognition of speech by said user. The suggestions all seem rather vague, e.g., by spreading service access points around a virtual field, speech recognition could then be made sensitive to the user turning to face the desired service while speaking the relevant words. There is also a proposal to make speech recognition sensitive to a speaker's volume, which would correlate with the distance of an access point in the audio field.—SAF

6,916,291

43.66.Sr SYSTEMS, METHODS AND PRODUCTS FOR DIAGNOSTIC HEARING ASSESSMENTS DISTRIBUTED VIA THE USE OF A COMPUTER NETWORK

Gregg D. Givens *et al.*, assignors to East Carolina University
12 July 2005 (Class 600/559); filed 5 February 2002

Systems, methods, and associated devices and computer programs are described here for executing diagnostic hearing tests that utilize a computer network to provide interaction between a test administration site and one or more remote patient sites. The test may be administered by an audiologist or a qualified clinician at a site remote from the patient, so that there is inter-

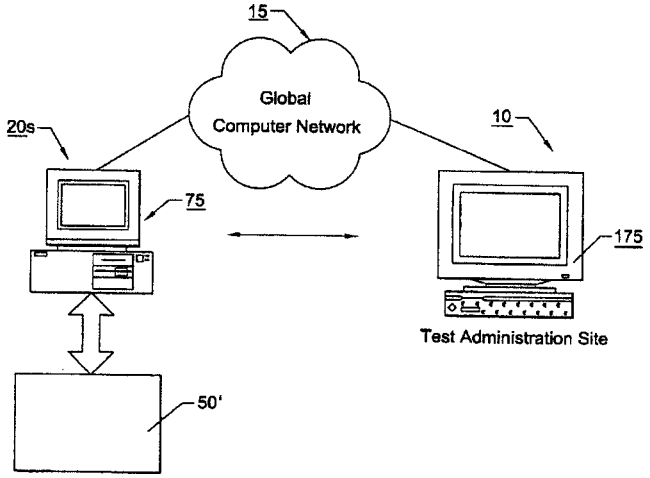

action between the user and the clinician during at least a portion of the test. The tests can be performed to meet standardized guidelines such as ANSI requirements or certification standards.—DRR

6,914,996

43.66.Ts PORTABLE TELEPHONE ATTACHMENT FOR PERSON HARD OF HEARING

Takeshi Takeda, assignor to Temco Japan Company, Limited
5 July 2005 (Class 381/380); filed in Japan 24 November 2000

A cellular phone attachment for use by a hearing-impaired person includes a microphone to be positioned close to the receiver portion of the cellular phone and a bone conduction speaker that is placed in contact at the appropriate location on a user's head. A main body contains the amplifier, a battery, and means for mounting the microphone next to the receiver and the bone conduction speaker on the user's head.—DRR

6,912,289

43.66.Ts HEARING AID AND PROCESSES FOR ADAPTIVELY PROCESSING SIGNALS THEREIN

André Vonlanthen *et al.*, assignors to Unitron Hearing Limited
28 June 2005 (Class 381/312); filed 9 October 2003

The particular signal processing method selected is determined by comparing in each of several frequency bands the input signal level and the amount of amplitude modulation in the input signal to at least one threshold

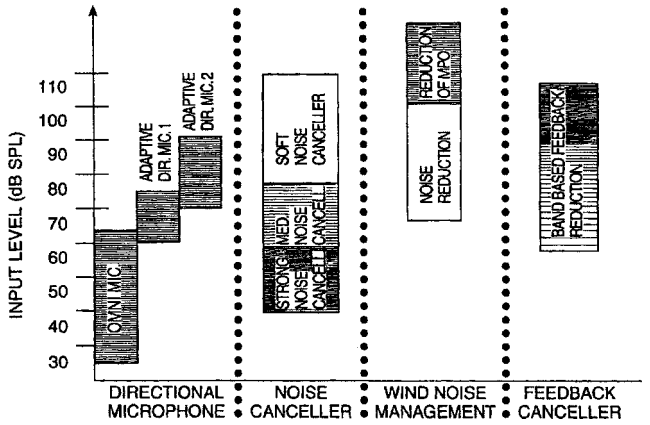

value for each. The threshold values are associated with particular signal processing methods including adaptive directionality, noise and acoustic feedback cancellation, and adaptive wind noise management.—DAP

6,914,994

43.66.Ts CANAL HEARING DEVICE WITH TRANSPARENT MODE

Adnan Shennib and Ross G. Baker, Jr., assignors to InSound Medical, Incorporated
5 July 2005 (Class 381/312); filed 7 September 2001

During long periods of inactivity, the wearer of a canal hearing aid would select a power-saving transparent mode without removing the device from the ear canal. The transparent mode compensates for the insertion loss

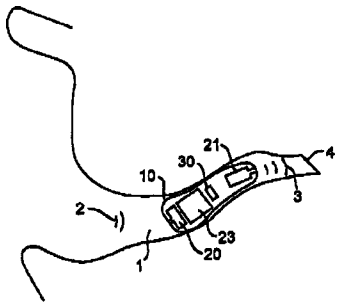

of ear canal resonance caused by inserting the hearing aid and provides approximately the same frequency response in the ear canal as the unoccluded ear.—DAP

6,915,209

43.66.Ts VISUAL AND AUDIBLE BUS ROUTING SYSTEM

David I. Spann, Savannah, Georgia
5 July 2005 (Class 701/213); filed 19 May 2003

This is a route information system that automatically provides both visual and audible information to hearing and visually impaired bus riders. A combined computer/global positioning system automatically displays the location on screen displays and makes announcements through loudspeakers.

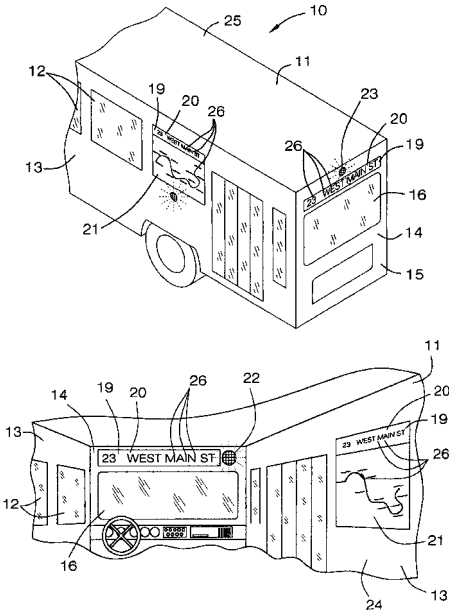

The displays and speakers are located inside the bus and also on the exterior, so the handicapped riders would know when to get on or off. Hopefully, the loudspeaker system would be clearer than is usually the case in bus and airline terminals.—DRR

6,912,495

43.72.Ar SPEECH MODEL AND ANALYSIS, SYNTHESIS, AND QUANTIZATION METHODS

Daniel W. Griffin and John C. Hardwick, assignors to Digital Voice Systems, Incorporated
28 June 2005 (Class 704/208); filed 20 November 2001

This patent proposes improved methods for parametric representation of speech for coding or synthesis, but the underlying specifics are not provided here. Generally, speech is to be represented using three parameters, viz., time-frequency distributions of voiced speech power (harmonics), unvoiced speech power (noise), and ''pulse component'' power. To obtain these, the authors cite prior patents. This patent chiefly runs through a laundry list of ways of using the three parameters to quantize various aspects of speech.—SAF

6,912,497

43.72.Ar CALIBRATION OF SPEECH DATA ACQUISITION PATH

Yifan Gong, assignor to Texas Instruments Incorporated
28 June 2005 (Class 704/228); filed 18 January 2002

How good is a speech transmission channel? Where multiple choices are available, such parsing may be essential. This patent uses a number of advanced analytical techniques to verify the accuracy and calibration of a speech acquisition path. As stated in the abstract, ''The processing uses

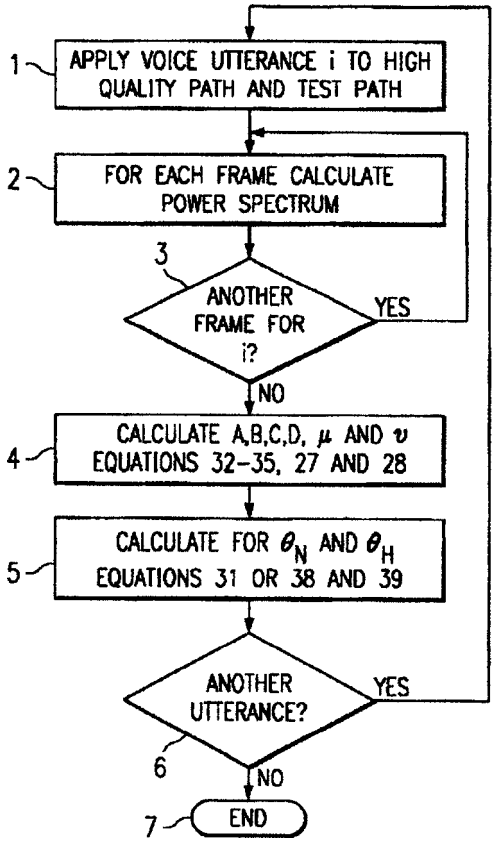

equations derived by modeling convolutive and additive noise as polynomials with different orders and estimating model parameters using maximum likelihood criteria and simultaneously solving linear equations for different orders.'' The patent is short but complex and should be read by all who are in related fields.—JME

6,915,260

43.72.Ar METHOD OF DETERMINING AN EIGENSPACE FOR REPRESENTING A PLURALITY OF TRAINING SPEAKERS

Henrik Botterweck, assignor to Koninklijke Philips Electronics, N.V.
5 July 2005 (Class 704/250); filed in Germany 27 September 2000

This patent proposes an improvement to the ''eigenvoice'' approach to speech recognition, patents pertaining to which have been reviewed here recently. In this approach, each training speaker's parameters are concatenated into a ''supervector,'' and from the space of supervectors an eigenspace is obtained by a linear transformation such that its basis vectors represent either correlation among training speakers or discriminatory attributes among speaker models. As pointed out in this patent, the number of model

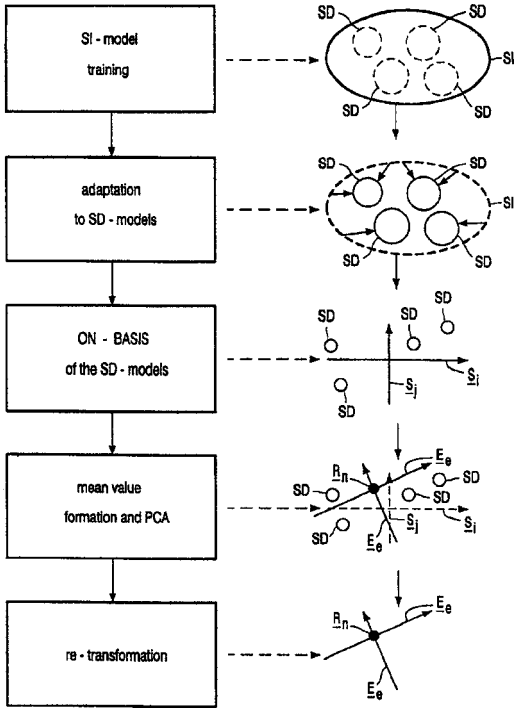

parameters for the training database leads to an unmanageably high-dimensional model space from large vocabulary ASR training, making it computationally impossible to actually carry out the eigenspace transformation. The proposal here involves any number of well-known change-of-basis algorithms, such as Gram-Schmidt orthogonalization, to obtain a ''speaker subspace,'' performing the desired transformation to the eigenspace basis vectors in each speaker model, and then reconverting.—SAF

6,915,256

43.72.Gy PITCH QUANTIZATION FOR DISTRIBUTED SPEECH RECOGNITION

Tenkasi V. Ramabadran and Alexander Sorin, assignors to Motorola, Incorporated
5 July 2005 (Class 704/207); filed 7 February 2003

Distributed speech recognition refers to allowing a wireless device to perform feature extraction, leaving pattern recognition to a back-end server. This necessitates encoded transmission of extracted features such as pitch using as few bits as possible. This patent proposes quantization methods which reduce the bit requirements of the prior art standards by such methods as intermingling frame class (e.g., voiced/unvoiced) and pitch information rather than separately encoding these with multiple code words.—SAF

6,915,263

43.72.Gy DIGITAL AUDIO DECODER HAVING ERROR CONCEALMENT USING A DYNAMIC RECOVERY DELAY AND FRAME REPEATING AND ALSO HAVING FAST AUDIO MUTING CAPABILITIES

Hua Chen *et al.*, assignors to Sony Corporation
5 July 2005 (Class 704/500); filed 20 October 1999

A decoder is proposed in which recovery delay is adaptive and based on an error rate. When the error rate is high, the silent period between error frames is extended. Error concealment is performed by repeating previous audio frames. Fast muting is accomplished within two frames of a mute signal.—DAP

6,910,007

43.72.Ja STOCHASTIC MODELING OF SPECTRAL ADJUSTMENT FOR HIGH QUALITY PITCH MODIFICATION

Ioannis G. (Yannis) Stylianou and Alexander Kain, assignors to AT&T Corporation
21 June 2005 (Class 704/207); filed 25 January 2001

This patent addresses a problem in speech synthesis, viz., that the clean modification of the pitch of voiced speech sounds is hampered by a correlation between pitch and power spectrum (line spectral frequencies) that exists in real speech. The authors propose to set up a large database of speech sounds (either actual or encoded by parameters) including information about these correlations from the actual speech of one speaker. Subsequent speech synthesis using that speaker as a template will refer to the database to select the best possible exemplar of the desired speech sound for the desired fundamental frequency.—SAF

6,890,180

43.72.Kb PHONETIC TRANSLITERATION CARD DISPLAY

Ronni S. Sterns *et al.*, assignors to Creative Action LLC
10 May 2005 (Class 434/157); filed 22 August 2003

This system would provide a physical display of multiple phrase cue cards in a speaker's native language while that person is trying to communicate in a second language. Each card would include a phonetically spelled version of the phrase in the second language. The idea is that the speaker would be able to pronounce the foreign-language phrase by reading the phonetic text such that the listener would understand. In general, both the speaker and the listener would likely find this cumbersome and time consuming, but it could prove useful in situations, such as a hospital, where the staff members do not speak the local language. However, while the staff members might be familiar with the device, understanding the reply could be a problem. There is no mention of the obvious possibility of setting up such a system with an electronic display.—DLR

6,910,005

43.72.Ne RECORDING APPARATUS INCLUDING QUALITY TEST AND FEEDBACK FEATURES FOR RECORDING SPEECH INFORMATION TO A SUBSEQUENT OFF-LINE SPEECH RECOGNITION

Heinrich Franz Bartosik, assignor to Koninklijke Philips Electronics N.V.
21 June 2005 (Class 704/201); filed in the European Patent Office 29 June 2000

This patent addresses a problem seeming to arise when voice material is recorded in a dictation mode for later transfer to a computer system to be recognized and transcribed. If errors in the transfer process or the recognition operations seriously disrupt the transcription, the user is not likely to be satisfied. But such errors should be made known, if possible, at the time of recording. The patented device has an error processor which evaluates the speech quality and, knowing the details of the transfer and recognition processes, provides, as nearly as possible, a prediction of the recognition results. A feedback mechanism allows real-time updates of the current system conditions to the recording device.—DLR

6,891,932

43.72.Ne SYSTEM AND METHODOLOGY FOR VOICE ACTIVATED ACCESS TO MULTIPLE DATA SOURCES AND VOICE REPOSITORIES IN A SINGLE SESSION

Gautam Bhargava *et al.*, assignors to Cisco Technology, Incorporated
10 May 2005 (Class 379/88.02); filed 11 December 2001

With this system, a "backbone" controller program, written in the VoiceXML language, provides voice access to a large number of diverse databases, software services, or outside telephone connections, using a network. An example grammar presented in the patent text is a Perl-like script, which would function something like a CGI server to provide access to the various services.—DLR

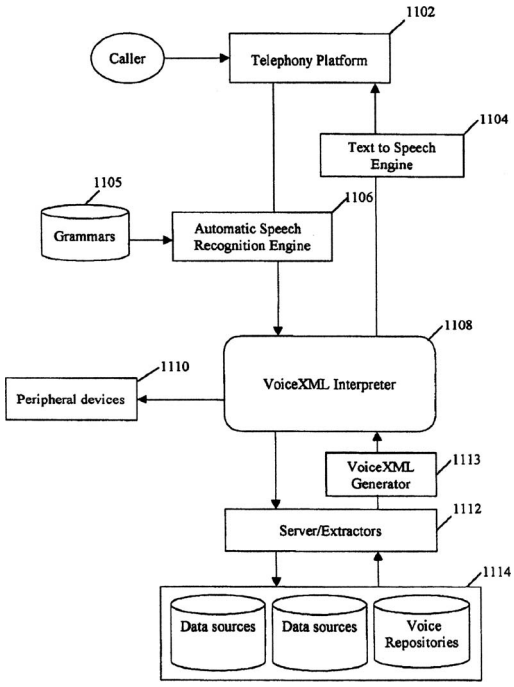

6,917,917

43.72.Ne APPARATUS AND METHOD FOR VOICE RECOGNITION AND DISPLAYING OF CHARACTERS IN MOBILE TELECOMMUNICATION SYSTEM

Yeon-Joo Kim, assignor to Samsung Electronics Company, Limited
12 July 2005 (Class 704/235); filed in the Republic of Korea 30 August 1999

To enable a caller to transfer a message to a called user at any time, voice messages are recognized via speech recognition, converted to characters, and put on the display of the user's mobile phone or paging unit when the user is not available.—DAP

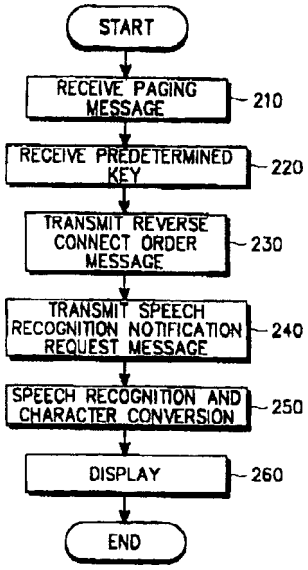

6,917,802

43.72.Ne MOBILE KEYLESS TELEPHONE INSTRUMENTS AND WIRELESS TELECOMMUNICATIONS SYSTEM HAVING VOICE DIALING AND VOICE PROGRAMMING CAPABILITIES

Byard G. Nilsson, Fallbrook, California
12 July 2005 (Class 455/419); filed 17 May 2001

Small, customized, inexpensive, voice-actuated, remote keyless devices may be activated via voice recognition to dial and perform such operations as call screening and call routing. Operations may be customized using single nonnumerical words to dial specific numbers.—DAP

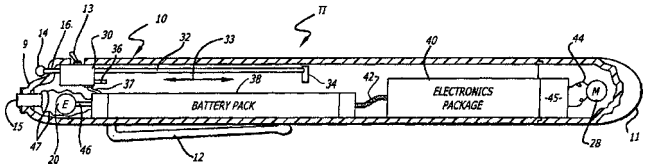

6,889,188

43.72.Ne METHODS AND APPARATUS FOR CONTROLLING AN ELECTRONIC DEVICE

Benjamin T. Metzler and Wayne D. Trantow, assignors to Intel Corporation
3 May 2005 (Class 704/270); filed 22 November 2002

Described here is what might be called a superstructure for using spoken commands to control electronic devices which were not designed for voice control. Basically, the system would have a database of the attached devices, including interface specifications suitable for controlling each of the devices electronically. A generic speech interface can then use the database to convert voice commands to device commands. Running through the 30 claims is the common thread that the devices must all be interconnected by a local-area network, assuming the use of TCP/IP protocols. Presumably, other patents have already been issued covering this obvious idea for the case of direct connections.—DLR

6,917,918

43.72.Ne METHOD AND SYSTEM FOR FRAME ALIGNMENT AND UNSUPERVISED ADAPTATION OF ACOUSTIC MODELS

William H. Rockenbeck *et al.*, assignors to Microsoft Corporation
12 July 2005 (Class 704/244); filed 22 December 2000

The goal is to reduce the storage and time requirements associated with aligning individual frames of speech with acoustic units during adaptation. In the proposed method, utterances are converted into feature vectors, which are decoded to produce a transcript and alignment unit boundaries for each utterance, resulting in fewer required feature vectors.—DAP

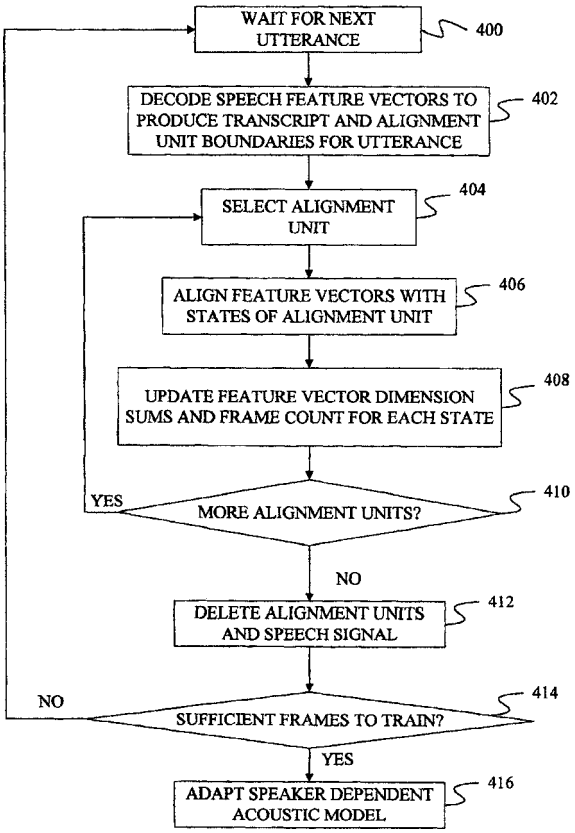

6,889,192

43.72.Ne GENERATING VISUAL FEEDBACK SIGNALS FOR EYE-TRACKING CONTROLLED SPEECH PROCESSING

Wolfgang Friedrich *et al.*, assignors to Siemens Aktiengesellschaft
3 May 2005 (Class 704/275); filed in Germany 27 January 2000

This is a minor variation of the setup covered by United States Patent 6,853,972 [reviewed in J. Acoust. Soc. Am. **118**(4), 2101–2115 (2005)] for controlling a complex system, such as a manufacturing plant, using eye-movement tracking as well as speech recognition. While similar to those in the earlier patent, the claims here have been rewritten.—DLR

6,917,920

43.72.Ne SPEECH TRANSLATION DEVICE AND COMPUTER READABLE MEDIUM

Atsuko Koizumi *et al.*, assignors to Hitachi, Limited
12 July 2005 (Class 704/277); filed in Japan 7 January 1999

This language translation device purports to be able to provide coverage of a wider range of situations and dialogue than prior examples. Intended for use by, e.g., a traveler to a foreign country, the device would include a template system for sentence construction and a speech recognizer able to convert spoken phrases into search items to aid in filling in the sentence forms. It seems obvious that one would want as much computer power as could be available in an artificial intelligence mode to provide estimates of the situation, to generate word lists, etc. That is left to a follow-up patent. Many examples in the Japanese language are provided.—DLR

6,911,592

43.75.Wx PORTABLE TELEPHONY APPARATUS WITH MUSIC TONE GENERATOR

Tsuyoshi Futamase *et al.*, assignors to Yamaha Corporation
28 June 2005 (Class 84/622); filed in Japan 28 July 1999

This patent runs to 56 pages. It is assigned to a major Japanese manufacturer and represents the combined effort of eight highly trained engineers. How will modern civilization benefit from this stupendous display of brain

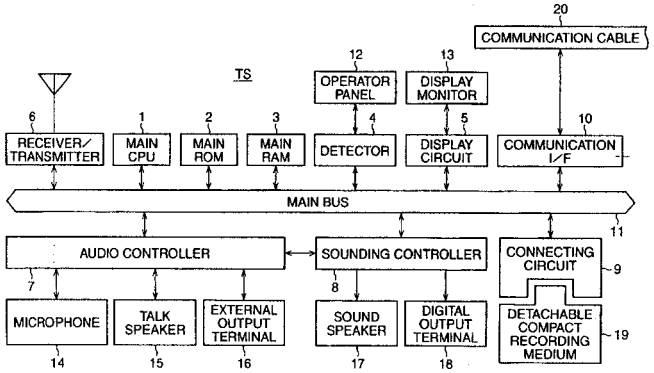

power? Why, in providing cellular phone users more options in programming their individual ring signals. The circuitry described here accommodates not only polyphonic tunes but the ability to receive spoken information and background music as well.—GLA

6,913,581

43.80.Sh HIGH OUTPUT THERAPEUTIC ULTRASOUND TRANSDUCER

Paul D. Corl, Palo Alto, California *et al.*
5 July 2005 (Class 601/2); filed 24 October 2002

The design of this transducer is said to provide very high-amplitude vibrational signals without failure of the system. In the preferred embodiment, the therapeutic ultrasound delivery system consists of a catheter body with multiple axially spaced-apart, hollow, cylindrical vibrational transducers distributed along its length, a spring connector wrapped around the outer surfaces of the piezoelectric vibrational transducers, and another connector that contacts the inner surfaces of these transducers.—DRR

6,908,434

43.80.Vj ULTRASOUND IMAGING CATHETER ISOLATION SYSTEM WITH TEMPERATURE SENSOR

David Jenkins and Simcha Borovsky, assignors to EP MedSystems, Incorporated
21 June 2005 (Class 600/466); filed 16 January 2003

A thermistor mounted on the catheter near the ultrasound transducer senses the temperature in the region of the transducer. The temperature is used to control the power output of the transducer. Electrical isolation is

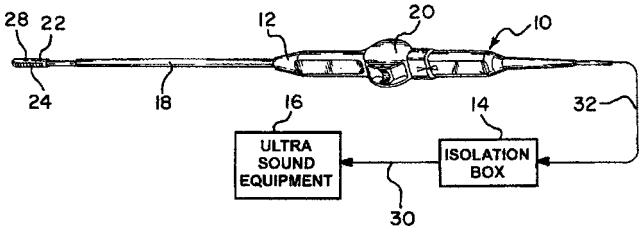

provided by a transformer box in the cable between the catheter and the ultrasonic imaging electronics.—RCW

6,911,008

43.80.Vj COMPOUND ULTRASOUND IMAGING METHOD

Laurent Pelissier *et al.*, assignors to Ultrasonix Medical Corporation
28 June 2005 (Class 600/443); filed 19 February 2003

Frames of b-scan echo data are acquired with different scanline prop-

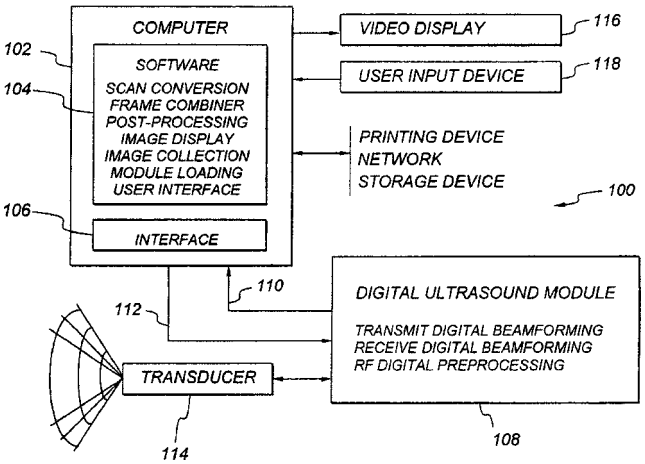

erties such as angle, length, and geometry and are compounded in real time.—RCW

LETTERS TO THE EDITOR

This Letters section is for publishing (a) brief acoustical research or applied acoustical reports, (b) comments on articles or letters previously published in this Journal, and (c) a reply by the article author to criticism by the Letter author in (b). Extensive reports should be submitted as articles, not in a letter series. Letters are peer-reviewed on the same basis as articles, but usually require less review time before acceptance. Letters cannot exceed four printed pages (approximately 3000–4000 words) including figures, tables, references, and a required abstract of about 100 words.

Equivalence of expressions for the acoustic radiation force on cylinders (L)

Wei Wei[a] and Philip L. Marston[b]
Department of Physics and Astronomy, Washington State University, Pullman, Washington 99164-2814

(Received 15 June 2005; revised 12 September 2005; accepted 25 September 2005)

Using an appropriate grouping of terms, a radiation force expression for cylinders in a standing wave based on far-field scattering [Wei *et al.*, J. Acoust. Soc. Am. **116**, 202–208 (2004)] is transformed to an expression given elsewhere [F. G. Mitri, Eur. Phys. J. B **44**, 71–78 (2005)]. Mitri's result is from a near-field derivation for the specific case of a circular cylinder. The far-field derivation also applies to noncircular objects having mirror symmetry about the incident wave vector. Some aspects of far-field derivations of optical and acoustical radiation forces are noted as are some implications for the radiation force on cylinders in travelling waves. © *2005 Acoustical Society of America.* [DOI: 10.1121/1.2126918]

PACS number(s): 43.25.Qp, 43.20.Fn [MFH] Pages: 3397–3399

I. INTRODUCTION

Recently Wei, *et al.*[1] showed how the radiation force-per-length on a symmetric cylinder in a dissipationless fluid can be expressed in terms of far-field scattering. The analysis assumed that the scattering is an even function of scattering angle so that partial wave series for the scattering has the form given by Eq. (2) of Ref. 1, which we refer to as Eq. (W2). As an example, Wei *et al.* applied this method to the scattering by a cylinder in a standing wave and obtained a simple series[2] for the dimensionless radiation force function Y_{st}, Eq. (W19). The series was expressed using the complex partial wave coefficients a_n for the scattering of a traveling wave by the cylinder. Subsequently, for a *circular* cylinder Mitri[3] obtained, by a near-field method, what may at first appear to be a different series for Y_{st}, Eq. (15) of Ref. 3. Furthermore, Mitri's discussion appears to suggest that derivations of radiation force based on far-field scattering are in some sense approximate. That is contrary to the derivation in Ref. 1. The purpose of this letter is (a) to show that Eq. (W19) reduces to Eq. (15) of Ref. 3 with an appropriate grouping of terms, (b) to clarify the significance and history of using far-field scattering for the analysis of radiation pressure, and (c) to note the generalization to progressive waves. In all cases the cylinder's axis is perpendicular to the axis of the incident wave. A partially analogous discussion of the equivalence of different derivations of traveling wave radiation pressure on spheres was given by Hasegawa.[4] The small rigid-cylinder limiting case was previously examined by Wu *et al.*[5]

II. ANALYSIS AND DISCUSSION

Equation (W19) for the dimensionless radiation force function Y_{st} is

$$Y_{\mathrm{st}} = (8/k_o R)\sum_{n=0}^{\infty}(-1)^n[\alpha_n\beta_{n+1} - \alpha_{n+1}\beta_n - (\varepsilon_n/2)\beta_n], \tag{1}$$

where $a_n = \alpha_n + i\beta_n$ is the complex partial wave scattering coefficient in Eq. (W2), k_o is the wave number in the outer medium, and $\varepsilon_n = 2 - \delta_{0n}$ where δ_{0n} is the Kronecker delta. For the case of a *circular* cylinder, R is the radius of the cylinder. The radiation force per unit length is

$$F_z/L = (R/4)P_a^2\kappa_o Y_{\mathrm{st}}\sin(2k_o h), \tag{2}$$

where P_a is the standing wave pressure amplitude, κ_o is the compressibility of the outer medium, and h denotes the position of the cylinder as explained above Eq. (W14). For the case of an *elliptical* cylinder, with a symmetric orientation as shown in Fig. 5 of Ref. 1, R becomes the same *reference radius* used in Eq. (2). The R in the denominator of Eq. (1) cancels the R in the numerator of Eq. (2) so that F_z/L does not depend on the value of the reference radius. Equation (1) may be rewritten as

$$Y_{\mathrm{st}} = (4/k_o R)\sum_{n=0}^{\infty}(-1)^{n+1}(2\alpha_{n+1}\beta_n - 2\alpha_n\beta_{n+1} + \varepsilon_n\beta_n), \tag{3}$$

where

[a]Present address: Apt. E103, 7711 NE 175th St., Kenmore, WA 98028.
[b]Electronic mail: marston@wsu.edu

$$\sum_{n=0}^{\infty}(-1)^{n+1}\varepsilon_n\beta_n = -(\beta_0-\beta_1)+(\beta_1-\beta_2)-(\beta_2-\beta_3)+\cdots$$

$$=\sum_{n=0}^{\infty}(-1)^{n+1}(\beta_n-\beta_{n+1}). \quad (4)$$

It follows that

$$Y_{\mathrm{st}} = (4/k_oR)\sum_{n=0}^{\infty}(-1)^{n+1}[\beta_n(1+2\alpha_{n+1})-\beta_{n+1}(1+2\alpha_n)], \quad (5)$$

which is Eq. (15) of Ref. 3. While the specific numerical examples in Wei *et al.* were for fluid circular cylinders, the derivation and discussion in Secs. I, II, and IV of Ref. 1 make it clear that the result in Eq. (1) applies also to symmetric solid or rigid cylinders and to shells when the appropriate partial-wave coefficients a_n are used. There have been recent advances in the evaluation of the coefficients a_n for solid elliptical cylinders.[6]

Beginning as early as Debye's 1909 analysis of the electromagnetic radiation force on spheres,[7,8] it has been recognized that calculations of radiation force based on far-field limits of the scattering do not introduce any approximation for the radiation force in the idealized case of loss-less media. Other examples in electromagnetics include the analysis of radiation torques and angular momentum flux.[9,10] In calculations of acoustical radiation force, the approach based on far-field scattering was used in the 1950s by Westervelt *et al.*,[11–14] by Gorkov,[15] and by Lee and Wang.[16] In the present case of a cylinder, the scattering contributions that fall off faster than $1/\sqrt{r}$ give a vanishing contribution to the cylindrical surface integral in Eq. (10) of Ref. 1 when the distance r goes to infinity. The analogous result for a spherical surface integral concerns contributions falling off faster than $1/r$.

III. RADIATION FORCE ON CYLINDERS IN PROGRESSIVE WAVES

Hasagawa *et al.*[17,18] expressed the radiation force per unit length on a circular cylinder of radius R in a *progressive wave* with a time-averaged intensity $\langle I\rangle$ using a dimensionless radiation force function Y_p. The radiation force per unit length F_z/L is given by $2(\langle I\rangle/c_o)RY_p$ where c_o is the speed of sound in the outer medium,

$$Y_p = -(2/k_oR)\sum_{n=0}^{\infty}[\alpha_n+\alpha_{n+1}+2(\alpha_n\alpha_{n+1}+\beta_n\beta_{n+1})], \quad (6)$$

and α_n and β_n are defined as in Eq. (1). This result was based on a near-field evaluation of the radiation stress on the cylinder. Equation (6) was confirmed by Mitri[3] as a special case in an analysis of the radiation force of quasistationary waves on a circular cylinder. From the equivalence of near- and far-field derivations leading to Eq. (W13), it follows that Eq. (6) is also applicable to *elliptical* cylinders for the case where either the semimajor or semiminor axis of the cylinder lies along the propagation direction as in Fig. 5 of Ref. 1. The R in the denominator of Eq. (6) cancels an R factor so that F_z/L does not depend on the value of the reference radius R as in the standing wave case. A similar generalization to elliptical cylinders applies to Mitri's analysis[3] of the radiation force in quasi-stationary waves. It is, of course, first necessary to evaluate the partial wave coefficients a_n for the corresponding elliptical cylinders traveling wave problem.[6]

IV. VISCOUS CORRECTIONS FOR CYLINDERS IN STANDING WAVES

Haydock[19] has recently presented extensions of Wu *et al.*[5] for the radiation force on small moveable and fixed rigid cylinders in standing waves in inviscid fluids. Haydock's formulation includes a quadrupole ($n=2$) term in the scattered field and is based on an extension of King's near-field method.[20] The expressions for the force are not in a form that can be easily compared with Eq. (1). Haydock[21] also computed (with a lattice-Boltzmann simulation) the time-averaged force on small cylinders in standing wave in a *viscous* fluid. Those computations of the force on small fixed rigid cylinders generally support the conjecture in Ref. 1 that viscous corrections for cylinders will be small when the oscillating viscous boundary layer thickness is much less than the cylinder radius. As explained by Haydock,[21] however, the implementation of the lattice-Boltzmann simulation did not allow for a detailed test of the thin-layer limit.

ACKNOWLEDGMENTS

We are grateful to David B. Thiessen for helpful comments. This research was supported by NASA.

[1] W. Wei, D. B. Thiessen, and P. L. Marston, "Acoustic radiation force on a compressible cylinder in a standing wave," J. Acoust. Soc. Am. **116**, 201–208 (2004); Erratum, *ibid.* **118**, 551 (2005).
[2] W. Wei, "Capillary bridge stability and dynamics: Active electrostatic stress control and acoustic radiation pressure," Ph.D. thesis, Washington State University, 2005, Chap. 6. This gives the detailed reduction of Eqs. (13) and (17) of Ref. 1 to Eqs. (18) and (19) of Ref. 1.
[3] F. G. Mitri, "Theoretical calculation of the acoustic radiation force acting on elastic and viscoelastic cylinders placed in a plane standing or quasi-standing wave field," Eur. Phys. J. B **44**, 71–78 (2005).
[4] T. Hasegawa, "Comparison of two solutions for acoustic radiation pressure on a sphere," J. Acoust. Soc. Am. **61**, 1445–1452 (1977).
[5] J. Wu, G. Du, S. Work, and S. Warshaw, "Acoustic radiation pressure on a rigid cylinder: An analytical theory and experiments," J. Acoust. Soc. Am. **87**, 581–586 (1990).
[6] F. Léon, F. Chati, and J.-M. Conoir, "Modal theory applied to the acoustic scattering by elastic cylinders of arbitrary cross section," J. Acoust. Soc. Am. **116**, 686–692 (2004).
[7] P. Debye, "Der Lichtdruck auf Kugeln von beliebigem Material," Ann. Phys. **30**, 57–136 (1909).
[8] H. C. van de Hulst, *Light Scattering by Small Particles* (Wiley, New York, 1957), pp. 124–130.
[9] P. L. Marston and J. H. Crichton, "Radiation torque on a sphere caused by a circularly polarized electromagnetic wave," Phys. Rev. A **30**, 2508–2516 (1984).
[10] J. H. Crichton and P. L. Marston, "The measurable distinction between the spin and orbital angular momenta of electromagnetic radiation," Electronic Journal of Differential Equations Conference 04, pp. 37–50 (2000). Available online at ⟨http://ejde.math.unt.edu⟩.
[11] P. J. Westervelt, "The theory of steady forces caused by sound waves," J. Acoust. Soc. Am. **23**, 312–315 (1951).
[12] P. J. Westervelt, "Acoustic radiation pressure," J. Acoust. Soc. Am. **29**, 26–29 (1957).
[13] G. Maidanik, "Acoustical radiation pressure due to incident plane progressive waves on spherical objects," J. Acoust. Soc. Am. **29**, 738–742 (1957).
[14] H. Olsen, H. Wergeland, and P. J. Westervelt, "Acoustic radiation force,"

J. Acoust. Soc. Am. **30**, 633–634 (1958).
[15]L. P. Gorkov, "On the forces acting on a small particle in an acoustical field in an ideal fluid," Sov. Phys. Dokl. **6**, 773–775 (1962).
[16]C. P. Lee and T. G. Wang, "Acoustic radiation force on a bubble," J. Acoust. Soc. Am. **93**, 1637–1640 (1993).
[17]T. Hasegawa, K. Saka, N. Inoue, and K. Matsuzawa, "Acoustic radiation force experienced by a solid cylinder in a plane progressive sound field," J. Acoust. Soc. Am. **83**, 1770–1775 (1988).
[18]T. Hasegawa, Y. Hino, A. Annou, H. Noda, M. Kato, and N. Inoue, "Acoustic radiation pressure acting on spherical and cylindrical shells," J. Acoust. Soc. Am. **93**, 154–161 (1993).
[19]D. Haydock, "Calculation of the radiation force on a cylinder in a standing wave acoustic field," J. Phys. A **38**, 3279–3285 (2005).
[20]L. V. King, "On the acoustic radiation on spheres," Proc. R. Soc. London, Ser. A **147**, 212–240 (1933).
[21]D. Haydock, "Lattice Boltzmann simulations of the time-averaged forces on a cylinder in a sound field," J. Phys. A **38**, 3265–3277 (2005).

Stiffness matrix method with improved efficiency for elastic wave propagation in layered anisotropic media

Eng Leong Tan[a)]
Nanyang Technological University, South Spine, Block S2, Nanyang Avenue, Singapore 639798, Singapore

(Received 7 February 2005; revised 22 July 2005; accepted 16 September 2005)

This paper presents the recursive algorithm of stiffness matrix method with improved efficiency for computing the total and surface stiffness matrices for a general multilayered anisotropic media. Based on the eigensolutions commonly available for analysis of such media, the recursive algorithm deals with eigen-submatrices directly and bypasses all intermediate layer stiffness submatrices. The improved algorithm obviates the need to compute certain inverse of the original scheme and makes the stiffness matrix recursion more robust. In situation where transfer matrix is numerically stable and easily accessible, an improved recursive algorithm is also given directly in terms of transfer submatrices without involving their explicit inverse. © *2005 Acoustical Society of America.* [DOI: 10.1121/1.2118287]

PACS number(s): 43.20.Bi, 43.20.Fn, 43.20.Gp [TDM] Pages: 3400–3403

I. INTRODUCTION

Elastic wave propagation in layered anisotropic media has been a topic of considerable interest for many years. One of the celebrated techniques for analysis of such media is based on the transfer matrix method.[1,2] This method has been known to suffer from the inherent numerical instabilities,[3] particularly when the layer thickness becomes large and/or the frequency is high. There have been various techniques proposed to overcome the numerical problem. Some of the popular ones include the direct global matrix approach[4–6] and the reflection or scattering matrix method.[7–11]

Recently, an alternative approach called the stiffness matrix method,[12–15] has been proposed to resolve the numerical instability of transfer matrix method. In this method, the layer stiffness matrix is calculated for each layer which is then applied in a recursive algorithm to determine the total stiffness matrix for a stack of multilayers. The method has been demonstrated to be efficient and computationally stable for large layer thickness and high frequency. Since the stiffness matrix operates with total stresses and displacements, it preserves the convenience of transfer matrix for incorporating imperfect interface between two layers. Furthermore, the modal solutions for different boundary value problems can be easily addressed through the total stiffness matrix. For problems where not all submatrices of the stiffness matrix are needed, e.g., for a layered half space, a partial algorithm of surface stiffness or impedance matrix method[16–18] can be utilized. This method reduces the dimension of matrices and the number of operations at each recursion, therefore it gives rise to higher computation speed.

In this paper, a more efficient recursive algorithm of stiffness matrix method is presented for computing both total and surface stiffness matrices for a general multilayered anisotropic media. Based on the eigensolutions commonly available for analysis of such media, the recursive algorithm deals with eigen-submatrices directly and bypasses all intermediate layer stiffness submatrices. In situation where transfer matrix is numerically stable and easily accessible, an improved recursive algorithm is also given directly in terms of transfer submatrices.

II. STIFFNESS MATRIX METHOD WITH IMPROVED EFFICIENCY

A. Improved algorithm for total stiffness matrix based on eigensolutions

Consider a planar multilayered structure comprising arbitrarily anisotropic media stratified in $\hat{\mathbf{z}}$ direction. Let the fields in each layer f be described by a 6×1 field vector $\mathbf{f}_f$ formed by the elements of displacement vector $\mathbf{u}_f$ and normal stress vector $\boldsymbol{\sigma}_f$, i.e., $\mathbf{f}_f=[\mathbf{u}_f;\boldsymbol{\sigma}_f]$. Assuming plane harmonic wave with $e^{-i\omega t}$ time dependence, each field vector satisfies a first-order 6×6 matrix differential system as

$$\frac{d}{dz}\mathbf{f}_f=-i\omega\mathbf{A}_f\mathbf{f}_f, \tag{1}$$

where the elements of $\mathbf{A}_f$ are functions of transverse slowness, mass density, and stiffness constants of layer f. Equation (1) admits solutions in terms of the superposition of eigenwaves:

$$\mathbf{f}_f(z)=\boldsymbol{\Psi}_f\mathbf{P}_f(z)\mathbf{c}_f. \tag{2}$$

Here, $\boldsymbol{\Psi}_f$ is a 6×6 eigenwave matrix comprising the eigenvectors $\psi_f^{(j)}$, $\mathbf{P}_f(z)$ is a diagonal matrix whose elements are $p_f^{(j)}(z)=\exp(ik_{zf}^{(j)}z)$ ($k_{zf}^{(j)}$ being the jth wave number), and $\mathbf{c}_f$ is a 6×1 coefficient vector containing the unknown constants to be determined. Henceforth, it will be assumed that the wave numbers for $j=1,2,3$ and $j=4,5,6$ along with their associated eigenwaves correspond to the upward-bounded and downward-bounded waves, respectively. Under such boundedness association, the matrices

a)Electronic mail: eeltan@ntu.edu.sg

(and vector) in Eq. (2) can be decomposed into 3×3 (and 3×1) partitions as

$$\mathbf{\Psi}_f = \begin{bmatrix} \mathbf{u}_f^{>} & \mathbf{u}_f^{<} \\ \boldsymbol{\sigma}_f^{>} & \boldsymbol{\sigma}_f^{<} \end{bmatrix}, \tag{3}$$

$$\mathbf{P}_f(z) = \begin{bmatrix} \mathbf{P}_f^{>}(z) & \mathbf{0} \\ \mathbf{0} & \mathbf{P}_f^{<}(z) \end{bmatrix}. \tag{4}$$

To keep our notations in coherence with the field vector, we have used the superscripts ">" and "<" to stand for "upward-bounded" and "downward-bounded" decomposition, respectively. $\mathbf{0}$ is the 3×3 null matrix.

With the eigensolutions available for each layer, the stiffness matrix method proceeds first by defining the layer stiffness matrix for layer f of thickness h_f as[13]

$$\mathbf{K}_f = \begin{bmatrix} \mathbf{K}_f^{11} & \mathbf{K}_f^{12} \\ \mathbf{K}_f^{21} & \mathbf{K}_f^{22} \end{bmatrix} = \mathbf{E}_f^{\boldsymbol{\sigma}}(\mathbf{E}_f^{\mathbf{u}})^{-1}, \tag{5}$$

$$\mathbf{E}_f^{\boldsymbol{\sigma}} = \begin{bmatrix} \boldsymbol{\sigma}_f^{>} & \boldsymbol{\sigma}_f^{<}\mathbf{P}_f^{<}(-h_f) \\ \boldsymbol{\sigma}_f^{>}\mathbf{P}_f^{>}(h_f) & \boldsymbol{\sigma}_f^{<} \end{bmatrix}, \tag{6}$$

$$\mathbf{E}_f^{\mathbf{u}} = \begin{bmatrix} \mathbf{u}_f^{>} & \mathbf{u}_f^{<}\mathbf{P}_f^{<}(-h_f) \\ \mathbf{u}_f^{>}\mathbf{P}_f^{>}(h_f) & \mathbf{u}_f^{<} \end{bmatrix}. \tag{7}$$

The layer stiffness matrix relates the stresses to displacements at both interfaces of the layer. For a stack of multilayers, the total stiffness matrix which relates the stresses to displacements at the top and bottom surfaces is obtained via a recursive algorithm:

$$\mathbf{K}_{(f)} = \begin{bmatrix} \mathbf{K}_{(f)}^{11} & \mathbf{K}_{(f)}^{12} \\ \mathbf{K}_{(f)}^{21} & \mathbf{K}_{(f)}^{22} \end{bmatrix}, \tag{8}$$

$$\mathbf{K}_{(f)}^{11} = \mathbf{K}_{(f-1)}^{11} + \mathbf{K}_{(f-1)}^{12}[\mathbf{K}_f^{11} - \mathbf{K}_{(f-1)}^{22}]^{-1}\mathbf{K}_{(f-1)}^{21}, \tag{9}$$

$$\mathbf{K}_{(f)}^{12} = -\mathbf{K}_{(f-1)}^{12}[\mathbf{K}_f^{11} - \mathbf{K}_{(f-1)}^{22}]^{-1}\mathbf{K}_f^{12}, \tag{10}$$

$$\mathbf{K}_{(f)}^{21} = \mathbf{K}_f^{21}[\mathbf{K}_f^{11} - \mathbf{K}_{(f-1)}^{22}]^{-1}\mathbf{K}_{(f-1)}^{21}, \tag{11}$$

$$\mathbf{K}_{(f)}^{22} = \mathbf{K}_f^{22} - \mathbf{K}_f^{21}[\mathbf{K}_f^{11} - \mathbf{K}_{(f-1)}^{22}]^{-1}\mathbf{K}_f^{12}. \tag{12}$$

Here, $\mathbf{K}_{(f)}$ denotes the total stiffness matrix for the bottom f layers, while $\mathbf{K}_{(f-1)}$ denotes that for the bottom $f-1$ layers. The recursion starts from the first bottom layer and progresses upward involving all intervening layer stiffness matrices one at a time.

To devise a more efficient recursive scheme, we rewrite Eqs. (9)–(12) in terms of the product of two matrices $\boldsymbol{\kappa}_1$ and $\boldsymbol{\kappa}_2$ defined as

$$\begin{bmatrix} \mathbf{K}_{(f)}^{11} - \mathbf{K}_{(f-1)}^{11} & \mathbf{K}_{(f)}^{12} \\ \mathbf{K}_{(f)}^{21} & \mathbf{K}_{(f)}^{22} \end{bmatrix} = \boldsymbol{\kappa}_1\boldsymbol{\kappa}_2 = \begin{bmatrix} \mathbf{K}_{(f-1)}^{12} & \mathbf{0} \\ \mathbf{K}_f^{21} & \mathbf{K}_f^{22} \end{bmatrix} \begin{bmatrix} [\mathbf{K}_f^{11} - \mathbf{K}_{(f-1)}^{22}]^{-1}\mathbf{K}_{(f-1)}^{21} & -[\mathbf{K}_f^{11} - \mathbf{K}_{(f-1)}^{22}]^{-1}\mathbf{K}_f^{12} \\ \mathbf{0} & \mathbf{I} \end{bmatrix}. \tag{13}$$

Using Eq. (5), the matrix $\boldsymbol{\kappa}_1$ can be split and factor out to give

$$\boldsymbol{\kappa}_1 = \left\{ \begin{bmatrix} \mathbf{K}_{(f-1)}^{12} & \mathbf{0} \\ \mathbf{0} & \mathbf{0} \end{bmatrix} \mathbf{E}_f^{\mathbf{u}} + \begin{bmatrix} \mathbf{0} & \mathbf{0} \\ \mathbf{0} & \mathbf{I} \end{bmatrix} \mathbf{E}_f^{\boldsymbol{\sigma}} \right\} (\mathbf{E}_f^{\mathbf{u}})^{-1}. \tag{14}$$

For the matrix $\boldsymbol{\kappa}_2$, it is transformed via partitioned inverse formula into

$$\boldsymbol{\kappa}_2 = \begin{bmatrix} \mathbf{K}_f^{11} - \mathbf{K}_{(f-1)}^{22} & \mathbf{K}_f^{12} \\ \mathbf{0} & \mathbf{I} \end{bmatrix}^{-1} \begin{bmatrix} \mathbf{K}_{(f-1)}^{21} & \mathbf{0} \\ \mathbf{0} & \mathbf{I} \end{bmatrix}. \tag{15}$$

Incorporating the inverse $(\mathbf{E}_f^{\mathbf{u}})^{-1}$ from Eq. (14) into Eq. (15) and carrying out the matrix products, we finally obtain

$$\begin{bmatrix} \mathbf{K}_{(f)}^{11} - \mathbf{K}_{(f-1)}^{11} & \mathbf{K}_{(f)}^{12} \\ \mathbf{K}_{(f)}^{21} & \mathbf{K}_{(f)}^{22} \end{bmatrix} = \begin{bmatrix} \mathbf{K}_{(f-1)}^{12}\mathbf{u}_f^{>} & \mathbf{K}_{(f-1)}^{12}\mathbf{u}_f^{<}\mathbf{P}_f^{<}(-h_f) \\ \boldsymbol{\sigma}_f^{>}\mathbf{P}_f^{>}(h_f) & \boldsymbol{\sigma}_f^{<} \end{bmatrix} \cdot \begin{bmatrix} \boldsymbol{\sigma}_f^{>} - \mathbf{K}_{(f-1)}^{22}\mathbf{u}_f^{>} & [\boldsymbol{\sigma}_f^{<} - \mathbf{K}_{(f-1)}^{22}\mathbf{u}_f^{<}]\mathbf{P}_f^{<}(-h_f) \\ \mathbf{u}_f^{>}\mathbf{P}_f^{>}(h_f) & \mathbf{u}_f^{<} \end{bmatrix}^{-1} \begin{bmatrix} \mathbf{K}_{(f-1)}^{21} & \mathbf{0} \\ \mathbf{0} & \mathbf{I} \end{bmatrix}. \tag{16}$$

Equation (16) constitutes the recursive algorithm of stiffness matrix method with improved efficiency. It is evident that the recursion step deals with eigen-submatrices directly and bypasses all intermediate layer stiffness submatrices. The algorithm thus obviates the need to compute the inverse $[\mathbf{K}_f^{11}-\mathbf{K}_{(f-1)}^{22}]^{-1}$ of the original stiffness matrix method, and no explicit inverse $(\mathbf{E}_f^{\mathbf{u}})^{-1}$ of the layer stiffness matrix is required. Besides improvement in efficiency, the exclusion of layer stiffness matrix circumvents the numerical difficulty when $\mathbf{E}_f^{\mathbf{u}}$ becomes singular, e.g., when $h_f \to 0$. This makes the stiffness matrix recursive algorithm in Eq. (16) more robust than that in Eq. (5) and Eqs. (9)–(12). Equation (16) can be solved directly as a linear system of equations, which are to be simplified further for the case when only partial solution is required as in the following.

B. Improved algorithm for surface stiffness matrix based on eigensolutions

Considering the improved version of stiffness matrix method for $\mathbf{K}_{(f)}^{22}$ (extracted in the following for convenience):

$$\mathbf{K}_{(f)}^{22}=[\boldsymbol{\sigma}_f^{>}\mathbf{P}_f^{>}(h_f)\ \boldsymbol{\sigma}_f^{<}]\times\begin{bmatrix}\boldsymbol{\sigma}_f^{>}-\mathbf{K}_{(f-1)}^{22}\mathbf{u}_f^{>} & [\boldsymbol{\sigma}_f^{<}-\mathbf{K}_{(f-1)}^{22}\mathbf{u}_f^{<}]\mathbf{P}_f^{<}(-h_f)\\ \mathbf{u}_f^{>}\mathbf{P}_f^{>}(h_f) & \mathbf{u}_f^{<}\end{bmatrix}^{-1}\begin{bmatrix}\mathbf{0}\\ \mathbf{I}\end{bmatrix}, \tag{17}$$

there is still one 6×6 inversion needed. Prior to its subsequent simplification, the form of Eq. (17) invites comparison with the efficient scheme of scattering matrix method, particularly[10,11]

$$\mathbf{R}_{(f)}=[\mathbf{P}_f^{>}(h_f)\ \mathbf{0}]\times\begin{bmatrix}-\mathbf{u}_f^{>} & \mathbf{u}_{f-1}^{>}\mathbf{R}_{(f-1)}+\mathbf{u}_{f-1}^{<}\\ -\boldsymbol{\sigma}_f^{>} & \boldsymbol{\sigma}_{f-1}^{>}\mathbf{R}_{(f-1)}+\boldsymbol{\sigma}_{f-1}^{<}\end{bmatrix}^{-1}\begin{bmatrix}\mathbf{u}_f^{<}\mathbf{P}_f^{<}(-h_f)\\ \boldsymbol{\sigma}_f^{<}\mathbf{P}_f^{<}(-h_f)\end{bmatrix}. \tag{18}$$

$\mathbf{R}_{(f)}$ is the reflection coefficient matrix describing the interactions between layer f and below, while $\mathbf{R}_{(f-1)}$ is that describing the interactions between layer $f-1$ and below. It can be seen that the matrix structures of Eqs. (17) and (18) bear much resemblance to each other. They both deal with eigen-submatrices directly in their recursion without introducing auxiliary intermediate notations. Thus they feature the same conciseness and high efficiency within their own realm of stiffness and scattering matrix methods, respectively.

By applying the partitioned inverse formula to Eq. (17), one can cast the equation into

$$\mathbf{K}_{(f)}^{22}=[\boldsymbol{\sigma}_f^{<}+\boldsymbol{\sigma}_f^{>}\mathbf{R}_{(f)}][\mathbf{u}_f^{<}+\mathbf{u}_f^{>}\mathbf{R}_{(f)}]^{-1}, \tag{19}$$

$$\mathbf{R}_{(f)}=-\mathbf{P}_f^{>}(h_f)[\boldsymbol{\sigma}_f^{>}-\mathbf{K}_{(f-1)}^{22}\mathbf{u}_f^{>}]^{-1}[\boldsymbol{\sigma}_f^{<}-\mathbf{K}_{(f-1)}^{22}\mathbf{u}_f^{<}]\times\mathbf{P}_f^{<}(-h_f). \tag{20}$$

Here, in place of the single 6×6 inverse, we have two simpler 3×3 inverses for each recursion. Hence the surface stiffness matrix method dictated by Eqs. (19) and (20) has resulted in even more improvement in efficiency over the original method of Eqs. (5) and (12).

C. Improved algorithms based on transfer matrix

The above-described efficiency improvements have been based on the eigensolutions commonly available for analysis of general multilayered anisotropic media. In this section, we consider the enhancement of stiffness matrix method when the transfer matrix solution of Eq. (1) is numerically stable and easily accessible. Denoting the transfer matrix of layer f by

$$\mathbf{T}_f=\begin{bmatrix}\mathbf{T}_f^{11} & \mathbf{T}_f^{12}\\ \mathbf{T}_f^{21} & \mathbf{T}_f^{22}\end{bmatrix}, \tag{21}$$

the original stiffness matrix method first converts the transfer matrix into layer stiffness matrix via[13]

$$\mathbf{K}_f=\begin{bmatrix}-(\mathbf{T}_f^{12})^{-1}\mathbf{T}_f^{11} & (\mathbf{T}_f^{12})^{-1}\\ \mathbf{T}_f^{21}-\mathbf{T}_f^{22}(\mathbf{T}_f^{12})^{-1}\mathbf{T}_f^{11} & \mathbf{T}_f^{22}(\mathbf{T}_f^{12})^{-1}\end{bmatrix}. \tag{22}$$

These submatrices are then substituted into the recursive algorithm (9)–(12) to obtain the total stiffness matrix as before.

By performing some manipulations as in the previous sections, an improved stiffness matrix recursive scheme can be developed with the algorithm given directly in terms of transfer submatrices as

$$\mathbf{K}_{(f)}^{11}=\mathbf{K}_{(f-1)}^{11}-\mathbf{K}_{(f)}^{12}\mathbf{T}_f^{12}\mathbf{K}_{(f-1)}^{21}, \tag{23}$$

$$\mathbf{K}_{(f)}^{12}=\mathbf{K}_{(f-1)}^{12}[\mathbf{T}_f^{11}+\mathbf{T}_f^{12}\mathbf{K}_{(f-1)}^{22}]^{-1}, \tag{24}$$

$$\mathbf{K}_{(f)}^{21}=[\mathbf{T}_f^{22}-\mathbf{K}_{(f)}^{22}\mathbf{T}_f^{12}]\mathbf{K}_{(f-1)}^{21}, \tag{25}$$

$$\mathbf{K}_{(f)}^{22}=[\mathbf{T}_f^{21}+\mathbf{T}_f^{22}\mathbf{K}_{(f-1)}^{22}][\mathbf{T}_f^{11}+\mathbf{T}_f^{12}\mathbf{K}_{(f-1)}^{22}]^{-1}. \tag{26}$$

Compared with Eq. (22) and Eqs. (9)–(12), Eqs. (23)–(26) have saved up one multiplication and one inversion of 3×3 matrix for the total stiffness matrix. For the surface stiffness matrix method pertaining to Eq. (26) only,[19] it allows more savings and achieves higher efficiency compared with the original method in Eqs. (22) and (12). Furthermore, the elimination of explicit inverse $(\mathbf{T}_f^{12})^{-1}$ extends the applicability of the recursion equation even when the inverse does not exist, e.g., when $\mathbf{T}_f$ is an identity matrix. This also makes the improved algorithm more robust apart from being more efficient.

D. Comparison of algorithms

For more detailed assessment and comparison of various improved algorithms above, we have acquired their floating point operations (flops) count using MATLAB®. The flops counting method is based on the following rules: additions or subtractions of complex numbers are two flops, multiplications or divisions of complex numbers are six flops, linear system of equations is solved using Gaussian elimination. Based on the relative flops count, Table I lists the gain in efficiency for each recursion of algorithm when given the eigensolutions $\boldsymbol{\Psi}_f$ (and $\mathbf{P}_f$) or the transfer matrix solution $\mathbf{T}_f$

TABLE I. Comparison of algorithms.

No.	Algorithm	Efficiency gain with respect to 1a or 2a	Condition as $h_f \to 0$
1a	$\boldsymbol{\Psi}_f \xrightarrow{(5)} \mathbf{K}_f \xrightarrow{(9)\text{-}(12)} \mathbf{K}_{(f)}$	1 (reference)	Singular
1b	$\boldsymbol{\Psi}_f \xrightarrow{(16)} \mathbf{K}_{(f)}$	1.18	Stable
1c	$\boldsymbol{\Psi}_f \xrightarrow{(5)} \mathbf{K}_f \xrightarrow{(12)} \mathbf{K}^{22}_{(f)}$	1.28	Singular
1d	$\boldsymbol{\Psi}_f \xrightarrow{(19)\text{-}(20)} \mathbf{K}^{22}_{(f)}$	2.50	Stable
2a	$\mathbf{T}_f \xrightarrow{(22)} \mathbf{K}_f \xrightarrow{(9)\text{-}(12)} \mathbf{K}_{(f)}$	1 (reference)	Singular
2b	$\mathbf{T}_f \xrightarrow{(23)\text{-}(26)} \mathbf{K}_{(f)}$	1.76	Stable
2c	$\mathbf{T}_f \xrightarrow{(22)} \mathbf{K}_f \xrightarrow{(12)} \mathbf{K}^{22}_{(f)}$	1.63	Singular
2d	$\mathbf{T}_f \xrightarrow{(26)} \mathbf{K}^{22}_{(f)}$	3.57	Stable

as input (for algorithms 1 or 2). The input will include as well the stack stiffness (sub)matrix $\mathbf{K}_{(f-1)}$ or $\mathbf{K}^{22}_{(f-1)}$ for the total or surface stiffness matrix method (dictated by algorithms a, b or c, d), respectively. Each algorithm then takes its input for computing the new stack stiffness (sub)matrix $\mathbf{K}_{(f)}$ or $\mathbf{K}^{22}_{(f)}$ directly or indirectly via the layer stiffness matrix $\mathbf{K}_f$. The efficiency gain has been estimated with reference to the original algorithm of Ref. 13, i.e., with respect to algorithm 1a or 2a for algorithms 1b–1d or 2b–2d, respectively.

From Table I, one can see that for the total stiffness matrix method, the improved algorithms 1b and 2b are 18% and 76% more efficient than the original algorithms 1a and 2a, respectively. For the surface stiffness matrix method that is sufficient in many problems of interest, the efficiency is higher by 28% and 63% using algorithms 1c and 2c, respectively, when compared to the original total stiffness matrix method. Even higher gains in efficiency can be achieved by resorting to the improved algorithms 1d and 2d, which lead to 2.5 and 3.6 times more efficient than the original algorithms 1a and 2a, respectively. Recall that the efficiency improvements described here are meant for each recursion per layer. Overall one will gain substantial savings in the total computation time when there are many layers and many calculations for different parameters to be dealt with. As an additional advantage of the improved algorithms 1b, 1d, 2b, and 2d, each recursion of these algorithms remains stable unlike the rest involving layer stiffness matrix that will approach being singular when the layer thickness shrinks to zero.

III. CONCLUSION

This paper has presented a more efficient recursive algorithm of stiffness matrix method for computing both total and surface stiffness matrices for a general multilayered anisotropic media. Based on the eigensolutions commonly available for analysis of such media, the recursive algorithm deals with eigen-submatrices directly and bypasses all intermediate layer stiffness submatrices. The improved algorithm obviates the need to compute certain inverse of the original scheme and makes the stiffness matrix recursion more robust. In the situation where transfer matrix is numerically stable and easily accessible, an improved recursive algorithm is also given directly in terms of transfer submatrices without involving their explicit inverse. The above-presented improved algorithms can be extended to more complex materials including piezoelectric media.

[1] W. T. Thomson, "Transmission of elastic waves through a stratified solid medium," J. Appl. Phys. **21**, 89–93 (1950).
[2] N. A. Haskell, "The dispersion of surface waves on multilayered media," Bull. Seismol. Soc. Am. **43**, 17–34 (1953).
[3] J. W. Dunkin, "Computation of modal solutions in layered elastic media at high frequencies," Bull. Seismol. Soc. Am. **55**, 335–358 (1965).
[4] L. Knopoff, "A matrix method for elastic wave problems," Bull. Seismol. Soc. Am. **54**, 431–438 (1964).
[5] H. Schmidt and F. B. Jensen, "A full wave solution for propagation in multilayered viscoelastic media with application to Gaussian beam reflection at fluid-solid interfaces," J. Acoust. Soc. Am. **77**, 813–825 (1985).
[6] A. K. Mal, "Wave propagation in layered composite laminates under periodic surface loads," Wave Motion **10**, 257–266 (1988).
[7] B. L. N. Kennett, *Seismic Wave Propagation in Stratified Media* (Cambridge University Press, Cambridge, 1983).
[8] D. C. Booth and S. Crampin, "The anisotropic reflectivity technique: theory," Geophys. J. R. Astron. Soc. **72**, 755–766 (1983).
[9] G. J. Fryer and L. N. Frazer, "Seismic waves in a stratified anisotropic media," Geophys. J. R. Astron. Soc. **78**, 691–710 (1984).
[10] E. L. Tan, "A robust formulation of SAW Green's functions for arbitrarily thick multilayers at high frequencies," IEEE Trans. Ultrason. Ferroelectr. Freq. Control **49**, 929–936 (2002).
[11] E. L. Tan, "A concise and efficient scattering matrix formalism for stable analysis of elastic wave propagation in multilayered anisotropic solids," Ultrasonics **41**, 229–236 (2003).
[12] L. Wang and S. I. Rokhlin, "Stable reformulation of transfer matrix method for wave propagation in layered anisotropic media," Ultrasonics **39**, 413–424 (2001).
[13] S. I. Rokhlin and L. Wang, "Stable recursive algorithm for elastic wave propagation in layered anisotropic media: Stiffness matrix method," J. Acoust. Soc. Am. **112**, 822–834 (2002).
[14] L. Wang and S. I. Rokhlin, "A compliance/stiffness matrix formulation of general Green's function and effective permittivity for piezoelectric multilayers," IEEE Trans. Ultrason. Ferroelectr. Freq. Control **51**, 453–463 (2004).
[15] L. Wang and S. I. Rokhlin, "Modeling of wave propagation in layered piezoelectric media by a recursive asymptotic matrix method," IEEE Trans. Ultrason. Ferroelectr. Freq. Control **51**, 1060–1071 (2004).
[16] B. Honein, A. M. B. Braga, P. Barbone, and G. Herrmann, "Wave propagation in piezoelectric layered media with some applications," Proceedings of the Conference on Recent Advances in Active Control of Sound and Vibration, 1991, pp. 50–63.
[17] B. Hosten and M. Castaings, "Surface impedance matrices to model the propagation in multilayered media," Ultrasonics **41**, 501–507 (2003).
[18] B. Collet, "Recursive surface impedance matrix methods for ultrasonic wave propagation in piezoelectric multilayers," Ultrasonics **42**, 189–197 (2004).
[19] A. L. Shuvalov, O. Poncelet, and M. Deschamps, "General formalism for plane guided waves in transversely inhomogeneous anisotropic plates," Wave Motion **40**, 413–426 (2004).

Click production during breathing in a sperm whale (*Physeter macrocephalus*) (L)

Magnus Wahlberg
Department of Zoophysiology, Aarhus University, C. F. Møllers Alle Building 131, DK-8000 Aarhus C, Denmark

Alexandros Frantzis and Paraskevi Alexiadou
Pelagos Cetacean Research Institute, Terpsichoris 21, 16671 Vouliagmeni, Greece

Peter T. Madsen
Department of Zoophysiology, Aarhus University, C. F. Møllers Alle Building 131, DK-8000 Aarhus C, Denmark and Biology Department, Woods Hole Oceanographic Institution, Woods Hole, Massachusetts 02543

Bertel Møhl
Department of Zoophysiology, Aarhus University, C. F. Møllers Alle Building 131, DK-8000 Aarhus C, Denmark

(Received 4 August 2005; revised 16 September 2005; accepted 28 September 2005)

A sperm whale (*Physeter macrocephalus*) was observed at the surface with above- and underwater video and synchronized underwater sound recordings. During seven instances the whale ventilated its lungs while clicking. From this observation it is inferred that click production is achieved by pressurizing air in the right nasal passage, pneumatically disconnected from the lungs and the left nasal passage, and that air flows anterior through the phonic lips into the distal air sac. The capability of breathing and clicking at the same time is unique among studied odontocetes and relates to the extreme asymmetry of the sperm whale sound-producing forehead. © *2005 Acoustical Society of America.* [DOI: 10.1121/1.2126930]

PACS number(s): 43.80.Ka [WA] Pages: 3404–3407

I. INTRODUCTION

The sperm whale (*Physeter macrocephalus*), the largest of the toothed whales, emits click sounds for echolocation (Møhl *et al.*, 2003a) and communication (Weilgart and Whitehead, 1993). During deep foraging dives, they emit so-called usual clicks with properties suited for long-range echolocation of mesopelagic fish and squid (Madsen *et al.*, 2002a; Møhl *et al.*, 2003a). When closing on prey they switch to creaks (Miller *et al.*, 2004) consisting of clicks repeated with much shorter intervals of about 20 ms (Madsen *et al.*, 2002a). For communication, sperm whales produce so-called codas, which are repetitive patterns of clicks (Watkins and Schevill, 1977) and other clicklike reverberant sounds known as "slow clicks," most commonly or exclusively heard from male sperm whales (Madsen *et al.*, 2002a).

Even though recent work has expanded the knowledge on the click properties and acoustic behavior of sperm whales, we still lack detailed knowledge on the sound-production mechanism and abilities of this species. The particular problem studied here is in which manner air is used to drive the sound-production system.

The nasal complex of the sperm whale is nature's largest sound generator. It consists of a set of wax-filled cavities, the largest being the spermaceti organ (Raven and Gregory, 1933). Below the spermaceti organ is the junk, consisting of wax-filled cavities interspaced by connective tissue. Two nasal passages extend through the nose from the separated bony nares to the blow hole on the left side of the tip of the nose (Fig. 1). Two air sacs divert from the right nasal passage, one at the front (the distal sac) and one at the posterior end of the spermaceti organ (the frontal sac). The anterior portion of the right nasal passage is surrounded by two lips of connective tissue called the monkey lips (Pouchet and Beauregard, 1885). This is the site of the initial sound production event (Madsen *et al.*, 2003). From anatomical observations (Norris and Harvey, 1972) it has been surmised that this initial event is created by pressurized air flowing through the monkey lips while opening slightly during a short instant of time (Cranford, 1999). This hypothesis is consistent with results from numerical modeling (Dubrovsky *et al.*, 2004) and acoustic recordings (Wahlberg, 2002). According to Møhl *et al.*'s (2003a) bent-horn model only a tiny fraction of the sound energy of a usual click is leaking out of the animal anteriorly (the p0 pulse in Fig. 1). The majority of the energy is channelled rearwards into the spermaceti organ, reflected at the frontal air sac and exits the whale through the junk. This is the p1 pulse (Fig. 1). Some stray energy is re-reflected at the distal air sac, makes another round through the spermaceti organ, and is detected in far-field recordings as p2 (Fig. 1). This process is repeated and gives rise to subsequent pulses of decreasing amplitude but fixed intervals, giving the sperm whale click its unique multi-pulsed structure (Backus and Schevill, 1966; Møhl, 2001; Møhl *et al.*, 2003b; Norris and Harvey, 1972). The p1 pulse is the

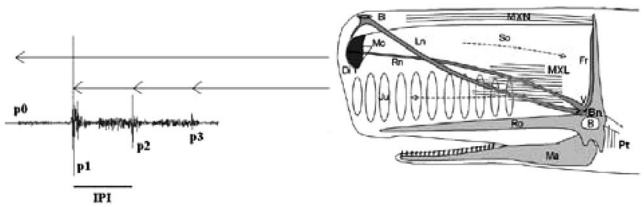

FIG. 1. Left: Sperm whale click, with the pulses labelled p0, p1, p2, p3. Right: The anatomy of the sperm whale head and suggested path of the p0 and p1 pulses. B=brain, Bn=bony naris, Bl=blowhole, Di=distal air sac, Fr=frontal air sac, Ju=junk, Ln=left naris, Ma=mandible, Mo=monkey muzzle, MXN=maxillo-nasalis muscle layer, MXL=maxillo-labialis muscle layer, Pt=pteropharynegel muscles, Rn=right naris, Ro=rostrum, So =spermaceti sac, and V=valve at the entrance of the bony naris. Modified after Madsen *et al.* (2002b) and Møhl *et al.* (2003a), with permission from the *Journal of Experimental Biology* and the *Journal of the Acoustical Society of America*.

most powerful transient sound produced in the animal kingdom and is at least as directional as dolphin clicks (Møhl *et al.*, 2003a; Zimmer *et al.*, 2005).

Even though the sound production system of the sperm whale is homologus to that of smaller toothed whales (Cranford *et al.*, 1996) there are some important differences in the anatomy and thereby possibly in the pneumatic operation of the two systems. In dolphins both pairs of monkey lips open dorsally into a set of of vestibular sacs connected to the blow hole for which reason the air for lung ventilation must pass through the sound generating structures (Dormer, 1979). This is different from the sperm whale, where only one set of monkey lips is found in conjunction with the right nasal passage. The left nasal passage bypasses the sound generator mechanism connecting the blow hole and the lungs (Fig. 1).

Previously, sperm whale sound production has been studied using anatomy (Norris and Harvey, 1972; Cranford *et al.*, 1996; Cranford and Amundin, 2004), hydrophones attached to a captive specimen (Madsen *et al.*, 2003), recordings of sound projected into recently dead specimens (Møhl, 2001; Møhl *et al.*, 2003b), hydrophones deployed from boats (Gordon, 1991; Goold, 1999; Møhl *et al.*, 2003a; Thode *et al.*, 2002; Zimmer *et al.*, 2003), and acoustic tags attached to the whale (Madsen *et al.*, 2002b; Zimmer *et al.*, 2005).

The data presented here complement the above-mentioned techniques through combined visual and acoustic observations of a clicking sperm whale close to the surface. The whale emitted series of rapid clicks similar to the creak-type vocalization described above. Usually such sounds are heard when the whale is at great depths (Miller *et al.*, 2004). However, we have also recorded rapid clicks when sperm whales explore nearby vessels. Here we combine visual and acoustical observations to study concomitant clicking and ventilation in a sperm whale and discuss the implications for air-driven sound production.

II. MATERIAL AND METHODS

Field work was made from a 16-m-long motor vessel as a part of the long-term "Greek Sperm Whale Program" of Pelagos Cetacean Research Institute (Frantzis *et al.*, 2003). Data were gathered on July 25 and August 3, 2000 off South-West Crete (Mediterranean Sea) during two encounters with a previously photo-identified sperm whale. The whale was a 9.7 m long male, length estimated from coda click interpulse intervals (Gordon, 1991) and sex determined through genetic analysis of sloughed skin. On July 25 the sperm whale was observed by a free-swimming diver using an underwater handheld mini-DV video camera (Sony DCR-TRV900E) with a digital stereo sound track, sampled with 12 bits at 32 kHz. The stereo microphone of the video camera was inside an Ikelite water-proof housing. Although the automatic gain control (AGC) is of unknown nature, analysis of the recorded noise indicated that its effect was negligible on the analysis presented here (assuming that any self-induced noise from the recording system would have been affected by the AGC). During the recordings the range between the diver and the whale was estimated to be 1–15 m and recordings were made in aspects to the whale ranging from approximately head-on to rearwards.

Simultaneous in-air filming was made from a distance of 10–30 m to the whale with a Sony Hi-8 hand-held video camera on the research vessel. The in-air video recordings were synchronized to underwater sound and video recordings to the closest video frame (1/25 of a second), i.e., with a resolution around 40 ms. This was possible through identifying the starting point of human vocalizations (diver) audible in both the in-air and underwater video. The acoustic travel time from the diver to the in-air video camera may have caused an additional delay in the in-air video recording of up to 100 ms relative to the underwater video recording. On August 3 the same individual sperm whale was recorded at a distance of 5–20 m from the vessel with the mini-DV video camera held above water. During this encounter sounds were recorded with a towed two-hydrohone array (Benthos AQ-4 elements, each with separate, 30 dB gain preamplifiers; frequency response: flat within 2 dB between 0.1 and 15 kHz) connected to a DAT recorder (Sony TCD-D8, 16 bits, 48 kHz sampling frequency). The array was left to sink into a nearly vertical orientation 100 m below the stern of the drifting vessel. The array recordings were synchronized to the in-air video recordings through connecting the signal from the array to the video camera a few minutes after the observations analyzed here were recorded. During this recording, the synchronization error was less than 110 ms, resulting from the video frame interval (40 ms) and the delay between the video and acoustic recordings (up to 70 ms) due to the travel time of sound from the whale to the array.

Twelve video sequences where the whale was close to the observer were selected for analysis. Sound and video recordings were digitally transferred to a computer. Clicks were extracted and their amplitude and interclick intervals were measured using Cool Edit Pro ver. 2 (Syntrillium, Inc.) and routines written with Matlab 6.2 (MathWorks, Inc.).

No other whales were observed by lookouts or detected acoustically. In addition to this, the correlation between the movements of the whale (e.g., reduction in click intensity as the whale emerged from the water with the nose; see below) made us confident that the whale we observed on the video was the same as the one we recorded with the hydrophone.

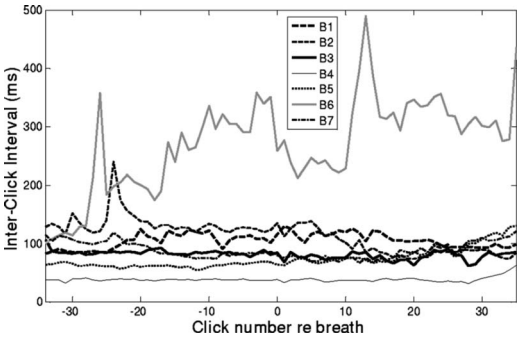

FIG. 2. Interclick intervals of clicks recorded right before until right after seven breaths (labelled B1–B7) made by a sperm whale. Breaths occur at the x value of 0 for each sequence.

III. RESULTS AND DISCUSSION

Instances of the whale ventilating were observed from the surface video recordings, shown by moist air being emitted from the blow hole. During seven such events the whale was clicking during lung ventilation. The few sudden excursions observed in the interclick intervals (ranging from 31 to 490 ms, Fig. 2) appeared to be independent of the breathing events. During ventilation of the lungs the blow hole is open and connects the left nasal passage and the lungs to the atmosphere (Raven and Gregory, 1933; Norris and Harvey, 1972; Schenkkan and Purves, 1973). There is no sphincter structure between the left nasal passage and the distal air sac (Fig. 3). Therefore it is not possible to build up pressure on the anterior side of the monkey lips while breathing. Air must be pressurized in the right nasal passage and flow anteriorly through the phonic lips into the frontal sac. This is consistent with the inferences made from anatomical observations by Norris and Harvey (1972) and analogous to the direction of airflow in other toothed whales (Cranford *et al.*, 1996).

Even though the sound generator system of sperm whales is homologous to that of other toothed whales (Cranford *et al.*, 1996) the observations made here indicate that the mechanism behind the air pressure build up for actuating the pneumatically driven sound generator might be quite different. In dolphins, click sound production is initiated by keeping the muscular sphincter around the epiglottal spout of the larynx closed and then pressurizing the bony nares by contraction of the palatopharyngeal and anteriorinternus muscles (Ridgway *et al.*, 1980; Cranford *et al.*, 1996). The pressurized air is metered past the two pairs of monkey lips [the right pair being homologous to the monkey lips of sperm whales (Cranford *et al.*, 1996)]. The internareal pressures in the two nasal passages rise and fall together during click production (Ridgway *et al.*, 1980; Amundin and Andersen, 1983). Thus the contracting palatopharyngeal and anteriorinternus muscles act on both nasal passages and dolphins are therefore not able to click and breathe simultaneously. However, sometimes during click production the two phonic lips can be actuated independently from each other (Cranford *et al.*, 2000), demonstrating some degree of separation in the control of sound production between the left and the right side.

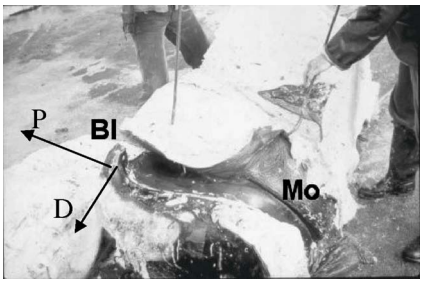

FIG. 3. Dissection of an adult male sperm whale showing the passage between the blowhole (Bl) and the monkey lips (Mo) through the distal air sac. P denotes posterior direction, D denotes dorsal direction.

The fact that the sperm whale can click and ventilate its lungs simultaneously shows that the right nasal passage can be pressurized independently of the left nasal passage which is connected to the lungs. This can either be achieved (1) if the open epiglottis inserts into the left bony naris during ventilation while the pterygopharyngeus muscle pressurizes the cavity beneath the bony nares and thereby the right nasal passage or (2) by closing the ventro-posterior entrance to the right naris disconnecting the right nasal passage from the ventilation pathway made up by the trachea, the open epiglottis, and the left nasal passage. The latter scenario is supported by the existence of a sphincter at the right bony naris (Raven and Gregory, 1933; Norris and Harvey, 1972; Schenkkan and Purves, 1973) The air pressure necessary for click production may in that case result from contracting the muscles below and above the right nasal passage [described in Schenkkan and Purves (1973) and Clark (1978)] throughout its course towards the monkey lips. The latter scenario will, however, be fundamentally different from the way air pressure for sound production is generated in other toothed whales (Ridgway *et al.*, 1980), whereby homologous structures would not serve homologous functions of actuating the sound generator among clicking toothed whales. These two conjectures remain to be tested.

When diving to great depths, the air available for sound production is seriously restricted (Madsen *et al.*, 2002b, Wahlberg, 2002). Recycling may be accomplished by opening the monkey lips and moving the air backwards into the right nasal passage through the action of the maxillonasalis and maxillolabialis muscles as well as additional muscles above and below the right nasal passage (Schenkkan and Purves, 1973; Clark, 1978; Madsen, 2002).

In the observations presented here, the peak-to-peak sound level of the clicks dropped with up to 28 dB when the whale partially raised its head out of the water surface (either to breathe or not), sometimes emerging the whole anterior area leading in to the junk. This is probably a minimum estimate, as the measurements were restricted by the low recording band width, dynamic range, and possibly also by the automatic gain control mechanism of the camera. These measurements are contradictory to Watkins and Daher's (2004) observation of a whale lifting its head completely out of the water without affecting the level nor the frequency content of the clicks.

In one of the surface video sequences analyzed here small drops of water jumped out from the emerged blowhole while the whale was clicking rapidly. This may be caused by

vibrations of the nose associated with sound production. Very powerful accelerations at the front of a sperm whale nose were observed by a diver in an earlier study (Norris and Møhl, 1983).

These observations were made on a single individual observed during two independent observations. *Ad libitum* observations that we made on another individual, unfortunately without recording it, indicates that breathing while clicking is not a unique behavior of the recorded individual, nor does it seems to be a rare phenomenon.

Future work will benefit from methods telling the distance and bearing to the whale, as well as from using a calibrated sound recording system sensitive in the entire frequency range of sperm whale vocalizations. With this information the sound production of sperm whales could be even further investigated, including variations in source level and frequency content with the direction to the whale. The synchronized observations of video and audio hold promise to contribute to the understanding of possible fine-scale changes in the nasal system during sound production not observable with other methods, e.g., to understand how the nose may become slightly deformed while producing different types of clicks.

ACKNOWLEDGMENTS

We wish to thank Olga Nikolaou, Varvara Kandia, and Giorgos Paximadis for their help in the field, Apostolos Armaganidis for providing some useful video shots, and all the ecovolunteers who supported the field work of Pelagos Cetacean Research Institute in 2000. We also thank Dan Engelhaupt for sex determination of sloughed skin samples from the sperm whale. MW was funded by the Carlsberg Foundation and the Pelagos Institute received support for instrumentation from Oracle corporation through a CAFAmerica grant. AF and PA wishes to thank Patroklos (the sperm whale) for its cooperation during the recordings.

Amundin, M., and Andersen, S. H. (**1983**). "Bony nares air pressure and nasal plug muscle activity during click production in the harbour porpoise, Phocoena phocoena, and the bottlenosed dolphin, Tursiops truncatus," J. Exp. Biol. **105**, 275–282.

Backus, R., and Schevill, W. E. (**1966**). "Physeter clicks," in *Whales, Porpoises and Dolphins*, edited by K. S. Norris (Univ. California, Berkeley, CA), pp. 510–528.

Clark, M. R. (**1978**). "Structure and proportions of the spermaceti organ in the sperm whale," J. Mar. Biol. Assoc. U.K. **58**, 1–17.

Cranford, T. W. (**1999**). "The sperm whale's nose: sexual selection on a grand scale?" Marine Mammal Sci. **15**(4), 1133–1157.

Cranford, T. W., and Amundin, M. (**2004**). "Biosonar pulse production in Odontocetes: The state of our knowledge," in *Echolocation in Bats and Dolphins*, edited by J. Thomas, C. F. Moss, and M. Vater (Univ. of Chigaco, IL), pp. 27–35.

Cranford, T. W., Amundin, M., and Norris, K. S. (**1996**). "Functional morphology and homology in the odontocete nasal complex: implications for sound generation," J. Morphol. **228**, 223–285.

Cranford, T. W., Elsberry, W. R., Blackwood, D. J., Carr, J. A., Kamolnick, T., Todd, M., Van Bonn, W. G., Carder, D. A., Ridgway, S. H., Bozlinski, D. M., and Decker, E. C. (**2000**). "Two independent sonar signal generators in the bottlenose dolphin: physiologic evidence and implications," J. Acoust. Soc. Am. **108**(5), 2613.

Dormer, K. J. (**1979**). "Mechanism of sound production and air recycling in dolphinids: Cineradiographic evidence," J. Acoust. Soc. Am. **65**(1), 229–239.

Dubrosky, N., Gladilin, A., Møhl, B., and Wahlberg, M. (**2004**). "Modelling of the dolphin's clicking sound source: the influence of the critical parameters," Acoust. Phys. **50**(4), 463–468.

Frantzis, A., Alexiadou, P., Paximadis, G., Politi, E., Gannier, A., and Corsini-Foka, M. (**2003**). "Current knowledge of the cetacean fauna of the Greek Seas," J. Cetacean Res. Manage. **5**(3), 219–232.

Goold, J. C. (**1999**). "Behavioural and acoustic observations of sperm whales in Scapa Flow, Orkney Islands," J. Mar. Biol. Assoc. U.K. **79**, 544–550.

Gordon, J. (**1991**). "Evaluation of a method for determining the length of sperm whales (Physeter catodon) from their vocalizations," J. Zool. **224**, 301–314.

Madsen, P. T. (**2002**). "Sperm whale sound production," Ph.D. thesis, Aarhus University.

Madsen, P. T., Wahlberg, M., and Møhl, B. (**2002a**). "Male sperm whale (Physeter macrocephalus) acoustics in a high-latitude habitat: implications for echolocation and communication," Behav. Ecol. Sociobiol. **53**, 32–41.

Madsen, P. T., Payne, R., Kristiansen, N. U., Wahlberg, M., Kerr, I., and Møhl, B. (**2002b**). "Sperm whale clicks: bimodal, pneumatic sound production at depth," J. Exp. Biol. **205**, 1899–1906.

Madsen, P. T., Carder, D. A., Au, W. W. L., Møhl, B., Nachtigall, P. E., and Ridgway, S. H. (**2003**). "Sound production in neonate sperm whales (L)," J. Acoust. Soc. Am. **113**(6), 2988–2991.

Miller, P. J. O., Johnson, M., and Tyack, P. L. (**2004**). "Sperm whale behaviour indicates the use of echolocation click buzzes 'creaks' in prey capture," Biol. Lett. **271**, 2239–2247.

Møhl, B. (**2001**). "Sound transmission in the nose of the sperm whale, *Physeter catodon*. A post mortem study," J. Comp. Physiol., A **187**, 335–340.

Møhl, B., Wahlberg, M., Madsen, P. T., Heerfordt, A., and Lund, A. (**2003a**). "The monopulsed nature of sperm whale clicks," J. Acoust. Soc. Am. **114**(2), 1143–1154.

Møhl, B., Madsen, P. T., Wahlberg, M., Au, W. W. L., Nachtigall, P. E., and Ridgway, S. H. (**2003b**). "Sound transmission in the spermaceti complex of a recently expired sperm whale calf," ARLO **4**(1), 19–24.

Norris, K. S., and Harvey, G. W. (1972). "A theory for the function of the spermaceti organ of the sperm whale," in *Animal Orientation and Navigation*, edited by S. R. Galler, NASA SP-262, pp. 393–417.

Norris, K. S., and Møhl, B. (**1983**). "Can odontocetes debilitate prey with sound?" Am. Nat. **122**, 85–104.

Pouchet, G., and Beauregard, H. (**1885**). "Note sur "l'Organe des Spermaceti"," C R. Seances Soc. Biol. Fil **2**(8), 342–344.

Raven, H. C., and Gregory, W. K. (**1933**). "The spermaceti organ and nasal passages of the sperm whale (*Physter catodon*) and other odontocetes," Am. Mus. Nov. **677**, 1–18.

Ridgway, S. H., Carder, D. A., Green, R. E., Gaunt, A. S., Gaunt, S. L. L., and Evans, W. E. (**1980**). "Electromyographic and pressure events in the nasolaryngeal system of dolphins during sound production," in *Animal Sonar Systems*, edited by R G. Busnel and J. F. Fish (Plenum, New York), pp. 239–249.

Schenkkan, E. J., and Purves, P. E. (**1973**). "The comparative anatomy of the nasal tract and the function of the spermaceti organ in the physeteridae (Mammalia, Odontoceti)," Bijdragen tot de dierkunde **43**(1), 93–112.

Thode, A., Mellinger, D. K., Stienessen, S., Martinez, A., and Mullin, K. (**2002**). "Depth-dependent acoustic features of diving sperm whales (*Physeter macrocephalus*) in the Gulf of Mexico," J. Acoust. Soc. Am. **112**(1), 308–321.

Wahlberg, M. (**2002**). "The acoustic behaviour of diving sperm whales observed with a hydrophone array," J. Exp. Mar. Biol. Ecol. **281**, 53–62.

Watkins, W. A., and Daher, M. A. (**2004**). "Variable spectra and nondirectional characteristics of clicks from near-surface sperm whales (*Physeter catodon*)," in *Echolocation in Bats and Dolphins*, edited by J. A. Thomas, C. F. Moss, and M. Vater (Chicago U. P., Chicago), pp. 410–413.

Watkins, W. A., and Schevill, W. E. (**1977**). "Spatial distribution of *Physeter catodon* (sperm whales) underwater," Deep-Sea Res. **24**, 693–699.

Weilgart, L. H., and Whitehead, H. (**1993**). "Coda communication by sperm whales (Physeter macrocephalus) off the Galàpagos Islands," Can. J. Zool. **71**, 744–752.

Zimmer, W. M. X., Johnson, M., D'Amico, A., and Tyack, P. L. (**2003**). "Combining data from a multisensor tag and passive sonar to determine the diving behaviour of a sperm whale (*Physeter macrocephalus*)," IEEE J. Ocean. Eng. **28**(1), 13–28.

Zimmer, W. M. X., Tyack, P. L., Johnson, M. P., and Madsen, P. T. (**2005**). "Three-dimensional beam pattern of regular sperm whale clicks confirms bent-horn hypothesis," J. Acoust. Soc. Am. **117**(3), Pt. 1, 1473–1485.

Time-domain calculation of acoustical wave propagation in discontinuous media using acoustical wave propagator with mapped pseudospectral method

Jing Lu[a)]
State Key Laboratory of Modern Acoustics and Institute of Acoustics, Nanjing University, Nanjing 210093, China

Jie Pan
Department of Mechanical and Materials Engineering, The University of Western Australia, Crawley WA 6009, Australia

Boling Xu
State Key Laboratory of Modern Acoustics and Institute of Acoustics, Nanjing University, Nanjing 210093, China

(Received 6 April 2005; revised 12 September 2005; accepted 16 September 2005)

The acoustical Wave Propagator (AWP) scheme involves an effective time-domain calculation of sound propagation using the combination of Chebyshev polynomial expansion and the Fourier pseudospectral method. The accuracy of this scheme degrades when the media has discontinuities due to the well-known Gibbs phenomenon. In this paper, several issues concerning AWP are addressed, including an analysis of the effect of Gibbs phenomenon on the accuracy. A mapped pseudospectral method is proposed wherein the grid points are redistributed, with the emphasis across the media discontinuities by a pre-determined smooth mapping curve, then the spatial derivatives are calculated through a modified Fourier pseudospectral method. Using this method, the influence of the Gibbs phenomenon is effectively alleviated while the computational efficiency of AWP is still maintained. The superiority of this improved AWP scheme is illustrated by three one-dimensional (1-D) numerical examples. © *2005 Acoustical Society of America.* [DOI: 10.1121/1.2114627]

PACS number(s): 43.20.Bi, 43.20.El [TDM] Pages: 3408–3419

I. INTRODUCTION

Over the last decade, the time-domain solution of acoustical wave propagation in inhomogeneous media, especially in media with discontinuities, has attracted attention of many researchers.[1–8] Most of the approaches[1–5] are based on the finite difference time-domain (FDTD) scheme due to its simplicity and versatility. Because the FDTD method has the disadvantage of the relatively large linear dispersion error that accumulates rapidly with time,[9] much higher grid density than that specified by the Nyquist limit (which is two nodes per minimum wavelength) is needed for an accurate result. The pseudospectral time-domain (PSTD) method[6] can achieve an exact spatial representation of wave equations with smoothly spatial-varying coefficients using the grid density of Nyquist limit, but they still use the conventional difference approaches (for example, Leap-frog method) to march the solution in time. Therefore, the dispersion error is still hard to be avoided and the overall accuracy is influenced strongly by the relatively poor approximation of the time derivative. The *k*-space method, which was first proposed by Bojarski[10,11] and newly developed in Refs. 7 and 8, uses a wave number–time space iteration scheme derived from the nonstandard finite difference model[12] to launch the time integration. It provides superior stability and accuracy over the normal FDTD and PSTD methods. The acoustical wave propagator (AWP)[13] scheme, which makes use of Chebyshev polynomial expansion, is another way to improve the time integration accuracy. Our first aim in this paper is to examine the accuracy of the AWP in the context of wave propagation in discontinuous media.

The idea of implementing Chebyshev polynomial expansion in calculating time integration was first proposed for solving the time-dependent Schrodinger equation.[14] In Ref. 15, this scheme was extended to solving linear, periodic, hyperbolic problems, then in Ref. 16 for seismic forward modeling. A rapid expansion method (REM) twice as efficient as that of Ref. 16 was proposed in Ref. 17, in which only even-order Chebyshev polynomials are needed. Recently, such a time integration strategy was also implemented in the electromagnetic field.[18,19] The AWP method[13] was introduced to investigate the time-domain evolution of acoustical waves. One of the merits of AWP is that the traditional boundary conditions for acoustical wave propagation are described in terms of the change of material or wave propagation properties of the media explicitly in the propagator matrix. Therefore, it forms a highly efficient calculation technique for research on the time-domain wave propagation in

[a)]Address for correspondence: Jing Lu, Institute of Acoustics, Nanjing University, Nanjing 210093, China. Telephone: 86-25-83593571; electronic mail: lujing@nju.edu.cn

inhomogeneous media and the advantages over the normal FDTD methods have been addressed in Refs. 13 and 20.

Unfortunately, for acoustical wave propagation in discontinuous media, the derivatives of the sound pressure and particle velocity are discontinuous across the media interfaces, giving rise to degradation of the accuracy of the pseudospectral method caused by Gibbs phenomenon.[21,22] A smooth technique is recommended in Ref. 13 to alleviate the problem caused by the discontinuities, and a similar technique is also used in Refs. 7 and 8, but we note that the physical nature of the interfaces at the media discontinuities is changed by such a smooth process. There is a postprocessing method[23] that increases the accuracy of the pseudospectral method when discontinuity exists through a Gegenbauer reconstruction procedure (GRP).[24,25] However, the computation burden of the method is quite heavy, and, more importantly, the choice of the reconstruction parameters is highly dependent on the specific features of the discontinuous function. Therefore this method is not suitable for the solution of the general time evolution problem.

A practical method to alleviate the influence of the Gibbs phenomenon on the accuracy of spatial derivative calculation is to increase the grid density of the whole computational domain, but this will greatly increase both the memory and the computation burden. Alternatively, a variable grid density pseudospectral method[6,26] has been proposed in which higher resolution is achieved across the interfaces of media discontinuities. By making use of the nonuniform fast Fourier transform (NUFFT) algorithm,[27,28] this method alleviates the influence of Gibbs phenomenon without high demands of the number of the grid points. However, the efficiency and the accuracy of the pseudospectral method will degrade due to the interpolation processes needed by NUFFT. A rather simplified and efficient technique of using a mapping method to obtain spatial derivatives appeared in Ref. 29 and 30 established a general procedure to construct mapping curves. A drawback of the procedure is found in the choice of initial grid points, although some rules in deciding the positions of grid points were proposed.

As the second aim of this paper, we launch the mapping method by designing the mapping curve directly and circumvent the difficulty of the choice of initial grid points. Using the pseudospectral method with a proper mapping curve, the mapped pseudospectral method is established and the spatial derivatives can be obtained efficiently through projecting the uniformly spaced grid points onto the nonuniform shape that concentrates more across the media interfaces. Combining the mapped pseudospectral method with Chebyshev polynomial expansion time integration method, an improved AWP scheme is obtained resulting in a more accurate solution for acoustical wave propagation in discontinuous media.

It should be noted that there are some limitations of the scheme proposed in this paper when it is extended to multidimensional applications. First of all, unlike the PSTD method[6] and the *k*-space method,[7,8] the form of AWP scheme makes it not easy to include currently the most successful absorbing boundary condition, the Perfectly Matched Layer (PML), which was originated from Ref. 31 and developed by many researchers thereafter. On the other hand, although the extension of AWP to multidimensional applications is straightforward,[32] many different mapping curves are needed when there are scattering objects with arbitrary shapes in the computation area. This will lead to the increase of the computation and storage burden. In the recent development of the multidomain PSTD method,[33,34] the computational domain is divided into several subdomains, conforming to the problem geometry in order to accurately model curved objects, and the solutions across subdomains are reconciled by using patching conditions derived in accordance with the physics of the problem to determine the global solution. Such an idea might also be useful to the extension of the scheme proposed in this paper. The detailed analysis concerning these problems is still ongoing and will be given in another paper.

The outline of the paper is as follows. In Sec. I, a brief review of AWP is given and some issues concerning this scheme are addressed. In Sec. III we analyze the influence of the discontinuous coefficients in the Euler's field equations on the accuracy of the pseudospectral method. Also, the idea of mapped pseudospectral method and the design of the mapping curves are described in Sec. III. In Sec. IV we show the superiority of the improved AWP method using some numerical examples. Conclusions are drawn in Sec. V.

II. SOME COMMENTS ON AWP

A. The validity of the Chebyshev polynomial expansion

Defining

$$\Phi(x,t)=\begin{bmatrix} p(x,t) \\ v(x,t) \end{bmatrix}, \quad \hat{\mathbf{H}}=\begin{bmatrix} 0 & \rho c^2 \dfrac{\partial}{\partial x} \\ \dfrac{1}{\rho}\dfrac{\partial}{\partial x} & 0 \end{bmatrix},$$

in which p and v are the sound pressure and the particle velocity respectively, the one-dimensional acoustical wave propagation is described as

$$\frac{\partial}{\partial t}\Phi(x,t)=-\hat{\mathbf{H}}\Phi(x,t). \tag{1}$$

The solution of Eq. (1) is

$$\Phi(x,t)=e^{-(t-t_0)\hat{\mathbf{H}}}\Phi(x,t_0). \tag{2}$$

If an N-grid-point Fourier pseudospectral method is applied to calculate the spatial derivatives in the domain $x_1 \leqslant x \leqslant x_2$, and $x_2-x_1=L$, the spatial derivative operator $\hat{\mathbf{H}}$ can be expressed in a discrete form as

$$\hat{\mathbf{H}}_N=\begin{bmatrix} 0 & \rho c^2 D_N \\ \dfrac{1}{\rho}D_N & 0 \end{bmatrix}, \tag{3}$$

where D_N is the Fourier differentiation matrix with N grid points, as described in Ref. 15 and Ref. 22,

$$(D_N)_{jk} = \begin{cases} \dfrac{\pi}{L}(-1)^{j+k}\cot\left(\dfrac{(j-k)}{2}\dfrac{L}{N}\right), & j \neq k \\ 0, & j = k \end{cases}, \tag{4}$$

where $(j,k)=1,2,\ldots,N$. When N is even (actually N must be even for the implementation of FFT in calculating the spatial derivatives), D_N is a normal skew-symmetric matrix with purely imaginary eigenvalues of $2\pi i/L\{-N/2+1, -N/2+2,-1,0,1,\ldots,N/2-1\}$ among which 0 is a 2-fold degenerate eigenvalue.[22] It can be deduced that the eigenvalues of $\hat{\mathbf{H}}_N$ are

$$\lambda = \frac{2\pi c i}{L}\{-N/2+1,-N/2+2,\ldots,-1,0,1,\ldots,N/2 - 2,N/2-1\}, \tag{5}$$

among which 0 is a 4-fold degenerate eigenvalue while all the other eigenvalues are 2-fold degenerate. Therefore the maximum eigenvalue is obtained as

$$|\lambda|_{\max} = \frac{2\pi c}{L}(N/2-1) = \frac{\pi c}{\Delta x} - \frac{2\pi c}{L} \approx \frac{\pi c}{\Delta x}, \tag{6}$$

for sufficiently large N.

Defining a diagonal matrix as

$$B = \begin{bmatrix} \dfrac{1}{c\sqrt{\rho}} I_N & 0 \\ 0 & \sqrt{\rho} I_N \end{bmatrix},$$

where I_N represents a $N\times N$ identity matrix, it is easy to find that $\hat{\mathbf{H}}_N$ can be obtained by a similarity transformation as

$$\hat{\mathbf{H}}_N = B^{-1}\mathbf{H}_N B, \tag{7}$$

where B^{-1} represents the inverse of matrix B, and $\mathbf{H}_N = \begin{bmatrix} 0 & cD_N \\ cD_N & 0 \end{bmatrix}$ is a normal symmetric matrix that possesses the eigenvalues of (5) and a complete orthonormal set of eigenvectors[35] denoted as $\{X_k\}(k=1,2,\ldots,2N)$.

The operator $e^{-(t-t_0)\hat{\mathbf{H}}}$ can be transformed as

$$e^{-(t-t_0)\hat{\mathbf{H}}_N} = e^{R\hat{\mathbf{H}}'_N} = B^{-1}e^{R\mathbf{H}'_N}B, \tag{8}$$

where $R=-(t-t_0)|\lambda|_{\max}$, $\hat{\mathbf{H}}'_N=\hat{\mathbf{H}}_N/|\lambda|_{\max}$, and $\mathbf{H}'_N = \mathbf{H}_N/|\lambda|_{\max}$. Note that $\mathbf{H}'_N$ is also a normal matrix containing eigenvalues $\lambda'=\lambda/|\lambda|_{\max}$ and eigenvectors $\{X_k\}(k=1,2,\ldots,2N)$, the multiplication of B and the initial vector of $\Phi_N(x,t_0)$ can be expressed as $B\Phi_N(x,t_0)=\sum_{k=1}^{2N}h_kX_k$; therefore from Eqs. (2) and (8), we obtain

$$\Phi_N(x,t) = B^{-1}\sum_{k=1}^{2N} h_k e^{R\lambda'_k}X_k, \tag{9}$$

where λ'_k denotes the eigenvalue corresponding to the eigenvector X_k.

For an M-order polynomial approximation of an exponential function, denoted as

$$e^{\xi} \approx G(\xi) = \sum_{j=0}^{M} g_j\xi^j, \tag{10}$$

imposing a matrix form argument of $\xi=R\hat{\mathbf{H}}'_N$, the state vector of the wave propagation is expressed as

$$\begin{aligned}\tilde{\Phi}(x,t) &= G(R\hat{\mathbf{H}}'_N)\Phi_N(x,t_0) = \sum_{j=0}^{M} g_j(R\hat{\mathbf{H}}'_N)^j\Phi_N(x,t_0) \\ &= B^{-1}\left(\sum_{j=0}^{M} g_j(R\mathbf{H}'_N)^j\right)B\Phi_N(x,t_0) \\ &= B^{-1}\sum_{k=1}^{2N} h_k\left(\sum_{j=0}^{M} g_j(R\lambda'_k)^j\right)X_k \\ &= B^{-1}\sum_{k=1}^{2N} h_k G(R\lambda'_k)X_k. \end{aligned} \tag{11}$$

The estimation error is defined as

$$\begin{aligned} E_N &= \|\Phi(x,t) - \tilde{\Phi}(x,t)\|^2 \\ &= \left\| B^{-1}\sum_{k=1}^{2N} h_k[e^{R\lambda'_k} - G(R\lambda'_k)]X_k \right\|^2. \end{aligned} \tag{12}$$

Note that B^{-1} is a diagonal matrix and $\|X_k\|=1$. Using Schwarz's inequality yields

$$E_N \leqslant \|W_{B^{-1}}\|^2\left\|\sum_{k=1}^{2N}\alpha_k X_k\right\|^2 \leqslant 2N\|W_{B^{-1}}\|^2\sum_{k=1}^{2N}|\alpha_k|^2, \tag{13}$$

where $W_{B^{-1}}$ is the vector composed of the diagonal elements of B^{-1} and $\alpha_k=h_k[e^{R\lambda'_k}-G(R\lambda'_k)]$. Equation (13) means that the upper bound of the error depends on the scalar polynomial approximation of $e^{R\lambda'_k}$.

It has been found that Chebyshev polynomial expansion is a near-optimal approximation to a function with argument defined in $[-1,1]$,[36] and it is a much better expansion than the Taylor expansion,[21] which is approximated to give several conventional finite difference methods.[37] We regard $e^{R\lambda'_k}$ as a function with respect to the argument $i\lambda'_k$, which is in $[-1,1]$, then for a polynomial estimation with fixed order M the Chebyshev polynomial expansion method will result in a near-minimized estimation error for every term on the right-hand side of Eq. (13). This explains that the high accuracy of the AWP scheme is largely due to the selection of the Chebyshev polynomial expansion method to launch the time integration operation. It should be noted that when the acoustical parameters ρ and c are not constant in the computation domain, the estimation error of the wave propagation calculation result is not restricted by some scalar polynomial approximations, as depicted in Eq. (13). However, from our numerical calculation experiences concerning AWP, as long as the operator $\hat{\mathbf{H}}_N$ does not show any extreme ill-condition property, by a moderate regulation of the time step, the AWP method is still superior over other conventional finite difference approaches.

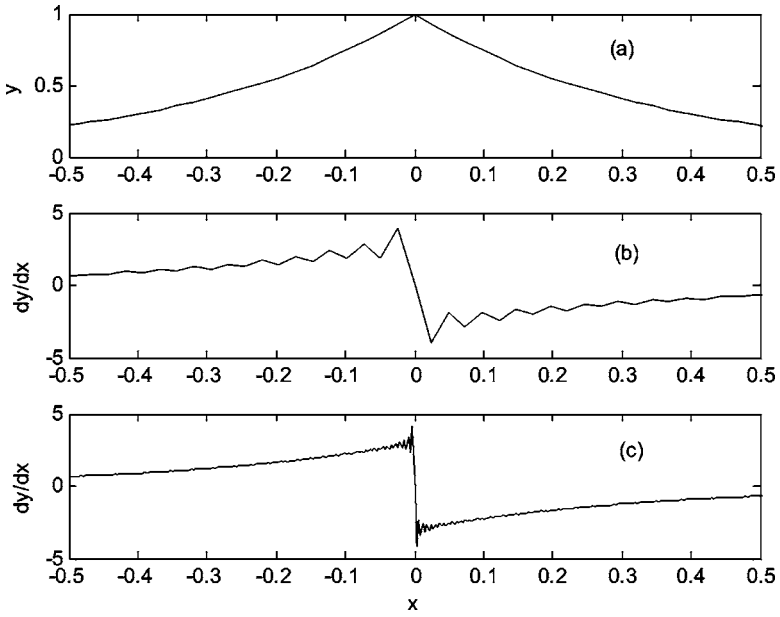

FIG. 1. Calculation of the first derivative of a C^0 function using a Fourier pseudospectral method with (a) the original function, (b) the calculation with 256 grid points, and (c) the calculation with 2048 grid points.

B. Different realizations of the Chebyshev polynomial expansion

The Chebyshev polynomial expansion of the acoustical wave propagator $e^{-(t-t_0)\hat{\mathbf{H}}}$ can be realized in two forms: one is

$$e^{-(t-t_0)\hat{\mathbf{H}}} = \sum_{k=0}^{\infty} \alpha_k(R) T_k(\hat{\mathbf{H}}'), \tag{14}$$

where $\alpha_k(R)=2I_k(R)$, except for $\alpha_0(R)=I_0(R)$ with $I_k(\cdot)$ representing the kth-order modified Bessel function of the first kind, and $T_k(\cdot)$ stands for the Chebyshev polynomials. (Note that all the above notations are similar to those in Ref. 13 with two modifications. First is the definition of R, without the minus notation; the wave propagation direction calculated by AWP will be opposite to the theoretical result. Second, the system operator should be normalized by $|\lambda|_{\max}$ instead of $\sqrt{\lambda_{\max}}$, as demonstrated in Sec. II A)

The alternative realization form to (14) is

$$e^{-(t-t_0)\hat{\mathbf{H}}} = \sum_{k=0}^{\infty} \beta_k(R) Q_k(\hat{\mathbf{H}}'), \tag{15}$$

where $\beta_k(R)=2J_k(R)$, except for $\beta_0(R)=J_0(R)$, with $J_k(\cdot)$ representing the kth-order Bessel function of the first kind, and $Q_k(\cdot)$ stands for the modified Chebyshev polynomials with $Q_0(\hat{\mathbf{H}}')=\mathbf{I}$, $Q_1(\hat{\mathbf{H}}')=\hat{\mathbf{H}}'$, and $Q_{k+1}(\hat{\mathbf{H}}')=2\hat{\mathbf{H}}'Q_k(\hat{\mathbf{H}}')+Q_{k-1}(\hat{\mathbf{H}}')$.

Reference 38 gives comparisons between these two expansion forms and demonstrates that (15) is recommended for the sake of numerical stability. Another interesting form of Chebyshev expansion method was proposed in Ref. 17, which is equivalent in efficiency to (15) unless the medium density ρ is constant.

III. THE MAPPED PSEUDOSPECTRAL METHOD

A. The influence of discontinuous coefficients on the pseudospectral methods

The pseudospectral methods have been developed since the 1970s[39] using trigonometric functions or Chebyshev polynomials to evaluate spatial derivatives. In an AWP scheme, the Fourier pseudospectral method is used to calculate the spatial derivative,

$$\frac{\partial^q}{\partial x^q}\Phi(x,t_0) = F^{-1}\{(ik)^q F[\Phi(x,t_0)]\}, \tag{16}$$

where $F[\cdot]$ and $F^{-1}[\cdot]$ represent the Fourier and inverse Fourier transforms, respectively, k is the wave number, and q denotes the order of the derivative.

The basic idea of the Fourier pseodospectral method is to estimate the spatial derivatives in the spectral transform domain on the grid (collocation) points, then approach the real value of the derivatives by inverse transform. Its superiority over the conventional difference methods has been well addressed in many references and books.[21,22,39] The accuracy of this method depends largely on the smoothness of the function with which we deal. Specifically, in the time domain calculation of acoustical wave propagation, the spatial smoothness of the sound pressure p and the particle velocity v dramatically influence the accuracy of our solution. For one-dimensional wave propagation in media with discontinuous acoustical parameters ρ and c, the derivatives of p and v are not continuous (or in mathematical notation as described as Ref. 3, p and c are in C^0) across the media interfaces. Reference 22 analyzed the relation between the function smoothness and the accuracy of the pseudospectral method and indicated that for a C^0 function, the error of the derivative calculated by the pseudospectral method will be $O(N^{q-1})$. This can be clarified by a simple example. Take a function as $y=e^{-3|x|}(-\pi<x\leqslant\pi)$; it can be easily seen that this function is in C^0 at the position of $x=0$. The original

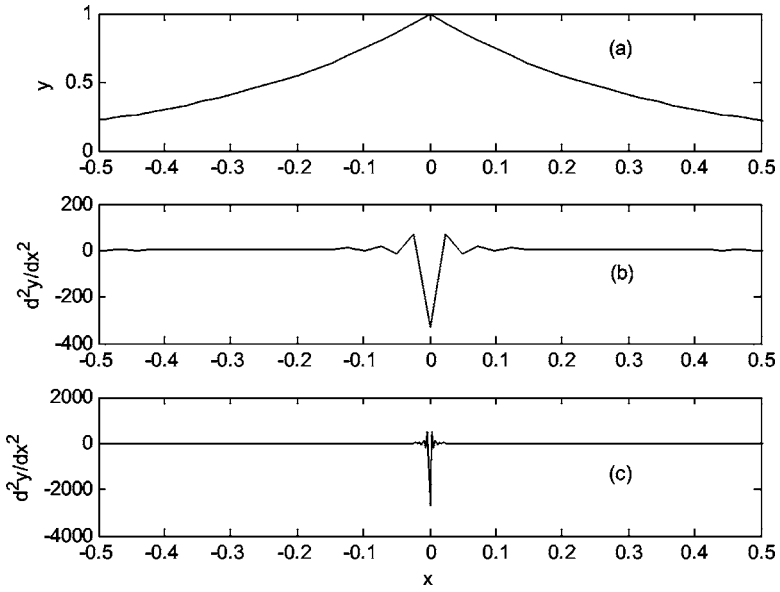

FIG. 2. Calculation of the second derivative of a C^0 function using a Fourier pseudospectral method with (a) the original function, (b) the calculation with 256 grid points, and (c) the calculation with 2048 grid points.

function and the first derivative calculated with 256 grid points and 2048 grid points are depicted in Fig. 1. Although with the increase of grid points the spurious vibration of dy/dt at positions around $x=0$ can be attenuated, the overshoot at the position of $x=0$ remains at the same level. This is consistent with the conclusion that the error of the first derivative is $O(1)$. Due to the fact that the first derivative of a C^0 is discontinuous, we attribute this to the Gibbs phenomenon, in spite of a little concept difference.

Figure 2 shows the calculation result of the second derivative. Obviously the error at the position of $x=0$ calculated with 2048 grid points is about ten times the value calculated with 256 grid points. This illustrates that the error of the second derivative is $O(N)$. With the increase of the grid density, the error of the high derivatives calculated by the pseudospectral method, especially at the positions across the interfaces, increases drastically. This is quite disadvantageous for the implementation of the pseudospectral method in the AWP scheme when dealing with acoustical wave propagation in discontinuous media, and the time step should be restricted to guarantee stability.

The calculation error of the spatial derivatives can be inspected from another viewpoint. It is inferred from Ref. 22 that for the C^0 function $\Phi(x,t_0)$, the error of the spectrum estimation by N-point FFT is $O(h^2)$, where h denotes the grids interval, e.g., $h=L/N$. Thus we describe the error in the wave number space as

$$E[\tilde{\Phi}(k,t_0)] = \varsigma(k)h^2, \tag{17}$$

where $\tilde{\Phi}(k,t_0)$ represents the function in the spectral transform domain and $\varsigma(k)$ is a bounded function. Since in the Fourier pseudospectral method, the estimation of the spectrum of the qth spatial derivatives is written as

$$\tilde{\Phi}^q(k,t_0) = (jk)^q\tilde{\Phi}(k,t_0), \tag{18}$$

the error of the spectrum estimation of the qth spatial derivatives becomes

$$E[\tilde{\Phi}^q(k,t_0)] = \varsigma(k)k^q\left(\frac{L}{N}\right)^2. \tag{19}$$

It can be seen from Sec. II B that the Chebyshev polynomial expansion method is actually a weighed summation of a series of spatial derivatives. Equation (19) suggests that increasing the grid points will effectively reduce the errors of spatial derivatives for low wave number components. For time domain acoustical wave propagation calculation, the energy of the commonly used Gaussian wave packet concentrates in the low wave number components. Therefore, the accuracy of the AWP scheme will be improved with the increase of the grid density. It should be noted that for high wave number components as $k\rightarrow N/2$, from (19) we can see that the error of the spectrum estimation is $O(N^{q-2})$, and due to the N summation operations included in the inverse FFT process, the error of the estimation of the derivatives in spatial domain is $O(N^{q-1})$. This is consistent with the statements concerning Figs. 1 and 2. Although increasing the number of grid points can directly improve the accuracy of AWP, the computation and storage burden will increase drastically. We then propose a rather efficient mapping technique to deal with the problem.

B. Mapping technique and mapping curve design

The basic idea of the mapping technique in the pseudospectral method is to project the uniform spaced grid points onto a nonuniform shape with higher grid density across the media interfaces, and retrieve the spatial derivatives at the nonuniform collocation points through a minor modification of the normal pseudospectral method. If the uniform series of collocation points $\{u_k\}k=1,2,\ldots,N$ are mapped into a series of nonuniform grids $\{x_k\}k=1,2,\ldots,N$, the spatial derivatives of the initial value function $\Phi(x,t_0)$ is obtained by the chain rule as

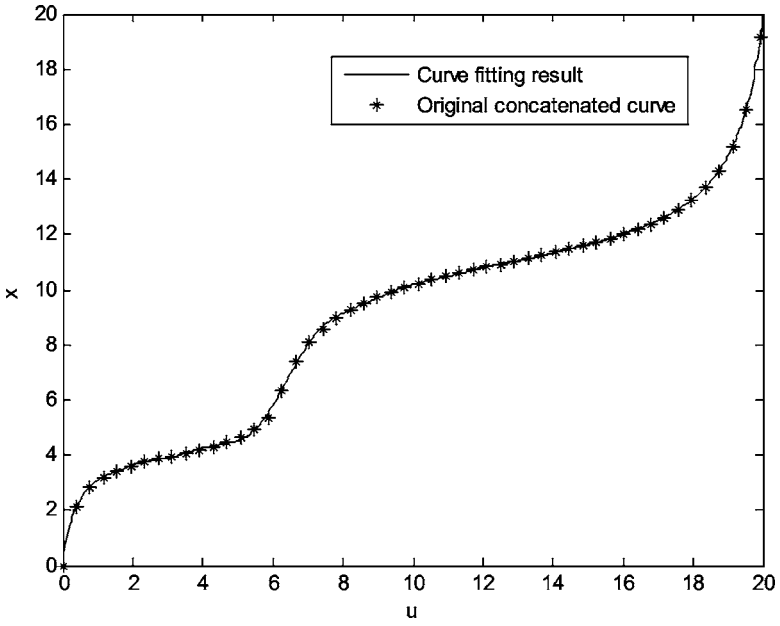

FIG. 3. An example of the mapping curve design. (Note that for clarity, not all the points on the original concatenated curve are shown.)

$$\left.\frac{d\Phi(x,t_0)}{dx}\right|_{x=x_k} = \left(\left.\frac{du}{dx}\right|_{x=x_k}\right)\left(\left.\frac{d\Phi'(u,t_0)}{du}\right|_{u=u_k}\right), \quad (20)$$

where $\Phi'(u,t_0)$ denotes the initial value function formed by the mapping process. The term in the first bracket on the right-hand side of (20) needs to be calculated only once for the whole AWP scheme and the second term can be calculated by the normal pseudospectral method.

There is a review of different mapping functions in Ref. 21, but most of them have only one concentration region, which means that only solutions with one media interface can be achieved successfully. An arbitrary mapping curve construction way was proposed in Ref. 30, but it demands a proper choice of the nonuniform initial collocation points. In this paper, we propose a simple procedure of designing the mapping curve, which can project the uniform grid points properly onto a series of nonuniform grid points that provide higher resolution across the media interfaces.

First of all, for a computation domain with only one media interface, the mapping curves reviewed in Ref. 21 can be implemented directly. For the computation domain of $[-1,1]$, the following is one example that was first proposed in Ref. 29.

$$x = \alpha_2 + \tan[(u-\beta)\gamma]/\alpha_1, \quad (21)$$

where

$$\beta = \frac{\kappa-1}{\kappa+1}, \quad \kappa = \tan^{-1}[\alpha_1(1+\alpha_2)]/\tan^{-1}[\alpha_1(1-\alpha_2)],$$

and $\gamma=\tan^{-1}[\alpha_1(1-\alpha_2)]/(1-\beta)$. Among all the parameters, α_2 is the location of the interface and α_1 determines the width of the concentration area. The other parameters are used so that (21) maps the computation domain on itself. For an arbitrary computation domain $[s_1,s_2]$, the mapping curve of (21) is extended by the scale and shift techniques as follows;

$$x = \frac{s_2-s_1}{2}\left\{\alpha_2 + \tan\left[\left(\frac{2u-(s_1+s_2)}{s_2-s_1}-\beta\right)\gamma\right]/\alpha_1\right\} + \frac{s_1+s_2}{2}. \quad (22)$$

Note that in (22), $\alpha_2=[2s-(s_1+s_2)]/(s_2-s_1)$, where s is the actual position of the media interface in $[s_1,s_2]$. If the media interface is at the center of the computation domain of $[-1,1]$, a much simpler mapping curve is proposed in Ref. 40,

$$x = (1-\eta)u^3 + \eta u, \quad (23)$$

where η controls the width of the concentration area. Also, for the computation domain of $[s_1,s_2]$, (23) is expanded as

$$x = \frac{s_2-s_1}{2}\left[(1-\eta)\left(\frac{2u-(s_1+s_2)}{s_2-s_1}\right)^3 + \eta\frac{2u-(s_1+s_2)}{s_2-s_1}\right] + \frac{s_1+s_2}{2}. \quad (24)$$

For computation domain with two or more media interfaces, the mapping curve can be constructed by the concatenation of two or several mapping curves with one concentration area such as (22) and (24). But such a direct concatenation will result in a C^0 function. Note that Eq. (20) implies that the mapping curve must correspond to at least a C^1 smooth function so that du/dx is continuous, otherwise additional Gibbs phenomenon will be introduced. Therefore it is necessary to postprocess the concatenation result using some curve fitting techniques. A normal least-squares polynomial function curve-fitting technique can give quite a satisfactory performance. For example, two media interfaces are set in the computation domain [0,20] at the positions of $x=4$ and $x=11$, and the number of the total grid points is 512. The computation domain can be divided into two subdomains, [0,6.2] and [6.2,20]. After applying mapping function (22) to each subdomain with $\alpha_1=5$, a 30-order polynomial

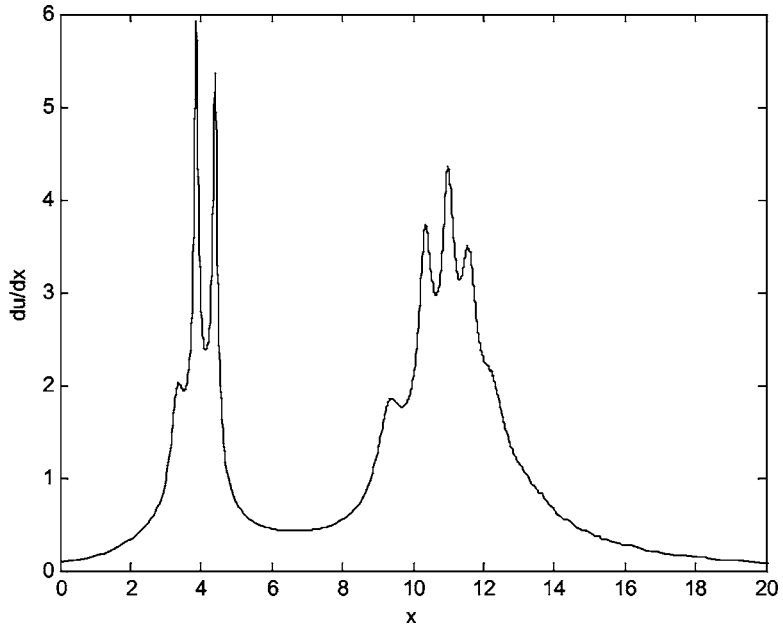

FIG. 4. $du/dx|_{x=x_i}$ of the mapping curve depicted in Fig. (3) at every collocation point.

function is used to fit the concatenation of the two mapping curves, as depicted in Fig. 3. It can be found that the effective curve fitting can be achieved with a polynomial function of sufficiently high order. It should be pointed out that the order of the polynomial function should be well limited in order to avoid the well-known Runge phenomenon[21] in polynomial curve fitting. Figure 4 shows the derivatives of $du/dx|_{x=x_i}$ at every collocation point, and it demonstrates that the non-uniform grids do have higher density across the media interfaces.

Another mapping curve design method of the above example is to divide the computation domain into three subdomains [0,8], [8,14], and [14,20]. Then apply the mapping function (24) to the first and the second subdomain and leave alone the third subdomain, i.e., $x=u$ for the third subdomain. The concatenation of the curves and a 15-order polynomial mapping curve are illustrated in Fig. 5. Figure 6 shows the derivatives of $du/dx|_{x=x_i}$ at every collocation point. The validity of the mapping curve is also demonstrated. Note that in Fig. 6, the derivative in the subdomain[14,20] is no longer a constant and varies around 1. This is caused by the polynomial curve-fitting procedure.

For the above mapping curve design procedures, we should rely on the features of the computation domain and the positions of the interfaces to determine which one should be used. A practical rule of choosing how to separate the computation domain into subdomains is to guarantee the first-order derivatives of the concatenated mapping curves meet as close as possible at the joint points, therefore making it easy for the curve-fitting process. This is why we choose 6.2 as the joint point for Figs. 3 and 4 and (8,14) as the joint points for Figs. 5 and 6. Although high resolution is needed across the interfaces, the residual grid points in the other areas should be kept rich enough to guarantee a sufficient

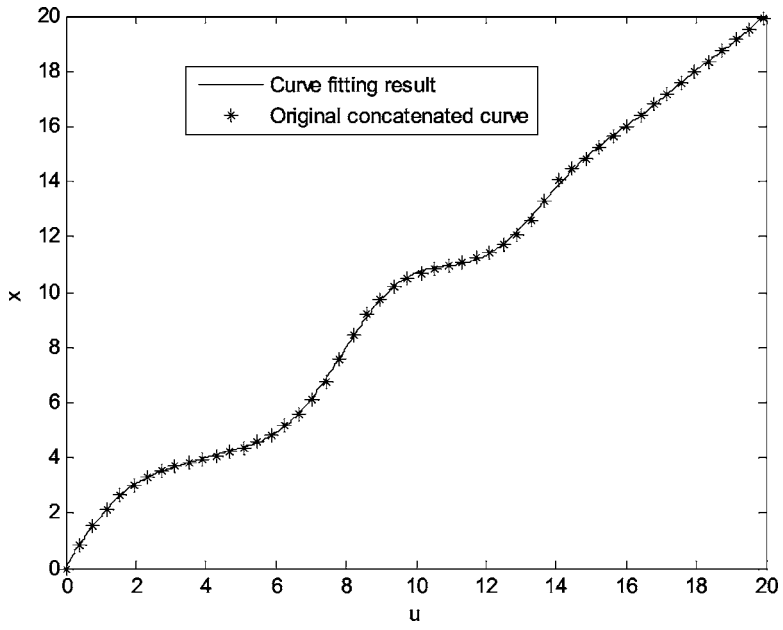

FIG. 5. Another example of the mapping curve design. (Note that for clarity, not all the points on the original concatenated curve are shown.)

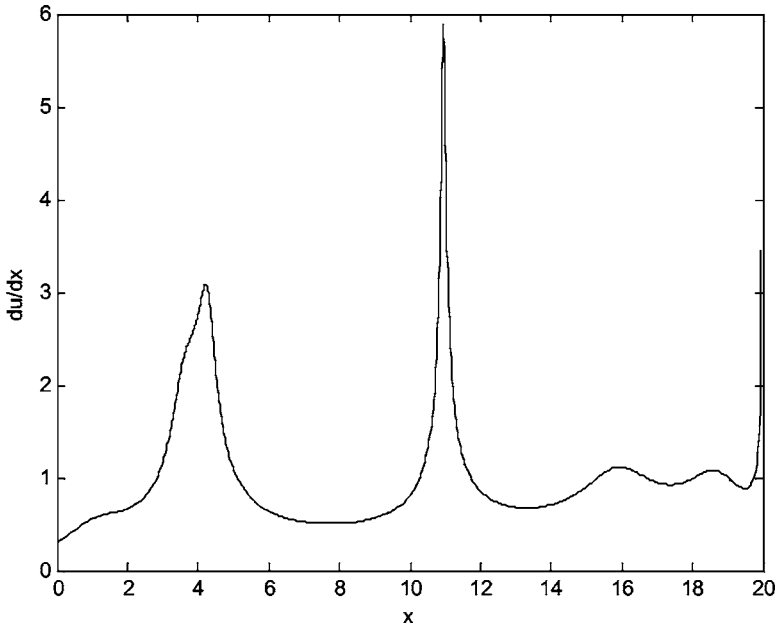

FIG. 6. $du/dx|_{x=x_i}$ of the mapping curve depicted in Fig. (5) at every collocation point.

description of the initial wave packet. It should be noted that the curve-fitting process and the calculation of du/dx at every collocation point are finished before the wave evolution calculation. Therefore the computation burden will not be affected by the mapping curve design procedure.

IV. ILLUSTRATING EXAMPLES

A. Reflection and transmission at a single interface

The computation domain is $[0\ \text{m}, 20\ \text{m}]$ and the media interface is set at $x=14$ m. The density of air is $\rho_0=1.21\ \text{kg/m}^3$ and the sound velocity in the air is $c_0=344$ m/s. The parameters of the medium on the left side of the interface are set as $\rho_1=\rho_0$ and $c_1=c_0$ while those on the right side are set as $\rho_2=1.5\rho_0$ and $c_2=3c_0$. The initial wave packet is a Gaussian wave packet centered at $x=7$ m, i.e., $p(x,0)=e^{-16(x-7)^2}$ and $v(x,0)=p(x,0)/\rho_1 c_1$. The number of the total grid points is 1024. The mapping curve function of (22) with $\alpha_1=5$ is used in this example. Figure 7 shows the initial sound pressure wave packet and the snapshot of the time domain waveform at $t=0.025$ s by the AWP scheme and the AWP scheme with a mapped pseudospectral method (named the mapped AWP hereafter), respectively. After extracting the reflected wave and the transmitted wave from the snapshot at $t=0.025$ s, the reflection coefficient $R(f)$ and the transmission coefficient $T(f)$ can be calculated, as depicted in Fig. 8. Note that the frequency for the reflection and transmission coefficients only covers the range in which the initial wave has sufficient energy content.

The reflection coefficient and the transmission coefficient are calculated in the following way. First, the dominant part of the initial Gaussian wave packet is guaranteed to be on the left side of the interface, which means that the value of the initial wave packet on the right side of the interface is near machine zero. Note that the frequency f is related to the wave number through $f=kc/2\pi$, then the amplitude of the

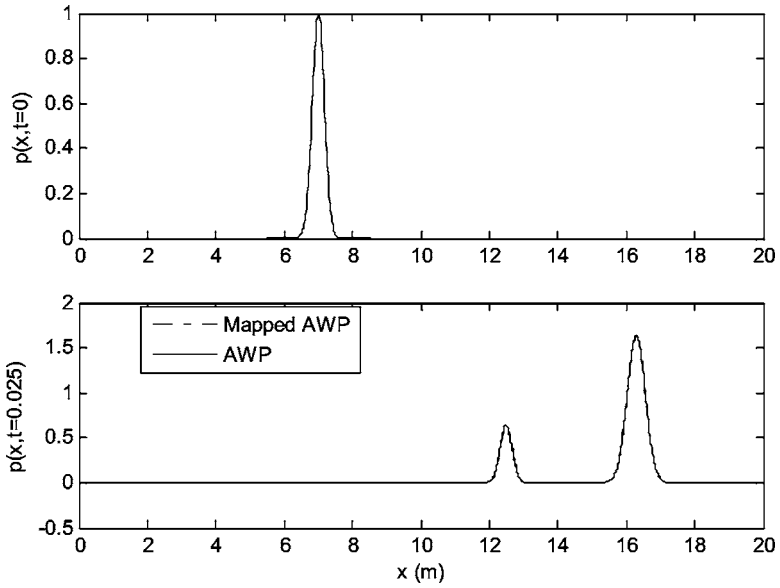

FIG. 7. The initial wave packet and the wave form at $t=0.025$ s calculated by the AWP and the mapped AWP scheme, respectively.

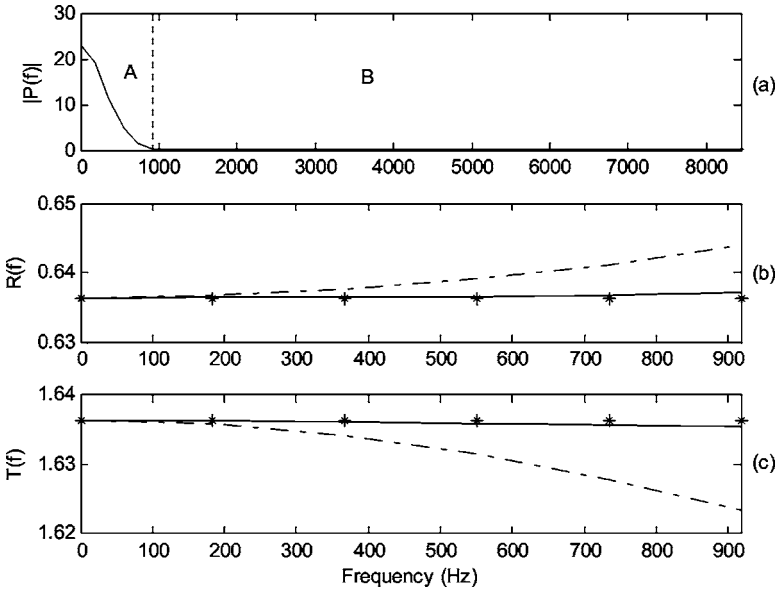

FIG. 8. (a) The energy distribution of the initial sound pressure in the frequency domain; (b) the reflection coefficient calculated by the AWP (dashed line) and the mapped AWP (solid line) within region A of (a); * stands for the theoretical result; (c) the transmission coefficient calculated by AWP (dashed line) and mapped AWP (solid line) within region A of (a); * stands for the theoretical result.

initial sound pressure at a specific frequency $Pi(f)$ can be calculated by Fourier transform. After the wave packet evolves for a sufficiently long time (which is 0.025 s in this example), extract the reflected wave packet and the transmitted wave packet, and the amplitudes of the reflected wave and the transmitted wave at a specific frequency, denoted as $Pr(f)$ and $Pt(f)$, respectively, can also be calculated by a Fourier transform. Finally, the reflection coefficient and the transmission coefficient are calculated by $R(f)=Pr(f)/Pi(f)$ and $T(f)=Pt(f)/Pi(f)$.

In Fig. 7, the difference between the time domain wave forms calculated by the two methods is not so obvious. For one-dimensional acoustical wave propagation, both the reflection coefficient $R(f)=(\rho_2 c_2-\rho_1 c_1)/(\rho_2 c_2+\rho_1 c_1)$, and the transmission coefficient $T(f)=2\rho_2 c_2/(\rho_2 c_2+\rho_1 c_1)$ should be independent of frequency.[41] In this example, $R(f)=0.6363$ and $T(f)=1.6364$. Therefore from Fig. 8 the superiority of mapped AWP can be clearly viewed in the frequency domain when the reflection coefficient and the transmission coefficient are concerned. Also, it can be seen that for AWP, the calculation error becomes larger with the increase of the frequency, this is consistent with the analysis in Sec. III A.

B. Acoustical wave propagation through a blockage

In this example, a blockage with width 1 m centered at $x=14$ m is set in the computation domain [0 m, 20 m]. The parameters in the blockage are $\rho_2=1.5\rho_0$ and $c_2=3c_0$, and $\rho_1=\rho_0$ and $c_1=c_0$ are for all the other areas. The initial wave packet is chosen as $p(x,0)=e^{-32(x-3)^2}$ and $v(x,0)=p(x,0)/\rho_1 c_1$. In this example, there are two media interfaces with quite close distance; thus the mapping curve with only one concentration area can still be used. However, since the initial wave packet (centered at 3 m) is quite far from the blockage, the direct implementation of the mapping curve function (22) may lead to extra computation error because of too sparse grid density around the initial wave packet. A mapping curve design procedure similar with that described in Fig. 5 of Sec. III B is implemented in this example. The computation domain is divided into two subdomains [0 m, 8 m], and [8 m, 20 m]. The mapping curve function of (24) with $\eta=0.2$ is applied to the second subdomain and the first subdomain is left alone, i.e., $x=u$ in the first subdomain. Figure 9 shows the initial wave packet of sound pressure and the snapshot of the wave form at $t=0.043$ s. Several reflection wave packets and transmitted wave packets can be clearly seen. The transmission coefficients of the first and third transmitted wave packet calculated by AWP and mapped AWP are depicted in Fig. 10. The theoretical transmission coefficients for the first and third transmitted wave packet are $T_1(f)=0.5950$ and $T_3(f)=0.0976$. Obviously, mapped AWP holds high accuracy, even when the energy decreases much in the third transmitted wave packet.

C. Acoustical wave evolution between two boundaries

The time domain acoustical wave packet evolution within an area between two boundaries is investigated in this example. The computational domain is set the same as the one described in Sec. III B, i.e., two media interfaces are set in the computation domain [0, 20] at the positions of $x=4$ and $x=11$. The acoustical parameters in the area between the interfaces are $\rho_1=\rho_0$, and $c_1=c_0$, and $\rho_2=1.5\rho_0$ and $c_2=3c_0$ are for the rest areas. The initial wave packet is set in the middle between the two interfaces, $p(x,0)=10e^{-64(x-7.5)^2}$ and $v(x,0)=p(x,0)/\rho_1 c_1$. The mapping curve described by Fig. 5 is implemented. To demonstrate the superiority of the mapped AWP, a comparatively extreme condition is considered. After 0.386 s evolution, the acoustical wave packet propagates 132.8 m and reflects 19 times from the interfaces and the energy of the wave packet decreases dramatically. The reflection coefficient can be calculated as $R_{19}(f)=0.0002$. Figure 11(b) shows the extracted wave packet within the two boundaries after 0.386 s evolution, the error of the AWP scheme can be clearly viewed. The reflection coefficient calculated by the AWP and the mapped AWP schemes are depicted in Fig. 11(c). It can be found that for such an extreme condition the error of the AWP scheme accumulates to the extent that the reflection coefficient is more

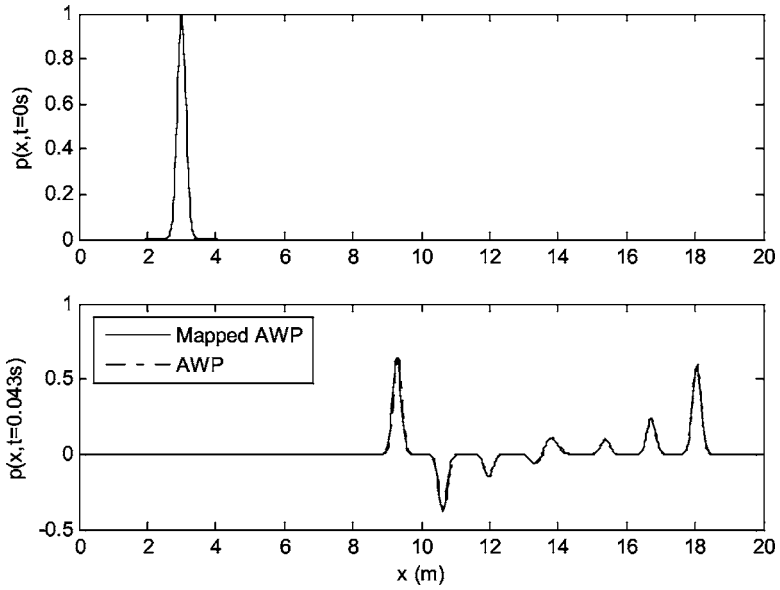

FIG. 9. The initial wave packet and the wave form at $t=0.043$ s calculated by the AWP and the mapped AWP scheme, respectively.

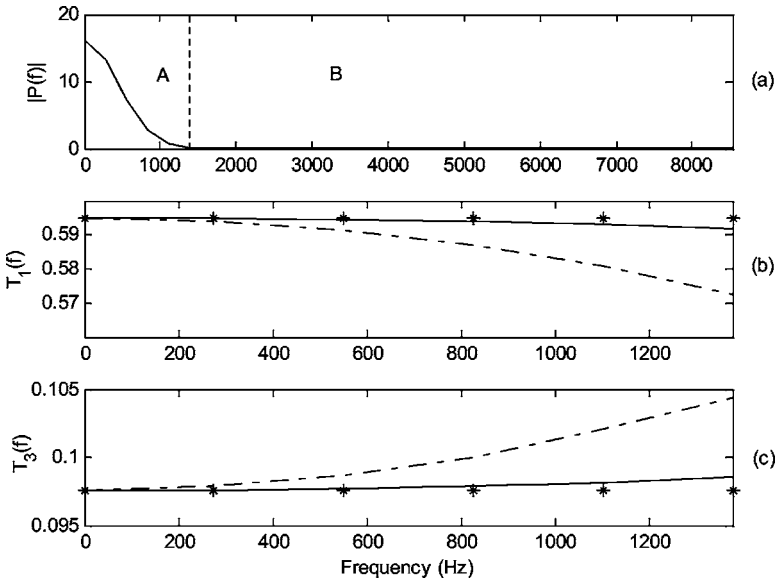

FIG. 10. (a) The energy distribution of the initial sound pressure in the frequency domain; (b) the transmission coefficient of the first transmitted wave packet calculated by the AWP (dashed line) and, the mapped AWP (solid line) within region A of (a); ∗ stands for the theoretical result; (c) the transmission coefficient of the third transmitted wave packet calculated by the AWP (dashed line) and the mapped AWP (solid line) within region A of (a) ∗ stands for the theoretical result.

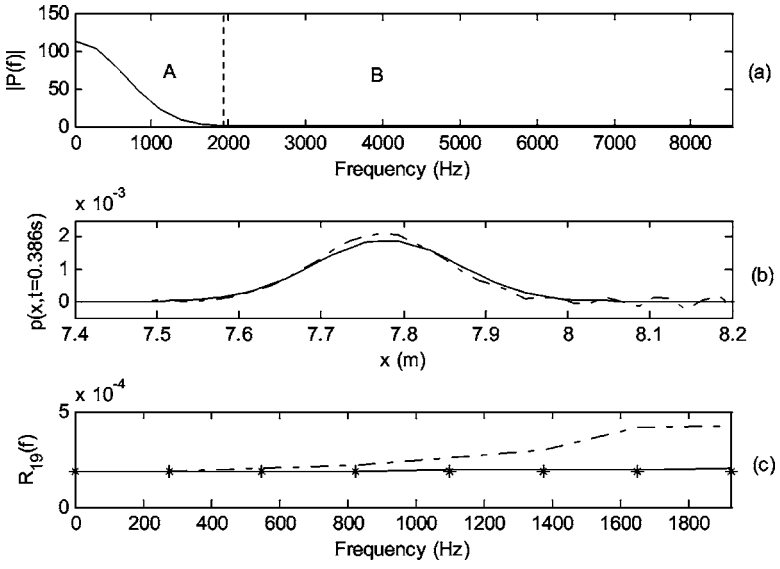

FIG. 11. (a) The energy distribution of the initial sound pressure in the frequency domain; (b) the extracted wave packet after 0.386 s evolution calculated by the AWP (dashed line) and the mapped AWP (solid line); (c) the reflection coefficient calculated by the AWP (dashed line) and the mapped AWP (solid line) within region A of (a); ∗ stands for the theoretical result.

than twice the correct value in the upper bound of the effective frequency range. This demonstrates the necessity of mapped AWP for the acoustical wave propagation problem when the wave packet interacts with the interfaces many times.

It should be pointed out that for the above illustrative examples and all the other numerical simulations that have not been included in this paper, as long as the requirement of two grid points per minimum wavelength is satisfied, mapped AWP outperforms the original AWP when discontinuities exist in the computational domain.

V. CONCLUSIONS

Due to the influence of Gibbs phenomenon, the error of AWP in calculating acoustical wave propagation in discontinuous media increases with the growth of frequency in the spectral domain. To alleviate this problem, an improved AWP scheme with mapped pseudospectral method is proposed in this paper. By projecting the uniform grid points onto a series of nonuniform grid points through a carefully designed smooth mapping function, the grid density across the media interfaces can be increased remarkably. Since the accuracy in the low-frequency range can be regarded as proportional to the square of the grid density, the mapped pseudospectral method effectively improve the performance of the AWP scheme. The superiority of the proposed scheme is demonstrated by several numerical examples. Compared with the normal method, the error of the improved AWP with a mapped pseudospectral method is negligible, even after quite a long propagation time when the media interfaces act many times on the wave packet. The improvement in calculation accuracy makes the improved AWP a reliable tool for the study of the evolution of acoustical waves in media with discontinuities. The research concerning some difficulties of this scheme when it is extended to multidimensional applications is still ongoing.

ACKNOWLEDGMENTS

This work was supported by the Chinese Natural Science Foundation No. 60340420325, the Research Fund for the Doctoral Program of Higher Education of China No. 20040284038, and the Australia Research Council discovery grant.

[1]G. Cohen and P. Joly, "Construction and analysis of fourth-order finite difference schemes for the acoustic wave equation in nonhomogeneous media," SIAM (Soc. Ind. Appl. Math.) J. Numer. Anal. **33**, 1266–1302 (1996).

[2]A. Bamberger, R. Glowinski, and Q. H. Tran, "A domain decomposition method for the acoustic wave equation with discontinuous coefficients and grid change," SIAM (Soc. Ind. Appl. Math.) J. Numer. Anal. **34**, 603–639 (1997).

[3]J. Piraux and B. Lombard, "A new interface method for hyperbolic problems with discontinuous coefficients: one-dimensional acoustic example," J. Comput. Phys. **168**, 227–248 (2001).

[4]B. Lombard and J. Piraux, "Numerical treatment of two-dimensional interfaces for acoustic and elastic waves," J. Comput. Phys. **195**, 90–116 (2004).

[5]B. Gustafsson and P. Wahlund, "Time compact difference methods for wave propagation in discontinuous media," SIAM J. Sci. Comput. (USA) **26**, 272–293 (2004).

[6]Q. H. Liu, "Large-scale simulations of electromagnetic and acoustic measurements using the pseudospectral time-domain (PSTD) algorithm," IEEE Trans. Geosci. Remote Sens. **GE–37**, 917–926 (1999).

[7]T. D. Mast, L. P. Souriau, D.-L. Liu, M. Tabei, A. I. Nachman, and R. C. Waag, "A *k*-space method for large-scale models of wave propagation in tissure," IEEE Trans. Ultrason. Ferroelectr. Freq. Control **48**, 341–354 (2001).

[8]M. Tabei, T. D. Mast, and R. C. Waag, "A *k*-space method for coupled first-order acoustic propagation equations," J. Acoust. Soc. Am. **111**, 53–63 (2002).

[9]B. Fornberg, "The pseudospectral method: comparisons with finite differences for he elastic wave equation," Geophysics **52**, 483–501 (1987).

[10]N. N. Bojarski, "The *k*-space formulation of the scattering problem in the time domain," J. Acoust. Soc. Am. **72**, 570–584 (1982).

[11]N. N. Bojarski, "The *k*-space formulation of the scattering problem in the time domain: an improved single propagator formulation," J. Acoust. Soc. Am. **77**, 826–831 (1985).

[12]R. E. Mickends, *Nonstandard Finite Difference Models of Differential Equations* (World Scientific, Singapore, 1994).

[13]J. Pan and J. B. Wang, "Acoustical wave propagator," J. Acoust. Soc. Am. **108**, 481–487 (2000).

[14]H. Tal-Ezer and R. Kosloff, "An accurate and efficient scheme for propagating the time-dependent Schrodinger equation," J. Chem. Phys. **81**, 3967–3971 (1984).

[15]H. Tal-Ezer, "Spectral methods in time for hyperbolic equations," SIAM (Soc. Ind. Appl. Math.) J. Numer. Anal. **23**, 11–26 (1986).

[16]H. Tal-Ezer, D. Kosloff, and Z. Koren, "An accurate scheme for seismic forward modelling," Geophys. Prospect. **35**, 479–490 (1987).

[17]D. Kosloff, A. Queiroz Filho, E. Tessmer, and A. Behle, "Numerical solution of the acoustic and elastic wave equations by a new rapid expansion method," Geophys. Prospect. **37**, 383–394 (1989).

[18]H. De Raedt, K. Michielsen, J. S. Kole, and M. T. Figge, "One-step finite-difference time-domain algorithm to solve Maxwell equations," Phys. Rev. E **67**, 056706-1–056706-12 (2003).

[19]H. De Raedt, K. Michielsen, J. S. Kole, and M. T. Figge, "Solving the Maxwell equations by the Chebyshev method: a one-step finite-difference time-domain algorithm," IEEE Trans. Antennas Propag. **51**, 3155–3160 (2003).

[20]H. M. Sun, J. B. Wang, and J. Pan, "An effective algorithm for simulating acoustical wave propagation," Comput. Phys. Commun. **151**, 241–249 (2003).

[21]J. P. Boyd, *Chebyshev and Fourier Spectral Methods*, 2nd ed. (Dover, Mineola, New York, 2001).

[22]L. N. Trefethen, *Spectral Methods in MATLAB* (SIAM, Philadelphia, 2000).

[23]S. A. Sarra, "Spectral methods with postprocessing for numerical hyperbolic heat transfer," Numer. Heat Transfer, Part A **43**, 717–730 (2003).

[24]D. Gottlieb and C. W. Shu, "On the Gibbs phenomenon V: recovering exponential accuracy from collocation point values of a piecewise analytic function," Numer. Math. **71**, 511–526 (1995).

[25]D. Gottlieb and C. W. Shu, "On the Gibbs phenomenon and its resolution," SIAM Rev. **39**, 644–668 (1997).

[26]Q. H. Liu, X. M. Xu, B. Tian, and Z. Q. Zhang, "Applications of nonuniform fast transform algorithms in numerical solutions of differential and integral equations," IEEE Trans. Geosci. Remote Sens. **GE–38**, 1551–1560 (2000).

[27]A. Dutt and V. Rokhlin, "Fast Fourier transform for nonequispaced data," SIAM J. Sci. Comput. (USA) **14**, 1368–1393 (1993).

[28]N. Nguyen and Q. H. Liu, "The regular Fourier matrices and non-uniform fast Fourier transforms," SIAM J. Sci. Comput. (USA) **21**, 283–293 (1999).

[29]A. Bayliss and E. Turkel, "Mapping and accuracy for Chebyshev pseudospectral approximations," J. Comput. Phys. **101**, 349–359 (1992).

[30]X. Gao, M. S. Mirotznik, S. Y. Shi, and D. W. Prather, "Applying a mapped pseudospectral time-domain method in simulating diffractive optical elements," J. Opt. Soc. Am. A **21**, 777–785 (2004).

[31]J.-P. Berenger, "A perfectly matched layer for the absorption of electromagnetic waves," J. Comput. Phys. **114**, 185–200 (1994).

[32]S. Z. Peng and J. Pan, "Acoustical wave propagator for time-domain flexural waves in thin plates," J. Acoust. Soc. Am. **115**, 467–474 (2004).

[33]G. X. Fan, Q. H. Liu, and J. S. Hesthaven, "Multidomain pseudospectral time-domain simulations of scattering by objects buried in lossy media," IEEE Trans. Geosci. Remote Sens. **GE–40**, 1366–1373 (2002).

[34]Y. Q. Zeng, Q. H. Liu, and G. Zhao, "Multidomain pseudospectral time-

domain method for acoustic waves in lossy media," J. Comput. Acoust. **12**, 277–299 (2004).
[35]C. D. Meyer, *Matrix Analysis and Applied Linear Algebra* (SIAM, Philadelphia, 2000).
[36]T. J. Rivlin, *Chebyshev Polynomials*, 2nd ed. (Wiley, New York, 1990).
[37]A. A. Samarskii, *The Theory of Difference Schemes* (Marcel Dekker, New York, 2001).
[38]J. Pan and J. B. Wang, "Further development of the acoustical wave propagator," *Proceedings of the 10th ICSV*, Stockholm, Sweden, 2003, pp. 5045–5051.
[39]D. Gottlieb and S. A. Orszag, *Numerical Analysis of Spectral Methods: Theory and Applications* (SIAM, Philadelphia, 1977).
[40]C. Basdevant, M. Deville *et al.*, "Spectral and finite difference solutions of Burgers' equation," Comput. Fluids **14**, 23–41 (1986).
[41]P. M. Morse and K. U. Ingard, *Theoretical Acoustics* (McGraw-Hill, New York, 1968).

Sound propagation through and scattering by internal gravity waves in a stably stratified atmosphere

Vladimir E. Ostashev
NOAA/Environmental Technology Laboratory, Boulder, Colorado 80305 and Department of Physics, New Mexico State University, Las Cruces, New Mexico 88003

Igor P. Chunchuzov
Obukhov Institute of Atmospheric Physics, Moscow, Russia

D. Keith Wilson
U.S. Army Engineer Research and Development Center, Hanover, New Hampshire 03755

(Received 8 March 2005; revised 28 September 2005; accepted 29 September 2005)

A stably stratified atmosphere supports propagation of internal gravity waves (IGW). These waves result in highly anisotropic fluctuations in temperature and wind velocity that are stretched in a horizontal direction. As a result, IGW can significantly affect propagation of sound waves in nighttime boundary layers and infrasound waves in the stratosphere. In this paper, a theory of sound propagation through, and scattering by, IGW is developed. First, 3D spectra of temperature and wind velocity fluctuations due to IGW, which were recently derived in the literature for the case of large wave numbers, are generalized to account for small wave numbers. The generalized 3D spectra are then used to calculate the sound scattering cross section in an atmosphere with IGW. The dependencies of the obtained scattering cross section on the sound frequency, scattering angle, and other parameters of the problem are qualitatively different from those for the case of sound scattering by isotropic turbulence with the von Kármán spectra of temperature and wind velocity fluctuations. Furthermore, the generalized 3D spectra are used to calculate the mean sound field and the transverse coherence function of a plane sound wave propagating through IGW. The results obtained also significantly differ from those for the case of sound propagation through isotropic turbulence. © *2005 Acoustical Society of America.* [DOI: 10.1121/1.2126938]

PACS number(s): 43.20.Fn, 43.28.Bj, 43.28.Lv [LCS] Pages: 3420–3429

I. INTRODUCTION

A stably stratified atmosphere often occurs in nighttime boundary layers (NBL) which extend from the ground to heights of about several hundred meters. Furthermore, the atmosphere is stably stratified in the stratosphere with the highest static stability in a range of heights from about 20 to 45 km.

A stably stratified atmosphere supports propagation of internal gravity waves (IGW). In NBL these waves can be trapped in a waveguide within a temperature inversion layer where the Brunt-Väisälä frequency is maximal. (The Brunt-Väisälä frequency is a characteristic frequency of IGW.[1]) The local maximum of this frequency near the stratopause (located about 45 km above the ground) can also be a barrier for IGW. In both cases, significant fluctuations in temperature T and wind velocity $\mathbf{v}$ are observed due to propagation of IGW.[1–4] These fluctuations are highly anisotropic and are stretched in a horizontal direction. The fluctuations can significantly affect sound propagation in NBL and infrasound propagation in the stratosphere. For example, facsimile records of sodars clearly show the presence of IGW in NBL (Refs. 1 and 2).

Despite the significance of sound propagation through, and scattering by, IGW, few theoretical studies of this phenomenon have been made. The reason for that is that such studies require combining results from two research topics: (1) 3D spectra of temperature and wind velocity fluctuations due to IGW in a stably stratified atmosphere; and (2) a general theory of sound propagation through, and scattering by, anisotropic turbulence with both temperature and wind velocity fluctuations. Significant progress in both research topics has been made only recently.

In the first of these research topics, 3D spectra of temperature and wind velocity fluctuations due to IGW were derived in Ref. 5 for the limiting case of large wave numbers (in comparison with the inverse outer scale of IGW). The spectra are very anisotropic: Their scale in a horizontal direction is much greater than that in a vertical direction. The 1D vertical spectra of temperature and wind velocity fluctuations obtained from these 3D spectra agree with those derived theoretically,[6,7] calculated numerically,[8,9] and measured in the stratosphere and troposphere, e.g., Refs. 3 and 10.

In the second research topic, a general theory of sound propagation through, and scattering by, anisotropic turbulence with temperature and wind velocity fluctuations has been developed in Refs. 11–14. Given the 3D spectra of T and $\mathbf{v}$ fluctuations, the theory provides formulas for calculations of the most widely used statistical moments of plane- and spherical sound waves: the sound scattering cross section, the variances and correlation functions of log-amplitude and phase fluctuations, the mean sound field, and the coherence function of the sound field.

The main goal of the present paper is to use the results obtained in these two research topics to develop a theory of sound propagation through, and scattering by, IGW. First, the 3D spectra of temperature and wind velocity fluctuations obtained in Ref. 5 for the case of large wave numbers are generalized to account for small wave numbers (of order of or smaller than the inverse outer scale of IGW). It is shown that the generalized 3D spectra have "realistic" 1D vertical spectra which, for large wave numbers, agree with those measured experimentally, and are bounded for small wave numbers.

Then, the generalized 3D spectra of temperature and wind velocity fluctuations are used to calculate the sound scattering cross section in the atmosphere with IGW. The obtained scattering cross section is compared with that due to sound scattering by isotropic turbulence with the von Kármán spectra of temperature and wind velocity fluctuations.

Furthermore, line-of-sight sound propagation through IGW with the 3D generalized spectra is studied. First, the extinction coefficient of the mean sound field is calculated. Then, the transverse coherence function of a plane sound wave is calculated and analyzed. The results obtained are also compared with those for the von Kármán spectra of temperature and wind velocity fluctuations.

The paper is organized as follows. In Sec. II, the spectra of temperature and wind velocity fluctuations due to IGW and von Kármán spectra of isotropic turbulence are considered. The sound scattering cross section in the atmosphere with IGW is calculated and analyzed in Sec. III. In Sec. IV, we consider line-of-sight sound propagation through IGW and calculate the mean sound field and the coherence function of a plane sound wave. The results obtained in the paper are summarized in Sec. V.

II. SPECTRA OF TEMPERATURE AND VELOCITY FLUCTUATIONS

A. 3D spectra for large wave numbers

At large wave numbers, the interaction between IGW modes is strongly nonlinear.[5–8] Such interaction transfers energy from random IGW sources to the modes with larger vertical and smaller horizontal scales than those in the source spectrum. This energy transfer is balanced by energy dissipation due to convective or shear instabilities at *very* large wave numbers.[15] As a result of the nonlinear interaction, 1D vertical spectra of temperature and horizontal wind velocity fluctuations have a universal form at large wave numbers that does not depend on the form of the spectrum for small wave numbers. These 1D vertical spectra have been studied extensively theoretically,[6,7] numerically,[8,9] and experimentally.[16–21]

However, when considering sound propagation through IGW, one needs to know 3D spectra of temperature and wind velocity fluctuations rather than 1D spectra. Using the mechanism of nonlinear interaction between IGW modes described above, the 3D spectra of temperature and horizontal wind velocity fluctuations were derived in Ref. 5. The 3D spectrum of temperature fluctuations is given by:

$$\Phi_T(\mathbf{K}) = \frac{AT_0^2N^4}{g^2|K_3|^5}\exp\left(-\frac{K_\perp^2}{4e_0K_3^2}\right), \tag{1}$$

where $\mathbf{K}=(K_1,K_2,K_3)$ is the turbulence wave vector, $K_\perp=\sqrt{K_1^2+K_2^2}$, N is the Brunt-Väisälä frequency, T_0 is the reference value of temperature, and g is the acceleration due to gravity. The components K_1, K_2, and K_3 of the turbulence wave vector are in the directions of the x-, y-, and z axes, with the z axis being vertical and the x- and y axes being in a horizontal plane. Furthermore, e_0 is a dimensionless parameter characterizing anisotropy of the spectrum. It is defined as a root-mean-square of the horizontal gradient of horizontal displacements due to IGW.[5,6] The value of e_0 depends on the degree of nonlinearity of IGW and can be in a wide range; however, e_0 is always much less than 1 (see the end of this section for more details). In Eq. (1), the numerical coefficient A is given by

$$A = \frac{\exp[-1/(32a_0)]}{2^{15}(2\pi)^{3/2}e_0a_0^{5/2}}. \tag{2}$$

Here, $a_0=M^2/8$, where M^2 is the mean-square vertical gradient of the vertical displacements due to IGW.[5] M characterizes the degree of nonlinearity of IGW and varies from 0 to about 0.5. (If $M>0.5$, IGW are unstable.) Therefore, in Eq. (2) the value of the parameter a_0 is in the range $0<a_0<0.03$.

Let $\Phi_{ij}(\mathbf{K})$ be the 3D spectral tensor of wind velocity fluctuations $\mathbf{v}=(v_1,v_2,v_3)=(v_x,v_y,v_z)$, where $i,j=1,2,3$. The theory developed in Ref. 5 results in isotropic velocity fluctuations in a horizontal plane so that $\Phi_{11}(\mathbf{K})=\Phi_{22}(\mathbf{K})$. Furthermore, $\Phi_{11}(\mathbf{K})$ has the same dependence on $\mathbf{K}$ as does the temperature spectrum

$$\Phi_{11}(\mathbf{K}) = \frac{AN^2}{2|K_3|^5}\exp\left(-\frac{K_\perp^2}{4e_0K_3^2}\right). \tag{3}$$

The vertical velocities due to IGW are significantly suppressed in comparison with the horizontal ones. Therefore, for the purpose of this paper, Φ_{i3} and Φ_{3i} can be ignored in comparison with Φ_{11}.

The 3D spectra of temperature and horizontal velocity fluctuations, Eqs. (1) and (3), were derived in Ref. 5 assuming that $K_3 \gg K_0$ and $K_3/K_0 \gg K_\perp/K_{0\perp}$. Here, K_0 and $K_{0\perp}$ are characteristic wave numbers of the spectra in vertical and horizontal directions, respectively, similar to the inverse outer scale of turbulence. Let $K_0=2\pi/L_0$, where L_0 is a characteristic spatial scale of the spectra. In NBL, $L_0\sim 300$ m, while in the stratosphere $L_0\sim 2-4$ km. $K_{0\perp}$ is much less than K_0 so that the ratio $\chi=K_0/K_{0\perp}$ is much greater than 1. Using the measurements of the vertical and horizontal velocities in NBL,[22] it can be shown that this ratio is in the range $3<\chi<10$. The range of values of χ in the stratosphere is not yet well known. Apparently, it can be as large as $\chi\sim 10$. This value of χ in the stratosphere will be assumed in numerical estimates below.

In Eqs. (1) and (3), the parameter e_0 is of the order of a_0/χ^2.[5] For the values of a_0 and χ given above, this parameter is in the range $0<e_0<3\cdot 10^{-3}$ in NBL, and in the range $0<e_0<3\cdot 10^{-4}$ in the stratosphere. Since $e_0 \ll 1$, the spectra

Φ_T and Φ_{11}, given by Eqs. (1) and (3), are very anisotropic: Their scale in a horizontal direction is much greater than that in the vertical direction.

Using the spectra Φ_T and Φ_{11}, given by Eqs. (1) and (3), the travel time fluctuations of sound propagation in NBL were calculated and compared with those measured experimentally.[23] The results obtained show good agreement between theoretical predictions and experimental data. This can be considered as an indirect experimental verification of the spectra (1) and (3). Note that direct measurements of the 3D spectra $\Phi_T(\mathbf{K})$ and $\Phi_{11}(\mathbf{K})$ are difficult to obtain; usually, 1D vertical spectra are measured experimentally by using different techniques, e.g., ground-based radars and lidars,[3,4,17] high-resolution radiosondes,[18,20] and measurements of stellar scintillations from space.[16] In the next section, starting from Eqs. (1) and (3), we derive 1D vertical spectra of temperature and wind velocity fluctuations, and discuss their agreement with experimental data and theoretical predictions.

B. 1D vertical spectra for large wave numbers

The 1D vertical spectrum $F_v(K_3)$ of temperature fluctuations is defined as

$$F_v(K_3) = \int_{-\infty}^{\infty} dK_1 \int_{-\infty}^{\infty} \Phi_T(K_1, K_2, K_3) dK_2. \tag{4}$$

Using this formula and Eq. (1) for Φ_T, the 1D vertical temperature spectrum can be calculated

$$F_v(K_3) = \frac{4\pi B e_0}{K_3^3}. \tag{5}$$

Here, $B = AT_0^2 N^4 / g^2$. Both the K_3^{-3} dependence and the coefficient $4\pi B e_0$ of the 1D vertical temperature spectrum, Eq. (5), agree with those measured experimentally in the stratosphere and troposphere.[3,4,16–19]

Using Eq. (3), it can be shown that the 1D vertical spectrum of v_x fluctuations is given by Eq. (5) if the constant B is replaced with $B' = AN^2/2$. It is shown in Refs. 5, 7, and 9 that the dependencies of this 1D vertical spectrum on K_3 and the coefficient $4\pi B' e_0$ are consistent with experimental data obtained in Refs. 10, 16, 20, and 21

The 1D vertical spectra of temperature and wind velocity fluctuations considered in this section also agree with those derived theoretically[6,21] and calculated numerically.[8,9]

C. Generalized 3D spectra

The spectrum Φ_T, given by Eq. (1), becomes unrealistic for small values of the vertical component of the turbulence wave vector, K_3. In this source region, Φ_T should be approximately constant. Therefore, it is worthwhile to generalize the spectrum (1) to account for small values of K_3.

In this paper, we propose the following generalization of the 3D temperature spectrum:

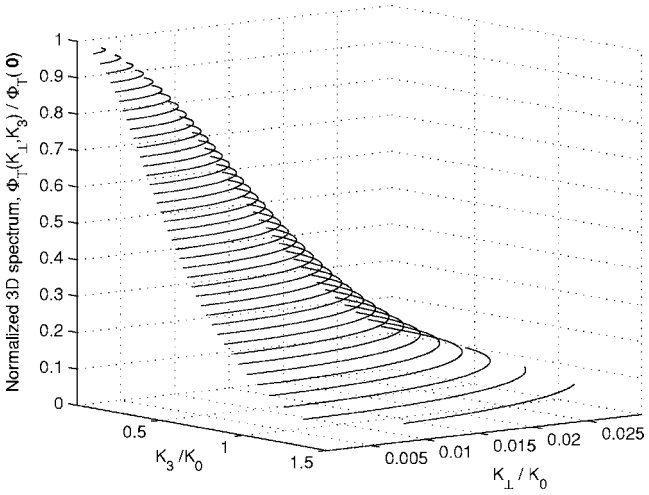

FIG. 1. The normalized generalized 3D spectrum of temperature fluctuations $\Phi_T(K_\perp, K_3)/\Phi_T(\mathbf{0})$. The anisotropy parameter is $e_0 = 10^{-4}$.

$$\Phi_T(\mathbf{K}) = \frac{AT_0^2 N^4}{g^2 (K_0^2 + K_3^2)^{5/2}} \exp\left(- \frac{K_\perp^2}{4e_0 (K_0^2 + K_3^2)} \right). \tag{6}$$

If $K_3 \gg K_0$, the spectrum (6) coincides with that given by Eq. (1). If $K_3 \ll K_0$ and $K_\perp \ll 2\sqrt{e_0} K_0$, the spectrum (6) does not depend on $\mathbf{K}$ and is constant: $\Phi_T = AT_0^2 N^4 / (g^2 K_0^5)$. The suggested generalization of the spectrum (1) is similar to the generalization of the Kolmogorov spectrum when it is replaced by the von Kármán spectrum.[11,24] Note that the von Kármán spectra of temperature and wind velocity fluctuations have been widely used for studies of sound propagation through a turbulent atmosphere, e.g., see Refs. 11 and 25 and references therein.

The variance of temperature fluctuations is determined as

$$\sigma_T^2 = \int_{-\infty}^{\infty} dK_1 \int_{-\infty}^{\infty} dK_2 \int_{-\infty}^{\infty} \Phi_T(K_1, K_2, K_3) dK_3. \tag{7}$$

Substituting the value of Φ_T given by Eq. (6) into Eq. (7) and calculating the integrals, the constant A can be expressed in terms of σ_T^2

$$A = \frac{\sigma_T^2 g^2 K_0^2}{8\pi e_0 T_0^2 N^4}. \tag{8}$$

Using this value of A in Eq. (6), we obtain a desired form of the generalized 3D spectrum of temperature fluctuations

$$\Phi_T(\mathbf{K}) = \frac{K_0^2 \sigma_T^2}{8\pi e_0 (K_0^2 + K_3^2)^{5/2}} \exp\left(- \frac{K_\perp^2}{4e_0 (K_0^2 + K_3^2)} \right). \tag{9}$$

Figure 1 shows $\Phi_T(K_\perp, K_3)$, given by this equation, normalized by $\Phi_T(\mathbf{0})$. In the figure, $e_0 = 10^{-4}$. It follows from Fig. 1 that $\Phi_T(K_\perp, K_3)$ reaches a maximum at $\mathbf{K} = 0$ and decreases along the $K_\perp$ axis (which corresponds to the horizontal components of the turbulence wave vector) much faster than along the K_3 axis (vertical components of the wave vector); i.e., the spectrum is highly anisotropic.

The proposed generalization of the 3D spectrum of horizontal velocity fluctuations, Eq. (3), is analogous to that of the 3D spectrum of temperature fluctuations

$$\Phi_{11}(\mathbf{K}) = \frac{AN^2}{2(K_0^2 + K_3^2)^{5/2}} \exp\left(- \frac{K_\perp^2}{4e_0(K_0^2 + K_3^2)} \right). \quad (10)$$

Thus, the generalized 3D spectra of temperature and wind velocity fluctuations, Eqs. (9) and (10), have the same dependence on $\mathbf{K}$ as do the corresponding spectra given by Eqs. (1) and (3).

The variance σ_v^2 of horizontal velocity fluctuations is given by a formula similar to Eq. (7): $\sigma_v^2 = \int \Phi_{11}(\mathbf{K}) d^3K$. Substituting Eq. (10) into this formula and calculating the integral over $\mathbf{K}$, we express the parameter A in terms of σ_v^2:

$$A = \frac{K_0^2 \sigma_v^2}{4\pi e_0 N^2}. \quad (11)$$

Using this value of A in Eq. (10), we obtain a desired form of the generalized 3D spectrum of horizontal velocity fluctuations

$$\Phi_{11}(\mathbf{K}) = \frac{K_0^2 \sigma_v^2}{8\pi e_0 (K_0^2 + K_3^2)^{5/2}} \exp\left(- \frac{K_\perp^2}{4e_0(K_0^2 + K_3^2)} \right). \quad (12)$$

Note that the variances of the temperature and horizontal velocity fluctuations in Eqs. (9) and (12) are related by a formula that can be obtained by eliminating the parameter A between Eqs. (8) and (11)

$$\sigma_v^2 = \frac{g^2}{2N^2} \frac{\sigma_T^2}{T_0^2}. \quad (13)$$

The generalized 3D spectra $\Phi_T(\mathbf{K})$ and $\Phi_{11}(\mathbf{K})$, given by Eqs. (9) and (12), will be used in Secs. III and IV for calculations of the statistical moments of a sound field propagating in an atmosphere with IGW.

D. Generalized 1D vertical spectra

In this section, we consider the generalized 1D temperature and horizontal velocity spectra. For the purpose of this section, it is more convenient to deal with Eqs. (6) and (10) for these spectra rather than with equivalent Eqs. (9) and (12).

Substituting Eq. (6) into Eq. (4) and calculating the integrals over K_1 and K_2, we obtain the generalized 1D vertical spectrum of temperature fluctuations

$$F_v(K_3) = \frac{4\pi B e_0}{(K_0^2 + K_3^2)^{3/2}}. \quad (14)$$

For $K_3 \gg K_0$, this spectrum coincides with that given by Eq. (5). Since the latter spectrum agrees with experimental data, so does the spectrum (14). For $K_3 \ll K_0$, the spectrum (14) is approximately constant. This is a more realistic behavior of the spectrum than an infinite increase of the spectrum (5) for small K_3.

It can be shown that the 1D vertical spectrum of horizontal velocity fluctuations is given by Eq. (14) if the constant B in this equation is replaced with the constant B'. This spectrum also agrees with experimental data for $K_3 \gg K_0$ and is approximately constant for $K_3 \ll K_0$.

E. von Kármán spectra of temperature and wind velocity fluctuations

The 3D von Kármán spectrum of isotropic temperature fluctuations is given by[11]

$$\Phi_T^{vK}(K) = \frac{2^{1/3}5}{3^{3/2}\Gamma^3(1/3)} \frac{K_T^{2/3} \sigma_{T,vK}^2}{(K_T^2 + K^2)^{11/6}}. \quad (15)$$

Here, K is the modulus of the turbulence wave number $\mathbf{K}$, Γ is the gamma function, $\sigma_{T,vK}^2$ is the variance of temperature fluctuations for the von Kármán spectrum, and K_T is a characteristic wave number inversely proportional to the outer scale of temperature fluctuations.

The 3D von Kármán spectral tensor of isotropic wind velocity fluctuations is given by[11]

$$\Phi_{ij}^{vK}(\mathbf{K}) = \frac{55}{2^{2/3}3^{5/2}\Gamma^3(1/3)} \left(\delta_{ij} - \frac{K_i K_j}{K^2} \right) \frac{K^2 K_v^{2/3} \sigma_{v,vK}^2}{(K_v^2 + K^2)^{17/6}}, \quad (16)$$

where δ_{ij} is the Kronecker symbol, $\sigma_{v,vK}^2$ is the variance of wind velocity fluctuations, and K_v is a characteristic wave number inversely proportional to the outer scale of velocity fluctuations.

Note that the von Kármán spectra $\Phi_T^{vK}(K)$ and $\Phi_{11}^{vK}(\mathbf{K})$ have different dependence on $\mathbf{K}$ even for $K \gg K_T$ and $K \gg K_v$, while the generalized 3D spectra given by Eqs. (9) and (12) have the same dependence.

III. SCATTERING OF SOUND BY IGW

The sound scattering cross section, σ, is an important statistical characteristic of a sound wave propagating in a medium with random inhomogeneities. In this section, we calculate σ for the case of sound scattering by IGW.

A. Sound scattering cross section

For anisotropic turbulence, the sound scattering cross section is given by[11]

$$\sigma = 2\pi k^4 \cos^2 \Theta \left[\frac{\Phi_T(\mathbf{q})}{4T_0^2} + \frac{n_{0,i} n_{0,j} \Phi_{ij}(\mathbf{q})}{c_0^2} \right]. \quad (17)$$

Here, k is the sound wave number, $\mathbf{q} = 2k(\mathbf{n}_0 - \mathbf{n})$ is the scattering vector, $\mathbf{n}_0 = (n_{0,1}, n_{0,2}, n_{0,3})$ is the unit vector in the direction of propagation of a sound wave incident on a scattering volume, $\mathbf{n}$ is the unit vector in the direction of propagation of a scattered wave, Θ is the scattering angle between the vectors $\mathbf{n}_0$ and $\mathbf{n}$, and summation is assumed over repeated subscripts.

In Eq. (17), it is worthwhile to express $\cos \Theta$ and $\mathbf{q}$ in terms of the spherical coordinates of the unit vectors $\mathbf{n}_0$ and $\mathbf{n}$. Without loss of generality, we assume that the vector $\mathbf{n}_0$ lies in the xz plane. Then, $\mathbf{n}_0 = (\sin \theta_0, 0, \cos \theta_0)$, where θ_0 is the angle between $\mathbf{n}_0$ and the vertical z axis; see Fig. 2. In the spherical coordinates, the unit vector $\mathbf{n}$ can be written as $\mathbf{n} = (\sin \theta \cos \phi, \sin \theta \sin \phi, \cos \theta)$. Here, θ is the angle between $\mathbf{n}$ and the vertical axis, and ϕ is the azimuthal angle between the projection of $\mathbf{n}$ on the horizontal plane and the x axis (Fig. 2).

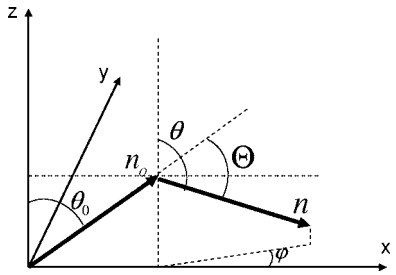

FIG. 2. The unit vectors $\mathbf{n}_0$ and $\mathbf{n}$ in the Cartesian coordinate system.

Using these representations of the unit vectors $\mathbf{n}_0$ and $\mathbf{n}$, the components of the scattering vector $\mathbf{q}=(q_1,q_2,q_3)$ can be expressed in terms of the spherical coordinates of $\mathbf{n}_0$ and $\mathbf{n}$

$$q_1 = 2k(\sin\theta_0 - \sin\theta\cos\phi), \quad q_2 = -2k\sin\theta\sin\phi,$$

$$q_3 = 2k(\cos\theta_0 - \cos\theta). \tag{18}$$

Furthermore, $\cos\Theta=\mathbf{n}_0\cdot\mathbf{n}$ can be written as

$$\cos\Theta = \sin\theta_0\sin\theta\cos\phi + \cos\theta_0\cos\theta. \tag{19}$$

Since $n_{0,2}=0$ in Eq. (17), the terms proportional to Φ_{i2} and Φ_{2j} do not contribute to σ. Furthermore, the terms proportional to Φ_{i3} and Φ_{3j} are much less than the term proportional to Φ_{11} if the angle θ_0 is not too small. If $\theta_0=0$, the terms proportional to Φ_{i3} and Φ_{3j} are small in comparison with the term proportional to Φ_T for most "reasonable" values of N.

Thus, in Eq. (17), the sum $n_{0,i}n_{0,j}\Phi_{ij}$ can be approximated as $\sin^2\theta_0\Phi_{11}$. Furthermore, in this equation, we replace Φ_T and Φ_{11} by their values given by Eqs. (9) and (12), respectively. Finally, using Eq. (18), we obtain a desired formula for the scattering cross section due to sound scattering by IGW

$$\sigma = \frac{K_0^2\cos^2\Theta\exp\left\{-\dfrac{\sin^2\theta_0+\sin^2\theta-2\sin\theta_0\sin\theta\cos\phi}{4e_0[K_0^2/(4k^2)+(\cos\theta_0-\cos\theta)^2]}\right\}}{2^9 e_0 k[K_0^2/(4k^2)+(\cos\theta_0-\cos\theta)^2]^{5/2}} \times\left[\frac{\sigma_T^2}{T_0^2}+4\sin^2\theta_0\frac{\sigma_v^2}{c_0^2}\right]. \tag{20}$$

It is worthwhile to compare the obtained value of σ with that for the case of sound scattering by isotropic temperature and wind velocity fluctuations with the von Kármán spectra. The latter scattering cross section was calculated in Ref. 26

$$\sigma_{vK} = \frac{b_1 k^{1/3}K_T^{2/3}\cos^2\Theta}{[K_T^2/(4k^2)+\sin^2(\Theta/2)]^{11/6}} \times\left[\frac{\sigma_{T,vK}^2}{T_0^2}+\frac{11\sin^2\Theta}{6[K_T^2/(4k^2)+\sin^2(\Theta/2)]}\frac{\sigma_{v,vK}^2}{c_0^2}\right]. \tag{21}$$

Hereinafter, for simplicity, $K_T=K_v$. Furthermore, in Eq. (21) and for some equations below, involved numerical coefficients are denoted by b with subscripts; in Eq. (21) $b_1=5\pi/(2^{13/3}3^{3/2}\Gamma^3(1/3))=0.0078$.

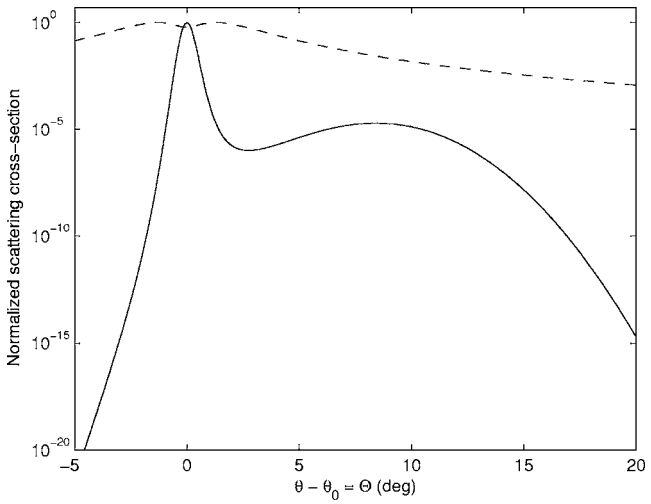

FIG. 3. The normalized scattering cross section versus the difference $\theta-\theta_0=\Theta$. For this plot, the sound frequency $f=3$ Hz, the anisotropy parameter $e_0=10^{-4}$, the angle $\theta_0=85°$, and the scale $L_0=3$ km. The solid and dashed lines correspond to σ and σ_{vK}, respectively, normalized by their maximum values.

B. Analysis

Let us compare the sound scattering cross sections σ and σ_{vK} given by Eqs. (20) and (21), respectively. In atmospheric acoustics, the terms $K_0^2/(4k^2)$ and $K_T^2/(4k^2)$ appearing in these equations are both small and can be neglected for most geometries of scattering.

There are several differences between σ and σ_{vK}. First, σ_{vK} depends only on the scattering angle Θ between the unit vectors $\mathbf{n}_0$ and $\mathbf{n}$, as must be the case for scattering by isotropic turbulence, while σ depends not only on Θ but also on the orientation of these unit vectors. Second, σ and σ_{vK} have different dependencies on the frequency $f=kc_0/(2\pi)$ of a sound wave: If $K_0^2/(4k^2)$ and $K_T^2/(4k^2)$ can be neglected in Eqs. (20) and (21), $\sigma\sim 1/f$ while $\sigma_{vK}\sim f^{1/3}$. Third, in Eqs. (20) and (21) the factors in front of the terms σ_v^2/c_0^2 and $\sigma_{v,vK}^2/c_0^2$ are different. Therefore, relative contributions to σ and σ_{vK} due to sound scattering by temperature and velocity fluctuations are different.

Finally, let us compare the dependence of the sound scattering cross sections σ and σ_{vK} on the scattering angle Θ. In Fig. 3, the solid curve corresponds to the dependence of σ, normalized by its maximum value, on the difference $\theta-\theta_0$. When plotting this curve, it was assumed that $\sigma_T^2/T_0^2=\sigma_v^2/c_0^2$, $e_0=10^{-4}$, $\theta_0=85°$, $f=3$ Hz, and $L_0=3$ km. (The numerical value of L_0 corresponds to IGW in the stratosphere; see Sec. II A.) Furthermore, it was assumed that the azimuthal angle $\phi=0$. In this case, both $\mathbf{n}_0$ and $\mathbf{n}$ lie in the xz plane (see Fig. 2) so that the difference $\theta-\theta_0$ is equal to the scattering angle Θ. The dashed curve in Fig. 3 corresponds to the dependence of σ_{vK}, also normalized by its maximum value, on the scattering angle Θ. When plotting the dashed curve, we assumed that $\sigma_{T,vK}^2/T_0^2=\sigma_{v,vK}^2/c_0^2$, $K_T=K_0$, and, as for the solid curve, $f=3$ Hz.

Figure 3 shows two maxima in the dependence of σ on $\theta-\theta_0=\Theta$. The first maximum occurs at $\theta=\theta_0$ (i.e., at $\Theta=0$) and corresponds to forward scattering of a sound wave. The appearance of this maximum is well known in theories of

sound scattering by isotropic turbulence: σ_{vK} reaches its maximum values for predominantly forward scattering. (In Fig. 3, a small dip in the dashed curve at $\Theta=0$ is due to the fact that sound scattering by isotropic velocity fluctuations is zero at $\Theta=0$; this dip would disappear for the case of sound scattering by only temperature fluctuations.) The second, much broader maximum in the dependence of σ on Θ occurs at $\Theta=\pi-2\theta_0=10°$. This maximum occurs in the direction of specular reflection of the incident wave from a horizontal plane. The appearance of this maximum is due to the fact that random inhomogeneities in temperature and wind velocity are highly stretched in horizontal planes, effectively producing a random layered medium. A plane wave incident on such a random layered medium is transmitted through, and reflected from, the medium. The transmitted and reflected waves correspond to two maxima in the solid curve in Fig. 3. Note that the dashed curve in this figure does not have a maximum at $\Theta=10°$.

The second maximum in the solid curve in Fig. 3 can explain an interesting phenomenon in infrasound propagation occurring at heights of about 35–45 km. The infrasound waves are often partially "reflected" from these heights even though the effective sound speed in the stratosphere is less than that near the ground, which prevents such reflection in geometrical acoustics.[27] The second maximum in the dependence of σ on Θ occurs at $\theta=105°$, i.e., when the scattered wave propagates back to the ground. Therefore, Fig. 3 shows that a significant portion of infrasound energy can be scattered back to the ground from the stratosphere.

C. Backscattering

An important particular case of sound scattering in the atmosphere is backscattering, which occurs for $\Theta=180°$. The backscattering cross section $\sigma(\Theta=180°)$ can be measured by monostatic sodars.[28,29]

For the case of backscattering, Eq. (20) can be simplified by taking into account that $\mathbf{n}=-\mathbf{n}_0$, $\theta=\pi-\theta_0$, and $\phi=\pi$. As a result, we obtain the following formula for the backscattering cross section due to sound scattering by IGW:

$$\sigma(180°)=\frac{K_0^2\exp\left\{-\dfrac{\sin^2\theta_0}{4e_0[K_0^2/(16k^2)+\cos^2\theta_0]}\right\}}{2^{14}e_0k[K_0^2/(16k^2)+\cos^2\theta_0]^{5/2}}\times\left[\frac{\sigma_T^2}{T_0^2}+4\sin^2\theta_0\frac{\sigma_v^2}{c_0^2}\right]. \tag{22}$$

For the von Kármán spectra of temperature and velocity fluctuations, the backscattering cross section is given by

$$\sigma_{vK}(180°)=\frac{b_1k^{1/3}K_T^{2/3}}{[1+K_T^2/(4k^2)]^{11/6}}\frac{\sigma_{T,vK}^2}{T_0^2}. \tag{23}$$

It follows from Eqs. (22) and (23) that velocity fluctuations can contribute to $\sigma(180°)$; however, they do not contribute to $\sigma_{vK}(180°)$. Furthermore, $\sigma(180°)$ significantly depends on θ_0 while $\sigma_{vK}(180°)$ does not.

Figure 4 shows the dependence of $\sigma(180°)$ (normalized by its value at $\theta_0=0$) on the angle θ_0 for different values of e_0: 3×10^{-4}—dash-dotted line; 10^{-3}—dashed line; and 3×10^{-3}—solid line. When plotting Fig. 4, it was assumed that $f=3$ kHz and $L_0=300$ m. (The numerical value of L_0 corresponds to IGW in NBL, see Sec. II A.) It follows from Fig. 4 that the backscattering cross section decreases rapidly with the increase of the angle θ_0. One would expect such dependence of $\sigma(180°)$ on θ_0 for a layered random medium.

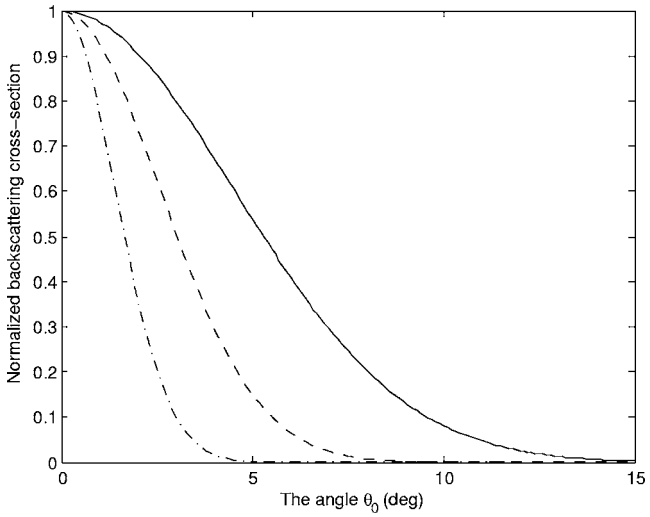

FIG. 4. The normalized backscattering cross section versus the angle θ_0. Dash-dotted line corresponds to $e_0=3\times10^{-4}$, dashed line to $e_0=10^{-3}$, and solid line to $e_0=3\times10^{-3}$. For this figure, the sound frequency $f=3$ kHz and the scale $L_0=300$ m.

IV. LINE-OF-SIGHT SOUND PROPAGATION THROUGH IGW

In this section, we will consider line-of-sight sound propagation in an atmosphere with temperature and wind velocity fluctuations induced by IGW. We will assume that a sound wave propagates nearly horizontally in the direction of the x axis. This is a reasonable assumption for many problems of atmospheric acoustics, e.g., for near-ground sound propagation.

A. Effective 3D spectrum

A theory of line-of-sight sound propagation through anisotropic, inhomogeneous turbulence with temperature and wind velocity fluctuations has been recently developed in Refs. 12–14. Using the Markov approximation and the Rytov or parabolic equation method, formulas for the variances and correlation functions of log-amplitude and phase fluctuations, the mean field, and the coherence function of plane and spherical sound waves were derived. These statistical moments of a sound field were expressed in terms of the effective 3D spectral density of random inhomogeneities[11–14]

$$\Phi_{\text{eff}}(\mathbf{K})=\frac{\Phi_T(\mathbf{K})}{T_0^2}+\frac{4\Phi_{11}(\mathbf{K})}{c_0^2}. \tag{24}$$

Using Eqs. (9) and (12), the effective 3D spectral density can be calculated for the case of sound propagation through IGW

$$\Phi_{\text{eff}}(\mathbf{K}) = \frac{K_0^2 \exp\left[-\dfrac{K_\perp^2}{4e_0(K_0^2+K_3^2)}\right]}{8\pi e_0 (K_0^2+K_3^2)^{5/2}} \left[\frac{\sigma_T^2}{T_0^2} + 4\frac{\sigma_v^2}{c_0^2}\right]. \quad (25)$$

Using this formula for $\Phi_{\text{eff}}(\mathbf{K})$ and equations obtained in Refs. 12–14, the above-mentioned statistical moments of plane- and spherical sound waves propagating through IGW can be readily calculated. In this section, we will calculate and analyze the mean sound field and the coherence function of a plane sound wave.

B. Mean sound field

The mean field $\langle p \rangle$ of a sound wave propagating in a random medium attenuates exponentially[11]

$$\langle p(\mathbf{R}) \rangle = p_0(\mathbf{R}) e^{-\gamma x}. \quad (26)$$

Here, $\mathbf{R}=(x,y,z)$, p_0 is the sound field in the absence of random inhomogeneities, x in the exponent indicates the distance of sound propagation in a turbulent atmosphere, and γ is the extinction coefficient given by[14]

$$\gamma = \frac{\pi k^2}{4} \int_{-\infty}^{\infty} dK_2 \int_{-\infty}^{\infty} \Phi_{\text{eff}}(0,K_2,K_3) dK_3. \quad (27)$$

The extinction coefficient γ is an important statistical characteristic of a field propagating in a random medium. It indicates the rate at which the coherent part of the field is transformed into the incoherent one.

Substituting the value of Φ_{eff} from Eq. (25) into Eq. (27), and calculating the integrals over K_2 and K_3, we obtain the following formula for the extinction coefficient of the mean sound field propagating through IGW:

$$\gamma = \frac{b_2 k^2}{\sqrt{e_0} K_0} \left[\frac{\sigma_T^2}{T_0^2} + 4\frac{\sigma_v^2}{c_0^2}\right], \quad (28)$$

where $b_2 = \pi^{3/2}/32 \cong 0.174$.

Let us compare Eq. (28) with the extinction coefficient γ_{vK} of the mean sound field propagating in a turbulent atmosphere with the von Kármán spectra of temperature and velocity fluctuations, which can be obtained with the use of Eqs. (7.110) and (7.111) from Ref. 11

$$\gamma_{vK} = \frac{b_3 k^2}{K_T} \left[\frac{\sigma_{T,vK}^2}{T_0^2} + 4\frac{\sigma_{v,vK}^2}{c_0^2}\right]. \quad (29)$$

Here, $b_3 = \pi^2/(2^{2/3}\sqrt{3}\Gamma^3(1/3)) \cong 0.187$. It follows from Eqs. (28) and (29) that the dependencies of γ and γ_{vK} on the parameters of the problem are similar with one exception: The denominator in Eq. (28) contains a small factor $\sqrt{e_0}$.

The inverse of the extinction coefficient, γ^{-1}, is equal to the distance x of sound propagation in a random medium at which the mean sound field has decayed by a factor $1/e$. It follows from Eq. (28) that $\gamma^{-1} = \sqrt{e_0} c_0^2/(2\pi b_2 f^2 M)$, where $M = L_0(\sigma_T^2/T_0^2 + 4\sigma_v^2/c_0^2)$ is the outer scale-variance product. The values of γ^{-1} versus f and M are depicted in Fig. 5(a). Similarly, it can be shown from Eq. (29) that $\gamma_{vK}^{-1} = c_0^2/(2\pi b_3 f^2 M_{vK})$, where $M_{vK} = L_T(\sigma_{T,vK}^2/T_0^2 + 4\sigma_{v,vK}^2/c_0^2)$ is the outer scale-variance product for the von Kármán spectra. Here, $L_T = 2\pi/K_T$. Figure 5(b) shows γ_{vK}^{-1} as a function of f and M_{vK}. Figures 5(a) and 5(b) give us typical values of γ^{-1} and γ_{vK}^{-1} in the atmosphere. It also follows from these figures that $\gamma^{-1} \ll \gamma_{vK}^{-1}$ provided that $M = M_{vK}$.

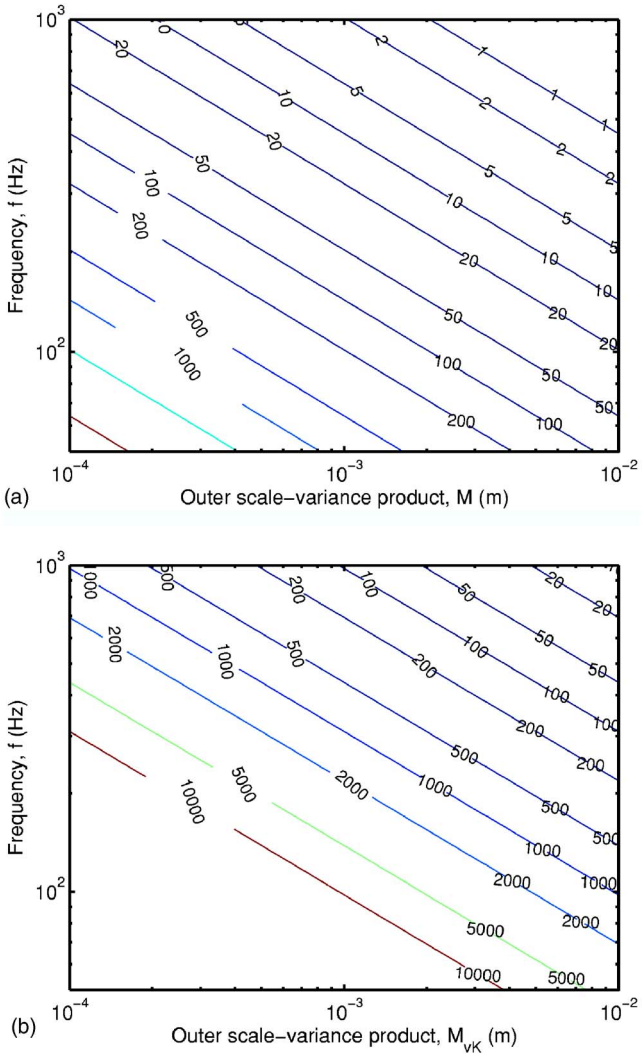

FIG. 5. (Color online) (a) The inverse of the extinction coefficient, γ^{-1}, for IGW as a function of the frequency f and the outer scale-variance product $M = L_0(\sigma_T^2/T_0^2 + 4\sigma_v^2/c_0^2)$. The values of γ^{-1} are in meters. For this plot, $e_0 = 4 \times 10^{-4}$. (b) The inverse of the extinction coefficient, γ_{vK}^{-1}, for the von Kármán spectra as a function of the frequency f and the outer scale-variance product $M_{vK} = L_T(\sigma_{T,vK}^2/T_0^2 + 4\sigma_{v,vK}^2/c_0^2)$. The values of γ_{vK}^{-1} are in meters.

C. Coherence function of a plane sound wave

Let the two points of observation (x, y_1+y, z_1+z) and (x, y_1, z_1) be located in a plane perpendicular to the x axis. Here, y and z are the distances between these two points along the y- and z axes. The transverse coherence function of a sound field p is determined by

$$\Gamma(x;y,z) = \langle p(x, y_1+y, z_1+z) p^*(x, y_1, z_1) \rangle. \quad (30)$$

For the considered case of plane-wave propagation, the transverse coherence function does not depend on the coordinates y_1 and z_1; e.g., see Ref. 30.

In Ref. 14, the following formula for Γ was derived:

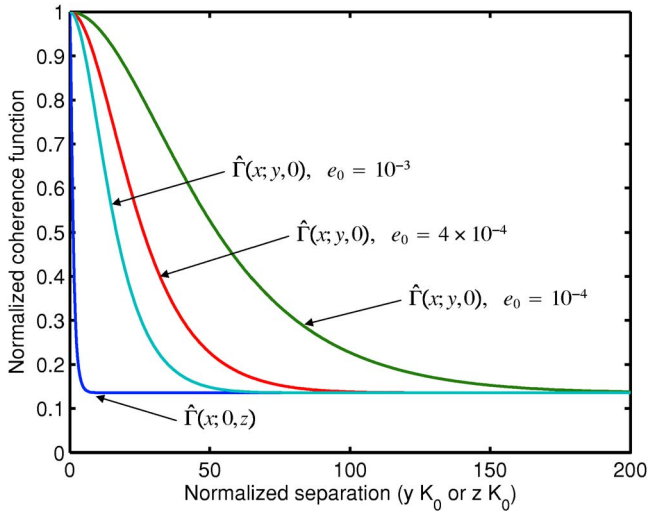

FIG. 6. (Color online) The normalized coherence function $\hat{\Gamma}(x;y,z)$ of a plane sound wave propagating through IGW. The curves show this function for $x=\gamma^{-1}$ and for either a vertical separation ($y=0$) or a horizontal separation ($z=0$) between two points of observation. The abscissa is yK_0 for horizontal separations or zK_0 for vertical separations. Three curves are shown for horizontal separations, which correspond to $e_0=10^{-4}$, $e_0=4\times10^{-4}$, and $e_0=10^{-3}$.

$$\Gamma(x;y,z)=|A_0^2|\exp\left\{-\frac{\pi k^2 x}{2}\int_{-\infty}^{\infty}dK_2 \times\int_{-\infty}^{\infty}[1-e^{i(yK_2+zK_3)}]\Phi_{\text{eff}}(0,K_2,K_3)\right\}dK_3. \tag{31}$$

Here, A_0 is the amplitude of the plane sound wave at $x=0$. After substituting the expression for Φ_{eff} given by Eq. (25) into Eq. (31), some algebra yields a formula for the coherence function of a plane sound wave propagating through IGW

$$\Gamma(x;y,z)=|A_0^2|\exp[-x\gamma F(y,z)]. \tag{32}$$

Here, the function F characterizes the dependence of the coherence function on y and z

$$F(y,z)=\frac{4}{\pi}\int_{-\infty}^{\infty}\frac{1-\exp[izK_0\xi-e_0y^2K_0^2(1+\xi^2)]}{(1+\xi^2)^2}d\xi. \tag{33}$$

Figure 6 shows the normalized coherence function of a plane sound wave $\hat{\Gamma}(x;y,z)=\Gamma(x;y,z)/|A_0^2|$ calculated with the use of Eqs. (32) and (33). The calculations were made for $x\gamma=1$ and three values of e_0. Results for both vertical ($y=0$) and horizontal ($z=0$) separations between two points of observation are shown. The coherence is observed to decay much more rapidly with increasing vertical separation than with increasing horizontal separation. This trend is enhanced for smaller values of e_0.

It is also worthwhile to consider two limiting cases when analytical formulas for $\Gamma(x;y,z)$ can be obtained. In the first limiting case, the values of y and z are relatively large

$$zK_0\gg1,\quad e_0y^2K_0^2\gg1. \tag{34}$$

It can be shown that, in this case, $F\approx2$, so that

$$\Gamma(x;y,z)=|A_0^2|\exp(-2x\gamma). \tag{35}$$

This formula represents the correct asymptotic behavior of the coherence function for relatively large distances between the observation points. Indeed, in this case $p(x,y_1+y,z_1+z)$ and $p^*(x,y_1,z_1)$ do not correlate, so that Eq. (30) takes the form: $\Gamma(x;y,z)=\langle p(x,y_1+y,z_1+z)\rangle\langle p^*(x,y_1,z_1)\rangle$. Replacing $\langle p\rangle$ and $\langle p^*\rangle$ in this formula with their values given by Eq. (26) results in Eq. (35). Note that, for $x\gamma=1$, it follows from Eq. (35) that $\Gamma(x;y,z)/|A_0^2|=1/e^2$. This result is in agreement with Fig. 6, where all four curves reach their asymptote $1/e^2$ for large values of y or z.

Let $\Gamma_{vK}(x;r)$ be the coherence function of a plane sound wave for the case of the von Kármán spectra of temperature and velocity fluctuations, where $r=\sqrt{y^2+z^2}$. The value of $\Gamma_{vK}(x;r)$ is given by Eq. (7.112) from Ref. 11. It can be shown that, if $rK_T\gg1$ [which is similar to inequalities Eq. (34)], Γ_{vK} is given by Eq. (35) if γ is replaced with γ_{vK}.

Let us now consider the other limiting case of $\Gamma(x;y,z)$ when the values of y and z are relatively small

$$zK_0\ll1,\quad e_0y^2K_0^2\ll1. \tag{36}$$

It can be shown that, in this case, $F\approx4e_0y^2K_0^2+z^2K_0^2$. Substituting this value of F into Eq. (32), we obtain

$$\Gamma(x;y,z)=|A_0^2|\exp[-x\gamma(4e_0y^2K_0^2+z^2K_0^2)]. \tag{37}$$

If $rK_T\ll1$ [which is similar to Eq. (36)], $\Gamma_{vK}(x;r)$ can also be simplified

$$\Gamma_{vK}(x;r)=|A_0^2|\exp(-b_4\eta x\gamma_{vK}K_T^{5/3}r^{5/3}). \tag{38}$$

Here, $b_4=3^{3/2}\Gamma^3(1/3)/(2^{1/3}5\Gamma(2/3)\pi)\cong3.73$, and the numerical coefficient η is given by

$$\eta=\frac{\sigma_{T,vK}^2/T_0^2+(22/3)\sigma_{v,vK}^2/c_0^2}{\sigma_{T,vK}^2/T_0^2+4\sigma_{v,vK}^2/c_0^2}. \tag{39}$$

This coefficient depends on the values of the variances of the temperature and velocity fluctuations for the von Kármán spectra, $\sigma_{T,vK}^2$ and $\sigma_{v,vK}^2$, and varies in the range $1\leqslant\eta\leqslant11/6$.

The most noticeable difference between the coherence functions given by Eqs. (37) and (38) is that $\Gamma(x;y,z)$ is a highly anisotropic function of the coordinates y and z, while $\Gamma_{vK}(x;r=\sqrt{y^2+z^2})$ is an isotropic function of these coordinates. Furthermore, in Eq. (37) y and z are both squared, while in Eq. (38) they have a different power.

D. Coherence radius

The coherence radius is an important characteristic of the coherence function. It indicates the distance between the two points of observation at which the coherence function decreases by a factor of e^{-1}.

Let us consider the limiting case of relatively small values of y and z when Eq. (36) holds and when the coherence radius can be determined analytically. In this case, the coherence radius y_c along the y axis can be determined by setting $z=0$ and equating the exponential term in Eq. (37) to e^{-1}

$$y_c = \frac{1}{2K_0\sqrt{e_0\gamma x}}. \tag{40}$$

Similarly, setting $y=0$, we obtain the coherence radius z_c along the z axis

$$z_c = \frac{1}{K_0\sqrt{\gamma x}}. \tag{41}$$

Comparing Eqs. (40) and (41) reveals that the coherence radius along the y axis is much greater than that along the z axis: $y_c = z_c/(2\sqrt{e_0})$. Since y and z must satisfy Eq. (36), the coherence radii y_c and z_c exist if $\gamma x > 1$.

Using the formula Eq. (38) for $\Gamma_{vK}(x;r)$, it can be shown that, for $rK_T \ll 1$, the coherence radii $y_{c,vK}$ and $z_{c,vK}$ for the von Kármán spectra of temperature and wind velocity fluctuations are given by

$$y_{c,vK} = z_{c,vK} = \frac{1}{K_T(b_4\eta x\gamma_{vK})^{3/5}}. \tag{42}$$

Comparing Eqs. (40)–(42) reveals that, for the case of sound propagation through IGW, the coherence radii have a different power dependence on the propagation distance and extinction coefficient than those for the case of the von Kármán spectra of temperature and velocity fluctuations.

V. CONCLUSIONS

In this paper, we have developed a theory of sound propagation through, and scattering by, IGW in a stably stratified atmosphere.

First, the 3D spectra of temperature and horizontal wind velocity fluctuations due to IGW recently developed in Ref. 5 for the case of large wave numbers were generalized to account for small wave numbers. The variances of temperature and wind velocity fluctuations of the generalized 3D spectra were calculated.

Then, the generalized 3D spectra of temperature and wind velocity fluctuations were used to study sound scattering by IGW. A formula for the sound scattering cross section σ was derived. It was shown that σ has different dependencies on the sound frequency, scattering angle, and other parameters of the problem than does the scattering cross section due to sound scattering by temperature and wind velocity fluctuations with the von Kármán spectra. Furthermore, the scattering cross section σ has two maxima as a function of the scattering angle. The first maximum occurs in the direction of propagation of a sound wave incident on the scattering volume. The second maximum appears in the direction at which the incident sound wave would be specularly reflected from a horizontal plane. This second maximum is due to the fact that temperature and wind velocity fluctuations induced by IGW are highly stretched in a horizontal direction. The second maximum can explain the interesting phenomenon of a partial infrasound "reflection" from the stratosphere which is observed experimentally.

The generalized 3D spectra of temperature and wind velocity fluctuations were also used to study line-of-sight sound propagation through an atmosphere with IGW. The extinction coefficient γ of the mean sound field was calculated and compared with that for the case of sound propagation through isotropic turbulence with the von Kármán spectra of temperature and wind velocity fluctuations. Furthermore, the transverse coherence function $\Gamma(x;y,z)$ of a plane sound wave propagating through an atmosphere with IGW was calculated. It was shown that $\Gamma(x;y,z)$ is an anisotropic function of the transverse coordinates y and z, while the coherence function for the von Kármán spectra of temperature and wind velocity fluctuations is an isotropic function of these coordinates.

Finally, note that the variances and correlation functions of log-amplitude and phase fluctuations of plane and spherical sound waves, and the transverse coherence function of a spherical sound wave can be readily calculated using the general formulas for these statistical moments obtained in Refs. 12–14 and Eq. (25) for the effective 3D spectral density, derived in the present paper.

ACKNOWLEDGMENTS

This article is partly based upon work supported by the U.S. Army Research Office Grant DAAG19-01-1-0640 and the Russian Foundation of Basic Research, Grant 03 05-04001.

[1] E. E. Gossard and W. H. Hoke, *Waves in the Atmosphere* (Elsevier, Amsterdam, 1975).
[2] R. B. Stull, *An Introduction to Boundary Layer Meteorology* (Kluwer, Dordrecht, 1988).
[3] D. C. Fritts, T. Tsuda, T. Sato, S. Fukao, and S. Kato, "Observational evidence of a saturated gravity wave spectrum in the troposphere and lower stratosphere," J. Atmos. Sci. **45**, 1741–1758 (1988).
[4] C. A. Hostetler and C. S. Gardner, "Observations of horizontal and vertical wave number spectra of gravity wave motions in the stratosphere and mesosphere over the mid-Pacific," J. Geophys. Res. **99**, 1283–1302 (1994).
[5] I. P. Chunchuzov, "On the high-wave number form of the Eulerian internal wave spectrum in the atmosphere," J. Atmos. Sci. **59**, 1753–1774 (2002).
[6] K. R. Allen and R. I. Joseph, "A canonical statistical theory of oceanic internal waves," J. Fluid Mech. **204**, 185–228 (1989).
[7] C. O. Hines, "Theory of the Eulerian tail in the spectra of atmospheric and oceanic internal gravity waves," J. Fluid Mech. **448**, 289–313 (2001).
[8] S. D. Eckermann, "Isentropic advection by gravity waves: Quasi-universal M^{-3} vertical wave number spectra near the onset of instability," Geophys. Res. Lett. **26**, 201–204 (1999).
[9] C. O. Hines, L. I. Childress, J. B. Kinney, and M. P. Sulzer, "Modeling of gravity-wave tail spectra in the middle atmosphere via numerical and Doppler-spread methods," J. Atmos. Sol.-Terr. Phys. **66**, 933–948 (2004).
[10] E. M. Dewan and R. E. Good, "Saturation and the 'universal' spectrum for vertical profiles of horizontal scalar winds in the atmosphere," J. Geophys. Res. **91**, 2742–2748 (1986).
[11] V. E. Ostashev, *Acoustics in Moving Inhomogeneous Media* (E&FN SPON, London, 1997).
[12] V. E. Ostashev and D. K. Wilson, "Log-amplitude and phase fluctuations of a plane wave propagating through anisotropic, inhomogeneous turbulence," Acust. Acta Acust. 87, No. 6, 685–694 (2001).
[13] V. E. Ostashev, D. K. Wilson, and G. H. Goedecke, "Spherical wave propagation through inhomogeneous, anisotropic turbulence: Studies of log-amplitude and phase fluctuations," J. Acoust. Soc. Am. **115**, 120–130 (2004).
[14] V. E. Ostashev and D. K. Wilson, "Coherence function and mean field of plane and spherical sound waves propagating through inhomogeneous anisotropic turbulence," J. Acoust. Soc. Am. **115**, 497–506 (2004).
[15] D. C. Fritts and P. K. Rastogi, "Convective and dynamic instabilities due to gravity wave motions in the lower and middle atmosphere: Theory and observations," Radio Sci. **20**, 1247–1277 (1985).
[16] A. S. Gurvich and I. P. Chunchuzov, "Parameters of the fine density structure in the stratosphere obtained from spacecraft observations of stellar scintillations," J. Geophys. Res. **108** (D5), ACL 6-1–ACL 6-4 (2003).

[17]J. A. Whiteway and T. J. Duck, "Evidence for critical level filtering of atmospheric gravity waves," Geophys. Res. Lett. **23**, 145–148 (1996).
[18]R. A. Vincent, S. J. Allen, and S. D. Eckermann, "Gravity wave parameters in the lower stratosphere," in *Gravity Wave Processes: Their Parameterization in Global Climate Models*, edited by K. Hamilton (Springer, Berlin, 1997), pp. 7–25.
[19]J. T. Bacmeister, S. D. Eckermann, A. Tsias, K. S. Carslaw, and T. Peter, "Mesoscale temperature fluctuations induced by a spectrum of gravity waves: A comparison of parametrization and their impact on stratospheric microphysics," J. Atmos. Sci. **56**, 1913–1924 (1999).
[20]E. M. Dewan, N. Grossbard, A. F. Queseda, and R. E. Good, "Spectral analysis of 10-m resolution scalar velocity profiles in the stratosphere," Geophys. Res. Lett. **11**, 80–83 (1984).
[21]C. O. Hines, "The saturation of gravity waves in the middle atmosphere. I. Critique of linear instability theory," J. Atmos. Sci. **48**, 1348–1359 (1991).
[22]*Atmospheric Turbulence and Air Pollution Modeling*, edited by F. T. M. Neuwstadt and Y. Van Dop (Reidel, London, 1982).
[23]I. P. Chunchuzov, "Influence of internal gravity waves on sound propagation in the lower atmosphere," Meteorol. Atmos. Phys. **85**, 61–76 (2004).
[24]J. Hinze, *Turbulence* (McGraw-Hill, New York, 1975).
[25]E. M. Salomons, *Computational Atmospheric Acoustics* (Kluwer Academic, Dordrecht, 2001).
[26]V. E. Ostashev and G. H. Goedecke, "Sound scattering cross section for von Kármán spectra of temperature and wind velocity fluctuations," in Proceedings 1997 Battlespace Atmospheric Conference, San Diego, 171–180 (1998).
[27]S. N. Kulichkov, "Long-range propagation and scattering of low-frequency sound pulses in the middle atmosphere," Meteor. Atmos. Phys. **85**, 47–60 (2004).
[28]E. H. Brown and F. F. Hall, "Advances in atmospheric acoustics," Rev. Geophys. Space Phys. **16**(1), 47–110 (1978).
[29]S. P. Singal, "Acoustic sounding stability studies," in *Encyclopedia of Environment Control Technology. V. 2: Air Pollution Control* (Gulf Publishing, Houston,1989), pp. 1003–1061.
[30]S. M. Rytov, Yu. A. Kravtsov, and V. I. Tatarskii, *Principles of Statistical Radio Physics. Part 4, Wave Propagation through Random Media* (Springer, Berlin, 1989).

Debye-series analysis of the transmission coefficient of a water-saturated porous plate obeying Biot's theory

Serge Derible[a)]
LAUE UMR 6068, Université du Havre, IUT Caucriauville, Place Robert Schuman, 76610 Le Havre, France

(Received 8 November 2004; revised 18 July 2005; accepted 22 July 2005)

We derive the Debye-series expansion of the normal transmitted plane wave through a water-saturated porous plate. By using relations from Biot's theory, the theoretical transmission coefficient of the plate is related to a limited number of unknown parameters (velocity, attenuation coefficient of the fast and slow wave, reflection coefficients at the interfaces of the plate). They are determined via a comparison with the experimental transmission coefficient. The measurements show that the attenuation of the dilatational waves scales as the second power of frequency. © *2005 Acoustical Society of America.* [DOI: 10.1121/1.2118248]

PACS number(s): 43.20.Gp, 43.20.Jr [ANN] Pages: 3430–3435

I. INTRODUCTION

Propagation of sound in fluid-saturated porous media is an important phenomenon developed by Biot[1] in two pioneering papers published in the mid-1950s. Later, Stoll *et al.*[2] extended Biot's theory with a mathematical model able to describe the propagation of elastic waves in water-saturated sediments. Their model was of considerable interest in theoretical and experimental aspects of sound reflection/transmission at water-sediment interface.[3–5] In several papers, Johnson *et al.*[6–10] studied the influence on sound propagation of some typical aspects of porous media: tortuosity, porosity, permeability. They investigated wave propagation in sand and also in commercially available plates made with a porous material named QF-20 and produced by Filtros®. In this paper, we propose an alternative way to find dispersion and attenuation of the compressional waves which propagate in a water-saturated QF-20 plate. Berryman[11] established the prominent role played by the permeability in wave attenuation in rocks and in partially consolidated porous materials. In much of this literature, the background question is in fact the loss mechanism and the resulting frequency dependence of the attenuation. An overview of this problem is presented by Buckingham.[12,13] Biot-Stoll's model allows us to study not only liquid-saturated media, but also gas-saturated porous materials.[14–16] However, the former case encounters some tricky points not found in the second configuration. The coupling between the liquid and the solid phases, which arises during wave propagation, brings supplementary difficulties. That is one of the reasons why recent advanced methods, elaborated for air-saturated porous materials, have limited success when applied on water-saturated porous media (page 38 of Ref. 16).

At normal incidence, only the two compressional bulk waves, the fast wave and the slow one, can propagate in the plate.[4,9,10] Three possibilities may occur at the interfaces and each of them gives three coefficients written into brackets:[17]

(1) a wave incident from fluid onto the plate generates a reflected wave ($r_{1,p}$), a fast transmitted wave ($t^f_{1,p}$), and a slow transmitted one ($t^s_{1,p}$).
(2) an incident fast wave onto the plate-fluid interface generates a fast reflected wave ($r^{f,f}_{p,1}$), a slow reflected one ($r^{f,s}_{p,1}$), and a transmitted wave ($t^f_{p,1}$).
(3) an incident slow wave onto the plate-fluid interface generates a slow reflected wave ($r^{s,s}_{p,1}$), a fast reflected one ($r^{s,f}_{p,1}$), and a transmitted wave ($t^s_{p,1}$).

Those nine coefficients are solutions of the matrix equations issued from the stress-strain relations and the boundary conditions at the interfaces.[8,17] This method leads to expressions of the refraction coefficients expanded into the complex parameters introduced by Biot and Stoll. However, relationships connecting exclusively the reflection and transmission coefficients at the interfaces of a porous plate imbedded in a fluid have not yet been established; it will be performed in this paper.

The organization of the paper is as follows. First, properties of the refraction coefficients at the interfaces of a fluid-saturated porous plate obeying Biot's theory are presented. For later convenience, these coefficients are called "local." Next, a theoretical expression of the transmission coefficient of the plate (ratio of the amplitude of the wave emerging from the second face to this of the incident one striking the front face) is obtained by means of the velocities, the attenuation coefficients of the fast and slow waves, and the local refraction coefficients. The transmission coefficient is represented as a Debye series.[18,19] Then, the experimental setup and the recorded signals are described. Finally, the parameters of the theoretical transmission coefficient are modified to fit the experimental transmission coefficient of the plate. As a result, the velocities, the attenuation coefficients, and some of the local refraction coefficients are measured. There is good agreement with the theoretical predictions and with other experimental determinations.

a)Electronic mail: serge.derible@univ-lehavre.fr

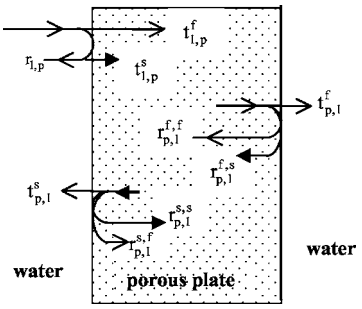

FIG. 1. The three cases of normal reflection/transmission at the interfaces and the related reflection or transmission coefficient. In the plate, a fast wave and a slow one are, respectively, represented by the symbols: →, ➛.

II. THEORY

A. Local reflection and transmission coefficients of interfaces

The three cases of normal reflection/transmission of the interfaces separating a porous media and water are shown in Fig. 1. For each kind of incident wave onto a given interface, these coefficients are the ratios of the amplitude of the reflected/transmitted wave divided by the amplitude of the incident wave. The notations used here, restricted to the dilatational waves, are those of Stoll's papers[3,4] in which the waves are written in the form $\exp[\boldsymbol{i}(\omega t - kx)]$. The wave number is $k_1 = \omega/c_1$ in water. In the porous media, the biquadratic equation presented by Stoll has two complex solutions with positive real parts: $k_f = \omega/c_f + \boldsymbol{i}k_i^f$ and $k_s = \omega/c_s + \boldsymbol{i}k_i^s$. The imaginary parts of the wave numbers express wave attenuation, provided they are negative.

On rearrangement, the boundary conditions lead to the following matrix equations satisfied by the local reflection and transmission coefficients;

$$\begin{pmatrix} 1 & m_{12} & m_{13} \\ -1 & m_{22} & m_{23} \\ -1 & m_{32} & m_{33} \end{pmatrix} \begin{pmatrix} r_{1,p} \\ t_{1,p}^f \\ t_{1,p}^s \end{pmatrix} = \begin{pmatrix} 1 \\ 1 \\ 1 \end{pmatrix}, \tag{1}$$

$$\begin{pmatrix} m_{12} & m_{13} & 1 \\ m_{32} & m_{33} & -1 \\ m_{22} & m_{23} & -1 \end{pmatrix} \begin{pmatrix} r_{p,1}^{f,f} \\ r_{p,1}^{f,s} \\ t_{p,1}^f \end{pmatrix} = \begin{pmatrix} m_{12} \\ -m_{32} \\ -m_{22} \end{pmatrix}, \tag{2}$$

$$\begin{pmatrix} m_{12} & m_{13} & 1 \\ m_{32} & m_{33} & -1 \\ m_{22} & m_{23} & -1 \end{pmatrix} \begin{pmatrix} r_{p,1}^{s,f} \\ r_{p,1}^{s,s} \\ t_{p,1}^s \end{pmatrix} = \begin{pmatrix} m_{13} \\ -m_{33} \\ -m_{23} \end{pmatrix}. \tag{3}$$

The terms of the matrices are

$$m_{12} = \frac{k_f}{k_1}(1+\gamma_f), \quad m_{13} = \frac{k_s}{k_1}(1+\gamma_s),$$

$$m_{22} = k_f^2\left(\frac{M\gamma_f + C}{\rho_1\omega^2}\right), \quad m_{23} = k_s^2\left(\frac{M\gamma_s + C}{\rho_1\omega^2}\right),$$

$$m_{32} = k_f^2\left(\frac{H + C\gamma_f}{\rho_1\omega^2}\right), \quad m_{33} = k_s^2\left(\frac{H + C\gamma_s}{\rho_1\omega^2}\right),$$

with

$$\gamma_f = \frac{Hk_f^2 - \rho\omega^2}{\rho_1\omega^2 - Ck_f^2}, \quad \gamma_s = \frac{Hk_s^2 - \rho\omega^2}{\rho_1\omega^2 - Ck_s^2}.$$

The C, H, and M parameters are connected to the bulk modulii of the materials through the following relationships:

$$C = \frac{Kr(Kr - Kb)}{Kr - Kb + Kr\beta_p\left(\frac{Kr}{Kf} - 1\right)},$$

$$H = \frac{(Kr - Kb)^2}{Kr - Kb + Kr\beta_p\left(\frac{Kr}{Kf} - 1\right)} + Kb + \frac{4\mu}{3},$$

$$M = \frac{Kr^2}{Kr - Kb + Kr\beta_p\left(\frac{Kr}{Kf} - 1\right)}.$$

The matrix equations (1)–(3) are solved. The nine reflection and transmission coefficients are expressed by means of the six terms of the matrices. Those terms can be eliminated between some of the reflection/transmission coefficients, associated in the following expressions:

$$t_{1,p}^f \cdot t_{p,1}^f = (1 + r_{1,p})(1 + r_{p,1}^{f,f}), \tag{4}$$

$$t_{1,p}^s \cdot t_{p,1}^s = (1 + r_{1,p})(1 + r_{p,1}^{s,s}), \tag{5}$$

$$r_{p,1}^{s,s} = r_{1,p} + r_{p,1}^{f,f} - 1, \tag{6}$$

$$r_{p,1}^{f,s} \cdot r_{p,1}^{s,f} = (1 + r_{p,1}^{f,f})(1 + r_{p,1}^{s,s}), \tag{7}$$

$$t_{1,p}^f \cdot r_{p,1}^{f,s} \cdot t_{p,1}^s = (1 + r_{1,p})(1 + r_{p,1}^{f,f})(1 + r_{p,1}^{s,s}), \tag{8}$$

$$t_{1,p}^s \cdot r_{p,1}^{s,f} \cdot t_{p,1}^f = (1 + r_{1,p})(1 + r_{p,1}^{f,f})(1 + r_{p,1}^{s,s}). \tag{9}$$

As can be seen, all the left-handed expressions can be expressed by means of $r_{1,p}$ and $r_{p,1}^{f,f}$.

B. Debye-series expansion of the transmission coefficient of the plate

The Debye-series decomposition of the partial-wave scattering and interior amplitudes was first proposed in 1908 by Debye to study the electromagnetic field around a cylinder and to justify the theory of the rainbow. Now, it is a very useful tool in electromagnetic scattering[20] as well as in acoustics.[18,19]

In this section, the transmission coefficient of the plate is written by means of the local reflection/transmission coefficients linked to the two interfaces of the plate, and to the acoustical trajectories of the fast and slow waves inside the plate. The Debye-series expansion comes from the summation of all the transmitted waves, taking into account for each of them the appropriate local reflection/transmission coefficients, the delay time, and the attenuation inside the plate.

Let us consider the principle of the summation in Fig. 2. For clarity, the angles are drawn different from zero and the amplitude of the incident harmonic wave on the plate is taken equal to 1. The emerging waves are numbered from 1

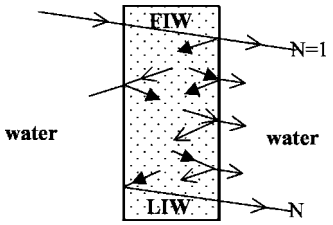

FIG. 2. Principle of the summation. In the plate, a fast wave and a slow one are, respectively, represented by the symbols: →, ➛. The successive emerging waves are numbered *N*.

to *N*. The expressions FIW and LIW, which mean first interior wave and last interior wave, play a prominent role. Indeed they govern the expression of the amplitude of the *N*th transmitted wave issued from N_f fast and N_s slow travels inside the plate. Along one internal travel the amplitude of the wave is multiplied by $\exp[-ik_fD]$ or $\exp[-ik_sD]$, whether it is a fast or a slow wave.

When both FIW and LIW are fast waves, the amplitude of the transmitted wave numbered *N* is

$$t^f_{1,p}\cdot(r^{f,f}_{p,1})^{\alpha}\cdot(r^{f,s}_{p,1}\cdot r^{s,f}_{p,1})^{\beta}\cdot(r^{s,s}_{p,1})^{\delta}\cdot\exp[-i(k_fN_f+k_sN_s)D]\cdot t^f_{p,1}. \quad (10)$$

This expression shows that the N_f fast and N_s slow travels are split in order to have α nonconverted reflections of a fast wave, δ nonconverted reflections of a slow wave and 2β converted reflections (fast to slow or slow to fast). N_f and N_s obey the relation $N_f+N_s=2N-1$, where N_f runs from 1 to $2N-1$ and N_s begins at 0. The three integers α,β,δ begin at 0 and obey the formula: $\alpha+2\beta+\delta=2N-2$.

When the two FIW and LIW are slow waves, a similar expression holds, but one must substitute $t^s_{1,p}\cdot t^s_{p,1}$ for $t^f_{1,p}\cdot t^f_{p,1}$ in the previous formula; N_s runs from 1 to $2N-1$ and N_f begins at 0.

The relations (7)–(9) allow us to express with the following relation the amplitude of the *N*th emergent wave, whether FIW and LIW are a fast/slow sequence or a slow/fast one,

$$t^f_{1,p}\cdot(r^{f,f}_{p,1})^{\alpha}\cdot(r^{f,s}_{p,1})^{1}\cdot(r^{f,s}_{p,1}\cdot r^{s,f}_{p,1})^{\beta}\cdot(r^{s,s}_{p,1})^{\delta}\cdot\exp[-i(k_fN_f+k_sN_s)D]\cdot t^s_{p,1}, \quad (11)$$

where $\alpha+2\beta+\delta=2N-3$ and $N_f+N_s=2N-1$ with $N\geqslant 2$.

Of course, in each case, the values of α, β, δ, N_f, and N_s are linked. For a given *N*, we use combinatorial tools of a software package MATHEMATICA® to establish their values and determine how many permutations of the fast and slow travels give a same emergent wave. Finally, the resultant transmitted amplitude comes from the summation over *N* of the previous expressions related to the four possible sequences of FIW and LIW. As a result, for a given frequency, via relations (4)–(9), the whole transmission coefficient of the plate only depends on the six variables: $r_{1,p}$, $r^{f,f}_{p,1}$, c_f, c_s, k^f_i, and k^s_i. It has a complex value noted $T_{\rm th}(\omega,r_{1,p},r^{f,f}_{p,1},c_f,c_s,k^f_i,k^s_i)$ in the following.

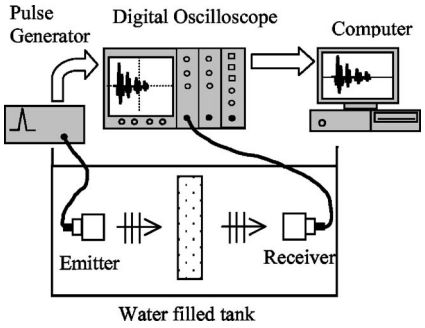

FIG. 3. Experimental setup.

III. EXPERIMENTAL TECHNIQUE

The porous plate (300 mm×200 mm×10 mm) stands vertically in water between two transducers (Fig. 3). The distances between the transducers and the plate are about 60 cm; the diffraction is negligible and a plane wave model is considered. The plate is insonified with a normal incident pulse, produced by the 300 V discharge of an internal capacitor of the generator, applied to the piezoelectric slab of the emitter. In order to cover a wide frequency range from 50 kHz to 1.8 MHz, three pairs of transducers, with different central frequency (Panametrics® nonfocused transducers, diameter of the active element: 1.5 in., 200 kHz, 500 kHz and 1 MHz), are successively utilized. For each pair, a direct signal is also recorded (the plate is simply removed). The signals are not amplified and the data are stored after the electronic perturbations have been removed thanks to an average of 300 acquisitions. The sampling frequency is 100 MHz and the recorded signals have 20 000 samples. The direct and transmitted signals—shifted for convenience—are plotted in Figs. 4–6.

Water saturated QF-20 plates have been yet studied by Johnson *et al.*,[10] who considered the bulk modulii: $Kr=36.6$ GPa, $Kb=9.47$ GPa, $\mu=7.63$ GPa, and $Kf=2.2$ GPa. The porosity of this material is $\beta_p\approx 0.4$ and its density $\rho=2056$ kg m^{-3}. In a recent paper, we have found for a

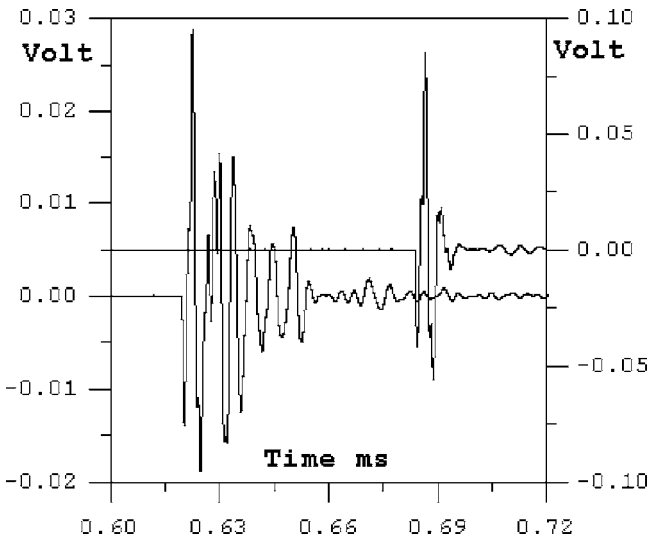

FIG. 4. Direct signal (right) and transmitted signal through the plate. 200 kHz transducers. The vertical axis on the right is for the amplitude of the direct signal.

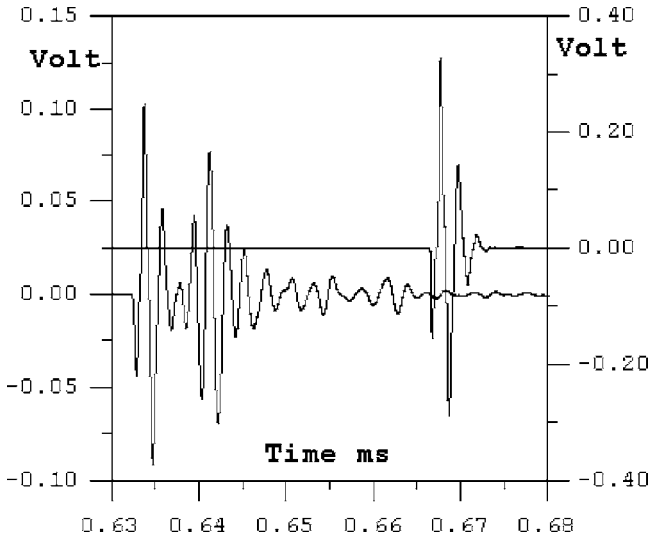

FIG. 5. Direct signal (right) and transmitted signal through the plate. 500 kHz transducers. The vertical axis on the right is for the amplitude of the direct signal.

2 cm-thick QF-20 plate the same results than those of Johnson. The velocities and the attenuation coefficients could have been obtained via different ways than these proposed here, for the thickness of the plate allowed to separate the successive temporal echoes on the transmitted signals.[21]

IV. NUMERICAL RESULTS

A. Experimental transmission coefficient

The experimental transmission coefficient is the ratio of the Fourier transform of the transmitted signal to the Fourier transform of the relevant direct signal. However, before performing this ratio, the direct signal must have been shifted of the delay time $-D/c_1$ to represent the incident wave onto the plate ($D=1$ cm, $c_1=1480$ m s^{-1}). The zero-padding technique is used to reduce the experimental frequency step to 190 Hz. The significant parts of the three normalized spectra

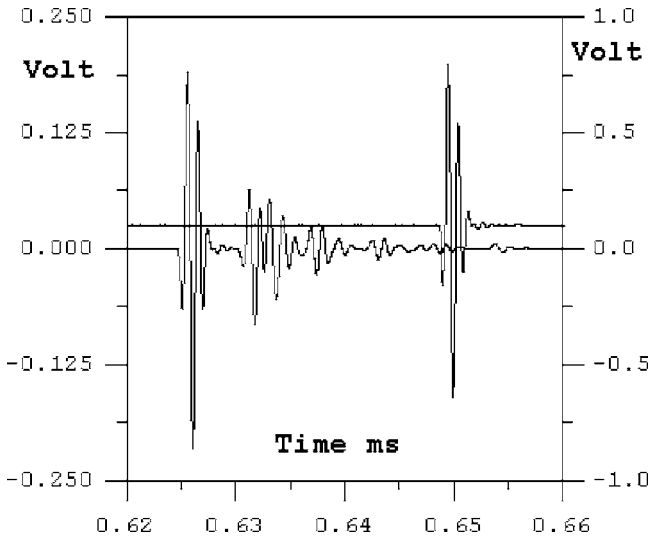

FIG. 6. Direct signal (right) and transmitted signal through the plate. 1 MHz transducers. The vertical axis on the right is for the amplitude of the direct signal.

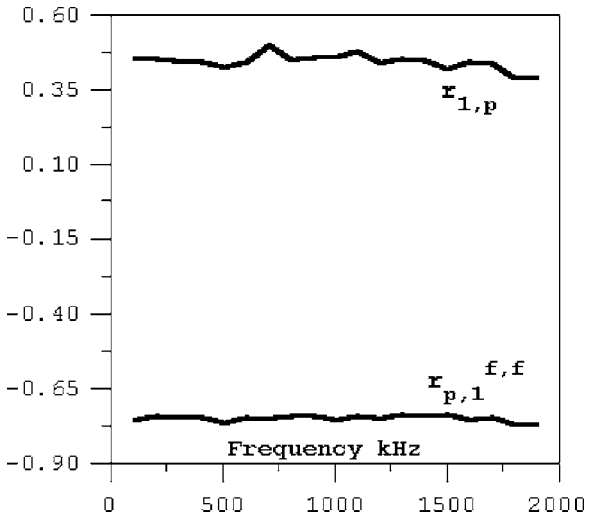

FIG. 7. Reflection coefficients $r_{1,p}$ and $r_{p,1}^{f,f}$ plotted vs frequency.

are extracted and associated to give the so-called experimental transmission coefficient noted $T_{\text{expt}}(\omega)$ and studied in the following section.

B. Experimental results

From 50 kHz to 1.8 MHz the spectrum is split into 100-kHz-wide frequency ranges. For each of them, a steepest descent technique is implemented to find the values of the six parameters giving the minimum of the summation:

$$\sum_{100\ \text{kHz/190 Hz}} \text{abs}(T_{\text{th}}(\omega, r_{1,p}, r_{p,1}^{f,f}, c_f, c_s, k_i^f, k_i^s) - T_{\text{exp}}(\omega)). \tag{12}$$

For a given set of the guess values of its six parameters, $T_{\text{th}}(\omega, r_{1,p}, r_{p,1}^{f,f}, c_f, c_s, k_i^f, k_i^s)$ is calculated up to $N=15$. Due to wave attenuation inside the plate, it remains unchanged for higher values of N. The so-obtained reflection coefficients $r_{1,p}$ and $r_{p,1}^{f,f}$ are plotted versus frequency in Fig. 7; the velocities are plotted in Fig. 8. These terms are nearly constant and their mean values are: $r_{1,p}=0.44$, $r_{p,1}^{f,f}=-0.75$,

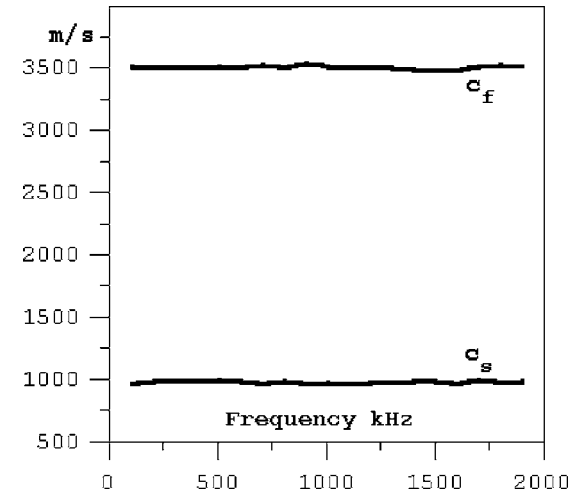

FIG. 8. Fast wave velocity c_f and slow wave velocity c_s plotted vs frequency.

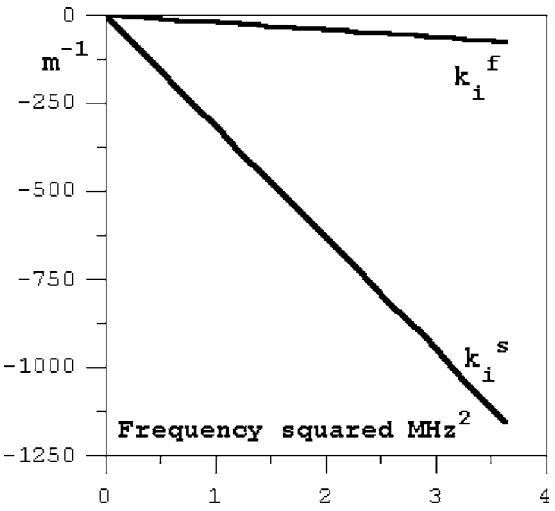

FIG. 9. Experimental attenuation coefficients k_i^f and k_i^s plotted vs the frequency squared.

c_f=3510 m s^{-1}, and c_s=977 m s^{-1}. The velocities are very close to those found by Johnson:[10] 3480 and 980 m s^{-1}. The attenuation coefficients k_i^f and k_i^s are successively plotted versus $\sqrt{\omega}$, ω, and ω^2. As a good linear fit is only obtained in the last option, k_i^f and k_i^s are plotted versus the frequency squared (Fig. 9). The linear fits are very good (correlation coefficients $\approx$0.99) and thus it is clearly established for the studied plate that the frequency dependence of the attenuation scales as the second power of frequency. As recalled by Buckingham,[13] such a behavior is predicted by Biot with viscous pore fluid. An attenuation coefficient scaling as $\sqrt{\omega}$ may occur for high frequencies, but simultaneously the velocities are no more independent of the frequency (they increase as $\sqrt{\omega}$ too). The experimental fits lead to the relations: $k_i^f = -5.5 \cdot 10^{-13} \omega^2$ and $k_i^s = -8.4 \cdot 10^{-12} \omega^2$. Now, $T_{\text{th}}(\omega, r_{1,p}, r_{p,1}^{f,f}, c_f, c_s, k_i^f, k_i^s)$ can be calculated on the experimental frequency range; its module is plotted and compared with this of $T_{\text{expt}}(\omega)$ in Fig. 10. The agreement is very good.

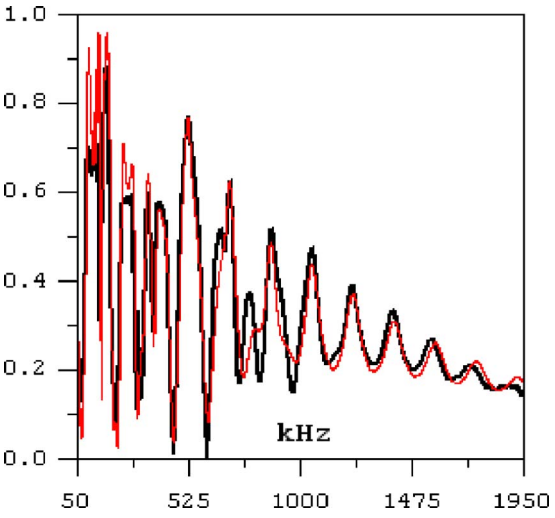

FIG. 10. Module of the calculated transmission coefficient (red) and module of the experimental transmission coefficient (black) plotted vs frequency.

V. CONCLUSION

In the framework of Biot's theory, the normal transmission coefficient of a water-saturated porous plate has been expanded in a Debye series taking into account the multiple reflection/conversion/transmission of the fast and slow waves inside the porous media. The comparison with the experimental transmission coefficient of the studied commercially available porous material (QF-20, Filtros®) allows us to determine the velocities and the attenuation coefficients of these waves. There is good agreement with other previous experimental determinations. Another outcome of our method is that the frequency dependence of the attenuation of both these waves in the studied material is established as the second power of frequency.

Nomenclature

c_1 = sound velocity in water
c_f = velocity of the fast wave
c_s = velocity of the slow wave
D = thickness of the porous plate
$\boldsymbol{i}$ = $\sqrt{-1}$
k_i^f = attenuation coefficient of the fast wave
k_i^s = attenuation coefficient of the slow wave
ρ_1 = density of water
ρ = density of the porous media
ω = circular frequency
β_p = porosity of the porous material
Kr = bulk modulus of mineral grains of the porous material
Kb = bulk modulus of frame
μ = shear modulus of frame
Kf = bulk modulus of fluid

[1]M. A. Biot, "Theory of propagation of elastic waves in a fluid-saturated porous solid. I and II," J. Acoust. Soc. Am. **28**, 168–191 (1956).
[2]R. D. Stoll and G. M. Bryan, "Wave attenuation in saturated sediments," J. Acoust. Soc. Am. **47**, 1440–1447 (1970).
[3]R. D. Stoll, "Theoretical aspects of sound transmission in sediments," J. Acoust. Soc. Am. **68**, 1341–1350 (1980).
[4]R. D. Stoll and T.-K. Kan, "Reflection of acoustic waves at a water-sediment interface," J. Acoust. Soc. Am. **70**, 149–156 (1981).
[5]R. D. Stoll, "Velocity dispersion in water-saturated granular sediment," J. Acoust. Soc. Am. **111**, 785–793 (2002).
[6]D. L. Johnson, T. J. Plona, C. Scala, F. Pasierb, and H. Kojima, "Tortuosity and acoustic slow wave," Phys. Rev. Lett. **49**, 1840–1843 (1982).
[7]D. L. Johnson, J. Koplik, and R. Dashen, "Theory of dynamic permeability and tortuosity in fluid-saturated porous media," J. Fluid Mech. **176**, 379–402 (1987).
[8]S. Feng and D. L. Johnson, "High-frequency acoustic properties of a fluid/porous solid interface. I. New surface mode," J. Acoust. Soc. Am. **74**, 906–914 (1993).
[9]D. L. Johnson, D. L. Hemmick, and H. Kojima, "Probing porous media with first and second sound. I. Dynamic permeability," J. Appl. Phys. **76**, 104–114 (1994).
[10]D. L. Johnson, T. J. Plona, and H. Kojima, "Probing porous media with first and second sound. II. Acoustic properties of water-saturated porous media," J. Appl. Phys. **76**, 115–125 (1994).
[11]J. Berryman, "Elastic wave attenuation in rocks containing fluids," Appl. Phys. Lett. **49**, 552–554 (1986).
[12]M. J. Buckingham, "Theory of acoustic attenuation, dispersion, and pulse propagation in unconsolidated granular materials including marine sediments," J. Acoust. Soc. Am. **102**, 2579–2596 (1997).
[13]M. J. Buckingham, "Theory of compressional and transverse wave propagation in consolidate porous media," J. Acoust. Soc. Am. **106**, 575–581

(1999).
[14]J. F. Allard, *Propagation of Sound in Porous Media. Modelling Sound Absorbing Materials* (Elsevier Applied Science, London, 1993).
[15]P. Leclaire, L. Kelders, W. Lauriks, C. Glorieux, and J. Thoen, "Determination of the viscous characteristic length in air filled porous materials by ultrasonic attenuation measurements," J. Acoust. Soc. Am. **99**, 1944–1948 (1996).
[16]Z. E. A. Fellah, C. Depollier, and M. Fellah, "Application of fractional calculus to the sound waves propagation in rigid porous materials: Validation via ultrasonic measurements," Acta. Acust. Acust. **88**, 34–39 (2002).
[17]K. Wu, Q. Xue, and L. Adler, "Reflection and transmission of elastic waves from a fluid-saturated porous solid boundary," J. Acoust. Soc. Am. **87**, 2349–2358 (1990).
[18]M. Deschamps and C. Chengwei, "Reflection/refraction of a solid layer by Debye's series expansion," Ultrasonics **29**, 288–293 (1991).
[19]J.-M. Conoir, O. Lenoir, and J.-L. Izbicki, "Interferences in elastic plates," in *Acoustic Interaction Width Submerged Elastic Structures*, Part I: Acoustic Scattering and Resonances, Series on Stability, Vibration and Control of Systems, series B Vol. **5**, edited by A. Guran, J. Ripoche, and F. Ziegler (World Scientific, Singapore, 1996), pp. 275–279.
[20]J. A. Lock and C. L. Adler, "Debye-series analysis of the first-order rainbow produced in scattering of a diagonally incident plane wave by a circular cylinder," J. Opt. Soc. Am. A **14**, 1316–1328 (1997).
[21]S. Derible, "Acoustical measurement of the bulk characteristics of a water-saturated porous plate obeying Biot's theory," Acta Acust. (Beijing) **90**, 85–90 (2004).

Approximate boundary conditions for a fluid-loaded elastic plate

M. Johansson, P. D. Folkow,[a] A. M. Hägglund, and P. Olsson
Department of Applied Mechanics, Chalmers University of Technology, SE-412 96 Göteborg, Sweden

(Received 12 November 2004; revised 26 September 2005; accepted 26 September 2005)

Approximate boundary conditions for an infinite elastic layer immersed in a fluid are derived. By using series expansions in the thickness coordinate of the plate fields, the displacements fields are eliminated, adopting the three-dimensional equations of motion. The sums and differences of the boundary pressure fields and their normal derivatives are related through a set of approximate boundary conditions, one symmetric and one antisymmetric. These equations involve powers in the layer thickness together with partial derivatives with respect to time as well as the spatial variables in the plate plane. The approximate boundary conditions can be truncated to an arbitrary order, and explicit relations are presented including terms of order five. Comparisons are made with effective boundary conditions using classical plate theories. The numerical examples involve reflection and transmission of plane waves incident on the plate at different angles, as well as the pressure fields due to a line force. Three fluid-loading cases are studied: modest, heavy, and light loadings. The results using truncated approximate boundary conditions are compared to exact and classical plate solutions. The examples show that the accuracies of the power series approximations of order three and higher are very good in the frequency interval considered. © *2005 Acoustical Society of America.* [DOI: 10.1121/1.2126927]

PACS number(s): 43.20.Gp, 43.20.Tb, 43.40.Rj [ANN] Pages: 3436–3446

I. INTRODUCTION

It is a well-known fact that interfaces between bodies and surfaces of bodies exhibit properties that may be strikingly different from those of the bulk of their interiors. Indeed, surface physics as well as the physics of thin films are distinct branches of physics, studied in their own right. In applied mechanics, there are quite a number of situations where properties of thin interface layers must be analyzed. One example of such is scattering of waves from structural elements, where the thickness of the element in question is small in comparison with the wavelengths involved. Here, the elementary theories for membranes, shells, and plates are often applicable. Besides these classical structural elements, there are other approximate theories that model various kinds of thin layers. As these theories may greatly simplify the analysis, thin-layer theories have been studied extensively in the literature.

The effects from thin layers on the surroundings may be studied using approximate (effective) boundary and interface conditions. Such methods have been used in many areas, for instance acoustics,[1] electromagnetics,[2] and elastodynamics.[1,3–5] Matrix formulations are adopted in Refs. 3 and 4 where the matrix elements are asymptotically expanded in the layer thickness. Elimination of the internal fields using series expansions together with boundary and interface conditions are used in Refs. 1 and 2. Another series expansion approach is presented by Johansson and Niklasson,[5] where methods for obtaining approximate boundary conditions to an (in principle) arbitrary order are presented. A somewhat different technique is adopted in the present paper, using systematic series expansions in the thickness coordinate. In spite of the seemingly different approaches used in the papers cited above, the various techniques are actually closely related.

In the work by Bövik,[1] various combinations of surrounding media and interface materials are treated. The approach allows for the thin layer to have a fairly general curved shape in three dimensions, albeit with a constant thickness. The method used is a systematic elimination of the internal fields, and the layer is replaced by a single curved mathematical surface of discontinuity for the field variables in the surrounding media. The discontinuities are specified in such a manner that the influence of the layer is reproduced to within terms of second order in the thickness. However, the work by Bövik does not cover all combinations that may in practice occur. In fact, the case of an elastic layer immersed in a (nonviscous) fluid is not covered (while some apparently more complex cases are). The reason for these lacunae are stated by Bövik to be the fact that the rational elimination process that is used breaks down when there are more degrees of freedom in the layer than in the surrounding medium.

The case of a planar thin elastic layer immersed in a fluid has been studied by many authors. In most works, the layer is modeled using the classical plate theories due to Kirchhoff[6] or Mindlin.[7] Various sorts of higher order plate theories may also be applicable in this context.[8–11] In the present paper, the approximate boundary conditions are obtained by adopting a series expansion technique previously used in the derivation of higher order plate equations by Losin.[12,13] The apparent restriction that hampered the elimination process used by Bövik is thus lifted, with a refinement of the method to include higher order terms. The present approach resembles the procedures employed in Ref. 5, which in turn is based on the higher order plate equation

[a]Electronic mail: peter.folkow@me.chalmers.se

derivation presented by Boström *et al.*[14] Hence, by generalizing the techniques adopted by Losin,[12,13] the structural form of the approximate boundary conditions to an arbitrary order is obtained. Explicit expressions including terms up to order five in the thickness are presented and compared to corresponding expressions using classical plate theories. In order to illustrate the results using different theories, numerical examples are presented for three fluid-loading cases. In the first examples, acoustic reflection from and transmission through an infinite elastic layer for plane waves are studied. This subject has been investigated by many authors.[6,15–18] The next examples consider the pressure fields on the plate surfaces due to either symmetric or antisymmetric harmonic line forces. Sound radiation by plates excited locally by forces is an important problem of structural acoustics, extensively studied in the literature.[6,19–23]

II. GOVERNING EQUATIONS

Consider a plate of thickness h, bounded by the two planes $z=\pm h/2$. The plate is surrounded by a linear nonviscous fluid with density ρ_f. The plate is homogeneous, isotropic, and linearly elastic with density ρ and Lamé constants λ and μ. The three-dimensional equations of motion in the plate for the displacement components u, v, and w are

$$(\lambda+\mu)(\partial_x^2 u+\partial_{xy}^2 v+\partial_{xz}^2 w)+\mu(\partial_x^2 u+\partial_y^2 u+\partial_z^2 u)=\rho\partial_t^2 u, \quad (1)$$

$$(\lambda+\mu)(\partial_{xy}^2 u+\partial_y^2 v+\partial_{yz}^2 w)+\mu(\partial_x^2 v+\partial_y^2 v+\partial_z^2 v)=\rho\partial_t^2 v, \quad (2)$$

$$(\lambda+\mu)(\partial_{xz}^2 u+\partial_{yz}^2 v+\partial_z^2 w)+\mu(\partial_x^2 w+\partial_y^2 w+\partial_z^2 w)=\rho\partial_t^2 w. \quad (3)$$

Partial derivatives are expressed in accordance with $\partial_x=\partial/\partial x$, etc. Stress continuity at $z=\pm h/2$ gives the boundary conditions (following Hooke's law)

$$\mu(\partial_z u+\partial_x w)=0, \quad (4)$$

$$\mu(\partial_z v+\partial_y w)=0, \quad (5)$$

$$\lambda(\partial_x u+\partial_y v)+(\lambda+2\mu)\partial_z w=-p+F. \quad (6)$$

The pressure from the surrounding fluid is denoted p, while F is due to additive distributed forces at the boundaries acting outward in the normal direction. Vertical displacement continuity at $z=\pm h/2$ together with the momentum equation for the fluid gives the additional boundary condition

$$\partial_t^2 w=-\partial_z p/\rho_f. \quad (7)$$

The main objective is to eliminate the plate fields u, v, and w in the equations above so as to obtain approximate differential equations in terms of the fluid pressure p and its normal derivative $\partial_z p$ at the boundaries. This is accomplished by first performing a power series expansion in the thickness coordinate h of the left-hand sides of the boundary conditions (4)–(7). These expansions are then combined with the equations of motion (1)–(3) to give the desired result.

So, for the elimination process, it is convenient to proceed in terms of the differences and sums of the boundary conditions, as is done by Losin.[12,13] The boundary conditions (4)–(7) may thus be rewritten using $\Delta f=f(x,y,h/2,t)-f(x,y,-h/2,t)$ and $\Sigma f=f(x,y,h/2,t)+f(x,y,-h/2,t)$, where f is any of the boundary fields. For the *plate* fields, the sums and differences can be expanded in power series according to Maclaurin's formula

$$\Delta f=2\sum_{j=0}^{n-1}\frac{\partial_z^{2j+1}f_0}{(2j+1)!}\left(\frac{h}{2}\right)^{2j+1}+\mathcal{O}(h^{2n+1}), \quad (8)$$

$$\Sigma f=2\sum_{j=0}^{n-1}\frac{\partial_z^{2j}f_0}{(2j)!}\left(\frac{h}{2}\right)^{2j}+\mathcal{O}(h^{2n}), \quad (9)$$

where $\partial_z^m f_0=(\partial_z^m f(x,y,z,t))|_{z=0}$.

The various plate fields present on the left-hand sides of the boundary conditions may be expanded in such a way, which for Eq. (6) gives

$$\Delta p-\Delta F=\sum_{j=0}^{n-1}\mathcal{A}_{1,j}\partial_z^{2j+1}u_0+\mathcal{A}_{2,j}\partial_z^{2j+1}v_0+\mathcal{A}_{3,j}\partial_z^{2j+2}w_0+\mathcal{O}(h^{2n+1}), \quad (10)$$

$$\Sigma p-\Sigma F=\sum_{j=0}^{n-1}\mathcal{A}_{4,j}\partial_z^{2j}u_0+\mathcal{A}_{5,j}\partial_z^{2j}v_0+\mathcal{A}_{6,j}\partial_z^{2j+1}w_0+\mathcal{O}(h^{2n}), \quad (11)$$

while Eq. (7) becomes

$$\Delta\partial_z p=\sum_{j=0}^{n-1}\mathcal{A}_{7,j}\partial_z^{2j+1}w_0+\mathcal{O}(h^{2n+1}), \quad (12)$$

$$\Sigma\partial_z p=\sum_{j=0}^{n-1}\mathcal{A}_{8,j}\partial_z^{2j}w_0+\mathcal{O}(h^{2n}). \quad (13)$$

The operators $\mathcal{A}_{i,j}$ involve powers of the plate thickness as well as possible time derivatives and spatial derivatives in the (xy) plane. When studying the differential orders ∂_z in Eqs. (10)–(13), it is seen that both Δp and $\Sigma\partial_z p$ involve even orders acting on w_0 while Δp involves odd orders acting on both u_0 and v_0. The opposite case holds for Σp and $\Delta\partial_z p$. It is therefore possible to obtain two separate relations between these fields, an antisymmetric case relating Δp and $\Sigma\partial_z p$ and a symmetric case relating Σp and $\Delta\partial_z p$. Both cases may be treated similarly. For the antisymmetric case, Eqs. (10) and (13) consist of $3n+3$ unknowns $(\Delta p,\Sigma\partial_z p,\partial_z u_0,\ldots,\partial_z^{2n-1}u_0,\partial_z v_0,\ldots,\partial_z^{2n-1}v_0,w_0,\ldots,\partial_z^{2n}w_0)$, so it is clear that $3n$ additional equations are needed in order to obtain a relation between Δp and $\Sigma\partial_z p$. The boundary conditions (4) and (5) can be expanded using either Eq. (8) or Eq. (9). For the antisymmetric case, Eq. (9) is to be used, giving

$$0=\sum_{j=0}^{n-1}\mathcal{B}_{1,j}\partial_z^{2j+1}u_0+\mathcal{B}_{2,j}\partial_z^{2j}w_0+\mathcal{O}(h^{2n}), \quad (14)$$

$$0 = \sum_{j=0}^{n-1} \mathcal{B}_{1,j} \partial_z^{2j+1} v_0 + \mathcal{B}_{3,j} \partial_z^{2j} w_0 + \mathcal{O}(h^{2n}), \tag{15}$$

where the operators $\mathcal{B}_{i,j}$ involve powers of the plate thickness as well as spatial derivatives in the (xy) plane. The last $3n-2$ equations are obtained by using the differential equations (1)–(3) for the midplane fields u_0, v_0, and w_0. Both Eqs. (1) and (2) involve solely even differential orders ∂_z on u_0 and v_0 and odd orders on w_0, while the opposite situation holds for (3). Differentiating Eqs. (1) and (2) an odd number of times with respect to z renders $2n-2$ more equations. The last n equations are obtained by using Eq. (3) and its even derivatives with respect to z.

Hence, it is possible to solve the two separate linear systems for the antisymmetric and symmetric cases, respectively, giving

$$\left(\sum_{j=0}^{n-1} h^{2j} \partial_t^2 \mathcal{C}_{1,j} \right) (\Delta p - \Delta F) = \left(\sum_{j=1}^{n} h^{2j-1} \mathcal{C}_{2,j} \right) \Sigma \partial_z p + \mathcal{O}(h^{2n}), \tag{16}$$

$$\left(\sum_{j=1}^{n} h^{2j} \partial_t^2 \mathcal{C}_{3,j} \right) (\Sigma p - \Sigma F) = \left(\sum_{j=1}^{n} h^{2j-1} \mathcal{C}_{4,j} \right) \Delta \partial_z p + \mathcal{O}(h^{2n}). \tag{17}$$

The differential operators $\mathcal{C}_{i,j}$ involve $\nabla_s^{2p} \partial_t^{2j-2p}$ for $p = 0, \ldots, j$ with $\nabla_s^2 = \partial_x^2 + \partial_y^2$. Thus, their highest order purely spatial derivatives are ∇_s^{2j}, and their highest order purely time derivatives are ∂_t^{2j}.

As the series expansion may be derived to any order, the accuracy of the solution can be made as good as one wishes.[24] The more terms involved in the series, the better approximation for shorter waves. However, the main interest in the results is perhaps to study expansions using a few terms which correspond to long wavelength and low-frequency approximations.

Presenting the explicit relations for the antisymmetric case, Eq. (16) gives up to order h^5

$$\begin{aligned}
&\frac{\rho_f}{\rho} \frac{\partial_t^2}{c_s^2} \left\{ 1 + \frac{1}{2}\left(\frac{h}{2}\right)^2 \left[-2\nabla_s^2 + (1+\gamma)\frac{\partial_t^2}{c_s^2} \right] + \frac{1}{24}\left(\frac{h}{2}\right)^4 \left[8\nabla_s^4 - 8(1+\gamma)\nabla_s^2 \frac{\partial_t^2}{c_s^2} + (1+6\gamma+\gamma^2)\frac{\partial_t^4}{c_s^4} \right] \right\} (\Delta p - \Delta F) \\
&\quad = \left\{ \frac{h}{2}\frac{\partial_t^2}{c_s^2} + \frac{1}{6}\left(\frac{h}{2}\right)^3 \left[8(1-\gamma)\nabla_s^4 - 4(3-2\gamma)\nabla_s^2 \frac{\partial_t^2}{c_s^2} + (3+\gamma)\frac{\partial_t^4}{c_s^4} \right] + \frac{1}{120}\left(\frac{h}{2}\right)^5 \left[-32(1-\gamma)\nabla_s^6 + 16(4-2\gamma-\gamma^2)\nabla_s^4 \frac{\partial_t^2}{c_s^2} \right. \right. \\
&\qquad \left. \left. - 4(9+3\gamma-4\gamma^2)\nabla_s^2 \frac{\partial_t^4}{c_s^4} + (5+10\gamma+\gamma^2)\frac{\partial_t^6}{c_s^6} \right] \right\} \Sigma \partial_z p.
\end{aligned} \tag{18}$$

In the symmetric case, Eq. (17) gives up to order h^5

$$\begin{aligned}
&\frac{\rho_f}{\rho} \frac{\partial_t^2}{c_s^2} \left(-\nabla_s^2 + \gamma \frac{\partial_t^2}{c_s^2} \right) \left\{ \frac{h}{2} + \frac{1}{6}\left(\frac{h}{2}\right)^3 \left[-2\nabla_s^2 + (1+\gamma)\frac{\partial_t^2}{c_s^2} \right] + \frac{1}{360}\left(\frac{h}{2}\right)^5 \left[4\nabla_s^2 - (1+3\gamma)\frac{\partial_t^2}{c_s^2} \right] \left[4\nabla_s^2 - (3+\gamma)\frac{\partial_t^2}{c_s^2} \right] \right\} (\Sigma p - \Sigma F) \\
&\quad = \left\{ \left[-4(1-\gamma)\nabla_s^2 + \frac{\partial_t^2}{c_s^2} \right] + \frac{1}{6}\left(\frac{h}{2}\right)^2 \left[8(1-\gamma)\nabla_s^4 - 4(2-\gamma^2)\nabla_s^2 \frac{\partial_t^2}{c_s^2} + (1+3\gamma)\frac{\partial_t^4}{c_s^4} \right] \right. \\
&\qquad \left. + \frac{1}{120}\left(\frac{h}{2}\right)^4 \left[-32(1-\gamma)\nabla_s^6 + 16(3-2\gamma^2)\nabla_s^4 \frac{\partial_t^2}{c_s^2} - 4(4+10\gamma-5\gamma^2-\gamma^3)\nabla_s^2 \frac{\partial_t^4}{c_s^4} + (1+10\gamma+5\gamma^2)\frac{\partial_t^6}{c_s^6} \right] \right\} \Delta \partial_z p.
\end{aligned} \tag{19}$$

In these equations, $c_s = \sqrt{\mu/\rho}$ is the transverse wave speed and $\gamma = \mu/(\lambda+2\mu)$ is the squared quotient between the transverse and the longitudinal wave speeds. Note the factorized differential operator on the left-hand side of Eq. (19). One consequence of this operator is that when $(-\nabla_s^2 + \gamma \partial_t^2/c_s^2)(\Sigma p - \Sigma F) = 0$, the normal motion of the plate boundaries is purely antisymmetric as $\Delta \partial_z p = 0$. Speaking in terms of plane time-harmonic waves, this occurs when the horizontal phase speed in the fluid is equal to the longitudinal wave speed in the elastic layer. The same result is obtained using exact theory, so the factorization of the operator probably holds to arbitrary order.

Asymptotic expansions for plates without surrounding fluids have been studied by Losin[12,13] and Boström *et al.*[14] In the works by Losin, where no boundary forces are included, the right-hand sides of Eqs. (18) and (19) can be identified. Boström *et al.* investigated the antisymmetric case including boundary forces, and the result may be shown to be in line with Eq. (18).

It is instructive to compare these asymptotic equations with the results from classical plate theory. For the *antisymmetric* case, the most simple approximation is to study the motion of a perfectly limp layer, giving

$$\frac{\rho_f}{\rho}(\Delta p - \Delta F) = \frac{h}{2}\Sigma\partial_z p. \tag{20}$$

This result is found in Eq. (18) when terms up to order h are included. A more refined theory that includes plate bending is the classic Kirchhoff equation, which in this context is written

$$\frac{\rho_f}{\rho}\frac{\partial_t^2}{c_s^2}(\Delta p - \Delta F) = \left\{\frac{h}{2}\frac{\partial_t^2}{c_s^2} + \frac{1}{6}\left(\frac{h}{2}\right)^3[8(1-\gamma)\nabla_s^4]\right\}\Sigma\partial_z p. \tag{21}$$

Hence, an extra term involving h^3 is added when compared to Eq. (20) due to the influence of the bending stiffness. It is clear from Eq. (18) that the Kirchhoff equation does not include the terms of order h^2 on the left-hand side and only the first term of the h^3 terms on the right-hand side. Turning into the Mindlin theory which includes both shear effects and rotary inertia, the equation becomes

$$\begin{aligned}\frac{\rho_f}{\rho}\frac{\partial_t^2}{c_s^2}&\left\{1 + \frac{1}{2}\left(\frac{h}{2}\right)^2\left[-\frac{8}{3\kappa}(1-\gamma)\nabla_s^2 + \frac{2}{3\kappa}\frac{\partial_t^2}{c_s^2}\right]\right\}(\Delta p - \Delta F)\\ &= \left\{\frac{h}{2}\frac{\partial_t^2}{c_s^2} + \frac{1}{6}\left(\frac{h}{2}\right)^3\left[8(1-\gamma)\nabla_s^4 - \left[2 + \frac{8}{\kappa}(1-\gamma)\right]\right.\right.\\ &\quad\left.\left.\times\nabla_s^2\frac{\partial_t^2}{c_s^2} + \frac{2}{\kappa}\frac{\partial_t^4}{c_s^4}\right]\right\}\Sigma\partial_z p.\end{aligned} \tag{22}$$

This equation involves various terms of order h^2 and h^3 of which the coefficients differ from the corresponding terms presented in Eq. (18). Here, κ is the much debated shear coefficient which is an adjustment coefficient not appearing in Eq. (18). In the numerical examples presented below, κ is chosen as $\kappa = 5/(6-\nu)$ in accordance with Ref. 14, where ν is the Poisson ratio.

In the *symmetric* case, the most simple approximation is to consider a layer in generalized plane stress giving

$$\begin{aligned}\frac{\rho_f}{\rho}\frac{\partial_t^2}{c_s^2}&\left\{\frac{h}{2}\left[-\nabla_s^2 + \gamma\frac{\partial_t^2}{c_s^2}\right]\right\}(\Sigma p - \Sigma F)\\ &= \left[-4(1-\gamma)\nabla_s^2 + \frac{\partial_t^2}{c_s^2}\right]\Delta\partial_z p,\end{aligned} \tag{23}$$

which is just Eq. (19) up to order h. A higher order plate theory is due to Kane and Mindlin,[25] which in this case becomes

$$\begin{aligned}\frac{\rho_f}{\rho}\frac{\partial_t^2}{c_s^2}&\left\{\frac{h}{2}\left[-\nabla_s^2 + \gamma\frac{\partial_t^2}{c_s^2}\right]\right\}(\Sigma p - \Sigma F)\\ &= \left\{\left[-4\kappa^2(1-\gamma)\nabla_s^2 + \kappa^2\frac{\partial_t^2}{c_s^2}\right] + \frac{1}{6}\left(\frac{h}{2}\right)^2\right.\\ &\quad\left.\times\left[2\nabla_s^4 - 2(1+\gamma)\nabla_s^2\frac{\partial_t^2}{c_s^2} + 2\gamma\frac{\partial_t^4}{c_s^4}\right]\right\}\Delta\partial_z p.\end{aligned} \tag{24}$$

This equation involves terms up to order h^2, but the coefficients of the differential operators on the right-hand side are different from the corresponding terms given in Eq. (19).

III. NUMERICAL CALCULATIONS OF TRANSMISSION AND REFLECTION

To validate the various approximate equations presented above, the reflection from and transmission through the plate may be considered for $F=0$. The wave propagation in the fluid medium is here assumed to follow the simple wave equation

$$\nabla^2 p = \partial_t^2 p/c_f^2, \tag{25}$$

where c_f is the wave speed and $\nabla^2 = \partial_x^2 + \partial_y^2 + \partial_z^2$. Consider $z < -h/2$ and let plane waves propagate in the (xz) plane towards $z=-h/2$, giving rise to reflected and transmitted plane waves. Thus, the incident, reflected, and transmitted waves may be expressed as

$$p_i = e^{i(k_f(\zeta x + \sqrt{1-\zeta^2}z) - \omega t)}, \quad z < -h/2,$$

$$p_r = Re^{i(k_f(\zeta x - \sqrt{1-\zeta^2}z) - \omega t)}, \quad z < -h/2,$$

$$p_t = Te^{i(k_f(\zeta x + \sqrt{1-\zeta^2}z) - \omega t)}, \quad z > h/2,$$

where $k_f = \omega/c_f$ and $\zeta = \sin\phi$; ϕ being the angle measured from the normal to the plate boundaries.

It is now straightforward to solve for R and T using either the exact three-dimensional equations of motion (1)–(3) with pertinent boundary conditions, or the asymptotic equations (18) and (19). As the loading is such that purely antisymmetric or symmetric modes will not be generated in the general case, Eqs. (18) and (19) are solved as a system. Only odd-order expansions in the plate thickness are here of interest. The reason for this is that the quotient between the differences and the sums of the pressure fields p and $\partial_z p$ are seen to be of order h. Hence, in Eqs. (18) and (19), every thickness order term on the left-hand side is to be paired to a corresponding term on the right-hand side for a correct truncation. The numerical results involve solutions based on the asymptotic h, h^3, and h^5 expansions, respectively. The range of applicability for each truncation level is hereby clearly visible. When performing comparisons to classical plate theories, mainly solutions involving Kirchhoff theory (21) and Mindlin theory (22) are presented. These equations have been used extensively in the literature and are suitable for comparisons since the antisymmetric motions are prevailing in most of the examples presented below. When the influence from the symmetric motions is pronounced, numerical results are explicitly given using classical theories covering both antisymmetric and symmetric motions. Note that in all the various plate equations that are studied, $R^2 + T^2 = 1$ as no losses are incorporated in the models.

It is convenient to introduce various nondimensional parameters, besides γ, that appear in the equations

$$\alpha = \rho_f/\rho, \quad \beta = c_f^2/c_s^2, \quad \Omega = k_s h, \tag{26}$$

where $k_s = \omega/c_s$.

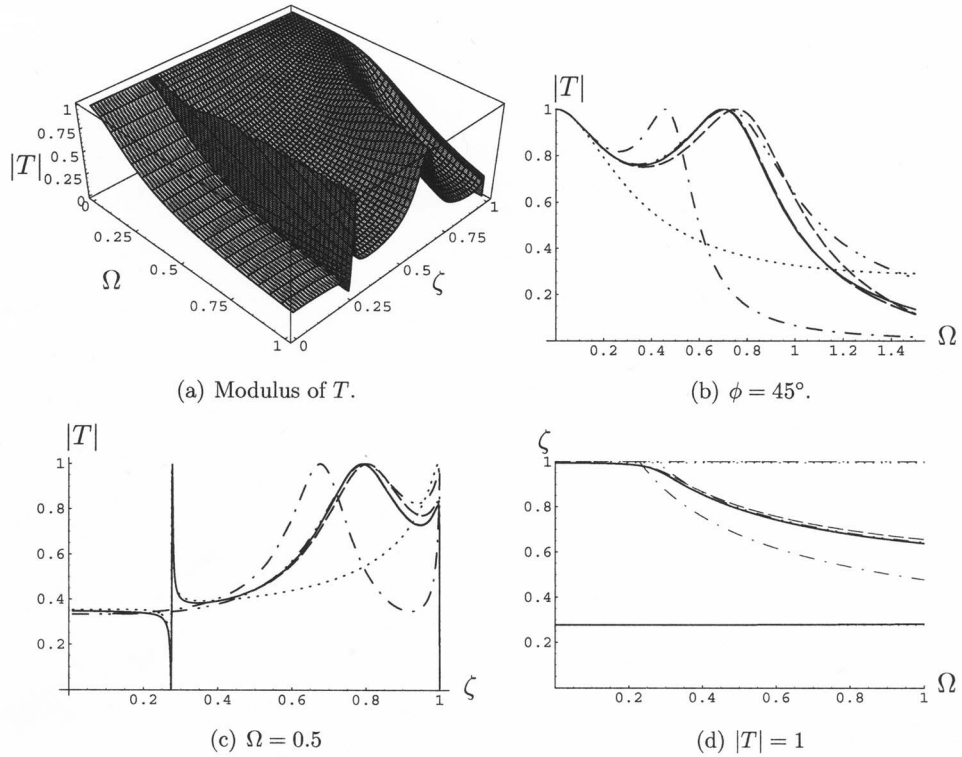

FIG. 1. Aluminum-water. —— exact; – – h^5; --- h^3; ··· h; -·- Kirchhoff, -·-· Mindlin.

A. Aluminum-water

Consider a case of modest loading, where an aluminum plate is surrounded by water. Here, the various nondimensional parameters become $\alpha \approx 0.37$, $\beta \approx 0.23$, and $\gamma \approx 0.25$.

Using exact theory, the transmission coefficient modulus is displayed in a 3D plot in Fig. 1(a). The figure shows the dependence of $|T|$ upon the frequency Ω and the angle of incidence, displayed through ζ. These results are to be compared to the asymptotic h, h^3, and h^5 expansions as well as the classical Kirchhoff and Mindlin theories. Figure 1(b) shows the modulus of T when the angle of incidence is $\phi = 45°$. The result using the h^5 expansion is almost indistinguishable from the exact result over a large frequency interval. Mindlin and the h^3 results are of the same accuracy, even though the former is somewhat better for lower frequencies, while the Kirchhoff theory is clearly inferior. The simple h expansion is valid for low frequencies only. It completely misses the total transmission effect due to the flexural motion (closely related to the zeroth antisymmetric Lamb mode for a free plate) as expected. Note that the total transmission for the Kirchhoff and Mindlin theories occurs when the horizontal wave number in the fluid, $k_f\zeta$, is equal to the plate wave number for a *free* plate. This behavior does not appear for the exact and asymptotic theories in the general case.

The dependence of $|T|$ upon the angle of incidence is presented in Fig. 1(c) for the frequency $\Omega = 0.5$. The accuracy of the different approximations shows a similar behavior as in Fig. 1(b). Note the rapid transition of the transmission coefficient from zero to unity around $\zeta \approx 0.28$, that is $\phi \approx 16°$. This is associated with the first compressional mode (closely related to the zeroth symmetric Lamb mode for a free plate). The phenomenon is not captured by the Kirchhoff and Mindlin theories, since they do not take symmetric motion into account. Another minor incorrectness with the Kirchhoff and Mindlin equations is that $|T| = 1$ for the grazing angle, $\zeta = 1$. The exact and asymptotic equations predict that the transmission modulus falls quickly to zero as ζ approaches unity. This behavior is also illustrated in Fig. 1(d), where the curves of total transmission are displayed. The curve related to the loci of the lowest flexural mode shows once again that the Kirchhoff theory is inferior to the other higher order theories. Hence, the Kirchhoff equation is here not that well suited when predicting total transmission. The curve related to the lowest compressional mode shows very little frequency dependence. Here, the various asymptotic curves are indistinguishable from the exact curve. Moreover, there exists a curve just below $\zeta = 1$ due to the h expansion.

In order to perceive the range of accuracy for the different theories, the contour lines for 1% relative error in the transmission modulus are displayed in Fig. 2. The different theories involving terms of order h^3, that is Kirchhoff, Mindlin, and asymptotic h^3 expansions, are presented in Fig. 2(a). The latter theory is seen to be within the error limit over a larger frequency interval, especially for $\phi < 30°$. In Fig. 2(b) similar contours for the asymptotic h, h^3, and h^5 theories are depicted, showing the range improvement using higher order theories. Considering an explicit example using a 2-mm-thick aluminum plate immersed in water, the h theory applies within the error limit for frequencies up to around 25 kHz, while the h^3 theory is valid up to 0.1 MHz and h^5 theory up to 0.17 MHz.

In all the examples presented above, the comparisons are made with the purely antisymmetric classical plate equations due to Kirchhoff or Mindlin. As the asymptotic equations involve both symmetric and antisymmetric motions, the flexural plate equations can be combined with the classical sym-

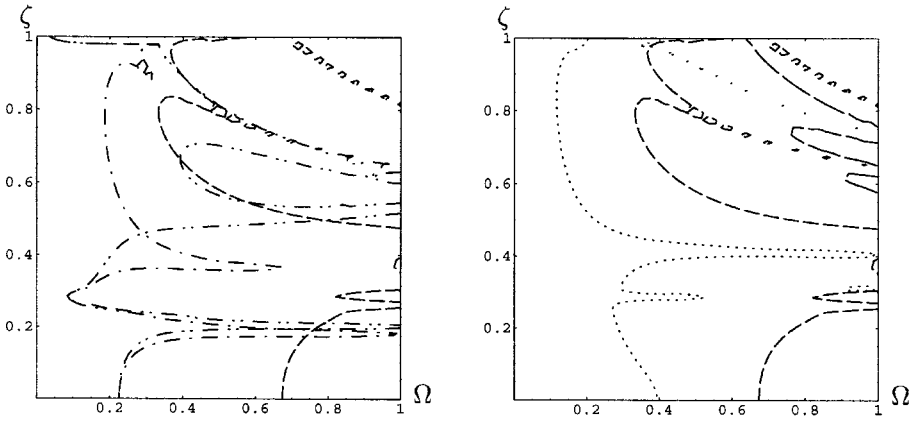

(a) 1% relative error contours for $|T|$. (b) 1% relative error contours for $|T|$.

FIG. 2. Aluminum-water. – – h^5; --- h^3; ··· h; -·- Kirchhoff; -···- Mindlin.

metrical plate equations as well. Two different combinations are considered here; the Kirchhoff equation (21) together with the generalized plane stress equation (23) (K-GPS), as well as the Mindlin equation (22) together with the equation due to Kane and Mindlin (24) (M-KM). The main reason for choosing the M-KM solution is that it is based on refined antisymmetric and symmetric theories when compared to K-GPS, thus resembling the asymptotic h^3 to a greater extent. Several authors have studied the effects of various such combined equations.[15,17,26,27] The equations derived by Lyamshev[26] are, after corrections, in line with the K-GPS relations. Freedman[15] adopted the generalized plane stress equation together with the Mindlin equation. However, some of his results exhibit some peculiar behavior not appearing when implemented here. The influence of the symmetric parts in both the K-GPS and the M-KM theories is best appreciated when compared to the results displayed in Fig. 1(c). First, both the combined classical theories feature the rapid transition of the transmission coefficient around $\zeta \approx 0.28$ due to the compressional mode, as expected. Second, the transmission modulus tends abruptly to zero as ζ approaches unity in both cases. Otherwise, there are small discrepancies between the combined theories (K-GPS and M-KM) and the corresponding antisymmetric theories (Kirchhoff and Mindlin) in this case.

B. Polyethylene-water

In this section a light solid is immersed in water. The solid parameters are those of polyethylene, which represents a typical plastic material. The amplitudes are assumed to be low, so that elastic theory is applicable. The system is an example of heavy loading, where the nondimensional parameters become $\alpha \approx 1.03$, $\beta \approx 0.71$, and $\gamma \approx 0.25$.

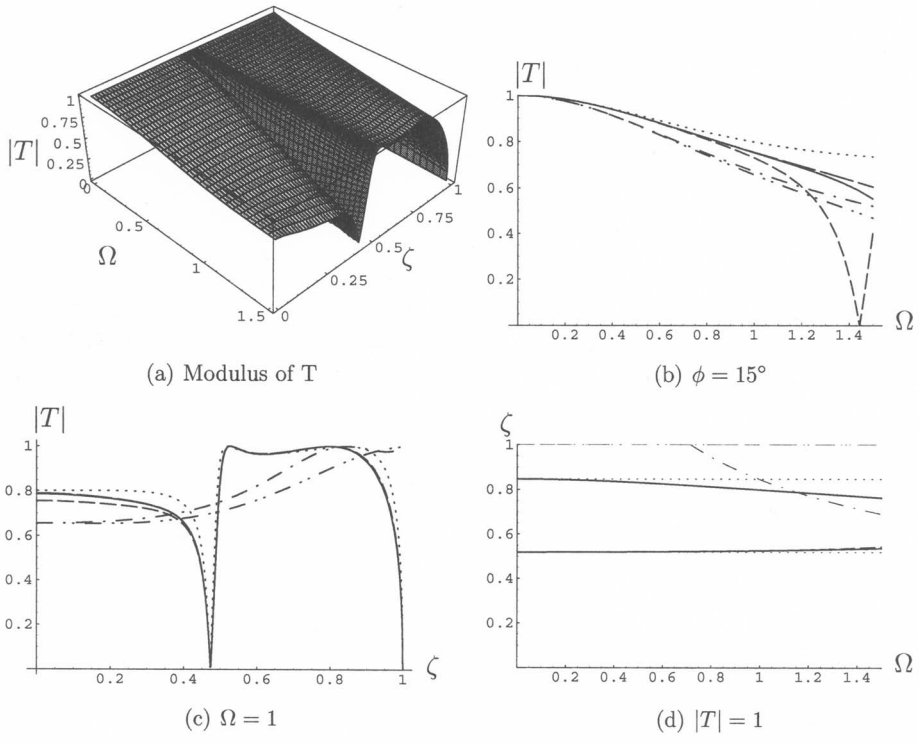

(a) Modulus of T (b) $\phi = 15°$

(c) $\Omega = 1$ (d) $|T| = 1$

FIG. 3. Polyethylene-water. —— exact; – –h^5; ---h^3; ··· h; -·- Kirchhoff; -···- Mindlin.

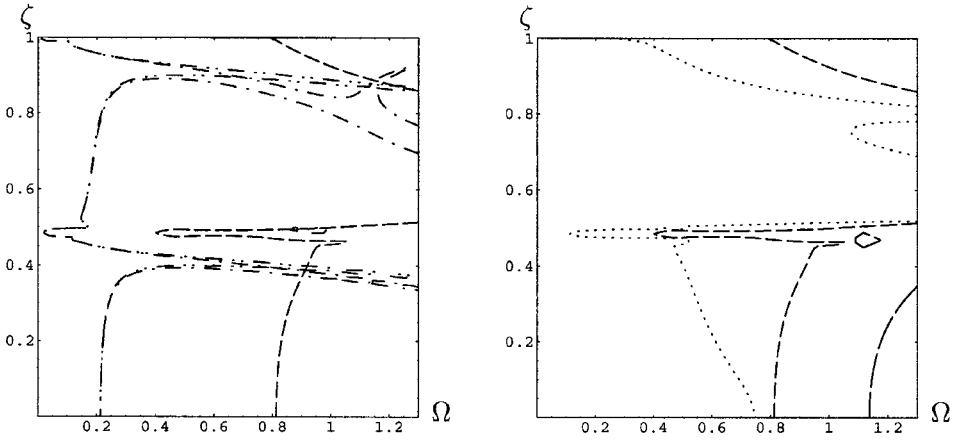

(a) 1% relative error contours for $|T|$. (b) 1% relative error contours for $|T|$.

FIG. 4. Polyethylene-water. – – h^5; --- h^3; ⋯ h; -·- Kirchhoff; -···- Mindlin.

The exact transmission coefficient modulus is displayed in Fig. 3(a). It is seen that the transmission through the plate is pronounced for a large interval of both the frequency and the angle of incidence, compared to the aluminum-water case, Fig. 1(a). This is due to the similarities in the plate and fluid impedances in this heavy loading example. When displaying the frequency dependence of the transmission coefficient modulus for the different approximate theories, it is seen that for most of the angles of incidence the classical plate equations reproduce the behavior less correctly than the asymptotic expansions, including the simple h expansion. This indicates that the symmetric motion is of importance in this frequency interval. In the case of small angles of incidence, the classical theories are rather good, as is shown in Fig. 3(b) when $\phi=15°$. The plot displays the discrepancy of the asymptotic expansions as the frequency increases. Note the total reflection according to the h^3 theory, which is at a lower frequency than according to exact theory; $\Omega\approx1.76$. The accuracies of the classical and asymptotic theories are clearly visible in Fig. 3(c), where the angle of incidence is varied for $\Omega=1$. The classical theories fail to illustrate the behavior of the transmission coefficient for most ζ. There exists a rapid transition of $|T|$ from zero to unity around $\zeta\approx0.5$ ($\phi\approx30°$) which corresponds to the lowest compressional mode. This behavior was also present in the aluminum-water case, Fig. 1(c), where the relation to the zeroth symmetric Lamb mode was stated. However, total transmission occurs at $\zeta\approx0.8$, which is not that close to the corresponding zeroth-order antisymmetric Lamb mode for a free plate. In this case, neither the symmetric nor the antisymmetric part of the motion is prevailing.[16] This is easily seen by analyzing the equations for the asymptotic h expansion, the solution of which is surprisingly accurate. Similar results are also clearly visible in Fig. 3(d), where the Kirchhoff and Mindlin plate theories obviously differ from the rest. Hence, comparisons to the free-plate Lamb modes are of less importance in this heavy loading example, as expected.[18]

As in the aluminum-water case, contour lines are displayed in Fig. 4. The results using Kirchhoff, Mindlin, and asymptotic h^3 expansions are presented in Fig. 4(a), showing the superiority of the latter theory. Here, the lines corresponding to the classical theories are mostly on top of each other. The various asymptotic expansions are displayed in Fig. 4(b). The accuracies are quite good for all the expansions, besides around $\zeta=0.5$, where the relative errors become pronounced due to the transition from $T=0$.

Due to the importance of the symmetric motion in this heavy loading case, it is interesting to study the combined classical theories according to K-GPS and M-KM. When

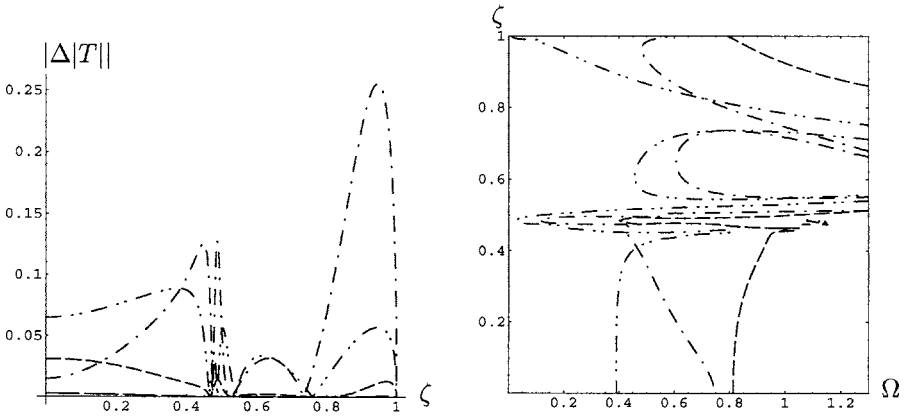

(a) $\Omega=1$ (b) 1% relative error contours for $|T|$.

FIG. 5. Polyethylene-water. – – h^5; --- h^3; -·- K-GPS; -···- M-KM.

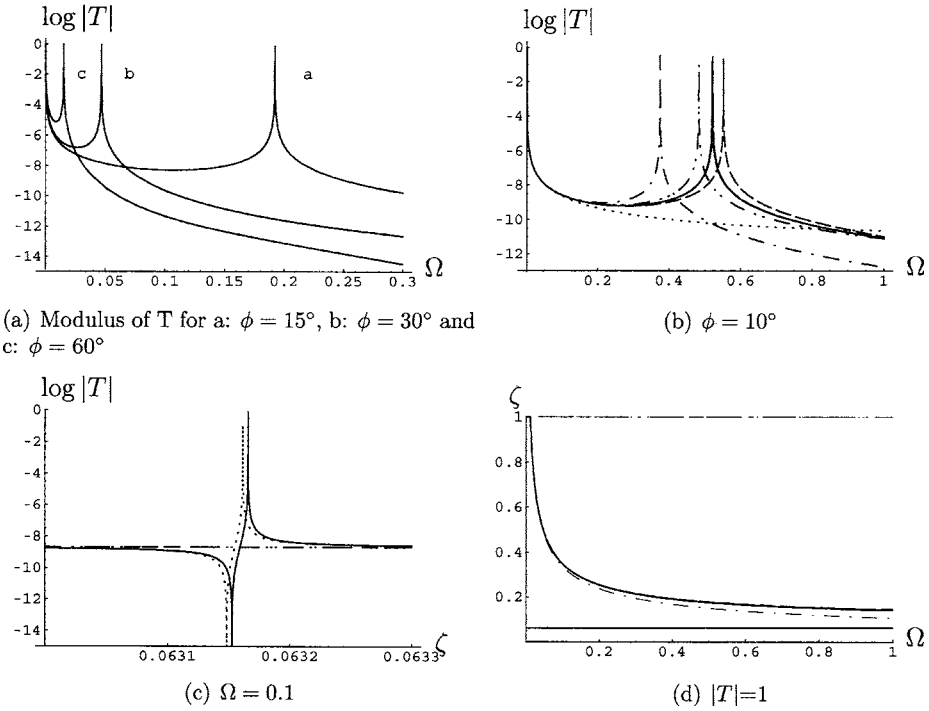

(a) Modulus of T for a: $\phi = 15°$, b: $\phi = 30°$ and c: $\phi = 60°$

(b) $\phi = 10°$

(c) $\Omega = 0.1$

(d) $|T|=1$

FIG. 6. Steel-air. —— exact; – – h^5; --- h^3; ⋯ h; -·- Kirchhoff; -···- Mindlin.

compared to the results presented in Fig. 3(c), both K-GPS and M-KM are considerably better than the classical antisymmetrical plate theories. The accuracies are displayed in Fig. 5(a), where the absolute values of the error in the transmission coefficient modulus, $|\Delta|T||$, are plotted. As in the aluminum-water case, the combined classical theories render more or less the correct behavior around the transition point $\zeta \approx 0.5$ as well as near $\zeta = 1$. The contour lines for the three theories of order h^3, that is K-GPS, M-KM, and asymptotic h^3, are given in Fig. 5(b). The improvement using the combined classical theories is clearly visible when compared to Fig. 4(a). However, Fig. 5 shows that the the asymptotic h^3 and h^5 expansions are, in most cases, the best approximations.

C. Steel-air

The last example considers a case of light fluid loading, a steel plate in air. The nondimensional parameters are $\alpha \approx 1.66 \times 10^{-4}$, $\beta \approx 0.011$, and $\gamma \approx 0.33$.

The pronounced impedance mismatch causes the plate to act as a sound barrier ($|T| \approx 0$) for most combinations of Ω and ζ. The transmission coefficient tends to unity for those (Ω, ζ) which are close to the solutions of the dispersion relation for a free plate. In Fig. 6(a) the exact value of $\log|T|$ is plotted for some different angles of incidence, resembling the results presented in the aluminum-water case, Fig. 1(a). The behavior of the transmission coefficient using the different plate equations is displayed in Fig. 6(b) for $\phi = 10°$. As in the aluminum-water case, the h^5 expansion result is very close to the exact one, while the h expansion does not include the flexural mode. Figure 6(c) shows the very sharp transition of the transmission coefficient from zero to unity for the compressional mode around $\phi = 3.6°$, which is not included in the Kirchhoff and Mindlin theories. The curves for total transmission are presented in Fig. 6(d), similar to Fig. 1(d).

IV. NUMERICAL CALCULATIONS FOR A LINE LOADING

To further evaluate the asymptotic equations, the pressure fields on the plate boundaries due to applied forces are calculated. As the fluid-plate responses from time-harmonic line forces have been studied by many authors,[19–23] such problems are addressed here. The line forces are modeled according to $\Delta F = F_a \delta(x) e^{-i\omega t}$ in the antisymmetric case and $\Sigma F = F_s \delta(x) e^{-i\omega t}$ in the symmetric case. Each case is studied separately. As the problems become y independent, this coordinate is suppressed throughout. The problems are solved by applying the Fourier transform in the x coordinate. If the fluid is assumed to follow the wave equation (25), the transformed pressure fields are given by

$$\hat{p}^+ = p^+ e^{i(kz-\omega t)}, \quad z > h/2, \tag{27}$$

$$\hat{p}^- = p^- e^{i(-kz-\omega t)}, \quad z < -h/2, \tag{28}$$

where $k = \sqrt{k_f^2 - q^2}$, q being the transform variable. In the antisymmetric case $p^- = -p^+$, while in the symmetric case $p^- = p^+$. Thus, it is clear that Eqs. (27) and (28) can be combined to give

$$\Delta\hat{p}(q) = \hat{p}_a(q), \quad \Sigma\partial_z\hat{p}(q) = ik(q)\hat{p}_a(q), \tag{29}$$

$$\Sigma\hat{p}(q) = \hat{p}_s(q), \quad \Delta\partial_z\hat{p}(q) = ik(q)\hat{p}_s(q). \tag{30}$$

By using the relations in (29) and (30), it is straightforward to relate p_a to F_a as well as p_s to F_s in the approximate boundary conditions (18)–(24). The transformed pressure

fields at the boundaries can in each such case be expressed in the form

$$\hat{p}_{a,s}(q) = \frac{N_{a,s}(q)}{N_{a,s}(q) + k(q)D_{a,s}(q)} F_{a,s}. \tag{31}$$

The various functions $N_{a,s}$ and $D_{a,s}$ involve polynomials in q^2. The numerators are recognized as the dispersion equations for fluid-loaded plates, while the functions $D_{a,s}$ appear when studying the dispersion relations for the corresponding free plates. For the *exact* theory, separate antisymmetric and symmetric modes are easily obtained.[28] The pressure relations may still be written in the form of Eq. (31). Here, $N_{a,s}$ and $D_{a,s}$ are even functions in q, including trigonometric functions. The functions $D_{a,s}$ are then recognized as the Rayleigh-Lamb frequency equations. It is instructive to note that the numerator and denominator of Eq. (31) in the exact cases may be expanded in the layer thickness coordinate h, giving the same quotients as for the asymptotic plate equations discussed above; see further Losin.[24]

By using the inversion formula, the pressure fields $p_{a,s}(x)$ are obtained from $\hat{p}_{a,s}(q)$ in Eq. (31) for each plate theory. The integrals are rewritten as cosine transforms, since the integrands are even in q. Analytical solution of these integrals is complicated to evaluate, even for the lowest order case. Therefore, it is computed numerically. The contour of integration is deformed into the fourth quadrant due to the poles and branch points on the real axis.

The numerical results, Figs. 7 and 8, show the plate boundary pressure as a function of the distance from the line force. Only the pressure component in phase with the line force is presented. All three fluid-loading situations are studied for both the antisymmetric and the symmetric cases. In order to easily distinguish between the results using various plate theories, the chosen frequency is quite high, $k_s h = 1$. In Fig. 7, the antisymmetric motions for the different theories are displayed. The lowest order h theory is not included here, as this simple approximation completely fails to predict the plate and fluid behavior in this loading case. From the figures, it is clear that the Kirchhoff theory is less accurate than the other more refined theories at this frequency level, as expected. The accuracies using the Mindlin equation and the asymptotic h^3 equation are of the same order. The results using the h^5 theory are very close to the exact curves. The corresponding symmetric cases are plotted in Fig. 8. Here, the curves using the approximate equations comprise the classic Kane-Mindlin equation as well as the three different asymptotic equations. It is seen from these results that the relations between the plate and fluid parameters influence the wave lengths in a more pronounced way than in the antisymmetric cases. In the modest and heavy loading cases, Figs. 8(a) and 8(b), the asymptotic theories are superior to the Kane-Mindlin theory. Since this relation holds even for the h theory, this is an unexpected outcome. However, for even higher frequencies, the results due to Kane-Mindlin are better than the asymptotic h theory. The different approximate equations behave quite poorly in the steel-air case, Fig. 8(c), especially close to $x=0$. This is probably due to the unphysical behavior of these approximate equations near a symmetric point load for a free plate, rendering infinite displacements.

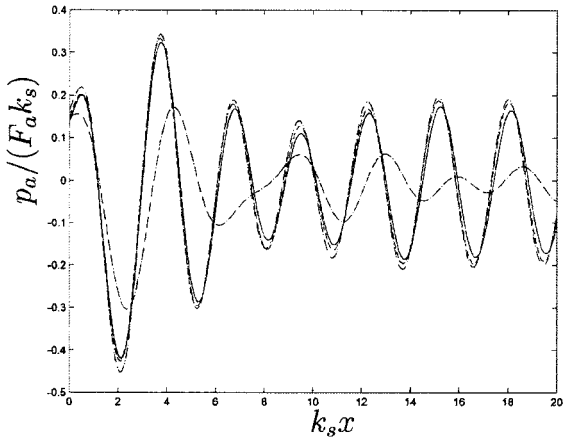

(a) Aluminum-Water.

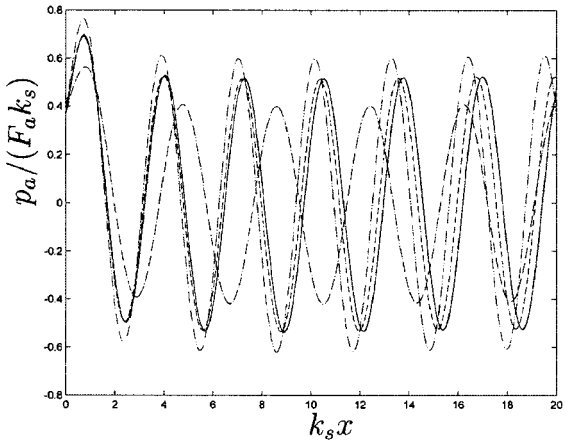

(b) Polyethylene-Water.

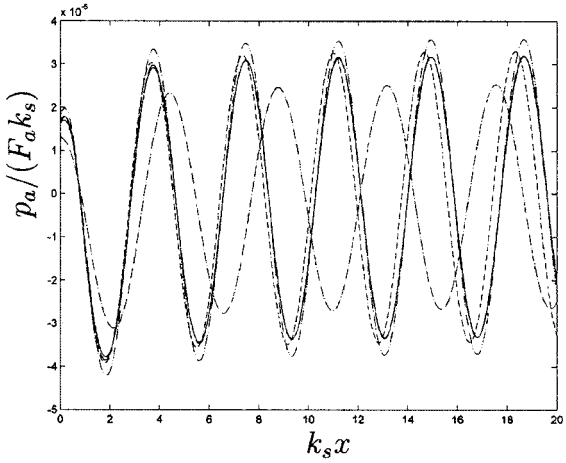

(c) Steel-Air.

FIG. 7. Antisymmetric plate boundary pressure $p_a/(F_a k_s)$ as a function of distance $k_s x$ for $k_s h = 1$. —— exact; – – h^5; --- h^3; -·- Kirchhoff; -···- Mindlin.

V. CONCLUSIONS

In this paper, the derivation of approximate boundary conditions for an elastic layer immersed in a fluid is pre-

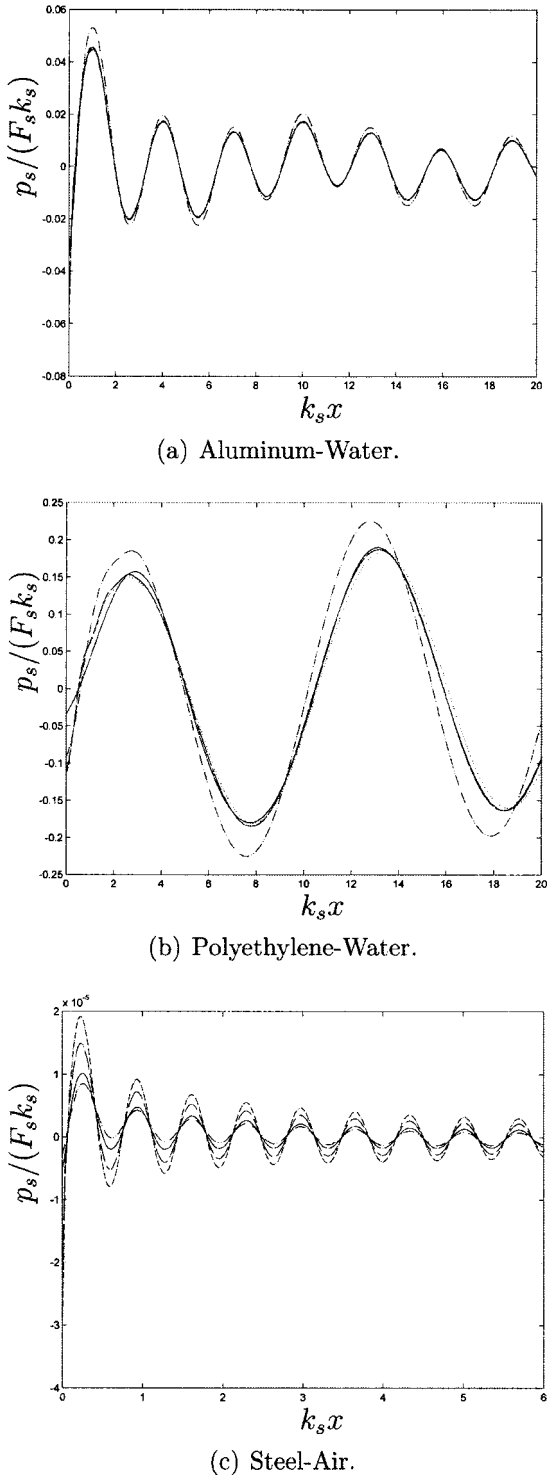

FIG. 8. Symmetric plate boundary pressure $p_s/(F_s k_s)$ as a function of distance $k_s x$ for $k_s h=1$. —— exact; – – h^5; --- h^3; ··· h; -·-· Kane-Mindlin.

sented. Starting from the three-dimensional equations of motion, the boundary conditions are stated in terms of the plate fields together with the pressure field and its normal derivative. By expressing the sums and differences of the boundary conditions, the terms involving the plate fields are expanded in Maclaurin's series in the plate thickness. In order to eliminate the plate fields (and their normal derivatives), the three-dimensional equations of motion (and normal derivatives thereof) are adopted. This gives two different linear systems, one antisymmetric involving Δp and $\Sigma \partial_z p$ and one symmetric involving Σp and $\Delta \partial_z p$. The operators relating Δp to $\Sigma \partial_z p$ and Σp to $\Delta \partial_z p$, respectively, are expressed in terms of time derivatives, spatial derivatives in the layer plane, and power series in the plate thickness. These equations can be truncated to any desired order, and the explicit relations up to and including order five are presented. Comparisons are made with different classic plate theories. Especially, the often-used antisymmetric equations due to Kirchhoff and Mindlin are here of interest.

In the numerical results, both the reflection and transmission from plane waves as well as the boundary pressure fields from line forces are studied. The results using exact three-dimensional theory, classical flexural equations (e.g., Kirchhoff, Mindlin), as well as asymptotic expansions (h, h^3, h^5) are compared. Three different cases are studied: modest loading (aluminum-water), heavy loading (polyethylene-water), and light loading (steel-air). In the planar scattering problems, the classical flexural theories are rather good for modest and light loading as the antisymmetric motion is prevailing. However, in the heavy loading example, the importance of including compressional motion is obvious. Taking all three loading cases into consideration, the asymptotic h^3 and h^5 expansions theories give more satisfying results than the different classic theories. In the line loading cases, purely antisymmetric and symmetric motions are examined separately. The accuracies of the Kirchhoff theory in the antisymmetric case are inferior to the other theories of order three (Mindlin and asymptotic h^3), which in turn are inferior to the asymptotic h^5 solutions. In the symmetric case, all the displayed results are here of the same order.

ACKNOWLEDGMENTS

The present work is partially supported by the Swedish Research Council (VR) and the Volvo-Chalmers Vehicle Research Program.

[1] P. Bövik, "On the modelling of thin interface layers in elastic and acoustic scattering problems," Q. J. Mech. Appl. Math. **47**(1), 17–42 (1994).
[2] H. Ammari and S. He, "Generalized effective impedance boundary conditions for an inhomogeneous thin layer in electromagnetic scattering," J. Electromagn. Waves Appl. **11**, 1197–1212 (1997).
[3] P. Olsson, S. K. Datta, and A. Boström, "Elastodynamic scattering from inclusions surrounded by thin interface layers," J. Appl. Mech. **57**, 672–676 (1990).
[4] S. I. Rokhlin and W. Huang, "Ultrasonic wave interaction with a thin anisotropic layer between two anisotropic solids. II. Second-order asymptotic boundary conditions," J. Acoust. Soc. Am. **94**(6), 3405–3420 (1993).
[5] G. Johansson and A. J. Niklasson, "Approximate dynamic boundary conditions for a thin piezoelectric layer," Int. J. Solids Struct. **40**(13–14), 3477–3492 (2003).
[6] P. M. Morse and K. U. Ingard, *Theoretical Acoustics* (McGraw-Hill, New York, 1968).
[7] R. D. Mindlin, "Influence of rotatory inertia and shear on flexural motion of isotropic, elastic plates," J. Appl. Mech. **18**, 31–38 (1951).
[8] B. L. Woolley, "Acoustic radiation from fluid-loaded elastic plates. I. Antisymmetric modes," J. Acoust. Soc. Am. **70**(3), 771–781 (1981).
[9] B. L. Woolley, "Acoustic radiation from fluid-loaded elastic plates. II. Symmetric modes," J. Acoust. Soc. Am. **72**(3), 859–869 (1982).
[10] G. Jemielita, "On kinematical assumptions of refined theories of plates: A survey," J. Appl. Mech. **57**, 1088–1091 (1990).
[11] A. L. Goldenveizer, J. D. Kaplunov, and E. V. Nolde, "On Timoshenko-

Reissner type theories of plates and shells," Int. J. Solids Struct. **30**(5), 675–694 (1993).
[12]N. A. Losin, "Asymptotics of flexural waves in isotropic elastic plates," Trans. ASME, J. Appl. Mech. **64**, 336–342 (1997).
[13]N. A. Losin, "Asymptotics of extensional waves in isotropic elastic plates," Trans. ASME, J. Appl. Mech. **65**, 1042–1047 (1998).
[14]A. Boström, G. Johansson, and P. Olsson, "On the rational derivation of a hierarchy of dynamic equations for a homogeneous, isotropic, elastic plate," Int. J. Solids Struct. **38**(15), 2487–2501 (2001).
[15]A. Freedman, "Reflectivity and transmittivity of elastic plates. I. Comparison of exact and approximate theories," J. Sound Vib. **59**(3), 369–393 (1978).
[16]R. Fiorito, W. Madigosky, and H. Überall, "Resonance theory of acoustic waves interacting with an elastic plate," J. Acoust. Soc. Am. **66**(6), 1857–1866 (1979).
[17]P. S. Dubbelday and A. J. Rudgers, "An analysis of effective shear modulus for flexural and extensional waves and its application to reflection of sound by a plate," J. Acoust. Soc. Am. **70**(2), 603–614 (1981).
[18]D. E. Chimenti and S. I. Rokhlin, "Relationship between leaky Lamb modes and reflection coefficient zeroes for a fluid-coupled elastic layer," J. Acoust. Soc. Am. **88**(3), 1603–1611 (1990).
[19]A. D. Stuart, "Acoustic radiation from submerged plates. I. Influence of leaky wave poles," J. Acoust. Soc. Am. **59**(5), 1160–1169 (1976).
[20]Y. D. Sergeev, "Influence of shear, rotary inertia, and longitudinal vibrations on the radiation of sound by a point-driven plate," Sov. Phys. Acoust. **25**(2), 174–176 (1979).
[21]A. J. Rudgers, P. S. Dubbelday, and L. A. Fagerstrom, "Extensional-wave and flexural-wave contributions to the sound field radiated by a fluid-loaded infinite plate," J. Acoust. Soc. Am. **80**(3), 932–950 (1986).
[22]A. J. Langley, "Exact and approximate theories for fluid-loaded, infinite, elastic plates," J. Acoust. Soc. Am. **83**(4), 1366–1376 (1988).
[23]A. J. DiPerna and D. Feit, "An approximate Green's function for a locally excited fluid-loaded thin elastic plate," J. Acoust. Soc. Am. **114**(1), 194–199 (2003).
[24]N. A. Losin, "On the equivalence of dispersion relations resulting from Rayleigh-Lamb frequency equation and the operator plate model," ASME J. Vibr. Acoust. **123**, 417–420 (2001).
[25]T. R. Kane and R. D. Mindlin, "High-frequency extensional vibrations of plates," J. Appl. Mech. **23**, 277–283 (1956).
[26]L. M. Lyamshev, "Reflection of sound from a moving thin plate," Sov. Phys. Acoust. **6**(4), 505–507 (1960).
[27]E. L. Shenderov, "Sound transmission through a transversely isotropic plate," Sov. Phys. Acoust. **30**(1), 69–73 (1984).
[28]J. D. Achenbach, *Wave Propagation in Elastic Solids* (North-Holland, Amsterdam, 1973).

The mean and variance of diffuse field correlations in finite bodies

Richard L. Weaver[a] and Oleg I. Lobkis
Department of Theoretical and Applied Mechanics, University of Illinois at Urbana-Champaign, 216 Talbot Lab, 104 S. Wright Street, Urbana, Illinois 61801

(Received 24 January 2005; revised 17 August 2005; accepted 12 September 2005)

A model consisting of uniformly distributed concentrated transient sources in closed reverberant systems is used to construct predictions for the diffuse field correlation function and its variance. Such correlations are useful for passive imaging. It is found that the variance is small compared with the square of the mean if estimates are based on a sufficient number of sources, and if a sufficiently long data record is taken from each source. Requirements are predicted to be most onerous at high frequency. Laboratory measurements support this theory. They furthermore indicate that the fidelity of the passively obtained correlation function to an actively obtained waveform depends, not only on having sufficient passive data, but also on an informed compensation for source spectrum and receiver characteristics. It is anticipated that these arguments will be relevant to convergence rates and fidelity for passive imaging in open systems such as are found in seismology and ocean acoustics. © *2005 Acoustical Society of America.* [DOI: 10.1121/1.2109307]

PACS number(s): 43.20.Gp, 43.40.Qi, 43.40.Ph [ANN] Pages: 3447–3456

I. INTRODUCTION

The recent arguments, proofs, and demonstrations that diffuse fields have correlations essentially equal to the Green's function[1–8] have been widely noted.[9–16] Laboratory demonstrations of the effect have been conducted in ultrasonics and in acoustics.[2,15,16] Applications have been suggested in ocean acoustics[7,13,14] and in seismology.[6,8–12] The potential for passive imaging is intriguing, especially in seismology where well-controlled sources are awkward. The idea is not entirely new. Helioseismology[17] correlates acoustic fluctuations in the sun to determine the speeds of such waves. Claerbout and Cole and Claerbout and Rickett[17] have speculated that correlations of ambient seismic waves would reveal geologic structures. Cole's attempts to verify and apply this were unsuccessful. Fehler *et al.*,[12] Wapenaar,[8] and Campillo and co-workers[9–11] have explored applications in seismology with promising results.

Norton *et al.*[18] have speculated in similar ways; they describe a method for analysis of ambient seismic noise to resolve deep structures, a method that they term "time exposure acoustics." Close examination, however, shows that their technique is not equivalent to that of Refs. 1–16. Similarly, the technique termed "acoustic daylight"[19] bears some similarities, but is not equivalent. Nor are the field-field correlation functions of Refs. 1–16 equivalent to the better-known process of correlating a noisy source function with a noisy response (e.g., Ref. 20) to construct impulse responses.

The proof by Weaver and Lobkis[1–4] was based on a modal expansion for the diffuse field in a finite reverberant body. They showed that convergence is most clear if correlation averaging could be carried out over ranges of time comparable to the Heisenberg time T_H (T_H is the inverse of the mean spacing of eigenfrequencies), and/or if sources are distributed over all space. This limitation was perhaps of small concern in the corresponding laboratory demonstrations conducted in finite bodies.[2] But in open systems, where T_H is infinite, the potential restrictions are problematic. Recently the proof was extended to open homogeneous[6,7] and open heterogeneous systems.[21]

Both in laboratory demonstrations,[2,15,16] and in applications to seismic waves, the correlation function has in practice only imperfectly matched the Green's function itself. Campillo and Paul[9] and Shapiro *et al.*[11] observed low-frequency Rayleigh and Love waves in the correlations of seismic codas on a regional scale. (The seismic coda is the low amplitude ringing that typically follows an earthquake for periods of minutes or more. It is widely believed to be multiply scattered and diffuse.) Shapiro and Campillo observed[10] very low frequency surface waves in correlations of ambient seismic noise on a continental scale. They did not observe other wave types or higher frequencies. In laboratory ultrasonic experiments Lobkis and Weaver[2] observed surface waves and reflections from nearby interfaces in finite bodies, but only after extensive averaging, in time and over a small ensemble of distinct sources. Even then, they observed convergence to be inadequate at higher frequencies. These papers have thus made it abundantly clear that there is a need for theoretical understanding of the *rate* of convergence. How much averaging is necessary? It is towards that question that this work is addressed. A separate question regarding the fidelity with which the limit matches the Green's function, and the quality of the retrieval when the diffuse field is insufficiently diffuse, is not addressed.

In a companion paper,[22] a theory was presented for the rate of convergence in open systems. The issue has also been addressed elsewhere.[6] Here we adapt the theory used in Ref. 22 to closed systems and compare its predictions to our observations in a finite aluminum block. Most applications ap-

[a]Author to whom all correspondence should be addressed. Electronic mail: r-weaver@uiuc.edu

pear to reside in open systems, but the possibility of well-controlled laboratory experiments in closed systems renders the theory worth adapting to that case.

In finite systems, ergodically filled by diffuse waves, it has proved convenient[1,2] to take a diffuse field in the form of a modal expansion with uncorrelated, equal mean square, modal amplitudes. Such a diffuse field fills the volume uniformly. Such an assumed form begs an important question, however, of whether the assumption is valid, or whether a particular diffuse field can be so represented. It may be that a practical correlation function will vary as the source of the diffuse field is varied.

It is unclear how quickly a measured correlation function will average to the Green's function as the source is varied. To address this question we do not make the assumption of incoherent modal amplitudes here, but rather take our diffuse field to have simple sources at random positions. This model is introduced in Sec. II, after which the field-field correlation functions are shown, in Sec. III, to have expectation equal to the Green's function of the medium. Thus the familiar proof[1–8] is rederived. The mean square correlation function is then derived in the following section, and the corresponding variance is compared with the square of the mean. It is found that the variance is small compared with the square of the mean if averaging is sufficient. The precise meaning of "sufficient" is described mathematically. In Sec. V these predictions are compared to our observations.

II. MODEL

Consider a finite elastic volume V with normalized modes $u^n(x)$ and natural frequencies ω_n. In terms of these modes we define a waveform that will prove useful in the following:

$$C_{ab}(t) \equiv \sum_n u^n(a)u^n(b)\cos(\omega_n t), \tag{1}$$

for all t, and all positions a,b. It is related to the velocity Green's function:

$$\dot{G}_{ab}(t) \equiv \Theta(t)\sum_n u^n(a)u^n(b)\cos(\omega_n t) \tag{2}$$

by

$$C_{ab}(t) \equiv \dot{G}_{ab}(t) + \dot{G}_{ab}(-t). \tag{3}$$

In the above $\Theta(t)$ is the unit step function.

We define a time-varying signal $\Psi_a^\sigma(t)$ as the response at position a to a spatially distributed source $\dot{s}_x^\sigma(t)$, after filtering by a receiver function $r(t)$. Ψ is given by a convolution of r and $\dot{s}$ with G:

$$\begin{aligned}\Psi_a^\sigma(t) &= \int dx \int d\phi d\alpha \dot{s}_x^\sigma(\phi) r(\alpha) G_{ax}(t-\phi-\alpha) \\ &= \int dx \int d\phi s_x^\sigma(\phi) r(\alpha) \dot{G}_{ax}(t-\phi-\alpha),\end{aligned} \tag{4}$$

where the second equality follows from an integration by parts. We consider a finite set of distinct transient source distributions $s_x^\sigma(t)$ $(\sigma=1,2,\ldots,N)$ concentrated at random positions p_σ

$$s_x^\sigma(t) = g_\sigma s(t)\delta(x-p_\sigma). \tag{5}$$

The g are independent random force amplitudes with zero mean; $g=\pm 1$. The points p_σ are randomly and uniformly and independently distributed in the volume V. The probability density in this ensemble is given by a product of differentials $dP=\Pi_\sigma dp_\sigma/V$. Thus $\int dP=1$. With ensemble averages defined by $\langle\cdots\rangle=\int\cdots dP$, we find

$$\langle s_x^\sigma\rangle = 0; \quad \langle s_x^\sigma(t)s_{x'}^{\sigma'}(t')\rangle = \delta(x-x')s(t)s(t')\delta_{\sigma\sigma'}/V, \tag{6}$$

$$\begin{aligned}&\langle s_x^\sigma(t)s_{x'}^\sigma(t')s_y^{\sigma'}(t'')s_{y'}^{\sigma'}(t''')\rangle \\ &\quad= \delta(x-x')\delta(y-y')s(t)s(t')s(t'')s(t''')[1-\delta_{\sigma\sigma'}]/V^2 \\ &\qquad+ s(t)s(t')s(t'')s(t''')\delta_{\sigma\sigma'}\int \delta(x-p)\delta(x'-p) \\ &\qquad\times\delta(y-p)\delta(y'-p)dp/V.\end{aligned} \tag{7}$$

An estimate of the correlation function is obtained by means of a sum, R^N, over N distinct sources, and an integral over a long time window W. The estimated correlation is

$$R_{ab}^N(\tau) = \frac{1}{N}\sum_\sigma \int dt W(t)\Psi_a^\sigma(t)\Psi_b^\sigma(t+\tau). \tag{8}$$

It is expected to converge to the Green's function as $N\to\infty$. It is convenient to take the window to be rectangular: $W=1$ if $t_o-T/2<t<t_o+T/2$ (and 0 otherwise), where $T=\int W(t)\,dt$ is the amount of time over which signal Ψ is collected. The center time t_o is understood to be large enough that $W(t=0)$ is zero; $t_o>T/2$. T and t_o are also taken to be much greater than the correlation times τ of interest. Under these conditions, we may replace $\dot{G}(t)$ with $C(t)$. Then

$$\begin{aligned}R_{ab}^N(\tau) &= \frac{1}{N}\sum_\sigma \int dt W(t)\Psi_a^\sigma(t)\Psi_b^\sigma(t+\tau) \\ &= \frac{1}{N}\sum_\sigma \int W(t)dtdxdyd\phi d\psi d\alpha d\beta s_x^\sigma(\phi)s_y^\sigma(\psi) \\ &\quad\times r(\alpha)r(\beta)C_{ax}(t-\phi-\alpha)C_{by}(t+\tau-\psi-\beta).\end{aligned} \tag{9}$$

For simplicity we have assumed that the receivers at a and b have identical transfer functions $r(t)$. The assumption is readily relaxed. Equation (9) is an expression for the correlation function that would be estimated from measurements of fields due to a finite set of distinct sources σ. It is the experimentalist's estimate for an ensemble average.

III. EXPECTATION OF ESTIMATED CORRELATOR $\langle R^N \rangle$

The expectation, over the ensemble of different sources, of the estimate R^N is $\langle R^N \rangle = \int R^N \, dP$.

$$\langle R^N_{ab}(\tau) \rangle = \int dt W(t) dx d\phi d\psi d\alpha d\beta s(\phi) s(\psi) r(\alpha) r(\beta) \times C_{ax}(t - \phi - \alpha) C_{bx}(t + \tau - \psi - \beta)/V. \quad (10)$$

The integral over x may be evaluated by use of a Ward identity[23]

$$\int dx C_{ax}(t) C_{bx}(t') = \frac{1}{2}[C_{ab}(t + t') + C_{ab}(t - t')], \quad (11)$$

which is readily proved by substituting for C in terms of the modes, as in Eq. (1), and invoking orthonormality of the modes: $\int u^n(x) u^m(x) \, dx = \delta_{nm}$.

Thus

$$\langle R^N_{ab}(\tau) \rangle = \int dt W(t) d\phi d\psi d\alpha d\beta r(\alpha) r(\beta) s(\phi) s(\psi) \times \frac{1}{2}[C_{ab}(2t + \tau - \phi - \psi - \alpha - \beta) + C_{ab}(\tau + \phi - \psi + \alpha - \beta)]/V. \quad (12)$$

The α, β, ϕ, and ψ integrations merely filter these C's. On denoting the quadruply filtered C's with superscripts = or ±, the above becomes

$$\langle R^N_{ab}(\tau) \rangle = \frac{1}{2V} \int dt W(t) [C^{=}_{ab}(2t + \tau) + C^{\pm}_{ab}(\tau)]. \quad (13)$$

Here the superscript = denotes two filterings by s and two by r. The superscript ± denotes a filtering by s and r and a filtering by the time-reversed s and the time-reversed r.

On integration with respect to t, the first term is essentially zero. (We assume the sources and receivers have no amplitude at zero frequency.) The second term then gives

$$\langle R^N_{ab}(\tau) \rangle = \frac{T}{2V} C^{\pm}_{ab}(\tau), \quad (14)$$

thus once again establishing the now-familiar identification of the expectation of field-field correlations R_{ab} with the (time derivative of the) Green's function C_{ab}.

In order to be able to compare $\langle R \rangle$ to its expected level of fluctuations, it is necessary to estimate its amplitude. At sufficiently large τ (greater than a few transits, i.e., an ergodic time), $\langle R \rangle$ should have achieved a stationary and diffuse character. Its mean square level (we denote averages over time or space with an overbar)

$$\overline{\langle R^N_{ab}(\tau) \rangle^2}^{\tau} = \frac{T^2}{4V^2} \overline{C^{\pm}_{ab}(\tau)^2}^{\tau} = \frac{T^2}{4V^2} E \quad (15)$$

is proportional to the mean square of C, i.e., to

$$E = \overline{\sum_n \sum_m u^n(a) u^n(b) u^m(a) u^m(b) |\tilde{s}(\omega_n)|^2 |\tilde{s}(\omega_m)|^2 |\tilde{r}(\omega_n)|^2 |\tilde{r}(\omega_m)|^2 \cos(\omega_n t) \cos(\omega_m t)}^{t}.$$

We have learned[24] that such double sums are well approximated by their diagonal part (if the time range over which they are averaged is beyond the ergodic time). We conclude

$$E = \frac{1}{2} \sum_n u^n(a)^2 u^n(b)^2 |\tilde{s}(\omega_n)|^4 |\tilde{r}(\omega_n)|^4 = \frac{1}{2V^2} \int D(\omega) |\tilde{s}(\omega)|^4 |\tilde{r}(\omega)|^4 \, d\omega. \quad (16)$$

The sum in (16) is well represented by the integral, with modal density D, because the functions $\tilde{r}$ and $\tilde{s}$ are smooth on a scale of natural frequency spacings:

$$\overline{\langle R^N_{ab}(\tau) \rangle^2}^{\tau} = \frac{T^2}{8V^4} \int D(\omega) |\tilde{s}(\omega)|^4 |\tilde{r}(\omega)|^4 \, d\omega. \quad (17)$$

It depends on source and receiver functions and on modal density.

IV. MEAN SQUARE CORRELATOR $\langle R^2 \rangle$

We now investigate the fluctuations of R and estimate the accuracy with which the estimate R^N may be expected to equal $\langle R \rangle$. The expected square of the correlation estimate [Eq. (9)] is, if the sources σ are independent,

$$\langle R^{N^2}_{ab}(\tau) \rangle = \langle R^N_{ab} \rangle^2 + \frac{\text{var } R}{N}, \quad (18)$$

where var R is the variance (over the ensemble of source positions p_σ) of the quantity

$$R_{ab}(\tau)=\int dt W(t)\Psi_a^\sigma(t)\Psi_b^\sigma(t+\tau),$$

$$\begin{aligned}\text{var}\,R&=\langle R^2\rangle-\langle R\rangle^2\\&=\left\langle\int W(t)W(t')dtdt'\Psi_a^\sigma(t)\Psi_b^\sigma(t+\tau)\Psi_a^\sigma(t')\Psi_b^\sigma(t'+\tau)\right\rangle-\langle R\rangle^2\\&=-\langle R\rangle^2+\int W(t)W(t')dtdt'd\phi d\phi' d\psi d\psi' d\alpha d\alpha' d\beta d\beta' dxdx' dydy' r(\alpha)r(\beta)r(\alpha')r(\beta')\\&\quad\times\langle s_x^\sigma(\phi)s_y^\sigma(\psi)s_{x'}^\sigma(\phi')s_{y'}^\sigma(\psi')\rangle C_{ax}(t-\phi-\alpha)C_{by}(t+\tau-\psi-\beta)C_{ax'}(t'-\phi'-\alpha')C_{by'}(t'+\tau-\psi'-\beta').\end{aligned}\tag{19}$$

The expectation of ssss is obtained from Eq. (7). The result is

$$\begin{aligned}\text{var}\,R(\tau)&=\frac{1}{V}\int W(t)W(t')dtdt'd\phi d\psi d\phi' d\psi' d\alpha d\alpha' d\beta d\beta' r(\alpha)r(\beta)r(\alpha')r(\beta')s(\phi)s(\psi)s(\phi')s(\psi')\\&\quad\times\int dp C_{ap}(t-\phi-\alpha)C_{bp}(t'+\tau-\psi'-\beta)C_{bp}(t+\tau-\psi-\beta')C_{ap}(t'-\phi'-\alpha')-\langle R\rangle^2.\end{aligned}\tag{20}$$

A procedure for evaluation of (20) is not obvious. It may be appropriate to treat C as a random Gaussian process as p is varied; this leads to writing the product of four factors of C in terms of its cumulants. Another possibility is to take an average over a and b. Two further invocations of the Ward identity (11) then yield a useful expression. While this option abandons any attempt to evaluate sensitivity to special places a b, it does have the virtue of being rigorous:

$$\begin{aligned}\overline{\text{var}_{ab}(\tau)}^{ab}&=-\overline{\langle R\rangle^2}^{ab}\\&\quad+\frac{1}{4V^3}\int dtdt' W(t)W(t')\int dp[C_{pp}^{=}(t+t')\\&\quad+C_{pp}^{\pm}(t-t')][C_{pp}^{=}(t+t'+2\tau)+C_{pp}^{\pm}(t-t')].\end{aligned}\tag{21}$$

The integrations over t and t' are best performed by first changing variables

$$\xi=t+t'-2t_o,\quad \eta=t-t'\tag{22}$$

such that

$$\int\cdots W(t)W(t')dtdt'=\frac{1}{2}\int_{\xi=-T}^{T}\int_{\eta=|\xi|-T}^{T-|\xi|}\cdots d\eta\, d\xi,\tag{23}$$

whereupon

$$\begin{aligned}\overline{\text{var}_{ab}(\tau)}^{ab}&=-\overline{\langle R\rangle^2}^{ab}+\frac{1}{8V^3}\int_{\xi=-T}^{T}\int_{\eta=|\xi|-T}^{T-|\xi|}d\eta\, d\xi\\&\quad\times\int dp[C_{pp}^{=}(\xi+2t_o)+C_{pp}^{\pm}(\eta)]\\&\quad\times[C_{pp}^{=}(\xi+2t_o+2\tau)+C_{pp}^{\pm}(\eta)].\end{aligned}\tag{24}$$

The cross terms $C^{=}C^{\pm}$ and $C^{\pm}C^{=}$ integrate to zero, leaving two nontrivial terms to evaluate.

The product of the first terms, $C^{=}C^{=}$, integrates with respect to η to a factor of $2T-2|\xi|$. It then integrates with respect to ξ and p to (at $\tau=0$)

$$[T^2/4V^2]\overline{C_{pp}^{=2}}^{\text{all } p \text{ and time range } 2t_o\pm T}.$$

The time average is taken over a range from $2t_o-T$ to $2t_o+T$, with a triangular weighting that emphasizes times near $2t_o$. Enhanced backscatter[25] tells us that $C_{pp}^{=2}$ is two (or three if $2t_o>T_{\text{H}}$) times greater than typical mean square signals $C_{pp'}^{=2}$ elsewhere. Furthermore, $\overline{C_{pp'}^{=2}}=\overline{C_{pp'}^{\pm 2}}$, as time reversing a filtering affects only phase, leaving mean square values unaffected. This latter quantity is E. Thus we replace the above with $(T^2/4V^2)$ (2 to 3) $E=$(2 to 3)$\overline{\langle R^2\rangle}$. At $\tau\neq 0$, this term is diminished by a factor related to s and r. Indeed, this term is simply the autocorrelation function of the random process $C_{pp}^{=}(\xi+2t_o)$. The diminishment factor is

$$d(\tau)=\left(\int|s(\omega)|^4|\tilde{r}(\omega)|^4\exp\{-2i\omega\tau\}d\omega\right)\Big/\left(\int|s(\omega)|^4|\tilde{r}(\omega)|^4 d\omega\right).\tag{25}$$

If we take $s(t)=\exp(-t^2/2\Delta^2)\cos\omega_c t$ and $r=\delta(t)$, we find the diminishment factor $d(\tau)\sim\exp(-\tau^2/2\Delta^2)\cos 2\omega_c\tau$. Thus the factor is negligible for τ long compared to the ring time Δ of the sources and receivers. Finally, the first two terms of var R, averaged over a and b, are

$$(T^2/4NV^2)(2\text{ to }3)Ed(\tau)-\overline{\langle R\rangle^2}^{ab}=\overline{\langle R\rangle^2}[(2\text{ or }3)d(\tau)-1].\tag{26}$$

The product of the second terms in (24), $C_{pp}^{\pm 2}(\eta)$, looks at first like another mean square backscatter signal. But there is an additional coherent contribution in the vicinity of $\eta=0$. Indeed, $C_{pp}(\eta)$ before filtering has a delta-function-like be-

havior $\delta(\eta)$ near $\eta=0$ leading to an infinite value for $\int C^2(\eta)d\eta$. After filtering, however, the integral is finite. We note

$$C_{pp}^{\pm}(\eta)=\sum_n (u_p^n)^2|\tilde{s}(\omega_n)|^2|\tilde{r}(\omega_n)|^2\cos(\omega_n\eta). \tag{27}$$

So,

$$\begin{aligned}
&\int_{|\xi|-T}^{T-|\xi|} d\eta C_{pp}^{\pm 2}(\eta)\\
&\quad=\sum_{n,m}(u_p^n)^2(u_p^m)^2|\tilde{s}(\omega_n)|^2|\tilde{s}(\omega_m)|^2|\tilde{r}(\omega_n)|^2|\tilde{r}(\omega_m)|^2\\
&\qquad\times\int_{|\xi|-T}^{T-|\xi|} d\eta\cos(\omega_m\eta)\cos(\omega_n\eta)\\
&\quad=\sum_{n,m}(u_p^n)^2(u_p^m)^2|\tilde{s}(\omega_n)|^2|\tilde{s}(\omega_m)|^2|\tilde{r}(\omega_n)|^2|\tilde{r}(\omega_m)|^2\\
&\qquad\times\int_{|\xi|-T}^{T-|\xi|} d\eta\frac{1}{2}[\cos((\omega_m+\omega_n)\eta)+\cos((\omega_m-\omega_n)\eta)].
\end{aligned} \tag{28}$$

The first term of (28) drops out on doing the integral over η. The second gives a sinc function:

$$\begin{aligned}
&=\sum_{n,m}(u_p^n)^2(u_p^m)^2|\tilde{s}(\omega_n)|^2|\tilde{s}(\omega_m)|^2|\tilde{r}(\omega_n)|^2|\tilde{r}(\omega_m)|^2\\
&\quad\times\frac{\sin\{(T-|\xi|)(\omega_n-\omega_m)\}}{(\omega_n-\omega_m)}.
\end{aligned} \tag{29}$$

Thus the contribution to var R from the product of the second terms of (24) is

$$\begin{aligned}
\overline{\mathrm{var}_{ab}(\tau)}^{ab}|_{\text{2nd terms}}&=\frac{1}{8V^3}\int_{\xi=-T}^{T}d\xi\int dp\sum_{n,m}(u_p^n)^2(u_p^m)^2|\tilde{s}(\omega_n)|^2\\
&\quad\times|\tilde{s}(\omega_m)|^2|\tilde{r}(\omega_n)|^2|\tilde{r}(\omega_m)|^2\\
&\quad\times\frac{\sin\{(T-|\xi|)(\omega_n-\omega_m)\}}{(\omega_n-\omega_m)}.
\end{aligned} \tag{30}$$

The $n=m$ parts evaluate to (we take the random matrix theory estimate $\langle u^4\rangle=3\langle u^2\rangle^2=3/V^2$)

$$\frac{3}{V^4}\frac{T^2}{8}\int D(\omega)|\tilde{s}(\omega)|^4|\tilde{r}(\omega)|^4\,d\omega=3\overline{\langle R\rangle^2}. \tag{31}$$

The $n\neq m$ parts are

$$\begin{aligned}
&\frac{1}{8V^4}\int_{\xi=-T}^{T}d\xi\int D(\omega_c)|\tilde{s}(\omega_c)|^4|\tilde{r}(\omega_c)|^4d\omega_cD(\omega_c)\\
&\quad\times\int d\omega_d\frac{\sin\{(T-|\xi|)\omega_d\}}{\omega_d}[1-Y_2(D\omega_d)].
\end{aligned} \tag{32}$$

where Y_2 is Dyson's level correlation function,[26] equal to unity at zero argument, and equal to zero at infinite argument; it integrates to unity.

We define

$$X=D(\omega_c)\int d\omega_d\frac{\sin\{(T-|\xi|)\omega_d\}}{\omega_d}Y_2(D\omega_d) \tag{33}$$

and note

$$\partial X/\partial\xi=-\operatorname{sgn}\xi D(\omega_c)\int d\omega_d\cos\{(T-|\xi|)\omega_d\}Y_2(D\omega_d), \tag{34}$$

which may be interpreted in terms of the Fourier transform $b(t)$ of the Y_2 function:

$$\frac{\partial X}{\partial\xi}=-\operatorname{sgn}\xi\, b\left(\frac{T-|\xi|}{2\pi D}\right). \tag{35}$$

The function $b(t)$ is known in closed, albeit nonanalytic, form.[27] It is convenient to approximate it as $b(t)=\exp(-2|t|)$.[27] On making this substitution, we may conclude

$$X=\pi D[1-\exp(-(T-|\xi|)/\pi D)] \tag{36}$$

and then write the $n\neq m$ parts as

$$\begin{aligned}
&\frac{1}{8V^4}\int D(\omega_c)|\tilde{s}(\omega_c)|^4|\tilde{r}(\omega_c)|^4\,d\omega_c\int_{\xi=-T}^{T}d\xi(\pi D-X)\\
&\quad=\frac{1}{8V^4}\int D(\omega_c)|\tilde{s}(\omega_c)|^4|\tilde{r}(\omega_c)|^4\,d\omega_c\pi D\\
&\qquad\times\int_{\xi=-T}^{T}d\xi\exp\{-(|T-|x|)/\pi D\}\\
&\quad=\overline{\langle R\rangle^2}2(\pi D/T)^2[1-\exp\{-T/\pi D\}].
\end{aligned} \tag{37}$$

Summing equations (37), (31), and (26), we find

$$\begin{aligned}
\overline{\mathrm{var}\,R}^{ab}&=\overline{\langle R\rangle^2}\Bigg[2+(2\text{ or }3)d(t)+\frac{1}{2}\left(\frac{T_{\mathrm{H}}}{T}\right)^2\\
&\qquad\times(1-\exp\{-2T/T_{\mathrm{H}}\})\Bigg],
\end{aligned} \tag{38}$$

where $T_{\mathrm{H}}=2\pi D$ is the Heisenberg time equal to the inverse of the mean spacing of eigenfrequencies $f_n=\omega_n/2\pi$. The normalized variance $n\,\mathrm{var}\,R=\mathrm{var}\,R/\overline{\langle R\rangle^2}$ takes particularly simple forms in the limit of large and small T. For $T\gg T_{\mathrm{H}}$, the normalized variance is

$$n\,\mathrm{var}\,R=[2+(2\text{ or }3)d(\tau)], \tag{39}$$

independent of the length T of the waveform analyzed. For $T\ll T_{\mathrm{H}}$, the normalized variance is

$$n\,\mathrm{var}\,R=[1+(2\text{ or }3)d(\tau)+T_{\mathrm{H}}/T], \tag{40}$$

which diminishes with increasing data capture T. It is this limit which is the more common; the ability to capture long data records T is limited by absorption. Typically, it is only at low frequencies or for small objects that absorption times will exceed Heisenberg times. In this limit the variance is a strong function of frequency ($T_{\mathrm{H}}\propto f^2$ in three dimensions). We therefore typically expect greater difficulty retrieving $\langle R\rangle$ at high frequencies.

We summarize: R^N has an expected value of $(T/2V)C^{\pm}(\tau)$, with expected rms deviation from that value of

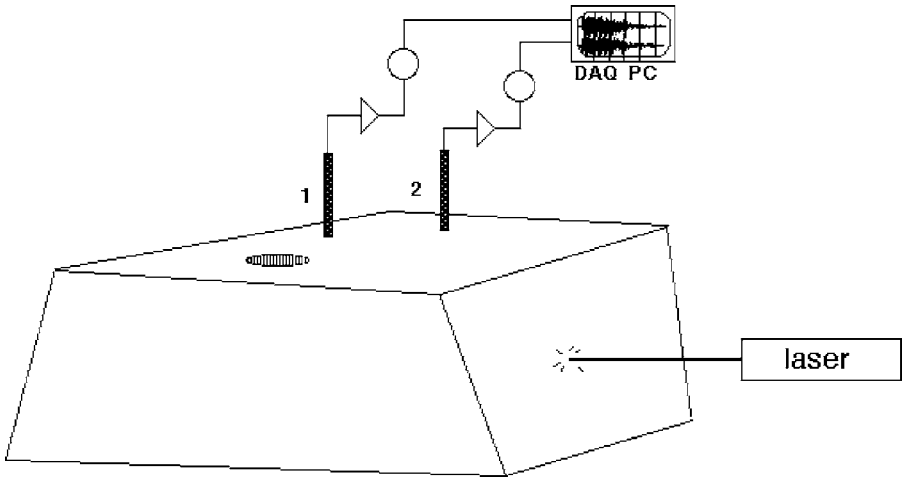

FIG. 1. Sketch of measurement system. A Q-switched Nd:YAG laser excites elastic waves in an irregular aluminum block of nominal dimension 15 cm. The signals from two piezoelectric transducers are amplified and low-pass filtered before being digitized by a PC.

$(n\ \mathrm{var}/N)^{1/2}$ times the rms value of $(T/2V)C^{\pm}(\tau)$ itself. In application to resolving early ray arrivals in a finite elastic block we note that the ray will be well discerned under certain conditions. The estimate R^Ns expected deviation will be small compared to the ray arrival itself if N is large, if T is large, and if the ray arrival is strong compared to the rms value of the rest of the waveform to be retrieved. Resolving weak ray arrivals from the correlations of diffuse fields will be difficult if the fields were generated by a modest number of sources N and only modest record lengths T were captured.

V. MEASUREMENTS

To investigate these predictions for variance and mean of R, we revisit the system of Ref. 2. We do so with a set of reproducible broadband sources and investigate the extent to which $\langle R\rangle$ is correctly given by (14), and the extent to which variance is correctly given by (38).

The experimental configuration is illustrated in Fig. 1. Two piezoelectric transducers are separated by 56 mm and oil-coupled to the top surface of an irregularly shaped object. A Q-switched 35-mJ Nd-Yag infrared laser with pulse duration ~8 ns and beam diameter ~4 mm excites elastic waves by means of a thermo-elastic mechanism, waves which then reverberate in the object. Absorption times vary with frequency and are of the order of tens of milliseconds. Transit times are of the order of tens of microseconds. The ensuing 100 ms of diffuse wave signals in each transducer is amplified, low-pass filtered, digitized, and passed to the computer for digital processing. Unlike other work,[2] no compensation for absorption is applied. Each decaying waveform is Fourier transformed. The result is two complex functions $\tilde{V}_1^{\sigma}(\omega)$ and $\tilde{V}_2^{\sigma}(\omega)$, where σ labels the position of the laser. We form the product $\tilde{P}^{\sigma}(\omega)=\tilde{V}_1^{\sigma}(\omega)\tilde{V}_2^{\sigma^*}(\omega)$ and average it over 100 different positions of the laser spot on one lateral face. Sources were spaced by ~1 cm in a square grid. This was repeated for each of three different lateral faces.

Figure 2(a) shows the direct "pitch-catch" signal transmitted between pin transducers when one is excited by a delta-function-like pulse. In spite of transducer dispersion, some of the arrivals can be identified. Figure 2(b) shows the inverse Fourier transform of the average (over the 300 source positions σ) of $\tilde{V}_1^{\sigma}(\omega)\tilde{V}_2^{\sigma^*}(\omega)$. One can identify the Rayleigh wave arrival at 20 μs, but little else. This is in part due to the ringing of the pinducers; they do not lend themselves to identifying sharp ray arrivals. It is also due to the presence in Eq. (14) of additional factors $|s|^2$ and $|r|^2$. It is also due to insufficient averaging; the variance is not zero. Rather than correct for these factors here, where the direct signal is so dispersive anyway, we use this data set only to investigate the variance amongst the $P^{\sigma}(\tau)$. The experimentally estimated variance is

$$\mathrm{var}=\frac{N}{N-1}\left[\frac{1}{N}\sum_{\sigma}(P^{\sigma}(\tau))^2-\left(\frac{1}{N}\sum_{\sigma}P^{\sigma}(\tau)\right)^2\right]. \tag{41}$$

This is smoothed and plotted in the form $\sqrt{\mathrm{var}/N}$ in Fig. 2(b) as a horizontal line at a level of 0.0002. The quantity $\sqrt{\mathrm{var}/N}$ is an estimate of the residual inaccuracy in $\langle P\rangle$.

Figure 3 shows the N dependence of var amongst this broadband set of signals $P^{\sigma}(\tau)$. As expected, it is independent of N except for statistical fluctuations. Small differences between the variances seen from sources on different faces are ascribed to differences between surface conditions and differences of angle of surface relative to laser beam.

A narrow-band version of the normalized variance is plotted versus frequency in Fig. 4. This is obtained by bandpassing $P^{\sigma}(\tau)$ at various frequencies, and for each such frequency and face constructing $\langle P\rangle$ and $n\ \mathrm{var}_P$. The quantity plotted is a smoothed-in-τ value of var divided by the time average of $\langle P(\tau)\rangle^2$. Thus it may be compared to the prediction Eq. (38),

$$n\ \mathrm{var}=\left[2+(2\text{ or }3)d(\tau)+\frac{1}{2}\left(\frac{T_{\mathrm{H}}}{T}\right)^2(1-\exp\{-2T/T_{\mathrm{H}}\})\right], \tag{42}$$

where T is replaced with T_{eff}

$$T_{\mathrm{eff}}=T_{\mathrm{absorption}}[1-\exp(-T/T_{\mathrm{absorption}})], \tag{43}$$

$1/T_{\mathrm{absortption}}$ being the rate of exponential dissipation of diffuse energy and readily measured (e.g., Refs. 2 and 27). The figure corroborates the prediction (42). This is important, because it confirms that higher frequencies have higher fluctuations in their diffuse field-diffuse field cor-

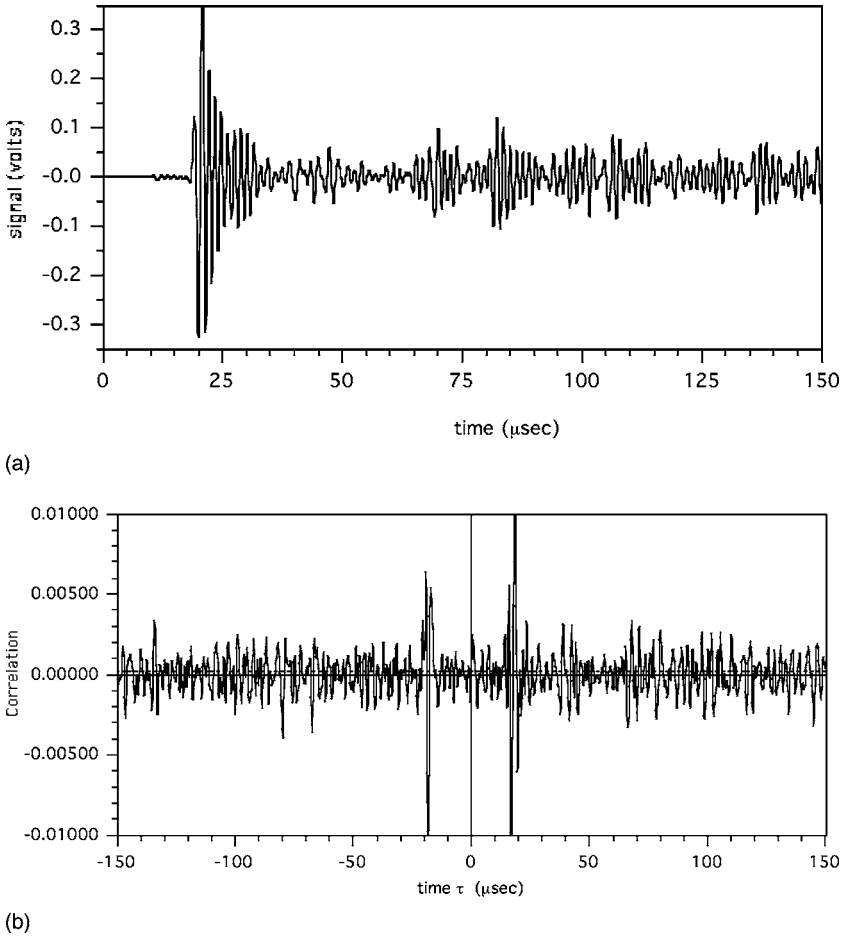

FIG. 2. (a) The direct signal received by one pinducer when the other is pulsed. The low-amplitude surface skimming P wave is first observed at $\tau \sim 9.8$ μs; the surface skimming shear wave arrives at 17.6 μs. A Rayleigh wave arrives at about 19 μs. Later arrivals corresponding to Rayleigh reflections from the edges are also seen. Transducer ringing is strong. (b) The correlation of two pinducer signals, over 100 ms of data taken from each of 300 laser source points. No attempt has been made to adjust for source and receiver functions s and $r(\omega)$. The Rayleigh arrivals at 19 μs are apparent; little else is. The estimated residual rms fluctuation $[\text{Eq. } (41)/N]^{1/2}$ is plotted as the horizontal dashed line.

relations, and that convergence will therefore be slower for such frequencies.

The interesting drop of variance at 100 kHz below that predicted may be ascribed to laser spot sources being within a half-wavelength of each other and so not independent.

In order to investigate the fidelity with which $\langle P \rangle$ accurately represents a direct "pitch-catch" signal, we adapt the above configuration to employ broader band and plane wave transducers with which crisper arrivals may be expected. The configuration is otherwise identical, except that the laser is aimed at 132 spots on one face of the object, spots separated by 0.75 cm. Figure 5(a) shows the direct pitch-catch signal, in which we may identify a direct surface-skimming P wave arrival, a direct Rayleigh surface wave arrival, R, a wave which has reflected once off the bottom LL, a wave that has reflected twice between top and bottom ($LLLL$) and another that is not identified but which may be LS. Figure 5(b) shows the raw average $\langle P \rangle$ and its square root of variance. Again very little is readily identified in $\langle P \rangle$. Nor can one detect much similarity between $\langle P \rangle$ and the pitch catch signal $V(t)$ in Fig. 5(a).

The lack of symmetry in τ is noteworthy. Theory predicts (14) such symmetry if $r_1 = r_2$. Even when $r_1 \neq r_2$, as in the present case, one might nevertheless expect to observe arrivals at both signs of τ. The absence of clear arrivals at negative τ is in this case due to heavy absorption by one of the transducers (the large one). The effective diffuse field is thereby rendered nonisotropic. Such effects would not be present had we used noninvasive detection, perhaps by laser interferometry. This behavior underscores how theory,[2,5–8] which presumes negligible absorption, may fail.

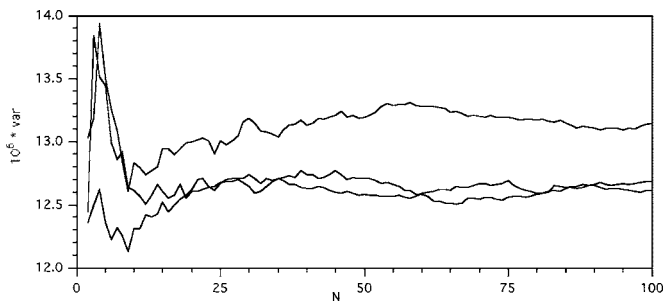

FIG. 3. The observed variance, Eq. (41), amongst the correlations taken from up to 100 laser source positions on each of the three lateral faces.

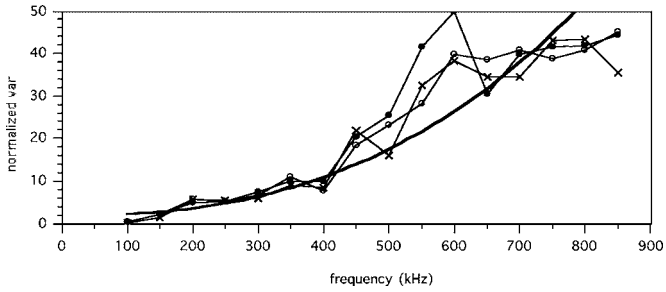

FIG. 4. Normalized variance from 100 sources on each of the three faces is plotted versus frequency. The bold line shows the theoretical prediction (38).

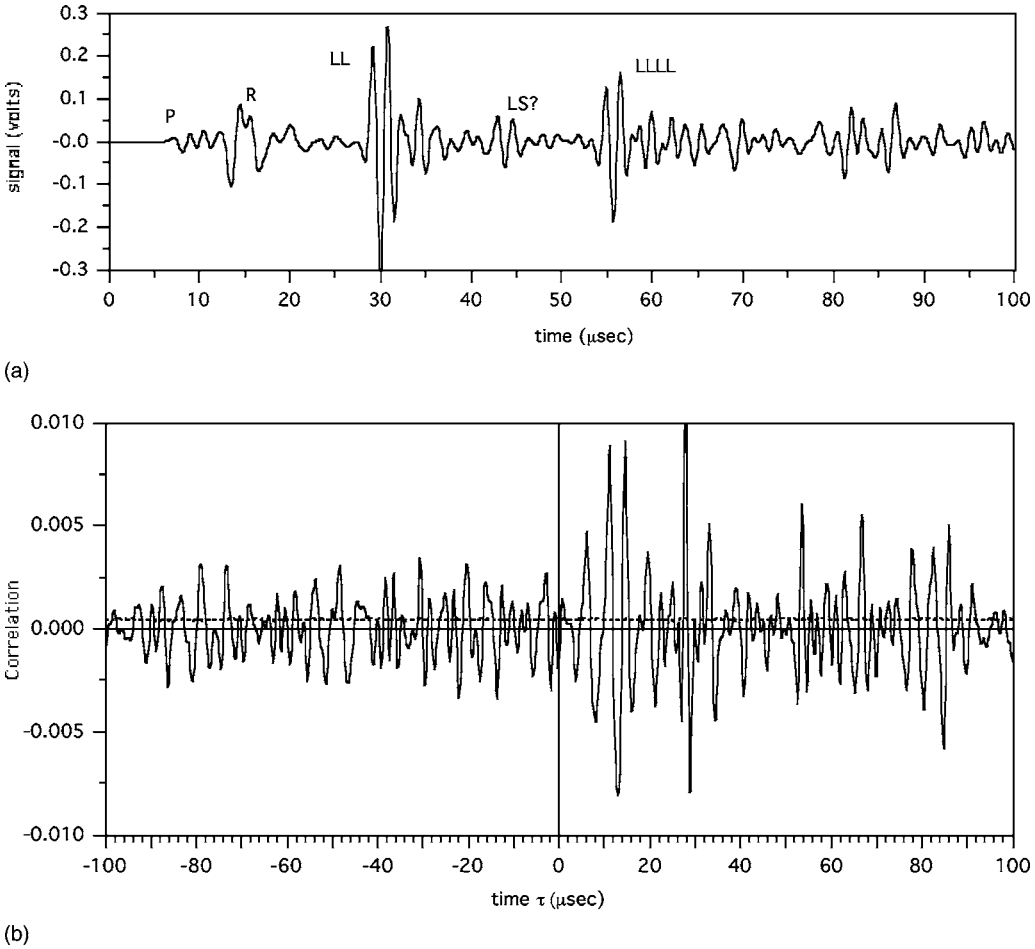

FIG. 5. (a) Direct signal $V(t)$ obtained actively between two conventional acoustic emission transducers. (b) As in Fig. 2(b), the raw correlator, and its expected rms deviation, between the two conventional transducers.

$V(t)$ is given by a convolution of source and receiver functions: $r_1 \otimes G_{12} \otimes t_2$ (where r_1 is the transfer function of transducer number 1, and $r_2 = t_2$ is the transfer function of transducer number 2), while $\langle P \rangle$, according to (14), is $s \otimes r_1 \otimes (\partial_t G_{12} - \partial_t G_{12}^{\text{time-reversed}}) \otimes r_2^{\text{time-reversed}} \otimes s^{\text{time reversed}}$. In the frequency domain they differ by a factor of $i\omega|s|^2 r_2^* / r_2$. In order to compare $\langle P \rangle$ and V, we must correct for the source and receiver spectra. Had we used flat-spectrum detectors, such as laser interferometry, these corrections would not be necessary.

The laser source spectrum $|s|$ was estimated by comparing a frequency-smoothed $|\tilde{V}(\omega)|^2$ with mean frequency smoothed product of $|\tilde{V}_1^\sigma(\omega)|^2$ and $|\tilde{V}_2^\sigma(\omega)|^2$. We identify $|s|^2$ by

$$|\tilde{s}(\omega)|^2 = \overline{|\tilde{V}_1^\sigma(\omega)|^2 |\tilde{V}_2^\sigma(\omega)|^2} / \overline{|\tilde{V}(\omega)|^2}, \tag{44}$$

where the overbars represent a frequency smoothing, over scales ~1 kHz. Figure 6 plots the value of $1/|s|^2$ resulting from this process. The curve is fit to a quadratic in order to suppress the noise, a process that is justified by our knowledge that the laser source is highly transient, with no long-range structure in time or space. While the laser pulse itself is a delta function on these time scales, it is less efficient at generating high frequencies than low frequencies, owing to its finite size. The spectrum $|s|$ falls off at higher frequency, as one might expect when laser beam radius times acoustic wave-number exceeds unity.

In Fig. 7 we plot the inverse Fourier transform of $\langle \tilde{P}(\omega) \rangle / |s|^2$, and compare it to $V(t)$. A uniform shift in time and an amplitude rescaling have been imposed. Here we see a substantial similarity. Arrivals are apparent, though their precise form and timing differ. The figure also shows the expected rms deviation $\sqrt{\text{var}/N}$ between the estimate and the waveform we would obtain if $N = \infty$. The arrivals rise well above this level and thus are statistically significant.

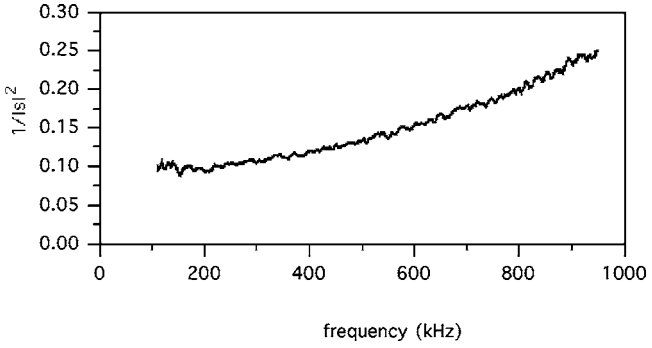

FIG. 6. The inverse of the effective power spectrum of the laser source used to generate the data of Figs. 5–8. Power is less at short wavelength, owing to the finite beam diameter.

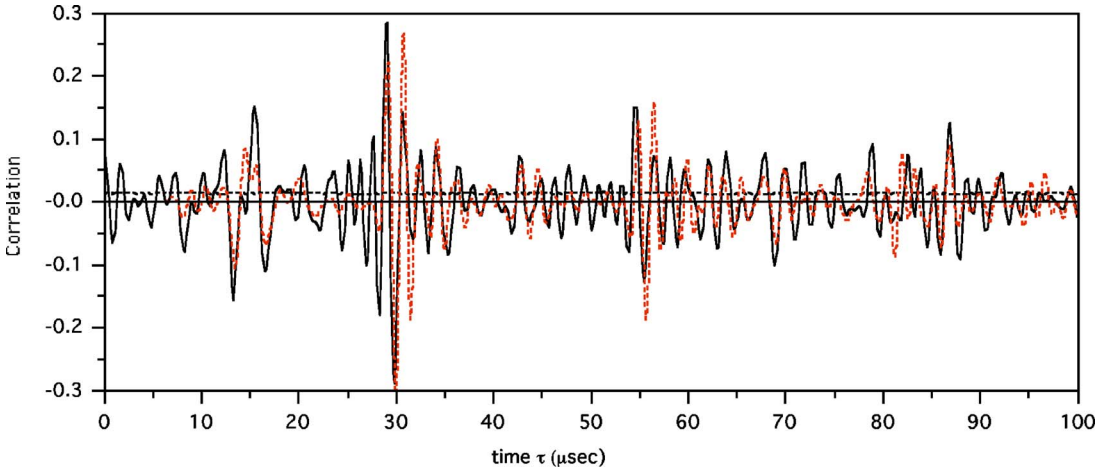

FIG. 7. The correlation (solid line) after compensating for the laser source spectrum is compared with the direct pitch catch waveform (dotted line).

Further improvement in correspondence is obtained by correcting for the phase of the receiver by the factor r_2^*/r_2. This factor is estimated by Fourier transforming the "pulse echo" signal $p(t)$ of the LL ray obtained by pulsing transducer number 2 and receiving with number 2 also. Except for the elastodynamics and in particular the time delay for the round trip travel of the LL ray, we may identify p with $t_2 r_2$, and $p(\omega)^*/|p(\omega)|$ with r_2^*/r_2. Figure 8 compares the inverse Fourier transform of $(p(\omega)^*/|p(\omega)|)\langle\tilde{P}(\omega)\rangle/|s|^2$ with $V(t)$. Further improvement is evident. There are remaining differences. One notable difference is the ringing, at ~900 kHz, that precedes the LL arrival in the correlation, but not in the direct $V(t)$. We ascribe the ringing to an effect of the low-pass filter. The signal received by transducer number 2 was filtered by a four-pole low-pass filter with its 3-dB point set at 900 kHz. This filter did not operate when the transducer was used as a source and so was not properly accounted for when the factor r^*/r was constructed. It may be shown that the effect of the filter on the comparison of V and $\langle P\rangle$ is an additional factor of $f(\omega)/|f(\omega)|$. The phase of the filter is known to be highly dispersive near its cutoff at 900 kHz, hence the dispersion at these frequencies.

There is an additional difference discernable at $t < 5$ μs, a difference which appears to be statistically significant in that it rises well above $\sqrt{\text{var}/N}$. It is our speculation that this is an artifact of our sources being imperfectly distributed over the full volume. That all sources were on the surface leads in principle to features in the source spectrum $|s|^2$ corresponding to time scales equal to round trip echo times t_{RT} from the source to the source. Our 132 sources were all at about the same distance from the far wall, a round trip P travel time of about 50 μs. To the extent that the set of 132 sources had coherent echoes, "ghost" versions of legitimate arrivals from time t will appear in the correlation at times $t \pm t_{RT}$. Such ghosts are also discussed by Sabra *et al.*[28] The imperfect correspondence in Fig. 8 may be compared with that seen when retrieving the Green's function from a thermal diffuse field.[1] In the thermal case, the diffuse field was fully equipartitioned, the theorem's requirements were fully satisfied, and the convergence was excellent. In Fig. 8 the field is imperfectly equipartitioned, and so the correspondence is also imperfect.

The remaining differences are of order $\sqrt{\text{var}/\text{N}}$ and may be ascribed to fluctuations that are still present in spite of

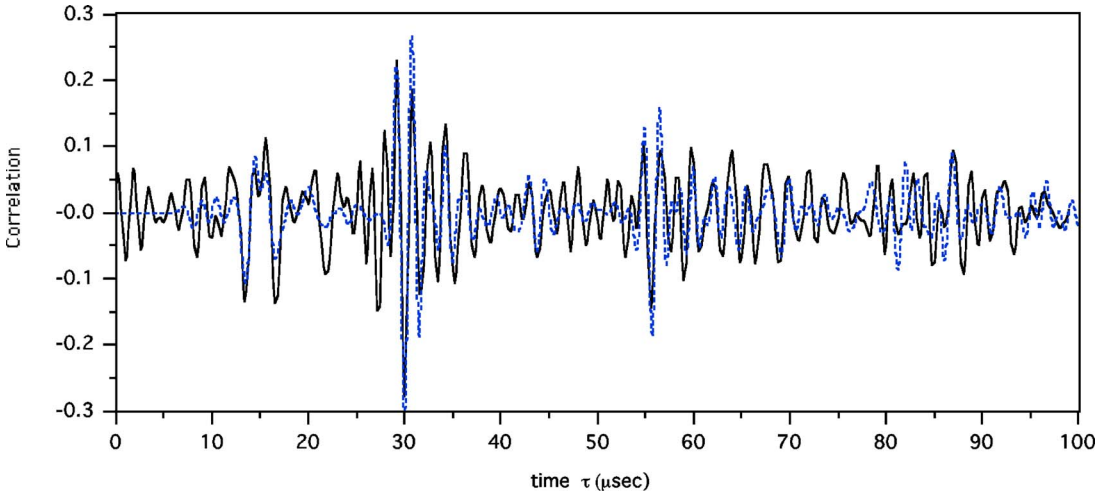

FIG. 8. The correlation (solid line) after compensating for the laser source spectrum and the receiver spectrum is compared with the direct pitch catch waveform (dotted line).

having averaged over a large amount of raw data, fluctuations that presumably would diminish further if more sources could be enlisted or more time captured from each source. The remaining differences are not statistically significant; whether they represent or hide deviations from theory cannot be determined from this data.

VI. CONCLUSION

A theory for the rate of convergence of diffuse field correlation functions in a closed system has been developed and favorably compared to laboratory measurements. A key prediction is that the amount of data needed for accurate retrieval of a Green's function scales with the square of the frequency. Close correspondence between the passively obtained correlation function and an actively obtained waveform is found to depend not only on having sufficient passive data, but also on an informed compensation for diffuse field spectrum and receiver characteristics. It is particularly noteworthy that coherent source environment can generate anomalies in the correlation function. If the sources are distributed uniformly, then such ghosts disappear. This is a warning for those attempting to retrieve Green's functions; the field must be sufficiently diffuse, and sources sufficiently distributed, in order to eliminate such ghosts. It is also indicates an opportunity: comparison of Green's functions to correlation functions obtained from single codas may allow determination of source environment.

It is anticipated that these arguments will be relevant to Green's function retrieval and convergence rates in open systems such as are found in seismology and ocean acoustics.

ACKNOWLEDGMENTS

This work was supported by the National Science Foundation Grant Nos. INT-0230312 and CMS-0201346. We thank Michel Campillo for discussions.

[1]R. L. Weaver and O. I. Lobkis, "Ultrasonics without a source, Thermal fluctuation correlations at MHz frequencies," Phys. Rev. Lett. **87**, 134301 (2001).
[2]O. I. Lobkis and R. L. Weaver, "On the emergence of the Greens function in the correlations of a diffuse field," J. Acoust. Soc. Am. **110**, 3011–3017 (2001).
[3]R. L. Weaver and O. I. Lobkis, "On the Emergence of the Greens Function in the Correlations of a Diffuse Field; Pulse-Echo using Thermal Phonons," Ultrasonics **40**, 435–439 (2002).
[4]R. L. Weaver and O. I. Lobkis, "Elastic wave thermal fluctuations, ultrasonic waveforms by correlation of thermal phonons," J. Acoust. Soc. Am. **113**, 2611–2621 (2003).
[5]B. A. van Tiggelen, "Green Function Retrieval and Time Reversal in a Disordered World," Phys. Rev. Lett. **91**, 243904 (2003).
[6]R. Snieder, "Extracting the Greens' function from the correlation of coda waves: a derivation based on stationary phase," Phys. Rev. E **69**, 046610 (2004).
[7]P. Roux, K. Sabra, W. A. Kupperman, and A. Roux, "Ambient noise cross-correlation in free space: theoretical approach," J. Acoust. Soc. Am. **117**, 79 (2005).
[8]K. Wapenaar, "Synthesis of an inhomogeneous medium from its acoustic transmission response," Geophysics **68**, 1756–1759 (2003); K. Wapenaar, J. Thorbecke, and D. Draganov, "Relations between reflection and transmission responses of three-dimensional inhomogeneous media," Geophys. J. Int. **156**(2), 179–194 (2004); K. Wapenaar, "Retrieving the Elastodynamic Green's Function of an Arbitrary Inhomogeneous Medium by Cross Correlation," Phys. Rev. Lett. **93**, 254301 (2004).
[9]M. Campillo and A. Paul, "Long range correlations in the diffuse seismic coda," Science **299**(5606), 547–549 (2003).
[10]N. M. Shapiro and M. Campillo, "Emergence of broadband Rayleigh waves from correlations of the ambient seismic noise," Geophys. Res. Lett. **31**, L07614 (2004).
[11]N. M. Shapiro, M. Campillo, L. Stehly, and M. Ritzwoller, "High resolution surface wave tomography from ambient seismic noise," Science **307**, 1615–1618 (2005).
[12]K. G. Sabra, P. Gerstoft, and P. Roux, "Extracting time-domain Green's function estimates from ambient seismic noise," Geophys. Res. Lett. **32**, L03310 (2005).
[13]P. Roux and M. Fink, "Green's function estimation using secondary sources in a shallow water environment," J. Acoust. Soc. Am. **113**, 1406–1416 (2003).
[14]P. Roux and W. A. Kuperman, "Coherent waveforms from ocean noise," J. Acoust. Soc. Am. **116**, 1995–2003 (2004).
[15]A. Derode, E. Larose, M. Campillo, and M. Fink, "How to estimate the Green's function of a heterogeneous medium between two passive sensors? Application to acoustic waves," Appl. Phys. Lett. **83**(15), 3054–3056 (2003); E. Larose, A. Derode, M. Campillo, and M. Fink, "Imaging from one-bit correlations of wideband diffuse wave fields," J. Appl. Phys. **95**, 8393–8399 (2004).
[16]A. E. Malcolm, J. A. Scales, and B. A. van Tiggelen, "Retrieving the Green Function from Diffuse, Equipartitioned Waves," Phys. Rev. E **70**, 015601(R) (2004).
[17]T. L. Duvall, S. M. Jefferies, J. W. Harvey, and M. A. Pomerantz, "Time-Distance Helioseismology," Nature (London) **362**, 430 (1993); J. Rickett and Jon Claerbout, "Acoustic daylight imaging via spectral factorization: Helioseismology and reservoir monitoring," The Leading Edge **18**, 957–960 (1999).
[18]S. J. Norton and I. J. Won, "Time exposure acoustics," IEEE Trans. Geosci. Remote Sens. **GE–38**(3), 1337–1343 (2000); S. J. Norton and T. Vo-Dinh, "Diffraction tomographic imaging with photon density waves: an explicit solution," J. Opt. Soc. Am. A **15**(10), 2670–2677 (1998); W. E. Doll, S. J. Norton, L. J. Gray, and M. D. Morris, "Passive seismic imaging of scatterers," Oak Ridge National Lab, Oak Ridge, TN, Tech. Rep. K/NSP-585 October (1997).
[19]J. R. Potter, "Acoustic imaging using ambient noise—some theory and simulation results," J. Acoust. Soc. Am. **95**, 21–33 (1994); J. R. Potter and M. Chitre, "Ambient noise imaging in warm shallow seas: second order moment and model based imaging algorithms," *ibid.* **106**, 3201 (1999).
[20]Y. Lee, *Statistical Theory of Communication* (Wiley, New York, 1960).
[21]R. L. Weaver and O. I. Lobkis, "Diffuse waves in open systems and the emergence of the Greens' function," J. Acoust. Soc. Am. **116**, 2731–2734 (2004).
[22]R. L. Weaver and O. I. Lobkis, "Fluctuations in diffuse field-field correlations and the emergence of the Green's function in open systems," J. Acoust. Soc. Am. **117**, 3432–3439 (2005).
[23]Closely related to conservation of energy and to reciprocity, this is one of a set of identities based on underlying symmetries that are used to constrain perturbation theories in quantum dynamics. It is easily proved using orthogonality of the modes.
[24]One argues that E is known to be constant, except for stochastic fluctuations, at all times after the ergodic time at which rays fill the volume. One then argues that terms $n \neq m$ will vanish on averaging over times greater than T_H at which all such terms lose coherence.
[25]R. Weaver and J. Burkhardt, "Weak Anderson localization and enhanced backscatter in reverberation rooms and quantum dots," J. Acoust. Soc. Am. **96**, 3186–3190 (1994); R. L. Weaver and O. I. Lobkis, "Enhanced Backscattering and Modal Echo of Reverberant Elastic Waves," Phys. Rev. Lett. **84**, 4942–4945 (2000).
[26]T. A. Brody, J. Flores, J. B. French, P. A. Mello, A. Pandey, and S. S. M. Wong, "Random Matrix Physics: Spectrum and strength fluctuations," Rev. Mod. Phys. **53**, 385–478 (1981); H.-J. Stöckmann, *Quantum Chaos: An Introduction* (Cambridge U. P., Cambridge, 1999); R. L. Weaver, "On the Ensemble Variance of Reverberation Room Transfer Functions, The Effect of Spectral Rigidity," J. Sound Vib. **130**, 487–491 (1989).
[27]O. I. Lobkis, R. L. Weaver, and I. Rozhkov, "Power Variances and Decay Curvature in a Reverberant System," J. Sound Vib. **237**, 281–302 (2000).
[28]K. G. Sabra, P. Roux, and W. A. Kuperman, J. Acoust. Soc. Am. **117**, 164–174 (2005).

Simplified expansions for radiation from a baffled circular piston

T. Douglas Mast
Department of Biomedical Engineering, University of Cincinnati, Cincinnati, Ohio 45267-0586

Feng Yu[a)]
Department of Aerospace Engineering and Engineering Mechanics, University of Cincinnati, Cincinnati, Ohio 45221-0070

(Received 31 May 2005; revised 1 September 2005; accepted 5 September 2005)

Computation of acoustic radiation from a baffled circular piston continues be an active area of investigation, both as a canonical problem and because of numerous practical applications. For time-harmonic radiation, exact series expansions are an attractive approach because they do not require numerical integration or limiting approximations. Here, series expansions due to Hasegawa, Inoue, and Matsuzawa [J. Acoust. Soc. Am. **74**, 1044–1047 (1983); **75**, 1048–1051 (1984)] are shown to reduce to simpler expressions suitable for numerical computations of piston fields in lossless and attenuative fluid media. For the region $r \geqslant a$, where a is the piston radius and r is the distance from the piston center, an exact solution is given by an series of spherical Hankel functions and Legendre polynomials with explicit, closed-form, position-independent coefficients. For the paraxial region $w \leqslant a$, where w is the distance from the piston axis, a second exact series expansion is valid for all axial distances z and reduces to the known analytic solution for $w=0$. These two expansions allow the radiated field to be computed at any point, with rapid convergence except for points near the circle bounding the piston. Example numerical results illustrate application of this method to ultrasonic sources. © *2005 Acoustical Society of America.* [DOI: 10.1121/1.2108997]

PACS number(s): 43.20.Rz, 43.20.El [JJM] Pages: 3457–3464

I. INTRODUCTION

Acoustic radiation from a circular piston is a canonical acoustics problem investigated by Rayleigh and many subsequent researchers. In this problem, a circular piston with radius a, within an infinite rigid baffle, vibrates uniformly at a radial frequency ω with a normal velocity $v_0 e^{-i\omega t}$ into a homogeneous fluid medium with speed of sound c and density ρ. The resulting radiated pressure is given by the Rayleigh integral[1]

$$p(\mathbf{r},t) = -\frac{ik}{2\pi} p_0 \int \frac{e^{ikR}}{R} dS e^{-i\omega t}, \tag{1}$$

where $p_0 = \rho c v_0$, $R = |\mathbf{r} - \mathbf{r}_s|$ is the distance from a field point $\mathbf{r}$ to a point on the piston surface $\mathbf{r}_s$, k is the wave number ω/c (which is complex in the case of a sound-absorbing medium), and S covers all points on the piston surface, $r_s \leqslant a$.

The Rayleigh integral is not directly solvable in a simple form, except for certain special cases, including the on-axis field and the asymptotic far field.[2] Piston fields have often been computed using numerical integration, including methods that transform the Rayleigh integral into single line integrals[3–6] and methods involving numerical integration of the space- and time-dependent piston impulse response.[7–9] Because of the problem's practical importance in ultrasonics and other areas of acoustics, the efficient computation of such numerical integrals,[10–12] as well as approximations to the piston field,[13–17] remain active areas of research.

An alternate approach to exact computation of piston fields involves expansion of the field in series of orthogonal functions. Series solutions have advantages including exactness, easily analyzed convergence properties, and amenability to analysis. Series of this form were derived by Backhaus[18] and Stenzel,[19] who presented equivalent expansions valid for the region $r \geqslant a$, where r is the distance from the piston center. These expansions are slow to converge for $r \approx a$, while an additional solution by Stenzel for the region $r \leqslant a$ is slow to converge over the entire region $r \leqslant a$.[19,20] More recently, Wittmann and Yaghjian[20] presented an alternate derivation of the Backhaus-Stenzel series for $r \geqslant a$ and a different expansion for $r \leqslant a$, which incurs similar convergence problems for $r \approx a$. Other available series expansions include an expression in oblate spheroidal coordinates by Spence[21] that is slow to converge for large ka, an expansion derived by Carter and Williams[22,23] and improved by Elrod[24] that is invalid for $z \leqslant a$ and is slow to converge outside the paraxial region, and a slowly-converging series derived by New as a limiting case of a radially vibrating polar cap on a rigid sphere.[25]

More general series expansions were derived by Hasegawa, Inoue, and Matsuzawa.[26,27] These series contain coefficients that depend on the spatial position and on the choice of an origin for the coordinate system employed. For a given field position, choice of an appropriate origin location provides a series with favorable local convergence properties. However, simpler expressions that do not depend on spatial position or choice of origin would be desirable for numerical computation of piston radiator fields.

[a)]Present address: Cessna Aircraft Company, Wichita, Kansas 67215.

Here, simplified series, which also result from special cases of the Hasegawa, Inoue, and Matsuzawa expansions, are derived. An expansion valid for $r \geqslant a$ is equivalent to previous series solutions,[18–20] but is presented here with explicit, closed-form coefficients. A second expansion is valid for $w \leqslant \sqrt{z^2+a^2}$, where w is the distance from the piston axis, and converges within a few terms for field points near the axis. Computational examples show that these two methods provide accurate solutions for the piston field, with favorable convergence properties except near the velocity discontinuity at the piston boundary, where $z \approx 0$ and $w \approx a$.

II. THEORY

A. General expansions

For simplicity, the following derivations will set $p_0 \equiv 1$ in Eq. (1) and suppress the $e^{-i\omega t}$ time dependence. An exact series solution of the Rayleigh integral by Hasegawa *et al.* is then given for the notation of Eq. (1) as[27]

$$p(r,\theta) = \sum_{n=0}^{\infty} (-1)^n (2n+1) f_n(kr_0, kr_a) P_n(\cos\theta) j_n(kr),$$
$$f_n(kr_0, kr_a) = \int_{kr_0}^{kr_a} P_n\left(\frac{kr_0}{\zeta}\right) h_n^{(1)}(\zeta)\zeta d\zeta. \tag{2}$$

Here, r_0 is distance from the piston center to the origin of the spherical coordinate system (r, θ, ϕ), which is placed arbitrarily along the piston's axis of symmetry $(r_0 > 0)$, $r_a = \sqrt{r_0^2 + a^2}$, j_n and $h_n^{(1)}$ are the spherical Bessel function and Hankel function of the first kind, and P_n is the Legendre polynomial. The integral $f_n(kr_0, kr_a)$ can be evaluated for successive indices n using a recurrence relation given in Ref. 26. According to Hasegawa *et al.*, the solution of Eq. (2) is appropriate for $r \leqslant r_a$, while for $r \geqslant r_a$ an appropriate series solution is[27]

$$p(r,\theta) = \sum_{n=0}^{\infty} (-1)^n (2n+1) \mathrm{Re}[f_n(kr_0, kr_a)] P_n(\cos\theta) h_n^{(1)}(kr). \tag{3}$$

Although exact and fairly general, computations employing Eqs. (2) and (3) are complicated by the requirement to choose an origin position r_0. The solution of Eq. (2) is slow to converge for large values of kr, and the convergence properties of Eq. (3) also depend on kr, so that the useful region for each of these expansions depends on the choice of the origin r_0. Two special cases of the above solutions can reduce these difficulties; a simplified derivation encompassing these special cases follows.

B. Simplified expansions

Below, simplified series expansions for the Rayleigh integral are derived directly from a series expansion of the integrand, As a starting point, the distance R from a field point $\mathbf{r}$ to a point on the piston surface $\mathbf{r}_s$ in Eq. (1) can be written in cylindrical coordinates as

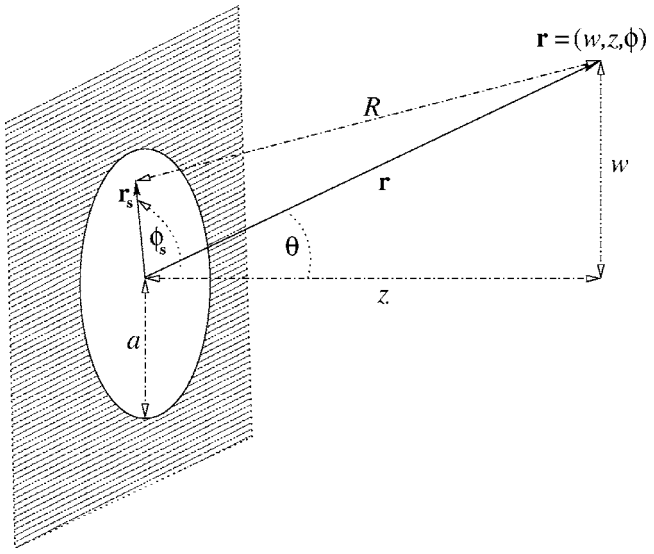

FIG. 1. Sketch of the problem geometry and notation. A piston of radius a, centered at the origin, radiates from within an infinite baffle into a semi-infinite space. The vector $\mathbf{r} = (w, z, \phi)$ is the position of a field point in cylindrical coordinates, where w is the azimuthal distance from the piston axis, z is the distance along the piston axis, and ϕ is the azimuthal angle. The vector $\mathbf{r}_s = (w_s, \phi_s)$ denotes a position on the piston surface. The angle between the z axis and the position vector $\mathbf{r}$ is denoted by θ.

$$R = \sqrt{z^2 + w^2 + w_s^2 - 2ww_s\cos\phi_s}, \tag{4}$$

where z and w are the axial and azimuthal coordinates of the field point, while w_s and ϕ_s are the azimuthal coordinate and angle of a point on the piston surface. This coordinate system, in which the origin is placed at the piston center, is sketched in Fig. 1. Without loss of generality, the azimuthal angle ϕ of the field point is taken here to be zero.

The distance defined by Eq. (4) can be rewritten as

$$R = \sqrt{r_1^2 + r_2^2 - 2r_1 r_2 \cos\phi_s \sin\beta}, \tag{5}$$

where the distances r_1 and r_2 must satisfy the relation $r_1^2 + r_2^2 = z^2 + w^2 + w_s^2$ and $\sin\beta = (ww_s)/(r_1 r_2)$ may not exceed unity.

Several different series expansions of the Rayleigh integral can then be obtained using the identity[28]

$$\frac{e^{ik\sqrt{r_1^2+r_2^2-2r_1r_2\cos\phi_s\sin\beta}}}{\sqrt{r_1^2 + r_2^2 - 2r_1 r_2 \cos\phi_s \sin\beta}} = ik\sum_{n=0}^{\infty} (2n+1) P_n(\cos\phi_s \sin\beta) j_n(kr_1) h_n^{(1)}(kr_2), \tag{6}$$

which converges for $r_1 \leqslant r_2$. Here, P_n is the Legendre polynomial, j_n is the spherical Bessel function, and h_n is the spherical Hankel function. Variants of this identity were employed in Refs. 19, 26, and 27. Inserting Eq. (6) into the Rayleigh integral (1), one obtains the series expansion

$$p(\mathbf{r}) = \frac{k^2}{2\pi}\sum_{n=0}^{\infty}(2n+1)\int_0^a\left[\int_0^{2\pi}P_n(\cos\phi_s\sin\beta)d\phi_s\right] \times j_n(kr_1)h_n^{(1)}(kr_2)w_s dw_s$$
$$= k^2\sum_{n=0}^{\infty}(2n+1)P_n(0)\int_0^a P_n(\cos\beta)j_n(kr_1)h_n^{(1)}(kr_2)w_s dw_s$$
$$= \frac{k^2}{\sqrt{\pi}}\sum_{n=0}^{\infty}(-1)^n(4n+1)\frac{\Gamma\left(n+\frac{1}{2}\right)}{\Gamma(n+1)} \times\int_0^a P_{2n}(\cos\beta)j_{2n}(kr_1)h_{2n}^{(1)}(kr_2)w_s dw_s. \quad (7)$$

Here, the integral over ϕ_s has been evaluated using the addition theorem for Legendre polynomials as in Refs. 19 and 26. The Legendre polynomial $P_n(0)$ has value zero for odd n, so that the series expansion of Eq. (7) contains only Legendre polynomials and spherical Bessel and Hankel functions of even order.

Given a choice of appropriate distances r_1 and r_2, construction of a series expansion solving the Rayleigh integral (1) in the region $r_1 \leqslant r_2$ requires only evaluation of the integral term in the last of Eqs. (7). One useful case is obtained by setting $r_1 = w_s$, $r_2 = \sqrt{z^2+w^2} = r$, which results in a valid series expansion if $r \geqslant a$. In this case, $\sin\beta = w/r = \sin\theta$ and Eq. (7) becomes

$$p(\mathbf{r}) = \frac{k^2}{\sqrt{\pi}}\sum_{n=0}^{\infty}(-1)^n(4n+1)\frac{\Gamma\left(n+\frac{1}{2}\right)}{\Gamma(n+1)}\left[\int_0^a j_{2n}(kw_s)w_s dw_s\right] \times P_{2n}(\cos\theta)h_{2n}^{(1)}(kr)$$
$$= \sum_{n=0}^{\infty}(-1)^n\left(\frac{ka}{2}\right)^{(2n+2)}\frac{(4n+1)\Gamma\left(n+\frac{1}{2}\right)}{\Gamma(n+2)\Gamma\left(2n+\frac{3}{2}\right)} \times {}_1F_2\left[n+1; n+2, 2n+\frac{3}{2}; -\left(\frac{ka}{2}\right)^2\right] \times P_{2n}(\cos\theta)h_{2n}^{(1)}(kr). \quad (8)$$

Here, evaluation of the integral term[29] has yielded explicit coefficients in terms of the generalized hypergeometric function ${}_1F_2$. Taken as a function of $\xi \equiv ka/2$, this function is well-behaved for all orders n, with value unity for $\xi \to 0$, positive for all $\xi \geqslant 0$, and zero for $\xi \to \infty$. For large order n, this hypergeometric function approaches a Gaussian distribution

$$\lim_{n\to\infty} {}_1F_2\left[n+1; n+2, 2n+\tfrac{3}{2}; -\xi^2\right] = e^{-\xi^2/2n}, \quad (9)$$

which can be verified by expanding the hypergeometric and exponential functions from Eq. (9) in powers of ξ and evaluating the limit $n \to \infty$ term by term. The general function ${}_1F_2(a_1; b_1, b_2; -\xi^2)$ has been analyzed previously[30] and can be computed numerically with available algorithms.[31,32] Equivalently, the integral appearing in Eq. (8) can be evaluated in terms of Bessel functions and Lommel functions.[29]

The series expansion of Eq. (8) is equivalent to series derived in Refs. 18–20 for the region $r \geqslant a$, although none of these references presented explicit series coefficients. This expansion, which is valid for $r \geqslant a$ and converges smoothly except for the region $r \approx a$, can also be obtained by setting $r_0 = 0$ in Eq. (3). Numerical computations suggest that outside the region $r \approx a$, the number of terms required for convergence is of the order $N \sim ka$. Below, the solution of Eq. (8) will be referred to as an "outer" expansion, since it is valid for the region exterior to the hemisphere $r = a$.

A second useful series expansion is obtained from the choices $r_1 = w$, $r_2 = \sqrt{z^2+w_s^2}$. In this case, $\cos\beta = z/\sqrt{z^2+w_s^2}$ and Eq. (7) reduces to

$$p(\mathbf{r}) = \frac{1}{\sqrt{\pi}}\sum_{n=0}^{\infty}(-1)^n(4n+1)\frac{\Gamma\left(n+\frac{1}{2}\right)}{\Gamma(n+1)} \times\left[\int_{kz}^{kr_a}P_{2n}\left(\frac{z}{\zeta}\right)h_{2n}^{(1)}(\zeta)\zeta d\zeta\right]j_{2n}(kw)$$
$$= \frac{1}{\sqrt{\pi}}\sum_{n=0}^{\infty}(-1)^n(4n+1)\frac{\Gamma\left(n+\frac{1}{2}\right)}{\Gamma(n+1)}f_{2n}(kz, kr_a)j_{2n}(kw), \quad (10)$$

where f_{2n} is the integral function from Eq. (2), which can be evaluated using the recurrence relation[26]

$$f_0 = e^{ikz} - e^{ikr_a},$$
$$f_{2n} = -f_{2n-2} - kr_a\left[P_{2n}\left(\frac{z}{r_a}\right) - P_{2n-2}\left(\frac{z}{r_a}\right)\right]h_{2n-1}^{(1)}(kr_a), \quad (11)$$

where $r_a = \sqrt{z^2+a^2}$. This solution corresponds to the special case $r_0 = z$ in Eq. (2). The series converges for the region $w \leqslant \sqrt{z^2+a^2}$, with fastest convergence near the piston axis $w = 0$ and slowest convergence for $w \approx \sqrt{z^2+a^2}$. Numerical experience suggests that, within the region of validity for this expansion, $N \sim kw$ terms are required for convergence at an azimuthal distance w. Because the solution of Eq. (10) converges fastest within the cylinder defined by $w \leqslant a$, this series will be referred to below as a paraxial expansion.

Notable is that the terms f_{2n} in Eq. (10) depend spatially only on the axial coordinate z. Thus, computations of the piston field at multiple spatial points (e.g., on a rectangular grid in the axial and azimuthal directions) can be performed more efficiently by computing these terms only once for each axial distance required.

Compared to the previous series expansions cited above, the expansion of Eq. (10) particularly simplifies computation of pressure fields near the piston axis. On the axis ($w = 0$), only the leading term from Eq. (10) is nonzero and the solution reduces identically to the known exact solution[2]

$$p(0,z) = e^{ikz} - e^{ikr_a} = -2ie^{ik(z+r_a)/2}\sin\left(\frac{kr_a - kz}{2}\right), \quad (12)$$

where, as above, $r_a = \sqrt{z^2+a^2}$.

Similarly, for points close to the piston axis, the paraxial expansion of Eq. (10) converges within a few terms, since each term of Eq. (10) is of order $(kw)^{2n}$. Thus, for example,

an expression valid to fourth order in the normalized azimuthal coordinate kw can be obtained from Taylor series for the first three terms of the paraxial expansion (10). The result is

$$p(w,z) = e^{ikz} - e^{ikr_a}\left[1 - \frac{a^2(kr_a+i)}{4kr_a^3}(kw)^2 + \psi(k,a,r_a)(kw)^4\right] + O[(kw)^6], \tag{13}$$

where the fourth-order term ψ is given by

$$\psi(k,a,r_a) = \frac{a^4}{64k^3r_a^7}\left\{\left[12\left(\frac{r_a}{a}\right)^2 - 15\right](kr_a+i) - i\left[4\left(\frac{r_a}{a}\right)^2 - 6\right](kr_a)^2 + (kr_a)^3\right\}. \tag{14}$$

The truncated series of Eq. (13) is accurate for points near the piston axis, relative to the acoustic wavelength. For $kw \ll 1$, this expression is more accurate than the approximate paraxial expression derived by Schoch,[2,4] and agrees to second order in kw with an improved approximation derived in Ref. 13. The fourth-order correction of Eq. (14) provides greater accuracy for small kw than either of these previous approximations.

The pressure field given by the paraxial expansion of Eq. (10) can also be used to derive a simplified expression for the output of an ideal coaxial receiver, which is given by the average pressure over a circular surface S_b with radius b, centered at $w=0$ and parallel to the piston at a distance z. This is a configuration of interest in ultrasonic measurements of attenuation[33,34] as well as hydrophone measurements of acoustic fields.[35] Acoustic reciprocity allows the spatially averaged pressure to be obtained in a similar manner for the cases $b \leqslant a$ and $b > a$. The results can compactly be written as

$$\begin{aligned}\bar{p}_b(z) &= \frac{1}{\pi b^2}\int p(\mathbf{r})\,dS_b \\ &= \frac{\alpha_1^2}{2b^2}\sum_{n=0}^{\infty}(-1)^n\left(\frac{k\alpha_1}{2}\right)^{2n} \\ &\quad\times\frac{(4n+1)\Gamma\left(n+\frac{1}{2}\right)}{\Gamma(n+2)\Gamma\left(2n+\frac{3}{2}\right)}f_{2n}(kz,k\sqrt{z^2+\alpha_2^2}) \\ &\quad\times{}_1F_2\left[n+1;n+2,2n+\frac{3}{2};-\left(\frac{k\alpha_1}{2}\right)^2\right],\end{aligned} \tag{15}$$

where $\alpha_1=b$, $\alpha_2=a$ if $b \leqslant a$, and $\alpha_1=a$, $\alpha_2=b$ if $b>a$. Due to acoustic reciprocity, interchange of source and receiver causes the spatially-averaged pressure to vary only by a multiplicative factor due to the change in relative source and receiver area.[34,35]

C. Recurrence relations for numerical evaluation

Because gamma functions of large order can take on exceedingly large values (e.g., $\Gamma(171) \approx 7.3\times10^{306}$ is the largest integer-order gamma function that can be computed as a double-precision real variable), it is helpful to define recurrence relations for the coefficients in the expansions of Eqs. (8) and (10). Using the recurrence and duplication formulas for the gamma function,[36] the outer expansion of Eq. (8), valid for $r \geqslant a$, is written as

$$\begin{aligned}p(\mathbf{r}) &= \sum_{n=0}^{\infty} A_n {}_1F_2\left[n+1;n+2,2n+\frac{3}{2};-\left(\frac{ka}{2}\right)^2\right] \\ &\quad\times P_{2n}(\cos\theta)h_{2n}^{(1)}(kr), \\ A_0 &= \frac{(ka)^2}{2}, \\ A_n &= -\frac{2n-1}{32n^3-26n+6}(ka)^2A_{n-1}, \quad n>0,\end{aligned} \tag{16}$$

while the paraxial expansion of Eq. (8), valid for $w \geqslant \sqrt{z^2+a^2}$, is written as

$$\begin{aligned}p(\mathbf{r}) &= \sum_{n=0}^{\infty} B_n f_{2n}(kz,kr_a)j_{2n}(kw), \\ B_0 &= 1, \\ B_n &= -\frac{8n^2-2n-1}{8n^2-6n}B_{n-1}, \quad n>0,\end{aligned} \tag{17}$$

with $f_{2n}(kz,kr_a)$ defined by the recurrence relation of Eq. (11).

Similarly, the expansion of Eq. (15) for the pressure averaged over a coaxial circular surface of radius b can be written

$$\begin{aligned}\bar{p}_b(z) &= \sum_{n=0}^{\infty} C_n f_{2n}(kz,k\sqrt{z^2+\alpha_2^2}) \\ &\quad\times{}_1F_2\left[n+1;n+2,2n+\frac{3}{2};-\left(\frac{k\alpha_1}{2}\right)^2\right], \\ C_0 &= \left(\frac{\alpha_1}{b}\right)^2, \\ C_n &= -\frac{2n-1}{32n^3-26n+6}(k\alpha_1)^2C_{n-1}, \quad n>0,\end{aligned} \tag{18}$$

where $\alpha_1=b$, $\alpha_2=a$ if $b \leqslant a$, and $\alpha_1=a$, $\alpha_2=b$ if $b>a$.

III. COMPUTATIONS

Example computations were performed by directly applying the outer series expansion of Eq. (16), the paraxial series expansion of Eq. (17), and the expansion of Eq. (18) for computations of averaged pressure over a circular aperture. In each case, series were truncated after the convergence criterion

$$\frac{|p_n - p_{n-1}|}{|p_{n-1}|} < \epsilon \tag{19}$$

was met for two successive terms, where p_n is the pressure estimate obtained by truncation of an exact series expansion after the nth term. Given this convergence criterion, a

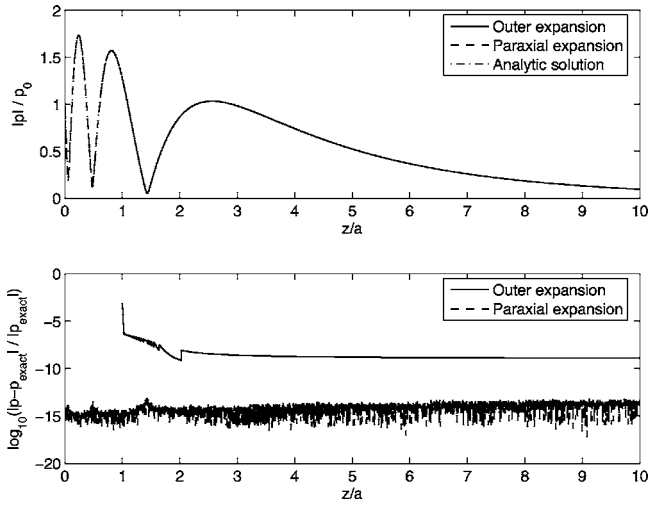

FIG. 2. Computed pressure amplitudes and base-10 logarithm of relative error for paraxial and outer series expansions of the on-axis field of a baffled piston in a lossy medium, computed for $ka=20+0.1i$.

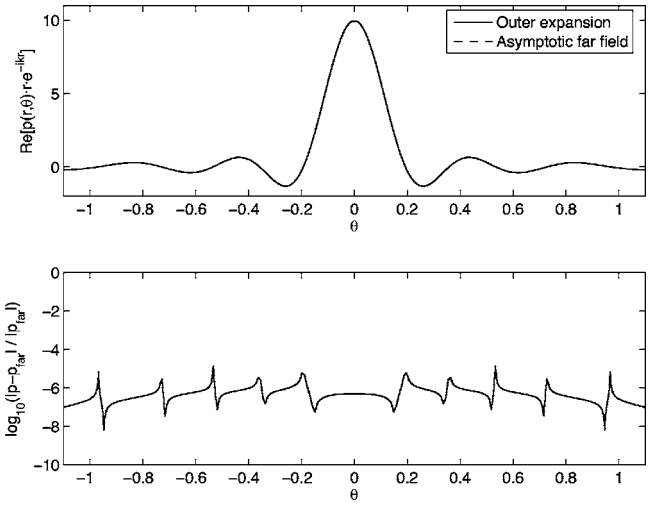

FIG. 3. Computed far-field pattern and base-10 logarithm of error relative to the asymptotic far-field solution for the outer series expansion, computed for $ka=20$, $kz=20\times10^7$.

minimum of three terms is required to compute the piston field at any point. The small parameter ϵ was taken in these computations to be 10^{-6}. If a series computation diverged or caused a floating-point overflow before meeting the convergence criterion, as can occur near the boundaries of convergence for each series type, the sum was taken to be the value obtained by truncating the series at the term of minimum error ϵ.

Results from the exact series expansions derived above can be compared with known analytic solutions for special cases of the piston field. For the on-axis case $w=0$, the paraxial series expansion given by Eq. (10) is mathematically equivalent to the analytic solution of Eq. (12). In Fig. 2, the exact on-axis field for $ka=20+0.1i$ is plotted against the expansions of Eqs. (8) and (10), where the former solution is only valid for $z\geqslant a$. Also shown is the logarithmically scaled relative error $\log_{10}(|p-p_{\text{exact}}|/|p_{\text{exact}}|)$, where p_{exact} is the analytic on-axis solution of Eq. (12). The corresponding plot of error relative to the analytic solution shows that the outer expansion of Eqs. (8) has a numerical error comparable to the truncation error expected for $\epsilon=10^{-6}$, except for the region $z\approx a$. The paraxial expansion of Eq. (10) shows error comparable to the precision limit for double-precision numerical computations.

The solutions can also be compared to the asymptotic far field for the piston radiator, given by

$$p(r,\theta)\rightarrow -ika^2\frac{J_1(ka\sin\theta)}{ka\sin\theta}\frac{e^{ikr}}{r}, \tag{20}$$

where J_1 is the Bessel function of order 1. Figure 3 shows plots of the far-field pattern $p(r,\theta)\cdot re^{-ikr}$ for the asymptotic $(r\rightarrow\infty)$ solution and the present series solutions, computed for a piston with normalized radius $ka=20$, a normalized axial distance of $kz=20\times10^7$, and azimuthal distances of $w<2z$, corresponding to $|\theta|<1.11$ radians or an angular span of 127°. The second panel of the plot shows the logarithmically scaled relative error $\log_{10}(|p-p_{\text{far}}|/|p_{\text{far}}|)$, where p_{far} is the asymptotic far-field solution of Eq. (20). Agreement is good, with error exceeding the series truncation precision only near nulls of the asymptotic far-field pattern.

Convergence of the outer and paraxial series expansions is illustrated in Fig. 4. Here, the number of terms required to meet the convergence criteria described above are plotted as a function of position for a piston with normalized radius $ka=50$. The outer expansion from Eqs. (8) and (16) converges uniformly outside the vicinity $r\approx a$, requiring 35 to 38 terms for most of the field. The paraxial expansion from Eqs. (10) and (17) converges immediately on-axis, with the number of required terms increasing approximately linearly $(N\sim kw)$ as the azimuthal distance w approaches $\sqrt{z^2+a^2}$. For the case illustrated here, convergence occurs in less than 38 terms throughout the cylinder $w\leqslant a$, except for the vicinity where $z\approx0$ and $w\approx a$. Although the number of terms required for convergence depends on ka, the spatial regions of convergence for each expansion are determined only by the piston geometry, as seen from the conditions for validity of Eq. (6).

The two expansions derived above have overlapping regions of validity that enable accurate computation of the radiated pressure field for the entire half-plane $z\geqslant0$. An effective use of these series employs Eqs. (8) or (16) for the region $w\geqslant a$ and Eqs. (10) or (17) for the region $w<a$. The number of terms required for convergence using this combination of series is illustrated in Fig. 4(c). The region of validity for each solution results in rapid convergence everywhere (number of terms $\sim ka$) except for points near the piston boundary, where $z\approx0$ and $w\approx a$.

An example simulation shows the application of these methods to computation of fields induced by high-frequency sources in lossless and absorbing media. This computation employed the outer expansion of Eq. (16) for the region $w\geqslant a$ and the paraxial expansion of Eq. (17) for the region $w<a$. The parameters employed correspond to a transducer of frequency 4 MHz and diameter 6.1 cm radiating into a tissue-like fluid medium with sound speed 1.54 mm/μs. Figure 5 shows pressure amplitudes for the lossless case, with a normalized wave number $ka=500$, and for a case with ab-

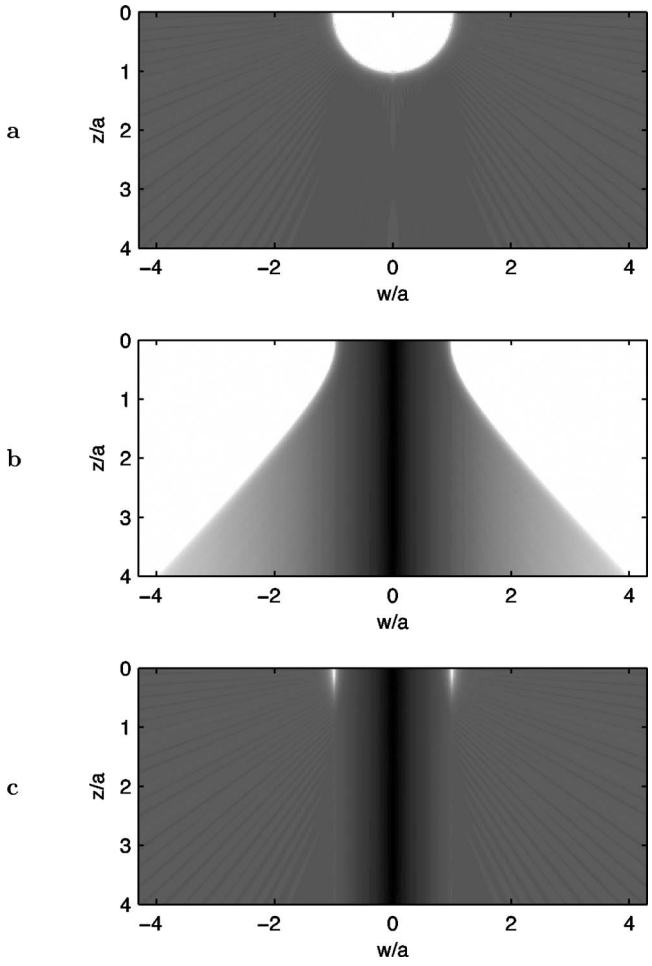

FIG. 4. Number of terms required for convergence, $ka=50$, $\epsilon=10^{-6}$. The number of required terms is shown using a linear gray scale where black represents three terms (the minimum possible for the convergence criteria employed) and white represents 200 terms. To show detail, points requiring more than 200 terms are plotted with a value of 200. (a) Outer expansion. (b) Paraxial expansion. (c) Combined solution, requiring <40 terms in most of the half-space. The solid white regions in panels (a) and (b) represent the spatial regions where the respective expansions do not converge.

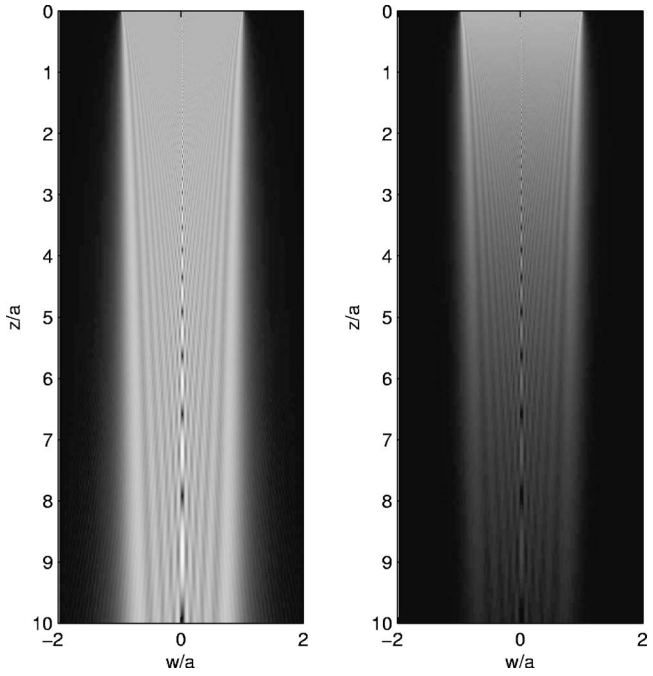

FIG. 5. Pressure amplitude computed using simplified series expansions. Left: field in a lossless medium, $ka=500$. Right: field in an absorbing medium, $ka=500+0.2303i$. Both fields are shown using a linear gray scale in which black represents $|p|=0$ and white represents $|p|=2p_0$.

sorption of 2 dB per piston radius, or 0.16 dB/(cm MHz), corresponding to a normalized complex wave number $ka=500+0.2303i$.

The accuracy and computational efficiency of the exact series expansion approach can be compared with numerical integration using the impulse response method. For the straightforward implementation of the impulse response method employed here, the single-frequency field was obtained here as a single Fourier component of the analytic piston impulse response[9] The Fourier integral defined in Ref. 9 was evaluated analytically for the constant portion of the impulse response, and using midpoint integration for the duration over which the impulse response is not constant. The number of summation points used for the numerical integration was adjusted so that the time step employed was an integer fraction of the time span integrated.

The impulse response method was used to compute the lossless field of a piston with $ka=500$ described above and plotted in Fig. 5. For accuracy comparable to the series method, a sampling rate of about 1000 points per period, or 4 GHz for the present example, is required for the impulse response method. This fine sampling is consistent with previous findings that gigahertz (GHz)-range sampling rates are required for accurate impulse-response computations of megahertz (MHz)-range ultrasound fields.[37] To compute one field point, the impulse response method as implemented here thus required summation of up to 1.59×10^5 terms for each field point. This may be compared to the $\sim$300 summation terms required for the series solution with comparable accuracy in this case. Also notable is that the impulse response must be recomputed for each spatial position, while the series solutions of Eqs. (16) and (17) contain coefficients that need only to be evaluated once for multiple spatial positions. The result is that the impulse-response method required 1.8×10^{-2} CPU s per field point for the computation shown, while the series expansion method required 1.6×10^{-4} CPU s per field point. Thus, for the implementations employed here, the series method can improve computational speed by two orders of magnitude compared to numerical integration. Both computations were implemented here in GNU Fortran 77 (g77), running under Linux on an AMD Athlon 64 3000+ processor with clock speed 1.8 GHz.

Use of the series expansion method to model a pitch-catch measurement is illustrated in Fig. 6. In the modeled configuration, the acoustic pressure radiated by a baffled piston is detected by an idealized coaxial receiver that averages the free-field pressure over a circle of radius a. The averaged pressure was computed using Eqs. (18) for normalized wave numbers $ka=1$, 4, 10, and 100 and axial distances $0<z/a<10$. The results show the expected axial variations in the measured pressure due to near-field diffraction effects, as well as amplitude changes due to beam spreading. The accuracy of these results can be gauged by numerical com-

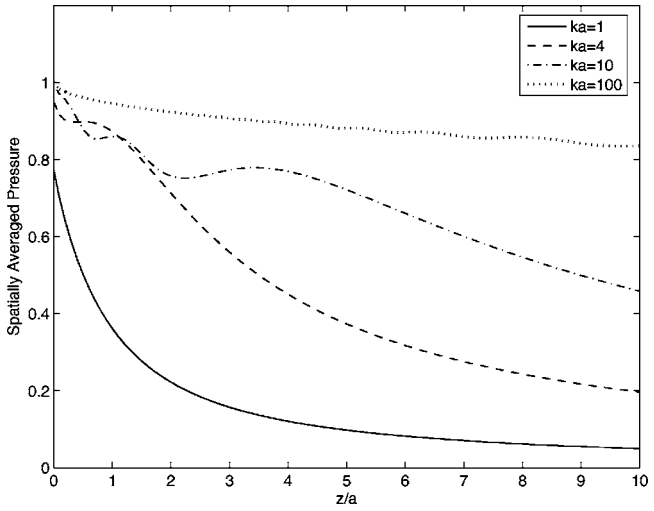

FIG. 6. Acoustic pressure field of a baffled piston averaged over a coaxial circle of equal radius, plotted as a function of normalized axial distance z/a for four values of the normalized wave number ka.

parisons with the exact solution for $a=b$, $z=0$ given by Rayleigh[1,2] and with the numerical integration approach from Ref. 34 for arbitrary a, b, and z. The series method from Eqs. (18) is thus found to provide acceptable accuracy (relative error magnitude $\sim 10^{-4}-10^{-5}$) for $z=0$ and high accuracy (relative error magnitude $<10^{-6}$, limited by the series truncation error) for z greater than about $0.1a$.

IV. DISCUSSION

The work presented here provides accurate solutions for the fields of piston radiators, with favorable analytic and computational simplicity as well as convergence properties compared to previous exact solutions. The outer and paraxial series expansions presented here can be regarded as special cases of those given in Refs. 26 and 27, but consideration of these special cases has resulted in simpler analytic forms for the expansions. Compared to the general expansions given in Refs. 26 and 27, those presented here have one-half the number of terms, take simpler forms including closed-form coefficients for the outer expansion of Eq. (8), and do not require choice of an arbitrary origin position.

The series methods presented here can be considered a complementary alternative to numerical integration approaches. Methods for computing exact piston fields by numerical integration include transformations of the Rayleigh integral into single line integrals[3–6] as well as approaches to integration of the space- and time-dependent piston impulse response.[7–9] Recent progress has been made in efficient numerical computation of such integrals.[10–12] Several approaches are reviewed in Ref. 12, where application of a grid-sectoring method to a modified impulse-response integral is shown to significantly improve computational efficiency for single-frequency computations of the piston nearfield. Compared to the present series approaches, numerical integration approaches based on the piston impulse response may incur greater computational difficulties in the acoustic far field,[10,12] but may provide more accurate results for points near the velocity discontinuity at the piston boundary, where $z\approx 0$ and $w\approx a$.

The series solutions presented here are expected to be useful for computations of single-frequency piston fields at multiple spatial positions. This is the configuration of interest, for example, in ultrasonic heating of tissue, where the acoustic heat deposition in an absorbing medium needs to be known with high spatial resolution.[13] In highly absorbing media, such as soft tissue at sufficiently high ultrasonic frequencies, acoustic absorption may substantially affect diffraction of ultrasound beams. Thus, the series methods presented here, which treat attenuation effects exactly by incorporation of a complex wave number, may have advantages over other approaches that treat attenuation approximately.[13,17,38]

Another application for the series solutions presented here is benchmarking of numerical methods for radiation from arbitrary sources, as has been previously done using numerical integration methods.[16,39] The easily-characterized accuracy of the series solutions allows numerical evaluation of piston radiator fields with accuracy limited only by the floating-point resolution employed in the computations. Thus, this method is expected to be useful for computing reference solutions in both lossless and absorbing media. Using Fourier synthesis of piston fields computed for multiple frequencies, time-domain reference solutions can also be computed. However, the series methods considered here are not expected to be as efficient as time-domain integration methods for computation of transient radiation.

The capability of the series solutions for exact nearfield computations of spatially-averaged piston fields in absorbing media should also be useful for measurements of attenuation in transmission mode.[33,34] In highly absorbing media, the presence of large attenuation may measurably affect the spatial distribution of acoustic pressure in the near field. For this reason, rigorously accounting for the effects of absorption may provide increased accuracy in diffraction correction for attenuation measurements.

[1] J. W. S. Rayleigh, *The Theory of Sound*, Vol. 2, 1896 (reprinted by Dover, New York, 1945), Secs. 278, 302.
[2] A. D. Pierce, *Acoustics: An Introduction to its Physical Principles and Applications*, 2nd ed. (Acoustical Society of America, Woodbury, NY, 1989), pp. 213–245.
[3] L. V. King, "On the acoustic radiation field of the piezo-electric oscillator and the effect of viscosity on transmission," Can. J. Res. **11**, 135–155 (1934).
[4] A. Schoch, "Betrachtungen über das Schallfeld einer Kolbenmembran," Akust. Z. **6**, 318–326 (1941).
[5] S. Ohtsuki, "Ring function method for calculating nearfield of sound source," J. Bronchol. **123**, 23–31 (1974).
[6] G.-P. J. Too, "New phenomena on King integral with dissipation," J. Acoust. Soc. Am. **101**, 119–124 (1997).
[7] F. Oberhettinger, "On transient solutions of the baffled piston Problem," J. Res. Natl. Bur. Stand., Sect. B **65B**, 1–6 (1961).
[8] P. R. Stepanishen, "The time-dependent force and radiation impedance on a piston in a rigid infinite planar baffle," J. Acoust. Soc. Am. **49**, 841–849 (1970).
[9] J. C. Lockwood and J. G. Willette, "High-speed method for computing the exact solution for the pressure variations in the nearfield of a baffled piston," J. Acoust. Soc. Am. **53**, 735–741 (1973).
[10] J. D'hooge, J. Nuyts, B. Bijnens, B. De Man, P. Suetens, J. Thoen, M.-C. Herregods, and F. Van de Werf, "The calculation of the transient near and

far field of a baffled piston using low sampling frequencies," J. Acoust. Soc. Am. **102**, 78–86 (1997).
[11]U. P. Svensson, K. Sakagami, and M. Morimoto, "Line integral model of transient radiation from planar pistons in baffles," Acust. Acta Acust. **87**, 307–315 (2001).
[12]R. J. McGough, T. V. Samulski, and J. F. Kelly, "An efficient grid sectoring method for calculations of the near-field pressure generated by a circular piston," J. Acoust. Soc. Am. **115**, 1942–1954 (2004).
[13]W. L. Nyborg and R. B. Steele, "Nearfield of a piston source of ultrasound in an absorbing medium," J. Acoust. Soc. Am. **78**, 1882–1891 (1985).
[14]H. O. Berktay and M. J. Lancaster, "An analytical expression for the near field of a circular piston radiator," J. Sound Vib. **137**, 319–325 (1990).
[15]A. Freedman, "Acoustic field of a pulsed circular piston," J. Sound Vib. **170**, 495–519 (1994).
[16]T. Xue, W. Lord, and S. Udpa, "Numerical analysis of the radiated fields of circular pistons and time-delay spherically focused arrays," IEEE Trans. Ultrason. Ferroelectr. Freq. Control **43**, 78–87 (1996).
[17]A. Goldstein, "Steady state unfocused circular aperture beam patterns in nonattenuating and attenuating fluids," J. Acoust. Soc. Am. **115**, 99–110 (2004).
[18]H. Backhaus, "Das Schallfeld der kreisförmigen Kolbenmembran," Ann. Phys. **5**, 1–35 (1930).
[19]H. Stenzel, "Über die Berechnung des Schallfeldes einer kreisförmigen Kolbenmembran," Elektr. Nachr. Tech. **12**, 16–30 (1935).
[20]R. C. Wittmann and A. D. Yaghjian, "Spherical-wave expansions of piston-radiator fields," J. Acoust. Soc. Am. **90**, 1647–1655 (1991).
[21]R. D. Spence, "The diffraction of sound by circular disks and apertures," J. Acoust. Soc. Am. **20**, 380–386 (1948).
[22]A. H. Carter and A. O. Williams, Jr., "A new expansion for the velocity potential of a piston source," J. Acoust. Soc. Am. **23**, 179–184 (1951).
[23]A. H. Carter and A. O. Williams, Jr., "A new expansion for the velocity potential of a piston source," [Erratum], J. Acoust. Soc. Am. **24**, 230 (1952).
[24]H. Elrod, "A more rapidly-convergent expansion for the velocity potential of a piston source," J. Acoust. Soc. Am. **24**, 325–326 (1952).
[25]R. New, "A limiting form for the nearfield of the baffled piston," J. Acoust. Soc. Am. **70**, 1518–1526 (1981).
[26]T. Hasegawa, N. Inoue, and K. Matsuzawa, "A new rigorous expansion for the velocity potential of a circular piston source," J. Acoust. Soc. Am. **74**, 1044–1047 (1983).
[27]T. Hasegawa, N. Inoue, and K. Matsuzawa, "Fresnel diffraction: Some extensions of the theory," J. Acoust. Soc. Am. **75**, 1048–1051 (1984).
[28]G. N. Watson, *A Treatise on the Theory of Bessel Functions* (Cambridge University Press, Cambridge, 1922), p. 366.
[29]A. P. Prudnikov, Yu. A. Brychkov, and O. I. Marichev, *Integrals and Series, Volume 2: Special Functions* (Gordon and Breach Science, New York, 1986), p. 37.
[30]A. P. Prudnikov, Yu. A. Brychkov, and O. I. Marichev, *Integrals and Series, Volume 3: More Special Functions* (Gordon and Breach Science, New York, 1990), pp. 608–609.
[31]W. F. Perger, A. Bhalla, and M. Nardin, "A numerical evaluator for the generalized hypergeometric series," Comput. Phys. Commun. **77**, 249–254 (1993).
[32]S. Wolfram, *The Mathematica Book*, 4th ed. (Cambridge University Press, New York, 1999), pp. 772, 1158.
[33]H. Seki, A. Granato, and R. Truell, "Diffraction effects in the ultrasonic field of a piston source and their importance in the accurate measurement of attenuation," J. Acoust. Soc. Am. **28**, 230–238 (1956).
[34]K. Beissner, "Exact integral expression for the diffraction loss of a circular piston source," Acustica **49**, 212–217 (1981).
[35]A. Goldstein, D. R. Gandhi, and W. D. O'Brien, "Diffraction effects in hydrophone measurements," IEEE Trans. Ultrason. Ferroelectr. Freq. Control **45**, 972–979 (1998).
[36]P. J. Davis, "Gamma function and related functions," in *Handbook of Mathematical Functions*, edited by M. Abramowitz and I. A. Stegun (National Bureau of Standards, reprinted by Dover, New York, 1974), Chap. 6.
[37]J. A. Jensen, "A model for the propagation and scattering of ultrasound in tissue," J. Acoust. Soc. Am. **89**, 182–191 (1991).
[38]J. A. Jensen, D. Gandhi, and W. D. O'Brien, "Ultrasound fields in an attenuating medium," 1993 IEEE Ultrasonics Symposium Proceedings, pp. 943–946.
[39]D. Ding and Y. Zhang, "Notes on the Gaussian beam expansion," J. Acoust. Soc. Am. **116**, 1401–1405 (2004).

Measuring the phase of vibration of spheres in a viscoelastic medium as an image contrast modality[a)]

Matthew W. Urban, Randall R. Kinnick, and James F. Greenleaf[b)]
Department of Physiology and Biomedical Engineering, Mayo Clinic College of Medicine, 200 First Street SW, Rochester, Minnesota 55905

(Received 16 June 2005; revised 6 October 2005; accepted 7 October 2005)

Detection of calcifications in breast is an important problem in the diagnosis of breast cancer. Vibro-acoustography is a recently developed method that uses the radiation force of ultrasound to create images of the mechanical response of an object at a low frequency using the magnitude or phase of the response. Small spheres are used to explore the use of the phase of vibration as a contrast modality for use in detection and identification of calcifications in breast tissue. An experiment is presented to measure the magnitude and phase of vibration at different frequencies. The theoretical and experimental results are compared for spheres of two different sizes. Phase images are shown in which five spheres of different density can be clearly distinguished from each other. With phase measurements and images, it is demonstrated that predictable image contrast exists for spheres of different density embedded in a viscoelastic medium. © *2005 Acoustical Society of America.* [DOI: 10.1121/1.2130947]

PACS number(s): 43.20.Tb, 43.25.Qp, 43.30.Jx, 43.80.Qf [TDM] Pages: 3465–3472

I. INTRODUCTION

X-ray mammography is the standard clinical screening modality for breast cancer because of its good sensitivity, high specificity, and relatively low cost. Screening has been shown to reduce breast cancer mortality by 20%–35% in women aged 50 to 69 and slightly less in women of ages 40 to 49 [Elmore *et al.*, 2005]. The American Cancer Society currently recommends that women start receiving yearly screening mammograms starting at age 40 [American Cancer Society, 2005].

It has been found that breast x-ray density and age are factors that decrease the sensitivity and specificity of the mammography screening process [Carney *et al.*, 2003]. Increased breast density reduces contrast in mammograms, making calcifications and tumors harder to find. Women aged 40 to 49 typically have denser breast tissue than older women, making this group susceptible to mitigated benefits from the screening process.

The roles of medical ultrasound and magnetic resonance imaging (MRI) techniques are actively being explored to address some of the limitations of current x-ray mammography. Medical ultrasound is often used as an adjunct for women who have suspicious lesions identified on the mammogram, and for women with dense breast tissue. However, medical ultrasound is not always able to detect microcalcifications due to a number of factors including the spatial resolution of the imaging system, speckle noise, and phase aberration [Anderson *et al.*, 1997]. MRI has shown increased sensitivity in detection of lesions in studies of women with increased risk of breast cancer, but specificity is lower than x-ray mammography [Elmore *et al.*, 2005]. Also, the cost of MRI scanning and the need for injection of a contrast agent are other reasons it has not supplanted x-ray mammography as a widespread clinical screening modality. A recently developed ultrasound method called vibro-acoustography is being explored as a new modality for medical imaging with applicability to breast imaging [Fatemi and Greenleaf, 1998, 1999; Fatemi *et al.*, 2002].

Vibro-acoustography typically uses two ultrasound beams at slightly different frequencies, f_0 and $f_0+\Delta f$, where Δf is typically in the kilohertz range. When the two sound beams interfere at the intersecting foci of the two beams, the resulting acoustic radiation force causes the object within the intersection or focal region to vibrate at Δf. When the object vibrates, it creates a sound field which is called acoustic emission. The acoustic emission is measured with a low-frequency hydrophone or microphone. An image of the acoustic emission can be formed by scanning the object in a raster pattern with a transducer.

Vibro-acoustography has been used for various medical applications such as imaging of mass lesions in liver tissue and calcified arteries [Alizad *et al.*, 2004a, 2004b]. The potential use of vibro-acoustography in breast imaging has been studied, and there have been good results including detection of mass lesions present in the mammogram as well as microcalcifications as small as 100 μm in diameter [Alizad *et al.*, 2004c].

Vibro-acoustography overcomes the obstacle of speckle noise that plagues conventional medical ultrasound. Speckle noise arises from ultrasound interactions with scatterers that are roughly the same size as the wavelength of the ultrasound. Since the acoustic emission is at very low frequencies, the wavelength is very large compared to the ultrasound wavelength, thereby avoiding the speckle noise from scattering. The spatial resolution obtained using vibro-

[a)]Portions of this work were presented in "Measuring the phase of vibration of spheres in a viscoelastic medium using vibrometry," 28th International Acoustical Imaging Symposium, San Diego, CA, March 2005.

[b)]Electronic mail: jfg@mayo.edu

acoustography is good. Using a confocal two-element 3.0 MHz transducer with an F number of 1.55, the point-spread function in the focal plane is about 0.7 mm wide in the focal plane, giving an excitation that is very localized [Chen *et al.*, 2004].

Breast microcalcifications can be associated with the presence of diseased tissue [Kumar *et al.*, 2005; Ikeda 2004]. The material properties of microcalcifications are very different from those of the surrounding soft tissue. Microcalcifications are composed of apatite, calcite, calcium oxalate, and other materials [Fandos-Merera *et al.*, 1988]. These materials have densities ranging from 2200 to 3350 kg/m^3 [Lide, 1991], while soft tissue has a density closer to that of water, which is 1000 kg/m^3. Because these materials are denser and harder than the soft tissue, an imaging modality that is sensitive to density could be used to better detect microcalcifications.

There are two reasons to model microcalcifications as small spheres. First, using a sphere simplifies the shape of the calcifications and the model can be extended easily for any size calcification. Second, extensive theoretical development on the motion of spheres in a viscoelastic medium excited by radiation force has already been carried out [Chen *et al.*, 2002]. We chose to model the spheres in a viscoelastic medium because soft tissue is inherently viscoelastic.

In the vibro-acoustography studies previously cited, the difference frequency ranged from 5 to 30 kHz, and the magnitude of the acoustic emission signal was used to create the images [Alizad *et al.*, 2004c]. As a new contrast mechanism, we will explore the phase of the vibration at very low frequencies, 100–3000 Hz.

II. METHODS

A. Dynamic motion of a sphere

The radiation force resulting from a plane wave incident on a sphere immersed in a fluid is given by $F=\pi a^2 Y\langle E\rangle$, where πa^2 is the projected area of the sphere, Y is the radiation force function, and $\langle E\rangle$ is short-term time average of the energy density of the ultrasound [Chen *et al.*, 2002]. The dynamic radiation force from two interfering plane waves is given by $F_d=\pi a^2 Y\langle E_0\rangle\cos((\omega_1-\omega_2)t-\theta_d)$ where $\langle E_0\rangle = 2P_0^2/\rho c^2$ and θ_d is the phase shift of the radiation force compared to the incident field. The difference frequency is defined as $\Delta\omega=\omega_1-\omega_2$. The velocity of the sphere can be calculated as

$$V=\frac{F_d}{Z_r+Z_m}. \tag{1}$$

The terms Z_r and Z_m are the radiation and mechanical impedances, respectively, given in Eqs. (2) and (4), where $k=\sqrt{\rho\Delta\omega^2/(2\mu+\lambda)}$, $h=\sqrt{\rho\Delta\omega^2/\mu}$, $\mu=\mu_1+i\Delta\omega\mu_2$, and $\lambda=\lambda_1+i\Delta\omega\lambda_2$, a is the radius of the sphere, ρ is the density of the medium, c is the speed of sound of the medium, μ_1 and μ_2 are shear elasticity and viscosity of the medium, respectively, and λ_1 and λ_2 are the bulk elasticity and viscosity of the medium, respectively [Ostreicher, 1951]. For soft tissues, $\lambda_1\sim 10^9$ Pa, $\lambda_2\sim 0$ Pa·s, $\mu_1\sim 10^4$ Pa, and $\mu_2\sim 10^{-2}$ Pa·s [Ostreicher, 1951; Frizzell *et al.*, 1976].

$$Z_r=-i\frac{4\pi a^3}{3}\rho\Delta\omega \times\frac{\left(1-\frac{3i}{ah}-\frac{3}{a^2h^2}\right)-2\left(\frac{i}{ah}+\frac{1}{a^2h^2}\right)\left(3-\frac{a^2k^2}{aki+1}\right)}{\left(\frac{i}{ah}+\frac{1}{a^2h^2}\right)\frac{a^2k^2}{aki+1}+\left(2-\frac{a^2k^2}{aki+1}\right)}. \tag{2}$$

For a sphere with mass m vibrating with harmonic velocity $Ve^{i\Delta\omega t}$, the force required to overcome the inertia of the sphere is given as

$$F=m\frac{dVe^{i\Delta\omega t}}{dt}=im\Delta\omega Ve^{i\Delta\omega t}. \tag{3}$$

The mechanical impedance is defined as the ratio of the applied force to the resulting velocity given in the following equation, where ρ_s is the density of the sphere material:

$$Z_m=\frac{-F}{Ve^{i\Delta\omega t}}=-im\Delta\omega=-i\rho_s\frac{4\pi a^3}{3}\Delta\omega. \tag{4}$$

Using these relationships, we can calculate the response of spheres of varying density over a range of frequencies.

B. Phase of vibration

Let us denote Z as the sum of Z_r and Z_m. Also, we introduce phasor notation where $F_d=|F_d|\angle\theta_d$, $Z_r=|Z_r|\angle\theta_r$, $Z_m=|Z_m|\angle\theta_m$. We can rewrite Eq. (1) as

$$V=\frac{|F_d|\angle\theta_d}{|Z_r|\angle\theta_r+|Z_m|\angle\theta_m}=\frac{|F_d|\angle\theta_d}{|Z|\angle\theta_Z}. \tag{5}$$

We would like to explore how the density of the sphere changes the phase of the velocity for the sphere. From Eq. (4), we know that $\theta_m=-90°$ so we substitute this value in Eq. (5) and find the phase of Z. We observe that the radiation impedance only depends on the medium parameters, and thus has no effect on the phase variance as the density of the sphere changes. The total impedance Z is given in Eq. (6) and the phase of Z is given in Eq. (7)

$$Z=|Z_r|\cos(\theta_r)+i|Z_r|\sin(\theta_r)-i|Z_m|, \tag{6}$$

$$\theta_Z=\tan^{-1}\left(\frac{|Z_r|\sin(\theta_r)-|Z_m|}{|Z_r|\cos(\theta_r)}\right). \tag{7}$$

We can calculate the impedance phase, θ_Z, for a sphere of radius $a=0.79$ mm, in a viscoelastic medium modeling tissue with parameters $\mu_1=6.7\times10^3$ Pa, $\mu_2=0.5$ Pa·s, $\lambda_1=10^9$ Pa, $\lambda_2=0$ Pa·s, $c=1500$ m/s, $\rho=1000$ kg/m^3. We will vary the density of the sphere, ρ_s, from 1000–8000 kg/m^3 and set $\Delta f=1.0$ kHz. The resulting curve is shown in Fig. 1 and shows a phase change of 54.75° over the range of density given.

To find an optimal value for Δf, the phase change is calculated over the given density range for different values of Δf. The optimal point for the curve shown in Fig. 2 is a phase change of 64.5° given at $\Delta f=600$ Hz.

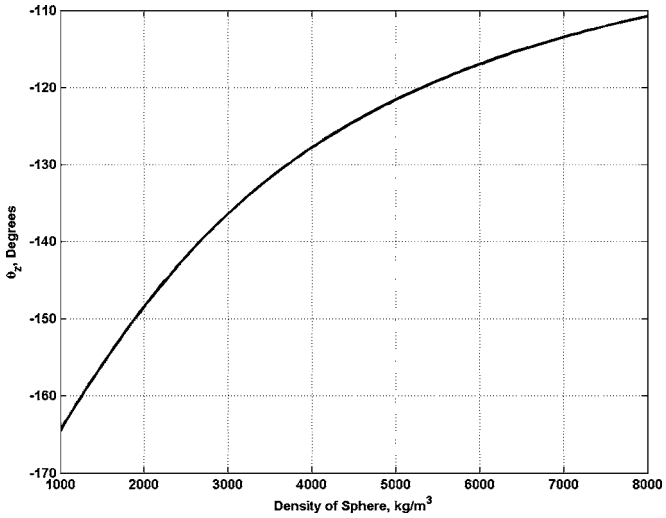

FIG. 1. Plot of θ_Z versus density of sphere for a sphere of radius $a=0.79$ mm at $\Delta f=1.0$ kHz.

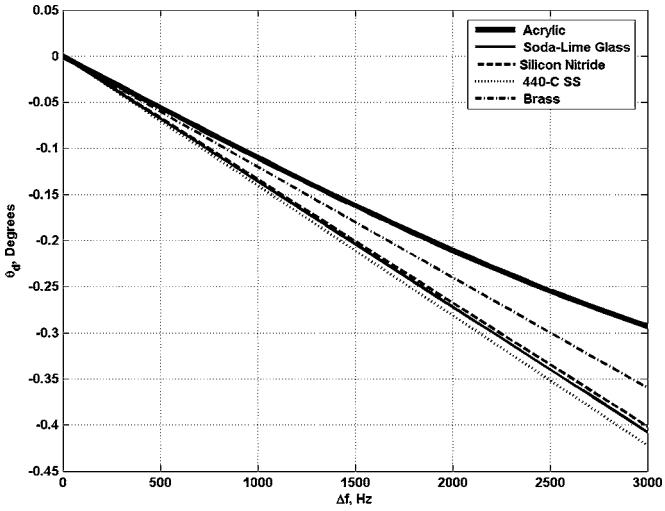

FIG. 3. Plot of θ_d for spheres of radius $a=0.79$ mm made of different materials.

The only parameter that can change the phase of the velocity in the force term is the radiation force function Y which introduces phase θ_d in Eq. (5). The radiation force function for five different spheres made of acrylic, soda lime glass, silicon nitride, 440-C stainless steel, and brass with densities of 1190, 2468, 3210, 7840, 8467 kg/m^3 over a range of $\Delta f=0-3000$ Hz was computed, and the results are shown in Fig. 3. The phase change of the radiation force function is less than 0.5° for this range of Δf, so it can be assumed that any contrast is due to the density change of the sphere. The velocity for the five different spheres mentioned above for a frequency range of $\Delta f=0-3000$ Hz was calculated. The magnitude and phase of the velocity are shown in Fig. 4, where the magnitude curves are normalized by the maximum value of the brass response.

Each sphere has a specific resonance frequency at which the magnitude of the velocity is maximal. The resonance frequency is dependent on the values of μ_1, μ_2, and a. It is important to note that for all values of Δf the phase shift is the least for the sphere of lowest density made of acrylic, and the greatest for the most dense sphere made of brass. As density increases, the phase shift increases as shown in Fig. 1. Therefore, the phase shift of the vibration is proportional to density, providing a predictable density contrast mechanism for evaluating images.

One way to view the magnitude and phase data in one plot is to use a feature space. The magnitude is plotted on the x axis and the phase on the y axis for the data plotted in Fig. 4. Before plotting the phase versus the magnitude, the brass response is subtracted at each frequency to use the brass response as a reference. The frequency range is limited from $\Delta f=750-3000$ Hz to avoid the effects of the resonances of the different spheres. The goal of this feature space diagram is to find a pictorial way to separate the contributions from each sphere over a range of frequencies. In the background, different gray scales define a discrimination surface to separate the responses from each sphere. The regions in Fig. 5 depict the discrimination regions for the acrylic, soda lime glass, silicon nitride, and stainless steel in decreasing levels of brightness. The points within those regions depict simulation results at individual frequencies. The discrimination surface adequately separates the responses of the different spheres.

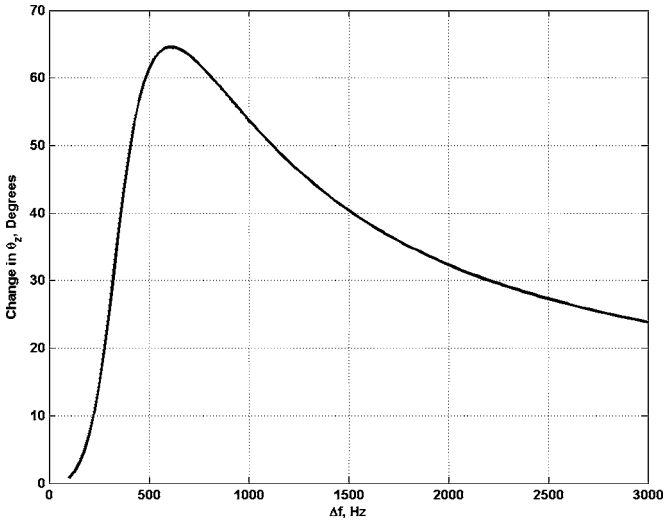

FIG. 2. Plot of change in θ_Z versus Δf for a sphere of radius $a=0.79$ mm and varying the density from 1000–8000 kg/m^3.

III. EXPERIMENT

A. Experimental setup

Spheres of equal diameters, either 1.5875 or 3.175 mm, and different materials including acrylic, soda lime glass, silicon nitride, 440-C stainless steel, and brass were suspended in an optically clear gelatin phantom in a line so that, when scanned, they would all be in the same focal plane. The spheres were separated by more than 1 cm to avoid interactions of shear waves in the gelatin and the sidelobes of the point-spread function. The spheres with diameters 1.5875 and 3.175 mm will henceforth be referred to as the small and large spheres, respectively. The spheres were spray painted white to provide a reflective surface for a Doppler laser vibrometer (Polytec, Waldbronn, Germany). The gelatin phan-

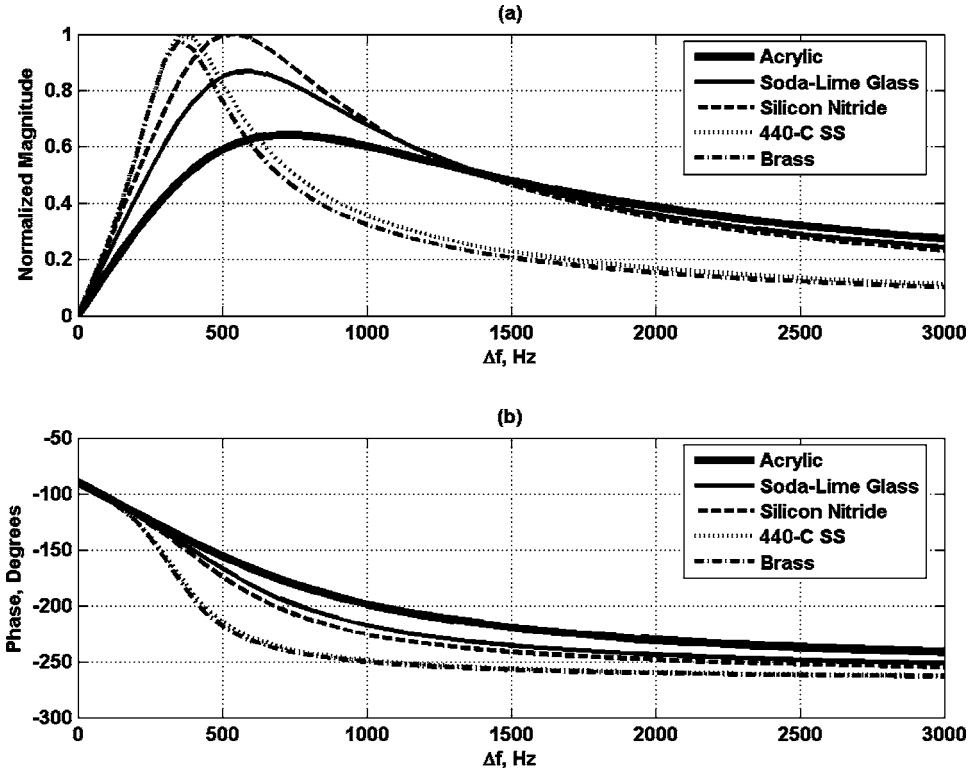

FIG. 4. (a) Normalized magnitude and (b) phase of velocity for five spheres of different materials with radius $a = 0.79$ mm.

tom was made using 300 Bloom gelatin powder (Sigma-Aldrich, St. Louis, MO) with a concentration of 10% by volume. A preservative of potassium sorbate (Sigma-Aldrich, St. Louis, MO) was also added with a concentration of 5%. A confocal, two-element transducer with a nominal frequency of 3.0 MHz and a focal distance of 70 mm was used to excite each sphere. One signal generator (33120A, Agilent, Palo Alto, CA) was set at f_0 and the other was set at $f_0+\Delta f$, where $f_0=3.0$ MHz. A pulse–echo technique was used to position the sphere in the focal region of the transducer. A Doppler laser vibrometer measured the velocity of the sphere, and this signal was subsequently processed by a lock-in amplifier (Signal Recovery, Oak Ridge, TN) to obtain the measurements of the magnitude and phase of the velocity. The phase was computed using a sinusoidal reference signal at the vibration frequency Δf, created by mixing the two ultrasound drive signals and passing the mixed signal through a low-pass filter. The block diagram of the experimental setup is shown in Fig. 6.

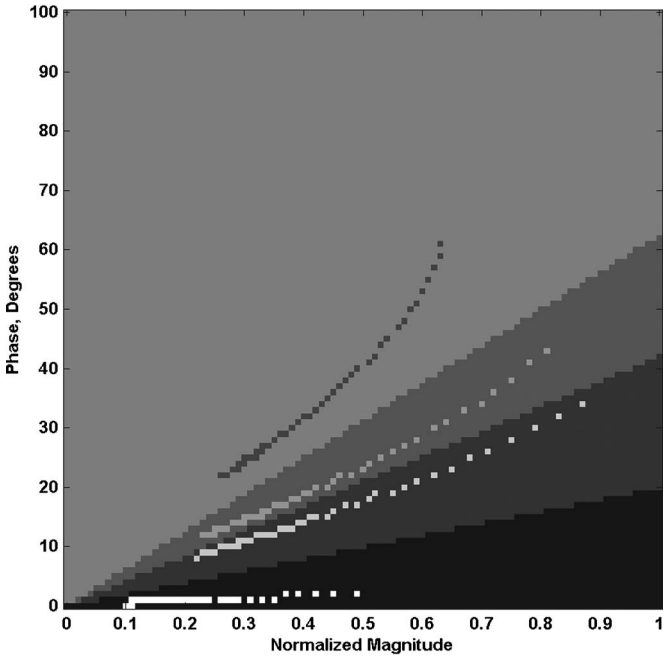

FIG. 5. Feature space for simulation results in Fig. 4.

The difference frequency was varied from 100–1250 Hz in increments of 50 Hz. The magnitude and phase of vibration at each frequency were measured while the transducer was spatially fixed on each sphere. With the measurement data, feature spaces are formed to evaluate the ability to separate the responses of the different spheres.

A magnitude and phase image was created for each sphere at $\Delta f=700$ Hz. This difference frequency was chosen because it was higher than the resonance frequencies so as to avoid confounding interactions due to resonance and to provide more predictable contrast between the spheres both in the magnitude and phase images. The laser was focused on one sphere while the transducer was raster scanned across the phantom with a pixel size of 0.2×0.2 mm. The laser was then focused on the other spheres one at a time, and the scanning was repeated, resulting in five images. The same field of view was scanned each time to assure registration of all the images.

B. Experimental results

The measured magnitude and unwrapped phase for the two phantoms are shown in Fig. 7. The magnitude and phase images from each of the five scans performed at $\Delta f = 700$ Hz were combined to create composite images for the

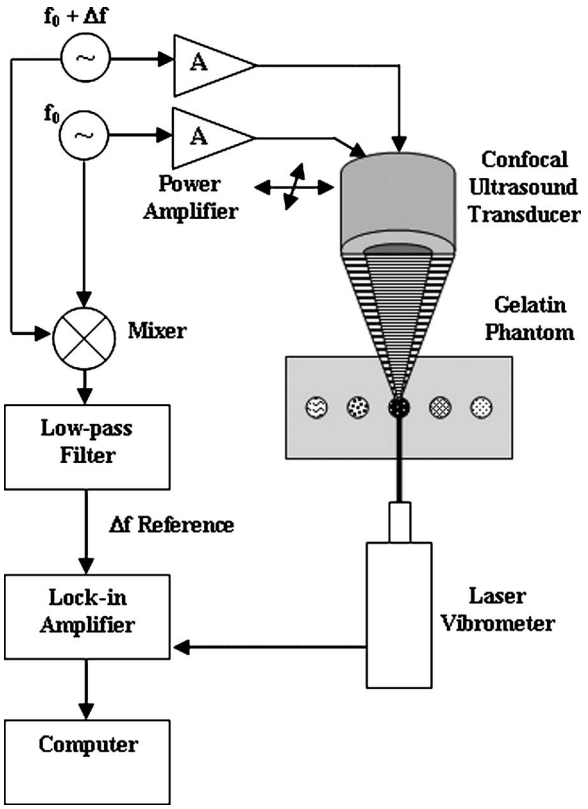

FIG. 6. Block diagram for experimental setup.

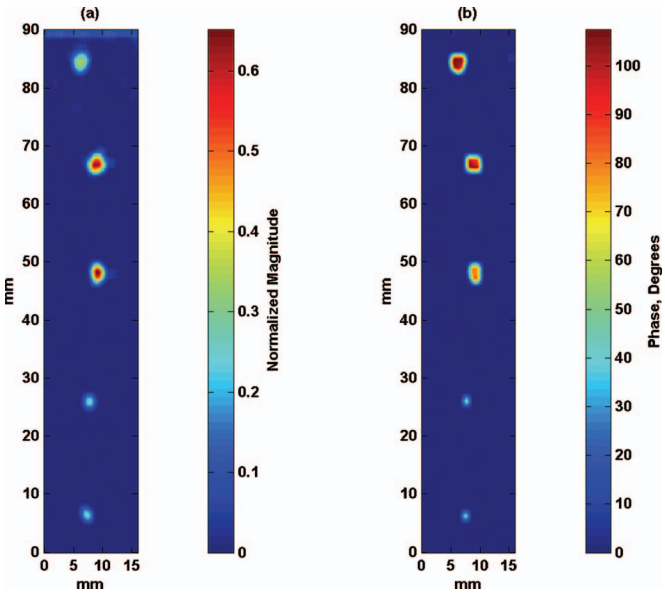

FIG. 8. Images of large spheres. (a) Normalized magnitude image of large spheres. (b) Phase image of large spheres. From top to bottom the spheres are made of acrylic, soda lime glass, silicon nitride, stainless steel, and brass. Brass is used as a reference.

phantom. Preprocessing was performed to reduce noise in the background of the images. The magnitude composite images were formed by adding all five magnitude images together. The phase composite images were created using threshold masks made from the magnitude images. The original phase images were multiplied by the mask images and then summed together. As a result of the threshold operation, the phase composite image had a blocky appearance, so it was spatially low-pass filtered to make the objects more resemble spheres. This filtering did not affect the image values in terms of comparing the magnitude and phase of the spheres. A bias was added to the background so that the relative phase differences could be better visualized. The composite images are shown in Figs. 8 and 9 for the large

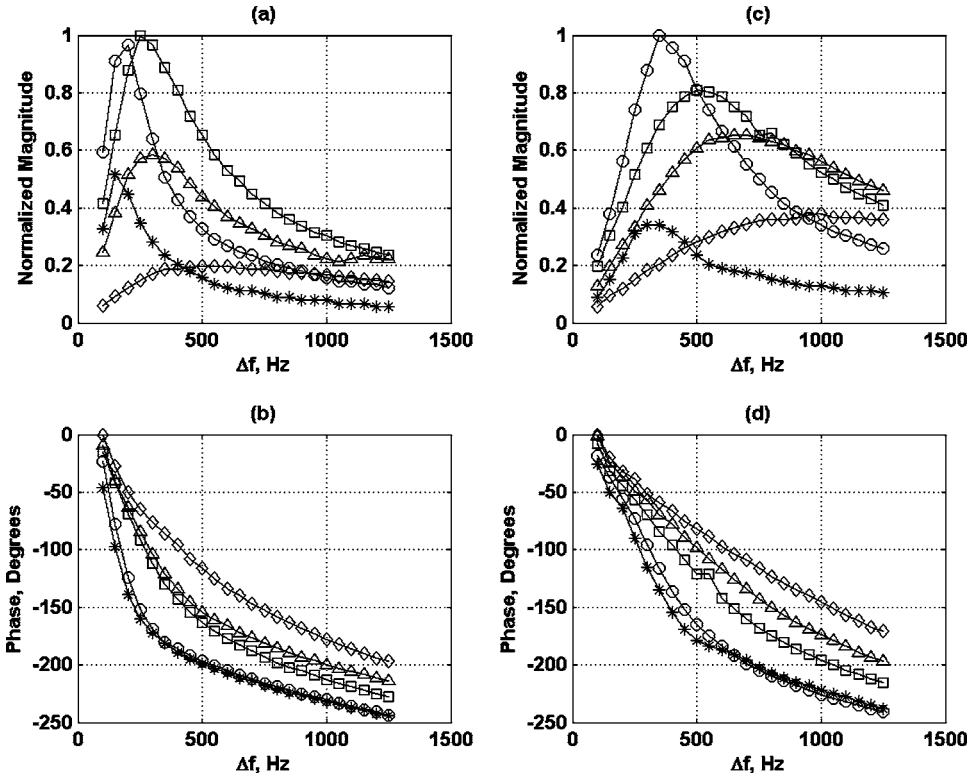

FIG. 7. Measurement results for large and small spheres. (a) Normalized magnitude of the velocity for the large spheres. (b) Phase of velocity for the large spheres. (c) Normalized magnitude of the velocity for the small spheres. (d) Phase of velocity for the small spheres. (◇—acrylic; △—soda lime glass; □—silicon nitride; □—stainless steel; *—brass).

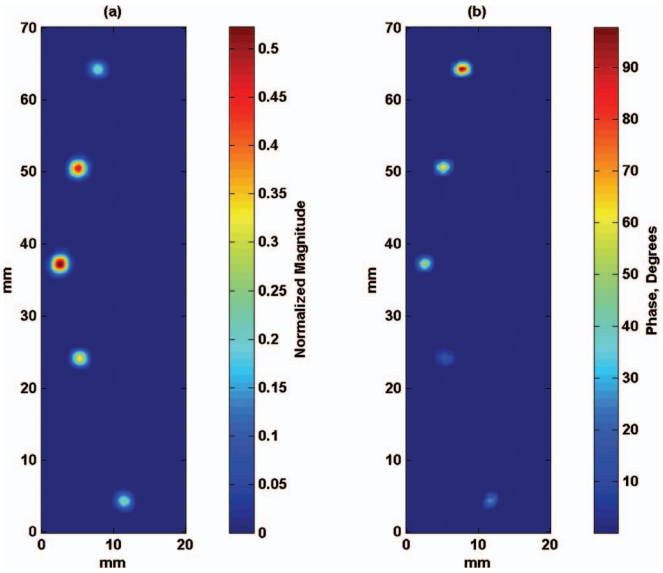

FIG. 9. Images of small spheres. (a) Normalized magnitude image of small spheres. (b) Phase image of small spheres. From top to bottom the spheres are made of acrylic, soda lime glass, silicon nitride, stainless steel, and brass. Brass is used as a reference.

and small spheres, respectively. From top to bottom, the spheres are made of acrylic, soda lime glass, silicon nitride, stainless steel, and brass. The brass and stainless spheres appear dark in the phase image because brass was used as the reference for comparison, and stainless steel has a phase value very close to the brass.

For feature space analysis the measurement data were used for frequency ranges of $\Delta f = 400-1250$ Hz and 700–1250 Hz for the large and small spheres, respectively. The two different lower cutoff frequencies were chosen to avoid the resonance characteristics of the spheres. The feature spaces for the large and small spheres are shown in Fig. 10. The feature space results are incorporated back into the images using the discrimination surface created with the feature spaces. In both feature spaces acrylic is identified by yellow, soda lime glass by red, silicon nitride by green, and stainless steel and brass by blue. The raw image data that were not biased were used for classification of the spheres using the feature space from the measurements. The resulting classified images are shown in Fig. 11.

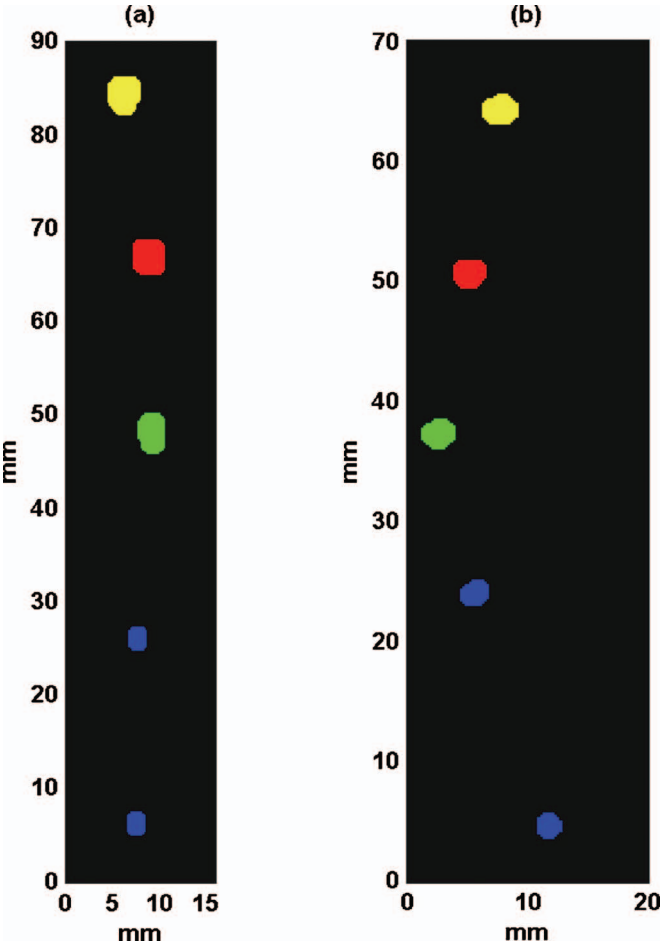

FIG. 11. Classification of images using feature spaces for large and small spheres. (a) Classified image for large spheres. (b) Classified image for small spheres.

IV. DISCUSSION

Comparing the phase responses in Figs. 4 and 7, we find that the spheres follow the same pattern, that is, the phase shift is proportional to the density of the sphere. The magnitude measurements provide no predictable contrast mechanism at a single Δf. The only density contrast evident in the magnitude measurements is that the resonance frequency is that inversely proportional to the density.

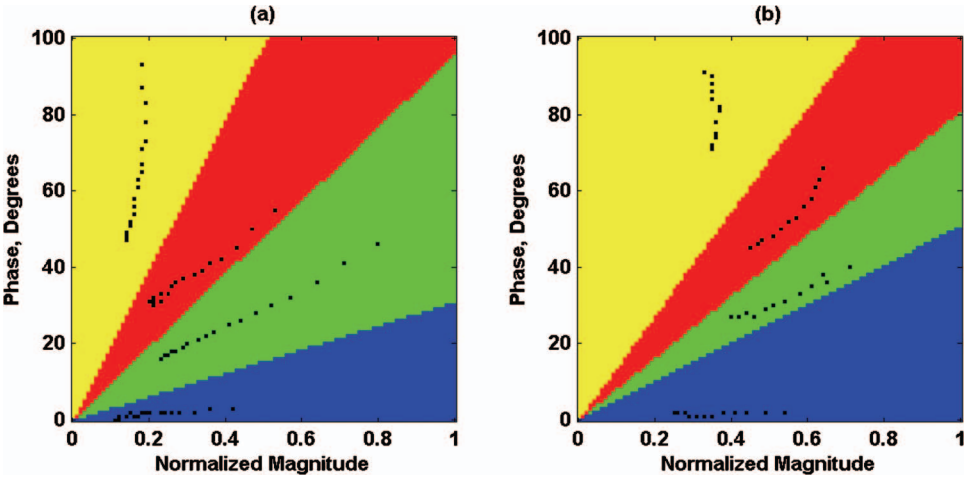

FIG. 10. Feature spaces for large and small spheres. (a) Feature space for measurements on large spheres for $\Delta f = 400-1250$ Hz. (b) Feature space for small spheres for $\Delta f = 700-1250$ Hz. (acrylic—yellow; soda lime glass—red; silicon nitride—green; stainless steel and brass—blue).

If we consider the magnitude image in Fig. 8(a), we observe that the acrylic, stainless steel, or brass spheres have similar image intensities. Also, the soda lime glass and silicon nitride appear similar. In the phase image, the intensity distinction between the acrylic and stainless steel spheres is very evident. We also note a difference between the soda lime glass and silicon nitride spheres in the phase image. The phase image in Fig 8(b) illustrates the same phase shift progression as the measurements, that is, compared to the most dense sphere made of brass, spheres of less dense material have larger phase shifts.

For the small spheres, the magnitude image in Fig. 9(a) would lead us to believe that the soda lime glass, silicon nitride, and stainless steel spheres are similar, and that the acrylic and brass spheres may be similar based on image intensity. However, the phase image in Fig. 9(b) provides evidence of the differences between the five spheres just as the phase image for the large spheres.

The feature space analysis in Fig. 10 provides very good separation of the different spheres for both sizes of spheres used. The discrimination surfaces are slightly different for the different-sized spheres due to different relationships between the magnitude and phase for each size. The colors yellow, red, green, and blue represent the divisions for the acrylic, soda lime glass, silicon nitride, and stainless steel and brass spheres. All of the large and small spheres were classified correctly in Fig. 11. This feature space analysis could be used for *in vivo* imaging to differentiate between objects of interest in an image. We see potential in this type of analysis being useful in classification of different types of calcifications and disease types, but that requires much more additional work.

To use this method *in vivo* a few points must be considered. Vibro-acoustography uses the acoustic emission signal to form images. In this paper, we demonstrated improved contrast from the laser measurement of the velocity of the spheres. To use acoustic emission instead of the velocity, we must develop the mathematical relationship relating the velocity to the acoustic emission. As an alternative to measuring the acoustic emission, we could measure the velocity of the sphere using Doppler ultrasound techniques. Motion detection using pulsed Doppler and a Kalman filter designed for detecting the magnitude and phase of motion due to a harmonic source has been developed and has demonstrated that phase and displacements down to 30 nm could be measured reliably [Zheng *et al.*, 2003].

These experiments detailed in this paper were carried out under continuous wave (cw) driving conditions. This type of implementation *in vivo* could be potentially damaging because of tissue heating effects. The method can be adapted for using tone bursts to prevent undesirable tissue heating.

Calcifications in the breast are not necessarily spherical in shape nor are they the same size within a sample. If the shape is close to spherical we could assume an equivalent sphere model where we use some effective radius to analyze objects in an image. To address size variations we can perform simulations using this equivalent sphere concept to better understand the potential contrast in magnitude and phase images.

The density of calcifications would probably not exceed 3500 kg/m^3, so the contrast in the phase images may only be about 30°, but that should be sufficient if the phase of the background is relatively constant. If Δf is kept in the low kilohertz range, phase wrapping in the phase image should not be a significant issue. However, two-dimensional phase unwrapping techniques have been developed and could be utilized if the need arose [Ghiglia and Pritt, 1998].

V. CONCLUSION

The ability to distinguish between different materials in an image is of great import in medical diagnosis. We have shown that we can provide predictable contrast between objects of different density, so that when an image is presented the density of different objects in the image can be compared. Finding the magnitude and phase responses of small spheres in a viscoelastic medium may give us more insight into how to choose the difference frequency when imaging microcalcifications in the breast. We may be able to provide better contrast in the phase images so that we can identify microcalcifications among other structures in the image, which would aid in diagnosis and treatment.

ACKNOWLEDGMENTS

The authors are grateful to Elaine Quarve and Jennifer Milliken for secretarial assistance. This study was supported in part by Grants EB002640 and EB002167 from the National Institute for Biomedical Imaging and Bioengineering.

Alizad, A., Wold, L. E., Greenleaf, J. F., and Fatemi, M., (**2004a**). "Imaging mass lesions by vibro-acoustography: Modeling and experiments," IEEE Trans. Med. Imaging **23**, 1087–1093.

Alizad, A., Fatemi, M., Whaley, D. H., and Greenleaf, J. F., (**2004b**). "Application of vibro-acoustography for detection of calcified arteries in breast tissue," J. Ultrasound Med. **23**, 267–273.

Alizad, A., Fatemi, M., Wold, L. E., and Greenleaf, J. F., (**2004c**). "Performance of vibro-acoustography in detecting microcalcifications in excised human breast tissue: A study of 74 tissue samples," IEEE Trans. Med. Imaging **23**, 307–312.

American Cancer Society (**2005**). *Cancer Facts and Figures 2005*, (American Cancer Society, Atlanta, GA).

Anderson, M. E., Soo, M. S., Bentley, R. C., and Trahey, G. E., (**1997**). "The detection of breast microcalcifications with medical ultrasound," J. Acoust. Soc. Am. **101**, 29–39.

Carney, P. A., Miglioretti, D. L., Yankaskas, B. C., Kerlikowske, K., Rosenburg, R., Rutter, C. M., Geller, B. M., Abraham, L. A., Taplin, S. H., Dignan, M., Cutter, G., and Ballard-Barbash, R., (**2003**). "Individual and combined effects of age, breast density, and hormone replacement therapy upon the accuracy of screening mammography," Ann. Intern Med. **138**, 168–175.

Chen, S., Fatemi, M., and Greenleaf, J. F., (**2002**). "Remote measurement of material properties from radiation force induced vibration of an embedded sphere," J. Acoust. Soc. Am. **112**, 884–889.

Chen, S., Fatemi, M., Kinnick, R., and Greenleaf, J. F., (**2004**). "Comparison of stress field forming methods for vibro-acoustography," IEEE Trans. Ultrason. Ferroelectr. Freq. Control **51**, 313–321.

Elmore, J. G., Armstrong, K., Lehman, C. D., and Fletcher, S. W., (**2005**). "Screening for breast cancer," J. Am. Med. Assoc. **293**, 1245–1256.

Fandos-Morera, A., Prats-Esteve, M., Tura-Soteras, J. M., and Traveria-Cros, A., (**1988**). "Breast tumors: Composition of microcalcifications," Radiology **169**, 325–327.

Fatemi, M., and Greenleaf, J. F., (**1998**). "Ultrasound-stimulated vibro-

acoustic spectrography," Science **280**, 82–85.
Fatemi, M., and Greenleaf, J. F., (**1999**). "Vibro-acoustography: An imaging modality based on ultrasound-stimulated acoustic emission," Proc. Natl. Acad. Sci. U.S.A. **96**, 6603–6608.
Fatemi, M., Wold, L. E., Alizad, A., and Greenleaf, J. F., (**2002**). "Vibro-acoustic tissue mammography," IEEE Trans. Med. Imaging **21**, 1–8.
Frizzell, L. A., Carstensen, E. L., and Dryo, J. F., (**1976**). "Shear properties of mammalian tissue at low megahertz frequencies," J. Acoust. Soc. Am. **60**, 1409–1411.
Ghiglia, D. C., and Pritt, M. D., (**1998**). *Two-Dimensional Phase Unwrapping—Theory, Algorithms, and Software* (Wiley, New York).
Ikeda, D. M., (**2004**). *Breast Imaging—The Requisites* (Elsevier Saunders, Philadelphia).
Kumar, V., Abbas, A. K., and Fausto, N., (**2005**). *Robbins and Cotran Pathologic Basis of Disease*, 7th ed. (Elsevier Mosby, Philadelphia) pp. 1119–1154.
Lide, David R., (ed.) (**1991**). *CRC Handbook of Chemistry and Physics*, 72nd ed. CRC Press, Boca Raton, pp. 4–49, 4–150.
Ostreicher, H. L., (**1951**). "Field and impedance of an oscillating sphere in a viscoelastic medium with an application to biophysics," J. Acoust. Soc. Am. **23**, 707–714.
Zheng, Y., Chen, S., Tan, W., and Greenleaf, J. F., (**2003**). "Kalman filter motion detection for vibro-acoustography using pulse echo ultrasound," Proc. 2003 IEEE Ultrason. Symp. 1812–1815.

On the holographic reconstruction of vibroacoustic fields using equivalent sources and inverse boundary element method

In-Youl Jeon and Jeong-Guon Ih[a)]
Center for Noise and Vibration Control, Department of Mechanical Engineering, Korea Advanced Institute of Science and Technology, Science Town, Taejon 305-701, Korea

(Received 31 August 2004; revised 13 September 2005; accepted 14 September 2005)

In using the near-field acoustical holography based on the inverse boundary element method (BEM) for the reconstruction of vibroacoustic source parameters, an enormous number of measurements required in practice have limited the extended application of this method. To obtain the sufficient field data with a small number of actual measured data, the regeneration method of the radiated field using the multipoint equivalent sources is attempted in this paper. In using the equivalent source method, a vibrating source can be represented by distributed spherical sources inside the actual source surface. In this paper, the radiated field is expressed with a series of spherical Hankel functions and spherical harmonics. For suppressing the adverse effect of high-order spherical functions, spatial filtering of coefficients and wave-vector components by a regularization scheme is adopted. Restored field data appended with actual measured data can be used as input for the inverse BEM to reconstruct the source field. Numerical tests for spherical sources were performed for investigating the characteristics of the proposed technique. In order to validate the usefulness of the proposed method to actual irregular sources, a vacuum cleaner was taken as a demonstration example and good agreement between measured and reconstructed results could be observed.
 [DOI: 10.1121/1.2114547]

PACS number(s): 43.20.Ye, 43.35.Sx, 43.40.Rj [SFW] Pages: 3473–3482

I. INTRODUCTION

Identification of source distribution is the starting condition for the effective noise control, notwithstanding the difficulties in dealing with the extended vibroacoustic radiators. As one of the indirect methods for the identification of such extended sources, near-field acoustical holography (NAH) has been recently highlighted. This method enables the precise estimation of the distribution of acoustical parameters on the source surface, i.e., surface pressure and normal velocity on a vibrating object, from which the radiation characteristics of the source such as radiated power from the surface, field pressure, and sound intensity can be easily predicted. In summary, NAH has been realized in three ways. One of them is based on the spatial Fourier transform[1,2] of measured data on the hologram plane into the target source plane, only in separable geometry. The second type is based on the inversion of the vibro-acoustic transfer matrix multiplied by the measured hologram data, which usually employs the source modeling by a direct[3,4] or indirect[5] boundary element method (BEM). Arbitrarily shaped sources can be dealt with, but a relatively high computational effort is required in comparison with the former method due to the numerical implementation of integral equations. The third type is to use a series expansion of spherical radiation functions for describing the sound field, in particular, in the hologram plane. The coefficient of each spherical function, centered at an origin located within the source volume, is determined by the numerical inverse process.[6–8]

Equivalent source method (ESM) was suggested[9–11] as an alternative to BEM that can be also used for the reconstruction of a sound field without numerical modeling and source information. This method is based on the principle of wave superposition, and it was successfully applied to many acoustic problems in both exterior[12–14] and interior[15,16] domains. The Helmholtz equation least-squares (HELS) method,[8,17] which is a special case of ESM by using spherical waves, emanating from a single point, has been suggested for reconstructing the sound field or source field in the spherical coordinates. It was recently shown[18,19] that the HELS method can be combined with the BEM-based NAH method, with relatively fewer measurements, for the reconstruction of source parameters of an arbitrarily shaped object.

When the inverse BEM is employed in the NAH, in spite of its advantageous feature in dealing with irregular sources, the method has not yet been used in many actual applications. This is mainly because a large number of measurements are required in practice in order to obtain a very fine source image. A reduction of the laborious effort in instrumentation and measurement has been needed for the extended application of this method. In this paper, in order to obtain the sufficient hologram data with a small number of actual measured data, the HELS method is reformulated by adopting multiple spherical sources distributed inside a source. This can be indeed regarded as a kind of interpolation of the measured field data. The contribution of each equivalent source can be determined by matching the assumed solution with the boundary conditions on the

[a)]All correspondence concerning this paper should be addressed to Jeong-Guon Ih, Department of Mechanical Engineering, KAIST, Science Town, Taejon 305-701, Korea. Telephone: +82.42.869.3035; fax: +82.42.869.8220; electronic mail: J.G.Ih@kaist.ac.kr

structure[9–11] or the measured acoustic pressures on the hologram plane.[9,17] Because the boundary conditions are, in general, the target values for holographic reconstruction, they are *a priori* unknown, so that the radiated field pressures, usually measured in the near field, are adopted as constraints on the assumed solution.

A difficulty in using ESM is that there exists little logical guidance to determine the location, order (or type), or number of equivalent sources, although the reconstruction resolution is highly affected by these characteristics. There were attempts to determine the optimal source locations and strengths numerically by adopting the natural algorithms for simple sources.[20,21] However, it seems that a proper guideline is needed for the selection of suitable locations for high-order spherical sources. In this paper, it is attempted to utilize the effective independence (EfI) method[4,22] for the positioning of linearly independent measurement sensors as well as equivalent sources.

The reconstruction accuracy may not be satisfactory because the system matrix is, in general, ill conditioned, mainly due to the radiated evanescent waves that are decaying at high rates away from the source. Consequently, the solution is very sensitive to the choice of the number of expansion terms,[9,17] in relation with the existence and uniqueness, and the measurement errors, in relation to stability. To determine the optimal expansion number, which is equivalent to designing a low-pass filter for suppressing the high-order spherical waves, the least-square error method (LSM) can be utilized in an iterative way by minimizing the sum of errors between actual and predicted pressures.[9] However, this process requires an additional field measurement to minimize the reconstruction error. Alternatively, spatial coefficient filtering (SCF) method is proposed here to determine the optimal truncation order. Additionally, regularization techniques[23–25] can be adopted to suppress the contribution of high-order wave vector components having small singular values. In this paper, the Landweber iterative method[24] is employed to improve the reconstruction accuracy. The generalized cross-validation (GCV) method[23] between the actual and reproduced model is adopted in determining the optimal parameters of regularization.

After regeneration of the radiated sound field in the hologram plane using the optimized ESM, the vibroacoustic source parameters can be efficiently recovered by using the inverse BEM, of which both the regenerated field data and the actually measured data are input. Numerical tests are performed for investigating the characteristics of the proposed method. In order to validate the applicability of the proposed method to practical complex-shaped sources, a canister-type vacuum cleaner is taken as a demonstration example, for which a comparison is made between measured and reconstructed results.

II. FORMULATION

A. Reformulation of the HELS method

Let the reference position $\mathbf{r}_s$ be the origin of the coordinate, then the time-harmonic acoustic field pressure at an arbitrary point $\mathbf{r}_m$ in the homogeneous free-field outside the source surface can be expressed in a truncated form to the order N in terms of spherical radiation functions ψ_j as[9]

$$p_f(\mathbf{r}_m;\omega) = \sum_{n=0}^{N}\sum_{l=-n}^{n} C_{n,l} h_n(kr_m) Y_n^l(\theta,\phi) \equiv \sum_{j=1}^{J} C_j \psi_j(\mathbf{r}_m;\omega) \quad (j=1,2,3,\ldots). \tag{1}$$

Here, ω is the circular frequency of time-harmonic variation ($e^{-i\omega t}$) and k is the wave number. h_n and Y_n^l represent the spherical Hankel function of the first kind of order $n(n=1,2,3,\ldots)$ and spherical harmonics of order (n,l), respectively, which are particular solutions to the Helmholtz equation in the spherical coordinates (r,θ,ϕ), C denotes the coefficient of each radiation function, and J is the total number of radiation functions. The total number of expansion terms is $J=(N+1)^2$, for which the relationship of $j=n^2+n+l+1$ holds. Equation (1) can be rewritten in the following matrix form when the field pressures are measured at $\mathbf{r}_m(m=1,\ldots,M)$ points on the hologram surface:

$$\mathbf{p}_f = \mathbf{\Psi}\mathbf{C}. \tag{2}$$

Here, $\mathbf{p}_f$ denotes the measured field pressure vector, $\mathbf{\Psi}$ denotes the spherical function matrix, and $\mathbf{C}$ represents the corresponding coefficient vector. If the field measurements are not duplicated, it is obvious that every column vectors of the matrix $\mathbf{\Psi}$ are linearly independent because the spherical functions satisfy the completeness and orthogonality.[26]

If multiple equivalent sources are adopted for modeling a vibroacoustic source, the radiated field pressure can be expressed by a superposition of spherical functions with respect to each equivalent source position $\mathbf{r}_e$ as

$$p_f(\mathbf{r}_m;\omega) = \sum_{e=1}^{E}\sum_{j=1}^{J} C_j^e \psi_j(\mathbf{r}_m - \mathbf{r}_e;\omega), \tag{3}$$

where E is the number of equivalent sources inside the actual vibroacoustic source. For M measurement points, one can rewrite Eq. (3) in a matrix form as

$$\mathbf{p}_f = \mathbf{\Psi}_1\mathbf{C}_1 + \cdots + \mathbf{\Psi}_J\mathbf{C}_J \equiv \mathbf{\Phi}\mathbf{D}, \tag{4}$$

where $\mathbf{\Psi}_j$ and $\mathbf{C}_j$ represent the spherical function matrix related to the jth expansion term and the corresponding coefficient vector, respectively. In addition, $\mathbf{\Psi}$ and $\mathbf{D}$ indicate the global spherical function matrix and coefficient vector corresponding to E-equivalent sources having J expansion terms, respectively. Thus, the total number of coefficients of multiple equivalent sources is $Q=E\times J$. The first term $\mathbf{\Psi}_1$ on the right-hand side of Eq. (4) signifies the system matrix only consisting of monopoles. High-order spherical functions are added up as the expansion order increases. Note that, for given M measurements, the maximum order of each spherical source is limited by the number of equivalent sources. Namely, the more equivalent sources are used, the lower-order spherical functions are involved in the matrix $\mathbf{\Psi}$.

Using the SVD technique, the spherical function matrix can be expressed as

$$\mathbf{\Phi} = \mathbf{U}\Lambda\mathbf{W}^{\mathrm{H}}, \tag{5}$$

where the operator "H" makes the matrix in a Hermitian form, Λ represents the diagonal matrix of which the diagonal elements λ_j are the singular values of the matrix $\mathbf{\Phi}$, and $\mathbf{U}$, $\mathbf{W}$ are two unitary matrices satisfying the orthonormality of $(\mathbf{u}_i)^{\mathrm{H}}(\mathbf{u}_j) = (\mathbf{w}_i)^{\mathrm{H}}(\mathbf{w}_j) = \delta_{ij}$. By combining Eqs. (4) and (5), the coefficients can be obtained by

$$\hat{\mathbf{D}} = \mathbf{W}\Lambda^{-1}\mathbf{U}^{\mathrm{H}}\tilde{\mathbf{p}}_f, \tag{6}$$

where $\tilde{\mathbf{p}}_f$ denotes the measured pressure vector at M field points. Once the coefficient of each spherical function is determined by Eq. (6), one can regenerate arbitrary field pressures at M_2 points outside the minimal spherical surface, enclosing a source as

$$\hat{\mathbf{p}}_{f_2} = \mathbf{\Phi}_{M_2}\hat{\mathbf{D}}, \tag{7}$$

where $\mathbf{\Phi}_{M_2}$ represents the spherical function matrix for M_2 field points.

B. Improvement of reconstruction accuracy with regularization

The spherical function matrix $\mathbf{\Phi}$ is ill conditioned, in general. Consequently, the condition number of the matrix $\mathbf{\Phi}$ is much larger than unity. During the inversion process, high-order spherical functions, which are closely correlated with evanescent waves, affect the reconstruction result significantly. Because the measured field pressures are always more or less contaminated by noise, small fast-varying noise signals, both measurement noise and high-order wave components can become a big contributor after the inversion. Due to this unnecessarily amplified component, the reconstructed results will be severely distorted from the actual target field, and the solutions are very sensitive to the choice of the number of expansion terms. From this reason, the system matrix should be truncated so that the error between measured and regenerated pressures at M_2 field points, in particular on the hologram plane, is minimized in the least square sense as follows:

$$\min_{q \leqslant Q} \|\tilde{\mathbf{p}}_{f_2} - \hat{\mathbf{p}}_{f_2}(q)\|. \tag{8}$$

Here, $\|\cdot\|$ denotes the L_2 norm and $\hat{\mathbf{p}}_{f_2}(q)$ represents the regenerated field pressure vector calculated by the first q coefficients. This process is called the least-square error method (LSM), which will need additional measurements for constraints. In principle, after finding an optimal truncation order q_{op} by the LSM, one can obtain a best fit of the restored acoustic image to the constrained field measurements.

Spherical radiation functions are directly associated with the acoustic radiation modes because each spherical function has its unique directivity pattern. In order to avoid the additional measurements for constraints, the spatial coefficients filtering (SCF) is considered as an alternative to LSM by truncating a part of high-order spherical functions. The truncated solution after eliminating the column vectors related to spherical waves of order $q+1$ to Q can be expressed as

$$\hat{\mathbf{D}}_q = (\mathbf{\Phi}\mathbf{F}_1^q)^{+}\tilde{\mathbf{p}}_f \equiv (\mathbf{\Phi}_q)^{+}\tilde{\mathbf{p}}_f, \tag{9}$$

where

$$\mathbf{F}_1^q = \mathrm{diag}(1, \ldots 1, 0, \ldots, 0) \quad [0 \leqslant \mathrm{rank}(\mathbf{F}_1^q) = q \leqslant Q]. \tag{10}$$

Here, the operator "+" signifies the pseudoinverse of a matrix and $\mathbf{\Phi}_q$ denotes the truncated spherical function matrix to the order q. In Eq. (10), the first q diagonal terms of $\mathbf{F}_1^q$ are unity while other terms are zero. Thus, the conditioning of the system of equations depends on the truncation order q. The optimal parameter q_{op} can be obtained by various parameter-choice tools.[23–25] In this paper, the GCV technique[23] is employed to determine the optimal parameter q_{op}.

Spatial filtering of wave vectors having small singular values of the spherical function matrix with a predetermined q_{op} can be thought of. By using a regularization technique, the solution can be given by

$$\hat{\mathbf{D}}_{q_{\mathrm{op}}}^{\alpha} = \mathbf{F}_1^{q_{\mathrm{op}}}\mathbf{W}\mathbf{F}_2^{\alpha}\Lambda^{-1}\mathbf{U}^{\mathrm{H}}\tilde{\mathbf{p}}_f \equiv (\mathbf{\Phi}_{q_{\mathrm{op}}}^{\alpha})^{+}\tilde{\mathbf{p}}_f, \tag{11}$$

where α is the regularization parameter. If the Landweber iterative method is employed, the regularization filter is given by[24]

$$\mathbf{F}_2^{\alpha} = \mathrm{diag}(F_1^{\alpha}, F_2^{\alpha}, \ldots, F_{q_{\mathrm{op}}}^{\alpha}), \tag{12}$$

where

$$F_q^{\alpha} = 1 - (1 - \beta\lambda_q^2)^{\alpha+1}. \tag{13}$$

Here, the diagonal elements of $\mathbf{F}_2^{\alpha}$ represent the wave vector filter coefficients at the αth iteration step and β denotes the convergence factor. The GCV function[23] between the actual and reproduced model after the truncation of coefficients can be modified as

$$\vartheta(\alpha)\big|_{Q=q_{\mathrm{op}}} = \frac{\|\tilde{\mathbf{p}}_f - \mathbf{\Phi}\hat{\mathbf{D}}_{q_{\mathrm{op}}}^{\alpha}\|^2}{\{\mathrm{tr}[\mathbf{I}_M - \mathbf{\Phi}(\mathbf{\Phi}_{q_{\mathrm{op}}}^{\alpha})^{+}]\}^2} = \frac{\|(\mathbf{I}_M - \mathbf{P}_{q_{\mathrm{op}}}^{\alpha})\tilde{\mathbf{p}}_f\|^2}{[\mathrm{tr}(\mathbf{I}_M - \mathbf{P}_{q_{\mathrm{op}}}^{\alpha})]^2}, \tag{14}$$

where

$$\mathbf{P}_{q_{\mathrm{op}}}^{\alpha} = \mathbf{U}\Lambda\mathbf{W}^{\mathrm{H}}\mathbf{F}_1^{q_{\mathrm{op}}}\mathbf{W}\mathbf{F}_2^{\alpha}\Lambda^{-1}\mathbf{U}^{\mathrm{H}}. \tag{15}$$

Here, "tr" signifies the trace of a matrix and $\mathbf{I}_M$ means the unity matrix with rank M. With a predetermined truncation order q_{op}, the optimal regularization parameter α_{op} can also be obtained by minimizing the GCV function. In practice, the regularization does not need any additional measurements for constraints.

C. Reconstruction of surface parameters by the inverse BEM

In acoustic problems, the Kirchhoff–Helmholtz boundary integral equation can be derived by taking Green's theorem of the volume integral equations as follows:[3,4]

$$c(\mathbf{r})p(\mathbf{r}) = \int_{S_0} \left[p(\mathbf{r}_0) \frac{\partial G(\mathbf{r},\mathbf{r}_0)}{\partial \mathbf{n}(\mathbf{r}_0)} - G(\mathbf{r},\mathbf{r}_0) \frac{\partial p(\mathbf{r}_0)}{\partial \mathbf{n}(\mathbf{r}_0)} \right] dS(\mathbf{r}_0), \tag{16}$$

where $\mathbf{r}$ and $\mathbf{r}_0$ are the field and surface points on S_0, respectively, $\mathbf{n}$ the unit normal vector toward a medium on S_0, $\partial/\partial\mathbf{n}$ the derivative operator in a normal direction to the surfaces, and $c(\mathbf{r})$ the solid angle. The matrix/vector representation of Eq. (16) can be obtained after utilizing the discretization and numerical integration as follows:

$$\mathbf{p}_f = \mathbf{G}_\nu \mathbf{v}_S. \tag{17}$$

Here, $\mathbf{G}_\nu$ is the vibroacoustic transfer matrix correlating the surface normal velocity with the field pressure and this contains the acoustic and geometric information of the system. The surface velocity can be reconstructed from the measured field pressure using the least-square solution as follows:[3,4]

$$\hat{\mathbf{v}}_S = (\mathbf{G}_\nu^{\mathrm{H}}\mathbf{G}_\nu)^{-1}\mathbf{G}_\nu^{\mathrm{H}}\tilde{\mathbf{p}}_f \equiv (\mathbf{G}_\nu)^{+}\tilde{\mathbf{p}}_f. \tag{18}$$

In applying the inverse BEM to reconstructing sound fields of a vibrating object, more than the number of discrete nodes considering a wavelength of interest is required to avoid distortions and take a considerable amount of measurements, since the surface quantities are described by spatial discretization. Such a procedure may be impractical, especially for a complex- shaped structure due to the fact that the discrete nodes and corresponding measurements may be excessive and the reconstruction process can be extremely complex and time consuming. To solve this problem and to enhance the reconstruction efficiency for the surface acoustic quantities on the noise source, a combined method of the inverse BEM with the regenerated field pressures can be thought of. When the field pressures at M_2 points are regenerated by ESM with the actually measured pressures at M points, one can enlarge the size of global matrix with the use of additionally regenerated field pressures. Therefore, the holography equation can be rewritten as

$$\hat{\mathbf{v}}_S = (\mathbf{G}_\nu)^{+}\mathbf{\Phi}_{M_2}(\mathbf{\Phi}^{\alpha}_{q_{\mathrm{op}}})^{+}\tilde{\mathbf{p}}_f. \tag{19}$$

Although the number of actual measured pressure data is less than that of velocity-known nodes of the source surface, the resultant matrix after appending such interpolated field information would be useful in improving the reconstruction. In order to suppress the undesirable contribution from high-order singular values and incorporated noise, a proper technique of wave-vector filtering should be taken and then the accuracy of restored result can be improved. In this study, the Landweber iterative filter with the GCV function is adopted, as discussed in the previous section. After obtaining the optimal regularization parameter μ for the matrix $\mathbf{G}_\nu$ with the optimally regenerated field pressures, the surface velocity can be expressed as

$$\hat{\mathbf{v}}_S^{\mu} = (\mathbf{G}_\nu^{\mu})^{+}\mathbf{\Phi}_{M_2}(\mathbf{\Phi}^{\alpha}_{q_{\mathrm{op}}})^{+}\tilde{\mathbf{p}}_f = \mathbf{W}_\nu \mathbf{F}_2^{\mu} \Lambda_\nu^{-1} \mathbf{U}_\nu^{\mathrm{H}} \mathbf{\Phi}_{M_2}(\mathbf{\Phi}^{\alpha}_{q_{\mathrm{op}}})^{+}\tilde{\mathbf{p}}_f, \tag{20}$$

where $\mathbf{F}_2^{\mu}$ represents the regularization filter at the μth iteration step, as defined in Eq. (13), and $\hat{\mathbf{v}}_S^{\mu}$ denotes the corresponding surface velocity vector. Here, the matrices with the subscript "ν" are related to the singular matrices of $\mathbf{G}_\nu$.

D. Selection of equivalent source locations

In the measurement of radiated sound field by array sensors, if the sensors are located at positions, which are linearly independent to the noise source, it is quite useful in the viewpoint of system singularity. It has been suggested that those locations can be selected by the EfI method.[5,22] The method ranks the candidate sensor locations according to their contribution to the linear independence of the target modal partitions. The contribution of each measurement location to the linear independence of the field pressure for a given measurement setup can be represented by the EfI value, $\{\mathbf{E}_f^M\}$, which is defined as

$$\{\mathbf{E}_f^M\} = \mathrm{diag}(\mathbf{U}_Q \mathbf{U}_Q^{\mathrm{H}}), \tag{21}$$

where $\mathbf{U}_Q$ is the matrix spanned by the first Q column vectors of the singular matrix $\mathbf{U}$.

In a similar way, the proper locations of equivalent sources for regenerating the hologram data can also be determined by switching the source and measurement locations. The linear independency of equivalent sources to the measurement locations is ensured by the application of the EfI method for a given set of equivalent sources. The EfI value for equivalent sources can be given by

$$\{\mathbf{E}_f^Q\} = \mathrm{diag}(\mathbf{W}_M \mathbf{W}_M^{\mathrm{H}}) = \mathrm{diag}(\underbrace{S_{e=1}^{j=1}, S_{e=2}^{j=1}, \ldots, S_{e=E}^{j=1}}_{\text{monopole}}, \ldots, \underbrace{S_{e=1}^{j=J}, S_{e=2}^{j=J}, \ldots, S_{e=E}^{j=J}}_{\text{spherical waves of order } J}). \tag{22}$$

Here, S_e^j represents the EfI value for the eth equivalent source of order j and $\mathbf{W}_M$ indicates the matrix spanned by the first M column vectors of the singular matrix $\mathbf{W}$, which described the source field consisting of E-equivalent sources with J expansion terms. Each diagonal element of $\{\mathbf{E}_f^Q\}$ represents the contribution of each equivalent source to the linear independence of the spherical function matrix. It is noted that the representative EfI value for each equivalent source position $\mathbf{r}_e$ can be obtained by the sum of the EfI values corresponding to the expansion order 1 to J. Thus, the linear independency of each equivalent source location for a given source system can be expressed as

$$\{\mathbf{E}_f^e\} = \sum_{j=1}^{J} \{S_e^j\}, \tag{23}$$

where $\{\mathbf{E}_f^e\}$ denotes the EfI value for each equivalent source position $\mathbf{r}_e$. As a result, the equivalent source location having the smallest EfI value among all the equivalent source positions can be eliminated one by one, or group by group, from the initial set of candidate positions until the predetermined number of equivalent sources is reached.

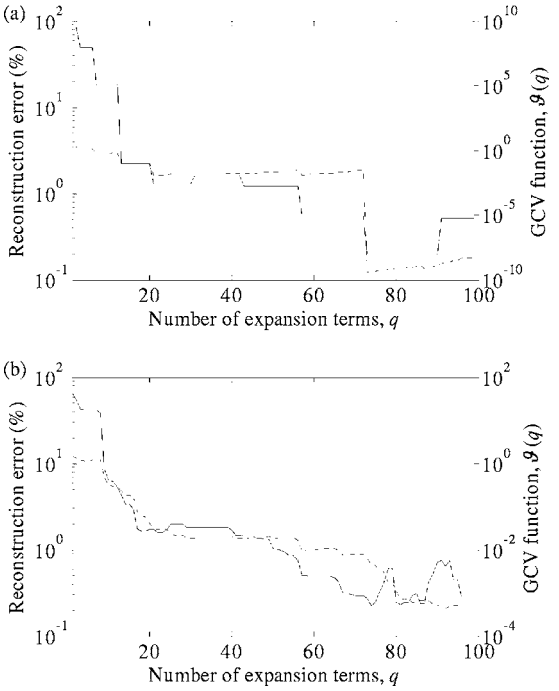

FIG. 1. A comparison of the reconstruction error and calculated GCV value of surface pressures on a partially pulsating sphere source increasing the number of expansion terms ($ka=3$; no input noise):—, reconstruction error;---, GCV function. (a) HELS; (b)ESM.

III. TEST EXAMPLES

A. Partially pulsating sphere

When a sphere with radius a is partially and harmonically pulsating at a velocity V_S with a half vertex angle θ_0 in an infinite, homogeneous, and quiescent medium, the field pressure at a distance r from the origin is given by[27]

$$p(r,\theta;\omega)=\frac{i\rho_0 cV_S}{2}\sum_{n=0}^{\infty}Z_n(\theta_0)\frac{h_n(kr)}{h_n'(ka)}P_a(\cos\theta), \tag{24}$$

where

$$Z_n(\theta_0)=P_{n-1}(\cos\theta_0)-P_{n+1}(\cos\theta_0). \tag{25}$$

Here, ρ_0 is the density of air, c the speed of sound, P_n the Legendre polynomial of order n, and h_n' the derivative of the spherical Hankel function of the first kind of order n.

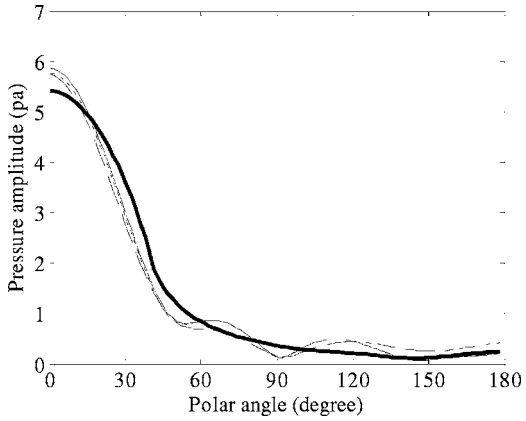

FIG. 3. A comparison of analytical and holographic methods in the reconstruction of surface pressures on a partially pulsating sphere source ($ka=3$; SNR=10).—, Analytical solution;– – –, HELS with LSM ($e=2.4\%$)---, HELS with SCF and regularization ($e=2.84\%$);——, ESM with SCF and regularization ($e=3.00\%$).

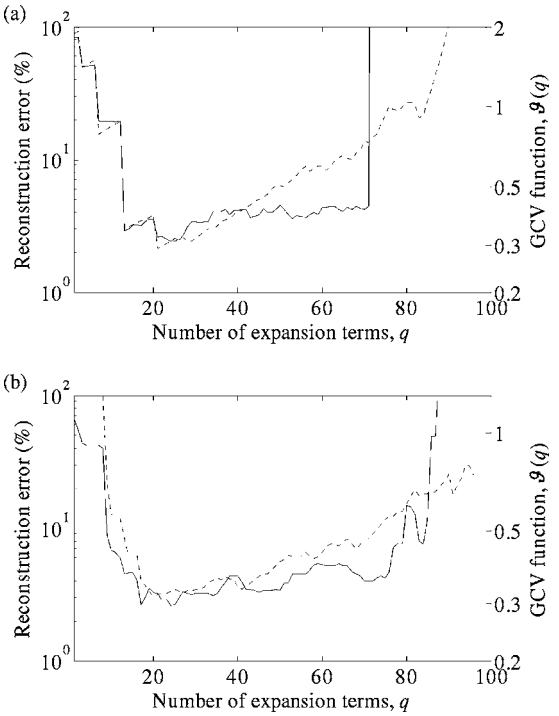

FIG. 2. A comparison of the reconstruction error and calculated GCV value of the surface pressures on a partially pulsating sphere source increasing the number of expansion terms ($ka=3$; SNR=10):—, reconstruction error;---, GCV function. (a) HELS; (b) ESM.

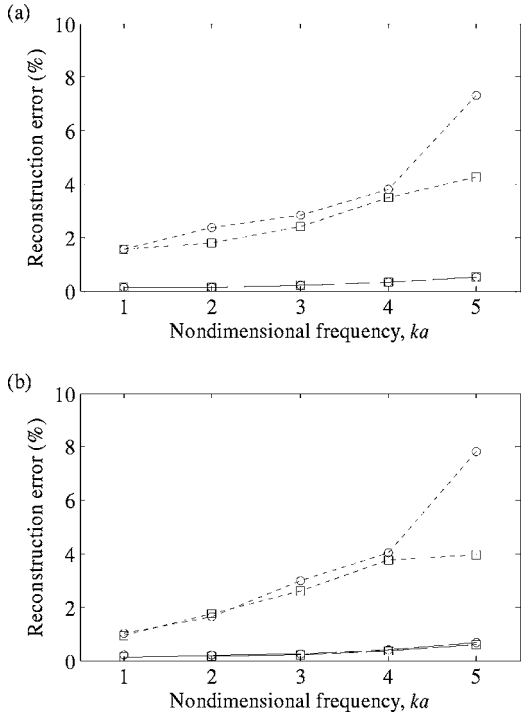

FIG. 4. A comparison of the reconstruction errors of surface pressures on a partially pulsating sphere source by applying (a) HELS and (b) ESM. □, LSM; ○, SCF and regularization (solid line, noise-free; dotted line, SNR =10).

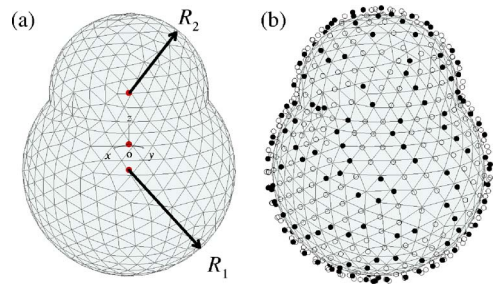

FIG. 5. (a) BEM model of a snowman-like spherical source in which two spheres of different size ($R_1=a$, $R_2=0.75a$) are merged with a center offset of $R=0.75a$; (b) spatial distribution of candidate field points on the conformal surface at a $0.1a$ clearance (●, $M=200$; ○, $M_2=600$).

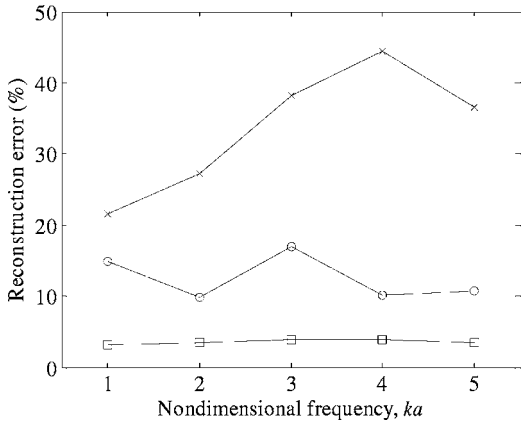

FIG. 6. Reconstruction errors of the normal surface velocities on a snowman-like spherical source (600 nodes) by using the inverse BEM ($C_p=5$; SNR=100). ○, using 600 regenerated pressures including 200 input data; □, using 600 input data without regeneration; ×, using 200 input data.

Assume that the sphere is partially vibrating with amplitude of $V_S=0.01$ m/s and with a solid angle of $\theta_0=40°$. Measurement points ($M=98$) are evenly distributed on the spherical surface of $r=1.05a$. The field pressure at each measurement point can be calculated by using Eq. (24) and used as the input data for simulation. The acoustic pressure on the surface of sphere was the target for reconstruction.

If a single source happens to be placed at the origin of a spherical system, the condition coincides with that of the conventional HELS method, as mentioned earlier. In dealing with the multiple equivalent spherical sources, apart from the measurement noise and among many possible factors, the configuration of equivalent sources and/or boundary conditions can also cause the instability of solution. The instability due to this condition can be avoided by taking a similar equivalent source system, which is chosen to conform to the geometric configuration of measurement points, into the actual noise source.[12] Therefore, eight equivalent sources ($E=8$) are uniformly placed on the surface of a small sphere with $r=0.3a$ inside the actual source. Consequently, the solution is obtained by using the SVD and regularization technique combined with the SCF method. The following percentage error of regenerated data is used for the calculation of the accuracy of reconstruction:

$$e=\frac{\|\text{actual value}-\text{reconstructed value}\|^2}{\|\text{actual value}\|^2}\times 100(\%). \tag{26}$$

Even though there is no noise added to the input data, the reconstruction error does not go to zero since the residual error still remains in the restored solution. If the solution is determined by HELS, the residual error between the analytical and assumed solution with the order N_{op} can be directly calculated by matching Eqs. (1) and (24) as follows:

$$\varepsilon(a,\theta;\omega)|_{N=N_{\text{op}}}=\frac{i\rho_0 cV_S}{2}\sum_{n=N_{\text{op}}+1}^{\infty}Z_n(\theta_0)\frac{h_n(ka)}{h_n'(ka)}P_n(\cos\theta), \tag{27}$$

where ε denotes the residual error of the solution and N_{op} represents the optimal order of spherical waves. It is noted that the residual error increases with the nondimensional frequency ka and decreases with the optimal order N_{op} of spherical waves. The residual error may also vary with polar angle.

Figure 1 shows a comparison of the reconstruction errors of surface pressures and the calculated GCV function, increasing the number of expansion terms at $ka=3$ when no input noise is added. It is observed that both the reconstruction error and the GCV function are minimized at the certain number of expansion order q_{op}. In this case, the maximum order of spherical waves for HELS ($N_{\max}=8$) is larger than that for ESM with $E=8$ ($N_{\max}=3$), although the optimal truncation order for HELS ($q_{\text{op}}=73$) is smaller than that for ESM with $E=8$ ($q_{\text{op}}=92$). Note that when the number of measurement M is increased, such a residual error would be decreased since the maximum order $N_{\max}$ can be increased.

It should be noted that the instabilities of the truncated solution are not only supposed to be due to the residual error, but also due to the added noise, because the signal deterioration by measurement noise is unavoidable in the actual situation. To simulate the inclusion of measurement noise, the calculated field pressures are mixed with the unbiased Gaussian random noise. In this case, an optimal number of expansion terms could be determined by utilizing the fact that the reconstruction error decreases first and then diverges as the number of expansion terms increases.

When the signal-to-noise ratio (SNR) is equal to 10, the optimal truncation order q_{op} is much smaller in comparison with the previous noise-free case, as shown in Fig. 2. In other words, the maximum order of spherical waves would be changed with the amount of the added noise because the high-order spherical waves are much more sensitive to the noise than low-order ones. The maximum order for ESM is determined as $N_{\max}=1$ and this reveals that the sound field could be reconstructed by using relatively simple equivalent sources such as a monopole and a dipole instead of using high-order spherical waves. Figure 3 shows the reconstructed surface pressures at $ka=3$ with an input noise of SNR=10. As a result, it is thought that the reconstruction accuracy of the present method is acceptable because the error for ESM (3%) is less than the input noise level (10%).

Figure 4 shows a comparison of the reconstruction er-

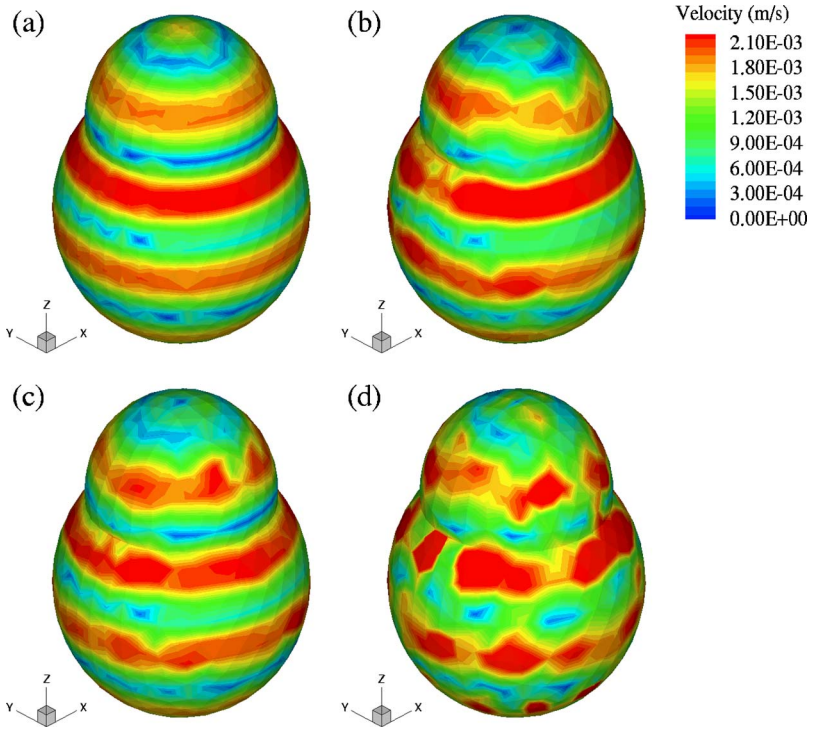

FIG. 7. (Color online) A comparison of the reconstructed surface velocity distributions by the inverse BEM ($ka=5$; $C_p=5$; SNR=100). (a) True value, (b) reconstructed value using 600 regenerated pressures with 200 input data, (c) reconstructed value using 600 input data, (d) reconstructed value using 200 input data.

rors by applying HELS and ESM with the change of the nondimensional frequency ka. As mentioned earlier, the reconstruction error increases with ka due to the existence of residual error. Under a noiseless condition, the final reconstruction results by both HELS and ESM with regularization are slightly deviated from the true value due to the effect of the residual error and the singularity of the system. In addition, the reconstruction results with regularization are quite similar to the results by LSM. It is reminded that LSM cannot be applied to the actual problems because the true solution is never known *a priori*. In summary, it is thought that multiple equivalent sources can be employed in reconstructing the sound field efficiently without extra measurements for constraints, resulting in a substantial reduction of measurement effort.

B. Snowman-like spherical source

In general, a partially pulsating sphere generates the uniform and continuous sound field. However, the irregularities of source shape and boundary condition, on which the radiation pattern highly depends, can also affect the reconstruction result, although the vibrating object is spherical. Therefore, it is needed to consider the effect of nonuniformities in the source shape and boundary condition on the reconstruction of the sound field. From this purpose, a snowman-like spherical source, in which two spheres of different radius ($R_1=a$ and $R_2=0.75a$) are merged with a center offset of $R=0.75a$, is taken as a second numerical example. This source is modeled by 600 nodes and 1206 linear triangular elements, as shown in Fig. 5. The maximum characteristic length of this model is $L_C=0.21a$, of which the applicable high frequency can be spanned up to $ka=5$ under the $\lambda/6$ criterion for linear elements. The following velocity profile is given on the source surface to simulate a rapid variation of the sound field in the polar direction as follows:

$$\bar{V}_S(r,\theta,\phi;\omega) = -V_S h_0(kr)\cos(C_p\theta)\exp(i\phi). \tag{28}$$

Here, C_p represents the polar constant.

Once the normal surface velocities are specified, the field pressure data is calculated using the BEM over a conformal surface around the source at a $0.1a$ clearance, which will be taken as the input data for simulation. Eight equivalent sources ($E=8$) are uniformly placed on the surface of a small sphere of radius $r=0.3a$, which is located at the center of the source.

In order to prevent the aliased result, the number of field points M should be determined appropriately, considering the interested frequency or the wavelength of the radiated sound of concern. Consider a case that the field pressures at 200 points ($M=200$) with SNR=100 (characteristic sensor distance, $L_S=0.34a$) are used to regenerate acoustic pressures at 600 points ($M_2=600$) on the conformal hologram surface, as shown in Fig. 5(b). Note that the acoustical wavelength in the direction of the polar angle on the source surface can be calculated as $\lambda_R=L_a\pi/C_p=6.81a/C_p$ with the average dimension L_a of the source. For $C_p=3.38$, the maximum characteristic distance between field points is less than $L_S=\lambda_R/6=0.34a$. Likewise, the characteristic sensor distances for $M_2=600$ can be determined as $0.21a$. It is found that, by adopting the regularized HELS and ESM, a satisfactory reconstruction could be achieved with an approximately 2% error over the frequency range of $ka=1-5$ for $C_p=5$. In this test example, the proposed scheme would be valid to within 10% error for $C_p<7$.

The normal surface velocity can be recovered by the inverse BEM with an optimal regularization as described in Sec. II C. Figure 6 shows the reconstruction errors of surface

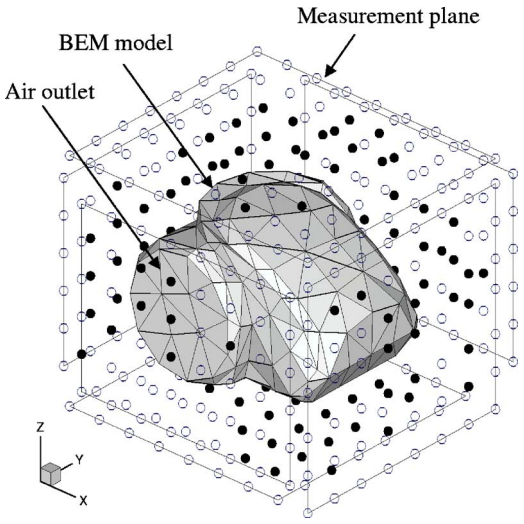

FIG. 8. BEM model of a canister-type vacuum cleaner and the locations of 336 candidate field points on a parallelepiped measurement plane. ●, measurement points selected by the EfI method; ○, field points to be regenerated by ESM.

velocities by the inverse BEM using 600 regenerated field pressures from 200 input data, and using 600 and 200 input data with respect to 600 discrete nodes. Here, the input data represents the simulation pressures, which are calculated by BEM using the given boundary condition in Eq. (28) and then contaminated with a random noise of SNR=100. Figure 7 depicts a comparison of the reconstructed surface velocity distributions by the inverse BEM at $ka=5$ and $C_p=5$. It is noted that, when 200 input data is taken as input to the inverse BEM, the restored image is distorted due to an insufficient number of equations, as shown in Fig. 7(d). Although the reconstruction error of surface velocities with regenerated field pressures is higher than that with 600 input data, a reasonably good agreement is observed with an error of $e=10.8\%$, as shown in Fig. 7(b). Therefore, it is thought that a combined method of the inverse BEM with regenerated field pressures using relatively fewer measurements can enhance the efficiency of reconstruction.

IV. APPLICATION TO AN IRREGULAR SOURCE

As an irregular-shaped, three-dimensional application example, a canister-type vacuum cleaner with the dimension of $303.3(\mathrm{L})\times 254.1(\mathrm{W})\times 206.8(\mathrm{H})$ mm was chosen. The vacuum cleaner was modeled by 170 nodes and 336 linear triangular boundary elements, as depicted in Fig. 8. The maximum characteristic length of this BEM model was $L_C=78.8$ mm, which limits the applicable high frequency to 725 Hz, considering the $\lambda/6$ criterion for linear elements. Uniformly distributed (50 mm spacing) 336 points were chosen as initial measurement positions. The parallelepiped hologram plane was separated from each nearest side of the vacuum cleaner by 60 mm, as shown in Fig. 8. Target frequencies were 120 and 240 Hz which were around the harmonic frequencies of the rotor installed inside the vacuum cleaner. All experimental works were performed in a full anechoic chamber.

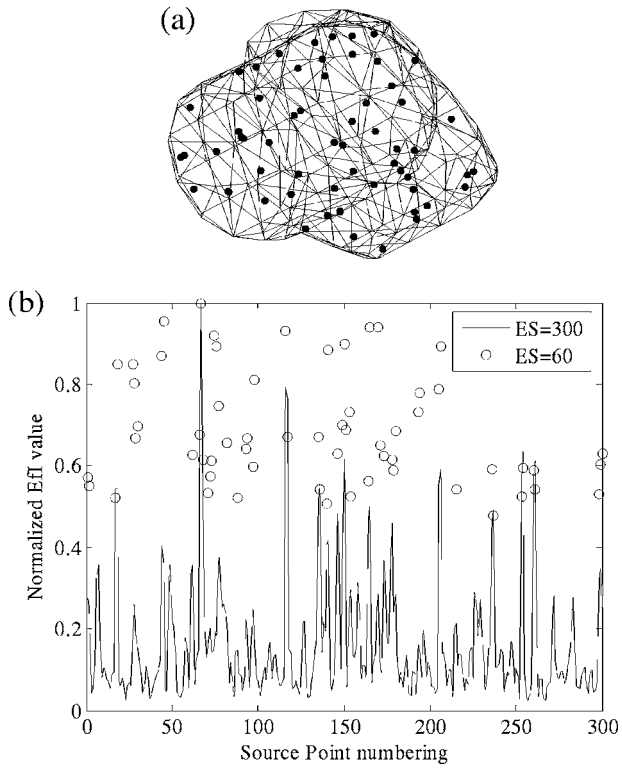

FIG. 9. (a) Equivalent sources determined by applying the EfI method ($E=60$); (b) EfI values of equivalent sources with respect to 100 measurement points during the EfI discarding process.

For the application of the inverse BEM to reconstructing the source field, more field measurements should be taken than the number of discrete surface nodes. In this paper, however, relatively fewer measurements were considered to extend the measured sound field by using the regularized ESM. To this end, the measured pressures at $M=100$ points were selected by the EfI method. They were taken as the input data to determine the regularized coefficients in Eq. (12) and then regenerate the acoustic pressures at all candidate measurement locations.

Locations of equivalent sources were also determined by the EfI technique. Initially, there were 300 candidate-equivalent sources randomly distributed inside the source. Thereafter, the EfI value of each equivalent source was calculated with the spherical function matrix $\mathbf{\Phi}$ in Eq. (23). The locations of 60 equivalent sources are finally chosen by the EfI method, as shown in Fig. 9(a). Figure 9(b) shows the EfI values of equivalent sources with respect to 100 measurement points. From this figure, 60 source positions having large EfI values were survived during the EfI discarding process. One can find that they are close to the source surface since the EfI values tend to be inversely proportional to the minimum distance between each equivalent source and measurement point.

It is noted that the number of expansion terms J of each equivalent source is limited by the number of measurements M, thus the maximum order of spherical wave functions decreases with the number of equivalent sources E. When 60 equivalent sources were used, simple sources such as monopoles and dipoles were only involved in the reconstruction process due to this rather small number J while high-order

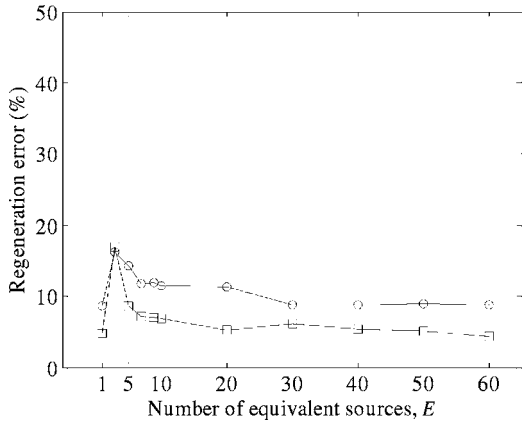

FIG. 10. Regeneration errors of field pressures on the parallelepiped hologram plane with increasing the number of equivalent sources: □, 120 Hz; ○, 240 Hz.

spherical waves could be involved in the HELS method. Note that the number of expansion terms and equivalent sources are very much related with the shapes of the measurement plane and the source surface as well as, of course, the distribution of the source strength, phase, and the frequency.

The field pressure at the measurement plane could be calculated from the final set of equivalent sources. Figure 10 shows the regeneration errors of field pressures on the measurement plane with increasing the number of equivalent sources at 120 and 240 Hz. As a result, one can say that reconstruction results are satisfactory and the error converges to a certain value when the adopted number of equivalent sources is more than about $E=10$ in this case.

Figure 11 illustrates the acoustic pressure distributions at the measurement plane in the right side of the vacuum cleaner by using HELS and ESM with $E=60$, which are compared with the actual measured pressures. A reasonably good agreement could be observed between measured and regenerated field data. Existence of an air outlet, directly

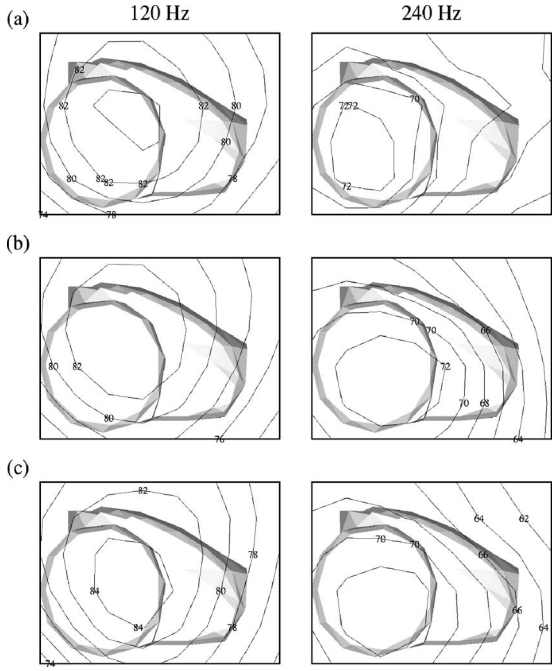

FIG. 11. A comparison of the measured and regenerated field pressure level in dB scale at the measurement plane on the right side of the vacuum cleaner at 120 Hz (left column) and 240 Hz (right column). (a) Measured, (b) HELS, (c) ESM with $E=60$.

radiating the noise, explains why the field pressure in the right side of the vacuum cleaner is largest of all the hologram data.

Combining the inverse BEM with the field data regenerated by the optimized ESM, the source or field parameters can be reconstructed more efficiently. Figure 12 illustrates the reconstructed normal surface velocities on the vacuum cleaner by the inverse BEM using 337 measured pressures and 337 regenerated pressures. As a result, a good agreement between two results could be obtained at both target frequencies. Once the surface acoustic parameters are identified, one

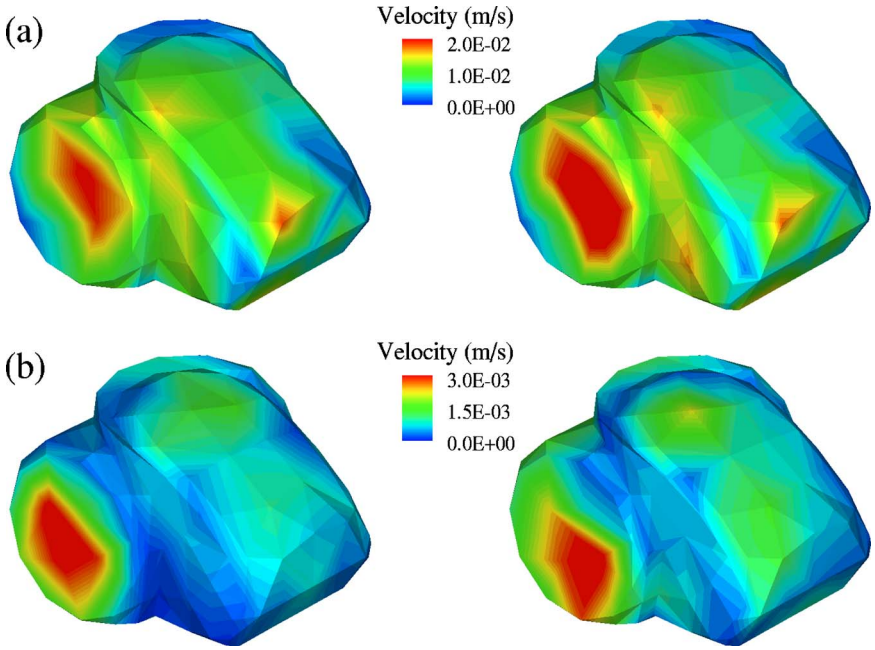

FIG. 12. (Color online) Reconstructed normal surface velocities on the vacuum cleaner by the inverse BEM using 336 measured pressures (left column) and 336 regenerated pressures ($E=60$) with 100 measured data (right column): (a) 120 Hz, (b) 240 Hz.

can predict the arbitrary sound field by using the forward BEM calculation. For example, the field pressures on the elliptical sphere, of which the size is two times bigger than the noise source, could be accurately predicted and the maximum difference between the peak pressures in amplitude was 0.12 dB at 120 Hz and 0.29 dB at 240 Hz.

V. CONCLUDING REMARKS

The generalized ESM with multipoint equivalent sources was employed to reconstruct the sound field in a holographic way. This method can supplement the NAH using the inverse BEM that requires a lot of computational and measurement effort. This study was inspired by the HELS method that employs the series expansion of spherical wave functions and approximates the wave field radiated from a single point source inside the real source. The optimal amount of expansion was obtained by adopting the spatial filtering of coefficients and wave vectors based on the regularization technique with the GCV function, thus a solution could be obtained without *a priori* knowledge of field constraints.

Once the regularized coefficients for the optimally truncated spherical functions are determined, the sound field can be regenerated as many as necessary on or outside the measurement plane. When the generalized ESM using the sufficiently meaningful number of simple sources is employed, it is shown that a robust result can be achieved. The positions of equivalent sources that ensure the linear independence to the measurement plane can be determined by the EfI method. After regeneration of the sound field, usually on the measurement plane, using the ESM with regularization, the source and field parameters can be effectively reconstructed from measured field data and additionally regenerated field data. Such a procedure allows a small number of field measurements in implementing the conventional inverse BEM, thus reducing the measurement effort substantially.

ACKNOWLEDGMENTS

This work was partially supported by the BK21 Project and the NRL.

[1]E. G. Williams and J. D. Maynard, "Holographic imaging without the wavelength resolution limit," Phys. Rev. Lett. **45**, 554–557 (1980).
[2]J. D. Maynard, E. G. Williams, and Y. Lee, "Near field acoustic holography: I. theory of generalized holography and the development of NAH," J. Acoust. Soc. Am. **78**, 1395–1413 (1985).
[3]M. R. Bai, "Application of BEM-based acoustic holography to radiation analysis of sound sources with arbitrarily shaped geometries," J. Acoust. Soc. Am. **92**, 533–549 (1992).
[4]B.-K. Kim and J.-G. Ih, "On the reconstruction of the vibro-acoustic field over the surface enclosing an interior space using the boundary element method," J. Acoust. Soc. Am. **100**, 3003–3016 (1996).
[5]Z. Zhang, N. Vlahopoulos, S. T. Raveendra, T. Allen, and K. Y. Zhang, "A computational acoustic field reconstruction process based on an indirect boundary element formulation," J. Acoust. Soc. Am. **108**, 2167–2178 (2000).
[6]W. Williams, N. G. Parke, D. A. Moran, and C. H. Sherman, "Acoustic radiation from a finite cylinder," J. Acoust. Soc. Am. **36**, 2316–2322 (1964).
[7]Y.-C. Chao, "An implicit least-square method for the inverse problem of acoustic radiation," J. Acoust. Soc. Am. **81**, 1288–1292 (1987).
[8]Z. Wang and S. F. Wu, "Helmholtz equation-least-squares method for reconstructing the acoustic pressure field," J. Acoust. Soc. Am. **102**, 2020–2032 (1997).
[9]G. H. Koopmann, L. Song, and J. B. Fahnline, "A method for computing acoustic fields based on the principle of wave superposition," J. Acoust. Soc. Am. **86**, 2433–2438 (1989).
[10]L. Song, G. H. Koopmann, and J. B. Fahnline, "Numerical errors associated with the method of superposition for computing acoustic fields," J. Acoust. Soc. Am. **89**, 2625–2633 (1991).
[11]J. B. Fahnline and G. H. Koopmann, "A numerical solution for the general radiation problem based on the combined methods of superposition and singular-value decomposition," J. Acoust. Soc. Am. **90**, 2808–2819 (1991).
[12]M. Ochmann, "The source simulation technique for acoustic radiation problems," Acustica **81**, 512–527 (1995).
[13]M. Ochmann, "The full-field equations for acoustic radiation and scattering," J. Acoust. Soc. Am. **105**, 2574–2584 (1999).
[14]M. E. Johnson, S. J. Elliott, K.-H. Baek, and J. Garcia-Bonito, "An equivalent source technique for calculating the sound field inside an enclosure containing scattering objects," J. Acoust. Soc. Am. **104**, 1221–1231 (1998).
[15]F. Holste, "An equivalent source method for calculation of the sound radiated from aircraft engines," J. Sound Vib. **203**, 667–695 (1997).
[16]L. Bouchet, T. Loyau, N. Hamzaoui, and C. Boisson, "Calculation of acoustic radiation using equivalent-sphere," J. Acoust. Soc. Am. **107**, 2387–2397 (2000).
[17]S. F. Wu, "On reconstruction of acoustic pressure fields using the Helmholtz equation least-squares method," J. Acoust. Soc. Am. **107**, 2511–2522 (2000).
[18]S. F. Wu and X. Zhao, "Combined Helmholtz equation least-squares method for reconstructing acoustic radiation from arbitrary shaped objects," J. Acoust. Soc. Am. **112**, 179–188 (2002).
[19]S. F. Wu, "Hybrid near-field acoustic holography," J. Acoust. Soc. Am. **115**, 207–217 (2004).
[20]K. H. Baek and S. J. Elliott, "Natural algorithms for choosing source locations in active control systems," J. Sound Vib. **186**, 245–267 (1995).
[21]Y. Gounot and R. E. Musafir, "Optimization of source positioning and strength in equivalent sources method using genetic algorithms," *Proceedings of Inter-Noise 2004*, Prague, 2004.
[22]D. C. Kammer, "Sensor placement for on-orbit modal identification and correlation of large space structures," J. Guid. Control Dyn. **14**, 251–259 (1991).
[23]P. C. Hansen, *Rank-Deficient and Discrete Ill-Posed Problems* (SIAM, Philadelphia, 1998).
[24]B.-K. Kim and J.-G. Ih, "Design of an optimal wave-vector filter for enhancing the resolution of reconstructed source field by NAH," J. Acoust. Soc. Am. **107**, 3289–3297 (2000).
[25]E. G. Williams, "Regularization methods for near-field acoustical holography," J. Acoust. Soc. Am. **110**, 1976–1988 (2001).
[26]E. G. Williams, *Fourier Acoustics: Sound Radiation and Nearfield Acoustical Holography* (Academic, London, 1999), Chap. 6, pp. 183–197.
[27]P. M. Morse and K. U. Ingard, *Theoretical Acoustics* (McGraw-Hill, New York, 1968), Chap. 7, pp. 332–356.

Measurements of the frame acoustic properties of porous and granular materials

Junhong Park[a)]
School of Mechanical Engineering, Hanyang University, 17 Haengdang-dong, Seongdong-gu, Seoul, 133-791, Korea

(Received 16 October 2004; revised 4 October 2005; accepted 4 October 2005)

For porous and granular materials, the dynamic characteristics of the solid component (frame) are important design factors that significantly affect the material's acoustic properties. The primary goal of this study was to present an experimental method for measuring the vibration characteristics of this frame. The experimental setup was designed to induce controlled vibration of the solid component while minimizing the influence from coupling between vibrations of the fluid and the solid component. The Biot theory was used to verify this assumption, taking the two dilatational wave propagations and interactions into account. The experimental method was applied to measure the dynamic properties of glass spheres, lightweight microspheres, acoustic foams, and fiberglass. A continuous variation of the frame vibration characteristics with frequency similar to that of typical viscoelastic materials was measured. The vibration amplitude had minimal effects on the dynamic characteristics of the porous material compared to those of the granular material. For the granular material, materials comprised of larger particles and those under larger vibration amplitudes exhibited lower frame wave speeds and larger decay rates. © *2005 Acoustical Society of America.*
[DOI: 10.1121/1.2130929]

PACS number(s): 43.20.Ye, 43.20.Jr, 43.58.Dj [RAS] Pages: 3483–3490

I. INTRODUCTION

As advanced structural elements such as honeycomb panels are used increasingly in vehicles, the total masses of those structures continue to decrease, especially in aerospace applications.[1] The decrease in airframe mass can result in increased cabin noise. To maintain interior noise levels, either the existing treatment must be supplemented, which adds mass, or a more efficient treatment must be developed. Structural vibration damping contributes to the minimization of these noise-related problems. Porous and granular materials have been widely used for vibration damping and noise-control applications. A unique characteristic of these materials is that the two separate dilatational waves propagate through the fluid and the solid component (frame).[2] In this paper, these are referred to as airborne and frame waves, respectively.[3]

To investigate and measure the acoustic properties of porous materials, it is often assumed that the frame of the porous materials is either rigid or limp. In the case of airborne wave propagation only, the acoustic properties are measured using several different methods.[4] Measurement of the vibration characteristics of the frame waves under time-varying external loads,[5,6] has received less attention than the airborne waves. However, these properties are important factors that affect the acoustic properties when the elasticity of the frame of the material is large as in the case of polyurethane acoustic foams.[3] Additionally, vibration characteristics of the frames of fibrous and granular materials significantly affect the materials' dynamic characteristics.[7,8]

There have been several different approaches to measuring the frame vibration.[5,6,9–12] Stoll[9] measured the vibration characteristics of sediments by analyzing the shear wave propagation in the torsional vibration of samples. The effects of fluid in torsional vibration are minimal since the shear stiffness of the fluid is negligible. To induce torsional vibration of a granular material, samples should be held in some type of container. Consequently, this method is applicable only when the effects of these containers on the material's dynamic properties are small. Liu and Nagel[10] measured the wave speed in glass spheres under longitudinal vibration. The vibration response was measured by attaching an accelerometer directly to a glass sphere, thus minimizing the effects of the airborne wave propagation. Using the measured results, the frame wave speed was calculated through two different methods—from the time delay between the generation of a pulse and its arrival at the detector, and from the phase difference between the two vibration measurements. These methods required assumptions of the longitudinal wave propagation and no reflection from the boundaries, which could be difficult to achieve in some cases. In addition, the methods may not be applicable when the size of each particle is small. Okudaira *et al.*[11] performed sound absorption measurements for various polymeric granular materials. The wave speed was estimated from the lowest frequency of the peaks of the absorption coefficients and was found to range from 28 to 40 m/s. However, the wave speed was obtained at only one frequency per measurement. A similar problem applies to the method suggested by Kuhl and Kaiser[12] in which the mechanical impedance of the tube containing the granular material was measured, and the wave

[a)]Electronic mail: parkj@hanyang.ac.kr

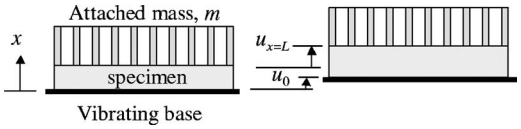

FIG. 1. Longitudinal vibration of the specimen.

speed was estimated by assuming that the height of the granular layer was equal to a quarter wavelength at the lowest observed natural frequency.

In this study, an experimental method was proposed to measure the dynamic characteristics of the frame of porous and granular materials. Under controlled longitudinal vibration of the granular material, the transfer function between the excitation and the response of the specimen was measured. The experimental setup was designed so that the effects of the interaction between the two dilatational waves due to the tortuosity and inertia coupling had negligible impacts on the measurements. The wave propagation characteristics (wave speeds and loss factors) were obtained from the measured transfer function. The proposed method was also applied to measuring the frame wave propagation characteristics of porous materials, specifically acoustic foams and fiberglass. The measured characteristics were compared to those of the typical viscoelastic materials. The impact of several parameters, such as vibration amplitude and particle size, on the measured dynamic properties was investigated. The measured properties can be used to study sound transmission characteristics and to understand the damping mechanisms of materials applied as damping treatments.[13,14]

II. VIBRATION CHARACTERISTICS OF THE FRAME OF POROUS AND GRANULAR MATERIALS

A. Measurement setup

For small amplitude harmonic vibration, complex elastic moduli are used to take account of the dissipation of vibration energy within materials. For uniaxial vibrations, the Young's modulus of the bulk solid phase in vacuum is defined as

$$\hat{E}(\omega) = E(\omega)[1 + i\eta_E(\omega)], \tag{1}$$

where E is the dynamic modulus, $i=\sqrt{-1}$, and η_E is the loss factor of the complex modulus. In order to measure these dynamic properties using the transfer function method, controlled excitation and precisely known boundary conditions are required. The dynamic properties of polymers are often measured using rodlike specimens excited to longitudinal vibrations.[15–17] However, it is difficult to induce a controlled vibration of a granular material formed into a rod because the material will collapse. If a container such as a tube is used to hold the specimen in the shape of the rod, the friction between the granular material and the container significantly affects material's vibration characteristics.[12] To minimize these friction-related problems, the longitudinal vibration of the material specimen was induced, as shown in Fig. 1.

The lateral dimensions of the specimen in the y and z directions are larger than the thickness of the specimen, L.

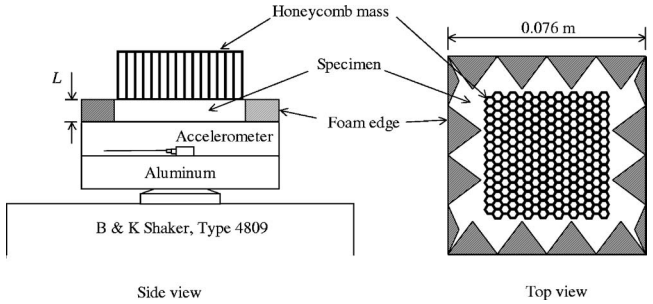

FIG. 2. Experimental setup to measure frame dynamic properties of granular materials.

This arrangement has several advantages. The effect of interaction between the frame and airborne wave propagations on the dynamic response due to tortuosity and inertial coupling is less for a sample of smaller thickness, which can be confirmed through Biot's theory, as shown in the following section. The strains in the y and z directions are negligibly small. Under these conditions, the vibration analysis of the granular media is reduced to one dimension.

In Fig. 1, the longitudinal vibration response of the specimen was measured at the attached mass. This attached mass prevented the shear or bending vibration of the specimen, so that the specimen vibrated longitudinally. To minimize the effects of structural deformation, the mass should be as rigid as possible in the frequency range of interest. However, the mass should also be as small as possible to minimize the initial static compression of the specimen due to the mass loading of the attached mass, especially when specimens of small elasticity are tested, as in lightweight microspheres and fiberglass. Additionally, airborne waves should be able to propagate freely through the attached mass so that the mass responds only to the frame vibration.

A schematic of the experimental setup used for the test is shown in Fig. 2. Nomex honeycomb was used as the attached mass. The cross-sectional dimensions, thickness, and mass of the honeycomb were 5.1×5.1 cm^2, 1.9 cm, and 3.6 g, respectively. The honeycomb cell cavity in the x direction provided free propagation of the acoustic wave. The first natural frequency of the honeycomb mass under free-free boundary conditions was 880 Hz. This suggests that its dynamic characteristics were similar to those of a rigid mass within the frequency range of interest. To prevent standing waves in the y and z directions, the edges of the granular specimens were terminated by corrugated acoustic foam. This acoustic foam border was required to hold the granular material in place.

B. Wave propagations in granular and porous media

In the wave propagation analysis of granular media, the particles are often assumed to be limp, i.e., the frame wave speeds are close to zero. In such cases, the airborne wave speed ranges from 100 to 300 m/s depending on the mechanical properties of the particles. In particular, the airborne wave speed increases with particle diameter. For complete analyses of the acoustic properties, the theoretical model presented by Biot[2] has been widely used. For one-dimensional

longitudinal wave propagation assuming harmonic motion, i.e., $u(x,t)=\mathrm{Re}\{\hat{u}(x)e^{i\omega t}\}$, the wave equation is

$$\hat{P}\frac{\partial^2\hat{u}}{\partial x^2}+\hat{Q}\frac{\partial^2\hat{U}}{\partial x^2}=-\omega^2[\hat{\rho}_{11}\hat{u}+\hat{\rho}_{12}\hat{U}], \tag{2}$$

$$\hat{R}\frac{\partial^2\hat{U}}{\partial x^2}+\hat{Q}\frac{\partial^2\hat{u}}{\partial x^2}=-\omega^2[\hat{\rho}_{12}\hat{u}+\hat{\rho}_{22}\hat{U}], \tag{3}$$

where $\hat{u}$ and $\hat{U}$ are the solid and fluid displacements, respectively, and $\hat{P}=\hat{E}(1-\nu)/(1+\nu)(1-2\nu)$ is the longitudinal stiffness. $\hat{Q}$ and $\hat{R}$ are the coupling factor and the elastic constant assumed here as $(1-h)\hat{E}_2$ and $h\hat{E}_2$, respectively, where $\hat{E}_2$ is the bulk modulus of elasticity of the fluid in the pores given by

$$\hat{E}_2=\rho_0c_0^2\{1+[2(\gamma-1)/N_{\mathrm{pr}}^{1/2}\lambda_c\sqrt{-i}]T_c(N_{\mathrm{pr}}^{1/2}\lambda_c\sqrt{-i})\},$$

γ is the ratio of specific heats, N_{pr} is the Prandtl number, $\lambda_c^2=8\omega\rho_0\varepsilon/h\sigma$, ε is the geometric structural factor, σ is the flow resistivity, h is the porosity, $T_c(\xi)=J_1(\xi)/J_0(\xi)$, and J_0 and J_1 are the Bessel functions of zeroth and first order, respectively.[3,18,19] The mass coefficients are given by $\hat{\rho}_{11}=\rho_1+\rho_2(\varepsilon\hat{\rho}_c/\rho_0-1)$, $\hat{\rho}_{22}=\rho_2\varepsilon\hat{\rho}_c/\rho_0$, and $\hat{\rho}_{12}=-\rho_2(\varepsilon\hat{\rho}_c/\rho_0-1)$, where ρ_1 and ρ_2 are the bulk densities of the fluid and the solid component, respectively, and $\hat{\rho}_c=\rho_0[1-(2/\lambda_c\sqrt{-i})T_c(\lambda_c\sqrt{-i})]$.[3]

The solution of the above wave equation is assumed as

$$\hat{u}(x)/u_0=C_1e^{-ik_1x}+C_2e^{ik_1(x-L)}+C_3e^{-ik_2x}+C_4e^{ik_2(x-L)}, \tag{4}$$

$$\hat{U}(x)=[(\hat{Q}\hat{\rho}_{12}-\hat{R}\hat{\rho}_{11})\omega^2\hat{u}+(\hat{Q}^2-\hat{R}\hat{P})\partial^2\hat{u}/\partial x^2]/(\omega^2\hat{\rho}_{12}\hat{R}-\omega^2\hat{\rho}_{22}\hat{Q}), \tag{5}$$

where k_1 and k_2 are the wave numbers obtained by solving the below quadratic equation in k^2:[3,18]

$$(\hat{P}\hat{R}-\hat{Q}^2)k^4-\omega^2(\hat{\rho}_{11}\hat{R}-2\hat{\rho}_{12}\hat{Q}+\hat{\rho}_{22}\hat{P})k^2+\omega^4(\hat{\rho}_{11}\hat{\rho}_{22}-\hat{\rho}_{12}^2)=0. \tag{6}$$

Subsequently, the four unknowns, C_1-C_4, were obtained by applying the boundary conditions. Four boundary conditions are imposed at $x=0$ and L as

$$\hat{u}_{x=0}=u_0, \tag{7}$$

$$\hat{U}_{x=0}=u_0, \tag{8}$$

$$\left(\hat{P}\frac{\partial\hat{u}}{\partial x}+\hat{Q}\frac{\partial\hat{U}}{\partial x}\right)_{x=L}=\omega^2\hat{u}_{x=L}m/A, \tag{9}$$

$$\left(\hat{R}\frac{\partial\hat{U}}{\partial x}+\hat{Q}\frac{\partial\hat{u}}{\partial x}\right)_{x=L}=0, \tag{10}$$

where m is the mass and A is the cross-sectional area of the attached mass block. After neglecting the effects of the surrounding air, the pressure release boundary condition was used to simplify the problem. In the transfer function methods, the measured values for $\hat{u}$ and $\hat{U}$ may be used in Eqs. (4) and (5) to obtain k_1 and k_2, from which the dynamic characteristics of the frame can be found. However, this requires measurement of the two transfer functions $\hat{u}_{x=L}/u_0$ and $\hat{U}_{x=L}/u_0$. Measuring the particle velocity to obtain $\hat{U}_{x=L}/u_0$ may require a complicated experimental setup. Measuring the inertia coupling and the tortuosity also requires separate measurement procedures. To avoid these complexities, the coupling between vibrations of the fluid and the solid component was neglected, and the transfer function methods were applied.

When the coupling between vibrations of solids and fluids is minimal, the equation of motion for the one-dimensional vibration of the solid component is simplified to

$$\frac{\partial^2\hat{u}}{\partial x^2}+\hat{k}^2\hat{u}=0, \tag{11}$$

where $\hat{k}^2=\rho_1\omega^2/\hat{P}$ is the complex wave number. The measurement procedures based on this longitudinal vibration of the specimen are well established.[15–17] In the transfer function method, a standing wave is analyzed to estimate the wave number from the measured transfer functions. From the measured wave number in the solid, the complex stiffness and the wave speed were obtained:

$$\hat{P}=\rho_1\omega^2/\hat{k}^2, \tag{12}$$

$$\hat{c}=\omega/\hat{k}. \tag{13}$$

For longitudinal vibration shown in Fig. 1, the measured transfer function between the input and output displacements is related to the wave number as

$$\hat{u}_{x=L}/u_0=(\cos\hat{k}L-(m/m_s)\hat{k}L\sin\hat{k}L)^{-1}, \tag{14}$$

where $m_s=\rho_1AL$ is the mass of the specimen.

After substituting $\hat{u}_{x=L}/u_0$ in Eq. (14) with the measured transfer function and separating the real and imaginary parts, two equations are obtained. The Newton-Rapson method is used to obtain the complex wave number $\hat{k}=k_r+ik_i$ from these two equations. There are an infinite number of solutions that satisfy Eq. (14). Among the possible solutions, only one is physically acceptable. This solution and Eq. (12) yield positive real and imaginary parts for the complex modulus, $\hat{P}$.

The application of the transfer function method requires minimal interaction between oscillations of the fluid and the solid component. The validity of this assumption was investigated by comparing the predicted responses of the specimen by two different methods—the Biot theory, Eq. (4), and the uncoupled longitudinal vibration analysis, Eq. (14). The effects of tortuosity and inertial coupling should be negligible when the thickness of the sample approaches zero. Figure 3 shows the predicted transfer functions of the acoustic foam. To predict the transfer functions, the material parameters were assumed to be $E=0.25$ MPa, $\eta_E=0.2$, $\nu=0.3$, $\rho_1=30$ kg/m^3, $\varepsilon=7.8$, and $\sigma=25000$ MKS Rayls/m. The mass per unit area of the attached mass, m/A, was 1.55 kg/m^2. The calculation was performed for different foam thicknesses: 8, 32, and 64 mm. In Fig. 3, the two predictions were

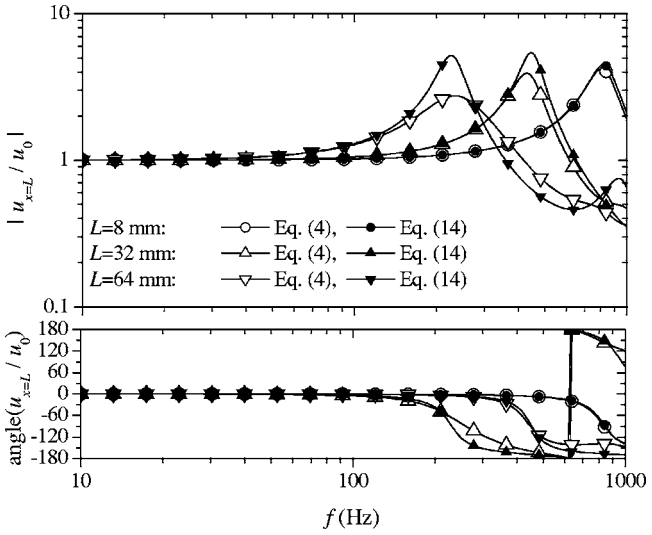

FIG. 3. Predicted transfer functions using two different methods—the Biot theory, calculated using Eq. (4), and the uncoupled longitudinal vibration analysis, calculated using Eq. (14).

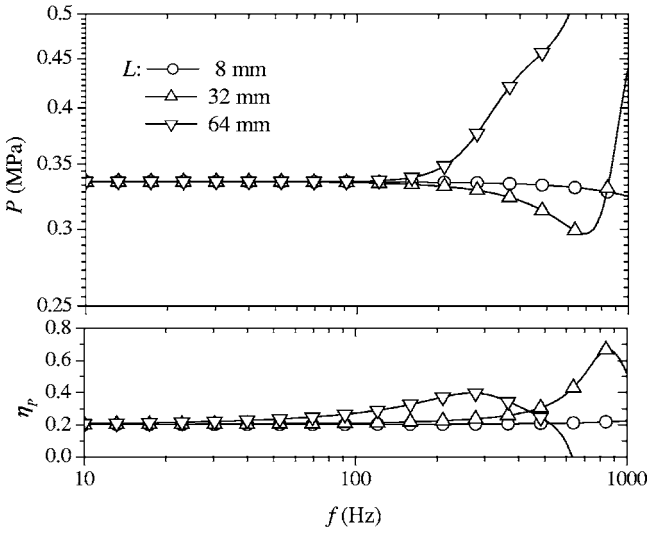

FIG. 4. Dynamic characteristics of the acoustic foam obtained by the transfer function methods. The dynamic response predicted by the Biot theory was assumed as the measured transfer function.

very similar when the thickness was 8 mm. As the thickness increased, the interaction increased and, consequently, there were considerable discrepancies between the two predicted responses. This suggests that the interaction between the two dilatational waves decreased with the decreasing specimen thickness. Obviously, the fluid and the solid component are completely uncoupled when the thickness is close to zero.

To further analyze the effects of interactions on the measurements of the frame dynamic properties, the transfer function method was applied to the predicted response of the Biot theory, and the obtained dynamic properties are shown in Fig. 4. Samples with a small thickness ($L=8$ mm) resulted in the dynamic properties assumed in the simulation. As the thickness increased, the obtained dynamic moduli deviated from the given value since the coupling of the fluid and the solid component which was not taken into account in the transfer function method increased and affected the transfer function, $\hat{u}_{x=L}/u_0$.

These results show that the specimen thickness should be as small as possible to measure the dynamic properties of the solid components of porous and granular materials using the transfer function method. However, too small thickness may increase the sensitivity, resulting in physically unacceptable values even if small experimental errors are included in the measurements.[14,16] A suitable compromise is required based on the material being tested.

III. RESULTS AND DISCUSSION

A. Measurements of transfer functions

In the experimental setup shown in Fig. 2, an electronic shaker (Brüel & Kjær type 4809) was used to induce the longitudinal vibration of the base panel. A random signal in the frequency range of 10 to 2000 Hz was supplied to the shaker. A miniature piezoelectric accelerometer (Endevco model 2250-A) was attached to the center of the base panel to measure the input acceleration level $a_0(=-\omega^2 u_0)$. The magnitude and phase of the acceleration measurements were calibrated with respect to the velocity measurement of a laser Doppler vibrometer that was used to measure the vibration of the attached mass. The transfer function between the two vibration measurements u_0 and $\hat{u}_{x=L}$ was used to obtain the wave propagation characteristics.

A wide range of specimens composed of different raw materials and particle diameters were tested. These specimens included lightweight microspheres made of polyimide (Teek-L and Teek-H), glass spheres, thermoplastic (TPV) pellets, fiberglass, polyurethane acoustic foam, and melamine foam. The densities and particle radii of the samples are given in Table I. The glass spheres and lightweight microspheres were spherical, but the TPV pellets were shaped more like circular cylinders. Each lightweight microsphere particle has a void in the center and the density

TABLE I. Diameter and density of porous and granular materials.

	Mean diameter, D (μm)	Density (kg/m^3)
polyimide (Teek—H)	400, 500, 600, 1200	38, 28, 23, 23
polyimide (Teek—L)	380, 480, 560	49, 34, 26
glass spheres	66, 120, 180, 254, 504, 1500, 2400	1590
TPV pellets	3800	630
acoustic foam	···	37
melamine foam	···	11
fiberglass	···	14

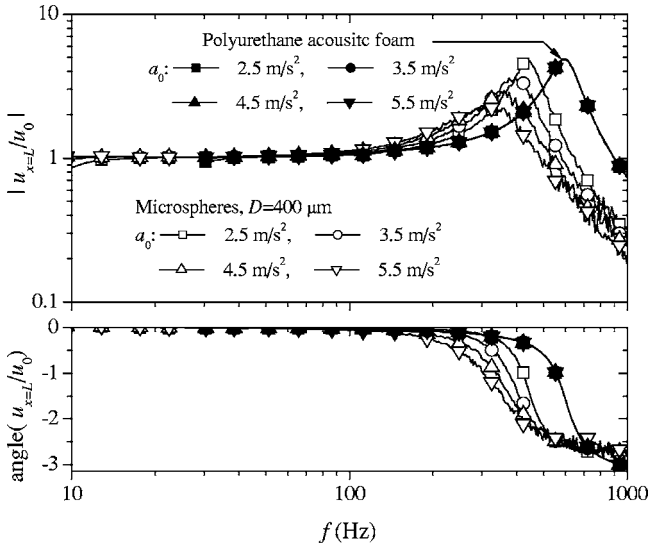

FIG. 5. Measured transfer functions of microspheres (D=400 μm) and polyurethane acoustic foam.

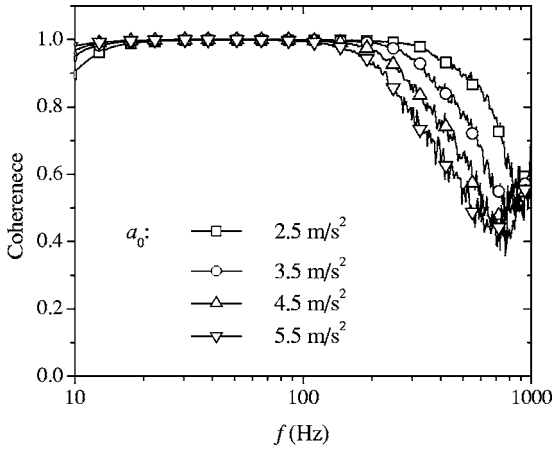

FIG. 6. Variation of coherence with excitation amplitudes for microspheres (D=400 μm).

varied with the particle diameter. Generally, the density decreased with the increasing diameter for the microspheres tested (Table I). For the glass spheres, the variation of the density with the particle diameter was negligible. The thickness of the specimen L when testing the microspheres, the glass spheres, and the TPV pellets was 0.75 cm. When the fiberglass and the acoustic foam were tested, the specimen thicknesses were 0.95 and 1.23 cm, respectively, and double-sided tape and spray epoxy were used on the surface of the base panel and the attached mass.

Figure 5 shows the variation of the measured transfer functions with the input acceleration level for the microspheres (D=400 μm) and the polyurethane acoustic foam. For the acoustic foam, the input and output response was coherent, and there was little variation in the measured transfer functions with the input excitation level. This suggested that the linear longitudinal vibration analysis presented in Sec. II was appropriate for use in the transfer function method when testing the porous materials. For the microspheres, there was considerable variation with excitation level. The natural frequency and peak amplitude decreased considerably with increases in the vibration amplitude. This indicated that the damping inside the granular material increased with the increasing vibration amplitude, as reported by Kuhl and Kaiser.[12] Figure 6 shows the variation of the coherence for the microspheres (D=400 μm). When the phase difference was larger than $\pi/2$, i.e., when the vibrating base and the attached mass vibrated out of phase, a complete disconnect between the particles was expected, especially at large vibration amplitudes. In these cases, the nonlinear response of the granular material induced decay in the coherence, and the application of the linear longitudinal vibration theory in Sec. II led to physically unacceptable values.

B. Frequency-dependent variation of the frame vibration characteristics

The dynamic properties of the granular materials were calculated from the measured transfer functions. Figure 7 shows the frame wave speeds obtained for microspheres of 400-μm diameter where $\hat{c}=c(1+i\eta_c)$. At frequencies close to 10 Hz, the measurements were influenced by experimental errors related to the small phase difference between the two vibration measurements, and physically acceptable solutions were not obtained. Except for those frequencies, a continuous variation of the measured wave speed and its loss factor with frequency was obtained, and no resonant variation was observed. For the microspheres, the measured wave speed was much smaller than the airborne wave speed which ranged from 100 to 200 m/s. The wave speeds and their loss factors increased with the increasing frequency. As expected from the dependence of the measured transfer functions on the excitation level, the wave speeds decreased, and the loss factor increased when the vibration amplitude was increased. Also, the loss factor and increase rate of the wave speed with frequency were greater when obtained with the larger excitation amplitude. However, the obtained loss factor showed large variation at frequencies larger than 400 Hz for a_0

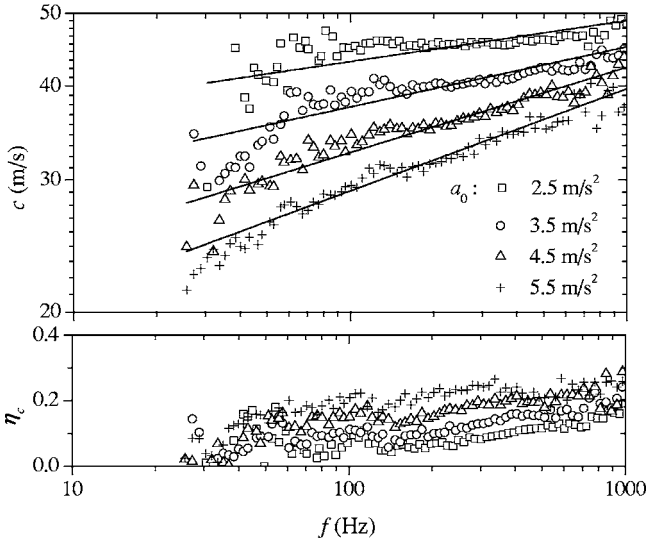

FIG. 7. Effects of excitation amplitudes on the wave speed and its loss factor measured for microspheres (D=400 μm).

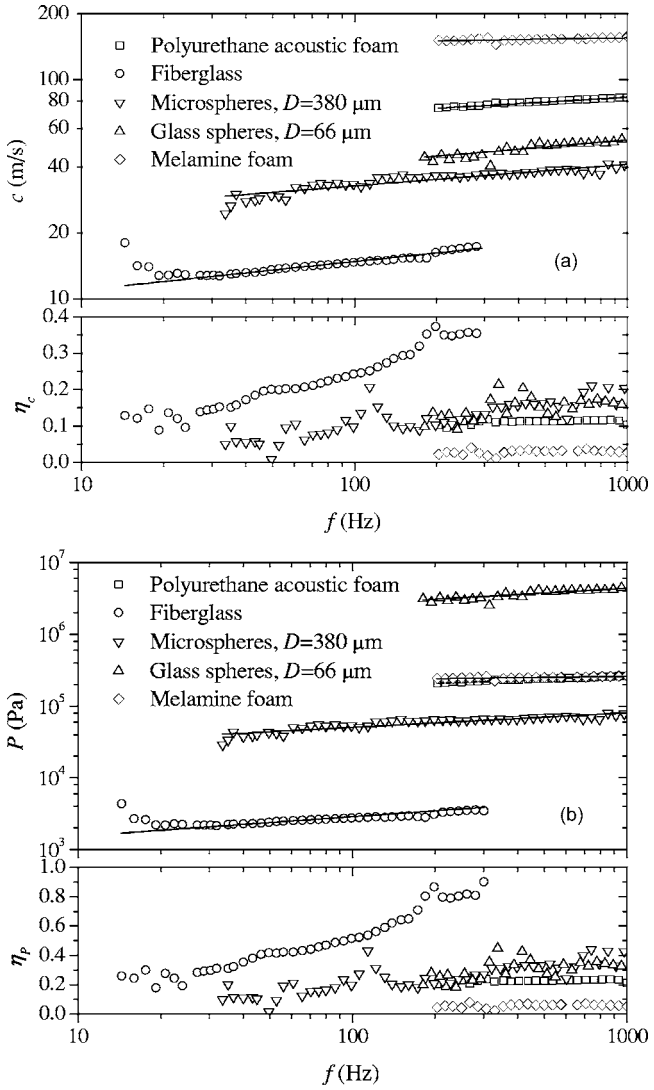

FIG. 8. The dynamic characteristics measured for polyurethane acoustic foam, melamine foam, fiberglass, microspheres, and glass spheres. $a_0 = 3.5\ \mathrm{m/s^2}$. (a) The wave speed and (b) the longitudinal stiffness, together with their loss factors.

$= 5.5\ \mathrm{m/s^2}$. At these frequencies the coherence between the two vibration measurements was less than 0.6 (Fig. 6), which is one indication of the nonlinear response.

The same measurement procedures were repeated for the other specimens. The measured dynamic properties are shown in Fig. 8. Figure 8(a) shows the measured wave propagation characteristics. The wave speeds of the microspheres and the glass spheres were higher than those of the fiberglass and lower than those of the polyurethane acoustic foam and the melamine foam. The loss factor of the fiberglass was much higher than the rest of the specimens for the excitation levels tested. Note that the sensitivity of the results to the measurement error depends on the natural frequency of the measured transfer function.[14,16] Therefore, the measured results were plotted in different frequency ranges where the error was not significant. Figure 8(b) shows the measured variation of the longitudinal stiffness. Although the wave speeds were similar to each other for several different porous and granular materials, a much wider variation in magnitude over four decades was observed for the dynamic stiffness.

The dynamic properties of viscoelastic materials show complex dependence on the frequency.[20,21] For example, the loss factor of the viscoelastic material has its maximum at the glass transition zone where the rate of change of the elastic moduli with frequency is the largest. To predict these behaviors, linear viscoelastic theory has been widely used. These behaviors are observed when measured over wide frequency ranges, typically more than seven to ten decades. At the current and much narrower frequency range of interest, from 10 to 1000 Hz, the frequency-dependent variation of the dynamic stiffness of the loss factor can be simplified as[20]

$$P(\omega) = P_d \omega^{2\eta_P/\pi}, \tag{15}$$

$$c(\omega) = c_d \omega^{2\eta_c/\pi}, \tag{16}$$

where P_d and c_d are constants. This frequency dependence shows that the dynamic stiffness of the material increases monotonically with increasing frequency, as measured in Figs. 7 and 8. The degree of frequency dependence is determined by the loss factor. For a material with a large loss factor, the dynamic stiffness increases more rapidly with frequency than that with a small loss factor.[20] In Eqs. (15) and (16), the assumption of a nonresonant variation of the dynamic properties with frequency is required. Additionally, it was assumed that the loss factor was constant. These interpolations will be more accurate if the interpolation is performed in closely spaced frequency ranges where the loss factor is constant. However, the measured loss factor in this study showed frequency-dependent variation in the frequency range of interest (Figs. 7 and 8). To take account of the frequency-dependent variation of the loss factor, which is the most significant for the fiberglass among the materials tested, more complicated frequency-dependent predictions that hold in entire frequency ranges should be applied. However, the frequency range of interest in this study, although important in noise control, was less than two decades. To increase the frequency ranges, measurements over several temperature ranges must be taken and extrapolation should be performed using the WLF (Williams, Landel, and Ferry) equation.[21] Without conducting measurements at different temperatures, interpolation was performed after assuming that the loss factor was constant.

The measured loss factor increased in the frequency ranges of interest for the materials tested, as shown in Figs. 7 and 8, except for the ranges where a nonlinear response was expected. The average loss factor in the different frequency ranges was used for the loss factor in Eqs. (15) and (16). The frequency-dependent relationships by Eq. (15) and (16) are shown by the straight lines in Figs. 7 and 8. The constants used to obtain the straight lines are summarized in Table II. As the excitation level increased for the granular material, the loss factor also increased. Consequently, the degree of the frequency dependence of the wave speed also increased as shown in Fig. 7. The frequency dependence of the frame wave speed that was predicted by curve-fitted values using Eq. (16) and plotted as straight lines agreed well with the

TABLE II. Constants of Eqs. (15) and (16) plotted as straight lines in Figs. 7 and 8.

	D (μm)	a_0 (m/s^2)	c_d	η_c	P_d	η_P
polyimide (Teek—H)	400	2.5	33.5	0.086	41 900	0.17
		3.5	25.9	0.14	24 500	0.26
		4.5	19.3	0.18	13 000	0.37
		5.5	15.5	0.21	8000	0.45
polyimide (Teek—L)	380	3.5	23.8	0.12	26 800	0.25
glass spheres	66	3.5	39.7	0.10	246 0000	0.21
acoustic foam	⋯	3.5	50.4	0.11	94 800	0.23
melamine foam	⋯	3.5	135.0	0.03	194 000	0.065
fiberglass	⋯	3.5	8.1	0.18	817	0.40

measured values for all specimens. Also, the slope of the frame wave speed curve for porous and granular materials increased with the increasing loss factor. The frequency dependence shown in Eqs. (15) and (16) is a typical characteristic of viscoelastic elastomers.[17,20] This suggests that the dynamic properties of the solid component of the porous and granular materials closely followed those of the viscoelastic materials.

C. Effects of particle diameter of the granular material

Figure 9 shows the dependence of the dynamic properties on the vibration amplitude. The measured dynamic properties were almost constant for the porous materials—polyurethane acoustic foam and fiberglass. In contrast, a considerable change was observed in the dynamic properties of the granular materials—the microspheres and glass spheres. The loss factor of the granular material increased with increasing vibration amplitude. As the vibration amplitude decreased, the loss factor approached that of the raw materials, i.e., glass for the glass spheres and polyimide for the microspheres. As the vibration amplitude increased, the wave speeds continued to decrease and gradually approached zero. This suggests that when an extremely high level of the input acceleration is applied, a complete disconnect between the particles occurs so that the force between the particles is negligible. Consequently, the particles become limp, i.e., the wave speeds are close to zero. The measured wave speeds continued to increase with decreasing vibration amplitude. The maximum measured wave speed should be less than the longitudinal wave speed of the raw material, which, for example, is 5600 m/s for glass.

Figure 10 shows the dependence of the wave speed on the diameter of the granular material. The elastic modulus of the hard TPV pellets was twice that of the soft one. The diameter of the particle had a strong influence on the wave speeds. The wave speeds decreased with increasing particle diameter, unlike the airborne wave speed. The loss factor generally increased with increasing diameter, except for the TPV pellets whose particle shape more closely resembled a circular cylinder than a sphere. The mechanical properties of the solid component also influenced the bulk material's dynamic properties. The frame wave speeds of the particles increased with the dynamic moduli of the raw material. These dependences of the dynamic properties on the mechanical and geometrical properties of the particle can be applied to the design of granular materials for vibration and sound transmission controls.[13,14]

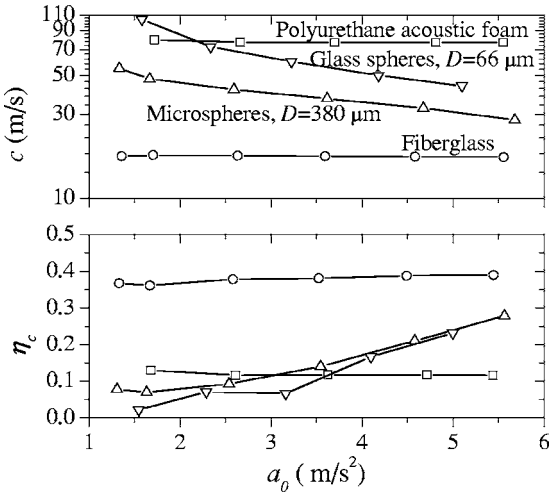

FIG. 9. Dependence of wave speed and its loss factors on the excitation amplitudes at f=700 Hz for glass spheres and f=300 Hz for other specimens.

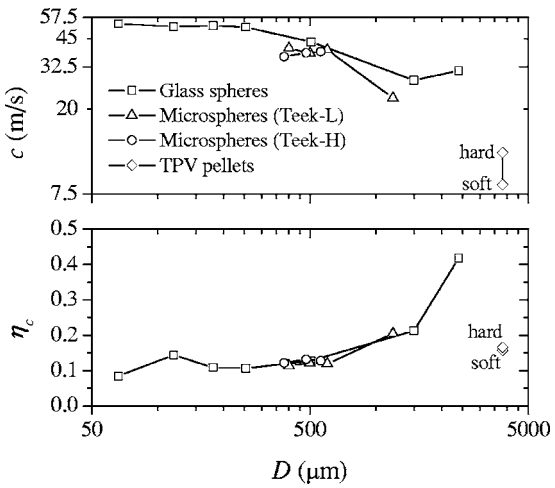

FIG. 10. Effects of particle sizes on the wave speed and its loss factor. a_0 =3.5 m/s^2.

IV. CONCLUSIONS

In this study, an experimental method for measuring the frame vibration characteristics of porous and granular materials was proposed and applied to a wide variety of materials. These materials included fiberglass, acoustic foams, glass spheres, and lightweight microspheres. To measure the frame dynamic characteristics without the effects of the interactions resulting from tortuosity and inertial coupling, the specimen thickness should be as small as possible. The measured dynamic properties followed the characteristics of typical viscoelastic materials: the dynamic moduli increased with frequency and its frequency dependence was influenced by its loss factor. The dependence of the measured properties on the vibration amplitude was not significant for fiberglass and acoustic foams. For granular materials, including glass spheres and lightweight microspheres, the dynamic properties depended on the vibration amplitude, bulk material's dynamic properties, and the particle size. The frictional force between the particles is expected to vary with vibration amplitude and has significant impact on the dynamic properties of the granular material. Consequently, the frame dynamic moduli of the granular material decreased and its loss factor increased with increasing vibration amplitude. The particle size had similar impacts on the dynamic properties as the vibration amplitude. The frame vibration characteristics measured in this study are useful in analyzing the acoustic properties and vibration dissipation capabilities.

ACKNOWLEDGMENTS

The financial support from the NASA Langley Research Center while in residence under a NRC Post-doctoral Research Associateship Award is gratefully acknowledged. The author sincerely appreciates Dr. Richard J. Silcox, Daniel L. Palumbo, and Jacob Klos for many discussions and suggestions.

[1]D. Zenkert, *An Introduction to Sandwich Construction* (Chameleon, London, 1997).
[2]M. A. Biot, "Theory of propagation of elastic waves in a fluid-saturated porous solid. I. Low-frequency range," J. Acoust. Soc. Am. **28**, 168–178 (1956).
[3]J. S. Bolton, N. M. Shiau, and Y. J. Kang, "Sound transmission through multi-panel structures lined with elastic porous materials," J. Sound Vib. **191**, 317–347 (1996).
[4]B. H. Song and J. S. Bolton, "A transfer-matrix approach for estimating the characteristic impedance and wave numbers of limp and rigid porous materials," J. Acoust. Soc. Am. **107**, 1131–1152 (2000).
[5]K. Khirnykh and A. Cummings, "The measurement of frame motion in flexible porous materials," J. Acoust. Soc. Am. **105**, 755–761 (1999).
[6]T. Pritz, "Frequency-dependence of frame dynamic characteristics of mineral and glass wool materials," J. Sound Vib. **106**, 161–169 (1986).
[7]M. D. Dahl, E. J. Rice, and D. E. Groesbeck, "Effects of fiber motion on the acoustic behavior of an anisotropic, flexible fibrous material," J. Acoust. Soc. Am. **87**, 54–66 (1990).
[8]D. L. Johnson and T. J. Plona, "Acoustic slow waves and the consolidation transition," J. Acoust. Soc. Am. **72**, 556–565 (1982).
[9]R. D. Stoll, "Experimental studies of attenuation in sediments," J. Acoust. Soc. Am. **66**, 1152–1160 (1979).
[10]C.-H. Liu and S. R. Nagel, "Sound in sand," Phys. Rev. Lett. **68**, 2301–2304 (1992).
[11]Y. Okudaira, Y. Kurihara, H. Ando, M. Satoh, and K. Miyanami, "Sound absorption measurements for evaluating dynamic physical properties of a powder bed," Powder Technol. **77**, 39–48 (1993).
[12]W. Kuhl and H. Kaiser, "Absorption of structure-borne sound in building materials without and with sand-filled cavities," Acustica **2**, 179–188 (1962).
[13]J. Park and D. L. Palumbo, "Measurements of Acoustic Properties of Porous and Granular Materials and Application to Vibration Control," *Proc. NOISE-CON 2004*, Baltimore, MD, 12–14 July 2004.
[14]J. Park, "Transfer function methods to measure dynamic mechanical properties of complex structures," J. Sound Vib. **288**, 57–79 (2005).
[15]ANSI S2.22-1998, "Resonance method for measuring the dynamic mechanical properties of viscoelastic materials," (American National Standards Institute, published through the Acoustical Society of America, New York, 1998).
[16]T.-K. Ahn and K.-J. Kim, "Sensitivity analysis for estimation of complex modulus of viscoelastic materials by non-resonance method," J. Sound Vib. **176**, 543–561 (1994).
[17]J. Park, T. Siegmund, and L. Mongeau, "Viscoelastic properties of foamed thermoplastic vulcanizates and their dependence on void fraction," Cell. Polym. **22**, 137–156 (2003).
[18]J. F. Allard, A. Aknine, and C. Depollier, "Acoustical properties of partially reticulated foams with high and medium flow resistance," J. Acoust. Soc. Am. **79**, 1734–1740 (1986).
[19]K. Attenborough, "Acoustical characteristics of rigid fibrous absorbents and granular-materials," J. Acoust. Soc. Am. **73**, 785–799 (1983).
[20]T. Pritz, "Frequency dependences of complex moduli and complex Poisson's ratio of real solid materials," J. Sound Vib. **214**, 83–104 (1998).
[21]J. D. Ferry, *Viscoelastic Properties of Polymers* (Wiley, New York, 1980).

Two-dimensional numerical simulation of acoustic wave phase conjugation in magnetostrictive elastic media

Peter Voinovich[a)]
St. Petersburg Branch of Joint Supercomputer Center, Russian Academy of Sciences, Polytekhnicheskaya 26, St. Petersburg 194021, Russia

Alain Merlen[b)]
Joint European Laboratory in Magneto-Acoustics, Laboratoire de Mécanique de Lille, UMR CNRS 8107, Bd Paul Langevin, Cité Scientifique, 59655 Villeneuve d'Ascq Cédex, France

(Received 20 April 2005; revised 13 September 2005; accepted 8 October 2005)

The effect of parametric wave phase conjugation (WPC) in application to ultrasound or acoustic waves in magnetostrictive solids has been addressed numerically by Ben Khelil *et al.* [J. Acoust. Soc. Am. **109**, 75–83 (2001)] using 1-D unsteady formulation. Here the numerical method presented by Voinovich *et al.* [Shock waves **13**(3), 221–230 (2003)] extends the analysis to the 2-D effects. The employed model describes universally elastic solids and liquids. A source term similar to Ben Khelil *et al.*'s accounts for the coupling between deformation and magnetostriction due to external periodic magnetic field. The compatibility between the isotropic constitutive law of the medium and the model of magnetostriction has been considered. Supplementary to the 1-D simulations, the present model involves longitudinal/transversal mode conversion at the sample boundaries and separate magnetic field coupling with dilatation and shear stress. The influence of those factors in a 2-D geometry on the potential output of a magneto-elastic wave phase conjugator is analyzed in this paper. The process under study includes propagation of a wave burst of a given frequency from a point source in a liquid into the active solid, amplification of the waves due to parametric resonance, and formation of time-reversed waves, their radiation into liquid, and focusing. The considered subject is particularly important for ultrasonic applications in acoustic imaging, nondestructive testing, or medical diagnostics and therapy. © *2005 Acoustical Society of America.* [DOI: 10.1121/1.2130964]

PACS number(s): 43.25.Dc, 43.25.Lj [MFH] Pages: 3491–3498

I. INTRODUCTION

This paper presents a logical two-dimensional extension of the previous numerical analysis of wave phase conjugation (WPC) in an active solid[1] performed using a one-dimensional model. The subject is particularly important for ultrasonic applications in acoustic imaging,[2,3] nondestructive testing, or medical diagnostics and therapy.[4] The technology of such active solids is currently under intensive development, particularly on the basis of magnetostrictive properties. The active materials and WPC technique are still in a phase of research prior to potential applications.[5,6]

Among many questions and discrepancies between the theory and experiments that inevitably arise in such a new field of research, one is particularly important: how to isolate each factor to analyze its effect separately from the others. An obvious answer to this question is linked with the development of reliable numerical tools where various parameters can be explored one by one. This is the aim of the work presented here. The paper is focused on the effects of oblique reflections of waves at the boundaries of a two-dimensional sample of magnetostrictive solid. The code has been tested in terms of numerical dispersion and dissipation and the geometrical effects are analyzed in the case of an isotropic elastic magnetostrictive medium under linear magnetic pumping.

II. THE NUMERICAL MODEL

A. Governing equations

Here we use the following governing equations (see, e.g., Ref. 7):

$$\frac{\partial}{\partial t}\int_V \mathbf{Q}\,\mathrm{d}v = \oint_S (\mathbf{F}n_x + \mathbf{G}n_y)\mathrm{d}s + \int_V \mathbf{H}\,\mathrm{d}v, \tag{1}$$

n_x, n_y being Cartesian projections of the outward normal vector $\mathbf{n}$ to the closed surface S bounding volume V, and $\mathbf{Q}$, $\mathbf{F}$, $\mathbf{G}$, $\mathbf{H}$ are given as follows:

$$\mathbf{Q} = \begin{pmatrix} \rho\dot{U}_x \\ \rho\dot{U}_y \\ \sigma_{xx} \\ \sigma_{xy} \\ \sigma_{yy} \end{pmatrix}, \quad \mathbf{F} = \begin{pmatrix} \sigma_{xx} \\ \sigma_{xy} \\ \rho c_1^2 \dot{U}_x \\ \rho c_2^2 \dot{U}_y \\ \rho c_3^2 \dot{U}_x \end{pmatrix},$$

a)Electronic address: vpeter@scc.ioffe.ru
b)Electronic address: alain.merlen@univ-lille1.fr

$$\mathbf{G}=\begin{pmatrix}\sigma_{xy}\\ \sigma_{yy}\\ \rho c_3^2\dot{U}_y\\ \rho c_2^2\dot{U}_x\\ \rho c_1^2\dot{U}_y\end{pmatrix},\quad \mathbf{H}=\begin{pmatrix}0\\ 0\\ H_{xx}\\ H_{yy}\\ H_{xy}\end{pmatrix}, \tag{2}$$

where ρ is the material density, $\dot{U}_x$ and $\dot{U}_y$ are Cartesian projections of the displacement velocity $\dot{\mathbf{U}}$, σ_{xx} and σ_{yy} are compression stresses, and σ_{xy} is shear stress. Constants c_1, c_2, c_3 are expressed through the Lamé coefficients as follows:

$$c_1=\sqrt{\frac{\lambda+2\mu}{\rho}},\quad c_2=\sqrt{\frac{\mu}{\rho}},\quad c_3=\sqrt{\frac{\lambda}{\rho}}. \tag{3}$$

In an elastic solid, c_1 and c_2 correspond to the propagation speeds of longitudinal c_L and transversal c_T waves, respectively.

The first two equations in (1) and (2) represent Cartesian projections of the equation of motion. The last three equations are obtained by differentiating in time and integrating over an arbitrary volume V bounded by surface S the classical stress-strain relations, i.e., the generalized Hooke law for an isotropic elastic material under a small strain. The divergence theorem is applied then to the right-hand side of the equations, converting them into the surface integrals.

The source term $\mathbf{H}$ with nonzero components H_{xx}, H_{yy}, and H_{xy} in the last three equations is introduced to describe coupling between the stress and external magnetic field in a magnetostrictive solid and is specified in Sec. II B below.

The governing equations (1) and (2) represent a set of hyperbolic conservation laws allowing application of well-developed numerical technologies from classical gasdynamics.

The Lamé coefficients in Eqs. (3) are evaluated using the fundamental characteristics of an isotropic elastic body—the bulk (compression) modulus K and Poisson's ratio ν:

$$\lambda=\frac{3\nu K}{(1+\nu)},\quad \mu=\frac{3(1-2\nu)K}{2(1+\nu)}.$$

This makes the governing equations (1) and (2) valid universally for elastic solids and liquids, as unlike the Young modulus E, the bulk modulus K remains finite for liquids. For a liquid we have

$$\nu=1/2,\quad K=\rho_0 c_0^2,\quad E=0,$$

$$\lambda=\rho_0 c_0^2,\quad \mu=0,$$

$$\sigma_{xy}=0,\quad \sigma_{xx}=\sigma_{yy}=-p,$$

with c_0 representing the sound speed in liquid and p the acoustic pressure. The fourth equation of the system (1) and (2) degenerates in this case, and the third and fifth equations become identical.

B. The source term

In the classical formulation of elastic problems, the derivation in time of the Hooke law resulting in the latter three lines of Eqs. (1) and (2) does not provide any source term because the Lamé coefficients are constant. In the problem under study, however, those coefficients are known functions of time, introducing the additional term

$$H_{ij}=\frac{1}{\lambda}\frac{\partial\lambda}{\partial t}(\lambda\epsilon_{kk}\delta_{ij})+\frac{1}{\mu}\frac{\partial\mu}{\partial t}(2\mu\epsilon_{ij}),$$

where ϵ_{ij} is a component of the strain tensor, ϵ_{kk} is the trace of this tensor, and δ_{ij} is the Kronecker symbol. Using the Hooke law again, this expression can be written as a function of the stress tensor itself:

$$H_{ij}=\frac{\lambda}{3\lambda+2\mu}\sigma_{kk}\left[\frac{1}{\lambda}\frac{\partial\lambda}{\partial t}-\frac{1}{\mu}\frac{\partial\mu}{\partial t}\right]\delta_{ij}+\frac{1}{\mu}\frac{\partial\mu}{\partial t}\sigma_{ij}.$$

Applying relations (3), this can be rewritten in terms of the sound speeds:

$$H_{ij}=\frac{c_L^2-2c_T^2}{3c_L^2-4c_T^2}\sigma_{kk}\left[\frac{1}{c_L^2-2c_T^2}\frac{\partial(c_L^2-2c_T^2)}{\partial t}-\frac{1}{c_T^2}\frac{\partial c_T^2}{\partial t}\right]\delta_{ij}+\frac{1}{c_T^2}\frac{\partial c_T^2}{\partial t}\sigma_{ij}.$$

For realistic parameters of magnetostrictive coupling,[1] the effect of a variable magnetic field can be taken into account as a small perturbation of the sound velocities. In order to focus on the boundary effects and not on the complex nonlinear properties of the material, the magnetic pumping is assumed to be linear (i.e., the modulation depths M_L and M_T below are constants), which means that the following modulation is applied to the sound velocities:

$$\begin{aligned}c_L^2&=c_{L0}^2[1+M_L\cos(\omega_B t+\varphi_L)],\\ c_T^2&=c_{T0}^2[(1+M_T\cos(\omega_B t+\varphi_T)\ ].\end{aligned} \tag{4}$$

This leads to an explicit form of the source term:

$$\begin{aligned}H_{xx}(t)&=-M_T\omega_B\sin(\omega_B t+\varphi_T)\sigma_{xx}\\ &\quad+\frac{c_L^2}{2(c_L^2-c_T^2)}(\sigma_{xx}+\sigma_{yy})(M_T-M_L)\omega_B\sin(\omega_B t+\varphi_L),\\ H_{yy}(t)&=-M_T\omega_B\sin(\omega_B t+\varphi_T)\sigma_{yy}\\ &\quad+\frac{c_L^2}{2(c_L^2-c_T^2)}(\sigma_{xx}+\sigma_{yy})(M_T-M_L)\omega_B\sin(\omega_B t+\varphi_L),\\ H_{xy}(t)&=-M_T\omega_B\sin(\omega_B t+\varphi_T)\sigma_{xy}.\end{aligned} \tag{5}$$

The question naturally arises as to why this source, which is a small disturbance, is important for the system dynamics. It turns out that the source term can be neglected except when parametric resonance occurs through WPC. In general, the pumping is just a small disturbance of the incident wave, but if the pumping frequency ω_B equals a doubled frequency from the spectrum of the incident wave, the source

term becomes secular and the amplitude of this particular component of the incident wave starts growing exponentially.[1] As this process occurs without any force applied to the solid, the conservation of momentum infers that a conjugate wave is created, traveling in the opposite direction but with the same phase as the direct wave. This is a way to obtain a time-reversed signal with exponentially growing amplitude. In a multidimensional problem, the phenomenon becomes much more complicated because reflections at the boundaries cause energy exchange between the shear and longitudinal waves and consequent variations in the way the energy is transmitted. This may become crucial for applications involving wave focusing and hence is a subject of the present numerical study.

The coefficients in (2) depending on the sound speeds are also modulated according to expressions (4).

C. Isotropy and modulation depth

The problem (1) and (2) is formulated in terms of stress components and displacement velocities. The displacement field $\mathbf{U}$ is never used explicitly and can be obtained only as a subproduct by integrating the velocity field. One well-known consequence of this formulation is the disconnection between the displacement field and the strain tensor. The latter can be formally deduced from the stress tensor through the Hooke law, but nothing in the problem seems to ensure that this tensor is really the symmetric part of $\nabla\mathbf{U}$. This is only possible if some integrabillity conditions are fulfilled. Often referred to as compatibility equations, these conditions can be expressed by

$$\nabla\nabla\cdot\mathbf{E}+\nabla^t\Delta\cdot\mathbf{E}-\nabla\nabla e-\nabla\mathbf{E}=0, \tag{6}$$

where $\mathbf{E}$ is the strain tensor, $e=tr(\mathbf{E})$, and ∇^t is the transposed nabla operator. Using the Hooke law, Eq. (6) can be expressed in terms of stress by

$$\nabla\nabla\cdot\boldsymbol{\sigma}+\nabla^t\nabla\cdot\boldsymbol{\sigma}-\frac{1}{1+\nu}\nabla s+\frac{1}{1+\nu}\Delta s\mathbf{I}-\Delta\boldsymbol{\sigma}=0, \tag{7}$$

where $\boldsymbol{\sigma}$ is the stress tensor, $s=tr(\boldsymbol{\sigma})$, and $\mathbf{I}$ is the unit tensor. This equation is often refered to as the Beltrami-Michell equation.[8] Introducing parameter $\eta=c_1/c_2$, $\boldsymbol{\sigma}$, s, and ν can be written

$$\boldsymbol{\sigma}=\rho c_2^2[(\eta-2)e\mathbf{I}+2\mathbf{E}],$$

$$s=\rho c_2^2(3\eta-4)e,$$

$$\nu=\frac{\eta-2}{2(\eta-1)},$$

and Eq. (7) becomes

$$\nabla\nabla\cdot\boldsymbol{\sigma}+\nabla^t\nabla\cdot\boldsymbol{\sigma}-\frac{2(\eta-1)}{3\eta-4}\nabla s+\frac{\eta-2}{3\eta-4}\Delta s\mathbf{I}-\Delta\boldsymbol{\sigma}=0. \tag{8}$$

In the present formulation, tensor $\boldsymbol{\sigma}_t=\partial\boldsymbol{\sigma}/\partial t$ plays the most important role: it must satisfy the equation obtained by the time derivation of (8):

$$\nabla\nabla\cdot\boldsymbol{\sigma}_t+\nabla^t\nabla\cdot\boldsymbol{\sigma}_t-\frac{2(\eta-1)}{3\eta-4}\nabla s_t+\frac{\eta-2}{3\eta-4}\Delta s_t\mathbf{I}-\Delta\boldsymbol{\sigma}_t+\frac{2}{(3\eta-4)^2}\eta_t(\nabla\nabla s+\Delta s\mathbf{I})=0, \tag{9}$$

where $\eta_t=\partial\eta/\partial t$. It is easy to verify that, if $\boldsymbol{\sigma}$ fulfills (8), Eq. (9) is fulfilled by

$$\boldsymbol{\sigma}_t=\rho c_2^2[(\eta-2)e_t\mathbf{I}+2\mathbf{E}_t+\eta_t e r\mathbf{I}]+2\frac{c_{2t}}{c_2}\boldsymbol{\sigma}$$

and

$$s_t=\rho c_2^2[(3\eta-4)e_t\mathbf{I}+3\eta_t e]+2\frac{c_{2t}}{c_2}s$$

with c_{2t} the time derivative of c_2. Consequently, if a stress tensor represents a physically realistic solution of problem (1) and (2) at time t, its time derivative must be a solution of (9), but this does not ensure that the incremented stress tensor at time $t+dt$ is a physical solution. For that, $\boldsymbol{\sigma}(t+dt)$ must fulfill (8). Developing $\boldsymbol{\sigma}(t+dt)$ in (8) around t for any dt as

$$\boldsymbol{\sigma}(t+dt)=\boldsymbol{\sigma}(t)+dt\boldsymbol{\sigma}_t+\frac{dt}{2}\boldsymbol{\sigma}_{tt}+\cdots,$$

one would have, for example, for the first term of expansion,

$$\nabla\nabla\cdot\boldsymbol{\sigma}_t+\nabla^t\nabla\cdot\boldsymbol{\sigma}_t-\frac{2(\eta-1)}{3\eta-4}\nabla s_t+\frac{\eta-2}{3\eta-4}\Delta s_t\mathbf{I}-\Delta\boldsymbol{\sigma}_t=0, \tag{10}$$

and the same for all the derivatives in time.

The preceeding results can be summarized as follows: if $\dot{\mathbf{U}}(t)$, $\boldsymbol{\sigma}(t)$ is a physical solution of the elastic problem (1) and (2), which implies that (9) is fulfilled, then $\dot{\mathbf{U}}(t+dt)$, $\boldsymbol{\sigma}(t+dt)$ is also a physical solution if (8) is fulfilled. It is clear that both Eqs. (9) and (10) are only compatible if $\eta_t=0$. From the definition of η and the expressions of the modulation of $c_1=c_L$ and $c_2=c_T$ (4), this leads to $M_L=M_T$.

The above analysis shows, first, that formulation (1) and (2) provides a physical solution of any 2-D elasto-dynamical problem if the initial conditions are physically correct and the medium isotropic at each time step. This is particularly true in the case $M_L=M_T=0$, which represents the standard elasto-dynamic problem of a linearly elastic isotropic and passive medium.

But here the validity of the formulation is extended to active media under the condition that the modulation depths of both sound velocities are the same. This assumption does not mean that magnetostriction must only be an isotropic phenomenon, but that a magnetostrictive medium that respects the Hooke law when no magnetic field is present remains isotropic under excitation only if the modulation depth is the same on both sound velocities. In that case the Hooke law is valid at any time t. On the contrary, if the modulation depths are independent, the medium becomes anisotropic under excitation, but the present formulation cannot account for this situation. Effectively, this independent modulation of the Hooke law does not fit with any constitutive law of physi-

cally possible anisotropic elastic medium. A correct approach would be to rewrite (1) and (2) for a general, anisotropic constituive law assuming that the coefficients coincide with their values in the isotropic Hooke law when the pumping is switched off. This is a promising direction to follow in the future for magnetostrictive simulations and specifically for WPC.

The nonphysical solution patterns induced by violation of the equality $M_L = M_T$ have been observed in our computations using the described model resulting in stationary residual stresses inside the solid after the end of the pumping and evacuation of all the waves. These spurious stresses are divergence-free and compatible with the steady state, however they are not linked to the displacement field by the constitutive law, but are rather an artificial product of the source term which does not respect the compatibility criteria.

D. A split scheme in a rectangular domain

Our numerical approach is based on the scheme described in Ref. 7 for an arbitrary 2-D grid. Here we use an operator-split implementation of that technique.

The governing equations of the previous sections are applied to the control volumes of a regular Cartesian grid with indices i,j and uniform spacings Δx, Δy in each direction. The scheme is written in a split form with separate explicit time steps accounting for fluxes **F**, **G**, and for the source term **H**, so in a symbolic operator form one full time step can be written as

$$L(\Delta t) = L_F(\Delta t) L_G(\Delta t) L_H(\Delta t). \tag{11}$$

Each quasi-one-dimensional advection operator in (11) is realized by an explicit second-order Godunov-type finite-volume scheme. The advection time steps $L_F(\Delta t)$ and $L_G(\Delta t)$ are computed in a similar way; for example, the split advection step in x direction $L_F(\Delta t)$ is performed for each grid line $j=$const as follows.

First, limited spatial derivatives of primitive variables $\dot{U}_x$, $\dot{U}_y$, σ_{xx}, σ_{xy} are computed for each control volume:

$$\nabla_x r_i^n = \mathrm{minmod}\left(\frac{r_{i+1}^n - r_{i-1}^n}{2\Delta x}, C\frac{r_i^n - r_{i-1}^n}{\Delta x}, C\frac{r_{i+1}^n - r_i^n}{\Delta x} \right),$$

where r denotes any variable of $\dot{U}_x$, $\dot{U}_y$, σ_{xx}, σ_{xy}; C is the "compression" coefficient ($C=2$ in our computations), and the "minmod" operator is given as follows:

$$\mathrm{minmod}(a,b) = \begin{cases} 0, & ab \leqslant 0 \\ \dfrac{a}{|a|}\min(|a|,|b|), & ab > 0 \end{cases}.$$

Then, a nonconservative predictor step is performed using the above spatial derivatives:

$$\tilde{\mathbf{Q}}_i^{n+1} = \mathbf{Q}_i^n - \frac{\Delta t}{\Delta x}\left[\mathbf{F}\left(\mathbf{Q}_i^n + \frac{1}{2}\nabla_x \mathbf{Q}_i^n \Delta x \right) - \mathbf{F}\left(\mathbf{Q}_i^n - \frac{1}{2}\nabla_x \mathbf{Q}_i^n \Delta x \right) \right].$$

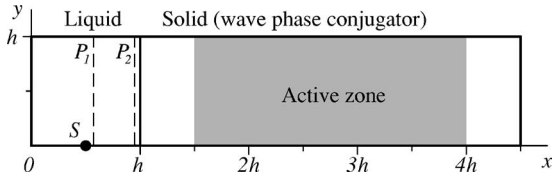

FIG. 1. Computational domain: S: the primary acoustic signal source; P_1, P_2: observation planes of the acoustic energy flux.

Finally, the main conservative (or "corrector") step is computed:

$$\mathbf{Q}_i^{n+1} = \mathbf{Q}_i^n - \frac{\Delta t}{V_i}[\mathbf{F}(\tilde{\mathbf{Q}}_{i+1/2}^*) S_{xi+1/2} - \mathbf{F}(\tilde{\mathbf{Q}}_{i-1/2}^*) S_{xi-1/2}],$$

using the following initial data for the Riemann problem solution $\tilde{\mathbf{Q}}_{i+1/2}^*$ at the face $i+\frac{1}{2}$:

$$\tilde{\mathbf{Q}}_L = 0.5(\mathbf{Q}_i^n + \tilde{\mathbf{Q}}_i^{n+1} + \nabla_x \mathbf{Q}_i^n \Delta x),$$

$$\tilde{\mathbf{Q}}_R = 0.5(\mathbf{Q}_{i+1}^n + \tilde{\mathbf{Q}}_{i+1}^{n+1} - \nabla_x \mathbf{Q}_{i+1}^n \Delta x)$$

(see Ref. 7 for details).

The value of σ_{yy} after this split advection step is obtained from

$$\Delta\sigma_{yy} = \frac{\nu}{1-\nu}\Delta\sigma_{xx},$$

where ν is the Poisson ratio.

According to the long-established operator splitting technology,[9] the order of convective operators $L_F(\Delta t)$ and $L_G(\Delta t)$ in (11) is reversed for accuracy reasons at every even time step.

The effect of external magnetic field on the stress components described by the source term (1), (2), and (5) is simulated by a separate split step $L_H(\Delta t)$ for each control volume i,j as follows:

$$\sigma_{xx}^{n+1} = \sigma_{xx}^n + \mathrm{H}_{xx}^{n+1/2}\Delta t,$$

$$\sigma_{yy}^{n+1} = \sigma_{yy}^n + \mathrm{H}_{yy}^{n+1/2}\Delta t,$$

$$\sigma_{xy}^{n+1} = \sigma_{xy}^n + \mathrm{H}_{xy}^{n+1/2}\Delta t.$$

III. THE NUMERICAL ANALYSIS

A. Problem setting

Figure 1 presents the computational domain in the x,y plane ($0 \leqslant x \leqslant 4.5h, 0 \leqslant y \leqslant h$) containing liquid at $0 \leqslant x \leqslant 1$ and magnetostrictive solid at $1 \leqslant x \leqslant 4.5h$. All planar sections $z=$const are considered equivalent. The active or pumping zone, i.e., the zone where the source term (1), (2), and (5) is applied, is sharply limited by $1.5h \leqslant x \leqslant 4h$. After Ref. 1, the following parameters were used for the magnetostrictive material: density $\rho = 3.3$ kg/m^3, longitudinal sound speed $c_L = 7170$ m/s, and Poisson ratio $\nu = 0.25$.

Parameters of water were used for liquid in one-dimensional simulations[1] with the sound speed $c_0 = 1470$ m/s and density $\rho = 1$ kg/m^3. Here, to reduce the grid resolution restrictions imposed by the short wave length in

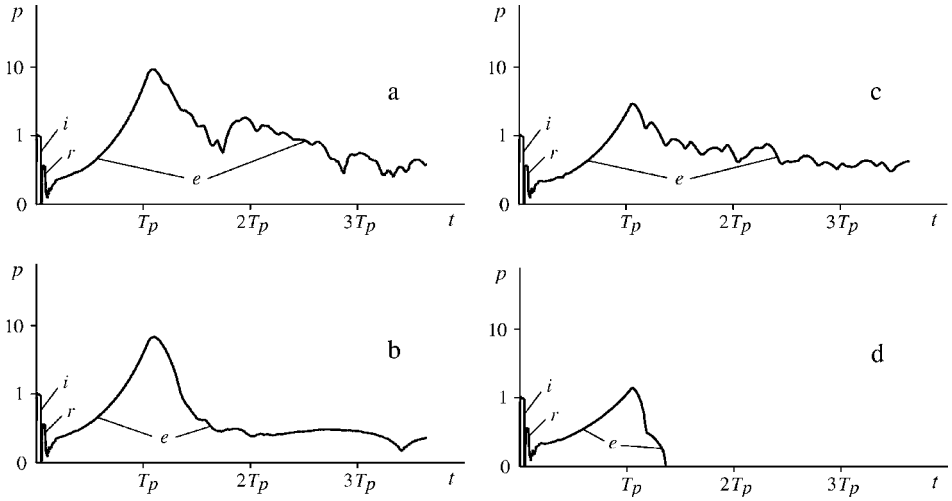

FIG. 2. Temporal evolution of dimensionless acoustic pressure (signal's amplitude) at the point of initial excitation for different boundary conditions at the solid upper and right-hand side boundaries: (a) stress-free upper and right-hand side boundaries; (b) stress-free upper and absorbing right-hand side boundaries; (c) stress-free right-hand side and absorbing upper boundaries; and (d) absorbing upper and right-hand side boundaries. Initial signal: *i*, reflection from liquid-solid boundary: *r*, emission from the solid due to WPS and internal reflection at the solid boundaries: *e*.

the liquid, the sound speed c_0 has been set up equal to the longitudinal sound speed in the solid c_L. The liquid density was modified accordingly ($\rho=1470/7170$ kg/m^3) resulting in the acoustic impedance $Z=c_0\rho$ equal to that of water.

The boundary conditions at the external boundaries of the computational domain were applied using a double layer of ghost cells. The symmetry boundary condition has been set up at $y=0$. The "absorbing" condition was used at the boundaries $x=0$ and $0<x<h$, $y=h$. For that, spatial derivatives of stress components and displacement velocities were set up to zero across the boundary. The internal boundary between the liquid and solid at $x=h$ has been treated assuming the inviscid slip condition (see Ref. 7 for details). The boundary conditions at the solid boundaries $x>h$, $y=h$ and $x=4.5h$ were toggled separately in different computations between the "absorbing" and "stress-free" boundary. The presented results have been obtained using an equally spaced grid ($\Delta x=\Delta y=0.01h$) containing $n_x\times n_y=454\times 104$ grid cells, which includes the double layer of ghost cells surrounding the domain and used to implement boundary conditions.

The initial wave train was generated at a small spot (*S* in Fig. 1) in the liquid at the symmetry plane by harmonic modulation of σ_{xx} and σ_{yy} at a frequency ω with the corresponding period T during a time of three full periods, i.e., $3T$, in four grid cells surrounding point $x=0.5h$, $y=0$. The wavelength of the generated wave train used in the following results was $\lambda=c_0T=2\pi c_0/\omega=0.205h$. The code has been thoroughly tested and selected grid resolution found sufficient providing relative error by the convection operators within 5% for a harmonic wave of the given wavelength.

The pumping (actuation of the WPC source term) at frequency $\omega_B=2\omega$ has been performed during the time $T_p=95T\approx 19.5h/c_0$ at a constant intensity characterized by the modulation depths $M_L=M_T=0.041$.

B. The influence of boundaries

Computations have been performed for different boundary conditions at the external boundaries of the solid: the upper and the right-hand side boundaries were separately treated as either "stress-free" or "absorbing" ones. The acoustic pressure histories at the location of original wave excitation (*S* in Fig. 1) are presented in Fig. 2. Due to the high frequency, the principal harmonic component of the signal cannot be presented in the figure, but rather evolution of the signal amplitude. The first short pulse *i* seen in the plots starting at time $t=0$ is the initial signal, which is followed by reflection *r* of the former from the liquid-solid boundary. After that, an exponentially growing amplitude indicates arriving at *S* of the conjugate wave amplified in the solid by the magnetostrictive effect. The exponential growth finishes shortly after the pumping terminates. Numerous reflections at the solid boundaries together with the mismatched acoustic impedance at the solid-liquid boundary cause a long-lasting radiation with gradually decaying ampitude. Comparison with the one-dimensional computations from Ref. 1 clearly indicates much more sophisticated signal shape for our case of diverging initial waves from the source. Variations in the boundary settings essentially affect both the signal intensity and its shape. A qualitative analogy to the one-dimensional case is better observed for reflecting stress-free conditions at the right-hand side solid boundary and absorbing condition at the upper boundary, though the amplitude pulsates at higher frequency. The first radiated pulse representing the amplified conjugate wave is of primary interest for applications.

Figure 3 shows the evolution of mechanical energy in the solid for considered cases. Naturally, the highest energy in the solid is achieved by reflecting stress-free boundaries. The exponential growth of the acoustic energy terminates sharply together with the pumping. The highest accumulated acoustic energy in the case of stress-free boundaries suggests that nonlinear pumping effects and saturation[10] can be more critical in that case.

To analyze the focusing ability of the radiated conjugate wave, energy fluxes through planes P_1 close to the source and P_2 close to the solid in liquid (see Fig. 1) have been recorded and compared, as shown in Fig. 4. The flux through the solid-liquid boundary (plane P_2) was computed across the whole domain $0<y<h$. The fluxes through plane P_1 are given separately for three segments: $0<y<0.1h$, $0.1h<y<0.2h$, and $0.2h<y<0.3h$. Averaged values over the signal period T have been used for the energy and energy fluxes presented in the figures.

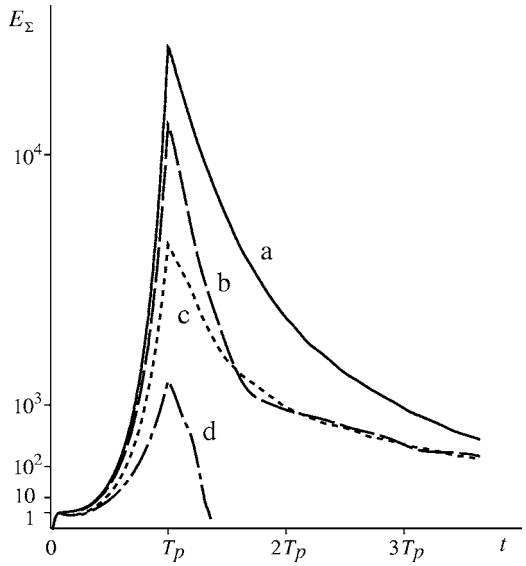

FIG. 3. Temporal evolution of dimensionless total energy in the solid. T_p indicates pumping duration. Different curves display results for different boundary conditions at the boundaries of the solid corresponding to Fig. 2.

A good energy flux concentration (focusing) of the conjugate wave (flux maximum following exponential growth) is observed by stress-free external solid boundaries [Fig. 4(a)]. The flux maximum through the first segment of plane P_1 comprises an essential part of the whole radiated flux (plane P_2) with considerably lower flux values through segments located off the symmetry plane. A similar flux concentration for the conjugate wave is achieved also by the sress-free upper solid boundary and absorbing right-hand side boundary [Fig. 4(b)]. A remarkable feature of this case is a rapid decay of the signal right after the conjugate wave pulse, which can be preferrable for applications. Alternatively, a rather long-lasting radiation and unfocused flux intensity at the initial signal level after conjugate wave focusing can be seen in Fig. 4(c) for absorbing upper and stress-free right-hand side boundaries. Figure 4(d) corresponds to absorbing external solid boundaries and demonstrates a good focusing with no extra signals after the conjugate wave, but at very low amplitude.

More detailed information on the acoustic energy flux distribution with its time variations across the pane P_1 can be obtained from the $y-t$ carpet diagrams given in Fig. 5. A small-amplitude negative flux seen in the figures close to $y=0$, $t=0$ corresponds to the initial signal from the source. The amplitude of that flux is taken as a reference unit Φ_0. One can note the best localized conjugate wave signal by the stress-free solid boundaries [Fig. 5(a)]. However, some signals of relatively high intensity are observed also at locations far from the expected focusing area and during a rather long time. A better spatial and temporal localization of radiated signal corresponds to the stress-free upper solid boundary and absorbing right-hand side boundary [Fig. 5(b)]. Though, quite intensive side lobes in the flux appear next to the focus point. An absorbing upper boundary effectively reduces the angle at which the diverging incident signal receives amplification in the solid and is radiated back into liquid as a conjugate wave, resulting in essentially less sharp energy flux localization [Figs. 5(c) and 5(d)].

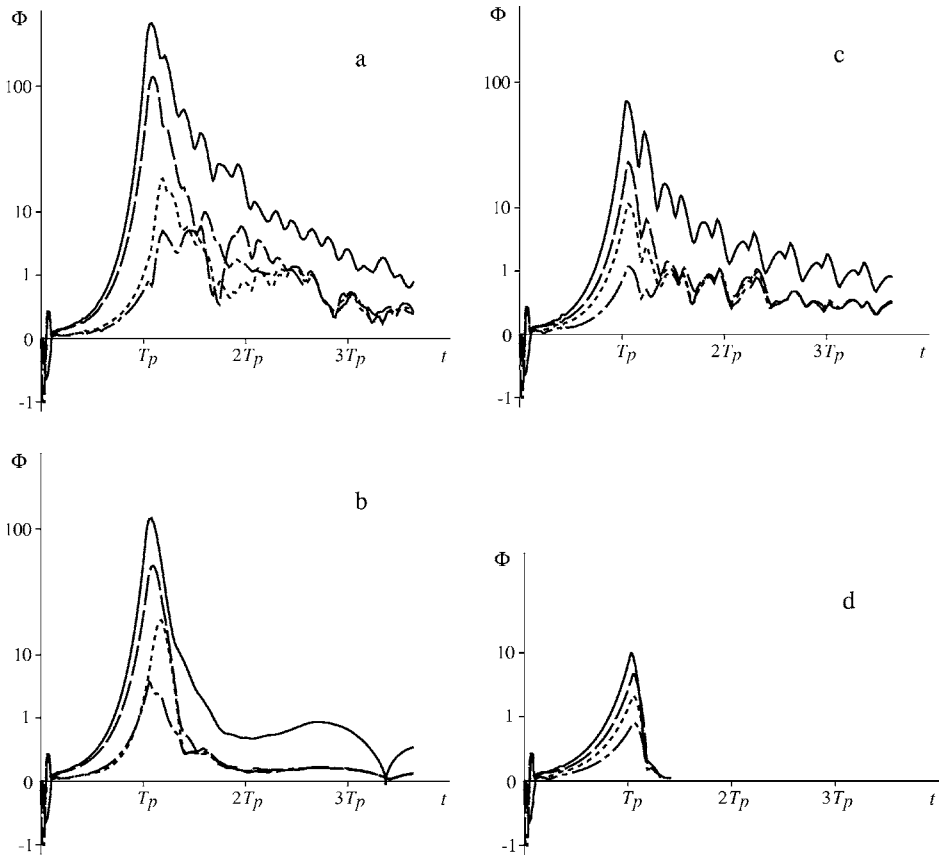

FIG. 4. Temporal evolution of dimensionless acoustic energy flux through the solid-liquid boundary (solid lines) and through different segments of the observation plane P_1 (Fig. 1) near the focusing area (dashed lines). (a)–(d) same as in Fig. 2.

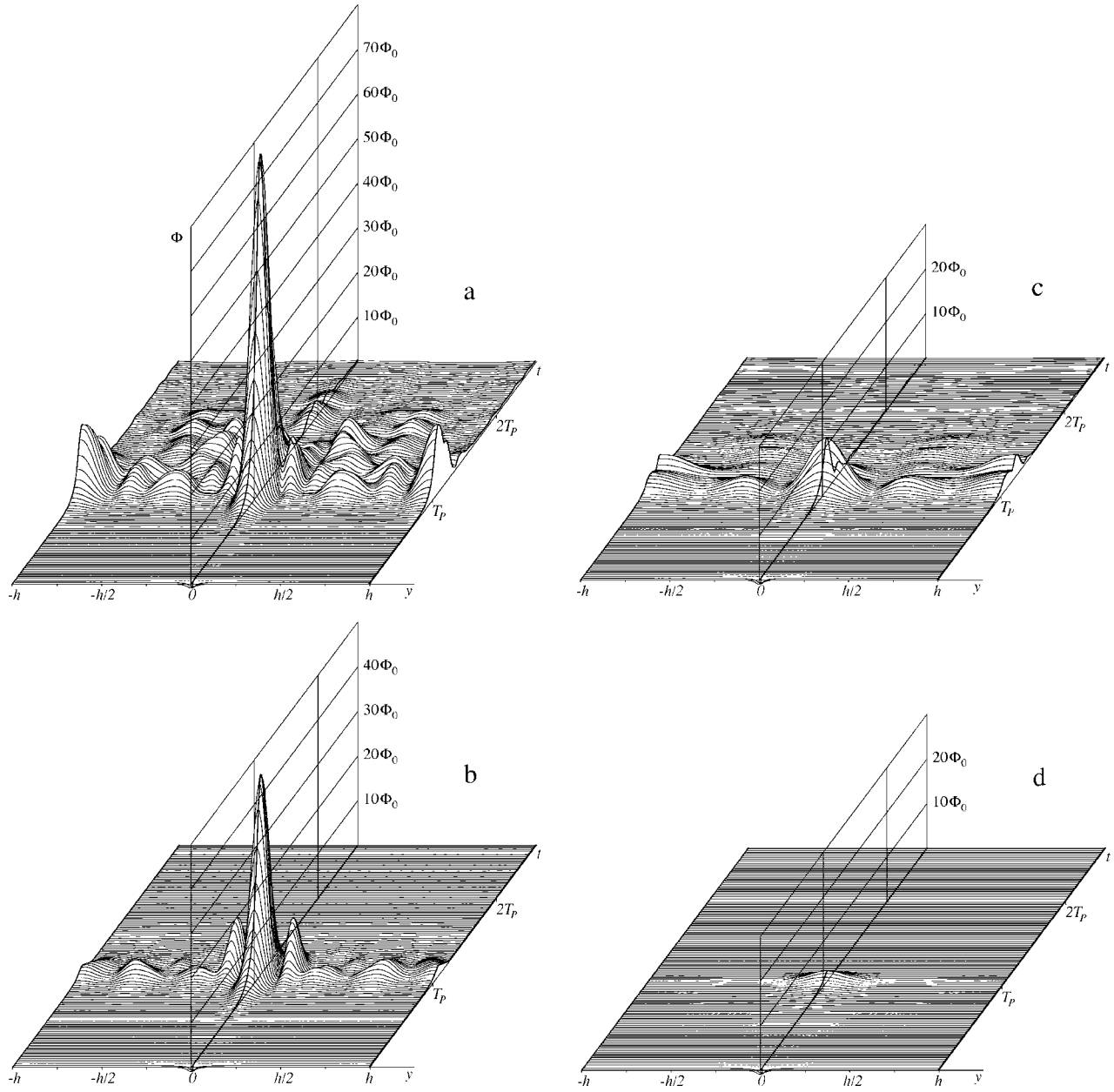

FIG. 5. Space-resolved temporal evolution of dimensionless acoustic energy flux through the observation plane P_1 (Fig. 1) near the focusing area. (a)–(d) same as in Fig. 2.

IV. CONCLUDING REMARKS

The main results of the present work can be summarized as follows.

(a) A mathematical model has been developed to simulate two-dimensional effects by ultrasonic wave phase conjugation (WPC) in magnetostrictive solids. The model is written in a form of integral conservation equations and universally includes elastic solids and liquids.

(b) A source term and variable transport coefficients are introduced in the model to describe coupling between the acoustic field and external magnetic field through the modulation of longitudinal and transversal sound speeds.

(c) A compatibility criterion has been derived ensuring physical realism of the solution with modulated sound speeds. It has been shown that for an isotropic magnetostrictive solid, only equal modulation of longitudinal and transversal sound speeds results in a realistic solution without spurious effects like residual divergence-free stationary stress in the solid.

(d) The model is implemented in a computer code using an operator-split modification of a second-order-accurate quasi-monotone Godunov-type finite-volume numerical scheme developed earlier by the authors.

(e) The potentialities of the model and code have been demonstrated on a representative problem of WPC essentially involving two-dimensional effects and studied earlier in a one-dimensional formulation. Radiation of a short diverging harmonic acoustic signal from a point source in liquid, its transmision into a finite sample of magnetostrictive solid, amplification of the signal and

conjugate wave formation under magnetic pumping, radiation back into the liquid, and focusing of the amplified conjugate wave at the primary signal source—all these effects have been obtained in simulations and presented using a range of problem-specific postprocessing technologies.

(f) A strong sensitivity of the conjugate wave intensity and focusing ability has been detected relative to the boundary conditions at the external boundaries of the magnetostrictive solid.

As an immediate application of the developed techniques, the authors are planning a comprehensive study of conjugate wave formation and focusing under various conditions, particularly related to the shape and location of the primary signal source; dimensions of the magnetostrictive solid; shape, location, and properties of the active zone in the solid; and more elaborated boundary effects. The earlier unstructured grid implementation of the elastic model[7] used in this work can be easily upgraded to simulate WPC in curvilinear geometries. An axi-symmetric formulation of the problem represents another natural extension of the study. The use of massively parallel processing computer platforms is planned to overcome restrictions imposed by essentially different sound speeds in the liquid and solid under parameters of the media and signal frequency used in experiments. An extension to anisotropic media is also a development direction of substantial interest in order to widen the models of magnetostriction.

Quantitative verification of the results is a serious aspect of any numerical analysis and involves various methodological approaches, including comparisons with the available experimental data and/or conduction of verification experiments (which is mostly to validate the model of magnetostriction used) as well as convergence tests and comparisons with analytical solutions (to demonstrate accuracy of the method). Extensive data accumulated on the above subject and related to the numerical techniques used in this paper must be compared with other numerical approaches (i.e., spectral). The emergence of analytical solutions in nontrivial situations would be a great improvement for the field and the best way to validate the computational accuracy. An intensive effort is in progress in this direction.

ACKNOWLEDGMENTS

The authors wish to thank Professor Ph. Pernod and Professor V. Preobrazhensky of Institut d'Electronique, de Microélectronique et de Nanotechnologie, Ecole Centrale de Lille, France, and Professor E. Timofeev of McGill University, Canada, for their encouraging interest and valuable advice. Financial support by CNRS, France (Décision SPRH 234/2004) is kindly acknowledged.

[1] S. Ben Khelil, A. Merlen, V. Preobrazhensky, and P. Pernod, "Numerical simulation of acoustic wave phase conjugation in active media," J. Acoust. Soc. Am. **109**, 75–83 (2001).

[2] A. Brysev, L. Krutyansky, P. Pernod, and V. Preobrazhensky, "Acoustic microscope based on magneto-elastic wave phase congugator," Appl. Phys. Lett. **76**(12), 3133–3135 (2000).

[3] Y. Pyl'nov, P. Pernod, and V. Preobrazhensky, "Acoustic imaging by second harmonic of phase-conjugate wave in inhomogeneous medium," Appl. Phys. Lett. **78**(4), 553–555 (2001).

[4] K. Yamamoto, P. Pernod, and V. Preobrazhensky, "Visualization of phase conjugate ultrasound waves passed through inhomogeneous layer," Ultrasonics **42**(1–9), 1049–1052 (2004).

[5] A. P. Brysev, F. V. Bunkin, M. F. Hamilton, L. M. Krutyansky, K. B. Cunningham, V. L. Preobrazhensky, Y. V. Pyl'nov, A. D. Stakhnovsky, and S. J. Younghouse, "Nonlinear propagation of quasi-plane conjugate ultrasonic beam," Acoust. Phys. **44**, 641–650 (1998).

[6] V. Preobrazhensky and P. Pernod, "Phase conjugation of second acoustic harmonic and retrofocusing in nonlinear inhomogeneous medium," Phys. Wave Phenom. **11**(2), 63–67 (2003).

[7] P. Voinovich, A. Merlen, E. Timofeev, and K. Takayama, "A Godunov-type finite-volume scheme for unified solid-liquid elastodynamics on arbitrary two-dimensional grids," Shock Waves **13**(3), 221–230 (2003).

[8] L. I. Sedov, *A Course on Continuum Mechanics* (Wolters-Noordhoff, Groningen, 1972), Vol. 4, pp. 41–42.

[9] G. Strang, "On the construction and comparison of difference schemes," SIAM (Soc. Ind. Appl. Math.) J. Numer. Anal. **5**(3), 506–517 (1968).

[10] A. Merlen, V. Preobrazhensky, and P. Pernod, "Supercritical parametric phase conjugation of ultrasound. Numerical simulation of nonlinear and nonstationary mode," J. Acoust. Soc. Am. **112**(6), 2656–2665 (2002).

A model for large amplitude oscillations of coated bubbles accounting for buckling and rupture

Philippe Marmottant,[a] Sander van der Meer, Marcia Emmer, and Michel Versluis
Department of Science and Technology, University of Twente, P.O. Box 217, 7500AE Enschede, The Netherlands

Nico de Jong
Department of Science and Technology, University of Twente, P.O. Box 217, 7500AE Enschede, The Netherlands and Department of Experimental Echocardiography, Thoraxcentre, Erasmus MC, Rotterdam, The Netherlands

Sascha Hilgenfeldt[b] and Detlef Lohse
Department of Science and Technology, University of Twente, P.O. Box 217, 7500AE Enschede, The Netherlands

(Received 31 March 2005; revised 25 August 2005; accepted 13 September 2005)

We present a model applicable to ultrasound contrast agent bubbles that takes into account the physical properties of a lipid monolayer coating on a gas microbubble. Three parameters describe the properties of the shell: a buckling radius, the compressibility of the shell, and a break-up shell tension. The model presents an original non-linear behavior at large amplitude oscillations, termed compression-only, induced by the buckling of the lipid monolayer. This prediction is validated by experimental recordings with the high-speed camera Brandaris 128, operated at several millions of frames per second. The effect of aging, or the resultant of repeated acoustic pressure pulses on bubbles, is predicted by the model. It corrects a flaw in the shell elasticity term previously used in the dynamical equation for coated bubbles. The break-up is modeled by a critical shell tension above which gas is directly exposed to water. © *2005 Acoustical Society of America.*
[DOI: 10.1121/1.2109427]

PACS number(s): 43.25.Yw, 43.35.Ei [AJS] Pages: 3499–3505

I. INTRODUCTION

To enhance ultrasound echographic imaging, micrometric coated bubbles are used as contrast agents. Coating materials include lipid monolayers, polymer shells, or thick solid shells. The coating stabilizes the bubbles and prevents their coalescence. Pulmonary alveoli in the lungs have a lipidic coating for the same reason.[1] The coating modifies the effective surface tension. Since surface tension plays a crucial role in the dynamics of small bubbles, when the capillary pressure term is of the order of the static ambient pressure, the coating is expected to strongly influence the dynamics.

All current models developed to describe coated bubble oscillations implicitly assume small deformations of the bubble surface: however, in practice, insonifying contrast agent bubbles produces oscillations with large variations in the surface area. We will present in this article a model designed to incorporate the effect of a coating on the microbubble response to ultrasound, and to specifically capture the high-amplitude dynamics.

We focus on phospholipidic monolayer coatings, used in several contrast agent bubbles.[2] The phospholipid molecules naturally adsorb to the interface[3] and shield the water from the air, reducing the surface tension σ to a value lower than that of pure water (73 mN/m). Surface tension can be measured in a flat monolayer with the Langmuir-Blodgett balance, or on centimetric bubbles,[4] showing its dependence on the surface concentration of molecules.

The compression of the monolayer decreases the area available per molecule. When this area reaches that covered by the lipid molecules (typically 0.4 nm^2 for phospholipids in the transconfiguration normal to the interface), the effective surface tension decreases sharply, see Fig. 1. The variation of surface tension with the area A is expressed with the elastic compression modulus defined by $\chi = A(d\sigma/dA)$ (of order 0.2 N/m for a slow compression, as derived from the steepest slopes of Fig. 1). Further compression leads to an unstable situation where the monolayer buckles out of plane, while the surface tension nearly vanishes. A spectacular demonstration of the buckling is the appearance of wrinkles on coated bubbles when their gas dissolves out.[8] Buckling can be reversible.[9,10] Vanishing surface tensions were revealed by the microscopic observation of bubbles with a monolayer lipid coating in a solid state: these bubbles could assume a steady nonspherical shape[11] when deformed with a micropipette, and dissolution was greatly reduced by the absence of the capillary overpressure.[12]

In contrast, a slow expansion separates molecules from each other: surface tension rises. A monolayer made from pure lipid (one species only) will show phase changes from a

[a]Present address: Laboratoire de Spectrométrie Physique, CNRS-Université Joseph Fourier, Boîte Postale 87, F-38402 Saint Martin d'Hères, France.
[b]Present address: Engineering Sciences and Applied Mathematics and Department of Mechanical Engineering, Northwestern University, 2145 Sheridan Road, Evanston, IL 60208.

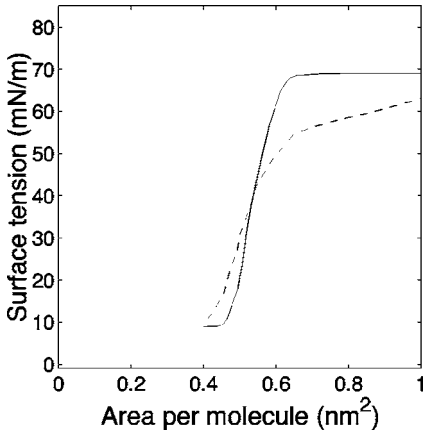

FIG. 1. Effective surface tension versus area per molecule at the interface for two phopholipids (both present in the contrast agent SonoVue®) (see Ref. 5) under *slow compression* at a few percent per minute: distearoylphosphatidylcholine, solid line; and dipalmytoylphosphatidylglycerol, broken line. Curves redrawn from Ref. 6 and 7.

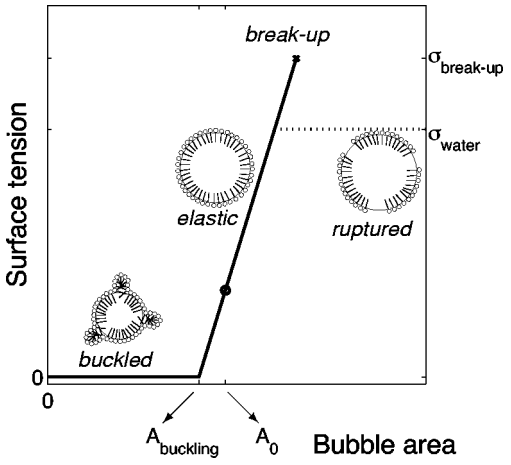

FIG. 2. Model for the dynamic surface tension of a monolayer coated bubble (continuous line). The coating has a fixed number of lipid molecules, which corresponds to a monolayer at equilibrium (when area is A_0). The tension saturates to the water value σ_{water} (broken line) after the break-up tension has been reached ($\sigma_{break-up} > \sigma_{water}$).

two-dimensional (2D) solid state, to a liquid and eventually gaseous state, where surface tension is close to that of water. With a mixture of lipid molecules the phase changes are not necessarily present, and a 2D solid can rupture during expansion, leaving rafts of solid phospholipid molecules separated by clean interfaces.[13]

Most previous existing experimental data on phospholipidic monolayers were collected at very slow compression/expansion rates, when molecules at the interface could equilibrate. Only a few experiments tackled the high-frequency and thus out-of-equilibrium trends: the buckling surface tension comes closer to zero and the elastic modulus becomes higher (see reported experiments[1] with pulmonary surfactant compressed within 0.2 s). These findings give some hint to the extrapolation of surface properties to the realm of high frequency oscillations, the one we are going to explore with oscillating contrast agent bubbles.

II. MODEL

A. Effective surface tension of a bubble during its oscillation

At high frequencies, we propose to model the effective surface tension σ of the lipidic monolayer of a bubble along three linear regimes inspired from the low frequency observations. The regimes depend on the bubble area $A=4\pi R^2$, with R the bubble radius (see Fig. 2). This simplified model is designed to capture the coated bubble dynamics with a minimum of parameters.

The model has three parameters only to describe the surface tension: the buckling area of the bubble $A_{buckling}$ below which the surface buckles, an elastic modulus χ that gives the slope of the elastic regime. The third parameter is incorporated to describe the moment of rupture: the elastic regime holds until a critical break-up tension called $\sigma_{break-up}$. When this limit has been reached the maximum surface tension saturates at σ_{water}.

We motivate here the modeling of the three states.

- Buckled state, $\sigma=0$.

  Consistent with experimental findings on the fast compression of pulmonary phospholipid monolayers, we assume a near vanishing surface tension in the buckled state.[1] The buckling area of the bubble depends on the number n of lipid molecules at the interface and on the molecular area at buckling $a_{buckling}$, with $A_{buckling}=na_{buckling}$, with $a_{buckling}$ typically of the order of 0.4 nm^2, see previous section. Note that a first compression of the bubble might *expel* in bulk some molecules into the bulk,[14] decreasing the number n. After this transient expulsion, and for moderate driving amplitudes and short exposures, we expect the number of molecules to remain constant, as phospholipids with long carbon chains are poorly soluble.
- Elastic state, $\sigma=\chi(A/A_{buckling}-1)$.

  The shell is elastic only in a narrow area range. The lower limit is $A_{buckling}$ for the area, or equivalently $R_{buckling}$ for the radius. The upper limit radius is fixed by the maximum surface tension, which is $\sigma_{break-up}$ before rupture of the shell giving $R_{break-up}=R_{buckling}(1+\sigma_{break-up}/\chi)^{1/2}$, or σ_{water} after rupture giving $R_{ruptured}=R_{buckling}(1+\sigma_{water}/\chi)^{1/2}$. The elastic regime holds only in a narrow range of radii, since χ is usually large compared to $\sigma_{break-up}$ or σ_{water}. The value of the elastic modulus can also incorporate the presence of any solid-like shell material that sustains tensile stress (such as the polyethyleneglycol polymer in SonoVue® contrast agent bubbles[5]). We assign a constant elastic modulus in this state, slightly caricaturing the quasi-static profiles of Fig. 1, a simplification of the model to facilitate calculation.

  Within this regime the surface tension is a linear function of the area, or of the square of the radius, and for small variations around a given radius R_0, it can be written as:

$$\sigma(R)=\sigma(R_0)+\chi\left(\frac{R^2}{R_0^2}-1\right)\simeq\sigma(R_0)+2\chi\left(\frac{R}{R_0}-1\right)\quad\text{when } |R-R_0|\ll R_0. \tag{1}$$

  The lipid monolayer behaves as if composed of a thin solid

and elastic material, see the appendix for the derivation of the tension of a thin elastic shell.

- Ruptured state, $\sigma=\sigma_{\text{water}}$.
  A fast expansion, such as the one triggered on a bubble by an ultrasonic pressure pulse, does not allow much time for any phase change and the monolayer is likely to break at a critical tension $\sigma_{\text{break-up}}$, exposing bare gas interfaces to the liquid. The bare interface has a tension value of σ_{water}. The break-up tension can be higher than σ_{water}, since any polymer component confers more cohesion to the shell, and shifts the break-up to higher tensions. The introduction of a high tension break-up was motivated by the observation of resistant bubbles, as will be exposed further.
  After break-up we assume that surface tension relaxes to σ_{water}. Even if the phospholipid monolayer rafts are likely to display non-isotropic tensions and shear stresses (being solid), the expansion is uniform before rupture, and the stress is likely to remain close to uniformity on average. The average tension value is settled in this case by the local mechanical equilibrium between the solid rafts and the bare interfaces, the latter pulling with the tension σ_{water}.

B. Dynamics of the coated bubble

During the oscillation, the dynamical surface tension will vary, since it is a function of the bubble area and therefore of the bubble radius. We therefore write the effective surface tension $\sigma(R)$ to emphasize this dependence. In motion, the balance of normal stresses at the interface reads

$$P_g(t) - P_l(t) = \frac{2\sigma(R)}{R} + 4\mu\frac{\dot{R}}{R} + 4\kappa_s\frac{\dot{R}}{R^2}, \tag{2}$$

with P_g as the gas pressure in the bubble, P_l as the liquid pressure, μ as the surrounding liquid viscosity, and κ_s as the surface dilatational viscosity from the monolayer. The first term on right-hand side is the capillary pressure term, while the second is the stress arising from the frictions in the liquid and the third from frictions in the shell. The last term was initially derived for a layer of finite and constant thickness ϵ ($\epsilon \ll R$) by Morgan *et al.*,[15] the dilatational viscosity writing $\kappa_s=3\epsilon\mu_{\text{lipid}}$, with μ_{lipid} as the bulk lipid viscosity. Here we use only κ_s to describe the monolayer shell surface viscosity, following Chatterjee and Sarkar.[16] In this model κ_s does not depend on the surface area, nor does it exhibit any hysteresis. Note that the shear viscosity of the surface does not come into play in the present situation, because of the radial motion of the bubble.

The Laplace capillary pressure term writes $2\sigma(R)/R$ including the effective surface tension, *without any additional terms*, contrary to a previous statement in an article by Glazman,[17] who expressed the capillary pressure by the erroneous expression $2\sigma/R+\partial\sigma/\partial R=2/R[\sigma+\chi(R_0/R)^2]$. We demonstrate here why: the capillary overpressure derives from the mechanical equilibrium of all forces acting on the interface (of vanishing mass), that is the infinitesimal work δW of the forces cancels out for small bubble radius variation. By definition, the work associated with a variation dA of the area is σdA,[18] while the pressure work from a variation dV of the volume is $-(P_g-P_l)dV$. Owing to the mechanical equilibrium of the interface, the sum of these works vanishes, and we obtain the static capillary term of Eq. (2). In the analysis by Glazman, the surface work is expressed incorrectly by $\sigma dA+Ad\sigma$ (instead of σdA) from the differentiation of a surface potential energy $E=\sigma A$: actually this last expression of the surface potential energy ($E=\int \delta W_{surface}$ by definition) is valid only when σ is constant.

The popular model of Morgan *et al.*[15] for coated microbubbles improves the description of viscous frictions, but is based on the analysis of Glazman for the elasticity of the lipid shell, equivalent to the introduction of an effective surface tension $\sigma(R)=\sigma_0+\chi(R_0/R)^2$ that fails to describe a coated bubble. Physically it would mean that surface tension always decreases when the bubble is inflated, in contrast with the behavior of lipid monolayers or elastic solid shells.

The hydrodynamics of the liquid motion around the bubble is modeled by the (modified) Rayleigh-Plesset equation $\rho_l\left(R\ddot{R}+\frac{3}{2}\dot{R}^2\right)=P_l(t)-P_0-P_{\text{ac}}(t)-(R/c)[dP_g(t)/dt]$, with P_0 as the ambient pressure, $P_{\text{ac}}(t)$ as the acoustic pressure, and c as the velocity of sound in the liquid. This equation proved to be accurate and robust even in the extreme conditions of sonoluminescence.[19] We choose an ideal polytropic ideal gas law $P_g \propto R^{-3\kappa}$, with κ as the polytropic gas exponent. It is 1 for bubbles behaving isothermally, and equal to the ratio of specific heats for bubbles behaving adiabatically[20] (close to 1.095 for SF_6). In the following, the thermal diffusion length in the gas during a period being small compared to the radius, we use the adiabatic version.

Combining the Rayleigh-Plesset equation and the polytropic gas law with the boundary condition (2) we obtain the model for the bubble dynamics

$$\rho_l\left(R\ddot{R}+\frac{3}{2}\dot{R}^2\right)=\left[P_0+\frac{2\sigma(R_0)}{R_0}\right]\left(\frac{R}{R_0}\right)^{-3\kappa}\left(1-\frac{3\kappa}{c}\dot{R}\right) - P_0-\frac{2\sigma(R)}{R}-\frac{4\mu\dot{R}}{R}-\frac{4\kappa_s\dot{R}}{R^2}-P_{\text{ac}}(t), \tag{3}$$

with R_0 the equilibrium radius of the bubble. This equation is identical to a free gas bubble equation, except from the effective surface tension $\sigma(R)$ term and the shell viscosity term. The tension expressed in our monolayer model described above, and expressed here in terms of the bubble radius writes:

$$\sigma(R)=\begin{cases} 0 & \text{if } R \leqslant R_{\text{buckling}} \\ \chi\left(\dfrac{R^2}{R_{\text{buckling}}^2}-1\right) & \text{if } R_{\text{buckling}} \leqslant R \leqslant R_{\text{break-up}} \\ \sigma_{\text{water}} & \text{if ruptured and } R \geqslant R_{\text{ruptured}}. \end{cases} \tag{4}$$

The third regime appears after rupture of the shell, when $\sigma_{\text{break-up}}$ has been reached (see broken line in Fig. 2).

For small vibration amplitudes within the tensed elastic state, the surface tension can be linearized around a constant value, with $\sigma(R)\simeq\sigma(R_0)+2\chi(R/R_0-1)$, from Eq. (1). Implemented in the dynamical equation its yields the same

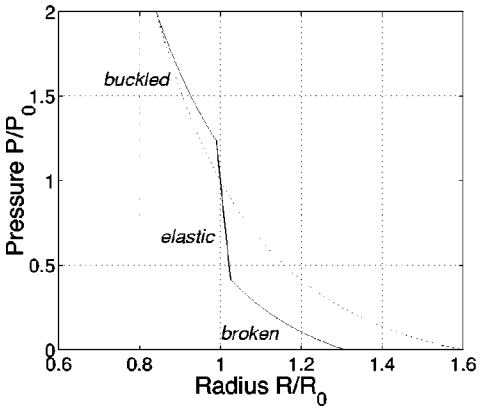

FIG. 3. Ambient pressure vs equilibrium radius for a coated bubble (continuous line) and a free gas bubble (dotted line). At atmospheric pressure, the bubble radius is $R_0=2$ μm. The coated bubble is initially in the elastic state ($R_{\text{buckling}}=1.98$ μm, $\chi=1$ N/m).

pressure term $-2\sigma(R)/R=-2\sigma(R_0)/R-4\chi(1/R_0-1/R)$ as in the model proposed by de Jong *et al.*[21] for thin elastic shells. The shell stiffness coefficient S_p they introduced is simply related to the present shell elasticity by $S_p=2\chi$, while their shell friction coefficient writes $S_f=12\pi\kappa_s$. We stress here again that the model by de Jong *et al.*[21] is limited to small amplitudes of vibration (for effective tensions bounded between 0 and σ_{water}, or for R in between R_{buckling} and R_{collapse}), while the present model extends the oscillation to unbounded, large amplitudes.

C. Implications of the model: Bubble compressibility

The effective tension model drastically changes the compressibility of the bubble. For slow variations of the ambient pressure P, at frequencies small compared to the resonance frequency, we can compute the equilibrium radius response, see Fig. 3, setting $\dot{R}=0$ in Eqs. (3) and (4).

From the equilibrium, we also derive the compression modulus of the bubble, K_V, with

$$K_V=-V\left(\frac{dP}{dV}\right)=\begin{cases}\kappa P & \text{for the buckled state}\\ \kappa P+\dfrac{4}{3}\dfrac{\chi}{R} & \text{for the elastic state}\\ \kappa P+\dfrac{3\kappa-1}{3}\dfrac{2\sigma_{\text{water}}}{R} & \text{for the free bubble/broken shell state}\end{cases} \tag{5}$$

with V as the bubble volume, a polytropic exponent κ close to 1 for slow and isothermal compressions, and in the limit of $\chi \gg \sigma_{\text{water}}$ (usual for phospholipids). The compression modulus is much higher when the bubble is in the elastic state: this is reflected in the much steeper slope of the curve in Fig. 3. When the pressure is increased enough the bubble buckles, and becomes very compressible, even more than an uncoated free gas bubble of the same radius (whose internal pressure is increased by capillarity).

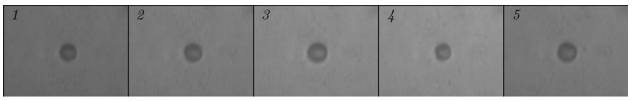

FIG. 4. Consecutive images of a contrast agent bubble from the high speed camera Brandaris operated at 14.3 million frames per second (time intervals between images are thus 69.8 ns), during one ultrasound cycle, of frequency 2.6 MHz. The bubble radius is initially 1.95 μm, and frame number 4 shows the bubble compression.

The change in compressibility is reflected on the dynamics of small amplitude oscillations as well. The linearization of the equations, setting $R(t)=R_0[1+x(t)]$, provides a damped oscillator equation $\ddot{x}+2\gamma\dot{x}+\omega_0^2 x=-P_{\text{ac}}(t)/\rho_l R_0^2$, with a damping coefficient $\gamma=2\mu/\rho_l R_0^2+2\kappa_s/\rho_l R_0^3+3\kappa[P_0+2\sigma(R_0)/R_0]/2c\rho_l R_0$, and an eigenfrequency simply writing

$$\omega_0^2=\frac{3}{\rho_l R_0^2}K_V. \tag{6}$$

In the free bubble state, this equation provides the Minnaert frequency as expected. It can be concluded that bubbles in the elastic state have a much higher resonance frequency than free or buckled bubbles, because their compression modulus is higher, consistently with the derivation of de Jong.[21]

III. RESULTS

A. Compression-only behavior

At small acoustic amplitudes, the model presented earlier provides a linear radius response to the pressure similar to other Rayleigh-Plesset models with constant surface tension.

Under large pressure amplitudes, the bubble will experience an original non-linear response. It will likely buckle in its compression phase, which cancels out any surface tension. On the other hand, the surface tension rapidly rises during the expansion phase, and this asymmetry in surface tension provides an asymmetry in capillary pressure, especially strong for small bubbles. The radius response curve displays this asymmetry by a "compression-only" behavior.

Recent experiments, realized with the high-speed camera Brandaris 128,[22] reveal the existence of such asymmetric oscillations of bubbles. The experiment was conducted as follows: SonoVue® and BR14 contrast bubbles, supplied by Bracco Research SA, Geneva, Switzerland, were prepared in the vial about 24 h prior to the recording of their dynamics. Both types of bubbles present a phospholipidic coating, SonoVue® containing SF_6 gas,[5] while BR14 contains the even less soluble C_4F_{10} gas.[23] The contrast bubbles were led through a capillary fiber inside a small water-filled container. An Olympus microscope with a 60× high resolution water immersed objective and a 2× magnifier produced an image of the contrast bubbles. The image was then relayed to the high speed framing camera Brandaris 128. A broadband single element transducer was mounted at 75 mm from the capillary. A Tektronix AWG 520 arbitrary waveform generator provided a signal amplified by an ENI A-500 amplifier. The bubble response was investigated with sequential ultrasound bursts of 8 cycles at frequencies ranging from

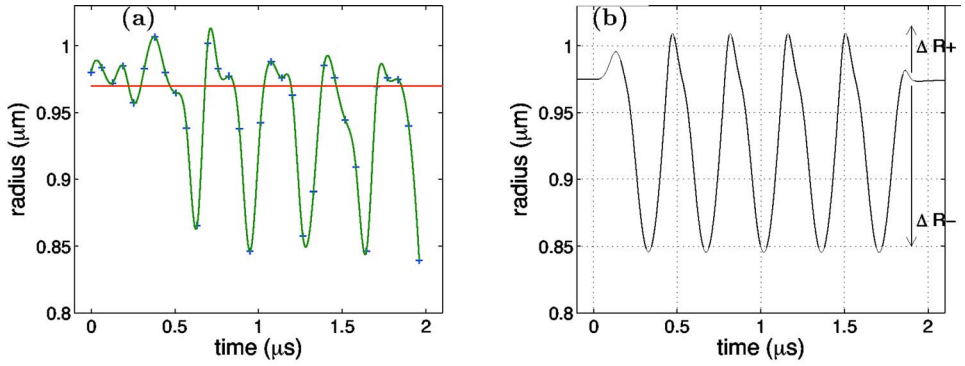

FIG. 5. (Color online) (a) Experimental recording of the radius of a SonoVue® bubble vs time, with the fast framing camera Brandaris (beginning of a 2.9 MHz pulse with an acoustic pressure of 130 kPa). (b) Simulation. The fitted shell parameters are $R_{buckling}=R_0=0.975$ μm, $\chi=1$ N/m, $\kappa_s=15\times10^{-9}$ N and $\sigma_{break\text{-}up}>1$ N/m (resistant shell). The liquid properties are $\rho_l=10^3$ kg/m^3, $\mu=0.001$ Pa s, $c=1480$ m/s, and the polytropic gas exponent is $\kappa=1.095$.

1.5 to 5 MHz. The camera was operated at a framing rate of 15 million frames per second, resolving the insonified microbubble dynamics. From the images (see Fig. 4) the radius versus time curves for each individual bubble were extracted [Fig. 5(a)], from which the compression-only behavior is apparent.

This phenomenon is very well modeled with our effective surface tension model, see Fig. 5(b), assuming the bubble to be initially in a tension-less state ($R_{buckling}=R_0$), and allowing the shell to support elevated tensions. Note that the fitted elastic modulus and shell viscosity of this shell are of the same order of magnitude than the average ones from attenuation measurements on bubble populations by Gorce *et al.*,[24] who deduced an average shell elasticity $\chi=S_p/2=0.55$ N/m and shell friction $\kappa_s=S_f/12\pi=7.2\times10^{-9}$ N.

B. Aging of micro-bubbles: Effect on the oscillation response

The initial effective tension of the monolayer depends on the history of the bubble. During their formation in the vial, lipid molecules are adsorbed at the interface, which reduces the effective surface tension, in proportion to the surface concentration n/A of adsorbed lipid molecules. The bubble is initiated in the tensed elastic state, its area being above the buckling area, $A_{buckling}=n*a_{buckling}$.

Dissolution of the gas in the surrounding liquid will "deflate" the bubble and reduce its area towards a tension-less state (like the deflation of a rubber balloon), below which the bubble will buckle. In the tension-less state dissolution is much slower, since the capillary overpressure (typically an atmospheric pressure for micrometric bubbles) vanishes and the rate of radius decrease is proportional to inside pressure (which determines the dissolution concentration in the liquid according to Henry's law). Bubbles therefore *spontaneously tend to their buckling radius*, and then shrink much more slowly, compared to bubbles of constant surface tension. The reduction of surface tension is the main mechanism to account for increased longevity from the coating, since the gas permeability of 16- and 18-carbons phospholipids coatings is high.[8]

Experiments show that asymmetric oscillations become more pronounced in the course of dissolution, see Fig. 6. Our interpretation is that the bubble reaches the tension-less state, where buckling occurs. According to the present model, the asymmetry is the signature of the variation in surface tension during each cycle, and this variation is the highest near buckling.

The asymmetry can be monitored by the ratio $\Delta R^+/\Delta R^-$ of the positive and negative radius excursions [defined by $\Delta R^+=\max(R)-R_0$ and $\Delta R^-=R_0-\min(R)$, both materialized in Fig. 5(b)]. Simulations demonstrate indeed that the compression-only asymmetry ($\Delta R^+/\Delta R^-<1$), is the more pronounced when $R_0/R_{buckling}\sim1$ (see Fig. 7), the tension asymmetry during the oscillation being maximal.

This behavior is to be contrasted with the large amplitude oscillation of bubbles with a constant surface tension, which tends to produce higher positive excursions. It is seen in the same figure when the bubble radius is well above $R_{buckling}$ (free bubble state, $\sigma=\sigma_{water}$) or well below $R_{buckling}$ (tension-less state, $\sigma=0$). The response curve slightly depends on frequency: varying the frequency between 1 and 4 MHz changes $\Delta R^+/\Delta R^-$ by about 10%.

Repeated pulses on a bubble accelerate the gas dissolution, as evidenced in Fig. 6 by the sudden decrease after the first pulse and the subsequent pulses. Two mechanisms could account for this effect. First, the initial pulses may expel

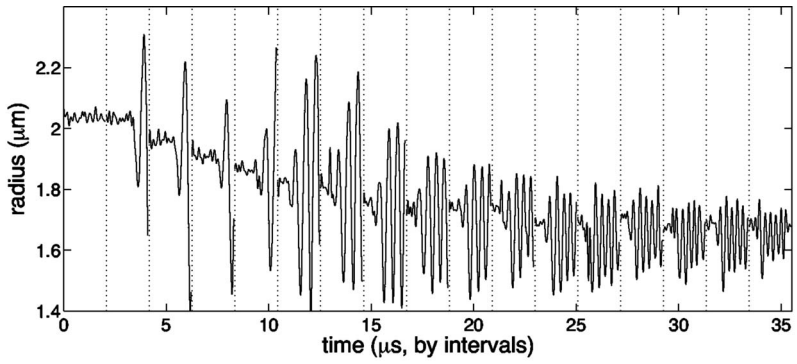

FIG. 6. Experimental recordings of repeated acoustic pulses of 100 kPa on a single bubble, separated by 50 ms (break of time at vertical lines). The oscillation asymmetry increases pulse after pulse. (Frequency is increasing from 1.5 to 4 MHz, inducing amplitude changes).

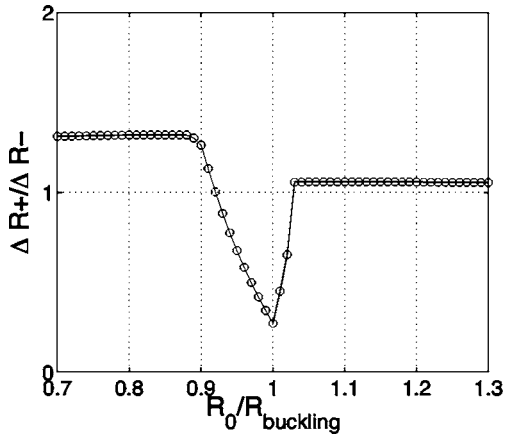

FIG. 7. Simulated asymmetry of the oscillation for varying starting radii. Acoustic pulse and shell properties: same as Fig. 5.

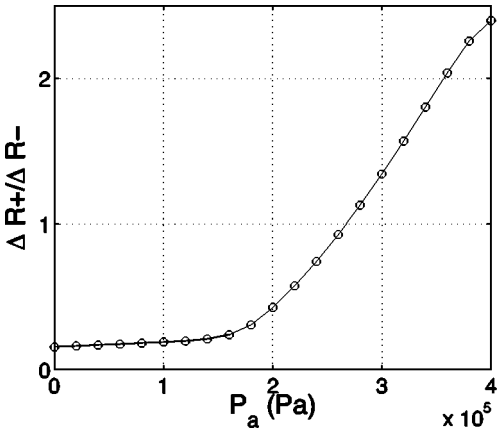

FIG. 9. Effect of an increasing acoustic pressure on the asymmetry of the response [same parameters as in Fig. 8(b)].

some lipid molecules and reduce the buckling radius, to which the bubble will relax. Another explanation would be an "inverse" rectified-diffusion generated by compression-only behaviors. The gas pressure increases during the compression phase, while it remains close to the pressure at rest during expansion (a symmetric oscillation would alternately compress and expand the gas). The concentration of gas in the liquid near the interface being proportional to gas pressure (Henry's law), the asymmetry, even small, tends to force more gas out of the bubble. This "inverted" rectified-diffusion would be the opposite of the usual rectified-diffusion effect that counteracts dissolution for free gas bubbles.[25]

A quantitative evaluation of this effect follows from the expression of the rate of dissolution of an oscillating bubble[25,26]

$$\frac{d}{dt}\overline{R(t)} = \frac{Dc_0}{\rho_g \overline{R(t)}^2}\left[\frac{c_\infty}{c_0} - \frac{\overline{P_g(t)R(t)^4}}{P_0\overline{R(t)^4}}\right] \times \left\{\int_0^\infty \frac{dh'}{\overline{[3h'+R(t)^3]^{4/3}}}\right\}^{-1}, \quad (7)$$

where the overline is the average over one period, this equation being valid for an evolution slow at the scale of the period. The diffusivity of the gas is D, its volumic mass ρ_g, its saturation concentration c_0, and its concentration far from the bubble c_∞. The last factor containing an integration along the variable h' does not change sign, and tends to R^4 for small amplitude oscillations. A compression-only signal produces a stronger "averaged" pressure term $\overline{P_g(t)R(t)^4}/\overline{R(t)^4}$ [for instance it amounts to $1.2P_0$ from the simulation in Fig. 5(b)], which accelerates dissolution. Even at R_{buckling}, where the capillary overpressure vanishes, inverted rectified diffusion can force dissolution in a fully saturated liquid with $c_\infty/c_0=1$.

C. Rupture of the shell

The shell can withstand finite tensions only in its shell: starting from a compression-only signal and increasing the acoustic pressure step by step shows that a strong positive radius excursion suddenly appears above a critical pressure [see Fig. 8(a)]. In this new state, the bubble oscillates as a free bubble: we interpret this behavior as the effect of the shell rupture.

To model the rupture, we assume that above a critical tension, $\sigma_{\text{break-up}}$, the shell breaks up and that part of the bubble surface is uncovered. Once this threshold has been reached, the surface tension upper bound will be the surface tension of water, σ_{water}. We can therefore simulate the effect of an increasing acoustic pressure on a bubble [see Fig. 8(b)].

The compression-only behavior ($\Delta R^+/\Delta R^- < 1$) is interrupted by the break-up of the shell: the non-linear behavior then favors positive excursions of the radius, as seen in experiment, as for standard large pressure Rayleigh-Plesset dynamics (see Fig. 9).

IV. CONCLUSIONS

We presented a simple model for the dynamical properties of coated contrast agents bubbles, with three parameters:

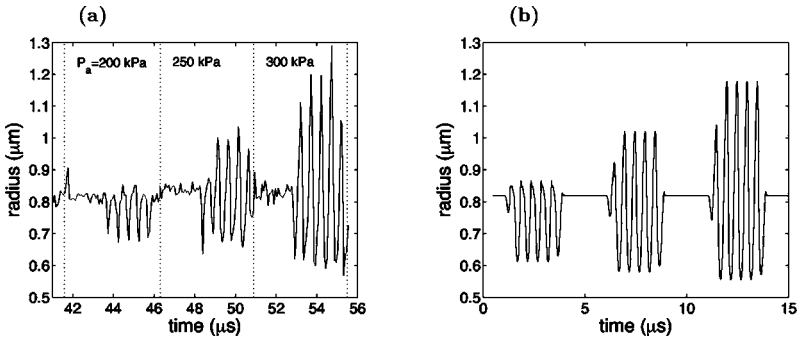

FIG. 8. (a) Experimental recordings of a BR14 bubble response to repeated 2 MHz pulses separated by 60 ms, with an increasing acoustic pressure. (b) Simulation with the same acoustic pressures. The fitted shell parameters are $R_{\text{buckling}}=R_0=0.82\ \mu$m, $\chi=1$ N/m, $\kappa_s=7.2\times10^{-9}$ N, while the critical break-up is $\sigma_{\text{break-up}}=0.13$ N/m.

a buckling surface radius, a shell compressibility, and a break-up shell tension. It predicts a compression-only behavior of the bubble, a highly non-linear response. It occurs when its radius is close to the buckling radius, a state that naturally occurs with dissolution of gas, or that can be accelerated by repeated pulses. High-frequency image recordings with lipid coated microbubbles reveal the existence of such asymmetric oscillations, and validate the model. The break-up of the shell is modeled by a third parameter, a finite tension of the bubble shell above which bare interfaces are created, with a corresponding change in bubble dynamics.

Possible applications of the model include: the characterization of coated microbubbles, the description of acoustic echoes and their use in non-linear or pulse-inversion imaging, and the prediction of the effect of repeated pulses or of long-term experiments.

ACKNOWLEDGMENTS

The authors would like to thank Joris Timmermans for his help in computations. They appreciated fruitful discussions with François Graner and Wouter den Otter.

APPENDIX: COMPARISON WITH THE ELASTICITY OF A SOLID SHELL LAYER

Like monolayer coatings, the elasticity of a thin solid shell of thickness $\epsilon \ll R$ is characterized by a two-dimensional compression modulus $\chi = A(d\sigma/dA)$, where σ is the isotropic in-plane tension (shear of the surface does not occur with a radial expansion, and bending is neglected assuming an initial curvature close to the spontaneous curvature). Additionally, the solid shell has two interfaces, with a surface tension σ_1 for the inner interface and σ_2 for the outer interface. The mechanical equilibrium balance for any small change in bubble area around the tensionless shell area A_0 reads $\delta W = \chi(A/A_0 - 1)dA + \sigma_1 dA + \sigma_2 dA - (P_g - P_l)dV = 0$, from which we obtain the pressure jump at the liquid-gas interface $P_g - P_l = 2[\sigma_1 + \sigma_2 + \chi(A/A_0 - 1)]/R$. The effective surface tension of the shell thus reads

$$\sigma = \sigma_1 + \sigma_2 + \chi\left(\frac{R^2}{R_0^2} - 1\right), \tag{A1}$$

it is a linear function of the bubble area, like in the lipid *monolayer* coated bubble model [Eq. (1) for the elastic state, with $\sigma(R_0) = \sigma_1 + \sigma_2$].

The model for a thick elastic shell by Church[27] provides the same effective surface tension law when the shell thickness ϵ tends to be small compared to the radius. In this model the shell has a bulk shear modulus G_s and is incompressible in volume (the thickness thus varies around its equilibrium value during the oscillation). From the Church model at small thicknesses we find that the shell contribution can be expressed with an effective tension law as in Eq. (A1), using a two-dimensional elastic modulus $\chi = 3G_s\epsilon$, which is a classical result of the elasticity of thin plates.[28]

[1] J. M. Crane and S. B. Hall, "Rapid compression transforms interfacial monolayers of pulmonary surfactant," Biophys. J. **80**, 1863 (2001).
[2] A. L. Klibanov, "Ultrasound contrast agents: Development of the field and current status," Top. Curr. Chem. **222**, 73 (2002).
[3] S. Lee, D. H. Kim, and D. Needham, "Equilibrium and dynamic interfacial tension measurements at microscopic interfaces using a micropipet technique. 2: Dynamics of phospholipid monolayer formation and equilibrium tensions at the water-air interface," Langmuir **17**, 5544 (2001).
[4] J. M. Crane, G. Putz, and S. B. Hall, "Persistence of phase coexistence in disaturated phosphatidylcholine monolayers at high surface pressures," Biophys. J. **77**, 3134 (1999).
[5] M. Schneider, M. Arditi, M.-B. Barrau, J. Brochot, A. Broillet, R. Ventrone, and F. Yan, "BR1: A new ultrasonic contrast agent based on sulfur hexafluoride-filled microbubbles," Invest. Radiol. **30**, 451 (1995).
[6] F. Pétriat, E. Roux, J.-C. Leroux, and S. Giasson, "Study of molecular interactions between a phospholipidic layer and a *p*H-sensitive polymer using the langmuir balance technique," Langmuir **20**, 1393 (2004).
[7] M. I. Sández, A. Suárez, and A. Gil, "Surface pressure-area isotherms and fluorescent behavior of phospholipids containing labeled pyrene," J. Colloid Interface Sci. **250**, 128 (2002).
[8] M. A. Borden and M. L. Longo, "Dissolution behavior of lipid monolayer-coated, air-filled microbubbles: Effect of lipid hydrophobic chain length," Langmuir **18**, 9225 (2002).
[9] A. Saint-Jalmes, F. Graner, F. Gallet, and B. Houchmandzadeh, "Buckling of a bidimensional solid," Europhys. Lett. **28**, 565 (1994).
[10] A. Saint-Jalmes and F. Gallet, "Buckling in a solid langmuir monolayer: Light scattering measurements and elastic model," Eur. Phys. J. B **2**, 489 (1998).
[11] D. H. Kim, M. J. Costello, P. B. Duncan, and D. Needham, "Mechanical properties and microstructure of polycrystalline phospholipid monolayer shells: Novel solid microparticles," Langmuir **19**, 8455 (2003).
[12] P. B. Duncan and D. Needham, "Test of the epstein-plesset model for gas microparticle dissolution in aqueous media: Effect of surface tension and gas undersaturation in solution," Langmuir **20**, 2567 (2004).
[13] F. Graner, S. Perez-Oyarzun, A. Saint-Jalmes, C. Flament, and F. Gallet, "Phospholipidic monolayers on formamide," J. Phys. II **5**, 313 (1995).
[14] G. Gaines and L. George, *Insoluble Monolayers at Liquid-Gas Interfaces* (Interscience, New York, 1966).
[15] K. E. Morgan, J. S. Allen, P. A. Dayton, J. E. Chomas, A. L. Klibanov, and K. W. Ferrara, "Experimental and theoretical evaluation of microbubble behaviour: Effect of transmitted phase and bubble size," IEEE Trans. Ultrason. Ferroelectr. Freq. Control **47**, 1494 (2000).
[16] D. Chatterjee and K. Sarkar, "A newtonian rheological model for the interface of microbubble contrast agents," Ultrasound Med. Biol. **29**, 1749 (2003).
[17] R. E. Glazman, "Effects of an adsorbed film on gas bubble radial oscillations," J. Acoust. Soc. Am. **74**, 980 (1983).
[18] P.-G. de Gennes, F. Brochard-Wyart, and D. Quéré, *Capillarity and Wetting Phenomena: Drops, Bubbles, Pearls, Waves* (Springer, New York, 2004).
[19] M. P. Brenner, S. Hilgenfeldt, and D. Lohse, "Single-bubble sonoluminescence," Rev. Mod. Phys. **74**, 425 (2002).
[20] A. Properetti, "Bubble phenomena in sound fields: Part one," Ultrasonics **22**, 69 (1984).
[21] N. de Jong, R. Cornet, and C. Lancée, "Higher harmonics of vibration gas-filled microspheres. part one: simulations," Ultrasonics **32**, 447 (1994).
[22] C. T. Chin, C. Lancée, J. Borsboom, F. Mastik, M. Frijlink, N. de Jong, M. Versluis, and D. Lohse, "Brandaris 128: A digital 25 million frames per second camera with 128 highly sensitive frames," Rev. Sci. Instrum. **74**, 5026 (2003).
[23] M. Schneider, A. Broillet, P. Bussat, N. Giessinger, J. Puginier, R. Ventrone, and F. Yan, "Grayscale liver enhancement in VX2 tumor-bearing rabbits using BR14, a new ultrasonographic contrast agent," Invest. Radiol. **32**, 410 (1997).
[24] J. M. Gorce, M. Arditi, and M. Schneider, "Influence of bubble size distribution on the echogenicity of ultrasound contrast agents: A study of Sonovue," Invest. Radiol. **35**, 661 (2000).
[25] S. Hilgenfeldt, D. Lohse, and M. P. Brenner, "Phase diagrams for sonoluminescing bubbles," Phys. Fluids **8**, 2808 (1996).
[26] M. Fyrillas and A. J. Szeri, "Dissolution or growth of soluble spherical oscillating bubbles," J. Fluid Mech. **277**, 381 (1994).
[27] C. C. Church, "The effects of an elastic solid surface layer on the radial pulsations of gas bubbles," J. Acoust. Soc. Am. **97**, 1510 (1995).
[28] D. Boal, *Mechanics of the cell* (Cambridge University Press, Cambridge, 2002).

Effect of a downstream ventilated gas cavity on turbulent boundary layer wall pressure fluctuation spectra[a)]

Steven D. Young, Timothy A. Brungart, and Gerald C. Lauchle[b)]
Applied Research Laboratory, The Pennsylvania State University, P.O. Box 30, State College, Pennsylvania 16804-0030

Michael S. Howe
College of Engineering, Boston University, 110 Cummington Street, Boston, Massachusetts 02215

(Received 3 February 2005; revised 2 September 2005; accepted 12 September 2005)

An analytical and experimental investigation is made of the effect of a 2-D ventilated gas cavity on the spectrum of turbulent boundary layer wall pressure fluctuations upstream of a gas cavity on a plane rigid surface. The analytical model predicts the ratio of the wall pressure spectrum in the presence of the cavity to the blocked wall pressure spectrum that would exist if the cavity were absent. The ratio is found to oscillate in amplitude with upstream distance $(-x)$ from the edge of the cavity. It approaches unity as $-\omega x/U_c \to \infty$, where ω is the radian frequency and U_c is the upstream turbulence convection velocity. To validate these predictions an experiment was performed in a water tunnel over a range of mean flow velocities. Dynamic wall pressure sensors were flush mounted to a flat plate at various distances upstream from a backward facing step. The cavity was formed downstream of the step by injecting carbon dioxide gas. The water tunnel measurements confirm the predicted oscillatory behavior of the spectral ratio, as well as its relaxation to unity as $-\omega x/U_c \to \infty$. For $-\omega x/U_c > 7$ the cavity has a negligible influence on the upstream wall pressure fluctuations. © *2005 Acoustical Society of America.* [DOI: 10.1121/1.2109367]

PACS number(s): 43.28.Ra, 43.30.Nb [SFW] Pages: 3506–3512

I. INTRODUCTION

The application of supercavitation technology to undersea vehicles has made possible order-of-magnitude increases in speed compared to the speeds achieved with fully wetted vehicles. The technology employs a wetted upstream cavitator to generate a separated flow that is ventilated with gas to envelope the entire vehicle downstream from the cavitator. The gas/water interface may be viewed as a pressure release surface originating at the cavitator edge. Therefore, any unsteady pressures that develop on the cavitator surface must decay to zero as they approach and convect across the edge and onto the gas/water interface. This decay must occur in practice starting at some finite, frequency-dependent distance upstream from the cavitator edge and could reduce the need for techniques to minimize turbulence effects on sensors placed within this distance. With turbulence or near-field noise sources sufficiently suppressed, attention can be focused on suppressing the acoustic field stemming from cavity-related sources such as (*i*) turbulence quadrupoles adjacent to the nominally pressure release interface; (*ii*) surface normal velocity fluctuations produced by the impinging jet of gas from the gas source maintaining the cavity; (*iii*) the unsteady volume velocity of gas input from the gas jet; and (*iv*) the break-up of the interface into spray. It is the objective of this work to identify the distances from the cavitator edge and frequencies associated with the decay in the spectra of the turbulent boundary layer wall pressure fluctuations. An analytical model is developed to predict the trends, which is then validated experimentally.

II. ANALYTICAL MODEL

Figure 1 displays a schematic of the configuration modeled. Water flows in the x direction where the upstream surface $(x<0, y=0)$ supports a fully developed turbulent boundary layer (TBL). The TBL separates from the backward facing step at $x=0$. The separated flow encounters a stream of gas entering from a 2-D side branch that inhibits contact between the water and the wall downstream of the side branch. Wall pressure fluctuations are generated by the TBL for $x<0$. These fluctuations interact with both the edge and the gas stream interface, causing the wall pressures upstream of the edge to differ from those generated beneath a nonseparating TBL. The edge diffraction interaction is modeled in terms of the blocked wall pressure fluctuation spectra for a 2-D TBL in a manner similar to that of Chase[1] and Chandiramani[2] for calculating trailing edge noise.

Let $p_I(\vec{x},t)$ be the fluctuating pressure that would be produced by the boundary layer turbulence if the rigid wall were absent and water alone filled all of space, where t denotes time and $\vec{x}$ is position. The pressure $p'(\vec{x},t)$ is then defined to be the additional, scattered pressure produced by the interaction of the turbulence with the solid surface and edge. The pressures p_I and p' are required to satisfy the condition that

[a)]Portions of this work were presented in "Effect of a downstream ventilated gas cavity on the spectrum of turbulent boundary layer wall pressure fluctuations," Proceedings of the 2004 ASME International Mechanical Engineering Conference and RD&D Expo, Anaheim, CA, November 2004.
[b)]Also with the Graduate Program in Acoustics.

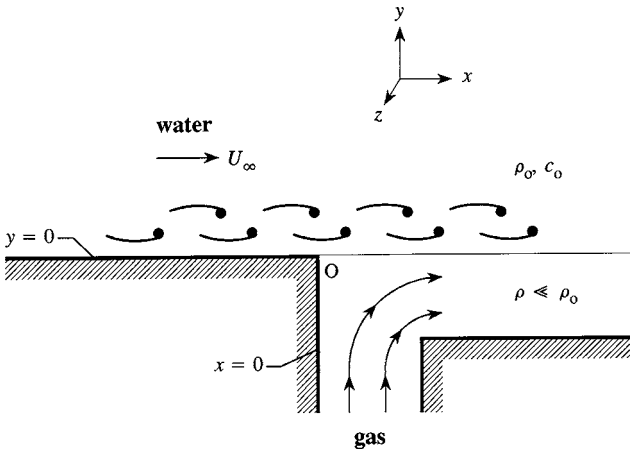

FIG. 1. Schematic of the two-phase flow problem that is investigated theoretically and experimentally. Gas is injected into the separated flow region downstream of a backward facing step ($x=0$) to form a ventilated cavity. The cavity interface is modeled as a free streamline with pressure release surface for $x>0$ at $y=0$.

the normal velocity component must be zero on the wall $y=0$ upstream of the cavity. At high Reynolds numbers this means that

$$\frac{\partial p_I}{\partial y} + \frac{\partial p'}{\partial y} = 0, \quad x < 0,\ y = 0. \tag{1}$$

In turbulence-free regions, and at very low Mach numbers, radian frequency-dependent pressure fluctuations, $p(\vec{x},\omega)$, satisfy the Helmholtz equation:

$$(\nabla^2 + k_0^2)p = 0, \quad y > 0, \tag{2}$$

where $k_0=\omega/c_0$ is the acoustic wavenumber, c_0 being the sound speed. The concept of a turbulence-free region involves the assumption[1–3] that the turbulence may be ignored except as a source that generates the pressure p_I.

The interface between the gas and water is modeled as a free streamline parallel to the undisturbed mean flow and, therefore, coincides with the positive x axis. This should be an adequate first approximation, at least close to the separation point O, where the dominant interactions occur. The very large density differential across the free streamline permits the interface to be regarded as a pressure release surface expressed by the condition

$$p_I + p' = 0, \quad x > 0,\ y = 0. \tag{3}$$

The error incurred in modeling the interface as a pressure release boundary is of the order of the gas-to-water density ratio. The edge-generated pressure fluctuations in the water are assumed to be independent of the side branch geometry due to either the large density differential between the gas and the water, intrinsic damping of the cavity's gas, or the natural leakage of acoustic energy due to the waveguide's open, effectively infinite shape.

The pressure $p_I(\vec{x},\omega)$ is an outgoing solution of Eq. (2) just "below" the boundary layer sources. The incident pressure is set equal to half the boundary layer blocked pressure, $p_s(x,z,t)$, that the same turbulence would exert on an infinite, rigid plane wall coinciding with $y=0$. This "halving" assumption is used only to calculate the diffracted field at the edge and is based on the hypothesis that the turbulence may be regarded as frozen as it passes over the edge. Therefore, just above $y=0$, the incident pressure can be written as

$$p_I(\vec{x},\omega) = \frac{1}{2}\int_{-\infty}^{\infty} p_s(\vec{k},\omega) e^{i(k_1 x + k_3 z - \gamma(k_1,k_3)y)}\, dk_1 dk_3,$$
$$\vec{k} = (k_1, \gamma, k_3), \tag{4}$$

where z or subscript "3" denotes the cross-stream coordinate direction, $p_s(\vec{k},\omega)$ is the wavevector-frequency representation of the blocked pressure, and $\gamma(k_1,k_3)=\sqrt{k_0^2-k_3^2-k_1^2}$. Equations (1)–(3) are then used to determine the scattered pressure p' produced by each Fourier component $\frac{1}{2}p_s(\vec{k},\omega)e^{i(k_1x+k_3z-\gamma(k_1,k_3)y)}$ of p_I. With both p_I and p' written in terms of $p_s(\vec{k},\omega)$, the equations may be manipulated and combined to express the wall pressure as

$$p_w(x,z,t) = \int_{-\infty}^{\infty}\int_{-\infty}^{\infty} p_s(\vec{k},\omega)\mathrm{erf}(e^{-i\pi/4}|x|^{1/2}\sqrt{(k_0^2-k_3^2)^{1/2}+k_1})$$
$$\times e^{i(k_1x+k_3z-\omega t)}\, dk_1 dk_3\, d\omega. \tag{5}$$

Here the error function is defined by

$$\mathrm{erf}(x) = \frac{2}{\sqrt{\pi}}\int_0^x e^{-\mu^2}\, d\mu. \tag{6}$$

The argument of the error function has a positive real part for all real values of k_1, so that the error function is approximately unity as $x\to\infty$. Thus, $p_w\to p_s$ far upstream of the edge, at distances exceeding the characteristic eddy dimension. On the other hand, the error function vanishes as $x\to 0$, where the net surface pressure fluctuations vanish, in accordance with the pressure release condition. Note that the error function's complex argument, whose phase is $-\pi/4$, may be replaced using an alternate combination of real-valued Fresnel integrals.[4]

Equation (5) can be transformed to supply the frequency pressure spectrum in the form

$$\phi_{pp}(\omega,x) = \int_{-\infty}^{\infty}\int_{-\infty}^{\infty} \Phi(k_1,k_3,\omega)|E(k_1,k_3,k_0,x)|^2\, dk_1\, dk_3, \tag{7}$$

$$|E(k_1,k_3,k_0,x)|^2 = |\mathrm{erf}(e^{-i\pi/4}|x|^{1/2}\sqrt{(k_0^2-k_3^2)^{1/2}+k_1})|^2. \tag{8}$$

The parameter $\Phi(k_1,k_3,\omega)$ is the wavevector-frequency spectrum of the TBL blocked wall pressure fluctuations. If a finite size sensor is used in the measurement of $\phi_{pp}(\omega,x)$, then $\Phi(k_1,k_3,\omega)$ must be weighted by the sensor's wavevector response function, $|H(k_1,k_3,\vec{\ell})|^2$, say, where the parameter $\vec{\ell}$ depends on the geometry of the pressure transducer. The point pressure spectrum measured by such a transducer is then determined by

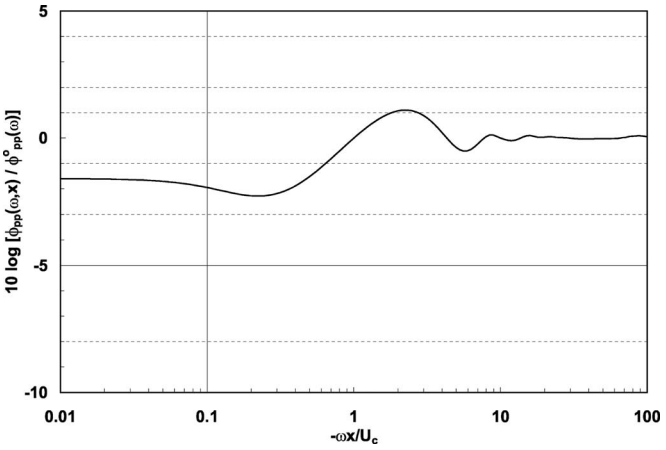

FIG. 2. Model prediction of the ratio of the point spectrum of the TBL wall pressure fluctuations upstream of the step edge to the blocked point pressure spectrum. Equation (11) is a numerical integration over all wavenumbers.

$$\phi_{pp}(\omega,x) = \int_{-\infty}^{\infty}\int_{-\infty}^{\infty} \Phi(k_1,k_3,\omega) \times |H(k_1,k_3,\vec{\ell})|^2 |E(k_1,k_3,k_0,x)|^2 \, dk_1 \, dk_3. \quad (9)$$

For a circular transducer of radius R with a uniform sensitivity distribution over the face of the sensing element,

$$|H(k_1,k_3,R)|^2 = \left| \frac{2J_1(kR)}{kR} \right|^2, \quad (10)$$

where $J_1(kR)$ is the Bessel function of the first kind and $k = \sqrt{k_1^2+k_3^2}$.

Note that far upstream of the step edge, the blocked point TBL wall pressure fluctuation frequency spectrum will correspond to the actual wall pressure frequency spectrum. Thus, the ratio of the point spectrum of the TBL wall pressure fluctuations at a given distance upstream from the step edge, $\phi_{pp}(\omega,x)$, to the blocked point pressure spectrum, $\phi_{pp}^0(\omega)$, can be evaluated numerically from

$$\frac{\phi_{pp}(\omega,x)}{\phi_{pp}^0(\omega)} = \frac{\int_{-\infty}^{\infty}\int_{-\infty}^{\infty}\Phi(k_1,k_3,\omega)|H(k_1,k_3,R)|^2|E(k_1,k_3,k_0,x)|^2 \, dk_1 \, dk_3}{\int_{-\infty}^{\infty}\int_{-\infty}^{\infty}\Phi(k_1,k_3,\omega)|H(k_1,k_3,R)|^2 \, dk_1 \, dk_3}. \quad (11)$$

Figure 2 shows the spectral ratio computed from Eq. (11), using the Chase model[3] of $\Phi(k_1,k_3,\omega)$ and an assumed circular sensor diameter of $2R=2.54$ mm. The spectral ratio exhibits a decaying oscillation that approaches unity with increasing $-\omega x/U_c$, indicating that, at constant frequency, the TBL wall pressure fluctuations become independent of the effects of the ventilated cavity as the distance upstream of the step increases. Furthermore, as a result of contributions from cross-stream and nonconvective streamwise wavevector components retained in the integrand of (11), the spectral ratio converges to −1.6 dB as $-\omega x/U_c$ approaches zero. The transducer wavevector response function, $|H(k_1,k_3,R)|^2$, was found to have a negligible effect on the spectral ratio determined by (11), either when evaluated numerically or when replaced by unity. Thus, the spectral ratio shown in Fig. 2 may be considered as "universal."

III. EXPERIMENTAL SETUP

The experiments were performed in the rectangular test section of the 304.8-mm-diam water tunnel at ARL Penn State.[5] This tunnel is shown schematically in Fig. 3. A 152 by 318-mm plate assembly, shown schematically in Fig. 4, was mounted to the tunnel wall in place of one of the test section's standard windows. The plate assembly consisted of a 7.9-mm-high backward facing step located 102 mm downstream of the leading edge. Three cover plates were fastened downstream from the step. The axial positions of the cover plates were adjustable and created slots for gas injection into the water. Compressed carbon dioxide (CO_2) was injected to form the ventilated cavity behind the step. The CO_2 passed through manifolds beneath the cover plates and then into the water through two slots. An additional cover plate could be placed over the recessed area downstream from the step to form a flat surface, flush with the tunnel wall (i.e., a canonical flat plate arrangement).

Eight PCB Model 105M147 piezoelectric pressure transducers with 2.52-mm-diam sensing elements were flush-mounted into the plate assembly as shown in Fig. 4. Six of the eight pressure sensors were paired axially along the plate, each pair separated by 63.5 mm and located 3.2 mm (sensors P5 and P6), 6.4 mm (sensors P2 and P3), and 9.5 mm (sensors P1 and P4) upstream from the step. Two additional pressure sensors were located 22.2 mm (sensor P7) and 41.3 mm (sensor P8) upstream from the step. A Zonic System 7000

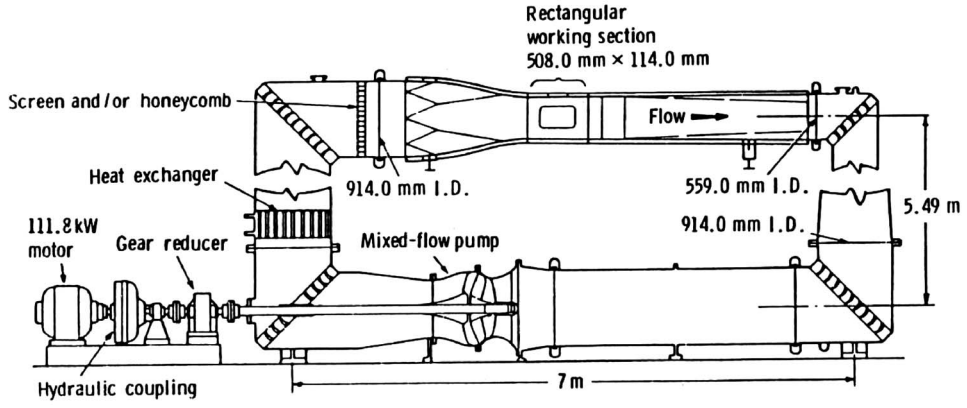

FIG. 3. Schematic of the ARL Penn State 304.8-mm-diam water tunnel facility with rectangular test section.

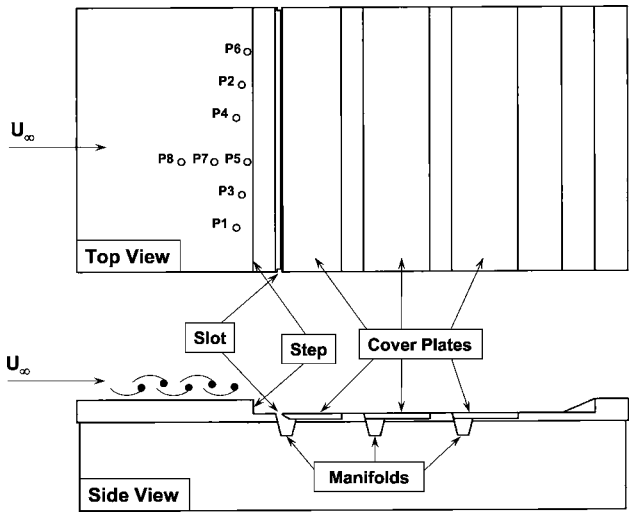

FIG. 4. Schematic of the instrumented plate assembly used in the experimental investigation. Measurements of the TBL wall pressure fluctuation spectra were made upstream of the backward facing step using eight flush-mounted pressure transducers (labeled P1–P8). Carbon dioxide gas was injected into the separated flow region downstream of the step through the plate manifolds to form the ventilated cavity. A cover plate was inserted into the recessed area downstream of the step for the canonical TBL wall pressure fluctuation measurements.

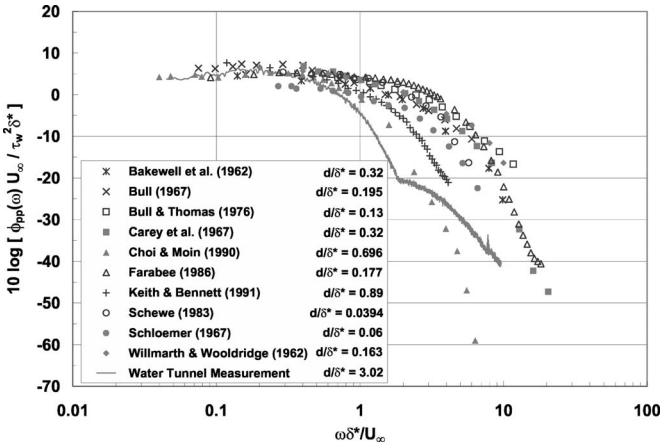

FIG. 5. Comparison of the water tunnel-measured TBL wall pressure fluctuation spectrum with archival spectra.[9] Collapse is expected[10] over the nondimensional frequency range $0.03 \leqslant \omega\delta^*/U_\infty \leqslant 0.6$.

digital signal processor was used for acquiring and processing the transducer signals into frequency spectra. The frequency spectra were acquired out to 20 kHz at 6.25 Hz resolution and linearly averaged over 256 data records for all wall pressure fluctuation measurements. The normalized random error for an autospectrum, ε_r, is given as[6]

$$\varepsilon_r[\phi_{pp}(\omega,x)] = \frac{1}{\sqrt{n_d}}, \tag{12}$$

where n_d is the number of realizations. Equation (12) gives a value of 0.063 for 256 averages and corresponds to a spectral estimate, with a 95% confidence interval, of ±12.5%. Increasing the number of averages taken during cavity ventilation was not feasible due to gas build-up inside the water tunnel.

Frequency and time domain signal processing techniques were used to reduce the effect of low-frequency acoustic plane wave propagation in the tunnel on the measured TBL wall pressure fluctuation spectra. The time domain technique relied on the subtraction of the signals from two amplitude- and phase-matched pressure sensors that were flush-mounted at the same axial location in the tunnel. The spectrum of the difference signal is a measurement of the TBL wall pressure spectrum signal with the coherent acoustic noise components removed.[7] The frequency domain technique applied the coherence function measured between the two cross-stream pressure sensors to the autospectrum of each sensor in the pair according to[7]

$$\phi^O_{pp-11} = \hat{\phi}^O_{pp-11}[1 - \sqrt{\gamma^2_{12}}]. \tag{13}$$

Here ϕ^O_{pp-11} is the spectrum of the TBL wall pressure fluctuations free from tunnel acoustic plane wave contamination. The quantity $\hat{\phi}^O_{pp-11}$ is the spectrum measured by the pressure sensor mounted flush to the plate containing contributions from both the turbulence-induced pressures and tunnel acoustic plane waves, and γ^2_{12} is the coherence measured between the two pressure sensors mounted at a common axial location on the plate. An advantage of the frequency domain noise cancellation technique is that it does not require any additional signal processing for the subtraction of the two time domain signals or the use of phase- and amplitude-matched sensors. The time and frequency domain noise cancellation techniques were effective at removing up to 24 and 29 dB, respectively, of noise contamination from the measured spectral levels at frequencies below 200 Hz. The reduced effectiveness of the time domain noise cancellation technique, compared to the frequency domain technique, stemmed from slight phase and amplitude mismatching between the sensors.[7] Pressures induced by tunnel vibration at the sensor measurement location are not cancelled with either of these techniques.

Initial spectral measurements were performed with all the cover plates in place which eliminated the step and formed a flat surface. This allowed for measurements of the blocked wall pressure fluctuation spectra beneath a canonical TBL whose velocity statistics are well established[8] and serve as a baseline for comparison to the spectra measured with a downstream ventilated cavity. It was anticipated that the assumptions inherent to Eq. (11) would be met reasonably well with the experimental setup in the water tunnel, given the small thickness of the boundary layer (δ^*=0.932 mm) relative to both the distance separating the tunnel's surfaces from the measurement locations of interest (114 mm) and the thickness of the ventilated gas cavity (7.9 mm). The tunnel velocity ranged from approximately 4.6 to 18.3 m/s for the subject experiments. Gas injection rates varied from 4.0 to 7.5 m^3/h, depending on the tunnel velocity.

IV. CANONICAL TBL WALL PRESSURE FLUCTUATION SPECTRA

Figure 5 shows a typical TBL wall pressure fluctuation spectrum for the equilibrium TBL configuration (P5 at 12.2 m/s), nondimensionalized with mixed flow variables

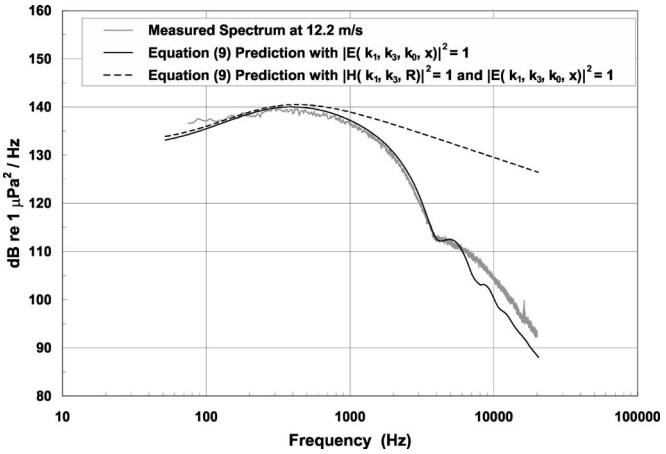

FIG. 6. Comparison of the measured and predicted spectra of the TBL wall pressure fluctuations for the canonical flat plate arrangement at 12.2 m/s. For the equilibrium TBL, the error function in the theoretical prediction [Eq. (9)] is set to unity. In addition, Eq. (9) predictions are computed with the transducer spatial averaging effects included and with $|H(k_1,k_3,R)|^2$ set equal to unity.

and compared to the archival wall pressure fluctuation spectra compiled by Keith *et al.*[9] According to Farabee and Casarella,[10] the TBL wall pressure fluctuation spectra should collapse over the nondimensional frequency range of $0.03 \leqslant \omega\delta^*/U_\infty \leqslant 0.6$ when mixed flow variables are used. Here δ^* is the TBL displacement thickness at the measurement point, and mixed flow variables means that both inner and outer flow variables are used in spectral normalization. At sensor P5 and a 12.2 m/s tunnel velocity, $\delta^*=0.932$ mm and adheres to the $\delta^* \propto U^{-1/5}x^{4/5}$ power law given by Schlichting[11] for other streamwise locations and tunnel velocities.

Transducer spatial averaging effects must be considered in assessing how well the spectra collapse in Fig. 5. According to Corcos,[12] the water tunnel-measured wall pressure fluctuation spectrum shown in Fig. 5 is attenuated by more than 1 dB for $\omega\delta^*/U_\infty \geqslant 0.17$. For $0.03 \leqslant \omega\delta^*/U_\infty \leqslant 0.17$, the water-tunnel-measured spectrum is attenuated by less than 1 dB and is observed to fall within the ±2-dB scatter of the archival spectra presented by Keith *et al.*[9] For $0.17 \leqslant \omega\delta^*/U_\infty \leqslant 0.6$ the measured spectrum is attenuated by more than 1 dB. Nevertheless, the water tunnel-measured wall pressure fluctuation spectrum is within the ±3-dB scatter of the archival spectra.

Figure 6 compares the spectrum of TBL wall pressure fluctuations measured with sensor P5 at 12.2 m/s to spectra predicted using Eq. (9) with the error function term set equal to unity. Here Eq. (9) uses the Chase model[3] of $\Phi(k_1,k_3,\omega)$, and the predictions are computed with $|H(k_1,k_3,R)|^2$ both evaluated numerically to account for spatial averaging effects and set to unity. When an assumed circular sensor diameter of $2R=2.54$ mm is used in $|H(k_1,k_3,R)|^2$, this operation effectively accounts for transducer spatial averaging effects in the point pressure spectrum prediction. See Refs. 7 and 13 for additional details regarding Eq. (9).

The predicted TBL wall pressure fluctuation spectrum that includes the spatial averaging effects is within 2 dB of the measured spectrum for frequencies below 6 kHz. At frequencies above 6 kHz, the measured spectrum is ~5 dB above the predicted spectrum, which may be an effect of background noise (possibly due to bubble-related noise) in the water tunnel. The notch in both spectra at approximately 4 kHz has been identified as the first zero of the transducer wavevector response function, Eq. (10).

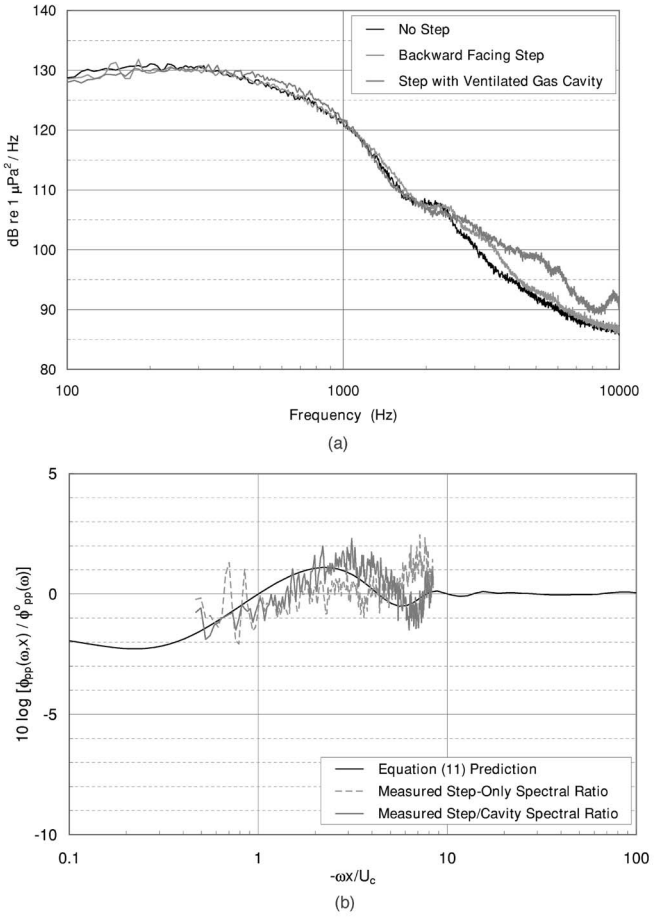

FIG. 7. (a) Comparison of the measured wall pressure fluctuation spectra for the equilibrium TBL (i.e., no step), the TBL with the backward facing step, and the TBL with the backward facing step and ventilated gas cavity for $x=-3.2$ mm and $U_\infty=6.1$ m/s. (b) Comparison of the measured step/cavity and step-only wall pressure fluctuation spectral ratio with that predicted by Eq. (11) for $x=-3.2$ mm and $U_\infty=6.1$ m/s.

V. PERTURBED FLOW TBL WALL PRESSURE FLUCTUATION SPECTRA

The cover plate downstream of the step, used to generate the canonical TBL, was removed and spectra of the TBL wall pressure fluctuations were measured just upstream of the backward facing step with and without the ventilated gas cavity. Differences in the wall pressure fluctuation spectral levels for the perturbed TBL with ventilation and the equilibrium TBL are expected to follow the expression given in Eq. (11). Figures 7–10 show the measured spectra for the equilibrium TBL (i.e., no step), the perturbed TBL with backward facing step but without ventilation, and the perturbed TBL with backward facing step and ventilated cavity. In addition, the measured spectral ratios of the perturbed TBL with and without the ventilated cavity to the equilibrium TBL (i.e., step/cavity and step-only) are compared to

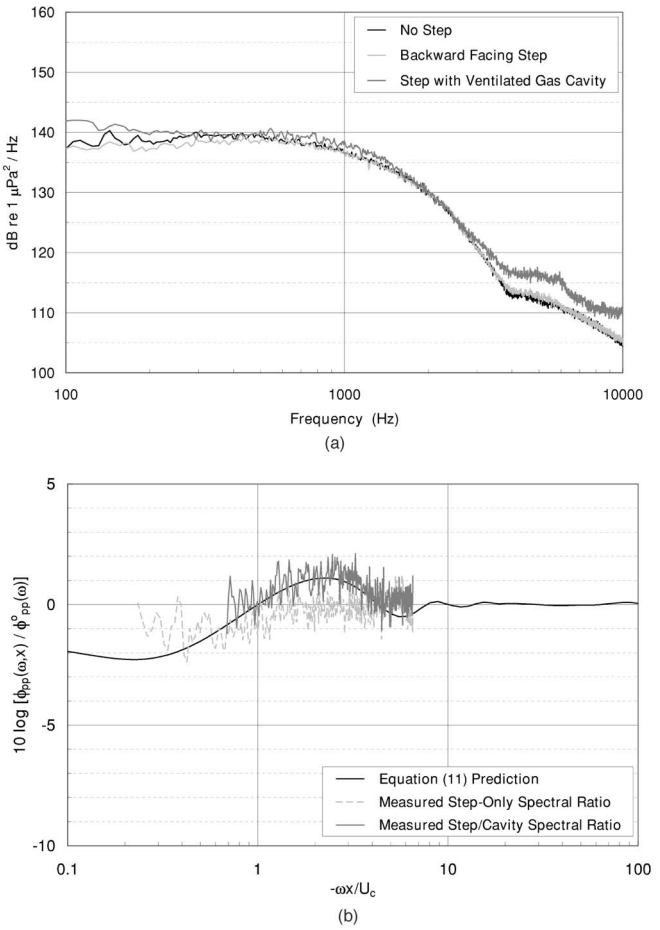

FIG. 8. (a) Comparison of the measured wall pressure fluctuation spectra for the equilibrium TBL (i.e., no step), the TBL with the backward facing step, and the TBL with the backward facing step and ventilated gas cavity for $x=-3.2$ mm and $U_\infty=12.2$ m/s. (b) Comparison of the measured step/cavity and step-only wall pressure fluctuation spectral ratio with that predicted by Eq. (11) for $x=-3.2$ mm and $U_\infty=12.2$ m/s.

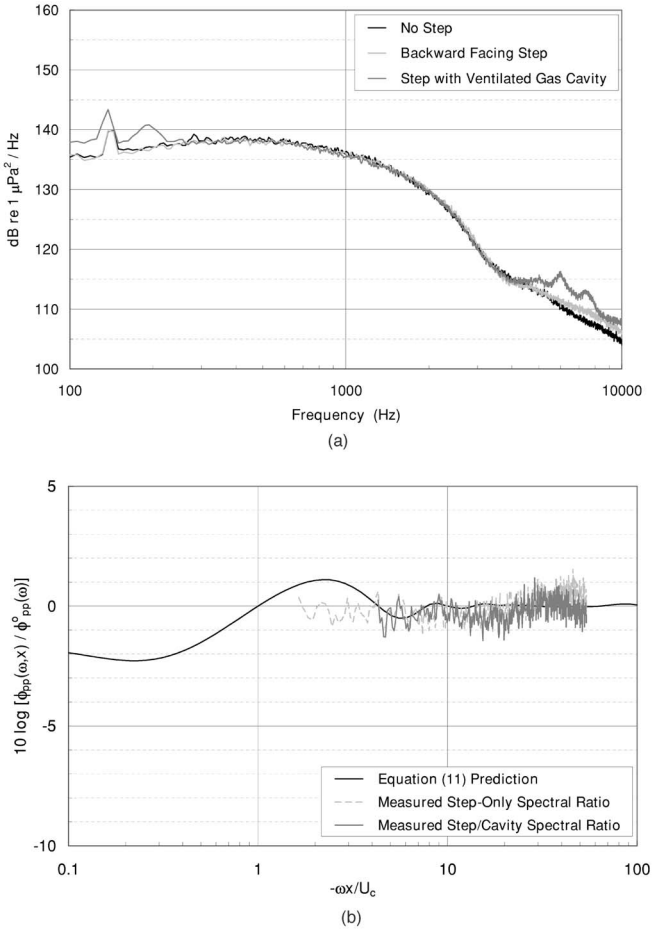

FIG. 9. (a) Comparison of the measured wall pressure fluctuation spectra for the equilibrium TBL (i.e., no step), the TBL with the backward facing step, and the TBL with the backward facing step and ventilated gas cavity for $x=-22.2$ mm and $U_\infty=12.2$ m/s. (b) Comparison of the measured step/cavity and step-only wall pressure fluctuation spectral ratio with that predicted by Eq. (11) for $x=-22.2$ mm and $U_\infty=12.2$ m/s.

the Eq. (11) prediction. Due to plate vibration from the gas injection system, the spectral ratio comparisons are only shown for frequencies where the coherence between the wall pressure sensor and an accelerometer mounted beneath the plate was below 0.05.

Figure 7 considers $U_\infty=6.1$ m/s and $x=-3.2$ mm. The difference in measured spectral level between the TBL wall pressure fluctuations perturbed with the step/cavity and the equilibrium varies, on average, between ±1.4 dB. This lies within 0.3 dB of the ±1.1 dB variations predicted by Eq. (11) over the nondimensional frequency range corresponding to the measurements. Equation (11) reaches its positive peak of 1.1 dB at $-\omega x/U_c=2.4$, whereas the measured levels peak at approximately 1.4 dB at $-\omega x/U_c=3.1$. The positive peak is followed by a valley for both the step/cavity measurements and the prediction. The average measured minimum of −0.7 dB is consistent with the −0.5 dB minimum predicted by Eq. (11). Note that the step/cavity measured spectral ratio exhibits a sinusoidal behavior similar to the prediction whereas the step-only ratio clearly does not. The measured spectral ratios are only shown out to $-\omega x/U_c=8.5$ because of the deviation in the measured spectral levels due to vibration from the gas injection system.

Figure 8 shows additional comparisons between experiment and model prediction at $x=-3.2$ mm, but at the higher speed $U_\infty=12.2$ m/s. The sinusoidal character of the step/cavity spectral ratio remains, and the nondimensional frequency at which the primary peak occurs has decreased in accordance to the prediction. Again, the step-only spectral ratio does not display the same sinusoidal character as the step/cavity ratio.

Figures 9 and 10 compare the prediction with data measured 22.2 and 41.3 mm upstream of the step for $U_\infty=12.2$ m/s. At $x=-22.2$ mm (Fig. 9), the step/cavity spectral ratio remains relatively constant over the range $7<-\omega x/U_c<50$. In addition, the step-only spectral ratio shows no evidence of the primary oscillation that was measured at the 3.2 mm upstream location near $-\omega x/U_c=2.4$. Similarly at $x=-41.3$ mm (Fig. 10), the step/cavity spectral ratio remains relatively constant over the range $8<-\omega x/U_c<100$. Thus, the average step/cavity spectral results fall within ±0.5 dB over the range $7<-\omega x/U_c<100$, indicating the effect of the ventilated cavity on the upstream TBL wall pressure fluctuations diminishes rapidly with increasing $-\omega x/U_c$.

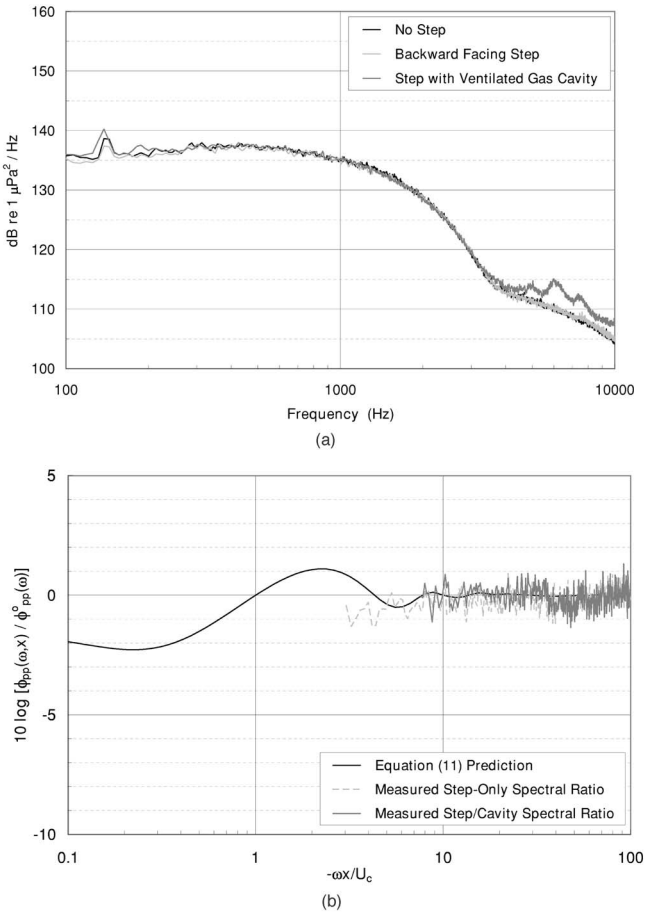

FIG. 10. (a) Comparison of the measured wall pressure fluctuation spectra for the equilibrium TBL (i.e., no step), the TBL with the backward facing step, and the TBL with the backward facing step and ventilated gas cavity for $x=-41.3$ mm and $U_\infty=12.2$ m/s. (b) Comparison of the measured step/cavity and step-only wall pressure fluctuation spectral ratio with that predicted by Eq. (11) for $x=-41.3$ mm and $U_\infty=12.2$ m/s.

VI. CONCLUSIONS

The frequency spectrum of the TBL wall pressure fluctuations upstream of a gas ventilated separated flow over a backward facing step has been investigated analytically and experimentally. Our predictions of the ratio of the TBL wall pressure spectrum upstream of the edge of the cavity to the corresponding blocked pressure spectrum in the absence of the cavity are in general accord with measurements performed in the water tunnel using a two-dimensional flat plate geometry equipped with the means to produce a ventilated gas cavity. This ratio is found to oscillate with the parameter $-\omega x/U_c$, but the oscillations damp out as $-\omega x/U_c \to \infty$. The principal conclusion of this investigation is that the ventilated cavity has a negligible effect on the upstream TBL wall pressure fluctuations when $-\omega x/U_c > 7$.

ACKNOWLEDGMENTS

The authors gratefully acknowledge the support from the Office of Naval Research, specifically Dr. Kam Ng of Code 333.

[1]D. M. Chase, "Noise radiated from an edge in turbulent flow," AIAA J. **13**, 1041–1047 (1975).
[2]K. L. Chandiramani, "Diffraction of evanescent waves with application to aerodynamically scattered sound and radiation from unbaffled plates," J. Acoust. Soc. Am. **55**, 19–29 (1974).
[3]D. M. Chase, "The character of the turbulent wall pressure spectrum at subconvective wavenumbers and a suggested comprehensive model," J. Sound Vib. **112**, 1041–1047 (1987).
[4]M. Abramowitz and I. A. Stegun (eds.), *Handbook of Mathematical Functions*, *Applied Mathematics Series No. 55*, U.S. Department of Commerce, National Bureau of Standards, 1970.
[5]G. C. Lauchle, M. L. Billet, and S. Deutsch, "High-Reynolds number liquid flow measurements," Lecture Notes in Engineering, Vol. **46** *Frontiers in Experimental Fluid Mechanics*, edited by M. Gad-el-Hak (Springer-Verlag, Berlin, 1989), Chap. 3, pp. 95–158.
[6]J. S. Bendat and A. G. Piersol, *Random Data: Analysis and Measurement Procedures*, 2nd ed. (Wiley, New York, 1986).
[7]S. D. Young, "Effect of ventilated gas cavity on turbulent boundary layer wall pressure fluctuations," M.S. thesis in Acoustics, The Pennsylvania State University, 2004.
[8]N. K. Madavan, S. Deutsch, and C. L. Merkle, "Reduction of turbulent skin friction by microbubbles," Phys. Fluids **27**, 356–363 (1984).
[9]W. L. Keith, D. A. Hurdis, and B. M. Abraham, "A comparison of turbulent boundary layer wall-pressure spectra," J. Fluids Eng. **114**, 338–347 (1992).
[10]T. M. Farabee and M. J. Casarella, "Spectral features of wall pressure fluctuations beneath turbulent boundary layers," Phys. Fluids A **3**, 2410–2420 (1991).
[11]H. Schlichting, *Boundary Layer Theory* (McGraw Hill, New York, 1979).
[12]G. M. Corcos, "Resolution of pressure in turbulence," J. Acoust. Soc. Am. **35**, 192–199 (1963).
[13]D. E. Capone and G. C. Lauchle, "Calculation of turbulent boundary layer wall pressure spectra," J. Acoust. Soc. Am. **98**, 2226–2234 (1995).

Effect of wind-generated bubbles on fixed range acoustic attenuation in shallow water at 1–4 kHz

Michael A. Ainslie
Underwater Technology Department, TNO Defence, Security and Safety, Oude Waalsdorperweg 63, 2509 JG The Hague, The Netherlands

(Received 7 February 2005; revised 13 September 2005; accepted 13 September 2005)

Long-range acoustic propagation in isothermal conditions is considered, involving multiple reflections from the sea surface. If the sea is calm there is almost perfect reflection and hence little loss of acoustic energy or coherence. The effect of wind is to increase propagation loss due to rough surface scattering and the interaction with near-surface bubble clouds. Previously published measurements of wind-related attenuation in shallow water, at a fixed range of 23 km, are converted to surface reflection loss by dividing the total attenuation by the expected number of surface interactions. Theoretical predictions of coherent reflection loss are compared with these measurements in the frequency range 0.9–4.0 kHz and wind speeds up to 13 m/s. Apart from an unexplained seasonal dependence, it is shown that the magnitude of the predicted rough surface scattering loss is sufficient to explain the measurements if the effect of bubbles is included, and not otherwise. The bubbles are found to play an important *catalytic* role, not by scattering or absorbing sound, but by refracting it up towards the sea surface and thus enhancing the scattering loss associated with the rough air–sea boundary. Possible explanations for the apparent seasonal variations in the measurements are explored.
[DOI: 10.1121/1.2114527]

PACS number(s): 43.30.Hw, 43.30.Cq, 43.30.Es [AJS] Pages: 3513–3523

I. INTRODUCTION

The coherent reflection loss due to scattering of sound from a rough sea surface is well understood theoretically.[1] However, reported reflection loss measurements, though of the same functional form as expected from rough surface scattering theory, are a factor of 3 or so higher in magnitude than theoretical predictions.[2] Specifically, while both predicted and observed losses, for acoustic frequency f and wind speed v, are proportional to the product $f^{3/2}v^4$, measured values of the constant of proportionality for two different observation periods, 8 months apart, are shown by Weston and Ching[2] (hereafter abbreviated as WC89) to be 2.3 and 4.5 times larger than theoretical values. The two periods are September–October 1968, and May–June 1969. The discrepancy between theory and observation is partially explained by Norton and Novarini[3] (hereafter abbreviated as NN01), who attribute the extra losses to scattering from aggregations of bubbles in the form of vertical protrusions (plumes). Their model predicts losses of magnitude in approximate agreement with observation at frequencies of 2 and 4 kHz and for one of the two measurement periods, but provides no explanation for the observed frequency, wind speed, or seasonal dependence.

The agreement in functional form between theory and measurement makes one reluctant to abandon the notion of rough surface scattering as the main loss mechanism, with the magnitude somehow enhanced. At the same time, the magnitude of the effects predicted by the detailed modeling work of NN01 makes it foolhardy to ignore the influence of bubbles. The hypothesis investigated here is that the bubbles may act primarily as a catalyst, enhancing the rough surface scattering loss by refracting the sound up towards the sea surface. Such an enhancement was suggested originally by Christian[4] and considered further by Tielbürger.[5] Here, the hypothesis is tested by a quantitative comparison with the measurements of WC89.

Section II of the present article summarizes the measurements of WC89, and this is followed in Sec. III by a description of the acoustical environment pertinent to the interaction with the sea surface, namely the sea surface roughness spectrum and the near-surface bubble population. Theoretical predictions of the coherent reflection coefficient are presented in Sec. IV, with and without the effect of bubbles, followed by comparisons with the WC89 measurements in Sec. V, including a discussion of the seasonal dependence. Conclusions are listed in Sec. VI.

II. WESTON-CHING MEASUREMENTS

The measurements of WC89 were made in the Bristol Channel, near Perranporth (UK), during two observation periods in Sept.–Oct. 1968 and May–June 1969. Propagation loss data for frequencies 0.87–4.0 kHz were collected for a fixed range of 23 km (see Fig. 1). The source and receiver are described by WC89 as a "type 14" projector and "hydrophone unit K." They are indicated on the map, respectively, by the number "14" and letter "K." The bathymetry data used to derive water depth contours are from Refs. 6 and 7. Both source and receiver were mounted on the seabed, which is described by WC89 as "a sand and shell bottom." The water depth along the K-14 track is mostly about 30 m, increasing to slightly more than 50 m at the receiver. In order to facilitate comparison with related work,[2,3] a nominal water

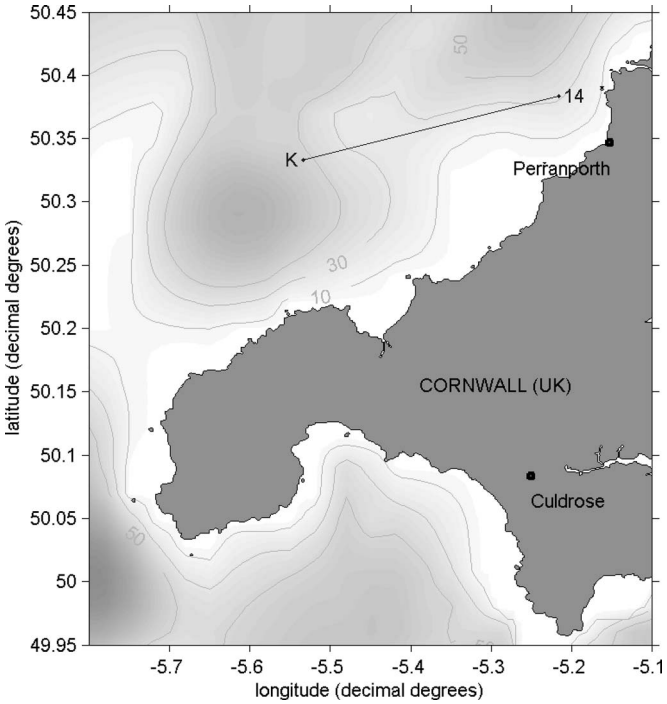

FIG. 1. Map of the measurement area. The symbols "14" and "K" mark the transmitter and receiver, respectively. The horizontal distance between them is 23 km. The contours denote water depths in meters.

depth of 39 m is used here for subsequent theoretical calculations. For both measurement periods the conditions were approximately isothermal, with "never more than 0.5 °C variation through the water column" [WC89] and predominantly westerly winds of up to 26 knots (13.4 m/s) in 1968 and up to 22 knots (11.3 m/s) in 1969. The wind-speed measurements were made on land at a nearby Royal Navy Air Station (RNAS Culdrose). Further details of the experiment can be found in Refs. 2 and 8.

The wind-induced reflection loss in shallow water is found by WC89 to vary according to a simple empirical formula, relating the magnitude of the reflection coefficient $|R|$ to frequency f and wind speed v. It is convenient to write this relationship in the form

$$-\ln|R| = \alpha\left(\frac{f}{1\ \text{kHz}}\right)^{3/2}\left(\frac{v_{10}}{10\ \text{m/s}}\right)^{4}, \tag{1}$$

where the coefficient α is the reflection loss at a frequency of 1 kHz and wind speed of 10 m/s, and the subscript "10" for the wind speed indicates that this parameter is measured at a nominal height of 10 m [WC89]. The measured value of α appears to depend on the time of year. Assuming a cycle distance of 5.34 km (the limiting ray cycle distance for isothermal and isohaline water of depth 39 m), it is numerically equal to[2]

$$\alpha = \begin{cases} 0.0677 & \text{Sept.} - \text{Oct. 1968} \\ 0.132 & \text{May} - \text{June 1969} \end{cases}. \tag{2}$$

Although the language of ray theory is used here for convenience, it should not be taken too seriously. For the frequencies used in this experiment there are never more than three water-borne modes excited. For a complete understanding a mode interpretation is necessary. In particular, if any one mode contributes to the acoustic field at a given range on the seabed, say that of a limiting eigenray after N cycles, it will do so also after $N+1$ cycles and *at all intermediate ranges*. Thus, the concept of an eigenray is not a useful one, and there is no need for the number of ray cycles to be an integer. The value used to derive the quoted numerical values of α is 4.31.

Although α is dimensionless, it can be assigned units of nepers per cycle or per surface reflection. One neper is equivalent to $20\log_{10}\mathrm{e}$ decibels (8.686 dB).

III. ACOUSTICAL ENVIRONMENT

The purpose of this section is to establish a scenario for the theoretical calculations of Sec. IV. It is assumed that conditions are isothermal, and that all energy arriving at the 23-km receiver does so via the resulting surface duct. With this assumption there is no need to describe the seabed. It is justified by the observation that, even in calm conditions, only one third of the energy arrives via bottom-interacting paths.[8] This proportion is expected to decrease with increasing wind speed. The main parameters controlling the surface interaction are the surface roughness spectrum and the near-surface bubble population. The properties of these, as assumed for the purpose of Sec. IV, are described in Secs. III A and III B below.

Acoustic effects of bubbles include refraction, absorption, and scattering of sound.[9] At the frequencies of interest here, the combined extinction effect on surface reflection loss of absorption and scattering due to bubbles is believed to be small.[3,10–12] For simplicity, it is assumed that the bubble population density can be characterized by a function of depth only (i.e., independent of horizontal range), meaning that scattering from bubble plumes[3,13] is excluded from the present study. In reality, there will be regions of locally higher concentration (e.g., near whitecaps), but it is hoped that long-range propagation will average out the effects of these. Neglecting absorption and scattering, the main acoustic effect of the bubbles is refraction, resulting from the increased compressibility (and hence reduced sound speed). The effect of the refraction is to increase the near-surface grazing angle, decreasing the coherence of the reflected wave because of the increased spread in phase differences at the sea surface, and thus increasing the scattering loss.

A. Surface waves

1. Surface wave spectra

Two different surface wave spectra $F(\Omega)$ are of interest: the Neumann–Pierson (NP) spectrum[14,15] and the Pierson–Moskowitz (PM) spectrum.[16] Both are applicable to a fully developed sea and both are of the form (for surface wave frequency Ω)

$$F(\Omega) = \frac{A}{\Omega^{n}}\exp\left[-B\left(\frac{g}{\Omega v}\right)^{m}\right] \quad (\Omega > 0), \tag{3}$$

where g is the acceleration due to gravity. The remaining four parameters A, B, n, and m are empirical constants. Numerical values associated with the NP and PM spectra are

TABLE I. Numerical constants associated with the Neuman–Pierson (NP) and Pierson–Moskowitz (PM) spectra.

Symbol	NP spectrum	PM spectrum
n	6	5
m	2	4
A	2.4 $m^2 s^{-5}$	0.0081 g^2
B	2	0.74

given by Table I. Of the two spectra, NP was in use for early research on sea surface scattering,[1,17] whereas PM is prevalent in more recent work.[3,18–21]

The wind-speed measurement height for the PM spectrum is 19.5 m. The measurement height for the NP spectrum is not specified explicitly, but a height close to 18 ft (5.5 m) is implied.[14] For the present purpose, rounded values of 20 and 5 m are assumed, and the corresponding wind speeds are denoted v_{20} and v_5, respectively.

Wave height spectra of the general form of Eq. (3) are referred to henceforth as generalized Pierson spectra (GPS). This form is used wherever possible to maintain generality, specializing to NP and PM cases where necessary.

2. rms roughness

The rms roughness σ follows from the spectral density according to

$$\sigma^2 \equiv \int_0^\infty F(\Omega)\mathrm{d}\Omega = AX_{n-1,m}\left(\frac{v}{g}\right)^{n-1}, \tag{4}$$

where $X_{n,m}$ is defined as

$$X_{n,m} \equiv \int_0^\infty x^{n-1}\exp[-Bx^m]\mathrm{d}x,$$

and therefore (Ref. 22, p. 342)

$$X_{n,m} = \frac{\Gamma(n/m)}{mB^{n/m}}, \tag{5}$$

where $\Gamma(x)$ is the gamma function.[23] For the NP and PM spectra, respectively, it follows that

$$\sigma_{\mathrm{NP}}^2 = S_{\mathrm{NP}}v_5^5, \tag{6}$$

and

$$\sigma_{\mathrm{PM}}^2 = S_{\mathrm{PM}}v_{20}^4 \tag{7}$$

where, using $g=9.807\ \mathrm{m/s^2}$, the coefficients are $S_{\mathrm{NP}} \approx 3.11\times10^{-6}\ \mathrm{m^{-3}\,s^5}$ and $S_{\mathrm{PM}} \approx 2.85\times10^{-5}\ \mathrm{m^{-2}\,s^4}$, consistent with Eq. (19) of Ref. 1 and Eq. (28) of Ref. 18, respectively. Equations (6) and (7) are special cases of the more general Eq. (4).

B. Bubbles

An important acoustical property of the near-surface bubble population is the volume gas fraction of air close to the sea surface, abbreviated henceforth as "air fraction" or "gas fraction." This parameter is estimated here using Hall's bubble population model,[24] as modified by Novarini (see Ref. 25), henceforth referred to as the "Hall–Novarini" model.

1. Bubble population model

Here, the near-surface Hall–Novarini (HN) bubble population is described. The HN model assumes that no bubbles exist with a radius less than $a_{\min}=10\ \mu$m, or greater than $a_{\max}=1000\ \mu$m. Between these limits, the bubble population distribution (i.e., the population density per unit increment in bubble radius) close to the sea surface, correcting some typographical errors in Eq. (10) of Ref. 25, is

$$n(a) = (1.6\times10^{10}\ \mathrm{m^{-4}})G(a,z)\left(\frac{v_{10}}{13\ \mathrm{m/s}}\right)^3 \times\exp\left[-\frac{z}{L(v_{10})}\right], \tag{8}$$

where

$$L(v) = \begin{cases} 0.4\ \mathrm{m} & v \leqslant 7.5\ \mathrm{m/s} \\ 0.4\ \mathrm{m} + 0.115\ \mathrm{s}(v - 7.5\ \mathrm{m/s}) & v > 7.5\ \mathrm{m/s} \end{cases},$$

$$G(a,z) = \begin{cases} [a_{\mathrm{ref}}(z)/a]^4 & a_{\min} \leqslant a \leqslant a_{\mathrm{ref}}(z) \\ [a_{\mathrm{ref}}(z)/a]^{x(z)} & a_{\mathrm{ref}}(z) < a \leqslant a_{\max} \end{cases},$$

$$a_{\mathrm{ref}}(z) = 54.4\ \mu\mathrm{m} + 1.984\times10^{-6}z, \tag{9}$$

and

$$x(z) = 4.37 + \left(\frac{z}{2.55\ \mathrm{m}}\right)^2.$$

2. Air fraction

It follows from Eq. (8) that the surface air fraction can be written

$$U(0) = U_{10}\left(\frac{v_{10}}{10\ \mathrm{m/s}}\right)^3, \tag{10}$$

where the dimensionless parameter U_{10} (the near-surface air fraction for a wind speed of 10 m/s) is equal to 9.29×10^{-7}.

3. Effect of bubbles on sound speed

The main acoustic effect of the air fraction is to reduce the sound speed of the air–water mixture (denoted c_{m}) to a value significantly below that of bubble-free water (c_{w}). Extinction effects are thought to be small on theoretical grounds,[26] and this is confirmed for frequencies of up to 4 kHz by numerical demonstrations.[3,11,12]

If the gas fraction is small (U_{10} is of order 10^{-6}) and neglecting extinction, c_{m} is related to c_{w} by[24]

$$c_{\mathrm{m}}^2 = \frac{c_{\mathrm{w}}^2}{1+\rho_{\mathrm{w}}c_{\mathrm{w}}^2\Delta K}, \tag{11}$$

where ρ_{w} is the density of water and ΔK is the contribution to the compressibility of water due to the gas fraction, given by Hall's Eq. (A7). Neglecting also the effect of surface

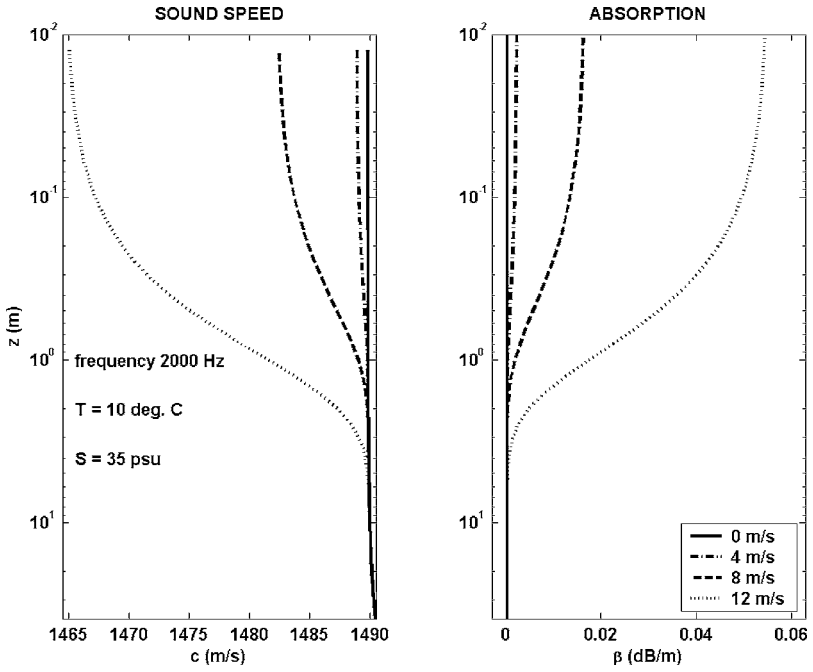

FIG. 2. Predicted variation of sound speed and extinction coefficient with depth from the sea surface for frequency 2 kHz. Wind speeds (at 10-m height) are 0 to 12 m/s as marked.

tension, and assuming that the frequency is below the resonance frequency of the largest bubbles, it follows that

$$\Delta K(f) \approx \frac{1}{P}\int_{a_{\min}}^{a_{\max}} \frac{V(a)n(a)}{\mathrm{Re}\,\kappa(a,f)}\mathrm{d}a, \tag{12}$$

where $\kappa(a,f)$ is the polytropic index,[9] $V(a)$ is the volume of a single spherical bubble of radius a, and P is the hydrostatic pressure. Defining κ_0 as

$$\kappa_0 \equiv \frac{U}{P\Delta K}, \tag{13}$$

it follows that

$$\Delta K(f) = \frac{U}{\kappa_0(f)P},$$

and therefore (making the near-surface depth dependence explicit)

$$\frac{c_{\mathrm{w}}^2}{c_{\mathrm{m}}(z)^2} = 1 + \frac{\rho_{\mathrm{w}}c_{\mathrm{w}}^2}{\kappa_0(z)P(z)}U(z). \tag{14}$$

The value of Re κ varies between unity for small bubbles and the specific heat ratio for large ones, so κ_0 is expected to vary between 1.0 and 1.4, depending on the acoustic frequency. By a small (large) bubble we mean one whose radius is small (large) compared with the thermal diffusion length $(D/\pi f)^{1/2}$, where D is the thermal diffusivity of air,[27] and whose behavior is thus isothermal (adiabatic). For a frequency of 2 kHz, the diffusion length is about 60 μm.

Numerical values used in the following for sound speed and density of bubble-free seawater are $c_w = 1490$ m/s and $\rho_{\mathrm{w}} = 1027$ kg/m^3. For example, evaluation of Eq. (14) at the sea surface ($z=0$), assuming a hydrostatic pressure P equal to 101.3 kPa, results in

$$\frac{c_{\mathrm{w}}^2}{c_{\mathrm{m}}(0)^2} = 1 + \frac{2.25\times 10^4}{\kappa_0(0)}U(0). \tag{15}$$

Figure 2 shows the variation of the sound speed c and extinction coefficient β (i.e., the combined decay constant due to both absorption and scattering effects) with depth for a frequency of 2 kHz and wind speeds up to 12 m/s as marked, calculated from the complex variable c_{m} using the algorithm of Hall[24] for the HN bubble population. The assumed temperature and salinity values for this and subsequent calculations are 10 °C and 35 psu. The main feature of interest is the large sound-speed defect at the sea surface for the higher wind speeds. Notice also that the predicted extinction coefficient at this frequency exceeds

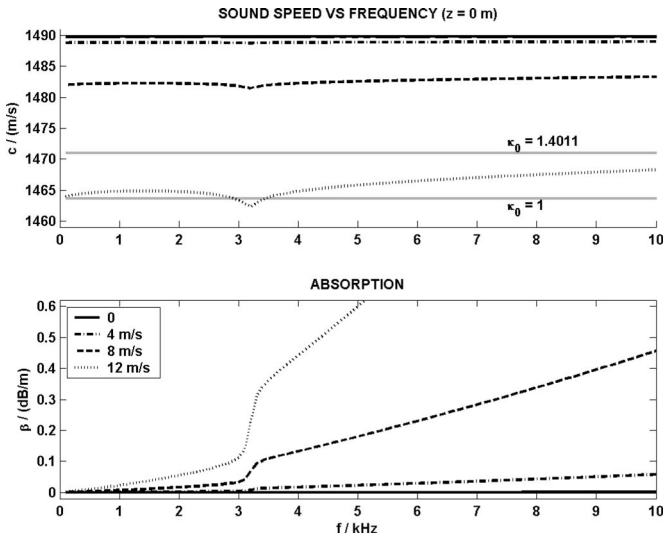

FIG. 3. Predicted variation of sound speed and extinction coefficient with frequency for $z=0$. Wind speeds are as Fig. 2. The horizontal gray lines in the upper graph are calculated using Eq. (15) with the values of κ_0 as marked (12 m/s only).

0.05 dB/m only for the highest wind speed considered, and then only in the uppermost 10 cm.

The frequency dependence of c and β at the sea surface is illustrated by Fig. 3, calculated in the same way as for Fig. 2. For the highest wind speed only (12 m/s), the isothermal and adiabatic predictions of Eq. (15) are also shown, and from these it is clear that the isothermal limit ($\kappa_0=1$) provides a reasonable approximation to the sound speed for frequencies less than about 4 kHz. The kink at 3.2 kHz results from the onset of resonance for the largest bubbles at this frequency, illustrating a transition between one regime that includes some resonant bubbles ($f>3.2$ kHz) and another that does not ($f<3.2$ kHz). Above this transition frequency, the predicted extinction coefficient increases rapidly with increasing frequency. The transition frequency is inversely proportional to the choice of $a_{\max}$, equal to 1 mm for the HN model.

A convenient approximation to the sound-speed profile (at low frequency) is obtained by substituting the depth-dependent air fraction into Eq. (14) with $\kappa_0=1$. The air fraction corresponding to the HN bubble model can be found by integrating Eq. (8). The result, assuming $a_{\text{ref}}<a_{\max}$, is

$$U(z)=\frac{U(0)}{J(0)}e^{-z/L}J(z), \tag{16}$$

where

$$J(z)\equiv\int_{a_{\min}}^{a_{\max}}V(a)G(a,z)\mathrm{d}a=\frac{4}{3}\pi a_{\text{ref}}^4(z)\left\{\ln\frac{a_{\text{ref}}(z)}{a_{\min}}+\frac{1-[a_{\text{ref}}(z)/a_{\max}]^{x(z)-4}}{x(z)-4}\right\}, \tag{17}$$

and

$$J(0)=1.275\times10^{-16}\ \text{m}^4.$$

IV. THEORETICAL REFLECTION COEFFICIENT

For the modeling of long-range propagation at low frequency, it is often assumed that the incoherent field contributes little to the total, and recent studies have provided some justification for this assumption.[21,28] In this situation it is useful to define a "coherent" reflection coefficient $|R|$ as the ratio of the mean reflected pressure amplitude to the incident amplitude. The average is usually over an ensemble of different realizations of a randomly rough surface, but it can also be thought of as an average in time over a randomly varying rough surface. Following Brekhovskikh and Lysanov,[29] the coherent reflection coefficient is calculated below for the case of large-scale roughness, both with and without effects of near-surface bubbles.

A. Large-scale roughness reflection coefficient in bubble-free water

For an isotropic wave number spectrum, the coherent reflection coefficient for large-scale roughness, and near-grazing incidence, can be written as a function of grazing angle θ and acoustic wave number k

$$|R|^2=1-4E\left(\frac{2k^3}{g}\right)^{1/2}I\sin\theta, \tag{18}$$

where

$$E=\left(\frac{8}{\pi}\right)^{1/2}\frac{\Gamma(3/4)}{\Gamma(1/4)}\approx0.3814,$$

and I is the integral

$$I=\int_0^\infty\Omega F(\Omega)\mathrm{d}\Omega.$$

For the GPS this reduces to

$$I=AX_{n-2,m}\left(\frac{v}{g}\right)^{n-2}, \tag{19}$$

so that the reflection coefficient can be written

$$|R|^2=1-Df^{3/2}v^{n-2}\sin\theta, \tag{20}$$

where

$$D=\frac{16E\Gamma(\mu)}{mB^\mu}\frac{A}{g^n}\left(\frac{\pi g}{c_w}\right)^{3/2},$$

and

$$\mu=\frac{n-2}{m}.$$

It follows from Eq. (20) that

$$|R_{\text{NP}}|^2=1-D_{\text{NP}}f^{3/2}v_5^4\sin\theta, \tag{21}$$

and

$$|R_{\text{PM}}|^2=1-D_{\text{PM}}f^{3/2}v_{20}^3\sin\theta, \tag{22}$$

where $D_{\text{NP}}\approx6.12\times10^{-9}\ \text{Hz}^{-3/2}\,\text{s}^4\,\text{m}^{-4}$ and $D_{\text{PM}}\approx5.98\times10^{-8}\ \text{Hz}^{-3/2}\,\text{s}^3\,\text{m}^{-3}$. Equation (21) is consistent with Eq. 9.6.7 from Ref. 29.

For comparison with measurements [i.e., Eq. (1)] it is convenient to rewrite Eqs. (21) and (22) using the approximation, valid for $|R|\approx1$

$$-2\ln|R|\approx1-|R|^2. \tag{23}$$

With this approximation, and converting to a common reference height of 10 m using[30] $v_{10}/v_{20}=0.94$ and $v_{10}/v_5=1.07$, it follows that

$$-\ln|R_{\text{PM}}|\approx1.14\left(\frac{f}{1\ \text{kHz}}\right)^{3/2}\left(\frac{v_{10}}{10\ \text{m/s}}\right)^3\sin\theta, \tag{24}$$

and

$$-\ln|R_{\text{NP}}|\approx0.74\left(\frac{f}{1\ \text{kHz}}\right)^{3/2}\left(\frac{v_{10}}{10\ \text{m/s}}\right)^4\sin\theta. \tag{25}$$

Notice that the scattering theory naturally gives an $f^{3/2}$ dependence on frequency, in agreement with observation. If one insists on reproducing the observed v^4 wind-speed dependence from Eq. (20), this restricts possible spectra to those satisfying $n=6$ only, consistent with the NP spectrum, but not with PM. However, the predicted value of α is 0.022, significantly lower than the measured values of Eq. (2).

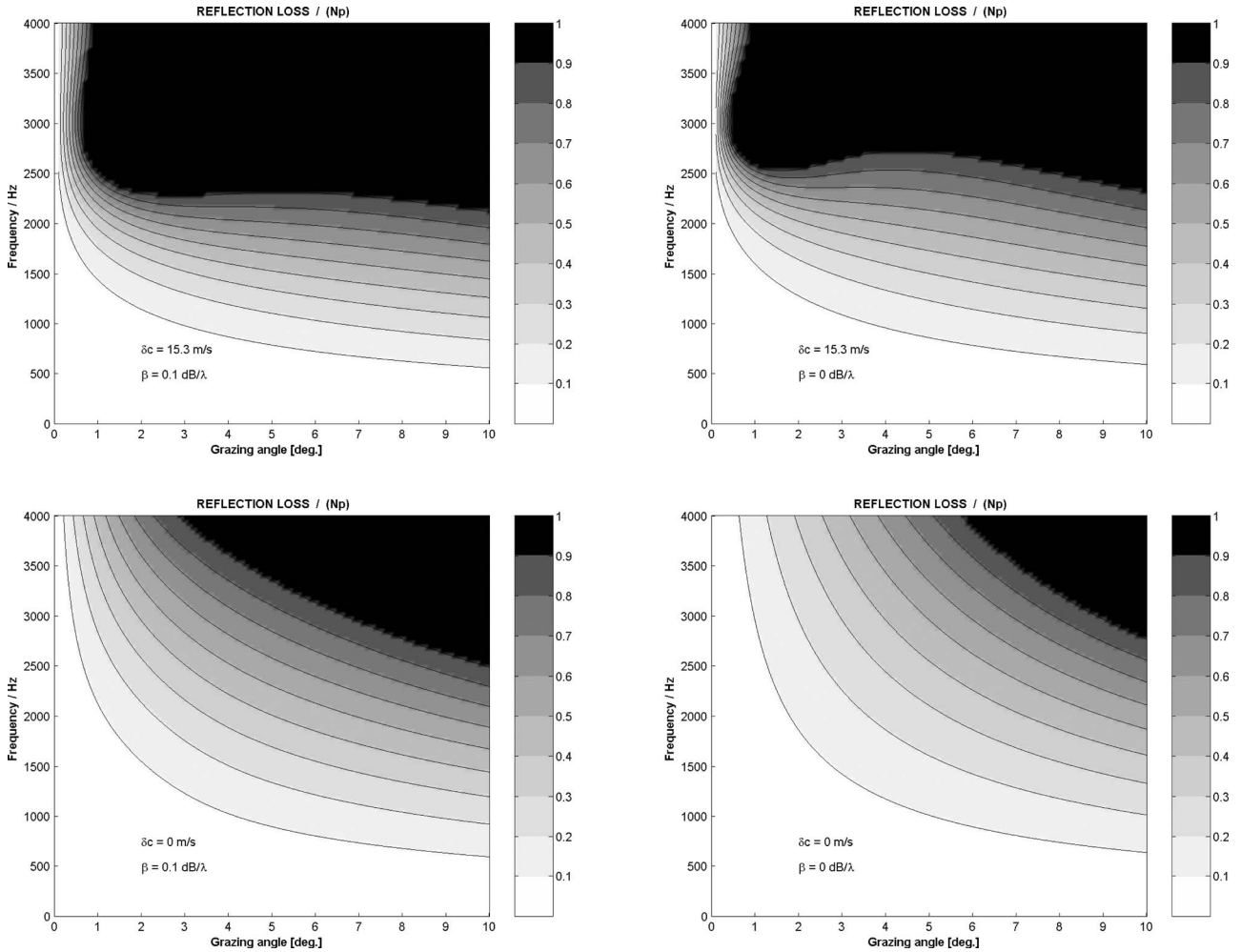

FIG. 4. Theoretical reflection loss in nepers ($-\ln|R|$), vs grazing angle and frequency, evaluated using RELAY for a wind speed (v_{10}) of 10 m/s; Top left: refraction+extinction; top right: refraction only; bottom left: extinction only; bottom right: no refraction+no extinction.

B. Influence of bubbles on scattering theory

The effect of a near-surface bubble layer on the above theoretical results is considered in this section, for a nominal wind speed (v_{10}) of 10 m/s. The two effects of the bubble cloud considered are sound extinction and refraction. It is shown above that, for frequencies up to 4 kHz, the sound speed in bubbly water can be estimated using the isothermal limit of Eq. (14). Figure 4 shows the coherent reflection loss calculated for the sound-speed profile thus calculated, which features a sound-speed deficit at the sea surface of 15.3 m/s. The bubbles are assumed to behave isothermally [i.e., $\kappa_0 = 1$ is used in Eq. (14)], here and throughout the remainder of this article. The corresponding extinction profile is estimated using a surface value of 0.1 dB/λ (equivalent to approximately 0.2 dB/m at 3 kHz) and assuming that the extinction coefficient varies with depth in proportion with the local air fraction.

The top left graph of Fig. 4 shows the result for the theoretical reflection loss for the sound-speed and extinction profiles described above. The remaining three graphs demonstrate the effects of switching off either extinction (top right), refraction (bottom left), or both (bottom right). The effect of the extinction coefficient β becomes important at frequencies above 2 kHz, but only if refraction is excluded (lower graphs). When the full sound-speed profile is taken into account (upper graphs), the effect of extinction is swamped by the much larger refraction effects. The low sensitivity to β in the latter case is consistent with the findings of Refs. 3, 11, and 12 that extinction has a small effect on propagation loss in the frequency range 1–4 kHz.

The predictions of Fig. 4 are made using the recursive method of Jensen *et al.* (Ref. 31, p. 53). A total of 100 sublayers was used to represent the bubbly medium, each of equal thickness and spanning a total depth of 10 m from the sea surface. Beneath this depth the properties of uniform, bubble-free water are assumed. All boundaries between sublayers are perfectly smooth except the top one, between the atmosphere and the uppermost sublayer of bubbly water, which is attributed a roughness (σ_{PM}) of 0.60 m, determined by Eq. (7). The effect of this roughness is modeled by scaling the reflection coefficient of the uppermost boundary by the factor $|R_{\mathrm{PM}}|$ from Eq. (24), taking account of Snell's law for the angle θ. The recursive method described above, including Eq. (24) for the effect of scattering, is abbreviated henceforth as RELAY, the name of the computer program in which it is implemented.

Figure 4 can be compared with the simpler approxima-

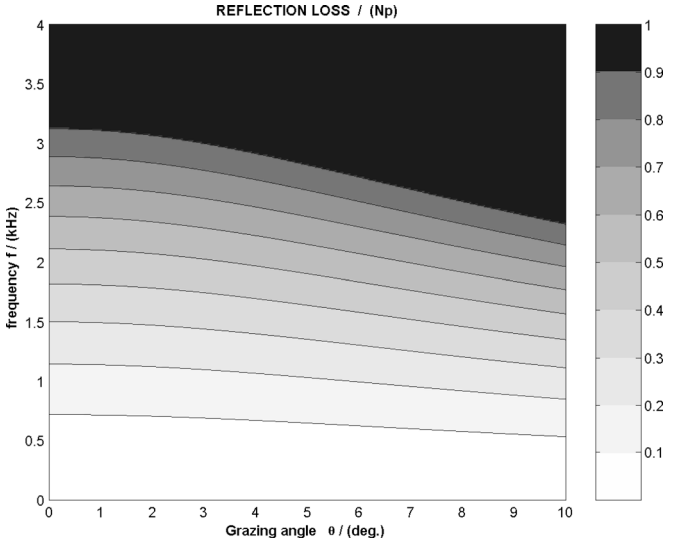

FIG. 5. Theoretical reflection loss in nepers ($-\ln|R_{PM}|$), vs grazing angle and frequency, evaluated using Eq. (24) for a wind speed (v_{10}) of 10 m/s. Equation (24) is evaluated using the angle at the sea surface calculated according to Snell's law. The x-axis variable is the grazing angle in bubble-free water.

tion of Eq. (24), which is insensitive to the layering. The result without refraction is not shown because it is identical to the bottom right graph of Fig. 4, as expected. The result *including* refraction, shown in Fig. 5, resembles the upper two graphs of Fig. 4 for angles 5–10°, but, by comparison with RELAY, Eq. (24) overestimates reflection loss at angles less than about 5°.

V. ANALYSIS OF WC89 MEASUREMENTS

A. Comparison with theory

The WC89 measurements for a wind speed of 10.3 m/s (i.e., 20 knots) are plotted in Fig. 6 vs frequency as a series of circles (1968 measurements) and squares (1969). The gray reference curves are calculated using Eq. (24) (i.e., using the PM spectrum) and Eq. (25) (NP spectrum), without any effects due to bubbles. Both spectra predict losses that are significantly lower than the measured values, as expected from the findings of WC89. When refraction is included (black solid and dashed curves), PM is close to 1969 and NP is between the two data sets—both exhibit the correct ($f^{3/2}$) frequency dependence. The remaining (dash-dot) curve in Fig. 6 is evaluated using RELAY, predicting a reflection loss magnitude that is intermediate between the 1968 and 1969 measurements. However, the frequency dependence is too steep, similar to that of the OASES predictions of Fig. 3 from Ref. 12. Closer inspection of the predictions of RELAY used to produce the present Fig. 4 reveal a deep interference null close to grazing incidence, at a frequency close to 3 kHz, suggesting that the rapid increase in loss with frequency predicted by RELAY may be an interference effect as this null is approached. Such a null is unlikely to manifest itself in the measured attenuation, due to the averaging effect resulting from multiple sea surface interactions.

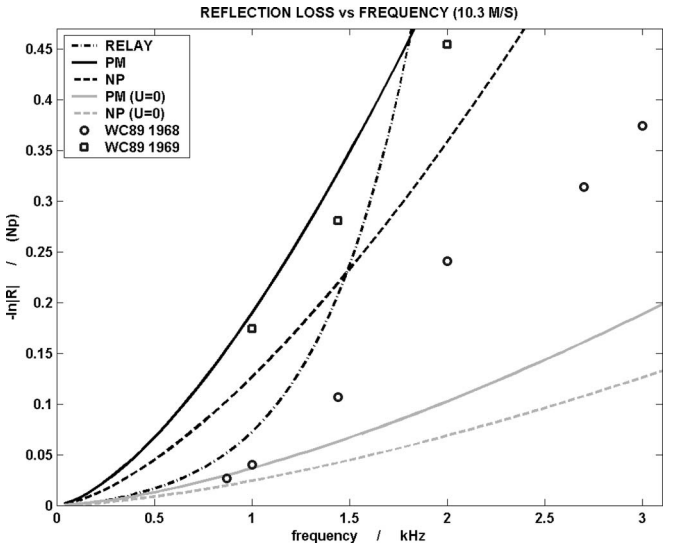

FIG. 6. Measured (symbols) and predicted (curves) reflection loss vs frequency for a wind speed (v_{10}) of 10.3 m/s. Predictions are for a grazing angle of 1.67°.

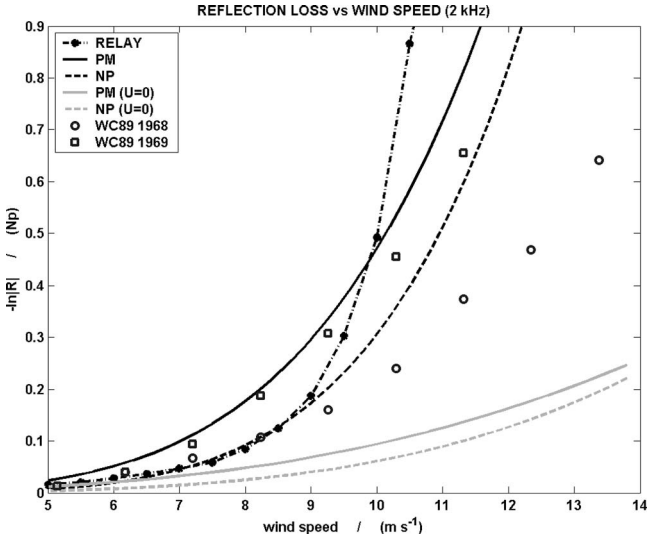

FIG. 7. Measured (symbols) and predicted (curves) reflection loss vs wind speed for a frequency of 2 kHz. Predictions are for a grazing angle of 1.67°.

The dependence on wind speed is also of interest. Figure 7 shows WC89 measurements and theoretical predictions vs wind speed for a frequency of 2 kHz. As for Fig. 6 above, PM agrees well for 1969 if bubbles are included, and overestimates the 1968 data. The behavior of the NP prediction is similar. RELAY also predicts the correct magnitude, but the scattering loss increases too steeply with increasing wind speed compared with the measurements.

Regardless of the precise explanation, it is clear from Figs. 6 and 7 that Eq. (24) does a better job than RELAY in predicting both the frequency and wind-speed dependence of the WC89 measurements, even though it is believed to overestimate the theoretical reflection loss in the angle region 0–5°, where it is being used. This success of Eq. (24) is especially surprising considering the small loss assumption made in its derivation.

Figure 8 shows all of the measurements from Tables III and IV from WC89 in a similar format to that of their Figs. 6 and 7. Specifically, what is plotted here is the quantity $(-\ln R)/f^{3/2}$ as a function of v_{10}^4. It is remarkable that (as Weston and Ching point out themselves) when presented in

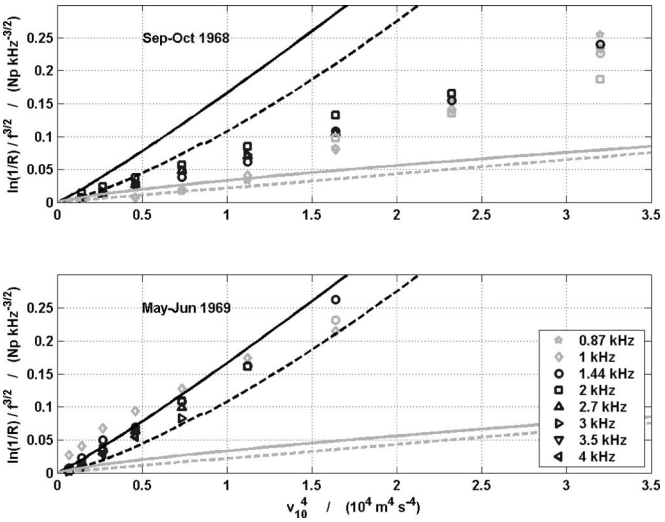

FIG. 8. Measured and predicted surface reflection loss, divided by $f^{3/2}$: symbols are WC89 measurements, with selected points shaded in gray as described in the text; the black lines are theoretical predictions with $\kappa_0=1$ using the HN bubble population ($U_{10}=9.29\times10^{-7}$); the gray lines are for the reference case without bubbles ($U=0$). For details, see the legends of Figs. 6 and 7. Symbols that are drawn in both black and gray (e.g., squares) appear in the legend only in black.

this way the measurements collapse to something approaching a straight line. Also plotted in Fig. 8, for comparison, are the theoretical predictions of Eqs. (24) and (25) with and without bubbles. The main justifications for using these simple approximate equations in preference to RELAY are that they appear to work and are free from artifacts caused by interference associated with a single range-averaged (and hence deterministic) realization of the bubble population. This approach also has the attraction of simplicity of presentation: the division by $f^{3/2}$ results in a theoretical prediction that depends only on wind speed, so that measurements at all frequencies can be compared with a single line in the graphs. From this line an estimate of the parameter α can be made by reading off the value from each curve at $v_{10}=10$ m/s, namely about 0.16 (0.11) for the PM (NP) spectrum, roughly consistent with the measured values between 0.07 and 0.13.

The conversion from total along-track attenuation to reflection loss per cycle requires a well cut-on duct and so may not be applicable to low-frequency data points, which are shaded gray in Fig. 8 to reflect this. (The cutoff frequencies of the first two modes are about 0.7 and 1.7 kHz). Also shaded, bearing in mind the perturbational nature of the theory, are those points whose loss per cycle exceeds an arbitrarily chosen threshold of 0.5 Np.

The theoretical predictions of Figs. 6–8 are calculated with the parameter U_{10} equal to 9.29×10^{-7}, the air fraction corresponding to the HN bubble population model. In fact, the value of this parameter is subject to considerable uncertainty. For example, Trevorrow's[32] Fig. 10 shows an order of magnitude spread in the near-surface bubble population density for the same wind speed. If U_{10} is treated as a free parameter, an improved fit using Eq. (24) can be obtained for 1968, again for isothermal conditions, with $U_{10}=1.3\times10^{-7}$. However, bearing in mind the tendency of Eq. (24) to overestimate the theoretical scattering loss for small grazing angles, it seems likely that the true U_{10} values during the WC89 measurements are higher than those discussed here.

B. Seasonal dependence

An outstanding puzzle is the cause of the seasonal dependence in the measured data. According to WC89, between August and October there is a period of relatively low wind-induced losses, exemplified by the measurements of Sept–Oct 1968. Conversely, between November and June, these losses, characterized by the May–June 1969 data, are significantly higher.

The theoretical predictions of Sec. IV B above are sensitive to the air fraction U at the sea surface, and in particular to the parameter U_{10}. The relation between U and v is subject to considerable uncertainty,[32] and a potential seasonal variation in U_{10} is considered a strong candidate for explaining the seasonal dependence in wind-related propagation loss. Possible explanations of the observed seasonal dependence are described below. The first three mechanisms all affect the value of U_{10}.

1. Stability in air column

Stable atmospheric conditions (caused by the air temperature T_a exceeding the water temperature T_w) lead to lower values of near-surface wind speed, and hence fewer bubbles in the water, for fixed v_{10}. A reduction in the bubble population has been proposed[33,34] as an explanation for anomalously low underwater wind noise associated with stable atmospheric conditions. It follows from Ref. 20 that the effect could be modeled empirically by the introduction of an effective wind speed

$$v_{\mathrm{eff}}=\begin{cases} v_{10} & \Delta T\leqslant 1\ ^\circ\mathrm{C} \\ v_{10}10^{-0.0116(\Delta T-1)^2} & \Delta T>1\ ^\circ\mathrm{C} \end{cases},$$

where

$$\Delta T\equiv T_a-T_w.$$

The ratio v_{eff}/v_{10} is equal to 0.79 and 0.65 for ΔT of 4 °C and 5 °C, respectively, implying factors of 0.38 and 0.18 in v^4, and hence a large reduction in surface loss for summer conditions. Thus, the effect is of the correct order of magnitude, and is also in the right direction to explain the higher loss measured in the winter months. Unfortunately, the timing of the summer months is off by about 2 months.[2] In principle, air stability might also affect the surface roughness, but Pierson and Moskowitz[16] find no evidence of a correlation between the surface wave spectrum and air–sea temperature difference.

2. Stability in water column

Acoustic effects of the bubble population are determined primarily by the gas fraction U at the sea surface, which depends on the depth distribution of the bubbles, depending in turn on the dynamics of the upper ocean and hence on the stability of the top few meters of water. So, there exists a potential connection between water column stability and U_{10}. While there is some anecdotal evidence to support the idea

that bubbles might be transported away from the surface in unstable conditions,[35] it predicts highest instability, lowest U_{10}, and therefore lowest scattering loss throughout the winter months, opposite to what is observed.

3. Gas saturation

It is known that a seasonal dependence can exist in gas saturation,[36] and that the supersaturation of seawater can have a significant impact on the bubble population[37,38] for otherwise unchanged conditions. However, higher bubble concentrations would then be expected in the late spring, when the sea is warming up, which does not explain the high losses throughout the winter months.[2]

4. Patchiness in bubble population

The acknowledged presence of patchiness in the bubble distribution raises the possibility of scattering by discrete aggregations of bubbles as considered by NN01. This is the first mechanism discussed here that does not influence the value of U_{10}.

Thus, the columnar clouds observed in unstable conditions by Thorpe[35] can also be used to explain the higher loss observed in winter, although the timing of the summer months is again problematic.[2] Furthermore, the success of surface scattering theory in predicting the functional form of the measurement makes alternative explanations seem less attractive, unless they can be shown to predict the same f and v dependence.

5. Surface tension

Leighton[9] points out that the surface tension of seawater can vary by a factor of 2 or so. A seasonal variation in this parameter would result in a corresponding change in the compressibility of small bubbles, and hence in the sound speed. This effect is considered unlikely to be large enough to explain the observed changes in the apparent gas fraction, primarily because it only affects the smallest bubbles.

6. Variations in sound-speed profile

The sound-speed profile in the ocean is prone to variation with season. If any changes to the profile are not correctly accounted for, artifacts will result. The assumption is made here that the profile is approximately isothermal for all of the measurements.[2] The main justification for this is that the measurements of most interest are those associated with moderate to high wind speeds, i.e., the ones most likely to correspond to a well-mixed layer.

A related effect of surface warming is to increase the surface sound speed and hence reduce the resulting scattering loss. However, the effect of temperature changes on the sound speed is minor compared with that of a typical bubble population.

7. Variations in wind or wave direction

If there are seasonal variations in the wave direction (possibly but not necessarily caused by changes in wind direction), this would affect the correlation length of the surface wave spectrum in the sound propagation direction,[39,40] and hence also the scattering loss.[41] Another potential consequence of changing *wind* direction arises from the land-based nature of the wind-speed measurements reported in WC89. A land-based anemometer is expected to "underestimate marine winds during periods of offshore winds."[42] This might manifest itself as an apparent seasonal dependence in scattering loss, when actually the only change was in the Culdrose measurement for essentially unchanged conditions at sea. However, RNAS Culdrose is at an exposed location, most of the measurements are for a westerly wind, and there is no obvious direction dependence in the WC89 loss measurements. Therefore, this effect is considered minor.

VI. CONCLUSIONS

A. Dependence of reflection loss on frequency and wind speed

Measured wind-related attenuation of the form $f^{3/2}v^4$, converted to reflection loss by dividing by the number of cycles, can be explained heuristically [through Eq. (24)] by means of scattering from a Pierson–Moskowitz (PM) rough surface, enhanced by the presence of a layer of near-surface bubbles. First-order perturbation theory applied to rough surface scattering has a built-in $f^{3/2}$ frequency dependence, independent of the assumed surface wave spectrum. Perturbation theory, in combination with the Hall–Novarini (HN) surface gas fraction and PM surface wave spectrum, predicts the correct order of magnitude for the wind-related reflection loss, with a dependence on wind speed that is very close to the observed v^4. The behavior with the Neumann–Pierson (NP) spectrum is similar, with a slightly stronger dependence on wind speed.

A more complete theoretical calculation (referred to in this article as "RELAY"), taking account of the full depth dependence of the HN model, while still of the correct magnitude predicts a different dependence on frequency and wind speed that does not agree with the measurements, as illustrated by Figs. 6 and 7. A possible explanation for the discrepancy is the presence of a deep interference null in the RELAY prediction.

B. Main mechanism of wind-related attenuation

From the available evidence, it seems likely that refraction due to bubbles and rough surface scattering are both essential ingredients for a complete explanation of long-range wind-induced attenuation in the frequency range 1–4 kHz. The bubbly layer is thought to act as a catalyst by refracting the sound upwards, and thus multiplying the theoretical scattering loss by a factor of order 3. It follows that surface loss models that neglect the effect of bubbles are likely to underestimate wind-related attenuation by a similar amount. The magnitude of the Perranporth measurements can be explained without the need to invoke bubble absorption, scattering from individual bubbles, or scattering from aggregations of bubbles. A related effect is the enhancement to *back*-scattering strength predicted by Keiffer *et al.*,[25,43] also due to upward refraction in the bubble layer.

Thus, rough surface scattering, enhanced by refraction due to near-surface bubbles, is offered as an alternative explanation for wind-related attenuation to that of scattering from discrete bubble plumes suggested by NN01. There are several important differences between the present work and that of NN01 that may be partly responsible for the differences between the present conclusions and theirs. The modeling of NN01 generally pays more attention to environmental detail, including the effects of scattering from bubble plumes, multiple reflections from the seabed, and an ensemble average over multiple deterministic realizations of a randomly rough sea surface; they compromise only on the sound-speed profile in the water which they assume to be isovelocity (apart from refraction in the bubble layer—included automatically with their approach). By comparison, in the present article this level of realism is deliberately sacrificed in exchange for the simplicity required to gain insight into the minimal set of physical effects required to explain the observations.

C. Seasonal effects

While a convincing explanation for the significant seasonal variation apparent in the WC89 measurements is not yet available, the main candidates involve a seasonal change in U_{10}. The most plausible explanation is through a seasonal dependence in wind stress for a fixed wind speed (at 10 m), although there is a problem with the timing of the summer months. Perhaps the only way to identify the cause of the seasonal change unambiguously is to repeat the experiment at a fixed location and different seasons, with *in situ* bubble, wind, temperature, and acoustic measurements.

ACKNOWLEDGMENTS

The author acknowledges several discussions about possible seasonal variation of bubble populations with Professor G. de Leeuw. He thanks Dr. Guy Norton of NRL and an anonymous reviewer for their constructive comments, and Wilco Boek for providing the software used to make Fig. 1.

[1]E. Y. T. Kuo, "Sea surface scattering and propagation loss: Review, update, and new predictions," IEEE J. Ocean. Eng. **13**, 229–234 (1988).
[2]D. E. Weston and P. A. Ching, "Wind effects in shallow-water transmission," J. Acoust. Soc. Am. **86**, 1530–1545 (1989).
[3]G. V. Norton and J. C. Novarini, "On the relative role of sea-surface roughness and bubble plumes in shallow-water propagation in the low-kilohertz region," J. Acoust. Soc. Am. **110**, 2946–2955 (2001).
[4]R. J. Christian, "The influence of a bubbly layer on near-surface acoustic propagation and surface loss modeling," J. Acoust. Soc. Am. **92**, No. 4, Pt.2, 2323 (1992); see also NUWC-NL Technical Document 10,229 (Naval Undersea Warfare Center, Detachment New London, Connecticut, 11 December 1992).
[5]D. Tielbürger, "Die Schallausbreitung im kHz-Bereich unter dem Einfluß von Blasen" ("The influence of bubbles on kHz-sound transmission"), Scientific Report FB 1994-3 FWG Research Project No. 1.1 (Forschungsanstalt der Bundeswehr für Wasserschall- und Geophysik, Kiel, 1994). In German.
[6]W. H. F. Smith and D. T. Sandwell, "Global sea floor topography from satellite altimetry and ship depth soundings," Science **277**, 1956–1962 (1997).
[7]D. T. Sandwell, W. H. F. Smith, S. M. Smith, and C. Small, "Measured and estimated seafloor topography," http://topex.ucsd.edu/marine_topo, last accessed 28 Dec 2004.
[8]D. E. Weston, K. J. Stevens, J. Revie, and M. Pengelly, "Multiple frequency studies of sound transmission fluctuations in shallow water," J. Sound Vib. **18**(4), 487–497 (1971).
[9]T. G. Leighton, *The Acoustic Bubble* (Academic, London, 1994).
[10]G. V. Norton and J. C. Novarini, "Enhancement of the total acoustic field due to the coupling effects from a rough sea surface and a bubble layer," J. Acoust. Soc. Am. **103**, 1836–1844 (1998).
[11]M. A. Ainslie, "Losses due to rough surface scattering and wind-generated bubble clouds," TNO Report FEL-04-A066, June 2004.
[12]M. A. Ainslie, "Effect of wind on long range propagation in shallow water," in Proceedings of the Seventh European Conference on Underwater Acoustics, ECUA 2004, Delft, The Netherlands, 5–8 July 2004, pp. 167–172.
[13]J. C. Novarini, R. S. Keiffer, and G. V. Norton, "A model for variations in the range and depth dependence of the sound speed and attenuation induced by bubble clouds under wind-driven sea surfaces," IEEE J. Ocean. Eng. **23**, No. 4, 423–438 (1998).
[14]G. Neumann and W. J. Pierson, "A detailed comparison of theoretical wave spectra and wave forecasting methods," Dtsch. Hydrogr. Z. **10**, Part 3, 73–92 (1957).
[15]G. Neumann and W. J. Pierson, *Principles of Physical Oceanography* (Prentice-Hall, Englewood Cliffs, NJ, 1966).
[16]W. J. Pierson and L. Moscowitz, "A proposed spectral form for fully developed wind seas based on the similarity theory of S. A. Kitaigorodskii," J. Geophys. Res. **69**(24), 5181–5190 (1964).
[17]H. W. Marsh, M. Schulkin, and S. G. Kneale, "Scattering of underwater sound by the sea surface," J. Acoust. Soc. Am. **33**, 334–340 (1961).
[18]D. M. F. Chapman, "An improved Kirchhoff formula for reflection loss at a rough ocean surface at low grazing angles," J. Acoust. Soc. Am. **73**, 520–527 (1983).
[19]E. I. Thorsos, "Acoustic scattering from a 'Pierson–Moskowitz' sea surface," J. Acoust. Soc. Am. **88**, 335–349 (1990).
[20]APL-UW, "High-Frequency Ocean Environmental Acoustic Models Handbook," Technical Report APL-UW TR 9407, AEAS 9501, October 1994.
[21]K. L. Williams, E. I. Thorsos, and W. T. Elam, "Examination of coherent surface reflection coefficient (CSRC) approximations in shallow-water propagation," J. Acoust. Soc. Am. **116**, 1975–1984 (2004).
[22]*Tables of Integrals, Series and Products*, edited by I. S. Gradshteyn and I. M. Ryzhik (Academic, New York, 1980).
[23]*Handbook of Mathematical Functions*, edited by M. Abramowitz and I. Stegun (Dover, New York, 1965).
[24]M. V. Hall, "A comprehensive model of wind-generated bubbles in the ocean and predictions of the effects on sound propagation at frequencies up to 40 kHz," J. Acoust. Soc. Am. **86**, 1103–1117 (1989).
[25]R. S. Keiffer, J. C. Novarini, and G. V. Norton, "The impact of the background bubble layer on reverberation-derived scattering strengths in the low to moderate frequency range," J. Acoust. Soc. Am. **97**, 227–234 (1995).
[26]D. E. Weston, "On the losses due to storm bubbles in oceanic sound transmission," J. Acoust. Soc. Am. **86**, 1546–1553 (1989).
[27]C. L. Morfey, *Dictionary of Acoustics* (Academic, San Diego, 2001).
[28]E. I. Thorsos, W. T. Elam, F. S. Henyey, S. A. Reynolds, and K. L. Williams, "Scattering from rough surfaces in shallow water propagation," in Proceedings of the Seventh European Conference on Underwater Acoustics, ECUA 2004, Delft, The Netherlands, 5–8 July 2004, pp. 559–564.
[29]L. M. Brekhovskikh and Yu Lysanov, *Fundamentals of Ocean Acoustics* (Springer, Berlin, 1982).
[30]F. W. Dobson, "Review of reference height for and averaging time of surface wind measurements at sea," Marine Meteorology and Related Oceanographic Activities, Report No. 3 (World Meteorological Organization, 1981).
[31]F. B. Jensen, W. A. Kuperman, M. B. Porter, and H. Schmidt, *Computational Ocean Acoustics* (AIP, New York, 1994).
[32]M. V. Trevorrow, "Measurements of near-surface bubble plumes in the open ocean with implications for high-frequency sonar performance," J. Acoust. Soc. Am. **114**, 2672–2684 (2003).
[33]S. O. McConnell, M. P. Schilt, and J. G. Dworski, "Ambient noise measurements from 100 Hz to 80 kHz in an Alaskan fjord," J. Acoust. Soc. Am. **91**, 1990–2003 (1992).
[34]P. C. Wille and D. Geyer, "Measurements on the origin of the wind-dependent ambient noise variability in shallow water," J. Acoust. Soc. Am. **75**, 173–185 (1984).
[35]S. A. Thorpe, "On the clouds of bubbles formed by breaking wind waves

in deep water and their role in air-sea gas transfer," Philos. Trans. R. Soc. London, Ser. A **304**, 155–210 (1982).
[36]S. Emerson, P. Quay, C. Stump, D. Wilbur, and M. Knox, "O_2, Ar, N_2, and ^{222}Rn in surface waters of the subarctic ocean: Net biological O_2 production," Global Biogeochem. Cycles **5**, 49–69 (1991).
[37]E. C. Monahan and M. Lu, "Acoustically relevant bubble assemblages and their dependence on meteorological parameters," IEEE J. Ocean. Eng. **11**(4), 340–349 (1990).
[38]S. T. McDaniel, "Sea surface reverberation: A review," J. Acoust. Soc. Am. **94**, 1905–1922 (1993).
[39]L. Fortuin, "The sea surface as a random filter for underwater sound waves," Ph.D., Technological University of Twente (Uitgeverij Waltman, Delft, The Netherlands, 1973) SACLANTCEN Report SR-7.
[40]L. Fortuin and J. G. de Boer, "Spatial and temporal correlation of the sea surface," J. Acoust. Soc. Am. **49**, 1677–1679 (1971).
[41]W. A. Kuperman, "Coherent component of specular reflection and transmission at a randomly rough two-fluid interface," J. Acoust. Soc. Am. **58**, 365–370 (1975).
[42]S. D. Smith, "Coefficients for sea surface wind stress, heat flux, and wind profiles as a function of wind speed and temperature," J. Geophys. Res. **93**, No. C12, 15467–15472 (1988).
[43]R. S. Keiffer, J. C. Novarini, and R. A. Zingarelli, "Finite-difference time-domain modeling of low to moderate frequency sea-surface reverberation in the presence of a near-surface bubble layer," J. Acoust. Soc. Am. **110**, 782–785 (2001).

Emergence rate of the time-domain Green's function from the ambient noise cross-correlation function

Karim G. Sabra,[a] Philippe Roux, and W. A. Kuperman
Marine Physical Laboratory, Scripps Institution of Oceanography, La Jolla, California 92093-0238

(Received 20 June 2005; revised 25 August 2005; accepted 8 September 2005)

It has been demonstrated experimentally and theoretically that an estimate of the Green's function between two receivers can be obtained from the time derivative of the long-time average ambient noise function cross-correlation function between these two receivers. The emergence rate of the deterministic coherent arrival times of the cross-correlation function, which yield an estimate of the Green's function, from the recordings of an isotropic distribution of random noise sources is studied by evaluating the amplitude of the variance of the cross-correlation function. The leading term in the expression of the variance depends on the recorded energy by both receivers and the time-bandwidth product of the recordings. The variance of the time derivative of the correlation function has a similar dependency. These simple analytic formulas show a good agreement with the variance determined experimentally for the correlation of ocean ambient noise for averaging time varying from 1 to 33 min. The data were recorded in shallow water at a depth of 21-m water depth in the frequency band [300–530 Hz] for receivers separation up to 28 m. © *2005 Acoustical Society of America.* [DOI: 10.1121/1.2109059]

PACS number(s): 43.30.Nb, 43.50.Rq, 43.60.Tj [RLW] Pages: 3524–3531

I. INTRODUCTION

Experimental and theoretical analysis have shown that the arrival-time structure of the time-domain Green's function (TDGF) can be estimated from the time derivative of the time-averaged ambient noise cross-correlation function (NCF) in various environments and frequency ranges of interest: helioseismology,[1] ultrasonics,[2–6] underwater acoustics,[7–9] and seismology.[10–14] The physical process underlying this noise cross-correlation technique is similar for all these environments. Initially, the small coherent component of the noise field at each receiver is buried in the spatially and temporally incoherent field produced by the distribution of noise sources. The coherent wavefronts emerge from a correlation process that accumulates contributions over time from noise sources whose propagation path passes through both receivers.

Based on theoretical and experimental results,[6,8,11,12,15] the following relationship between the TDGF between two receivers a and b, located respectively at $\vec{r}_a$ and $\vec{r}_b$, and the time derivative of the expected value of the NCF $\langle C_{a,b}(\tau)\rangle$ can be stated:

$$\frac{d\langle C_{a,b}(\tau)\rangle}{d\tau} \approx -G(\vec{r}_a,\vec{r}_b;\tau) + G(\vec{r}_b,\vec{r}_a;-\tau). \tag{1}$$

In Eq. (1), the terms on the rhs are respectively (1) the TDGF, which comes from noise events that propagate from receiver a to b and yields a positive correlation time-delay τ, and (2) the time-reversed TDGF, which comes from noise events that propagate from receiver b to a and yields a negative correlation time delay $-\tau$. Thus, for a uniform noise source distribution or a fully diffuse noise field, the derivative of the NCF is an antisymmetric function with respect to time, the NCF itself being a symmetric function. The exact relationship (in amplitude and arrival times) between the time derivative of the time-averaged NCF and the deterministic TDGF generally depends of specific noise source distribution and the environment. For instance, the source directionality creates shading of the wavefronts of the NCF with respect to the true TDGF.[7,8]

Experimental results typically show that a sufficiently long time-averaging interval (as long as environmental changes do not modify the acoustic propagation paths) and a spatially homogeneous noise distribution helps in estimating the arrival-time structure of the TDGF from this correlation process.[2,7,9] Determining precisely the dependence of the emergence rate of the coherent wavefronts of the NCF on the noise recording duration and the various environment parameters is essential for practical applications. This emergence rate (or convergence rate) can be defined based on the variance of the NCF. Indeed, the variance corresponds to the fluctuations of the NCF around its expected value whose time derivative is an estimate of the TDGF.

An upper bound on the variance of the NCF has been previously derived in the case of a homogeneous medium with embedded scatterers.[11] Furthermore, a formulation of the variance of the NCF for open systems and closed systems based on a modal expansion of the Green's function for the case of local diffuse fields has also been presented.[16] In this paper, an expression of the variance of the NCF is derived independently of the particular expression of the Green's function (free space, modal or rays expansion,…) for the environment of interest (e.g., ultrasonic experiments, underwater acoustics, seismology,…) and of the shape of the noise spectrum. This resulting analytic formula variance of the NCF is derived assuming only (1) an isotropic distribution of impulsive random noise sources and (2) a finite duration

[a]Electronic mail: ksabra@mpl.ucsd.edu

Green's function, which is true for any physical systems in the presence of attenuation. Furthermore, this formulation is readily extended to the variance of the time derivative of the NCF. In the case of a white noise model and finite bandwidth recordings, this analytic formula reduces to previous derivations when using a homogeneous free-space model[11] or a modal expansion of the Green's function.[16,17] The analytic results are compared to the variance of experimental NCF obtained from ocean noise recordings of various duration up to 33 min in the frequency band [300–530 Hz]. The ambient noise data were recorded on a bottom array in shallow water during the Adaptive Beach Monitoring (ABM 95) experiment.[9]

This article is divided into five sections. Section II presents a time-domain formulation of the NCF. Section III derives an analytic formula for the variance of the NCF and the time derivative of the NCF. Section IV provides an overview of the ABM 95 experiment and discusses the ambient NCFs obtained. Experimental measures of the variance of the NCF are then compared to the theoretical predictions of Sec. III. Section V summarizes the findings and conclusions drawn from this study.

II. FORMULATION OF THE AMBIENT NOISE CROSS-CORRELATION FUNCTION (NCF)

The signal recorded at two receivers a and b located respectively at $\vec{r}_a$ and $\vec{r}_b$ from a single random noise source (located at $\vec{r}_1$, broadcasting at a time t_1) is fully determined by the TDGF in the environment of interest, which for instance is noted $G(\vec{r}_1,\vec{r}_a;t-t_1)$ between this random source and receiver a.[18] Here, the causality requires that the noise source in $(\vec{r}_1;t_1)$ that contributes to the pressure field in a at a given time t satisfy the condition $t>t_1$. We assumed that the (impulse) response of both receiver a and b is embedded in the TDGF. The random impulse noise sources are assumed to follow a shot-noise model which is appropriate for broadband noise sources realizations.[8,19] In this model each noise source broadcasts, at a random time t_1, a signal $S(\vec{r}_1;t_1)$. The resulting noise waveforms are represented by a random pulse train consisting of similarly shaped pulses randomly distributed in time. In the case of white noise, the noise sources have a flat frequency spectrum.[19] In the present context, *random* means that the discrete events giving rise to the pulses are temporally and spatially incoherent in the limit of infinite recording time and infinite bandwidth (due to the impulsive nature of the sources) and have the same amplitude Q (whose unit depends on the variable being measured, e.g., pressure or displacement). The statistical law governing the distribution of the events in time is the Poisson probability density function and has a creation rate ν ($\mathrm{m}^{-3}\mathrm{s}^{-1}$) per unit time per unit volume. Hence the second-order moment of the uncorrelated noise sources can be written as[8,15]

$$\langle S(\vec{r}_1;t_1)S(\vec{r}_2;t_2)\rangle = \nu Q^2 \delta(\vec{r}_1-\vec{r}_2)\cdot\delta(t_1-t_2). \tag{2}$$

In practice, the contribution of the noise sources is limited in range due to attenuation. The total field at receiver a location is then

$$P(\vec{r}_a;t) = \int_{-\infty}^{+\infty} d\vec{r}_1 \int_{-\infty}^{t} dt_1 S(\vec{r}_1;t_1) G(\vec{r}_1,z_1,\vec{r}_a,z_a;t-t_1). \tag{3}$$

In a stationary medium, the temporal NCF $C_{a,b}(\tau)$ between the signals recorded by both receivers is defined as

$$C_{a,b}(\tau) = \int_{-T_r/2}^{T_r/2} dt P(\vec{r}_a;t) P(\vec{r}_b;t+\tau). \tag{4}$$

In practice, the NCF is constructed from ensemble averages, denoted by $\langle\ \rangle$, over realizations of the noise source signals $S(\vec{r}_1;t_1)$. The integration over the variable t, i.e., the recording time for receiver a and b, corresponds to an accumulation of noise sources events over time. In practice, the signals recorded by receivers a and b are correlated only over a finite interval T_r (including both positive and negative time delays).[15] For short correlation time τ (i.e., $\tau \ll T_r$) with respect to the recording duration at each receiver T_r, the tapering of the NCF which occurs otherwise on the edges of the finite correlation interval, i.e., for $\tau \approx T_r$, can be neglected.

Assuming a noise statistical model given by Eq. (2), using Eq. (3), and after performing a change of variables $u = t - t_1$, the ambient noise cross-correlation function defined in Eq. (4) can be expressed as

$$\langle C_{a,b}(\tau)\rangle = \nu Q^2 T_r \int_{-\infty}^{+\infty} d\vec{r}_1 \int_{0}^{+\infty} du G(\vec{r}_1,\vec{r}_a;u) G(\vec{r}_1,\vec{r}_b;\tau+u). \tag{5}$$

The TDGF has typically a finite temporal length noted T_{Green}, i.e., the time duration after which no more multipath arrivals can be detected. In practice, the value of the parameter T_{Green} depends on absorption, on the ambient noise level, and on the receiver dynamics (and sensitivity). Hence the relationship between the TDGF between the receivers a and b and the time derivative of the expected value of the NCF given by Eq. (1) shows that after sufficient averaging of the NCF and for time delay $\tau > T_{\mathrm{Green}}$, only small residual fluctuations are measured by the NCF. The level of these fluctuations corresponds to the square of the variance (or standard deviation) of this noise correlation process noted $\mathrm{Var}(C_{a,b}(\tau))$. A measure of the variance $\mathrm{Var}(C_{a,b}(\tau))$ gives an estimate of the residual error done when approximating the TDGF by the time derivative of the NCF and is thus a key quantity to evaluate. Based on the time-domain formalism developed in this section, a simplified formulation of the variance of this noise correlation process $\mathrm{Var}(C_{a,b}(\tau))$ is developed in the following section for an arbitrary TDGF with a finite temporal length T_{Green}.

III. VARIANCE OF THE AMBIENT NOISE CORRELATION FUNCTION. THEORY

A. Variance of the NCF

The variance of the ambient noise cross-correlation process, i.e., the square of the mean level of the fluctuations, is defined as[16]

$$\mathrm{Var}(C_{a,b}(\tau)) = \langle C_{a,b}^2(\tau)\rangle - \langle C_{a,b}(\tau)\rangle^2, \tag{6}$$

where the expected value of $\langle C_{a,b}(\tau)\rangle$ is given by Eq. (5). By combining Eqs. (3) and (4), the expression of $C_{a,b}^2(\tau)$ can be expanded as

$$\begin{aligned} C_{a,b}^2(\tau) = & \int_{-T_r/2}^{T_r/2} dt \int_{-T_r/2}^{T_r/2} d\tilde{t} \int_{-\infty}^{+\infty} d\vec{r}_1 \int_{-\infty}^{+\infty} d\vec{r}_2 \int_{-\infty}^{+\infty} d\vec{r}_3 \\ & \times \int_{-\infty}^{+\infty} d\vec{r}_4 \int_{-\infty}^{t} dt_1 \int_{-\infty}^{t} dt_2 \int_{-\infty}^{\tilde{t}} dt_3 \int_{-\infty}^{\tilde{t}} dt_4 \\ & \times S(\vec{r}_1;t_1) S(\vec{r}_2;t_2) S(\vec{r}_3;t_3) S(\vec{r}_4;t_4) \\ & \times G(\vec{r}_1,\vec{r}_a;t-t_1) G(\vec{r}_2,\vec{r}_b;\tau+t-t_2) \\ & \times G(\vec{r}_3,\vec{r}_a;\tilde{t}-t_3) G(\vec{r}_4,\vec{r}_b;\tau+\tilde{t}-t_4). \end{aligned} \tag{7}$$

Assuming that the random sources are temporally and spatially incoherent with Gaussian statistics, the expression of the fourth-order moment $\langle S(\vec{r}_1;t_1) S(\vec{r}_2;t_2) S(\vec{r}_3;t_3) S(\vec{r}_4;t_4)\rangle$ reduces to

$$\begin{aligned} & \langle S(\vec{r}_1;t_1) S(\vec{r}_2;t_2) S(\vec{r}_3;t_3) S(\vec{r}_4;t_4)\rangle \\ & \quad = \langle S(\vec{r}_1;t_1) S(\vec{r}_2;t_2)\rangle \langle S(\vec{r}_3;t_3) S(\vec{r}_4;t_4)\rangle \\ & \qquad + \langle S(\vec{r}_1;t_1) S(\vec{r}_3;t_3)\rangle \langle S(\vec{r}_2;t_2) S(\vec{r}_4;t_4)\rangle \\ & \qquad + \langle S(\vec{r}_1;t_1) S(\vec{r}_4;t_4)\rangle \langle S(\vec{r}_2;t_2) S(\vec{r}_3;t_3)\rangle. \end{aligned} \tag{8}$$

Each of the three terms on the rhs in Eq. (8) can be further simplified by using Eq. (2) for each of the second-order moments. By substituting this simplified form Eq. (8) in Eq. (7) and after performing spatial and temporal integration of the noise source distribution for the dirac terms $\delta(t_i - t_j)$ and $\delta(\vec{r}_i - \vec{r}_j)$ where $i,j = 1,\ldots,4$ are the indices of the source terms in Eqs. (7) and (8), the expression of $\langle C_{a,b}^2(\tau)\rangle$ reduces to three integral terms:

$$\langle C_{a,b}^2(\tau)\rangle = I(\tau) + J(\tau) + K(\tau). \tag{9}$$

The first integral term $I(\tau)$ is obtained after spatial and temporal integration over source indices $i=2$ and $i=4$. Its expression reduces to $\langle C_{a,b}(\tau)\rangle^2$ by comparison with Eq. (5):

$$\begin{aligned} I(\tau) = & Q^4 \nu^2 \left(\int_{-T_r/2}^{T_r/2} dt \int_{-\infty}^{+\infty} d\vec{r}_1 \int_{-\infty}^{t} dt_1 G(\vec{r}_1,\vec{r}_a;t-t_1) \right. \\ & \left. \times G(\vec{r}_1,\vec{r}_b;\tau+t-t_1) \right) \\ & \times \left(\int_{-T_r/2}^{T_r/2} d\tilde{t} \int_{-\infty}^{+\infty} d\vec{r}_3 \int_{-\infty}^{\tilde{t}} dt_3 G(\vec{r}_3,\vec{r}_a;\tilde{t}-t_3) \right. \\ & \left. \times G(\vec{r}_3,\vec{r}_b;\tau+\tilde{t}-t_3) \right) \\ = & \langle C_{a,b}(\tau)\rangle^2. \end{aligned} \tag{10}$$

The second integral term $J(\tau)$ in Eq. (9) is obtained after spatial and temporal integration over source indices $i=3$ and $i=4$,

$$\begin{aligned} J(\tau) = & Q^4 \nu^2 \int_{-T_r/2}^{T_r/2} dt \int_{-T_r/2}^{T_r/2} d\tilde{t} \left(\int_{-\infty}^{+\infty} d\vec{r}_1 \int_{-\infty}^{t} dt_1 G(\vec{r}_1,\vec{r}_a;t-t_1) \right. \\ & \left. \times G(\vec{r}_1,\vec{r}_a;\tilde{t}-t_1) \right) \left(\int_{-\infty}^{+\infty} d\vec{r}_2 \int_{-\infty}^{t} dt_2 G(\vec{r}_2,\vec{r}_b;\tau+t-t_2) \right. \\ & \left. \times G(\vec{r}_2,\vec{r}_b;\tau+\tilde{t}-t_2) \right). \end{aligned} \tag{11}$$

This expression of the integral term $J(\tau)$ can be simplified by performing the following change of variables $u=t-t_1$, $v=t-t_2$ and $q=t-\tilde{t}$:

$$\begin{aligned} J(\tau) = & Q^4 \nu^2 \int_{-T_r/2}^{T_r/2} dt \int_{-T_r}^{T_r} dq \left(\int_{-\infty}^{+\infty} d\vec{r}_1 \int_{0}^{+\infty} du G(\vec{r}_1,\vec{r}_a;u) \right. \\ & \left. \times G(\vec{r}_1,\vec{r}_a;q+u) \right) \left(\int_{-\infty}^{+\infty} d\vec{r}_2 \int_{0}^{-\infty} dv G(\vec{r}_2,\vec{r}_b;\tau+v) \right. \\ & \left. \times G(\vec{r}_2,\vec{r}_b;q+\tau+v) \right). \end{aligned} \tag{12}$$

By identification with the simplified form of $\langle C_{a,b}(\tau)\rangle$ in Eq. (5), $J(\tau)$ further reduces to

$$J(\tau) = \frac{1}{T_r} \int_{-T_r}^{T_r} dq \langle C_{a,a}(q)\rangle \langle C_{b,b}(q)\rangle, \tag{13}$$

where the autocorrelation functions of the ambient noise signals recorded at receivers a and b are noted respectively as $C_{a,a}(q)$ and $C_{b,b}(q)$.

The third integral term $K(\tau)$ in Eq. (9) is obtained after spatial and temporal integration over the remaining source indices $i=4$ and $i=3$,

$$\begin{aligned} K(\tau) = & Q^4 \nu^2 \int_{-T_r/2}^{T_r/2} dt \int_{-T_r/2}^{T_r/2} d\tilde{t} \left(\int_{-\infty}^{+\infty} d\vec{r}_1 \int_{-\infty}^{t} dt_1 \right. \\ & \left. \times G(\vec{r}_1,\vec{r}_a;t-t_1) G(\vec{r}_1,\vec{r}_b;\tau+\tilde{t}-t_1) \right) \\ & \times \left(\int_{-\infty}^{+\infty} d\vec{r}_2 \int_{-\infty}^{t} dt_2 G(\vec{r}_2,\vec{r}_a;\tilde{t}-t_2) G(\vec{r}_2,\vec{r}_b;\tau+t-t_2) \right). \end{aligned} \tag{14}$$

In a similar way, we can simplify the expression of the integral term $K(\tau)$ in Eq. (14) by performing the following change of variables $u=t-t_1$, $v=\tilde{t}-t_2$ and $q=t-\tilde{t}$:

$$\begin{aligned} K(\tau) = & Q^4 \nu^2 \int_{-T_r/2}^{T_r/2} dt \int_{-T_r}^{T_r} dq \left(\int_{-\infty}^{+\infty} d\vec{r}_1 \int_{0}^{+\infty} du \right. \\ & \left. \times G(\vec{r}_1,\vec{r}_a;u) G(\vec{r}_1,\vec{r}_b;\tau+q+u) \right) \\ & \times \left(\int_{-\infty}^{+\infty} d\vec{r}_2 \int_{0}^{+\infty} dv G(\vec{r}_2,\vec{r}_a;v) G(\vec{r}_2,\vec{r}_b;\tau-q+v) \right). \end{aligned} \tag{15}$$

By identification with the simplified form of $\langle C_{a,b}(\tau)\rangle$ in Eq. (5) we then get

$$K(\tau) = \frac{1}{T_r}\int_{-T_r}^{T_r} dq \langle C_{a,b}(\tau+q)\rangle\langle C_{a,b}(\tau-q)\rangle. \quad (16)$$

Based on Eq. (1), the arrival-time structure of the NCF $\langle C_{a,b}(\tau \pm q)\rangle$ is determined by TDGF $G_{a,b}(\tau \pm q)$. Furthermore, the measured TDGF has a finite duration, i.e., has zero values for running time larger than the temporal length of the retrived TDGF T_{Green} (i.e., $|\tau \pm q| > T_{\text{Green}}$). Hence, using the following approximation,

$$\int_{-T_r}^{T_r} dq \langle C_{a,b}(\tau+q)\rangle\langle C_{a,b}(\tau-q)\rangle \approx G_{a,b}(\tau)^2 \to 0, \quad \text{if } \tau > T_{\text{Green}}, \quad (17)$$

the value of $K(\tau)$ for large correlation time delay $\tau > T_{\text{Green}}$ can be neglected compared to the value of $J(\tau)$ [see Eq. (13)]. Thus using Eqs. (9) and (10) and substituting the result in Eq. (6) and for large correlation time-delay $\tau > T_{\text{Green}}$, the leading term in the expression of the variance of the NCF is $J(\tau)$:

$$[\text{Var}(C_{a,b})]_{\tau > T_{\text{Green}}} = J(\tau) + K(\tau) \approx \frac{\int_{-\infty}^{+\infty} dq \langle C_{a,a}(q)\rangle\langle C_{b,b}(q)\rangle}{T_r}. \quad (18)$$

Equation (18) gives a formulation of the variance *without* making specific assumptions on the particular expression of the TDGF nor for the spectral properties of the noise sources. Indeed, this formulation holds for *any* linear systems as long as the corresponding TDGF has a finite temporal response, which is generally the case due to the presence of attenuation.

Under the assumption of white noise model and finite bandwidth recordings B_ω, the expression of the variance of the NCF given in Eq. (18) can be further reduced. The power spectral densities of receivers a and b are noted respectively $\Phi_{a,a}(\omega)$ and $\Phi_{b,b}(\omega)$. Assuming that the recorded noise has a white spectrum, or after perfoming an preliminar noise whitening operation in practice (see Sec. IV A), the noise spectrum power densities are then a constant in the frequency band of interest: $\Phi_{a,a}(\omega) = C_{a,a}(0)/2B_\omega$ and $\Phi_{b,b}(\omega) = C_{b,b}(0)/2B_\omega$, where B_ω is the frequency bandwidth of interest. Thus, using the Wiener-Khintchine theorem, and assuming that the recording time T_r is sufficiently long so that $\int_{-T_r}^{T_r} \exp(i(\omega+\omega')q)\, dq = \delta(\omega+\omega')$, the following approximation can be made for finite bandwidth recordings:

$$\int_{-T_r}^{T_r} dq \langle C_{a,a}(q)\rangle\langle C_{b,b}(q)\rangle = 4\int_{\omega_c - B_\omega/2}^{\omega_c + B_\omega/2} d\omega \Phi_{a,a}(\omega) \int_{\omega_c - B_\omega/2}^{\omega_c + B_\omega/2} d\omega' \Phi_{b,b}(\omega')\delta(\omega+\omega') = \frac{\langle C_{a,a}(0)\rangle\langle C_{b,b}(0)\rangle}{2B_\omega}, \quad (19)$$

where ω_c is the center frequency of the noise recordings. Hence, for this simplified white noise model, the variance of the NCF reduces to

$$[\text{Var}(C_{a,b})]_{\tau > T_{\text{Green}}} \approx \frac{\langle C_{a,a}(0)\rangle\langle C_{b,b}(0)\rangle}{2B_\omega T_r} = \frac{\int_0^{T_r} dt P(\vec{r}_a;t)^2 \cdot \int_0^{T_r} dt P(\vec{r}_b;t)^2}{2B_\omega T_r}. \quad (20)$$

The simplified expression of the variance $[\text{Var}(C_{a,b})]_{\tau > T_{\text{Green}}}$ given by Eq. (20) is a constant proportional to the product of the total recorded energy by each receiver (which includes the receiver response, noise source amplitude, and potential site effects) and inversely proportional to the recorded time-bandwidth product $T_r B_\omega$ where T_r is the recording time and B_ω is the frequency bandwidth of interest. A similar dependency of the variance on the recorded time-bandwidth product has been previously derived for the case of a finite number of scatterers (or source events) embedded in a homogeneous medium.[11] Furthermore, this simple formulation in Eq. (20) reduces to previous derivations for the case of modal expansions in local diffuse fields.[16,17] For open systems using finite bandwidth Gaussian tone bursts, Eq. (20) corresponds to the leading term in Eq. (41) in Ref. 16. For finite bodies with constant modal density, Eq. (20) corresponds to Eq. (17) in Ref. 17, which is also the leading term in Eq. (38) of the same reference article.

B. Variance of the time derivative of the NCF

As shown in Eq. (1), the arrival-time structure of the TDGF should be estimated in practice using the time derivative of the NCF and not the NCF itself. From Eq. (5) we have

$$\frac{d\langle C_{a,b}(\tau)\rangle}{d\tau} = \nu Q^2 T_r \int_{-\infty}^{+\infty} d\vec{r}_1 \int_0^{+\infty} du G(\vec{r}_1,\vec{r}_a;u) \times \frac{dG(\vec{r}_1,\vec{r}_b;\tau+u)}{d\tau}. \quad (21)$$

The variance $\text{Var}(d(C_{a,b}(\tau)/d\tau))$ of the time derivative of the NCF is defined similarly as in Eq. (6),

$$\text{Var}\left(\frac{dC_{a,b}(\tau)}{d\tau}\right) = \left\langle \left(\frac{d\langle C_{a,b}(\tau)\rangle}{d\tau}\right)^2 \right\rangle - \left\langle \frac{d\langle C_{a,b}(\tau)\rangle}{d\tau} \right\rangle^2, \quad (22)$$

and can be readily estimated following similar derivations presented in the previous section. The main difference is the substitution of terms containing a Green's function with the time-delay variable τ [e.g., $G(\vec{r}_i,\vec{r}_b;\tau+u)$, $i=1,\ldots,4$] by their time derivative [i.e., $dG(\vec{r}_i,\vec{r}_b;\tau+u)/d\tau$]. Hence

$$\text{Var}\left(\frac{dC_{a,b}(\tau)}{d\tau}\right) = DJ(\tau) + DK(\tau). \quad (23)$$

The first integral term $DJ(\tau)$ in Eq. (23) reduces to

$$DJ(\tau) = \frac{1}{T_r}\int_{-T_r}^{+T_r} dq\langle C_{a,a}(q)\rangle\langle DC_{b,b}(q)\rangle, \tag{24}$$

where $\langle DC_{b,b}(q)\rangle$ is the autocorrelation of the *derivative* of the signals recorded at b, $dP(\vec{r}_b;t)/dt$:

$$\langle DC_{b,b}(q)\rangle = \left\langle \int_{-\infty}^{+\infty} dt \frac{dP(\vec{r}_b;t)}{dt}\frac{dP(\vec{r}_b;t+q)}{dt}\right\rangle. \tag{25}$$

The second integral term $DK(\tau)$ in Eq. (23) reduces to

$$DK(\tau) = \frac{1}{T_r}\int_{-T_r}^{T_r} dq\left\langle \frac{dC_{a,b}(\tau+q)}{d\tau}\frac{dC_{a,b}(\tau-q)}{d\tau}\right\rangle. \tag{26}$$

Based on Eq. (1), we can use the following approximation

$$\left\langle \frac{dC_{a,b}(\tau+q)}{d\tau}\right\rangle\left\langle \frac{dC_{a,b}(\tau-q)}{d\tau}\right\rangle \approx G_{a,b}(\tau)^2\delta(p). \tag{27}$$

Hence using similar arguments to the previous section the value of DK for large correlation time delay $\tau > T_{\text{Green}}$ is negligible compare to the expression DJ [see Eq. (24)]. Thus to first order for large correlation time delay $\tau > T_{\text{Green}}$, the leading term in the expression of the variance $\text{Var}(dC_{a,b}(\tau)/d\tau)$ is DJ:

$$\left[\text{Var}\left(\frac{dC_{a,b}(\tau)}{d\tau}\right)\right]_{\tau>T_{\text{Green}}} = \frac{\int_{-\infty}^{+\infty} dq\langle C_{a,a}(q)\rangle\langle DC_{b,b}(q)\rangle}{T_r}. \tag{28}$$

Note that this expression in Eq. (28) does not seem to be symmetric with respect to the role of receivers a and b since only the signal recorded in b is derived. However, if the ambient noise sources are uniformly distributed in space and time, have similar statistics, and the receiver responses are identical, then the signals recorded by receivers a and b have the same characteristics. Note the requirement on the noise source statistics to correctly estimate the TDGF from the NCF. In this case $C_{a,a}(q) \approx C_{b,b}(q)$ and $DC_{a,a}(q) \approx DC_{b,b}(q)$. Thus the roles of receiver a and b in Eq. (28) are indeed interchangeable.

Assuming a white noise model and a finite bandwidth recordings B_ω and using similar derivations done for Eq. (19), the general expression of the variance of the time derivative of the NCF given in Eq. (28) reduces to

$$\left[\text{Var}\left(\frac{dC_{a,b}(\tau)}{d\tau}\right)\right]_{\tau>T_{\text{Green}}} \approx \frac{\langle C_{a,a}(0)\rangle\langle DC_{b,b}(0)\rangle}{2B_\omega T_r}. \tag{29}$$

The simplified expression of the variance of the time derivative of the NCF given by Eq. (29) is a constant proportional to the product of the recorded energy by receiver a and the energy of the time derivative of the signal recorded by receiver b (which includes the receiver responses, site effects, and noise source amplitude) and inversely proportional to the time bandwidth product $T_r B_\omega$.

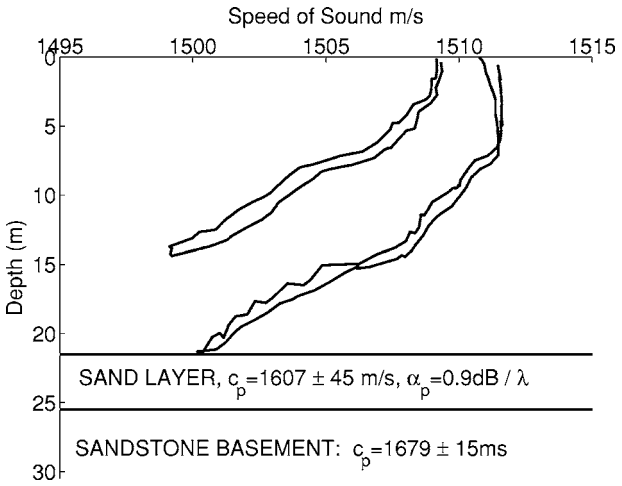

FIG. 1. Model of the range-independent environment in the vicinity of the *NS* array during the ABM95 experiment. The two closest CTD casts were not measured exactly above the location of the arrays but instead in shallower depth (around 15 m, closer to the shoreline) or deeper depth (around 40 m, in the offshore direction from the array). These up and down CTD casts (double lines) are from 0 to 21 m (the water depth at the array location) only.

IV. EXPERIMENTAL RESULTS

A. Experimental measure of the NCF

Ambient noise recordings were collected during the Adaptive Beach Monitoring experiment (ABM 95) near the southern California coast.[9] A bottom horizontal array was deployed along roughly a north-south direction at an average depth of 21 m in a range-independent environment (see Fig. 1). This low frequency (2–750 Hz) hydrophone array had 64 elements with an interelement spacing of $D_{\max}=1.875$ m (equal to half-wavelength spacing at 400 Hz) (see Fig. 2). The sampling frequency was $f_s=1500$ Hz and the array elements had a flat response between approximately 3 and 720 Hz. All array elements were time synchronized. In the

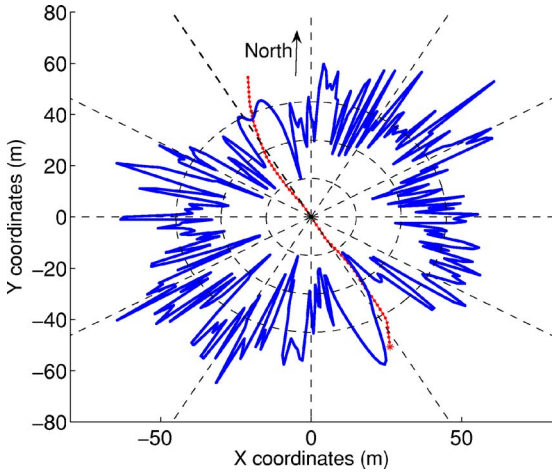

FIG. 2. (Color online) Shape of the bottom array obtained from inversion results.[9] Array elements location are indicated by dots. The origin of the axis coordinates is centered on the middle of the array. The normalized plane wave beamformer output of the array is superimposed on the array shape. Dashed lines shows angular direction with increment of 30°. Three dashed circles indicate the 10-, 20-, and 30-dB level contour levels of the beamformer output.

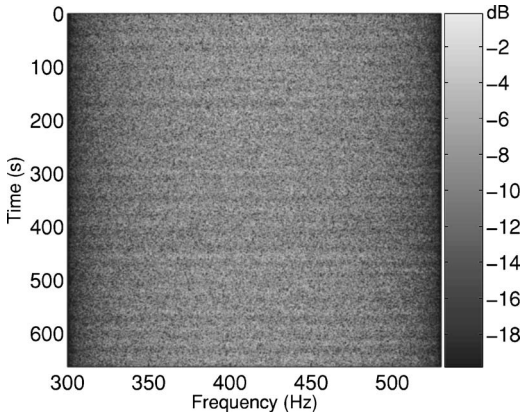

FIG. 3. Normalized spectrogram of 11 min of ambient noise recordings after time-frequency equalization (in the frequency band 300–530 Hz) from JD160 (starting at 0530 UTC), recorded by element 30 of the bottom array (see Fig. 2).

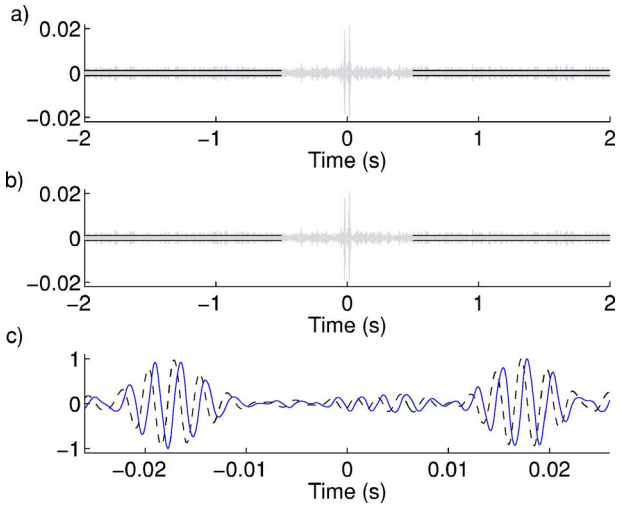

FIG. 4. (Color online) (a) Ambient noise cross-correlation function (NCF) $C_{i,j}(\tau)$, between element $i=30$ and $i=15$ of the bottom array (see Fig. 2). Thirty-three minutes of ambient noise recordings (in the frequency band $B_\omega=300-530$ Hz) were used. The amplitude of the square root of the variance, measured between $0.5<\tau<2s$, is indicated by the black lines. (b) Time derivative of the same NCF which can be used to estimate the arrival time structure of the Green's function. (c) Zoom around the positive and negative arrival times to compare the two time series: the negative time derivative of the NCF $-dC_{i,j}(\tau)/d\tau$ (solid line) and the NCF itself $C_{i,j}(\tau)$ (dashed line). The two time series were resampled at 15 kHz and normalized to their maxima.

vicinity of the array location, the water sound speed at the ocean bottom remained nearly constant at approximately 1495 m/s during this experiment. Details of the experimental setup have been previously presented.[9]

At night, the underwater acoustic ambient noise field was dominated by biological sounds over the 50-Hz to 1-kHz frequency band and the nighttime spectral levels in this band were raised by as much 30 dB over those measured during daylight.[20] The ambient noise field was generated mainly by members of the croaker fish (Sciaenidae) family which migrated at night from the surf zone out to the 21-m water where the bottom hydrophone arrays were located. These noise power spectra exhibit repeatable features of similar intensity throughout the ABM experiment in the 300–700-Hz bandwidth dominated by the croaker sounds consisting of a dominant spectral energy peak between 300 and 530 Hz and a weaker secondary peak between 600 and 700 Hz.[9] Ambient noise data were filtered in the frequency band [300–530 Hz] where the recording amplitude was maximal and the noise field was then created mainly by the distributed croaker fishes. The filtered data were further equalized in the frequency band [300–530 Hz] and a smoothing window was also applied (using a Haning window raised to the power 0.25) in order to render the noise spectrum more uniform before cross correlation. This corresponds to a noise whitening operation for the recorded noise waveforms in the frequency bandwidth of interest. The noise cross-correlation technique works best when the noise distribution is uniform in space and time.[4,7,11,10] Hence data clipping is used subsequently to reduce eventual influence of episodic energetic events (e.g., a loud fish sound close to an hydrophone) which would otherwise dominate the cross correlation. An amplitude threshold of three times the standard deviation of the filtered and equalized noise data was used instead of using a simple but rougher one-bit truncation.[4,14] Figure 3 shows the normalized spectrogram of the 30th array element, in the frequency band 300–530 Hz using 11 min of ambient noise after time-frequency equalization.

Conventional plane wave beamforming was used to verify that the spatial distribution of noise sources surrounding the array was almost uniform. The beamformer output from the noise data was normalized by the beamformer output for the case of uniform superposition of plane waves coming from all directions (i.e., from 0° to 360°) to compensate for the array directivity pattern (or array theoretical response) in the case of a perfectly isotropic noise source distribution. The normalized beamformer output was averaged incoherently across 70 frequencies spanning the whole frequency band 300–530 Hz with a 3.3-Hz increment. The resulting nearly uniform normalized beamformer output shows that the directionality of the croaker sounds was nearly isotropic (see Fig. 2). This confirms previous observations that the bottom hydrophone array was located in the midst of the fish schools.[20] Based on Figs. 2 and 3, the ambient noise field appears to be uniform in space and time in this frequency band. Thus theoretical predictions developed in Sec. II can be used to estimate the variance of the NCF computed from this experimental data set.

Figure 4(a) represents the NCF between the 15th and 30th elements of the north-south array which were separated approximately by 28 m (see Fig. 1). The NCF was obtained using 33 min of ambient noise recordings [see Fig. 3]. The normalized NCF $NC_{a,b}(\tau)$ was computed as the ratio of the NCF and the square root of the recorded energy of each receiver so that the autocorrelation is equal to 1:

$$NC_{a,b}(\tau)=\frac{C_{a,b}(\tau)}{C_{a,a}(0)C_{b,b}(0)}. \tag{30}$$

As expected, the time delays obtained from the NCF are symmetric in time because of the uniform surface noise distribution around the horizontal array (as shown in Fig. 2). Thus, for a pair of receivers $i=30$ and $j=15$, the corresponding NCF $C_{i,j}(\tau)$, for $\tau>0$, is a mirror image of the NCF,

$C_{i,j}(\tau)$, for $\tau<0$, with respect to the time-delay origin $\tau=0$ [see Eq. (1)]. Figure 4(b) represents the time derivative of the NCF displayed in Fig. 4(a). The derivative of the NCF is an antisymmetric function with respect to time, the NCF itself being a symmetric function. The time derivative of the NCF exhibits a clear double-peak structure associated with direct arrival of the TDGF.[9] The ambient noise recorded on the hydrophone array has a relatively small bandwidth B_ω =[300 Hz, 530 Hz]. Hence at first sight the time series of the NCF and its time derivative will look nearly identical. Figure 4(c) compares more closely the two time series $-dC_{i,j}(\tau)/d\tau$ (solid line), which yields the theoretical estimate of the true TDGF, to the NCF $C_{i,j}(\tau)$ (dashed line). The waveforms are similar but with a phase shift (for narrowband signals) corresponding here to a small time delay of 0.5 ms, which yields an error estimate in separation distance of 0.75 m. For a stationary pair separated by large distances with respect to the wavelength, thus yielding large arrival times, this small time delay is often insignificant and within the error bound associated with travel-time measurements. However, for small distances, e.g., 28 m in this case or roughly 7.5 wavelengths, this small time delay can cause a significant error in travel-time measurements. Thus, using the derivative of the NCF yields a crucial difference for the precise measurement required for array element localization[9] or small-scale tomography.

The time derivative of the NCF clearly shows the direct arrivals of the TDGF between two array elements; however, other multipath arrivals of the TDGF do not appear as clearly. This is most likely due to the multiple interaction with the moving free surface and the high attenuation bottom for the coherent components of the noise field propagating between the receivers along high angle paths. Indeed, in the presence of environmental fluctuation, the contribution of these noise components to the time-averaged NCF may not average coherently over long recording time period, i.e., T_r in the order of tenths of minutes. Thus the high angle paths may not emerge as reliably over time from the time-averaged NCF. Furthermore, even though the dominant noise sources (croakers) are uniformly distributed around the array, they may be quite directional since the croakers are typically located close to the hard ocean bottom (thus approaching baffled sources). Hence the shading introduced by the directionality of the noise sources may also further reduce the emergence of the high angle paths in the NCF.[7,8]

B. Experimental measure of the variance of the NCF

Following the theoretical discussions in Sec. II, the variance of the NCF was computed for long time-delay 0.5 s $\leqslant|\tau|\leqslant$2 s, much larger than the maximal travel time between array elements which is $(N-1)D_{\max}/c_0\approx 0.08$ s, where $N=64$ and $D_{\max}=1.875$ m. For instance, the square root of the variance is indicated by a thick line for respectively the NCF and its time derivative in Figs. 4(a) and 4(b), corresponding to a receiver separation distance of 28 m and a recording time $T_r=33$ min. To investigate the variations of the variance of the NCF, the experimental NCF was computed for six receiver pairs spaced from 1.82 to 27.65 m

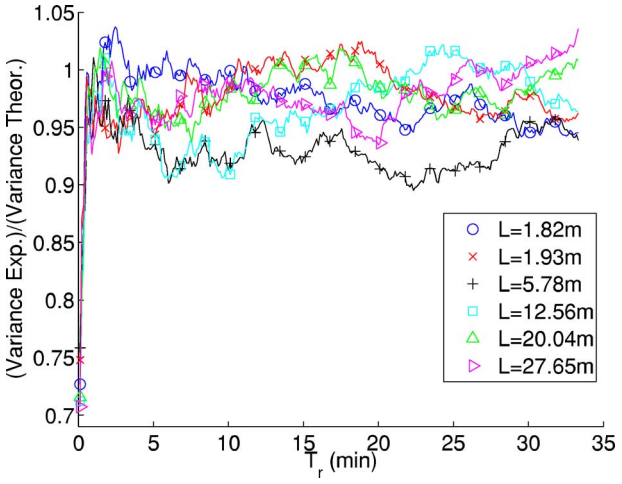

FIG. 5. (Color online) Ratio of the experimental measurements of the variance and the simplified theoretical predictions for the variance of the NCF given by Eq. (20) for increasing recording time T_r and for six receiver pairs with increasing separation distance L. This ratio is $\mathrm{Var}(C_{a,b})\times(2B_\omega^E T_r)/(\langle C_{a,a}(0)\rangle\langle C_{b,b}(0)\rangle)$ for two receivers a and b. The effective bandwidth was set to $B_\omega^E\approx 180$ Hz.

(using element 30 as the first receiver and by using different hydrophones as the second receivers) for increasing recording time from 6.6 s to 33 min by increments of 6.6 s.

Since the ambient noise recordings were windowed in the frequency bandwidth [300–530 Hz], the effective frequency bandwidth B_ω^E was indeed smaller: $B_\omega^E\approx 180$ Hz for most receiver pairs. Figure 5 compares the ratio of the experimental measurements of the variance of the NCF and the theoretical predictions for the variance of the NCF given by Eq. (20) for increasing recording time T_r and for each of the six receiver pairs using the effective bandwidth B_ω^E. The ratio $\mathrm{Var}(C_{a,b})\cdot(2B_\omega^E T_r)/(\langle C_{a,a}(0)\rangle\langle C_{b,b}(0)\rangle)$ remains close to one for all receiver pairs and recording time T_r larger than 1 min. For this short bandwidth, the amplitudes of the time derivative of NCF and of the NCF itself were almost identical (see Fig. 4). The ratio between the variance of the time derivative of the NCF and the corresponding theoretical predictions given by Eq. (29) yielded identical curves as in Fig. 5, all very close to 1. The theoretical predictions deviate from the experimental results for a small recording time-window length T_r (below 1 min here), which is insufficient for the time averaging for the ambient noise statistics to converge. Furthermore, the deviations of the noise source distributions from the case of an isotropic distribution may also affect the results.[9]

V. CONCLUSIONS

Theoretical predictions of the variance of the ambient noise cross-correlation function (NCF) between two receivers (and of its time derivative) have been derived and were simplified assuming a finite temporal length for the Green's function and a white noise nodel. The dominant term for simplified expression of the variance of the NCF is a constant proportional to the product of the recorded energy by both receivers and inversely proportional to the time-bandwidth product $T_r B_\omega$ where T_r is the recording time and B_ω is the frequency bandwidth of the recordings [see Eq.

(20)]. The expression of the recorded energy includes the receiver responses, site effects, and noise source amplitude. The variance of the time derivative of the NCF has a similar dependency but the recorded energy by one of the receivers is now replaced by the energy of the time derivative of the recorded signals instead [see Eq. (29)]. These simple analytic formulas provide a way to quantify the signal-to-noise ratio of the NCF and its time derivative.[9,13] A good agreement with experimental measurement of the variance of the NCF was found for ocean ambient noise recordings in shallow water in the frequency band [300–530 Hz] for receiver separations up to 28 m.

For such short separation distances between elements and strong bottom absorption, it was mentioned in Sec. III A that multipath arrivals of the NCF are not likely to be observed since they should have indeed a weak amplitude. Provided there is a simple estimate of the amplitude of the multipath arrivals (e.g., using a ray code[18]), the theoretical predictions given by Eq. (20) can be used to estimate the minimal duration of the noise recordings for the variance of the NCF to fall below a certain detection threshold for those arrivals. For the ABM95 environment and noise statistics the recording time should amount to several hours in order to have sufficient averaging time for the weak multipath arrivals to emerge from the NCF. However, fluctuations of the environment (e.g., tides, moving free surface, change of water sound speeds) render the acoustic paths nonstationary over such long durations and thus would prevent the coherent emergence of these multipath arrivals. On the other hand, for a more stable environment such as the earth crust in seismology applications, the theoretical predictions given by Eq. (20) can help to specify the amount of averaging necessary to recover both surface waves as well as body waves from seismic noise recordings.[13,14]

ACKNOWLEDGMENTS

This works was supported by the Office of Naval Research. We thank the two anonymous reviewers for their constructive comments.

[1]J. Rickett and J. Claerbout, "Acoustic daylight imaging via spectral factorization: Helioseismology and reservoir monitoring," The Leading Edge **18**, 957–960 (1999).

[2]O. I. Lobkis and R. L. Weaver, "On the emergence of the green's function in the correlations of a diffuse field," J. Acoust. Soc. Am. **110**, 3011–3017 (2001).

[3]R. L. Weaver and O. I. Lobkis, "Elastic wave thermal fluctuations, ultrasonic waveforms by correlation of thermal phonon," J. Acoust. Soc. Am. **113**, 2611–2621 (2003).

[4]E. Larose, A. Derode, M. Campillo, and M. Fink, "Imaging from one-bit correlations of wideband diffuse wavefields," J. Appl. Phys. **95**, 8393–8399 (2004).

[5]A. E. Malcolm, J. A. Scales, and B. van der Tiggelen, "Retrieving the green function from diffuse equipartitioned waves," Phys. Rev. E **70**, 015601(R) (2004).

[6]R. L. Weaver and O. I. Lobkis, "Diffuse fields in open systems and the emergence of the greens function," J. Acoust. Soc. Am. **116**, 2731–2734 (2004).

[7]P. Roux, W. A. Kuperman, and the NPAL Group, "Extracting coherent wavefronts from acoustic ambient noise in the ocean," J. Acoust. Soc. Am. **116**, 1995–2003 (2004).

[8]K. G. Sabra, P. Roux, and W. A. Kuperman, "Arrival-time structure of the time-averaged ambient noise cross-correlation function in an oceanic waveguide," J. Acoust. Soc. Am. **117**, 164–174 (2005).

[9]K. G. Sabra, P. Roux, A. M. Thode, G. L. D'Spain, W. S. Hodgkiss, and W. A. Kuperman, "Using ocean ambient noise for array self-localization and self-synchronization," IEEE J. Ocean. Eng. (unpublished).

[10]N. M. Shapiro and M. Campillo, "Emergence of broadband rayleigh waves from correlations of the ambient seismic noise," Geophys. Res. Lett. **31**, L07614 (2004).

[11]R. Snieder, "Extracting the green's function from the correlation of coda waves: A derivation based on stationary phase," Phys. Rev. E **69**, 046610 (2004).

[12]K. Wapenaar, "Retrieving the elastodynamic greens function of an arbitrary inhomogeneous medium by cross correlation," Phys. Rev. Lett. **93**, 254301 (2004).

[13]K. G. Sabra, P. Gerstoft, P. Roux, W. Kuperman, and M. C. Fehler, "Extracting time-domain greens function estimates from ambient seismic noise," Geophys. Res. Lett. **32**, L03310 (2005).

[14]N. M. Shapiro, M. Campillo, L. Stehly, and M. Ritzwoller, "High-resolution surface-wave tomography from ambient seismic noise," Science **29**, 1615–1617 (2005).

[15]P. Roux, K. Sabra, W. Kuperman, and A. Roux, "Ambient noise cross-correlation in free space: theoretical approach," J. Acoust. Soc. Am. **117**, 79–84 (2005).

[16]R. L. Weaver and O. I. Lobkis, "Fluctuations in diffuse field-field correlations and the emergence of the green's function in open systems," J. Acoust. Soc. Am. **117**, 3432–3439 (2005).

[17]R. L. Weaver and O. I. Lobkis, "The mean and variance of diffuse-field correlations in finite bodies," J. Acoust. Soc. Am. (unpublished).

[18]F. B. Jensen, W. A. Kuperman, M. B. Porter, and H. Schmidt, *Computational Ocean Acoustics* (AIP, New York, 2000).

[19]M. Buckingham, in *Noise in Electronic Devices and Systems*, edited by E. Horwood (Wiley, New York, 1983), p. 30.

[20]G. L. D'Spain, L. Berger, W. A. Kuperman, and W. S. Hodgkiss, "Summer night sounds by fish in shallow water," in *Proc. Int. Conf. on Shallow-Water acoustics* (China Ocean Press, Beijing, 1997), pp. 379–384.

Mean and covariance of the forward field propagated through a stratified ocean waveguide with three-dimensional random inhomogeneities

Purnima Ratilal and Nicholas C. Makris
Department of Ocean Engineering, Massachusetts Institute of Technology, Cambridge, Massachusetts 02139

(Received 22 May 2004; revised 3 June 2005; accepted 12 June 2005)

Compact analytic expressions are derived for the mean, mutual intensity, and spatial covariance of the acoustic field forward propagated though a stratified ocean waveguide containing three-dimensional random surface and volume inhomogeneities. The inhomogeneities need not obey a stationary random process in space, can be of arbitrary composition and size relative to the wavelength, or can have large surface roughness and slope. The form of the mean forward field after multiple scattering through the random waveguide is similar to that of the incident field, except for a complex change in the horizontal wave number of each mode. This change describes attenuation and dispersion induced by the medium's inhomogeneities, including potential mode coupling along the propagation path. The spatial covariance of the forward field between two receivers includes the accumulated effects of both coherent and incoherent multiple forward scattering through the random waveguide. It is expressed as a sum of modal covariance terms. Each term depends on the medium's expected modal extinction densities as well as the covariance of its scattering properties, which potentially couple each mode to every other mode. Three-dimensional scattering effects can become important at ranges where the Fresnel width exceeds the cross-range coherence scale of the medium's inhomogeneities. © *2005 Acoustical Society of America.* [DOI: 10.1121/1.1993087]

PACS number(s): 43.30.Re [WLS] Pages: 3532–3559

I. INTRODUCTION

Compact analytic expressions are derived for the mean, mutual intensity, and spatial covariance of the acoustic field forward propagated through a stratified ocean waveguide with three-dimensional (3-D) random surface and volume inhomogeneities. The novelty and advantages of the approach stem from the fact that 3-D multiple forward scattering is included in a formulation where received field moments are analytically expressed in terms of the moments of the random medium's spatially varying scatter function[1,2] density. This makes it possible to describe volume and surface scatterers of arbitrary composition and size relative to the wavelength that individually may strongly scatter the acoustic field. This differs substantially from restrictive perturbation theory and Rayleigh[3]-Born[4] approximation methods, where parameters such as surface roughness, slope, or changes in medium properties must be small. It also differs from parabolic equation approaches, where field moments must be obtained by numerical marching algorithms. Since the inhomogeneities need not obey a stationary random process in space, the formulation accounts for expected range, cross-range, and depth-dependent variations in the medium's scatter function density. It is based upon a modal formulation for coherent 3-D scattering in an ocean waveguide[1,5] and the waveguide extinction or generalized forward scatter theorem,[6] both of which stem directly from Green's theorem.

After describing the approach in the context of previous work, an analytic expression is derived for the acoustic field forward scattered from a single elemental shell of random inhomogeneities between a point source and distant receiver in an ocean waveguide. This is done in Sec. II via a single-scatter approximation. Difference and integral equations are then developed to march the mean field and expected power through a randomly inhomogeneous waveguide in Secs. III and IV. This includes the accumulated effects of multiple forward scattering through the medium for both the *mean and covariance* of the forward field.

Compact solutions for the mean, variance, and second moment of the forward propagated field are given in terms of parameters necessary to describe the incident field as well as the mean and spatial covariance of the medium's scatter function density in Sec. V. Compact solutions for transmitted power and the signal-to-noise ratio of the forward field are also presented in Sec. V. They are used to analytically show that 3-D scattering effects can become important at ranges between the source and receiver, where the Fresnel width approaches and exceeds the cross-range coherence scale of the medium's inhomogeneities.

The approach is generalized to determine the mutual intensity and spatial covariance of the forward propagated field in Sec. VI. Compact solutions are given in Sec. VI B. These can be used to the quantify the effect of randomness in the ocean medium on ocean acoustic remote sensing with receiving arrays of arbitrary configuration.

The fundamental assumptions of the present paper are that (1) in the absence of inhomogeneities, the waveguide is horizontally stratified; (2) the medium can be described by a scattering process where single scattering is valid in horizontal range increments large enough for the modal diagonalization condition of Eq. (57) to be valid; (3) the medium's 3-D

inhomogeneities obey a stationary random process within the incremental range scales described in (2) and the local Fresnel width in cross-range, but may not be stationary in the vertical or across larger horizontal scales; (4) the forward scattered field is approximated as that which successively forward scatterers through the inhomogeneous medium by interactions within the Fresnel width in cross-range from source to receiver; (5) the field scattered solely from inhomogeneities within any *single* horizontal range increment described in (2) must be small compared to the incident field; (6) to obtain mutual intensity from the power equations, waveguide modes are assumed to be uncorrelated, as is consistent with the central limit theorem, which is supported by many observations[7] and statistical theories for ocean-acoustic fluctuations.[8,9]

A. Approach in the context of previous developments

Some of the basic ideas behind the approach were inspired by the intuitive and physically compelling work of Rayleigh[10] in his explanation for the blue sky and red sunset, both of which have analogies in acoustic reverberation and transmission through the ocean. To study forward propagation in free space with random inhomogeneities, or the red sunset problem, Rayleigh first analyzed the effect of scattering by a thin slab of inhomogeneities in what we now call the *mean* forward field. He used this result to show that multiple forward scattering by inhomogeneities leads to an altered wave number in the mean field, which can be interpreted in terms of an effective medium when the scattered field from any slab is small compared to the incident field. The expected wave number change, ν, is directly proportional to the expected number of inhomogeneities per unit volume of the medium, n_V, multiplied by the forward scatter function of the inhomogeneities, S_f, and $2\pi/k^2$, where k is the wave number in free space; $\nu=(2\pi/k^2)\langle n_V S_f\rangle$. This wave number change leads to dispersion and attenuation in the mean forward field, and causes temporal distortion of the original signal waveform. A more modern version of Rayleigh's approach is given by van de Hulst,[11] where statistical operations leading to a mean field are again only implicit. The same results were later obtained by Foldy[12] using a significantly different multiple scatter series formulation, akin to Dyson's later more general formulation,[13] with ensemble averaging concepts but essentially the same physical assumptions as Rayleigh. Rayleigh implicitly, and van de Hulst explicitly, used a stationary phase approximation[14] to arrive at what we refer to here as the mean *direct wave*, following Rayleigh's intuitive terminology. The direct wave is comprised of the incident field and multiply scattered field contributions propagating within the Fresnel angle of forward from any inhomogeneous slab to the receiver. The latter are those contributions that travel with and can coherently interfere with the incident field. We refer to scattered field contributions that involve longer propagation paths, where some or all multiple scattering falls outside the Fresnel angle, to be *coda*. Coda is equivalent to *reverberation*. Many classic continuum models for optical and laser beam propagation through the turbulent atmosphere are based on assumptions similar to those in Rayleigh's original slab and direct wave formulation of forward scatter.[15]

The signal measured at a receiver from a point source in a waveguide is typically composed of multiple arrivals due to multimodal propagation effects, even when the medium is not random. We consider the *direct wave* in an inhomogeneous waveguide to be comprised of the incident and multiply scattered field contributions propagating within the Fresnel *azimuth* of forward from any cylindrical shell of inhomogeneities about the source to the receiver. Arrivals involving wider azimuthal scattering angles tend to form coda. The direct wave typically contains the most important information for signal transmission through the medium. Coda is important primarily in reverberation studies since it typically falls below the dynamic range or noise level of measurement systems designed for direct wave reception.

In a shallow-water waveguide, the effect of scattering by a single object leads to mode coupling and a redistribution of mode amplitudes that can be expressed in terms of the scatter function of the object.[1,5] We show that a distribution of volume or surface inhomogeneities over a sufficiently large range or depth increment causes the waveguide modes to decouple in the *mean* forward field under widely satisfied conditions. This allows the *mean* forward field to be analytically *marched* through range to include multiple forward scattering via a single modal sum by an explicit procedure analogous to Rayleigh's implicit marching procedure in free space. The resulting mean field has a form similar to the incident field, but with a change in the complex horizontal wave number for each mode due to scattering that leads to additional attenuation and dispersion. This wave number change is determined by the medium's expected scatter function density, which may vary as a function of range, depth, and azimuth. By invoking the generalized waveguide extinction theorem,[6] we show that attenuation from forward scattering for each mode can be expressed in terms of the expected waveguide modal extinction density of the medium. This provides a convenient method for estimating power losses after multiple forward scattering, given knowledge of the intrinsic scattering properties of the random medium.[16] We then apply a similar marching approach to derive analytic expressions for the mutual intensity and covariance of the forward field between two receivers in a random waveguide from a distant point source. We show that the resulting covariance can be expressed as a sum of modal covariance terms. Each term depends on the medium's expected modal extinction density as well as the covariance of the medium's scatter function density, which potentially couples each mode to all other modes.

While our method for obtaining the second moments of the forward field requires explicit statistical operations, it is still consistent with the implicit first moment analysis in Rayleigh's original explanation of the red sunset. To see this, let us follow Rayleigh's[10] notation in this Introduction and take m to be the dimensionless ratio of the scattered field to the incident field from a single slab of random inhomogeneities with surface normal in the direction of forward propagation. Rayleigh makes no distinction between m and its expectation $\langle m\rangle$ in his analysis, although his analysis is

undoubtedly for the mean field. Let us assume then that m is a random variable, so that by m, Rayleigh is referring to what we here call $\langle m \rangle$. Rayleigh finds that $\langle m \rangle$ must be small but not negligible compared to unity in order to march the field and obtain his effective medium result. In our second moment analysis, we follow a similar asymptotic approach and find that if $\langle m \rangle$ is small, $\langle m \rangle^2$ must be negligible, since it is totally determined by $\langle m \rangle$. The second moment $\langle m^2 \rangle$, however, is not negligible since it contains the variance of m that need not depend on $\langle m \rangle$. So, we take $\langle m^2 \rangle$ to be small but not negligible compared to unity. This enables us to obtain the forward field's second moment by an analytic marching procedure similar to that used to obtain the mean. As Foldy has noted, the second moment of the field is often more important than the first in many experimental scenarios.[12]

Since Rayleigh, there has been a long history of development in the study of wave propagation through random media, especially in free space for which a number of excellent references exist, including those by Strobehn,[15] Tsang, Kong, and Shin,[17] Ishimaru,[18] and van de Hulst.[11] Rayleigh's effective medium approach, however, is still one of the most widely used since it conveniently expresses effective wave number changes in terms of the scatter function of medium inhomogeneities. For the ocean, analytic approaches using ray theory have been investigated for deep water applications by a number of authors.[19,20] More recently, ray and other approaches for the ocean, such as the 2-D parabolic equation, are now widely used to generate statistical realizations of the acoustic field.[21–24] In shallow water it has also become increasingly common to determine field moments via Monte Carlo simulations using the 2-D parabolic equation.[25]

Even with the current availability of computing power, analytic methods and solutions still offer advantages because they provide insight into the mechanisms that lead to the observed phenomena. This is one of the primary motivations for the present paper. Another motivation is that it is still very difficult to perform 3-D Monte-Carlo simulations of propagation through a random ocean waveguide. The present analytic technique is then also valuable because it can be employed to efficiently solve a wide range of practical 3-D problems. A modal formulation was selected because modes are the most clearly identifiable entities that may propagate with statistical independence in a random waveguide.

A number of modal formulations for propagation through a waveguide with randomness have been previously developed. To our knowledge, however, they are all based upon perturbation theory and either require surface roughness and slope to be small or variations in medium sound speed and density to be small. For mean field propagation, Bass, Freulicher, and Fuks[26,27] investigated the specific problem of propagation through a waveguide with small boundary roughness. They expressed the mean field in terms of complex modal wave number changes by solving Dyson's equation with perturbation theory.[26] Kuperman and Ingenito[28] later used Bass, Freulicher, and Fuks[26] results to investigate the attenuation of the mean sound field propagating through a shallow water waveguide with rough boundaries, following experimental work by Ingenito.[29] Their approach, however, neglects the effect of dispersion in the mean field. Kuperman and Schmidt[30,31] extended Kuperman and Ingenito's[28] 3-D perturbation theory approach for mean field attenuation to a more generalized wave number formulation for small amplitude and slope roughness at multiple layers. Tracey and Schmidt[32] used this to develop a 2-D modal formulation to describe mean field attenuation from small perturbations in medium sound speed and density or surface roughness and slope. They later extended this to describe the effect of small 3-D perturbations in seabed sound speed and density on mean field modal attenuation for inhomogeneities with vertical scales small compared to the acoustic wavelength.[33]

A number of purely single scatter approaches for estimating the second moment of the received field in a waveguide have been developed, including those by Sutton and McCoy[34] and Tracey and Schmidt.[32] While these second moment approaches include a single scatter contribution from each inhomogeneity, they ignore the multiple scattering effects between inhomogeneities along the forward propagation path. This limits their applicability to relatively short ranges, as noted by Sutton and McCoy.[34]

A number of formulations for second moment propagation in a waveguide that include multiple scattering between medium inhomogeneities along the propagation path have been developed. Bass, Freulicher, and Fuks[27] again investigated a waveguide with small boundary roughness, but this time started with the general Bethe-Salpeter equations.[35] They obtained approximate transfer equations for modal intensities, but no explicit solution for the field moments. Dozier and Tappert,[36] and later Creamer,[37] derived expressions for the second moment of the forward field in a 2-D ocean waveguide with small sound speed perturbations by following the perturbed coupled-mode approach of Marcuse[38] in fiber optics. Penland[39] addressed 3-D effects neglected by Dozier and Tappert[36] for small sound speed fluctuations that have slow range variation with respect to the acoustic wavelength by making a number of adiabatic assumptions, as noted by Frankenthal and Beran.[40] Continuing the small sound speed perturbation approximation and adopting a slab formulation, Frankenthal and Beran[40] derived difference equations for the mean and second moment of the field forward propagated through a 3-D random channel with a rigid bottom and a pressure-release top, but apparently did not solve these equations. They found, as do we, that energy is not eventually equipartioned among the modes, as has been suggested based on analysis of 2-D models such as those of Dozier and Tappert.[36] They also found that Penland's[39] approximations are inconsistent with their equation for the propagation of modal power.[40]

Here we present a formulation for 3-D propagation through a stratified waveguide with random surface or volume inhomogenieties of arbitrary size relative to the acoustic wavelength and arbitrary contrast in compressibility and density from the pure medium. Since the inhomogenieties may strongly scatter the incident field individually, this formulation is more general than approaches based on small perturbations in sound speed and density or surface roughness and slope. Our formulation also describes the accumulated effects of *multiple forward scattering* on the *mean and cova-*

riance of the forward propagated field. These include coherent, partially coherent, and incoherent interactions with the incident field that lead to attenuation, dispersion, and exponential coefficients of field variance that describe mode coupling induced by the medium's inhomogeneities. We obtain difference equations, integral equations, and *analytic solutions* to these equations for the mean field, the expected intensity and the mutual intensity, including evanscent effects. We find in a following paper[16] that the present 3-D formulation is consistent with standard 2-D Monte-Carlo simulations at ranges within which the 2-D simulations should be valid, i.e., where the Fresnel angle of the incident field is less than the angle spanned by the cross-range extent of the inhomogeneity. This follows the analytic predictions of the present paper. This work has been presented at numerous meetings of the Acoustical Society of America,[41,42] including applications involving random internal waves,[43–46] random seabed inhomogeneities,[43,44,47] random bubble clouds,[43,48] and source localization in a random ocean waveguide.[49]

II. SCATTERED FIELD CONTRIBUTION TO THE DIRECT WAVE FROM A SHELL OF INHOMOGENEITIES

An analytic expression is derived for the scattered field contribution to the direct wave from an elemental cylindrical shell of inhomogeneities between the source and receiver. This is the portion of the field scattered from the shell that coherently interferes with the incident field, on average.

The origin of the coordinate system is placed at the air-water interface with the positive z axis pointing downward. The source is located at the horizontal origin $\mathbf{r_0}=(0,0,z_0)$, while receiver coordinates are given by $\mathbf{r}=(x,y,z)$ and those of inhomogeneity centers by $\mathbf{r_t}=(x_t,y_t,z_t)$. Spatial cylindrical (ρ,ϕ,z) and spherical systems (r,θ,ϕ) are defined by $x=r\sin\theta\cos\phi$, $y=r\sin\theta\sin\phi$, $z=r\cos\theta$, and $\rho^2=x^2+y^2$. The horizontal and vertical wave number components for the nth mode are, respectively, $\xi_n=k\sin\alpha_n$ and $\gamma_n=k\cos\alpha_n$, where α_n is the elevation angle of the mode measured from the z axis. Here, $0\leqslant\alpha_n\leqslant\pi/2$ so that the down and upgoing plane wave components of each mode have elevation angles α_n and $\pi-\alpha_n$, respectively. The corresponding vertical wave number of the down- and upgoing components of the nth mode are γ_n and $-\gamma_n$, respectively, where $\Re\{\gamma_n\}\geqslant 0$. The azimuth angle of the mode is denoted by β. The wave number magnitude k equals the angular frequency ω divided by the sound speed c in the object layer, where $k^2=\xi_n^2+\gamma_n^2$. The geometry of spatial and wave number coordinates is shown in Ref. 50.

The field scattered to $\mathbf{r}$ from inhomogeneities within a cylindrical shell of radius ρ_s and thickness $\Delta\rho_s$ is found by integrating volumetric contributions with a single scatter approximation,

$$\Phi_s(\mathbf{r}|\mathbf{r_0},\Delta\rho_s(\rho_s))=\iiint_{\Delta V_s}\varphi_s(\mathbf{r}|\mathbf{r_0},\mathbf{r_t})\mathrm{d}V_t, \tag{1}$$

where ΔV_s is the volume of the cylindrical shell element and $\varphi_s(\mathbf{r}|\mathbf{r_0},\mathbf{r_t})$ is the scattered field per unit volume from inhomogeneities *centered* at $\mathbf{r_t}$.

A modal solution for the 3-D bistatic scattered field from an inhomogeneity of arbitrary size, shape, and material properties in an ocean waveguide has been derived from Green's theorem in Refs. 1, 5, and 51. With this, the scattered field per unit volume can be written as

$$\begin{aligned}\varphi_s(\mathbf{r}|\mathbf{r_0},\mathbf{r_t})&=\sum_{m=1}^{M_{\max}}\sum_{n=1}^{M_{\max}}\frac{(4\pi)^2}{k}\\&\times[A_m(\mathbf{r}-\mathbf{r_t})A_n(\mathbf{r_t}-\mathbf{r}_0)s_{\mathbf{r_t}}(\pi-\alpha_m,\beta_s(\phi,\phi_t);\alpha_n,\phi_t)\\&-B_m(\mathbf{r}-\mathbf{r_t})A_n(\mathbf{r_t}-\mathbf{r}_0)s_{\mathbf{r_t}}(\alpha_m,\beta_s(\phi,\phi_t);\alpha_n,\phi_t)\\&-A_m(\mathbf{r}-\mathbf{r_t})B_n(\mathbf{r_t}-\mathbf{r}_0)s_{\mathbf{r_t}}(\pi-\alpha_m,\beta_s(\phi,\phi_t);\pi-\alpha_n,\phi_t)\\&+B_m(\mathbf{r}-\mathbf{r_t})B_n(\mathbf{r_t}-\mathbf{r}_0)s_{\mathbf{r_t}}(\alpha_m,\beta_s(\phi,\phi_t);\pi-\alpha_n,\phi_t)],\end{aligned} \tag{2}$$

where $A_n(\mathbf{r_t}-\mathbf{r}_0)$ and $B_n(\mathbf{r_t}-\mathbf{r}_0)$ are the amplitudes of the *down-* and *upgoing* modal plane wave components incident on the inhomogeneity at $\mathbf{r_t}$, $A_m(\mathbf{r}-\mathbf{r_t})$ and $B_m(\mathbf{r}-\mathbf{r_t})$ are the amplitudes of the *up-* and *downgoing* modal components scattered from the inhomogeneity,[51] $s_{\mathbf{r_t}}(\alpha,\beta;\alpha_i,\beta_i)$ is the scatter function[2] density of the medium at $\mathbf{r_t}$, $\beta_s(\phi,\phi_t)=\phi-\arcsin\{(\rho_t/|\boldsymbol{\rho}-\boldsymbol{\rho_t}|)\sin(\phi_t-\phi)\}$ is the azimuth of the receiver from the target, α_n are the previously defined modal elevation angles, and $M_{\max}$ is the mode number at which the modal summations can be truncated and still accurately represent the field. We abbreviate the modal summation notation in subsequent equations with the understanding that the sum is taken to $M_{\max}$ modes.

The scatter function density describes scattering from both discrete and continuously varying inhomogeneities, as shown in Appendix A. The scattered field must be described in terms of a double modal sum to account for coupling of incident and scattered modes by the inhomogeneity. Equation (2) is applicable when the source and receiver ranges are sufficiently far from the target that the plane wave scatter function description is valid.[5,52,54]

For a single shell, the incident field has modal plane wave amplitudes given by,[1,5,51]

$$A_n(\mathbf{r_t}-\mathbf{r_0})=\frac{i}{d(z_0)}\frac{1}{\sqrt{8\pi\xi_n\rho_t}}u_n(z_0)N_n^{(1)}\mathrm{e}^{i(\xi_n\rho_t+\gamma_n z_t-\pi/4)}, \tag{3}$$

$$B_n(\mathbf{r_t}-\mathbf{r_0})=\frac{i}{d(z_0)}\frac{1}{\sqrt{8\pi\xi_n\rho_t}}u_n(z_0)N_n^{(2)}\mathrm{e}^{i(\xi_n\rho_t-\gamma_n z_t-\pi/4)}, \tag{4}$$

while the scattered modal plane wave amplitudes in Eq. (2) are[1,5,51]

$$A_m(\mathbf{r}-\mathbf{r_t})=\frac{i}{d(z_t)}\frac{1}{\sqrt{8\pi\xi_m|\boldsymbol{\rho}-\boldsymbol{\rho_t}|}}u_m(z)N_m^{(1)}\mathrm{e}^{i(\xi_m|\boldsymbol{\rho}-\boldsymbol{\rho_t}|+\gamma_m z_t-\pi/4)}, \tag{5}$$

$$B_m(\mathbf{r}-\mathbf{r_t}) = \frac{i}{d(z_t)}\frac{1}{\sqrt{8\pi\xi_m|\boldsymbol{\rho}-\boldsymbol{\rho_t}|}}u_m(z)N_m^{(2)}e^{i(\xi_m|\boldsymbol{\rho}-\boldsymbol{\rho_t}|-\gamma_m z_t-\pi/4)}. \tag{6}$$

Upon substituting Eqs. (3), (4), (5), and (6) into Eq. (2), and Eq. (2) into Eq. (1), the scattered field from the shell becomes

$$\begin{aligned}
&\Phi_s(\mathbf{r}|\mathbf{r_0},\Delta\rho_s(\rho_s))\\
&= \sum_m\sum_n \iiint_{\Delta V_s} \frac{2\pi}{k}\frac{i}{d(z_0)d(z_t)}\frac{1}{\sqrt{\xi_m\xi_n|\boldsymbol{\rho}-\boldsymbol{\rho_t}|\rho_t}}u_m(z)u_n(z_0)e^{i(\xi_m|\boldsymbol{\rho}-\boldsymbol{\rho_t}|+\xi_n\rho_t)}\\
&\quad\times[N_m^{(1)}N_n^{(1)}e^{i(\gamma_m+\gamma_n)z_t}s_{\mathbf{r_t}}(\pi-\alpha_m,\beta_s(\phi,\phi_t);\alpha_n,\phi_t)\\
&\quad- N_m^{(2)}N_n^{(1)}e^{i(-\gamma_m+\gamma_n)z_t}s_{\mathbf{r_t}}(\alpha_m,\beta_s(\phi,\phi_t);\alpha_n,\phi_t)\\
&\quad- N_m^{(1)}N_n^{(2)}e^{i(\gamma_m-\gamma_n)z_t}s_{\mathbf{r_t}}(\pi-\alpha_m,\beta_s(\phi,\phi_t);\pi-\alpha_n,\phi_t)\\
&\quad+ N_m^{(2)}N_n^{(2)}e^{i(-\gamma_m-\gamma_n)z_t}s_{\mathbf{r_t}}(\alpha_m,\beta_s(\phi,\phi_t);\pi-\alpha_n,\phi_t)]\rho_t\,d\rho_t\,d\phi_t\,dz_t,
\end{aligned} \tag{7}$$

where $\xi_m|\boldsymbol{\rho}-\boldsymbol{\rho_t}| = \xi_m\sqrt{\rho^2+\rho_t^2-2\rho\rho_t\cos(\phi_t-\phi)}$.

The integration over shell azimuth ϕ_t leads on average to two stationary phase contributions centered at $\phi_t=\phi$ and $\phi_t=\phi+\pi$ over angular widths $\phi_F(\rho,\rho_t)=\sqrt{2\pi(\rho-\rho_t)/\xi_m\rho\rho_t}$ and $\phi_B(\rho,\rho_t)=\sqrt{2\pi(\rho+\rho_t)/\xi_m\rho\rho_t}$, respectively, via approximations of the form

$$\begin{aligned}
&\int_0^{2\pi}\frac{1}{\sqrt{|\boldsymbol{\rho}-\boldsymbol{\rho_t}|}}e^{i\xi_m|\boldsymbol{\rho}-\boldsymbol{\rho_t}|}s_{\mathbf{r_t}}(\pi-\alpha_m,\beta_s(\phi,\phi_t);\alpha_n,\phi_t)d\phi_t\\
&= \int_0^{2\pi}\frac{1}{[\rho^2+\rho_t^2-2\rho\rho_t\cos(\phi_t-\phi)]^{(1/4)}}e^{i\xi_m\sqrt{\rho^2+\rho_t^2-2\rho\rho_t\cos(\phi_t-\phi)}}s_{\mathbf{r_t}}(\pi-\alpha_m,\beta_s(\phi,\phi_t);\alpha_n,\phi_t)d\phi_t\\
&\approx e^{i\pi/4}\frac{e^{i\xi_m(\rho-\rho_t)}}{\sqrt{\rho-\rho_t}}\int_{\phi-\phi_F/2}^{\phi+\phi_F/2}s_{\mathbf{r_t}}(\pi-\alpha_m,\beta_s(\phi,\phi_t);\alpha_n,\phi_t)e^{i\xi_m[\rho\rho_t/2(\rho-\rho_t)](\phi_t-\phi)^2}\,d\phi_t\\
&\quad+ e^{-i\pi/4}\frac{e^{i\xi_m(\rho+\rho_t)}}{\sqrt{\rho+\rho_t}}\int_{\phi+\pi-\phi_B/2}^{\phi+\pi+\phi_B/2}s_{\mathbf{r_t}}(\pi-\alpha_m,\beta_s(\phi,\phi_t);\alpha_n,\phi_t)e^{i\xi_m[\rho\rho_t/2(\rho+\rho_t)](\phi_t-\phi-\pi)^2}\,d\phi_t.
\end{aligned} \tag{8}$$

These define the active region from which dominant contributions to the scattered field are expected to arise. The first term describes forward scatter through the shell within the Fresnel angle ϕ_F, while the second describes backscatter from the rear of the shell. The backscatter term tends not to contribute significantly to the direct wave because it requires longer propagation paths and so tends to (1) suffer greater transmission loss and (2) not arrive with the direct wave in pulsed transmissions. The backscattered contributions also tend to cancel on average since they have phases that oscillate with shell thickness $\Delta\rho_s$.

By applying the type of integral approximations made in Eq. (8) to Eq. (7), the direct wave portion of the scattered field from the shell is found to be

$$\begin{aligned}
&\Phi_s(\mathbf{r}|\mathbf{r_0},\Delta\rho_s(\rho_s))\\
&= \sum_m\sum_n \int_0^{\infty}dz_t\int_{\rho_s-\Delta\rho_s/2}^{\rho_s+\Delta\rho_s/2}d\rho_t\int_{\phi-\phi_F/2}^{\phi+\phi_F/2}\rho_t\,d\phi_t\,e^{i\xi_m[\rho\rho_t/2(\rho-\rho_t)](\phi_t-\phi)^2}\\
&\quad\times\frac{2\pi}{k}\frac{i}{d(z_0)d(z_t)}\frac{1}{\sqrt{\xi_m\xi_n(\rho-\rho_t)\rho_t}}u_m(z)u_n(z_0)e^{i\pi/4}e^{i\xi_m\rho}e^{i(\xi_n-\xi_m)\rho_t}\\
&\quad\times[N_m^{(1)}N_n^{(1)}e^{i(\gamma_m+\gamma_n)z_t}s_{\mathbf{r_t}}(\pi-\alpha_m,\beta_s(\phi,\phi_t);\alpha_n,\phi_t)\\
&\quad- N_m^{(2)}N_n^{(1)}e^{i(-\gamma_m+\gamma_n)z_t}s_{\mathbf{r_t}}(\alpha_m,\beta_s(\phi,\phi_t);\alpha_n,\phi_t)\\
&\quad- N_m^{(1)}N_n^{(2)}e^{i(\gamma_m-\gamma_n)z_t}s_{\mathbf{r_t}}(\pi-\alpha_m,\beta_s(\phi,\phi_t);\pi-\alpha_n,\phi_t)\\
&\quad+ N_m^{(2)}N_n^{(2)}e^{i(-\gamma_m-\gamma_n)z_t}s_{\mathbf{r_t}}(\alpha_m,\beta_s(\phi,\phi_t);\pi-\alpha_n,\phi_t)].
\end{aligned} \tag{9}$$

The active region for forward scattering on the shell then occurs over a Fresnel width $Y_F(\rho,\rho_s)=\rho_s\phi_F(\rho,\rho_s)=\sqrt{2\pi(\rho-\rho_s)\rho_s/\xi_m\rho}$, which is a function of the horizontal wave number of the mth mode. Long-range propagation is directed near the horizontal in most ocean waveguides, so that the mode-independent $Y_F(\rho,\rho_s)\approx\sqrt{\lambda(\rho-\rho_s)\rho_s/\rho}$ is both a good and practical approximation. The Fresnel width varies symmetrically between the source and receiver as a consequence of reciprocity. The maximum Fresnel width $Y_F(\rho,\rho/2)=(\rho/2)\phi_F(\rho,\rho/2)=\sqrt{\lambda\rho/4}$ occurs at the midpoint between source and receiver and increases with the square root of their separation.

III. DIFFERENCE AND INTEGRAL EQUATIONS TO MARCH THE MEAN FIELD, POWER, AND EXPECTED INTENSITY THROUGH A WAVEGUIDE WITH RANDOM INHOMOGENEITIES

A. Mean forward field

An analytic expression is derived for the mean forward field propagated from a point source to a distant receiver through a stratified ocean waveguide containing random volume or surface inhomogeneities. This is done by first developing a difference equation that describes the change in the mean forward field at the receiver due to scattering from an elemental shell of inhomogeneities between the source and receiver. The mean field is then analytically marched through all shells to determine the effect of multiple forward scattering between the source and the receiver. The derivation of the mean scattered field from a single elemental shell and limiting conditions on its validity are given in Sec. IV.

It is first assumed that the inhomogeneities are confined within a cylinder of radius ρ_s centered at the source so that there are no inhomogeneities in the medium outside this cylinder. Let $\Phi(\mathbf{r}|\mathbf{r_0})$ be the direct wave measured at receiver $\mathbf{r}$ from the source at $\mathbf{r_0}$. The thickness of the cylinder containing inhomogeneities is now augmented by a small amount, $\Delta\rho_s$. Let $\Phi_s(\mathbf{r}|\mathbf{r_0},\Delta\rho_s(\rho_s))$ be the *scattered* field at the receiver from inhomogeneities in this new cylindrical shell of thickness $\Delta\rho_s$. Let the *total* field at the receiver given the new cylinder of radius $\rho_s+\Delta\rho_s$ be $\Phi(\mathbf{r}|\mathbf{r_0},\Delta\rho_s(\rho_s))$. Then the difference equation,

$$\Phi(\mathbf{r}|\mathbf{r_0},\Delta\rho_s(\rho_s))=\Phi(\mathbf{r}|\mathbf{r_0})+\Phi_s(\mathbf{r}|\mathbf{r_0},\Delta\rho_s(\rho_s)), \tag{10}$$

is obtained where $\Phi_s(\mathbf{r}|\mathbf{r_0},\Delta\rho_s(\rho_s))$ is given by Eq. (9), as long as the width $\Delta\rho_s$ is sufficiently small for the single scatter approximation to be valid within it.

The mean field can be obtained by taking the expected value of Eq. (10),

$$\langle\Phi(\mathbf{r}|\mathbf{r_0},\Delta\rho_s(\rho_s))\rangle=\langle\Phi(\mathbf{r}|\mathbf{r_0})\rangle+\langle\Phi_s(\mathbf{r}|\mathbf{r_0},\Delta\rho_s(\rho_s))\rangle. \tag{11}$$

The mean field in the absence of the shell can be expressed as a sum of normal modes,

$$\langle\Phi(\mathbf{r}|\mathbf{r_0})\rangle=\sum_n\langle\Phi^{(n)}(\mathbf{r}|\mathbf{r_0})\rangle, \tag{12}$$

where $\langle\Phi^{(n)}(\mathbf{r}|\mathbf{r_0})\rangle$ is the contribution to the field by mode n. Equation (12) is generally valid even when the modes are coupled by scatterers in the waveguide since another modal summation can always be embedded within $\langle\Phi^{(n)}(\mathbf{r}|\mathbf{r_0})\rangle$.

The scattered field contribution to the direct wave was found using a stationary phase approximation in Sec. II. The mean of this scattered field is expressible as a single modal sum,

$$\langle\Phi_s(\mathbf{r}|\mathbf{r_0},\Delta\rho_s(\rho_s))\rangle=\sum_n\langle\Phi^{(n)}(\mathbf{r}|\mathbf{r_0})\rangle i\nu_n(\rho_s)\Delta\rho_s, \tag{13}$$

under widely applicable conditions, as will be shown in Sec. IV A, where ν_n is the horizontal wave number change of the nth mode due to scattering by inhomogeneities in the medium. An analytic expression for this wave number change is given in Eq. (60). It depends on the expected scattering properties of the inhomogeneities in the *forward azimuth*.

Expressing the mean total field at the receiver as a modal sum,

$$\langle\Phi(\mathbf{r}|\mathbf{r_0},\Delta\rho_s(\rho_s))\rangle=\sum_n\langle\Phi^{(n)}(\mathbf{r}|\mathbf{r_0},\Delta\rho_s(\rho_s))\rangle \tag{14}$$

and substituting Eqs. (12), (13), and (14) into Eq. (11), it follows that for each mode n,

$$\langle\Phi^{(n)}(\mathbf{r}|\mathbf{r_0},\Delta\rho_s(\rho_s))\rangle=\langle\Phi^{(n)}(\mathbf{r}|\mathbf{r_0})\rangle(1+i\nu_n(\rho_s)\Delta\rho_s). \tag{15}$$

This can be rewritten as the difference equation,

$$\Delta\langle\Phi^{(n)}(\mathbf{r}|\mathbf{r_0})\rangle=\langle\Phi^{(n)}(\mathbf{r}|\mathbf{r_0})\rangle i\nu_n(\rho_s)\Delta\rho_s, \tag{16}$$

where $\Delta\langle\Phi^{(n)}(\mathbf{r}|\mathbf{r_0})\rangle=(\langle\Phi^{(n)}(\mathbf{r}|\mathbf{r_0},\Delta\rho_s(\rho_s))\rangle-\langle\Phi^{(n)}(\mathbf{r}|\mathbf{r_0})\rangle)$ describes the change in the nth mode's contribution to the mean field at the receiver as a result of scattering by inhomogeneities in the shell. From Eqs. (13) and (16), the modal sum of these changes equals the forward scattered field from the shell. Equation (16) can be recast as the integral equation,

$$\int_{\Psi_i^{(n)}}^{\langle\Psi_T^{(n)}\rangle}\frac{\mathrm{d}\langle\Phi^{(n)}(\mathbf{r}|\mathbf{r_0})\rangle}{\langle\Phi^{(n)}(\mathbf{r}|\mathbf{r_0})\rangle}=i\int_0^{\rho}\nu_n(\rho_s)\mathrm{d}\rho_s, \tag{17}$$

which marches the mean forward field for each mode through the inhomogeneous medium since the inhomogeneities in adjacent single-scatter shells are assumed to be uncorrelated with each other. This includes multiple forward scattering from source to receiver in a manner analogous to that used by Rayleigh[10,11] and others[15,18] for free space.

In the absence of inhomogeneities in the medium, the field measured at the receiver for each mode is simply the incident field,[53]

$$\Psi_i^{(n)}(\mathbf{r}|\mathbf{r_0})=4\pi\frac{i}{d(z_0)\sqrt{8\pi}}\mathrm{e}^{-i\pi/4}u_n(z)u_n(z_0)\frac{\mathrm{e}^{i\xi_n\rho}}{\sqrt{\xi_n\rho}}, \tag{18}$$

where $u_n(z)$ is the amplitude of the mode shape and $d(z)$ is the density at depth z. Within any approximately isovelocity layer of the waveguide, the mode shape can be expressed as

$$u_n(z)=N_n^{(1)}(z)\mathrm{e}^{i\gamma_n z}-N_n^{(2)}(z)\mathrm{e}^{-i\gamma_n z}, \tag{19}$$

integrating Eq. (17), we have

$$\langle \Psi_T^{(n)}(\mathbf{r}|\mathbf{r_0})\rangle = \Psi_i^{(n)}(\mathbf{r}|\mathbf{r_0}) e^{i\int_0^\rho \nu_n(\rho_s)d\rho_s}. \quad (20)$$

Summing the contribution from all the modes, the total mean forward field at the receiver in a waveguide containing inhomogeneities is then

$$\langle \Psi_T(\mathbf{r}|\mathbf{r_0})\rangle = \sum_n \langle \Psi_T^{(n)}(\mathbf{r}|\mathbf{r_0})\rangle, \quad (21)$$

$$= \sum_n \Psi_i^{(n)}(\mathbf{r}|\mathbf{r_0}) e^{i\int_0^\rho \nu_n(\rho_s)d\rho_s}. \quad (22)$$

Here ν_n, given in Eq. (60), describes the change in the horizontal wave number of mode n as it propagates through the random inhomogeneous waveguide. It is a complex quantity that provides a measure of the attenuation and dispersion of each mode per unit horizontal range due to scattering by inhomogeneities in the medium. The real part of ν_n determines modal dispersion while the imaginary part of ν_n determines modal attenuation. If the source is at a null for a particular mode, that mode may still contribute to the field at a distant receiver through scattering. This is because the imaginary part of ν_n includes the effect of mode coupling along the propagation path through a sum over all modes by the waveguide extinction theorem.[6]

For the present formulation to be valid, the change in the mean forward field at the receiver due to scattering from any shell increment $\Delta\rho_s$ must be small relative to the incident field, as can be seen from Eqs. (15) and (22). Here $\Delta\rho_s$ must be small enough for the single scatter approximation to be valid within it, and large enough for the modal decoupling conditions derived in Sec. IV to be valid. Any individual inhomogeneity may have a large scattered field in its vicinity, on the order of the incident field, as is typical in shadow formation. In such cases, the present theory is still valid as long as the separation between inhomogeneities in the forward direction is large enough for the scattered field from the previous interaction to be small in comparison to the total incident field of the current interaction.

Both the difference equation (16) and integral equation (17) account for range-dependent variation in the medium's expected scatter function density. If the inhomogeneities are contained in an evanescent layer, such as in the sea bottom, Eq. (19) can still be used if the given mode is evanescent. In this case, we set $N_n^{(2)}=0$ and can write $N_n^{(1)}=u_n(H)e^{\Im\{\gamma_n\}H}$, where H is the water depth, since the vertical wave number becomes purely imaginary.

B. Power of the forward field

Here we develop a difference equation that describes the change in the expected depth-integrated second moment of the forward field due to scattering from an elemental shell of inhomogeneities between the source and receiver. This is proportional to the corresponding change in power at a given range for a receiver of fixed area spanning the water column. The depth integrated second moment is then marched through the random waveguide to include multiple forward scattering between the source and receiver. The derivation of the expected power transmission through a single elemental shell of inhomogeneities is given in Sec. IV along with its validity conditions.

From Eq. (10), the second moment of the total field at receiver $\mathbf{r}$ from a source at $\mathbf{r_0}$ after scattering from a shell of inhomogeneities of thickness $\Delta\rho_s$ at range ρ_s can be expressed as

$$\begin{aligned}\langle |\Phi(\mathbf{r}|\mathbf{r_0},\Delta\rho_s(\rho_s))|^2\rangle &= \langle |\Phi(\mathbf{r}|\mathbf{r_0})|^2\rangle + \langle |\Phi_s(\mathbf{r}|\mathbf{r_0},\Delta\rho_s(\rho_s))|^2\rangle \\ &+ \langle \Phi(\mathbf{r}|\mathbf{r_0})\Phi_s^*(\mathbf{r}|\mathbf{r_0},\Delta\rho_s(\rho_s))\rangle \\ &+ \langle \Phi^*(\mathbf{r}|\mathbf{r_0})\Phi_s(\mathbf{r}|\mathbf{r_0},\Delta\rho_s(\rho_s))\rangle. \quad (23)\end{aligned}$$

The first term on the right-hand side of Eq. (23) is the second moment of the received field in the absence of the shell. Next is the second moment of the field scattered from the shell. This is followed by two cross-terms arising from coherent interaction between incident and scattered fields.

We next integrate Eq. (23) over receiver depth to obtain the depth-integrated second moment of the field at horizontal range ρ. Integrating the first term to the right of Eq. (23), leads to the depth-integrated second moment of the field in the absence of the shell. It can always be expressed as a single modal sum,

$$\int_0^\infty \frac{1}{d(z)}\langle |\Phi(\mathbf{r}|\mathbf{r_0})|^2\rangle dz = \sum_n \langle W^{(n)}(\boldsymbol{\rho}|\mathbf{r_0})\rangle, \quad (24)$$

even when the modes are coupled due to scattering in the waveguide, since other modal summations can always be embedded within $W^{(n)}(\boldsymbol{\rho}|\mathbf{r_0})$.

The depth integral of the second moment of the scattered field from the shell is expressible as a single modal sum,

$$\begin{aligned}&\int_0^\infty \frac{1}{d(z)}\langle |\Phi_s(\mathbf{r}|\mathbf{r_0},\Delta\rho_s(\rho_s))|^2\rangle dz \\ &= \sum_n \langle W^{(n)}(\boldsymbol{\rho}|\mathbf{r_0})\rangle \mu_n(\rho_s)\Delta\rho_s, \quad (25)\end{aligned}$$

under widely satisfied conditions, as shown in Sec. IV B. Here $\mu_n(\rho_s)$ is what we refer to as the *exponential coefficient of modal field variance*. It accounts for the covariance of the medium's scatter function density and the potential coupling of energy from each mode n to every other mode in the waveguide as a result of the random scattering process. It is expressible as a single modal sum, as shown in Sec. IV B.

Depth-integration of the last two terms on the right in Eq. (23) leads to

$$\begin{aligned}&\int_0^\infty \frac{1}{d(z)}[\langle \Phi(\mathbf{r}|\mathbf{r_0})\Phi_s^*(\mathbf{r}|\mathbf{r_0},\Delta\rho_s(\rho_s))\rangle \\ &+ \langle \Phi^*(\mathbf{r}|\mathbf{r_0})\Phi_s(\mathbf{r}|\mathbf{r_0},\Delta\rho_s(\rho_s))\rangle]dz \\ &= -\sum_n \langle W^{(n)}(\boldsymbol{\rho}|\mathbf{r_0})\rangle 2\Im\{\nu_n(\rho_s)\}\Delta\rho_s, \quad (26)\end{aligned}$$

which depends on the attenuation coefficient $\Im\{\nu_n\}$, as shown in Sec. IV C. Equation (26) reflects the fact that it is the coherent interaction between the incident and forward

scattered fields that leads to extinction of the total forward field.

Each term on the right-hand side of Eq. (23) is now expressed as a single modal sum after depth-integration throughout the waveguide. As before, the depth integral of the left-hand side of Eq. (23) can always be expressed as a single modal sum via

$$\int_0^\infty \frac{1}{d(z)}\langle \Phi(\mathbf{r}|\mathbf{r_0},\Delta\rho_s(\rho_s))\Phi^*(\mathbf{r}|\mathbf{r_0},\Delta\rho_s(\rho_s))\rangle \mathrm{d}z = \sum_n \langle W^{(n)}(\boldsymbol{\rho}|\mathbf{r_0},\Delta\rho_s(\rho_s))\rangle. \quad (27)$$

Substituting Eqs. (24), (25), (26), and (27) for the various terms obtained after integrating Eq. (23) over depth leads to

$$\langle W^{(n)}(\boldsymbol{\rho}|\mathbf{r_0},\Delta\rho_s(\rho_s))\rangle = \langle W^{(n)}(\boldsymbol{\rho}|\mathbf{r_0})\rangle[1+(\mu_n(\rho_s)-2\Im\{\nu_n(\rho_s)\})\Delta\rho_s]. \quad (28)$$

This can be rewritten as the difference equation,

$$\Delta\langle W^{(n)}(\boldsymbol{\rho}|\mathbf{r_0})\rangle = \langle W^{(n)}(\boldsymbol{\rho}|\mathbf{r_0})\rangle(\mu_n(\rho_s)-2\Im\{\nu_n(\rho_s)\})\Delta\rho_s, \quad (29)$$

where $\Delta\langle W^{(n)}(\boldsymbol{\rho}|\mathbf{r_0})\rangle = (\langle W^{(n)}(\boldsymbol{\rho}|\mathbf{r_0},\Delta\rho_s(\rho_s))\rangle - \langle W^{(n)}(\boldsymbol{\rho}|\mathbf{r_0})\rangle)$ is the change in the depth-integrated second moment of the forward field due to scattering from inhomogeneities in the shell. This change has a component that depends on the interference between the incident and forward scattered fields.

Equation (29) can be recast as an integral equation,

$$\int_{W_i^{(n)}}^{\langle W_T^{(n)}\rangle} \frac{\mathrm{d}\langle W^{(n)}(\boldsymbol{\rho}|\mathbf{r_0})\rangle}{\langle W^{(n)}(\boldsymbol{\rho}|\mathbf{r_0})\rangle} = \int_0^\rho (\mu_n(\rho_s)-2\Im\{\nu_n(\rho_s)\})\mathrm{d}\rho_s, \quad (30)$$

which marches the depth-integrated second moment of the forward field for each mode through the inhomogeneous medium to include multiple forward scattering along the way. This approach is based on the assumption that inhomogeneities in adjacent single-scatter shells are uncorrelated with each other. This is related to the classic Markov assumptions and ladder approximations made to describe optical and laser beam propagation through the turbulent atmosphere.[15]

Here the lower limit of the integral occurs in the absence of inhomogeneities. It is defined in terms of the depth-integrated second moment of the incident field,

$$W_i(\boldsymbol{\rho}|\mathbf{r_0}) = \int_0^\infty \frac{1}{d(z)}|\Psi_i(\mathbf{r}|\mathbf{r_0})|^2\,\mathrm{d}z = \sum_n W_i^{(n)}(\boldsymbol{\rho}|\mathbf{r_0}), \quad (31)$$

where

$$W_i^{(n)}(\boldsymbol{\rho}|\mathbf{r_0}) = \frac{2\pi}{d^2(z_0)}|u_n(z_0)|^2\frac{1}{\rho|\xi_n|}\mathrm{e}^{-2\Im\{\xi_n\}\rho}, \quad (32)$$

decays as a function of horizontal range as a result of cylindrical spreading in the waveguide through the $1/\rho$ dependence and absorption loss in the water column and bottom through $\mathrm{e}^{-2\Im\{\xi_n\}\rho}$.

Integrating Eq. (30), we then have

$$\langle W_T^{(n)}(\boldsymbol{\rho}|\mathbf{r_0})\rangle = W_i^{(n)}(\boldsymbol{\rho}|\mathbf{r_0})\mathrm{e}^{\int_0^\rho(\mu_n(\rho_s)-2\Im\{\nu_n(\rho_s)\})\mathrm{d}\rho_s}. \quad (33)$$

Summing the contributions from all modes, the depth-integrated second moment of the forward field in the randomly inhomogeneous waveguide is

$$\langle W_T(\boldsymbol{\rho}|\mathbf{r_0})\rangle = \sum_n \langle W_T^{(n)}(\boldsymbol{\rho}|\mathbf{r_0})\rangle = \sum_n W_i^{(n)}(\boldsymbol{\rho}|\mathbf{r_0})\mathrm{e}^{\int_0^\rho(\mu_n(\rho_s)-2\Im\{\nu_n(\rho_s)\})\mathrm{d}\rho_s}, \quad (34)$$

which decays with range due to (1) spreading and absorption loss in the incident field and (2) modal extinction from scattering by inhomogeneities as seen in the argument of the exponential. It is important to point out that Eq. (34) accounts for possible range-dependent variation in the expected scattering properties of the inhomogeneities.

C. Second moment and variance of the forward field

Here we develop analytic expressions for the second moment and variance of the forward field after propagating through a random inhomogeneous waveguide to a single receiver.

The forward field $\Psi_T(\mathbf{r}|\mathbf{r_0})$ received at $\mathbf{r}$ after propagation through a waveguide containing inhomogeneities can be expressed as a modal sum of the form

$$\Psi_T(\mathbf{r}|\mathbf{r_0}) = \sum_n \chi_T^{(n)}(\boldsymbol{\rho}|\mathbf{r_0})u_n(z), \quad (35)$$

where the range-dependent part of the field given by $\chi_T^{(n)}(\boldsymbol{\rho}|\mathbf{r_0})$ is separated from the depth-dependent part given by the mode amplitude $u_n(z)$ at receiver depth z.

The mean forward field from Eq. (35) is

$$\langle \Psi_T(\mathbf{r}|\mathbf{r_0})\rangle = \sum_n \langle \chi_T^{(n)}(\boldsymbol{\rho}|\mathbf{r_0})\rangle u_n(z), \quad (36)$$

where the expectation is taken over the range-dependent part of the field. The mean forward field is then expressed in terms of the modes of the incident field in the medium without random inhomogeneities. This follows from successive application of Green's theorem to describe multiple forward scattering through consecutive single scatter shells, as has been noted in previous sections and will be discussed again in Sec. IV. From Eqs. (18), (22), and (36), we observe that $\chi_T^{(n)}(\boldsymbol{\rho}|\mathbf{r_0})$ has a mean given by

$$\langle \chi_T^{(n)}(\boldsymbol{\rho}|\mathbf{r_0})\rangle = 4\pi\frac{i}{d(z_0)\sqrt{8\pi}}e^{-i\pi/4}u_n(z_0)\frac{\mathrm{e}^{i\xi_n\rho}}{\sqrt{\xi_n\rho}}\mathrm{e}^{i\int_0^\rho\nu_n(\rho_s)\mathrm{d}\rho_s}. \quad (37)$$

The second moment of the forward field at receiver $\mathbf{r}$ is

$$\langle|\Psi_T(\mathbf{r}|\mathbf{r_0})|^2\rangle = \langle\Psi_T(\mathbf{r}|\mathbf{r_0})\Psi_T^*(\mathbf{r}|\mathbf{r_0})\rangle = \sum_n \sum_m \langle\chi_T^{(n)}(\boldsymbol{\rho}|\mathbf{r_0})\chi_T^{*(m)}(\boldsymbol{\rho}|\mathbf{r_0})\rangle u_n(z)u_m^*(z). \quad (38)$$

We assume that the modes are statistically independent. This is a valid assumption beyond several waveguide depths in range after significant multiple forward scattering. The cross-modal coherence of the range-dependent part of the forward field can then be expressed as

$$\langle\chi_T^{(n)}(\boldsymbol{\rho}|\mathbf{r_0})\chi_T^{*(m)}(\boldsymbol{\rho}|\mathbf{r_0})\rangle = \langle\chi_T^{(n)}(\boldsymbol{\rho}|\mathbf{r_0})\rangle\langle\chi_T^{*(m)}(\boldsymbol{\rho}|\mathbf{r_0})\rangle + \delta_{nm}\,\mathrm{Var}(\chi_T^{(n)}(\boldsymbol{\rho}|\mathbf{r_0})), \quad (39)$$

where

$$\mathrm{Var}(\chi_T^{(n)}(\boldsymbol{\rho}|\mathbf{r}_0)) = \langle|\chi_T^{(n)}(\boldsymbol{\rho}|\mathbf{r_0})|^2\rangle - |\langle\chi_T^{(n)}(\boldsymbol{\rho}|\mathbf{r_0})\rangle|^2, \quad (40)$$

is the variance of the range-dependent part of the forward field for each mode n. Substituting Eq. (39) into Eq. (38), the expected intensity of the forward field becomes

$$\langle|\Psi_T(\mathbf{r}|\mathbf{r_0})|^2\rangle = \sum_n \sum_m \langle\chi_T^{(n)}(\boldsymbol{\rho}|\mathbf{r_0})\rangle\langle\chi_T^{*(m)}(\boldsymbol{\rho}|\mathbf{r_0})\rangle u_n(z)u_m^*(z), + \sum_n \mathrm{Var}(\chi_T^{(n)}(\boldsymbol{\rho}|\mathbf{r_0}))|u_n(z)|^2, \quad (41)$$

$$= |\langle\Psi_T(\mathbf{r}|\mathbf{r_0})\rangle|^2 + \mathrm{Var}(\Psi_T(\mathbf{r}|\mathbf{r_0})). \quad (42)$$

The last equality follows from the use of Eq. (36) and the definition of the variance of the forward field, where

$$\mathrm{Var}(\Psi_T(\mathbf{r}|\mathbf{r_0})) = \langle|\Psi_T(\mathbf{r}|\mathbf{r_0})|^2\rangle - |\langle\Psi_T(\mathbf{r}|\mathbf{r_0})\rangle|^2 \quad (43)$$

$$= \sum_n \mathrm{Var}(\chi_T^{(n)}(\boldsymbol{\rho}|\mathbf{r_0}))|u_n(z)|^2. \quad (44)$$

In Eq. (42), the second moment of the forward field is expressed as a sum of the square of the mean field $|\langle\Psi_T(\mathbf{r}|\mathbf{r_0})\rangle|^2$ which is proportional to the coherent direct wave intensity, and the variance of the forward field $\mathrm{Var}(\Psi_T(\mathbf{r}|\mathbf{r_0}))$, which is proportional to the incoherent direct wave intensity.

The second moment and variance of the forward field at a single receiver can be calculated using Eqs. (40), (41), and (44) from knowledge of the mean and second moment of $\chi_T^{(n)}(\boldsymbol{\rho}|\mathbf{r_0})$ for each mode n, where the mean is given in Eq. (37), and the second moment can be computed from the depth-integrated second moment of the forward field.

The depth-integrated second moment of the forward field can be written as

$$\langle W_T(\boldsymbol{\rho}|\mathbf{r_0})\rangle = \int_0^\infty \frac{1}{d(z)}\langle|\Psi_T(\mathbf{r}|\mathbf{r_0})|^2\rangle \mathrm{d}z \quad (45)$$

$$= \sum_n \langle|\chi_T^{(n)}(\boldsymbol{\rho}|\mathbf{r_0})|^2\rangle, \quad (46)$$

where modal orthogonality,

$$\int_0^\infty \frac{1}{d(z)} u_m(z)u_n(z)\mathrm{d}z = \delta_{nm} \quad (47)$$

collapses the double modal sum in Eq. (38) into the final single sum.

The second moment of $\chi_T^{(n)}(\boldsymbol{\rho}|\mathbf{r_0})$ for each mode n can be obtained from the depth-integrated second moment of the forward field using Eq. (46). In Sec. III B, we derive analytic expressions for $W_T(\boldsymbol{\rho}|\mathbf{r_0})$ and hence $\langle|\chi_T^{(n)}(\boldsymbol{\rho}|\mathbf{r_0})|^2\rangle$.

Comparing Eq. (34) with Eq. (46), the second moment of $\chi_T^{(n)}(\boldsymbol{\rho}|\mathbf{r_0})$ becomes

$$\langle|\chi_T^{(n)}(\boldsymbol{\rho}|\mathbf{r_0})|^2\rangle = W_i^{(n)}(\boldsymbol{\rho}|\mathbf{r_0})\mathrm{e}^{\int_0^\rho(\mu_n(\rho_s)-2\Im\{\nu_n(\rho_s)\})\mathrm{d}\rho_s}. \quad (48)$$

The variance of the forward field at any receiver depth in the waveguide can now be analytically expressed as the single modal sum,

$$\mathrm{Var}(\Psi_T(\mathbf{r}|\mathbf{r_0})) = \sum_n W_i^{(n)}(\boldsymbol{\rho}|\mathbf{r_0})|u_n(z)|^2\mathrm{e}^{-\int_0^\rho 2\Im\{\nu_n(\rho_s)\}\mathrm{d}\rho_s}\left(\mathrm{e}^{\int_0^\rho \mu_n(\rho_s)\mathrm{d}\rho_s} - 1\right), \quad (49)$$

from Eqs. (37), (40), (44), and (48).

IV. DERIVATION OF DIRECT WAVE MOMENTS FOR A SHELL OF INHOMOGENEITIES IN TERMS OF EXPONENTIAL COEFFICIENTS OF MODAL ATTENUATION, DISPERSION, AND FIELD VARIANCE

Here we derive the first and second statistical moments of the direct wave after propagation through an elemental shell of inhomogeneities within which the single scatter approximation is valid. These moments are expressed in terms of exponential coefficients of modal attenuation, dispersion, and field variance. It is shown that both the first and depth-integrated second moment can be written as a single sum over the waveguide modes as long as the shell width within which the single scatter approximation is valid is sufficiently large for modal decoupling to occur.

A. Modal attenuation and dispersion coefficients

Here it is shown that the mean scattered field contribution to the direct wave from a cylindrical shell of inhomogeneities is given by the single modal sum of Eq. (13), which is a linear function of shell thickness and the horizontal wave number change ν_n of mode n, under widely satisfied conditions.

The *mean* scattered field from any shell that contributes to the direct wave is found by taking the expected value of Eq. (9),

$$\langle \Phi_s(\mathbf{r}|\mathbf{r_0}, \Delta\rho_s(\rho_s))\rangle$$
$$= \sum_m \sum_n \int_0^\infty \mathrm{d}z_t \int_{\rho_s-\Delta\rho_s/2}^{\rho_s+\Delta\rho_s/2} \mathrm{d}\rho_t \int_{\phi-\phi_F/2}^{\phi+\phi_F/2} \rho_t \,\mathrm{d}\phi_t \, \mathrm{e}^{i\xi_m[\rho\rho_t/2(\rho-\rho_t)](\phi_t-\phi)^2}$$
$$\times \frac{2\pi}{k} \frac{i}{d(z_0)d(z_t)} \frac{1}{\sqrt{\xi_m\xi_n(\rho-\rho_t)\rho_t}} u_m(z)u_n(z_0)\mathrm{e}^{i\pi/4}\mathrm{e}^{i\xi_m\rho}\mathrm{e}^{i(\xi_n-\xi_m)\rho_t}$$
$$\times [N_m^{(1)}N_n^{(1)}\mathrm{e}^{i(\gamma_m+\gamma_n)z_t}\langle s_{\mathbf{r_t}}(\pi-\alpha_m, \beta_s(\phi,\phi_t); \alpha_n, \phi_t)\rangle - N_m^{(2)}N_n^{(1)}\mathrm{e}^{i(-\gamma_m+\gamma_n)z_t}\langle s_{\mathbf{r_t}}(\alpha_m, \beta_s(\phi,\phi_t); \alpha_n, \phi_t)\rangle$$
$$- N_m^{(1)}N_n^{(2)}\mathrm{e}^{i(\gamma_m-\gamma_n)z_t}\langle s_{\mathbf{r_t}}(\pi-\alpha_m, \beta_s(\phi,\phi_t); \pi-\alpha_n, \phi_t)\rangle + N_m^{(2)}N_n^{(2)}\mathrm{e}^{i(-\gamma_m-\gamma_n)z_t}\langle s_{\mathbf{r_t}}(\alpha_m, \beta_s(\phi,\phi_t); \pi-\alpha_n, \phi_t)\rangle]. \quad (50)$$

So long as the single scatter approximation is valid within the given inhomogeneous shell, the Green functions from the source to the shell and from the shell to the receiver can be treated deterministically. The expectation values then operate only on the scatter functions of random shell inhomogeneities, as noted in the derivation of Eq. (8) of Ref. 5.

We assume that the inhomogeneities only need to obey a horizontally stationary random process within the Fresnel width in any given shell, but not over larger separations. The expected scattering properties of the medium then may be both range and azimuth dependent in the present formulation. Also, the scattering properties need not be stationary over depth. This makes it possible to adopt the abbreviated notation $\langle s_{\mathbf{r_t}}(\alpha,\beta;\alpha_i,\beta_i)\rangle = \langle s_{\rho_s,z_t}(\alpha,\beta;\alpha_i,\beta_i)\rangle$ within the Fresnel width in any given shell.

Given the assumed statistical stationarity of the scatter function density within the integrand of Eq. (50), the integral over azimuth can be evaluated by conventional stationary phase methods to yield

$$\langle \Phi_s(\mathbf{r}|\mathbf{r_0}, \Delta\rho_s(\rho_s))\rangle = \sum_m \sum_n \int_0^\infty \mathrm{d}z_t \int_{\rho_s-\Delta\rho_s/2}^{\rho_s+\Delta\rho_s/2} \mathrm{d}\rho_t \sqrt{\frac{2\pi(\rho-\rho_t)}{\xi_m\rho\rho_t}} \rho_t \frac{2\pi}{k} \frac{i}{d(z_0)d(z_t)} \frac{1}{\sqrt{\xi_m\xi_n(\rho-\rho_t)\rho_t}} u_m(z)u_n(z_0)\mathrm{e}^{i\pi/4}\mathrm{e}^{i\xi_m\rho}\mathrm{e}^{i(\xi_n-\xi_m)\rho_t}$$
$$\times [N_m^{(1)}N_n^{(1)}\mathrm{e}^{i(\gamma_m+\gamma_n)z_t}\langle s_{\rho_s,z_t}(\pi-\alpha_m, \phi; \alpha_n, \phi)\rangle - N_m^{(2)}N_n^{(1)}\mathrm{e}^{i(-\gamma_m+\gamma_n)z_t}\langle s_{\rho_s,z_t}(\alpha_m, \phi; \alpha_n, \phi)\rangle$$
$$- N_m^{(1)}N_n^{(2)}\mathrm{e}^{i(\gamma_m-\gamma_n)z_t}\langle s_{\rho_s,z_t}(\pi-\alpha_m, \phi; \pi-\alpha_n, \phi)\rangle + N_m^{(2)}N_n^{(2)}\mathrm{e}^{i(-\gamma_m-\gamma_n)z_t}\langle s_{\rho_s,z_t}(\alpha_m, \phi; \pi-\alpha_n, \phi)\rangle]. \quad (51)$$

Equation (51) is then integrated in range ρ_t over the shell width $\Delta\rho_s$ about ρ_s. Applying exponential integration of the form

$$\int_{\rho_s-\Delta\rho_s/2}^{\rho_s+\Delta\rho_s/2} \mathrm{e}^{i(\xi_n-\xi_m)\rho_t}\mathrm{d}\rho_t = \mathrm{e}^{i(\xi_n-\xi_m)\rho_s}\Delta\rho_s \,\mathrm{sinc}\left((\xi_n-\xi_m)\frac{\Delta\rho_s}{2}\right), \quad (52)$$

leads to

$$\langle \Phi_s(\mathbf{r}|\mathbf{r_0}, \Delta\rho_s(\rho_s))\rangle = \sum_m \sum_n \int_0^\infty \mathrm{d}z_t \frac{2\pi}{k} \frac{i}{d(z_0)d(z_t)} \frac{\sqrt{2\pi}}{\xi_m} \frac{\mathrm{e}^{i\xi_m\rho}}{\sqrt{\xi_n\rho}} u_m(z)u_n(z_0)\mathrm{e}^{i\pi/4}\mathrm{e}^{i(\xi_n-\xi_m)\rho_s}\,\mathrm{sinc}\left((\xi_n-\xi_m)\frac{\Delta\rho_s}{2}\right)$$
$$\times [N_m^{(1)}N_n^{(1)}\mathrm{e}^{i(\gamma_m+\gamma_n)z_t}\langle s_{\rho_s,z_t}(\alpha_m, \phi; \pi-\alpha_n, \phi)\rangle - N_m^{(2)}N_n^{(1)}\mathrm{e}^{i(-\gamma_m+\gamma_n)z_t}\langle s_{\rho_s,z_t}(\alpha_m, \phi; \alpha_n, \phi)\rangle$$
$$- N_m^{(1)}N_n^{(2)}\mathrm{e}^{i(\gamma_m-\gamma_n)z_t}\langle s_{\rho_s,z_t}(\pi-\alpha_m, \phi; \pi-\alpha_n, \phi)\rangle + N_m^{(2)}N_n^{(2)}\mathrm{e}^{i(-\gamma_m-\gamma_n)z_t}\langle s_{\rho_s,z_t}(\pi-\alpha_m, \phi; \alpha_n, \phi)\rangle]\Delta\rho_s. \quad (53)$$

The field scattered from the shell given in Eq. (53) reduces to a single modal sum by modal orthogonality for compact scatterers that obey a stationary random process in depth throughout the waveguide, as will be shown in Sec. IV A 1. For general inhomogeneities with arbitrary depth distribution, a single modal sum is obtained under the widely satisfied conditions derived in Sec. IV A 2.

1. Compact inhomogeneities that obey a stationary random process in depth

Acoustically compact inhomogeneities, those small compared to the wavelength, or inhomogeneities following the sonar equation in a waveguide[54] that obey a stationary random process in depth have expected scatter function densities that are independent of both direction and depth, so that $\langle s_{\rho_s,z_t}(\alpha,\beta;\alpha_i,\beta_i)\rangle=\langle s_0(\rho_s)\rangle$, can be factored from Eq. (53).

Equation (53) for the mean scattered field from the shell then reduces to the single modal sum,

$$\langle \Phi_s(\mathbf{r}|\mathbf{r_0},\Delta\rho_s(\rho_s))\rangle = \sum_n 4\pi \frac{i}{d(z_0)\sqrt{8\pi}} e^{-i\pi/4} u_n(z)u_n(z_0) \times \frac{e^{i\xi_n\rho}}{\sqrt{\xi_n\rho}} i\left(\frac{2\pi}{k\xi_n}\langle s_0(\rho_s)\rangle\right)\Delta\rho_s, \tag{54}$$

by modal orthogonality, via Eq. (47).

The mean scattered field from the shell can then be expressed in terms of the incident field,

$$\langle \Phi_s(\mathbf{r}|\mathbf{r_0},\Delta\rho_s(\rho_s))\rangle = \sum_n \Phi_i^{(n)}(\mathbf{r}|\mathbf{r_0}) i\nu_n(\rho_s)\Delta\rho_s, \tag{55}$$

by substituting Eq. (18) into Eq. (54), where,

$$\nu_n(\rho_s) = \frac{2\pi}{k\xi_n}\langle s_0(\rho_s)\rangle. \tag{56}$$

Equation (56) defines the horizontal wave number change of each mode due to scattering from 3-D compact inhomogeneities that obey a stationary random process over waveguide depth. For mode 1, $\xi_1 \approx k$ is an excellent approximation that makes the corresponding wave number change approximately equal to that found for propagation through inhomogeneities in free space.[11] Higher-order modes travel at steeper elevation angles, have longer propagation paths, interact more with the inhomogeneities, and so experience greater attenuation and dispersion. This is seen in Eq. (56), where modal attenuation and dispersion coefficients are inversely proportional to the horizontal wave number of the given mode.

2. General inhomogeneities with arbitrary depth dependence

All terms in Eq. (53) are proportional to $\mathrm{sinc}[(\xi_n-\xi_m)(\Delta\rho_s/2)]$, which is unity for diagonal terms, where $n=m$, but becomes negligibly small for off-diagonal terms, where $n\neq m$, when the shell thickness is large enough that $\mathrm{sinc}[(\xi_n-\xi_m)(\Delta\rho_s/2)]_{\Delta\rho_s=\Delta\rho_{\max}} \ll 1$ or equivalently the condition

$$\Delta\rho_{\max}(\sin\alpha_n - \sin\alpha_m) \gg \lambda, \tag{57}$$

is satisfied.[51]

The mean forward field then reduces to a single modal sum when the maximum shell thickness $\Delta\rho_{\max}$ for which the single scatter approximation is valid satisfies condition (57). A similar condition has been presented by Frankenthal and Beran[40] for forward propagation and in Ref. 5 for reverberation.

Condition (57) is most easily interpreted in terms of diffraction theory by considering plane wave propagation through an aperture of length $\Delta\rho_{\max}\cos(\pi/2-\alpha_n)$, which equals the projected length of $\Delta\rho_{\max}$ in the equivalent plane wave propagation direction of mode n. In the forward azimuth, condition (57) requires the difference in projected apertures between modes n and m for $n\neq m$ to be much larger than the wavelength. For typical low-frequency applications, $\Delta\rho_{\max}$ will range in scale from the minumum channel depth, or water depth in Continental Shelf environments, to at most one order of magnitude larger.

The mean scattered field from the shell, under condition (57), is then the single modal sum

$$\langle \Phi_s(\mathbf{r}|\mathbf{r_0},\Delta\rho_s(\rho_s))\rangle = \sum_n 4\pi \frac{i}{d(z_0)\sqrt{8\pi}} e^{-i\pi/4} u_n(z)u_n(z_0) \frac{e^{i\xi_n\rho}}{\sqrt{\xi_n\rho}} \times i\int \frac{1}{d(z_t)}\frac{2\pi}{k}\frac{1}{\xi_n}[(N_n^{(1)})^2 e^{i2\gamma_n z_t}\langle s_{\rho_s,z_t}(\pi-\alpha_n,\phi;\alpha_n,\phi)\rangle - N_n^{(2)}N_n^{(1)}\langle s_{\rho_s,z_t}(\alpha_n,\phi;\alpha_n,\phi)\rangle - N_n^{(1)}N_n^{(2)}\langle s_{\rho_s,z_t}(\pi-\alpha_n,\phi;\pi-\alpha_n,\phi)\rangle + (N_n^{(2)})^2 e^{-i2\gamma_n z_t}\langle s_{\rho_s,z_t}(\alpha_n,\phi;\pi-\alpha_n,\phi)\rangle]dz_t\Delta\rho_{\max}. \tag{58}$$

Substituting Eq. (18) into Eq. (58), the mean scattered field from the shell is then expressible in terms of the incident field via

$$\langle \Phi_s(\mathbf{r}|\mathbf{r_0},\Delta\rho_s(\rho_s))\rangle = \sum_n \Phi_i^{(n)}(\mathbf{r}|\mathbf{r_0}) i\nu_n(\rho_s)\Delta\rho_{\max}, \tag{59}$$

where

$$\nu_n(\rho_s) = \int_0^\infty \frac{2\pi}{k}\frac{1}{\xi_n}\frac{1}{d(z_t)}[(N_n^{(1)})^2 e^{i2\gamma_n z_t}\langle s_{\rho_s,z_t}(\pi-\alpha_n,\phi;\alpha_n,\phi)\rangle$$
$$- N_n^{(2)}N_n^{(1)}\langle s_{\rho_s,z_t}(\alpha_n,\phi;\alpha_n,\phi)\rangle$$
$$- N_n^{(1)}N_n^{(2)}\langle s_{\rho_s,z_t}(\pi-\alpha_n,\phi;\pi-\alpha_n,\phi)\rangle$$
$$+ (N_n^{(2)})^2 e^{-i2\gamma_n z_t}\langle s_{\rho_s,z_t}(\alpha_n,\phi;\pi-\alpha_n,\phi)\rangle]dz_t. \quad (60a)$$

Equation (60) defines the horizontal wave number change of the nth mode due to scattering in a waveguide with general inhomogeneities arbitrarily distributed in depth. For compact scatterers that follow a stationary random process in depth, Eq. (60) reduces to Eq. (56).

By applying the generalized waveguide extinction theorem, Eq. (20) of Ref. 6 with $x=0$, the attenuation coefficient due to scattering for each mode n can be expressed in terms of the waveguide extinction cross-section σ_n of the medium inhomogeneities as,

$$\Im\{\nu_n(\rho_s)\} = \frac{1}{V_c}\int_0^\infty \frac{1}{2}\frac{1}{d(z_t)}\frac{1}{|u_n(z_t)|^2}\langle\sigma_n\rangle dz_t. \quad (60b)$$

Equation (60b) is convenient because it can be used to compute attenuation due to scattering in the randomly inhomogeneous waveguide directly from a knowledge of the expected waveguide extinction cross-section density of the medium's inhomogeneities.

B. Coefficient of modal field variance

We now derive an analytic expression for the exponential coefficient of modal field variance μ_n for a random inhomogeneous waveguide. Here, we show that Eq. (25) is valid for scattering from a cylindrical shell element containing inhomogeneities under widely applicable conditions.

Again employing the single scatter approximation within a shell of inhomogeneities of thickness $\Delta\rho_s$ at range ρ_s, from Eq. (9), the second moment of the direct-wave component of the scattered field from the shell is found to be

$$\langle|\Phi_s(\mathbf{r}|\mathbf{r_0},\Delta\rho_s(\rho_s))|^2\rangle$$
$$= \Bigg\langle \sum_m\sum_n\sum_{m'}\sum_{n'}\int_0^\infty dz_t\int_0^\infty dz_{t'}\int_{\rho_s-\Delta\rho_s/2}^{\rho_s+\Delta\rho_s/2} d\rho_t\int_{\rho_s-\Delta\rho_s/2}^{\rho_s+\Delta\rho_s/2} d\rho_{t'}$$
$$\times\int_{\phi-\phi_F/2}^{\phi+\phi_F/2}\rho_t\,d\phi_t\, e^{i\xi_m[\rho\rho_t/2(\rho-\rho_t)](\phi_t-\phi)^2}\int_{\phi-\phi_F/2}^{\phi+\phi_F/2}\rho_{t'}\,d\phi_{t'}\, e^{-i\xi_{m'}[\rho\rho_{t'}/2(\rho-\rho_{t'})](\phi_{t'}-\phi)^2}$$
$$\times\frac{4\pi^2}{k(z_t)k(z_{t'})d(z_t)d(z_{t'})}\frac{1}{d^2(z_0)}\frac{1}{\sqrt{\xi_m\xi_{m'}^*}}\frac{1}{\sqrt{\xi_n\xi_{n'}^*}}\frac{1}{\sqrt{(\rho-\rho_t)(\rho-\rho_{t'})\rho_t\rho_{t'}}}u_m(z)u_{m'}^*(z)u_n(z_0)u_{n'}^*(z_0)$$
$$\times[N_m^{(1)}(z_t)N_n^{(1)}(z_t)e^{i\Re(\gamma_m+\gamma_n)z_t}s_{\mathbf{r_t}}(\pi-\alpha_m,\beta_s(\phi,\phi_t);\alpha_n,\phi_t)$$
$$- N_m^{(2)}(z_t)N_n^{(1)}(z_t)e^{i\Re(-\gamma_m+\gamma_n)z_t}s_{\mathbf{r_t}}(\alpha_m,\beta_s(\phi,\phi_t);\alpha_n,\phi_t)$$
$$- N_m^{(1)}(z_t)N_n^{(2)}(z_t)e^{i\Re(\gamma_m-\gamma_n)z_t}s_{\mathbf{r_t}}(\pi-\alpha_m,\beta_s(\phi,\phi_t);\pi-\alpha_n,\phi_t)$$
$$+ N_m^{(2)}(z_t)N_n^{(2)}(z_t)e^{i\Re(-\gamma_m-\gamma_n)z_t}s_{\mathbf{r_t}}(\alpha_m,\beta_s(\phi,\phi_t);\pi-\alpha_n,\phi_t)]$$
$$\times[N_{m'}^{*(1)}(z_{t'})N_{n'}^{*(1)}(z_{t'})e^{i\Re(-\gamma_{m'}-\gamma_{n'})z_{t'}}s_{\mathbf{r_{t'}}}(\pi-\alpha_{m'},\beta_s(\phi,\phi_{t'});\alpha_{n'},\phi_{t'})$$
$$- N_{m'}^{*(2)}(z_{t'})N_{n'}^{*(1)}(z_{t'})e^{i\Re(\gamma_{m'}-\gamma_{n'})z_{t'}}s_{\mathbf{r_{t'}}}(\alpha_{m'},\beta_s(\phi,\phi_{t'});\alpha_{n'},\phi_{t'})$$
$$- N_{m'}^{*(1)}(z_{t'})N_{n'}^{*(2)}(z_{t'})e^{i\Re(-\gamma_{m'}+\gamma_{n'})z_{t'}}s_{\mathbf{r_{t'}}}(\pi-\alpha_{m'},\beta_s(\phi,\phi_{t'});\pi-\alpha_{n'},\phi_{t'})$$
$$+ N_{m'}^{*(2)}(z_{t'})N_{n'}^{*(2)}(z_{t'})e^{i\Re(\gamma_{m'}+\gamma_{n'})z_{t'}}s_{\mathbf{r_{t'}}}(\alpha_{m'},\beta_s(\phi,\phi_{t'});\pi-\alpha_{n'},\phi_{t'})]$$
$$\times e^{i\Re\{\xi_m(\rho-\rho_t)-\xi_{m'}(\rho-\rho_{t'})\}}e^{i\Re\{\xi_n\rho_t-\xi_{n'}\rho_{t'}\}}$$
$$\times e^{-\Im\{\xi_m+\xi_{m'}\}(\rho-\rho_t)}e^{-\Im\{\xi_n+\xi_{n'}\}\rho_t}e^{-\Im\{(\gamma_m+\gamma_n)z_t+(\gamma_{m'}+\gamma_{n'})z_{t'}\}}\Bigg\rangle, \quad (61)$$

where the expectation values only operate on scatter function density products following the assumed statistical decorrelation between inhomogenieties in adjacent shells, as discussed previously.

Equation (61) can only be further evaluated if the cross-correlation of the scatter function density of the medium at $\mathbf{r_t}$ and $\mathbf{r_{t'}}$ is known. We will assume that the inhomogeneities obey a stationary random process within the Fresnel width in each single scatter shell. The second moment of the scattered field contribution to the direct wave from a given shell then

depends on whether the cross-range coherence length l_y of the random process, defined in Appendix A, is greater or less than the Fresnel width Y_F at the given shell range ρ_s. Scatterers are fully correlated across the active region or Fresnel width of the shell when $l_y > Y_F$, but are uncorrelated in range and possibly depth. When, $l_y < Y_F$, fluctuations arise from scatterers uncorrelated in both range, cross-range, and possibly depth.

1. Fully correlated scatterers within the Fresnel width

Inhomogeneities within the shell at range ρ_s are now assumed to satisfy $l_y > Y_F(\rho, \rho_s)$ or $|\rho_s - \rho/2| > (\rho/2)\sqrt{1 - 4l_y^2/\lambda\rho}$. Their scatter function densities are then taken to be fully correlated in cross-range within the active region of the shell, but become uncorrelated when their separation in range exceeds the coherence length $l_x(\rho_s, z_t, z_{t'})$, defined in Appendix A, so that

$$
\begin{aligned}
&\langle s_{\mathbf{r_t}}(\pi - \alpha_m, \beta_s(\phi, \phi_t); \alpha_n, \phi_t) s^*_{\mathbf{r_{t'}}}(\pi - \alpha_{m'}, \beta_s(\phi, \phi_{t'}); \alpha_{n'}, \phi_{t'})\rangle \\
&\quad \approx l_x(\rho_s, z_t, z_t')[\langle s_{\rho_s, z_t}(\pi - \alpha_m, \beta_s(\phi, \phi_t); \alpha_n, \phi_t) s^*_{\rho_s, z_{t'}}(\pi - \alpha_{m'}, \beta_s(\phi, \phi_{t'}); \alpha_{n'}, \phi_{t'})\rangle \\
&\qquad - \langle s_{\rho_s, z_t}(\pi - \alpha_m, \beta_s(\phi, \phi_t); \alpha_n, \phi_t)\rangle \langle s^*_{\rho_s, z_{t'}}(\pi - \alpha_{m'}, \beta_s(\phi, \phi_{t'}); \alpha_{n'}, \phi_{t'})\rangle] \delta(x_t - x_{t'}) \\
&\qquad + \langle s_{\rho_s, z_t}(\pi - \alpha_m, \beta_s(\phi, \phi_t); \alpha_n, \phi_t)\rangle \langle s^*_{\rho_s, z_{t'}}(\pi - \alpha_{m'}, \beta_s(\phi, \phi_{t'}); \alpha_{n'}, \phi_{t'})\rangle. \qquad (62)
\end{aligned}
$$

The second moment of the scattered field, obtained by substituting Eq. (62) into Eq. (61), has 16 similar terms, the first of which is

$$
\begin{aligned}
&\langle |\Phi_s(\mathbf{r}|\mathbf{r}_0, \Delta\rho_s(\rho_s))|^2\rangle_1 \\
&\quad = \sum_m \sum_n \sum_{m'} \sum_{n'} \int_0^\infty dz_t \int_0^\infty dz_{t'} \int_{\rho_s - \Delta\rho_s/2}^{\rho_s + \Delta\rho_s/2} d\rho_t l_x(\rho_s, z_t, z_{t'}) \\
&\qquad \times \int_{\phi - \phi_F/2}^{\phi + \phi_F/2} \rho_t \, d\phi_t \, e^{i\xi_m[\rho\rho_t/2(\rho - \rho_t)](\phi_t - \phi)^2} \int_{\phi - \phi_F/2}^{\phi + \phi_F/2} \rho_t \, d\phi_{t'} \, e^{-i\xi_{m'}[\rho\rho_t/2(\rho - \rho_t)](\phi_{t'} - \phi)^2} \\
&\qquad \times \frac{4\pi^2}{k(z_t)k(z_{t'})d(z_t)d(z_{t'})} \frac{1}{d^2(z_0)} \frac{1}{\sqrt{\xi_m \xi^*_{m'}}} \frac{1}{\sqrt{\xi_n \xi^*_{n'}}} \frac{1}{(\rho - \rho_t)\rho_t} \\
&\qquad \times u_m(z) u^*_{m'}(z) u_n(z_0) u^*_{n'}(z_0) N^{(1)}_m(z_t) N^{(1)}_n(z_t) N^{*(1)}_{m'}(z_{t'}) N^{*(1)}_{n'}(z_{t'}) \\
&\qquad \times [\langle s_{\rho_s, z_t}(\pi - \alpha_m, \beta_s(\phi, \phi_t); \alpha_n, \phi_t) s^*_{\rho_s, z_{t'}}(\pi - \alpha_{m'}, \beta_s(\phi, \phi_{t'}); \alpha_{n'}, \phi_{t'})\rangle \\
&\qquad - \langle s_{\rho_s, z_t}(\pi - \alpha_m, \beta_s(\phi, \phi_t); \alpha_n, \phi_t)\rangle \langle s^*_{\rho_s, z_{t'}}(\pi - \alpha_{m'}, \beta_s(\phi, \phi_{t'}); \alpha_{n'}, \phi_{t'})\rangle] \\
&\qquad \times e^{i\Re\{\xi_m - \xi_{m'}\}(\rho - \rho_t)} e^{i\Re\{\xi_n - \xi_{n'}\}\rho_t} e^{-\Im\{\xi_m + \xi_{m'}\}(\rho - \rho_t)} e^{-\Im\{\xi_n + \xi_{n'}\}\rho_t} \\
&\qquad \times e^{i\Re\{(\gamma_m + \gamma_n)z_t - (\gamma_{m'} + \gamma_{n'})z_{t'}\}} e^{-\Im\{(\gamma_m + \gamma_n)z_t + (\gamma_{m'} + \gamma_{n'})z_{t'}\}} \\
&\qquad + |\langle \Phi_s(\mathbf{r}|\mathbf{r}_0, \Delta\rho_s(\rho_s))\rangle_1|^2, \qquad (63)
\end{aligned}
$$

where $|\langle \Phi_s(\mathbf{r}|\mathbf{r_0}, \Delta\rho_s(\rho_s))\rangle_1|^2$ is the first term of the square of the mean scattered field from the shell given by Eq. (13).

Since one of our fundamental assumptions is that the *mean* scattered field from a shell must be small in comparison to the incident field, as discussed in the Introduction and Sec. III A, the square of the mean scattered field from the shell must be negligible in the second moment. Since the variance of the scattered field, which is comprised of the remaining terms to the right in Eq. (63), is a statistical quantity that need not depend on the mean, it is not necessarily negligible and must be retained in the second moment, where it is assumed to simply be small compared to the squared magnitude of the incident field. This leads to a consistent asymptotic analysis of the field moments, as we will see in Sec. V A 2.

Since the inhomogeneities are fully correlated over the Fresnel width of the shell, the integral over azimuth in Eq. (63) can be evaluated by stationary phase methods to yield

$$\langle|\Phi_s(\mathbf{r}|\mathbf{r_0},\Delta\rho_s(\rho_s))|^2\rangle_1$$
$$= \sum_m \sum_n \sum_{m'} \sum_{n'} \int_0^\infty \mathrm{d}z_t \int_0^\infty \mathrm{d}z_{t'} \int_{\rho_s-\Delta\rho_s/2}^{\rho_s+\Delta\rho_s/2} \mathrm{d}\rho_t \, l_x(\rho_s,z_t,z_{t'}) \rho_t^2 \frac{2\pi(\rho-\rho_t)}{\sqrt{\xi_m\xi_{m'}}\rho\rho_t}$$
$$\times \frac{4\pi^2}{k(z_t)k(z_{t'})d(z_t)d(z_{t'})} \frac{1}{d^2(z_0)} \frac{1}{\sqrt{\xi_m\xi_{m'}^*}} \frac{1}{\sqrt{\xi_n\xi_{n'}^*}} \frac{1}{(\rho-\rho_t)\rho_t}$$
$$\times u_m(z)u_{m'}^*(z)u_n(z_0)u_{n'}^*(z_0)N_m^{(1)}(z_t)N_n^{(1)}(z_t)N_{m'}^{*(1)}(z_{t'})N_{n'}^{*(1)}(z_{t'})$$
$$\times[\langle s_{\rho_s,z_t}(\pi-\alpha_m,\phi;\alpha_n,\phi)s_{\rho_s,z_{t'}}^*(\pi-\alpha_{m'},\phi;\alpha_{n'},\phi)\rangle$$
$$-\langle s_{\rho_s,z_t}(\pi-\alpha_m,\phi;\alpha_n,\phi)\rangle\langle s_{\rho_s,z_{t'}}^*(\pi-\alpha_{m'},\phi;\alpha_{n'},\phi)\rangle]$$
$$\times e^{i\Re\{(\xi_m-\xi_{m'})(\rho-\rho_t)}e^{i\Re\{\xi_n-\xi_{n'}\}\rho_t}e^{-\Im\{\xi_m+\xi_{m'}\}(\rho-\rho_t)}e^{-\Im\{\xi_n+\xi_{n'}\}\rho_t}$$
$$\times e^{i\Re\{(\gamma_m+\gamma_n)z_t-(\gamma_{m'}+\gamma_{n'})z_{t'}\}}e^{-\Im\{(\gamma_m+\gamma_n)z_t+(\gamma_{m'}+\gamma_{n'})z_{t'}\}}. \quad (64)$$

We next integrate over the shell thickness $\Delta\rho_s$. Applying exponential integration of the form

$$\int_{\rho_s-\Delta\rho_s/2}^{\rho_s+\Delta\rho_s/2} e^{i\Re\{(\xi_n-\xi_{n'})-(\xi_m-\xi_{m'})\}\rho_t}\,\mathrm{d}\rho_t = e^{i\Re\{(\xi_n-\xi_{n'})-(\xi_m-\xi_{m'})\}\rho_s}\,\Delta\rho_s\,\mathrm{sinc}\left(\Re\{(\xi_n-\xi_{n'})-(\xi_m-\xi_{m'})\}\frac{\Delta\rho_s}{2}\right), \quad (65)$$

to Eq. (64), we find

$$\langle|\Phi_s(\mathbf{r}|\mathbf{r_0},\Delta\rho_s(\rho_s))|^2\rangle_1$$
$$= \sum_m \sum_n \sum_{m'} \sum_{n'} \int_0^\infty \mathrm{d}z_t \int_0^\infty \mathrm{d}z_{t'}\, 2\pi l_x(\rho_s,z_t,z_{t'}) \frac{1}{\sqrt{\xi_m\xi_{m'}}}$$
$$\times \frac{4\pi^2}{k(z_t)k(z_{t'})d(z_t)d(z_{t'})} \frac{1}{d^2(z_0)} \frac{1}{\sqrt{\xi_m\xi_{m'}^*}} \frac{1}{\sqrt{\xi_n\xi_{n'}^*}} \frac{1}{\rho}$$
$$\times u_m(z)u_{m'}^*(z)u_n(z_0)u_{n'}^*(z_0)N_m^{(1)}(z_t)N_n^{(1)}(z_t)N_{m'}^{*(1)}(z_{t'})N_{n'}^{*(1)}(z_{t'})$$
$$\times[\langle s_{\rho_s,z_t}(\pi-\alpha_m,\phi;\alpha_n,\phi)s_{\rho_s,z_{t'}}^*(\pi-\alpha_{m'},\phi;\alpha_{n'},\phi)\rangle$$
$$-\langle s_{\rho_s,z_t}(\pi-\alpha_m,\phi;\alpha_n,\phi)\rangle\langle s_{\rho_s,z_{t'}}^*(\pi-\alpha_{m'},\phi;\alpha_{n'},\phi)\rangle]$$
$$\times e^{i\Re\{\xi_m-\xi_{m'}\}\rho}e^{i\Re\{(\xi_n-\xi_{n'})-(\xi_m-\xi_{m'})\}\rho_s}e^{-\Im\{\xi_m+\xi_{m'}\}\rho}e^{-\Im\{(\xi_n+\xi_{n'})-(\xi_m+\xi_{m'})\}\rho_s}$$
$$\times e^{i\Re\{(\gamma_m+\gamma_n)z_t-(\gamma_{m'}+\gamma_{n'})z_{t'}\}}e^{-\Im\{(\gamma_m+\gamma_n)z_t+(\gamma_{m'}+\gamma_{n'})z_{t'}\}}$$
$$\times\Delta\rho_s\,\mathrm{sinc}\left(\Re\{(\xi_n-\xi_{n'})-(\xi_m-\xi_{m'})\}\frac{\Delta\rho_s}{2}\right). \quad (66)$$

We next integrate Eq. (66) over receiver depth to obtain the depth-integrated second moment of the scattered field from the shell. Applying modal orthogonality, Eq. (47), to Eq. (66), leads to,

$$\int_0^\infty \frac{1}{d(z)}\langle|\Phi_s(\mathbf{r}|\mathbf{r_0},\Delta\rho_s(\rho_s))|^2\rangle_1\mathrm{d}z$$
$$= \sum_m \sum_n \sum_{n'} \int_0^\infty \mathrm{d}z_t \int_0^\infty \mathrm{d}z_{t'} 2\pi\ell_x(\rho_s,z_t,z_{t'}) \frac{1}{\xi_m}$$
$$\times \frac{4\pi^2}{k(z_t)k(z_{t'})d(z_t)d(z_{t'})} \frac{1}{d^2(z_0)} \frac{1}{|\xi_m|} \frac{1}{\sqrt{\xi_n\xi_{n'}^*}} \frac{1}{\rho}$$
$$\times u_n(z_0)u_{n'}^*(z_0)N_m^{(1)}(z_t)N_n^{(1)}(z_t)N_m^{*(1)}(z_{t'})N_{n'}^{*(1)}(z_{t'})$$
$$\times[\langle s_{\rho_s,z_t}(\pi-\alpha_m,\phi;\alpha_n,\phi)s_{\rho_s,z_{t'}}^*(\pi-\alpha_m,\phi;\alpha_{n'},\phi)\rangle$$
$$-\langle s_{\rho_s,z_t}(\pi-\alpha_m,\phi;\alpha_n,\phi)\rangle\langle s_{\rho_s,z_{t'}}^*(\pi-\alpha_m,\phi;\alpha_{n'},\phi)\rangle]$$

$$\times e^{i\Re\{\xi_n-\xi_{n'}\}\rho_s}e^{-2\Im\{\xi_m\}\rho}e^{-\Im\{(\xi_n+\xi_{n'})-2\xi_m\}\rho_s}$$
$$\times e^{i\Re\{(\gamma_m+\gamma_n)z_t-(\gamma_m+\gamma_{n'})z_{t'}\}}e^{-\Im\{(\gamma_m+\gamma_n)z_t+(\gamma_m+\gamma_{n'})z_{t'}\}}$$
$$\times \Delta\rho_s \mathrm{sinc}\left[\Re\{\xi_n-\xi_{n'}\}\frac{\Delta\rho_s}{2}\right], \tag{67}$$

which has a triple modal sum.

In Eq. (67), terms with $n\neq n'$ have fluctuating phases proportional to $e^{i\Re\{\xi_n-\xi_{n'}\}\rho_s}$. These terms are negligibly small compared to terms for which $n=n'$ when the shell thickness is large enough that

$$\mathrm{sinc}\left[\Re\{\xi_n-\xi_{n'}\}\frac{\Delta\rho_s}{2}\right] \ll 1. \tag{68}$$

This leads to a condition that is identical to Eq. (57) when we let $m=n'$ in Eq. (57).

Under condition (57), the triple sum over the modes in Eq. (67) for the depth-integrated second moment of the scattered field from the shell reduces to a double modal sum,

$$\int_0^\infty \frac{1}{d(z)}\langle|\Phi_s(\mathbf{r}|\mathbf{r_0},\Delta\rho_s(\rho_s))|^2\rangle_1 dz = \sum_m\sum_n \Delta\rho_s\int_0^\infty dz_t\int_0^\infty dz_{t'} 2\pi\frac{\ell_x(\rho_s,z_t,z_{t'})}{\xi_m}\frac{4\pi^2}{k(z_t)k(z_{t'})d(z_t)d(z_{t'})}\frac{1}{d^2(z_0)}\frac{1}{|\xi_m|}\frac{1}{|\xi_n|}\frac{1}{\rho}$$
$$\times |u_n(z_0)|^2 N_m^{(1)}(z_t)N_n^{(1)}(z_t)N_m^{*(1)}(z_{t'})N_n^{*(1)}(z_{t'})\mathrm{Cov}(s_{\rho_s,z_t}(m_u;n_d),s_{\rho_s,z_{t'}}(m_u;n_d))$$
$$\times e^{-2\Im\{\xi_m\}\rho}e^{-2\Im\{\xi_n-\xi_m\}\rho_s}e^{i\Re\{(\gamma_m+\gamma_n)\}(z_t-z_{t'})}e^{-\Im\{(\gamma_m+\gamma_n)\}(z_t+z_{t'})}, \tag{69}$$

where,

$$\mathrm{Cov}(s_{\rho_s,z_t}(m_u;n_d),s_{\rho_s,z_{t'}}(m_u;n_d)) = \langle s_{\rho_s,z_t}(\pi-\alpha_m,\phi;\alpha_n,\phi)s^*_{\rho_s,z_{t'}}(\pi-\alpha_m,\phi;\alpha_n,\phi)\rangle$$
$$-\langle s_{\rho_s,z_t}(\pi-\alpha_m,\phi;\alpha_n,\phi)\rangle\langle s^*_{\rho_s,z_{t'}}(\pi-\alpha_m,\phi;\alpha_n,\phi)\rangle. \tag{70}$$

Combining all sixteen terms leads to the depth-integrated second moment of the scattered field from the shell,

$$\int_0^\infty \frac{1}{d(z)}\langle|\Phi_s(\mathbf{r}|\mathbf{r_0},\Delta\rho_s(\rho_s))|^2\rangle dz = \sum_n \frac{2\pi}{d^2(z_0)}|u_n(z_0)|^2\frac{1}{|\xi_n|\rho}e^{-2\Im\{\xi_n\}\rho}\Delta\rho_s$$
$$\times\sum_m \frac{e^{-2\Im\{\xi_n-\xi_m\}(\rho_s-\rho)}}{|\xi_m|}\int_0^\infty dz_t\int_0^\infty dz_{t'}\frac{\ell_x(\rho_s,z_t,z_{t'})}{\xi_m}\frac{4\pi^2}{k(z_t)k(z_{t'})d(z_t)d(z_{t'})}\mathrm{C}_{s,s}(\rho_s,z_t,z_{t'},m,n), \tag{71}$$

where,

$$\begin{aligned}
\mathrm{C}_{s,s}(\rho_s,z_t,z_{t'},m,n) = {} & [N_m^{(1)}(z_t)N_n^{(1)}(z_t)N_m^{*(1)}(z_{t'})N_n^{*(1)}(z_{t'})e^{i\Re\{(\gamma_m+\gamma_n)z_t-(\gamma_m+\gamma_n)z_{t'}\}}\mathrm{Cov}(s_{\rho_s,z_t}(m_u;n_d),s_{\rho_s,z_{t'}}(m_u;n_d))\\
& - N_m^{(1)}(z_t)N_n^{(1)}(z_t)N_m^{*(2)}(z_{t'})N_n^{*(1)}(z_{t'})e^{i\Re\{(\gamma_m+\gamma_n)z_t-(-\gamma_m+\gamma_n)z_{t'}\}}\mathrm{Cov}(s_{\rho_s,z_t}(m_u;n_d),s_{\rho_s,z_{t'}}(m_d;n_d))\\
& - N_m^{(1)}(z_t)N_n^{(1)}(z_t)N_m^{*(1)}(z_{t'})N_n^{*(2)}(z_{t'})e^{i\Re\{(\gamma_m+\gamma_n)z_t-(\gamma_m-\gamma_n)z_{t'}\}}\mathrm{Cov}(s_{\rho_s,z_t}(m_u;n_d),s_{\rho_s,z_{t'}}(m_u;n_u))\\
& + N_m^{(1)}(z_t)N_n^{(1)}(z_t)N_m^{*(2)}(z_{t'})N_n^{*(2)}(z_{t'})e^{i\Re\{(\gamma_m+\gamma_n)z_t-(-\gamma_m-\gamma_n)z_{t'}\}}\mathrm{Cov}(s_{\rho_s,z_t}(m_u;n_d),s_{\rho_s,z_{t'}}(m_d;n_u))\\
& - N_m^{(2)}(z_t)N_n^{(1)}(z_t)N_m^{*(1)}(z_{t'})N_n^{*(1)}(z_{t'})e^{i\Re\{(-\gamma_m+\gamma_n)z_t-(\gamma_m+\gamma_n)z_{t'}\}}\mathrm{Cov}(s_{\rho_s,z_t}(m_d;n_d),s_{\rho_s,z_{t'}}(m_u;n_d))\\
& + N_m^{(2)}(z_t)N_n^{(1)}(z_t)N_m^{*(2)}(z_{t'})N_n^{*(1)}(z_{t'})e^{i\Re\{(-\gamma_m+\gamma_n)z_t-(-\gamma_m+\gamma_n)z_{t'}\}}\mathrm{Cov}(s_{\rho_s,z_t}(m_d;n_d),s_{\rho_s,z_{t'}}(m_d;n_d))\\
& + N_m^{(2)}(z_t)N_n^{(1)}(z_t)N_m^{*(1)}(z_{t'})N_n^{*(2)}(z_{t'})e^{i\Re\{(-\gamma_m+\gamma_n)z_t-(\gamma_m-\gamma_n)z_{t'}\}}\mathrm{Cov}(s_{\rho_s,z_t}(m_d;n_d),s_{\rho_s,z_t}(m_u;n_u))\\
& - N_m^{(2)}(z_t)N_n^{(1)}(z_t)N_m^{*(2)}(z_{t'})N_n^{*(2)}(z_{t'})e^{i\Re\{(-\gamma_m+\gamma_n)z_t-(-\gamma_m-\gamma_n)z_{t'}\}}\mathrm{Cov}(s_{\rho_s,z_t}(m_d;n_d),s_{\rho_s,z_{t'}}(m_d;n_u))\\
& - N_m^{(1)}(z_t)N_n^{(2)}(z_t)N_m^{*(1)}(z_{t'})N_n^{*(1)}(z_{t'})e^{i\Re\{(\gamma_m-\gamma_n)z_t-(\gamma_m+\gamma_n)z_{t'}\}}\mathrm{Cov}(s_{\rho_s,z_t}(m_u;n_u),s_{\rho_s,z_{t'}}(m_u;n_d))\\
& + N_m^{(1)}(z_t)N_n^{(2)}(z_t)N_m^{*(2)}(z_{t'})N_n^{*(1)}(z_{t'})e^{i\Re\{(\gamma_m-\gamma_n)z_t-(-\gamma_m+\gamma_n)z_{t'}\}}\mathrm{Cov}(s_{\rho_s,z_t}(m_u;n_u),s_{\rho_s,z_{t'}}(m_d;n_d))\\
& + N_m^{(1)}(z_t)N_n^{(2)}(z_t)N_m^{*(1)}(z_{t'})N_n^{*(2)}(z_{t'})e^{i\Re\{(\gamma_m-\gamma_n)z_t-(\gamma_m-\gamma_n)z_{t'}\}}\mathrm{Cov}(s_{\rho_s,z_t}(m_u;n_u),s_{\rho_s,z_{t'}}(m_u;n_u))\\
& - N_m^{(1)}(z_t)N_n^{(2)}(z_t)N_m^{*(2)}(z_{t'})N_n^{*(2)}(z_{t'})e^{i\Re\{(\gamma_m-\gamma_n)z_t-(-\gamma_m-\gamma_n)z_{t'}\}}\mathrm{Cov}(s_{\rho_s,z_t}(m_u;n_u),s_{\rho_s,z_{t'}}(m_d;n_u))
\end{aligned}$$

$$+ N_m^{(2)}(z_t)N_n^{(2)}(z_t)N_m^{*(1)}(z_{t'})N_n^{*(1)}(z_{t'})e^{i\Re\{(-\gamma_m-\gamma_n)z_t-(\gamma_m+\gamma_n)z_{t'}\}}\mathrm{Cov}(s_{\rho_s,z_t}(m_d;n_u),s_{\rho_s,z_{t'}}(m_u;n_d))$$
$$- N_m^{(2)}(z_t)N_n^{(2)}(z_t)N_m^{*(2)}(z_{t'})N_n^{*(1)}(z_{t'})e^{i\Re\{(-\gamma_m-\gamma_n)z_t-(-\gamma_m+\gamma_n)z_{t'}\}}\mathrm{Cov}(s_{\rho_s,z_t}(m_d;n_u),s_{\rho_s,z_{t'}}(m_d;n_d))$$
$$- N_m^{(2)}(z_t)N_n^{(2)}(z_t)N_m^{*(1)}(z_{t'})N_n^{*(2)}(z_{t'})e^{i\Re\{(-\gamma_m-\gamma_n)z_t-(\gamma_m-\gamma_n)z_{t'}\}}\mathrm{Cov}(s_{\rho_s,z_t}(m_d;n_u),s_{\rho_s,z_{t'}}(m_u;n_u))$$
$$+ N_m^{(2)}(z_t)N_n^{(2)}(z_t)N_m^{*(2)}(z_{t'})N_n^{*(2)}(z_{t'})e^{i\Re\{(-\gamma_m-\gamma_n)z_t-(-\gamma_m-\gamma_n)z_{t'}\}}\mathrm{Cov}(s_{\rho_s,z_t}(m_d;n_u),s_{\rho_s,z_t}(m_d;n_u))]$$
$$\times e^{-\Im\{(\gamma_m+\gamma_n)(z_t+z_{t'})\}}, \tag{72}$$

depends on the covariances of the scatter function density in the forward azimuth that couple incident mode n to scattered mode m.

When Eq. (71) is expressed in terms of the depth-integrated second moment of the incident field in the absence of the shell using Eq. (32), it is found that

$$\int_0^\infty \frac{1}{d(z)}\langle|\Phi_s(\mathbf{r}|\mathbf{r_0},\Delta\rho_s(\rho_s))|^2\rangle dz = \sum_{n=1}^{\infty} W_i^{(n)}(\boldsymbol{\rho}|\mathbf{r_0})\mu_n^{\mathrm{cor}}\,\Delta\rho_s, \tag{73}$$

which is the desired form of general Eq. (25), where

$$\mu_n^{\mathrm{cor}}(\rho_s) = \sum_m \frac{1}{|\xi_m|}\int_0^\infty dz_t \int_0^\infty dz_{t'} \frac{l_x(\rho_s,z_t,z_{t'})}{\xi_m} \times \frac{4\pi^2}{k(z_t)k(z_{t'})d(z_t)d(z_{t'})} C_{s,s}(\rho_s,z_t,z_{t'},m,n) \tag{74}$$

is the *exponential coefficient of modal field variance*. It contains a modal sum that accounts for coupling between the nth mode and every other mode in the waveguide due to the *random* scattering process. If the scattering process is not random, the covariance of the scatter function density is zero and, consequently, μ_n is also zero.

Attenuation due to deterministic absorption in the medium is already included in the incident field through $W_i^{(n)}$ of Eq. (32) in Eq. (73). The effect of scattering must be determined separately to conserve energy in the current marching formulation. This requires $-2\Im\{\xi_n-\xi_m\}$ to be set to zero in going from Eq. (71) to Eqs. (73) and (74), following an approach similar to that described in deriving the waveguide extinction theorem.[6] An equivalent route with much historical precedence would be to derive the total field moments without absorption and then include it in the incident field at the final stage.

It is noteworthy that μ_n may depend on shell range ρ_s since it describes the potentially range-dependent variations of the medium's inhomogeneities. When the inhomogeneities obey a stationary random process in range, μ_n is a constant, independent of shell range ρ_s.

2. Uncorrelated scatterers within the Fresnel width

Here inhomogeneities within the shell at range ρ_s satisfy $l_y < Y_F(\rho,\rho_s)$ or $|\rho_s-\rho/2| < (\rho/2)\sqrt{1-4l_y^2/\lambda\rho}$. Their scatter function densities then decorrelate in both range and cross-range within the Fresnel width. For scatter function density separations greater than that which can fall within the coherence area $A_c(\rho_s,z_t,z_{t'})$, defined in Appendix A, scatter function densities are assumed to be uncorrelated, so that

$$\langle s_{\mathbf{r_t}}(\pi-\alpha_m,\beta_s(\phi,\phi_t);\alpha_n,\phi_t)s^*_{\mathbf{r_{t'}}}(\pi-\alpha_{m'},\beta_s(\phi,\phi_{t'});\alpha_{n'},\phi_{t'})\rangle$$
$$\approx A_c(\rho_s,z_t,z_t')[\langle s_{\rho_s,z_t}(\pi-\alpha_m,\beta_s(\phi,\phi_t);\alpha_n,\phi_t)s^*_{\rho_s,z_{t'}}(\pi-\alpha_{m'},\beta_s(\phi,\phi_t);\alpha_{n'},\phi_t)\rangle - \langle s_{\rho_s,z_t}(\pi-\alpha_m,\beta_s(\phi,\phi_t);\alpha_n,\phi_t)\rangle$$
$$\times\langle s^*_{\rho_s,z_{t'}}(\pi-\alpha_{m'},\beta_s(\phi,\phi_t);\alpha_{n'},\phi_t)\rangle]\delta(\boldsymbol{\rho}_t-\boldsymbol{\rho}_{\mathbf{t}'}) + \langle s_{\rho_s,z_t}(\pi-\alpha_m,\beta_s(\phi,\phi_t);\alpha_n,\phi_t)\rangle\langle s^*_{\rho_s,z_{t'}}(\pi-\alpha_{m'},\beta_s(\phi,\phi_{t'});\alpha_{n'},\phi_{t'})\rangle. \tag{75}$$

Substituting Eq. (75) into Eq. (61), leads to the second moment of the direct wave portion of the scattered field from the shell, which has 16 terms of similar form. The first of these is

$$\langle|\Phi_s(\mathbf{r}|\mathbf{r_0},\Delta\rho_s(\rho_s))|^2\rangle_1$$
$$= \sum_m\sum_n\sum_{m'}\sum_{n'}\int_0^\infty dz_t\int_0^\infty dz_{t'}\int_{\rho_s-\Delta\rho_s/2}^{\rho_s+\Delta\rho_s/2} d\rho_t\int_{\phi-\phi_F/2}^{\phi+\phi_F/2}\rho_t\,d\phi_t\,e^{i(\xi_m-\xi_{m'})[\rho\rho_t/2(\rho-\rho_t)](\phi_t-\phi)^2}$$
$$\times A_c(\rho_s,z_t,z_{t'})\frac{4\pi^2}{k(z_t)k(z_{t'})d(z_t)d(z_{t'})}\frac{1}{d^2(z_0)}\frac{1}{\sqrt{\xi_m\xi^*_{m'}}}\frac{1}{\sqrt{\xi_n\xi^*_{n'}}}\frac{1}{(\rho-\rho_t)\rho_t}$$
$$\times u_m(z)u^*_{m'}(z)u_n(z_0)u^*_{n'}(z_0)N_m^{(1)}(z_t)N_n^{(1)}(z_t)N_{m'}^{*(1)}(z_{t'})N_{n'}^{*(1)}(z_{t'})$$

$$\times[\langle s_{\rho_s,z_t}(\pi-\alpha_m,\beta_s(\phi,\phi_t);\alpha_n,\phi_t)s^*_{\rho_s,z_{t'}}(\pi-\alpha_{m'},\beta_s(\phi,\phi_t);\alpha_{n'},\phi_t)\rangle$$
$$-\langle s_{\rho_s,z_t}(\pi-\alpha_m,\beta_s(\phi,\phi_t);\alpha_n,\phi_t)\rangle\langle s^*_{\rho_s,z_{t'}}(\pi-\alpha_{m'},\beta_s(\phi,\phi_t);\alpha_{n'},\phi_t)\rangle]$$
$$\times e^{i\Re\{\xi_m-\xi_{m'}\}(\rho-\rho_t)}e^{i\Re\{\xi_n-\xi_{n'}\}\rho_t}e^{-\Im\{\xi_m+\xi_{m'}\}(\rho-\rho_t)}e^{-\Im\{\xi_n+\xi_{n'}\}\rho_t}$$
$$\times e^{i\Re\{(\gamma_m+\gamma_n)z_t-(\gamma_{m'}+\gamma_{n'})z_{t'}\}}e^{-\Im\{(\gamma_m+\gamma_n)z_t+(\gamma_{m'}+\gamma_{n'})z_{t'}\}}$$
$$+|\langle\Phi_s(\mathbf{r}|\mathbf{r_0},\Delta\rho_s(\rho_s))\rangle_1|^2. \tag{76}$$

Here $|\langle\Phi_s(\mathbf{r}|\mathbf{r_0},\Delta\rho_s(\rho_s))\rangle_1|^2$ is the first term of the square of the mean scattered field from the shell, from Eq. (13). It is negligible, as noted in previous sections.

Following on analysis analogous to that in Sec. IV B 1, the exponential coefficient of modal field variance is found to be

$$\mu_n^{\text{uncor}}(\rho_s)=\sum_m\sqrt{\frac{\rho}{2\pi\xi_m\rho_s(\rho-\rho_s)}}\frac{1}{|\xi_m|}\times\int_0^\infty dz_t\int_0^\infty dz_{t'}\,A_c(\rho_s,z_t,z_{t'})\times\frac{4\pi^2}{k(z_t)k(z_{t'})d(z_t)d(z_{t'})}C_{s,s}(\rho_s,z_t,z_{t'},m,n), \tag{77}$$

which strongly depends on shell range ρ_s.

C. Coherent second moment interference between incident and scattered fields

We now derive Eq. (26) for the depth-integrated cross terms between the incident and scattered field from the isolated shell. One of the two cross-terms can be approximated as

$$\langle\Phi(\mathbf{r}|\mathbf{r_0})\Phi_s^*(\mathbf{r}|\mathbf{r_0},\Delta\rho_s(\rho_s))\rangle=\langle\Phi_i(\mathbf{r}|\mathbf{r_0})\Phi_s^*(\mathbf{r}|\mathbf{r_0},\Delta\rho_s(\rho_s))\rangle=\sum_n\Phi_i^{(n)}(\mathbf{r}|\mathbf{r_0})\sum_m\Phi_i^{*(m)}(\mathbf{r}|\mathbf{r_0})(-i\nu_m^*)\Delta\rho_s \tag{78}$$

$$=\sum_n\sum_m\frac{2\pi}{d^2(z_0)}u_n(z)u_m^*(z)u_n(z_0)u_m^*(z_0)\frac{e^{i\Re\{\xi_n-\xi_m\}\rho}}{\rho\sqrt{\xi_n\xi_m^*}}\times e^{-\Im\{\xi_n+\xi_m\}\rho}(-i\nu_m^*)\Delta\rho_s, \tag{79}$$

by application of Eq. (59) with the same single scatter approximation as before. A similar expression can be obtained for the other cross-term.

Integrating Eq. (79) over the receiver depth, invoking modal orthogonality Eq. (47), and applying Eq. (32) leads to

$$\int_0^\infty\langle\Phi_i(\mathbf{r}|\mathbf{r_0})\Phi_s^*(\mathbf{r}|\mathbf{r_0},\Delta\rho_s(\rho_s))\rangle dz=\sum_n W_i^{(n)}(\boldsymbol{\rho}|\mathbf{r_0})(-i\nu_n^*(\rho_s))\Delta\rho_s. \tag{80}$$

Similarly, it can be shown that

$$\int_0^\infty\langle\Phi_i^*(\mathbf{r}|\mathbf{r_0})\Phi_s(\mathbf{r}|\mathbf{r_0},\Delta\rho_s(\rho_s))\rangle dz=\sum_n W_i^{(n)}(\boldsymbol{\rho}|\mathbf{r_0})(i\nu_n(\rho_s))\Delta\rho_s. \tag{81}$$

Summing Eqs. (80) and (81), we find

$$\int_0^\infty[\langle\Phi_i(\mathbf{r}|\mathbf{r_0})\Phi_s^*(\mathbf{r}|\mathbf{r_0},\Delta\rho_s(\rho_s))\rangle+\langle\Phi_i^*(\mathbf{r}|\mathbf{r_0})\Phi_s(\mathbf{r}|\mathbf{r_0},\Delta\rho_s(\rho_s))\rangle]dz=-\sum_n W_i^{(n)}(\boldsymbol{\rho}|\mathbf{r_0})2\Im\{\nu_n(\rho_s)\}\Delta\rho_s, \tag{82}$$

which depends on the modal attenuation coefficient $\Im\{\nu_n\}$. This is a consequence of the extinction or forward scatter theorem that states that it is the coherent interference between the incident and scattered fields that leads to shadow formation and the eventual attenuation of the forward field.

The modal power equation (28) and the corresponding difference equation (29) for scattering from a single shell follow directly from the derivation for Eq. (26) and the fact that the depth-integrated intensity at the receiver in the absence of inhomogeneities is described by Eq. (32).

V. SOLUTIONS FOR THE MEAN, VARIANCE, INTENSITY, POWER, AND SIGNAL-TO-NOISE RATIO OF THE FORWARD FIELD

Within the framework of the present formulation, we now provide general solutions for the mean, second moment, variance, and power of the forward field in terms of the parameters needed to describe the incident field and the first two statistical moments of the random medium's scatter function density, which obeys a spatial random process that need not be stationary. These solutions include the accumulated effects of multiple forward scatter from source to receiver through range integrals of the horizontal wave number change ν_n and the coefficient of field variance μ_n for the nth

mode. We then evaluate these integrals analytically for the special case when the inhomogeneities obey a stationary random process along the forward propagation path from source to receiver.

A. Field moments at a single receiver, power, and signal-to-noise ratio

1. Mean forward field

The mean of the forward field received at $\mathbf{r}$ from a source at $\mathbf{r_0}$ after propagation through a random inhomogeneous waveguide can be expressed as a sum of modal contributions,

$$\langle \Psi_T(\mathbf{r}|\mathbf{r_0})\rangle = \sum_{n=1}^{M_{max}} 4\pi \frac{i}{d(z_0)\sqrt{8\pi}} e^{-i\pi/4} u_n(z)u_n(z_0) \times \frac{e^{i\xi_n\rho}}{\sqrt{\xi_n\rho}} e^{i\int_0^\rho \nu_n(\rho_s)d\rho_s}, \quad (83)$$

from Eqs. (18) and (22). Here the wave number change $\nu_n(\rho_s)$ defined in Eq. (60) depends on the expected scattering properties of the random medium, which may be spatially nonstationary.

2. Variance of the forward field

The variance of the forward field received at $\mathbf{r}$ from the source at $\mathbf{r_0}$ can be expressed as a sum of modal variance terms,

$$\mathrm{Var}(\Psi_T(\mathbf{r}|\mathbf{r_0})) = \sum_{n=1}^{M_{max}} \frac{2\pi}{d^2(z_0)} \frac{1}{|\xi_n|\rho} |u_n(z_0)|^2 |u_n(z)|^2 \times e^{-2\Im\left\{\xi_n\rho+\int_0^\rho \nu_n(\rho_s)d\rho_s\right\}}\left(e^{\int_0^\rho \mu_n(\rho_s)d\rho_s}-1\right), \quad (84)$$

from Eq. (49), with the use of Eq. (32). For each mode n, the forward field variance depends on the expected modal extinction cross section of medium inhomogeneities through $\Im\{\nu_n\}$, and the covariance of the scatter function density of these inhomogeneities through μ_n. Both coefficients account for coupling of each mode n to every other mode in the random waveguide. Both coefficients may vary with range to account for nonstationarity in the inhomogeneous medium and variation of the medium's cross-range coherence length with respect to the local Fresnel width. The exponential coefficient of field variance $\mu_n(\rho_s)$ is given in Eq. (74) for the case when scatterers are correlated, and in Eq. (77) uncorrelated, within the local Fresnel width. The integral of $\mu_n(\rho_s)$ over range ρ_s is evaluated in Sec. V B for the important special case, where the medium's inhomogeneities obey a stationary random process between the source and the receiver.

This theory is consistent with the fact that in the limiting case of a nonrandom waveguide, the variance of the forward field must be zero. For example, in a waveguide with a static and uniform distribution of nonrandom inhomogeneities, the covariance of the scatter function density is zero. This then makes the exponential coefficient of field variance $\mu_n(\rho_s)$ zero for each mode from Eq. (74) or (77). The variance of the forward field in Eq. (84) is then zero, as it should be for a completely deterministic and coherent field.

3. Second moment of the forward field

The second moment of the forward field received at $\mathbf{r}$ from a source at $\mathbf{r_0}$ in the random inhomogeneous waveguide is found to be

$$\langle |\Psi_T(\mathbf{r}|\mathbf{r}_0)|^2\rangle = \sum_{n=1}^{M_{\max}} \frac{2\pi}{d^2(z_0)} \frac{1}{|\xi_n|\rho} |u_n(z_0)|^2 |u_n(z)|^2 e^{-2\Im\left\{\xi_n\rho+\int_0^\rho \nu_n(\rho_s)d\rho_s\right\}}\left(e^{\int_0^\rho \mu_n(\rho_s)d\rho_s}-1\right) + \sum_{n=1}^{M_{\max}}\sum_{m=1}^{M_{\max}} \frac{2\pi}{d^2(z_0)} \frac{1}{\sqrt{\xi_n\xi_m^*}\rho} u_n(z_0)u_m^*(z_0)u_n(z)u_m^*(z) e^{i\Re\left\{(\xi_n-\xi_m)\rho+\int_0^\rho(\nu_n(\rho_s)-\nu_m(\rho_s))d\rho_s\right\}} \times e^{-\Im\left\{(\xi_n+\xi_m)\rho+\int_0^\rho(\nu_n(\rho_s)+\nu_m(\rho_s))d\rho_s\right\}} \quad (85)$$

by inserting Eqs. (36), (37), and (84) into Eq. (42). The first term in Eq. (85) corresponds to the field variance and the second to the mean field squared. When the mean field dominates, the expected total intensity will fluctuate as a function of range due to coherent interference between waveguide modes. This interference is maintained even in the presence of inhomogeneities but may be significantly different from that of the incident field due to dispersion induced by the inhomogeneities. When the variance dominates, the modal interference patterns become insignificant, and the expected total intensity decays monotonically as the range becomes large.[16]

4. Forward field power

The second moment of the forward field integrated over the receiver depth is directly proportional to the net power propagated to range ρ in the waveguide. With the use of Eqs. (32) and (34), it can be expressed as

$$\langle W_T(\mathbf{r}|\mathbf{r_0})\rangle = \sum_{n=1}^{M_{\max}} \frac{2\pi}{d^2(z_0)} \frac{1}{|\xi_n|\rho} |u_n(z_0)|^2 e^{-2\Im\{\xi_n\rho + \int_0^\rho \nu_n(\rho_s)d\rho_s\}} \times e^{\int_0^\rho \mu_n(\rho_s)d\rho_s}, \quad (86)$$

which decays both monotonically with range, by the waveguide extinction theorem,[6] and uniformly since depth integration eliminates modal interference. This decay reflects the total power loss in the waveguide due to both scattering and absorption in the present formulation.

5. Signal to noise ratio

Here we define the signal to noise ratio $\mathrm{SNR}_n(\rho)$ for the nth mode of the forward field as the ratio of the depth-integrated square of the mean forward field to the depth-integrated variance. It is found to be

$$\mathrm{SNR}_n(\rho) = 1/\left(e^{\int_0^\rho \mu_n(\rho_s)d\rho_s} - 1\right), \quad (87)$$

by integrating Eqs. (83) and (84) over receiver depth. We observe that the signal to noise ratio for each mode only depends on the coefficient of modal field variance μ_n, is independent of the wave number change ν_n, and decreases with increasing receiver range ρ.

B. Special solutions when inhomogeneities obey a stationary random process along the path from source to receiver

The mean, second moment, and variance of the forward field can be readily obtained from Eqs. (83), (84), and (85), respectively, if statistical properties of the medium's inhomogeneities are known. The horizontal wave number change ν_n and the coefficient of modal field variance μ_n can then be determined as a function of range from source to receiver for each mode n.

Here we will assume that the scatter function density of the inhomogeneities follows the same stationary random process across all active regions from source to receiver. We can then analytically integrate ν_n and μ_n across range to obtain closed form expressions for the field moments. In this case, from Eq. (60), ν_n is simply a constant independent of shell range ρ_s so that $\int_0^\rho \nu_n\, d\rho_s = \nu_n\rho$. Since μ_n depends on the relative size of the cross-range coherence length l_y to the Fresnel width at the given shell range, however, three forms of solution are possible and must be considered.

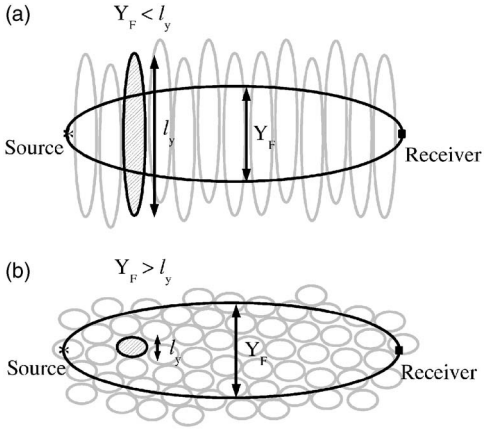

FIG. 1. (a) The maximum Fresnel width $Y_F(\rho,\rho/2)$ is smaller than the cross-range coherence length l_y of the local inhomogeneities for the given source-receiver separation ρ. (b) The maximum Fresnel width $Y_F(\rho,\rho/2)$ is larger than the cross-range coherence length l_y of the local inhomogeneities for the given source receiver separation ρ. Local inhomogeneities are fully correlated in cross-range within the Fresnel width for all single scatter shells in (a), while in (b) the active region within the Fresnel width contains inhomogeneities uncorrelated in cross-range for single scatter shells located at ρ_s that satisfy $\rho-\rho_s^{\mathrm{cor}} < \rho_s < \rho+\rho_s^{\mathrm{cor}}$. Figure not to scale.

1. The Fresnel width exceeds the cross-range coherence length of the scatter function density over part of the propagation path

This is the most general situation. The Fresnel width exceeds the cross-range coherence length l_y of the medium's scatter function density over the middle segment ($\rho_s^{\mathrm{cor}} < \rho_s < \rho-\rho_s^{\mathrm{cor}}$) of the propagation path, but not at the beginning ($\rho_s \le \rho_s^{\mathrm{cor}}$) or end ($\rho_s > \rho-\rho_s^{\mathrm{cor}}$), where $\rho_s^{\mathrm{cor}} = \rho/2(1-\sqrt{1-4l_y^2/\lambda\rho})$. Cross-range decorrelation of the scatter function density then only occurs over the middle segment. The exponential coefficient for field variance then takes on a different form for each of these segments in the marching solution from source to receiver,

$$\int_0^\rho \mu_n(\rho_s)d\rho_s = \int_0^{\rho_s^{\mathrm{cor}}} \mu_n^{\mathrm{cor}}(\rho_s)d\rho_s + \int_{\rho_s^{\mathrm{cor}}}^{\rho-\rho_s^{\mathrm{cor}}} \mu_n^{\mathrm{uncor}}(\rho_s)d\rho_s + \int_{\rho-\rho_s^{\mathrm{cor}}}^{\rho} \mu_n^{\mathrm{cor}}(\rho_s)d\rho_s. \quad (88)$$

If the coherence scales, l_y and A_c are independent of depth, substituting Eqs. (74) and (77) for $\mu_n^{\mathrm{cor}}(\rho_s)$ and $\mu_n^{\mathrm{uncor}}(\rho_s)$, respectively, into Eq. (88), leads to

$$\int_0^\rho \mu_n(\rho_s)d\rho_s = \sum_m \left(\frac{l_x}{\xi_m} \int_0^{\rho_s^{\mathrm{cor}}} d\rho_s + A_c \int_{\rho_s^{\mathrm{cor}}}^{\rho-\rho_s^{\mathrm{cor}}} \sqrt{\frac{\rho}{2\pi\xi_m\rho_s(\rho-\rho_s)}}\, d\rho_s + \frac{l_x}{\xi_m} \int_{\rho-\rho_s^{\mathrm{cor}}}^{\rho} d\rho_s \right) \frac{1}{|\xi_m|} \times \int_0^\infty dz_t \int_0^\infty dz_{t'} \frac{4\pi^2}{k(z_t)k(z_{t'})d(z_t)d(z_{t'})} C_{s,s}(z_t, z_{t'}, m, n). \quad (89)$$

Evaluting the integrals over the three segments then leads to the solution

$$\int_0^{\rho} \mu_n(\rho_s)\mathrm{d}\rho_s = \sum_m 2\left(\frac{l_x}{\xi_m}\rho_s^{\mathrm{cor}} + A_c\sqrt{\frac{\rho}{2\pi\xi_m}}\left[\sin^{-1}\sqrt{1-\frac{\rho_s^{\mathrm{cor}}}{\rho}} - \sin^{-1}\sqrt{\frac{\rho_s^{\mathrm{cor}}}{\rho}}\right]\right)\frac{1}{|\xi_m|}$$
$$\times \int_0^{\infty}\mathrm{d}z_t \int_0^{\infty}\mathrm{d}z_{t'}\frac{4\pi^2}{k(z_t)k(z_{t'})d(z_t)d(z_{t'})}C_{s,s}(z_t,z_{t'},m,n). \tag{90}$$

2. The cross-range coherence length of the scatter function density exceeds the Fresnel width over the entire propagation path

Here the scatterers are assumed to be fully correlated in cross-range across the entire propagation path. This is valid when $l_y > Y_{\mathrm{F}}(\rho,\rho/2)$ or $\rho < 4l_y^2/\lambda$, since the maximum Fresnel width falls midway between the source and the receiver. This case is illustrated in Fig. 1(a). Integrating Eq. (74) leads to the solution

$$\int_0^{\rho}\mu_n(\rho_s)\mathrm{d}\rho_s = \int_0^{\rho}\mu_n^{\mathrm{cor}}(\rho_s)\mathrm{d}\rho_s = \mu_n^{\mathrm{cor}}\rho, \tag{91}$$

since μ_n^{cor} is range independent here.

The signal to noise ratio for each incident mode n is then approximately

$$\mathrm{SNR}_n(\rho) = 1/(\mathrm{e}^{\mu_n^{\mathrm{cor}}\rho} - 1), \tag{92}$$

which becomes $\mathrm{SNR}_n(\rho) \approx 1/\mu_n^{\mathrm{cor}}\rho$ for sufficiently small ranges and $\mathrm{SNR}_n(\rho) \approx \mathrm{e}^{-\mu_n^{\mathrm{cor}}\rho}$ for sufficiently large ranges as long as Eq. (92) remains valid.

3. Fresnel length exceeds the cross-range coherence length and waveguide depth exceeds the vertical coherence length over the entire propagation path

Here it is assumed that scatterers may be uncorrelated in all three dimensions within the active region of any shell along the propagation path. This case is illustrated in Fig. 1(b). This is particularly applicable to propagation through bubble clouds, schools of fish, or fine-scale turbulence in the ocean. It can be described by taking the scatter function densities at $\mathbf{r_t}$ and $\mathbf{r_{t'}}$ to be uncorrelated when their separation is greater than that which can fall within a coherence volume $V_c(z_t)$, so that

$$\begin{aligned}
&\langle s_{\mathbf{r_t}}(\pi-\alpha_m,\beta_s(\phi,\phi_t);\alpha_n,\phi_t)s^*_{\mathbf{r_{t'}}}(\pi-\alpha_{m'},\beta_s(\phi,\phi_{t'});\alpha_{n'},\phi_{t'})\rangle \\
&\quad = V_c(z_t)[\langle s_{z_t}(\pi-\alpha_m,\beta_s(\phi,\phi_t);\alpha_n,\phi_t)s^*_{z_t}(\pi-\alpha_{m'},\beta_s(\phi,\phi_t);\alpha_{n'},\phi_t)\rangle \\
&\qquad - \langle s_{z_t}(\pi-\alpha_m,\beta_s(\phi,\phi_t);\alpha_n,\phi_t)\rangle\langle s^*_{z_t}(\pi-\alpha_{m'},\beta_s(\phi,\phi_t);\alpha_{n'},\phi_t)\rangle]\delta(\mathbf{r_t}-\mathbf{r_{t'}}) \\
&\qquad + \langle s_{z_t}(\pi-\alpha_m,\beta_s(\phi,\phi_t);\alpha_n,\phi_t)\rangle\langle s^*_{z_{t'}}(\pi-\alpha_{m'},\beta_s(\phi,\phi_{t'});\alpha_{n'},\phi_{t'})\rangle.
\end{aligned} \tag{93}$$

Following the analysis of Sec. IV B, but instead using Eq. (93) for the correlation of the scatter function density in Eq. (61), the coefficient of modal field variance becomes

$$\mu_n^{\mathrm{uncor,3\text{-}D}}(\rho_s) = \sum_m \sqrt{\frac{\rho}{2\pi\xi_m\rho_s(\rho-\rho_s)}}\frac{1}{|\xi_m|}\int_0^{\infty}\mathrm{d}z_t\, V_c(z_t)\frac{4\pi^2}{k^2(z_t)d^2(z_t)}C_{s,s}(z_t,z_t,m,n). \tag{94a}$$

Integrating Eq. (94a) leads to the solution

$$\int_0^{\rho}\mu_n(\rho_s)\mathrm{d}\rho_s = \int_0^{\rho}\mu_n^{\mathrm{uncor,3\text{-}D}}(\rho_s)\mathrm{d}\rho_s = \sum_m \sqrt{\frac{\rho\pi}{2\xi_m}}\frac{1}{|\xi_m|}\int_0^{\infty}\mathrm{d}z_t\, V_c(z_t)\frac{4\pi^2}{k^2(z_t)d^2(z_t)}C_{s,s}(z_t,z_t,m,n). \tag{94b}$$

The signal to noise ratio for each incident mode n is

$$\mathrm{SNR}_n(\rho) = 1/(\mathrm{e}^{\mathcal{M}_n^{\mathrm{uncor,3\text{-}D}}\sqrt{\rho}} - 1), \tag{95}$$

where

$$\mathcal{M}_n^{\mathrm{uncor,3\text{-}D}} = \sum_m \sqrt{\frac{\pi}{2\xi_m}}\frac{1}{|\xi_m|}\int_0^{\infty}\mathrm{d}z_t\, V_c(z_t)\frac{4\pi^2}{k^2(z_t)d^2(z_t)}C_{s,s}(z_t,z_t,m,n). \tag{96}$$

The signal to noise ratio becomes $\mathrm{SNR}_n(\rho) \approx 1/\mathcal{M}_n^{\text{uncor,3-D}}\sqrt{\rho}$ for sufficiently small ranges, and $\mathrm{SNR}_n(\rho) \approx e^{-\mathcal{M}_n^{\text{uncor,3-D}}\sqrt{\rho}}$ for sufficiently large ranges as long as Eq. (95) is valid.

By comparing Eqs. (92) and (95), it is observed that the direct wave for each mode is more coherent when decorrelation occurs in depth and azimuth as well as in range within the active region. This analytically shows that 3-D scattering effects become important as the Fresnel width exceeds the medium's local cross-range coherence length.

In the present scenario of three-dimensional decorrelation within the active region, the modal attenuation coefficient, from Eq. (60), can be expressed as

$$\mathfrak{T}\{\nu_n\} = \int_0^\infty \frac{1}{2}|u_n(z_t)|^2 \frac{1}{d(z_t)} \frac{1}{V_c(z_t)} \langle \sigma_n(0,z_t)\rangle dz_t. \tag{97}$$

This follows from Eq. (20) of Ref. 6 for the modal extinction cross-section σ_n of an inhomogeneity and Eq. (A5), which relates its scatter function to a corresponding scatter function density. Equation (97) is convenient because it can be used to calculate the attenuation due to scattering of each mode.

VI. MUTUAL INTENSITY AND THE SPATIAL COVARIANCE OF THE FORWARD FIELD

Here we provide analytic expressions for the mutual intensity and covariance of the forward field for two receivers at $\mathbf{r_1}=(\rho_1,\phi_1,z_1)$ and $\mathbf{r_2}=(\rho_2,\phi_2,z_2)$ in a random inhomogeneous ocean waveguide. This analysis is applicable to any two receivers in an arbitrary array configuration.

A. Difference and integral equations

Following an analysis similar to that in Sec. III B, it can be shown that by considering scattering from an elemental cylindrical shell of inhomogeneities, the change in the depth-integrated cross-moment, or the depth-integrated mutual intensity, of the forward field $\Delta W^{(n)}(\boldsymbol{\rho}_1,\boldsymbol{\rho}_2|\mathbf{r}_0)$ at ρ_1 and ρ_2 for each mode m satisfies

$$\begin{aligned}\Delta\langle W^{(n)}(\boldsymbol{\rho}_1,\boldsymbol{\rho}_2|\mathbf{r}_0)\rangle = \langle W^{(n)}(\boldsymbol{\rho}_1,\boldsymbol{\rho}_2|\mathbf{r}_0)\rangle(\mu_{n,1,2}(\rho_s) \\ + i\Re\{\nu_{n,1}(\rho_s) - \nu_{n,2}(\rho_s)\} \\ - \mathfrak{T}\{\nu_{n,1}(\rho_s) + \nu_{n,2}(\rho_s)\})\Delta\rho_s.\end{aligned} \tag{98}$$

Here $\langle W^{(n)}(\boldsymbol{\rho}_1,\boldsymbol{\rho}_2|\mathbf{r}_0)\rangle$ is defined in

$$\int_0^\infty \frac{1}{d(z)}\langle \Phi(\mathbf{r}_1|\mathbf{r}_0)\Phi^*(\mathbf{r}_2|\mathbf{r}_0)\rangle \mathrm{d}z = \sum_n \langle W^{(n)}(\boldsymbol{\rho}_1,\boldsymbol{\rho}_2|\mathbf{r}_0)\rangle, \tag{99}$$

and $\nu_{n,1}$ and $\nu_{n,2}$ are the modal horizontal wave number changes given in Eq. (60) with scatter functions evaluated at the forward azimuths $\phi=\phi_1$ and $\phi=\phi_2$, respectively, and $\mu_{n,1,2}$ is the exponential coefficient of modal field *covariance*, which will be derived in Sec. VI C.

If the receivers are within a single-scatter shell width in horizontal range, their depth-integrated mutual coherence can be approximated by marching Eq. (98) to a range at the midpoint between the two receivers,

$$\begin{aligned}\int_{W_i^{(n)}}^{W_T^{(n)}} \frac{\mathrm{d}W^{(n)}(\boldsymbol{\rho}_1,\boldsymbol{\rho}_2|\mathbf{r_0})}{W^{(n)}(\boldsymbol{\rho}_1,\boldsymbol{\rho}_2|\mathbf{r_0})} \\ = \int_0^{\rho_1+\Delta\rho/2} (\mu_{n,1,2}(\rho_s) + i\Re\{\nu_{n,1}(\rho_s) - \nu_{n,2}(\rho_s)\} - \mathfrak{T}\{\nu_{n,1}(\rho_s) + \nu_{n,2}(\rho_s)\})\mathrm{d}\rho_s,\end{aligned} \tag{100}$$

where

$$W_i^{(n)}(\boldsymbol{\rho}_1,\boldsymbol{\rho}_2|\mathbf{r}_0) = \frac{2\pi}{d^2(z_0)} \frac{1}{|\xi_n|\sqrt{\rho_1\rho_2}} |u_n(z_0)|^2 e^{i\Re\{\xi_n\}(\rho_1-\rho_2)} e^{-\mathfrak{T}\{\xi_n\}(\rho_1+\rho_2)} \tag{101}$$

is the depth-integrated mutual intensity of the incident field for mode n at receiver ranges ρ_1 and ρ_2.

The resulting contribution to the depth-integrated mutual intensity of the forward field for the nth mode is then

$$\begin{aligned}W_T^{(n)}(\boldsymbol{\rho}_1,\boldsymbol{\rho}_2|\mathbf{r_0}) \\ = W_i^{(n)}(\boldsymbol{\rho}_1,\boldsymbol{\rho}_2|\mathbf{r_0}) \exp\left(\int_0^{\rho_1+\Delta\rho/2} (\mu_{n,1,2}(\rho_s) + i\Re\{\nu_{n,1}(\rho_s) - \nu_{n,2}(\rho_s)\} - \mathfrak{T}\{\nu_{n,1}(\rho_s) + \nu_{n,2}(\rho_s)\})\mathrm{d}\rho_s\right),\end{aligned} \tag{102}$$

which is valid when $(\mu_{n,1,2} - \mathfrak{T}\{\nu_{n,1}+\nu_{n,2}\})\Delta\rho/2 \ll 1$. This condition is satisfied when the effect of scattering over the horizontal range separation $\Delta\rho$ between the two receivers is small. It is consistent with our basic assumption that the scattered field from any individual single-scatter shell must be small compared to the incident field at the receiver. The condition is only necessary for receivers that are separated in range. It is not required for receivers at different azimuths with the same horizontal range.

B. Solutions

1. Spatial covariance of the forward field

The covariance of the forward fields received at $\mathbf{r_1}$ and $\mathbf{r_2}$ can be expressed as the single modal sum

$$\begin{aligned}
&\mathrm{Cov}(\Psi_T(\mathbf{r_1}|\mathbf{r_0}),\Psi_T(\mathbf{r_2}|\mathbf{r_0}))\\
&\quad=\langle\Psi_T(\mathbf{r_1}|\mathbf{r_0})\Psi_T^*(\mathbf{r_2}|\mathbf{r_0})\rangle-\langle\Psi_T(\mathbf{r_1}|\mathbf{r_0})\rangle\langle\Psi_T^*(\mathbf{r_2}|\mathbf{r_0})\rangle\\
&\quad=\sum_n W_i^{(n)}(\boldsymbol{\rho}_1,\boldsymbol{\rho}_2|\mathbf{r_0})u_n(z_1)u_n^*(z_2)\exp\left(\int_0^{\rho_1+\Delta\rho/2}(i\Re\{\nu_{n,1}(\rho_s)-\nu_{n,2}(\rho_s)\}-\Im\{\nu_{n,1}(\rho_s)+\nu_{n,2}(\rho_s)\})\mathrm{d}\rho_s\right)\\
&\qquad\times\left(\mathrm{e}^{\int_0^{\rho1+\Delta\rho/2}\mu_{n,1,2}(\rho_s)\mathrm{d}\rho_s}-1\right) \qquad (103)\\
&\quad=\sum_n\frac{2\pi}{d^2(z_0)}\frac{1}{|\xi_n|\sqrt{\rho_1\rho_2}}|u_n(z_0)|^2u_n(z_1)u_n^*(z_2)\mathrm{e}^{i\Re\{\xi_n\}(\rho_1-\rho_2)}\mathrm{e}^{-\Im\{\xi_n\}(\rho_1+\rho_2)}\\
&\qquad\times\exp\left(\int_0^{\rho_1+\Delta\rho/2}(i\Re\{\nu_{n,1}(\rho_s)-\nu_{n,2}(\rho_s)\}-\Im\{\nu_{n,1}(\rho_s)+\nu_{n,2}(\rho_s)\})\mathrm{d}\rho_s\right)\left(\mathrm{e}^{\int_0^{\rho_1+\Delta\rho/2}\mu_{n,1,2}(\rho_s)\mathrm{d}\rho_s}-1\right), \qquad (104)
\end{aligned}$$

using Eqs. (22), (101), and (102).

2. Mutual intensity of forward field

The spatial cross-correlation of the forward fields received at $\mathbf{r_1}$ and $\mathbf{r_2}$ is given by

$$\begin{aligned}
\langle\Psi_T(\mathbf{r_1}|\mathbf{r_0})\Psi_T^*(\mathbf{r_2}|\mathbf{r_0})\rangle&=\sum_n\frac{2\pi}{d^2(z_0)}\frac{1}{|\xi_n|\sqrt{\rho_1\rho_2}}|u_n(z_0)|^2u_n(z_1)u_n^*(z_2)\mathrm{e}^{i\Re\{\xi_n\}(\rho_1-\rho_2)}\mathrm{e}^{-\Im\{\xi_n\}(\rho_1+\rho_2)}\\
&\quad\times\exp\left(\int_0^{\rho_1+\Delta\rho/2}(i\Re\{\nu_{n,1}(\rho_s)-\nu_{n,2}(\rho_s)\}-\Im\{\nu_{n,1}(\rho_s)+\nu_{n,2}(\rho_s)\})\mathrm{d}\rho_s\right)\left(\mathrm{e}^{\int_0^{\rho_1+\Delta\rho/2}\mu_{n,1,2}(\rho_s)\mathrm{d}\rho_s}-1\right)\\
&\quad+\sum_n\sum_m\frac{2\pi}{d^2(z_0)}\frac{1}{\sqrt{\xi_n\xi_m^*\rho_1\rho_2}}u_n(z_0)u_m^*(z_0)u_n(z_1)u_m^*(z_2)\mathrm{e}^{i\Re\{\xi_n\rho_1-\xi_m\rho_2\}}\mathrm{e}^{-\Im\{\xi_n\rho_1+\xi_m\rho_2\}}\\
&\quad\times\exp\left(\int_0^{\rho_1+\Delta\rho/2}(i\Re\{\nu_{n,1}(\rho_s)-\nu_{m,2}(\rho_s)\}-\Im\{\nu_{n,1}(\rho_s)+\nu_{m,2}(\rho_s)\})\mathrm{d}\rho_s,\right) \qquad (105)
\end{aligned}$$

from Eqs. (22) and (104). This spatial cross-correlation is proportional to the mutual intensity of the two receivers.

C. Exponential coefficient of modal covariance

Here we derive an analytic expression for the exponential coefficient of modal covariance $\mu_{m,1,2}$. The spatial cross-correlation of the scattered fields received at $\mathbf{r_1}$ and $\mathbf{r_2}$ from an elemental shell of inhomogeneities obtained from Eq. (9) is

$$\begin{aligned}
&\langle\Phi_s(\mathbf{r_1}|\mathbf{r_0},\Delta\rho_s(\rho_s))\Phi_s^*(\mathbf{r_2}|\mathbf{r_0},\Delta\rho_s(\rho_s))\rangle\\
&\quad\approx\Bigg\langle\sum_m\sum_n\sum_{m'}\sum_{n'}\int_0^\infty\mathrm{d}z_t\int_0^\infty\mathrm{d}z_{t'}\int_{\rho_s-\Delta\rho_s/2}^{\rho_s+\Delta\rho_s/2}\mathrm{d}\rho_t\int_{\rho_s-\Delta\rho_s/2}^{\rho_s+\Delta\rho_s/2}\mathrm{d}\rho_{t'}\\
&\qquad\times\int_{\phi_1-\phi_F/2}^{\phi_1+\phi_F/2}\rho_t\,\mathrm{d}\phi_t\,\mathrm{e}^{i\xi_m[\rho_1\rho_t/2(\rho_1-\rho_t)](\phi_t-\phi_1)^2}\int_{\phi_2-\phi_F/2}^{\phi_2+\phi_F/2}\rho_{t'}\,\mathrm{d}\phi_{t'}\,\mathrm{e}^{-i\xi_{m'}[\rho_2\rho_{t'}/2(\rho_2-\rho_{t'})](\phi_{t'}-\phi_2)^2}\\
&\qquad\times\frac{4\pi^2}{k(z_t)k(z_{t'})d(z_t)d(z_{t'})}\frac{1}{d^2(z_0)}\frac{1}{\sqrt{\xi_m\xi_{m'}^*}}\frac{1}{\sqrt{\xi_n\xi_{n'}^*}}\frac{1}{\sqrt{(\rho_1-\rho_t)(\rho_2-\rho_t')\rho_t\rho_{t'}}}\\
&\qquad\times u_m(z_1)u_{m'}^*(z_2)u_n(z_0)u_{n'}^*(z_0)\\
&\qquad\times[N_m^{(1)}(z_t)N_n^{(1)}(z_t)\mathrm{e}^{i\Re(\gamma_m+\gamma_n)z_t}s_{\mathbf{r_t}}(\pi-\alpha_m,\beta_s(\phi_1,\phi_t);\alpha_n,\phi_t)\\
&\qquad-N_m^{(2)}(z_t)N_n^{(1)}(z_t)\mathrm{e}^{i\Re(-\gamma_m+\gamma_n)z_t}s_{\mathbf{r_t}}(\alpha_m,\beta_s(\phi_1,\phi_t);\alpha_n,\phi_t)\\
&\qquad-N_m^{(1)}(z_t)N_n^{(2)}(z_t)\mathrm{e}^{i\Re(\gamma_m-\gamma_n)z_t}s_{\mathbf{r_t}}(\pi-\alpha_m,\beta_s(\phi_1,\phi_t);\pi-\alpha_n,\phi_t)\\
&\qquad+N_m^{(2)}(z_t)N_n^{(2)}(z_t)\mathrm{e}^{i\Re(-\gamma_m-\gamma_n)z_t}s_{\mathbf{r_t}}(\alpha_m,\beta_s(\phi_1,\phi_t);\pi-\alpha_n,\phi_t)]\\
&\qquad\times[N_{m'}^{*(1)}(z_{t'})N_{n'}^{*(1)}(z_{t'})\mathrm{e}^{i\Re(-\gamma_{m'}-\gamma_{n'})z_{t'}}s_{\mathbf{r_{t'}}}(\pi-\alpha_{m'},\beta_s(\phi_2,\phi_{t'});\alpha_{n'},\phi_{t'})
\end{aligned}$$

$$
\begin{aligned}
&- N^{*(2)}_{m'}(z_{t'})N^{*(1)}_{n'}(z_{t'})e^{i\Re(\gamma_{m'}-\gamma_{n'})z_{t'}}s_{\mathbf{r}_{t'}}(\alpha_{m'},\beta_s(\phi_2,\phi_{t'});\alpha_{n'},\phi_{t'})\\
&- N^{*(1)}_{m'}(z_{t'})N^{*(2)}_{n'}(z_{t'})e^{i\Re(-\gamma_{m'}+\gamma_{n'})z_{t'}}s_{\mathbf{r}_{t'}}(\pi-\alpha_{m'},\beta_s(\phi_2,\phi_{t'});\pi-\alpha_{n'},\phi_{t'})\\
&+ N^{*(2)}_{m'}(z_{t'})N^{*(2)}_{n'}(z_{t'})e^{i\Re(\gamma_{m'}+\gamma_{n'})z_{t'}}s_{\mathbf{r}_{t'}}(\alpha_{m'},\beta_s(\phi_2,\phi_{t'});\pi-\alpha_{n'},\phi_{t'})]\\
&\times e^{i\Re\{\xi_m(\rho_1-\rho_t)-\xi_{m'}(\rho_2-\rho_{t'})\}}e^{i\Re\{\xi_n\rho_t-\xi_{n'}\rho_{t'}\}}\\
&\times e^{-\Im\{\xi_m(\rho_1-\rho_t)+\xi_{m'}(\rho_2-\rho_{t'})\}}e^{-\Im\{\xi_n+\xi_{n'}\}\rho_t}e^{-\Im\{(\gamma_m+\gamma_n)z_t+(\gamma_{m'}+\gamma_{n'})z_{t'}\}}\Big\rangle. \qquad (106)
\end{aligned}
$$

Equation (106) cannot be further evaluated unless the cross-correlation of the scatter function densities at $\mathbf{r_t}$ and $\mathbf{r_{t'}}$ is known. As before, we examine the two cases. The first is when inhomogeneities are fully correlated and the second is when they are uncorrelated within the Fresnel width for both receivers.

1. Scatterers fully correlated within Fresnel width

This analysis is applicable to shells where $l_y > Y_F(\rho_p,\rho_s)$ or $|\rho_s-\rho_p/2| > (\rho_p/2)\sqrt{1-4l_y^2/\lambda\rho}$ for $p=1,2$. The exponential coefficient of field covariance for the two receiver azimuths is found to be

$$
\mu^{\mathrm{cor}}_{n,1,2}(\rho_s) = \sum_m \frac{1}{|\xi_m|}\int_0^\infty dz_t \int_0^\infty dz_{t'} \frac{l_x(\rho_s,z_t,z_{t'})}{\xi_m}\frac{4\pi^2}{k(z_t)k(z_{t'})d(z_t)d(z_{t'})}C_{s,s}(\rho_s,z_t,z_{t'},m,n), \qquad (107)
$$

by setting $\rho_1=\rho_2=\rho$ in Eq. (106) and following an approach similar to that in Sec. IV B 1. Here $C_{s,s}(\rho_s,z_t,z_{t'},m,n)$ is given by Eq. (72), but with the covariance of the scatter function density defined as

$$
\begin{aligned}
&\mathrm{Cov}(s_{\rho_s,z_t}(m_u;n_d),s_{\rho_s,z_{t'}}(m_u;n_d))\\
&= \langle s_{\rho_s,z_t}(\pi-\alpha_m,\phi_1;\alpha_n,\phi_1)s^*_{\rho_s,z_{t'}}(\pi-\alpha_m,\phi_2;\alpha_n,\phi_2)\rangle - \langle s_{\rho_s,z_t}(\pi-\alpha_m,\phi_1;\alpha_n,\phi_1)\rangle\langle s^*_{\rho_s,z_{t'}}(\pi-\alpha_m,\phi_2;\alpha_n,\phi_2)\rangle. \qquad (108)
\end{aligned}
$$

The solutions for receivers at different ranges and azimuths are then obtained by substituting Eq. (107) into Eqs. (104) and (105).

2. Uncorrelated scatterers within the Fresnel width

This analysis is applicable to shells where $l_y < Y_F(\rho_p,\rho_s)$ or $|\rho_s-\rho_p/2| < (\rho_p/2)\sqrt{1-4l_y^2/\lambda\rho_p}$ for $p=1,2$. The scatter function densities centered at $\mathbf{r_t}$ as well as $\mathbf{r_{t'}}$ are assumed to be fully correlated if they fall within both a coherence area A_c of each other and the overlapping active regions of the given shell for the two receivers. Let $W_{\mathrm{overlap}}(\phi_t)$ be an azimuthal window function that describes this overlap region,

$$
W_{\mathrm{overlap}}(\phi_t) = \begin{cases} 1, & \text{if } (\phi_1-\phi_F/2<\phi_t<\phi_1+\phi_F/2)\&(\phi_2-\phi_F/2<\phi_t<\phi_2+\phi_F/2),\\ 0, & \text{otherwise.}\end{cases} \qquad (109)
$$

The coefficient of modal field variance for the two receiver azimuths becomes

$$
\mu^{\mathrm{uncor}}_n(\rho_s) = \sum_m \sqrt{\frac{\rho}{2\pi\xi_m\rho_s(\rho-\rho_s)}}\frac{1}{|\xi_m|}\mathcal{B}(\rho,\rho_s,\phi_1,\phi_2)\int_0^\infty dz_t\int_0^\infty dz_{t'}\, A_c(\rho_s,z_t,z_{t'})\frac{4\pi^2}{k(z_t)k(z_{t'})d(z_t)d(z_{t'})}C_{s,s}(\rho_s,z_t,z_{t'},m,n), \qquad (110)
$$

by setting $\rho_1=\rho_2=\rho$ in Eq. (106) and following an analysis similar to that in Sec. IV B 2. Here,

$$
\mathcal{B}(\rho,\rho_s,\phi_1,\phi_2) = e^{i\xi_m[\rho\rho_s/2(\rho-\rho_s)](\phi_1^2-\phi_2^2)}\sqrt{\frac{\xi_m\rho}{2\pi\rho_s(\rho-\rho_s)}}\int_0^{2\pi} W_{\mathrm{overlap}}(\phi_t)e^{i\xi_m\rho_s\phi_t[\rho/2(\rho-\rho_s)](\phi_2-\phi_1)}\rho_s\, d\phi_t, \qquad (111)
$$

and $C_{z_t,z_{t'}}(n,m)$ is given by Eq. (72), but with the covariance of the scatter function defined by

$$\mathrm{Cov}(s_{z_t}(m_u;n_d),s_{z_{t'}}(m_u;n_d)) = \left\langle s_{z_t}\left(\pi-\alpha_m,\beta_s\left(\phi_1,\frac{\phi_1+\phi_2}{2}\right);\alpha_n,\frac{\phi_1+\phi_2}{2}\right)s^*_{z_{t'}}\left(\pi-\alpha_m,\beta_s\left(\phi_2,\frac{\phi_1+\phi_2}{2}\right);\alpha_n,\frac{\phi_1+\phi_2}{2}\right)\right\rangle$$
$$-\left\langle s_{z_t}\left(\pi-\alpha_m,\beta_s\left(\phi_1,\frac{\phi_1+\phi_2}{2}\right);\alpha_n,\frac{\phi_1+\phi_2}{2}\right)\right\rangle\left\langle s^*_{z_{t'}}\left(\pi-\alpha_m,\beta_s\left(\phi_2,\frac{\phi_1+\phi_2}{2}\right);\alpha_n,\frac{\phi_1+\phi_2}{2}\right)\right\rangle. \quad (112)$$

The solutions for receivers at different ranges and azimuths are then obtained by substituting Eq. (110) into Eqs. (104) and (105). For two receivers that are colocated so that $\phi_1=\phi_2=\phi$, $\mathcal{B}(\rho,\rho_s,\phi,\phi)=1$ and Eq. (110) reduces to Eq. (77) for a single receiver.

VII. CONCLUSION

Compact analytic expressions are derived for the mean, mutual intensity, and spatial covariance of the acoustic field foward propagated through a stratified ocean waveguide containing 3-D random surface or volume inhomogeneities. They include the accumulated effect of multiple forward scattering through the random inhomogeneous waveguide. They are given as a modal solution in terms of the parameters necessary to describe the incident field as well as the mean and spatial covariance of the medium's inhomogeneities. They are applicable to a broad range of remote sensing and communication problems in the ocean. This includes propagation through bubble clouds, fish schools, internal waves, turbulence, and seabed anomalies in waveguides with rough boundaries.

Multiple scattering through the randomly inhomogeneous medium leads to a mean field where each mode propagates with a new horizontal wave number that depends on the expected scatter function density of the random medium. The new wave number describes attenuation and dispersion induced by the medium's randomness, including potential mode coupling along the propagation path. Expressions for the mutual intensity and spatial covariance of the forward field depend on both the random medium's expected modal extinction density as well as the covariance of its scatter function density, which couples each mode to all other modes due to multiple forward scattering. These are used to analytically show that 3-D scattering effects can become important for scatterers at ranges where the Fresnel width exceeds the medium's local cross-range coherence length. The expressions can also be applied to determine how the coherence of an acoustic signal received by an array of arbitrary configuration is degraded by random multiple forward scattering through the fluctuating ocean.

APPENDIX A: SCATTER FUNCTION DENSITY

Discretion must be used in choosing a parametrization for the scatter function density that properly describes the random characteristics of the medium and their relationship to the scattering process, which must conserve energy. Here we present representations of the scatter function density $s_{\mathbf{r_t}}(\alpha,\beta;\alpha_i,\beta_i)$ for both continuous and discrete random scatterers.

1. Continuous random inhomogeneities

Random inhomogeneitites in the acoustic medium are in essence stochastic spatial variations in density and compressibility. Continuous random inhomogeneities in ocean waveguides include turbulence, internal waves, sea-surface and seabed roughness, as well as anomalies in the seabed.

a. Local 3-D stationary random process, potentially nonisotropic

If the inhomogeneities obey a 3-D stationary random process within the single scatter shell, the coherence volume can be defined as

$$V_c(\rho_s,z_t) = \frac{\int_0^{2\pi}\int_0^{\pi}\int_0^{R_{\max}} |C_{\mathcal{FF}}(R,\Omega_1,\Omega_2,\rho_s,z_t)|^2 R^2 \sin\Omega_1\, dR\, d\Omega_1\, d\Omega_2}{|C_{\mathcal{FF}}(0,0,0,\rho_s,z_t)|^2}, \quad (A1)$$

where the scattering density $\mathcal{F}$ of an elemental volume of the randomly inhomogeneous medium can be defined by the Rayleigh-Born single scatter approximation as

$$\Re\{\mathcal{F}(\alpha,\beta,\alpha_i,\beta_i)\} = \frac{k^3}{4\pi}(\Gamma_\kappa(\mathbf{r_t}) + \eta(\mathbf{k},\mathbf{k}_i)\Gamma_d(\mathbf{r_t})), \quad (A2)$$

where Γ_κ is the fractional change in compressibility and Γ_d is the fractional change in density of the local inhomogeneity with respect to the original homogeneous medium,[4] and

$$\eta(\mathbf{k},\mathbf{k}_i) = \frac{\mathbf{k}_i\cdot\mathbf{k}}{k^2} \quad (A3)$$

is the cosine of the angle between the incident and scattered plane wave directions. When density changes are important to acoustic scattering, perturbation expansions in *sound speed* and density alone are typically not sufficient to de-

scribe even first-order effects. To include all necessary effects, expansions in *compressibility* and density must be made.[3]

Here the covariance of the elemental scattering density $\mathrm{Cov}(\mathcal{F}_{\mathbf{r_t}}, \mathcal{F}^*_{\mathbf{r_{t'}}}) = C_{\mathcal{FF}}(R, \Omega_1, \Omega_2, \rho_s, z_t)$ depends only on the separation $\mathbf{R} = (R, \Omega_1, \Omega_2) = \mathbf{r_t} - \mathbf{r'_t}$, where $R = \sqrt{(x_t - x_{t'})^2 + (y_t - y_{t'})^2 + (z_t - z_{t'})^2}$. The coherence radius for any direction specified by the elevation angle Ω_1 and azimuth angle Ω_2 is given by

$$l_c^3(\Omega_1, \Omega_2, \rho_s, z_t) = \frac{3\int_0^{R_{\max}} |C_{\mathcal{FF}}(R, \Omega_1, \Omega_2, \rho_s, z_t)|^2 \, \mathrm{d}R}{|C_{\mathcal{FF}}(0,0,0,\rho_s,z_t)|^2}. \tag{A4}$$

The coherence lengths for the random process in the x, y, and z directions are then given by $l_x(\rho_s, z_t) = l_c(\Omega_1 = \pi/2, \Omega_2 = 0, \rho_s, z_t) + l_c(\Omega_1 = \pi/2, \Omega_2 = \pi, \rho_s, z_t)$, $l_y(\rho_s, z_t) = l_c(\Omega_1 = \pi/2, \Omega_2 = \pi/2, \rho_s, z_t) + l_c(\Omega_1 = \pi/2, \Omega_2 = 3\pi/2, \rho_s, z_t)$, and $l_z(\rho_s, z_t) = l_c(\Omega_1 = 0, \Omega_2 = 0, \rho_s, z_t) + l_c(\Omega_1 = \pi, \Omega_2 = 0, \rho_s, z_t)$. In Eq. (A1), $R_{\max}$ should be larger than l_c.

The 3-D delta-function covariance assumed in Eq. (93) is consistent with the interpretion that

$$s_{\rho_s, z_t}(\alpha, \beta, \alpha_i, \beta_i) = \frac{1}{V_c} \iiint_{V_c} \mathcal{F}_{\mathbf{r_t}+\mathbf{u}}(\alpha, \beta, \alpha_i, \beta_i) \mathrm{e}^{i(\mathbf{k_i} - \mathbf{k_s})\cdot\mathbf{u}} \mathrm{d}^3\mathbf{u}, \tag{A5}$$

be used on the right-hand side of Eq. (93), given continuous inhomogeneities. Here $\mathbf{k_i}$ and $\mathbf{k_s}$ are the incident and scattered wave number vectors, and $\mathbf{u} = (u_x, u_y, u_z)$ are locations within the coherence volume relative to $\mathbf{r_t}$. The corresponding free-space plane wave scatter function S_{z_t} for the coherence volume is then obtained by multiplying Eq. (A5) by V_c.

b. Local 2-D stationary random process, potentially nonisotropic

Given the 2-D delta-function covariance assumed in Eq. (75), the interpretation,

$$s_{\rho_s, z_t}(\alpha, \beta, \alpha_i, \beta_i) = \frac{1}{A_c} \iint_{A_c} \mathcal{F}_{\mathbf{r_t}+\mathbf{u}}(\alpha, \beta, \alpha_i, \beta_i) \mathrm{e}^{i(\boldsymbol{\xi_i} - \boldsymbol{\xi_s})\cdot\mathbf{u}} \mathrm{d}^2\mathbf{u} \tag{A6}$$

can be made on the right-hand side of Eq. (75) for continuous inhomogeneities. Here $\boldsymbol{\xi_i}$ and $\boldsymbol{\xi_s}$ are the incident and scattered horizontal wave number vectors and $\mathbf{u} = (u_x, u_y)$ are horizontal locations within the coherence area relative to $\boldsymbol{\rho}_t$.

Here the horizontal coherence area A_c is defined under the assumption that the inhomogeneities obey a stationary random process in the horizontal within the Fresnel width in each single scatter shell. The horizontal covariance of their scattering densities can then be expressed as $\mathrm{Cov}(\mathcal{F}_{\mathbf{r_t}}, \mathcal{F}^*_{\mathbf{r_{t'}}}) = C_{\mathcal{FF}}(P, \Omega, \rho_s, z_t, z_{t'})$, which depends on the separation between their horizontal coordinates, $P = \sqrt{(x_t - x_{t'})^2 + (y_t - y_{t'})^2}$, and $\Omega = \tan^{-1}[(y_t - y_{t'})/(x_t - x_{t'})]$ but not on their absolute position within the shell.

The generalized parametric coherence area for the random process in the horizontal is then defined as[55]

$$A_c(\rho_s, z_t, z_{t'}) = \frac{\int_0^{2\pi} \int_0^{P_{\max}} |C_{\mathcal{FF}}(P, \Omega, \rho_s, z_t, z_{t'})|^2 P \, \mathrm{d}P \, \mathrm{d}\Omega}{|C_{\mathcal{FF}}(0,0,\rho_s,z_t,z_{t'})|^2}, \tag{A7}$$

with coherence radius $l_c(\Omega, \rho_s, z_t, z_{t'})$ for any direction Ω, given by

$$l_c^2(\Omega, \rho_s, z_t, z_{t'}) = \frac{2\int_0^{P_{\max}} |C_{\mathcal{FF}}(P, \Omega, \rho_s, z_t, z_{t'})|^2 P \, \mathrm{d}P}{|C_{\mathcal{FF}}(0,0,\rho_s,z_t,z_{t'})|^2}. \tag{A8}$$

The coherence lengths for the random process in the x and y directions are then given by $l_x(\rho_s, z_t, z_{t'}) = l_c(\Omega = 0, \rho_s, z_t, z_{t'}) + l_c(\Omega = \pi, \rho_s, z_t, z_{t'})$ and $l_y(\rho_s, z_t, z_{t'}) = l_c(\Omega = \pi/2, \rho_s, z_t, z_{t'}) + l_c(\Omega = 3\pi/2, \rho_s, z_t, z_{t'})$, where $P_{\max}$ in Eq. (A7) is larger than l_c.

2. Discrete inhomogeneities or particles

Consider a volume of space V centered at location $\mathbf{r}_t$ containing discrete inhomogeneities or particles. Each particle may be large compared to the waveglength and have arbitrary shape and material properties. Examples of such discrete scatterers include fish, marine mammals, bubbles, and underwater vehicles. The location of the qth particle in this volume is $\mathbf{r}_{t,q} = \mathbf{r}_t + \mathbf{u}_q$, where $\mathbf{u}_q$ is its displacement from the volume center $\mathbf{r}_t$. The scatter function of the qth particle relative to the volume center is $S_q(\mathbf{r}_t)\mathrm{e}^{i(\mathbf{k}_i - \mathbf{k}_s)\cdot\mathbf{u}_q}$, where $S_q(\mathbf{r}_t)$ is its scatter function, $\mathbf{k}_i$ and $\mathbf{k}_s$ are the incident and scattered plane wave vectors, respectively. For discussions in this section, we suppress the angular dependence of the scatter function to abbreviate the notation.

When the single scatter approximation is valid, the expected total scatter function $\langle S_T(\mathbf{r}_t) \rangle$ of the volume V is then

$$\langle S_T(\mathbf{r}_t) \rangle = \int\int\int \sum_q^N S_q(\mathbf{r}_t) \mathrm{e}^{i(\mathbf{k}_i - \mathbf{k}_s)\cdot\mathbf{u}_q} p(\mathbf{u}_q, S_q | N) \times p(N) \mathrm{d}^3\mathbf{u}_q \, \mathrm{d}S_q \, \mathrm{d}N, \tag{A9}$$

where $p(\mathbf{u}_q, S_q | N)$ is the probability density of finding the qth particle at location $\mathbf{u}_q$ with scatter function amplitude S_q given that there are N particles in the volume, and $p(N)$ is the probability density of finding N particles in this volume.

If the particles in V are each identically distributed in space and their spatial distribution is uniform and independent of the scatter function amplitude and the number of particles in the volume, then $p(\mathbf{u}_q, S_q | N) = p(\mathbf{u}_q) p(S_q | N)$, and $p(\mathbf{u}_q) = 1/V$. Equation (A9) then becomes

$$\langle S_T(\mathbf{r}_t)\rangle = U \int \int \sum_q^N S_q(\mathbf{r}_t) p(S_q|N) p(N) \mathrm{d}S_q \, \mathrm{d}N, \quad \text{(A10)}$$

where

$$U = \int \frac{1}{V} \mathrm{e}^{i(\mathbf{k}_i - \mathbf{k}_s)\cdot \mathbf{u}_q} \mathrm{d}^3 \mathbf{u}_q \quad \text{(A11)}$$

is an elementary integral over V that is a function of $\mathbf{k}_i$ and $\mathbf{k}_s$. For forward scatter in free space, $U=1$, since $\mathbf{k}_i$ and $\mathbf{k}_s$ are identical in the forward direction. This point was essentially made long ago by Rayleigh.[10] In a multimodal waveguide, however, U will not necessarily be unity, even for scattering in the forward azimuth due to variations in modal elevation angles. It is always approximately unity when the dimensions of V can be made small compared to the acoustic wavelength, assuming due attention is paid to the actual size of the particles.

If the particles are also identically distributed in their scatter function amplitude, and N is large, the total scatter function of the volume from Eq. (A10) then reduces to

$$\langle S_T(\mathbf{r}_t)\rangle = U \int N \overline{S(\mathbf{r}_t|N)} p(N) \mathrm{d}N, \quad \text{(A12)}$$

$$= U \langle N \overline{S(\mathbf{r}_t|N)} \rangle, \quad \text{(A13)}$$

where $\overline{S(\mathbf{r}_t|N)} = \int S_q(\mathbf{r}_t) p(S_q|N) \mathrm{d}S_q$ is the expected scatter function amplitude of each of the identically distributed particles, given that there are a total of N particles in the volume.

The expected scatter function density at location $\mathbf{r}_t$ is then given by

$$\langle s_{\mathbf{r}_t} \rangle = \frac{\langle S_T(\mathbf{r}_t)\rangle}{V} = U \langle n_V \overline{S(\mathbf{r}_t|n_V)} \rangle, \quad \text{(A14)}$$

where $n_V = N/V$ is the number of particles per unit volume.

The second moment of the scatter function of the particles within V is

$$\langle S_T(\mathbf{r}_t) S_T^*(\mathbf{r}_t)\rangle = \int \int \int \int \int \sum_q^N \sum_l^N S_q(\mathbf{r}_t) S_l^*(\mathbf{r}_t) \mathrm{e}^{i(\mathbf{k}_i - \mathbf{k}_s)\cdot \mathbf{u}_q} \times \mathrm{e}^{-i(\mathbf{k}_i - \mathbf{k}_s)\cdot \mathbf{u}_l} p(\mathbf{u}_q, \mathbf{u}_l, S_q, S_l|N) p(N) \times \mathrm{d}\mathbf{u}_q \, \mathrm{d}\mathbf{u}_l \, \mathrm{d}S_q \, \mathrm{d}S_l \, \mathrm{d}N. \quad \text{(A15)}$$

If we assume that the scatter functions and positions of the particles are uncorrelated, Eq. (A15) then reduces to

$$\langle S_T(\mathbf{r}_t) S_T^*(\mathbf{r}_t)\rangle = \int \sum_q^N \sum_l^N \left([\mathrm{Var}(S_q(\mathbf{r}_t|N)) + (1 - |U|^2) |\overline{S_q(\mathbf{r}_t|N)}|^2] \delta_{ql} + |U|^2 \overline{S_q(\mathbf{r}_t|N)} \; \overline{S_l^*(\mathbf{r}_t|N)} \right) p(N) \mathrm{d}N, \quad \text{(A16)}$$

where $\mathrm{Var}(S_q(\mathbf{r}_t|N)) = \int |S_q(\mathbf{r}_t)|^2 p(S_q|N) \mathrm{d}S_q - |\overline{S_q(\mathbf{r}_t|N)}|^2$, and the second term in the square bracket is a variance component that arises solely from randomness in the particle position.

Since the scatterers are also taken to be identically distributed, and N is large, Eq. (A16) further simplifies to

$$\langle S_T(\mathbf{r}_t) S_T^*(\mathbf{r}_t)\rangle = \int (N \, \mathrm{Var}(S(\mathbf{r}_t|N)) + (1 - |U|^2) N |\overline{S(\mathbf{r}_t|N)}|^2 + |U|^2 N^2 |\overline{S(\mathbf{r}_t|N)}|^2) p(N) \mathrm{d}N, \quad \text{(A17)}$$

$$= \langle N \, \mathrm{Var}(S(\mathbf{r}_t|N)) \rangle + (1 - |U|^2) \langle N |\overline{S(\mathbf{r}_t|N)}|^2 \rangle + |U|^2 \langle N^2 |\overline{S(\mathbf{r}_t|N)}|^2 \rangle. \quad \text{(A18)}$$

The second moment of the scatter function density then becomes

$$\langle |s_{\mathbf{r}_t}|^2 \rangle = \frac{\langle |S_T(\mathbf{r}_t)|^2 \rangle}{(V)^2} = \frac{1}{V} \left[\langle n_V \, \mathrm{Var}(S(\mathbf{r}_t|N)) \rangle + (1 - |U|^2) \langle n_V |\overline{S(\mathbf{r}_t|n_V)}|^2 \rangle \right] + |U|^2 \langle n_V^2 |\overline{S(\mathbf{r}_t|n_V)}|^2 \rangle, \quad \text{(A19)}$$

and its variance is

$$\mathrm{Var}(s_{\mathbf{r}_t}) = \langle |s_{\mathbf{r}_t}|^2 \rangle - |\langle s_{\mathbf{r}_t} \rangle|^2, \quad \text{(A20)}$$

$$= \frac{1}{V} [\langle n_V \, \mathrm{Var}(S(\mathbf{r}_t|N)) \rangle + (1 - |U|^2) \langle n_V |\overline{S(\mathbf{r}_t|n_V)}|^2 \rangle] + |U|^2 \langle n_V^2 |\overline{S(\mathbf{r}_t|n_V)}|^2 \rangle - |U|^2 |\langle n_V \overline{S(\mathbf{r}_t|n_V)} \rangle|^2. \quad \text{(A21)}$$

If scattering by the particles is independent of the number of particles per unit volume in the medium, the mean and variance of the scatter function density then, respectively, become

$$\langle s_{\mathbf{r}_t} \rangle = U \langle n_V \rangle \langle S(\mathbf{r}_t) \rangle, \quad \text{(A22)}$$

and

$$\mathrm{Var}(s_{\mathbf{r}_t}) = \frac{1}{V} [\langle n_V \rangle \mathrm{Var}(S(\mathbf{r}_t)) + (1 - |U|^2) \langle n_V \rangle |\langle S(\mathbf{r}_t) \rangle|^2] + |U|^2 \, \mathrm{Var}(n_V) |\langle S(\mathbf{r}_t) \rangle|^2. \quad \text{(A23)}$$

For forward scatter in free space $|U|^2 = 1$ and the variance of the scatter function density in Eq. (A23) reduces to

$$\mathrm{Var}(s_{\mathbf{r}_t}) = \frac{1}{V} \langle n_V \rangle \mathrm{Var}(S(\mathbf{r}_t)) + \mathrm{Var}(n_V) |\langle S(\mathbf{r}_t) \rangle|^2. \quad \text{(A24)}$$

Under the assumptions and approximations leading to Eq. (A24), the variance of the scatter function density for discrete scatterers in the forward direction in free space is zero when both the variance of the scatter function of an individual particle and the variance of the number density of particles are zero. Otherwise, the scatter function variance and, consequently, the field variance cannot be zero. This result is especially intuitive in forward scatter, where changes in the configuration of a fixed number of like and uncorrelated particles within a farfield volume can have no effect on the forward field. We again note that essentially this same point was made long ago by Rayleigh[10] and can be obtained in the appropriate limiting case of Eqs. (7.3.13) and (7.3.18) in the Tsang, Kong, and Ding[56] analysis for omnidirectional scatterers.

It is interesting that in Twersky's formulation of forward scattering through a slab of discrete scatterers, he implicitly assumed the variances of the scatter function and the number density to be zero and also obtains zero variance for the forward field for his q small, which corresponds to what we refer to here as the direct wave, as can be seen in Sec. 14-6 of Ishimaru.[18] It is not clear that Twersky's formulation is valid when his q is not small, given the numerous small angle approximations he makes for the scattered field about the incident direction.

Similarly, the cross-correlation of the scatter function densities centered at $\mathbf{r}_{t1}$ and $\mathbf{r}_{t2}$ can be approximated as

$$\langle s_{\mathbf{r_{t1}}} s^*_{\mathbf{r_{t2}}} \rangle = \frac{\langle S_T(\mathbf{r}_{t1}) S_T^*(\mathbf{r}_{t2}) \rangle}{(V_c)^2} = V_c \delta(\mathbf{r}_{t1} - \mathbf{r}_{t2}) \left\{ \frac{\langle n_V(\mathbf{r}_{t1}) \rangle}{V_c} \mathrm{Var}(S(\mathbf{r}_{t1})) + \left[\frac{\langle n_V(\mathbf{r}_{t1}) \rangle}{V_c} (1 - |U(\mathbf{r}_{t1})|^2) + |U(\mathbf{r}_{t1})|^2 \, \mathrm{Var}(n_V(\mathbf{r}_{t1})) \right] |\langle S(\mathbf{r}_{t1}) \rangle|^2 \right\}$$
$$+ U(\mathbf{r}_{t1}) U^*(\mathbf{r}_{t2}) \langle n_V(\mathbf{r}_{t1}) \rangle \langle n_V(\mathbf{r}_{t2}) \rangle \langle S(\mathbf{r}_{t1}) \rangle \langle S^*(\mathbf{r}_{t2}) \rangle, \tag{A25}$$

if the coherence volume V_c falls within the active region of a given single scatter shell. Here the coherence volume is defined entirely by the spatial covariance of the number density through

$$V_c = \frac{\iiint |C_{n_V n_V}(\mathbf{R})|^2 \, \mathrm{d}^3\mathbf{R}}{|C_{n_V n_V}(0)|^2}, \tag{A26}$$

where the covariance of the number density $\mathrm{Cov}(n_{V\mathbf{r_t}}, n_{V\mathbf{r_t}'}) = C_{n_V n_V}(\mathbf{R})$ depends only the separation $\mathbf{R} = \mathbf{r_t} - \mathbf{r}'_\mathbf{t}$.

If $|U|^2 V_c \, \mathrm{Var}(n_V)$ is negligible, then

$$\langle s_{\mathbf{r_{t1}}} s^*_{\mathbf{r_{t2}}} \rangle = \frac{\langle S_T(\mathbf{r}_{t1}) S_T^*(\mathbf{r}_{t2}) \rangle}{(V)^2}$$
$$= \langle n_V(\mathbf{r}_{t1}) \rangle \delta(\mathbf{r}_{t1} - \mathbf{r}_{t2}) \{ \mathrm{Var}(S(\mathbf{r}_{t1})) + [(1 - |U(\mathbf{r}_{t1})|^2)] |\langle S(\mathbf{r}_{t1}) \rangle|^2 \} + U(\mathbf{r}_{t1}) U^*(\mathbf{r}_{t2}) \langle n_V(\mathbf{r}_{t1}) \rangle \langle n_V(\mathbf{r}_{t2}) \rangle \langle S(\mathbf{r}_{t1}) \rangle \langle S^*(\mathbf{r}_{t2}) \rangle, \tag{A27}$$

as long as V can be limited to the active region and have the corresponding number of particles N within it be large. Equations (A25) or (A27) can be used in Eq. (93) for scattering from discrete particles or objects that decorrelate in three dimensions. The spatial correlation of scattering from objects that decorrelate in only one or two dimensions can be readily obtained by analogous means.

[1] F. Ingenito, "Scattering from an object in a stratified medium," J. Acoust. Soc. Am. **82**, 2051–2059 (1987).

[2] J. J. Bowman, T. B. A. Senior, and P. L. E. Uslenghi, in *Electromagnetic and Acoustic Scattering by Simple Shapes* (North-Holland, Amsterdam, 1969).

[3] Lord Rayleigh, *The Theory of Sound* (Dover, New York, 1896), Vol. 2, Ch. 15, p. 296.

[4] P. M. Morse and K. U. Ingard, *Theoretical Acoustics* (Princeton University Press, Princeton, NJ, 1986).

[5] N. C. Makris and P. Ratilal, "A unified model for reverberation and submerged object scattering in a stratified ocean waveguide," J. Acoust. Soc. Am. **109**, 909–941 (2001).

[6] P. Ratilal and N. C. Makris, "Extinction theorem for object scattering in a stratified medium," J. Acoust. Soc. Am. **110**, 2924–2945 (2001).

[7] P. G. Bergmann, "Intensity fluctuations," in *The Physics of Sound in the Sea, Part I: Transmission* (National Defense Research Committee, Washington, DC, 1946).

[8] I. Dyer, "Statistics of sound propagation in the ocean," J. Acoust. Soc. Am. **47**, 337–345 (1970)

[9] N. C. Makris, "The effect of saturated transmission scintillation on ocean acoustic intensity measurements," J. Acoust. Soc. Am. **100**, 769–783 (1996).

[10] Lord Rayleigh, "On the transmission of light through an atmosphere containing small particles in suspension, and on the origin of the blue of the sky," Philos. Mag. **47**, 375–384 (1899).

[11] H. C. van de Hulst, *Light Scattering by Small Particles* (Dover, New York, 1957).

[12] L. L. Foldy, "The multiple scattering of waves," Phys. Rev. **67**, 107–119 (1945).

[13] F. Dyson, "The S. Matrix in Quantum Electrodynamics," Phys. Rev. **75**, 1736-1755 (1949).

[14] C. M. Bender and S. A. Orszag, *Advanced Mathematical Methods for Scientists and Engineers* (McGraw-Hill, New York, 1978).

[15] J. W. Strobehn, in *Laser Beam Propagation in the Atmosphere* (Springer-Verlag, Germany, 1978).

[16] T. Chen, P. Ratilal, and N. C. Makris, "Mean and variance of the forward field propagated through three-dimensional random internal waves in a continental-shelf waveguide" (unpublished).

[17] L. Tsang, J. A. Kong, and R. T. Shin, *Theory of Microwave Remote Sensing* (Wiley, New York, 1985).

[18] A. Ishimaru, *Wave Propagation and Scattering in Random Media* (Academic, New York, 1978).

[19] S. Flatte, in *Sound Propagation Through a Fluctuating Ocean* (Cambridge University Press, Cambridge, UK, 1979).

[20] F. Dyson, W. Munk, and B. Zetler, "Interpretation of multipath scintillation Eleuthera to Bermuda in terms of internal waves and tides," J. Acoust. Soc. Am. **59**, 1121–1133 (1976).

[21] M. G. Brown, J. A. Colosi, S. Tomosovic, A. L. Virovlyansky, M. A. Aolfson, and G. M. Zaslavsky, "Ray dynamics in long-range deep ocean sound propagation," J. Acoust. Soc. Am. **113**, 2533–2547, (2003).

[22] J. A. Colosi and S. M. Flatte, "Mode coupling by internal waves for multi-megameter acoustic propagation in the ocean," J. Acoust. Soc. Am. **100** 3607–3620 (1996).

[23] T. E. Ewart, C. Macaskill, and B. J. Uscinski, "Intensity fluctuations. Part II: Comparson with the Cobb Experiment," J. Acoust. Soc. Am. **74** 1484–1499 (1983).

[24] J. Simmen, S. M. Flatte, and G. Y. Wang "Wavefront folding, chaos, and diffraction for sound propagation through ocean internal waves," J. Acoust. Soc. Am. **102**, 239–255 (1997).

[25] D. Tielburger, S. Finette, and S. Wolf, "Acoustic propagation through an internal wave field in a shallow water waveguide," J. Acoust. Soc. Am. **101**, 789–808 (1997).

[26] F. G. Bass, V. D. Freulicher, and I. M. Fuks, "Propagation in statistically irregular waveguides—Part I: Average field," IEEE Trans. Antennas Propag. **AP-22**, 278-288 (1974).

[27] F. G. Bass, V. D. Freulicher, and I. M. Fuks, "Propagation in Statistically Irregular Waveguides—Part II: Second Order Statistical Moments," IEEE Trans. Antennas Propag. **AP-22**, 288-295 (1974).

[28]W. A. Kuperman and F. Ingenito, "Attenuation of the coherent component of sound propagating in shallow water with rough boundaries," J. Acoust. Soc. Am. **61**, 1178–1187 (1977).
[29]F. Ingenito, "Measurements of mode attenuation coefficients in shallow water," J. Acoust. Soc. Am. **53**, 858-863 (1972).
[30]W. A. Kuperman and H. Schmidt, "Rough surface elastic wave scattering in a horizontally stratified ocean," J. Acoust. Soc. Am. **79**, 1767-1777 (1986).
[31]W. A. Kuperman and H. Schmidt, "Self-consistent perturbation approach to rough surface scattering in stratified elastic media," J. Acoust. Soc. Am. **86**, 1511-1522 (1989).
[32]B. Tracey and H. Schmidt "Seismo-acoustic field statistics in shallow water," IEEE J. Ocean. Eng. **22** 317-331 (1997).
[33]B. Tracey and H. Schmidt "A self-consistent theory for seabed volume scattering," J. Acoust. Soc. Am. **106** 2524-2534 (1999).
[34]G. R. Sutton and J. J. McCoy, "Scattering of acoustics signals by inhomogeneities in a waveguide—a single scatter treatment," J. Acoust. Soc. Am. **60**, 833-839 (1976).
[35]E. E. Salpeter and H. A. Bethe, "A relativistic equation for bound-state problems," Phys. Rev. **84**, 1232-1242 (1951).
[36]L. B. Dozier and F. D. Tappert, "Statistics of normal mode amplitudes in a random ocean. I. Theory," J. Acoust. Soc. Am. **63**, 353-365 (1978).
[37]D. B. Creamer, "Scintillating shallow water waveguides," J. Acoust. Soc. Am. **99**, 2825-2838 (1996).
[38]D. Marcuse, *Theory of Dielectric Optical Waveguides* (Academic, New York, 1974).
[39]C. Penland, "Acoustic normal mode propagation through a three-dimensional internal wave field," J. Acoust. Soc. Am. **78** 1356-1365, (1985).
[40]S. Frankenthal and M. J. Beran, "Propagation in random stratified waveguides—A modal-spectral treatment," J. Acoust. Soc. Am. **104**, 3282-3295 (1998).
[41]P. Ratilal and N. C. Makris, "Propagation through a stratified ocean waveguide with random volume and surface inhomogeneities, Part I. Theory: Attenuation, dispersion and acoustic mirages," J. Acoust. Soc. Am. **112**, 2402 (2002).
[42]P. Ratilal and N. C. Makris, "Covariance of the forward propagated field through a waveguide containing random inhomogeneities," J. Acoust. Soc. Am. **114**, 2428 (2003).
[43]T. Chen, P. Ratilal, and N. C. Makris, "Propagation through a stratified ocean waveguide with random volume and surface inhomogeneities, Part II. Application: Internal waves, bubbles, sub-bottom and seafloor anomalies," J. Acoust. Soc. Am. **112**, 2402 (2002).
[44]P. Ratilal, T. Chen, and N. C. Makris, "Analytic mean and variance of forward propagated field through random internal waves and subbottom anomalies with Rayleigh-Born scattering," J. Acoust. Soc. Am. **115**, 2549 (2004).
[45]T. Chen, S. Lee, Y. Lai, P. Ratilal, and N. C. Makris, "Analysis of acoustic intensity fluctuations measured after one-way transmission and bistatic target scattering on the New Jersey continental shelf during MAE 2003," J. Acoust. Soc. Am. **115**, 2549 (2004).
[46]P. Ratilal, T. Chen, and N. C. Makris, "Estimating internal wave statistics from underwater acoustic transmission scintillation measurements on the New Jersey shelf with a 3-D stochastic model," J. Acoust. Soc. Am. **116**, 2506 (2004).
[47]P. Ratilal and N. C. Makris, "Unified model for 3-D scattering and forward propagation in a stratified ocean waveguide with random seabed inhomogeneities," J. Acoust. Soc. Am. **116**, 2527 (2004).
[48]T. Chen, P. Ratilal, and N. C. Makris, "Analytic expressions for time-domain forward propagation through a waveguide with random inhomogeneities including causality and dispersion relations," J. Acoust. Soc. Am. **114**, 2302 (2003).
[49]P. Ratilal, I. Bertsatos, T. Chen, M. Zanolin, and N. C. Makris, "Optimal passive source localization in a fluctuating ocean waveguide based on an analytic model for the mean field and covariance," J. Acoust. Soc. Am. **115**, 2473 (2004).
[50]N. C. Makris, F. Ingenito, and W. A. Kuperman, "Detection of a submerged object insonified by surface noise in an ocean waveguide," J. Acoust. Soc. Am. **96**, 1703-1724 (1994).
[51]P. Ratilal, "Remote sensing of submerged objects and geomorphology in continental shelf waters with acoustic waveguide scattering," Ph.D thesis, Massachusetts Institute of Technology, 2002.
[52]N. C. Makris, "A spectral approach to 3-D object scattering in layered media applied to scattering from submerged spheres," J. Acoust. Soc. Am. **104**, 2105-2113 (1998); erratum, **106**, 518 (1999).
[53]G. V. Frisk, *Ocean and Seabed Acoustics, A Theory of Wave Propagation* (Prentice–Hall, Englewood Cliffs, NJ, 1994).
[54]P. Ratilal, N. C. Makris, and Y. Lai, "Validity of the sonar equation and Babinet's principle for scattering in a stratified medium," J. Acoust. Soc. Am. **112**, 1797-1816 (2002).
[55]L. Mandel and E. Wolf, *Optical Coherence and Quantum Optics* (Cambridge University Press, Cambridge, (1995).
[56]L. Tsang, J. A. Kong, and K.-H. Ding, *Scattering of Electromagnetic Waves: Theories and Applications* (Wiley, New York, 2000).

Mean and variance of the forward field propagated through three-dimensional random internal waves in a continental-shelf waveguide

Tianrun Chen
Department of Mechanical Engineering, Massachusetts Institute of Technology, Cambridge, Massachusetts 02139

Purnima Ratilal
Department of Electrical and Computer Engineering, Northeastern University, Boston, Massachusetts 02115

Nicholas C. Makris
Department of Mechanical Engineering, Massachusetts Institute of Technology, Cambridge, Massachusetts 02139

(Received 30 May 2004; revised 3 June 2005; accepted 12 June 2005)

The mean and variance of the acoustic field forward propagated through a stratified ocean waveguide containing three-dimensional (3-D) random internal waves is modeled using an analytic normal mode formulation. The formulation accounts for the accumulated effects of *multiple forward scattering*. These lead to redistribution of both coherent and incoherent modal energies, including attenuation and dispersion. The inhomogeneous medium's scatter function density is modeled using the Rayleigh-Born approximation to Green's theorem to account for random fluctuations in both density and compressibility caused by internal waves. The generalized waveguide extinction theorem is applied to determine attenuation due to scattering from internal wave inhomogeneities. Simulations for typical continental-shelf environments show that when internal wave height exceeds the acoustic wavelength, the acoustic field becomes so randomized that the expected total intensity is dominated by the field variance beyond moderate ranges. This leads to an effectively saturated field that decays monotonically and no longer exhibits the periodic range-dependent modal interference structure present in nonrandom waveguides. Three-dimensional scattering effects can become important when the Fresnel width approaches and exceeds the cross-range coherence length of the internal wave field. Density fluctuations caused by internal waves are found to noticably affect acoustic transmission in certain Arctic environments. [DOI: 10.1121/1.1993107]

PACS number(s): 43.30.Re [WLS] Pages: 3560–3574

I. INTRODUCTION

When an acoustic field propagates through a multimodal waveguide, random variations in medium properties can have a cumulative effect over range. This can drastically alter the delicate modal interference structure of the incident field, leading to significant randomization in the received field. Here, we model the mean, variance, and total intensity of the forward field propagated through an ocean waveguide containing temporally and spatially random 3-D internal waves using a general modal formulation described in Ref. 1. This formulation is convenient because it takes into account the accumulated effects of *multiple forward scattering* on the *mean and covariance* of the forward propagated field. These include coherent, partially coherent, and incoherent interactions with the incident field, which lead to attenuation, dispersion, and exponential coefficients of field variance that describe mode coupling induced by the medium's inhomogeneities. An advantage of the formulation is that the first and second moments of the forward field can be analytically expressed in terms of the first and second moments of the inhomogeneous medium's spatially varying scatter function density. These inhomogeneities can be arbitrarily large relative to the acoustic wavelength and have arbitrary compressibility and density contrast from the surrounding medium.

Inhomogeneities arising from internal wave disturbances typically have relatively small differences in density and compressibility from the surrounding medium. A convenient approach for modeling their scattering properties is to apply the first-order Rayleigh-Born approximation to Green's theorem.[2] Internal wave scattering properties are then expressed in terms of the statistical variations in compressibility and density caused by the disturbance. This requires knowledge of the probability distributions of the compressibility and density variations, which can be expressed in terms of internal-wave wave number spectra. The first-order Rayleigh-Born approximation leads to a purely real scatter function that can directly account for scattering-induced dispersion in the mean forward field, but not attenuation, which requires the imaginary part. Attenuation in the mean forward field due to scattering is then determined from the waveguide extinction theorem.[3,4] The waveguide extinction theorem for any given mode relates power loss in the *forward* azimuth to

the total scattered power in all directions, which can be estimated with high accuracy using the first-order Rayleigh-Born approximation.

Following the trend of ever-increasing ocean utilization has come a greater interest in developing models to help understand and accurately predict the effect of internal wave fields on underwater acoustic transmission through continental shelf environments. Significant fluctuations have been observed[5–7] and predicted[8,9] in signal transmission. These fluctuations lead to signal-dependent noise[8] that can significantly degrade sonar system performance. Since internal waves in continental shelf environments often have large displacements compared to the acoustic wavelength and large slopes, standard perturbation theory methods for modeling the effect of rough surface scattering[10–13] on acoustic transmission through an ocean waveguide may often be unsuitable. If the accumulated effects of multiple forward scattering on dispersion and field variance are important in acoustic propagation through extended internal wave fields, approaches that neglect them[10–13] may be inappropriate, as noted in Ref. 14. It is possible that acoustic transmission through such complicated environments may be seriously altered by three-dimensional (3-D) scattering effects beyond relatively short ranges. Two-dimensional models,[6,13,15–17] 2-D Monte-Carlo simulations,[18] and adiabatic 3-D models[19] may then also become unreliable.

The present formulation is advantageous because the mean and variance of the acoustic field multiply forward scattered through a 3-D random waveguide can be rapidly obtained from the compact analytic expressions of Ref. 1, given the mean and spatial covariance of the internal wave displacement field, without restriction on internal wave amplitude or slope. It can be readily applied to solve a variety of underwater remote sensing and communication problems in continental shelf environments. This includes the detection and localization of sources[20,21] and targets by passive and active sonar, as well as the estimation of biological,[22,23] geological,[24] and oceanographic parameters[25] by seismoacoustic inverse methods.

We show that the accumulated effect of multiple forward scattering through random internal wave fields typically must be included to properly model the statistical moments of the acoustic field forward propagated through continental shelf environments. We also show that 3-D multiple scattering effects can become important in both the mean and variance of the forward field. This is because, as the source-receiver range increases, the Fresnel width of the forward field eventually exceeds the cross-range coherence length of the internal waves, making out-of-plane scattering important when internal wave amplitudes exceed the acoustic wavelength and slopes become higher. Out-of-plane scattering cannot be accounted for in 2-D models. We illustrate this effect by comparing the present 3-D model with a current standard approach, which is to compute field moments by Monte-Carlo simulations with the 2-D parabolic equation.

We show that the acoustic field moments are highly dependent on both the rms displacements and coherence scales of the 3-D internal waves. In a waveguide where the rms internal wave height is small compared to the acoustic wavelength, the forward field remains coherent and exhibits the range and depth-dependent structure expected from the coherent interference between waveguide modes. The moderate dispersion and attenuation induced by multiple forward scatter through the internal wave disturbances still noticeably alters the mean field. Scattering in such a slightly random waveguide may not be strong enough to make 3-D effects noticable.

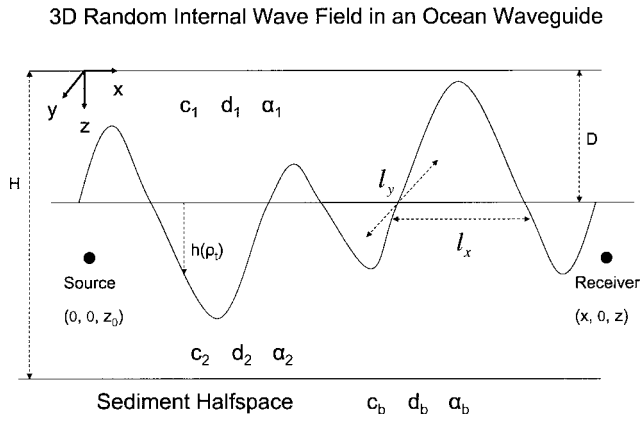

FIG. 1. Geometry of mid-latitude Atlantic continental shelf and Arctic environments with two-layer water column of total depth $H_w = 100$ m, and upper layer depth of $D = 30$ m. The bottom sediment half-space is composed of sand. The internal wave disturbances have coherence length scales l_x and l_y in the x and y directions, respectively, and are measured with positive height h measured downward from the interface between the upper and lower water layers.

When the rms internal wave height becomes larger than the acoustic wavelength, 3-D scattering effects become significant. The field variance or incoherent intensity is found to dominate the total intensity of the forward field beyond moderate propagation ranges. This causes the acoustic field to become fully saturated. In this case, the coherent modal interference structure in range and depth is lost, and the intensity of the forward field then decays monotonically. This makes standard processing techniques that rely upon model coherence, such as matched field processing and the waveguide-invariant method[26] for source range and depth localization, far less effective.

The effects on acoustic transmission of random density fluctations in the medium due to internal waves are also quantified. We show that internal-wave-induced density effects can significantly affect acoustic propagation in specific environments, such as Arctic seas.

II. FORMULATION IN A TWO-LAYER WATER COLUMN

Internal waves in mid-latitude continental shelf environments often occur at the interface between warm water near the sea surface and cooler water below.[7,27,28] In high latitude, the reverse is usually true where the cooler less dense water above comes from recently melted ice. Here, we model the internal wave field as disturbances propagating along the boundary between strata in a two-layer water-column, as illustrated in Fig. 1. Although many other internal wave models and parametrizations could have been used to implement the general formulation of Ref. 1, the two-layer model is chosen here because it clearly illustrates the fundamental

physics of internal waves in a continental shelf environment. This has made it probably the most frequently used model in the literature.[29–31] We focus on the baroclinic mode of the internal wave, which has negligible displacement at the sea surface.[30] In the absence of internal waves, the boundary separating the upper medium with density d_1 and sound speed c_1 from the lower medium with density d_2 and sound speed c_2 is at a constant depth. In the presence of internal waves, a part of the lower medium protrudes into the upper medium and a part of the upper medium protrudes into the lower medium. We model protrusion of the lower medium into the upper medium as a volumetric inhomogeneity that scatters the sound field by Green's theorem, and *vice versa* for the lower medium.

To formulate the problem, we place the origin of the coordinate system at the sea surface. The z axis points downward and normal to the interface between horizontal strata. The water depth is H and the boundary separating the upper and lower medium is at depth $z=D$. Let coordinates of the source be defined by $\mathbf{r}_0=(0,0,z_0)$, and receiver coordinates by $\mathbf{r}=(x,0,z)$. Spatial cylindrical (ρ,ϕ,z) and spherical systems (r,θ,ϕ) are defined by $x=r\sin\theta\cos\phi$, $y=r\sin\theta\sin\phi$, $z=r\cos\theta$, and $\rho=x^2+y^2$. The horizontal and vertical wave number components for the nth mode are, respectively, $\xi_n=k\sin\alpha_n$ and $\gamma_n=k\cos\alpha_n$, where α_n is the elevation angle of the mode measured from the z axis. Here, $0\leqslant\alpha_n\leqslant\pi/2$ so that the down- and upgoing plane wave components of each mode will then have elevation angles α_n and $\pi-\alpha_n$, respectively. The corresponding vertical wave number of the down- and upgoing components of the nth mode are γ_n and $-\gamma_n$, respectively, where $\Re\{\gamma_n\}\geqslant 0$. The wave number magnitude k equals the angular frequency ω divided by the sound speed c in the object layer so that $k^2=\xi_n^2+\gamma_n^2$. The azimuth angle of the modal plane wave is denoted by β, where $0\leqslant\beta\leqslant 2\pi$. The geometry of spatial and wave number coordinates is shown in Ref. 32.

A. Statistical description of internal waves

1. Joint spatial probability density of internal wave displacement

The displacement $h(\boldsymbol{\rho}_t)$ of the internal wave boundary at horizontal location $\boldsymbol{\rho}_t$, as illustrated in Fig. 1, can be modeled as a Gaussian random process in space and time with mean $\langle h\rangle$, and variance $\eta_h^2=\langle h^2\rangle-\langle h\rangle^2$. Since the baroclinic internal wave displacement cannot penetrate the water surface or the sea bottom, we limit unphysical tails of the probability density function by windowing h. The probability density function of the internal wave displacement is,

$$p_h(h)=\begin{cases} T\dfrac{1}{\sqrt{2\pi}\eta_h}\mathrm{e}^{-(h-\langle h\rangle)^2/2\eta_h^2}, & \text{for } \langle h\rangle-h_1\leqslant h\leqslant\langle h\rangle+h_2,\\ 0 \quad \text{elsewhere}, \end{cases} \tag{1}$$

where $T=1/[P((\langle h\rangle+h_2)/\eta_h)-P((\langle h\rangle-h_1)/\eta_h)]$ is a normalization constant, and $P(b)$ is the cumulative distribution function,

$$P(b)=\frac{1}{\sqrt{2\pi}}\int_{-\infty}^{b}\mathrm{e}^{-m^2/2}\,dm. \tag{2}$$

Linear internal wave displacements are expected to follow a zero-mean circular complex Gaussian random process by the central limit theorem, given that they arise from the superposition of many statistically independent sources in space and time. The same model can also be used to describe nonlinear solitary internal waves in some cases when they are incompletely evolved[33] or broadly distributed in peak amplitude.[34] For nonlinear internal wave fields, nonzero mean displacements and much larger standard deviations are expected.

The joint probability density function of the internal wave displacement at horizontal locations $\boldsymbol{\rho}_t$ and $\boldsymbol{\rho}_t'$ can be expressed as

$$p(h(\boldsymbol{\rho}_t),h(\boldsymbol{\rho}_t'))=\frac{1}{2\pi\eta_{h(\boldsymbol{\rho}_t)}\eta_{h(\boldsymbol{\rho}_t')}(1-\varrho^2)^{1/2}}\exp\left(-\frac{[(h^2(\boldsymbol{\rho}_t)\eta^2_{h(\boldsymbol{\rho}_t')}-2h(\boldsymbol{\rho}_t)h(\boldsymbol{\rho}_t')\varrho\,\eta_{h(\boldsymbol{\rho}_t)}\eta_{h(\boldsymbol{\rho}_t')}+h^2(\boldsymbol{\rho}_t')\eta^2_{h(\boldsymbol{\rho}_t)})]}{2\eta^2_{h(\boldsymbol{\rho}_t)}\eta^2_{h(\boldsymbol{\rho}_t')}(1-\varrho^2)}\right), \tag{3}$$

where ϱ is the correlation coefficient defined as

$$\varrho=\frac{\langle h(\boldsymbol{\rho}_t)h(\boldsymbol{\rho}_t')\rangle-\langle h(\boldsymbol{\rho}_t)\rangle\langle h(\boldsymbol{\rho}_t')\rangle}{\sqrt{(\langle|h(\boldsymbol{\rho}_t)|^2\rangle-|\langle h(\boldsymbol{\rho}_t)\rangle|^2)(\langle|h(\boldsymbol{\rho}_t')|^2\rangle-|\langle h(\boldsymbol{\rho}_t')\rangle|^2)}}. \tag{4}$$

2. Linear internal wave field as a stationary random process

For random internal wave fields that follow a stationary random process in space, the internal wave displacement correlation function and standard deviation η_h can be expressed in terms of the internal wave spectrum $\mathcal{G}(\boldsymbol{\kappa})$. For instance, the correlation function is

$$\langle h(\boldsymbol{\rho}_t)h(\boldsymbol{\rho}_t')\rangle=C_{hh}(\boldsymbol{\rho}_t-\boldsymbol{\rho}_t')=\frac{1}{(2\pi)^2}\int_0^{2\pi}\int_0^{\infty}\mathcal{G}(\boldsymbol{\kappa})e^{i\boldsymbol{\kappa}\cdot(\boldsymbol{\rho}_t-\boldsymbol{\rho}_t')}\kappa\,\mathrm{d}\kappa\,\mathrm{d}\Theta, \tag{5}$$

where $\boldsymbol{\kappa}=(\kappa_x,\kappa_y)=(\kappa\cos\Theta,\kappa\sin\Theta)$ is the internal-wave wave number vector with magnitude κ and azimuthal di-

rection Θ. The internal wave height standard deviation η_h is defined by

$$\eta_h^2 = C_{hh}(0), \tag{6}$$

when $\langle h \rangle = 0$, as is the case for linear internal waves.

The internal wave disturbance has a horizontal coherence area given by[35]

$$A_c = \frac{\int_0^{2\pi}\int_0^{\infty} |C_{hh}(\rho,\Theta)|^2 \rho \, d\rho \, d\Theta}{|C_{hh}(0)|^2}, \tag{7}$$

where $\boldsymbol{\rho} = \boldsymbol{\rho}_t - \boldsymbol{\rho}_t' = \rho \cos\Theta \mathbf{x} + \rho \sin\Theta \mathbf{y}$, outside of which internal wave displacements can be assumed to be uncorrelated.[1] The corresponding coherence length scale of the internal wave disturbance $l_c(\Theta)$ in any azimuthal direction Θ is then given by

$$l_c^2(\Theta) = \frac{2\int_0^{\infty} |C_{hh}(\rho,\Theta)|^2 \rho \, d\rho}{|C_{hh}(0)|^2}. \tag{8}$$

Here $l_c(\Theta)$ defines a coherence shape function for the internal wave disturbance that is determined as its wave number spectrum spans the 2π azimuthal radians of Θ. The full coherence lengths l_x and l_y of the internal wave disturbance in the x and y directions are then, respectively,

$$l_x = l_c(\Theta = 0) + l_c(\Theta = \pi) \tag{9}$$

and

$$l_y = l_c(\Theta = \pi/2) + l_c(\Theta = 3\pi/2). \tag{10}$$

For an isotropic internal wave field, Eq. (5) reduces to

$$C_{hh}(\boldsymbol{\rho}_t - \boldsymbol{\rho}_t') = \frac{1}{2\pi}\int_0^{\infty} \mathcal{G}(\kappa) J_0(\kappa|\boldsymbol{\rho}_t - \boldsymbol{\rho}_t'|) \kappa \, d\kappa, \tag{11}$$

since its wave number spectrum $\mathcal{G}(\kappa)$ is independent of the azimuth angle Θ.

B. Scatter function of an internal wave inhomogeneity

To determine the plane wave scatter function of a coherence volume of internal wave inhomogeneity, we apply Green's theorem,[2]

$$\Phi_s(\mathbf{r}|\mathbf{r_0}) = \iiint [k^2 \Gamma_\kappa(\mathbf{r_t}) \Phi(\mathbf{r_t}|\mathbf{r_0}) G(\mathbf{r}|\mathbf{r}_t) + \Gamma_d(\mathbf{r_t}) \nabla \Phi(\mathbf{r_t}|\mathbf{r_0}) \cdot \nabla G(\mathbf{r}|\mathbf{r_t})] dV_t, \tag{12}$$

where Γ_κ is the fractional change in compressibility and Γ_d is the fractional change in density of the inhomogeneity centered at $\mathbf{r}_t$ relative to the original medium, $G(\mathbf{r}|\mathbf{r_t})$ is the free space Green's function, and $\Phi(\mathbf{r_t}|\mathbf{r_0})$ is the total acoustic field in the volume of inhomogeneity. To integrate Eq. (12) analytically, we need to know the total field within the volume of the inhomogeneity. But this is the sum of the known incident and unknown scattered field in the volume. In the first-order Rayleigh-Born approximation, the total field inside the inhomogeneity is approximated by the incident field. This is a good approximation when the scattered field within the inhomogeneity is small compared to the incident field as it typically is when the fractional compressibility and density changes are small, as they are in the present scenario. Green's theorem evaluated using the first-order Rayleigh-Born approximation then provides a first-order estimate of the scattered field from an inhomogeneity. From this we can obtain a first-order estimate of the inhomogeneity's plane wave scatter function.

We first derive the plane wave scatter function for a coherent volume of internal wave inhomogeneity centered at horizontal location $\boldsymbol{\rho}_s$, where $\boldsymbol{\rho}_t = \boldsymbol{\rho}_s + \mathbf{u}_t$. For an incoming plane wave in the direction $\mathbf{k}_i = (k, \alpha_i, \beta_i) = (\boldsymbol{\xi}_i, \gamma_i)$ and scattered plane wave in the direction $\mathbf{k} = (k, \alpha, \beta) = (\boldsymbol{\xi}, \gamma)$, the first-order scatter function of an internal wave inhomogeneity is

$$\Re\{S_{\boldsymbol{\rho}_s}(\alpha,\beta,\alpha_i,\beta_i)\} = \iint_{A_c}\int_0^H \frac{k^3}{4\pi}[\Gamma_\kappa(\mathbf{r}_t) + \eta(\mathbf{k},\mathbf{k}_i)\Gamma_d(\mathbf{r}_t)] \times e^{i[(\boldsymbol{\xi}_i - \boldsymbol{\xi})\cdot\mathbf{u}_t + (\gamma_i - \gamma)z_t]} d^2\mathbf{u}_t \, dz_t, \tag{13}$$

by application of Green's theorem, Eq. (12), where

$$\eta(\mathbf{k},\mathbf{k}_i) = (\mathbf{k}_i \cdot \mathbf{k})/k^2 = \cos\alpha_i \cos\alpha + \sin\alpha_i \sin\alpha \cos(\beta_i - \beta) \tag{14}$$

is the cosine of the angle between the incident and scattered plane wave directions. The fractional changes in compressibility and density depend on the displacement of the inhomogeneities at $\mathbf{r_t}$ and are given by

$$\Gamma_\kappa(\mathbf{r}_t) = \Gamma_\kappa(h(\boldsymbol{\rho}_t), z_t) = \frac{\kappa_1 - \kappa_2}{\kappa_2} U[h(\boldsymbol{\rho}_t) - (z_t - D)] U(z_t - D) + \frac{\kappa_2 - \kappa_1}{\kappa_1} U[(z_t - D) - h(\boldsymbol{\rho}_t)] U(-(z_t - D)), \tag{15}$$

and

$$\Gamma_d(\mathbf{r}_t) = \Gamma_d(h(\boldsymbol{\rho}_t), z_t) = \frac{d_1 - d_2}{d_1} U[h(\boldsymbol{\rho}_t) - (z_t - D)] U(z_t - D) + \frac{d_2 - d_1}{d_2} U[(z_t - D) - h(\boldsymbol{\rho}_t)] U(-(z_t - D)), \tag{16}$$

where U is the unit step function.

The areal scatter function density $s_{\boldsymbol{\rho}_s, z_t}(\alpha,\beta,\alpha_i,\beta_i)$ centered at $(\boldsymbol{\rho}_s, z_t)$ is related to the scatter function $S_{\boldsymbol{\rho}_s}(\alpha,\beta,\alpha_i,\beta_i)$ of Eq. (13) by

$$S_{\boldsymbol{\rho}_s}(\alpha,\beta,\alpha_i,\beta_i) = A_c \int_0^H s_{\boldsymbol{\rho}_s, z_t}(\alpha,\beta,\alpha_i,\beta_i) e^{i(\gamma_i - \gamma)z_t} \, dz_t, \tag{17}$$

where

$$s_{\boldsymbol{\rho}_s, z_t}(\alpha,\beta,\alpha_i,\beta_i) = \frac{1}{A_c}\iint_{A_c} \frac{k^3}{4\pi}[\Gamma_\kappa(\mathbf{r}_t) + \eta(\mathbf{k},\mathbf{k}_i)\Gamma_d(\mathbf{r}_t)] e^{i(\boldsymbol{\xi}_i - \boldsymbol{\xi})\cdot\mathbf{u}_t} \, d^2\mathbf{u}_t. \tag{18}$$

1. Mean and correlation function of the scatter function density of internal wave inhomogeneities

The scatter function density $s_{\boldsymbol{\rho}_s,z_t}(\alpha,\beta,\alpha_i,\beta_i)$ of Eq. (18) is a random variable since it depends on the internal wave displacement $h(\boldsymbol{\rho}_t)$. The mean of the scatter function density is

$$\langle s_{\boldsymbol{\rho}_s,z_t}(\alpha,\beta,\alpha_i,\beta_i)\rangle = \frac{1}{A_c}\iint_{A_c}\left[\int \frac{k^3}{4\pi}[\Gamma_\kappa(h(\boldsymbol{\rho}_t),z_t)+\eta(\mathbf{k},\mathbf{k}_i)\Gamma_d(h(\boldsymbol{\rho}_t),z_t)]p_h(h)\mathrm{d}h\right]e^{i(\boldsymbol{\xi}_i-\boldsymbol{\xi})\cdot\mathbf{u_t}}\,\mathrm{d}^2\mathbf{u_t}$$
$$= \frac{1}{A_c}\left\langle \frac{k^3}{4\pi}[\Gamma_\kappa(h(\boldsymbol{\rho}_t),z_t)+\eta(\mathbf{k},\mathbf{k}_i)\Gamma_d(h(\boldsymbol{\rho}_t),z_t)]\right\rangle \iint_{A_c} e^{i(\boldsymbol{\xi}_i-\boldsymbol{\xi})\cdot\mathbf{u_t}}\,\mathrm{d}^2\mathbf{u_t}. \tag{19}$$

For two inhomogeneities centered at $(\boldsymbol{\rho}_s,z_t)$ and $(\boldsymbol{\rho}_s',z_t')$, respectively, the correlation of their scatter function densities is

$$\langle s_{\boldsymbol{\rho}_s,z_t}(\alpha,\beta,\alpha_i,\beta_i)s^*_{\boldsymbol{\rho}_s',z_t'}(\alpha',\beta',\alpha_i',\beta_i')\rangle = \left(\frac{1}{A_c}\right)^2\iint_{A_c}\iint_{A_c'} e^{i[(\boldsymbol{\xi}_i-\boldsymbol{\xi})\cdot\boldsymbol{\rho}_t-(\boldsymbol{\xi}_i'-\boldsymbol{\xi}')\cdot\boldsymbol{\rho}_t']}C_{\mathcal{FF}}(\boldsymbol{\rho}_t-\boldsymbol{\rho}_t',z_t,z_t')\mathrm{d}^2\mathbf{u}_t\,\mathrm{d}^2\mathbf{u}_t', \tag{20}$$

where

$$C_{\mathcal{FF}}(\boldsymbol{\rho}_t-\boldsymbol{\rho}_t',z_t,z_t')$$
$$= \iint\left(\frac{k^3}{4\pi}\right)^2[\Gamma_\kappa(h(\boldsymbol{\rho}_t),z_t)+\eta(\mathbf{k},\mathbf{k}_i)\Gamma_d(h(\boldsymbol{\rho}_t),z_t)][\Gamma_\kappa(h(\boldsymbol{\rho}_t'),z_t')+\eta(\mathbf{k}',\mathbf{k}_i')\Gamma_d(h(\boldsymbol{\rho}_t'),z_t')]p(h(\boldsymbol{\rho}_t),h(\boldsymbol{\rho}_t'))\mathrm{d}h(\boldsymbol{\rho}_t)\mathrm{d}h(\boldsymbol{\rho}_t'), \tag{21}$$

following the notation of Ref. 1, Appendix A.

The joint probability function $p(h(\boldsymbol{\rho}_t),h(\boldsymbol{\rho}_{t'}))$ requires the internal wave spectrum to be specified, as can be seen from Eqs. (3)–(5).

2. Isotropic internal waves

We must calculate the mean and spatial covariance of the scatter function density $s_{\boldsymbol{\rho}_s,z_t}(\alpha,\beta,\alpha_i,\beta_i)$ to determine the forward field moments. This requires the internal wave spectrum defined in Eq. (5) to be specified. Following Refs. 18 and 6, we assume the internal waves follow the isotropic Garret-Munk spectrum,

$$\mathcal{G}(\boldsymbol{\kappa}) = E_0\frac{2}{\pi^2}\frac{\omega_c\sqrt{\kappa^2c_g^2-\omega_c^2}}{\kappa^4c_g^2}, \tag{22}$$

for the relatively high wave numbers of interest in our analysis, where E_0 is the average energy density that determines the strength of the internal wave fluctuation, ω_c is the Coriolis frequency, which is roughly 1.16×10^{-5} Hz at 30° lattitude, and $c_g\approx0.4$ m/s is the phase speed of the internal waves in the two-layer ocean, given by $c_g^2=g[(\rho_2-\rho_1)/\rho_2][D(H-D)/H]$, where g is the gravitational acceleration. The corresponding coherence radius $l_c(\theta_t)=l_c$ is then independent of azimuth.

In this paper, we focus our analysis on internal wave fluctuations that occur within a measurement time scale T. Within this time, only internal wave disturbances that occur with frequencies that are larger than $f_{\min}=1/T$ or equivalently have wave numbers larger than $\kappa_{\min}=2\pi f_{\min}/c_g=2\pi/c_gT$ can cause temporal fluctuation in the acoustic field. From Eq. (22), Eq. (8) and Eq. (7), the coherence radius is then $l_c=\sqrt{2}/\kappa_{\min}$, the x and y coherence lengths are $l_x=l_y=2\sqrt{2}/\kappa_{\min}$, and the coherence area is $A_c=\pi l_c^2=2\pi/\kappa_{\min}^2$.

As noted in Ref. 1, the cross-range coherence length l_y of internal wave inhomogeneities can be greater or less than the Fresnel width $Y_{\mathrm{F}}(\rho,\rho_s)\approx\sqrt{\lambda(\rho-\rho_s)\rho_s/\rho}$, which depends on the range ρ from source to receiver and the range ρ_s from source to the inhomogeneities. When $l_y<Y_{\mathrm{F}}$, decorrelation in the cross-range occurs within the Fresnel width or active region. But when $l_y>Y_{\mathrm{F}}$, internal wave inhomogeneities are fully correlated across the active region. In this case, only the portion of the coherence area A_{F} within the Fresnel width is important to forward scatter, where $A_{\mathrm{F}}\leqslant A_c$.

C. Statistical moments of the forward propagated field

The mean field, variance, and expected total intensity of the forward field propagated through the ocean waveguide containing random internal waves can be expressed analytically using the formulation of Ref. 1. We assume that the internal wave inhomogeneities obey a stationary random process in range. For a source at $\mathbf{r_0}=(0,0,z_0)$ and a receiver at $\mathbf{r}=(x,0,z)$, the mean forward field is given by Eq. (83) of Ref. 1 as

$$\langle\Psi_T(\mathbf{r}|\mathbf{r_0})\rangle = \sum_n \Psi_i^{(n)}(\mathbf{r}|\mathbf{r_0})\mathrm{e}^{i\int_0^\rho\nu_n(\rho_s)\mathrm{d}\rho_s}, \tag{23}$$

where

$$\Psi_i^{(n)}(\mathbf{r}|\mathbf{r_0}) = 4\pi\frac{i}{d(z_0)\sqrt{8\pi}}\mathrm{e}^{-i\pi/4}u_n(z)u_n(z_0)\frac{\mathrm{e}^{i\xi_n\rho}}{\sqrt{\xi_n\rho}} \tag{24}$$

is the incident field contribution from mode n, given no inhomogeneities in the medium, $u_n(z)$ is the modal amplitude at depth z, and ν_n is the horizontal wave number change due to multiple scattering from the inhomogeneities. The modal horizontal wave number change is complex, and it leads to both dispersion and attenuation in the mean forward field.

The real part $\Re\{\nu_n\}$ is the modal dispersion coefficient and the imaginary part $\Im\{\nu_n\}$ is the modal attenuation coefficient.

For the present case, where the random inhomogeneities are due to internal waves,

$$\int_0^\rho \nu_n(\rho_s)\mathrm{d}\rho_s = \int_0^\rho \frac{1}{\xi_n}\langle \Xi_h(n,n,0,0)\rangle \mathrm{d}\rho_s, \tag{25}$$

from Eq. (60) of Ref. 1, where

$$\begin{aligned}
&\Xi_h(m,n,\beta,\beta_i) \\
&= \int_0^H \frac{2\pi}{k(z_t)d(z_t)}[N_m^{(1)}N_n^{(1)}\mathrm{e}^{i\Re\{\gamma_m+\gamma_n\}z_t}s_{\rho_s,z_t}(\pi-\alpha_m,\beta;\alpha_n,\beta_i) \\
&\quad - N_m^{(2)}N_n^{(1)}\mathrm{e}^{i\Re\{-\gamma_m+\gamma_n\}z_t}s_{\rho_s,z_t}(\alpha_m,\beta;\alpha_n,\beta_i) \\
&\quad - N_m^{(1)}N_n^{(2)}\mathrm{e}^{i\Re\{\gamma_m-\gamma_n\}z_t}s_{\rho_s,z_t}(\pi-\alpha_m,\beta;\pi-\alpha_n,\beta_i) \\
&\quad + N_m^{(2)}N_n^{(2)}\mathrm{e}^{i\Re\{-\gamma_m-\gamma_n\}z_t}s_{\rho_s,z_t}(\alpha_m,\beta;\pi-\alpha_n,\beta_i)] \\
&\quad \times \mathrm{e}^{-\Im\{\gamma_m+\gamma_n\}z_t}\,\mathrm{d}z_t.
\end{aligned} \tag{26}$$

As discussed in Sec. II B, substituting Eq. (18) into Eq. (25) leads to a modal horizontal wave number change that is purely real. This accounts for the dispersion, but not the attenuation in the mean forward field due to scattering. The modal attenuation coefficients $\Im\{\nu_m\}$ will be derived in Sec. II D from the waveguide extinction theorem.[3]

From Eq. (25), we see that the modal dispersion coefficients depend on the expected scatter function density in the forward azimuth. This is independent of the cross-range extent of the internal wave inhomogeneities, so the dispersion coefficients are also range independent.

The variance of the forward field at the receiver can be expressed by Eq. (84) of Ref. 1 as

$$\begin{aligned}
\mathrm{Var}(\Psi_T(\mathbf{r}|\mathbf{r_0})) = \sum_n \frac{2\pi}{d^2(z_0)}\frac{1}{|\xi_n|\rho}|u_n(z_0)|^2|u_n(z)|^2 \\
\times \mathrm{e}^{-2\Im\left\{\xi_n\rho+\int_0^\rho \nu_n(\rho_s)\mathrm{d}\rho_s\right\}}\left(\mathrm{e}^{\int_0^\rho \mu_n(\rho_s)\mathrm{d}\rho_s}-1\right),
\end{aligned} \tag{27}$$

where μ_n is defined in Ref. 1 as the exponential coefficient of modal field variance. The variance of the forward field depends on the first- and second-order moments of the scatter function density of the random medium. An analytic expression for μ_n for general surface and volume inhomogeneities is provided in Ref. 1.

For receiver ranges $\rho < 4l_y^2/\lambda$, where the internal wave inhomogeneities are fully correlated within the Fresnel width, from Eq. (74) of Ref. 1, we have

$$\begin{aligned}
&\int_0^\rho \mu_n(\rho_s)\mathrm{d}\rho_s \\
&= \sum_m \rho\frac{l_x}{\xi_m}\frac{1}{|\xi_m|}[\langle|\Xi_h(m,n,0,0)|^2\rangle - |\langle\Xi_h(m,n,0,0)\rangle|^2],
\end{aligned} \tag{28}$$

and for receiver ranges $\rho > 4l_y^2/\lambda$, where the Fresnel width exceeds the internal wave cross-range coherence length, from Eq. (90) of Ref. 1, we have

$$\int_0^\rho \mu_n(\rho_s)\mathrm{d}\rho_s = \sum_m 2\left(\frac{l_x}{\xi_m}\rho_s^{\mathrm{cor}} + A_c\sqrt{\frac{\rho}{2\pi\xi_m}}\left[\sin^{-1}\sqrt{1-\frac{\rho_s^{\mathrm{cor}}}{\rho}} - \sin^{-1}\sqrt{\frac{\rho_s^{\mathrm{cor}}}{\rho}}\right]\right)\frac{1}{|\xi_m|}[\langle|\Xi_h(m,n,0,0)|^2\rangle - |\langle\Xi_h(m,n,0,0)\rangle|^2], \tag{29}$$

where $\rho_s^{\mathrm{cor}} = \rho/2(1-\sqrt{1-4l_y^2/\lambda\rho})$. These equations show how the exponential coefficient of modal field variance couples energy in incident mode n to all scattered modes m after random multiple forward scattering through the waveguide.

The mean forward field of Eq. (23) is also called the coherent field, the magnitude square of which is proportional to the coherent intensity. The variance of the forward field in Eq. (27) provides a measure of the incoherent intensity. The total intensity of the forward field is the sum of the coherent and incoherent intensities. The coherent field tends to dominate at short ranges from the source and in slightly random media, while the incoherent field tends to dominate in highly random media. It should be noted that in a nonrandom waveguide $\mu_n = 0$ so that the variance of the forward field is zero, from Eq. (27). This is expected since the field is fully coherent in this case.

D. Modal attenuation from generalized waveguide extinction theorem

Attenuation or extinction of the forward field arises from scattering by inhomogeneities and intrinsic absorption in the medium. As mentioned in Secs. I and II C, the purely real scatter function of Eq. (13) can only account for dispersion due to scattering. In order to include attenuation in the mean forward field, we apply the waveguide extinction theorem.[3,4] The modal extinction cross section of an object, for incident mode n, is the ratio of the extinction $\mathcal{E}_n$ or power loss caused by the object to the incident intensity $I_{i,n}$,[3,4]

$$\sigma_n(x=0) = \frac{\mathcal{E}_n(x=0|\mathbf{r_0})}{I_{i,n}(z_h|\mathbf{r_0})\cdot\mathbf{i}_x}, \tag{30}$$

where $\mathbf{i}_x$ is the propagation direction. The notation $x=0$ means that the medium's intrinsic absorption is set to zero

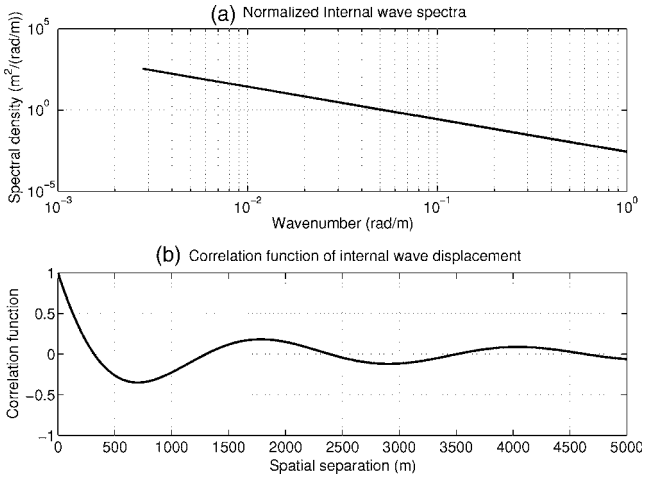

FIG. 2. (a) Normalized spectrum of internal wave field over an observation period of approximately 10 min with minimum wave number $\kappa_{\min}=0.028$ rad/m. The spectrum is computed using Eq. (22) with a κ^{-2} dependence at high frequencies. (b) Correlation function of the isotropic internal wave field with a coherence length of 100 m. The correlation function was obtained from the inverse Fourier transform of the internal wave spectrum plotted in (a).

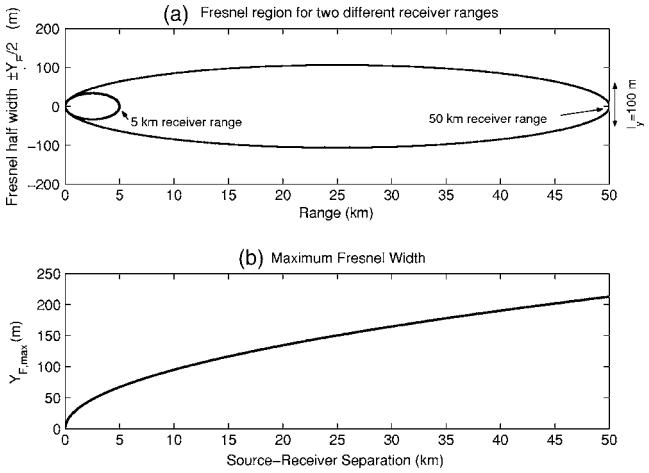

FIG. 3. (a) Fresnel half-width for receiver ranges $\rho=5$ km and $\rho=50$ km. The Fresnel width $Y_F(\rho,\rho_s)$ is approximately equal to $\sqrt{\lambda(\rho-\rho_s)\rho_s/\rho}$, where ρ is the source-receiver separation and ρ_s is the range from source to inhomogeneity. (b) The maximum Fresnel width $Y_{F,\max}=Y_F(\rho,\rho/2)=\sqrt{\lambda\rho}/2$ as a function of source-receiver separation ρ.

during the calculation, as described in Ref. 3, to properly determine the extinction cross section of a given scatterer.

In a waveguide with random internal wave inhomogeneities, the modal attenuation coefficient $\Im\{\nu_n\}$ can be be expressed in terms of the modal extinction cross section[3] $\sigma_n(x=0|h)$ of the inhomogeneities as

$$\Im\{\nu_n(\rho_s)\}=\frac{1}{2A_c(\rho_s)}\left\langle\frac{1}{d(z_h)}\sigma_n(x=0|h)|u_n(z_h)|^2\right\rangle, \tag{31}$$

from Eq. (60) of Ref. 1 and Eq. (20) of Ref. 3, where the expectation in Eq. (31) is taken over the height of the internal waves. Note that

$$A_c(\rho_s)=\begin{cases}A_F, & l_y>Y_F(\rho_s)\\ A_c, & l_y<Y_F(\rho_s),\end{cases} \tag{32}$$

is dependent on the range location ρ_s of the inhomogeneity within the Fresnel width from source to receiver, where A_F is defined in Sec. II B 2.

For nonabsorbing objects, the extinction $\mathcal{E}_m$ caused by the object is equal to the total scattered power $W_{s,n}$. By placing the object within a closed control surface, we can calculate $W_{s,n}$ as the total scattered power flux through the surface. A general analytic expression for the total scattered power flux from an object centered at depth z_h within a closed cylindrical control surface with a radius of x and height spanning the entire waveguide depth for incident mode n is provided by Eq. (16) of Ref. 3. We assume that the internal wave elements remove power from the incident field by scattering only so that intrinsic absorption losses from the inhomogeneities are negligible. This is a valid assumption since the internal wave inhomogeneities do not lead to absorption other than that already present in the medium. For a characteristic internal wave inhomogeneity given height h, the total scattered power flux is

$$W_{s,n}(x|\mathbf{r_0},h)=\Re\left\{\frac{1}{\omega d^2(z_0)}\frac{|u_n(z_0)|^2}{|\xi_n|x_0}\sum_{m=1}^{\infty}\frac{\xi_m}{|\xi_m|}A_c^2(\rho_s)\times e^{-2\Im\{\xi_n x_0+\xi_m x\}}\int_0^{2\pi}|\Xi_h(m,n,\beta,0)|^2\,d\beta\right\}. \tag{33}$$

The x component of incident intensity from mode n on this inhomogeneity is

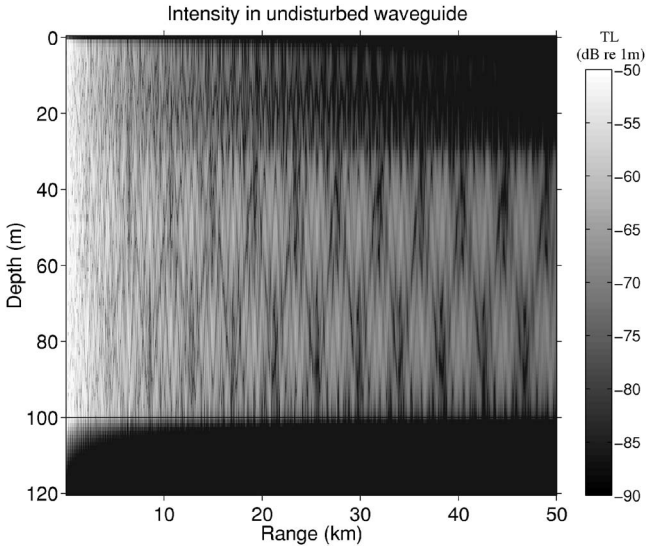

FIG. 4. Acoustic field intensity at 415 Hz as a function of range and depth in the mid-latitude Atlantic continental shelf waveguide of Fig. 1, when there are no internal waves present so that the waveguide is undisturbed. The boundary between the warm and cool water is at the depth of 30 m from the water surface in this static waveguide. The source is at 50 m depth with source level 0 dB *re* 1 μPa at 1 m. The acoustic intensity exhibits range- and depth-dependent variations due to coherent interference between waveguide modes.

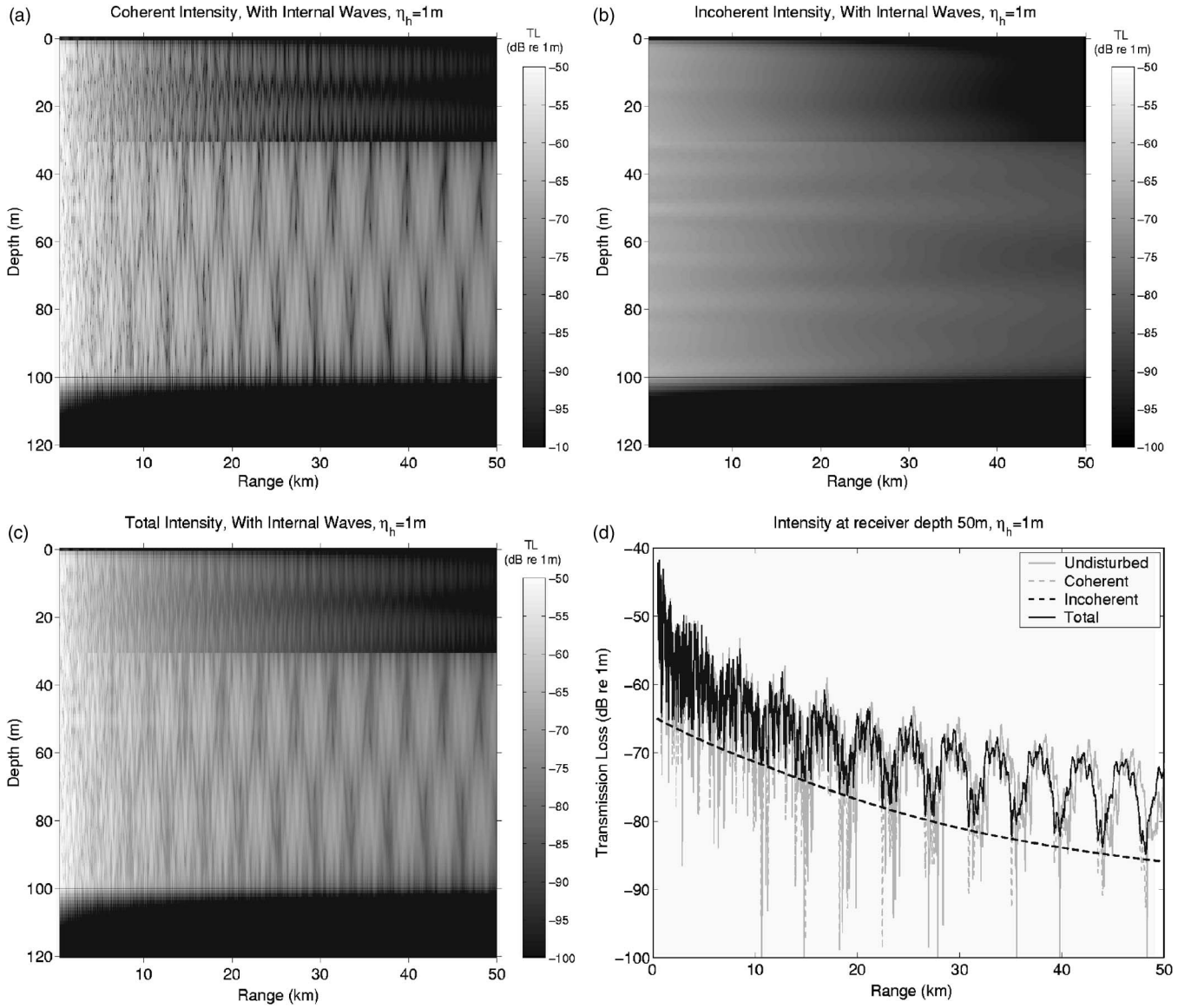

FIG. 5. Intensities of the (a) mean or coherent field, (b) variance or incoherent field, and (c) the total field at 415 Hz as functions of range and depth in the mid-latitude Atlantic continental shelf waveguide of Fig. 1 when there is a random internal wave field present in the waveguide. The internal wave disturbances have a height standard deviation of σ_h=1 m and coherence lengths of l_x=l_y=100 m. The source is at 50 m depth with source level 0 dB *re* 1 μPa at 1 m. This medium is only slightly random and the total intensity in (c) is dominated by the coherent intensity out to 50 km range and exhibits range- and depth-dependent variations due to coherent interference between waveguide modes, similar to the static waveguide example in Fig. 4. Figure 5(d) shows the acoustic intensity as a function of range at a single receiver depth of 50 m for the fields shown in (a)–(c). For a comparison, the acoustic intensity of the static waveguide is also plotted.

$$I_{i,n}(z_t|\mathbf{r_0})\cdot\mathbf{i}_x=\frac{2\pi}{\omega d^2(z_0)d(z_h)}\frac{1}{x_0}|u_n(z_0)|^2|u_n(z_h)|^2\frac{\Re\{\xi_n^*\}}{|\xi_n|}\times e^{-2\Im\{\xi_n\}x_0}, \tag{34}$$

from Eq. (19) of Ref. 3. Following Eq. (30), the modal extinction cross section of the internal wave inhomogeneity is found from dividing Eq. (33) by Eq. (34) and setting x=0,

$$\sigma_n(x=0|h)=\Re\left\{\frac{1}{2\pi}d(z_h)\frac{1}{|u_n(z_h)|^2}\sum_{m=1}^{\infty}\frac{\xi_m^*}{|\xi_m|\Re\{\xi_n^*\}}A_c^2(\rho_s)\times\int_0^{2\pi}|\Xi_h(m,n,\beta,0)|^2\,\mathrm{d}\beta\right\}. \tag{35}$$

The attenuation coefficient of mode n due to scattering in the random waveguide can then be found to be

$$\Im\{\nu_n(\rho_s)\}=\frac{1}{4\pi}A_c(\rho_s)\sum_{m=1}^{\infty}\Re\left\{\frac{\xi_m^*}{|\xi_m|\Re\{\xi_n^*\}}\int_0^{2\pi}\langle|\Xi_h(m,n,\beta,0)|^2\rangle\mathrm{d}\beta\right\}, \tag{36}$$

by substituting Eq. (35) into Eq. (31).

III. COMPUTING 2-D SPATIAL REALIZATIONS OF A RANDOM INTERNAL WAVE FIELD

To compare statistical moments of the forward field from the 3-D analytical formulation with Monte-Carlo simu-

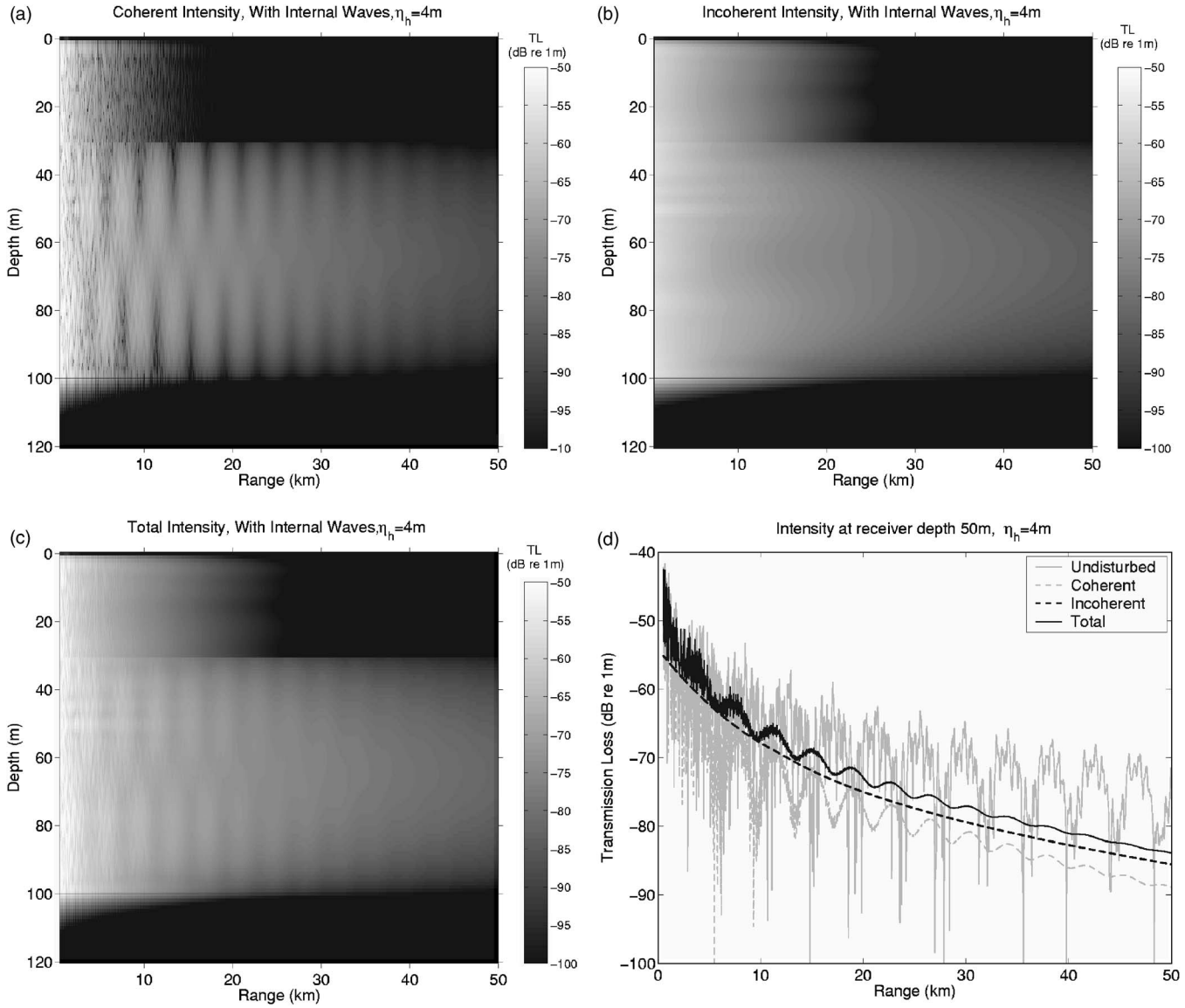

FIG. 6. Similar to Fig. 5, but for a waveguide with an internal wave height standard deviation of η_h=4 m. This medium is highly random and the total intensity in (c) is dominated by the variance or incoherent intensity beyond the 11 km range. The total acoustic intensity decays monotonically as a function of range at sufficiently long ranges since the field is now completely incoherent and the waveguide loses the coherent range- and depth-dependent variations due to modal interference.

lations based on the 2-D parabolic equation, we must compute spatial realizations of the internal wave height $h(x_t)$. We assume that the Gaussian random internal wave field $h(x_t)$ is a stationary random process that follows the correlation function shown in Fig. 2(b). The Fourier transform of internal wave height $h(x_t)$ over a finite spatial window is then

$$H(\kappa) = \int_{-L/2}^{L/2} h(x_t) e^{-i\kappa x_t} \, dx_t,$$

where $H(\kappa)$ is a zero-mean Gaussian random process due to its linear dependence on $h(x_t)$. According to Parseval's theorem,

$$\eta_h^2 \approx \frac{1}{L} \int_{L/2}^{L/2} \langle |h(x_t)|^2 \rangle dx_t = \frac{1}{L} \int \langle |H(\kappa)|^2 \rangle d\kappa, \tag{37}$$

while, from Eq. (6), $\eta_h^2 = C_{hh}(0)$, so that $\langle |H(\kappa)|^2 \rangle \approx L\mathcal{G}(\boldsymbol{\kappa})\kappa/2\pi$. As L becomes arbitrarily large, the delta-function correlation is achieved across the wave number domain,

$$\langle H(\kappa) H(\kappa') \rangle \approx \frac{\mathcal{G}(\boldsymbol{\kappa})\kappa}{2\pi} \delta(\kappa - \kappa'), \tag{38}$$

indicating that components of $H(\kappa)$ with wave number separations exceeding $2\pi/L$ are uncorrelated.

So, a random realization of the internal wave height $h(x_t)$ can be computed as the inverse Fourier transform of $H(\kappa)$ under the assumption that the $H(\kappa)$ are zero mean Gaussian random variables that are uncorrelated when sampled at wave number intervals of at least $2\pi/L$ and have variance $L\mathcal{G}(\boldsymbol{\kappa})\kappa/2\pi$.

IV. ILLUSTRATIVE EXAMPLES

Here we provide examples illustrating the dependence of acoustic field moments on internal wave parameters. We

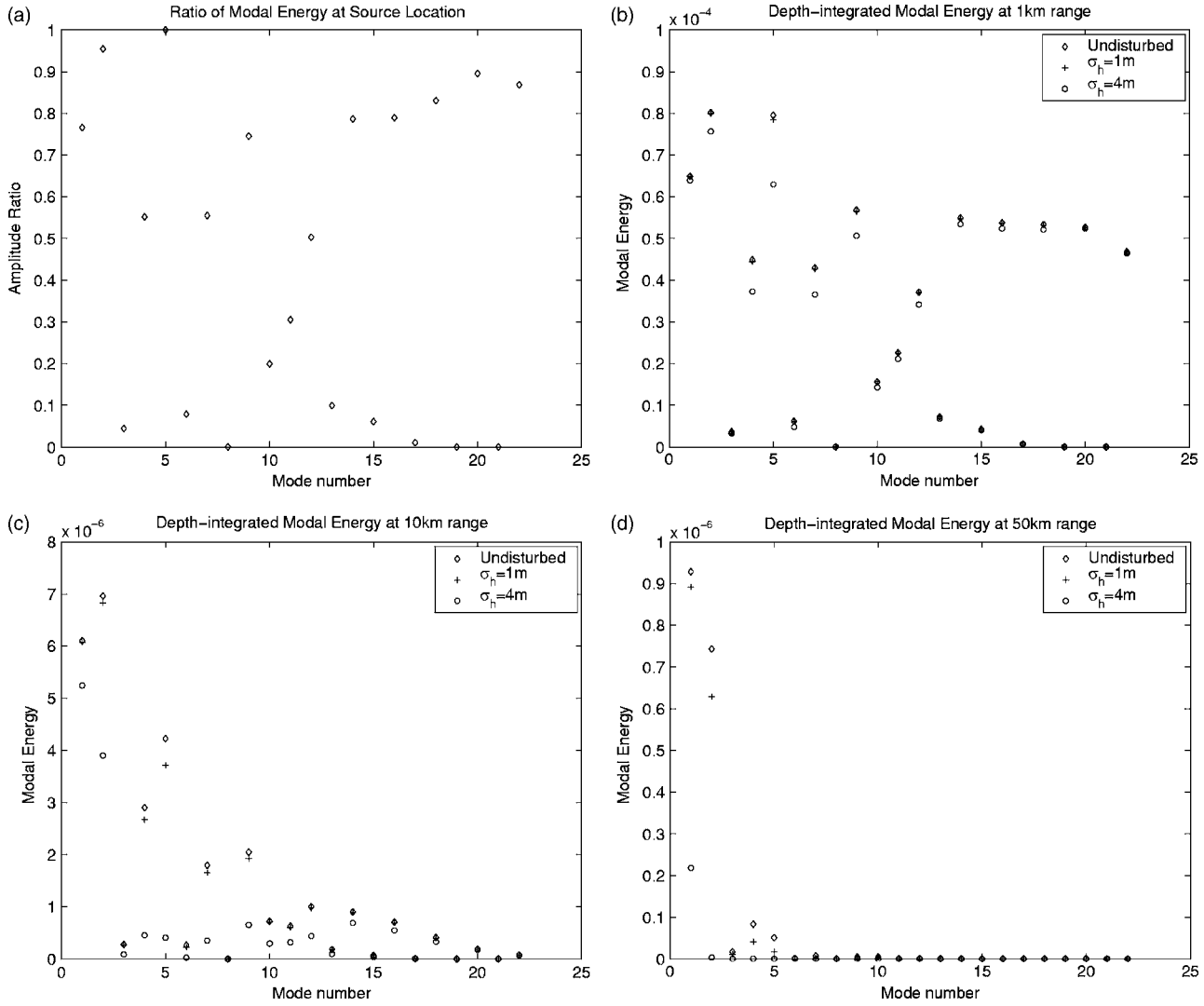

FIG. 7. Contributions of the waveguide modes to the depth-integrated total intensity of the forward field at (a) the source location, (b) 1 km, (c) 10 km, and (d) 50 km ranges from the source for a source strength of 0 dB *re* 1 μPa at 1 m. All values are absolute except those in (a), which are normalized by the maximum modal contribution.

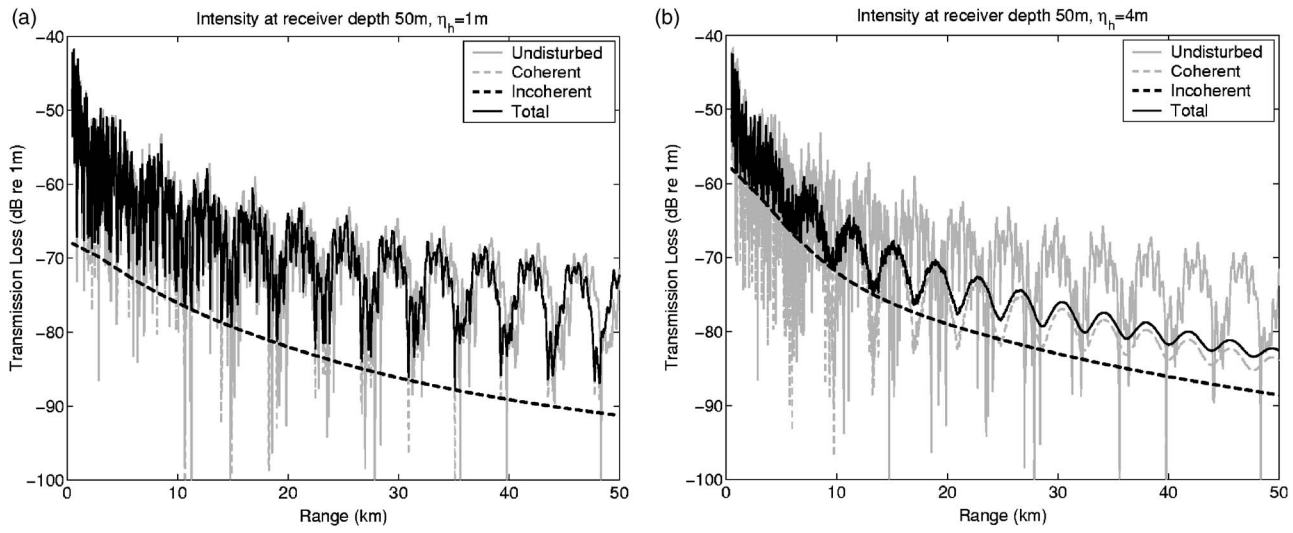

FIG. 8. Acoustic intensity at a single receiver depth of 50 m in the presence of an internal wave field with coherence lengths $l_x = l_y = 50$ m and height standard deviations of (a) $\eta_h = 1$ m and (b) $\eta_h = 4$ m.

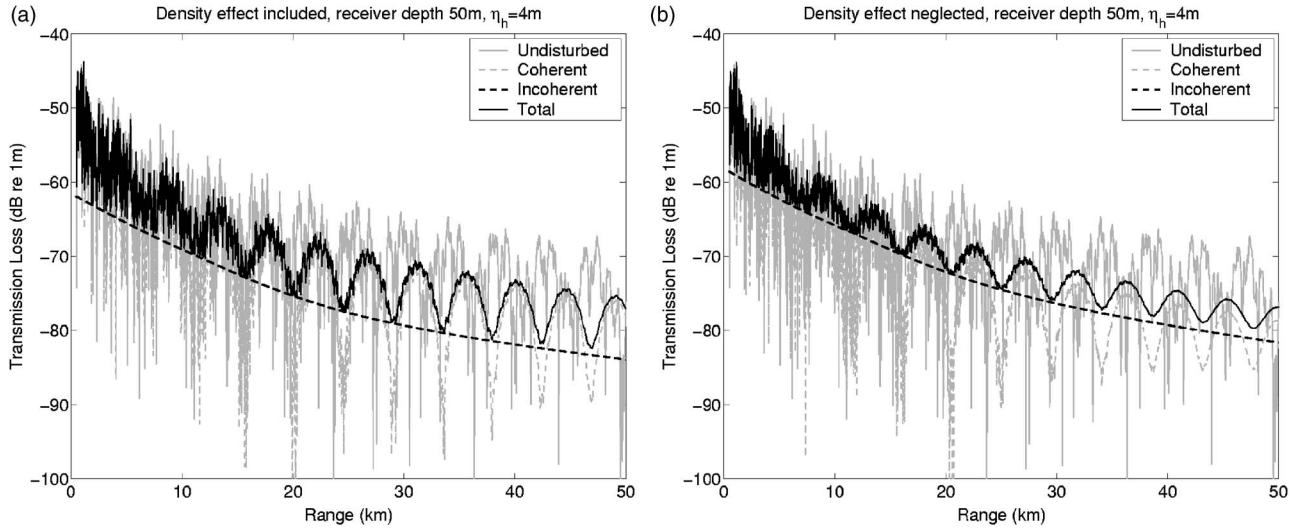

FIG. 9. Effect of (a) including and (b) neglecting internal wave density fluctuations on acoustic transmission in an Arctic waveguide with geometry described in Fig. 1. The internal wave field has coherence lengths of $l_x = l_y = 100$ m and a height standard deviation of $\eta_h = 4$ m. The acoustic intensity is plotted as a function of range for the source and receiver at 50 m depth.

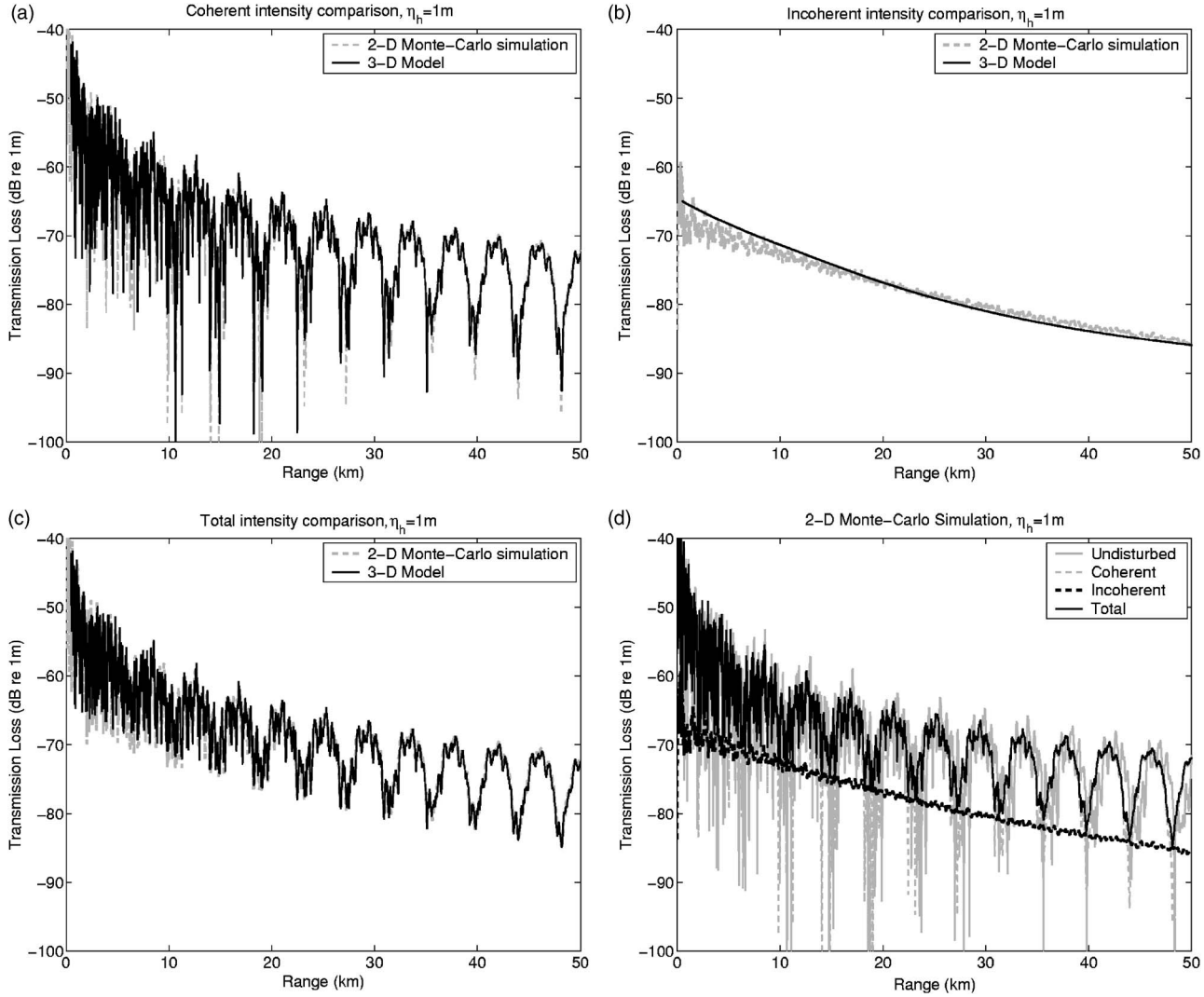

FIG. 10. Comparison of intensities from 2-D Monte-Carlo simulations and 3-D analytical model at the single receiver depth of 50 m in the presence of an internal wave field with height standard deviation of $\eta_h = 1$ m. A total of 1000 simulations were made using the parabolic equation to compute the 2-D Monte Carlo field statistics. (a) Coherent field comparison, (b) incoherent field comparison, (c) total field comparison, (d) only the 2-D Monte-Carlo simulated acoustic intensities of the coherent, incoherent, and total fields used in (a)–(c).

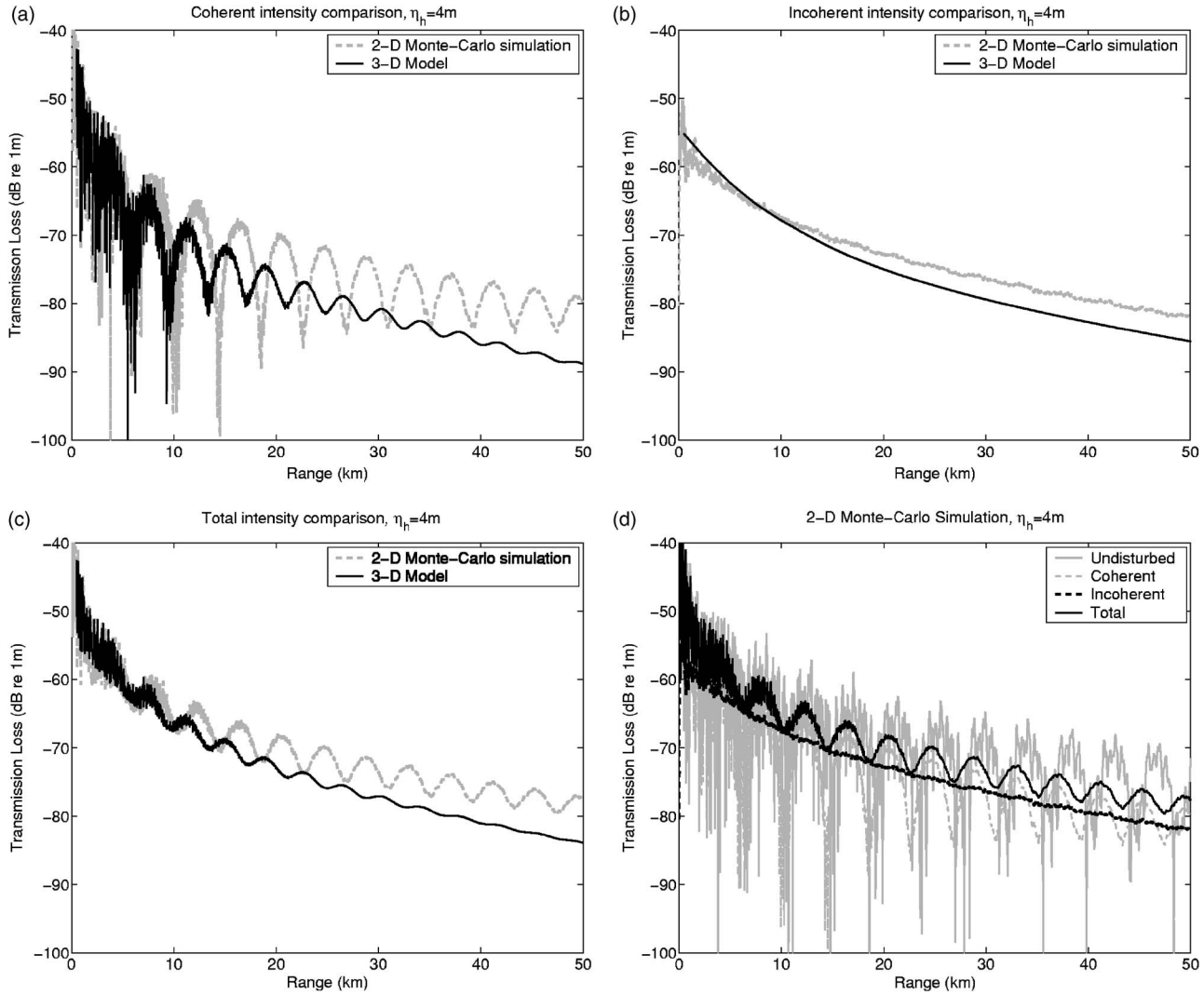

FIG. 11. Similar to Fig. 10, but for a waveguide with an internal wave height standard deviation of η_h=4 m.

study random and isotropic internal waves in typical continental shelf environments. In Sec. IV A, we investigate the effect of rms internal wave height and coherence length on acoustic transmission in a typical mid-latitude Atlantic continental shelf waveguide. In Sec. IV B, the coherent, incoherent, and total intensities of the forward acoustic field are compared when density fluctuations due to internal waves are first included and then neglected. We also compare our 3-D analytical model with 2-D Monte-Carlo simulations of the forward propagated acoustic field in Sec. IV C.

We examine the effect of internal waves on acoustic transmission over a measurement time period of approximately 10 min in our simulations. Over this time period, internal wave disturbances with wave numbers larger than $\kappa_{\min}$=0.028 rad/m will undergo spatial-temporal variation. The normalized power spectrum of the internal wave field is shown in Fig. 2(a) and the correlation function in Fig. 2(b). The corresponding coherence length of the isotropic internal waves is l_x=l_y=100 m from Fig. 2 and Eqs. (8), (9), and (10). The maximum Fresnel width $\sqrt{\lambda\rho/2}$ then exceeds the cross-range coherence length for source-receiver separations larger than 11 km, as shown in Fig. 3. These are the ranges

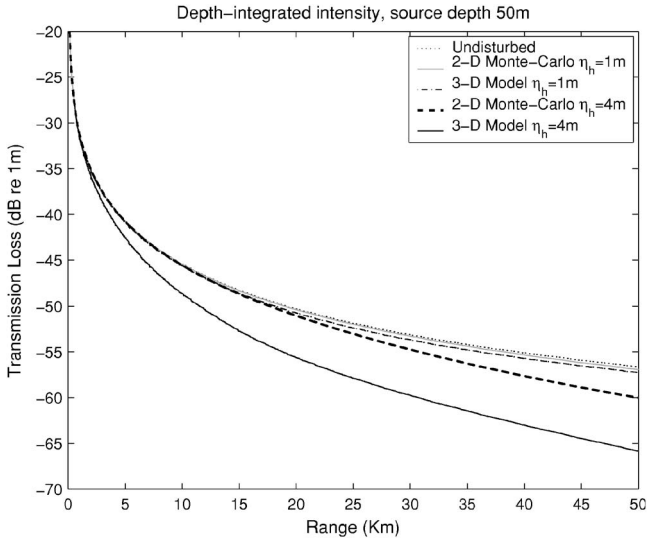

FIG. 12. Total depth-integrated intensities for the waveguide used in Fig. 4. The static case with no internal waves in the medium is compared to the 3-D analytical model and 2-D Monte-Carlo simulations with internal wave height standard deviations of η_h=1 m and η_h=4 m. The attenuation or power loss due to scattering is most significant in the 3-D analytical model for the highly random waveguide.

where 3-D scattering effects can become pronounced when internal wave displacements exceed the acoustic wavelength.

A. Mid-latitude Atlantic continental shelf environment

Here, a water column of $H=100$ m depth is used to simulate the geometry of a typical continental shelf environment, as shown in Fig. 1. The water column is comprised of a warm upper layer with density $d_1=1024$ kg/m^3 and sound speed $c_1=1520$ m/s overlying a cool lower layer with density $d_2=1025$ kg/m^3 and sound speed $c_2=1500$ m/s. The bottom sediment half-space is composed of sand with density $d_b=1.9$ g/cm^3 and sound speed $c_b=1700$ m/s. The attenuations in the water column and bottom are $\alpha=6\times10^{-5}$ dB/λ and $\alpha_b=0.8$ dB/λ, respectively. The 3-D internal wave field is assumed to propagate along the boundary between the two layers at a depth of $D=30$ m from the surface. The receiver and source with frequency 415 Hz and source level of 0 dB *re* 1 μPa at 1 m are both located at 50 m depth in the water column.

We consider two scenarios. In the first scenario, the internal wave disturbances have a height standard deviation of $\eta_h=1$ m that is smaller than the acoustic wavelength of $\lambda=3.6$ m. For the ranges considered, we find the acoustic field to be slightly random. The internal wave spectrum has an amplitude of approximately 2 m^2/cph at $\kappa_{\min}$ for this example. In the second scenario, the internal wave disturbances have a height standard deviation of $\eta_h=4$ m, which is slightly larger than the acoustic wavelength. We find that the acoustic field becomes highly random within a few kilometers of the source. The internal wave spectrum has an amplitude of approximately 30 m^2/cph at $\kappa_{\min}$ in this case. The internal wave correlation length and height standard deviations modeled here are typical of those measured on the Strataform area of the New Jersey continental shelf. For instance, they would correspond to the disturbances shown as Segment C of Fig. 24 in Ref. 7.

The acoustic field intensity is plotted as a function of range and depth in Fig. 4 for the shallow water waveguide of Fig. 1 when there are no internal waves present in the medium. The waveguide is static and undisturbed by inhomogeneities in this case. The forward acoustic field is then fully coherent, since the variance in the forward field is zero everywhere in the medium. The acoustic intensity exhibits a range- and depth-dependent structure arising from coherent interference between the waveguide modes. Figure 5 shows the coherent, incoherent, and expected total intensity for the slightly random waveguide. In this case, the incoherent intensity is small compared to the coherent intensity even at long ranges up to 50 km. The total field still maintains the range- and depth-dependent structure due to modal interference, but shows the effect of some moderate dispersion and attenuation. The situation changes, however, in the highly random waveguide, as shown in Fig. 6. The coherent intensity decays rapidly as a function of range from the source due to severe attenuation arising from internal wave scattering. The incoherent component dominates the expected total intensity beyond the 11 km range, where 3-D scattering begins to take effect. The expected total intensity eventually decays monotonically with range and no longer exhibits a significant coherent modal interference structure in range and depth beyond roughly 30 km in range.

The relative contributions of the waveguide modes to the depth-integrated total intensity of the forward field at the source location and at 1, 10, and 50 km range from the source are shown in Fig. 7. There it can be seen that the highly random waveguide redistributes modal energies far more than the nonrandom waveguide and also has much less energy across the modal spectrum.

We next investigate the dependence of the forward field moments on the coherence lengths of the internal wave disturbances by letting them decrease to $l_x=l_y=50$ m. Figures 8(a) and 8(b) show the coherent, incoherent, and total acoustic intensities for internal wave height standard deviations of $\eta_h=1$ m and $\eta_h=4$ m, respectively. Comparing the coherent field in Figs. 8(a) and 8(b) with Figs. 5(d) and 6(d), we find that attenuation due to scattering increases with increasing coherence length, especially in the highly random waveguide. This can be explained by noting that in Eq. (36) the attenuation coefficient is linearly related to the coherence area since the second moment of scatter function density is effectively independent of coherence area in the forward azimuth. The larger attenuation from multiple scattering leads to lower coherent intensity. The level of incoherent intensity, on the other hand, increases with increasing coherence area in the highly random waveguide. This is expected, since in the limiting case where the cross-range coherence length exceeds the Fresnel width, incoherent intensity arises from a more multiplicative process of transmission through single scatter shells decorrelated solely in range as in a 2-D multiple scattering scenario.[37,38]

B. Effect of internal wave density fluctuations on acoustic transmission in an Arctic environment

Internal waves cause not only sound speed, but also density fluctuations in the water column that can sometimes affect acoustic transmission statistics. Density effects are expected to be pronounced in deep estuaries such as Norwegian Fjords, where "fresh river water tends to move seaward above the heavier salt water[29]," before sufficient tidal motions occur to cause mixing,[29] and in the Arctic seas, where cold fresh water near the melting temperature of ice flows above warm and salty seawater.[36]

Here we give an example of acoustic propagation though a 3-D linear internal wave field in an Arctic sea with 100 m water depth, as illustrated in Fig. 1. The interface between the cold fresh water above with density $d_1=1022$ kg/m^3 and sound speed $c_1=1433$ m/s and the warm salty water below with density $d_2=1028$ kg/m^3 and sound speed $c_2=1443$ m/s is also assumed to be at 30 m depth from the sea surface.[36] In Fig. 9, we determine the effect of internal wave density fluctuations on the forward acoustic field by including and then neglecting them in our calculations. Significant differences occur between these two cases for both the coherent and incoherent field components. Attenuation due to scattering is reduced when density fluctuations are included. This is because scattering from density and compressibility inhomogeneities are exactly out of phase

in the forward direction, as can be seen by substituting sound speeds and densities for the two layers of the water column into Γ_κ and Γ_d in Eq. (18). Internal wave density fluctuations should then not be neglected in estimating acoustic transmission statistics in certain environments.

C. Comparison of 3-D analytic model with 2-D Monte-Carlo simulations

Comparisons of the coherent, incoherent, and total acoustic field intensity determined by our 3-D analytic model and 2-D Monte-Carlo simulations using the parabolic equation for a slightly random waveguide with $\eta_h = 1$ m are illustrated in Figs. 10(a), 10(b), and 10(c). The coherent, incoherent, and total intensities calculated with the 3-D and 2-D approaches match very well out to the 50 km ranges shown. Both the 3-D and 2-D simulations agree on the moderate dispersion, attenuation, and low variance or incoherent intensity found at the longer ranges shown. This is a consequence of the weak scattering found for rms internal wave displacements, small compared to the acoustic wavelength. The situation changes, however, in a highly random waveguide, where rms internal wave displacements exceed the acoustic wavelength, with $\eta_h = 4$ m. As shown in Figs. 11(a), 11(b), and 11(c), the coherent and incoherent fields determined by the two approaches show a reasonable match within 11 km, where the cross-range coherence is larger than the Fresnel width. This is the range within which the 2-D simulations are expected to be valid. Beyond 11 km range, the 2-D Monte-Carlo simulations of coherent and incoherent intensities are far less attenuated than those of the 3-D model and the 2-D coherent intensities are far less dispersed. This is because the 2-D parabolic equation cannot account for scattering of acoustic energy out of the forward direction and subsequent loss of coherence incurred by random cross-range variations in the 3-D medium. Figures 10(d) and 11(d) show 2-D Monte-Carlo simulations of the coherent, incoherent and total field for the slightly and highly random waveguides for comparison with the 3-D model examples of Figs. 5(d) and Fig. 6(d).

The expected values of depth-integrated total intensity for our 3-D model and 2-D Monte-Carlo simulations are compared in Fig. 12. They decay with range as a result of spreading, intrinsic absorption and the accumulated effect of multiple forward scattering through internal wave inhomogeneities in the medium. In the slightly random waveguide, the curves for the 3-D and 2-D models show close agreement with each other and with the curve for the undisturbed waveguide, as expected, since scattering is weak. In the highly random waveguide, the 3-D model shows far greater power loss than the 2-D Monte-Carlo simulations. This is because the 2-D model cannot account for the out-of-plane scattering that must occur when the Fresnel width exceeds the cross-range coherence length of the internal waves.

V. CONCLUSION

Statistical moments of the acoustic field forward propagated through an ocean waveguide with random internal waves are modeled with a normal mode formulation that accounts for 3-D multiple forward scattering through medium inhomogeneities. The formulation analytically describes the accumulated effects of *multiple forward scattering*. These redistribute both coherent and incoherent modal energy, including attenuation and dispersion. Calculations for typical continental shelf environments show that the acoustic field becomes effectively incoherent at typical operational ranges when the rms internal wave height is on the order of the acoustic wavelength. It is found that two-dimensional models for the mean and variance of the acoustic field propagated through a 3-D random internal wave field then become inaccurate when the Fresnel width approaches and exceeds the cross-range coherence length of the internal wave field. Density fluctuations caused by internal waves may have a non-negligible effect on acoustic transmission in certain continental shelf environments, such as in Arctic seas.

[1] P. Ratilal and N. C. Makris, "Mean and covariance of the forward field propagated through a stratified ocean waveguide with three-dimensional random inhomogeneities," submitted to J. Acoust. Soc. Am.

[2] P. M. Morse and K. U. Ingard, *Theoretical Acoustics* (Princeton University Press, Princeton, NJ, 1986).

[3] P. Ratilal and N. C. Makris, "Extinction theorem for object scattering in a stratified medium," J. Acoust. Soc. Am. **110**, 2924–2945 (2001).

[4] P. Ratilal, "Remote sensing of submerged objects and geomorphology in continental shelf waters with acoustic waveguide scattering," Ph.D thesis, Massachusetts Institute of Technology, 2002.

[5] J. Colosi, R. Beardsley, J. Lynch, G. Gawarkiewicz, C. Chiu, and A. Scotti, "Observations of nonlinear internal waves on the outer New England continental shelf during the summer Shelfbreak Primer study," J. Geophys. Res. **106**, 9587–9601 (2001).

[6] J. Lynch, G. Jin, R. Pawlowicz, D. Ray, A. Plueddeman, C. Chiu, J. Miller, R. Bourke, A. Parsons, and R. Muench, "Acoustic travel-time perturbations due to shallow-water internal waves and internal tides in the Barents Sea Polar Front: Theory and experiment," J. Acoust. Soc. Am. **99**, 803–821 (1996).

[7] J. R. Apel, M. Badiey, C.-S. Chiu, S. Finette, R. Headrick, J. Kemp, J. F. Lynch, A. Newhall, M. H. Orr, B. H. Pasewark, D. Tielbuerger, A. Turgut, K. Heydt, and S. Wolf, "An overview of the 1995 SWARM shallow-water internal wave acoustic scattering experiment," IEEE J. Ocean. Eng. **22**, 465-500 (1997).

[8] N. C. Makris, "The effect of saturated transmission scintillation on ocean acoustic intensity measurements," J. Acoust. Soc. Am. **100**, 769-783 (1996).

[9] I. Dyer, "Statistics of sound propagation in the ocean," J. Acoust. Soc. Am. **47**, 337–345 (1970)

[10] W. A. Kuperman and F. Ingenito, "Attenuation of the Coherent Component of Sound Propagation in Shallow Water with Rough Boundaries," J. Acoust. Soc. Am. **61**, 1178-1187 (1977).

[11] W. A. Kuperman and H. Schmidt, "Rough surface elastic wave scattering in a horizontally stratified ocean," J. Acoust. Soc. Am. **79**, 1767-1777 (1986).

[12] W. A. Kuperman and H. Schmidt, "Self-consistent perturbation approach to rough surface scattering in stratified elastic media," J. Acoust. Soc. Am. **86**, 1511-1522 (1989).

[13] B. H. Tracey and H. Schmidt, "Seismo-acoustic field statistic in shallow water," IEEE J. Ocean. Eng. **22**, 317-331 (1997).

[14] G. R. Sutton and J. J. McCoy, "Scattering of acoustics signals by inhomogeneities in a waveguide—a single scatter treatment," J. Acoust. Soc. Am. **60**, 833-839 (1976).

[15] D. B. Creamer, "Scintillating shallow water waveguides," J. Acoust. Soc. Am. **99**, 2825-2838 (1996).

[16] L. B. Dozier and F. D. Tappert, "Statistics of normal mode amplitudes in a random ocean. I. Theory," J. Acoust. Soc. Am. **63**, 353-365 (1978).

[17] T. Duda and J. Preisig, "A modeling study of acoustic propagation through moving shallow water solitary wave packets," IEEE J. Ocean. Eng. **24**, 16–32 (1999).

[18] D. Tilbürger, S. Finette, and S. Wolf, "Acoustic propagation through an internal wave field in a shallow water waveguide," J. Acoust. Soc. Am. **101**, 789-807 (1997).

[19]C. Penland, "Acoustic normal mode propagation through a three-dimensional internal wave field," J. Acoust. Soc. Am. **78** 1356-1365 (1985).
[20]P. Ratilal, I. Bersatos, T. Chen, M. Zanolin, and N. C. Makris, "Optimal passive source localization in a fluctuating ocean waveguide based on an analytic model for the mean field and covariance," J. Acoust. Soc. Am. **115**, 2473 (2004).
[21]N. C. Makris, P. Ratilal, M. Zanolin, and I. Bersatos, "Obtaining optimal time-delay, source localization and tracking estimates in free space and in an ocean waveguide," J. Acoust. Soc. Am. **116**, 2606 (2004).
[22]D. T. Symonds, P. Ratilal, N. C. Makris, and R. W. Nero "Inferring fish school distributions from long range acoustic images: Main acoustic clutter experiment 2003," J. Acoust. Soc. Am. **115**, 2618 (2004).
[23]P. Ratilal, D. T. Symonds, N. C. Makris, and R. W. Nero, "Fish population dynamics revealed by instantaneous continental-shelf scale acoustic imaging," J. Acoust. Soc. Am. **117**, 2382 (2005).
[24]M. Zanolin, I. Ingram, A. Thode, and N. C. Makris, "Asymptotic accuracy of geoacoustic inversions," J. Acoust. Soc. Am. **116**, 2031–2042 (2004).
[25]P. Ratilal, T. Chen, and N. C. Makris, "Estimating internal wave statistics from underwater acoustic transmission scintillation measurements on the New Jersey shelf with a 3-D stochastic model," J. Acoust. Soc. Am. **116**, 2506 (2004).
[26]L. M. Brekhovskikh and Y. Lysanov, *Fundamentals of Ocean Acoustics* (Springer-Verlag, New York, 1991).
[27]P. Hursky, M. B. Porter, B. D. Cornuelle, W. S. Hodgkiss, and W. A. Kuperman, "Adjoint modeling for acoustic inversion," J. Acoust. Soc. Am. **115**, 607-619 (2004).
[28]P. Ratilal, Y. Lai, D. T. Symonds, L. A. Ruhlmann, J. Goff, C. W. Holland, J. R. Preston, E. K. Scheer, M. T. Garr, and N. C. Makris, "Long range acoustic imaging in Continental Shelf Environment: The Acoustic Clutter reconnaisance Experiment 2001," J. Acoust. Soc. Am. **117**, 1977-1998 (2005). (Appendix A).
[29]J. Lighthill, *Waves in Fluids* (Cambridge University Press, Cambridge, 1978).
[30]A. E. Gill, *Atmosphere-Ocean Dynamics* (Academic Press, San Diego, 1082).
[31]W. A. Kuperman and J. F. Lynch, "Shallow-water acoustics," Phys. Today, **11**, 55–61 (2004).
[32]N. C. Makris, F. Ingenito, and W. A. Kuperman, "Detection of a submerged object insonified by surface noise in an ocean waveguide," J. Acoust. Soc. Am. **96**, 1703-1724 (1994).
[33]J. R. Apel, J. R. Holbrook, A. K. Liu, and J. J. Tsai, "The Sulu Sea Internal Soliton Experiment," J. Phys. Oceanogr. **15**, 1625-1651 (1985).
[34]L. A. Ostrovsky and Y. A. Stepanyants, "Do internal solitons exist in the ocean?," Rev. Geophys. **3**, 293-310 (1989).
[35]L. Mandel and E. Wolf, *Optical Coherence and Quantum Optics* (Cambridge University Press, Cambridge, 1995).
[36]N. C. Makris, "Environmental correlates of arctic ice edge noise," MIT Ph.D. thesis, 1991.
[37]B. R. Frieden, *Probability, Statistical Optics, and Data Testing* (Springer-Verlag, Berlin, (1936).
[38]J. W. Strobehn, in *Laser Beam Propagation in the Atmosphere* (Springer-Verlag, Germany, 1978).

Three-dimensional passive acoustic tracking of sperm whales (*Physeter macrocephalus*) in ray-refracting environments

Aaron Thode[a)]
Marine Physical Laboratory, Scripps Institution of Oceanography, San Diego, California 92093-0205

(Received 8 April 2005; revised 3 August 2005; accepted 11 August 2005)

A wide-aperture towed passive acoustic array is used to obtain ranges and depths of acoustically active sperm whales in the Gulf of Mexico in June 2004, by extending a technique previously reported [Thode, J. Acoust. Soc. Am. **116**, 245–253 (2004)] to explicitly account for ray-refraction effects arising from a depth-dependent sound speed profile. Under this expanded approach, three quantities are measured from an impulsive sound: the time difference between direct-path arrivals on a forward and rear subarray, the time difference between the direct and surface-reflected paths on the rear subarray, and the acoustic bearing measured on the rear subarray. These quantities, combined with independent measurements of hydrophone depths and cable inclination, are converted into range-depth position fixes by implementing an efficient numerical procedure that uses a ray-tracing code to account for ray-refraction effects caused by depth-dependent sound speed profiles. Analytic expressions that assume a constant waterborne sound speed are also derived. Foraging depths of various sperm whales over 10 days in June, 2004 are estimated using the numerical technique. © *2005 Acoustical Society of America.*
[DOI: 10.1121/1.2049068]

PACS number(s): 43.30.Sf, 43.80.Ka [WWA] Pages: 3575–3584

I. INTRODUCTION

Sperm whales are a vocally active species, and detecting their signals, or "clicks," using towed passive acoustic arrays has become a standard procedure for detecting, locating, and monitoring these animals.[1,2] The seismic exploration industry is considering implementing passive acoustic monitoring systems as part of standard mitigation procedures during deep-water seismic exploration, due to concerns about the potential effects of deep-water airgun activity on deep-diving marine mammals such as the sperm whale.[3]

Most passive array systems have the ability to estimate a sound's bearing relative to the tow cable axis. They achieve this by measuring the signal's arrival time difference between two hydrophones spaced a few meters apart, and then assuming a planar wave front, yielding a monotonic relationship between arrival time difference and arrival angle. Using a single short-aperture array, the range to an animal can then be estimated by measuring how the measured bearings from a particular animal shift over time while the observation platform is moving.[1,2,4] If the velocity of the platform is much greater than that of the animal, then a time-motion analysis will yield a set of bearings that intersect at an animal's range over a 3–10 minute interval.

Unfortunately, typical seismic vessels operational speeds of 1–2 m/s are not much greater than estimated sperm whale swimming speeds,[5,6] invalidating the assumptions of time-motion analysis. Furthermore, obtaining a range estimate via this approach usually requires several minutes of continuous vocalizing, and assumes that individuals vocalizing simultaneously can clearly be distinguished, conditions which are not always met. Other algorithms assume that measuring the received level of a signal, and comparing this level to a reference database of typical source levels, can provide a range estimate. However, data on source levels are scarce, individuals can create sounds with varying source levels, and several marine mammal sounds, including sperm whale sounds, are now understood to be highly directional.[7–9] Thus at present there is no reliable way to range sperm whales, or any broadband biological underwater sound, using standard acoustic monitoring and mitigation equipment.

The situation is even more difficult for certain species of deep-diving mammals, including sperm and beaked whales, as a deep animal's depth must be determined in order to distinguish the "slant range," or the distance between the array and the animal, from the "horizontal range," or horizontal separation between the array and the animal. For directional sources like seismic airgun arrays this distinction may be important—the received sound level obtained by an animal 1 km directly below a towed airgun array is predicted to be 20 dB rms greater from that received by an animal at 1 km horizontal range,[10,11] even though the slant ranges for both animals would be the same.

In 2003 the US Minerals Management Service (MMS) and the Industry Research Funders Coalition supported efforts to develop a three-dimensional (3D) passive acoustic tracking method for sperm whales, by exploiting surface-reflected acoustic arrivals to create a virtual planar array out of a large-aperture towed array. During 2003 the Sperm Whale Seismic Study (SWSS) conducted a research cruise in the Gulf of Mexico, and the tracking concept was demonstrated using data collected from an autonomous recorder attached to the end of a short-aperture towed array. The analysis of this data has been previously reported.[12] If the

a)Electronic mail: thode@mpl.ucsd.edu

horizontal separation between two widely spaced hydrophones was at least 200 m, range/depth estimates could be obtained from sperm whale clicks out to 1 km horizontal range. Bottom-reflected acoustic multipath were not required for tracking, but when bottom returns were detected they provided an independent confirmation of the tracking procedure.[8]

The two-hydrophone analytic method presented in Ref. 12, however, suffers from two weaknesses. The first is that a surface-reflected path must be recorded on both hydrophones. Whenever this situation occurs, it permits a simple and straightforward analytical solution, but under many practical circumstances noise from the towing vessel may degrade or eliminate the ability to detect surface reflections on the hydrophones closest to the ship. A more serious limitation is that the assumption of a uniform spatially independent waterborne sound speed limits the accuracy of the method to ranges of 1 km or less in regions like the Gulf of Mexico, where stratified conditions produce strongly depth-dependent sound speed profiles. These profiles can cause substantial ray refraction of both direct and surface-reflected paths when the initial propagation angle of the departing acoustic energy lies close to the horizontal, and thus the rectilinear approximations behind the analytical formulas are violated.

Both problems were encountered during the 2004 SWSS field season, when data were collected from a tandem towed-array system constructed specifically for passive acoustic range-depth tracking. The surface-reflected paths were difficult to detect on the hydrophones closest to the ship, due to self-noise from the ship's propeller. Thus Sec. II presents a new analytic solution that only requires surface-reflected paths to be detected on one hydrophone, but requires an estimate of the acoustic bearing of a signal at the same hydrophone. The new tracking solution also has the advantage of being more robust to uncertainties in hydrophone depth. However, the new formulas in Sec. II still neglect the potential effects of ray refraction due to a depth-dependent sound speed profile, so in Sec. III numerical procedures for incorporating refraction effects are presented. Section IV presents details of the experimental deployment and automated data analyses, discusses how the tracking hardware and procedures were tested using data from June 16, 2004, and concludes with estimates of foraging depths of several animals over several days in the Gulf of Mexico.

II. ANALYTICAL TRACKING SOLUTION

An analytical solution for a 3D whale position can be obtained if a constant underwater sound speed is assumed, and thus ray paths are rectilinear. In Sec. III this assumption is dropped and the effects of a depth-dependent sound speed profile are incorporated into a numerical tracking procedure.

The geometry and parameters of the required array system are illustrated and defined in Fig. 1, and an example of a realistic tow configuration is shown in Fig. 2. Along a single towed array cable four array elements are arranged as two short-aperture subarrays separated by a cable distance L, with the forward subarray at a depth $z_{a,f}$ and the rear subarray at a depth $z_{a,r}$. In all future expressions, "f" or "r" subscripts designate measurements at the forward or rear subarray, respectively, and i designates a dummy variable that can represent either location. It is assumed that the cable lies in a two-dimensional plane perpendicular to the ocean surface, e.g., the ship is not turning and current velocity is depth independent. The separation between the two elements in each subarray is small enough that any signal wave front moving across the array aperture can be modeled as a plane wave (i.e., a Fraunhoffer approximation). Thus the bearing of a direct-path signal relative to the array cable, $\eta_{d,I}$, can be defined and estimated at both subarrays using standard cross-

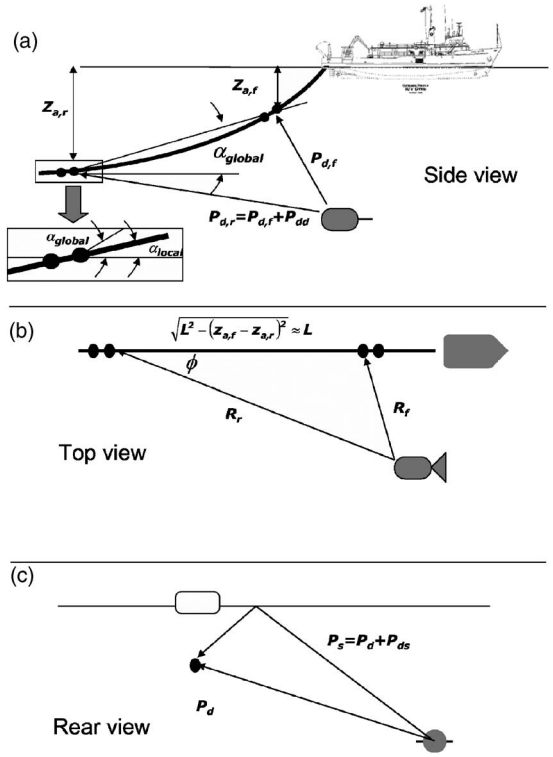

FIG. 1. Schematic of tandem array deployment geometry, defining symbols used in Sec. II, (a) side view of system; inset, expanded view of rear subarray illustrating the difference between the local tilt α_{local} and global cable inclination α_{global}. (b) Top view of system illustrating horizontal ranges; (c) rear view looking forward, illustrating notation for direct and surface-reflected paths.

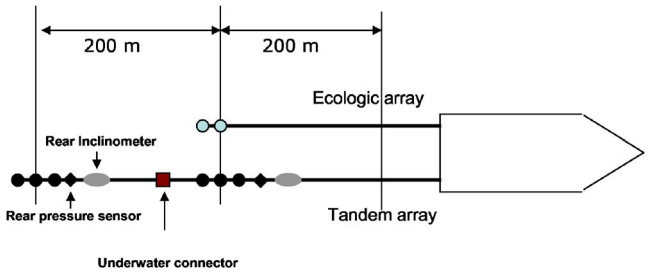

FIG. 2. Illustration of 3D deployment off R/V Gyre in 2004, viewed from above. The tandem array deployed off the starboard stern was specifically built for the project, and consisted of two subarrays separated by 200 m, each subarray consisting of three hydrophones and a pressure transducer. The tandem array and a second (Ecologic) array were deployed in parallel, permitting bearings of sounds to be determined without a port/starboard ambiguity. Round circle, calibrated hydrophone; diamonds, pressure (depth) sensors; oval, autonomous inclinometer package; square, underwater connector.

correlation methods. The formulas presented here use only $\eta_{d,r}$, or the bearing measured from the rear subarray, to minimize potential signal masking from ship noise interference.

A whale position is specified by the coordinates (R_i, z_w, ϕ_i) for the whale's horizontal range, depth, and azimuth from subarray i, respectively, where $\phi=0$ represents a position directly ahead of the ship. The "slant range" traveled by a sound along the direct propagation path to a given subarray i is $P_{d,i}=\sqrt{R_i^2+(z_w-z_{a,i})^2}$, and the distance traveled along the surface-reflected path to the same subarray is $P_{s,i}=\sqrt{R_i^2+(z_w+z_{a,i})^2}$. From these two expressions one obtains the useful formula

$$z_w = \frac{P_{ds,r}(2P_{d,f}+2P_{dd}+P_{ds,r})}{4z_{a,r}}, \tag{1}$$

where $P_{ds,r}=P_{s,r}-P_{d,r}$ is the difference between the direct and surface-reflected paths on the rear subarray, and the difference between the direct path slant ranges at the forward and rear locations is defined by $P_{dd}=P_{d,r}-P_{d,f}$. From estimates of $P_{ds,r}$, P_{dd}, and $\eta_{d,r}$ it should be possible to derive the whale's spatial coordinates. The first two estimates can be derived by measuring the relative arrival times $t_{ds,r}$ and t_{dd} and converting them to path length differences using an effective medium sound speed c. Estimates of $P_{ds,f}$ and $\eta_{d,f}$ will not be required in the derivation, anticipating the realities of noise contamination on the forward subarray. However, whenever these quantities are measurable, they can be used to verify the position fix.

Besides knowledge of both subarray tow depths, some additional ancillary measurements of the towed array cable are needed. In particular, information about the cable vertical inclination and curvature, or "sag," must be incorporated, in the form of a "local" tilt and "global" tilt. The rear subarray local tilt α_{local} is the angle between a horizontal line and a line connecting the two rear subarray elements [Fig. 1(a)]. The global tilt α_{global} is the angle between the horizontal line and a line connecting the front elements of the front and rear subarrays, or $\alpha_{\text{global}}=\sin^{-1}[(z_{a,r}-z_{a,f})/L]$. If the array cable has no sag, then the local and global tilt angles will be equal.

The relationship between an animal's azimuth, local tilt, and direct-path bearing $\eta_{d,r}$ is governed by

$$\cos\,\eta_{d,r} = \cos\,\phi\,\cos\,\alpha_{\text{local},r}\,\sin\,\theta_{d,r} + \sin\,\alpha_{\text{local},r}\,\cos\,\theta_{d,r}, \tag{2}$$

where $\theta_{d,r}$ is the elevation angle of the direct-path arrival on the rear subarray, defined relative to the upward z axis such that $\cos\,\theta_{d,r}=(z_{a,r}-z_w)/P_{d,r}$ and $\sin\,\theta_{d,r}=R_r/P_{d,r}$.

From the law of cosines a relationship between the forward and rear slant ranges can be obtained

$$P_{d,f}^2 = L^2 + P_{d,r}^2 - 2LP_{d,r}\cos\,\eta_{\text{global}} \tag{3}$$

with

$$\cos\,\eta_{\text{global}} = \cos\,\phi\,\cos\,\alpha_{\text{global}}\,\sin\,\theta_{d,r} + \sin\,\alpha_{\text{global}}\,\cos\,\theta_{d,r}. \tag{4}$$

Substituting Eqs. (2)–(4) into Eq. (1) one obtains an expression for the rear slant range,

$$P_{d,r} = P_{dd} + \frac{LP_{dd}\cos\,\alpha_{\text{global}}\cos\,\eta_{d,r} - \cos\,\alpha_{\text{local},r}(L^2+P_{dd}^2)/2 - L\sin(\alpha_{\text{local},r}-\alpha_{\text{global}})[z_{a,r}-P_{ds,r}(2P_{dd}+P_{ds,r})/4z_{a,r}]}{\cos\,\alpha_{\text{local},r}P_{dd} - L\cos\,\eta_{d,r}\cos\,\alpha_{\text{global}} - LP_{ds,r}\sin(\alpha_{\text{local},r}-\alpha_{\text{global}})/z_{a,r}}. \tag{5}$$

For the special case where the array cable is straight, or $\alpha_{\text{global}}=\alpha_{\text{local}}$, one finds

$$P_{d,r} = P_{dd} + \frac{LP_{dd}\cos\,\eta_{d,r} - (L^2+P_{dd}^2)/2}{P_{dd} - L\cos\,\eta_{d,r}}. \tag{6}$$

Substituting $P_{d,r}$ into Eq. (1) yields the whale depth, from which the range R_r and azimuth ϕ_r can be derived. Thus if independent estimates of $z_{a,f}, z_{a,r}$ and the local array tilt α_{local} are available, the whale position may be obtained by measuring the relative arrival times of a direct-path arrival between subarrays, and relative arrival times between the direct- and surface-reflected-path arrivals on the rear subarray alone.

The denominator of Eq. (6) indicates that in order for the slant range to be finite the signal wave front across aperture L must have significant curvature (i.e., be in the Fresnel zone). Alternatively stated, the bearings of the signal measured between the forward and rear subarrays must be sufficiently different to allow the animal's slant range to be calculated, even though the procedure here does not explicitly incorporate the forward subarray bearing. A general rule of thumb is that if the hydrophone elements are separated by a distance L then a broadside slant range of $5-10L$ should be resolvable.[13]

To estimate the inverted location uncertainties, a sensitivity analysis for the technique was conducted for a whale located at 1 km range and 400 m depth, using representative subarray depths and $L=200$ m (Table I). The 1 km range corresponds to the expected outer limit of the tracking algorithm for this subarray separation. Each of the input parameters was varied by an amount representative of the typical uncertainty of that measurement, 1 ms for relative time-of-arrival measurements, 1 m for subarray depth measurements, and up to 1 degree for the local tilt measurements. The spread in output values indicates that a whale depth can be estimated to within ±50 m, with most of the uncertainty dominated by imprecise estimates of t_{dd} and α_{local}. The impact of the local tilt is particularly felt whenever the whale's azimuth moves toward 0° or 180°. If $L=500$ m these depth uncertainties drop to ±20 m.

TABLE I. Sensitivity of analytic tracking algorithm to input uncertainties. Forward and rear subarray depths are 30 m and 50 m, respectively, with local tilt of 3 degrees on rear subarray.

Perturbation	Horizontal range (R_r) in m	Whale depth (z_w) in m
Baseline (L=200 m, ϕ_R=90°)	1000	400
Increase $t_{ds,r}$ by 1 ms	1002	420
Increase t_{dd} by 1 ms	1090	436
Increase $z_{a,R}$ by 1 m	1016	397
Increase α_{local} 1 degree	940	376
Baseline (L=200 m, ϕ_R=25°)	1000	400
Increase $t_{ds,r}$ by 1 ms	1016	425
Increase t_{dd} by 1 ms	1231	492
Increase $z_{a,R}$ by 1 m	1052	411
Increase α_{local} 1 degree	845	338

III. NUMERICAL TRACKING PROCEDURE

The localization formulas in Eqs. (1), (5), and (6) neglect potential ray refraction effects caused by depth-dependent sound speed profiles in the Gulf of Mexico. To explicitly account for these effects, a numerical procedure was created that implements a standard ray-tracing propagation code to compute the travel times, elevation angles, and t_{ds} values produced by a set of impulsive sources placed along a grid of horizontal ranges and depths. The most straightforward approach to implementing the algorithm would be to compute and store the ray paths and travel times of sources arranged along a three-dimensional grid surrounding the tandem towed array system, and then to construct an error function that indicates the mismatch between the measured relative arrival times and arrival angles with the modeled arrival times and angles. The 3D location that generates the error minimum would be chosen as the true location. This "matched-field" processing approach has been successfully demonstrated on large-aperture distributed array systems, where the sensors are permanently mounted on the ocean floor.[14,15] The problem with this approach when applied to the current situation is the dynamic nature of the array geometry. The towed array depths are constantly changing with time, and thus ray computations of all possible combinations of the 3D source locations and receiver depths becomes daunting.

Fortunately the problem can be reduced to a two-dimensional grid search over range and depth by using the ray-tracing code to precompute three L by M by N matrices, which represent a grid of L depths, M ranges, and N receiver depths. Thus the modeled values at the l,m,n coordinate represent an impulsive source at depth z_l and range R_m propagating to a receiver at depth z_n. The first matrix contains the computed travel distance $\mathbf{P_d}$ between the source and receiver combinations, the second matrix contains the elevation angle $\boldsymbol{\theta}_\mathbf{d}$ measured at the receiver, with the elevation angle defined as in Eq. (2), and the third matrix contains $\mathbf{t_{ds}}$, the modeled arrival-time difference between the direct and surface-reflected ray paths, t_{ds}.

For each measurement of t_{dd}, $t_{ds,r}$, and η_d, the following steps are taken:

(1) The receiver depth z_n that best matches the measured depth of the rear subarray, $z_{a,r}$, is used to extract the appropriate L by M matrices $\mathbf{P_d}(z_{a,r})$, $\boldsymbol{\theta}_\mathbf{d}(z_{a,r})$, and $\mathbf{t_{ds}}(z_{a,r})$. The matrix $\mathbf{P_d}(z_{a,f})$ that corresponds with the forward subarray depth $z_{a,f}$ is also extracted.
(2) A grid search along source depth z_l is conducted. For each value of z_l, the following steps are performed.
  (a) Interpolate along R_m to find a modeled value of $t_{ds,lm}=\mathbf{t_{ds}}(z_l,R_m,z_{a,r})$ that best matches the measured $t_{ds,r}$. Determine the corresponding interpolated values of $\theta_{d,lm}=\boldsymbol{\theta}_\mathbf{d}(z_l,R_m,z_{a,r})$, and $P_{d,lm}=\mathbf{P_d}(z_l,R_m,z_{a,r})$ for this interpolated range $R_{m,r}$.
  (b) Estimate the source azimuth relative to the rear subarray by rearranging Eq. (2),

$$\cos\phi^{(1)}=\frac{\cos\eta_{d,r}-\sin\alpha_{\text{local},r}\cos\theta_{d,lm}}{\cos\alpha_{\text{local},r}\sin\theta_{d,lm}}. \tag{7a}$$

  (c) Interpolate along R_m to find a modeled value of $\mathbf{P_d}(z_l,R_m,z_{a,f})$ that best matches $P_{d,lm}-P_{dd}$, and assign a value of $R_{m,f}$ to this range.
  (d) Make a second estimate of source azimuth using the law of cosines relationship

$$\cos\phi^{(2)}=\frac{R_{m,f}^2-L^2-R_{m,r}^2}{2LR_{m,r}}. \tag{7b}$$

  (e) Define an error function $E(z_l)=\cos\phi^{(2)}-\cos\phi^{(1)}$.
(3) Interpolate along $E(z_l)$ to find the modeled source depth z_l^* such that $E(z_l^*)=0$.
(4) Repeat steps (2a) and (2b) to obtain the best-fit source range and azimuth.

The top subplot of Fig. 3 shows a typical sound speed profile in the Gulf of Mexico (GOM) acquired from CTD casts during June, 2004. Generally, the sound speed profile was very stable with only slight changes over a 3 week period. The downward-refracting tendency of this environment is clearly indicated by the monotonic decrease of the water sound speed from over 1540 m/s at the surface to 1490 m/s at the bottom. The next three subplots show contour plots of ray path length P_d, arrival time differences between the direct and surface-reflected path t_{ds}, and elevation angle for a

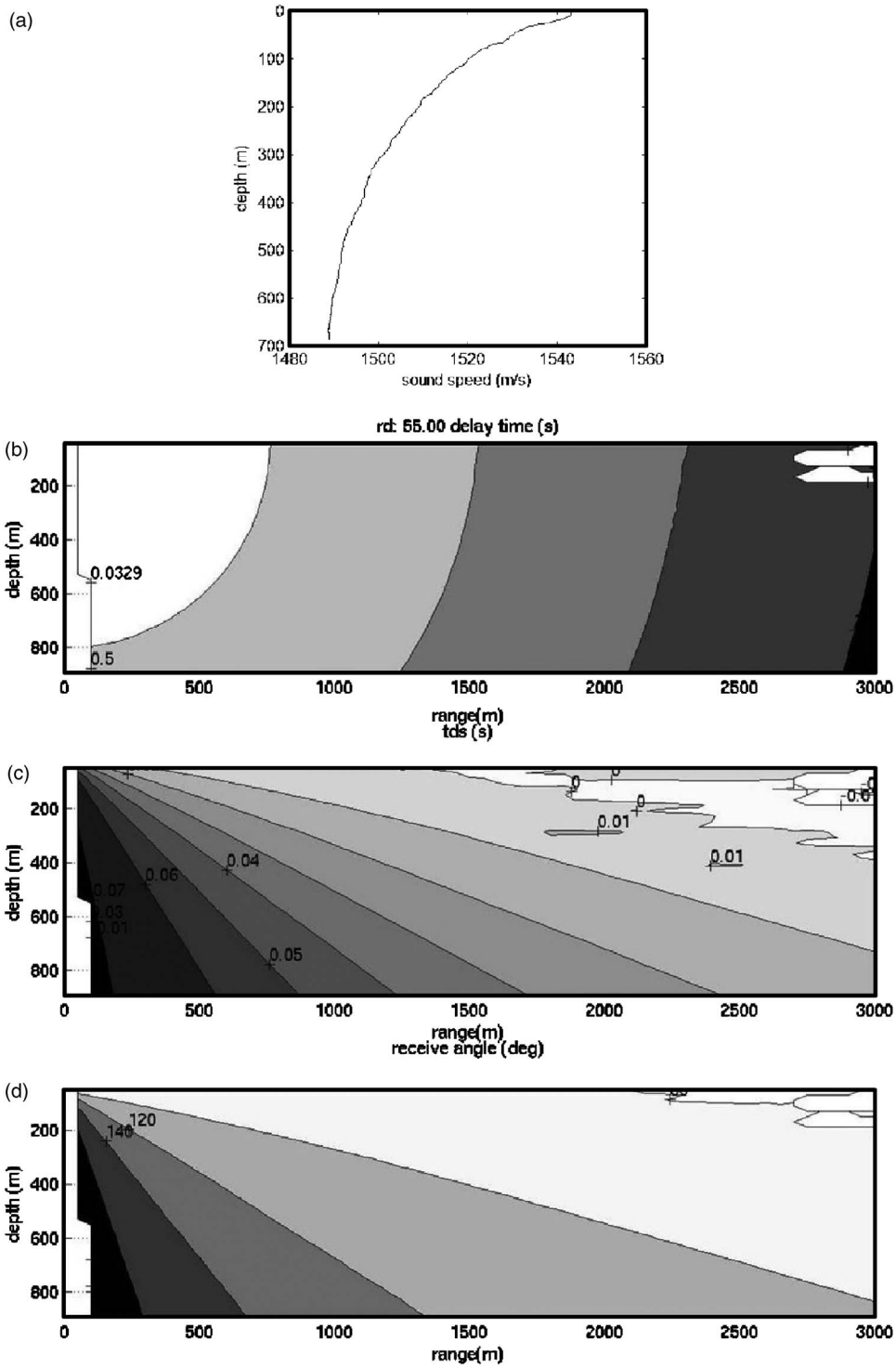

FIG. 3. (a) Downward-refracting sound speed profile measured on June 13, 2004. (b)–(d) Effect of sound speed profile on localization parameters, for a receiving hydrophone at 55 m depth. (b) Ray path length vs source range and depth; (c) direct-surface time delay vs source range and depth; (d) received ray elevation angle vs source range and depth. Note the appearance of a "shadow" zone beginning at shallow depths at 2 km range.

receiver depth of 55 m. The path-length contour map, which would consist of concentric circles in a constant-speed (isovelocity) profile, shows that the greatest horizontal range a receiver can detect a direct path from a surface source is 2.8 km in the GOM. Beyond this range, a source would have to be at progressively deeper depths to be detected via its direct path. The elevation angle contour map in the bottom subplot also illustrates this tendency.

Given that the duration of a sperm whale click is on the order of 10 ms, distinguishing t_{ds} values below this value becomes problematic, although cepstral methods can be successfully applied.[12,16–18] The contour map of t_{ds} shows that beyond 2.0 km range the direct-surface arrival time difference exceeds 10 ms only for sources deeper than 200 m, and the required source depth to attain this minimum interval increases with greater range. In general the deeper the receiving hydrophone, the greater the range over which the depth and horizontal range components of an animal's location can be teased apart.

The computations shown in Fig. 3 were repeated for receiving hydrophone depths from 15 m to 80 m, increasing in 5 m increments.

IV. EXPERIMENTAL SETUP

A. Equipment and deployment

A dedicated towed "tandem" array for the SWSS 3D tracking project was built between December 2003 and May 2004, and deployed during the SWSS 2004 cruise between May 27 and June 17, 2004 (Fig. 2). Designed according to the geometry in Fig. 1, the tandem array consists of two calibrated subarrays of three elements each, separated by $L = 200$ m of cable, with an additional 200 m of lead-in to the deck winch. Thus the rear subarray is deployed 400 m behind the ship stern. The 200 m aperture would be sufficient for tracking animals within 1–2 km of the vessel, based on a consideration of Eq. (6). An underwater connector (square in Fig. 2) at the base of the first array permits the arrays to be interchangeable, or even converted into two single arrays, providing emergency redundancy for the S-tag cruise requirements. Both subarrays incorporate pressure sensors, and a breakout box provided separate acoustic and pressure outputs. Each hydrophone on the tandem array has between −165 to −170 dB re 1 V sensitivity, with a flat frequency response between 100 Hz to over 24 kHz, although usable signal could be obtained past 30 kHz. The presence of a third hydrophone in each subarray provides redundancy in case of a sensor failure. An estimated total of 30 lb. of lead forms were added to the cable about 50 m ahead of the forward subarray to increase the array tow depths. For example, at 3 knots (around 2 m/s) the tow depth for the forward array was 30 m and the rear array about 55 m.

Between June 12 and June 18 two autonomous inclinometer packages were attached to both the forward and rear subarray to provide independent measurements of α_{local}, thus determining whether the simplified Eq. (6) was adequate for most situations. A second array, provided by Ecologic Inc., was deployed off the port side of the Gyre (Fig. 2). When combined with data from the rear subarray of the tandem array, acoustic observers were able to distinguish port/starboard ambiguities in the bearings without having to alter vessel course.

Data from two hydrophones in the forward array and two hydrophones in the rear array were filtered using a Khron-hite model 3944 filter/amplifier before being recorded onto an Alesis ADAT HD24XR hard disk digital recorder, along with two channels from the Ecologic array. Thus a total of six hydrophones were sampled at 96 kHz and stored in 24 bit WAV format. The start time of each recording was entered into both an Excel spreadsheet and a Microsoft Access database. The signal was high-pass filtered above 100 Hz to eliminate potential dc and 60 Hz line noise. The two pressure sensors were sampled by two process indicators in the breakout box, with output both a digital LED display and a serial port signal. The serial port signals were sampled by a Labview program on a dedicated laptop, which saved the time-stamped data to file.

B. Automated parameter extraction

The data were post-processed after the cruise, using automated procedures for extracting the localization parameters, similar to those discussed in Ref. 12. The recorded data were first rearranged into two stereo audio files, one for each subarray. The bioacoustic analysis software Ishmael[19] then detected impulses by monitoring the spectral energy content between 4 kHz and 15 kHz, and activating a MATLAB subroutine that identified whether a particular pulse was a direct arrival or a surface-reflected path. A direct path was identified as any pulse that was not preceded by another pulse during the previous 50 ms, which would be a typical value of $t_{ds,r}$ given the array depths and whale ranges considered here. Even when multiple animals are vocalizing, the odds of two direct path arrivals being detected within 50 ms of each other were small enough that direct-path arrivals from animals calling simultaneously could be distinguished. Pulse detections with acoustic bearings of less than 25 degrees were also rejected, in order to remove impulsive sounds generated by the tow vessel. For each direct-path detection, the MATLAB script estimated the acoustic bearing via standard cross-correlation methods, and then computed $t_{ds,r}$ simply by assuming the next detected pulse after a direct-path arrival was the surface-reflected path.

Once both subarrays had been processed this way, a second MATLAB script examined each direct-path arrival time on the rear subarray, and for every such "focal" click determined an appropriate set of interclick-intervals (ICIs) for that particular animal, by identifying other direct paths within a 10 second window that arrived within 10° of the acoustic bearing of the focal click. The program then scanned the direct-path arrivals on the forward subarray for a similar ICI pattern. Once a matching ICI set was found, the arrival-time difference t_{dd} for the direct path was determined. This "rhythm analysis" is a standard technique for many sperm whale acoustic analysis programs over widely spaced apertures.[1,14,20,21]

The hydrophone depths and cable inclination, which had been sampled every 10 seconds, were interpolated to assign a value to each direct-path arrival. Equations (5) and (6) then provided a slant range, and Eq. (1) a depth. As a check that the array cable is laterally straight, the values of $\eta_{d,f}$ and $t_{ds,f}$ were derived and compared with the measurements on the forward array. Navigation data from the ship GPS was also plotted to check whether the ship was changing course or speed during the time of interest.

V. RESULTS

A. Confirmation of tracking approach using bottom-reflected data and inclinometer measurements

Acoustic data were collected from the tandem array from May 27 through June 17, 2004. A particularly clean dive sequence from a single whale at close range was recorded on June 16, shortly before midnight of the last full cruise day. Numerous bottom-reflected returns were audible throughout the dive, making this data set a good candidate for an initial check of the tracking sequence. A MATLAB graphical-user interface (GUI) was written to permit convenient review of spectrograms from the forward and rear array simultaneously, and Fig. 4 shows a few seconds from the data set. Surface reflections are clearly visible on both sub-

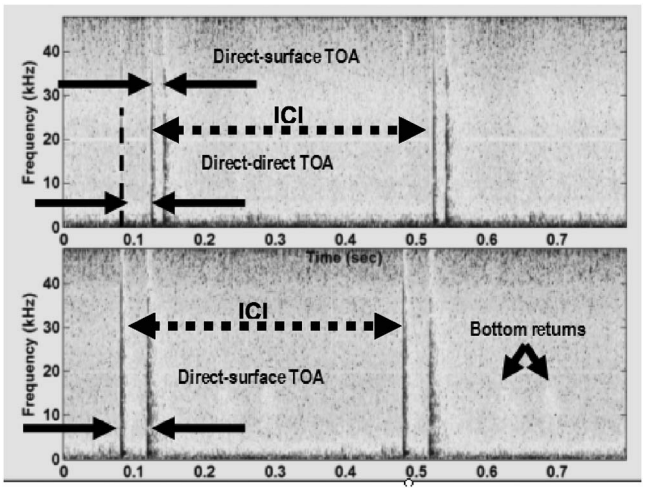

FIG. 4. Spectrograms of data collected during 2004 3D tracking experiment, as viewed with a MATLAB graphical user interface. All time units are in seconds. The top and bottom spectrograms (48 kHz sample rate, 1024 pt. FFT samples, 75% overlap) image data from the forward and rear subarrays. Up to five pieces of information can be obtained from each individual click, the differences between the arrival times of the direct and surface-reflected paths on the forward ($t_{ds,f}$) and rear ($t_{ds,r}$) hydrophones, the arrival time difference between the direct arrivals on both hydrophones (t_{dd}), and the acoustic bearings of both signals ($\eta_{d,f}$ and $\eta_{d,r}$). If both hydrophone depths are known, the animal's position can be fixed. Also shown is the interclick interval (ICI), which is used to identify the same whale on both hydrophones; and bottom-reflected paths, which permit an independent check of the tracking algorithm.

arrays, as are bottom-reflected returns. The interclick interval is shorter than the travel time of the bottom-reflected returns.

Figure 5 shows the output of the automated parameter detection routines. The $t_{ds,r}$ value for the whale in question

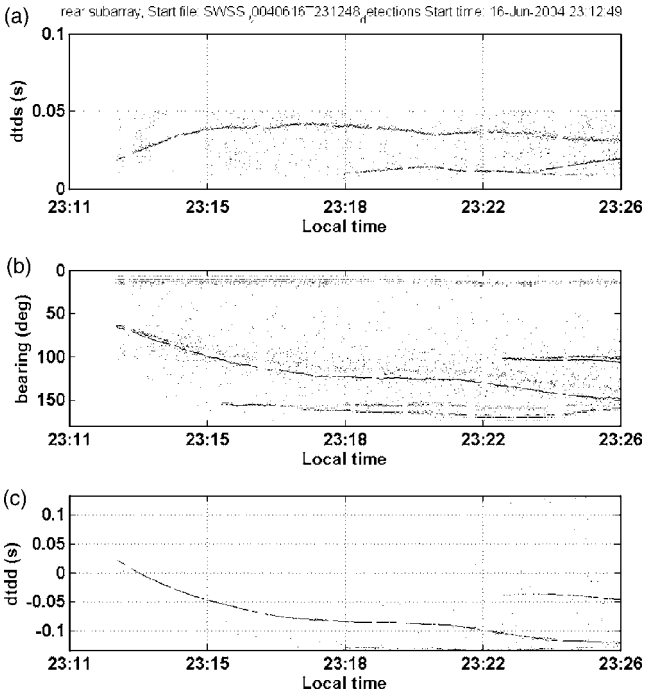

FIG. 5. Tracking parameters extracted automatically from the acoustic data on June 16. (a) Arrival time difference between the direct and surface-reflected sound arrivals on the rear subarray; (b) acoustic bearings measured on the rear subarray; and (c) arrival time difference t_{dd} between the forward and rear subarrays.

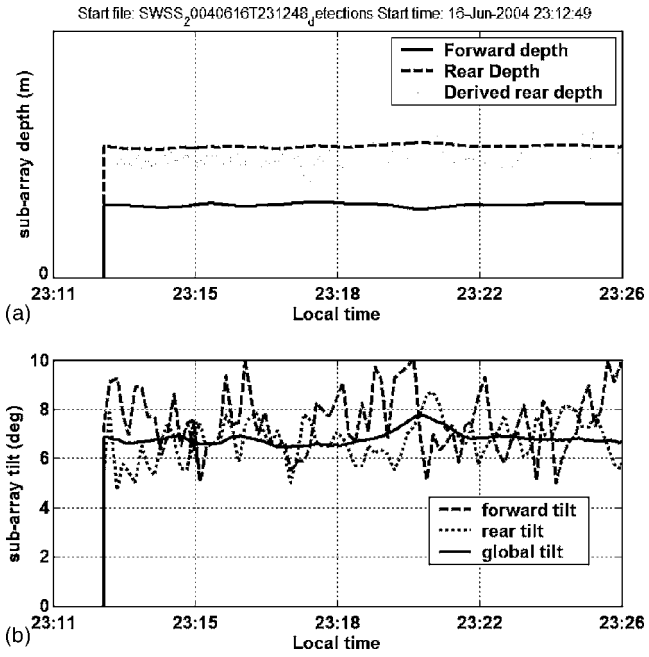

FIG. 6. Measurements of tandem array tow shape during the same time interval shown in Fig. 5. (a) Subarray depths of the forward (solid line) and rear (dashed line) subarrays, as measured by embedded pressure transducers. Rear subarray depths are also independently derived using bottom-reflected sperm whale clicks (hollow squares). (b) Comparison of α_{local} and α_{global} of tandem array. The local tilt was measured on the forward (dashed line) and rear (dotted line) subarrays. The global tilt (solid line) was derived from array depths in (a).

reaches nearly 50 ms at 23:17, then decreases as the array passes the whale, as is seen by the plots of acoustic bearing and t_{dd} shown in Figs. 5(b) and 5(c), respectively. Measurements of $t_{ds,r}$ less than 10 ms are not attempted.

Figure 6 shows independent checks of the geometry of the towed array cable. The top subplot shows the measured depths of the two subarray pressure transducers, along with rear subarray depths derived from bottom-reflected returns. The measured and derived rear subarray depths are within a few meters of each other. The bottom subplot compares the output of the inclinometers, which directly measure α_{local}, with the value of α_{global} derived from the hydrophone depths and knowledge of the cable length. Despite the large variance in the inclinometer readings, the mean values of α_{local} are within a degree of α_{global}, indicating that the array cable is relatively straight, and that Eq. (6) is valid for the cable at this tow speed. Measurements at other times and other ship speeds indicate that setting $\alpha_{\text{local}} \sim \alpha_{\text{global}}$ is a good approximation.

Figure 7 shows range and depth fixes using the single-phone localization procedure described in Ref. 8, along with the tracking results derived in Sec. II. Until 23:19 the results agree extremely well as the animal dives from 100 m down to 550 m. After this time, however, the single-phone measurements indicate that the animal remains at depth, while the tracking method introduced here determines that the animal's range and depth decreases substantially—effectively, that the path length $P_{d,r}$ is decreasing. The answer to this inconsistency appears in the bottom subplot, which plots the ship speed in knots and the vessel course over ground (COG)

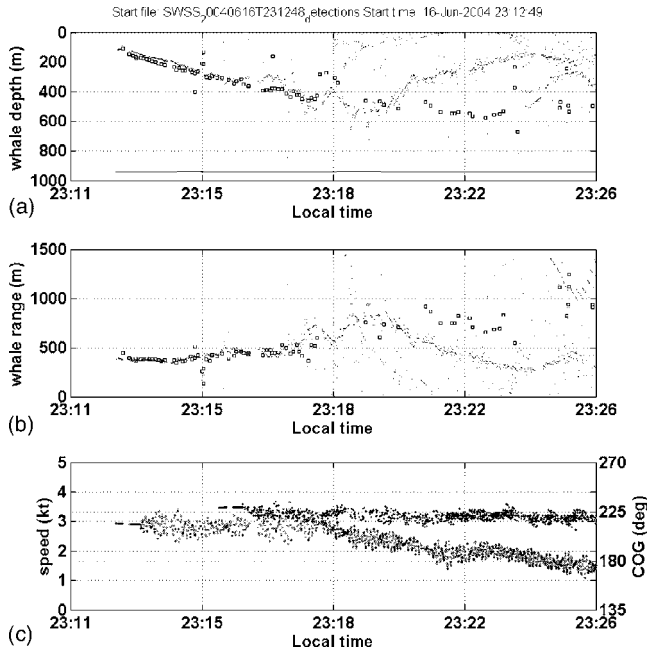

FIG. 7. Analytic range-depth track estimates, using data beginning at June 16, 2004, 11:13 CDT, covering the same time period as Figs. 5 and 6. Positions derived using methods derived in Sec. II are shown as dots, and positions derived by exploiting bottom multipath on a single hydrophone as shown by squares. The whale depths are shown in (a), the horizontal ranges from the forward hydrophone are shown in (b), and (c) shows the ship speed (plus signs) and course over ground (circles) measured by GPS over the same interval. Note divergence of tracking methods when ship course changes at 23:17.

in degrees. At 23:19 the ship begins a 40 degree port turn that continues past 23:37. This turn throws the tow cable out of a two-dimensional vertical plane, violating the assumptions of Sec. II. Thus the course of the towing vessel must be monitored carefully for the tracking techniques presented here to work.

B. Effect of ray refraction

Applying the numerical ray-refraction tracking procedure to Fig. 7 did not yield any substantial differences from the analytical formulas. However, clicks generated by animals at ranges greater than 1 km show effects of ray refraction. To illustrate this, Fig. 8 shows a 30 minute tracking segment from June 8, 2004, using the analytic formulas. The bottom subplot illustrates that the ship course and speed were steady through the encounter. Although it is difficult to distinguish, two animals are present at the same depth in the first half of the sequence, while one animal is present in the latter half. Figure 9 shows the same data analyzed using the numerical procedure outlined in Sec. III. Comparing plots reveals that at horizontal ranges greater than roughly 1 km animals that appear to be at 300–400 m depth using the analytic formulas are actually 100 m deeper when an accurate propagation model is taken into account. This example demonstrates that as tracking is extended to greater ranges, the effects of the depth-dependent sound speed profile cannot be neglected if accurate dive depths of animals are to be inferred from passive acoustics.

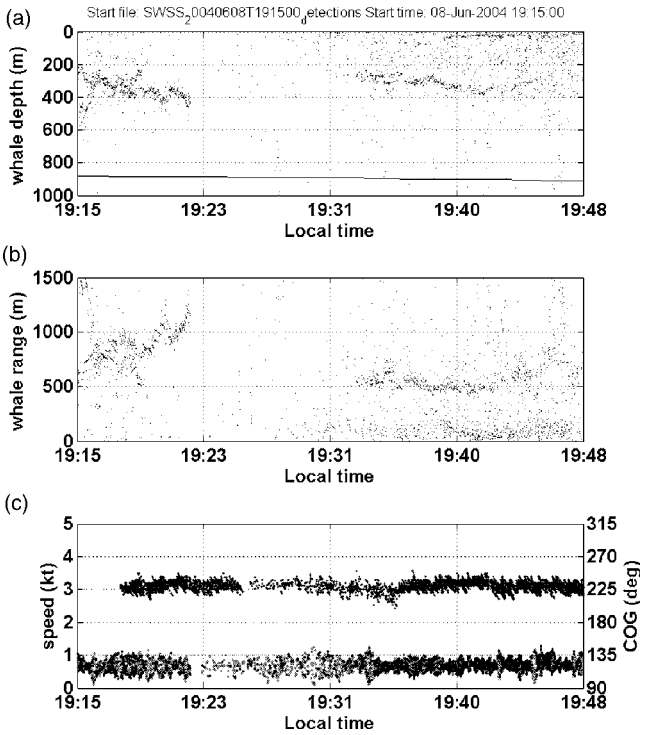

FIG. 8. Same as Fig. 7, except analytically derived tracks are shown for three whales beginning June 8, 19:15 local time.

C. Foraging depths over several days

A selection of the 2004 data have been selectively analyzed to determine depth ranges of individual animals over a 10 day period, during times where the ship course and speed is constant over long periods. Table II shows the results of measured foraging depths, with an asterisk indicating that at least part of an animal's initial dive profile was detected. This is not meant to be an exhaustive list of encounters, but a selection intending to show the diversity of the dive depths encountered during the cruise. Many of these measurements

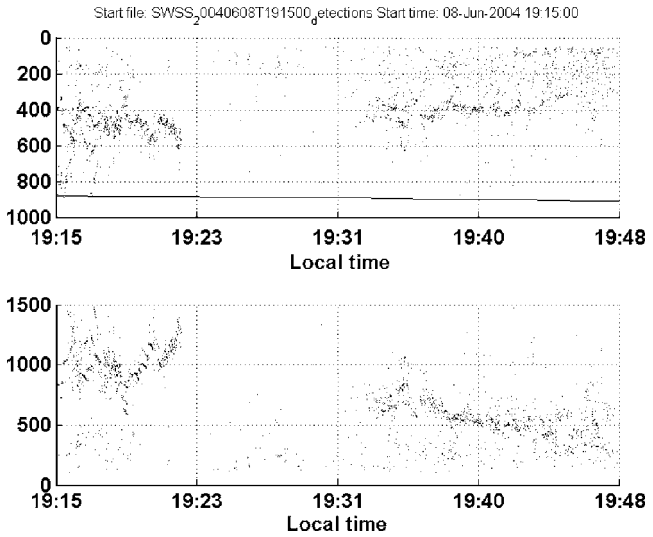

FIG. 9. Same as Fig. 8, but tracks are derived using the numerical procedure discussed in Sec. III. At horizontal ranges greater than 1 km, the effects of ray refraction due to a depth-dependent sound speed profile are not negligible.

TABLE II. Depths traversed by individual whales during SWSS 2004 cruise, corrected for ray-refraction effects. Times are rounded to the nearest 5 minute increment, and depths to the nearest 50 m increment (the depth uncertainty from Table I). A single depth is shown if an animal remained within ±50 m of that depth. Ship coordinates shown are the ship location midway through the dive profile measurement. An asterisk (*) indicates the observation of what appears to be an initial dive descent.

Date	Time	Latitude	Longitude	Depth range(m)	Description
June 7	8:38–9:30	28.112	−89.800	400–600 m	
June 7	11:30–12:00	28.154	−87.707	250 m	
June 8	16:45–17:45	28.274	−89.584	200–300 m	
June 8	16:40–17:30	Same	Same	300–400 m	
June 8	18:00–18:10	28.316	−89.596	200 m	
June 8	18:00–18:30	Same	Same	200–400 m	
June 8	18:30–19:00	Same	Same	300 m	
June 8	19:15–19:20	28.327	−89.538	350–600 m*	Section IV B
June 8	19:15–19:25	Same	Same	400–500 m	
June 8	19:35–19:45	Same	Same	400 m	
June 13	19:55–20:00	28.267	−89.578	250 m	
June 13	20:00–20:10	Same	Same	300 m	
June 13	20:10–20:15	Same	Same	400 m	
June 13	22:15–22:25	28.287	−89.573	200–400 m	
June 13	22:40–23:00	Same	Same	400–500 m	
June 16	13:25–13:30	Same	Same	300 m	
June 16	16:30–16:55	28.163	−89.382	200–450 m	
June 16	16:45–17:05	Same	Same	350 m	
June 16	16:40–17:05	Same	Same	300–500 m	
June 16	16:45–17:10	Same	Same	200–400 m	
June 16	23:15–23:20	28.000	−89.584	150–500 m*	Section IV A
June 17	1:15–1:20	27.99	−89.590	150–450 m	
June 17	1:25–1:30	Same	Same	250–400 m	
June 17	16:05–16:20	28.178	−89.632	150–350 m	
June 17	16:45–17:00	Same	Same	300 m	

were taken during the night or during days of poor weather, whenever tagging activities and visual observations were infeasible.

During these time periods, the range-depth tracks of animals are computed using both the methods of Sec. II and the refraction-corrected methods of Sec. III, but only the refraction-corrected results are shown here. The derived animal depths are rounded to the nearest 50 m, on the basis of the sensitivity analysis presented in Table I. The quality of the tracks obtained improved as the acoustic observers gained more experience in directing the vessel course and speed. By June 16 and 17, up to three animals could be tracked simultaneously using the system.

VI. CONCLUSION

An automated 3D passive acoustic tracking system has been developed and tested on a 200 m aperture towed array system built specifically for this purpose, and animals out to 1.5 km range have been successfully tracked. Information from bottom-reflected returns and additional parameters measured from the forward subarray has been used to confirm the tracking results when possible. At ranges of around 1 km or greater, the effects of a depth-dependent sound speed profile must be incorporated into the tracking procedure to obtain accurate results. In addition, the ship course must be steady and true to avoid large localization biases.

Direct inclinometer measurements of the tow cable dynamics have revealed that under many conditions the cable's vertical curvature is small, permitting substantial simplification of the analytical formulas. However, the sensitivity analysis presented in Table I indicates that small changes in local tilt can cause large variations in estimated animal depth when the animal is either directly ahead or behind the system. The technique presented here thus complements the procedure outlined in Ref. 12, which works best when an animal is directly ahead of or behind a vessel.

Further refinements in modeling the tow cable dynamics are expected, to determine under what circumstances precise information about the cable sag would be required. Eventually data collected using these techniques may not only find use in marine mammal mitigation efforts, but might also be combined with measurements of acoustic backscattering depths to gain insight into foraging ecology.

ACKNOWLEDGMENTS

The author thanks Bruce Mate of Oregon State University for permitting the deployment of the tracking system for the summer S-tag cruise, and the Industrial Research Funders Coalition (IRFC) for providing support to build the towed array system. Tom Norris, Elizabeth Zele, Sarah Tsoflias, and Alyson Azzara helped monitor and record acoustic data during that cruise. Matt Howard of Texas A&M provided data on the water depth beneath the R/V Gyre in 2004. This work

was supported by the U.S. Minerals Management Service, under Cooperative Agreement 1435-01-02-CA-85186. Ann Jochens and Doug Biggs of Texas A&M University helped arrange this support, and have been supportive of this research since its inception.

[1]R. Leaper, O. Chappell, and J. Gordon, "The development of practical techniques for surveying sperm whale populations acoustically," Rep. Int. Whal. Comm. **42**, 549–560 (1992).
[2]J. Barlow and B. L. Taylor, "Estimates of sperm whale abundance in the northeastern temperate Pacific from a combined acoustic and visual survey," Marine Mammal Sci. **21**(3), 429–445 (2005).
[3]J. Gordon, D. Gillespie, J. Potter, A. Frantzis, M. P. Simmonds, R. Swift, and D. Thompson, "A review of the effects of seismic surveys on marine mammals," Mar. Technol. Soc. J. **37**, 16–33 (2004).
[4]D. Gillespie, "An acoustic survey for sperm whales in the Southern Ocean Sanctuary conducted from the RSV Aurora Australis," Rep. Int. Whal. Comm. **47**, 897–907 (1997).
[5]H. Whitehead, *Sperm Whales: Social Evolution in the Ocean* (University of Chicago Press, Chicago, 2003).
[6]J. C. Gordon, "The behavior and ecology of sperm whales off Sri Lanka," Ph.D. thesis, University of Cambridge, Cambridge, UK, 1987.
[7]B. Møhl, M. Wahlberg, P. T. Madsen, L. A. Miller, and A. Surlykke, "Sperm whale clicks: Directionality and source level revisited," J. Acoust. Soc. Am. **107**, 638–648 (2000).
[8]A. Thode, D. K. Mellinger, S. Stienessen, A. Martinez, and K. Mullin, "Depth-dependent acoustic features of diving sperm whales (Physeter macrocephalus) in the Gulf of Mexico," J. Acoust. Soc. Am. **112**, 308–321 (2002).
[9]W. M. X. Zimmer, P. L. Tyack, M. P. Johnson, and P. T. Madsen, "Three-dimensional beam pattern of regular sperm whale clicks confirms bentho rn hypothesis," J. Acoust. Soc. Am. **117**, 1473–1485 (2005).
[10]J. J. Nooteboom, "Signature and amplitude of linear airgun arrays," Geophys. Prospect. **26**, 194–201 (1978).
[11]S. Vaage and B. Ursin, "Computation of signatures of linear airgun arrays," Geophys. Prospect. **35**, 281–287 (1987).
[12]A. Thode, "Tracking sperm whale (Physeter macrocephalus) dive profiles using a towed passive acoustic array," J. Acoust. Soc. Am. **116**, 245–253 (2004).
[13]C. R. Greene and M. W. McLennan, *Passive Acoustic Localization and Tracking of Vocalizing Marine Mammals Using Buoy and Line Arrays* (Hobart, Tasmania, 1996).
[14]J. Ward, M. Fitzpatrick, N. DiMarzio, D. Moretti, and R. Morrissey, "New algorithms for open ocean marine mammal monitoring," *OCEANS 2000 MTS/IEEE Conference and Exhibition. Conference Proceedings (Cat. No. 00CH37158)* (IEEE, Piscataway, NJ, 2000), pp. 1749–1752.
[15]C. O. Tiemann, M. B. Porter, and L. N. Frazer, "Localization of marine mammals near Hawaii using an acoustic propagation model," J. Acoust. Soc. Am. **115**, 2834–2843 (2004).
[16]W. M. X. Zimmer, M. P. Johnson, A. D'Amico, and P. L. Tyack, "Combining data from a multisensor tag and passive sonar to determine the diving behavior of a sperm whale (Physeter macrocephalus)," IEEE J. Ocean. Eng. **28**, 13–28 (2003).
[17]A. V. Oppenheim and R. W. Schafer, *Discrete-Time Signal Processing* (Prentice-Hall, Englewood Cliffs, NJ, 1989).
[18]J. M. Tribolet, *Seismic Applications of Homomorphic Signal Processing* (Prentice-Hall, Englewood Cliffs, NJ, 1979).
[19]D. K. Mellinger, "Ishmael 1.0 User's Guide," NOAA/PMEL Tech. Mem. Report PMEL-120, 2002.
[20]R. J. Barton III, S. Jarvis, R. J. Rowland, and D. Moretti, "The application of EZ-Gram sonar display aids to the Marine Mammal Monitoring on Navy Undersea Ranges (M3R) system," *Oceans 2002 Conference and Exhibition. Conference Proceedings (Cat. No. 02CH37362)* (IEEE, Piscataway, NJ, 2002), Vol. **2**, pp. 1064–1070.
[21]D. Gillespie and R. Leaper, "Detection of sperm whales (Physeter macrocephalus) clicks, and discrimination of individual vocalisations," Eur. Res. Cetaceans **10**, 87–91 (1997).

Analysis of the near-field ultrasonic scattering at a surface crack

Bernard Masserey[a] and Edoardo Mazza[b]
Institute of Mechanical Systems, ETH Zurich, Swiss Federal Institute of Technology, CH-8092 Zurich, Switzerland

(Received 2 June 2005; revised 12 September 2005; accepted 13 September 2005)

The near-field scattering of a Rayleigh wave at a surface crack is analyzed with analytical and numerical calculations complemented by detailed experimental observations. These investigations are directed towards the development of inversion schemes for surface crack sizing in mechanical components. The near-field analysis is based on a procedure that allows filtering the Rayleigh wave from the other wave modes scattered at the defect. Pointwise measurements of the out-of-plane displacement using a laser interferometer lead to a complete displacement field image in the crack near field with high spatial resolution. The numerical calculations are compared with the analytical solution and the experimental data in order to validate specific crack modeling approaches and to identify parameters for surface crack characterization. The evaluation is carried out with respect to the stress fields at the crack tip, the surface displacement near field, Rayleigh wave transmission and reflection coefficients, and the time delay of Rayleigh wave transmission. The latter appears as the most suitable parameter for crack characterization due to the relative insensitivity of the measured values on the variability of the experimental conditions. The results of the present work also highlight differences between the scatterings at cracks and narrow slots ("artificial cracks"). © *2005 Acoustical Society of America.* [DOI: 10.1121/1.2109407]

PACS number(s): 43.35.Cg, 43.35.Pt, 43.35.Zc [YHB] Pages: 3585–3594

I. INTRODUCTION

The assessment of engineering components using fracture mechanics has driven researchers to develop quantitative nondestructive evaluation (QNDE) methods for damage detection and crack characterization. In fact, knowledge of position, size, and geometry of the defect is essential for predicting the loading conditions under which failure might occur. One widely used nondestructive technique is based on the scattering of ultrasonic waves in the presence of defects.[1] In fact, the scattered or diffracted ultrasonic pulses can be used for crack detection and crack sizing.[2] Among the many ultrasonic methods, Rayleigh waves are particularly suitable for characterization of defects at the free surface of a component, since the energy of the wave is confined in a thin layer along the surface of the material. Different far-field evaluation methods based on the analysis of pulse amplitude, time-of-flight methods, or ultrasonic spectroscopic analysis have been investigated for the characterization of surface cracks by Rayleigh waves. Recent work[3–5] has shown that the scattered near field contains valuable information for a nondestructive evaluation of the crack size. The development of characterization techniques based on measurements of the defect near field is particularly important in the case of components with complex geometry, where the far-field evaluation is hampered by the influence of geometry discontinuities.

A prerequisite for the correct interpretation of experimental data and the development of inversion schemes is the understanding of the interaction of Rayleigh waves with surface features. Achenbach *et al.*[6] investigated the basic diffraction mechanisms in the high-frequency range on the basis of elastodynamic ray theory. Kundu and Mal[7] studied the scattering of time harmonic elastic waves at a surface crack using an asymptotic theory of diffraction. Similarly, other works[8,9] have investigated the problem of reflection and transmission of Rayleigh waves at surface grooves using perturbation techniques. An exact solution for the scattering of a time-harmonic elastic wave at a surface crack has been obtained by Mendelsohn *et al.*[10,11] The scattering problem is reduced to singular integral equations and the exact analytical representation of the displacement field is obtained in the form of finite integrals, which can be solved numerically.

When the specimens under investigation have complex geometries, numerical methods represent the only viable approach for understanding the multiple reflections and diffractions of the ultrasonic waves within the component. Among the many numerical methods simulating the interaction of acoustic surface waves with discontinuities, the finite difference method (FDM) has been most widely applied to geophysical problems as well as nondestructive material evaluation. Saffari and Bond[12] investigated the interaction of acoustic waves at steps and slots; Fuyuki and Matsumoto[13] dealt with reflection and transmission coefficients at a trench with variable width. The scattering at a surface-breaking crack was investigated using FDM by Hirao *et al.*,[14] Scandrett and Achenbach,[15] and Harker.[16] Wu *et al.*[17] studied the transient diffracted wave field of a plate containing a normal surface crack using a finite difference formulation with staggered grid, as proposed by Madariaga.[18] Further numerical methods used for the investigation of scattering at surface

[a]Electronic mail: masserey@imes.mavt.ethz.ch
[b]Electronic mail: mazza@imes.mavt.ethz.ch

discontinuities are the boundary element method (BEM)[19,20] and the finite element method (FEM).[21] Liu *et al.*[22] proposed a combined boundary integral and finite element technique to analyze the transient scattering at a surface crack. Sohn and Krishnaswamy[5] used a hybrid model based on the mass-spring lattice model (MSLM)[23] for elastic wave propagation combined with a FDM formulation of the boundary conditions.

The interaction of Rayleigh waves with surface defects has been studied experimentally through investigations that involve the far-field evaluation of the scattered field. In most cases a measurement probe of finite size is applied at locations far from the defect, resulting in an average over the significantly large surface area of the measurement transducer. Only few experimental works were conducted focusing on the near-field scattering of Rayleigh waves at a surface crack. Vu and Kinra[24] reported near-field measurements using a small receiver in order to approximate a pointwise displacement measurement on the free surface. A nonconducting technique by means of laser interferometry measurements in close proximity to surface cracks was applied by Cooper *et al.*[25] In a recent work Blackshire and Sathish[26] presented an experimental observation of the intensification of the ultrasonic scattered field at a surface crack using optical interferometric detection.

In this paper a comprehensive approach is presented with analytical and numerical calculations of the near-field scattering of a Rayleigh wave at a surface crack complemented by detailed experimental observations. This approach, applied on a standard scattering problem, allows validating specific modeling techniques and identifying parameters to be used for the characterization of surface cracks. These results are relevant for the numerical analysis of diffraction mechanisms in complex specimens, which are required to develop inversion schemes for crack characterization in engineering components.

The analytical solution of the transient scattered near field of a Rayleigh wave at a normal surface crack is obtained using an extension of the steady-state exact solution proposed by Mendelsohn *et al.*[10] and is presented in Sec. II. Section III introduces the finite difference code used for the FDM calculations. The FDM results are validated in the near-field regime on the basis of the analytical calculations and the experimental results. The experiments, described in Sec. IV, are performed on steel specimens with narrow slots of different depths. Pointwise measurements of the out-of-plane scattered displacement field are performed by means of a laser interferometer mounted on a positioning system. This noncontacting scanning procedure leads to a complete displacement field image in the crack near field with high spatial resolution.

The FDM results are compared with the analytical solution and the experimental data in Sec. V. This approach allows evaluating the influence of the spatial discretization and the effectiveness of specific crack tip modeling techniques. The analysis of the near-field scattering is made possible by a procedure, which allows filtering the Rayleigh-wave pulse from the other wave modes scattered at the defect. The near-field scattering process is analyzed with respect to (*i*) the stress near field at the crack tip, (*ii*) Rayleigh wave transmission and reflection coefficients, (*iii*) the time delay of the transmitted Rayleigh pulse due to the presence of the defect, and (*iv*) the surface displacement in the near field. The parameters in (*ii*) and (*iii*) are particularly important since they can be used for crack characterization.[27] The comparison of the displacement near field shows good agreement between measurements, simulation, and analytical solution. The present work also highlights differences between the scattering at narrow slots and cracks which have to be considered when developing nondestructive characterization techniques based on experiments with artificial cracks or slots.

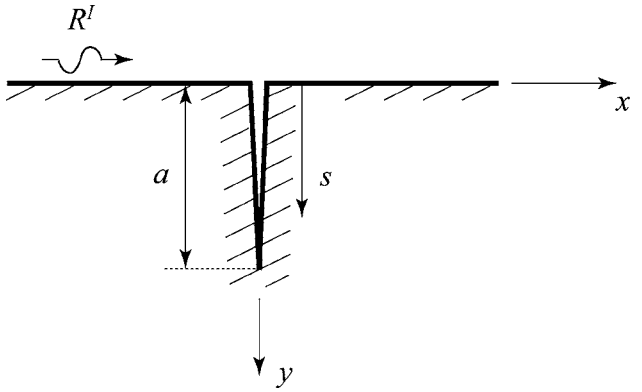

FIG. 1. Incident surface wave at a surface crack of depth *a*.

II. ANALYTICAL SOLUTION

The two-dimensional model of a normal surface crack of depth a in a homogeneous, isotropic, linearly elastic half-plane is shown in Fig. 1. The origin of the coordinate system is located at the mouth of the crack and plane strain deformation is assumed. The incident time-harmonic surface wave R^I propagating in the positive x direction generates surface tractions on the faces of the crack. To satisfy the stress-free boundary conditions

$$\sigma_{xx} = \sigma_{xy} = 0, \quad x = 0, \quad 0 \leqslant y \leqslant a, \tag{1}$$

a scattered wave must occur. Following the work of Mendelsohn *et al.*,[10] the scattered field in the half plane is decomposed into a symmetric and an antisymmetric field relative to $x=0$. The symmetric problem is related to mode-I crack deformation and the antisymmetric problem to mode-II deformation. The boundary conditions on the half-plane surface $y=0$ for both symmetric and antisymmetric fields are

$$\sigma_{yy} = \sigma_{xy} = 0. \tag{2}$$

Solutions to the displacement equations of motion in the two-dimensional half plane can be obtained in the form of Fourier transforms.[28] Application of the boundary conditions [Eqs. (1) and (2)] leads to two uncoupled singular integral equations, which are solved numerically using a collocation scheme. The exact representations of the components of the symmetric and antisymmetric fields in the form of finite integrals over the crack length are given by Mendelsohn *et al.*[10] for a steady-state time-harmonic elastodynamic problem. The total displacement field is obtained by addition of

the incident field $\mathbf{u}^I$ and both symmetric ($\mathbf{U}_s$) and antisymmetric ($\mathbf{U}_a$) fields:

$$\mathbf{u}(X,Y) = \mathbf{u}^I + \int_0^1 \int_0^\infty (\mathbf{U}_s(X,Y,\zeta,S) + \mathbf{U}_a(X,Y,\zeta,S))\, d\zeta\, dS. \tag{3}$$

In Eq. (3) the following dimensionless variables have been used:

$$X = \frac{x}{a}, \quad Y = \frac{y}{a}, \quad S = \frac{s}{a}, \tag{4}$$

where $s \in [0,a]$ is a running variable over the crack length (see Fig. 1) and $\mathbf{U}_s$ and $\mathbf{U}_a$ are two-dimensional vector functions. The displacement components are evaluated numerically in the complex ζ plane using a standard Gauss-Legendre quadrature. The integral contour proposed by Achenbach *et al.*[11] is applied and the upper integration limit for the variable ζ is chosen on the basis of convergence properties of the numerical integration.

The relevant stress fields σ_{xx}, σ_{yy}, and σ_{xy} are calculated analytically in terms of displacement derivatives using Hooke's law and the kinematic relations. The total steady-state stress field can be written in a similar way as the displacement field in Eq. (3). For $X=0$ the integrand of the scattered stress field has terms of $O(1)$ as $\zeta \to \infty$ and consequently does not converge. The numerical solution evaluated using Gauss-Legendre quadrature is a function of the upper integration limit $\zeta_{\max}$ and oscillates around the exact value. Following the idea of Mendelsohn *et al.*,[10] the first term of the asymptotic expansion of the integrand for large ζ is subtracted, so that the integral converges, and is subsequently evaluated by means of the following Fourier representations of generalized functions:

$$\int_0^\infty \cos(KY\zeta)\sin(KS\zeta)d\zeta = \frac{1}{K}\frac{S}{S^2 - Y^2},$$
$$\int_0^\infty \sin(KY\zeta)\sin(KS\zeta)d\zeta = \frac{\pi}{2K}(\delta(S-Y) - \delta(S+Y)), \tag{5}$$

where δ is the delta function. In this way the solution of the stress field at $X=0$ can be evaluated numerically for $Y>1$. For $Y<1$ the Fourier representations have a singularity at $S=Y$; the integral over S does not converge so that the stress field can only be obtained for $y>a$.

The analytical solution of Mendelsohn *et al.*[10] for a steady-state time-harmonic excitation has been extended here to the time domain for any excitation signal $f(t)$. To this end, the discrete Fourier coefficients $F(f_i)$ of the time series are computed using FFT (fast Fourier transform). The steady-state displacement fields $\mathbf{u}(f_i)$ or stress fields $\sigma(f_i)$ are calculated at any observation point in the frequency domain for every discrete frequency f_i, multiplied by the Fourier coefficients, and the transient field is finally synthesized by inverse Fourier transform.

III. NUMERICAL SIMULATION

A. Finite difference formulation

Second-order finite difference methods (FDMs) are used to simulate the two-dimensional scattering of an incident surface wave at a surface crack. The equations of momentum conservation and the stress-strain relations for a two-dimensional, isotropic, linear elastic medium are discretized on a Cartesian, staggered grid. This type of grid, first proposed by Madariaga,[18] has the useful property to minimize the number of variables per grid cell. As in the analytical solution of the scattering problem, plane strain wave propagation is assumed. The stress-free boundary conditions at the material boundaries are imposed by adding a fictitious layer just outside the free surface and assigning specific values to the variables of the "pseudonodes" of the fictitious layer so to give zero stress at the material surface. The usual criteria[29] must be satisfied in order to obtain a stable and accurate simulation. The accuracy of the FDM simulation with respect to the spatial discretization is discussed further below in Sec. V.

The initial conditions are defined by imposing the whole displacement field in the two initial time steps. The input displacements at every node are evaluated using FFT as described by Munasinghe.[30] In this work a sinusoid multiplied by a Hanning window is chosen as the excitation signal. The number of cycles within the Hanning window is chosen to obtain either a narrow-band signal for investigations in frequency domain or a short-time pulse for evaluations in time domain.[27] However, the finite difference code is appropriate for any broadband pulses as long as the spatial sampling is chosen as a function of the smallest Rayleigh wavelength corresponding to the maximum frequency present in the spectrum. This allows us to minimize the effect of the numerical dispersion and therefore to avoid a distortion of the pulse.

B. Implementation of the surface crack

Two different grid configurations have been used to simulate the scattering at an open, vertical surface crack with traction-free surfaces. In the first one the crack is approximated by a slot with a flat end and a width of $2\Delta x$ and the stress-free boundary conditions at the surfaces of the defect are implemented by introducing pseudonodes for the corresponding stress components, as shown in Fig. 2(a).

In the second grid configuration the crack is implemented with a zero small width [see Fig. 2(b)]. The crack faces are traction-free and have no interaction so that the corresponding displacement u has to be split into a left component u_l and a right component u_r. The displacement components are evaluated using the equilibrium condition in the x direction and considering the boundary conditions, yielding the following equations:

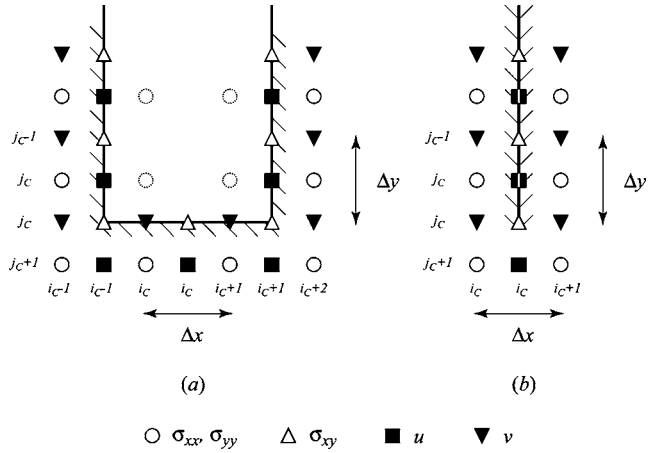

FIG. 2. Discretization in the vicinity of the crack tip using a staggered grid: (a) slot with a width of $2\Delta x$ and (b) crack with an infinitely small width.

$$u_l^{n+1}(i_C,j) = -\frac{(\Delta t)^2}{\rho}\frac{2\sigma_{xx}^n(i_C,j)}{\Delta x} + 2u_l^n(i_C,j) - u_l^{n-1}(i_C,j),$$

$$u_r^{n+1}(i_C,j) = \frac{(\Delta t)^2}{\rho}\frac{2\sigma_{xx}^n(i_C+1,j)}{\Delta x} + 2u_r^n(i_C,j) - u_r^{n-1}(i_C,j), \tag{6}$$

where $1 \leqslant j \leqslant j_C - 1$ (see Fig. 2) and n represents the time step. Hirao *et al.*[14] implemented a crack with infinitely small width using a standard grid and assuming $\sigma_{xx}=\sigma_{xy}=0$ at the crack tip. In the present work the use of a staggered grid leads to a vertical mismatch of $\Delta y/2$ between normal stress and shear stress, as can be seen in Fig. 2(b). The shear stress $\sigma_{xy}(i_C,j_C)$ is therefore evaluated at the crack tip where the stress field is singular. Two alternatives are proposed for the calculation of the shear stress component at the crack tip. In the first one, denoted by crack model type 1, the shear stress is assumed to be zero at the crack tip. The displacement components u_l and u_r at $j=j_C$ are calculated using Eq. (6). This leads to a transition interval $y \in [a, a+\Delta y/2]$ beyond the crack tip where transverse slip can occur ($\sigma_{xy}=0$). In the second crack model, called crack model type 2, the shear stress at the crack tip is calculated on the basis of the displacement near field as described by the following equation, discretized according to Fig. 2(b):

$$\sigma_{xy}(i_C,j_C) = \mu\left(\frac{u(i_C,j_C+1) - (u_l(i_C,j_C) + u_r(i_C,j_C))/2}{\Delta y} + \frac{v(i_C+1,j_C) - v(i_C,j_C)}{\Delta x}\right). \tag{7}$$

This results in a transition region in the interval $y \in [a - \Delta y/2, a]$ with vanishing normal stress σ_{xx} and shear stress described by Eq. (7). The nonvanishing shear stress at the tip of the crack has to be incorporated in the equilibrium condition in the x direction. Therefore the term

$$\frac{\Delta t^2}{\rho}\frac{\sigma_{xy}(i_C,j_C)}{\Delta y} \tag{8}$$

has to be added to Eq. (6) for the evaluation of the displacement components u_l and u_r at $j=j_C$. In summary, three different crack models are investigated here: the slot model, crack model type 1, and crack model type 2. Comparison of FDM calculations with analytical solutions and experimental results allows evaluating each modeling approach.

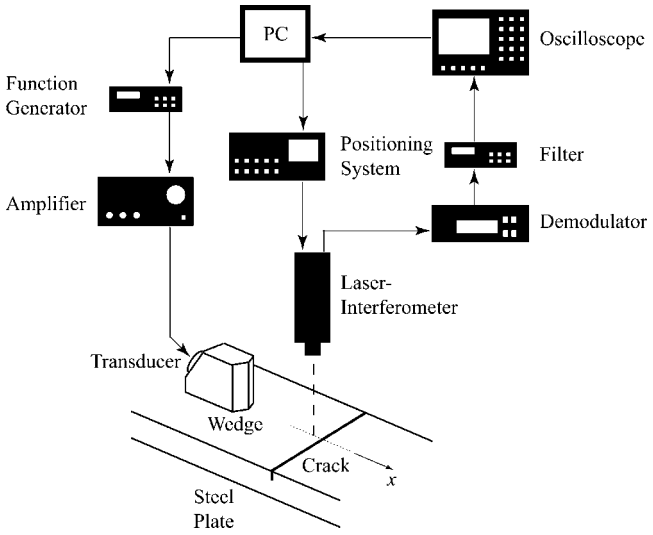

FIG. 3. Schematic representation of the experimental setup.

IV. EXPERIMENTAL SETUP

A schematic representation of the experimental setup is shown in Fig. 3. The samples are 10-mm-thick steel plates (St37-2) with a size of 30 by 200 mm. There were 0.2- to 1-mm-deep slots produced by electrical discharge machining (EDM) with a wire of 0.1-mm diameter. The surface wave is excited on the steel surface using standard angle beam transducers and wedges. Voltage proportional to the desired waveform is applied to the transducer. The excitation consists of a sinusoid multiplied by a Hanning window. Center frequencies of 2.25 to 5 MHz are used, resulting in Rayleigh wavelength of $\lambda=1.33$ mm to $\lambda=0.6$ mm. The experimental configuration is selected so that the incident surface wave reaches the crack perpendicularly to the crack length direction. The measurements are performed in the plate center so that plane strain deformation can be assumed.

A heterodyne laser interferometer is used for single point measurement of the out-of-plane surface displacement with high sensitivity and high spatial resolution. The measurement spot of the laser beam has a diameter below 50 μm. A complete displacement field image is obtained by moving the laser interferometer parallel to the surface of the specimen by means of a positioning system. For a detailed measurement of the near-field scattering process, the spatial resolution and the step size are typically 30 times smaller than the wavelength λ of the Rayleigh wave. The demodulator output is band-pass filtered around the center frequency and averaged in a digital oscilloscope. The measured time series are stored in a computer for further analysis.

V. RESULTS AND DISCUSSION

A. Analysis of the stress field at the crack tip

As described in Sec. II, the stress field on the crack line ($x=0$) can be calculated analytically for $y>a$. Figure 4 illus-

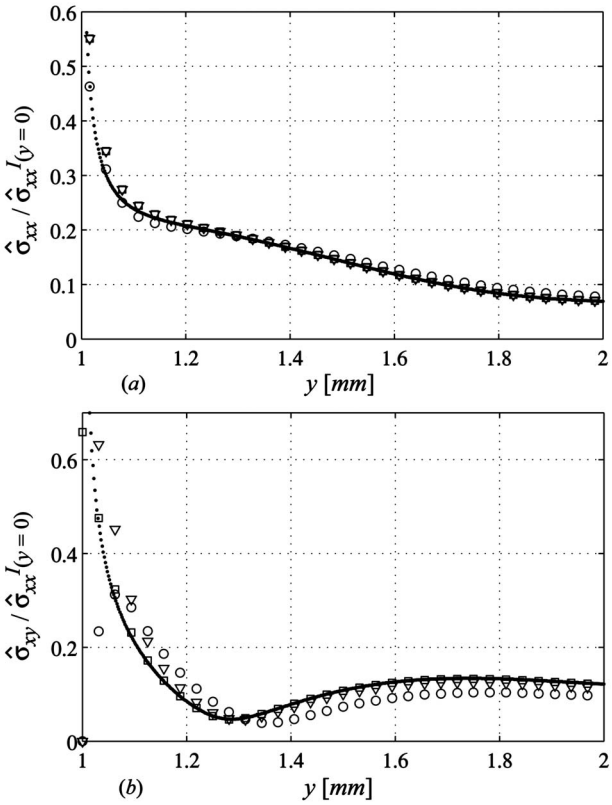

FIG. 4. Stress field singularity below the crack tip ($x=0$, $y>a$) normalized with respect to the normal stress amplitude of the incident field at the surface, $f_0=3$ MHz, $\lambda=1$ mm, $a/\lambda=1$: analytical solution (dotted line), simulation with a slot (open points), simulation using crack model type 1 (triangles) and type 2 (squares): (a) normal stress and (b) shear stress.

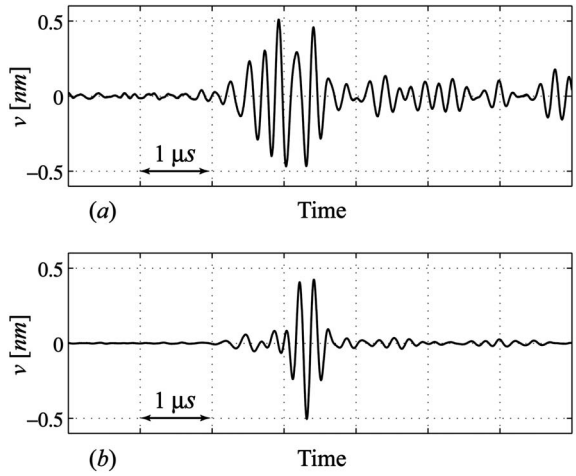

FIG. 5. Time series of the measured out-of-plane displacement v, $f_0=5$ MHz, four cycles, crack depth $a=1$ mm: (a) measurement at $x=2$ mm and (b) average of 31 measurements from $x=2$ mm to $x=5$ mm after phase shifting and addition.

trates the amplitude of normal stress σ_{xx} and shear stress σ_{xy} at $x=0, y>a$ for a 1-mm-deep crack using an input signal with frequency $f_0=3$ MHz ($a/\lambda=1$). The evaluation using the steady-state analytical solution for a time-harmonic excitation at frequency f_0 (solid points) is characterized by the stress field singularity at the crack tip.

The simulations are performed using a signal with eight cycles and center frequency $f_0=3$ MHz, so as to obtain a narrow-band excitation that closely approximates the steady-state conditions of the analytical solution. The time series of the stress field are calculated at every node on the crack line and the amplitude is extracted at the center frequency using FFT. The normal stress amplitude [Fig. 4(a)] calculated using crack model types 1 and 2 agrees very well with the analytical values. The simulation of the normal stress field using the slot model shows a good agreement as well. The results of the amplitude of the shear stress field are presented in Fig. 4(b). The simulation of the shear stress using a crack tip of type 2 (squares) shows an excellent agreement with the analytical solution, of course with the exception of the shear stress value at the crack tip, which cannot be infinite in the simulation. The evaluation of the simulated shear stress obtained with a crack tip of type 1 (triangles) leads to a slight shift of the amplitude curve towards the positive y direction, resulting in an apparent deeper crack. Clear differences can be seen between the shear field calculated with the slot model as compared with the other solutions: in the near field of the slot model (open points) the shear stress diminishes and vanishes at the slot tip according to the boundary conditions on the flat end. The influence of the approximations in the stress field calculations from the different crack model types on the relevant scattering parameters is analyzed in the following section.

B. Comparison of the scattering parameters in the near field

In the near field of the crack the reflected and transmitted Rayleigh pulses are superimposed with other wave modes scattered at the mouth or the tip of the crack and are therefore difficult to identify. Figure 5(a) illustrates a point measurement of the transmitted out-of-plane displacement field for a 1-mm-deep slot. The Rayleigh pulse with a frequency $f_0=5$ MHz and four cycles is hardly recognizable. In order to avert this problem, a method based on the nondispersive characteristics of the Rayleigh wave propagation[27] is applied here. The field variables are calculated or measured for all grid points in the near field of the crack. The transmitted Rayleigh wave is enhanced by (*i*) selecting a reference point after the crack, (*ii*) phase shifting the time series of the successive points with the predicted Rayleigh wave velocity, so that the Rayleigh wave reaches all the points at the same time, and (*iii*) summing the resulting time series. Figure 5(b) shows the result using 31 points of measurement. A strong enhancement of the transmitted Rayleigh pulse can be observed as well as a cancellation of the majority of the other modes. This novel approach has similarities with the delay-line systems commonly used for beam forming in ultrasound phased-array imaging equipments.[31] The signal thus obtained is used for the calculation of the amplitude coefficients and the time delay of the transmitted surface wave. The same approach is applied to the reflected field for the evaluation of the reflection coefficients.

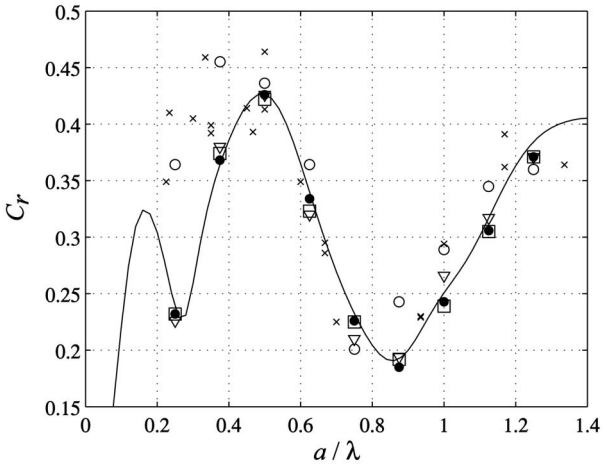

FIG. 6. Reflection coefficient C_r at the surface crack versus a/λ: analytical solution in the far field (solid line), analytical solution in the near field (solid points), simulation with a slot (open points), simulation with crack model type 1 (triangles) and type 2 (squares), and measurements (crosses).

1. Reflection and transmission coefficients

Figures 6 and 7 show the reflection and transmission coefficients for different ratios of crack depth to Rayleigh wavelength. The solid line represents the coefficients in the far field for a harmonic excitation calculated according to the steady-state analytical solution. The solid points are the results of the transient analytical solution in the near field which have been obtained using the enhancement procedure described previously. The agreement with the solid line can be considered as a validation of the proposed enhancement procedure for near-field analysis. The scattering simulation has been performed using the slot model (open points), crack model type 1 (triangles), and crack model type 2 (squares). For very short cracks ($a/\lambda=0.25$), the results of the simulation with the slot model differ greatly from the analytical solution. This discrepancy can be attributed to the fact that in this case the depth and width of the slot are of the same order of magnitude, so that the slot becomes a two-dimensional feature. The deviation of the shear-stress curve at the crack tip using crack model type 1 (described in the previous subsection) influences the simulation results for shorter cracks ($a/\lambda<0.3$) and results in a clear deviation of the calculated transmission coefficient (Fig. 7). The influence of the crack tip modeling approach on the energy distribution among the diffracted modes can be seen also for ratios of the order $a/\lambda=1$, where the results using the slot model and crack model type 1 differ from the analytical results. As expected from the analysis of the stress near-field approximation, the coefficients obtained from the simulations with the shear stress at the crack tip calculated on the basis of the displacement near field (crack model type 2) agree to a great extent with the analytical solution over the whole range of a/λ.

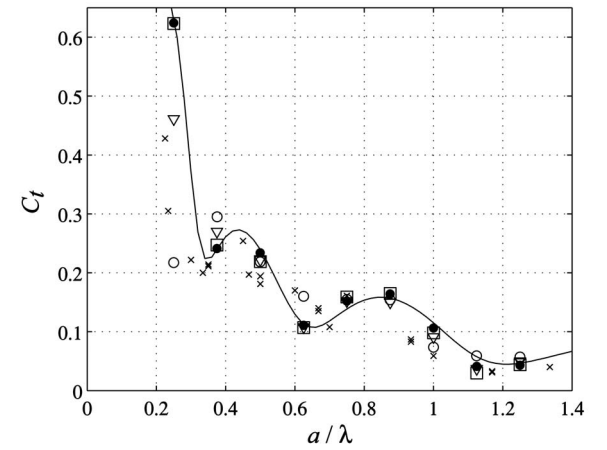

FIG. 7. Transmission coefficient C_t at the surface crack versus a/λ: analytical solution in the far field (solid line), analytical solution in the near field (solid points), simulation with a slot (open points), simulation with crack model type 1 (triangles) and type 2 (squares), and measurements (crosses).

The results of the experiments conducted using different combinations of excitation frequencies and slot depths are reported in Figs. 6 and 7 (crosses). In the measurements the incident displacement field is characterized by an amplitude attenuation in the far field of the excitation source. This attenuation strongly depends on the coupling and the pressure distribution of the contact surface between angle probe and specimen and is therefore difficult to quantify precisely. The measurement of the parameters in the near field of the crack enables us to minimize the impact of the amplitude attenuation on the surface scattering coefficients and to obtain results that are directly comparable with the theoretical values. The enhancement procedure described previously for the analysis of the near-field calculation results has been applied also to the experimental data in order to identify reflected and transmitted Rayleigh waves and thus determine the corresponding reflection and transmission coefficients. For $a/\lambda>0.5$ the agreement between experiments and analytical solution is good. For smaller defects the experimental values diverge from the analytical solution and approach the FDM results obtained with the slot model. These results represent an indication of the difference in the scattering field at a slot with respect to a crack, when the width of the slot is of the same order of magnitude as its depth. The differences in experimental C_r and C_t values at similar a/λ ratios are due to the fact that the measurements have been performed with different frequencies on slots with a constant width $w=0.1$ mm. This leads to different base-width-to-depth ratios w/a for measurements with a similar ratio of crack depth to wavelength a/λ.

2. Time delay of the transmitted Rayleigh wave

Figure 8 shows the time delay of the transmitted wave as a function of the ratio of crack depth to wavelength. It is obtained by (*i*) computing the cross correlation between incident and transmitted Rayleigh wave and (*ii*) calculating the envelope of the correlation function using Hilbert transformation.[27] The maximum of the envelope leads to the measured time-of-flight between incident and transmitted pulses. The time delay Δt is obtained after subtraction of the undisturbed propagation time along the surface and corresponds to the delay due to the presence of the defect. The diagram of Fig. 8, similar to the curve obtained by Hirao *et al.*,[14] can be used for sizing of cracks in the range $a/\lambda \in [0.7, 1.5]$.[27] The narrow-band approach yields negative time-delay values in the short-crack range. In reality the

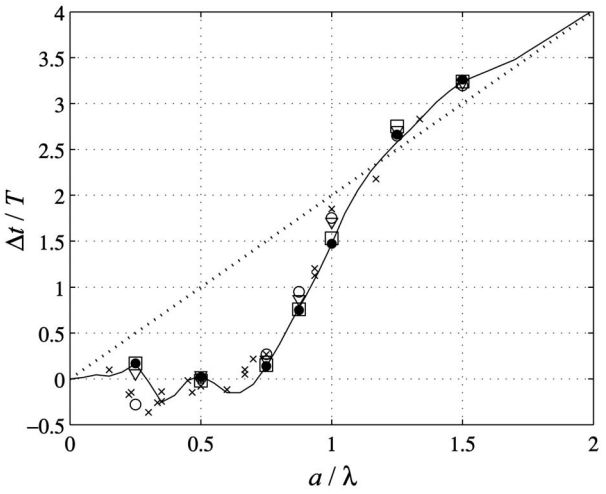

FIG. 8. Normalized time delay versus normalized crack depth and asymptote (dotted line), using a four-cycle excitation signal: analytical solution in the far field (solid line), analytical solution in the near field (solid points), simulation with a slot (open points), simulation with crack model type 1 (triangles) and type 2 (squares), and measurements (crosses).

transmitted wave is characterized by a negative phase shift in this range.[13] The evaluation of the time delay using the envelope of the cross correlation between incident and transmitted Rayleigh pulses leads to these apparent negative time-delay values. A detailed analysis of the starting time of incident and transmitted pulses shows that, as expected, the transmitted Rayleigh pulse does not exist behind the crack until the incident Rayleigh pulse has reached the defect.

The simulations with crack model type 2 agree to a great extent with the analytical values. The deviation of the simulations with crack model type 1 and a slot model with respect to the analytical solution are evident also in the case of the time delay calculation. The measurements, denoted here by crosses, show a good agreement with the analytical curve for $a/\lambda > 0.7$, i.e., in the range in which the time delay can be used for crack sizing. As for the surface scattering coefficients, a discrepancy between the experimental results and the analytical solution can be observed for smaller defects. Here the experimental values approach the time delay obtained from the scattering simulation with the slot model. It is interesting to note that measurement errors in the time-of-flight and therewith the scattering of the experimental time delay values are smaller than in the case of the coefficients C_r and C_t. This is due to the fact that the field attenuation (which affects the amplitude measurements) has a negligible influence on measurements in the time domain and the time parameters are therefore less sensitive to the variability of the experimental conditions.

3. Influence of the spatial discretization on the scattering parameters

The dependence of the results of second-order FDM simulations on the spatial discretization has been widely investigated, with particular attention to the so-called "numerical dispersion." As a general rule a minimum of ten nodes are needed inside a wavelength for correct modeling.[32] In the case of Rayleigh wave scattering simulations the depth dependence of the displacement field has to be considered so that the sampling of the wavelength found in the literature varies from 30 nodes by Munasinghe and Farnell[30] to 48 nodes by Blake and Bond.[33] The dispersion curve of the numerical propagation velocity as a function of the discretization parameter $\Delta x/\lambda$, normalized with respect to the Rayleigh wave velocity c_R, is shown in Fig. 9 (open points). The curve converges toward unity for a discretization parameter going to zero. All the results of the present work have been calculated with 32 nodes per Rayleigh wavelength. By this spatial sampling, corresponding to the minimum values plotted in Fig. 9 ($\Delta x/\lambda = 0.031$), the error in the numerical Rayleigh wave velocity is below 0.3%.

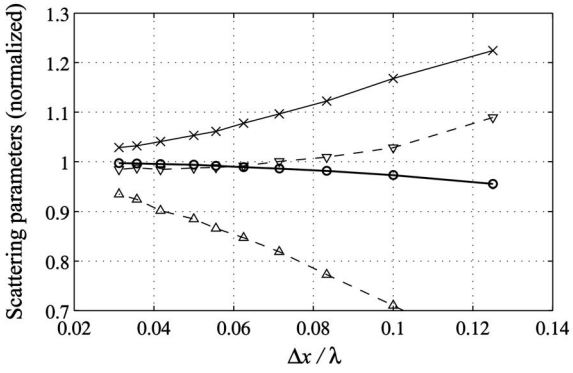

FIG. 9. Normalized numerical dispersion curve and normalized scattering parameters versus discretization parameter $\Delta x/\lambda$, simulation using crack model type 2, $a/\lambda = 1$: phase velocity c_R (open points), reflection coefficient (triangle-down), transmission coefficient (triangle-up), and time delay (crosses).

In addition to the phase velocity, usually taken as the relevant parameter for the numerical accuracy of FDM codes in the literature, the influence of the discretization on the scattering process is investigated here with respect to the surface scattering coefficients and the time delay of the transmitted pulse. Simulations have been performed for various discretization parameters $\Delta x/\lambda$ using a ratio of crack depth to wavelength $a/\lambda = 1$ and the crack model with the shear stress at the crack tip calculated on the basis of the displacement near field (crack model type 2). The calculated parameters have been normalized with their corresponding analytical values. Thereby, the error in the phase velocity has been taken into account by evaluating the parameters with respect to the apparent propagation velocity. The parameters converge as the discretization parameter decreases. The largest error is found for the coefficient of transmission (triangle-up), which could be more accurately calculated by using a higher spatial sampling. The reflection coefficient (triangle-down) converges toward a value about 1.5% smaller than the analytical one, this being in line with the lower reflection coefficient calculated with crack model type 2 with respect to the analytical solution (compare square and solid point for $a/\lambda = 1$ in Fig. 6). The deviation of the numerical parameters from the corresponding analytical values is translated in terms of error in crack size evaluation in Fig. 10. The values of apparent crack depth normalized with respect to the crack depth (a_{app}/a) are calculated as function of the discretization parameter for the reflection and transmission coefficients as

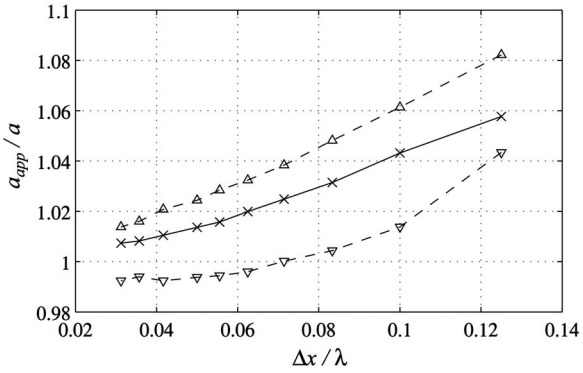

FIG. 10. Apparent crack depth normalized with respect to the crack depth versus discretization parameter $\Delta x/\lambda$, simulation using crack model type 2, $a/\lambda=1$: crack depth extracted from the reflection coefficient (triangle-down), the transmission coefficient (triangle-up), and the time delay (crosses).

well as for the time delay. The relative errors are small, with maximum depth overestimation of about 6% for a sampling rate of 10 nodes per wavelength. The apparent crack size decreases for all scattering parameters with a smaller grid size and the errors for 32 nodes per Rayleigh wavelength are in the order of 1%. The errors due to spatial discretization are, for all scattering parameters, smaller than the error in crack sizing which arises if a crack model with vanishing shear stress at the crack tip (crack model type 1) is used, for which the deviation between apparent and real crack depth is in the order of 5% (see Figs. 6–8 for $a/\lambda=1$).

C. Analysis of the surface displacement in the near field

In the last part of this section the amplitude of the surface displacement field in the vicinity of the crack is investigated. Analytical and numerical results are compared with measurements performed on a line perpendicular to the machined slots, as described in Sec. IV. The measured amplitudes are normalized with respect to the amplitude curve of the Rayleigh wave on an undamaged sample in order to eliminate the characteristic attenuation of the sound field with distance from the excitation source. The excitation consists of a sinusoid in a Hanning window with a central frequency $f_0=2.25$ MHz and eight cycles. The corresponding Rayleigh wavelength is $\lambda=1.33$ mm. The measurements are performed using a step size of 40 μm. A grid with $\Delta x=50$ μm is used in the FDM simulations. The amplitude of the out-of-plane displacement component is extracted at center frequency using FFT and plotted for each point of the grid.

Figure 11 shows the scattered field for a ratio $a/\lambda=0.75$, the crack mouth being at $x=0$. Close to the crack the constructive and destructive interferences of the incident and scattered fields yield a characteristic hill and valley pattern. The high amplitude directly at the crack results from the scattering at the traction-free crack faces. On the right-hand side of the crack the displacement is significantly lower and converges with increasing distance from the crack to an amplitude corresponding to the far-field transmission coefficient. Measurement, simulation, and analytical calculation

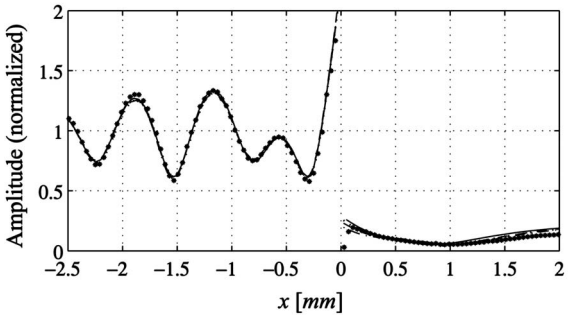

FIG. 11. Scattered field in the vicinity of a surface crack, $f_0=2.25$ MHz, $a/\lambda=0.75$: measurements (asterisk), analytical solution (solid line), slot simulation with $w/a=0.1$ (dash-dot line), and simulation with crack model type 1 (dashed line) and type 2 (dotted line).

show an excellent quantitative agreement and are hardly distinguishable. The measured and simulated scattered field at a narrow slot with a width $w=0.1$ mm ($w/a=0.1$) is very similar to the one at a crack with infinitely small width (analytical solution and simulation with both crack model types 1 and 2).

A smaller ratio of $a/\lambda=0.15$ is selected for the next comparison. For clarity purposes the evaluation is limited to the interference domain in front of the crack. Figure 12(a) shows a good agreement between measurements (asterisk) and simulation (dash-dot line) with a slot model (0.1 mm width, corresponding to a ratio of width to depth $w/a=0.5$). Figure 12(b) illustrates the comparison between analytical solution and scattering simulation using crack model types 1 and 2. The analytical near field (solid line) and the simulated near field using crack model type 2 (dotted line) are almost identical. A slight difference is found in the vicinity of the crack for the simulation with crack model type 1 (dashed line). The clear deviation between the interference pattern at

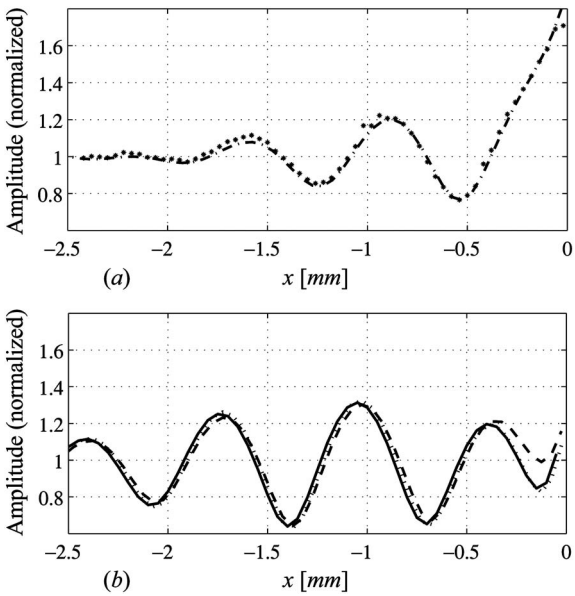

FIG. 12. Scattered field in the vicinity of a surface crack, $f_0=2.25$ MHz, $a/\lambda=0.15$: (a) measurements (asterisk) and slot simulation with $w/a=0.5$ (dash-dot line) and (b) analytical solution (solid line) and simulation with crack model type 1 (dashed line) and type 2 (dotted line).

a slot and a crack [compare Figs. 12(a) and 12(b)] is due to a significant discrepancy between reflection coefficients and phase shifts, leading to a smaller amplitude of the domain of interference and a shift of the extrema positions relative to the x axis.

VI. CONCLUSIONS

The reliability of FDM simulations of the Rayleigh wave near-field scattering at a surface crack was analyzed by comparison with analytical results and experimental data. The analytical solution by Mendelsohn *et al.*[10] has been extended here to an arbitrary transient excitation function so as to enable a direct comparison with the numerical and experimental results. The evaluation of the scattering parameters in the near field has been possible thanks to an enhancement technique (applied to both theoretical and experimental data) that allows filtering the Rayleigh wave from the other wave modes scattered at the defect. Different modeling approaches were applied for FDM simulation of a surface crack and their effectiveness evaluated with respect to different parameters. The calculation of the shear stress at the crack tip based on the displacement near field (crack model type 2) proved most reliable with excellent agreement to the exact solution in terms of stress and displacement fields and scattering coefficients. Good agreement between FDM results and analytical and experimental values demonstrates that the stability criteria applied in the numerical simulation leads to a faithful reproduction of the scattered near field.

The investigation of the influence of the spatial discretization on the scattering process at a crack with $a/\lambda=1$ has shown that (*i*) the errors in the calculation of the scattering parameters are in the range of 20% for a sampling rate of 10 nodes per wavelength and reduce to about 5% with 30 nodes per wavelength and (*ii*) when crack characterization is based on the scattering coefficients, the corresponding errors in crack sizing are in the order of 1% (for 30 nodes per wavelength).

The error in crack sizing that arises when a vanishing shear stress is imposed at the crack tip in the FDM simulation (crack model type 1) instead of calculating the shear stress at the crack tip based on the displacement near field (crack model type 2) is about 5%. It can be concluded, therefore, that the selection of the crack tip modeling technique is more relevant for crack sizing purposes than the enhancement of the spatial sampling rate.

The time delay of Rayleigh wave transmission appears as the most suitable parameter for crack characterization purposes due to the relative insensitivity of the measured values on the variability of the experimental conditions. The time delay approach allows characterizing the crack depth down to a ratio $a/\lambda=0.7$, which corresponds to a minimum crack size of about 0.4 mm at the maximum frequency applied in this work.

The comparison of theoretical and experimental results has shown that narrow slots lead to a scattered field representative to the one of a crack when the slot-width-to-depth ratio is smaller than 0.1. For larger values, relevant differences were observed between the slot and crack near fields. This limitation has to be taken into consideration when using narrow slots as "artificial cracks" for development of QNDE techniques of crack characterization.

The FDM model proposed and validated with the results presented in this paper will be used in future work as the basis for analyzing scattering in specimens with complex geometry for which no analytical solution is available and for development of inversion schemes for crack sizing in mechanical components.

[1] J. D. Achenbach, "Quantitative nondestructive evaluation," Int. J. Solids Struct. **37**, 13–27 (2000).
[2] M. G. Silk, "The transfer of ultrasonic energy in the diffraction technique for crack sizing," Ultrasonics **17**, 113–121 (1979).
[3] C. M. Scala and S. J. Bowles, "Laser ultrasonics for surface-crack depth measurement using transmitted near-field Rayleigh waves," in *Review of Progress in QNDE*, AIP Conference Proceedings 509, edited by D. O. Thompson and D. E. Chimenti (AIP, New York, 2000), Vol. **19**, pp. 327–334.
[4] J. C. Aldrin, J. Knopp, J. L. Blackshire, and S. Sathish, "Models and methodology for the characterization of surface-breaking cracks using an ultrasonic near-field scattering measurement," in *Review of Progress in QNDE*, AIP Conference Proceedings 700, edited by D. O. Thompson and D. E. Chimenti (AIP, New York, 2004), Vol. **23**, pp. 87–94.
[5] Y. Sohn and S. Krishnaswamy, "Interaction of a scanning laser-generated ultrasonic line source with a surface-breaking flaw," J. Acoust. Soc. Am. **115**, 172–181 (2004).
[6] J. D. Achenbach, A. K. Gautesen, and D. A. Mendelsohn, "Ray analysis of surface-wave interaction with an edge crack," IEEE Trans. Sonics Ultrason. **27**, 124–129 (1980).
[7] T. Kundu and A. K. Mal, "Diffraction of elastic waves by a surface crack on a plate," J. Appl. Mech. **48**, 570–576 (1981).
[8] H. S. Tuan and R. C. M. Li, "Rayleigh wave reflection from groove and step discontinuities," J. Acoust. Soc. Am. **55**, 1212–1217 (1974).
[9] D. A. Simons, "Reflection of Rayleigh waves by strips, grooves, and periodic arrays of strips or grooves," J. Acoust. Soc. Am. **63**, 1292–1301 (1978).
[10] D. A. Mendelsohn, J. D. Achenbach, and L. M. Keer, "Scattering of elastic waves by a surface-breaking crack," Wave Motion **2**, 277–292 (1980).
[11] J. D. Achenbach, L. M. Keer, and D. A. Mendelsohn, "Elastodynamic analysis of an edge crack," J. Appl. Mech. **47**, 551–556 (1980).
[12] N. Saffari and L. J. Bond, "Body to Rayleigh wave mode-conversion at steps and slots," J. Nondestruct. Eval. **6**, 1–22 (1987).
[13] M. Fuyuki and Y. Matsumoto, "Finite difference analysis of Rayleigh wave scattering at a trench," Bull. Seismol. Soc. Am. **70**, 2051–2069 (1980).
[14] M. Hirao, H. Fukuoka, and Y. Miura, "Scattering of Rayleigh surface waves by edge cracks: Numerical simulation and experiment," J. Acoust. Soc. Am. **72**, 602–606 (1982).
[15] C. L. Scandrett and J. D. Achenbach, "Time-domain finite difference calculations for interaction of an ultrasonic wave with a surface-breaking crack," Wave Motion **9**, 171–190 (1987).
[16] A. H. Harker, "Numerical modeling of the scattering of elastic waves in plates," J. Nondestruct. Eval. **4**, 89–106 (1984).
[17] T. T. Wu, J. S. Fang, and P. L. Liu, "Detection of the depth of a surface-breaking crack using transient elastic waves," J. Acoust. Soc. Am. **97**, 1678–1686 (1995).
[18] R. Madariaga, "Dynamics of an expanding circular fault," Bull. Seismol. Soc. Am. **66**, 639–666 (1976).
[19] C. Zhang and J. D. Achenbach, "Numerical analysis of surface-wave scattering by the boundary element method," Wave Motion **10**, 365–374 (1988).
[20] G. Hévin, O. Abraham, H. A. Pedersen, and M. Campillo, "Characterization of surface cracks with Rayleigh waves: A numerical model," NDT & E Int. **31**, 289–297 (1998).
[21] W. Hassan and W. Veronesi, "Finite element analysis of Rayleigh wave interaction with finite-size, surface-breaking cracks," Ultrasonics **41**, 41–52 (2003).
[22] S. W. Liu, J. C. Sung, and C. S. Chang, "Transient scattering of Rayleigh waves by surface-breaking and sub-surface cracks," Int. J. Eng. Sci. **34**, 1059–1075 (1996).
[23] H. Yim and Y. Choi, "Simulation of ultrasonic waves in various types of

elastic media using the mass spring lattice model," Mater. Eval. **58**, 889–896 (2000).
[24]B. Q. Vu and V. K. Kinra, "Diffraction of Rayleigh waves in a half-space. I. Normal edge crack," J. Acoust. Soc. Am. **77**, 1425–1430 (1985).
[25]J. A. Cooper, R. A. Crosbie, R. J. Dewhurst, A. D. W. McKie, and S. B. Palmer, "Surface acoustic-wave interactions with cracks and slots: a non-contacting study using lasers," IEEE Trans. Ultrason. Ferroelectr. Freq. Control **33**, 462–470 (1986).
[26]J. L. Blackshire and S. Sathish, "Near-field ultrasonic scattering from surface-breaking cracks," Appl. Phys. Lett. **80**, 3442–3444 (2002).
[27]B. Masserey and E. Mazza, "Characterization of surface cracks using Rayleigh waves," in *Review of Progress in QNDE*, AIP Conference Proceedings 760, edited by D. O. Thompson and D. E. Chimenti (AIP, New York, 2005), Vol. **24**, pp. 805–812.
[28]W. C. Luong, L. M. Keer, and J. D. Achenbach, "Elastodynamic stress intensity factors of a crack near an interface," Int. J. Solids Struct. **11**, 919–925 (1975).
[29]P. Fellinger, R. Marklein, K. J. Langenberg, and S. Klaholz, "Numerical modeling of elastic wave propagation and scattering with EFIT-elastodynamic finite integration technique," Wave Motion **21**, 47–66 (1995).
[30]M. Munasinghe and G. W. Farnell, "Finite difference analysis of Rayleigh wave scattering at vertical discontinuities," J. Geophys. Res. **78**, 2454–2466 (1973).
[31]G. F. Manes, C. Atzeni, and C. Susini, "Design of a simplified delay system for ultrasound phased array imaging," IEEE Trans. Sonics Ultrason. **30**, 350–354 (1983).
[32]J. Virieux, "P-SV wave propagation in heterogeneous media: Velocity-stress finite-difference method," Geophysics **51**, 889–901 (1986).
[33]R. J. Blake and L. J. Bond, "Rayleigh wave scattering from surface features: Wedges and down-steps," Ultrasonics **28**, 214–228 (1990).

A model for the dynamics of gas bubbles in soft tissue

Xinmai Yang[a] and Charles C. Church
National Center for Physical Acoustics, The University of Mississippi, University, Mississippi 38677

(Received 21 April 2005; revised 16 September 2005; accepted 17 September 2005)

Understanding the behavior of cavitation bubbles driven by ultrasonic fields is an important problem in biomedical acoustics. Keller-Miksis equation, which can account for the large amplitude oscillations of bubbles, is rederived in this paper and combined with a viscoelastic model to account for the strain-stress relation. The viscoelastic model used in this study is the Voigt model. It is shown that only the viscous damping term in the original equation needs to be modified to account for the effect of elasticity. With experiment determined viscoelastic properties, the effects of elasticity on bubble oscillations are studied. Specifically, the inertial cavitation thresholds are determined using R_{max}/R_0, and subharmonic signals from the emission of an oscillating bubble are estimated. The results show that the presence of the elasticity increases the threshold pressure for a bubble to oscillate inertially, and subharmonic signals may only be detectable in certain ranges of radius and pressure amplitude. These results should be easy to verify experimentally, and they may also be useful in cavitation detection and bubble-enhanced imaging. © *2005 Acoustical Society of America.* [DOI: 10.1121/1.2118307]

PACS number(s): 43.35.Wa, 43.80.Sh, 43.35.Ei [FD] Pages: 3595–3606

I. INTRODUCTION

Cavitation phenomena are very complicated due to the nonlinear oscillations of small bubbles and the interactions between these bubbles. In most cases, cavitation occurs in water, which is the most familiar fluid to us, and as a result, studies of bubble dynamics in water have been undertaken for over 80 years. Bubble dynamic models are well established for bubbles in water or simple Newtonian fluids. With the development of new materials and new techniques, the study of bubble dynamics in viscoelastic media becomes necessary. The increasing interest in cavitation is partly related to the application of medical ultrasound. For example, the use of bubble-based contrast agents in diagnostic ultrasound has significantly increased the quality of imaging. Recently, this issue has become more important due to the development of the high intensity focused ultrasound (HIFU) for therapeutic medicine. High intensity ultrasound will induce cavitation in soft tissue, and these microbubbles have a huge impact on the distribution of the ultrasound energy. In these situations, the surrounding media, i.e., biological tissues, often exhibit non-Newtonian behavior. Understanding the behavior of cavitation *in vivo* may provide a powerful tool to improve the quality of medical ultrasound.

The study of these microbubbles involves bubble oscillations in viscoelastic media. Many researchers have extended the analysis of bubble dynamics in Newtonian fluids to non-Newtonian fluids. Fogler and Goddard[1] combined the linear Maxwell model with the Rayleigh-Plesset equation and examined the collapse of a spherical cavity in a large body of an incompressible viscoelastic liquid. The bubble was modeled as a void, and the effect of elasticity was investigated. Their results showed that the elasticity in the liquid can significantly retard the collapse of a bubble. A three parameter linear Oldroyd model was employed by Tanasawa and Yang[2] to study the free oscillation of a gas bubble in viscoelastic fluids. They investigated the effects of the viscous damping in the presence of elasticity, and found that in the presence of elasticity, the effect of viscous damping on bubble collapse is less than that in the pure fluid. Later, Shima, Tsujina, and Nanjo[3] investigated the nonlinear oscillations of gas bubbles in viscoelastic fluids using the model first derived by Tanasawa and Yang,[2] and the effects of relaxation time and retardation time were clarified. A fully numerical scheme was developed by Kim[4] to investigate collapse of a spherical bubble in a large body of Upper-Convective Maxwell fluid. He observed that fluid elasticity accelerated the collapse in the early stage of collapse while in the later stages it retarded the collapse. His approach was very computationally intensive. Alekseev and Rybak[5] presented the resonance frequency of gas bubbles in elastic media. The dispersion equation in a viscoelastic medium was also derived for bubble clouds in their study. Allen and Roy[6] chose the linear Maxwell and Jeffreys models as the liquid constitutive equation to study bubble oscillations in linear viscoelastic fluids. After linearization of the original nonlinear differential equation (a Rayleigh-Plesset type equation), analytical solutions were obtained and compared with the Newtonian results. In a later study of nonlinear viscoelasticity, they[7] employed the Upper-Convective Maxwell model as the constitutive equation with the Rayleigh-Plesset equation. A fully numerical study was conducted to solve the governing system of equations. The results of the linear and nonlinear viscoelastic approaches were compared. Their results showed that tissue viscoelasticity may be important for the potential cavitation bioeffects.

For diagnostic ultrasound examinations, the acoustic intensity is usually insufficient to induce inertial cavitation in soft tissue directly.[8] The only source of microbubbles in soft tissue would be direct injection of a bubble-based contrast

[a]Electronic mail: xmyang@olemiss.edu

agent, an uncommon procedure. However, the use of higher intensity ultrasound, e.g., HIFU therapy, will cause cavitation in soft tissue directly. Different from contrast agent bubbles, this cavitation involves free bubbles oscillating nonlinearly because of the high intensity of the sound field. Previous models for viscoelastic media are all based on the Rayleigh-Plesset equation, which is not very appropriate for large amplitude oscillations. In this work, we seek a model that is capable of accounting for the potentially large-amplitude oscillations of bubbles exposed to HIFU fields. In addition, the bubble model must incorporate a viscoelastic model consistent with measured tissue properties. Although the data on viscoelastic properties of soft tissue at megahertz frequencies are very limited, the linear Voigt model has proven appropriate for the tissues studied;[9,10] none of the above-mentioned models incorporates these experimental results. The Keller-Miksis equation[11] has been shown to be suitable for large amplitude bubble oscillations.[12] In this study, we combine the general form of the Keller-Miksis equation with the linear Voigt model for viscoelastic solids to study the dynamics of bubbles in soft tissue.

The importance of the inertial cavitation threshold has been addressed by many authors. In a medical context, severe bioeffects, including both thermal and nonthermal effects, may be induced or exacerbated by inertial cavitation during high intensity ultrasound insonations. When inertial cavitation occurs, strong nonlinear acoustic emissions can be detected. A sudden change in the emission signals from a bubble is often used to monitor the occurrence of inertial cavitation in experiments.[13,14] In addition to the familiar second, third, and higher harmonics, bubbles may also generate subharmonic signals when they oscillate nonlinearly. Therefore, monitoring the generation of subharmonics can be used to detect inertial cavitation. Higher frequency emissions are very easily attenuated, and the signal that needs to be detected may become very weak. At the same time, the nonlinear propagation of ultrasound will also generate higher harmonics, and this can be a noise source for higher harmonic detection. Compared to harmonic detectors, subharmonic detectors have the advantages that the low frequency signal is less attenuated in soft tissue, and bubbles are the only sources generating subharmonics in soft tissue.

Subharmonic signals have been seen in experiments during cavitation events, but mechanisms for the generation of subharmonics are still not entirely clear. Possible explanations include that a single bubble will emit subharmonics when it breaks up, or interactions inside a bubble cloud can emit subharmonics, or chaotic oscillations of a single bubble will generate subharmonics. In this study, we focus on single bubble dynamics, and simply predict subharmonic signals from the chaotic oscillation of a single bubble. The effect of elasticity on inertial cavitation thresholds and subharmonic emissions will be investigated, providing data that may be useful for cavitation detection and bubble imaging.

II. THEORY AND METHOD

Consider a spherical bubble in an unbounded viscoelastic medium. The equation of continuity has the following form in a spherical coordinate system,

$$\frac{\partial \rho}{\partial t} + \frac{\partial(\rho v_r)}{\partial r} + \frac{2\rho v_r}{r} = 0, \tag{1}$$

where ρ is the density, v_r is the radial velocity, t is time, and r is the radial axis. Conservation of radial momentum for a spherically symmetric radial flow yields,[15,16]

$$\rho\left(\frac{\partial v_r}{\partial t} + v_r\frac{\partial v_r}{\partial r}\right) = -\frac{\partial p}{\partial r} + \frac{\partial \tau_{rr}}{\partial r} + \frac{2}{r}[\tau_{rr} - \tau_{\theta\theta}], \tag{2}$$

where p is the pressure in the surrounding medium, and τ_{rr} and $\tau_{\theta\theta}$ are the stresses in the r and θ directions, respectively. The boundary and initial conditions are:

$$p = p_g - \frac{2\sigma}{R} + \tau_{rr} \quad \text{at } r = R,$$

$$p = p_\infty \quad \text{at } r = \infty,$$

$$R = R_0, \quad \dot{R} = 0 \quad \text{at } t = 0,$$

where p_g is the gas pressure inside the bubble, R is the position of the gas-tissue interface, the dot indicates the time derivative, R_0 is the bubble equilibrium radius, and σ is the surface tension.

To derive the Keller-Miksis equation, which can account for the compressibility of the surrounding medium to first order, an asymptotic solution is employed in the near field and far field.

A. Near field approximation

In the near field $[r = O(R)]$, the effects of compression and expansion of the bubble are dominant, and the surrounding medium may be considered incompressible. From the Bernoulli integral (momentum equation), one can find the solution for the pressure distribution in the internal zone (near field),

$$v_r = -\frac{\dot{R}R^2}{r^2}, \tag{3}$$

$$p_{\text{in}} = p_a - \rho_0\left(R\ddot{R} + \frac{3}{2}\dot{R}^2\right) + \frac{\rho_0}{r}(R^2\dot{R})' - \frac{\rho_0}{2}\frac{R^4\dot{R}^2}{r^4} + \tau_{rr}|_R^r + 3\int_R^r \frac{\tau_{rr}}{r}dr, \tag{4}$$

where p_a is the pressure at the bubble surface, $\ddot{R}$ is the bubble wall acceleration, and $'$ indicates the time derivative.

B. Far field approximation

In the far field $(r \gg R)$, the pressure fluctuations and the density fluctuations are small, and the stress components become negligible, as do the nonlinear convection terms. Ignoring these terms, the governing equation in the far field is essentially the linear acoustic equation. The solutions for the linear acoustic equation are

$$\varphi_{\text{ex}} = \frac{1}{r}\left[\psi_1\left(t - \frac{r}{c}\right) + \psi_2\left(t + \frac{r}{c}\right)\right], \tag{5}$$

$$p_{ex} = p_0 - \rho_0 \frac{\partial \varphi_{ex}}{\partial t}, \tag{6}$$

where p_0 is the static pressure, ρ_0 is density at equilibrium, φ is the velocity potential, ψ_1 and ψ_2 characterize the outgoing and incident acoustic waves, respectively, and c is the sound speed in the medium.

C. Matching of the solutions

To obtain the equation of the radial motion of bubbles for a given driving pressure and to take account of compressibility of the surrounding medium, we need to match the asymptotic solutions in the internal and external zones in the intermediate zone. For the internal solution, the intermediate zone is at $r \to \infty$, and for the external solution, the intermediate zone is at $r \to 0$. The matching conditions in the intermediate zone are the equality of the volumetric flow and of the pressure,

$$4\pi r^2 v_{r(\mathrm{in})}|_{r\to\infty} = 4\pi r^2 v_{r(\mathrm{ex})}|_{r\to 0} \quad p_{\mathrm{in}}|_{r\to\infty} = p_{\mathrm{ex}}|_{r\to 0}. \tag{7}$$

For the internal solution, shear stresses vanish as $r \to \infty$. By matching the solutions we finally get

$$R\ddot{R} + \frac{3}{2}R^2 = \frac{p_a - p_0}{\rho} + \frac{1}{c}[2\psi_2'' + f''] - \frac{\tau_{rr}(R,t)}{\rho} + \frac{3}{\rho}\int_R^\infty \frac{\tau_{rr}}{r} dr, \tag{8}$$

where $f = R^2\dot{R}$, and ψ_2 is the incident wave. Note that the above equation includes f'', which will cause a third derivative of R. This was first noticed by Prosperetti *et al.*[12] This third derivative can be eliminated by assuming that f''/c is small, and evaluating the f from the above-mentioned equation. Then the equation becomes

$$R\ddot{R} + \frac{3}{2}R^2 = \frac{p_a - p_I}{\rho}, \tag{9}$$

where p_I is the pressure at infinity, $p_I = p_0 - 2\rho/c\psi_2'' + \tau_{rr}(R,t) - 3\int_R^\infty \tau_{rr}/r dr$. This is the form of classic Rayleigh equation, indicating that the evaluation of f from this equation is accurate to leading order. Equation (9) may be rewritten as

$$\frac{f'}{R} - \frac{1}{2}\frac{f^2}{R^4} = \frac{p_a - p_I}{\rho}, \tag{10}$$

then f' is evaluated as

$$f' = R\left[\frac{\dot{R}^2}{2} + \frac{p_a - p_I}{\rho}\right], \tag{11}$$

Substitution of Eq. (11) into Eq. (8) results in the final equation,

$$\left(1 - \frac{\dot{R}}{c}\right)R\ddot{R} + \frac{3}{2}\left(1 - \frac{\dot{R}}{3c}\right)\dot{R}^2 = \left(1 + \frac{\dot{R}}{c}\right)\frac{p_a - p_I}{\rho} + \frac{R}{\rho c}\frac{d}{dt}[p_a - p_I], \tag{12}$$

where $(2\rho/c)\psi_2'' = P_A g(t)$ is the driving pressure,

$$p_a = p_g - \frac{2\sigma}{R} + \tau_{rr}(R,t), \tag{13}$$

and

$$p_a - p_I = p_g - \frac{2\sigma}{R} - p_0 + \frac{2\rho}{c}\psi_2'' + 3\int_R^\infty \frac{\tau_{rr}}{r} dr. \tag{14}$$

D. Evaluating stress components

Since stress components will vanish in the far field, we then only evaluate τ_{rr} in the near field, i.e., in an incompressible material. Because soft tissue is viscoelastic, we need to choose a proper viscoelastic model to determine stresses. We choose the linear Voigt model for this study because it is a simple linear model and previous studies have shown that it is appropriate in the low megahertz frequency range.[9,10] More important, some experimental data for soft tissues are also available for this model.[9,10] This also creates the potential for comparing the resulting predictions with the experimental measurements *in vivo*.

Because the material is incompressible, $\tau_{rr} = 2(G\gamma_{rr} + \mu\dot{\gamma}_{rr})$, where γ_{rr} is the strain, $\dot{\gamma}_{rr}$ is the strain rate with $\dot{\gamma}_{rr} = \partial u/\partial r$, u is the velocity, and G is the shear modulus (or rigidity).[17] In the near field (near the bubble surface), $u = (R^2/r^2)\dot{R}$, therefore, $\gamma_{rr} = -(2/3r^3)(R^3 - R_0^3)$ and $\dot{\gamma}_{rr} = -(2R^2/r^3)\dot{R}$.

Then, we have

$$3\int_R^\infty \frac{\tau_{rr}}{r} dr = -\left[\frac{4G}{3R^3}(R^3 - R_0^3) + \frac{4\mu\dot{R}}{R}\right], \tag{15}$$

and

$$\frac{d}{dt}\left(3\int_R^\infty \frac{\tau_{rr}}{r} dr\right) = -4G\frac{R_0^3\dot{R}}{R^4} - 4\mu\left(-\frac{\dot{R}^2}{R^2} + \frac{\ddot{R}}{R}\right). \tag{16}$$

Expanding $(p_a - p_I)$, finally we have

$$p_a - p_I = p_g - \frac{2\sigma}{R} - p_0 + P_A g(t) - \left[\frac{4G}{3R^3}(R^3 - R_0^3) + \frac{4\mu\dot{R}}{R}\right], \tag{17}$$

and

$$\frac{d}{dt}(p_a - p_l)$$
$$= \frac{d}{dt}\left(p_g - \frac{2\sigma}{R} - p_0 + P_A g(t)\right) + \frac{d}{dt}\left[3\int_R^\infty \frac{\tau_{rr}}{r} dr\right]$$
$$= \frac{dp_g}{dt} + \frac{2\sigma\dot{R}}{R^2} + P_A \frac{dg(t)}{dt} - 4G\frac{R_0^3\dot{R}}{R^4} - 4\mu\left(-\frac{\dot{R}^2}{R^2} + \frac{\ddot{R}}{R}\right). \tag{18a}$$

Equations (12), (17), and (18a) provide the desired formulation describing the dynamics of gas bubbles in soft (i.e., viscoelastic) tissue. We note that this equation is actually just the Keller-Miksis equation with extra terms to account for the elasticity of soft tissue. The equation accounts for the compressibility of the surrounding medium to first order, and thus it is better suited than the Rayleigh-Plesset equation to simulate large amplitude bubble oscillations. The validity of this equation is limited to small Mach numbers.[12]

For the results presented here, the gas inside the bubble is assumed ideal, allowing the pressure to be estimated by use of a polytropic relation, $p_g = p_{g0}(R_0/R)^{3\kappa}$, where κ is the polytropic index. In this case, Eq. (18a) may be written as:

$$\frac{d}{dt}(p_a - p_l) = \left(\frac{2\sigma}{R} - 3\kappa p_g\right)\frac{\dot{R}}{R} + P_A\frac{dg(t)}{dt} - 4G\frac{R_0^3\dot{R}}{R^4} - 4\mu\left(-\frac{\dot{R}^2}{R^2} + \frac{\ddot{R}}{R}\right). \tag{18b}$$

E. Analytical solutions

Although Eq. (12) was specifically to investigate nonlinear bubble activity in tissue, it is instructive to consider the effects of the various physical parameters on bubble dynamics at low pressure amplitudes. An analytical solution to Eq. (12) may be obtained by assuming that the pulsation amplitude $R_0 x(t)$, is small, making the usual substitutions of Eq. (19) into Eq. (12):[18]

$$R = R_0(1+x), \quad U = R_0\dot{x}, \quad \dot{U} = R_0\ddot{x},$$
$$R^{-3\kappa} = R_0^{-3\kappa}(1-3\kappa), \text{ etc.}, \tag{19}$$

and recognizing that the term $i\omega R_0 P_A e^{i\omega t}/c$ is to first order equivalent to the linear expression for the radiated pressure wave:[15,18]

$$P_{\text{sac}} = \frac{\rho\ddot{R}R_0}{\left(1 - \frac{i\omega R_0}{c}\right)}, \tag{20}$$

The resulting equation has the form:

$$m\ddot{x} + b\dot{x} + kx = -P_A e^{i\omega t}, \tag{21}$$

where the effective mass, m, total damping, b_{tot}, and stiffness, k, are given by

$$m = \rho R_0^2 + \frac{4\mu R_0}{c},$$
$$b_{\text{tot}} = \left(3\kappa P_{g0} - \frac{2\sigma}{R_0} + 4G\right)\frac{R_0}{c} + 4\mu + \frac{\omega R_0/c}{1+(\omega R_0/c)^2}\omega(\rho R_0^2),$$
$$k = 3\kappa p_{g0} - \frac{2\sigma}{R_0} + 4G + \frac{\omega^2}{1+(\omega R_0/c)^2}(\rho R_0^2).$$

Notice that each term is greater than would be found from a purely linear analysis of a gas bubble in water.[18] The effective mass contains a small additional increment due to the effect of viscosity. There are two additional damping terms, one arising from variation in the surface energy of the bubble (and directed opposite to the other damping terms), the other from the rigidity of the surrounding tissue, respectively. The rigidity of the tissue also contributes to the total stiffness of the system, as has been noted previously.[1–6]

Comparison of Eq. (21) with that of a damped harmonic oscillator:

$$\ddot{x} + 2\beta_{\text{tot}}\dot{x} + \omega_0^2 x = \frac{-P_A}{m}e^{i\omega t}, \tag{22}$$

in which β_{tot} is the total damping constant and ω_0 is the natural frequency, allows identification of five components (viscous, thermal, acoustic, interfacial, and elastic) to the total damping, given by

$$\beta_{\text{vis}} = b_{\text{vis}}/2m = 2\mu \Big/ \left(\rho R_0^2 + \frac{4\mu R_0}{c}\right), \tag{23a}$$

$$\beta_{\text{th}} = b_{\text{th}}/2m = 3\kappa p_{g0}R_0 \Big/ \left[2c\left(\rho R_0^2 + \frac{4\mu R_0}{c}\right)\right] = 3\kappa p_{g0}/(2\rho c R_0 + 8\mu), \tag{23b}$$

$$\beta_{\text{ac}} = b_{\text{ac}}/2m = \frac{\omega R_0/c}{1+(\omega R_0/c)^2}\frac{\omega}{2}(\rho R_0^2) \Big/ \left(\rho R_0^2 + \frac{4\mu R_0}{c}\right), \tag{23c}$$

$$\beta_{\text{int}} = b_{\text{int}}/2m = -\sigma \Big/ \left[c\left(\rho R_0^2 + \frac{4\mu R_0}{c}\right)\right] = -\sigma/(\rho c R_0^2 + 4\mu R_0), \tag{23d}$$

$$\beta_{\text{el}} = b_{\text{el}}/2m = 2GR_0 \Big/ \left[c\left(\rho R_0^2 + \frac{4\mu R_0}{c}\right)\right] = 2G/(\rho c R_0 + 4\mu), \tag{23e}$$

and the expression for the natural frequency:

$$\omega_0^2 = k/m = \left[3\kappa p_{g0} - \frac{2\sigma}{R_0} + 4G + \frac{\omega^2}{1+(\omega R_0/c)^2}(\rho R_0^2)\right] \Big/ \left(\rho R_0^2 + \frac{4\mu R_0}{c}\right). \tag{24}$$

In this last expression, the contributions of the acoustic and viscous terms are important only for large bubbles, while the

elastic term either dominates or is of the same order as the pressure term except for very small bubbles. Note that if the acoustic, viscous, and elastic terms are neglected, the well-known expression for the resonance frequency of a gas bubble in liquid is recovered.

The scattering cross section may be defined as the ratio of the total acoustic power scattered by an object at a given frequency to the incoming acoustic intensity.[17] For a spherical bubble oscillating at low amplitude, the expression for the scattering cross section is

$$\sigma_S = \frac{4\pi R_0^2 \omega^4}{(\omega_0^2 - \omega^2)^2 + \beta_{\text{tot}}^2 \omega^2}. \tag{25}$$

F. Numerical solutions

To obtain predictions for the nonlinear oscillation of a bubble in soft tissue, Eq. (12) must be solved numerically. Results for individual $R(t)$ curves, inertial cavitation thresholds, and subharmonic emissions are presented in the following. Determination of the cavitation thresholds requires selection of a threshold criterion. Several criteria for the inertial cavitation threshold have appeared in literature, e.g., $R_{\max}/R_0=2$,[19,20] $T_{\max}=5000$ K,[21] etc. In this study, we use $R_{\max}/R_0=2$ as the threshold criterion. This choice is consistent with the assumption that the air in the bubble expands and contracts adiabatically since the amplitude $R(t)/R_0$ is fairly insensitive to the thermodynamic processes within the bubble.[22] For subharmonics, the relative strength of the emission with respect to that of the strongest frequency component emitted by a single bubble is shown. The reason to choose this relative strength is from consideration of experimental detection. After passing a preamp, whether a frequency component is detectable by a spectral analyzer or not depends on its strength relative to the strongest component. A frequency component is only detectable when this relative number is within the vertical resolution of the instrument. Otherwise, it will be suppressed as noise. The relative number is obtained by the following method: first the R-t curve is obtained, next the radiation pressure is determined by

$$p_{\text{sac}}(r,t) = \frac{\rho R}{r}(2\dot{R}^2 + R\ddot{R}), \tag{26}$$

where r is assumed to be a unit constant, and then frequency components are determined by FFT. The amplitude of the subharmonic is expressed in decibels relative to the maximum amplitude over all frequency components.

The following material properties are used in the current simulations: $p_0=1.01\times10^5$ Pa, $\rho=1060$ kg/m^3, $c=1540$ m/s, and $\sigma=0.056$ N/m (the value for blood assumed by Apfel and Holland[19]). These parameters are chosen to be close to values appropriate to soft tissue. The actual properties of specific soft tissues may be slightly different from these values (except for surface tension, which is unknown), but the differences will generally be small. The polytropic index $\kappa=1.4$, a value appropriate for adiabatic oscillations of air bubbles. The rigidity and the viscosity of tissue are assumed to be $G=0$, 0.5, 1.0, and 1.5 MPa and $\mu=0.015$ Pa s. These values span the range obtained by previous measurements,[9,10] with the exception of $G=0$, which is included for comparison. The effect of viscosity has been investigated previously for a Newtonian medium. We will focus on the effects of elasticity on bubble motion in this study, but to allow easy comparison with previous work, results for water ($G=0$, $\mu=0.001$) and blood ($G=0$, $\mu=0.005$) are also presented. The driving frequencies studied are 1 and 3.5 MHz, which are frequently used in HIFU. All the bubble oscillations are solved for 30 cycles.

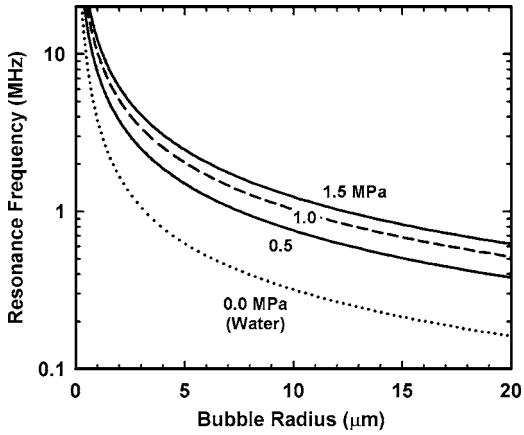

FIG. 1. Calculated values of linear resonance frequency for free air bubbles in water (···) and air bubbles surrounded by tissue having values of $G=1.5$ (upper—), 1.0 (– – –), and 0.5 MPa (lower—).

III. RESULTS

A. Analytical results

The following results were obtained for the case of air-filled bubbles in tissues having a modulus of rigidity equal to 0.5, 1.0, or 1.5 MPa (as discussed earlier). In addition, results for either water or blood or both are presented for comparison. The effects of the surrounding tissue on resonance frequency, damping, and the scattering cross section for individual single bubbles will be illustrated in the following.

1. Resonance frequency

The undamped linear resonance frequency for bubbles larger than 1–2 μm and surrounded by viscoelastic tissue is dominated by the shear modulus G. For these bubbles, as shown in Fig. 1, ω_0, increases approximately as the square root of G. The bottom curve in Fig. 1, labeled "Water," shows the resonance frequency for a free bubble with $G=0$. The three curves above it, for tissues with increasing values of G, demonstrate that the increase in stiffness provided by the tissue can increase the resonance frequency considerably. The effect of rigidity is much greater than the effect of surface tension, meaning that a larger bubble will exhibit a much greater stiffness than a free bubble of equivalent size. For example, the value of ω_0, for a 5-μm bubble is about 0.63 MHz, while replacing the water with tissue increases this value by a factor of 2.4, 3.3, and 4.0 times for the three rigidities studied here. Because these larger bubbles resonate at higher frequencies than free bubbles of equivalent size, they will tend to appear acoustically smaller than they actually are.

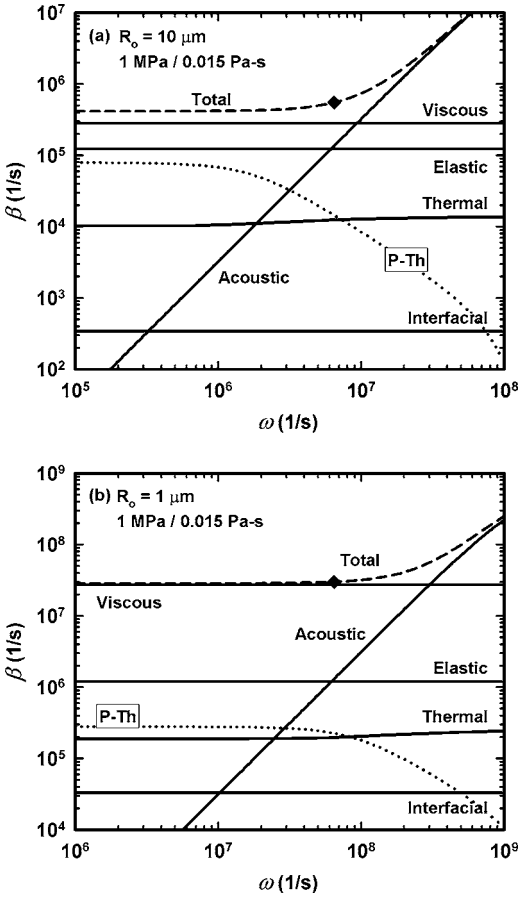

FIG. 2. Dimensional linear damping constants vs radial frequency for equilibrium bubble radii of (a) 10 μm and (b) 1 μm, surrounded by tissue with $G=1.0$ MPa and $\mu=0.015$ Pa s; resonance radius (♦), thermal damping constant given by Prosperetti—Ref. 25 (···).

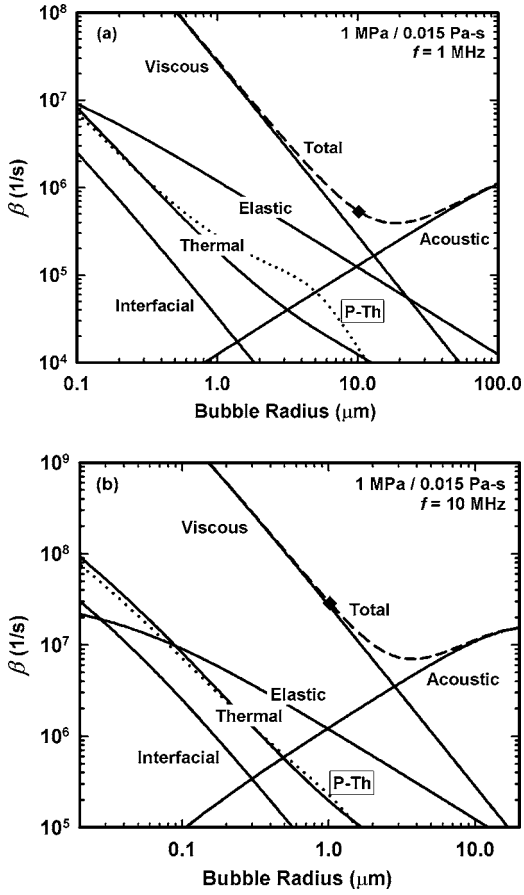

FIG. 3. Dimensional linear damping constants vs equilibrium bubble radius for radial frequencies of (a) 1 MHz and (b) 10 MHz, for air bubbles surrounded by tissue with $G=1.0$ MPa and $\mu=0.015$ Pa s; resonance radius (♦), thermal damping constant given by Prosperetti—Ref. 25 (···).

2. Linear damping coefficients

Five sources of damping for bubbles surrounding by viscoelastic tissue were identified earlier and quantified by Eq. (23). Two of these expressions, for viscous and acoustic damping, are identical to those given by Prosperetti[18] for a gas bubble in liquid, see Eqs. (23a) and (23c), respectively. The expression for thermal damping, Eq. (23b), differs markedly from those given by either Prosperetti[18] or Eller,[23] which is not surprising given the assumption of a polytropic pressure-volume relation for the gas. However, the numerical values obtained for bubbles smaller than the linear resonance radius are remarkably similar, often to within a few percent, of those obtained using more exact theories.[18,23] The two additional damping terms, due to the surface energy of the bubble and the rigidity of the surrounding tissue, see Eqs. (23d) and (23e), respectively, have a form similar to that for thermal damping, Eq. (23b). It is worth noting that a combination of four of the damping terms, Eqs. (23b)–(23e), is proportional to the stiffness, and thus also to the resonance frequency, of the system.

The results of calculations for the damping constants as a function of radial frequency are shown in Fig. 2 for bubble radii of 1 and 10 μm, assuming $G=1.0$ MPa and $\mu=0.015$ Pa s. Because the term for interfacial tension is negative, only its magnitude has been plotted here. In any case, the contribution of β_{int} to β_{tot} is quite modest. The figures have been drawn in such a way as to allow easy comparison with previous results for free[18,23] and encapsulated bubbles.[17] Due to the high value of μ, the total damping is dominated by β_{vis} for frequencies less than ω_0 and $R_0<10$ μm, while the acoustic term β_{ac} dominates at higher frequencies. The elastic term becomes increasingly important as R_0 increases, with $\beta_{el}\sim\beta_{vis}$ at $R_0=30$ μm. As noted earlier, the expression for β_{th} differs from those obtained using more exact approaches. This is reflected in both the shape and the magnitude of the curves labeled "Thermal" in Fig. 2, as may be seen by comparison with the dotted curves labeled "P-Th," obtained using the theory of Prosperetti.[18] Thus, while $\beta_{th}<\beta_{el}$ for all values of R_0 when employing the polytropic assumption (as is done here), β_{th} would come to dominate other sources of damping for $R_0>30$ μm and $\omega<\omega_0$ in a more rigorous treatment of thermal effects.

The results of calculations for damping constants as a function of radius are given in Fig. 3 for frequencies of 1 and 10 MHz, again assuming $G=1.0$ MPa and $\mu=0.015$ Pa s. The total damping is dominated by β_{vis} for bubbles smaller than the linear resonance radius, while β_{ac} dominates at larger sizes. The contribution of β_{el} is never more than about 20% of β_{tot}, which occurs near the resonance radius at 1 MHz, see Fig. 3(a). For frequencies above about 1 MHz and radii less than the resonance size, the values for β_{th}

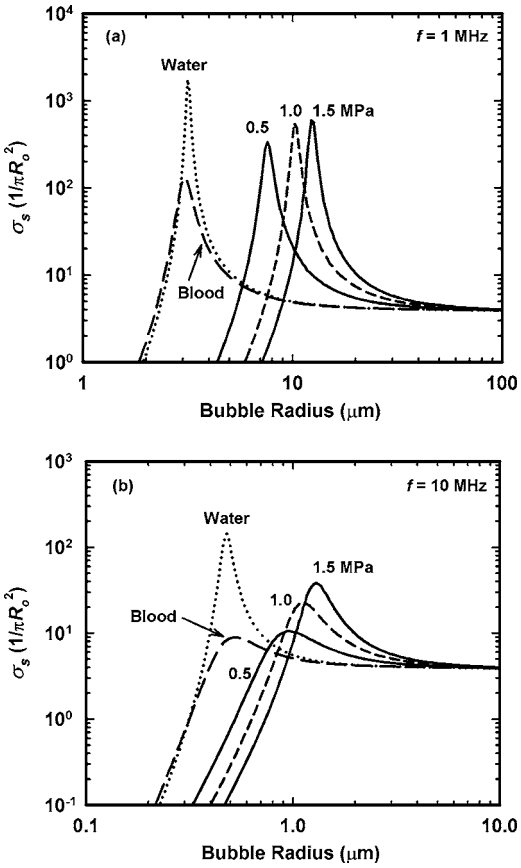

FIG. 4. Linear scattering cross sections vs equilibrium bubble radius for frequencies of (a) 1 MHz and (b) 10 MHz, for air bubbles surrounded by tissue having values of G=1.5 (right—), 1.0 (– – –), and 0.5 MPa (left—) with μ=0.015 Pa s, and for water (···) and blood (– – –).

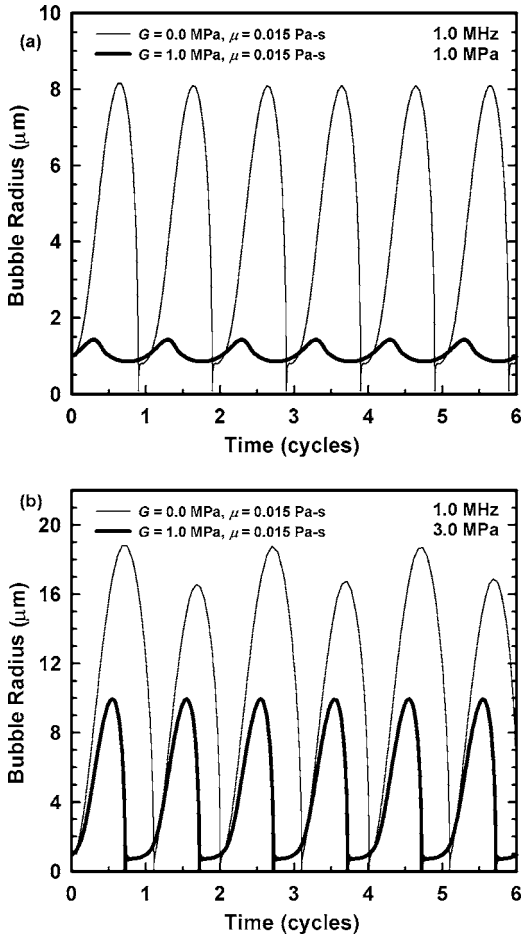

FIG. 5. A comparison of radial responses for 1-μm bubbles driven by a 1-MHz pulse at (a) 1 MPa and (b) 3 MPa, for G=0 (thin line), and G=1.0 MPa (thick line); the viscosity was fixed at 0.015 Pa s.

calculated using Eq. (23b) and the theory of Prosperetti,[18] (dotted curves labeled "P-Th") agree rather closely, although the contribution of β_{th} to β_{tot} is not significant. The contribution of β_{int} to β_{tot} is also trivial.

3. Scattering cross section

Calculated values of the linear scattering cross sections of individual air bubbles, normalized to their respective geometrical cross sections, are given in Fig. 4 for driving frequencies of 1 and 10 MHz. The strong effect of tissue elasticity (i.e., G) is apparent in these results, causing the resonance peaks to shift to bubble radii two to four times larger than for the resonance peak in water. Even though they are larger, the cross sections for bubbles surrounded by tissue are less, and sometimes much less, than for resonant bubbles in water. It is also seen that the curves broaden and diminish as either the rigidity G decreases or the frequency f increases, indicating that bubbles in tissue may be more difficult to detect acoustically than are bubbles in water at the same frequency. The cross sections for blood exhibit maxima at about the same radii as for water, but their magnitudes are less due to the higher viscosity of that fluid.

B. Numerical results

In this part of the paper, simulation results will be given for numerical solutions of Eq. (12). The effects of elasticity on R-t curves will be examined first. Next, initial cavitation thresholds will be presented for different elasticities and compared to the result in water. Finally, maps of the strength of subharmonic signals emitted by oscillating bubbles will highlight a common way to detect cavitation and will illustrate the ranges of bubble radii that may be easily detected using this method.

1. The effect of elasticity on $R(t)$ curves

Examples of $R(t)$ curves for a 1-μm bubble oscillating under 1-MHz driving pressures of 1 and 3 MPa are shown in Figs. 5(a) and 5(b), respectively. The viscosity is fixed at 0.015 Pa s and the rigidity is chosen as 0 and 1.0 MPa. The effect of the elasticity is very obvious that it greatly reduces the amplitude, and hence the nonlinearity, of the oscillation. At 1 MPa, the amplitude of the oscillation is much smaller when elasticity is included. When the driving pressure increases to 3 MPa, the amplitude of the oscillation with nonzero elasticity is still smaller than that with zero elasticity, but the difference between the two cases is less. This indicates that the effect of elasticity will be less when the driving pressure is strong. Another feature which is worthy of comment is that for the zero-elasticity case, the bubble oscillation approaches a steady-state resonance[22,24] of order 2/2, an example of period doubling and an indication of the start of

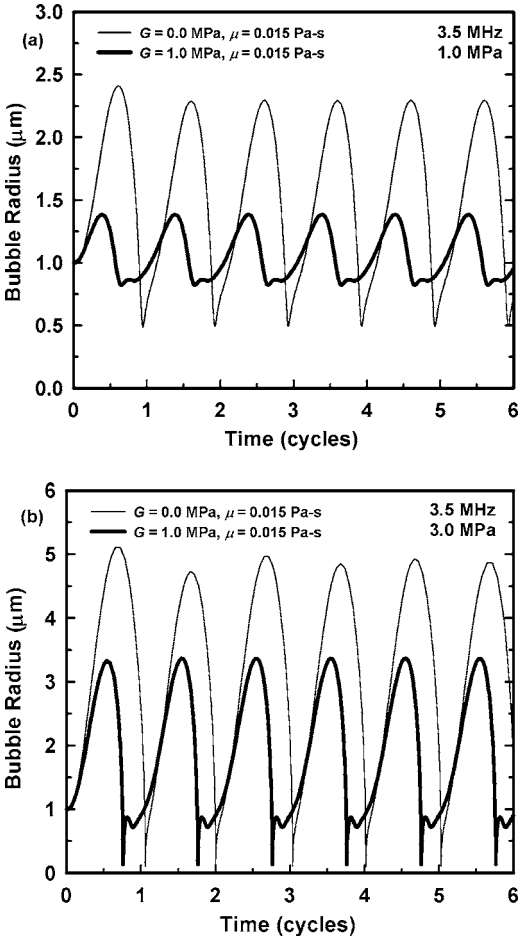

FIG. 6. A comparison of radial responses for 1-μm bubbles driven by a 3.5-MHz pulse at (a) 1 MPa and (b) 3 MPa, for $G=0$ (thin line), and $G=1.0$ MPa (thick line); the viscosity was fixed at 0.015 Pa s.

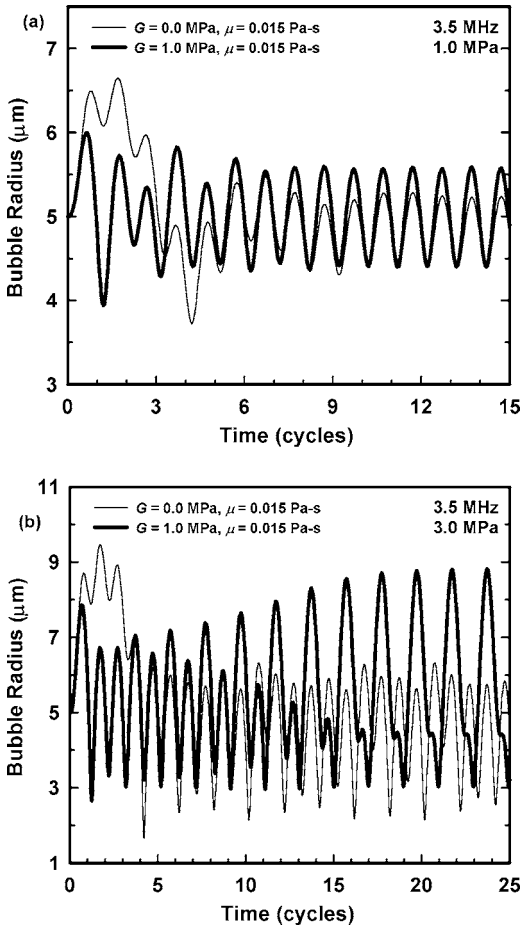

FIG. 7. A comparison of radial responses for 5-μm bubbles driven by a 3.5-MHz pulse at (a) 1 MPa and (b) 3 MPa, for $G=0$ (thin line), and $G=1.0$ MPa (thick line); the viscosity was fixed at 0.015 Pa s.

chaotic oscillation and very strong nonlinearity. For the nonzero-elasticity case, no period doubling is observed under this driving pressure, although the inertial collapses are still very strong. Clearly, the presence of the elasticity has reduced or eliminated some nonlinear components of the bubble oscillation.

Figure 6 shows examples of $R(t)$ curves for a 1-μm bubble driven by (a) 1 MPa and (b) 3 MPa at 3.5 MHz. Similar conclusions as those at 1 MHz can be drawn from these results. For the same driving pressure and the same size bubble, the nonlinearity appears to be weaker at the higher frequency because no period doubling is observed. Figure 7 shows the results for a 5-μm bubble at 1 MHz driven by (a) 1 MPa and (b) 3 MPa. For zero elasticity, bubbles oscillate with larger amplitudes during the first few cycles than that for the nonzero-elasticity case. Interestingly, after the initial state, the presence of the elasticity increases the amplitude of oscillation in both cases. In Fig. 7(a), at zero-elasticity, the bubble oscillation exhibits strong nonlinear behavior by a decrease at the average radius, and the presence of elasticity recovers the linear oscillation around the bubble equilibrium radius. In Fig. 7(b), although the oscillation amplitude is smaller at zero-elasticity case, the oscillation itself becomes chaotic, while it is periodic when elasticity is included. Compared to bubbles of smaller size, a stronger nonlinearity is observed, which is indicated by the approach to chaotic oscillations. Certainly, the nonlinearity does not always increase when the bubble size increases.

2. The effect of elasticity on the inertial cavitation threshold

In Fig. 8, predicted inertial cavitation thresholds are shown for a driving frequency of 1 MHz, $G=0$, 0.5, 1.0, and 1.5 MPa, and $\mu=0.015$ Pa s. The thresholds in water and

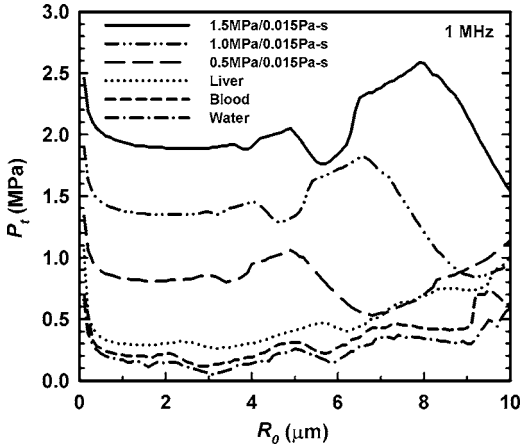

FIG. 8. Predicted thresholds for inertial cavitation at 1 MHz.

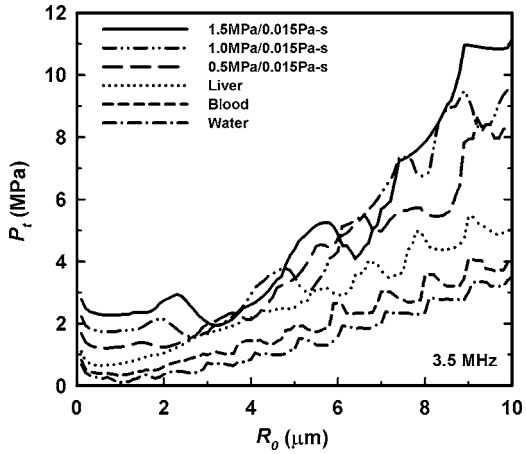

FIG. 9. Predicted thresholds for inertial cavitation at 3.5 MHz.

blood are also shown in the plot for reference. The effect of elasticity on the threshold is obvious. Threshold values increase as the elasticity increases, as expected based on the results for the $R(t)$ curves given earlier. For nonzero elasticity, the thresholds have significant structure that deserves comment. For example, at $G=1.5$ MPa, for small bubble sizes, the threshold value is consistent with the Blake threshold. As the bubble size increases, the threshold value reaches a minimum value and then slowly rises. At around 4 μm, the threshold value suddenly drops and then comes back. The same shape occurs at around 6 μm, and another drop in threshold occurs around 8 μm. The lowest threshold attained following each drop is less than the preceding minimum at a smaller bubble size. Similar structures are observed for the lower elasticity cases, the only difference being that these drops occur at different positions. This resonant structure appears to be related to the fractional-order subharmonic resonance minima described previously.[22] The positions of the minima are determined by the elasticity of the surrounding medium, shifting to larger radii as G increases.

Figure 9 shows the same thresholds but at a driving frequency of 3.5 MHz. At this higher frequency, the threshold values are greater than at 1 MHz, and the increase in thresholds for larger bubble sizes is much faster than that at 1 MHz. The resonant structures appearing in the nonzero-elasticity cases at 1 MHz are also observed on these threshold curves. The resonance structure differs significantly however in that the minimum values attained following the drops in the curves at 3.5 MHz are not less than the immediately preceding minima.

The effect of viscosity on the threshold can be observed by comparing the threshold for $G=0$ MPa and those of blood and water (the only difference among the three is the value of viscosity, $\mu=0.015$, 0.005, and 0.001 Pa s, respectively). In comparing, we conclude that thresholds increase and have less structure as viscosity increases.

3. The map of the strength of subharmonics

Figure 10 shows subharmonic emissions at a driving frequency of 1 MHz as a function of driving pressure and bubble equilibrium radius. Results for tissues with $G=0$, 0.5, and 1.0 MPa and $\mu=0.015$ Pa s are shown, with the result for blood also shown for reference ($G=0$ MPa, $\mu=0.005$ Pa s). We will define a subharmonic signal as "strong" when it is greater than −30 dB because above this level, the subharmonic signal can be easily detected by an instrument with an 8-bit dynamic range. From Figs. 10(a)–10(c), it is seen that as the elasticity increases, the strong subharmonic signal region moves toward larger bubble sizes and higher driving pressures. The strong subharmonic signal region generally lies above the corresponding inertial cavitation threshold. For small values of elasticity, the inertial threshold coincides with the lower boundary of the strong subharmonic emission region better than does that for higher elasticity cases. This result is expected because the subharmonic signal investigated here arises from chaotic bubble oscillations, and chaotic oscillations usually occur after the bubble motion becomes strongly nonlinear. In comparing the map for blood and that for tissue with $G=0$ MPa, we find that the strong subharmonic signal region becomes smaller when the viscosity increases. The contour lines on these plots indicate the boundaries between regions in which the maximum emission occurs at a particular frequency. The results show that all strong subharmonic emissions occur only when the fundamental frequency component has the maximum emission level.

Figure 11 shows results for the same cases as in Fig. 10, but at a driving frequency of 3.5 MHz. As the elasticity increases, the strong subharmonic emission region shrinks and moves toward higher pressure amplitudes. Significantly perhaps, the relative signal also seems stronger. Compared to results at 1 MHz, the strong subharmonic emission region at 3.5 MHz is much smaller and is limited to the small bubble region. This limitation to the small bubble region probably is related to the resonance structure of these bubble responses. At 3.5 MHz, the linear bubble resonance size is smaller than that at 1 MHz (3.07 vs 10.67 μm). Again, all strong-emission regions are above the inertial cavitation thresholds for the corresponding elasticity, and strong subharmonic emissions occur only when the fundamental frequency component has the maximum emission level.

IV. DISCUSSION AND CONCLUSIONS

In this study, we developed a theoretical model for the pulsations of gas bubbles in simple linear viscoelastic solids and presented some potentially useful results for the case of soft tissues. As pointed out in the text, although the model is simple, it is consistent with experimental data taken for some soft tissues. However, at high intensity, bubble oscillations are strongly nonlinear. Although strong nonlinear oscillations do not automatically imply that a nonlinear viscoelastic model is necessary to describe the bubble motion, the suitability of this linear model also remains unclear. As a matter of fact, there is little evidence that the strain-stress relation in tissue is not linear. Even though the change in bubble radius is significant compared to its initial dimension, the overall strain in the tissue could still be considered small if this change were compared to the dimension of the soft tissue. Use of a different viscoelastic model certainly would result in different predictions, but the sparse measurement data at

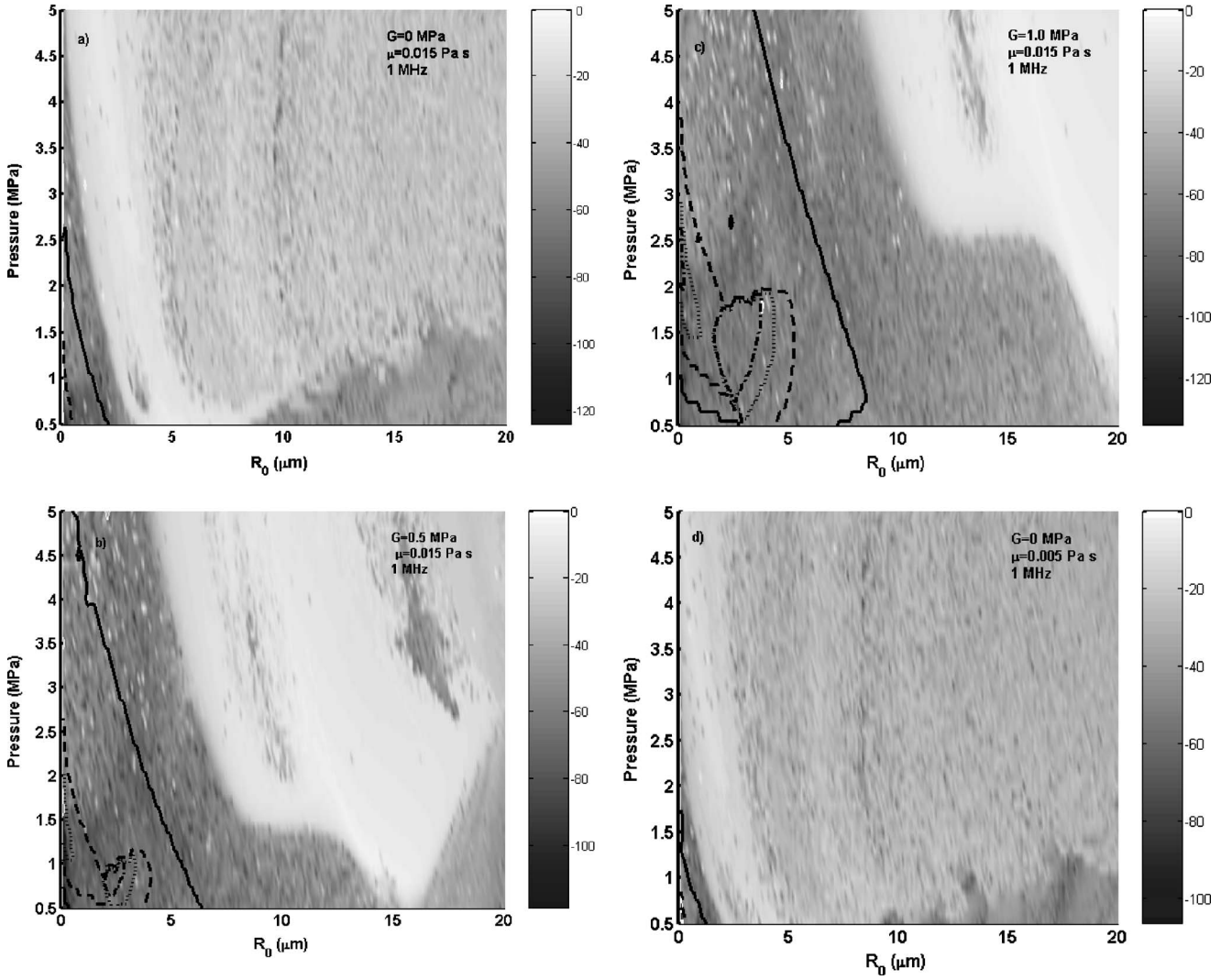

FIG. 10. Subharmonic emissions in dB relative to the peak emission at a driving frequency of 1 MHz as a function of driving pressure and bubble equilibrium radius for three "tissues:" (a) $G=0$ MPa and $\mu=0.015$ Pa s; (b) $G=0.5$, $\mu=0.015$; (c) $G=1.0$, $\mu=0.015$; and for (d) blood, $G=0$, $\mu=0.005$. The contour lines indicate the boundaries between regions in which maximum emissions occur only at one frequency component: fundamental (right-most region) and second harmonic (solid line); second harmonic and third harmonic (dashed line); third harmonic and fourth harmonic (dotted line); fourth harmonic and fifth harmonic (dash-dot line).

megahertz frequencies limits the study of verified viscoelastic models for soft tissue. Also, the present study provides predictions that can be examined experimentally. Verification of this model will be pursued in the future.

Linear analysis of this inherently nonlinear formulation provided analytical predictions of bubble responses to insonation at low pressure amplitudes. The result for resonance frequency increases as the modulus of rigidity increases, as was expected based on previous work.[17] The results for damping constants showed that the viscosity of the tissue tends to dominate either thermal or elastic damping for bubbles smaller than ~ 30 μm for frequencies smaller than the linear resonance size, while acoustic damping predominates at higher frequencies. It is also expected that thermal damping would dominate other sources of damping for $R_0 > 30$ μm and $\omega < \omega_0$ in a more rigorous treatment of thermal effects than is given by the polytropic assumption used here. The peaks in the curves for scattering cross section shift to larger radii as the rigidity increases due to the increase in resonance frequency, although their magnitudes are less, and sometimes much less, than is the case for resonant bubbles in water. This is consistent with the numerical results used in producing Figs. 10 and 11.

The effect of elasticity on bubble dynamics was investigated in some detail. Overall, the presence of the elasticity in a bubble dynamics equation will reduce, sometimes greatly, the nonlinearity of bubble oscillations. As might be expected, the inertial cavitation threshold was shown to be greater in tissue than in liquids such as water or blood, in contrast to the assumptions underlying the mechanical index.[19,25] This result should prove useful for understanding the prevalence of potentially damaging inertial cavitation *in vivo*. This will be the subject of a later study.

Subharmonic emissions from an oscillating viscoelastic bubble were also studied. Since soft tissue generally is not transparent, detecting acoustic emissions is often the best way to gain information about a bubble. A passive or active cavitation detector system can easily provide information about bubbles inside soft tissues. When interpreting such re-

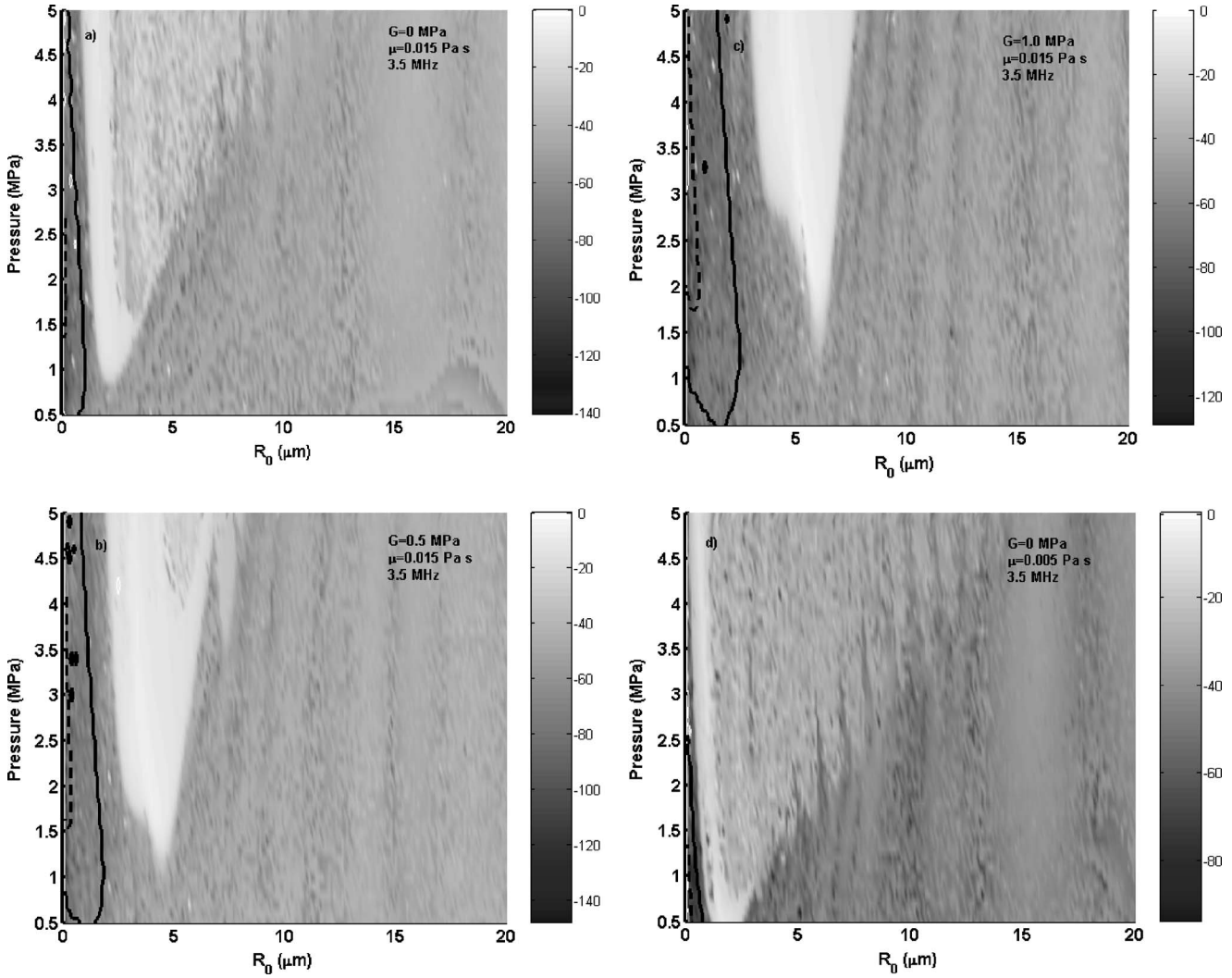

FIG. 11. Subharmonic emissions in dB relative to the peak emission at a driving frequency of 3.5 MHz as a function of driving pressure and bubble equilibrium radius for three "tissues:" (a) $G=0$ MPa and $\mu=0.015$ Pa s; (b) $G=0.5$, $\mu=0.015$; (c) $G=1.0$, $\mu=0.015$; and for (d) blood, $G=0$, $\mu=0.005$. The contour lines indicate the boundaries between regions in which maximum emissions occur only at one frequency component: fundamental (right-most region) and second harmonic (solid line); second harmonic and third harmonic (dashed line); third harmonic and fourth harmonic (dotted line); fourth harmonic and fifth harmonic (dash-dot line).

sults however, it will be important to keep in mind that the sizes of the bubbles detected will be greater than estimated using linear theory for water.

Shape oscillations and rectified diffusion are not considered in this study, although they are very important to predicting the stability and equilibrium size of a bubble.[26] Shape oscillations could also generate larger stresses that could cause severe mechanical damage to soft tissue. Rectified diffusion will change the equilibrium size of a bubble, and the bubble motion can thereby be greatly affected. These effects will be the focus of future studies.

ACKNOWLEDGMENTS

The suggestions and support of the Biomedical Acoustic group at NCPA are gratefully acknowledged. This work was supported by Award No. DAMD17-02-2-0014, administered by the US Army Medical Research Acquisition activity, Fort Detrick, MD. The information contained herein does not necessarily reflect the position or policy of the US government, and no official endorsement should be inferred.

[1]H. S. Fogler and J. D. Goddard, "Collapse of spherical cavities in viscoelastic fluids," Phys. Fluids **13**, 1135–1141 (1970).
[2]I. Tanasawa and W. J. Yang, "Dynamic behavior of a gas bubble in viscoelastic liquids," J. Appl. Phys. **41**, 4526–4531 (1970).
[3]A. Shima, T. Tsujino, and H. Nanjo, "Nonlinear oscillations of gas bubbles in viscoelastic fluids," Ultrasonics **24**, 142–147 (1986).
[4]C. Kim, "Collapse of spherical bubbles in Maxwell fluids," J. Non-Newtonian Fluid Mech. **55**, 33–58 (1994).
[5]V. N. Alekseev and S. A. Rybak, "The behavior of gas bubbles in insonated biological tissues," Acoust. Phys. **44**, 243–247 (1998).
[6]J. S. Allen and R. A. Roy, "Dynamics of gas bubbles in viscoelastic fluids. I. Linear viscoelasticity," J. Acoust. Soc. Am. **107**, 3167–3178 (2000).
[7]J. S. Allen and R. A. Roy, "Dynamics of gas bubbles in viscoelastic fluids. II. Nonlinear viscoelasticity," J. Acoust. Soc. Am. **108**, 1640–1650 (2000).
[8]C. C. Church, "Spontaneous homogeneous nucleation, inertial cavitation and the safety of diagnostic ultrasound," Ultrasound Med. Biol. **28**, 1349–1364 (2002).
[9]L. A. Frizzell, E. L. Carstensen, and J. F. Dyro, "Shear properties of mammalian tissues at low megahertz frequencies," J. Acoust. Soc. Am. **60**, 1409–1411 (1977).

[10]E. L. Madsen, H. J. Sathoff, and H. J. Zagzebski, "Ultrasonic shear wave properties of soft tissues and tissuelike materials," J. Acoust. Soc. Am. **74**, 1346–1355 (1983).
[11]J. B. Keller and M. J. Miksis, "Bubble oscillations of large amplitude," J. Acoust. Soc. Am. **68**, 628–633 (1980).
[12]A. Prosperetti and A. Lezzi, "Bubble dynamics in a compressible liquid. 1. First order theory," J. Fluid Mech. **168**, 457–478 (1986).
[13]R. A. Roy, S. I. Madanshetty, and R. E. Apfel, "An acoustic backscattering technique for the detection of transient cavitation produced by microsecond pulses of ultrasound," J. Acoust. Soc. Am. **87**, 2451–2458 (1990).
[14]ANSI Technical Report, "Bubble Detection and Cavitation Monitoring," American National Standards Institute, Document ANSI S1.24 TR-2002, 2002.
[15]L. D. Landau and E. M. Lifshitz, *Fluid Mechanics* (Pergamon, Oxford, 1959), Chap. II.
[16]A. Prosperetti, "A generalization of the Rayleigh-Plesset equation of bubble dynamics," Phys. Fluids **25**, 409–410 (1982).
[17]C. C. Church, "The effects of an elastic solid surface layer on the radial pulsations of gas bubbles," J. Acoust. Soc. Am. **97**, 1510–1521 (1995).
[18]A. Prosperetti, "Thermal effects and damping mechanisms in the forced radial oscillations of gas bubbles in liquids," J. Acoust. Soc. Am. **61**, 17–27 (1977).
[19]R. E. Apfel and C. K. Holland, "Gauging the likelihood of cavitation from short-pulse, low-duty cycle diagnostic ultrasound," Ultrasound Med. Biol. **17**, 179–185 (1991).
[20]B. E. Noltingk and E. A. Neppiras, "Cavitation produced by ultrasonics," Proc. Phys. Soc. London, Sect. B **63**, 674–685 (1950).
[21]H. G. Flynn, "Cavitation dynamics. II. Free pulsations and models for cavitation bubbles," J. Acoust. Soc. Am. **58**, 1160–1170 (1975).
[22]H. G. Flynn and C. C. Church, "Transient pulsations of small gas bubbles in water," J. Acoust. Soc. Am. **84**, 985–998 (1988).
[23]A. I. Eller, "Damping constants of pulsating bubbles," J. Acoust. Soc. Am. **47**, 1469–1470 (1970).
[24]W. Lauterborn, "Numerical investigation of nonlinear oscillations of gas bubbles in liquids," J. Acoust. Soc. Am. **59**, 283–293 (1976).
[25]C. K. Holland and R. E. Apfel, "An improved theory for the prediction of microcavitation thresholds," IEEE Trans. Ultrason. Ferroelectr. Freq. Control **36**, 204–208 (1989).
[26]X. Yang, R. A. Roy, and R. G. Holt, "Bubble dynamics and size distributions during focused ultrasound insonation," J. Acoust. Soc. Am. **116**, 3423–3431 (2004).

Coupled flexural-longitudinal wave motion in a finite periodic structure with asymmetrically arranged transverse beams

Lars Friis[a] and Mogens Ohlrich[b]
Acoustic Technology, Ørsted•DTU, Technical University of Denmark, Building 352, DK-2800 Kgs. Lyngby, Denmark

(Received 17 February 2005; revised 26 September 2005; accepted 26 September 2005)

A companion paper [J. Acoust. Soc. Am. **118**, 3010–3020 2005] has examined the phenomena of flexural-longitudinal wave coupling in a practically undamped and semi-infinite periodic waveguide with structural side-branches. The effect of structural damping on wave coupling in such a waveguide is examined in the first part of the present paper, and the damping-dependent decrease in wave coupling is revealed for a structure with multiresonant side-branches. In the second part, the simplifying semi-infinite assumption is relaxed and general expressions for the junction responses of *finite* and *multicoupled* periodic systems are derived as a generalization of the governing expressions for finite, mono-coupled periodic systems [Ohlrich, J. Sound Vib. **107**, 411–434 (1986)]. The present derivation of the general frequency response of a finite system utilizes the eigenvectors of displacement responses and wave forces that are associated with the characteristic wave-types, which can exist in a multicoupled periodic system [Mead, J. Sound Vib. **40**, 19–39 (1975)]. The third part of the paper considers a finite specific test-structure with eight periodic elements and with structural terminations at the extreme ends. Audio-frequency vibration responses of this tri-coupled periodic structure are predicted numerically over a broad range of frequencies and a very good agreement is found with the measurement results obtained from an experiment with a nominally identical, periodic test-structure which is freely suspended. [DOI: 10.1121/1.2126928]

PACS number(s): 43.40.At, 43.40.Cw, 43.20.Bi [MO] Pages: 3607–3618

I. INTRODUCTION

Flexural-longitudinal wave coupling in a periodic waveguide with structural side-branches was examined in a companion paper.[1] For a specific choice of side-branches in the form of relatively short transverse beams attached at regular intervals the coupling phenomena were clearly demonstrated, and it was found that the long-range transmission of structural wave motion was significantly enhanced in broad frequency bands due to this wave coupling between flexural and longitudinal motion. Such coupled motion in spatially periodic structures can be "provoked" in various ways but is most often a result of geometrical asymmetry as is the case for rib-stiffened plates or building columns with beams and floors attached at regular intervals as in multi-story buildings. A simple model of such a transmission path is shown in Fig. 1 as a periodic assembly of beam-type components, or as an idealized plane-wave, normal incidence model of a similar plate assembly; the transverse beams are attached asymmetrically—to one side only—on an otherwise continuous waveguide, that is, a continuous beam, column or plate structure. It is this type of *asymmetrical* periodic structure that is the subject of the present investigation.

The wave propagation characteristics of a practically *undamped* and *semi-infinite* periodic structure of this type were examined in Ref. 1. Numerical results for a system with relatively short-length transverse beams ($l_t = l/8$), which were still resonant within the frequency range considered, showed that the flexural-longitudinal wave coupling has a drastic effect on the wave propagation properties in comparison to those of a corresponding system with *symmetrically* attached cross beams, which are known to generate significant broadband attenuation of flexural waves.[2] Although the asymmetrical system[1] was excited by an external point moment—that was anticipated to excite a predominantly flexural wave, which is governed by a broad "stopband" at mid-frequencies—the inherent wave coupling resulted in a highly enhanced wave transmission with very little attenuation of flexural motion from element to element. This enhanced transmission is caused by another wave-type, which is predominantly longitudinal and propagates with significant components of both flexural and longitudinal displacements. So, the wave conversion implies that both flexural and longitudinal wave-energies are transported by *whichever* wave-type that is able to propagate, and that wave transmission is only effectively reduced in frequency bands where *all* the wave-types present are sufficiently attenuated. Whether this also applies for periodic structures with extended (long) and multiresonant side-branches and for systems with typical values of structural damping (as opposed to undamped systems) is examined in this paper. An understanding of this type of transmission path is of considerable practical interest, for example, in the prediction of structureborne sound transmission in web-stiffened panels, in ship hulls that have decks to one side only, and in supporting column-structures in building-skeletons.

[a]Electronic mail: lf@oersted.dtu.dk
[b]Electronic mail: mo@oersted.dtu.dk

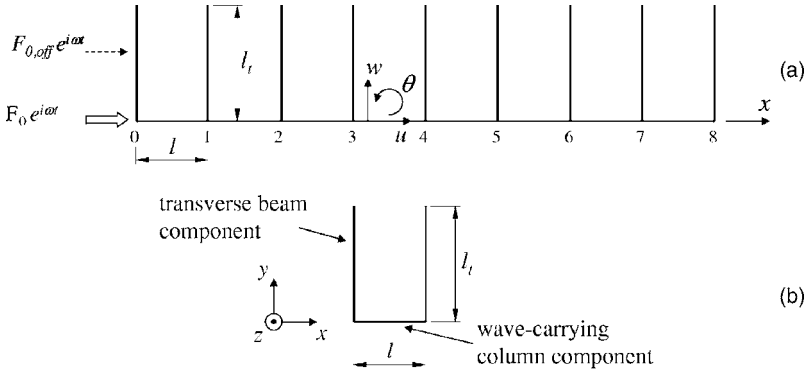

FIG. 1. (a) Periodic structure with asymmetrical side-branches in the form of transverse beams; (b) corresponding periodic element that is symmetrical with respect to its center $x=l/2$.

Periodic structures have been studied for many years but only a few authors have considered the problem of wave coupling and the effect of structural damping thereon. In an experimental investigation Gösele[3] measured the structure-borne sound transmission in a model structure representing the outer wall and flanking columns of a building structure, which was loaded asymmetrically with thick floor plates, causing a significant characteristic mobility-mismatch in the order of 1:70. It was shown that stiffening of the wall by two flanking columns significantly enhanced the wave transmission, as vibrational energy was transported through the columns rather than the wall. Presumably flexural-longitudinal wave coupling or flexural-torsional wave coupling or combinations thereof caused this. Mead and Markus[4] studied flexural-longitudinal wave coupling in a simple multisupported beam loaded eccentrically with single degree-of-freedom oscillators on levers, and they demonstrated that a *high value* of structural damping in the wave-carrying beam resulted in a very substantial decrease in the coupling between flexural and longitudinal motions. Whether such a decrease occurs in a moderately damped engineering structure like that sketched in Fig. 1 is examined in the present paper.

A. Fundamental relations for periodic structures

Periodic structure theory is briefly summarized in a companion paper,[1] so it is only the most basic relations that will be given here. Wave propagation in infinite periodic structures can be determined from knowledge of the dynamic properties of just a single "periodic element." Consider harmonic wave motion in an undamped and infinite periodic structure composed of repeated elements that are coupled with one another through the smallest possible number of motion coordinates n. The response of such a structure is governed by n characteristic free, harmonic wave-types, which can exist simultaneously and independently at any frequency.[5–7] These wave-types occur in n pairs of positive and negative-going waves, with the corresponding propagation characteristics being described by a pair of complex and frequency-dependent characteristic "propagation constants" $\mu=\pm(\mu_R+i\mu_I)$. Usually, μ_R is called the "attenuation constant" and μ_I the "phase constant;" both quantities are defined as being positive. So, if only a single positive-going characteristic harmonic wave with propagation constant μ and angular frequency ω travels through the system, then the complex displacements $q(x)=q(\xi)$ and $q(\xi+l)$ at identical positions ξ in adjacent elements of length l are related by $q(\xi+l)e^{i\omega t}=e^{\mu}q(\xi)e^{i\omega t}$. Hence, if the solution of μ takes on negative values the wave is progressing in the positive direction. These relationships show that free wave motion is possible only in frequency bands where μ is purely imaginary, that is, $\mu=\pm i\mu_I$. These bands are known as "propagation zones" or "passbands." For negligible structural damping a wave thus propagates throughout the system without change in amplitude. The frequency bands in which μ is real, that is, $\mu=\pm\mu_R$ or $\mu=\pm\mu_R\pm i\pi$, are called "attenuation zones" or "stopbands," since no transport of vibrational energy is possible and the wave amplitude is attenuated (reduced) from element to element.

B. Background and outline of paper

The paper examines wave propagation and response in asymmetrical periodic structures of the type shown in Fig. 1, which exemplifies a tri-coupled periodic structure with multiresonant point loadings caused by continuous cross-members (or side-branches). Damping loss factors in building structures, for example, typically take values in the range of 0.01–0.05, and this cannot be neglected in a prediction of wave transmission. The influence of structural damping on wave propagation and flexural-longitudinal wave coupling in a semi-infinite periodic structure is therefore examined numerically in Sec. II by using the expression derived in a companion paper.[1] The simplifying assumption behind the use of *infinite* or *semi-infinite* periodic systems is well justified for such analyses of wave propagation phenomena. However, most engineering structures consist of a relatively small number of periodic elements, which are only moderately damped. This means that reflections from the ends of a periodic system cannot be ignored and the system thus has to be treated as a *finite* periodic system, which, for a multicoupled periodic system, complicates the analysis considerably. A derivation of the frequency response functions of such finite periodic structures is of course very important, but has not been done before to the authors' knowledge.

Section III therefore presents an extensive derivation of a general expression for the junction-response of *finite* and *multicoupled* periodic systems. This is derived as a generalization of the governing expression for finite, *mono-coupled* periodic systems.[8] Together with a set of generalized wave coordinates the present derivation also utilizes the eigenvectors of displacements and wave forces that are associated with the characteristic wave-types, which can exist in a multicoupled periodic system;[9] the present analysis is based on

the receptance approach to the periodic structure theory.[7,9,10] Basically, this approach utilizes that harmonic displacements and forces at the terminals of a single periodic element are related by its dynamic receptances—or mobilities if these are preferred. With the harmonic time variation omitted, and by denoting the left- and right-hand ends of a periodic element by indices l and r, respectively, these relations between displacements q and forces F read $q_l = \alpha_{ll} F_l + \alpha_{lr} F_r$ and $q_r = \alpha_{rl} F_l + \alpha_{rr} F_r$, where α_{ll} and α_{rr} are the direct receptances of the periodic element and α_{lr} and α_{rl} are the transfer receptances. Now, relationships between displacement amplitudes in adjacent periodic elements and between corresponding forces were given in Sec. I A; evaluating these at the left- and right-hand ends of a single periodic element yield $q_r = e^{\mu} q_l$ and $F_r = -e^{\mu} F_l$. So, by substitution, the propagation constant μ is readily expressed in terms of the element receptances.[1]

Finally, in Sec. IV the derived junction-receptance is put into use in response predictions of a specific test-structure with eight periodic elements and with structural terminations at the extreme ends. Audio-frequency vibration responses of this tri-coupled periodic structure are predicted numerically over a broad range of frequencies and the results are compared with experimental measurements on a nominally identical periodic test-structure.

II. NUMERICAL INVESTIGATION OF THE EFFECT OF DAMPING

A wave analysis and numerical parameter study have been conducted for investigating the effect of structural damping on wave coupling and response of asymmetrical periodic structures that undergo flexural and longitudinal vibration. We consider a *semi-infinite* periodic structure similar to that depicted in Fig. 1, albeit extending toward infinity in the positive x-direction. This free or semidefinite system is driven by an external forcing vector $\mathbf{F}_0 e^{i\omega t}$ that represents both longitudinal and transverse force excitations as well as moment excitation. Note that application of any *single one* of these force components will generate a *coupled* or *mixed* response comprising both longitudinal and flexural motions because of the structural asymmetry. The vibration response of the wave-carrying components (and elsewhere) is governed by *three* motion degrees-of-freedom, comprising displacements $u(x,t)$, $w(x,t)$, and $\theta(x,t)$ in the longitudinal, transverse, and rotational directions.

The *periodic element* of the structure, shown in Fig. 1(b), consists of a wave-carrying beam or column component of length l, and two multiresonant load components in the form of transverse beams of length l_t. For convenience in analysis the periodic element is chosen to be symmetrical about the middle of the column component, which means that the element can be rotated 180° about the y axis without changing its dynamic properties. This symmetry of the periodic element is achieved by halving each transverse beam in the z direction into beams of half-width. Thus, when every second periodic element is rotated 180° about its vertical center axis and periodic elements are physically connected to one another, then the transverse beams of half-width become sideways interconnected to form transverse beams of full width.

The structural properties and dimensions of the components used in the present simulations are identical to those used in the predictions and experimental investigation in Sec. IV. The wave-carrying component has length $l = 235$ mm, thickness $h = 15$ mm, and width $b = 20$ mm, whereas the appended transverse beam has length $l_t = 380$ mm (i.e., $l_t \approx 1.6 \cdot l$), thickness-parameter $h_t = h$, and width-parameter $b_t = b$. The structure is made of acrylic with Young's modulus $E = 5.4 \cdot 10^9$ N/m^2 and density $\rho = 1200$ kg/m^3. Material damping is modeled by letting Young's modulus become complex as $\underline{E} = E(1 + i\eta)$, where η is the damping loss factor. Calculations have been made for three values of damping loss factor η, namely 0.001, 0.01, and 0.056, where the high value is identical to the experimentally determined loss factor for an acrylic test beam sample.

The semi-infinite structure considered is similar to the one investigated in a companion paper,[1] except for dimensions of the transverse beam components. Hence, the expressions used in the present numerical simulations for calculating the required quantities like element receptances, propagation constants, associated force and displacement vectors, energy ratios and vibration responses, can all be found in Ref. 1 and will not be repeated here. It should be mentioned that the element's components are modeled using Bernoulli-Euler beam theory, albeit with correction for shear deformation,[11] and that the computations have been done using MATLAB.

A. Propagation constants

Since the periodic structure is tri-coupled, asymmetrical, and semi-infinite, its response thus results from the sum of contributions from three positive-going characteristic waves, which all include components of the displacements $u(x,t)$, $w(x,t)$, and $\theta(x,t)$. The wave-field in each wave-carrying beam component is of course composed of both positive and negative-going waves; these waves result in the positive-going characteristic waves. Note that for the finite system studied later on, one also has to include three corresponding negative-going characteristic waves due to reflections from boundaries. Accordingly, the waves-types in the periodic structure are associated with three pairs of propagation constants $\mu_i = \pm(\mu_{i,R} + \mu_{i,I})$ where $i = A, B, C$. Here $\mu_{i,R}$ and $\mu_{i,I}$ are defined as positive and thus the three positive-going waves are associated with the values $\mu_{i,+} = -\mu_i = -(\mu_{i,R} + i\mu_{i,I})$, (and the three negative-going waves are associated with $\mu_{i,-} = \mu_i = \mu_{i,R} + i\mu_{i,I}$).

The calculated wave characteristics for the semi-infinite structure are presented in Fig. 2. This shows the frequency variation of the real and imaginary parts of the propagation constants, that is, the attenuation constants μ_R and the phase constants μ_I, associated with the three pairs of wave-types. In Fig. 2(a) results are shown for a very low damping value of $\eta = 0.001$; this shows that for frequencies above 35 Hz one wave-type, say type C, is governed by a very high attenuation constant and this wave can thus be regarded as a flexural near-field.[1] The two other wave-types, say A and B, which

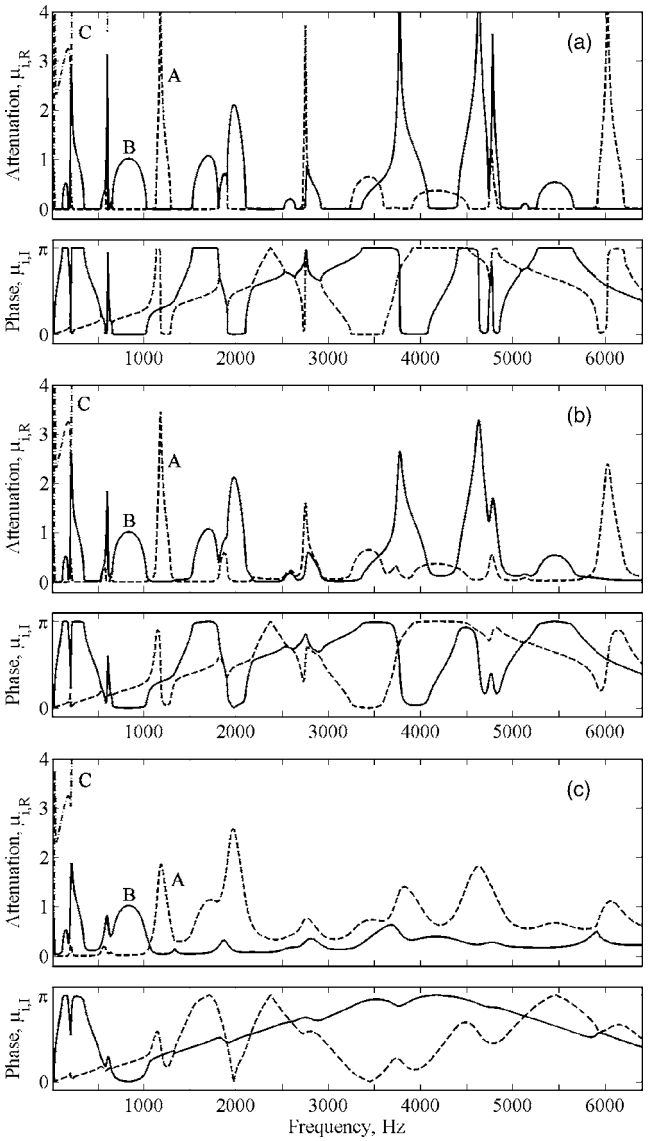

FIG. 2. Frequency variation of the real and imaginary parts of the propagation constants $\mu_i = \mu_{i,R} + \mu_{i,I}$ for the three wave-types: (---) flexural-longitudinal wave *A*; (—) flexural-longitudinal wave *B*; (-·-) predominantly flexural near-field *C*. Damping loss factors: (a) $\eta = 0.001$; (b) $\eta = 0.01$; (c) $\eta = 0.056$.

alternate between being either propagating or attenuated, must be regarded as being of both longitudinal and flexural nature. The very complicated pattern of propagation zones and attenuation zones shown here are to a large extent caused by the various modes of the transverse beams; the occurrence of both smooth and resonant type attenuation zones is explained in detail in Ref. 1. Still, it should be mentioned that no direct *crossing* of the phase constants of wave-type *A* and *B* occurs; the phase constants either (i) diverge or (ii) merge, so that the propagation constants become almost complex conjugates with nonzero attenuation constant. The first phenomenon is most pronounced at 1066, 1330, and 2175 Hz; at these frequencies the phase constant of each wave "jumps to" the slope of the other wave and the flexural-longitudinal wave coupling is found to be particularly strong. Usually the steeper phase characteristic is associated with a flexural-type wave whereas the more gradual and nearly linear phase characteristic is associated with a longitudinal-type wave. The second phenomenon occurs at several frequencies but may be seen to be most apparent in the bands around 560, 1860, 2580, 2830, 4755, and 5125 Hz. In these bands the wave with strongly coupled longitudinal-flexural motions is *attenuated* as it progresses through the periodic structure.

With a "moderate value" of structural damping of $\eta = 0.01$, the results in Fig. 2(b) show that this increased damping causes a weak widening of the attenuation zones into previous propagation zones as well as a decrease in magnitude of the attenuation constants at peak attenuation frequencies. Furthermore, the attenuation constants and phase constants slightly separate in the frequency bands, which were previously assigned as complex conjugate zones in Fig. 2(a). This indicates that flexural-longitudinal wave coupling decreases when structural damping is increased, and this is clearly demonstrated in Fig. 2(c), which shows results for a damping value of $\eta = 0.056$; in contrast to the results in Fig. 2(a) the phase constants are now seen to *cross-over* directly and become almost linear in certain frequency bands. This is the case in the frequency range from 0 to 1066 Hz for wave-type *A* and from 1066 Hz and upwards for wave-type *B*. As mentioned before, this almost linear phase characteristic is typically associated with a longitudinal wave. Figure 2(c) also reveals that the predominantly longitudinal wave is able to progress through the structure with relatively little attenuation in wave amplitude, since the associated attenuation constant is less than 0.3 in most parts of the frequency range considered. The predominantly flexural wave, however, which is associated with the steeper phase characteristic, is more significantly attenuated in nearly the whole frequency range.

Now, a more quantitative characterization of the wave-types than inspections of the propagation constant curves can provide, requires a determination of the displacement contributions and associated energies in the different wave-types. Such a characterization can be revealed by computing the normalized displacement vector associated with each wave-type and from this the corresponding wave energy.[1,4]

B. Nature of wave-types

The relative amounts of flexural and longitudinal motions contained in each wave-type can be quantified by the associated kinetic energy ratio ($E_{\mathrm{kin},F}/E_{\mathrm{kin},L}$), being the ratio between maximum kinetic energies of flexural and longitudinal motions in the wave-carrying column component. Figure 3 shows these energy ratio levels corresponding to the propagation constants given in Fig. 2. From Fig. 3(a), where $\eta = 0.001$, it is readily seen that wave-types *A* and *B* must both be classified as being longitudinal-flexural, since each of them alternates in a complicated manner between being either predominantly longitudinal or flexural, or occasionally fully mixed, with approximately equal contributions. Wave-type *C*, however, has an energy ratio level of more than 70 dB in almost the entire frequency range and thus can be regarded as a flexural near-field. In complex conjugate zones the energy levels of the two mixed wave-types are seen to be

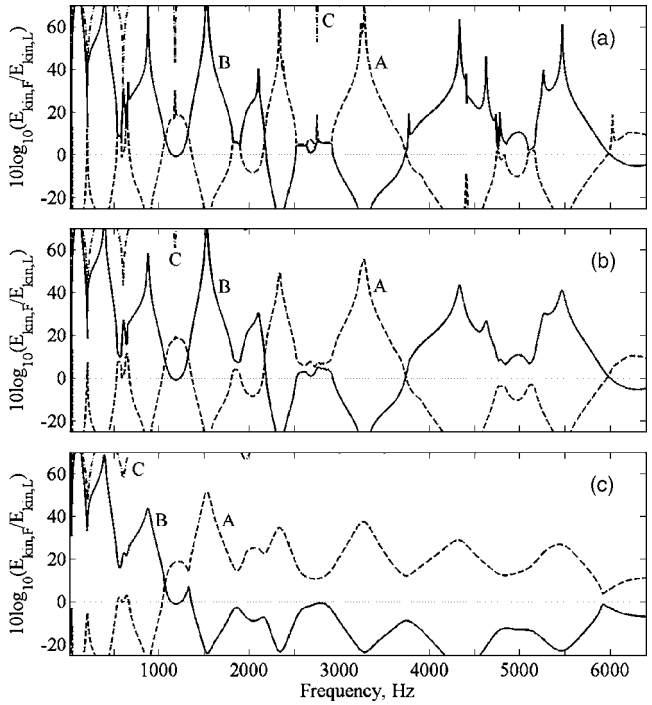

FIG. 3. Energy ratios $E_{kin,F}/E_{kin,L}$ for the three wave-types: (---) flexural-longitudinal wave A; (—) flexural-longitudinal wave B; (---) predominantly flexural near-field C. Damping loss factors: (a) $\eta=0.001$; (b) $\eta=0.01$; (c) $\eta=0.056$.

equal. The crossing of the energy ratios occurs only in the earlier mentioned regions where the phase constants of Fig. 2(a) diverge from one another.

When the loss factor is increased to $\eta=0.01$, Fig. 3(b) shows that the two mixed wave-types A and B separate in the frequency bands, which were formerly complex conjugate zones. Furthermore, peaks and troughs are smoothed especially at high frequencies. The pattern of the energy ratios, though, is the same as in Fig. 3(a), but a further *increase* of the loss factor to $\eta=0.056$ drastically changes this, as the two wave-types become almost completely separated, see Fig. 3(c). Now, the two energy ratios cross only at 1066 Hz, which is the region where the two phase constants in Fig. 2(c) diverge from one another. Consistent with earlier statements it is seen that the linear parts of the phase constants in Fig. 2(c) are associated with a predominantly longitudinal wave, whereas the steeper phase characteristic is associated with a predominantly flexural wave.

C. Junction responses

Finally the effect of damping on the response of the semi-infinite structure is investigated. For a harmonic *moment* excitation of unit magnitude Fig. 4 shows the maximum flexural displacement responses of the column component in the first eight periodic elements. For a loss factor of $\eta=0.001$, it is seen from Fig. 4(a) that flexural waves are propagating with practically no attenuation from element to element in approximately half the frequency range considered. A closer inspection reveals that some of the attenuation bands in Fig. 2(a) have little or no influence on the response. This phenomenon, which is due to flexural-longitudinal

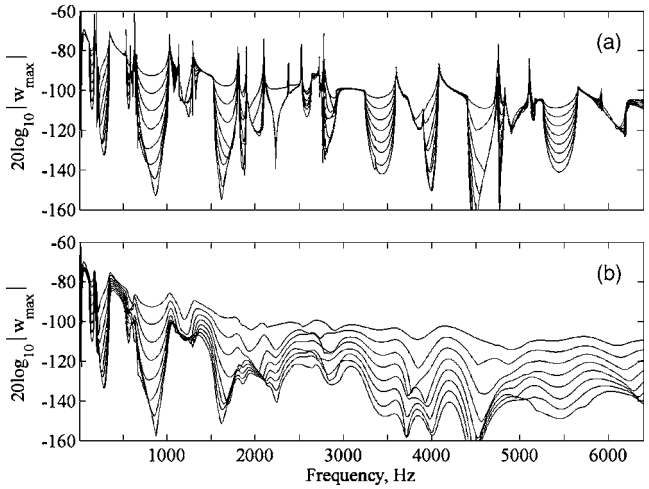

FIG. 4. Maximum transverse displacements w_{max} in column component of the first eight elements of semi-infinite periodic structure. Excitation by a harmonic point moment of unit amplitude. Damping loss factors: (a) $\eta=0.001$; (b) $\eta=0.056$.

wave coupling, is readily seen in the frequency bands around 1200, 3750, and 6000 Hz, and occurs whenever one wave-type is propagating and the other wave-type is *strongly* attenuated and their energy ratio levels in Fig. 3(a) are less than, say, 20 dB apart. Nevertheless, because of the moment excitation the predominantly flexural wave will dominate the response once the energy ratio levels are more than 20 dB apart; this evidently occur in the bands around the frequencies 150, 310, 875, 1595, 3440, 4010, 4450, and 5440 Hz. In complex conjugate zones, e.g., around 1860, 2580, and 2830 Hz, both wave-types are attenuated and the flexural responses and longitudinal responses are thus both reduced from element to element.

Figure 4(b) shows the flexural responses for a high loss factor of $\eta=0.056$. This increase of structural damping drastically affects the junction responses of the semi-infinite periodic structure; at all frequencies from about 1600 Hz and *upwards* the flexural responses are significantly reduced from element to element. This is because the flexural motion is dominated by wave-type A, which is considerably attenuated. However, in frequency bands where wave-type A is *strongly* attenuated, e.g., around 1200, 2000, and 4600 Hz, this wave becomes insignificant after just a few elements and the *less* attenuated wave-type B then takes over and dominates the flexural response of the elements that follows. Gösele[3] observed a similar wave conversion behavior and Mead and Markus[4] also discussed this phenomenon.

For a harmonic *longitudinal* unit force excitation Fig. 5 shows the maximum longitudinal displacement responses of the column component in the first eight elements. For a loss factor of $\eta=0.001$, Fig. 5(a) shows that longitudinal waves are propagating in almost the whole frequency range. Up to 3400 Hz and from 4500 Hz and upwards, this wave propagation is only interrupted by narrow bands of attenuation arising mostly from complex conjugate zones. In the frequency band from 3400 to 4500 Hz wider attenuation zones occur, as the predominantly longitudinal wave is signifi-

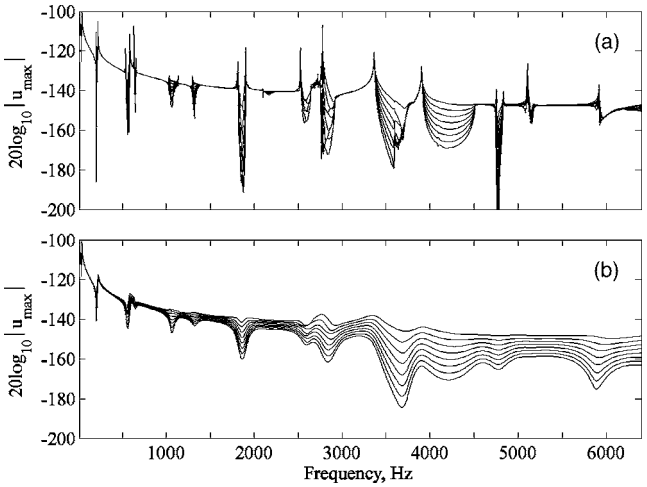

FIG. 5. Maximum longitudinal displacements u_{max} in column component of the first eight elements of semi-infinite periodic structure. Excitation by a harmonic longitudinal point force of unit amplitude. Damping loss factors: (a) $\eta=0.001$; (b) $\eta=0.056$.

cantly attenuated and the energy ratio levels in Fig. 3(a) are more than 20 dB apart.

In the present case of relatively light modal point loadings posed by the transverse beams, it can be shown that the longitudinal displacement responses—apart from minor deviations—follow closely the asymptotic response of a *simple continuous* and semi-infinite column structure of the same cross-sectional area S. Essentially, this implies that the corresponding longitudinal *velocity* responses of the system are almost independent of frequency in the range considered.

Figure 5(b) shows the longitudinal responses for the high loss factor of $\eta=0.056$. This increase of damping enhances only the attenuation slightly at higher frequencies. Furthermore, the damping enforces no particular change in the response pattern as attenuation occurs at the same frequencies as in Fig. 5(a). As the predominantly longitudinal wave-type has the lowest value of attenuation constant at all frequencies, then this is governing the longitudinal responses at all junctions of the structure.

III. FINITE PERIODIC STRUCTURES

Engineering structures that are spatially periodic often consist of relatively few periodic elements; this means that reflections from the extreme boundaries cannot be neglected and the periodic structures must therefore be treated as *finite*. Ohlrich[8] derived governing expressions for the response of finite, *mono-coupled* periodic systems in terms of the system's junction-receptances. The same derivation procedure is generalized herein and used for determining the junction-receptances of *finite* and *multicoupled* periodic systems. A general expression for a $n\times n$ junction-receptance matrix is derived for a system with arbitrary terminations. In this derivation use is also made of a wave-reflection technique developed by Mead,[9] and this was outlined and extended in the companion paper.[1]

Figure 6 shows schematically a finite system with N periodic elements and arbitrary terminations A and B at junctions O and N, respectively. These terminations may be defined by their $n\times n$ receptance matrices $\boldsymbol{\alpha}_A$ and $\boldsymbol{\alpha}_B$. It is assumed that the structure is excited at junction j by an *external* harmonic force vector $\mathbf{F}_j e^{i\omega t}$, which introduces a discontinuity. In order to determine the harmonic response at an arbitrary junction of the total system, it is expedient[8] to analyze the system as being composed of two subsystems in parallel, as shown by the block diagram in Fig. 6(b). The motions generated in each subsystem can be represented by n characteristic positive-going waves and n characteristic negative-going waves, of which each wave is associated with the propagation constants $\mu_{i,+}=-\mu_i$ and $\mu_{i,-}=\mu_i$, respectively, and where $i=1,2,3,\ldots,n$. The effect of the terminations can be taken into account by determining the corresponding reflection matrices.

A. Reflection from system boundaries

A relationship between the n waves incident on a boundary and the n waves being reflected by this is derived in the following. Consider the ith positive-going wave at angular frequency ω impinging on boundary B. This wave has the propagation constant $\mu_{i,+}=-(\mu_{i,R}+\mu_{i,I})$ and is associated with an n-element force eigenvector $\mathbf{F}_{i,B+}$ given by

$$\mathbf{F}_{i,B+}=\mathbf{f}_{i,+}\psi_{i,B+}, \tag{1}$$

where $\mathbf{f}_{i,+}$ is a *normalized force vector* with n entries and $\psi_{i,B+}$ is a *generalized wave coordinate* at boundary B. This force vector $\mathbf{f}_{i,+}$ only depends upon the receptances and propagation constants of the periodic element, whereas $\psi_{i,B+}$ is also a function of the position in the structure and the type of external excitation. The normalized force vector $\mathbf{f}_{i,+}$ is an eigenvector obtained for each wave-type as described in a

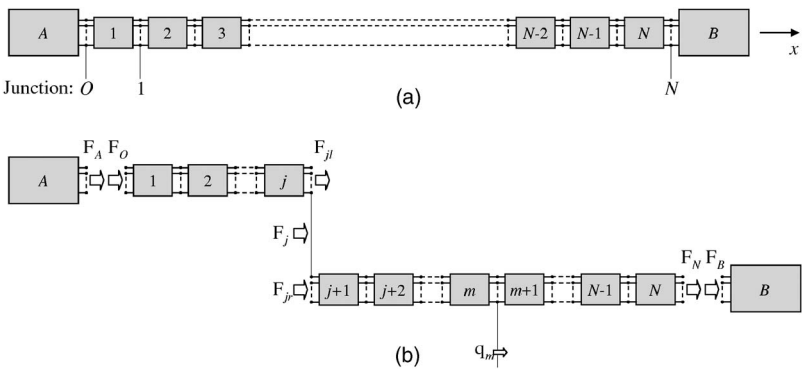

FIG. 6. (a) Block diagram of a finite multicoupled periodic structure with arbitrary terminations A and B. (b) Free body diagram for interior junction excitation.

companion paper.[1] Corresponding to the force eigenvector there is a displacement vector given as

$$\mathbf{q}_{i,B+} = \boldsymbol{\zeta}_{i,+}\psi_{i,B+}, \tag{2}$$

where $\boldsymbol{\zeta}_{i,+}$ is a *normalized displacement vector*.

The relationship between the normalized force vector $\mathbf{f}_{i,+}$ and the corresponding displacement vector $\boldsymbol{\zeta}_{i,+}$ yields[1]

$$\boldsymbol{\zeta}_{i,+} = \boldsymbol{\alpha}_{ll}\mathbf{f}_{i,+} - \boldsymbol{\alpha}_{lr}\mathbf{f}_{i,+}e^{-\mu_i}, \tag{3}$$

where $\boldsymbol{\alpha}_{ll}$ and $\boldsymbol{\alpha}_{lr}$, respectively, are the direct and transfer receptance matrices of the *periodic element*. At boundary B this particular positive-going wave causes n characteristic negative-going waves to be reflected back into the periodic system. So, if not only one but n characteristic waves impinge on the boundary B, then each of these is reflected into n negative-going waves. These $n\times n$ reflected waves form n negative-going waves, each of which consists of n wave contributions. Associated with each of these n negative-going waves there is a propagation constant μ_i, a force eigenvector $\mathbf{F}_{i,B-}$, and a corresponding displacement vector $\mathbf{q}_{i,B-}$ that are given by

$$\mathbf{F}_{i,B-} = \mathbf{f}_{i,-}\psi_{i,B-}, \quad \mathbf{q}_{i,B-} = \boldsymbol{\zeta}_{i,-}\psi_{i,B-}, \tag{4}$$

respectively. By analogy to Eq. (3) the normalized displacement vector and force vector are related as

$$\boldsymbol{\zeta}_{i,-} = \boldsymbol{\alpha}_{ll}\mathbf{f}_{i,-} - \boldsymbol{\alpha}_{lr}\mathbf{f}_{i,-}e^{\mu_i}. \tag{5}$$

Now, the total force vector $\mathbf{F}_B$ at boundary B is a sum of $2n$ force eigenvectors from n impinging waves and n reflected waves, which yields

$$\mathbf{F}_B = \sum_{i=1}^{n}\mathbf{f}_{i,+}\psi_{i,B+} + \sum_{i=1}^{n}\mathbf{f}_{i,-}\psi_{i,B-} = \mathbf{f}_+\boldsymbol{\psi}_{B+} + \mathbf{f}_-\boldsymbol{\psi}_{B-}, \tag{6}$$

where $\mathbf{f}_+$ and $\mathbf{f}_-$ are $n\times n$ element matrices containing n normalized force eigenvectors and $\boldsymbol{\psi}_{B+}$ and $\boldsymbol{\psi}_{B-}$ are column vectors containing n generalized coordinates associated with the positive and negative-going waves, respectively. In a similar manner the total displacement vector at boundary B can be expressed as a sum of contributions from n impinging and n reflected waves giving

$$\mathbf{q}_B = \sum_{i=1}^{n}\boldsymbol{\zeta}_{i,+}\psi_{B,i,+} + \sum_{i=1}^{n}\boldsymbol{\zeta}_{i,-}\psi_{B,i,-} = \boldsymbol{\zeta}_+\boldsymbol{\psi}_{B+} + \boldsymbol{\zeta}_-\boldsymbol{\psi}_{B-}, \tag{7}$$

where $\boldsymbol{\zeta}_+$ and $\boldsymbol{\zeta}_-$ are matrices with $n\times n$ entries containing normalized displacement vectors of the n positive and negative-going waves, respectively. Using Eqs. (3) and (5) these can be written as

$$\boldsymbol{\zeta}_+ = \boldsymbol{\alpha}_{ll}\mathbf{f}_+ - \boldsymbol{\alpha}_{lr}\mathbf{f}_+\mathbf{e}_d^{-\boldsymbol{\mu}}, \tag{8}$$

$$\boldsymbol{\zeta}_- = \boldsymbol{\alpha}_{ll}\mathbf{f}_- - \boldsymbol{\alpha}_{lr}\mathbf{f}_-\mathbf{e}_d^{\boldsymbol{\mu}}. \tag{9}$$

Here, the notations $\mathbf{e}_d^{-\boldsymbol{\mu}}$ and $\mathbf{e}_d^{\boldsymbol{\mu}}$ represent *diagonal matrices* containing all values of $e^{-\mu_i}$ and e^{μ_i}, respectively. The boundary condition at B is given by $\mathbf{q}_B = \boldsymbol{\alpha}_B\mathbf{F}_B$, and inserting Eqs. (6) and (7) into this gives

$$\boldsymbol{\zeta}_+\boldsymbol{\psi}_{B+} + \boldsymbol{\zeta}_-\boldsymbol{\psi}_{B-} = \boldsymbol{\alpha}_B(\mathbf{f}_+\boldsymbol{\psi}_{B+} + \mathbf{f}_-\boldsymbol{\psi}_{B-}). \tag{10}$$

This yields a relationship between the generalized wave coordinate vectors of the reflected waves $\boldsymbol{\psi}_{B-}$ and the incident waves $\boldsymbol{\psi}_{B+}$:

$$\boldsymbol{\psi}_{B,-} = -(\boldsymbol{\alpha}_B\mathbf{f}_- - \boldsymbol{\zeta}_-)^{-1}(\boldsymbol{\alpha}_B\mathbf{f}_+ - \boldsymbol{\zeta}_+)\boldsymbol{\psi}_{B+}, \tag{11}$$

where superscript -1 denotes a matrix inversion. This may be expressed in short form as

$$\boldsymbol{\psi}_{B-} = \mathbf{r}_B\boldsymbol{\psi}_{B+}, \tag{12}$$

where $\mathbf{r}_B$ is the matrix of reflection factors at boundary B.

The reflection matrix of boundary A can be found similarly by noting that the incident waves on A are negative-going and the reflected waves are positive-going. Thus, let the force vectors of the incident and reflected waves be given by

$$\mathbf{F}_{i,A-} = \mathbf{f}_{i,-}\psi_{i,A-}, \quad \mathbf{F}_{i,A+} = \mathbf{f}_{i,+}\psi_{i,A+}, \tag{13}$$

respectively. The total force vector at boundary A is a sum of force eigenvectors corresponding to n incident and n reflected waves, i.e.,

$$\mathbf{F}_A = -\mathbf{f}_+\boldsymbol{\psi}_{A+} - \mathbf{f}_-\boldsymbol{\psi}_{A-}, \tag{14}$$

and the total displacement is given by

$$\mathbf{q}_A = \boldsymbol{\zeta}_+\boldsymbol{\psi}_{A+} + \boldsymbol{\zeta}_-\boldsymbol{\psi}_{A-}. \tag{15}$$

Now, the boundary condition at A is $\mathbf{q}_A = \boldsymbol{\alpha}_A\mathbf{F}_A$, and substitution of Eqs. (14) and (15) into this finally yields a relationship between the generalized wave coordinate vectors of the reflected waves $\boldsymbol{\psi}_{A+}$ and the incident waves $\boldsymbol{\psi}_{A-}$:

$$\boldsymbol{\psi}_{A+} = -(\boldsymbol{\alpha}_A\mathbf{f}_+ + \boldsymbol{\zeta}_+)^{-1}(\boldsymbol{\alpha}_A\mathbf{f}_- + \boldsymbol{\zeta}_-)\boldsymbol{\psi}_{A-}. \tag{16}$$

In short form this reads

$$\boldsymbol{\psi}_{A+} = \mathbf{r}_A\boldsymbol{\psi}_{A-}, \tag{17}$$

where $\mathbf{r}_A$ is the reflection matrix of boundary A.

B. Matrix of direct receptances of *j*-element subsystem

An expression for the $n\times n$ direct receptance matrix of the left-hand subsystem with j elements in Fig. 6(b) will now be derived. The displacement vector $\mathbf{q}_O$ at junction O is a sum of contributions from displacement vectors associated with n positive-going and n negative-going waves. This can be expressed as

$$\mathbf{q}_O = \mathbf{q}_{O+} + \mathbf{q}_{O-} = \boldsymbol{\zeta}_+\boldsymbol{\psi}_{O+} + \boldsymbol{\zeta}_-\boldsymbol{\psi}_{O-}. \tag{18}$$

Further, the generalized wave coordinate vectors for the positive and negative-going waves at the other end of the subsystem, j junctions to the right, yield

$$\boldsymbol{\psi}_{jl+} = \mathbf{e}_d^{-j\boldsymbol{\mu}}\boldsymbol{\psi}_{O+}, \tag{19}$$

$$\boldsymbol{\psi}_{jl-} = \mathbf{e}_d^{j\boldsymbol{\mu}}\boldsymbol{\psi}_{O-}, \tag{20}$$

respectively. Here the notation $\mathbf{e}_d^{-j\boldsymbol{\mu}}$ and $\mathbf{e}_d^{j\boldsymbol{\mu}}$ represent *diagonal matrices* containing all values of $e^{-j\mu_i}$ and $e^{j\mu_i}$, respectively. By utilizing these expressions the total displacement vector $\mathbf{q}_{jl}$ at this position reads

$$\mathbf{q}_{jl} = \mathbf{q}_{jl+} + \mathbf{q}_{jl-} = \boldsymbol{\zeta}_+ \boldsymbol{\psi}_{jl+} + \boldsymbol{\zeta}_- \boldsymbol{\psi}_{jl-} = \boldsymbol{\zeta}_+ \mathbf{e}_d^{-j\boldsymbol{\mu}} \boldsymbol{\psi}_{O+} + \boldsymbol{\zeta}_- \mathbf{e}_d^{j\boldsymbol{\mu}} \boldsymbol{\psi}_{O-}. \quad (21)$$

Now, $\boldsymbol{\psi}_{O,+}$ and $\boldsymbol{\psi}_{O,-}$ are related through the reflection matrix $\mathbf{r}_A$ of boundary A given by Eq. (17) and utilizing this yields

$$\mathbf{q}_{jl} = (\boldsymbol{\zeta}_+ \mathbf{e}_d^{-j\boldsymbol{\mu}} \mathbf{r}_A + \boldsymbol{\zeta}_- \mathbf{e}_d^{j\boldsymbol{\mu}}) \boldsymbol{\psi}_{O-}. \quad (22)$$

In a similar way the corresponding force eigenvector $\mathbf{F}_{jl}$ is obtained as

$$\mathbf{F}_{jl} = \mathbf{F}_{jl+} + \mathbf{F}_{jl-} = -\mathbf{f}_+ \boldsymbol{\psi}_{jl+} - \mathbf{f}_- \boldsymbol{\psi}_{jl-} = -\mathbf{f}_+ \mathbf{e}_d^{-j\boldsymbol{\mu}} \boldsymbol{\psi}_{O+} - \mathbf{f}_- \mathbf{e}_d^{j\boldsymbol{\mu}} \boldsymbol{\psi}_{O-}, \quad (23)$$

and further use of the reflection matrix $\mathbf{r}_A$ gives

$$\mathbf{F}_{jl} = (-\mathbf{f}_+ \mathbf{e}_d^{-j\boldsymbol{\mu}} \mathbf{r}_A - \mathbf{f}_- \mathbf{e}_d^{j\boldsymbol{\mu}}) \boldsymbol{\psi}_{O-}. \quad (24)$$

Solving for $\boldsymbol{\psi}_{O,-}$ and substitution in Eq. (22) finally yields a relationship between the displacement vector $\mathbf{q}_{jl}$ and force vector $\mathbf{F}_{jl}$ at junction j,

$$\mathbf{q}_{jl} = \boldsymbol{\gamma}_{jj} \mathbf{F}_{jl}, \quad (25)$$

where the *direct* receptance matrix $\boldsymbol{\gamma}_{jj}$ of the j-element subsystem is given by

$$\boldsymbol{\gamma}_{jj} = (\boldsymbol{\zeta}_+ \mathbf{e}_d^{-j\boldsymbol{\mu}} \mathbf{r}_A + \boldsymbol{\zeta}_- \mathbf{e}_d^{j\boldsymbol{\mu}})(-\mathbf{f}_+ \mathbf{e}_d^{-j\boldsymbol{\mu}} \mathbf{r}_A - \mathbf{f}_- \mathbf{e}_d^{j\boldsymbol{\mu}})^{-1}. \quad (26)$$

C. Matrix of transfer receptances of $(N-j)$-element subsystem

Consider the subsystem with $(N-j)$ elements lying to the right of the external force discontinuity in Fig. 6(b). For this subsystem driven at j the transfer receptance matrix $\boldsymbol{\delta}_{mj}$ of junction m can be derived using a procedure similar to that above. So, the displacement vector $\mathbf{q}_{jr}$ at the excited junction j is expressed as a sum of contributions from n positive-going waves and n negative-going waves, that is,

$$\mathbf{q}_{jr} = \mathbf{q}_{jr+} + \mathbf{q}_{jr-} = \boldsymbol{\zeta}_+ \boldsymbol{\psi}_{jr+} + \boldsymbol{\zeta}_- \boldsymbol{\psi}_{jr-}, \quad (27)$$

and the total force vector $\mathbf{F}_{jr}$ at junction j reads correspondingly

$$\mathbf{F}_{jr} = \mathbf{F}_{jr+} + \mathbf{F}_{jr-} = \mathbf{f}_+ \boldsymbol{\psi}_{jr+} + \mathbf{f}_- \boldsymbol{\psi}_{jr-}. \quad (28)$$

Further, the displacement vector at junction m, that is $(m-j)$ junctions to the right, is

$$\mathbf{q}_m = \boldsymbol{\zeta}_+ \mathbf{e}_d^{-(m-j)\boldsymbol{\mu}} \boldsymbol{\psi}_{jr+} + \boldsymbol{\zeta}_- \mathbf{e}_d^{(m-j)\boldsymbol{\mu}} \boldsymbol{\psi}_{jr-}. \quad (29)$$

At boundary B, which is $(N-j)$ junctions to the right, the generalized wave coordinate vectors $\boldsymbol{\psi}_{B+}$ and $\boldsymbol{\psi}_{B-}$ of the incident and reflecting waves are given as

$$\boldsymbol{\psi}_{B+} = \mathbf{e}_d^{-(N-j)\boldsymbol{\mu}} \boldsymbol{\psi}_{jr+}, \quad \boldsymbol{\psi}_{B-} = \mathbf{e}_d^{(N-j)\boldsymbol{\mu}} \boldsymbol{\psi}_{jr-}, \quad (30)$$

respectively, and since these two vectors are related in Eq. (12) by the reflection matrix $\mathbf{r}_B$ of boundary B, the following identity is obtained:

$$\mathbf{e}_d^{(N-j)\boldsymbol{\mu}} \boldsymbol{\psi}_{jr-} = \mathbf{r}_B \mathbf{e}_d^{-(N-j)\boldsymbol{\mu}} \boldsymbol{\psi}_{jr+}. \quad (31)$$

Rearranging this gives

$$\boldsymbol{\psi}_{jr-} = \mathbf{e}_d^{-(N-j)\boldsymbol{\mu}} \mathbf{r}_B \mathbf{e}_d^{-(N-j)\boldsymbol{\mu}} \boldsymbol{\psi}_{jr+}, \quad (32)$$

which by substitution in Eqs. (28) and (29) yields

$$\mathbf{q}_m = (\boldsymbol{\zeta}_+ \mathbf{e}_d^{-(m-j)\boldsymbol{\mu}} + \boldsymbol{\zeta}_- \mathbf{e}_d^{(m-j)\boldsymbol{\mu}} \mathbf{e}_d^{-(N-j)\boldsymbol{\mu}} \mathbf{r}_B \mathbf{e}_d^{-(N-j)\boldsymbol{\mu}}) \boldsymbol{\psi}_{jr+} \quad (33)$$

and

$$\mathbf{F}_{jr} = (\mathbf{f}_+ + \mathbf{f}_- \mathbf{e}_d^{-(N-j)\boldsymbol{\mu}} \mathbf{r}_B \mathbf{e}_d^{-(N-j)\boldsymbol{\mu}}) \boldsymbol{\psi}_{jr+}, \quad (34)$$

respectively. From Eq. (34) a relation between the external force vector $\mathbf{F}_{jr}$ and $\boldsymbol{\psi}_{jr,+}$ is obtained

$$\boldsymbol{\psi}_{jr,+} = (\mathbf{f}_+ + \mathbf{f}_- \mathbf{e}_d^{-(N-j)\boldsymbol{\mu}} \mathbf{r}_B \mathbf{e}_d^{-(N-j)\boldsymbol{\mu}})^{-1} \mathbf{F}_{jr}. \quad (35)$$

Finally, substituting this into Eq. (33) gives the displacement vector $\mathbf{q}_m$ at junction m resulting from the force vector $\mathbf{F}_{jr}$ at junction j, that is

$$\mathbf{q}_m = \boldsymbol{\delta}_{mj} \mathbf{F}_{jr}, \quad (36)$$

where we have introduced the *transfer* receptance matrix $\boldsymbol{\delta}_{mj}$ of the right-hand subsystem:

$$\boldsymbol{\delta}_{mj} = (\boldsymbol{\zeta}_+ \mathbf{e}_d^{-(m-j)\boldsymbol{\mu}} + \boldsymbol{\zeta}_- \mathbf{e}_d^{(m-j)\boldsymbol{\mu}} \mathbf{e}_d^{-(N-j)\boldsymbol{\mu}} \mathbf{r}_B \mathbf{e}_d^{-(N-j)\boldsymbol{\mu}}) \times (\mathbf{f}_+ + \mathbf{f}_- \mathbf{e}_d^{-(N-j)\boldsymbol{\mu}} \mathbf{r}_B \mathbf{e}_d^{-(N-j)\boldsymbol{\mu}})^{-1}. \quad (37)$$

Thus, the corresponding *direct* receptance matrix $\boldsymbol{\delta}_{jj}$ is obtained by letting $m=j$, so that

$$\boldsymbol{\delta}_{jj} = (\boldsymbol{\zeta}_+ + \boldsymbol{\zeta}_- \mathbf{e}_d^{-(N-j)\boldsymbol{\mu}} \mathbf{r}_B \mathbf{e}_d^{-(N-j)\boldsymbol{\mu}}) \times (\mathbf{f}_+ + \mathbf{f}_- \mathbf{e}_d^{-(N-j)\boldsymbol{\mu}} \mathbf{r}_B \mathbf{e}_d^{-(N-j)\boldsymbol{\mu}})^{-1}. \quad (38)$$

D. Matrix of junction-receptances of total system

What remains is the determination of the junction-receptances of the total system in terms of the receptance matrices $\boldsymbol{\gamma}_{jj}$, $\boldsymbol{\delta}_{mj}$, and $\boldsymbol{\delta}_{jj}$ of the two subsystems. Since the two subsystems are in parallel the externally applied force vector $\mathbf{F}_j$ must be in equilibrium with the internal forces acting on the subsystems, that is, $\mathbf{F}_j = \mathbf{F}_{jl} + \mathbf{F}_{jr}$. Continuity of displacements at the excitation point furthermore yields $\mathbf{q}_j = \mathbf{q}_{jl} = \mathbf{q}_{jr}$.

Inserting Eqs. (25) and (38) into the last part of this continuity condition gives

$$\mathbf{F}_{jl} = \boldsymbol{\gamma}_{jj}^{-1} \boldsymbol{\delta}_{jj} \mathbf{F}_{jr}, \quad (39)$$

and substituting this into the stated force equilibrium condition leads to

$$\mathbf{F}_j = (\mathbf{I} + \boldsymbol{\gamma}_{jj}^{-1} \boldsymbol{\delta}_{jj}) \mathbf{F}_{jr}, \quad (40)$$

where $\mathbf{I}$ is the unity matrix. Now, $\mathbf{F}_{jr}$ can be eliminated by combining Eqs. (36) and (40), and solving for $\mathbf{q}_m$ finally gives

$$\mathbf{q}_m = \boldsymbol{\alpha}_{mj} \mathbf{F}_j, \quad (41)$$

where $\boldsymbol{\alpha}_{mj}$ is the matrix of transfer receptances of the *total* system:

$$\boldsymbol{\alpha}_{mj} = \boldsymbol{\delta}_{mj} (\mathbf{I} + \boldsymbol{\gamma}_{jj}^{-1} \boldsymbol{\delta}_{jj})^{-1}. \quad (42)$$

Substituting the expressions derived above for $\boldsymbol{\gamma}_{jj}$, $\boldsymbol{\delta}_{mj}$, and $\boldsymbol{\delta}_{jj}$ in Eq. (42) results in a rather complicated expression for the transfer receptance $\boldsymbol{\alpha}_{mj}$. Nevertheless, the solution of this can be implemented numerically and receptances have been calculated without computational difficulties for the limited number of cases studied.

FIG. 7. Experimental arrangement. Point force excitation in longitudinal direction at junction 0.

IV. RESPONSE PREDICTION AND EXPERIMENTAL VERIFICATION

Responses in all three junction coordinates of the eight-element periodic structure in Fig. 1(a) were predicted numerically using calculated propagation constants and the junction-receptances calculated from Eqs. (26), (37), (38), and (42). Since the transverse beams of each periodic element are taken to be of half-width to sustain element symmetry, the *end terminations* of the finite periodic structure are in this case also modeled as transverse beams of half-width in order to form the full-width physical beams at the ends of the structure in question. This implies that the boundary receptance matrices $\boldsymbol{\alpha}_A$ and $\boldsymbol{\alpha}_B$ are given by those of the transverse beam components as can be found in Ref. 1. Other end terminations complying with motion in the *xy* plane may readily be included.

In order to verify the theoretical model an experimental investigation was performed on a nominally identical periodic structure; Fig. 7 shows the experimental arrangement. The structure was made of acrylic, and was suspended in elastic wires so it could vibrate freely in all directions. The structure was forced at the end by an electro-dynamic vibration exciter (Brüel & Kjær Type 4809) fed by a white noise signal. A force transducer (B&K Type 8200) measured the input force and junction responses in all three motion coordinates were measured by using 2.5 g accelerometers (Brüel & Kjær Type 4393). The data acquisition and analysis were performed by a dual-channel FFT analyser (Brüel & Kjær Type 3160 C, "Pulse-System") using a frequency resolution of 1 Hz in the band from 0 to 6400 Hz.

For ease of comparison the propagation constants from Fig. 2(c) are shown in Fig. 8 with a *logarithmic* frequency axis. In the following the numerical predictions for the finite periodic structure are compared with the measured junction-mobilities.

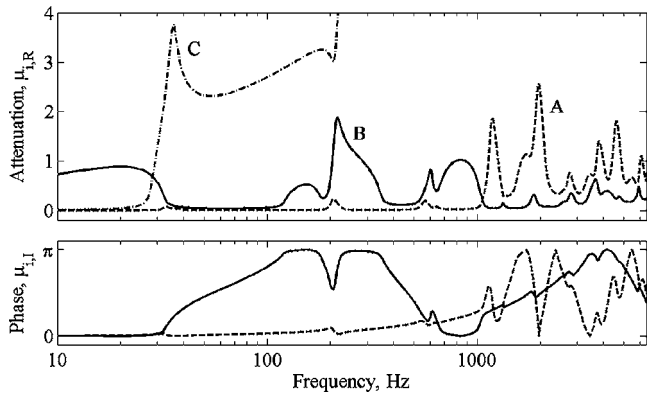

FIG. 8. Wave propagation constants; as in Fig. 2(c), but with logarithmic frequency axis.

A. Response to longitudinal (axial) force excitation

The finite periodic structure was first examined for excitation by a longitudinal force $F_0(t)$ acting at junction 0 as shown in Figs. 1 and 7. Longitudinal velocity responses $\dot{u}_j(t)$ were determined at all junctions $j=0-8$, giving the complex transfer mobilities $Y_{u,j0}=\dot{u}_j/F_0$. As examples of predicted and measured mobilities Fig. 9 shows results for junctions 0 and 8, in terms of magnitude and phase spectra. These results clearly reveal that there is a very good agreement between the predicted and measured mobilities. It is only at very low frequencies, below 50 Hz, that predicted and measured results deviate slightly. This is because the experimental structure oscillates to and through like a pendulum in its thin wire-suspensions, which were not sufficiently resilient at such low frequencies. Thus, below 50 Hz the experimental periodic structure cannot be regarded as being truly *semidefinite*, that is to say, totally *free* in space. The same phenom-

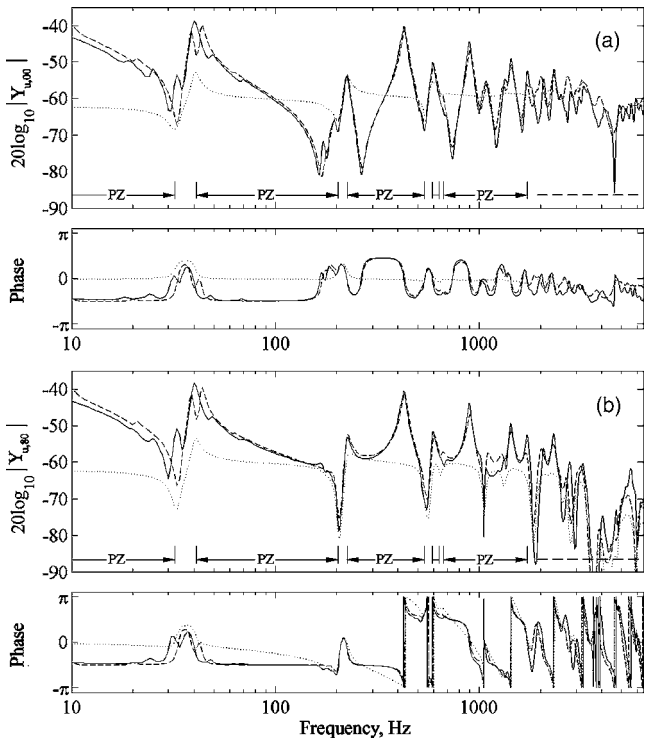

FIG. 9. Junction longitudinal mobility of finite periodic structure with eight elements; the system is driven at junction 0 by a longitudinal (axial) point force: (—) measurements; (- - -) numerical prediction using Eq. (42); (···) numerical prediction for a corresponding semi-infinite periodic structure. (a) Direct mobility $Y_{u,00}=\dot{u}_0/F_0$, and (b) transfer mobility $Y_{u,80}=\dot{u}_8/F_0$.

enon also causes calculated mobilities to be slightly higher than measured results at frequencies *below* 20 Hz, where the structure vibrates as a rigid mass, i.e., with a negative slope in magnitude and a phase of $-\pi/2$.

Also shown in Fig. 9 are calculated junction-mobilities for a corresponding, but *semi-infinite* periodic structure. By comparison with the calculated mobilities of the *finite* periodic structure, it is evident that this mostly behaves strongly resonant despite its relatively high damping loss factor. In frequency zones of sufficiently high attenuation constant μ_R, however, it is also apparent that the finite periodic structure can be treated approximately as being semi-infinite. In Fig. 9(b) this is seen around 1900 Hz and from 2800 Hz and upwards, where $\mu_R \geqslant 0.25$ and the mobilities of the semi-infinite and finite periodic structure are close to being identical. This is in agreement with the "10%-limit-condition" $N\mu_R > 1.5$ for applying the valuable semi-infinite-structure-assumption that was derived in Ref. 8 for maximum allowable response deviations of 10%, albeit for the case of mono-coupled periodic structures.

According to Sec. II and Fig. 3(c) the longitudinal motion is controlled mainly by wave-type *A* up until 1066 Hz. Thus, below this frequency, up until $N=8$ natural frequencies are expected[8,9] to occur within each propagation zone associated with wave-type *A*, provided that there is a full π-change of the phase constant μ_l. However, μ_l varies only little at frequencies below 1066 Hz because the finite periodic structure is significantly damped, and it is therefore very few of these resonances of the "eight-mode groups" that are visible in Fig. 9. The first, second, and third propagation zones, for example, lie in the bands from 0 to 32 Hz, 41 to 205 Hz, and 224 to 540 Hz, respectively. These bounding frequencies occur at the peaks and troughs in the dotted response curve for the semi-infinite structure. The peaks, which identify the *lower* bounding frequencies, correspond to the natural frequencies of a *single* periodic element when its longitudinal and rotational motion coordinates at junctions are *free* whereas transverse coordinates are *locked.* Upper bounding frequencies are identified by the troughs, which occur at the natural frequencies of an element with longitudinal and rotational junction coordinates being *locked* and transverse coordinates being *free*.[9] The mode of vibration at the lower bounding frequency of 41 Hz, for example, is strongly influenced by the transverse beams, which all vibrate in-phase virtually in their fundamental *sliding-free* mode. All junction longitudinal responses are also in-phase. The upper bound at 205 Hz is controlled by the "resonating" transverse beams vibrating in their second, virtually *clamped-free* mode. Longitudinal motions at junctions are thus virtually locked, and in the absence of damping the transverse beams will all vibrate in anti-phase with one another, because the junction-to-junction phase change is π. This influence of the transverse beams corresponds to the action of multiple dynamic neutralizer—or "absorbers". The same pattern is repeated in the next propagation zone from 224 to 540 Hz, just with increasing mode order, i.e., basically governed by the second sliding-free mode and the third clamped-free mode of the transverse beams.

Figure 10 shows calculated and measured cross mobilities $Y_{\theta,j0}=\dot{\theta}_j/F_0$ relating *rotational* velocities $\dot{\theta}_j(t)$ at junctions to the *longitudinal* driving force $F_0(t)$ at junction 0. These rotational velocities, which were measured using the finite difference from two accelerometers placed concentrically with respect to the column's neutral axis, are caused exclusively by longitudinal-flexural wave coupling in the structure. Disregarding results below 50 Hz, we find good overall agreement up until about 1200 Hz between predictions and measurements for these cross-coupled responses. Especially the peak values are almost the same at the frequencies 65, 185, 224, 420, 600, and 1100 Hz. These peaks are caused mainly by the strong longitudinal responses, which couple into rotational responses. The broadband and low-valued troughs centered around 100, 300, and 750 Hz are also in agreement. These are caused mainly by the low energy ratio of the predominantly longitudinal wave-type, that is, wave-type *A* from 0 to 1066 Hz and wave-type *B* from 1066 to 6400 Hz, see Fig. 3(c). Finally, with an overall level difference of about 5 dB the agreement is less good in the range from 1200 to 3000 Hz.

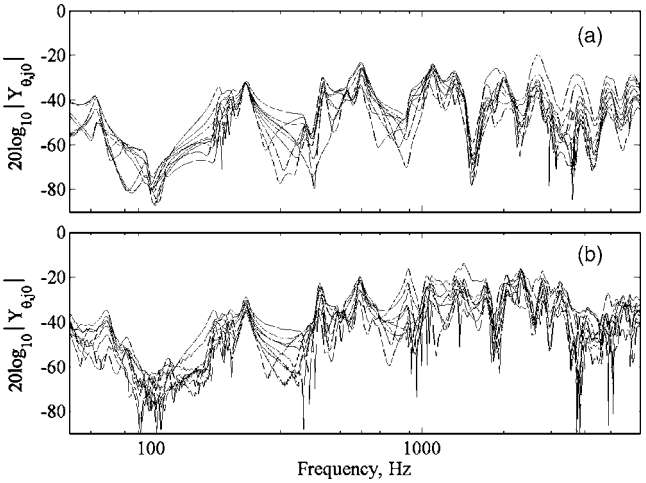

FIG. 10. Junction rotational mobilities $Y_{\theta,j0}=\dot{\theta}_j/F_0$, for $j=0-8$, of finite periodic structure with eight elements; the system is driven at junction 0 by a longitudinal point force. (a) Numerical predictions using Eq. (42), and (b) measurements.

B. Response to offset force excitation

In a second investigation the periodic structure was driven by an offset force $F_{0,\text{off}}(t)$ in order to excite primarily flexural-type waves. Figure 1 shows how the force was applied perpendicular to the first transverse beam, at a vertical distance of 183 mm from the previous driving point. This excitation resulted in a combined force and moment excitation at junction 0, of which the effect of the moment excitation was anticipated to dominate. For the prediction, this combined excitation was determined by calculating the transfer responses of the driven transverse beam and then using reciprocity between the offset point and junction 0.

For this forcing Fig. 11 shows an example of numerical predictions and measurements, in the form of junction rotational velocities per unit offset force, that is, the rotational cross mobilities $Y_{\theta,j0,\text{off}}=\dot{\theta}_j/F_{0,\text{off}}$. These single point junction mobilities are largely representative descriptors for the

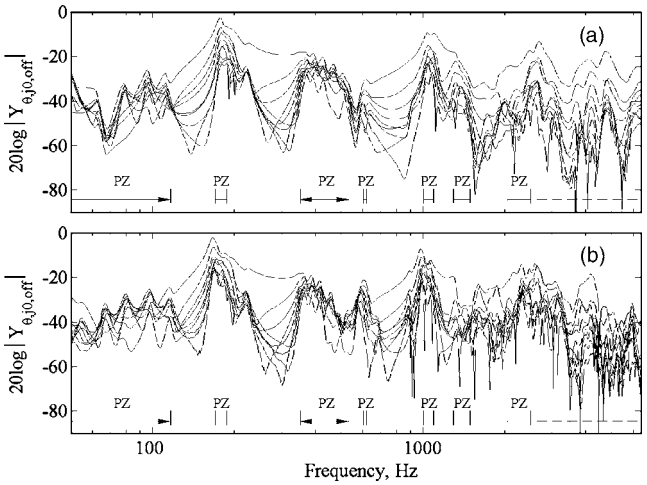

FIG. 11. Junction rotational mobilities $Y_{\theta,j0,\text{off}}=\dot{\theta}_j/F_{0,\text{off}}$, for $j=0-8$, of finite periodic structure with eight elements; the system is driven by an offset harmonic point force $F_{0,\text{off}}$ acting on the first transverse beam at 183 mm below junction 0. (a) Numerical predictions using Eq. (42), and (b) measurements.

flexural vibration in both the transverse beams and the wave-carrying column components. The responses are here seen to be governed by relatively narrow propagation zones, which are separated by strong, broadband attenuation zones. There is a fine agreement between predicted and measured results from 50 to about 1400 Hz. At the higher frequencies, however, discrepancies are noted particularly at the deep trough in the attenuation zone at about 1500 Hz. These deviations probably originate from finite-difference measurement problems associated with small rotational responses at high frequency troughs. Several moderate peaks from finite-system resonances can be observed especially in the bands from approximately 50 to 115 Hz and from 350 to 540 Hz. Furthermore, at most frequencies from 1066 Hz and upwards, where the attenuation constant of the predominantly flexural wave-type A takes values of $\mu_R \geqslant 0.35$, the vibrations are attenuated by more than 20 dB from junction 0 to junction 8. In the band from 3300 to 4800 Hz this attenuation is even 40 dB or more. This is again in accordance with the strong attenuation constant of wave-type A in Fig. 8, and this complies also with the predicted responses of the corresponding semi-infinite structure in Fig. 4(b).

Below 1066 Hz the rotational motion is expected to be controlled by the predominantly *flexural* wave-type B. However, since this wave-type is strongly attenuated in some bands, the contributions from the less attenuated and predominantly *longitudinal* wave-type A "takes over" after a few periodic elements and then dominates the transmission in the remaining parts of the periodic structure. This flexural-longitudinal wave coupling, which results in a spatially dual-rate decrease in magnitudes occurs in several narrow bands in Fig. 11, but is most clearly observed from 200 to 250 Hz and around 1200 and 2000 Hz, as is also seen in Fig. 4(b).

V. CONCLUSIONS

Periodic structure analysis has been further developed in this study of multicoupled periodic structures of both semi-infinite and finite extent. Specifically examined are propagation characteristics of flexural and longitudinal-type waves in tri-coupled periodic structures with multiresonant side-branches in the form of asymmetrically appended transverse beams. The fundamental understanding obtained for this type of transmission path is of considerable practical interest, if generalized to represent a plane-wave, normal incidence model of a similar plate assembly such as web-stiffened panels, ship hulls with decks, and floor-loaded columns in buildings.

Numerical results for semi-infinite and tri-coupled periodic systems show that the wave transmission is governed by a complicated pattern of propagation zones (passbands) for the two wave solutions which can carry energy, and that these zones are intervened by many stopbands of both moderate and high-valued attenuation. It is revealed that flexural and longitudinal motions are coupled in such systems with multiresonant side-branches, but a parameter study also shows that structural damping has a significant influence on this phenomenon. The otherwise strong coupling between flexural and longitudinal motions occurring in lightly damped structures decreases when structural damping is increased. For a tri-coupled periodic structure it is found that this damping-dependent decrease in coupling takes place at most frequencies for a damping loss factor value of, say, 0.01 or higher. This results in a separation of the wave-field into a primarily longitudinal wave-type and a primarily flexural wave-type, of which the latter is attenuated in approximately half the frequency range considered.

By relaxing the simplifying semi-infinite-structure assumption, a general expression for the junction receptances of *finite* and *multicoupled* periodic systems is derived as a generalization of the governing expression of mono-coupled periodic systems.[8] This new expression is used for predicting audio-frequency vibration responses of an eight-element, tri-coupled periodic structure to two types of point excitations applied at its end. These predictions are compared with measurements from a freely suspended and nominally identical finite test-structure. In the case of longitudinal force excitation a very good agreement is found with measured results of the longitudinal velocity responses at junctions. Moreover, a comparison with calculated responses for a corresponding, but *semi-infinite* periodic structure, shows that the finite periodic structure behaves strongly resonant in most propagation zones despite its relatively high damping loss factor of 0.056. A good correspondence is also achieved from 50 to 3000 Hz for junction *rotational* velocities caused by either the longitudinal force or a combined moment and force excitation. For the longitudinal excitation these junction rotational velocities are caused exclusively by the predominantly longitudinal wave-type and hence by the coupling between longitudinal and flexural motions. The combined moment and force excitation is found to generate strong rotational responses in a low frequency band from 80 to 400 Hz. However, at the higher frequencies the rotational responses are of the same order of magnitude as those resulting "indirectly" from pure longitudinal force excitation. Further, with the combined excitation it is found that the junction rotational velocities are controlled by a predominantly *flexural* wave-

type. However, since this wave is strongly attenuated the motion contributions from the significantly *less* attenuated and predominantly *longitudinal* wave-type "takes over" after a few periodic elements, and hence dominate the transmission and responses in the remaining parts of the periodic structure. This type of coupling is observed in narrow frequency bands for the examined structure, and this phenomenon would explain the spatially *dual-rate* exponential decrease in vibration magnitudes, observed in nominally periodic multi-story buildings.

[1]L. Friis, M. Ohlrich, "Coupling of flexural and longitudinal wave motion in a periodic structure with asymmetrically arranged transverse beams," J. Acoust. Soc. Am. **118**, 3010–3020 (2005).

[2]M. Ohlrich, "Harmonic vibration of a column structure with transverse beams," *Proceedings of the Institute of Acoustics, Spring Meeting*, Southampton, England, 1979, Paper 20.I2.

[3]K. Gösele, *Über das Schalltechnische Verhalten von Skelettbauten (Acoustic Properties of Skeleton Building Structures)*, Körperschall in Gebäuden (Ernst, Berlin 1960).

[4]D. J. Mead and S. Markus, "Coupled flexural-longitudinal wave motion in a periodic beam," J. Sound Vib. **90**, 1–24 (1983).

[5]L. Cremer and H. O. Leilich, "Zur Theorie der Biegekettenleiter" ("On theory of flexural periodic systems"), Arch. Elektr. Uebertrag. **7**, 261–270 (1953).

[6]L. Cremer, M. Heckl, and E. E. Ungar, *Structure-borne Sound* (Springer, Berlin, 1973). Translated from German, original 1967.

[7]D. J. Mead, "A general theory of harmonic wave propagation in linear periodic systems with multiple coupling," J. Sound Vib. **27**, 235–260 (1973).

[8]M. Ohlrich, "Forced vibration and wave propagation in mono-coupled periodic structures," J. Sound Vib. **107**, 411–434 (1986).

[9]D. J. Mead, "Wave propagation and natural modes in periodic systems. II. Multi-coupled systems, with and without damping," J. Sound Vib. **40**, 19–39 (1975).

[10]D. J. Mead, "Wave propagation and natural modes in periodic systems. I. Mono-coupled systems," J. Sound Vib. **40**, 1–18 (1975).

[11]G. L. Rodgers, *Dynamics of Framed Structures* (Wiley, New York, 1959).

Structural vibrations of buried land mines

Andrei Zagrai,[a] Dimitri Donskoy, and Alexander Ekimov
Davidson Laboratory, Stevens Institute of Technology, 711 Hudson Street, Hoboken, New Jersey 07030

(Received 30 December 2004; revised 20 July 2005; accepted 7 September 2005)

Buried landmines exhibit complex structural vibrations, which are dependent on interaction between soil and mines as well as on their respective properties. This paper presents experimental and theoretical studies of multimodal vibrations of buried mines and discusses the effects of burial depth and soil properties on dynamics of the soil-mine system. The two-dimensional model of the soil-mine system that accounts for soil-coupled mine's multiple vibration modes and spatial distribution of vibrations over the soil surface is introduced. The model was tested using experiments with the plastic mine simulant. The study reveals that the soil shear stiffness is one of the key governing parameters determining the resonance vibration frequency and the amplitude of the soil-mine system. Burial depth, soil moisture, and consolidation are among factors leading to the increase of the soil shear stiffness, therefore effectively influencing modal vibrations of buried mines. © *2005 Acoustical Society of America.* [DOI: 10.1121/1.2108754]

PACS number(s): 43.40.At, 43.28.En, 43.20.Tb [ANN] Pages: 3619–3628

I. INTRODUCTION

Recent studies[1–9] have demonstrated that acoustic detection and discrimination of landmines is a complex problem dependent upon interaction between soil and buried mines and their respective properties. Although significant progress has been achieved in developing a practical seismoacoustic technique, the dynamics of soil-mine interaction are not understood thoroughly. Improving current understanding of this complex phenomenon is a key element in enhancing detection capabilities, reducing false alarm rate, and developing fast, adaptable, and synergetic land mine detection systems.

The traditional approach of modeling the acoustic detection problem utilizes wave equations for an elastic or poroelastic medium and considers a diffraction/scattering of the propagating waves interacting with a target (mine). This approach is widely used for the sonar mine detection modeling and works well for the underwater mine detection. The problem of seismic detection of buried landmines is quite different: The medium (soil) is more complex than water because of the shear stresses, soil variability and structure, porosity, moisture, and other factors. Land mines are buried close to the soil surface at the depths much smaller than the wavelengths of the interrogating acoustic or seismic waves. In contrast to underwater mine-searching sonars working at the ultrasonic frequencies of tens to hundreds of kHz, seismoacoustic land mine detection utilizes much lower frequencies, i.e., below 1 kHz. At the lower frequencies, the structural dynamics (vibration) of a mine's housing is quite different from the dynamics at the high (ultrasonic) frequencies. Specifically, thin-shell mine housing exhibits very pronounced structural (flexural) vibrations that are manifested in the target response to the acoustic/seismic excitation. Another very important difference between the underwater and the land mine detection is due to a different interaction at the mine-medium interface.

All of these differences, in our view, require a different approach for the modeling of the seismoacoustic land mine detection. Thus, a simple practical lump-element dynamic model (LEDM) of the soil-mine system has been developed explaining dynamic interaction between mines and soil.[3,4] This model treats the soil-mine system as a combination of springs, masses, and dashpots, which represent inertial, elastic, and absorptive properties of mines and soil. Although this model explains many experimental observations and provides insights into underlying physical mechanisms of the soil-mine interaction, it has several limitations. Particularly, LEDM treats a mine as a single degree of freedom (SDOF) system ignoring spatial variability of the system's vibration response. In its current state, this model significantly simplifies soil dynamic properties, introducing effective shear and compressional stiffnesses of a soil column above a buried mine without a detailed discussion of their dependencies on soil properties, such as morphology, porosity, texture, and moisture.

In this paper, we investigate mine's structural vibrations (mode shapes and natural frequencies), their dependence on soil mass (burial depth), and consolidating factors, such as moisture. We use this analysis to further advance the LEDM to account for mine's modal properties and soil characteristics.

II. MULTIMODAL VIBRATION OF LAND MINES

Numerous field measurements[1,4,7,8] revealed that many mines exhibit well-defined resonances. It has been shown that these resonances are indeed mine's structural resonances and are strongly dependent on mine geometry, design, and condition, which suggests that mines might have complex vibrational characteristics. Figure 1 shows a dynamic impedance of an antipersonnel mine TS-50 as well as its vibration modes at the indicated frequencies. Among more than 50 different "live" mines (real mines with explosives) measured,[4] the strongest resonances were observed in mines which featured a relatively compliant upper casing. The dif-

[a]Electronic mail: azagrai@stevens.edu

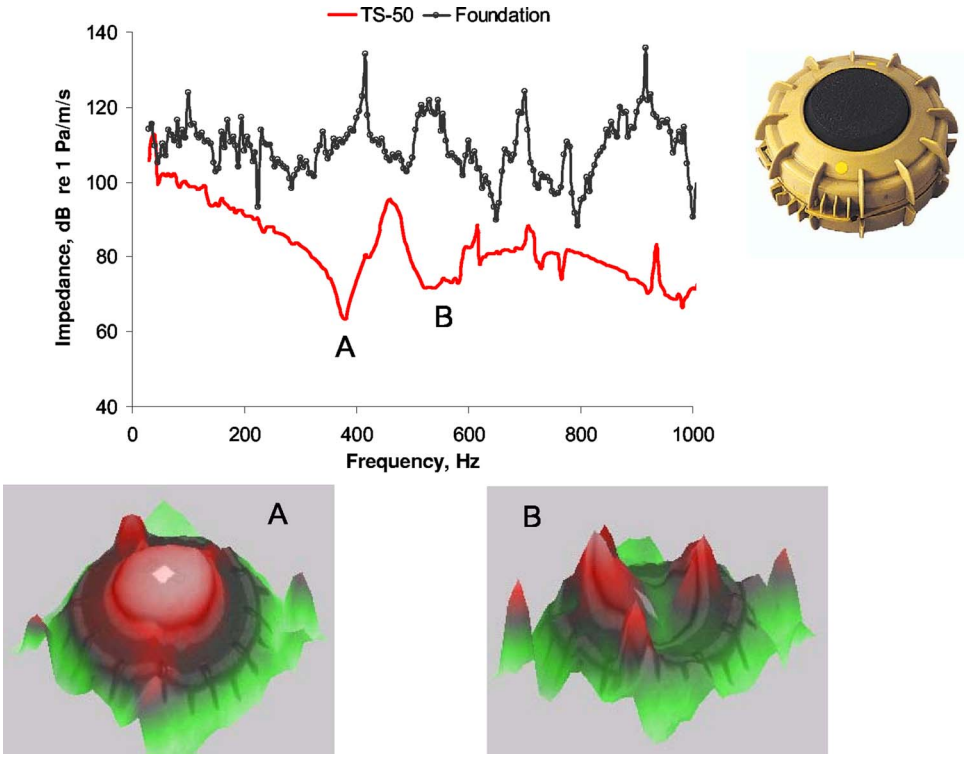

FIG. 1. (Color online) Impedance of the AP mine TS-50 and images of vibration velocity of the mine's surface measured at the indicated frequencies.

ference (contrast) between dynamic impedances of the casing and surrounding soil allows for land mine detection using a linear acoustic approach.[1,7–10]

Our measurements of real mines,[4,11] conducted during 2000–2003 field tests, demonstrated that in addition to profound response at the lowest resonance frequency, a buried mine exhibits multimodal vibrations in a higher-frequency range. The system utilized for the field measurements is described in Ref. 12. Soil surface was excited using the acoustic signal in 30–1000 Hz frequency range. Simultaneously, vibration of the soil surface was measured with a scanning Laser-Doppler vibrometer (LDV) and processed yielding a frequency dependent spatial distribution of vibration velocity over the scanned area. When plotted in narrow bands, which include subsequent resonance frequencies, these distributions feature distinctive patterns that correspond to mine's vibration modes as shown in Fig. 2. It is convenient to represent results of the seismoacoustic land mine detection as two- and

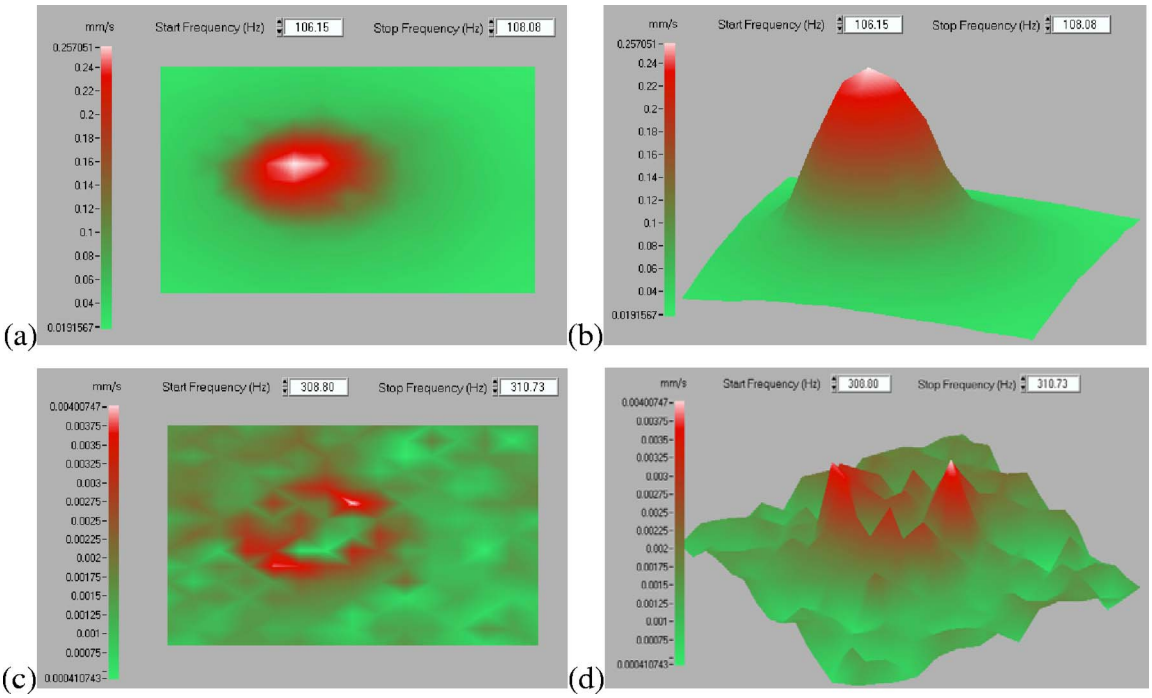

FIG. 2. (Color online) Vibration velocity profiles (linear scale) for the AT mine M-19 buried at 2.54 cm (1 inch) in gravel: (a) 2D and (b) 3D representations of the response at the first resonance frequency; (c) 2D and (d) 3D representations of the response at the second resonance frequency.

three-dimensional projections of the vibration velocity distribution. Figure 2 presents such projections for two vibration modes of an antitank (AT) mine M-19 buried at 2.54 cm (1 in.) in gravel. To visualize vibrations of this mine, we measured vibration velocity in 225 points that, considering a spatial step of 3.81 cm (or 1.5 in.), covered a rectangular area of 58.42 cm $\times$ 58.42 cm (or 23 $\times$ 23 in.). Figures 2(a) and 2(b) show vibration distribution for the lowest (first) vibration mode observed in the 106–108 Hz frequency range. This mode is clearly visible because of a relatively high contrast between on/off mine vibrations. On the contrary, Figs. 2(c) and 2(d) of the second vibration mode are contaminated with noise. The amplitude of the second mode is two orders of magnitude (20 dB) lower than the first mode resulting in poor contrast. However, even for such small vibration amplitudes, this mode reveals a distinctive modal pattern.

Although higher vibration modes have a much lower amplitude than the first mode, their presence (even if not visible on the surface) could have important implications. Due to coupling between vibration modes, the higher modes in the frequency response affect the lowest fundamental vibration mode paramount for detecting the buried mine. Therefore, higher vibration modes should not be ignored especially for the model-based detection algorithms. Moreover, multiple vibration modes could provide additional information for classification and discrimination of the buried landmines.

Vibration velocities distributions shown in Figs. 1 and 2, can be easily associated with familiar vibration modes, particularly for mines with mechanically simple uniform structures, such as a plate or membrane. Obviously, mines with more complicated structures (stiffening ribs, varying thickness, cavities for buster charges) may exhibit much more complicated vibration distribution.

III. SOIL-MINE DYNAMIC SYSTEM MODELING

A. Modeling of the mine vibrations

In the seismoacoustic detection, a land mine's detectability significantly depends on the compliance of its upper diaphragm. In the previous version of the model,[4] the diaphragm was presented as a SDOF system having a mass M_M and stiffness K_M related to its flexural rigidity. Although the SDOF model adequately represented the lowest resonance of the soil-mine system, it did not account for multiple resonances and spatial vibration modes. One of the aims of this development is to address these two issues by further extending the dynamic model for the soil-mine system to include multiple resonances and a spatial distribution of vibrations coupled with soil. For the modeling purposes, we represent the mine's upper casing as a thin uniform circular plate with elastic edge supports. It is suggested that the linear theory of thin plates could yield reasonable predictions because the thickness/radius ratio of the mine's casings are in the range of 0.1–0.01, and the dynamic displacements are much smaller than the casing's thickness (three orders of magnitude). Figure 3 illustrates the geometry of the problem in which a thin uniform circular plate is elastically supported

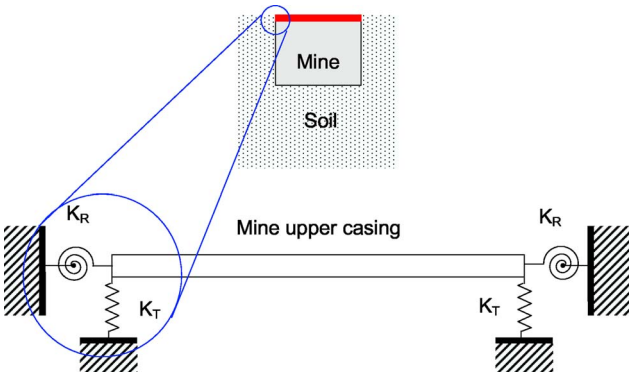

FIG. 3. (Color online) Geometry of the problem in which mine's upper casing is represented as a circular plate with the elastic edge support.

around its circumference. The reason for considering the elastic supports lies in the fact that the upper part of the casing is rarely clamped; in most cases, it is also neither pinned nor free, representing an intermediate state. In addition, when buried, mine experiences constraints due to adjoining soil. This also affects the upper casing and, therefore, its boundary conditions.

Forced flexural vibrations of a circular plate with viscous damping are described by the fourth-order differential equation of the following form,[13]

$$D_M \cdot \nabla^4 w_M(r,\theta,t) + c_M \cdot \frac{\partial}{\partial t} w_M(r,\theta,t) + \rho_M h_M \cdot \frac{\partial^2 w_M}{\partial t^2}(r,\theta,t) = p(r,\theta,t), \quad (1)$$

where c_M is the damping coefficient, ρ_M is the density of a plate, and $D_M = E_M h_M^3 / 12(1-\nu_M^2)$ is the flexural rigidity expressed in terms of the plate's thickness h_M, Poisson's ratio ν_M, and Young's modulus E_M, $p(r,\theta,t)$ is the applied external force.

Assuming the harmonic excitation with the frequency ω,

$$p(r,\theta,t) = P(r,\theta) \cdot e^{i\omega t}, \quad (2)$$

it can be shown that the steady-state solution of Eq. (1) is a modal expansion

$$w_M(r,\theta,t) = W(r,\theta) \cdot T(t) = \sum_m \sum_n W_{mn}(r,\theta) \cdot T_{mn}(t), \quad (3)$$

where the temporal solution

$$T_{mn}(t) = G_{mn} \cdot e^{i\cdot(\omega t - \varphi_{mn})}, \quad (4)$$

includes an amplitude parameter G_{mn} and a phase lag behind the excitation φ_{mn}.

The spatial mode shapes in solution (3)

$$W_{mn}(r,\theta) = A_{mn} \cdot [J_n(\lambda_{mn} r/a) + C_{mn} \cdot I_n(\lambda_{mn} r/a)] \cdot \cos(n\theta) \quad n \geq 0, \quad (5)$$

are expressed in terms of the Bessel functions of the first, J_n, and the second, I_n, kinds,[14] and a is a radius of the plate. The constants C_{mn}, A_{mn}, and eigenvalues λ_{mn} are dependent on the number of circles m and diameters n in each mode shape and could be obtained by imposing the boundary and orthonormalization conditions.

The elastic edge support is modeled as a combination of the linear elastic translational and rotation springs with the effective stiffnesses K_R and K_T:

$$M_r(a,\theta,t) = K_R \cdot \frac{\partial W(a,\theta)}{\partial r} \tag{6}$$

and

$$V_r(a,\theta,t) = -K_T \cdot W(a,\theta), \tag{7}$$

where M_r and V_r are the bending moment and Kelvin–Kirchhoff edge reaction expressed as Ref. 14

$$M_r(a,\theta) = -D_M \cdot \left[\frac{\partial^2 W(a,\theta)}{\partial r^2} + \nu_M \cdot \left(\frac{1}{r}\frac{\partial W(a,\theta)}{\partial r} + \frac{1}{r^2}\frac{\partial^2 W(a,\theta)}{\partial \theta^2} \right) \right] \tag{8}$$

and

$$V_r(a,\theta) = -D_M \cdot \left[\frac{\partial}{\partial r}\nabla^2 W(a,\theta) + (1-\nu_M) \cdot \frac{1}{r}\frac{\partial}{\partial \theta} \times \left(\frac{1}{r}\frac{\partial^2 W(a,\theta)}{\partial r \partial \theta} - \frac{1}{r^2}\frac{\partial W(a,\theta)}{\partial \theta} \right) \right]. \tag{9}$$

Using Eqs. (8) and (9), Eqs. (6) and (7) could be reformulated in terms of $W(a,\theta)$. Following Leissa[14] and Kang *et al.*,[15] we substitute Eq. (5) into the boundary conditions (6) and (7) and arrive at the frequency equation, which allows for obtaining the eigenvalues λ_{mn} and the mode shape parameters C_{mn}. The constant A_{mn} in Eq. (5) is an amplitude coefficient determined from the condition for the orthonormal modes:

$$\int_0^{2\pi}\int_0^a \rho h \cdot W_{mn}(r,\theta) \cdot W_{pq}(r,\theta) r dr d\theta = m_M \cdot \delta_{mp}\delta_{nq}, \tag{10}$$

where modal numbers $m,n,p,q=0,1,2,\ldots,\delta$ denotes the Kronecker delta (i.e., $\delta_{mp}=1$, if $m=p$ and $\delta_{mp}=0$, if $m\neq p$), and m_M is mass of the plate.

Substituting Eq. (3) into Eq. (1) and employing a method of separation of variables[16,17] and condition (10), we obtain an expression for the displacement:

$$w_M(r,\theta,t) = \sum_m \sum_n \frac{W_{mn}(r,\theta) \cdot \int_0^{2\pi}\int_0^a P(r,\theta) \cdot W_{mn}(r,\theta) r dr d\theta}{m_M \cdot \sqrt{(\omega_{mn}^2-\omega^2)^2 + (i\omega\eta_{mn})^2}} \cdot e^{i\cdot(\omega t - \tan^{-1}(\omega\eta_{mn}/(\omega_{mn}^2-\omega^2)))}, \tag{11}$$

that reflects contribution of G_{mn} and φ_{mn}. Rearranging Eq. (11) yields the complex frequency response:

$$H_M(r,\theta,\omega) = \sum_m \sum_n \frac{\chi_{mn}(r,\theta)}{M_{mn}(r,\theta) \cdot (\omega_{mn}^2 + i\omega\eta_{mn} - \omega^2)}, \tag{12}$$

where $\omega_{mn} = \sqrt{D_M/\rho_M h_M} \cdot \lambda_{mn}^2/a^2$ is the natural frequency of the plate, $\eta_{mn} = c_{Mmn}/(h_M\rho_M)$ is the damping coefficient for each individual mode, and

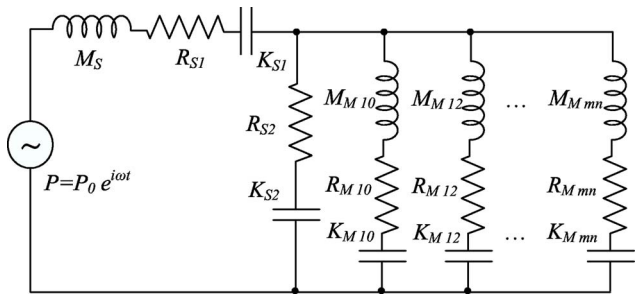

FIG. 4. Equivalent electrical diagram for the soil-mine mechanical system.

$$\chi_{mn}(r,\theta) = \frac{1}{P_0} \cdot \frac{1}{W_{mn}(r,\theta)} \int_0^{2\pi}\int_0^a P(r,\theta) \cdot W_{mn}(r,\theta) r dr d\theta, \tag{13}$$

$$P_0 = \int_0^{2\pi}\int_0^a P(r,\theta) r dr d\theta, \tag{14}$$

$$M_{mn}(r,\theta) = m_M / W_{mn}^2(r,\theta). \tag{15}$$

It is convenient to represent the soil-mine system as an assembly of springs, masses, and dashpots corresponding to the elastic, inertial, and absorptive properties of mines and soil. The advantage of such a representation is that a complex phenomenon can be modeled with relatively simple and straightforward formulations. This approach allows for utilization of the electromechanical analogies and a respective equivalent electric circuit analysis yielding simple analytical solutions. To benefit from this advantage, we suggest substituting the previous SDOF mine model[4] with the multidegree of freedom model (MDOF), where each vibration mode of the mine's casing is represented as a serial connection of elastic, inertial, and absorptive elements. Using analogies between mechanical and electrical systems,[17] we obtained an equivalent electric circuit shown in Fig. 4. In the circuit, elements that account for modal vibrations of the mine's casing are denoted with the subscript M. The serially connected capacitor, resistance, and inductance in each parallel branch can be further reduced to a parallel connection of the admittance elements Y_M. Reformulation of the response (12) in terms of the admittance yields

$$Y_M(r,\theta,\omega) = \sum_m \sum_n [R_{mn}^*(r,\theta) + i(\omega \cdot M_{mn}^*(r,\theta) - K_{mn}^*(r,\theta)/\omega)]^{-1}, \tag{16}$$

where the modal mass, M_{mn}^*, the stiffness, K_{mn}^*, and the damping parameter, R_{mn}^*, are defined as

$$M_{mn}^*(r,\theta) = M_{mn}(r,\theta)/\chi_{mn}(r,\theta), \tag{17}$$

$$K_{mn}^*(r,\theta) = \omega_{mn}^2 \cdot M_{mn}^*(r,\theta), \tag{18}$$

$$R_{mn}^*(r,\theta) = \eta_{mn} \cdot M_{mn}^*(r,\theta). \tag{19}$$

It should be noted that modal parameters M_{mn}^*, K_{mn}^*, and R_{mn}^* are dependent on radial and angular coordinates r and θ, thus unequally describing in space each vibration mode. The spa-

tially distributed dynamic impedance of the mine is inversely proportional to the admittance (16):

$$Z_M(\omega) = 1/Y_M(\omega), \tag{20}$$

B. Two-dimensional model for the soil-mine dynamic system

In the Fig. 4, elements of the circuit M_S, K_{S1}, K_{S2}, R_{S1}, R_{S2} correspond to the dynamic mass, and respective shear and compression stiffnesses, and damping coefficients of the soil layer above the mine. These parameters characterize the contribution of the soil into the joint vibration of the soil-mine system, and are dependent on soil properties and condition. Although soil is a complex medium comprised of interacting discrete particles, its equivalent continuum model is used for many engineering problems.[18] In the soil layer above a buried mine, the wavelength of a propagating elastic wave is much larger than a characteristic dimension of the soil granular assembly supporting the assumption of a continuous medium. When no slipping between particles occurs and the contact behavior is neglected—such soil could be represented as a linear elastic solid medium, providing that contribution of pores is small. The no-slipping condition implies that an internal friction allows soil to support the shear stress and "liquefaction" (sudden loss of the shear strength resulting in a fluidlike behavior) is not possible.

It is important to note that the dynamic response of soil without mines is very different from the response of a soil layer above the buried mine. In contrast to the vibration of soil without a mine, the soil layer above the buried mine follows bending vibrations of the mine's casing that result in bending of the soil layer due to its shear strength. Therefore, the soil-mine system could be represented as two connected plates with respective ρ_S, E_S and ρ_M, E_M. Equation (1) will hold for the system of such two plates providing that displacements of the soil layer and the mine's casing are equal, i.e., $w_S(r,\theta,t)=w_M(r,\theta,t)=w(r,\theta,t)$. The flexural rigidity and the mass per unit area, however, will be different:

$$D = D_S + D_M \text{ and } \rho h = \rho_S h_S + \rho_M h_M. \tag{21}$$

By substituting Eq. (21) into Eq. (1), we derive the expression for the natural frequency of the two-plates soil-mine undamped system,

$$\omega_{mn} = \frac{\lambda_{mn}^2}{a^2}\sqrt{\frac{E_S h_S^3/12(1-\nu_S^2) + E_M h_M^3/12(1-\nu_M^2)}{\rho_S h_S + \rho_M h_M}} \sim \sqrt{\frac{K_{S1}+K_M}{M_S+M_M}}, \tag{22}$$

where K_{S1} is a stiffness due to the shear strength of the soil layer. Equation (22) illustrates that K_{S1} is proportional to the third power of the burial depth h_S, i.e., $K_{S1}\sim h_S^3$. In practice, the natural frequency of the buried mine is also dependent on soil compression stiffness $K_{S2}=E_S A_S/h_S$ that does not appear in expression (22) but is accounted for in the dynamic model (Fig. 4). The choice of the elastic modulus E_S in elastic continuum model depends on a number of factors that determine soil composition, grain structure, and condition. Empirical dependencies of the form,

$$E_S = 2(1+\nu_S)\cdot A \cdot F(e)\sigma_0^n, \tag{23}$$

are suggested in literature[19,20] to describe the effects of confining pressure σ_0 and void ratio e. $F(e)$ and the constants A and n are determined for each type of soil. For example, for the fine angular-grained sands $F(e)=(2.973-e)^2/(1+e)$, $A=2.227$, and n is approximately equal to 0.5.[20] Other soil parameters participating in the dynamic model in Fig. 4 include:[4] Damping coefficients R_{S1}, R_{S2} which are both proportional to the soil depth, and mass $M_S=\rho_S A_S h_S$, where the effective area $A_S=\pi a_S^2$. These dynamic parameters allow for determining soil dynamic impedances in the equivalent electrical diagram depicted in Fig. 4:

$$Z_{S1}(\omega) = R_{S1} + i(M_S\omega - K_{S1}/\omega) \text{ and } Z_{S2}(\omega) = R_{S2} + iK_{S2}/\omega. \tag{24}$$

The total dynamic impedance of the soil-mine system is therefore

$$Z(\omega) = Z_{S1}(\omega) + Z_\Sigma(\omega), \text{ where } Z_\Sigma(\omega) = \frac{Z_{S2}(\omega)\cdot Z_M(\omega)}{Z_{S2}(\omega)+Z_M(\omega)}. \tag{25}$$

C. Experimental validation of the model

A suggested modeling approach was tested in the laboratory experiment using a plastic mine simulant. The mine simulant is essentially a 24.8 cm (9.75 in. diameter) cylindrical plastic container, which is used by the U.S. Army as a practice target. In the experiment, the flush-buried mine simulant was exposed to the acoustic excitation from a loudspeaker in 30–1000 Hz frequency range, and the resulting vibration velocity was measured with a LDV. To obtain the dynamic admittance of the target depicted in Fig. 5, its vibration velocity was divided by the acoustic pressure measured with a microphone located in close proximity to the LDV measuring point. Figure 5 presents an admittance in that particular point on the surface of the plastic mine simulant. Scanning the area over the mine's casing with the LDV allowed for presenting, in Fig. 5, spatially distributed vibration velocity profiles at the resonance frequencies.

In order to compare these experimental results with the results calculated using the analytical model described in the preceding section, we have to find the boundary condition parameters defined in Eqs. (6) and (7). The flush-buried mine is constrained by the adjacent soil in the radial direction. Although this condition significantly restrains radial vibrations, it also affects the boundary condition of the mine's upper plate. Therefore, we consider a general case of boundary conditions modeled as a combination of translational and rotational edge stiffnesses. To fit the experimental data, the following constraints were chosen for a numerical example: Translational factor $K_T\cdot a^3/D=32$, rotational factor $K_R\cdot Da^{-1}=1$. Parameters of the plastic mine included the plate's radius $a=12.4$ cm, thickness $h_M=2.3$ mm, density $\rho_M=1150$ kg/m^3, Young's modulus $E_M=17\times10^9$ Pa, and Poisson ratio $\nu_M=0.3$.

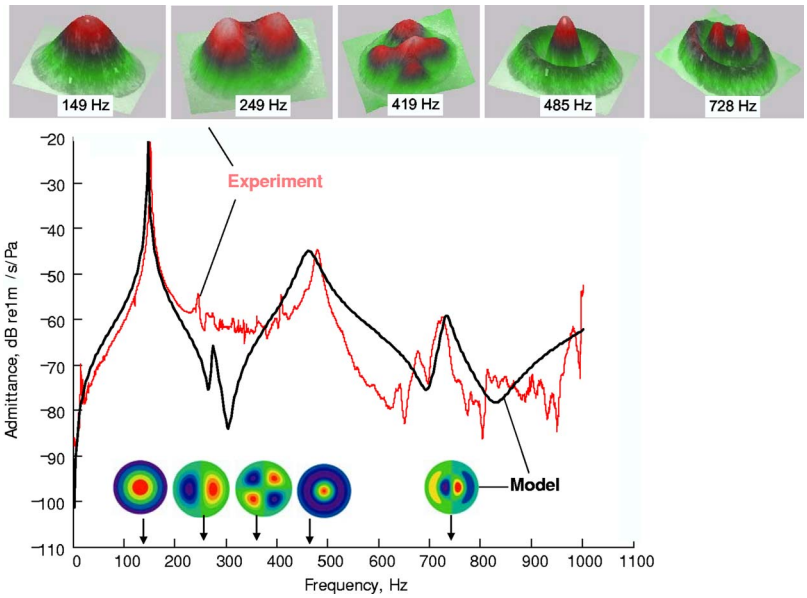

FIG. 5. (Color online) Experimental and modeling results for the flush-buried plastic mine.

The parameters above were substituted into the boundary conditions (6)–(9) to yield eigenvalues λ_{mn} and modal constants C_{mn}. Using the expression for the mode shapes (5) and the condition (10), we obtain the normalization coefficients A_{mn} that control respective amplitudes of vibration modes. Detailed procedure and a MATLAB code for calculating λ_{mn}, C_{mn}, and A_{mn} is described in Ref. 21. Equation (5), combined with Eqs. (13)–(15), allows for calculating the dynamic admittance (16). This admittance includes modal mass, stiffness, and damping parameters described by Eqs. (17)–(19). The results of the modeling are presented in Fig. 5, which shows good agreement between calculated and measured admittances. Although our model predicts five vibration modes in the mine's frequency response, only three are noticeable in the experimental curve because the response was measured in a particular location. Indeed, as illustrated in Fig. 5, scanning the surface of the mine's casing with the LDV revealed the "missing" modes at 249 and 419 Hz.

IV. SOIL EFFECT ON MINES' VIBRATIONS

A. Soil effect on the vibration amplitude

A range of factors influences manifestation of the mine's vibration modes on the soil surface; suggested that contributing factors include the soil mechanical loading, the inhomogeneity of the soil content, the soil layering, the distribution of moisture in the soil, vegetation, and weathering.[22,23] As a result, the soil layer above the buried mine considerably affects its dynamic response, diminishing vibration amplitudes and shifting resonant frequencies. At deeper depths, the soil vibration amplitude measured above the buried mine is comparable with the "off mine" level resulting in poor detection and discrimination. Figure 6 shows vibration velocity profiles at various resonance frequencies of a plastic mine buried at gradually increasing depths. The images were obtained by scanning the surface over the buried mine with the LDV. The experimental setup for the measurements was identical to the setup previously used for a flush-buried mine, with the only difference being that during this test uniform layers of dry sand were distributed over the mine simulating burial depths in the range of 2 mm to 80 mm. According to Fig. 6, in the frequency range below 1 kHz, a flush-buried (zero-burial depth) plastic mine exhibits at least three well-defined vibration modes. The vibration amplitude of each higher mode is approximately 20 dB lower than the preceding mode. Introduction of a 40 mm soil layer above the mine results in considerable diminishing of the second- and first-modal vibration amplitudes. The third vibration mode becomes invisible. A further increase in the burial depth leads to a gradual amplitude reduction, until the mine's vibration response reaches the off mine level and the mine is indistinguishable from the surrounding soil.

Another representation of the vibration amplitude reduction due to burial depth is given in Fig. 7, which shows dynamic admittances of the plastic mine simulant measured in a particular location next to its center. The peaks of the lowest resonance in the figure are labeled with the letters A–F, that correspond to the gradually increasing depth of the sand column above the mine. The other resonance noticeable in the frequency response is denoted with letters B2, C2, D2, and E2. The figure demonstrates that the amplitudes of both modes decrease as the thickness of the sand column increases. Multimodal behavior for the studied mine is observable up to the depths of 40 mm, although for the burial depths above 20 mm the high-frequency responses are indistinguishable from the off mine vibrations and were simply removed from the figure for the clarity of presentation.

Understanding physical mechanisms that contribute to the reduction in vibration amplitude is crucially important, since the amplitude is a key parameter used in the land mine detection. Certainly, dissipation of the elastic energy in an increasing layer of soil plays an important role. Figure 8 illustrates that the damping ratio $\zeta = 1/(2 \cdot Q)$, where Q is a quality factor obtained for the first vibration mode in Fig. 7, is nonlinearly dependent on the burial depth. This suggests that, in addition to friction, there could be other mechanisms contributing into the amplitude reduction. We believe that the

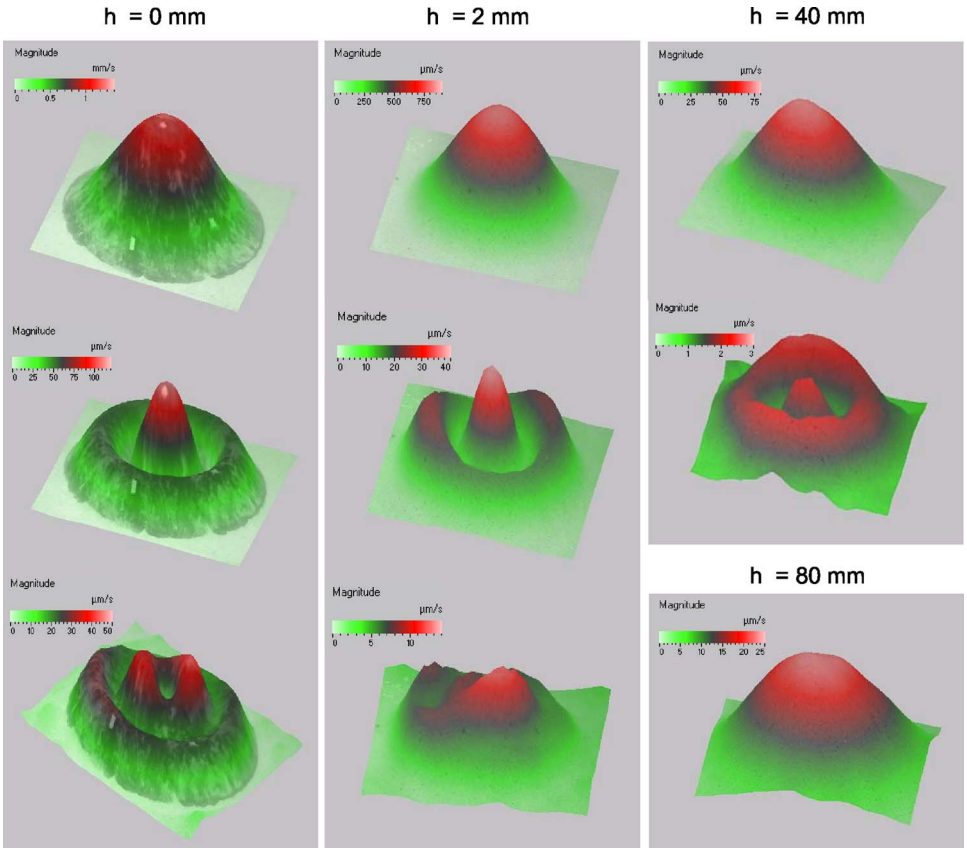

FIG. 6. (Color online) Vibration velocity profiles measured on the soil surface above the mine buried at different depths.

increasing shear stiffness, K_{S1}, plays a considerable role affecting both the amplitude and the frequency of the resonance vibration.

It is well known that in the SDOF system, the increasing stiffness shifts the natural frequency upward without affecting the vibration amplitude. However, in the MDOF system, the increasing stiffness may result in diminishing the vibration amplitude as it shifts the resonance frequency toward the antiresonance, where the amplitude is minimal. In the soil-mine dynamic system, these so-called "transmission zeros" were discussed by Yu *et al.*[24,25] We suggest that in the presence of the antiresonances, the increasing soil shear stiffness affects the vibration amplitude of the buried mine. This phenomenon is illustrated in Fig. 9, showing calculated admittances for the VS.-1.6 AT mine that features two resonances and one antiresonance at approximately 380 Hz. The solid line in the figure is the admittance of the unburied mine obtained by fitting the experimental data.[4] The dotted line represents the admittance of the mine buried at 1 cm, where $K_{S1}=2\times10^6$ Pa/m. Then, without modifying other parameters in the model, we calculated admittances for the higher shear stiffness: $K_{S1}=7\times10^7$ Pa/m (dashed line) and $K_{S1}=1.2\times10^8$ Pa/m (dashed-dotted line). As could be seen from the figure, the vibration amplitude of the mine buried in the stiffer soil decreased substantially. Depending on the soil type and condition, the stiffness could vary in a wide range; but compacted or consolidated soil, in general, is stiffer than the loose soil. There are many factors that can lead to the soil stiffening,[18] among them are moistening and freezing. There-

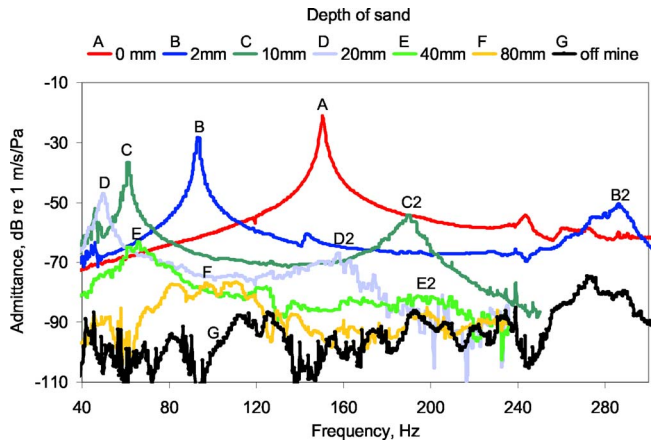

FIG. 7. (Color online) Soil admittances measured above the mine buried at increasing depths.

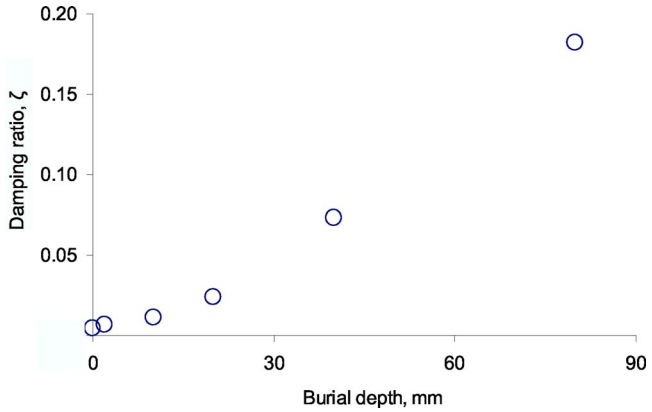

FIG. 8. Damping ratio versus burial depth.

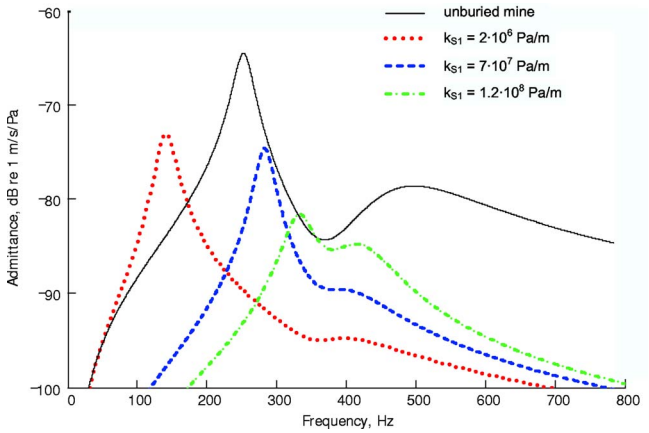

FIG. 9. (Color online) Calculated admittances of the AT mine VS-1.6 illustrating diminishing of the vibration amplitude due to soil stiffening.

fore, under these conditions, the soil stiffening may reduce the vibration amplitude of the buried mine. This observation has an important practical implication since it may explain some difficulties in detecting mines buried in consolidated or frozen soils. The effect of amplitude reduction due to soil stiffening is also accompanied by the upward resonance frequency shift that we discuss next.

B. Effect of burial depth on the resonance frequency

In addition to reduction of the vibration amplitude, the soil layer above the mine causes the resonance frequency shift. For relatively small depths, Fig. 7 clearly shows a downward resonance frequency shift attributed to the contribution of additional soil mass. The downward resonance frequency shift is observable not only for the first vibration mode, but for higher modes as well.

It should be noted that effects of the amplitude reduction and the downward resonance frequency shift caused by the soil distributed over the mine surface are well understood and have been observed for the lowest mine resonance in both laboratory measurements and field tests.[1–6,8] However, recent investigations[10,11,22,23] revealed that at certain depths buried mines exhibit an unexpected upward frequency shift, suggesting more complex dynamics of the soil-mine system. Figure 7 indicates that the first resonance frequency decreases and then, at a certain burial depth, starts to increase exhibiting an upward frequency shift at greater depths. The initial decrease of the resonance frequency, i.e., A (0 mm), B (2 mm), C (10 mm), D (20 mm), could be attributed to the effect of additional mass of the soil resting on the mine's upper plate. This phenomenon is consistent with the added mass theory and was observable up to the soil depth of 20 mm. However, after increasing the burial depth, we noticed an abnormal increase of the resonance frequency, so that E (40 mm) and F (80 mm) almost coincided with C (10 mm), and B (2 mm). The resonance frequency of the higher-mode exhibits comparable behavior. Although highly suppressed, the E2 resonance indicates the upward frequency shift similar to the one observed for the first resonance.

Another representation of the unusual upward frequency shift is given in Fig. 10(a) where we plotted a relative frequency of the first resonance versus the burial depth. The relative frequency in the figure is a ratio between the natural frequency at the current burial depth and the natural frequency of the flush-buried mine, i.e., at zero depth. Consistent with the previous observation, at small depths, the relative frequency decreases due to additional mass of the soil layer. However, at the depth of 15 mm, the frequency starts to increase contradicting assumption of the added mass. It is suggested that this frequency increase is caused by variation of the soil-mine dynamic stiffness as the burial depth increases. We considered two possible explanations of this phenomenon. The first deals with stiffening of the mine casing because of the nonlinear stress-strain relationship for the casing. In other words, additional soil mass modifies the stiffness of the casing and, therefore, the cumulative stiffness of the whole soil-mine system. This explanation, however, could hold for the exceedingly high stresses which are unlikely to occur under the given experimental conditions. To estimate the effect of the casing stiffening cased by the additional mass, we conducted an experiment where concentrated weights were placed on the casing and the frequency response was measured using the LDV and the microphone. The test data were superposed in Fig. 10(b) with results of the theoretical calculations. In contrast to Eq. (22), which accounts for both soil added mass and stiffness, formulation used in this case accounts for the effect of added mass only:

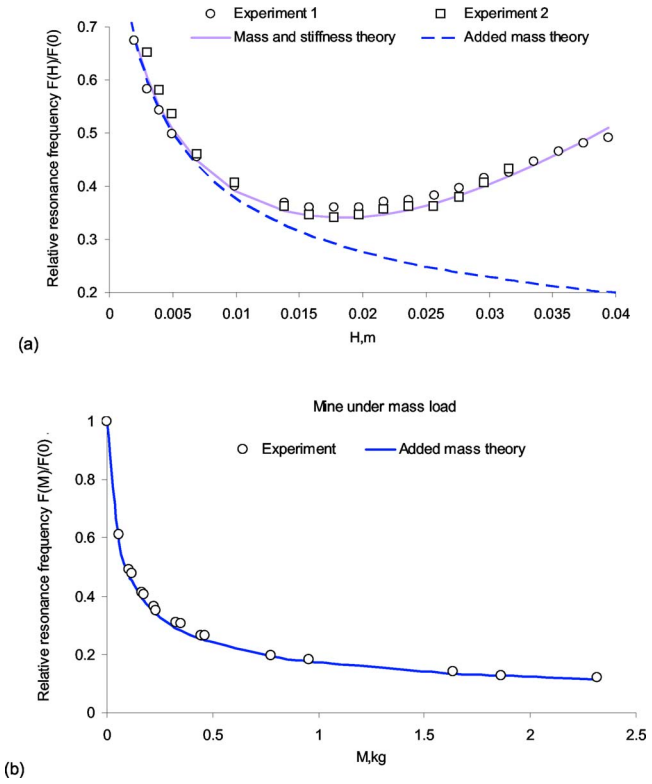

FIG. 10. (Color online) Relative resonance frequency of the first (lowest) mode versus (a) burial depth and (b) added mass.

$$f_h/f_0 = \sqrt{0.25 \cdot m_M/(M_S + 0.25 \cdot m_M)}. \quad (26)$$

Equation (26) predicts only a downward frequency shift, which is supported by the experimental data in Fig. 10(b). As can be seen from this figure, we obtained very good agree-

ment between the measured data and the theoretical prediction. Therefore, we conclude that the upward frequency shift is unlikely to result from the casing's stiffening, but is rather caused by a different physical mechanism.

We have indicated previously that the dynamic behavior of soil without a mine and a soil column above a buried mine differs significantly. Flexural vibrations of the mine casing result in bending of the soil layer above the mine. This effect occurs because soil, in contrast to fluid, supports shear stress. In the case of the bending vibrations, stiffness of the soil layer above the mine is proportional to the cube of the layer's thickness, as predicted by Eq. (22). We suggest that the upward frequency shift is related to the complex dependence of the soil stiffness on the burial depth. When the depth increases, so does the additional mass and the soil stiffness. According to Eq. (22), stiffness increases insignificantly at small depths, and its effect is negligible. However, at greater depths, the increase of the soil stiffness is considerable, and this effect overcomes contribution of the additional mass explaining the upward frequency shift. Figure 10(a) presents experimental data and results of the theoretical calculation where the shear stiffness of soil was considered as being proportional to the cube of the burial depth, $K_{S1} \sim h^3$, as our model suggests. Soil parameters that enter into the calculation according to Eqs. (22) and (23) corresponded to the well-graded sand: $e=0.4$, $\rho_S=1600$ kg/m^3, and $\nu_S=0.3$. As it could be seen from Fig. 10(a), theoretical calculations match well with the experimental data, supporting validity of the given explanation.

Recent experimental work[23] of Korman and Sabatier provided yet another confirmation of importance of the shear stiffness. To eliminate the contribution of the shear stiffness, authors substituted a soil layer above an oscillating plate with a water column. In contrast to experiments in which an upward frequency shift was observed for relatively thick soil layers, the test involving the water column has yielded only a continuous decrease of the resonance frequency.

In addition to laboratory experiments, we studied the effect of the upward frequency shift in field tests. Figure 11 shows the field data for AT mines VS-1.6 buried in sand and gravel. Despite differences in soil composition, the upward frequency shift was observed in both soils. Therefore, at relatively large depths, effects of additional stiffness due to the soil layer cannot be neglected and should be modeled appropriately using the soil stiffness proportional to the cube of the burial depth.

C. Effect of moisture

Depending on field and soil conditions, dynamic responses of buried mines could vary in a broad range. This variation occurs because environmental factors directly influence mechanical properties of the soil layer above the mine. For example, soil moisture could be particularly important because field conditions could vary from extremely dry weather to heavy rain. It has been observed that vibrations of a mine buried in wet soil could be considerably different from the one buried in dry soil. To understand and quantify the effect of moisture, we conducted a laboratory

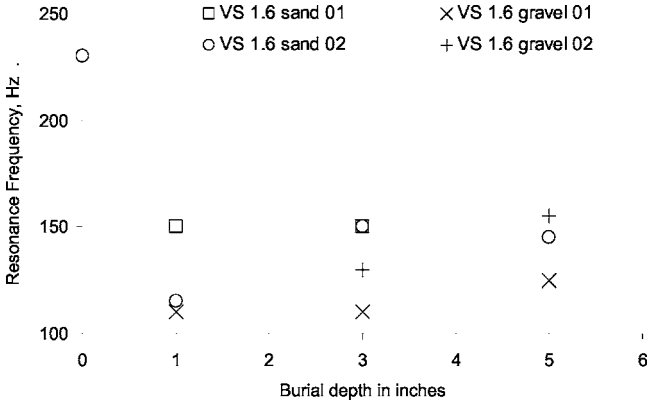

FIG. 11. The resonance frequency deviation versus the burial depth for VS-1.6 AT mine.

test in which the plastic mine simulant of radius 9.8 cm was buried under gradually increasing sand depths subjected to controlled levels of water saturation. Soil water content was calculated using a gravimetric method:

$$WC = W_{\text{water}}/W_{\text{soil}} \cdot 100\,\%\,, \tag{27}$$

where W_{soil} and W_{water} are respective weights of soil and water.

Initially, we repeated an experiment with the layers of dry sand shown in Fig. 10(a). A relative frequency shift of the first resonance frequency $F(h,0\%)/F(0,0\%)$ caused by increasing burial depths, h, was measured and results are presented in Fig. 12 with solid dots. Then, the test was repeated for sand layers of the same depths but different water contents, ranging from 2.6% to 18%. Moisture was uniformly distributed throughout the layers and was kept constant for each test run. Experimental results in Fig. 12 show that moisture considerably affects the resonance frequency of the buried mine, especially at deep depths.

It is interesting to note that a significant upward frequency shift occurs for a relatively small water content and does not change much at higher moisture levels. This observation, coupled with our previous conclusion that an upward frequency shift is due to the soil shear stiffness increase, leads us to believe that the introduction of moisture results in soil stiffening due to consolidation. As the test shows, even

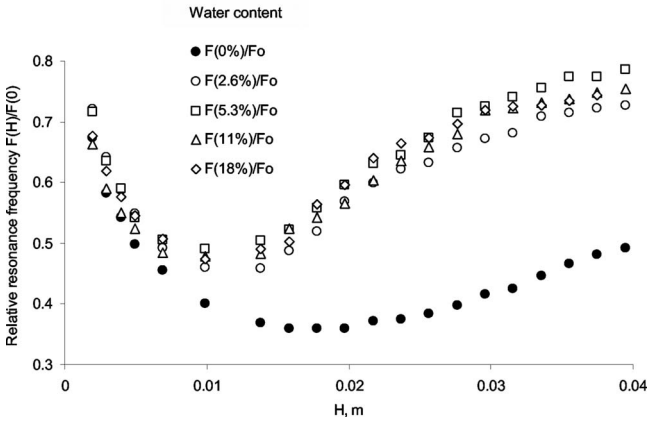

FIG. 12. Effect of the burial depth and water content on the resonance frequency of the buried mine.

relatively small water content creates an appreciable consolidation (stiffening) effect. Further increases of the water content adds little to already consolidated soil, resulting in an insignificant frequency shift.

V. CONCLUSIONS

Multimodal vibrations of buried landmines were observed in both field and laboratory experiments. These modes are modeled as oscillators with spatially distributed effective masses, stiffnesses, and damping parameters, and included into the previously developed lump-element model of the soil-mine dynamic system showing good agreement with the experimental data.

Vibration of buried mines is significantly affected by soil on top of the mine. The most noticeable effects include shifting the resonance frequencies and diminishing the vibration amplitudes as the burial depth increases. Decrease of the vibration amplitude is accompanied by an initial decrease of the resonance frequency due to additional soil mass. Interestingly, while the amplitude of vibrations continues to diminish, after a certain burial depth, the resonance frequency shifts upward. This phenomenon, observed in field and laboratory measurements, cannot be explained by a conventional approach that considers only the effect of additional soil mass. It is assumed that an upward frequency shift occurs because the soil shear stiffness increases with the burial depth. The upward frequency shift becomes apparent when, after a certain burial depth, the stiffening effect dominates over the contribution of additional soil mass. Consistent with the theory, experimental data show that the soil shear stiffness is proportional to the cube of the burial depth. Laboratory experiments revealed that the soil moisture results in further stiffening of the soil, thus amplifying the upward frequency shift. The soil stiffening has another interesting implication: The resonance frequencies shift toward the antiresonance resulting in reduction of the soil-mine vibration amplitude.

ACKNOWLEDGMENTS

The work was supported by the Office of Naval Research and the U.S. Army Communications-Electronics Command Night Vision and Electronics Sensors Directorate. The authors especially appreciate help and insights provided by Dr. Thomas Witten and Dr. Brad Libbey of NVESD and Dr. Clifford Anderson of ONR through the course of this work.

Portions of this work have been presented at the 147th Meeting of the Acoustical Society of America, 24–28 May 2004, New York and at the SPIE Defense and Security Symposium, 12–16 April 2004, Kissimmee, Fla.

[1] N. Xiang and J. M. Sabatier, "An experimental study on antipersonnel landmine detection using acoustic-to-seismic coupling," J. Acoust. Soc. Am. **113**(3), 1333–1341 (2003).
[2] J. M. Sabatier, M. S. Korman, and N. Xiang, "Linear and non-linear acoustic velocity profiles over buried landmines," Proc. SPIE **4742**, 695–700 (2002).
[3] D. M. Donskoy, "Nonlinear vibro-acoustic technique for land mine detection," Proc. SPIE **3392**, 211–217 (1998).
[4] D. Donskoy, A. Ekimov, N. Sedunov, and M. Tsionskiy, "Nonlinear seismo-acoustic land mine detection and discrimination," J. Acoust. Soc. Am. **111**(6), 2705–2714 (2002).
[5] W. R. Scott Jr., S. H. Lee, G. D. Larson, J. S. Martin, and G. S. McCall II, "Use of high-frequency seismic waves for the detection of buried land mines," Proc. SPIE **4394**, 543–552 (2001).
[6] S. H. Lee, W. R. Scott Jr., J. S. Martin, G. D. Larson, and G. S. McCall II, "Technical issues associated with the detection of buried land mines with high-frequency seismic waves," Proc. SPIE **4742**, 617–628 (2002).
[7] N. Xiang and J. M. Sabatier, "Acoustic-to-seismic landmine detection using a continuously scanning laser doppler vibrometer," Proc. SPIE **5089**, 591–595 (2003).
[8] J. M. Sabatier, R. Burgett, and V. Aranchuk, "High frequency A/S coupling for AP buried landmine detection using laser doppler vibrometers," Proc. SPIE **5415**, 35–41 (2004).
[9] J. C. van den Heuvel, V. Klein, P. Lutzmann, F. J. M. van Putten, M. Hebel, and H. M. A. Schleijpen, "Sound wave and laser excitation for acousto-optical landmine detection," Proc. SPIE **5089**, 569–578 (2003).
[10] D. Fenneman, C. Slick, and D. Velea, "Comparison of measured vs. predicted buried mine resonant behavior," Proc. SPIE **5089**, 495–504 (2003).
[11] A. Zagrai, D. Donskoy, and A. Ekimov, "Resonance vibrations of buried landmines," Proc. SPIE **5415**, 21–29 (2004).
[12] D. Donskoy, A. Reznik, A. Zagrai, and A. Ekimov, "Nonlinear vibrations of buried land mines," J. Acoust. Soc. Am. **117**(2), 690–700 (2005).
[13] A. W. Leissa, "Closed form exact solutions for the steady state vibrations of continuous systems subjected to distributed exciting forces," J. Sound Vib. **134**(3), 435–453 (1989).
[14] A. Liessa, *Vibration of Plates*, NASA SP-160 (NASA, 1969) (Reprinted for the Acoustical Society of America through the American Institute of Physics, Melville, 1993).
[15] K.-H. Kang and K.-J. Kim, "Modal properties of beams and plates on resilient supports with rotational and translational complex stiffness," J. Sound Vib. **190**(2), 207–220 (1996).
[16] L. K. Graff, *Wave Motion in Elastic Solids* (Dover, New York, 1991).
[17] E. Skudrzyk, *Simple and Complex Vibratory Systems* (University Press, University Park and London, 1968).
[18] J. C. Santamarina, K. A. Klein, and M. A. Fam, *Soils and Waves* (Wiley, New York, 2001).
[19] F. E. Richart, Jr., J. R. Hall Jr., and R. D. Woods, *Vibrations of Soils and Foundations* (Prentice–Hall, Englewood Cliffs, N.J., 1970).
[20] Y.-G. Zhou and Y.-M. Chen, "Influence of seismic cyclic loading history on small strain shear modulus of saturated sands," Soil Dyn. Earthquake Eng. **25**, 341–353 (2005).
[21] A. Zagrai and D. Donskoy, "A "soft table" for the natural frequencies and modal parameters of uniform circular plates with elastic edge support," J. Sound Vib. **287**(1-2), 343–351 (2005).
[22] J. M. Sabatier and M. S. Korman, "Nonlinear tuning curve vibration response of buried land mine," Proc. SPIE **5089**, 476–486 (2003).
[23] M. S. Korman and J. M. Sabatier, "Nonlinear acoustic technique for landmine detection," J. Acoust. Soc. Am. **116**, 3354–3369 (2004).
[24] S.-H. Yu, A. Gandhe, T. R. Witten, and R. K. Mehra, "Physically based method for automatic mine detection using acoustic data—A transmission zero approach," Proc. SPIE **4742**, 701–708 (2002).
[25] S.-H. Yu, T. R. Witten, and R. K. Mehra, "Acoustic-seismic mine detection based on spatial-spectral distribution of poles," Proc. SPIE **5089**, 606–613 (2003).

Noise levels in Johns Hopkins Hospital

Ilene J. Busch-Vishniac,[a] James E. West, Colin Barnhill, Tyrone Hunter, Douglas Orellana, and Ram Chivukula
Johns Hopkins University, 3400 N. Charles Street, Baltimore, Maryland 21218

(Received 25 May 2005; revised 12 September 2005; accepted 19 September 2005)

This article presents the results of a noise survey at Johns Hopkins Hospital in Baltimore, MD. Results include equivalent sound pressure levels (L_{eq}) as a function of location, frequency, and time of day. At all locations and all times of day, the L_{eq} indicate that a serious problem exists. No location is in compliance with current World Health Organization Guidelines, and a review of objective data indicates that this is true of hospitals throughout the world. Average equivalent sound levels are in the 50–60 dB(A) range for 1 min, $\frac{1}{2}$, and 24 h averaging time periods. The spectra are generally flat over the 63–2000 Hz octave bands, with higher sound levels at lower frequencies, and a gradual roll off above 2000 Hz. Many units exhibit little if any reduction of sound levels in the nighttime. Data gathered at various hospitals over the last 45 years indicate a trend of increasing noise levels during daytime and nighttime hours. The implications of these results are significant for patients, visitors, and hospital staff.
 [DOI: 10.1121/1.2118327]

PACS number(s): 43.50.Jh, 43.55.Gx [DKW] Pages: 3629–3645

I. INTRODUCTION

The importance of noise in health care has been recognized for years, as evidenced by a statement in 1859 by Florence Nightingale[1,2]

> "Unnecessary noise, then, is the most cruel absence of care which can be inflicted either on sick or well."

However, little work has been done to characterize and reduce hospital noise even though it routinely ranks among the top complaints of hospital patients, visitors, and staff.[3,4]

There are a small number of hospital noise surveys in the open literature,[4–21] and some studies that specifically consider intensive care units,[14,16,22–35] operating rooms,[36–42] and nurseries.[43–48] A few address tools found in hospitals, particularly incubators and instruments used in orthopedics.[10,49–53] All of these studies are generally conducted by physicians and nurses and reported in the medical literature, which is also replete with editorials and letters railing against noise.[54–58] Taken as a whole, this body of literature suggests that a significant problem exists, and that it is generally getting worse rather than better, even in new construction.

Interestingly, the literature on typical hospital noise levels is generally limited to overall noise levels (either linear or A-weighted). There is little mention of typical spectra and even less discussion of additional measures of the noise such as spectral quality, tonality, and time variance. This makes it quite difficult to discuss the noise in terms of human physiological and psychological response.

There are only a handful of reports dealing with control of hospital noise,[1,43,59] and these are almost entirely limited to administrative control measures such as closing doors and asking staff to speak softly. Such measures have not met with great success in industrial settings where there is, in theory, greater control over personal behavior than exists in hospitals. A notable exception to this is the recent study by Akhtar *et al.*[60] in which noise canceling headphones were given to medical staff and the parents of children in a pediatric intensive care unit (PICU). This study found that subjects generally perceived the headphones to offer an improvement in the environment, but overwhelmingly said they would prefer not wearing them in spite of this improvement.

Noise in hospitals is important for a number of reasons in addition to the obvious issue of annoyance. There is evidence that the high sound levels in the hospital contribute to stress in hospital staff[61] and a suggestion from one study that noise contributes to staff burn-out.[62,63] Further, there is some evidence that noise negatively affects the speed of wound healing. Fife[64] showed that hospital stays for cataract surgery patients increased during the time of higher noise due to construction of a new building. Also, Minckley[65] found that more medications were required for surgical patients in recovery when the sound levels present were high (over 60 dB re 20 μPa). Wysocki,[66] Toivanen *et al.*,[67] and Cohen[68] have all shown delays in wound healing in animals (mice and rats) when noise is present.

There are a few studies of the effects of noise on performance in hospitals, but these present conflicting results. Hawksworth *et al.*[69] looked at the performance of trainee anesthetists on a set of two standard psychomotor tests in the presence of music, white noise, and silence and found no difference in performance. Similarly Moorthy *et al.*[70] studied the ability of surgeons to place three laparoscopic sutures on a suture pad in quiet and noisy conditions using background operating room noise and music. They found no significant differences in performance with and without sound present. Park *et al.*[71] conducted a study of orthopedic surgeons in which they were asked to read x-rays in the presence of controlled levels of noise. It was found that there was no

[a]Electronic mail: ilenebv@jhu.edu

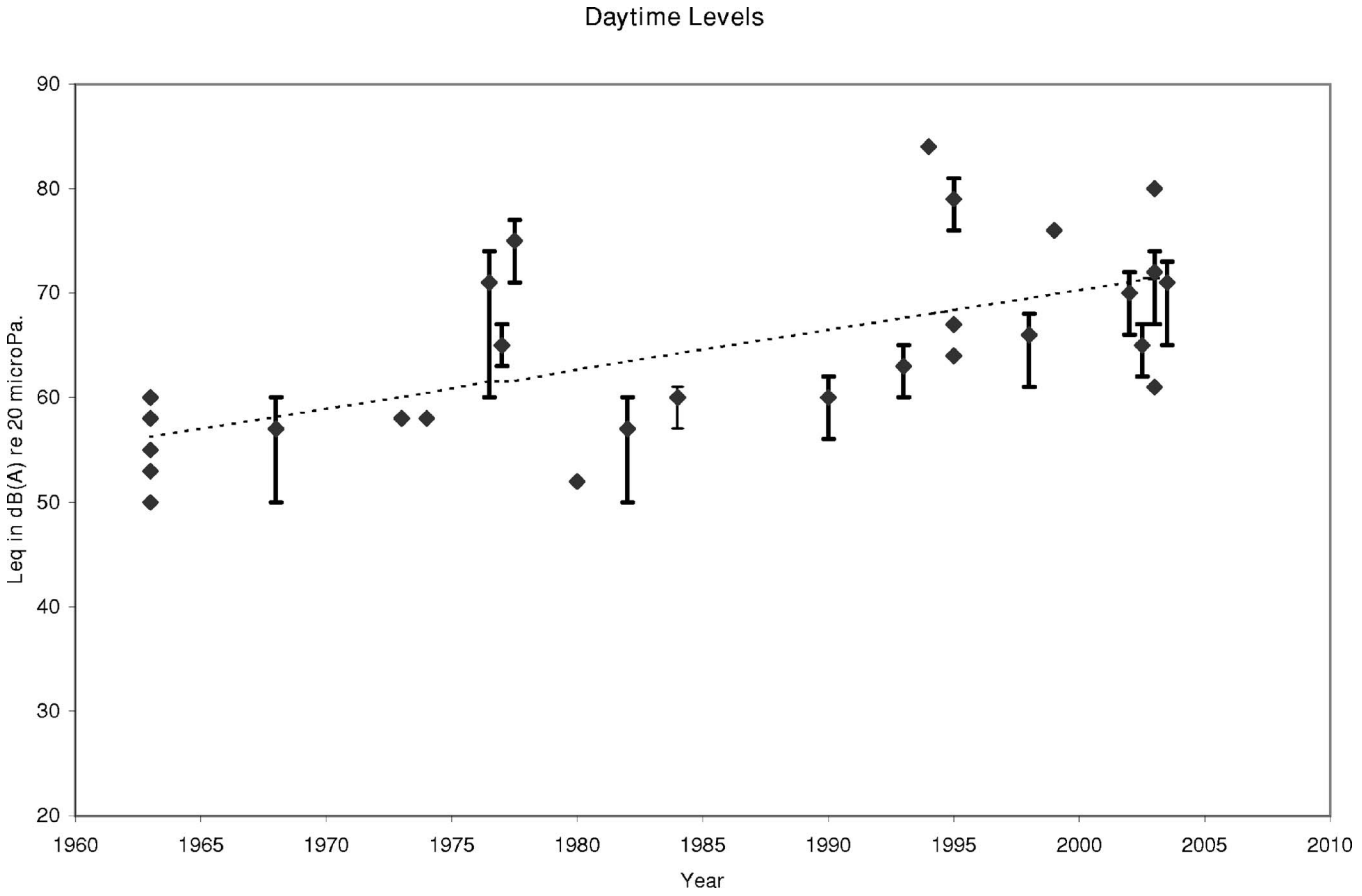

FIG. 1. A-weighted equivalent sound pressure levels measured in hospitals during daytime hours as a function of the year of study publication. Error bars indicate that data were given as a range spanned by the error bar. In these cases, the data point is shown as the logarithmic average of the range extreme values.

significant performance difference between noisy and quiet conditions, but overall residents who preferred quiet did better in quiet environments, and those who stated no preference performed equally as well in both noise and quiet. By contrast, Murthy *et al.*[39] found that mental efficiency and short-term memory declined in the presence of typical operating room noise for anesthetists. Murthy *et al.* also found that speech discrimination declined 23% and speech thresholds increased roughly 25% for the same level of comprehension[72]—a result with important implications for medical safety.

Finally, noise in hospitals could become important if it permits one facility in an area to advertise a better patient environment than other hospitals, i.e., if it offers a competitive advantage.

While the problem of hospital noise has not been adequately addressed, there are established guidelines and standards which deal with hospital noise. The World Health Organization (WHO) included guidelines for hospitals in their *Guidelines for Community Noise* published in 1995.[73] These guidelines recommend an L_{max} of no more than 40 dB(A) (re 20 μPa) at night measured on the fast setting. They also suggest patient room L_{eq} of no more than 35 dB(A) during the day and 30 dB(A) at night. The American National Standards Institute, Inc. (ANSI) also mentions hospital noise but uses different measures for their standard. ANSI S12.2, published in 1995, recommends a maximum RC(N) (neutral spectrum room criterion) value ranging from 25 to 40 depending on the room type, and a maximum NCB (balanced noise criterion) value ranging from from 25 to 40.[74] The Environmental Protection Agency (EPA) document which summarizes the significant community noise studies done in the late 1960s makes its recommendations in terms of the L_{dn} (day-night sound pressure level), which should not exceed 45 dB(A).[75] Of these standards and guidelines, we find the WHO values most frequently cited in the literature and thus we will rely on those in this article. We will show in the following that existing measures of sound pressure levels in hospitals exceed these guidelines significantly, and have for many years.

This article is the first step in a larger project to improve the sound environment in hospitals. It focuses on the existing sound pressure levels in a major US hospital and puts these in the context of sound pressure levels reported at hospitals in the last few decades. The measured data confirm the existence of a serious noise problem.

II. HOSPITAL NOISE LEVELS OVER THE YEARS

Although the literature on hospital noise is thin, some reliable noise measurements have been made at a variety of hospitals throughout the world over the last 40–50 years and published in the open literature. We reviewed these data carefully to enable us to answer the following basic ques-

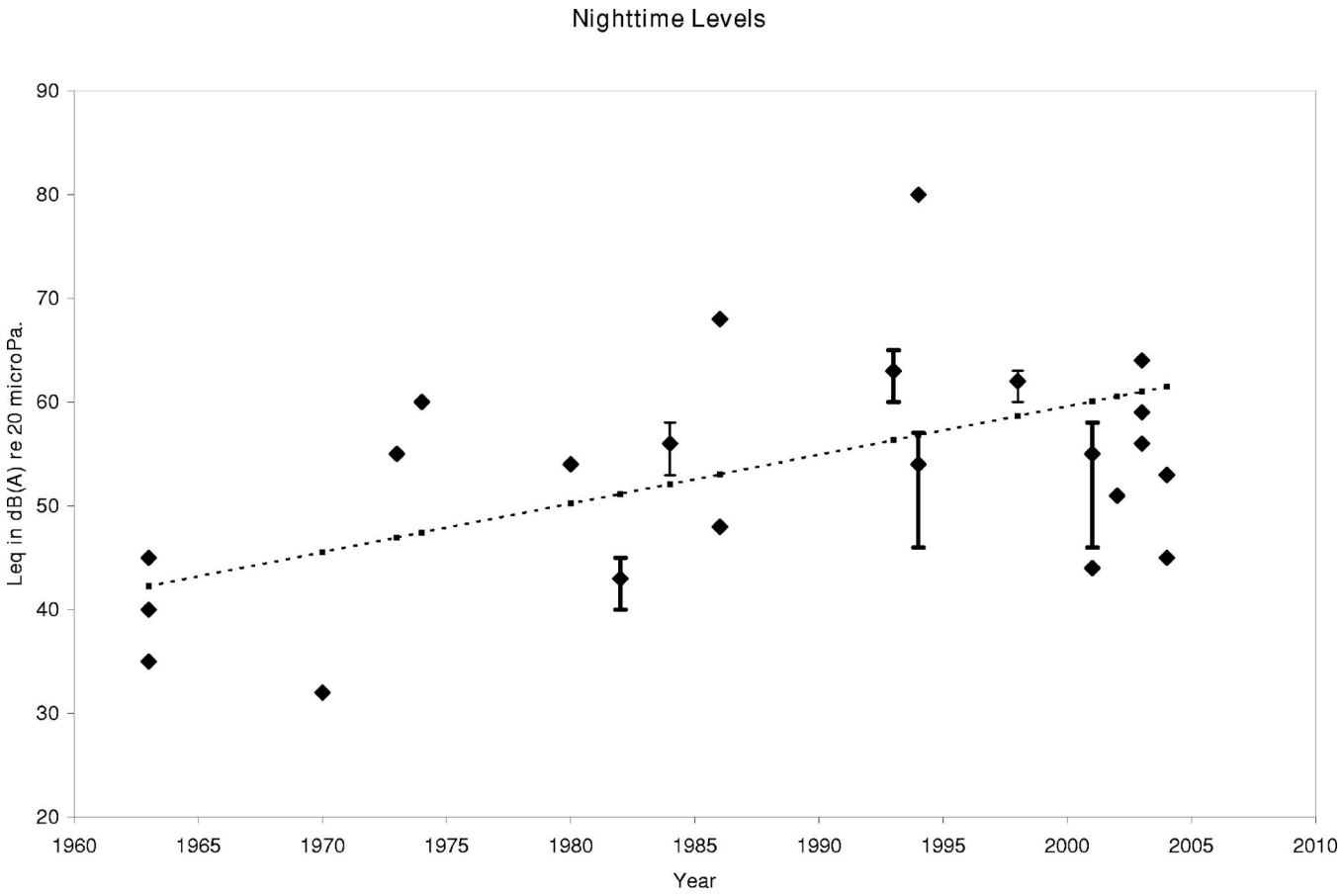

FIG. 2. A-weighted equivalent sound pressure levels measured in hospitals during nighttime hours as a function of the year of study publication.

tions: Is there any indication that hospital noise levels are changing over time? Do hospital noise levels vary dramatically from hospital to hospital? Do hospital noise levels vary significantly with type of unit?

In gathering data to answer these questions, we discovered a problem with the hospital noise literature that had been previously noted by Philbin.[48] The vast majority of the published literature on hospital noise has been written by medical staff with little or no training in acoustics. Unfortunately, there tends to be a consistent error in the presented results, namely that average sound pressure level information is published, but that the average has been computed erroneously by taking the mean of the decibel values read on a meter. The normal presentation gives a mean and a standard deviation (in decibels). To ensure the validity of our analysis, we considered all literature we could find that took correct averages, or presented raw data that we could average, or that presented a standard deviation of 1 dB or less. We also included data that were given as a range, and we show this as a data point at the decibel average of the range end points with error bars showing the span cited. Given the absence of a hospital noise standard, the measurements in the literature also vary from A-weighted L_{eq} to unweighted L_{eq} to L_{peak} or other measures. For consistency, we considered only A-weighted L_{eq} values, as these were most often measured. Even with this restriction, we should note that there is no known uniformity in the averaging time for the L_{eq}; nor is it known whether the sound level meter gathering data in each case were set to slow or fast.

Figures 1 and 2 show the results of our compilation of existing noise studies.[5–8,10–15,18–23,25,31–33,35,37–39,46,48,59,61,65,76–78] In these and all other figures in this article, dB(A) is referenced to 20 μPa and decibel averages refer to logarithmic or energy averages. The A-weighted L_{eq} are graphed as a function of the year of publication of the study. Figure 1 shows results for daytime hours and Fig. 2 for nighttime hours (using the same hourly division as in the L_{dn} when possible). When the data provided did not specify time, they were included in the daytime graph only. The results include hospitals of various types (major research facilities to community hospitals) located throughout the world. They make no distinction based on type of medical unit observed.

Figures 1 and 2 show three items of interest. First, not one published result shows a hospital which complies with the WHO guidelines for noise in hospitals. Most of the data, particularly that which is recent, shows sound levels 20–40 dB(A) higher. This certainly raises the question of what significance the guidelines have.

Second, there is a clear trend for rising hospital noise levels consistently since 1960. A straight line fit to the data (included in the figures) shows an increase, on average, of 0.38 dB per year for daytime levels, and 0.42 dB per year for the nighttime levels. The correlation coefficient for the straight line fit is $r=0.66$ for the daytime levels and $r=0.59$ for the nighttime levels. The (logarithmic) average A-weighted L_{eq} in hospitals have risen from 57 dB(A) in

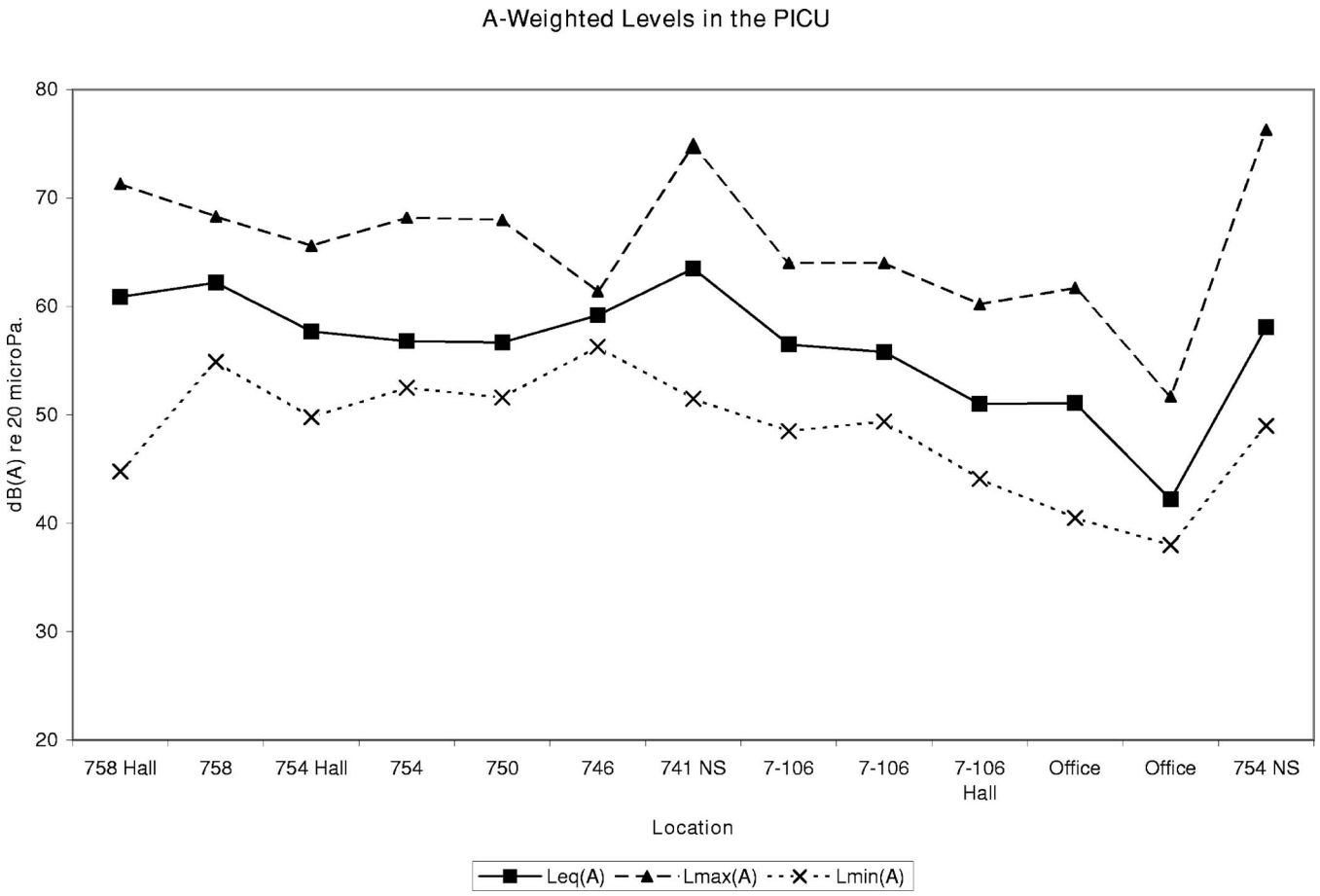

FIG. 3. A-weighted equivalent sound pressure levels measured in various locations in the PICU. Here and subsequently, NS indicates a nursing station.

1960 to 72 dB(A) today during daytime hours, and from 42 dB(A) in 1960 to 60 dB(A) today during nighttime hours.

Third, Figs. 1 and 2 show remarkably little variation given that the results are for widely different sorts of hospitals and medical units. Regardless of the reasons for this relative consistency, it suggests that the problem of hospital noise is universal, and that noise control techniques might also be expected to be applicable broadly. The bulk of the work on hospital noise has centered on intensive care units and operating rooms (with emphasis on orthopedic surgeries). These units do tend to show higher L_{eq} on average than other units included in measurement data, but not dramatically so.

The next sections of this article present new data on noise levels at a particular hospital—Johns Hopkins Hospital in Baltimore, MD. Johns Hopkins Hospital (JHH) is a large research medical facility which services a very broad community. It has been the top ranked hospital in the US (according to US News and World Report) for the last 14 years. As we will show in the following, the noise levels at JHH are completely consistent with the above-presented results.

III. EQUIVALENT A-WEIGHTED SOUND PRESSURE LEVELS IN JOHNS HOPKINS HOSPITAL

Over the last year, we have obtained sound pressure level measurements at five different locations in Johns Hopkins Hospital. These are the Pediatric Intensive Care Unit (PICU), Weinberg 4C, Weinberg 5C, the Children's Medical Services Center 4th floor (CMSC4), and Nelson 7. Weinberg is the oncology center of JHH. Weinberg 5C differs from Weinberg 4C in that Weinberg 5C has no acoustical tile ceiling because it houses immuno-compromised patients and there is concern about the holes in the standard acoustical tiles trapping bacteria. Weinberg is the newest patient care building in the hospital and came on line in 1999. CMSC4 and the PICU are pediatric units, with CMSC4 being a medical/surgical unit and the PICU housing intensive care children (but not neonates). Nelson 7 is an adult medical/surgical unit. Nelson 7, CMSC4, and the PICU are all housed in the older portions of the hospital, which are now roughly 50 years old.

At each unit we used a consistent protocol for measurements. We first measured one-minute L_{eq} at many locations on the unit, always including patient rooms, hallways, and nurses stations. We simultaneously obtained octave-band sound pressure levels at every location. Subsequently, we obtained 24-h measurements at a minimum of three places per unit—a patient room, a nurses station, and an examination room or empty patient room. In every case we requested that patients, staff, and visitors continue with their normal activity. All measurements were obtained with a Larson-Davis system 824. Results were downloaded to a PC for analysis. Measurements in hallways and patient rooms were

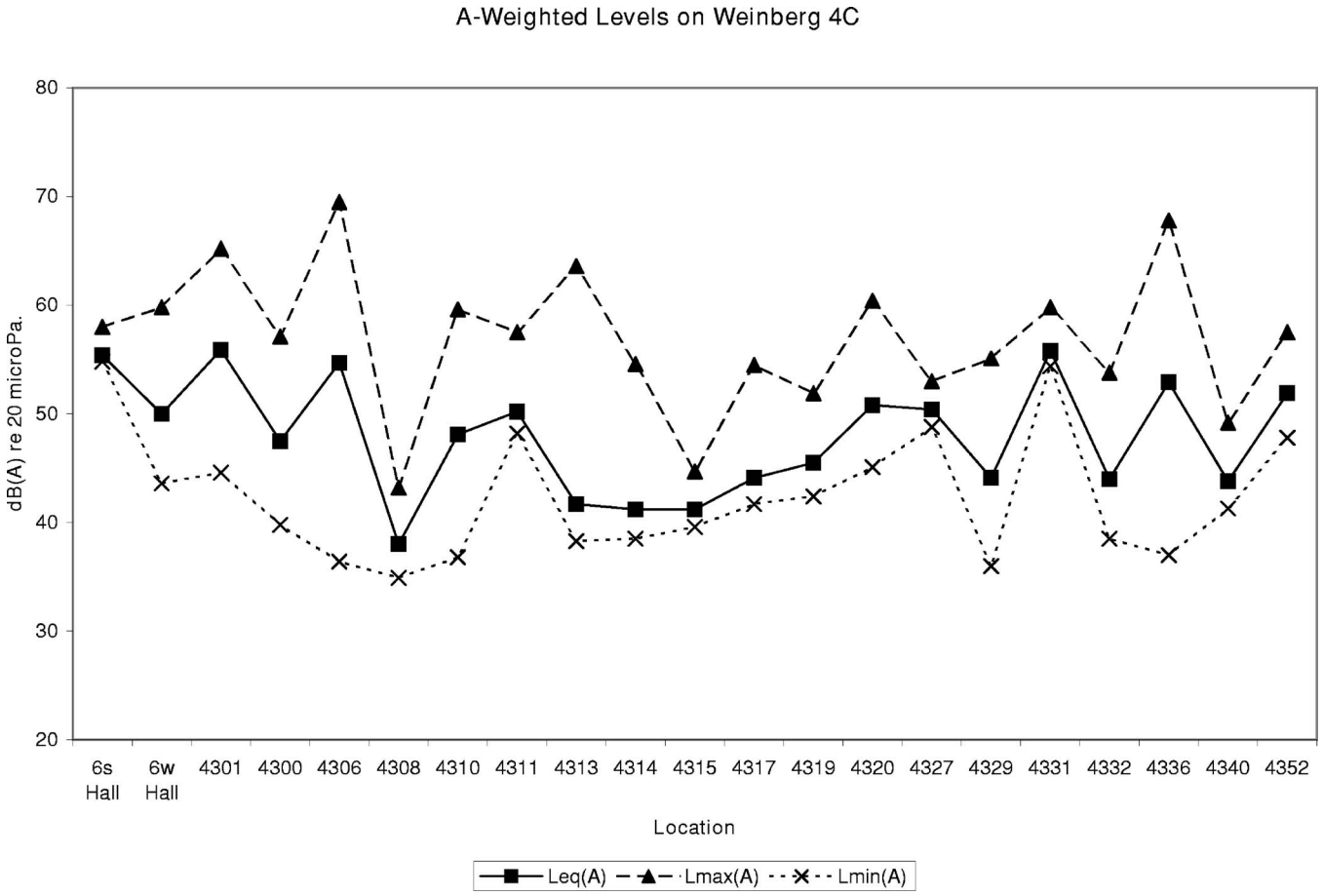

FIG. 4. A-weighted equivalent sound pressure levels measured in various locations in Weinberg 4C.

made near the room center at a height of roughly 4.5 ft. Some of the halls and some of the rooms had acoustical tile ceilings but no other acoustical treatment. Other locations had no acoustical treatment whatsoever. Thus, we found all of the facilities to be quite reverberant.

Figures 3–8 show the 1 min A-weighted L_{eq} as a function of location. In each case, the figure shows the L_{max}, L_{eq}, and L_{min} obtained using the slow averaging setting of the meter. In general, there is more variation between rooms on a unit than between hall measurements. This is almost certainly a reflection of the variations in activity in different patient rooms with higher levels corresponding to rooms with multiple visitors or louder playing of the TV.

Figure 3 shows an almost uniform set of sound levels throughout the PICU, which is somewhat surprising given its L-shaped geometry. The office measurements listed on this figure are two measurements at the office of Nurse Manager Claire Beers. Her office is at the extreme end of the unit. The higher sound level corresponds to the door open, and the lower value to the door closed. All rooms on the unit were occupied. Nurses stations are distributed throughout the larger patient rooms in addition to a main nurses station in the corridor.

Figures 4 and 5 show Weinberg results. From these we see that the new building is not particularly quieter than the older buildings. This is surprising given that noise was an issue considered during Weinberg design and construction. Indeed, the construction design called for NC-35 for the new, unoccupied building. Weinberg 4C is significantly quieter than 5C due to the acoustical tile ceiling there. Further, hospital air flow rates have increased significantly in the last 50 years so the older buildings are now driving more air through air ducts than the system was originally designed to handle, while Weinberg was built to handle the current HVAC standards.

Figure 6 shows the 1 min averaged A-weighted L_{eq} measured in CMSC4. CMSC4 is a particularly interesting location because it serves as a living laboratory for the study of hospitals. One of the corridors in this unit is the traditional straight corridor with small indentation places located along the walls which house computers for staff to enter patient data. These tend to be places where physicians congregate, particularly during rounds. The other corridor is nominally parallel to the conventional one, but has been built intentionally with a curvature to it. This prevents line of sight contact down the entire length of the hallway. On the curved corridor, there are small cubicles oriented at 90° to the corridor axis for staff to enter patient data. CMSC4 also has modified their nurses station so that there is a small reception area at the entry to the unit and a larger work area midway into the unit. This contrasts with the conventional approach of congregating the entire nurses station in a single location (except in intensive care units). Figure 6 shows that there is essentially no acoustical advantage gained by the curved corridor.

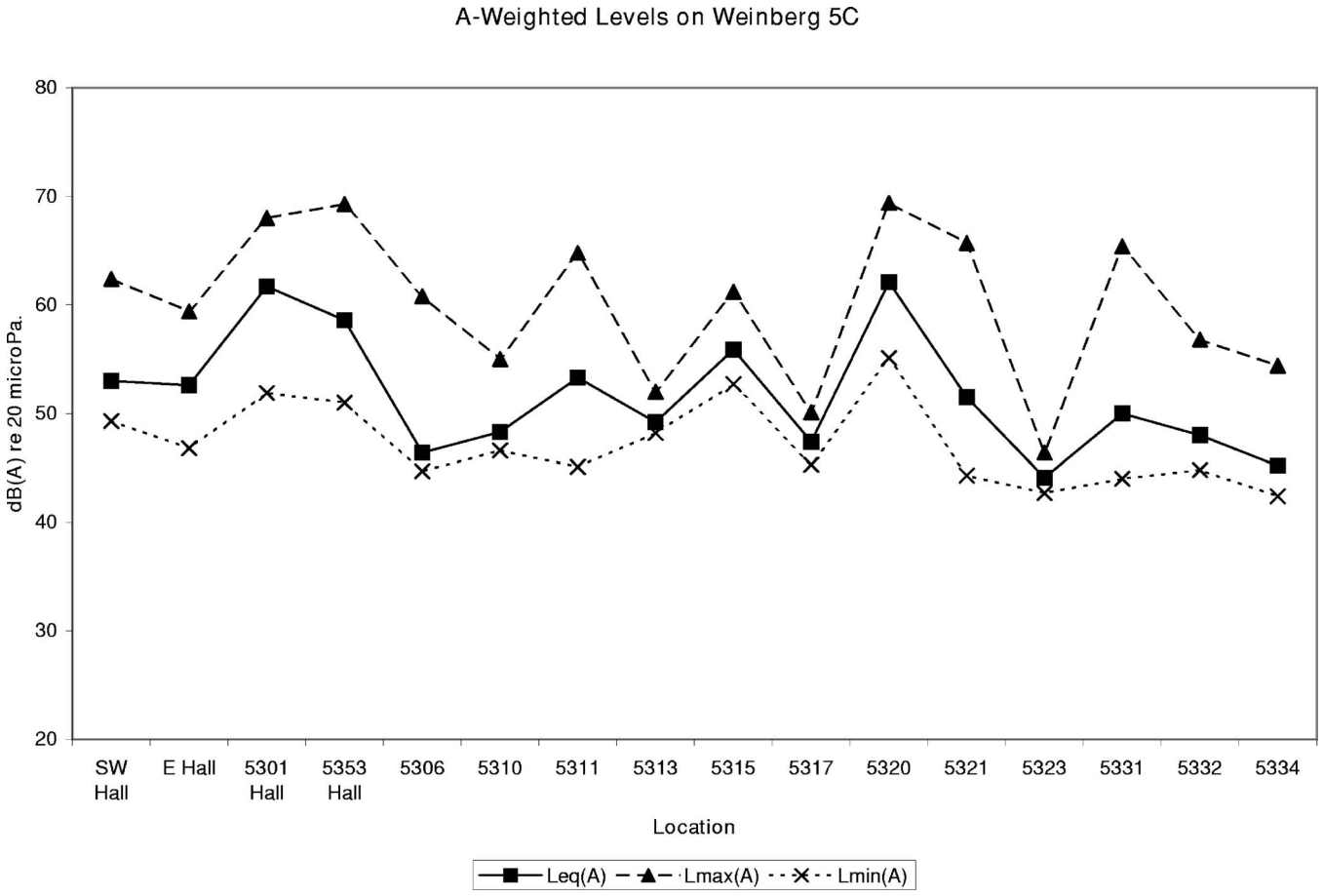

FIG. 5. A-weighted equivalent sound pressure levels measured in various locations in Weinberg 5C.

The results for straight corridor rooms (left half of the figure) are about the same as those for the curved corridor (right half of the figure).

Figures 7 and 8 show the sound levels on Nelson 7. Here we were able to get measurements in rooms with a greater range of uses, and this is reflected in the variability shown in Fig. 7. The rooms with the highest sound levels were a staff conference room and a patient room with loud conversation. The quietest room was an empty equipment room.

Figures 3–8 indicate which measurements were in hallways, which in rooms, and which at nurses stations. By considering the nurses stations separately, one sees a pattern emerge—they are generally noisier than the other areas on the unit by 1–2 dB(A). We can also consider the few rooms that were empty and note that they were generally quieter than the occupied rooms, but not always. In particular, when the empty rooms were near nurses stations, they were noisier rather than quieter than the other rooms on the unit. Finally, we had a single set of measurements with an empty room in which we were able to consider the effect of closing the room door. This yielded a noise reduction of 2.2 dB(A) only. Although we did not measure noise transmission through walls from one patient room to another, we did not hear any such sound transmission at any point during our measurements.

Figure 9 presents the logarithmic average L_{eq}, L_{max}, and L_{min} measured on each of the five units. Also shown in that figure are the WHO guidelines for operational hospital facilities, and representative levels for normal speech and shouting as measured at typical speaker/listener distances. This figure makes three compelling points. First, it is clear that there is little variation in the measured sound levels from among the five units studied at JHH. Average L_{eq} vary from 50 to 60 dB(A). The PICU is the noisiest unit of the five, while CMSC4, Weinberg 4C, and Nelson 7 are very similar in level and are quietest.

The second interesting observation comes from comparing the measured noise levels to WHO guidelines and the typical speech levels (as cited in the WHO report). Clearly, the observed sound levels exceed the WHO guidelines significantly—by at least 20 dB(A) on average levels, and by at least 15 dB(A) on L_{max}. Further, all of the measured logarithmic average sound levels exceed the typical speech level for communication between two people of 45–50 dB(A), suggesting that staff need to raise their voice routinely in order to be heard above the noise. Given the evidence that sound levels in hospitals are rising annually, there is reason to be concerned that it might eventually be difficult to communicate orally even by means of shouting.

Third, the values given in Fig. 9 are a little below those shown in Fig. 1 for 2004, but not dramatically so. They thus complement the pattern shown in Figs. 1 and 2 of a generally rising sound pressure level within hospitals regardless of their type or location.

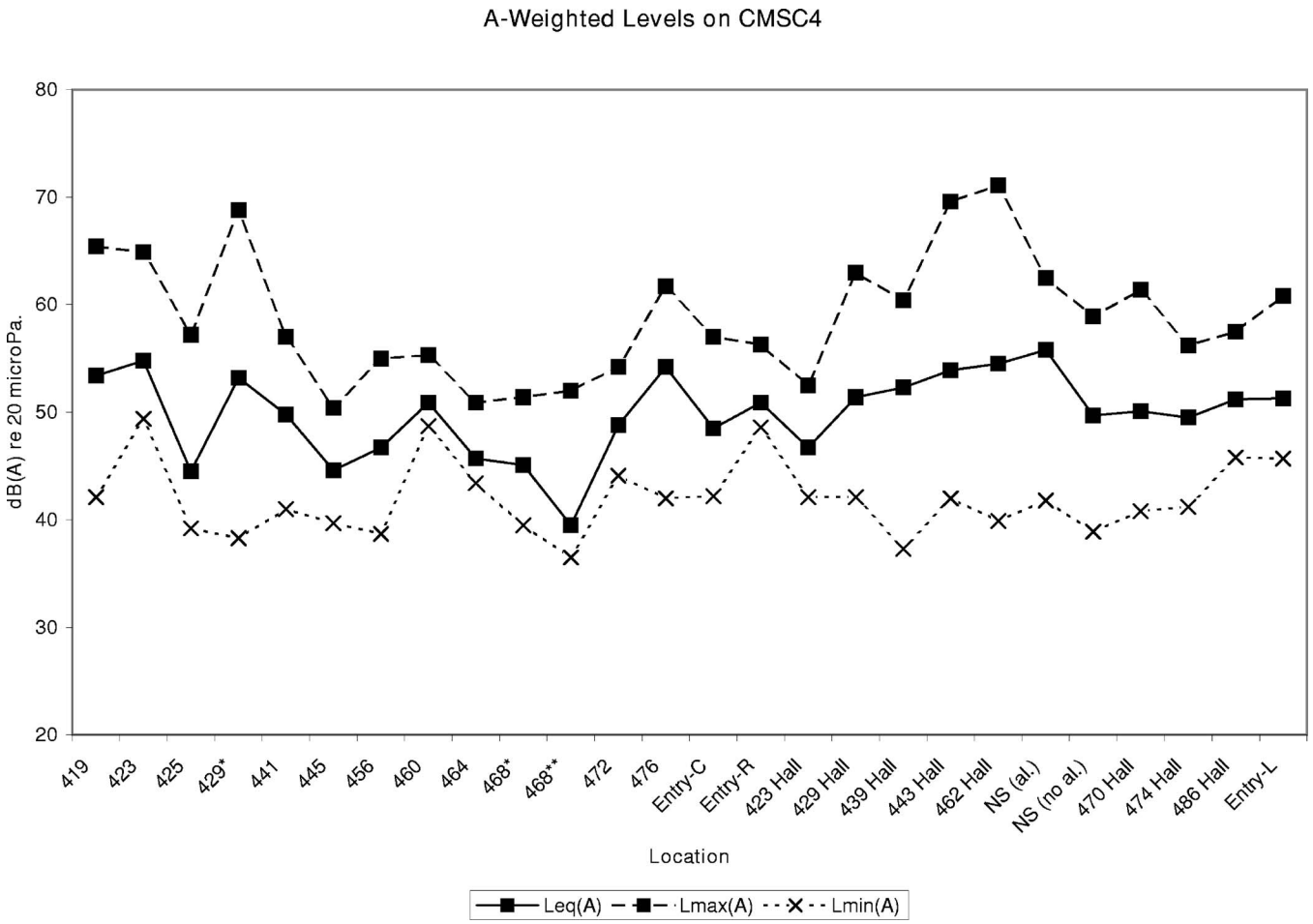

FIG. 6. A-weighted equivalent sound pressure levels measured in various locations in CMSC 4: (*) unoccupied rooms, (**) unoccupied and door closed.

IV. SOUND SPECTRA

Figure 10 shows the sound level in octave bands at the various measurement locations of the PICU. With the exception of the very lowest curve, measured at the Nurse Manager's office, the spectra are very similar in shape. The spectrum is nearly flat between the 63 and 1000 Hz octave bands, rolling off slowly at higher frequencies, and increasing at frequencies below the 63 Hz band. The flat sound spectrum region generally encompasses the speech band and, at the low frequency end, is almost certainly caused by heating, ventilating, and air conditioning noise. Given the constant chatter in hospitals and the mobile sources (doctors and nurses in halls for instance) it is not surprising to find the spectrum shown in Fig. 10.

The octave band levels for the other hospital units measured are quite similar in form to that shown in Fig. 10. What we present in Fig. 11 is the logarithmic average L_{eq} in each unit in each octave band. Note the similarity in shape of the curves, although there is a significant difference in the levels. The largest difference shown in Fig. 11 is 18 dB in the 16 kHz octave band, although the difference is more typically 5–10 dB. In JHH, then, there is significant difference from unit to unit, although the overall form of the spectra is quite similar.

The low frequency noise in the units is commonly found in buildings and likely relates to the air handling system. We obtained a small amount of data using a microphone directly under an air vent and an accelerometer mounted on the wall a short distance away. By considering the correlation between the two signals (with appropriate time delay for travel to the wall from the air vent) it is possible to determine whether the low frequency sound measured in the units is structure-born or airborne. On the basis of our few measurements, which produced generally low correlations, we believe the sound to be airborne.

The high frequency noise roll off in the hospital units we measured is more gradual than one often sees in buildings. We have not yet attempted to determine the source of the high frequency noise, although alarms and mobile medical equipment have been suggested as culprits. We cannot rule out high velocity flow in the air handling system.

V. EQUIVALENT A-WEIGHTED SOUND PRESSURE LEVELS AS A FUNCTION OF TIME OF DAY

In each unit we obtained a minimum of three 24 h measurements of the L_{eq}. When possible, one of these measurements was made at the main nurses station for the unit, one in an occupied patient room, and one in either an unoccupied patient room or an examination room (normally used only in daytime hours). The measurements were made using 30 min time averaging.

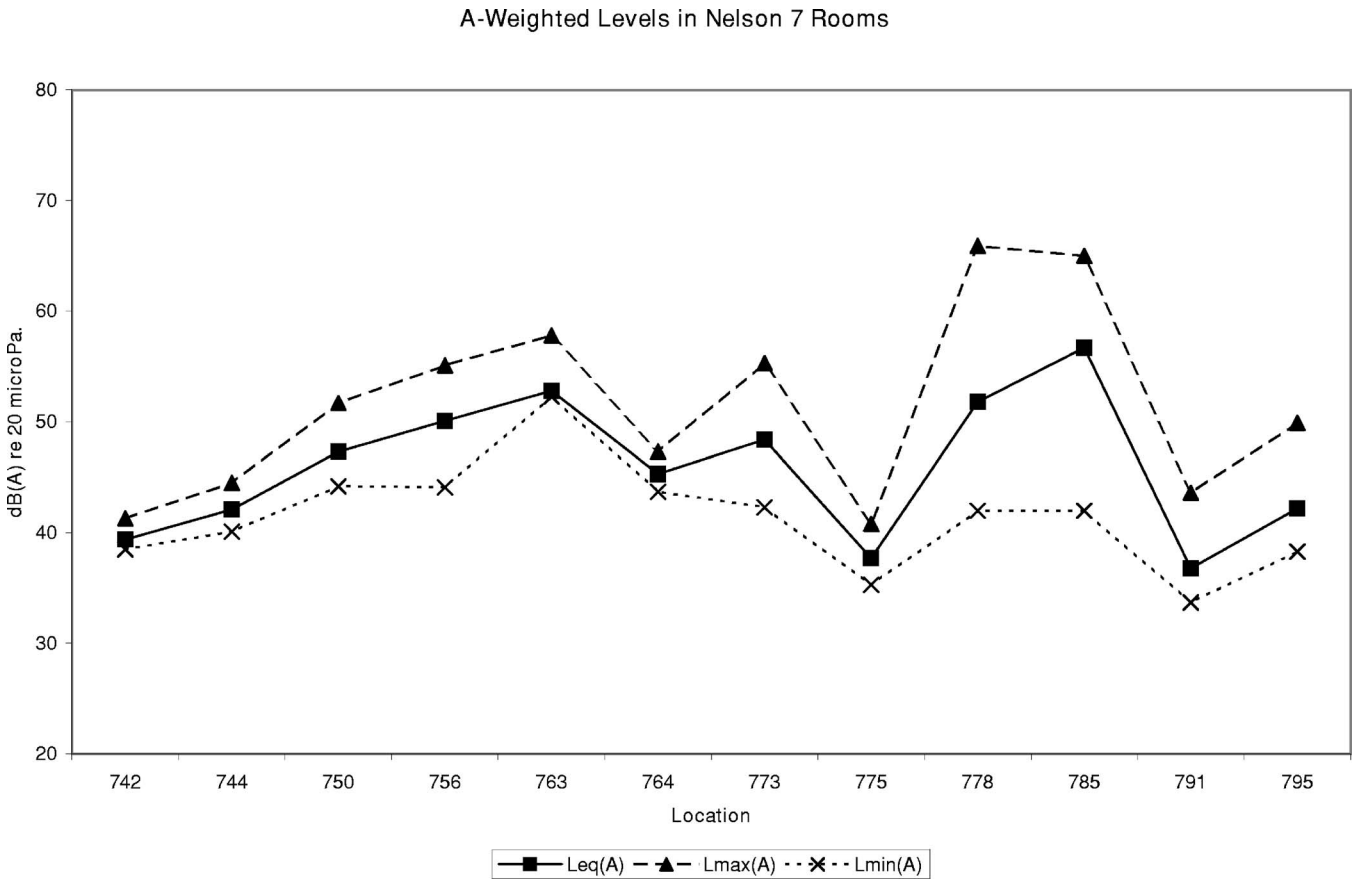

FIG. 7. A-weighted equivalent sound pressure levels measured in various rooms in Nelson 7.

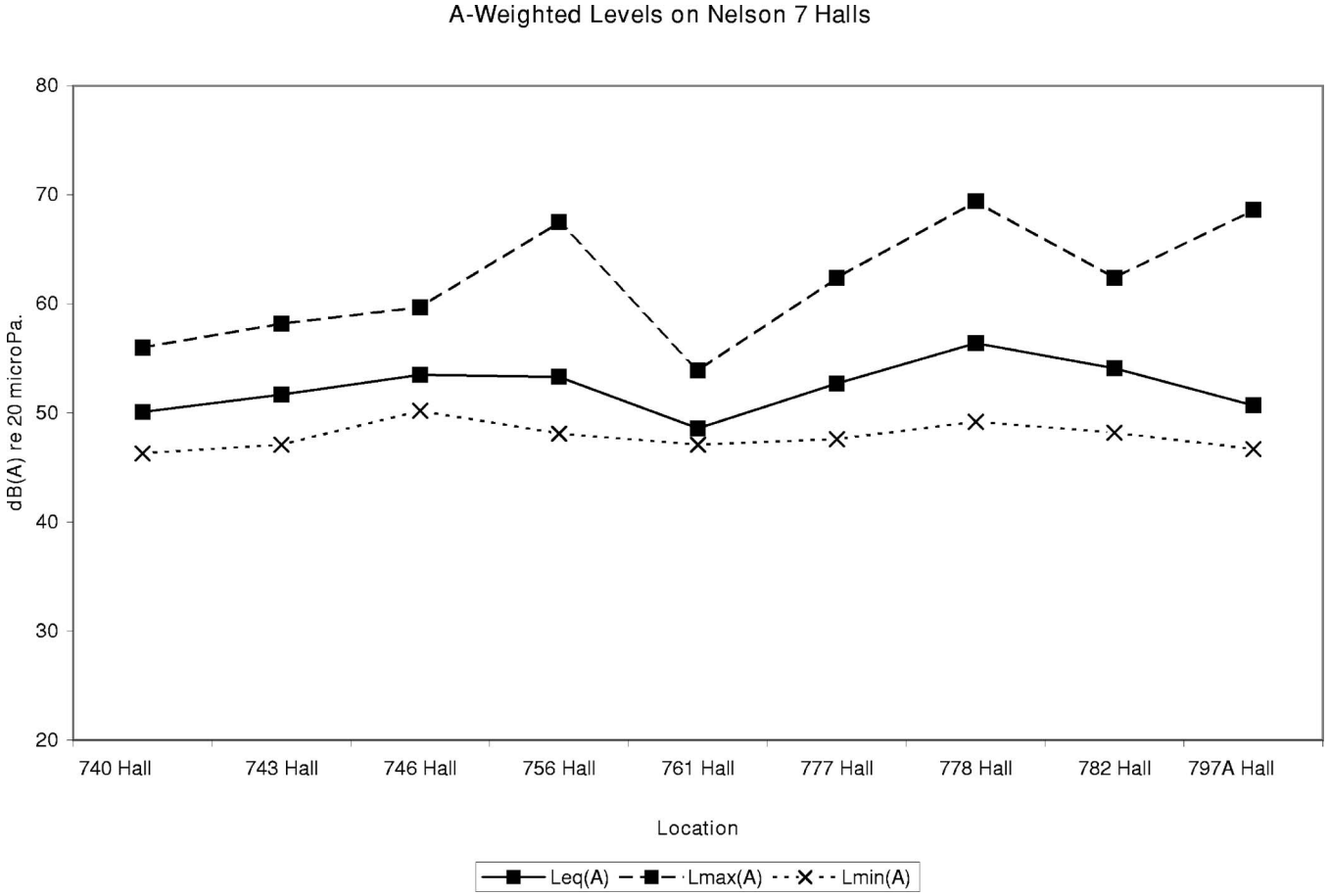

FIG. 8. A-weighted equivalent sound pressure levels measured in various hall locations in Nelson 7.

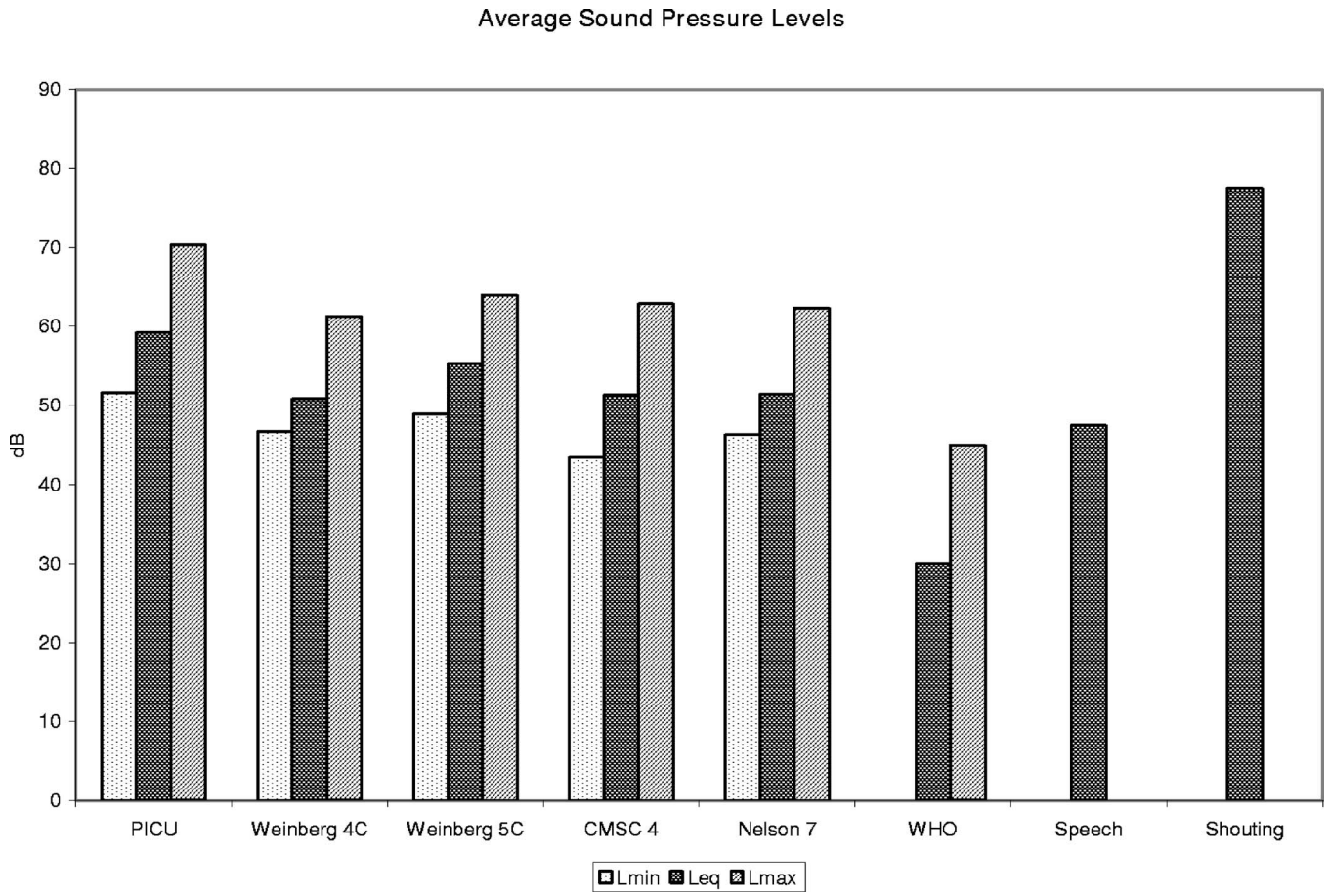

FIG. 9. Logarithmic average A-weighted sound pressure levels measured in JHH compared with WHO guidelines and typical levels for speech.

Figure 12 shows the A-weighted levels in the PICU as a function of time, running from midnight to midnight. Shown for comparison purposes only is the 24 h L_{eq} in the academic campus office of one of the authors. We note that in the PICU it is simply not possible to determine time of day from the sound level present. There is less than a 10 dB variation from the lowest to highest sound pressure level shown in Fig. 12. By contrast, the campus office shows a 15 dB variation and clearly shows when the office was occupied on this particular day.

Because an intensive care unit is for those in need of round-the-clock monitoring, it is not surprising that it is noisy 24 h a day. Indeed, it has been speculated that the incessant noise and constant light make sleep so difficult to achieve for patients in intensive care units that it might explain ICU-psychosis in patients, i.e., the development of psychotic episodes in patients with extended ICU stays.[79]

Figure 13 shows L_{eq} as a function of time in Weinberg 4C. Note that in these data there is a "quiet" period between roughly 11 p.m. and 7 a.m., but it is only about 7–8 dB quieter than the remainder of the day. The measurements in Fig. 13 include three sites near and in the main nurses station, one occupied patient room and one empty patient room. The three nurses station sites are very similar and have higher levels than the patient rooms. The occupied patient room is only slightly different, possessing brief periods of lower levels. The empty patient room is about 10 dB quieter across the board.

Figure 14 shows the L_{eq} results in Weinberg 5C. The results are quite similar to those in Fig. 13. However, the "quiet" period is shorter and more like the noisy period than is the case for Weinberg 4C. Again, the three measurements in and near the nurses station are the most intense. The occupied patient room is quite similar to the nurses station levels. The unoccupied patient room is significantly quieter. In this particular case, the unoccupied patient room was in a corner location and had two sets of doors blocking it from the corridor. The 37 dB level seen in quiet times thus defines the noise floor for this room (the lowest we observed in our measurements). What is also interesting is that hospital activity increased this noise level to about 50 dB (A) even though the room remained empty and both sets of doors were closed. We note that all doors in the hospital have large gaps at the floor so we are not surprised by their lack of acoustic insulation.

Figure 15 shows L_{eq} measurements on CMSC4. Here again the nurses station offered the highest noise levels—in this case significantly above those measured in an occupied patient room and in an examination room. These data show less evidence of a "quiet" time of day than was apparent in Figs. 13 and 14.

Figure 16 shows the L_{eq} results obtained on Nelson 7. Here there is evidence of a quiet period from about midnight until 7 a.m. Again, the nurses station is noisier than the patient room and examination room. The only surprise in this figure is that the examination room, which is rarely used and

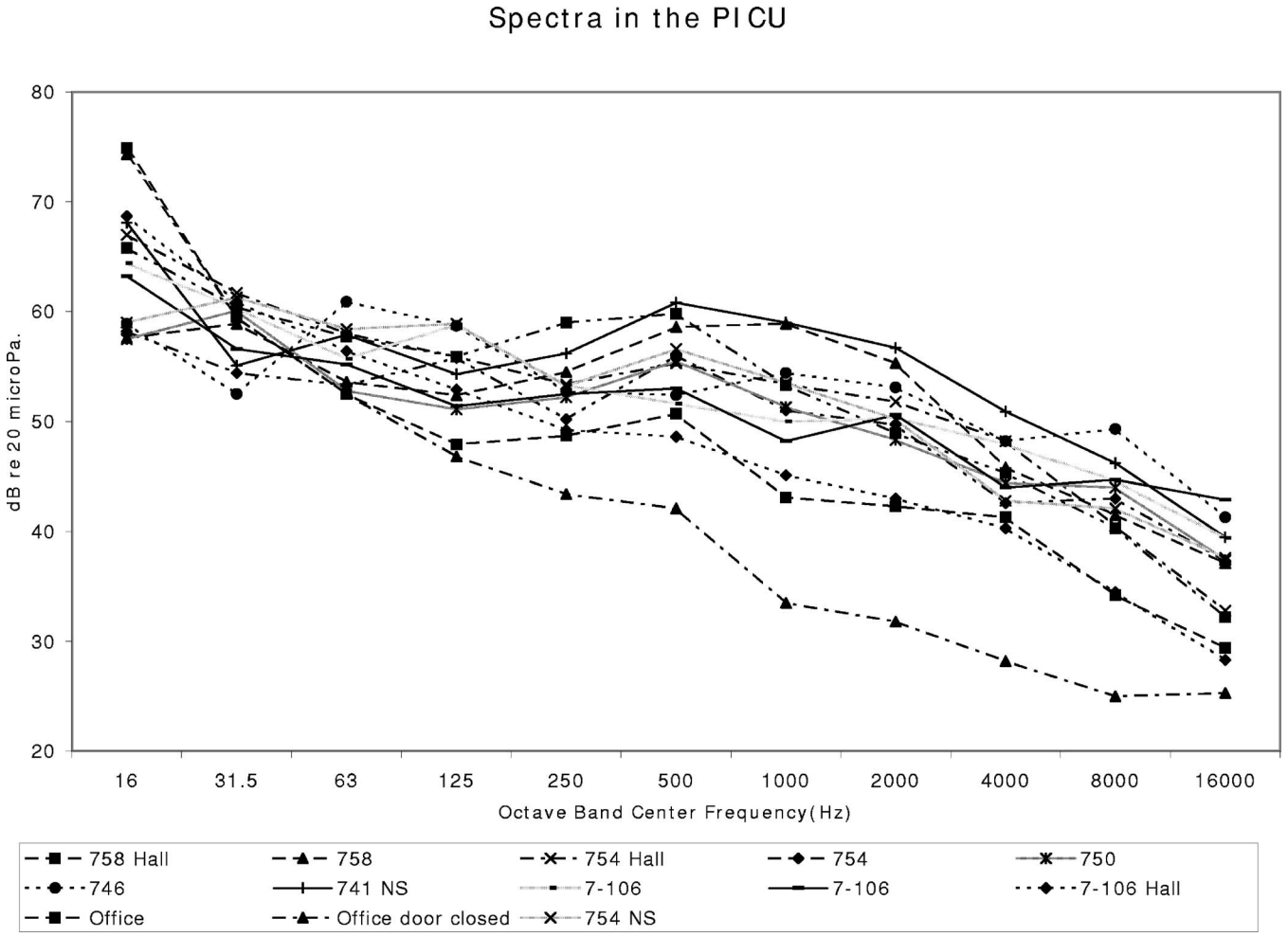

FIG. 10. Octave-band L_{eq}'s measured in various PICU locations.

has two sets of doors separating it from the hallway, exhibits a relatively high noise level. In this case, as for the other empty patient and treatment rooms shown in Figs. 13–15, the noise levels are directly attributable to HVAC noise and show that it is the mechanical systems which are largely responsible for this facility failing to meet the WHO noise guidelines.

Figure 17 summarizes the data shown in 24 h measurements by averaging the levels found in all five units in occupied patient rooms, unoccupied patient rooms or examination rooms, hallways, and nurses stations. The results show that halls tend to be the noisiest areas, with nurses stations and occupied patient rooms being very close to each other and next in line. Empty patient rooms are significantly quieter although they show evidence of noise intrusion during daytime hours (possibly due to the doors being opened for cleaning or other services). Among these divisions of location types, only the empty rooms show significant distinctions in noise as a function of time of day. On average, then, the hospital noise levels which most impact patients, staff, and visitors are at about the same sound level constantly.

VI. THE IMPACT OF PERSONAL PAGING

While the goal of our study is to characterize the current sound pressure levels in Johns Hopkins Hospital, we had a fortuitous opportunity to be involved in the implementation of a noise control measure in the PICU. When we first visited the PICU we noted their dependence on overhead paging. During these visits the overhead speakers throughout the unit would be active at least once every 5 min, typically for no more than 30 s per page. We investigated opportunities to replace overhead paging of everyone in the PICU with personal, hands-free call units which broadcast only to the individual desired to be reached. At the time, we found only one commercial manufacturer of such devices—Vocera, Inc. of San Jose, CA.

The idea of a personal, hands-free telecommunicator is to provide a lightweight, convenient microphone and loudspeaker or earphone to each staff member. These are typically linked via the existing telephone infrastructure or through a computer server and use wireless technology. Instead of a page, a call is instigated to an individual's personal communicator. The net effect is that an overhead page heard by everyone can be converted to a broadcast to a single individual.

During our noise characterization study, the PICU opted to run a trial of the Vocera, Inc. noise badges. Subsequently they purchased the devices and have been very successful in using them routinely. Today, overhead pages in the PICU

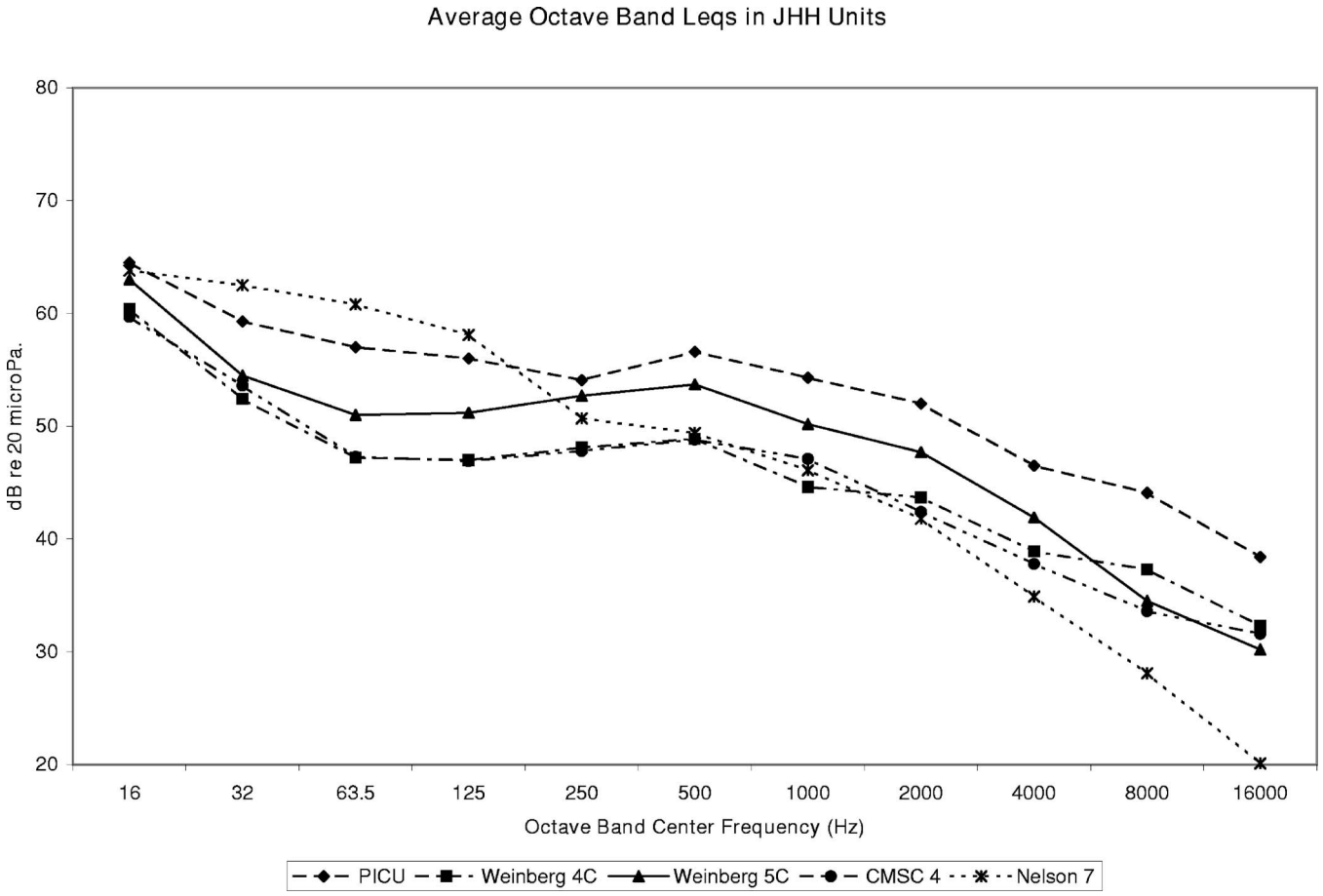

FIG. 11. Logarithmic average spectra measured on the five monitored units.

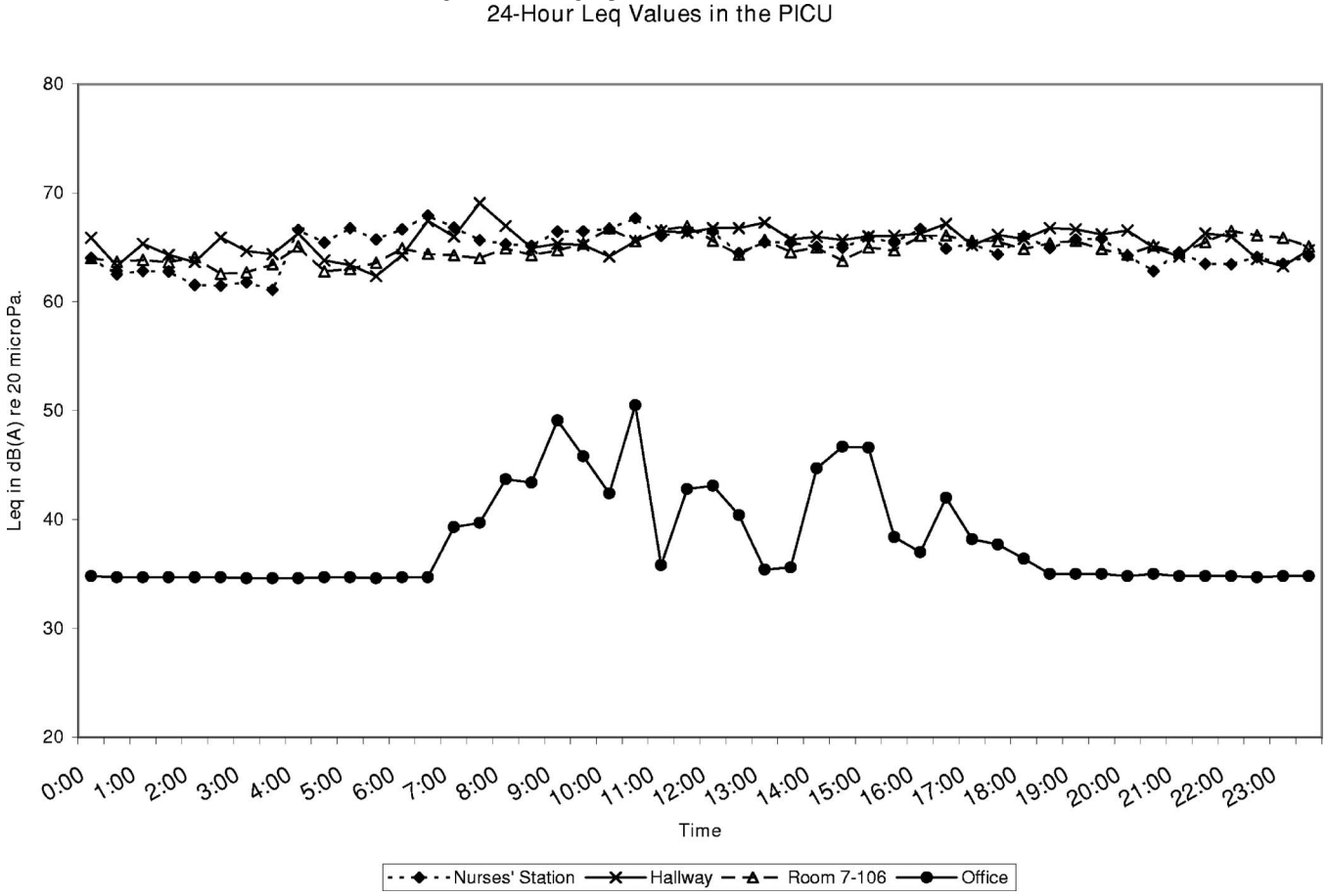

FIG. 12. L_{eq} vs time in the PICU.

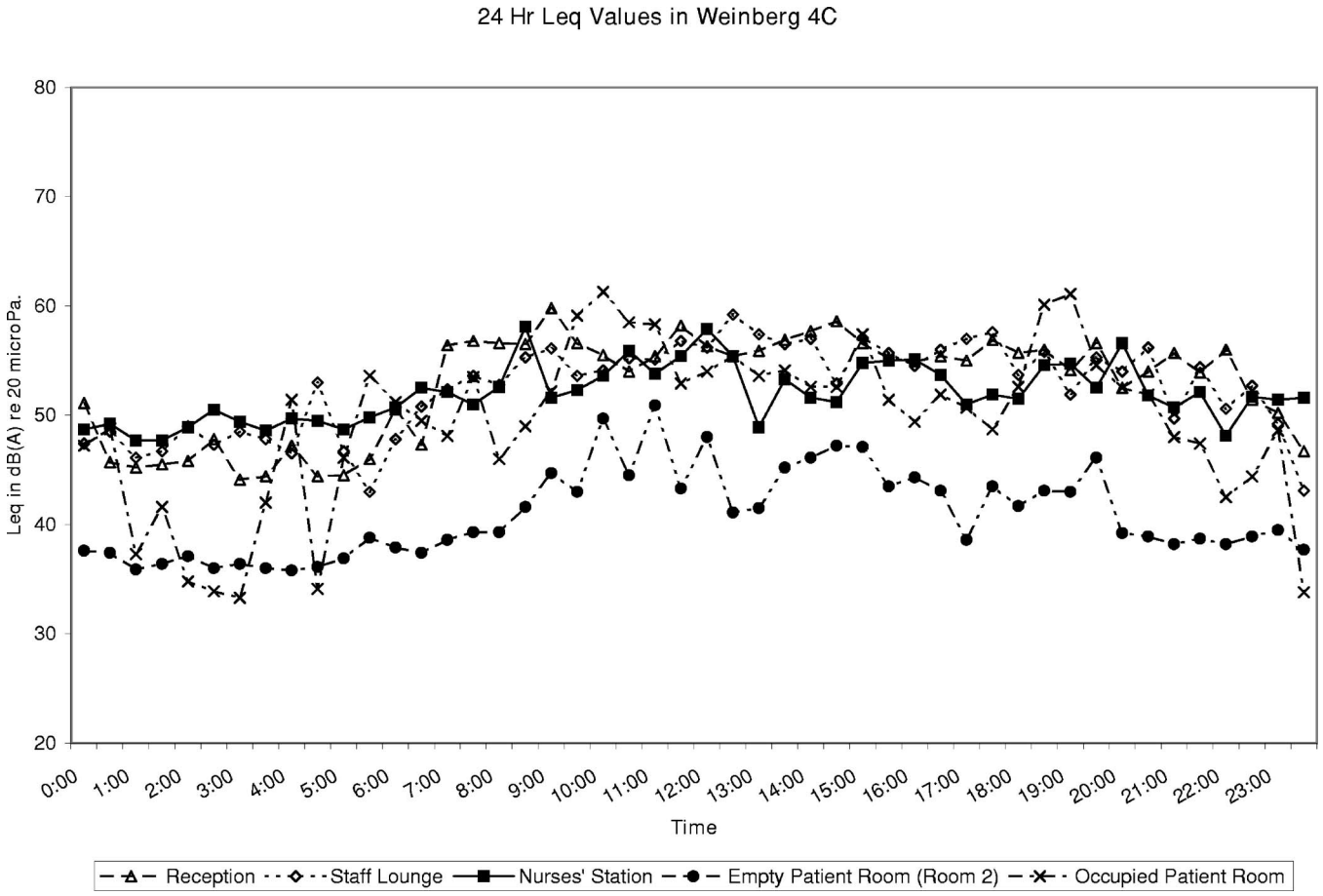

FIG. 13. L_{eq} vs time on Weinberg 4C.

have been reduced to roughly one or two per hour, generally for people on the unit temporarily (for a consult, for instance).

We assessed the difference between the overhead paging system and the personal communication system. Measurements were made during a scripted broadcast from the speakers and a badge at a distance of 3 ft (roughly the minimum distance to the ear from an overhead speaker) and 6 in (roughly the distance to the ears from a personal communicator badge). Results showed a 5.4 dB reduction of sound from the overhead at a distance of 3 ft to the badge at a distance of 6 in.. Of course, the reduction would be even greater comparing the badge at a distance of 3 ft to the overhead at 3 ft (a useful measure for privacy considerations). However, even these numbers are misleading, because the greatest gain is in the reduction of the population insonified using personal communicators compared to overhead paging.

Although personal communicators show significant promise in reducing noise from overhead paging, it should be noted that the speakers on these units are quite small in order to prevent them from being large and heavy. Thus, the quality of the sound produced is not as good as that generally available in overhead paging systems. Sound quality seems to be the single biggest compromise needed in conversion from an overhead to a personal communication unit. However, the advantages of efficiency, hands-free communication to prevent contamination, and noise reduction are seen by the PICU staff as far outweighing the quality reduction.

We also note that although we studied only the single commercial device available at the time, there are new entries into the market for personal, hands-free paging systems. We are actively interacting with a second project involving Avaya at Johns Hopkins Hospital for CMSC4.

VII. DISCUSSION

The above-presented results certainly demonstrate a noise problem in Johns Hopkins Hospital and suggest that this problem probably exists at virtually all other modern hospitals as well. The sound pressure levels are sufficiently high to interfere with sleep, to potentially affect speech intelligibility unless voices are raised, and to create a general din that is annoying to many. In addition to these direct effects of noise, there linger serious questions which have not been answered adequately by research studies, namely, whether elevated noise levels contribute to medical errors.

A related issue of great importance is the impact of noise on communication and the potential of safety hazards arising from an inability to be understood correctly. We have not found studies which directly relate to hospitals and medical errors, but we can offer some speculations. Normal hearing individuals are well adapted to detecting speech signals imbedded in noise, as is evidenced by their ability to correctly interpret speech even when the signal to noise ratio is as low as −6 dB. However, the same statement cannot be made for people with significant hearing impairments. Nor does it ap-

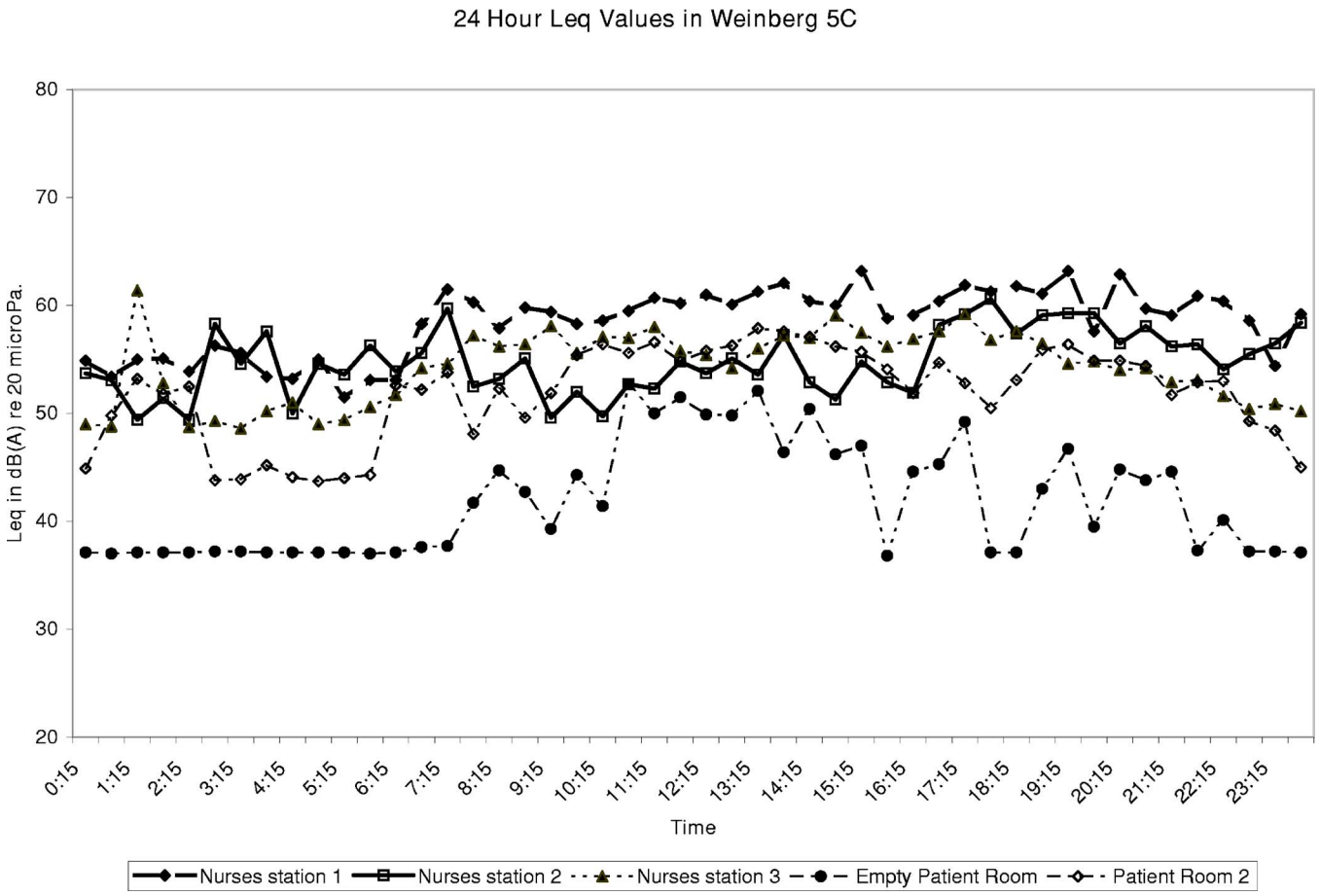

FIG. 14. L_{eq} vs time on Weinberg 5C.

ply to automated speech recognition systems, where one normally needs a signal to noise ratio of at least +15 dB in order to ensure correct interpretation of the signal. This distinction between human ears and automated speech recognizers is very important for the hospital setting, as there is a great desire to automate many hospital operations and this requires use of speech recognition. The move toward a digital hospital includes functions from automated transcription of doctors' notes spoken into recorders to automated dispensing of pharmaceuticals, and errors due to a poor acoustic environment simply cannot be tolerated. Further, when correct speech interpretation is critical, as is often the case in hospital situations, then a +15 dB signal to noise ratio requirement is appropriate. Thus, the high noise levels currently in place pose a real impediment to moving forward with plans for a digital hospital and with improved communication in general.

The study reported here simply documents the situation currently in place in a single hospital. What remains to be done is to study and demonstrate means of improving the noise environment in hospitals. There are several avenues for investigation along these lines, some of which we are pursuing.

First, although we have measured the noise in significant parts of JHH, there are many areas we have not yet studied. We will continue our work by measuring the noise environment in some of these areas as well. Of particular interest are the operating rooms and the emergency treatment facilities. Our study of operating room noise is just beginning. We have been invited to monitor the noise in every operating room for at least one 24 h period, and to correlate noise levels with the types of surgeries being performed. This will permit us to identify which surgical procedures are noisy and which are relatively quiet. This is particularly important when one considers that a prior study of orthopedic surgeons indicated that over half showed significant noise-induced hearing loss, presumably from exposure to bone drills and saws.[50,53]

Second, it is important to not only characterize the existing environment, but to understand why it is so noisy. To this end, we note that hospitals are notoriously lacking in the materials that one normally associates with acoustical absorption. This is largely the result of concerns about infection control, wear, and cost. However, there are materials available which meet hospital standards in these areas as well as in related areas such as flammability and smoke production. We are thus involved in a program to produce a series of prototype sound absorbing panels for ceilings and walls which meet hospital standards. We will demonstrate their impact by installing them in Weinberg 5C while carefully monitoring before and after ambient noise levels and reverberation times.

Third, communication in noise is an issue of increasing importance in hospitals as they move to smaller operating arenas and greater automation. We have embarked on a collaboration with medical personnel at JHH to consider technological solutions to communication problems which per-

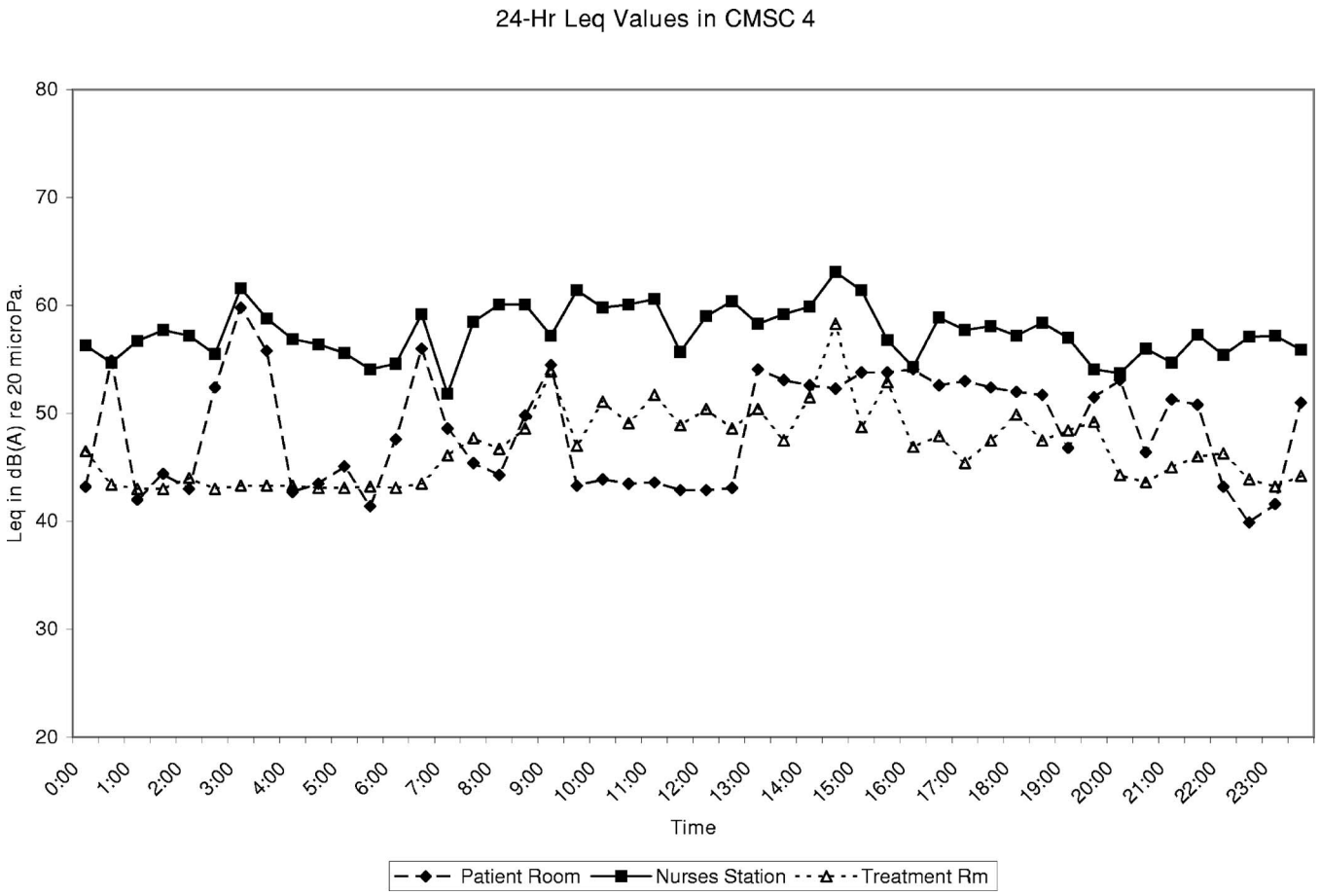

FIG. 15. L_{eq} vs time on CMSC 4.

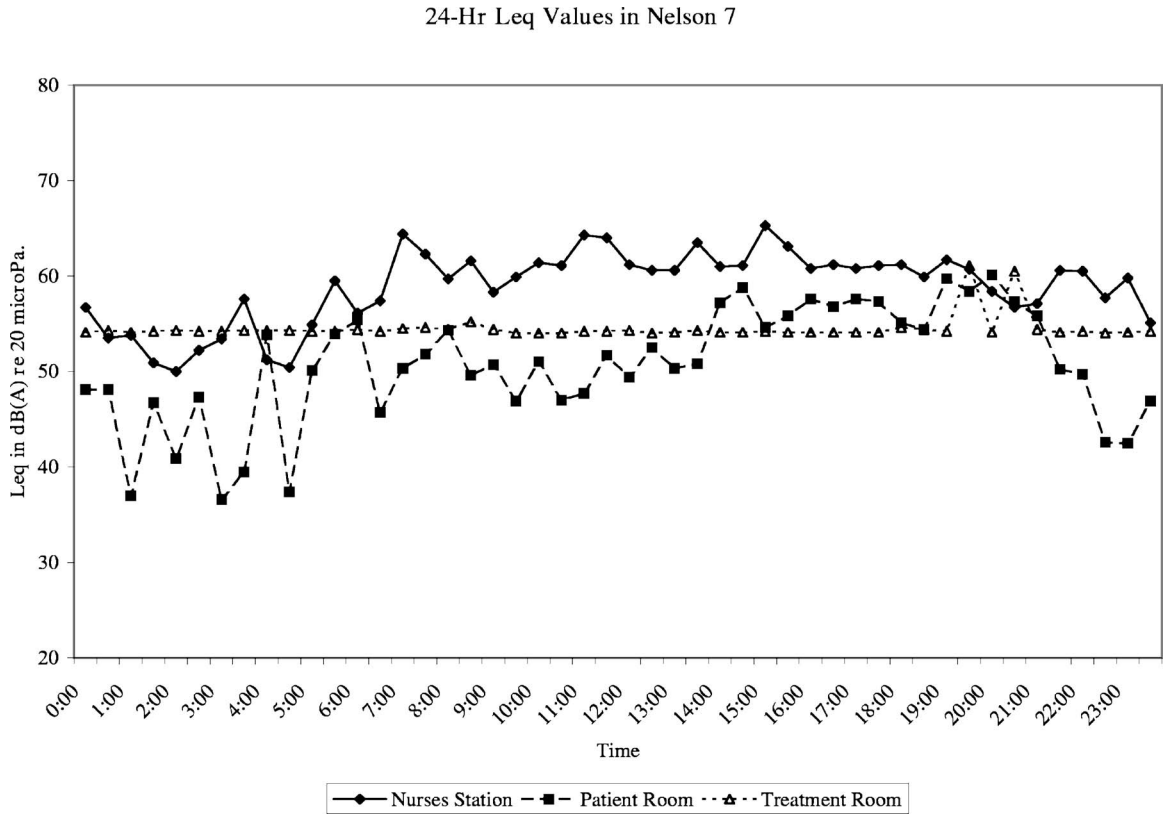

FIG. 16. L_{eq} vs time on Nelson 7.

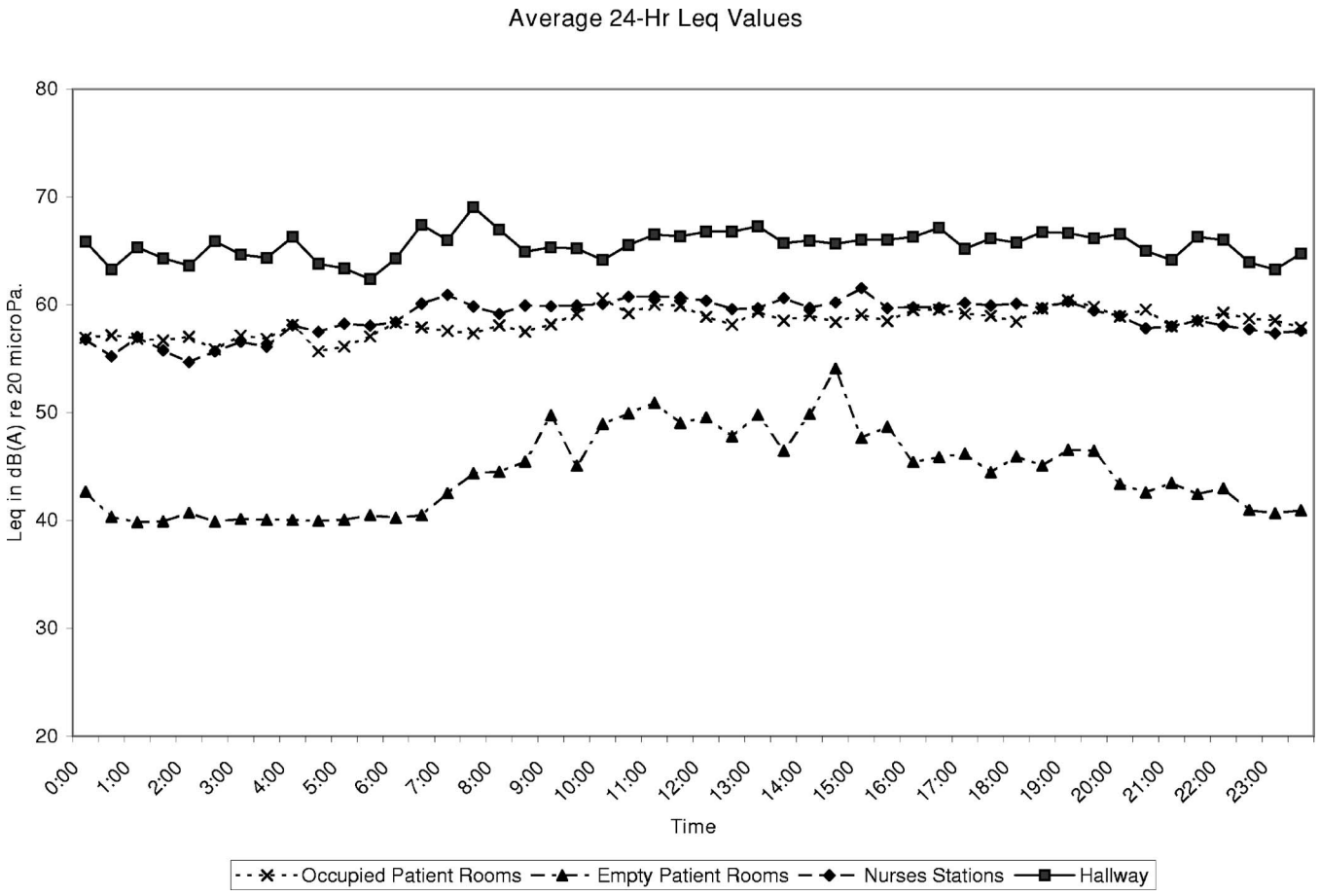

FIG. 17. Logarithmic average L_{eq} values vs time for halls, nurses stations, and occupied and empty patient rooms.

mit improved speech recognition. In particular, the advantage of stereophonic sound reception has not been exploited in hospital environments using sound systems so we are working to demonstrate such systems and incorporate their advantages.

Fourth, the literature shows that the overwhelming majority of audible alarms in hospitals result in no action being taken.[77,80–82] These alarms are, not surprisingly, a major source of irritation to patients and visitors. A ripe avenue for research is thus the effective use of audible alarms in hospitals, with the aim to preserve patient safety while reducing alarm noise.

Finally, although the current focus is on the major noise sources such as HVAC systems, overhead paging and speech, if we are successful in reducing the general din in hospital units it is likely that the noise of particular instruments or service objects (such as the meal tray carts) will become more identifiable and important as contributors to the noise. Here there will be a great opportunity for the design of quiet hospital items which could be tested and marketed on the basis of their ability to perform well while producing less noise.

Overall, most people will spend some time in a hospital and many will spend a large amount of time in them. The problem of hospital noise is clearly under-studied and not well understood. Our goal is to alter this landscape in meaningful ways.

ACKNOWLEDGMENTS

This work was supported by The Center for Quality Improvements and Patient Safety of Johns Hopkins Hospital. We are greatly indebted to Ron Peterson, President of Johns Hopkins Hospital, Chip Davis, Director of the Center for Quality Improvements and Patient Safety, and Josh Ettinger, also of the CQI. This work would not have been possible without the active encouragement of the nurse managers of the various units: Claire Beers, Anita Reedy, Jennifer Janicek, and Joanne Mills. We are also indebted to Claire Beers for her pioneering work on personal paging units for the PICU and for working with us to evaluate their impact on noise. Finally, we thank Stephanie Reel, Vice Provost and Chief Information Officer of Johns Hopkins, who brought this project to us and introduced us to a number of the JHH people whose assistance we need to improve the hospital sound quality.

[1]F. Biley, "Effects of noise in hospitals," Br. J. Nurs. **3**, 110–113 (1994).
[2]F. Nightingale, *Notes on Nursing* (Dover, New York, 1969).
[3]C. Baker, "Sensory overload and noise in the ICU: Sources of environmental stress," Crit. Care Nurs. Q. **6**, 66–79 (1984).
[4]A. Turner, C. King, and J. Craddock, "Measuring and reducing noise," Hospitals **49**, 85–90 (1975).
[5]R. Aitken, "Quantitative noise analysis in a modern hospital," Arch. Environ. Health **37**, 361–364 (1982).
[6]B. Allaouchiche, F. Duflo, R. Debon, A. Bergeret, and D. Chassard, "Noise in the postanaesthesia care unit," Br. J. Anaesth. **88**, 369–373

(2002).
[7]M. Bayo, A. Garcia, and G. Amando, "Noise levels in an urban hospital and workers' subjective responses," Arch. Environ. Health **50**, 247–251 (1995).
[8]M. Bovenzi and A. Collareta, "Noise levels in a hospital," Ind. Health **22**, 75–82 (1984).
[9]U. de Camp, "The measurement of sound levels in hospitals," Noise Control Eng. **13**, 24–27 (1979).
[10]S. Falk and N. Woods, "Hospital noise—Levels and potential health hazards," N. Engl. J. Med. **289**, 774–780 (1973).
[11]L. Goodfriend and R. Cardinell, "Noise in hospitals," Technical Report No. 930-D-11, Public Health Service, Division of Hospital and Medical Facilities, 1963.
[12]R. Guerrero, "Intermittent noise sampling and control strategies in the hospital environment," Master's thesis, NJIT, 2001.
[13]P. Haslam, "Noise in hospitals: Its effect on the patient," Nurs. Clin. North Am. **5**, 715–724 (1970).
[14]B. Hilton, "Noise in acute patient care areas," Res. Nurs. Health **8**, 283–291 (1985).
[15]S. Holmberg and S. Coon, "Ambient sound levels in a state psychiatric hospital," Arch. Psychiatr. Nurs. **XIII**, 117–126 (1999).
[16]D. Kahn, T. Cook, C. Carlisle, D. Nelson, N. Kramer, and R. Millman, "Identification and modification of environmental noise in an ICU setting," Chest **114**, 535–540 (1998).
[17]A. Ogilvie, "Sources and levels of noise on the ward at night," Nurs. Times **76**, 1363–1366 (1980).
[18]F. Omokhodian and M. Sridhar, "Noise levels in the hospital environment in Ibadan," Afr. J. Med. Med. Sci. **32**, 139–142 (2003).
[19]F. Pimentel-Souza, J. Carvalho, P. Alvares, C. Rodrigues, and A. Siqueira, "Noise and sleep quality in two hospitals in the city of Belo Horizonte, Brazil," 2003, http://www.icb.ufmg.br/lpf/2-19.html.
[20]N. Shankar, K. Malhotra, S. Ahuja, and O. Tandon, "Noise pollution: A study of noise levels in the operation theatres of a general hospital during various surgical procedures," J. Indian Med. Assoc. **99**, 244–247 (2001).
[21]N. Woods and S. Falk, "Noise stimuli in the acute care area," Nurs. Res. **23**, 144–150 (1974).
[22]D. Anagnostakis, J. Petmezakis, J. Messaritakis, and N. Matsaniotis, "Noise pollution in neonatal units: A potential health hazard," Acta Paediatr. Scand. **69**, 771–773 (1980).
[23]D. Balogh, E. Kittinger, A. Benzer, and J. Hackl, "Noise in the ICU," Intensive Care Med. **19**, 343–346 (1993).
[24]F. Benini, V. Magnavita, P. Lago, E. Arslan, and P. Piaso, "Evaluation of noise in the neonatal intensive care unit," Am. J. Perinatol **13**, 37–41 (1996).
[25]S. Bentley, F. Murphy, and H. Dudley, "Perceived noise in surgical wards and an intensive care area: An objective analysis," Br. Med. J. **2**, 1503–1506 (1977).
[26]G. Blennow, N. Svenningsen, and B. Almquist, "Noise levels in incubators (Adverse effects?)," Pediatrics **53**, 29–32 (1974).
[27]A. Gottfried, J. Hodgman, and K. Brown, "How intensive is newborn intensive care? An environmental analysis," Pediatrics **74**, 292–294 (1984).
[28]P. Kam, A. Kam, and J. Thompson, "Noise pollution in the anaesthetic and intensive care environment," Anaesthesia **49**, 982–986 (1994).
[29]J. Long, J. Lucey, and A. Philip, "Noise and hypoxemia in the intensive care nursery," Pediatrics **65**, 143–145 (1980).
[30]L. Marshall, "Patient reaction to sound in an intensive coronary care unit," Commun. Nurs. Res. **5**, 81–92 (1972).
[31]A. McLaughlin, J. Elliott, and G. Campalani, "Noise levels in a cardiac surgical intensive care unit: A preliminary study conducted in secret," Intensive Crit. Care Nurs. **12**, 226–230 (1996).
[32]T. Meyer, S. Eveloff, M. Bauer, W. Schwartz, N. Hill, and R. Millman, "Adverse environmental conditions in the respiratory and medical ICU settings," Chest **105**, 1211–1216 (1994).
[33]J. Redding, T. Hargest, and S. Minsky, "How noisy is intensive care?," Crit. Care Med. **5**, 275–276 (1977).
[34]K. Thomas and P. Martin, "The acoustic environment of hospital nurseries: NICU sound environment and the potential problems for caregivers," J. Perinatol **20**, S94–S99 (2000).
[35]C. Tsiou, D. Eftymiatos, E. Theodossopoulou, P. Notis, and K. Kiriakou, "Noise sources and levels in the Evgenidion Hospital intensive care unit," Intensive Care Med. **24**, 845–847 (1998).
[36]B. Hodge and J. Thompson, "Noise pollution in the operating theatre," Lancet **335**, 891–894 (1990).
[37]P. Lewis, J. Staniland, A. Cuppage, and J. Davies, "Operating room noise," Can. J. Anaesth. **37**, S79 (1990).
[38]H. Love, "Noise exposure in the orthopaedic operating theatre: A significant health hazard," ANZ J. Surg. **73**, 836–838 (2003).
[39]V. Murthy, S. Malhotra, I. Bala, and M. Raghunathan, "Detrimental effects of noise on anesthetists," Can. J. Anaesth. **42**, 608–611 (1995).
[40]M. Nott and P. West, "Orthopaedic theatre noise: A potential hazard to patients," Anaesthesia **58**, 784–787 (2003).
[41]C. Ray and R. Levinson, "Noise pollution in the operating room: A hazard to surgeons, personnel, and patients," J. Spinal Disord. **5**, 485–488 (1992).
[42]R. Shapiro and T. Berland, "Noise in the operating room," N. Engl. J. Med. **287**, 1236–1238 (1972).
[43]J. Evans and M. Philbin, "The acoustic environment of hospital nurseries: Facility and operations planning for quiet hospital nurseries," J. Perinatol **20**, S105–S112 (2000).
[44]R. Gädeke, B. Döring, F. Keller, and A. Vogel, "The noise level in a childrens hospital and the wake-up threshold in infants," Acta Paediatr. Scand. **58**, 164–170 (1969).
[45]L. Gray and M. Philbin, "The acoustic environment of hospital nurseries: Measuring sound in hospital nurseries," J. Perinatol **20**, S100–S104 (2000).
[46]M. Philbin and L. Gray, "Changing levels of quiet in an intensive care nursery," Acta Paediatr. Scand. **22**, 455–460 (2002).
[47]M. Philbin, A. Roberson, and J. W. Hall III, "Recommended permissible noise criteria for occupied, newly constructed or renovated hospital nurseries," J. Perinatol **19**, 559–563 (1999).
[48]M. Philbin, "The full-term and premature newborn: The influence of auditory experience on the behavior of preterm newborns," J. Perinatol **20**, S77–S87 (2000).
[49]R. Dodenhoff, "Noise in the orthopaedic operating theatre," Ann. R. Coll. Surg. Engl. **77**, 8–9 (1995).
[50]G. H. Jr, K. Goodman, D. Hang, and V. McCorvey, "Noise levels of orthopedic instruments and their potential health risks," Orthopedics **19**, 35–37 (1996).
[51]H. Mullett, K. Synnott, and W. Quinlan, "Occupational noise levels in orthopaedic surgery," Ir J. Med. Sci. **168**, 106 (1999).
[52]K. Prasad and K. Reddy, "Live recordings of sound levels during the use of powered instruments in ENT surgery," J. Laryngol. Otol. **117**, 532–535 (2003).
[53]K. Willett, "Noise-induced hearing loss in orthopaedic staff," J. Bone Joint Surg. Br. **OL-73B**, 113–115 (1991).
[54]V. Bredenberg, "Quiet, please!," Hosp. Prog. **42**, 104–108 (1961).
[55]A. Dellon, "To rid ORs of noise pollution," RN OR-6, 1975.
[56]G. Grumet, "Pandemonium in the modern hospital," N. Engl. J. Med. **328**, 433–437 (1993).
[57]A. Schneider and J. Beibuyck, "Music in the operating-room," Lancet **335**, 1407 (1990).
[58]D. Scalise, "Shhh, Quiet please!," Hosp. Health Netw. **78**, 16–17 (2004).
[59]C. Cmiel, D. Karr, D. Gasser, L. Oliphant, and A. Neveau, "Noise control: A nursing team's approach to sleep promotion," Am. J. Nurs. **104**, 40–48 (2004).
[60]S. Akhtar, C. Weigle, E. Cheng, R. Toohill, and R. Berens, "Use of active noise cancellation devices in caregivers in the intensive care unit," Crit. Care Med. **28**, 1157–1160 (2000).
[61]W. Morrison, E. Haas, D. Shaffner, E. Garrett, and J. Fackler, "Noise stress and annoyance in a pediatric intensive care unit," Crit. Care Med. **31**, 113–119 (2003).
[62]M. Topf, "Noise-induced occupational stress and health in critical care nurses," Hosp. Top. **66**, 30–34 (1988).
[63]M. Topf and E. Dillon, "Noise-induced stress as a predictor of burnout in critical care nurses," Heart Lung **17**, 567–574 (1988).
[64]D. Fife and E. Rappaport, "Noise and hospital stay," Am. J. Public Health **66**, 680–681 (1976).
[65]B. Minckley, "A study of noise and its relationship to patient discomfort in the recovery room," Nurs. Res. **17**, 247–250 (1968).
[66]A. Wysocki, "The effect of intermittent noise exposure on wound healing," Adv. Wound Care **9**, 35–39 (1996).
[67]P. Toivanen, S. Hulkko, and E. Naatanen, "Effect of psychic stress and certain hormone factors on the healing of wounds in rats," Ann. Med. Exp. Biol. Fenn **38**, 343–349 (1960).
[68]I. Cohen, "Stress and wound healing," Acta Anat. (Basel) **103**, 134–141 (1979).
[69]C. Hawksworth, P. Sivalingam, and A. Asbury, "The effect of music on

anesthetists' psychomotor performance," Anaesthesia **53**, 195–197 (1998).
[70]K. Moorthy, Y. Munz, S. Undre, and A. Darzi, "Objective evaluation of the effect of noise on the performance of a complex laparoscopic task," Surgery (St. Louis) **136**, 25–30 (2004).
[71]S. Park, H. Song, J. Han, J. Park, E. Lee, S. Park, K. Kang, J. Lee, S. Hwang, S. Rho, S. Jeong, H. Chung, and K. Shinn, "Effect of noise on the detection of rib fractures by residents," Invest. Radiol. **29**, 54–58 (1994).
[72]V. Murthy, S. Malhotra, I. Bala, and M. Raghunathan, "Auditory functions in anaesthesia residents during exposure to operating room noise," Indian J. Med. Res. **101**, 213–216 (1995).
[73]"Guidelines for community noise," edited by B. Berglund, T. Lindvall, D. H. Schwelaand K. T. Goh, Technical Report, World Health Organization, 1999.
[74]American National Standards Institute, "Criteria for evaluating room noise: S12.2," 1995, reaffirmed on 24 May, 1999.
[75]"Information on levels of environmental noise requisite to protect public health and welfare with an adequate margin of safety," EPA (1974).
[76]R. Soutar and J. Wilson, "Does hospital noise disturb patients?," Br. Med. J. **292**, 305 (1986).
[77]M. Wallace, M. Ashman, and M. Matjasko, "Hearing acuity of anesthesiologists and alarm detection," Anesthesiology **81**, 13–28 (1994).
[78]E. Liu and S.-M. Tan, "Patients' perception of sound levels in the surgical suite," J. Clin. Anesth. **12**, 298–302 (2000).
[79]N. Freedman, N. Kotzer, and R. Schwab, "Patient perception of sleep quality and etiology of sleep disruption in the intensive care unit," Am. J. Respir. Crit. Care Med. **159**, 1155–1162 (1999).
[80]L. Stanford, J. McIntyre, and J. Hogan, "Audible alarm signals for anaesthesia monitoring equipment," Int. J. Clin. Monit Comput. **1**, 251–256 (1985).
[81]A. Cropp, L. Woods, and D. Raney, "Name that tone: The proliferation of alarms in the intensive care unit," Chest **105**, 1217–1220 (1994).
[82]L. Biot, P. Carry, J. Perdrix, A. Eberhard, and P. Baconnier, "Èvaluation clinique de la pertinence des alarmes en rèanimation (clinical evaluation of the importance of alarms in recovery)," Ann. Fr. Anesth. Reanim **19**, 459–466 (2000).

Underwater and in-air sounds from a small hovercraft

Susanna B. Blackwell[a] and Charles R. Greene, Jr.
Greeneridge Sciences Inc., 1411 Firestone Road, Goleta, California 93117

(Received 3 August 2004; revised 9 September 2005; accepted 19 September 2005)

Underwater and in-air recordings were made from a boat anchored near Prudhoe Bay, Alaska, while a Griffon 2000TD hovercraft drove by at or near full power on four passes. At the closest point of approach (CPA, 6.5 m), underwater broadband (10–10 000 Hz) levels reached 133 and 131 dB *re*: 1 μPa at depths of 1 and 7 m, respectively. In-air unweighted and A-weighted broadband (10–10 000 Hz) levels reached 104 and 97 dB *re*: 20 μPa, respectively. The hovercraft produced sound at a wide range of frequencies. Both underwater and in air, the largest spectral peak was near 87 Hz, which corresponded to the blade rate of the thrust propeller. In addition, the spectral composition included several harmonics of this frequency. The shaft or blade rate of the lift fan was barely detectable underwater despite its proximity to the water. The hovercraft was considerably quieter underwater than similar-sized conventional vessels and may be an attractive alternative when there is concern over underwater sounds. © *2005 Acoustical Society of America.* [DOI: 10.1121/1.2118347]

PACS number(s): 43.50.Lj, 43.50.Rq, 43.30.Nb [DKW] Pages: 3646–3652

I. INTRODUCTION

Northstar Island is an artificial gravel island built for oil production by BP Exploration (Alaska) in nearshore waters of the Alaskan Beaufort Sea. Most of the sound emanating from the island operation is not produced on the island itself, which is relatively quiet, but by the vessels connected to the Northstar operation (Blackwell and Greene, submitted). The predominant sound sources are crew boats in particular, but also tugs, self-propelled barges, oil spill response vessels, and the vessel from which the hovercraft measurements were made. Vessel sounds are of concern because of potential disturbance to marine mammals (Richardson *et al.*, 1995), especially bowhead whales.

During the summer of 2003, BP tested a relatively small, diesel-powered hovercraft to ferry crew and supplies between the mainland and Northstar Island. Along with other advantages, it was anticipated that the hovercraft would produce less underwater sound than the crew boat.

The main objectives of this study are to characterize the sounds of this hovercraft in water and air by determining received levels, spectral characteristics, and transmission loss through both media, and to compare the findings with sounds from conventional vessels of approximately the same size.

II. METHODS

Underwater and airborne recordings were obtained on 8 August 2003 near Prudhoe Bay (Beaufort Sea), Alaska. The recording site was between the mainland and Northstar Island at a location 5.2 km north of the crew boat dock at West Dock. The recording vessel's position was 70° 26.48′ N, 148° 34.28′ W, and water depth was 7.3 m.

[a]Electronic mail: susanna@greeneridge.com

A. Acoustic equipment

The omnidirectional sensors included two hydrophones and a microphone, all calibrated. The hydrophones were model 6050C by International Transducer Corporation (ITC) and included a low-noise preamplifier next to the sensor and a 30-m cable. The hydrophone cables were attached with cable ties to a fairing to minimize strumming. Prior to recording, the hydrophone signals were amplified with an adjustable-gain postamplifier. The omnidirectional microphone was a G.R.A.S. Sound and Vibration $\frac{1}{2}$-in. prepolarized free field microphone model 40AE with an ICP preamplifier model TMS426C01 and a windscreen. Prior to recording, the microphone signals were amplified with an adjustable-gain postamplifier.

Hydrophone and microphone signals were recorded simultaneously on three channels of a SONY model PC208Ax instrumentation-quality digital audiotape (DAT) recorder. The sampling rate was 24 kHz, providing a frequency response that was nearly flat from $<$4 to 10 000 Hz on all channels. Both types of sensors were calibrated from 4 to 20 000 Hz. Quantization was 16 bits, providing a dynamic range of $>$80 dB between an overloaded signal and the instrumentation noise. A memo channel on the tape recorder was used for voice announcements, and the date and time were recorded automatically.

B. Field procedures

Recordings were obtained using the Alaska Clean Seas (ACS) vessel *Mikkelsen Bay* of length 12.8 m as a recording platform. After selecting a recording location that satisfied our acoustic needs as well as logistical and safety concerns, the *Mikkelsen Bay* was anchored, all engines and sound-generating devices were shut down, and the hydrophone string was lowered into the water with the two hydrophones at depths of 1 and 7 m. A microphone was positioned on the deck of the vessel, ~2 m above water level, with an unob-

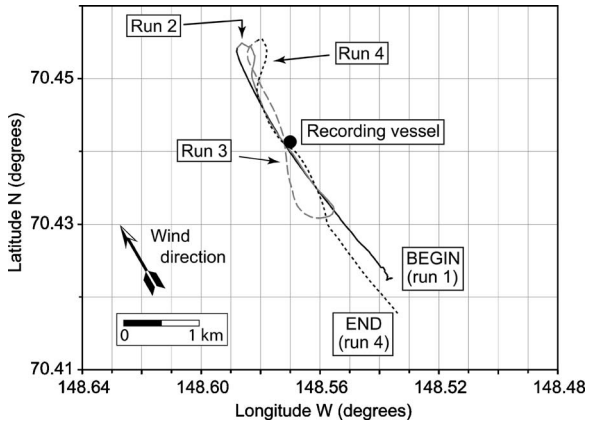

FIG. 1. Track of the hovercraft during its four passes near the recording vessel, shown as a filled circle. During the recordings the hovercraft was traveling on the same path as the wind, which was from the south-southeast.

structed path to the sound source at all times. The hovercraft was asked to drive by the recording vessel at full speed four different times, as shown in Fig. 1. A hand-held GPS (Garmin model 12XL), placed on the bridge of the hovercraft, logged its position every 5 s. During the nearby portion of the fly-by, the hovercraft's distance from the recording vessel was called out (and recorded) every few seconds by an observer on the *Mikkelsen Bay* using a laser rangefinder (Bushnell model # 20-0880). Wind speed, wind direction, and temperature were recorded over a period of 4 min with a Kestrel 2000 Pocket Thermo Wind meter (Nielsen Kellerman, Chester, PA 19013), and wave height (sea state) was estimated. A total of 27 min of boat-based recordings were obtained.

The hovercraft, shown in Fig. 2, was a Griffon 2000TD (length 11.9 m, width 4.8 m), capable of carrying 20 passengers at high speeds over a variety of surfaces. Its top speed with full payload was said to be 35 knots (18 m/s) in ideal conditions, i.e., calm water, no wind, and 15 °C ambient temperature. It was both lifted and propelled by a single Deutz air-cooled 355 hp (265 kW) diesel engine (BF8L513LC), running at a maximum speed of 2100 rpm. The 12-bladed lift fan turned at a maximum of 2100 rpm, as it was coupled directly to the engine; its blade rate was therefore 420 Hz. The thrust propeller had 4 blades with variable pitch. The pulley ratio between engine and propeller was 1.52 (70 to 46) so at an engine rpm of 2100 the propeller rpm was 1380 and the blade rate was 92 Hz. According to the manufacturer's specifications, maximum recommended wind speed for normal operations was 30 knots or 15 m/s (Force 7 Beaufort), and maximum recommended wave height was 1 m.

FIG. 2. Griffon 2000TD hovercraft landing on the slope protection mat at Northstar Island's southeastern shore.

C. Signal analysis

1. Underwater sounds

The recorded, digitized hydrophone signals were transferred as time series to a computer hard drive for processing. They were then equalized and calibrated in units of sound-pressure with flat frequency response over the data bandwidth (10–10 000 Hz). Analysis was done using MATLAB (The MathWorks, Natick, MA) routines and custom programs for analysis of both transient and continuous signals. For each recording, a sound-pressure time series (waveform) was inspected to help select samples for further analysis.

To assess variability in broadband levels during a fly-by of the hovercraft, acoustic recordings were partitioned into overlapping segments of length 0.25 s. Computing the mean square pressure of each segment yielded the broadband sound pressure level (SPL) for that segment. Each analysis segment was shifted in time by 0.1 s from the previous segment. This process produced a time series representing the fluctuation in broadband SPLs during the hovercraft's very rapid passage in front of the recording vessel.

Background levels (10–10 000 Hz) were obtained by computing the mean square pressure of 30-s segments, while the hovercraft was at least 1 km away or before the start of the experiment.

Spectral composition was examined by calculating the sound-pressure spectral density by Fourier analysis, using the Blackman-Harris minimum three-term window (Harris, 1978). A signal section of length 1.5 s was selected at the maximum broadband value on each run, i.e., at or near the CPA. Two 1-s segments overlapped by 50% were analyzed. This resulted in 1-Hz bin separation and 1.7-Hz bin resolution. One-third-octave band levels were derived from the narrow-band spectral densities by summing the mean square pressures in all frequency cells between the lower and upper frequency limits for the one-third-octave band in question. Proportional amounts were taken from the end cells as appropriate.

Distances from the hydrophones to the hovercraft were calculated based on a combination of GPS positions, rangefinder distances, and the travel speed of the hovercraft.

2. Airborne sounds

Microphone data were transcribed to disk files and analyzed in the same way as the hydrophone data. Microphone data were unweighted and are expressed in dB *re*: 20 μPa. To allow comparisons with published data for various sound sources, a few values were A-weighted and are expressed in dBA *re*: 20 μPa.

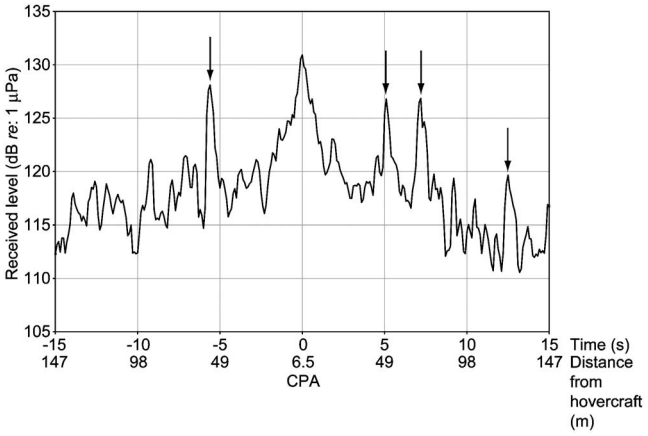

FIG. 3. Broadband (10–10 000 Hz) sound pressure time series for the deep hydrophone during run 4. The *x* axis shows time, centered on the closest point of approach (CPA), and the corresponding distance from the hovercraft, calculated using the vessel's mean speed during that particular run. Arrows indicate spikes in the sound pressure time series that were caused by waves slapping the recording vessel's hull.

We fitted a simple propagation model to broadband levels received by the microphone in order to develop equations that characterize propagation loss in air:

$$\mathbf{RL}(\text{received level}) = A - B\log(R). \quad (1)$$

In this equation, R is the range in m and the unit for **RL** is dB *re*: 20 μPa. The constant term A is the hypothetical extrapolated level at distance 1 m based on far-field measurements; B is the spreading loss. When applying the model to the data, recordings were included at increasing distances from the sound source until the point at which levels reached a minimum and remained constant (within $\sim\pm 2$ dB). This model is not ideal in that it ignores aspect dependence that is confounded with range dependence. Propagation loss modeling was inappropriate for the underwater data because the signal at all but the closest few meters was too close to background levels.

III. RESULTS

The hovercraft measurements were made during a short window of acceptable weather conditions on 8 August 2003. Wind was from the south-southeast, 5.1 m/s (10 knots) on average with peaks at 5.7 m/s (11 knots), temperature was 5.6 °C, and sea state was 1–2. The hovercraft runs were roughly NNW-SSE, i.e., either with or against the wind (see Fig. 1). The hovercraft was run at or near full throttle on all passes, but sea conditions kept its speed well below the theoretical maximum (35 knots). For runs 1–4, mean travel speed calculated from GPS positions, using straight stretches of the tracks centered on the closest point of approach (CPA) to the recording vessel, were as follows: 11.8 m/s (22.9 knots), 9.9 m/s (19.2 knots), 11.9 m/s (23.1 knots), and 9.8 m/s (19.0 knots), respectively. Runs 1 and 3 were downwind; runs 2 and 4 were upwind.

A. Underwater sounds

Figure 3 shows the broadband (10–10 000 Hz) SPL time series for the deep hydrophone during the fourth pass.

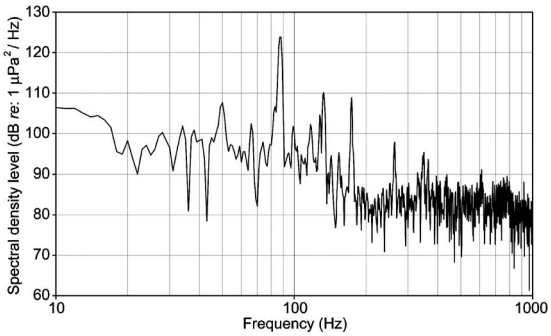

FIG. 4. Sound-pressure density spectrum (10–1000 Hz) for a 1.5-s sample recorded by the deep hydrophone and centered on the maximum broadband value for run 3.

Note that sound radiating from the hovercraft is likely to be directional, so that sound levels will vary both as a function of distance and of the aspect of the craft to the receiver. The latter variable was not taken into account in these measurements. Maximum SPLs were 122.5–130.9 dB *re*: 1 μPa for the four passes. The spikes before and after the CPA (indicated by arrows in Fig. 3) are caused by waves slapping on the vessel's hull. The shallow hydrophone data were more contaminated by wave noise than the deep hydrophone data, and the fourth pass did not yield any useable data. Maximum SPLs for the shallow hydrophone were 130.0–132.8 dB *re*: 1 μPa, on average 7.4 dB higher than the deep hydrophone values for the three runs for which both sets of data were available. Background levels on the deep hydrophone (computed over 30-s samples), obtained while the hovercraft was >1 km from the recording vessel or before the hovercraft was on location, were in the range 114–119 dB *re*: 1 μPa.

Sound spectral density levels are plotted in Fig. 4 to examine the tones (narrow spectral peaks) produced by the hovercraft during a fly-by. The largest peak was centered at $\sim$87 Hz, with smaller peaks at harmonics thereof, i.e., 173.5, 260, 346, and 432.5 Hz (Fig. 4). A comparison of spectral lines from different samples during the fly-by showed the expected amount of Doppler shift between approach and retreat.

The thrust propeller was expected to produce sound with a fundamental frequency near 92 Hz. This is based on the nominal 2100 rpm engine rotation rate at full power, the pulley ratio of 1.52 (resulting in a propeller shaft rate of 1382 rpm), and the presence of 4 blades on the propeller [$(1382\ \text{rpm} \times 4\ \text{blades})/60 = 92$ Hz]. The occurrence in the spectra of a strong narrow-band component centered between 86 and 87 Hz, but no strong component centered at 92 Hz, suggests that the actual engine and propeller rotation rates were slightly less (by $\sim$5.5%) than the nominal full-power values. These rotation rates are consistent with the lower speed appropriate to the sea conditions. The presence of narrow-band components centered at 173.5, 260, 346, and 432.5 Hz, which are very close to multiples of 86.5 Hz, strongly suggests that the component near 87 Hz was the fundamental frequency associated with the thrust propeller.

Both the lift fan and the thrust propeller were likely generators of airborne sound, but we expected sounds from the lift fan to be easier to detect on underwater recordings.

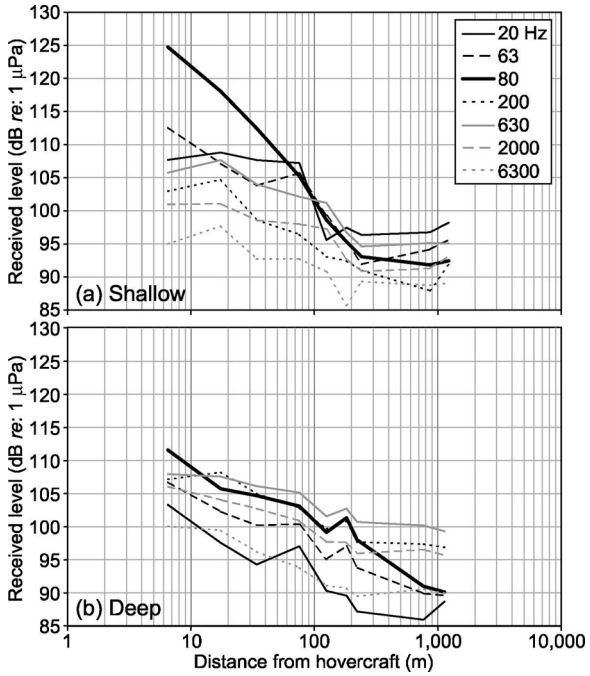

FIG. 5. Mean received levels as a function of mean distance from the hovercraft for seven selected one-third-octave bands and both hydrophones. (a) Shallow hydrophone. (b) Deep hydrophone. The indicated frequencies correspond to the bands' center frequencies.

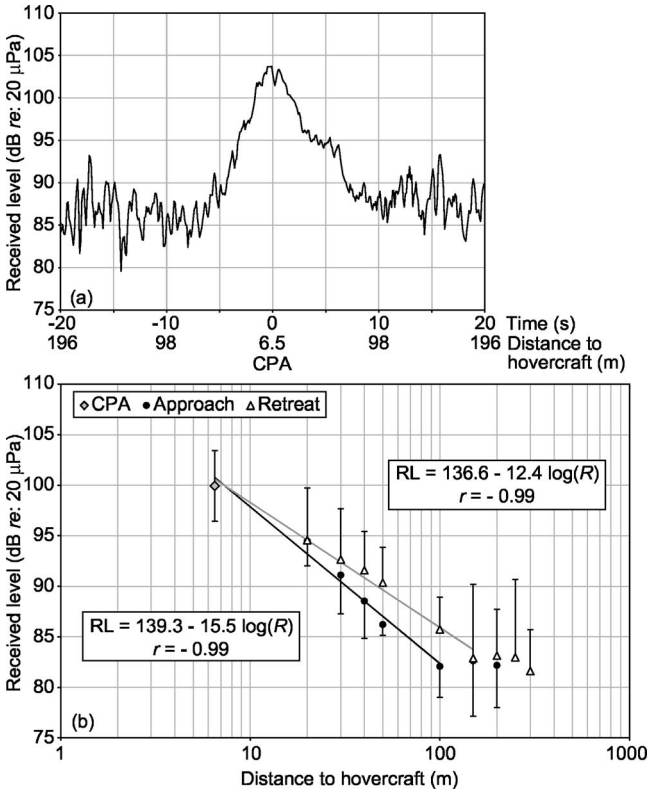

FIG. 6. (a) Broadband (10–10 000 Hz) sound pressure time series for the microphone during run 4. The x axis shows time, centered on the closest point of approach (CPA), and the corresponding distance from the hovercraft, calculated using the vessel's mean speed during that particular run. (b) Mean received broadband (10–10 000 Hz) levels in air (± one s.d.) for the hovercraft's approach (filled circles), CPA (gray diamond), and retreat (empty triangles), as a function of distance. The logarithmic spreading loss model (R in m) was applied to both data sets.

The lift fan was positioned under the hovercraft, close to the water, whereas the thrust propeller was upright on the stern deck (Fig. 2). However, contrary to expectation, lift fan components (i.e., 420 Hz blade rate −5.5% = ~397 Hz) were present but small in the underwater sound, even at the CPA.

Figure 5 shows levels of underwater sound for seven selected one-third-octave bands versus distance from the hovercraft for the two hydrophone depths. The one-third-octave band centered at 80 Hz is dominant at close distances on the shallow hydrophone. Levels for this band reach background values much faster on the shallow than on the deep hydrophone, which is what we would expect for an airborne sound source. Another difference in the sounds at the two depths involved the relative levels in the one-third-octave bands centered at 20 and 63 Hz: they contained some of the highest received levels at the shallow depth, but some of the lowest levels at the deeper depth.

B. Airborne sounds

Figure 6(a) shows the broadband (10–10 000 Hz) SPL time series for the microphone during the fourth pass. Maximum SPLs were 97–104 dB *re*: 20 μPa for the four passes (maximum A-weighted levels were 85–97 dBA *re*: 20 μPa). Broadband (10–10 000 Hz) levels of airborne sound as a function of distance from the hovercraft are shown in Fig. 6(b). The logarithmic sound propagation model represented by Eq. (1) was fitted separately to data from the hovercraft's approach and retreat. Spreading loss terms were 15.5 and 12.4 dB/tenfold change in distance, respectively. The effects of aspect and range dependence were confounded in the measurement geometry. This probably accounts for the deviations from expected spherical spreading (20 dB/tenfold change in distance), although other possible causes include atmospheric refraction and near-field effects. The spreading loss coefficient was smaller for the vessel's retreat in all four passes. Background in-air values were in the range 74–80 dB *re*: 20 μPa.

Sound spectral density levels are plotted in Fig. 7 to examine the tones or frequency peaks produced by the hovercraft in air during a fly-by. As seen in the underwater data the spectrum included a large peak at 87 Hz. In addition eight harmonics of this fundamental frequency were found up to ~870 Hz.

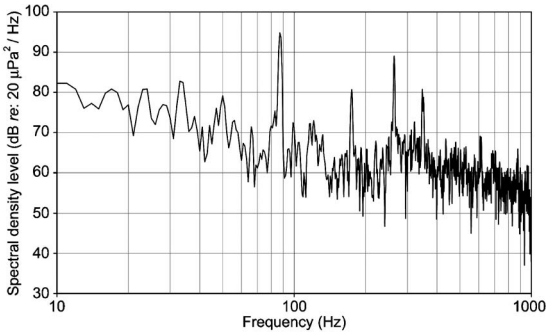

FIG. 7. Sound-pressure density spectrum (10–1000 Hz) for a 1.5-s sample recorded by the microphone and centered on the maximum broadband value for run 3.

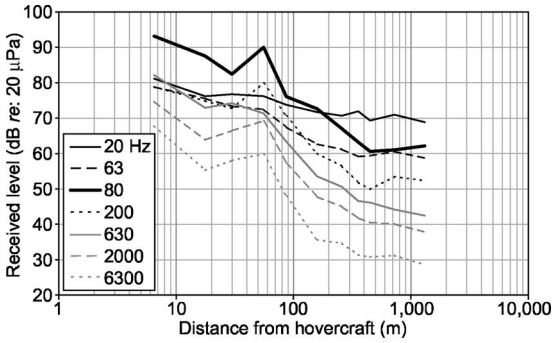

FIG. 8. Mean received levels of airborne sound as a function of mean distance from the hovercraft for seven selected one-third-octave bands. The indicated frequencies correspond to the bands' center frequencies.

The location of the thrust propeller on the stern deck of the hovercraft, in full view of the recording vessel, made it likely that tones produced by this propeller would be identified on the recordings. If we assume that the hovercraft was running somewhat below full power (see Sec. III A), then the peak centered at ~87 Hz very likely represents the thrust propeller's blade rate. Richards and Mead (1968) name the propeller rotational noise (at 80–800 Hz) as the major source of sound from a hovercraft.

Figure 8 shows that the one-third-octave band containing the thrust propeller's blade rate is dominant at close distances. Received one-third-octave levels of airborne sound generally decreased with distance at a higher rate for higher than for lower frequencies. For example, between the CPA (6.5 m) and 1310 m, received levels dropped by 12 dB for the band centered at 20 Hz, and by 39 dB for the band centered at 6300 Hz.

IV. DISCUSSION

The purpose of this paper is to present underwater and in-air sound measurement results for a small hovercraft in use for crew transfer to and from an island-based oil production facility. It might have been desirable to perform a physical acoustics study of the sources of sound on the hovercraft, including the directional effects, but such a study was well beyond the scope of the project. Good reviews of propeller and propfan noise are in Chap. 1 of Hubbard (1995) or Chaps. 9 and 10 in Richards and Mead (1968). These references do not include considerations of underwater sounds.

A. Underwater sounds

Few measurements of underwater sounds from hovercraft have been reported previously, and the limited existing data concern larger hovercraft. Slaney (1975) recorded the sounds from a Bell Voyageur hovercraft; in that study the hydrophone was at 1.8-m depth. The Bell Voyageur was a much larger hovercraft than the Griffon 2000TD used in this study: 20 m long, 11.2 m wide, and with a 23 720 kg payload, as compared to 11.9 m, 4.8 m, and 2268 kg for the Griffon 2000TD. The Bell Voyageur was powered by two marine gas turbines (2×1300 hp continuous) that drove two centrifugal lift fans and two propellers. At a horizontal distance of 46 m, received levels in one-third-octave bands centered at 80–630 Hz were ~110 dB *re*: 1 μPa. In our data set, the corresponding values were 97–105 dB (at a hydrophone depth of 1 m). Slaney (1975) also reported a 50–2000 Hz band level of 121 dB *re*: 1 μPa (also at a distance of 46 m), compared to ~111 dB in our data set for the same frequency range.

In another study, Brown (1988) reported broadband (22.5–22 500 Hz) levels of underwater sound generated by an AP.1-88 Hovercraft. Recordings were made with a hydrophone on the bottom in water 6–7 m deep. However, this hovercraft was also considerably larger than the Griffon 2000TD: 25 m long, 10.5 m wide, 7260 kg payload, powered by four diesel engines (two propulsion and two lift engines, at 2×500 and 2×390 hp continuous, respectively) driving six pairs of lift fans and two propellers. Maximum SPLs, as recorded on the bottom, were 122–126 dB and 117–119 dB *re*: 1 μPa at CPAs of 15 and 30 m, respectively. Brown (1988) presented one-third-octave band data from which we calculated a maximum level of 124 dB *re*: 1 μPa at a distance of 15 m for the 25–8000 Hz band. For that distance and frequency range (with hydrophone depth 7 m), our measured value is 122 dB *re*: 1 μPa, i.e., slightly lower.

In view of the differences in size and engine power between the hovercraft in this study and those studied by Slaney (1975) and Brown (1988), the lower received levels for the Griffon 2000TD are expected. However, large differences would not be expected, as (other factors being equal) a halving of power output would only result in a 3-dB drop in SPL. Similarly, dividing the power output by 5 would result in a 7-dB drop in SPL. If we limit our analysis to the propulsion (thrust) engine horse power, the differences between the vessels seem reasonable: the Bell Voyageur had 7.3 times the Griffon's hp and a 10 dB higher broadband level. The AP.1-88 had 2.8 times the Griffon's hp and a 2.5 dB higher broadband level.

The Griffon 2000TD hovercraft included three interlinked rotating components that might be expected to produce tonal sounds at particular frequencies: the vessel's diesel engine, the 12-bladed lift fan located under the vessel, close to the water, and a 4-bladed thrust propeller positioned vertically on the aft deck. When the hovercraft ran at full power, these sources were all in air. Therefore, we expected SPLs recorded by the shallower hydrophone (depth 1 m) during the fly-bys to be higher than those recorded by the deeper hydrophone (depth 7 m). This turned out to be true at the CPA where the difference was over 7 dB, indicating a rapid loss with depth. The experimental conditions (i.e., sea state) were such that the sounds produced by the hovercraft did not exceed ambient levels by a sufficient amount and duration to model transmission loss usefully.

Compared to the deep hydrophone, the shallow hydrophone recorded higher levels for the one-third-octave band centered at 20 Hz (Fig. 5). This is accounted for by the low-frequency cutoff caused by the shallow water at the recording site (Richardson *et al.*, 1995). The fact that the hovercraft is a sound source in air, where the low-frequency cutoff phenomenon does not apply, explains the presence of a range dependency at such a low frequency.

The distance at which broadband levels reached background values can be estimated by examining one-third-octave band levels (Fig. 5). For the shallow hydrophone [Fig 5(a)] levels for five out of seven bands shown did not decrease beyond 300 m. The exceptions were the bands centered at 80 and 200 Hz. For the deep hydrophone [Fig. 5(b)] the exceptions were the bands centered at 63 and 80 Hz. These exceptions had or were close to having reached their lowest value by a distance of 1 km. Consequently, for the particular set of sea state and water depth found during our recordings, we estimate that underwater sound levels had returned to background values by ~1 km fore and aft of a Griffon 2000TD hovercraft cruising by at full power.

The hovercraft recorded in this study was used as an alternative to conventional crew boats (length 19 m) at Northstar Island. Therefore, we compared levels of underwater sound produced by the hovercraft with conventional propeller-driven crafts of similar sizes. We have no close-up recordings of the Northstar crew boat, but unpublished measurements showed broadband (10–10 000 Hz) levels of 121 dB *re*: 1 μPa at a distance of 1820 m during cruising. A 15 log(R) propagation loss [which has been measured for this area, see Blackwell and Greene (submitted)] brings this value to 130.9 dB (the maximum hovercraft value at 6.5 m for the deep hydrophone) at a distance of ~400 m. Greene (1985) reported source levels of 156 dB *re*: 1 μPa-m for the 90-Hz tone of a 16-m crew boat. Buck and Chalfant (1972) reported source levels of 166 dB *re*: 1 μPa-m for a 37-Hz tone produced by a 25-m tug pulling an empty barge. In the two latter studies the broadband levels can only be higher than the values reported here. Thus, despite the paucity of comparable underwater measurements it is clear that conventional vessels of approximately the same size as the Griffon 2000TD hovercraft have higher source levels than the hovercraft. More importantly, because the hovercraft sound source is in air, it does not propagate well horizontally through the water. Consequently the amount of time that the two types of craft will be audible underwater while passing by a stationary underwater listener is on the order of 20–60 times longer for a conventional propeller-driven vessel.

Blackwell *et al.* (2004) also monitored underwater sounds from Northstar using an autonomous recorder located 550 m from the island. Broadband (10–500 Hz) sound levels were averaged for 1 min every 4.3 min. Whereas crew changes at the island by the crew boats raised broadband levels ~600 m away by ~15 dB, those by the hovercraft did not cause a noticeable change in broadband levels at that distance.

In conclusion, the Griffon 2000TD hovercraft was considerably quieter underwater than conventional vessels of comparable sizes. A hovercraft is therefore an attractive alternative when there is concern about the levels or the duration of vessel sounds produced underwater.

B. Airborne sounds

Maximum broadband values at the CPA were 97–104 dB *re*: 20 μPa or 85–97 dBA *re*: 20 μPa. For comparison, this corresponds to the sounds of a blender at the operator's position, or the cockpit of a light aircraft in the compilation of common airborne sounds by Kinsler *et al.* (2000). In one of the rare publications on hovercraft sounds in air, Lovesey (1972) reports maximum broadband SPLs for five types of hovercraft at a distance of 152 m during maneuvering in a terminal area. These were 94, 94, 95, 85, and 69 dBA for SRN2, SRN3, SRN5, SRN4, and VT1 hovercraft, respectively (the SRN2, 3, and 5 hovercraft were early models not optimized for reduced noise). The values for the SRN hovercraft are all higher than those recorded for the Griffon 2000TD, whereas the maximum value recorded for the VT1 is comparable. However, the hovercraft reported on by Lovesey (1972) were 3–80 times heavier than the Griffon 2000TD and had 2.5–38 times the horsepower. In addition, they were maneuvering, not flying by at full power as during our measurements. The Griffon 2000TD's specifications sheet states that the external noise level is less than 90 dBA at 150 ft (46 m). This statement is supported by our measurements (not shown).

The hovercraft's spectral composition in air was very similar to that underwater, with a peak at ~87 Hz accounted for by the thrust propeller's blade rate. Consequently, the one-third-octave bands centered at 80 Hz (and 160 Hz, not shown) showed marked increases, relative to neighboring bands, at all recorded distances. Slaney (1975) reported similar peaks in the one-third-octave bands centered at 100 and 200 Hz. Eight harmonics to the fundamental 87 Hz frequency were detected in the spectrum. In comparison, Wheeler and Donno (1966) detected up to 14 harmonics of this rotational noise on the SRN5 hovercraft.

Because all the hovercraft's sound sources (engine, lift fan, and propeller) were located in air during cruising, the craft was detectable in air out to distances exceeding the maximum distances where it would be detectable underwater. Mean broadband values in air reached a minimum and then remained constant at ~100 m and 150 m during approach and retreat, respectively [Fig. 6(b)]. However, there was a large amount of variation in background sound during the recording. In addition, many organisms are able to hear tones at levels below ambient—for example, the acoustics crew could clearly hear the hovercraft in air at distances of more than 400 m. Levels for three of the seven selected one-third-octave bands shown in Fig. 8 were still decreasing 1 km from the hovercraft, but only slightly. It is therefore reasonable to state that airborne broadband levels reached background values less than 2 km from the hovercraft for the conditions existing during our measurements.

ACKNOWLEDGMENTS

We thank A. Billings, G. Truitt, J. Nevels, and J. Hanover of Alaska Clean Seas (ACS) for their cooperation, enthusiasm, and expert boating skills. From Crowley Marine we thank R. Doughty for logistical help and D. Lockhart for being the hovercraft captain during the measurements. From LGL Alaska, we thank J. Leavitt for help with fieldwork and M. Williams for logistical support and for reviewing the manuscript. C. Leidersdorf of Coastal Frontiers Corporation provided the hovercraft picture (Fig. 2). For logistical sup-

port at Northstar we thank P. Pope and J. Huey of BP's island staff. W. Cullor of BP's Environmental Studies Group helped with logistics. Dr. W. J. Richardson, LGL Ltd., provided program direction and guidance as well as helpful comments on this paper. We also thank two anonymous reviewers who greatly improved the manuscript. Finally, we thank Dr. W. Streever of BP's Environmental Studies Group for his support of this project as well as valuable comments on the manuscript.

Blackwell, S. B., and Greene, C. R., Jr. "Sounds from an oil production island in the Beaufort Sea in summer: characteristics and contribution of vessels," J. Acoust. Soc. Am. (submitted).

Blackwell, S. B., Norman, R. G., Greene, C. R., Jr., McLennan, M. W., McDonald, T. L., and Richardson, W. J. (**2004**). "Acoustic monitoring of bowhead whale migration, autumn 2003," in "Monitoring of industrial sounds, seals, and bowhead whales near BP's Northstar oil development, Alaskan Beaufort Sea, 1999–2003," LGL Report TA4002, Rep. from LGL Ltd., King City, Ont., Greeneridge Sciences, Inc., Santa Barbara, CA, and WEST Inc., Cheyenne, WY, for BP Exploration (Alaska), Inc., Anchorage, AK, and Nat. Mar. Fish. Serv., Anchorage, AK, and Silver Spring, MD, edited by W. J. Richardson and M. T. Williams, pp. 7-1–7-45.

Brown, L. (**1988**). "Levels of underwater noise generated by the Hovermirage AP.1-88 hovercraft," Report for Hover Mirage, Brisbane, Qld.

Buck, B. M., and Chalfant, D. A. (**1972**). "Deep water narrowband radiated noise measurement of merchant ships," Delco TR72-28, Rep. from Delco Electronics, Santa Barbara, CA, for U.S. Navy Off. Naval Res., Arlington, VA.

Greene, C. R. (**1985**). "Characteristics of waterborne industrial noise, 1980–1984," p. 197–253, in "Behavior, disturbance responses and distribution of bowhead whales *Balaena mysticetus* in the eastern Beaufort Sea, 1980–84," OCS Study MMS 85-0034, Rep. from LGL Ecol. Res. Assoc. Inc., Bryan, TX, for U.S. Minerals Manage. Serv., Reston, VA, NTIS PB87-124376, edited by W. J. Richardson, pp. 197–253.

Harris, F. J. (**1978**). "On the use of windows for harmonic analysis with the discrete Fourier transform," Proc. IEEE **66**(1), 51–83.

Hubbard, H. H. (**1995**). *Aeroacoustics of Flight Vehicles: Theory and Practice* (Acoustical Society of America, Woodbury, NY), pp. 1–64.

Kinsler, L. E., Frey, A. R., Coppens, A. B., and Sanders, J. V. (**2000**). *Fundamentals of Acoustics*, 4th ed. (Wiley, New York), pp. 360–361.

Lovesey, E. J. (**1972**). "Hovercraft noise and vibration," J. Sound Vib. **20**(2), 241–245.

Richards, E. J., and Mead, D. J. (**1968**). *Noise and Acoustic Fatigue in Aeronautics* (Wiley, London), pp. 181–240.

Richardson, W. J., Greene, Jr., C. R., Malme, C. I., and Thomson, D. H. (**1995**). *Marine Mammals and Noise* (Academic, San Diego, CA), pp. 68–72, 110–117.

Slaney, F. F. (1975). "Bell Voyageur 002 ACV environmental assessment," Report for Transport Canada, Transportation Dev. Agency.

Wheeler, R. L., and Donno, G. F. (**1966**). "The hovercraft noise problem," J. Sound Vib. **4**(3), 415–422.

Optimal active noise control in large rooms using a "locally global" control strategy

Desheng Li and Murray Hodgson[a)]
School of Occupational and Environmental Hygiene, and Department of Mechanical Engineering, University of British Columbia, Vancouver, BC, V6T 1Z3, Canada

(Received 14 February 2005; revised 12 September 2005; accepted 14 September 2005)

The feasibility of applying active noise control in large rooms, in which global control is very difficult, is investigated. Local control can only ensure sound attenuation near error-sensor positions. Considering that workers usually work only in certain regions of a workroom, a new "locally global" control strategy is proposed. The objective is to reduce the acoustic potential energy in the target region. Compared to local control, "locally global" control ensures overall noise reduction over the target region. Compared to global control, it allows the number of control channels to be significantly reduced. The placements of the control loudspeakers and error microphones must be optimized to ensure that, while the sum of the squared sound pressures at the error sensors is minimized, the potential energy in the target region is reduced. Room sound fields are modeled using the image-source method and point sources. Genetic algorithms are used to optimize the locations of the control loudspeakers and error microphones. Both numerical and experimental results are presented. The sensitivities of control performance to variations in the excitation frequency, the control-source positions, and the error-sensor locations are investigated. © *2005 Acoustical Society of America.* [DOI: 10.1121/1.2114587]

PACS number(s): 43.55.Br, 43.50.Ki, 43.55.Ka [KAC] Pages: 3653–3661

I. INTRODUCTION

Active noise control (ANC) in sound cavities has been widely investigated in the past decade. Sutton, Elliott, and McDonald[1] and Elliott, Nelson, Stothers, and Boucher[2] investigated ANC in vehicle and aircraft cabins. Park and Sommerfeldt[3] and Parkins, Sommerfeldt, and Tichy[4] compared the performance of energy-density control using sound-intensity error sensors and squared-sound-pressure control. They used microphone error sensors in small enclosures, and found superior performance of the energy–density control. Lindqvist and Sjosten[5] used a method-of-images approach to address issues in local control, such as the number of secondary sources needed to obtain, for example, a 5 dB average sound-pressure-level reduction in a partial volume of 0.5 m^3 (around a microphone). Like the work discussed above, almost all of the work reported in the literature focused on very small enclosures. The sound fields considered were in most cases actually two or one dimensional because of the very small magnitudes of one or two of the room dimensions compared to the wavelength of sound. These results beg the question of whether ANC can be applied to large, three-dimensional rooms like industrial workrooms. The work reported here was a preliminary attempt to answer this question, and suggests that the answer is yes.

In many industrial workrooms, the low-frequency noise radiated from ventilation fans, engines, etc., is dominant. Investigations[6,7] have shown that exposure to low-frequency noise for long periods of time can contribute to hearing loss, and cause other detrimental effects. As is well known, active noise control can be very effective at controlling low-frequency noise. Therefore, it is of considerable interest to investigate the application of ANC technologies to large rooms like industrial workrooms. That is the objective of this paper.

Regarding the application of ANC in large, three-dimensional rooms, there is very little work reported in the literature. Lu and Clarkson[8] investigated the performance of active-noise-control systems in reverberant rooms. However, their work focused on the performance—for example, the convergence performance—of electronic controllers. Guo and Hodgson[9] used a method-of-images approach to study the active control of noise from a point source in an empty, rectangular room numerically and experimentally, using one or more control sources. Significant control was achieved when the location of the primary source was appropriate, and when the configuration of the control system was optimally arranged.

Ideally, as a result of active control, a global sound reduction is achieved with a limited number of control channels. In free-field environments, global control can be achieved by locating control sound sources at distances less than half a wavelength away from the primary source(s). In small enclosures, global control can be realized using the modal-coupling method. In cases when global control is difficult to achieve, local control can be used if the required control region is very small, such as when canceling noise at the positions of passengers' ears in vehicle cabins.

Because of the large volumes of many industrial rooms, global control becomes very difficult, if not impossible, to realize with reasonable cost. The local-control strategy is not

[a)]Full address: Professor Murray Hodgson, School of Occupational and Environmental Hygiene, University of British Columbia, 3rd Floor—2206 East Mall, Vancouver, British Columbia, V6T 1Z3, Canada. Electronic mail: hodgson@mech.ubc.ca

very useful, because workers usually occupy large regions of their workplaces. To resolve this problem, a new control strategy, called "locally global" control, is proposed here. The objective of this control strategy is to reduce the acoustic potential energy over a limited target region of the room. Hence, an overall noise reduction can be obtained in the target region of interest. Compared to the global-control strategy, the required number of control channels is significantly reduced. This control strategy is fundamentally different from traditional local control. As will be shown in this paper, with the "locally global" control strategy, an overall noise reduction can be achieved over a horizontal area of up to 20 m^2, with a depth of 0.5 m, using only two error microphones; a local-control strategy can only achieve noise attenuation in small regions around the error microphones.

The control strategy uses the acoustic potential energy over the target region as the cost function. Moreover, in practice, there are no error sensors that can sense acoustic potential energy directly. Therefore, the placement of the control loudspeakers and error microphones must be optimized. This ensures that, while the sum of the squared sound pressures at the error sensors is minimized, the potential energy in the control region is reduced. In this paper, following Lindqvist and Sjosten,[5] sound fields in rooms are modeled using the image-source method with phase.[9,10] Genetic Algorithms (GA's)[11] and the quadratic-optimization method[12] are combined to optimize the locations of the control loudspeakers and error microphones. Both numerical and experimental investigations conducted in the present research demonstrate the great effectiveness of the proposed "locally global" control strategy.

II. THEORETICAL DEVELOPMENT

A. "Locally global" control strategy

As discussed above, in many industrial rooms it is most effective to design a control system that ensures noise reduction only over particular regions of interest. To achieve this, a new control strategy, called "locally global" control, is proposed here. The acoustic potential energy in the target region is used as the cost function. In practice, there are no error sensors that can sense acoustic potential energy directly. To realize a control strategy, control systems have to be appropriately designed. In this study, a design system was developed using the image-source method with a phase to model the sound field. Genetic algorithms were used to optimize the locations of the control loudspeakers and error microphones. As shown below, the optimization process reduces the potential energy in the control region if the controller minimizes the sum of the squared sound pressures at the error sensors. The advantage of this control strategy is that it reduces the required number of control channels and, hence, the cost of active control, while ensuring noise attenuation over the desired region. In the following sections, the image-source method[9,10] and genetic algorithms are briefly described before the optimal-design method is introduced.

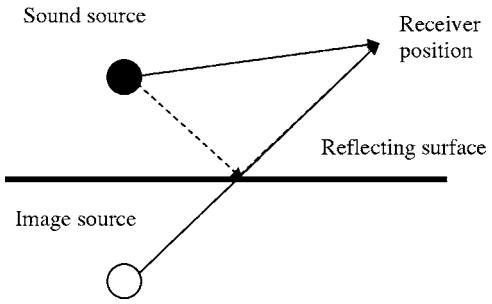

FIG. 1. Schematic diagram of a single reflection modeled by the image-source model.

B. Image-source method

In a free field, the sound pressure emitted by a point source can be expressed as

$$p(\mathbf{X},\mathbf{X}') = q\frac{i\omega\rho_0 e^{-ikR}}{4\pi R} = qZ_R, \tag{1}$$

in which q is the complex source strength, Z_R is the complex acoustic transfer impedance from the source position to the receiver position, ω is the angular frequency, k is the wave number, ρ_0 is the air density, $\mathbf{X}$ is the source position (x,y,z), $\mathbf{X}'$ is the receiver position (x',y',z'), and R is the distance between the source and the receiver.

When a rigid wall is present, the sound at a receiver position is the sum of the direct sound and reflections from the wall. In the image-source method, to model wall reflection, the wall is replaced by an image source located symmetrically on the other side of the wall (see Fig. 1). Thus, the sound pressure becomes the sum of the contributions from the original and image sources, expressed as

$$p(\mathbf{X},\mathbf{X}') = p_d + p_i = q\left(\frac{i\omega\rho_0 e^{-ikR_d}}{4\pi R_d} + \frac{i\omega\rho_0 e^{-ikR_i}}{4\pi R_i}\right), \tag{2}$$

where the subscripts d and i represent the direct and image sources, respectively.

Let the term in the bracket in Eq. (2) be the acoustic transfer impedance defined as

$$Z_R(\mathbf{X},\mathbf{X}') = \frac{i\omega\rho_0}{4\pi}\left(\frac{e^{-ikR_d}}{R_d} + \frac{e^{-ikR_i}}{R_i}\right). \tag{3}$$

Then, the sound pressure in a nonfree field can still be expressed as in Eq. (1).

In a rectangular enclosure with six rigid walls, the acoustic transfer impedance from the source to a receiver becomes

$$Z_R(\mathbf{X},\mathbf{X}') = \frac{i\omega\rho_0}{4\pi}\sum_{p=1}^{8}\sum_{r=-\infty}^{\infty}\frac{e^{-ik|\mathbf{R_p}+\mathbf{R_r}|}}{|\mathbf{R_p}+\mathbf{R_r}|}, \tag{4}$$

in which $\mathbf{R_p}$ represents the eight vectors given by the eight permutations over ± of

$$\mathbf{R_p} = (x \pm x', y \pm y', z \pm z'), \tag{5}$$

$\mathbf{r}$ is the integer vector triplet (n,l,m), and

$$\mathbf{R_r} = 2(nL_x, lL_y, mL_z). \tag{6}$$

If the room walls are not rigid, reflections from the walls can still be modeled with good accuracy using image sources as long as the absorption is small. In this case, the acoustic transfer impedance between the source and a receiver can be written as

$$Z_R(\mathbf{X},\mathbf{X}') = \frac{i\omega\rho_0}{4\pi}\sum_{p=0}^{1}\sum_{r=-\infty}^{\infty}\beta_{x1}^{|n-q|}\beta_{x2}^{|n|}\beta_{y1}^{|l-j|}\beta_{y2}^{|l|}\beta_{z1}^{|m-s|}\beta_{z2}^{|m|}\frac{e^{-ik|\mathbf{R_p}+\mathbf{R_r}|}}{|\mathbf{R_p}+\mathbf{R_r}|}, \quad (7)$$

in which $\mathbf{R_p}$ is now expressed in terms of the integer vector $\mathbf{p}=(q,j,s)$ as

$$R_p = (x-x'+2qx', y-y'+2jy', z-z'+2sz'). \quad (8)$$

The β's are the angle-independent pressure reflection coefficients of the six walls.

It should be mentioned that, in the present research, it was assumed that the overall dimensions of the noise sources and any obstacles in the room are much smaller than the sound wavelength of interest. Therefore, noise sources can be simplified as point sources, and the effect of obstacles can be neglected.

C. Genetic algorithms

Previous research[13,14] has shown that genetic algorithms are powerful and versatile tools for optimal design. Therefore, genetic algorithms were employed here to find the optimal locations of the control loudspeakers and error microphones of the active control systems.

Genetic algorithms are stochastic search techniques based on the mechanism of natural selection and natural genetics.[11] They start with an initial set of random solutions to the physical problem, called the "initial generation." In the present research, the solutions are a set of control-loudspeaker or error-microphone positions, which are coded into binary strings. Each solution in the generation is evaluated by a cost function (i.e., the reduction of the acoustic potential energy in the target region) and assigned a numerical fitness value. This value indicates the performance of the configuration of the control loudspeakers or error microphones in reducing the noise. Then, according to their fitness values, some solutions are selected as "parents" for "reproduction." Those solutions with higher fitness values have a higher probability of being selected, thus maintaining the rule of "survival of the fittest." Through a crossover operator (a process to create "children" by randomly copying information from two "parents") and/or a mutation operator (a process to create a "child" by randomly varying the information in a "parent"), "children" are produced to form a new generation. The children represent new configurations of the control loudspeakers or error microphones. Generally speaking, the solutions in the new generation are better than those in the previous generations. The "evolution" cycle is repeated until an optimal solution is found.

In the present investigation, advanced GA techniques, such as the steady-state genetic algorithm (SSGA) and the selection method of stochastic remainder sampling (SRS) without replacement,[11] were employed to improve the search performance.

D. Optimal control-system design

The design process is divided into two steps. First, the locations of the control loudspeakers are optimized to minimize the acoustic potential energy in the target region. At this stage, it is assumed that there is a virtual sensor that can sense the acoustic potential energy. After the optimal locations of the control loudspeakers are determined, the locations of the error microphones are optimized. The objective is to find the optimal locations of the error microphones, so that the acoustic potential energy in the target region can be significantly reduced, while the sum of the squared signals from the error microphones is minimized.

1. Location optimization of the control loudspeakers

During the design process, many location configurations are explored by the genetic algorithms. The location configurations are evaluated by the reduction of the acoustic potential energy in the target region. To do so, the optimal control strength of each explored configuration is obtained using the quadratic-optimization method. The acoustic potential energy in the target region can be expressed as

$$E_p = \frac{1}{4\rho_0 c_0^2}\int_V |p(r)|^2\, dr = \frac{1}{4\rho_0 c_0^2}\int_V p(r)^* p(r) dr, \quad (9)$$

in which c_0 is the sound speed in air, V is the volume of the target region, and * denotes a complex conjugate.

Since a linear system is being considered, the sound pressure at one point is the sum of the sound pressures induced by the primary and control sources, expressed as

$$p(r) = p_p(r) + p_c(r), \quad (10)$$

in which the subscripts p and c represent the primary and control sources, respectively.

Substituting Eq. (1) into Eq. (10), and then substituting the resulting equation into Eq. (9), one obtains

$$E_p = \mathbf{q_c^H A_E q_c} + \mathbf{q_c^H b_E} + \mathbf{b_E^H q_c} + \tilde{E}, \quad (11)$$

with

$$\mathbf{A_E} = \frac{1}{4\rho_0 c_0^2}\int_V \mathbf{Z}_{\mathbf{R_c}}^* \mathbf{Z}_{\mathbf{R_c}}^{\mathbf{T}}\, dV, \quad (12)$$

$$\mathbf{b_E} = \frac{1}{4\rho_0 c_0^2}\int_V \mathbf{Z}_{\mathbf{R_c}}^* \mathbf{Z}_{\mathbf{R_p}}^{\mathbf{T}}\, dV\, \mathbf{q_p}, \quad (13)$$

$$\tilde{E} = \frac{1}{4\rho_0 c_0^2}\mathbf{q_p^H}\int_V \mathbf{Z}_{\mathbf{R_p}}^* \mathbf{Z}_{\mathbf{R_p}}^{\mathbf{T}}\, dV\, \mathbf{q_p}. \quad (14)$$

Here $\tilde{E}$ is the acoustic potential energy induced by the primary sources, $\mathbf{q_c}$ is the vector of control-source strengths, $\mathbf{q_p}$ is the vector of primary-source strengths, $\mathbf{Z}_{\mathbf{R_c}}$ is a vector of the acoustic transfer-impedance functions of the control sources in the target region, and $\mathbf{Z}_{\mathbf{R_p}}$ is a vector of the acous-

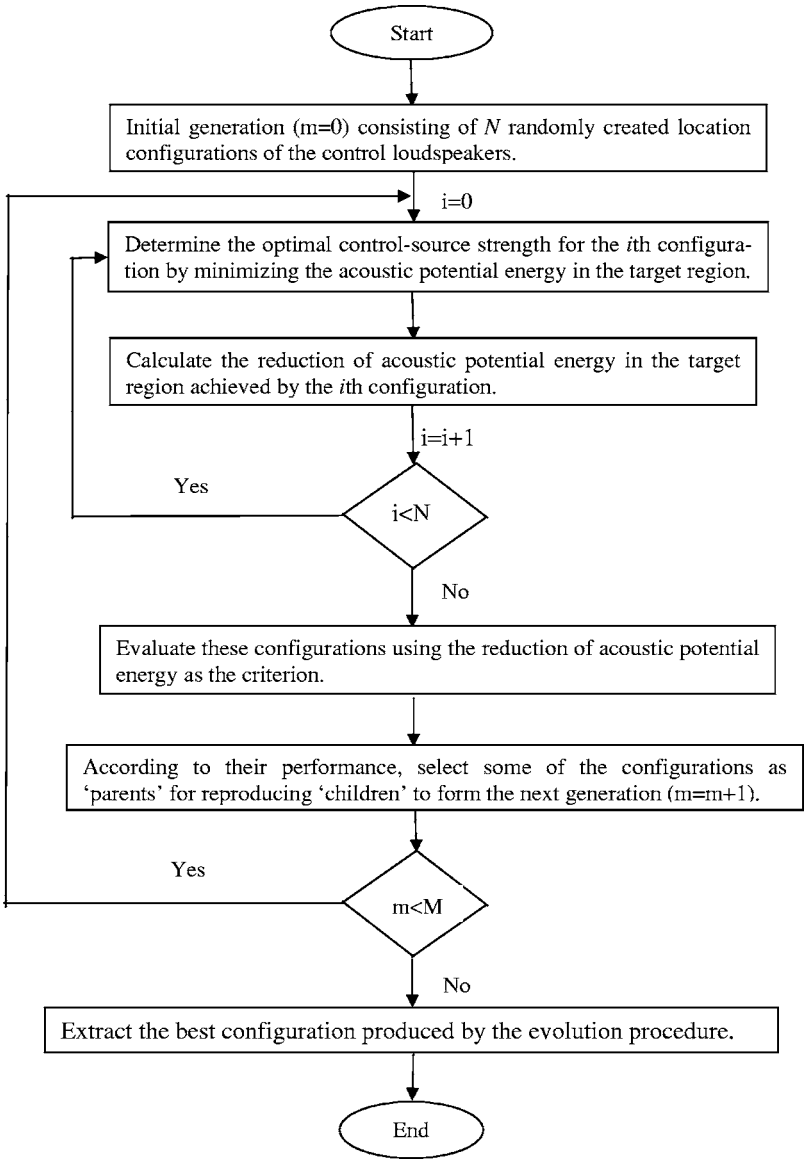

FIG. 2. Flow chart of the optimization procedure for control loudspeakers (note: M is the maximum generation number in the evolution).

tic transfer-impedance functions of the primary sources in the target region.

By taking the derivative of Eq. (11) with respect to $\mathbf{q_c}$, one can obtain the vector of optimal control-source strengths that minimizes the acoustic potential energy, as follows:

$$\mathbf{q_c} = -\mathbf{A_E^{-1}}\mathbf{b_E}. \tag{15}$$

Under this optimal control output, the reduction of the acoustic potential energy in the target region can be calculated as

$$E_{\text{reduction}} = -\mathbf{b_E^H}\mathbf{q_c}. \tag{16}$$

This is used as the cost function in the genetic algorithm to evaluate the fitness of the control-source configuration. The higher the reduction, the higher is the fitness value assigned to the configuration. At the end of the search, one optimal configuration—or at least a configuration close to the optimal—is obtained. For clarity, the whole design process is detailed in Fig. 2.

2. Location optimization of error microphones

After the optimal configuration of the control sources is obtained, the optimal positions of the error microphones are searched for in the target region, using genetic algorithms. The design procedure is similar to the location optimization of the control loudspeakers, except that, for each searched configuration, the optimal control strength is calculated by minimizing the sum of the squared sound pressures at the error-microphone positions, expressed as

$$\sum_{i=1}^{Ne} |p(r_i)|^2 = \mathbf{q_c^H}\mathbf{A}\mathbf{q_c} + \mathbf{q_c^H}\mathbf{b} + \mathbf{b^H}\mathbf{q_c} + p_{ps}, \tag{17}$$

with

$$\mathbf{A} = \mathbf{Z_c^H}\mathbf{Z_c}, \tag{18}$$

$$\mathbf{b} = \mathbf{Z_c^H}\mathbf{Z_p}\mathbf{q_p}, \tag{19}$$

$$p_{ps} = \mathbf{q_p^H Z_p^H Z_p q_p}. \tag{20}$$

Here $\mathbf{Z_c}$ and $\mathbf{Z_p}$ are the matrices of acoustic transfer impedances between the error-microphone locations and the control sources and primary sources, respectively. p_{ps} is the sum of the squared pressure amplitudes, at the *Ne* error-microphone locations, induced by the primary sources only.

By minimizing Eq. (17), the optimal control strengths can be obtained as

$$\mathbf{q_c} = -\mathbf{A^{-1}b}. \tag{21}$$

However, the control objective is to attenuate the noise over the whole target region, rather than only at the error-microphone positions. Thus, in the genetic algorithm, the performance of the *Ne* error-microphone configuration must be evaluated by the reduction of the acoustic potential energy in the target region. At the end of the search, the optimal configuration of the error microphones—or at least a configuration close to the optimal—is found. With this optimal configuration, a significant reduction of acoustic potential energy in the target region is achieved, while the sum of the squared outputs of the error microphones is minimized.

III. NUMERICAL INVESTIGATION

In this section, the locally global control strategy was implemented in small and large rooms. The small room (an empty office) was chosen because it was available for use for experimental validation. The large room was chosen to approximate a simplified industrial workroom; a suitable real industrial workroom, available for experimental work, could not be found.

A. Active control in a small room

Numerical investigations were first carried out for a small room with dimensions 5.3 m long, 3.95 m wide, and 2.72 m high. The reflection coefficients were assumed to be 0.94 for the four walls, 0.99 for the floor, and 0.81 for the ceiling (this choice is explained in Sec. IV). The primary source was assumed to be located at the corner of the room. A 2-by-2 control system was designed to control the noise in the 0.5 m thick horizontal layer centered around the horizontal plane 1.60 m above the floor. The source signal was a 100 Hz pure tone. Both the length and the width of the room are larger, while the height is a little smaller, than one wavelength of this noise signal. The source strength was 0.01 m^3/s. In theory, an infinite number of image sources should be used in the calculation; in practice, a finite number has to be used. Here an image-source order of 60 was used; this was determined to be sufficient to achieve high accuracy in studies of the convergence of the calculated sound-power output of the noise source.[9]

As is known, when a control source is placed within a half-wavelength of a noise source, global control can be realized. However, it is often inconvenient to put control sources close to noise sources in many practical situations. To make this research more meaningful and generalizable, control loudspeakers and the primary noise source were separated by at least one half-wavelength. Without this distance constraint, the control sources tend to be located at the same position as the noise source after optimization. In the genetic algorithm, the location region for the control-source optimization was the whole room; for the error-microphone optimization, it was the target region.

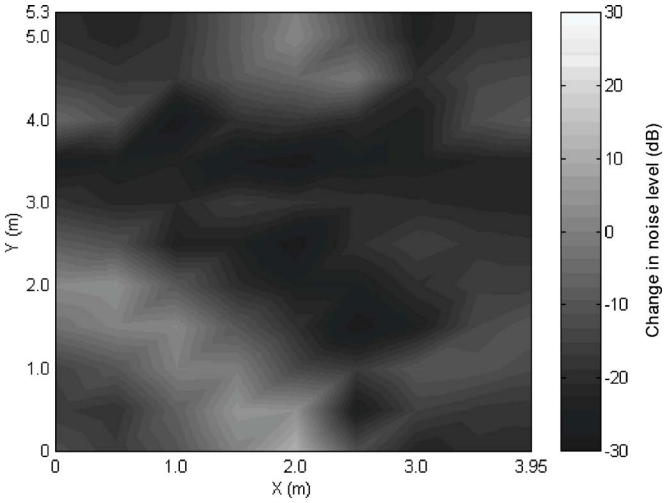

FIG. 3. Predicted control performance of an optimal two-by-two control system in a small, office-sized room.

A Cartesian coordinate system was established for the room, with one of the corners as the origin, the x and y axes in the two horizontal directions, and the z axis in the vertical direction. In the case of a noise source in the corner with coordinates (0, 0, 0), the optimal positions of the control sources were found to be (2.42, 0.85, 0.91) and (1.15, 2.22, 0.54). The two error microphones were optimally located at (2.29, 1.20, 1.6) and (1.91, 3.42, 1.6). Figure 3 shows the control performance, quantified by the change of the sound field in the plane 1.6 m high after control. Because of the long wavelength of the low-frequency sound, sound fields in other planes would be similar to that at 1.6 m high. In this figure and those discussed below, negative values in decibels represent sound reduction as a result of control, while positive values indicate a sound increase. From this figure, one can see that a significant sound reduction was achieved at most positions using the optimally designed two-by-two control system. Large reductions were achieved near the error-microphone locations. The average reduction in the target region was 15.3 dB. However, after control, the sound-pressure level increased slightly at a few positions that had relatively low noise levels before control. This phenomenon is very similar to that which occurs when a global-control strategy is used in control-system design.

To further show the effectiveness of, and the necessity for, optimal design, the control performance of various non-optimal configurations was investigated. The typical control performance of a nonoptimal system is shown here. In the control system, the two control loudspeakers were located at (2.0, 0.6, 0.0) and (1.8, 0.9, 1.5), respectively; the microphones were located at the same positions, as in the optimal case. The control performance is shown in Fig. 4. As is shown, sound reduction was not achieved at most positions. In fact, the average sound-pressure level increased by

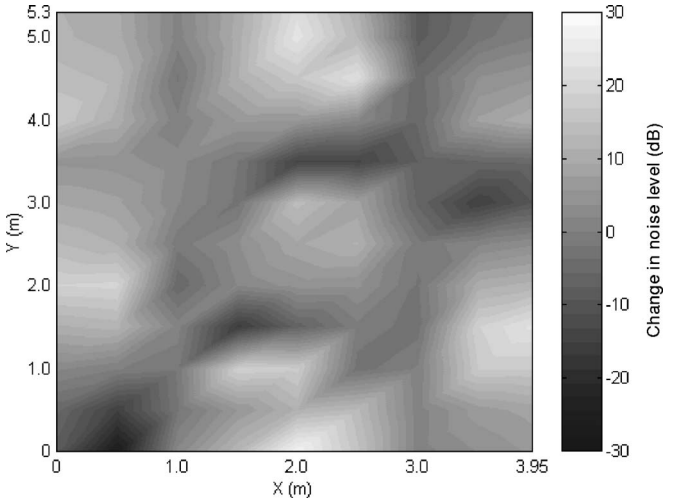

FIG. 4. Predicted control performance of a nonoptimal control system in a small, office-sized room.

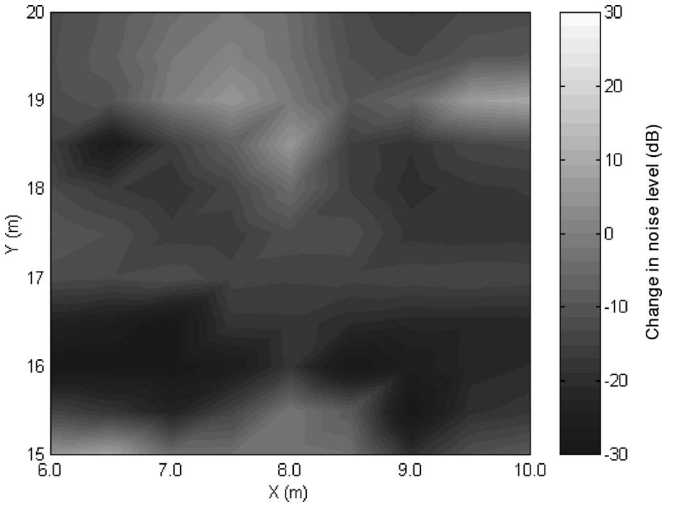

FIG. 5. Predicted control performance of an optimal control system in a large room at 100 Hz (reference configuration).

4.7 dB. It should be noted that the two control loudspeakers were closer to the noise source than in the optimal case. Despite this, the noise was not attenuated, but increased in the target region. This demonstrates that, in order to implement the proposed control strategy, a control system must be optimally designed.

B. Active control in a large room

To further test the proposed control strategy in a configuration more closely approximating an industrial workroom, noise control over a localized region of a large room was investigated. A typical result is reported here. A two-by-two control system was designed for a room 10 m wide by 20 m long by 5 m high. The reflection coefficients of the room surfaces, and the other conditions, were the same as for the small room discussed above. A 100 Hz pure tone was again used as the source signal. The noise source was placed in the corner with coordinates (0, 0, 0). The target region of control was $6 \leqslant x \leqslant 10$ and $15 \leqslant y \leqslant 20$ and $z = 1.6$. The optimal positions of the control loudspeakers were (4.13, 12.76, 2.58) and (0.32, 2.36, 0.65). The error microphones were optimally located at (8.58, 15.97, 1.60) and (7.03, 16.13, 1.60). Note that the error microphones were in the target region, but the control sources were well outside of it. Figure 5 shows the control performance in the target region. The noise is significantly reduced in the control region, using only two control channels. The average reduction is 13.5 dB.

C. Sensitivity studies

The sensitivities of the control performance to variations, with respect to a reference configuration, of the excitation frequency, control-source positions, and error-sensor locations were also analyzed in the research. This was done by varying these parameters around their optimal values. The optimal control system in the large room, discussed in the last section, at an excitation frequency of 100 Hz, was used as the reference configuration.

To investigate the sensitivity of the optimal control system to the excitation frequency, a 95 Hz signal, representing a 5 Hz deviation from the reference frequency, was used to excite the sound field. The control performance is shown in Fig. 6. Comparing Figs. 5 and 6, one can see that, with the change of excitation frequency, the quiet zone, where sound attenuation is achieved as a result of control, is reduced. Obvious sound increases are observed in some local regions. The overall sound reduction achieved is 5.3 dB, 8.2 dB less than that in the optimal reference case. Simulations with other excitation frequencies near the optimal frequency showed similar results. The results indicate that, as the excitation frequency varies around the optimal frequency, an overall sound attenuation is still achieved, but with a degradation of performance in both the quiet-zone size and the amplitude of the reduction.

The sensitivity to the positions of the control sources was analyzed by changing their optimal positions by small amounts. Two typical cases are presented here. The two control sources were first moved to (4.13, 12.46, 2.58) and (0.32, 2.06, 0.65), 0.3 m away from their corresponding optimal positions. The error sensors remained at their optimal loca-

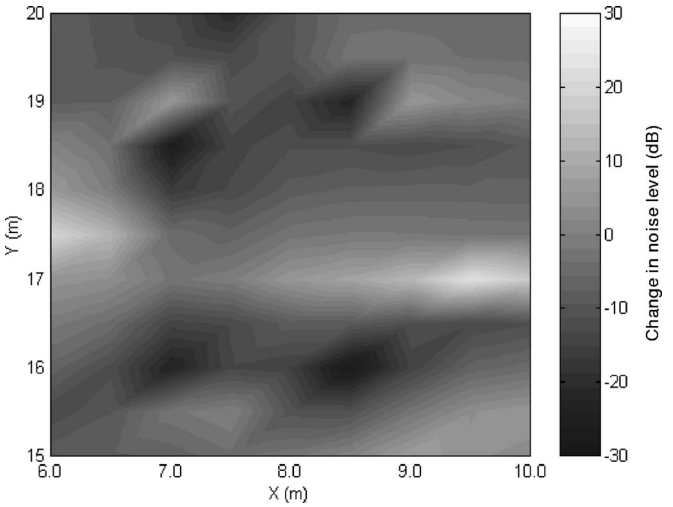

FIG. 6. Predicted control performance of the optimal control system in a large room with excitation frequency of 95 Hz.

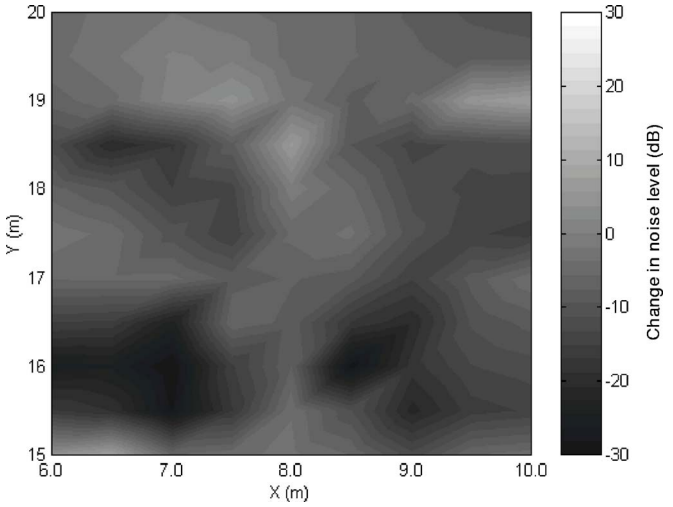

FIG. 7. Predicted control performance in a large room, with a 0.3 m deviation of the control-source locations from their optimal values.

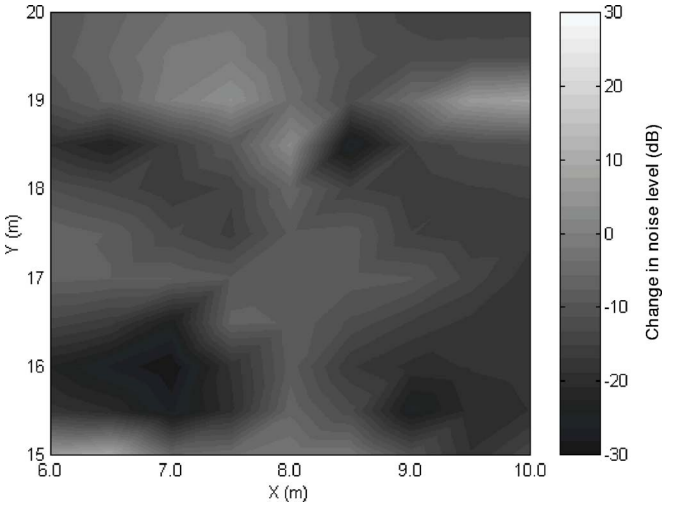

FIG. 9. Predicted control performance in a large room, with a 0.3 m deviation of error-sensor positions from their optimal values.

tions; the excitation frequency was 100 Hz. Figure 7 shows the resulting control performance. Compared to the optimal case (Fig. 5), the quiet zone decreases and the overall sound attenuation achieved is reduced by 4.1 dB. The control sources were then moved farther away from the optimal locations by 0.2 m (0.5 m in total) to (4.13, 12.26, 2.58) and (0.32, 1.86, 0.65). As shown in Fig. 8, the quiet zone becomes even smaller and the overall reduction achieved decreases to 7.6 dB, 5.9 dB less than the optimal case.

Finally, the error sensors were also moved a short distance from their optimal locations. The control sources were kept at their optimal locations; the excitation frequency was 100 Hz. When the error sensors were moved to (8.58, 15.67, 1.60) and (7.03, 15.83, 1.60), 0.3 m away from their optimal locations, both the quiet-zone size and the amplitude of the sound reduction decreased slightly, as shown in Fig. 9. The overall sound reduction is 1.9 dB less than that in the optimal case. When the error sensors are moved to (8.58, 15.47, 1.60) and (7.03, 15.63, 1.60), 0.5 m away from their optimal locations, the overall sound reduction achieved is 8.9 dB, 4.5 dB lower than that in the optimal case. As is shown in Fig. 10, the quiet zone further decreases as well.

Based on this analysis, it can be concluded that, when the excitation frequency or the locations of the control sources and error sensors vary around their optimal values, an overall sound reduction is still achieved, but the performance degrades to various extents. The control performance is more sensitive to a change of excitation frequency than to control-source and error-sensor locations. This is because the change of excitation frequency can result in a significant change in the sound field.

IV. EXPERIMENTAL INVESTIGATION

Simulation has shown that, through optimal design, noise reduction can be achieved in a target region using ANC. In order to validate the findings, experiments were carried out. The optimally designed two-by-two control system discussed in Sec. III A was implemented in a room (an empty office) with the same dimensions as in the simulation. The ceiling of the room was a suspended acoustic ceiling

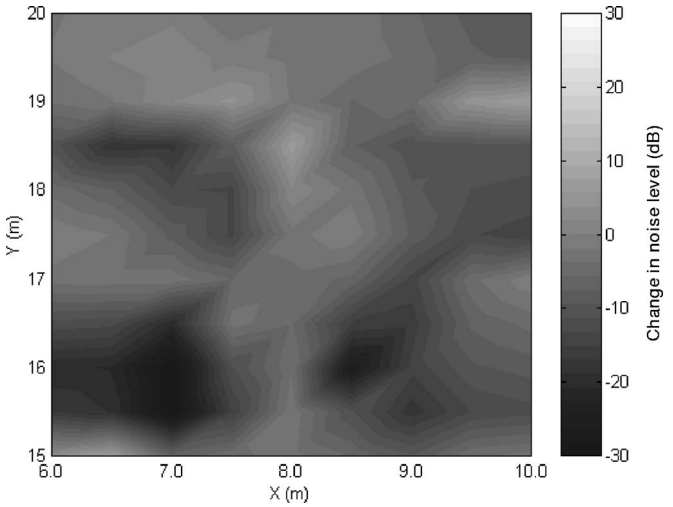

FIG. 8. Predicted control performance in a large room, with a 0.5 m deviation of the control-source locations from their optimal values.

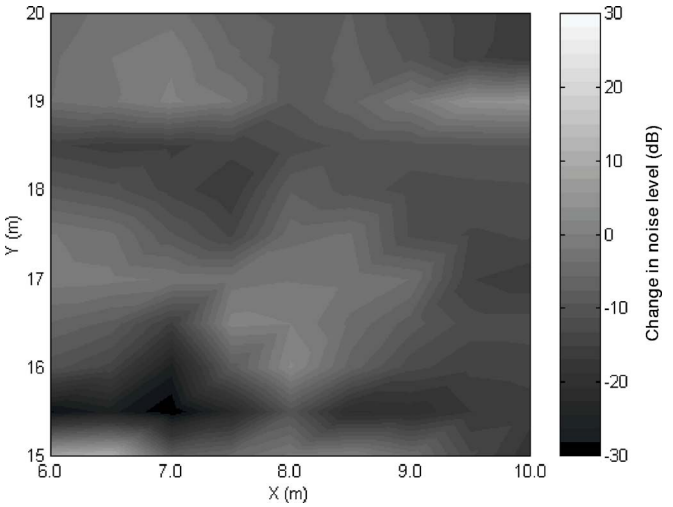

FIG. 10. Predicted control performance in a large room, with a 0.5 m deviation of the error-sensor positions from their optimal values.

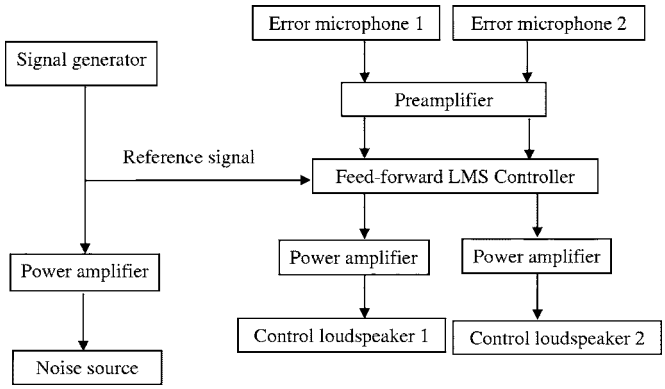

FIG. 11. Schematic of the active noise control system.

with mineral-fiber acoustic tiles. The floor was made of vinyl tiles on concrete. The walls were of double-plasterboard, stud construction. The reflection coefficients of the room surfaces were estimated by measuring the reverberation times of the room. The average room absorption was then estimated using diffuse-field theory. By distributing the absorption in a realistic way, reflection coefficients—0.94 for the walls, 0.99 for the floor, and 0.81 for the ceiling, as used in the simulation work—were obtained. An EZ-ANC controller[15] incorporating the Filtered-x, Feed-forward, LMS algorithm was used. At 100 Hz, the background-noise level from the ventilation system was as high as 65 dB.

Figure 11 shows the schematic of the active control system. Figure 12 shows the control signals to the control loudspeakers, and those from the error microphones. One can observe that, once control was enabled, the system converged very quickly and in a stable manner. The residual signals from the error microphones were due to background noise.

The noise attenuation was measured over the plane 1.60 m above the floor, as in the simulation. The measurement grid had 0.5 m intervals in both horizontal directions. Figure 13 shows the change of the sound field as a result of the control. The horizontal and vertical axes correspond to the width and length of the room, respectively. One can see

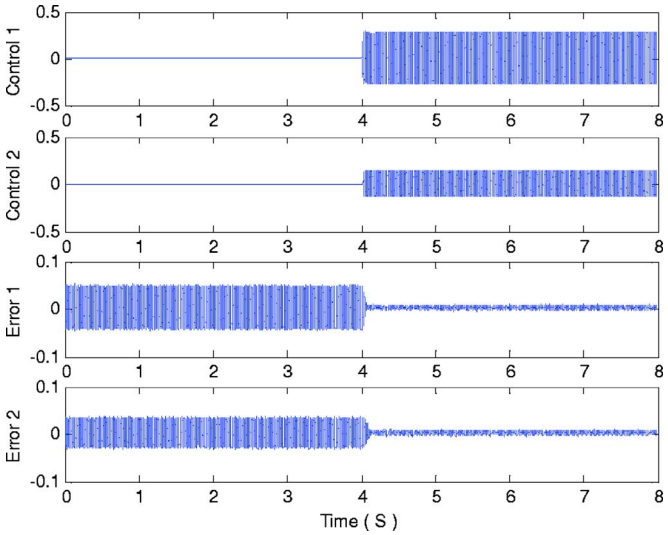

FIG. 12. Control and error signals.

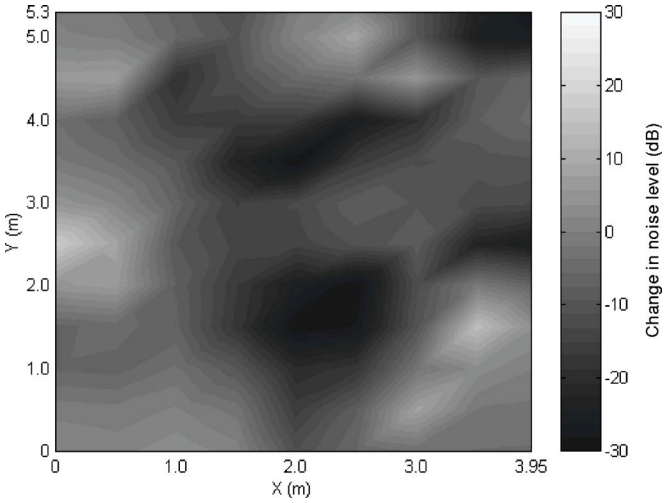

FIG. 13. Control performance of an optimal control system in the small room, measured on a 0.5 m receiver grid.

that, after control, sound reduction was achieved over most of the target region. At positions close to error microphones, significant sound reduction was achieved. The average sound reduction was 7.8 dB. It can also be observed that, at some positions where the original noise was low, the noise increased. This is because the "locally global" control strategy was employed in the design. With this control strategy, the control system tends to attenuate noise at positions where the noise is loud, but may increase the noise somewhat at positions where it is originally quiet.

It must be pointed out that the conditions in the experimental room were not identical to those assumed in the model. In the model, the room walls were assumed to be rigid. In practice, however, because the room walls were plasterboard, stud structures, they vibrated under the acoustic excitation in the experiment. The door to the room was not included in the model. Also, of course, the reflection coefficients of the room surfaces used in the model may not have been exactly the same as the actual values. Despite these differences, and the considerable background noise, substantial sound reduction was achieved by the designed control system using the sound-field model. This further suggests that the control strategy does not require a highly accurate sound-field prediction—that is, a highly accurate sound-field prediction model. If true, then the methods discussed here could be readily applied to the design of control systems in more complex enclosures.

To further show the effectiveness of optimal design, experiments were also done with a number of nonoptimal control systems. A typical experimental result is presented here. The positions of the two control loudspeakers were (2.15, 1.50, 0.91) and (0.75, 3.26, 0.54). The two error microphones were located at (2.46, 2.95, 1.6) and (2.20, 4.50, 1.6). The resulting control performance is shown in Fig. 14. Again, with a nonoptimal system, the noise increased at most positions, instead of being attenuated. The average increase was 9.7 dB in this case.

V. CONCLUSIONS

In this paper, the active control of low-frequency noise in rooms was investigated. To deal with difficulties associ-

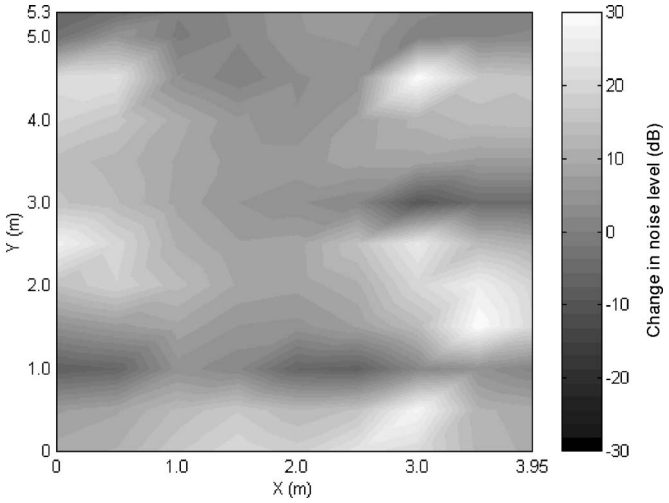

FIG. 14. Control performance of a nonoptimal control system in the small room, measured on a 0.5 m receiver grid.

ated with three-dimensional sound fields, a novel control strategy called "locally global" control was proposed. Compared to the local-control strategy, it ensures overall noise reduction over all of a target region. Compared to the global-control strategy, it requires a lower number of control channels and, therefore, reduces the cost of the application of ANC in rooms. Since the control strategy uses the acoustic potential energy over the target region as the cost function, and since, in practice, there are no error sensors that can sense acoustic potential energy directly, the placement of the control loudspeakers and error microphones must be optimized. This ensures that, while the sum of the squared sound pressures at the error sensors is minimized, the potential energy in the target region is significantly reduced.

Simulations were carried out for small and large rooms. Experiments were conducted in the small room to validate the simulation results. Both simulation and experimental results demonstrated the high effectiveness of the proposed control strategy. The sensitivity of the control performance to variations in the excitation frequency, and to control-source and error-sensor positions, were analyzed. The results indicate that, as these parameters vary around their optimal values, an overall sound reduction may still be achieved, with some performance degradation. The control performance is more sensitive to a change of excitation frequency than to the control-source and error-sensor locations. The research showed that it is feasible to apply ANC in three-dimensional rooms using the proposed "locally global" control strategy.

In the present research, in order to focus on the investigation of the proposed control strategy, a pure-tone noise and continuous room target regions were used. It would be of great interest to extend the research to broadband noise and to control over two or more unconnected regions.

ACKNOWLEDGMENTS

The authors would like to acknowledge financial support from the United States Center for Disease Prevention and Control (CDPC) and the National Institute of Safety and Health (NIOSH), the National Science and Engineering Research Council of Canada (NSERC), and the Bridge Program at the University of British Columbia. Thanks also to Dr. Jingnan Guo for his valuable comments on the work.

[1]T. J. Sutton, S. J. Elliott, and A. M. McDonald, "Active control of road noise inside vehicles," Noise Control Eng. J. **42**, 137–147 (1994).
[2]S. J. Elliott, P. A. Nelson, I. M. Stothers, and C. C. Boucher, "In flight experiments on the active control of propeller-induced cabin noise," J. Sound Vib. **140**, 219–238 (1990).
[3]Y. C. Park and S. D. Sommerfeldt, "Global attenuation of broadband noise fields using energy density control," J. Acoust. Soc. Am. **101**, 350–359 (1997).
[4]J. W. Parkins, S. D. Sommerfeldt, and J. Tichy, "Narrowband and broadband active control in an enclosure using the acoustic energy density," J. Acoust. Soc. Am. **108**, 192–203 (2000).
[5]E. A. Lindqvist and P. Sjosten, "System optimization for active control of sound fields in rooms," *Proceedings of Inter-Noise*, 1988, pp. 979–981.
[6]D. Radnoff, "Low frequency noise and hearing loss," *Proceedings of 3rd Biennial Spring Conference on Environmental and Occupational Noise*, 16–19 April 2000, pp. 95–103.
[7]K. Persson and R. Rylander, "The prevalence of annoyance and effects after long-term exposure to low-frequency noise," J. Sound Vib. **240**, 483–497 (2001).
[8]M. Lu and P. M. Clarkson, "The performance of adaptive noise cancellation systems in reverberant rooms," J. Acoust. Soc. Am. **93**, 1122–1135 (1993).
[9]J. Guo and M. Hodgson, "Investigation of active noise control in non-diffuse sound fields," *Proceedings of ACTIVE 99*, December 1999, pp. 621–632.
[10]J. B. Allen and D. A. Berkley, "Image method for efficiently simulating small-room acousticals," J. Acoust. Soc. Am. **65**, 943–950 (1979).
[11]D. E. Goldberg, *Genetic Algorithms in Search, Optimization and Machine Learning* (Addison-Wesley, New York, 1998).
[12]C. H. Hansen and S. D. Snyder, *Active Control of Noise and Vibration* (E&FN Spon, London 1997).
[13]D. S. Li, L. Cheng, and C. M. Gosselin, "Optimal design of PZT actuators in active structural acoustic control of a cylindrical shell with a floor partition," J. Sound Vib. **269**, 569–588 (2004).
[14]D. S. Li, "Active control of aircraft cabin noise and vibration using a physical model," Ph.D. thesis, Laval University, 2002.
[15]Causal Productions Pty Ltd., Adelaide, Australia.

Acoustic eigenvalues of rectangular rooms with arbitrary wall impedances using the interval Newton/generalized bisection method

Yusuke Naka[a)]
Department of Aerospace and Mechanical Engineering, Boston University, 677 Beacon Street, Boston, Massachusetts 02215

Assad A. Oberai
Department of Aerospace and Mechanical Engineering, Boston University, 110 Cummington Street, Boston, Massachusetts 02215

Barbara G. Shinn-Cunningham
Boston University Hearing Research Center, 677 Beacon Street, Boston, Massachusetts 02215

(Received 23 May 2005; revised 13 September 2005; accepted 15 September 2005)

Modal analysis of a rectangular room requires evaluation of the eigenvalues of the Helmholtz operator while taking into account the boundary conditions imposed on the walls of the room. When the walls have finite impedances, the acoustic eigenvalue equation becomes complicated and a numerical method that can find all roots within a given interval is required to solve it. In this study, the interval Newton/generalized bisection (IN/GB) method is adopted for solving this problem. For an efficient implementation of this method, bounds are derived for the acoustic eigenvalues and their asymptotic behavior explored. The accuracy of the IN/GB method is verified for a canonical problem by comparing the modal solution with the corresponding finite element solution. Furthermore, reverberation times estimated using the IN/GB method are compared to those calculated using the finite difference method. Through these examples, it is demonstrated that the IN/GB method provides a useful and efficient approach for estimating the acoustic responses of rectangular rooms with finite wall impedances. © *2005 Acoustical Society of America.* [DOI: 10.1121/1.2114607]

PACS number(s): 43.55.Br, 43.55.Ka, 43.20.Ks [NX] Pages: 3662–3671

I. INTRODUCTION

Modal analysis is a classical method for solving problems in room acoustics (see, for example, Refs. 1–5). Using this method, once all the normal modes are known, the acoustic pressure distribution for an arbitrary sound source in a room can be easily computed. Although the modal theory of room acoustics was established and fully formulated over a half century ago,[1] it is still incomplete in the sense that there is no well-developed, general method for finding eigenvalues that correspond to room modes for walls with arbitrary impedances. Only for rooms with perfectly or nearly rigid walls or rooms with the same impedance on each pair of parallel walls are the eigenvalues or their approximations easy to evaluate. Hence, only these cases have typically been considered in the acoustics literature.[1–6] However, the effect of finite wall impedances on quantities of interest, such as the reverberation time, is of general interest and important for real-world problems. Hence there is a need for an efficient and accurate method for evaluating eigenvalues for the more general case.

The difficulty in finding the acoustic eigenvalues arises from the nonlinear and transcendent nature of the acoustic eigenvalue equation,[1,2,5] which necessitates the use of numerical methods. In addition, for the modal solution to be accurate, these methods must be able to evaluate all the roots of this equation within a given interval. Classical numerical approaches for solving nonlinear equations such as Newton's iteration are not suitable for solving these equations because they yield one root for a single initial guess. Moreover, the initial guess must be "good" in order to obtain a root in the range of interest. If the number of roots in a range of interest is unknown, which is often the case in the acoustic eigenvalue problem for a room with finite wall impedances, these methods cannot be applied. Although several numerical methods have been developed to attack this problem (some of which work relatively well),[7,8] it is generally recognized that a simpler, more efficient, and stabler method would greatly increase the practicality of using modal analysis in studies of room acoustics.

In this study, the interval Newton/generalized bisection (IN/GB) method[9–11] is applied to the acoustic eigenvalue equation to overcome the above-mentioned difficulties. The IN/GB method is an extension of the classical Newton iterative method, combined with the concept of interval arithmetic.[9–12] The method is guaranteed to find all possible solutions of a system of equations within intervals specified for each variable. In addition, the quadratic convergence of the Newton method is preserved.[11]

[a)]Corresponding Author; Electronic mail: ynaka@bu.edu

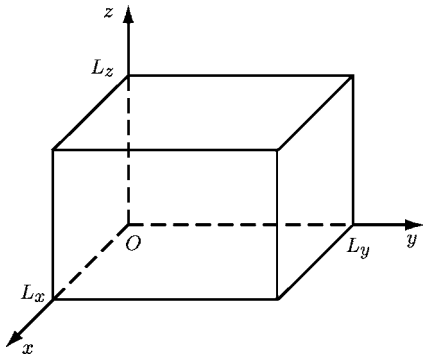

FIG. 1. Coordinate system of a rectangular room.

The remainder of this paper is organized as follows. In Sec. II, we derive the acoustic eigenvalue equation. In Sec. III, we discuss the application of the IN/GB method to the acoustic eigenvalue problem. In particular, we derive limits and approximations of eigenvalues that yield "good" initial guesses for intervals used in this method. These limits and approximations are useful not only for efficient implementation of the IN/GB method, but find more general applications. The subsequent sections describe three numerical experiments. In Sec. IV, we evaluate acoustic eigenvalues using the IN/GB method for a one-dimensional problem. In Sec. V, we evaluate the modal solution for a point source problem and compare our results with a benchmark solution obtained using the finite element method (FEM). In Sec. VI, we estimate room reverberation times using the acoustic eigenvalues, and compare our results with calculations using the finite-difference time-domain (FDTD) method.[13] We make concluding remarks in Sec. VII. In the Appendices, we review interval arithmetic first, and then describe the IN/BG method for single and multiple variable problems, of which the latter is required for solving the acoustic eigenvalue equation.

II. ACOUSTIC EIGENVALUE EQUATIONS

Normal modes of a rectangular room are obtained by solving the homogeneous Helmholtz (reduced wave) equation. For a room with uniform impedance on each of its walls, the three-dimensional homogeneous Helmholtz problem for the acoustic pressure $p(x,y,z)$ is described as

$$-\nabla^2 p - k^2 p = 0, \quad \text{in } \Omega, \tag{1}$$

$$\nabla p \cdot \mathbf{n} = -i\frac{\rho c}{Z_j} kp = -i\eta_j kp, \quad \text{on } \Gamma_j, \tag{2}$$

where Ω is the entire space of the room, Γ_j is the jth wall whose impedance is denoted by Z_j, i is the imaginary unit, $k=\omega/c$ is the driving wave number with angular frequency ω, c is the speed of sound, $\mathbf{n}$ is the outward normal unit vector on the walls, ρ is the density of the medium inside the room, and $\eta_j=\rho c/Z_j$ are the specific acoustic admittances of the walls. Figure 1 shows the coordinate system used for this problem. The domain is $\Omega=(0,L_x)\times(0,L_y)\times(0,L_z)$.

The solution of this homogeneous Helmholtz problem can be obtained by the separation of variables.[1–5] Exponentials are chosen as the eigenfunctions in this study; for example, the eigenfunction in the x direction is given in the form

$$\phi_x(x) = Ae^{ik_x x} + Be^{-ik_x x}, \tag{3}$$

where k_x (which is generally a complex value) is the eigenvalue in the x direction, and A and B are complex constants. After applying Eq. (3) to the boundary conditions Eqs. (2) at $x=0$ and $x=L_x$, the lth eigenfunction in the x direction is obtained as

$$\phi_{xl}(x) = (k_{xl} + \eta_1 k)e^{ik_{xl}x} + (k_{xl} - \eta_1 k)e^{-ik_{xl}x}, \tag{4}$$

where η_1 is the specific acoustic admittance at $x=0$. k_{xl} is the lth root of k_x for the following acoustic eigenvalue equation:

$$e^{i2k_x L_x} = \frac{(k_x - \eta_1 k)(k_x - \eta_2 k)}{(k_x + \eta_1 k)(k_x + \eta_2 k)}, \tag{5}$$

in which η_2 is the specific acoustic admittance at $x=L_x$. The eigenfunctions and eigenvalues in the y and z directions can be defined in the similar manner.

Since Eq. (5) is a nonlinear equation involving exponentials, its analytical solution is not feasible. Hence, it must be solved numerically, using a method that will yield all roots in a given interval. The solution of this problem using standard Newton's iteration with several initial guesses is fraught with difficulties, as different guesses might lead to the same root and it is impossible to determine if all roots within an interval have been estimated.

With this as motivation, the applicability of the IN/GB method for solving this problem is explored. The IN/GB method evaluates all possible solutions of a nonlinear equation system within a given range, and is therefore an appropriate method for finding all important eigenvalues of the acoustic eigenvalue equation. Interval arithmetic and the IN/GB method are reviewed in the Appendices. For a more detailed analysis of this method, the reader is referred to Refs. 9–12.

III. APPLICATION OF IN/GB METHOD TO ACOUSTIC EIGENVALUE EQUATIONS

A. Formulation of acoustic eigenvalue equation for IN/GB method

The IN/GB method is defined for real intervals (see the Appendices). However, the approach can be used to find complex roots in the acoustic eigenvalue equation, Eq. (5), by splitting the complex values into real and imaginary parts. Two separate equations derived from the real and imaginary components can then be written as $f_1(k_{xR},k_{xI})=0$ and $f_2(k_{xR},k_{xI})=0$, respectively. In this study, the following form is considered:

$$
\begin{aligned}
&f_1(k_{xR},k_{xI})\\
&\quad\equiv (k_{xR}-\eta_{1R}k)(k_{xR}-\eta_{2R}k)-(k_{xI}-\eta_{1I}k)(k_{xI}-\eta_{2I}k)\\
&\quad\quad -e^{-2k_{xI}L_x}\{\cos(2k_{xR}L_x)[(k_{xR}+\eta_{1R}k)(k_{xR}+\eta_{2R}k)\\
&\quad\quad -(k_{xI}+\eta_{1I}k)(k_{xI}+\eta_{2I}k)]-\sin(2k_{xR}L_x)[(k_{xR}+\eta_{1R}k)\\
&\quad\quad \times(k_{xI}+\eta_{2I}k)+(k_{xI}+\eta_{1I}k)(k_{xR}+\eta_{2R}k)]\}=0, \qquad (6)
\end{aligned}
$$

$$
\begin{aligned}
&f_2(k_{xR},k_{xI})\\
&\quad\equiv (k_{xR}-\eta_{1R}k)(k_{xI}-\eta_{2I}k)+(k_{xI}-\eta_{1I}k)(k_{xR}-\eta_{2R}k)\\
&\quad\quad -\{\cos(2k_{xR}L_x)[(k_{xR}+\eta_{1R}k)(k_{xI}+\eta_{2I}k)\\
&\quad\quad +(k_{xI}+\eta_{1I}k)(k_{xR}+\eta_{2R}k)]+\sin(2k_{xR}L_x)[(k_{xR}+\eta_{1R}k)\\
&\quad\quad \times(k_{xR}+\eta_{2R}k)-(k_{xI}+\eta_{1I}k)(k_{xI}+\eta_{2I}k)]\}=0. \qquad (7)
\end{aligned}
$$

The subscripts R and I denote the real and imaginary parts, respectively. Equations (6) and (7) are solved for k_{xR} and k_{xI} using the multivariate IN/GB method.

B. Limits and approximations of acoustic eigenvalues

Although the IN/GB method is guaranteed to find all roots in a given interval, an intelligent choice of the initial intervals makes it more efficient. In this section, the limits and the asymptotic behavior of the acoustic eigenvalues are derived in three theorems. Taken together, these three theorems significantly reduce the size of the initial intervals (from the entire complex plane).

Theorem 1: *The solutions of the acoustic eigenvalue equation appear in pairs of opposite signs.*

Proof: Replacing k_x by $-k_x$ in the acoustic eigenvalue equation, Eq. (5) leads to the same equation. Hence, if $\hat{k}_x$ is a solution of Eq. (5), then $-\hat{k}_x$ also satisfies this equation. ■

This theorem illustrates that it is sufficient to find solutions in only half of the complex plane. In this study, $k_{xI}\geqslant 0$ is considered. In this half-plane, $0<e^{-2k_{xI}L_x}\leqslant 1$ in Eqs. (6) and (7), while on the other half of the plane, it grows to infinity as k_{xI} decreases. For this reason, solutions are sought, even for $k_{xR}\leqslant 0$, although nonpositive values of k_{xR} are of no interest from a physical point of view. If a root with negative real part is found, then the root that has the opposite sign is an eigenvalue of interest.

While the lower limit of k_{xI} is determined from Theorem 1, the next theorem indicates that k_{xI} cannot be infinite. Taken together, these two theorems show that the interval to be searched for the imaginary parts of roots can be restricted to a moderate range.

Theorem 2: *Let $\hat{k}_{xR}$ and $\hat{k}_{xI}$ be the real and imaginary parts of a root of the acoustic eigenvalue equation, respectively. If $\hat{k}_{xI}\geqslant 0$, then $\hat{k}_{xI}$ is not much larger than* $\max\{1/2L_x,|\eta_1 k|,|\eta_2 k|\}$.

Proof: Let ε be a real number such that $|\varepsilon|\ll 1$. If $\hat{k}_{xI}\gg 1/2L_x,|\eta_1 k|,|\eta_2 k|$, then $e^{-2\hat{k}_{xI}L_x}$, $\eta_{1R}k/\hat{k}_{xI}$, $\eta_{1I}k/\hat{k}_{xI}$, $\eta_{2R}k/\hat{k}_{xI}$, and $\eta_{2I}k/\hat{k}_{xI}$ can be represented in terms of ε as $e^{-1/(a_e\varepsilon)}$, $a_{1R}\varepsilon$, $a_{1I}\varepsilon$, $a_{2R}\varepsilon$, and $a_{2I}\varepsilon$, respectively, where a's satisfy $|a|\leqslant 1$. Dividing Eqs. (6) and (7) by $\hat{k}_{xI}^2$ and denoting $\hat{k}_{xR}/\hat{k}_{xI}$ by ρ gives

$$
\begin{aligned}
&(\rho-a_{1R}\varepsilon)(\rho-\alpha_{2R}\varepsilon)-(1-a_{1I}\varepsilon)(1-a_{2I}\varepsilon)\\
&\quad=e^{-1/(a_e\varepsilon)}\{\cos(2\hat{k}_{xR}L_x)[(\rho+a_{1R}\varepsilon)(\rho+a_{2R}\varepsilon)\\
&\quad\quad -(1+a_{1I}\varepsilon)(1+a_{2I}\varepsilon)]\\
&\quad\quad -\sin(2\hat{k}_{xR}L_x)[(\rho+a_{1R}\varepsilon)(1+a_{2I}\varepsilon)\\
&\quad\quad +(1+a_{1I}\varepsilon)(\rho+a_{2R}\varepsilon)]\}, \qquad (8)
\end{aligned}
$$

$$
\begin{aligned}
&(\rho-a_{1R}\varepsilon)(1-a_{2I}\varepsilon)+(1-a_{1I}\varepsilon)(\rho-a_{2R}\varepsilon)\\
&\quad=e^{-1/(a_e\varepsilon)}\{\cos(2\hat{k}_{xR}L_x)[(\rho+a_{1R}\varepsilon)(1+a_{2I}\varepsilon)\\
&\quad\quad +(1+a_{1I}\varepsilon)(\rho+a_{2R}\varepsilon)]\\
&\quad\quad +\sin(2\hat{k}_{xR}L_x)[(\rho+a_{1R}\varepsilon)(\rho+a_{2R}\varepsilon)\\
&\quad\quad -(1+a_{1I}\varepsilon)(1+a_{2I}\varepsilon)]\}. \qquad (9)
\end{aligned}
$$

ρ can be expanded in a perturbation series as

$$\rho=\rho_0+\varepsilon\rho_1+\varepsilon^2\rho_2+\cdots . \qquad (10)$$

Substituting this expansion in Eqs. (8) and (9) and collecting terms of $O(\varepsilon^0)$ yields

$$\rho_0^2=1, \qquad (11)$$

$$\rho_0=0. \qquad (12)$$

As these two equations are contradictory, the assumption must be incorrect, and hence $\hat{k}_{xI}$ is not much larger than $\max\{1/2L_x,|\eta_1 k|,|\eta_2 k|\}$ if $\hat{k}_{xI}\geqslant 0$.

The next theorem shows that when the magnitude of the real part of the eigenvalue is large, the eigenvalue can be roughly estimated (see also Ref. 2).

Theorem 3: *Let $\hat{k}_{xR}$ and $\hat{k}_{xI}$ be the real and imaginary parts of a root of the acoustic eigenvalue equation, respectively. If $|\hat{k}_{xR}|\gg\max\{|\eta_1 k|,|\eta_2 k|\}$, then $|\hat{k}_{xR}|\approx n\pi/L_x$, where n is an integer, and $\hat{k}_{xI}\approx 0$.*

Proof: If $|\hat{k}_{xR}|\gg\max\{|\eta_1 k|,|\eta_2 k|\}$, then a real number ε with $|\varepsilon|\ll 1$ can be introduced to represent $\eta k/\hat{k}_{xR}$ as $\eta_{1R}k/\hat{k}_{xR}=a_{1R}\varepsilon$, $\eta_{1I}k/\hat{k}_{xR}=a_{1I}\varepsilon$, $\eta_{2R}k/\hat{k}_{xR}=a_{2R}\varepsilon$, and $\eta_{2I}k/\hat{k}_{xR}=a_{2I}\varepsilon$, respectively, where $|a|\leqslant 1$. Using the notation $\rho=\hat{k}_{xI}/\hat{k}_{xR}$, the division of Eqs. (6) and (7) by $\hat{k}_{xR}^2$ leads to

$$
\begin{aligned}
&(1-a_{1R}\varepsilon)(1-a_{2R}\varepsilon)-(\rho-a_{1I}\varepsilon)(\rho-a_{2I}\varepsilon)\\
&\quad=e^{-2\hat{k}_{xI}L_x}\{\cos(2\hat{k}_{xR}L_x)[(1+a_{1R}\varepsilon)(1+a_{2R}\varepsilon)\\
&\quad\quad -(\rho+a_{1I}\varepsilon)(\rho+a_{2I}\varepsilon)]\\
&\quad\quad -\sin(2\hat{k}_{xR}L_x)[(1+a_{1R}\varepsilon)(\rho+a_{2I}\varepsilon)\\
&\quad\quad +(\rho+a_{1I}\varepsilon)(1+a_{2R}\varepsilon)]\}, \qquad (13)
\end{aligned}
$$

$$
\begin{aligned}
&(1-a_{1R}\varepsilon)(\rho-a_{2I}\varepsilon)+(\rho-a_{1I}\varepsilon)(1-a_{2R}\varepsilon)\\
&\quad=e^{-2\hat{k}_{xI}L_x}\{\cos(2\hat{k}_{xR}L_x)[(1+a_{1R}\varepsilon)(\rho+a_{2I}\varepsilon)\\
&\quad\quad +(\rho+a_{1I}\varepsilon)(1+a_{2R}\varepsilon)]\\
&\quad\quad +\sin(2\hat{k}_{xR}L_x)[(1+a_{1R}\varepsilon)(1+a_{2R}\varepsilon)\\
&\quad\quad -(\rho+a_{1I}\varepsilon)(\rho+a_{2I}\varepsilon)]\}. \qquad (14)
\end{aligned}
$$

Substituting the perturbation expansion of ρ in Eq. (10) into Eqs. (13) and (14) and focusing on the terms of $O(\varepsilon^0)$ shows that

$$(\rho_0^2-1)[e^{-2\hat{k}_{xI}L_x}\cos(2\hat{k}_{xR}L_x)-1]+2\rho_0 e^{-2\hat{k}_{xI}L_x}\sin(2\hat{k}_{xR}L_x)=0, \tag{15}$$

$$2\rho_0[e^{-2\hat{k}_{xI}L_x}\cos(2\hat{k}_{xR}L_x)-1]-(\rho_0^2-1)e^{-2\hat{k}_{xI}L_x}\sin(2\hat{k}_{xR}L_x)=0. \tag{16}$$

The elimination of ρ_0 reduces these two equations to

$$[e^{-2\hat{k}_{xI}L_x}\cos(2\hat{k}_{xR}L_x)-1]^2+[e^{-2\hat{k}_{xI}L_x}\sin(2\hat{k}_{xR}L_x)]^2=0. \tag{17}$$

This implies that

$$e^{-2\hat{k}_{xI}L_x}\cos(2\hat{k}_{xR}L_x)=1, \tag{18}$$

$$e^{-2\hat{k}_{xI}L_x}\sin(2\hat{k}_{xR}L_x)=0. \tag{19}$$

The solutions of these equations are

$$\hat{k}_{xR}=\frac{n\pi}{L_x}, \tag{20}$$

$$\hat{k}_{xI}=0, \tag{21}$$

where n is an integer. ■

Theorem 3 indicates that if the magnitude of the real part of the solution is large relative to $|\eta_1 k|$ and $|\eta_2 k|$, then it is sufficient to find eigenvalues near $k_x=n\pi/L_x$, which are the eigenvalues when the walls are perfectly rigid both on $x=0$ and $x=L_x$. Therefore, the initial intervals used in the IN/GB method can be small and set only near $k_x=n\pi/L_x$ for large k_{xR}. Alternatively, the classical Newton iterative method can be used for Eq. (5) with the complex variable k_x for $|k_{xR}|\gg|\eta_1 k|,|\eta_2 k|$ with initial guesses $n\pi/L_x$. In either case, the knowledge of the approximate solutions can be used to vastly improve the computational efficiency.

In summary, the region on the complex plane in which the eigenvalues are sought can be restricted as follows:

(1) $0\leqslant k_{xI}$.
(2) k_{xI} is not much larger than $\max\{1/2L_x,|\eta_1 k|,|\eta_2 k|\}$.
(3) Near $k_x=n\pi/L_x$, if $|k_{xR}|\gg|\eta_1 k|,|\eta_2 k|$.

Although the limits and approximations of acoustic eigenvalues are derived to improve the efficiency of the IN/GB implementation, they may be applied to all methods for finding acoustic eigenvalues and are not restricted to the IN/GB method.

In the following sections, three numerical experiments are performed to show the accuracy, efficiency, and the utility of the IN/GB method.

IV. NUMERICAL EXPERIMENT 1: EIGENVALUE CALCULATION

Eigenvalues in the x direction were found by implementing the multivariate IN/GB method for solving the eigenvalue equations [Eqs. (6) and (7)] for driving wave numbers $k=2$, 10, and 20. These wave numbers correspond roughly to the frequencies of 100, 500, and 1000 Hz, respectively. In all calculations, $L_x=1$ m, and the specific acoustic admittances of the walls were set based on Fig. 1 in Ref. 14, which shows the specific acoustic impedances of some commercial acoustic materials with rigid wall backing. At each frequency, the specific impedances of Celotex C-4 1.25 in. and Johns-Manville Acoustex 0.88 in. were obtained from this figure. The impedances of the former material were used at $x=0$ and the latter at $x=1$. Table I shows the specific acoustic impedances used in the calculations. Because typical impedances of commercial materials were used, the resulting boundary conditions represent a real-world situation. Based on Theorems 2 and 3 derived in the previous section, the initial intervals for k_{xI} were set at $[0,10\max\{1/2L_x,|\eta_1 k|,|\eta_2 k|\}]$.

TABLE I. Specific acoustic impedances $Z_1/\rho c$ (on $x=0$) and $Z_2/\rho c$ (on $x=L_x$).

k	$Z_1/\rho c$	$Z_2/\rho c$
2	3.0−16.0 i	3.0−25.0 i
10	2.5−2.0 i	1.5−5.0 i
20	3.0+2.0 i	1.5−2.0 i

The implementation of the IN/GB algorithm requires an interval arithmetic software package. While some compilers support interval arithmetic,[15] public domain software is also available in several programming languages.[16] INTLIB[17] was used to implement interval arithmetic in this study.

The ten eigenvalues with the smallest real parts are shown in Fig. 2 and Table II for each driving wave number k. Results show that there are a few eigenvalues whose imaginary parts are much larger than the others, e.g., the first eigenvalue for $k=2$ and the second eigenvalues for $k=10$ and $k=20$. The magnitudes of the eigenfunctions corresponding to these roots change more rapidly in space than others [see Eq. (4)]. Although such roots are hard to find by some numerical methods,[7] the IN/GB method succeeds in finding them. Note that this method is guaranteed to find all roots

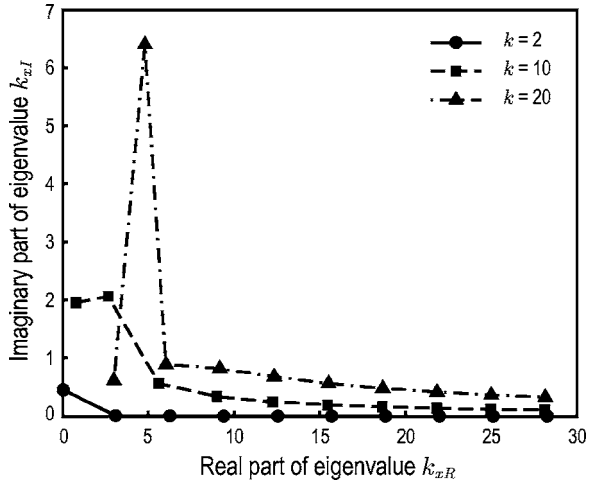

FIG. 2. The ten eigenvalues with the smallest real parts in the x direction with $L_x=1$ m and with boundary impedances shown in Table I.

TABLE II. The ten eigenvalues with the smallest real parts in the x direction with $L_x=1$ m and with boundary impedances shown in Table I.

	$k=2$	$k=10$	$k=20$
1	0.0370+0.4524 i	0.7631+1.9528 i	2.9873+0.6154 i
2	3.0768+0.0106 i	2.6597+2.0652 i	4.8000+6.4000 i
3	6.2513+0.0052 i	5.6177+0.5628 i	6.0268+0.8930 i
4	9.4036+0.0034 i	9.0063+0.3390 i	9.1681+0.8216 i
5	12.5505+0.0026 i	12.2582+0.2467 i	12.3426+0.6812 i
6	15.6952+0.0020 i	15.4635+0.1947 i	15.5169+0.5668 i
7	18.8390+0.0017 i	18.6467+0.1611 i	18.6849+0.4814 i
8	21.9821+0.0015 i	21.8177+0.1375 i	21.8473+0.4171 i
9	25.1248+0.0013 i	24.9813+0.1200 i	25.0053+0.3674 i
10	28.2672+0.0011 i	28.1398+0.1065 i	28.1602+0.3280 i

within a given interval. These results also indicate that it is not appropriate to assume $k_{xR} \gg k_{xI}$, an assumption that has been previously used.[1,2,5]

Whereas Table II and Fig. 2 also validate that the eigenvalues obey the limits and asymptotic behavior derived in Sec. III, these properties are more clearly seen in Fig. 3, which shows the first 1000 eigenvalues ordered by the magnitudes of their real parts. Results show that k_{xI} approaches zero with increasing k_{xR}, as indicated by Theorem 3, and that when k_{xR} is large, the rate of change of k_{xI} with respect to k_{xR} is approximately $O(k_{xR}^{-1})$ for all the driving wave numbers k. The behavior of k_{xR} is shown in more detail in Fig. 4. This figure shows the difference between k_{xlR}, the real part of the lth eigenvalue, and the nearest $n\pi/L_x$. As expected from Theorem 3, k_{xlR} converges to $n\pi/L_x$ as the mode number l grows, and the convergence rate is found to be approximately $O(l^{-1})$ for all driving frequencies.

The efficiency of the IN/GB algorithm is demonstrated by the observation that 1000 eigenvalues were calculated in about 10 s for all the wave numbers mentioned above on a computer with a 2.4 GHz CPU.

V. NUMERICAL EXPERIMENT 2: MODAL SOLUTION

As an application of the eigenvalues obtained using the IN/GB method, the modal solution of the Helmholtz problem

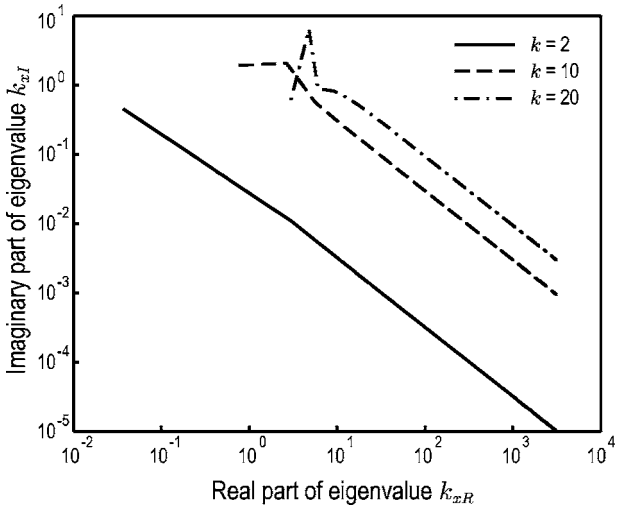

FIG. 3. The 1000 eigenvalues with the smallest real parts in the x direction with $L_x=1$ m and with boundary impedances shown in Table I.

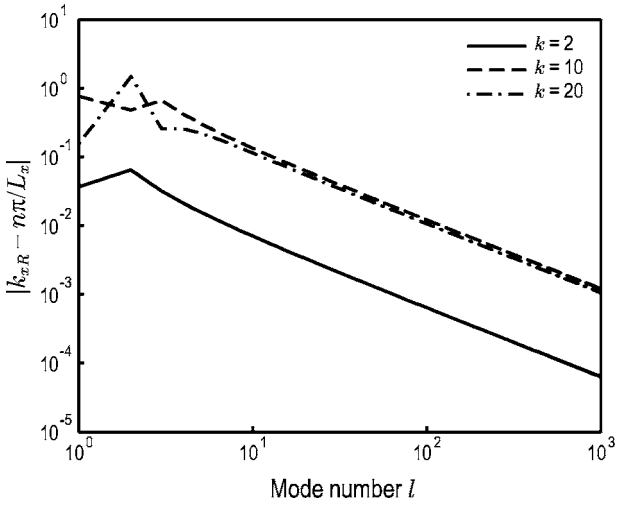

FIG. 4. Difference between the real part of each eigenvalue k_{xR} and the nearest $n\pi/L_x$, which is the eigenvalue when the walls are perfectly rigid.

in a two-dimensional rectangular room is calculated. The modal solution is then compared with the benchmark solution computed using the finite element method (FEM) to discuss the accuracy of the modal solution and hence the validity of the application of the IN/GB approach to the acoustic eigenvalue equation.

The problem domain is the rectangle on the xy plane in Fig. 1, and the size of the room is 1 m $\times$ 1 m (i.e., $L_x=L_y=1$ m). The governing equation is the inhomogeneous Helmholtz equation, given by

$$-\nabla^2 p - k^2 p = \delta(\mathbf{x}-\mathbf{x_s}), \tag{22}$$

in which $\mathbf{x_s}$ is the source position, set at the center of the room, i.e., $\mathbf{x_s}=(x_s,y_s)=(0.5,0.5)$. On the walls at $x=0$ and $x=L_x$, the impedance boundary conditions listed in Table I are imposed for driving wave numbers $k=2,10,20$. The walls on $y=0$ and $y=L_y$ are rigid with a specific acoustic admittance of zero.

A. Modal solution

1. Derivation of modal solution

Once all the eigenvalues in x and y directions are found, the modal solution of Eq. (22) is expressed in the series expansion in terms of the eigenfunctions as

$$p(x,y) = \sum_{l=1}^{\infty}\sum_{m=1}^{\infty} \tilde{A}_{lm}\phi_{xl}(x)\phi_{ym}(y), \tag{23}$$

where $\tilde{A}_{lm}$ are constants to be determined. The lth eigenfunction in the x direction $\phi_{xl}(x)$ is defined by Eq. (4), and similarly for $\phi_{ym}(y)$.

When walls have nonzero acoustic admittance, the eigenfunctions $\phi_{xl}(x)$ are orthogonal in the sense that

$$\int_0^{L_x} \phi_{xl}\phi_{xl'}\,dx = \Lambda_{xl}\delta_{ll'} \quad \text{(no sum on } l\text{)}, \tag{24}$$

where $\delta_{ll'}$ is the Kronecker delta function and

$$\Lambda_{xl} = \int_0^{L_x} \phi_{xl}^2 \, dx \tag{25}$$

$$= 2L_x[k_{xl}^2 - (\eta_1 k)^2] - \frac{i}{2k_{xl}}[(k_{xl} + \eta_1 k)^2(e^{i2k_{xl}L_x} - 1) - (k_{xl} - \eta_1 k)^2(e^{-i2k_{xl}L_x} - 1)]. \tag{26}$$

Note that in Eq. (24), ϕ_{xl} is multiplied by $\phi_{xl'}$, and not by the complex conjugate of $\phi_{xl'}$. This orthogonality can be proven by explicitly evaluating the integral in Eq. (24) and using the fact that k_{xl} satisfy the corresponding acoustic eigenvalue equation, Eq. (5). The eigenfunction is normalized as

$$\psi_{xl}(x) = \frac{\phi_{xl}(x)}{\sqrt{\Lambda_{xl}}}. \tag{27}$$

The modal solution is represented in terms of the orthonormal eigenfunctions as

$$p(x,y) = \sum_{l=1}^{\infty} \sum_{m=1}^{\infty} A_{lm} \psi_{xl}(x) \psi_{ym}(y). \tag{28}$$

A_{lm} are obtained by using the orthogonality of the eigenfunctions, an approach routinely used when the solution is sought for rigid walls. Substituting series expansion, Eq. (28), into the inhomogeneous Helmholtz equation Eq. (22) and making use of the orthonormal property of the eigenfunctions, the modal solution is given by

$$p(x,y) = \sum_{l=1}^{\infty} \sum_{m=1}^{\infty} \frac{1}{k_{lm}^2 - k^2} \psi_{xl}(x) \psi_{ym}(y) \psi_{xl}(x_s) \psi_{ym}(y_s), \tag{29}$$

where k_{lm} are the eigenvalues of the room defined by

$$k_{lm}^2 = k_{xl}^2 + k_{ym}^2. \tag{30}$$

The real parts of k_{lm} correspond to eigenfrequencies or resonance frequencies for the room, while the imaginary parts are the damping constants.[1,5]

Because of the rigid boundary conditions on $y=0$ and $y=L_y$, the eigenfunctions in the y direction are given by [see Eq. (4)]

$$\psi_{ym}(y) = \sqrt{\frac{\epsilon_m}{L_y}} \cos\left(\frac{m\pi}{L_y} y\right), \tag{31}$$

where ϵ_m is the Neumann factor with the value $\epsilon_m = 1$ if $m = 0$ but $\epsilon_m = 2$ if $m \geqslant 1$, and the eigenvalues are given by

$$k_{ym} = m\pi/L_y, \quad m = 0,1,2, \ldots . \tag{32}$$

Substituting these eigenfunctions and eigenvalues into Eq. (29), the modal solution for the entire problem is

$$p(x,y) = \sum_{l=1}^{\infty} \sum_{m=0}^{\infty} \frac{1}{k_{xl}^2 + (m\pi/L_y)^2 - k^2} \times \frac{\epsilon_m}{L_y} \psi_{xl}(x_s) \cos\left(\frac{m\pi}{L_y} y_s\right) \psi_{xl}(x) \cos\left(\frac{m\pi}{L_y} y\right). \tag{33}$$

2. Truncated modal solution

The modal solution is expressed by the infinite series given in Eq. (33); however, in practice, this series is truncated at a finite number of modes. As the truncation criterion, R is introduced such that all normal modes satisfying

$$r_{lm} \equiv |k_{lm}^2 - k^2|^{1/2} \leqslant R \tag{34}$$

are included in the summation. With this criterion, the truncated modal solution is defined as

$$p_R(x,y) = \sum_{\substack{l,m \\ r_{lm} \leqslant R}} \frac{\epsilon_m}{(k_{lm}^2 - k^2) L_y} \psi_{xl}(x_s) \cos\left(\frac{m\pi}{L_y} y_s\right) \psi_{xl}(x) \cos\left(\frac{m\pi}{L_y} y\right). \tag{35}$$

B. Finite element solution

For comparison, the same interior Helmholtz problem was solved using the FEM. In this simulation a uniform mesh of square elements with bilinear interpolations was used. The edge of each square element was 0.002 m long. This corresponded to 1571, 314, and 157 elements per wavelength for $k=2$, 10, and 20, respectively. With this resolution, the finite element solution converges well for all the driving wave numbers considered. Thus, the finite element solution provides a reliable benchmark solution and was used to check the validity of the modal solution.

C. Comparison of modal and finite element solutions

The modal solution was compared with the finite element solution at the nodal points used in the finite element analysis. Nodes inside a square region with a side length of 0.1 m centered at the source position were excluded from the comparison because the analytical solution is unbounded at the source and the finite element solution does not capture this behavior accurately.

The normalized error of the truncated modal solution with respect to the finite element solution is defined by

$$e_R = \sqrt{\frac{\sum_i |p_{\text{fem}}(\mathbf{x_i}) - p_R(\mathbf{x_i})|^2}{\sum_i |p_{\text{fem}}(\mathbf{x_i})|^2}}, \tag{36}$$

where p_{fem} is the finite element solution, and $\mathbf{x_i}$ are the nodal points. As the FEM solution is an accurate approximation of the exact solution, the convergence rate of the normalized error e_R with respect to the truncation criterion R must be the same as that of the analytical truncation error. Figure 5 shows the normalized error e_R as a function of R. The log–log plot shows that for all driving wave numbers k, the error decreases with increasing R with a convergence rate of approximately $O(R^{-1})$. It can be shown that the truncation error for a room with rigid walls also varies as R^{-1}. This observation validates the accuracy of the eigenvalues and the IN/GB method.

The result also strongly supports the assertion that the terms in the summation in Eq. (29) become increasingly less important as $|k_{lm}^2 - k^2|$ increases. Thus, there is an easy-to-

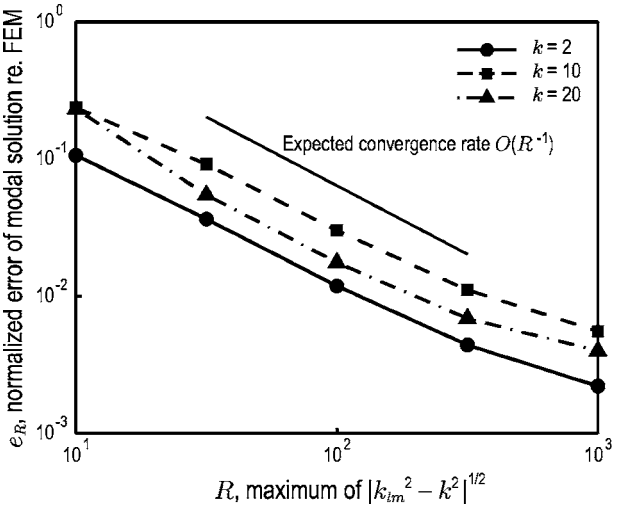

FIG. 5. Normalized difference between the modal solution and the finite element solution with a mesh size of 0.002 m as a function of R, the maximum value of $|k_{lm}^2 - k^2|^{1/2}$ included in the summation used to calculate the modal solution Eq. (35).

evaluate tradeoff between the accuracy of the modal solution and the number of terms included in the summation, and the IN/GB method can be used to find acoustic eigenvalues with whatever precision is desirable or necessary.

VI. NUMERICAL EXPERIMENT 3: ROOM REVERBERATION TIMES

As another example application of finding acoustic eigenvalues using the IN/GB approach, room reverberation times were calculated for three-dimensional rectangular rooms and then compared with the results obtained from the finite-difference time-domain (FDTD) method reported by Yasuda *et al.* in Ref. 13. The width and the depth of the room were L_x=24 m, L_y=12 m, respectively, and the height was either L_z=3 m or L_z=6 m. An absorber with absorption coefficient α=0.5 was installed either only at z=0 or both at z=0 and z=L_z. All other walls were assumed to have α =0.05. The corresponding specific acoustic impedances were all given as real values, i.e.,

$$\frac{Z}{\rho c} = \frac{1 + \sqrt{1-\alpha}}{1 - \sqrt{1-\alpha}}. \tag{37}$$

For these conditions, the reverberation times in 1/3 octave bands were calculated using the eigenvalues obtained by the IN/GB method.

In order to estimate the reverberation times, the collective modal decay curves were first obtained by

$$\langle p^2 \rangle(\Delta f, t) = 10 \log\left(\frac{\sum_{\Delta f} e^{-2k_{\mathbf{N}I}t}/k_{\mathbf{N}I}}{\sum_{\Delta f} 1/k_{\mathbf{N}I}} \right), \quad \text{in dB}, \tag{38}$$

where t is time, $\mathbf{N}$ is a trio of l, m, and n (the mode numbers in the x, y, and z directions, respectively), $k_{\mathbf{N}I}$ is the damping constant (the imaginary part of the eigenvalue $k_{\mathbf{N}}$), and the summation is over all eigenvalues whose eigenfrequencies (real parts of $k_{\mathbf{N}}$) are within the band Δf.[7,18] Although this decay curve is not exact, it roughly characterizes the energy

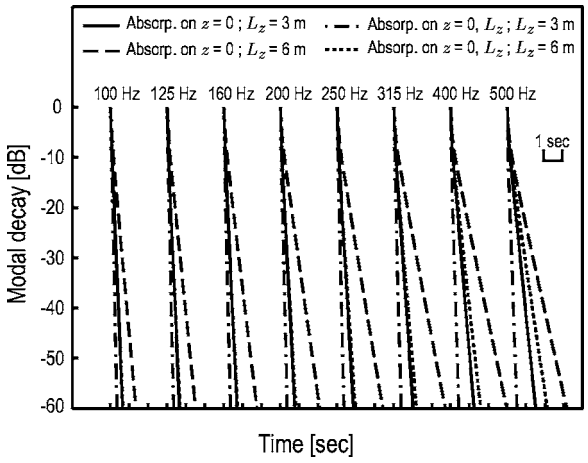

FIG. 6. Collective modal decay curves in 1/3 octave bands of rectangular rooms of size 24 m×12 m×L_z m. The height of the room is either L_z =3 m or 6 m, and an absorbing material is either only on z=0 or both on z=0 and z=L_z.

decay with time in a given frequency band. Figure 6 shows the decay curves obtained from Eq. (38) in 1/3 octave bands for all height and absorber configuration conditions mentioned above. The driving wave numbers k were set such that they correspond to the center frequencies of the 1/3 octave bands.

The reverberation times T_{60} were obtained from the modal decay curve, Fig. 6, and are plotted in Fig. 7 along with the reverberation times computed in Ref. 13, which used the FDTD approach to solve the same problem. A comparison between the room reverberation times using these two approaches shows that all trends are in close agreement. The only major distinction is that the reverberation times using the IN/GB method and decay curve, Eq. (38), are shorter than those found using the FDTD approach. However, the differences are consistent across all frequencies and conditions, and the correlation coefficient between the FDTD and modal decay with the IN/GB method (32 points corresponding to 8 frequency bands and 4 height/absorption con-

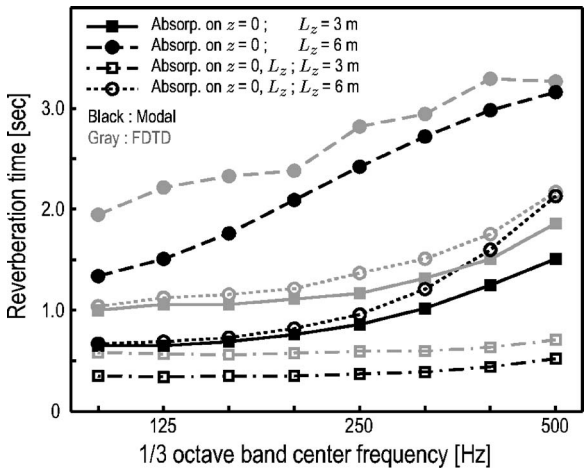

FIG. 7. Reverberation times of rectangular rooms of size 24 m×12 m ×L_z m. The height of the room is either L_z=3 or 6 m, and an absorbing material is either only on z=0 or both on z=0 and z=L_z. Data using the FDTD method were provided by Yasuda *et al.*, taken from their study, Ref. 13.

ditions for each method) is 0.9853. One possible reason for the systematic difference between the values found using the two approaches is that Eq. (38) is an approximation based on averaging the source and receiver positions over the entire room space, while the reverberation times were calculated in Ref. 13 for a specific source/receiver position.

Numerical approaches for finding reverberation times, such as finite element or finite difference methods, are computationally expensive, especially for large rooms or for high frequencies. On the other hand, the computational cost of finding reverberation times based on finding acoustic eigenvalues using the IN/GB method is considerably cheaper than these numerical methods.

VII. CONCLUSIONS

In this study, the IN/GB method was applied to the acoustic eigenvalue equation of a rectangular room with arbitrary, uniform wall impedances to find all eigenvalues within a given interval. Furthermore, the limits and asymptotic behavior of these eigenvalues were derived. These properties were used to restrict the interval range in the IN/GB method and to provide "good" initial guesses, increasing its efficiency in finding all eigenvalues. Several numerical tests were performed to validate the proposed method and to demonstrate its accuracy and efficiency. In the first test, it was verified that the roots obtained using the IN/GB method satisfied the analytical estimates we developed. In the second test, the IN/GB method was used to compute the modal solution corresponding to a point source in a two-dimensional room. This solution was compared with a well-resolved finite element solution, which was used as a benchmark. It was found that as the number of modes in the modal solution are increased, it converged to the FEM solution at the expected analytical rate. Finally, the IN/GB method was used to evaluate the reverberation times for a three-dimensional room with finite wall impedances. These results were compared with the FDTD results obtained by other researchers.[13] It was found that the IN/GB results were in good agreement with the FDTD results.

With the development of interval arithmetic software, it will become increasingly easy to apply the interval method. Therefore, in conjunction with the properties of acoustic eigenvalues derived in this study, the IN/GB method presents an efficient method for solving the acoustic eigenvalue equation for rectangular rooms with arbitrary, uniform wall impedances.

ACKNOWLEDGMENTS

This work was supported by a grant from the Air Force Office of Scientific Research. The authors are very grateful to Yosuke Yasuda, Shinichi Sakamoto, Ayumi Ushiyama, and Hideki Tachibana for their generosity in sharing with us the raw data from their paper, Ref. 13. Dr. Ning Xiang and two anonymous reviewers provided many helpful comments on earlier drafts of this paper.

APPENDIX A: INTERVAL ARITHMETIC

Real interval arithmetic operates on closed, real intervals. Let $X=[\underline{x},\overline{x}]$ denote a real interval with lower limit $\underline{x}$ and upper limit $\overline{x}$, and similarly define as $Y=[\underline{y},\overline{y}]$. The elementary interval operations are defined as follows:[9–12]

$$X+Y=[\underline{x}+\underline{y},\overline{x}+\overline{y}], \tag{A1}$$

$$X-Y=[\underline{x}-\overline{y},\overline{x}-\underline{y}], \tag{A2}$$

$$X\times Y=[\min\{\underline{x}\underline{y},\underline{x}\overline{y},\overline{x}\underline{y},\overline{x}\overline{y}\},\max\{\underline{x}\underline{y},\underline{x}\overline{y},\overline{x}\underline{y},\overline{x}\overline{y}\}], \tag{A3}$$

$$1/X=[1/\overline{x},1/\underline{x}], \quad \text{if } 0\notin X, \tag{A4}$$

$$X/Y=X\times 1/Y. \tag{A5}$$

Note that although the reciprocation $1/X$ or the division Y/X are undefined in ordinary interval arithmetic if $0\in X$, they can be defined in extended arithmetic.[11]

APPENDIX B: INTERVAL EXTENSION OF FUNCTIONS

Elementary functions, such as trigonometric functions and exponentials, can also be extended to work on intervals.[9–11] For a function $f(x):\mathbb{R}\rightarrow\mathbb{R}$, its interval extension $f(X)$ is defined such that

$$\{f(x)|x\in X\}\subseteq f(X). \tag{B1}$$

The definition of the interval extension of a function can also be more intuitively represented as

$$f(X)=[\min_{x\in X} f(x),\max_{x\in X} f(x)]. \tag{B2}$$

APPENDIX C: UNIVARIATE IN/GB METHOD

For a problem with only one variable, the mean value theorem implies

$$f(x)-f(x^*)=(x-x^*)f'(\xi), \tag{C1}$$

for some ξ satisfying $x\leqslant\xi\leqslant x^*$. In Eq. (C1), f' denotes the derivative of f. If x^* is the root of f [i.e., $f(x^*)=0$] and $f'(\xi)\neq 0$, then the root of f can be represented from Eq. (C1) as

$$x^*=x-\frac{f(x)}{f'(\xi)}. \tag{C2}$$

Now let X be an interval such that $x,x^*\in X$, and hence $\xi\in X$. If $f'(X)$ is the interval extension of $f'(x)$ over the interval X, then by definition $f'(\xi)\in f'(X)$. Therefore, the interval arithmetic formulation of Eq. (C2) becomes

$$x^*=x-\frac{f(x)}{f'(\xi)}\in x-\frac{f(x)}{f'(X)}\equiv N(x,X), \tag{C3}$$

where $N(x,X)$ is called the Newton operator. Thus, x^*, the root of f in X, must be in the intersection $X\cap N(x,X)$.

In each iteration step of the interval Newton method, the Newton operator is used to narrow the potential interval containing the roots. The nth iteration of the interval Newton method is defined as follows:

$$x^{(n)} = m(X^{(n)}), \tag{C4}$$

$$N(x^{(n)}, X^{(n)}) = x^{(n)} - \frac{f(x^{(n)})}{f'(X^{(n)})}, \tag{C5}$$

$$X^{(n+1)} = X^{(n)} \cap N(x^{(n)}, X^{(n)}), \tag{C6}$$

where $m(X)$ is the midpoint of X, calculated for $X=[\underline{x},\bar{x}]$ as

$$m(X) = \frac{\underline{x} + \bar{x}}{2}, \tag{C7}$$

and the number in parentheses in the superscripts denotes the iteration number. The input of the nth step is $X^{(n)}$ and the output is $X^{(n+1)}$.

The number of roots in X is then found from investigating the output interval based on the following properties:

(a) If $X^{(n+1)}=\emptyset$, i.e., if $N(x^{(n)},X^{(n)}) \cap X^{(n)}=\emptyset$, then there is no root of f in $X^{(n)}$.
(b) If $X^{(n+1)}=N(x^{(n)},X^{(n)},)$, i.e., if $N(x^{(n)},X^{(n)}) \subset X^{(n)}$, then f has a unique root in $X^{(n)}$.
(c) If neither (a) nor (b) is satisfied, then more than one root may exist in $X^{(n)}$.

Proofs of these properties can be found in Refs. 9–11 and 19. In case (a), the input interval $X^{(n)}$ can be discarded. In case (b) or (c), the output interval $X^{(n+1)}$ is used as the input of the next step to further narrow the interval.

If $X^{(n)}=X^{(n+1)}$, i.e., if $X^{(n)} \subseteq N(x^{(n)},X^{(n)})$, then the interval must be bisected. In such a case, the next step of the interval Newton method must be implemented for each of the divided intervals. The natural choice of the bisection point is the midpoint of the interval. When the interval Newton method is combined with this bisection technique, it is called the interval Newton/generalized bisection (IN/GB) method.

The number of roots in $X^{(n)}$ is known if $X^{(n+1)}$ satisfies the conditions of properties (a) or (b). In case (c), although the number of roots in $X^{(n)}$ is unknown, further IN/GB iterations lead all the subintervals of $X^{(n)}$ to either case (a) or (b). Therefore, after a certain number of iterations, it is assured that all subintervals that constitute the entire range of the initial interval have either zero or one root. Hence, once the roots are found in all subintervals in case (b), it is guaranteed that all roots in the initial interval are found.

The termination criteria of the iteration of the IN/GB implementation can be given by the residuals and/or the width of the intervals. Therefore, accuracy of the IN/GB solutions is easily controlled. Once the intervals containing unique roots are sufficiently small, any points inside these intervals can be taken as the approximate roots of the equation. Alternatively, a certain point inside such an interval can be used as the initial guess of a classical method to calculate a closer approximation of the root.

If $0 \in f'(X^{(n)})$, the division on the right-hand side of Eq. (C5) can be evaluated by extended interval arithmetic.[11] In this case, $N(x^{(n)},X^{(n)})$ may consist of two disjoint, semi-infinite intervals. However, after taking the intersection with the bounded interval $X^{(n)}$ in Eq. (C6), the output of nth iteration $X^{(n+1)}$ is bounded, although it may consist of two intervals. If the output of a certain iteration contains two intervals, the next IN/GB step must be implemented for each interval.

APPENDIX D: MULTIVARIATE IN/GB METHOD

For a problem with r variables, x, X, and f are extended in vector form as

$$\mathbf{x} = [x_1, x_2, \ldots, x_r]^T, \tag{D1}$$

$$\mathbf{X} = [X_1, X_2, \ldots, X_r]^T, \tag{D2}$$

$$\mathbf{f} = [f_1, f_2, \ldots, f_r]^T. \tag{D3}$$

Note that the components of $\mathbf{x}$ and $\mathbf{f}(\mathbf{x})$ are real numbers, while those of $\mathbf{X}$ and $\mathbf{f}(\mathbf{X})$ are real intervals. The simple multivariate extension of the Newton operator becomes

$$\mathbf{N}(\mathbf{x},\mathbf{X}) = \mathbf{x} - \mathbf{F}'(\mathbf{X})^{-1}\mathbf{f}(\mathbf{x}), \tag{D4}$$

where $\mathbf{F}'(\mathbf{X})$ is the interval extension of the Jacobian matrix of $\mathbf{f}(\mathbf{x})$. Unlike the univariate case, the multivariate Newton operator can be used only when the Jacobian matrix $\mathbf{F}'$ is not singular, i.e., $0 \notin \det\{\mathbf{F}'(\mathbf{X})\}$. If the Jacobian matrix is singular, computations of the matrix-vector product of $\mathbf{F}'(\mathbf{X})^{-1}$ and $\mathbf{f}(\mathbf{x})$ require the addition and/or subtraction of semi-infinite intervals; however, such operations are not defined. For this reason, the Krawczyk operator[9–11] is widely used for multivariate problems instead of the Newton operator.

In the Krawczyk method, the classical multivariate Newton method is treated as a fixed point iteration. The Krawczyk operator can be used even if the interval extension of the Jacobian matrix is singular. This operator is defined as

$$\mathbf{K}(\mathbf{x},\mathbf{X}) = \mathbf{x} - \mathbf{Y}\mathbf{f}(\mathbf{X}) + [\mathbf{I} - \mathbf{Y}\mathbf{F}'(\mathbf{X})](\mathbf{X} - \mathbf{x}), \tag{D5}$$

where $\mathbf{I}$ is the identity matrix. $\mathbf{Y}$ is an approximation of the inverse of the interval Jacobian matrix and $\mathbf{Y} = \{m[\mathbf{F}'(\mathbf{X})]\}^{-1}$ is frequently used, where m is the midpoint defined by Eq. (C7). The Krawczyk method can be used by extending Eqs. (C4)–(C6) to multivariate form and replacing the Newton operator by the Krawczyk operator.

[1] P. M. Morse and R. H. Bolt, "Sound waves in rooms," Rev. Mod. Phys. **16**, 69–150 (1944).
[2] L. Cremer and H. A. Müller, *Principles and Applications of Room Acoustics*, Vol. **2** (Applied Science Publishers, New York, 1982); english translation by T. J. Schultz.
[3] A. D. Pierce, *Acoustics—An Introduction to Its Physical Principles and Applications* (Acoustical Society of America, New York, 1994).
[4] D. T. Blackstock, *Fundamentals of Physical Acoustics* (Wiley-Interscience, New York, 2000).
[5] H. Kuttruff, *Room Acoustics*, 4th ed. (Spon Press, London, 2000).
[6] P. M. Morse, "The transmission of sound inside pipes," J. Acoust. Soc. Am. **11**, 205–210 (1939).
[7] S. R. Bistafa and J. W. Morrissey, "Numerical solutions of the acoustic eigenvalue equation in the rectangular room with arbitrary (uniform) wall impedances," J. Sound Vib. **263**, 205–218 (2003).
[8] S. L. Hodge, W. E. Zorumski, and W. R. Watson, "Solution of the three-dimensional Helmholtz equation with nonlocal boundary conditions," NASA Technical Memorandum 110174, 1995.
[9] R. E. Moore, *Methods and Applications of Interval Analysis* (SIAM, Philadelphia, 1979).
[10] A. Neumaier, *Interval Methods for Systems of Equations* (Cambridge University Press, Cambridge, 1990).

[11]R. B. Kearfott, *Rigorous Global Search: Continuous Problems* (Kluwer Academic, Dordrecht, 1996).
[12]T. Sunaga, "Theory of an interval algebra and its application to numerical analysis," in *RAAG Memoirs* (Gakujutsu Bunken Fukyu-kai, Tokyo, 1958), Vol. **2**, pp. 29–46 (547–564).
[13]Y. Yasuda, S. Sakamoto, A. Ushiyama, and H. Tachibana, "Reverberation characteristics in a room with unevenly-distributed absorbers: Numerical analysis," Acoust. Sci. Tech. **26**, 388–390 (2005).
[14]L. L. Beranek, "Acoustic impedance of commercial materials and the performance of rectangular rooms with one treated surface," J. Acoust. Soc. Am. **12**, 14–23 (1940).
[15]M. J. Schulte, A. Akkas, V. A. Zelov, and J. C. Burley, "Compiler support for interval arithmetic," in *Proceedings of the 16th IEEE Instrumentation and Measurement Technology Conference*, Venice, Italy, May 1999, pp. 1189–1193.
[16]C. Hu, S. Xu, and X. Yang, "A review on interval computation—Software and applications," Int. J. Comput. Numer. Anal. Appl. **1**, 149–162 (2002).
[17]R. B. Kearfott, M. Dawande, K. Du, and C. Hu, "INTLIB: A portable FORTRAN 77 interval standard-function library," ACM Trans. Math. Softw. **20**, 447–459 (1994).
[18]K. Bodlund, "Monotonic curvature of low frequency decay records in reverberation chambers," J. Sound Vib. **73**, 19–29 (1980).
[19]E. R. Hansen, *Topics in Interval Analysis* (Clarendon, Oxford, 1969).

Dynamic measurements of the elastic constants of glass wool

Viggo Tarnow[a)]
Department of Mechanical Engineering, Technical University of Denmark, Bygning 404, DK 2800 Lyngby, Denmark

(Received 29 November 2004; revised 16 September 2005; accepted 16 September 2005)

The sound wave in the air between the fibers of glass wool exerts an oscillatory viscous drag on the fibers and excites a mechanical wave in the fiber skeleton. Accurate calculations of sound attenuation in glass wool must take the mechanical wave in the fiber skeleton into account, and this requires knowledge of the dynamic elastic constants of the fiber skeleton. The mechanical properties of glass wool are highly anisotropic. Previously only one of the elastic constants has been measured dynamically, but here all the elastic constants are reported. The measurement method is well known. But a new mechanical design, which reduces mechanical resonance, is described. The measurements were carried out in atmospheric air at normal pressure, and this causes an oscillatory airflow in the sample. To obtain the elastic constants, the influence of the airflow was subtracted from the data by a new formula. The elastic constants were measured in the frequency range 20–160 Hz for glass wool of mass density 30 kg/m^3. The elastic constant C_{11} depended on the frequency; at 20 Hz it was $1.5+0.01i$ MPa, and at 160 Hz it was $2.6+0.06i$ MPa. The constant $C_{33}=12+0.6i$ kPa did not depend on frequency. The shear constant $C_{44}=40+2i$ kPa was constant. The two constants C_{12}, C_{13} were zero. © *2005 Acoustical Society of America.* [DOI: 10.1121/1.2118267]

PACS number(s): 43.55.Ev, 43.20.Jr, 43.58.Dj [AJZ] Pages: 3672–3678

I. INTRODUCTION

Glass wool is placed inside the fuselage of airplanes, where it reduces the noise transmissions from the outside to the inside of the cabin. Glass wool is also placed inside walls in buildings, where it reduces the transmission of noise through the walls.

Experiments in the last five years have shown that sound waves, in the air between fibers, drag the skeleton of fiber materials, and this causes movements of the fibers, which decreases the attenuation of sound waves.[1–4] Early measurements of sound attenuation in tubes did not show this, because samples were mounted in a way that prevented their movement. Recently[2,3] measurements have been carried out with thin samples fixed to the cylindrical surface of the tube. In this case, the skeleton of the material in the center of the tube can move.

The airborne sound wave is coupled to the fiber skeleton borne wave by an oscillatory viscous drag of air on the fibers. To take this into account by the Biot theory,[5] the dynamic elastic constants of the glass wool skeleton must be known.

Pritz[6] analyzed a measurement method where the glass wool sample is part of a spring as shown in Fig. 1. The shaker gave the lower part of the sample a displacement that was a sinusoidal function of time. Accelerometers measured the acceleration of the shaker table and the top plate. The amplitude and phase of the output from the two accelerometers were measured. From the complex ratio between the two accelerations, the length of the sample, the cross-section area, the mass of the sample, and the mass of the upper aluminum plate. Pritz calculated the complex Young modulus, and he made a detailed study of the measurement errors. Longitudinal wave movement was taken into account. It was assumed that the shaker and the upper aluminum plate moved translationally. In another paper[7] Pritz reported measurement, with the same setup, of the complex Young's modulus of glass wool of density 71 kg/m^3 for frequency 100–3 000 Hz. The measurements were carried out in air and vacuum.

Rice and Göransson[8] used a similar setup to measured a dynamic complex Young's modulus of glass wool with density 15 and 11 kg/m^3 for frequencies about 15 and 60 Hz. Measurement were carried out in air and vacuum. Ingard[9] used a similar setup to measure the complex Young's modulus of glass wool in vacuum.

To determine the complex Young's modulus of glass wool, Wilson and Cummings[10] used a setup with a force transducer that measured the force in the sample. The frequency range was 40–200 Hz. Figure 2 shows the principle. They first measured the complex mechanical impedance of one sample and then of a second sample with twice the thickness. From the two mechanical impedances and the length of the sample they calculated the complex wave number. The complex characteristic impedance was calculated from the measured impedances and the cross-sectional area. From frequency and the characteristic impedance, they calculated the effective mass density and Young's modulus. They assumed that their samples were homogeneous, and it was further assumed that there was no lateral movement of the sample—the Poisson's ratio was assumed to be zero. Langlois, Panneton, and Atalla[11] used an experimental arrangement similar to Fig. 2 to measure the elastic properties of isotropic plastic foam. They developed a new way to find Young's modulus and Poisson's ratio from measurements on samples of different thickness.

[a)]Electronic mail: vt@mek.dtu.dk

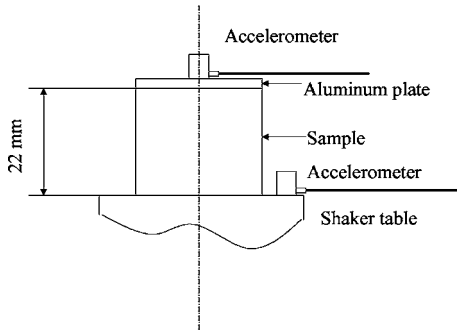

FIG. 1. Measurement principle with two moving surfaces, the sample is glued to the shaker table and the aluminum plate. The acceleration of the shaker table and the aluminum plate are measured.

The setup in Fig. 1 is attractive because it is simple. It was used in the beginning of the present study. The acceleration amplitude of the top plate and the shaker were recorded as a function of frequency. The acceleration amplitude of the top plate divided by the one of the shaker was plotted as a function of frequency. However, in many experiments the plot showed three resonance peaks between 200 and 300 Hz instead of only one as expected when the movement of the aluminum plate is a translation. The reason is that the top plate rocked, because the samples were not homogeneous. Pritz[6] assumed a translation; Cremer, Heckl, and Ungar[12] have observed excitation of rocking motions in similar experiments. Three modes of the top plate were excited. One mode is mainly a translation in the direction of dot-and-dash line in Fig. 1, the other modes are mainly rotations of the top plate. The movements of the top plate were detected by small accelerometers, which showed the accelerations of the three modes. Calculation of elastic constants from the data was unreliable, because three modes were excited.

The rotation of the upper plate was prevented in the setup in Fig. 2, and measurements reported in this paper were carried out with a similar setup. Measurements should ideally be carried out in a vacuum, but here they were performed in air. The movements of the shaker table pumped air through the sample, and the friction between air and fibers influence the measurement. Section II contains a derivation of a new formula used to corrects the data for the influence from airflow through the sample. Section II also shows a new way of correcting for wave movements in the fiber skeleton. The elastic constant can be measure with one sample, in

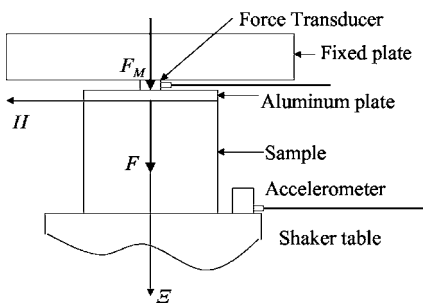

FIG. 2. Measurement principle with one moving surface, the force transducer fixes the aluminum plate. The force on the sample and the acceleration of the shaker table are measured. Ξ and H marks the axes of a coordinate system fixed on the aluminum plate.

contrast to the investigation by Wilson and Cummings[10] that requires two samples and assumed homogeneity of the samples. A new mechanical design is described in Sec. III, which also contains details of the electronic system.

Glass wool is anisotropic, but all the above-cited works present only measurements of one Young's modulus, the smallest one. Dynamic measurements of all the elastic constant are reported in Sec. IV, where all the dynamic elastic constants in the frequency range 20–160 Hz for glass wool of density 30 kg/m^3 are given. The results are compared with measurements of the elastic properties of glass wool in the papers Refs. 6–10.

II. PRINCIPLE OF MEASUREMENT

The elastic properties of glass wool are highly anisotropic. Glass wool mats are fabricated on a conveyer belt on which the glass fibers are laid. The glass wool is soft in the direction perpendicular to the conveyer belt and hard in all directions parallel to the belt. We use a coordinate system with Z axis in the soft direction, X axis in the direction the belt moves, and Y axis perpendicular to the first two axes. The standard nomenclature for elastic constants is used. Call the stress tensor σ_{pq} with p, $q=x$, y or z, and define a stress vector $\mathbf{\Sigma}=(\sigma_{xx},\sigma_{yy},\sigma_{zz},\sigma_{yz},\sigma_{xz},\sigma_{xy})$. Call the strain tensor ε_{pq}, and define the strain vector $\mathbf{E}=(\varepsilon_{xx},\varepsilon_{yy},\varepsilon_{zz},2\varepsilon_{yz},2\varepsilon_{xz},2\varepsilon_{xy})$: Then the elastic constants matrix $\mathbf{C}$ is defined by $\mathbf{\Sigma}=\mathbf{CE}$.

The $\mathbf{C}$ matrix is symmetrical. Rice and Göransson[8] state that their light glass wool is transversally isotropic. The glass wool studied her is also assumed transversally isotropic. Due to the symmetry, some components of the elastic constant matrix are zero, and some are equal, which is shown in the following matrix:

$$\begin{Bmatrix} C_{11} & C_{12} & C_{13} & 0 & 0 & 0 \\ . & C_{11} & C_{13} & 0 & 0 & 0 \\ . & . & C_{33} & 0 & 0 & 0 \\ . & . & . & C_{44} & 0 & 0 \\ . & . & . & . & C_{44} & 0 \\ . & . & . & . & . & \frac{1}{2}(C_{11}-C_{12}) \end{Bmatrix}. \quad (1)$$

The form of the matrix is given in Jones.[13]

Rice and Göransson[8] stated, based on static measurements, that the Poisson's ratios are zero. This is also assumed for the glass wool examined in this paper, and from Jones[13] it follows that $C_{12}=C_{12}=0$. Thus, the elastic constant matrix is diagonal, and it can be computed from the two Young's moduli E_1, E_3, and the shear module G,

$$\begin{Bmatrix} E_1 & 0 & 0 & 0 & 0 & 0 \\ . & E_1 & 0 & 0 & 0 & 0 \\ . & . & E_3 & 0 & 0 & 0 \\ . & . & . & G & 0 & 0 \\ . & . & . & . & G & 0 \\ . & . & . & . & . & \frac{1}{2}E_1 \end{Bmatrix}. \quad (2)$$

A. Calculating Young's modules from data

All samples were prismatic, cut perpendicular to one of the axes X, Y, and Z in the glass wool mats. Figure 2 shows the principle of the setup. The shaker was excited to give its table a simple harmonic motion, and the complex acceleration amplitude of the table A and the frequency f was recorded. The displacement of the table u_T can be calculated from the cyclic frequency $\omega=2\pi f$ and the amplitude of acceleration,

$$u_T = -A/\omega^2. \tag{3}$$

The complex force amplitude F_M measured by the force transducer was recorded. The force transducer was mounted on a plate that did not move, fixed plate in Fig. 2, and the force transducer was very stiff. Therefore the aluminum plate, on top of the sample, did not move, and the force on the transducer was equal to the force F on the sample, $F=F_M$. Airflow in the sample is neglected, but it will be considered in the next section. The frequency is assumed to be so low that wave motion in the sample may be neglected. This is the case when Young's module E_1 is determined. Then E_1 equals the stress divided by the strain, if the X axis of the sample is parallel to the Ξ axis of the apparatus. Stress is the force divided by the cross-section area of the sample S, and the strain is the displacement of the table divided by the length of the sample l. Thus,

$$E_1 = \frac{F/S}{u_T/l}. \tag{4}$$

There is no lateral strain because the elastic constants $C_{12}=0$ and $C_{13}=0$.

B. Airflow in the sample

During measurements air was pumped in and out of the sample by the movements of the shaker table. The airflow influenced the measurement of the imaginary part of the elastic constant, and this influence is calculated approximately in this section. First the energy loss P due to friction between air and fibers is calculated. An integral of the power loss density over the volume V of the sample gives P,

$$P = \int_V R_{rs} v_r v_s dV. \tag{5}$$

The velocity v_r is referred to the coordinate system in Fig. 2, with axes Ξ, H, and Z and coordinates (ξ, η, ς). The indices r, $s=\xi$, η, or ς, and repeated indices imply summation. The airflow resistivity R_{rs} is a tensor because the glass wool is anisotropic. Only the case where the resistivities are equal in all directions perpendicular to the Ξ axis is needed. It is assumed that the air is incompressible, because the wavelength of sound in the air between fibers is much longer than the dimension of the apparatus. The Ξ axis, Fig. 2, is the polar axis of a cylinder coordinate system with coordinates ξ, ρ, and φ, where ρ is the distance from the polar axis and φ the angle. The radial velocity of air v_ρ, perpendicular to the Ξ axis is, from the incompressibility of air, approximately

$$v_\rho = \frac{\pi\rho^2 v_T}{2\pi\rho l} = \frac{\rho v_T}{2l}, \tag{6}$$

where v_T is the velocity of the shaker table, Fig. 2, in the Ξ direction. The power P dissipated equals the volume integral over the sample

$$P = \int_V R_\perp v_\rho^2 dV, \tag{7}$$

where $R_\perp$ is the airflow resistivity perpendicular to the Ξ axis, and only radial flow is considered. Substitute Eq. (6) into Eq. (7), and get

$$P = \frac{R_\perp v_T^2}{4l^2}\int_V \rho^2 dV. \tag{8}$$

If the sample cross-section is square with side length a, then the integral becomes

$$P = \frac{R_\perp a^4 v_T^2}{24l}. \tag{9}$$

The power delivered from the shaker table to the sample is

$$P = v_T F_V, \tag{10}$$

where F_V is the viscous force. From Eqs. (9) and (10) one gets the force

$$F_V = \frac{R_\perp a^4}{24l} v_T. \tag{11}$$

We use a complex time factor $e^{i\omega t}$, where t is the time and $i^2=-1$. Then $v_T=i\omega u_T$, and Eq. (11) becomes

$$F_V = \frac{R_\perp a^4}{24l} i\omega u_T. \tag{12}$$

This force was subtracted from the direct measured force F_M to give the force F that would act on the fiber skeleton in vacuum. F is the force that should be used in Eq. (4),

$$F = F_M - F_V. \tag{13}$$

The real part of F_M was in principle also influenced by the airflow, but in the present measurement the influence was much smaller that the experimental uncertainty.

C. Wave motion in the fiber skeleton

The elastic constant E_3 is so small that the wavelength of waves in the sample skeleton becomes comparable to the length of the sample, and the strain is not constant in the sample. The calculation of the elastic constant from the data in this case follows in this section.

Figure 2 shows a coordinate system with Ξ axis perpendicular to the aluminum plate and origin in the center of this plate on the sample side. ξ is the coordinate in the Ξ direction, u is the displacement of the fiber skeleton in this direction, u_0 is a constant, and k is the wave number. The displacement of the sample at the aluminum plate, $\xi=0$, is zero. Therefore,

$$u = u_0 \sin k\xi. \tag{14}$$

The constant u_0 can be found from the displacement u_T of the shaker table,

$$u_0 = u_T / \sin kl. \tag{15}$$

To find E_3 the Z axis of the glass wool sample was parallel to the Ξ axis of the apparatus.

The force F on the aluminum plate is

$$F = SE_3 \left. \frac{\partial u}{\partial \xi} \right|_{\xi=0}. \tag{16}$$

Equations (14)–(16) give

$$\frac{F}{u_T} = \frac{SE_3 k}{\sin kl}. \tag{17}$$

Equation (17) is solved for E_3,

$$E_3 = \frac{F \sin kl}{u_T S k}. \tag{18}$$

The wave number is the cyclic frequency divided by the wave velocity. If the mass density of the fiber skeleton is ρ_W, then the wave number is

$$k = \frac{\omega}{\sqrt{\frac{E_3}{\rho_W}}}. \tag{19}$$

In the experiment the acceleration A of the shaker table, Fig. 2, was measured, and u_T was calculated from Eq. (3). The force transducer measured force F_M, and F was calculated from Eq. (13). [The correction for airflow Eq. (13) is not necessary when E_1 is calculated because the imaginary part of E_1 is much higher than the correction by Eq. (13).] ω, S, and l were recorded. The mass density ρ_W was assumed to be equal to the static mass density, 30 kg/m^3. All mechanical losses are attributed to the elastic constant. Equations (18) and (19) give implicitly E_3.

An iterative procedure was used to find E_3. A complex value of E_3 was assumed and k was calculated from Eq. (19). This k value was set into Eq. (18) and a new value for E_3 was computed. Then a new value of k was calculated from Eq. (19). The iteration was stopped when a stationary value of E_3 was obtained.

III. MEASUREMENT SETUP

The mechanical setup used to measure E_1 and E_3 is shown in Fig. 3. Four steel rods with threads and nuts held the two, 10-mm-thick, aluminum plates A and D. On plate D was mounted the shaker that carried a 5-mm-thick aluminum plate C, whose acceleration was measured by three piezoelectric accelerometers. They were placed at the vertices of an equilateral triangle with center in the center of the plate C. Three accelerometers were used, instead of one to detect possible rotations of the plate. The glass wool sample was glued to plates B and C. The plate B, 5-mm-thick aluminum, was mounted on plate A via a piezoelectric force transducer. The thickness of the sample was typical 50 mm.

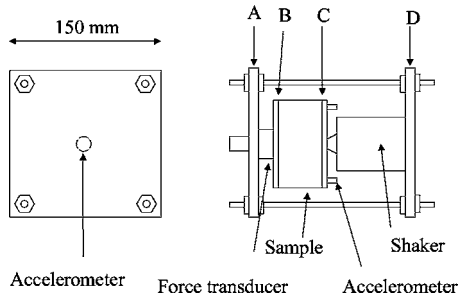

FIG. 3. The mechanical details of the setup used to measure Young's moduli. It uses the measurement principle in Fig. 2. The setup hung in 1 m long rubber bands. The sample is glued to the two plates B and C.

The whole assembly hung in two 1-m-long rubber bands. These bands are not shown in Fig. 3. In the early experiments, plate D was mounted horizontally on a concrete slab. But the suspension by rubber bands eliminated many resonance modes that disturbed the measurement and this greatly improved the data. Plate A, the force transducer, and plate B had a small acceleration, which was measured by an accelerometer mounted on plate A. The acceleration and the mass of plate B was used to correct the output from the force transducer to give the actual force from the sample on plate B. The derivation of Eq. (18) assumed that the displacement of plate B was zero. In the actual experiment the displacement was very small compared the movement of plate C, so Eq. (18) can still be used to calculate the influence from wave movement in the skeleton of the sample.

The shear constant G was measured with the setup in Fig. 4. The right picture gives the cut S-S shown on the left-hand side. The sample was glued to plates B and C. The shaker moved plate C horizontally, and its acceleration was measured by an accelerometer. Plate B was attached to a force transducer, which was fastened on plate A. The force transducer measured the horizontal force on plate B, and the displacement of plate C was calculated from its measured acceleration. The procedure in Sec. II C was used to correct for wave movements of the fiber skeleton. There was no airflow in the sample because it was subject to a shear deformation.

Figure 5 shows the electronic equipment. It used a Stanford Research System DSP Lock-In Amplifier SR850, which has an output voltage that is a sinusoidal function of time.

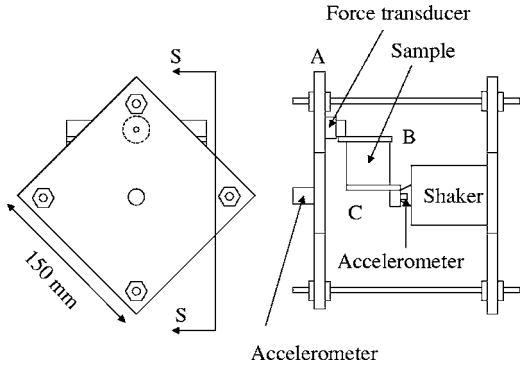

FIG. 4. The mechanical details of the setup used to measure the shear constant.

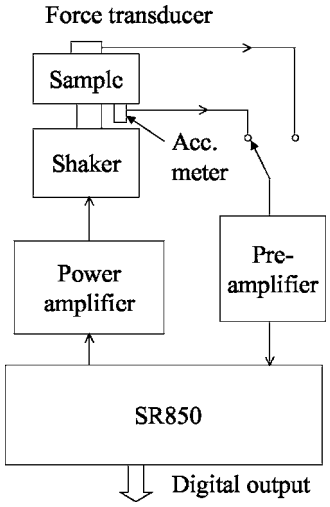

FIG. 5. The electronic setup used to record accelerations and force. The SR850 delivers a voltage that is a sinusoidal function of time. This voltage drove the power amplifier, which was connected to the shaker. The accelerometer or the force transducer was connected to the preamplifier. The amplitude and phase of the output from the preamplifier was measured and recorded by SR850.

The frequency can be programmed to sweep through a range. The output voltage from SR850 was connected to a power amplifier that drove the shaker. SR850 also has an input to a phase detector, and SR850 can record digitally the magnitude and phase of the input. One accelerometer on plate C was connected to a preamplifier, the output of which was connected to the input of SR850. The frequency was swept through a range, and the frequency, the magnitude, and phase of the signal from the accelerometer were recorded digitally. Then a new accelerometer was connected to the preamplifier and the procedure repeated. After all the accelerometer outputs were recorded, the force transducer was connected to the preamplifier, and the magnitude and phase of the force were recorded.

IV. RESULTS

The glass wool studied was of the type "Industriplade 1" produced by Saint-Gobain Isover a/s, Vamdrup, Denmark. Table I shows data for the glass wool.

The Z resistivity was measured with airflow in the Z direction in the glass wool, defined in Sec. II, and X resistivity was measured with airflow in the X direction. Resistivity in the X and Y directions are equal. The porosity was calculated from $1-\rho_W/\rho_F$, where ρ_W is the density of glass wool, and ρ_F is the density of fiber glass.

TABLE I. Acoustic data for "Industriplade 1."

Mass density of glass wool	30 kg/m^3
Mass density of fiber glass	2550 kg/m^3
Diameter of fiber	7 μm
Airflow Z-resistivity	16 kPa s m^{-2}
Airflow X-resistivity	8 kPa s m^{-2}
Concentration of phenol-formaldehyde resin	5%
Porosity	0.988

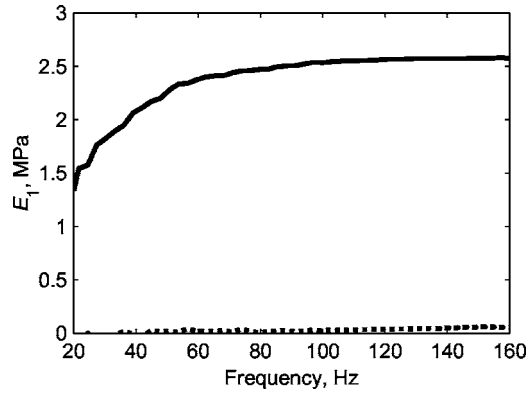

FIG. 6. The resulting Young's module E_1. The solid line shows the real part and the dotted one the imaginary part. Both real and imaginary part increases with frequency. At 20 Hz $E_1=1.5+0.01i$ MPa, and at 160 Hz $E_1=2.6+0.06i$ MPa.

A. Young module E_1

The sample had a cross-section area of $100\cdot100$ mm^2 perpendicular to the X axis in the glass wool. Its length was 50 mm. The sample was glued to the two plates B and C in Fig. 3. Figure 6 shows the resulting real and imaginary part of E_1. The solid curve is the real part and the dotted one the imaginary part. It was necessary to use a low level of acceleration to avoid elastic nonlinearity in the glass wool sample. The strain used for Fig. 6 was below 10^{-5}.

There are few data in the literature that the result can be compared with, and only static measurement seems to have been published. Rice and Göransson[8] reported a Young modulus $E_1=17.2$ kPa for glass wool of mass density 14 kg/m^3. Tarnow[14] found the static value 390 kPa for glass wool of mass density 30 kg/m^3, and the dynamic result for the real part was 1.5 MPa at 20 Hz. The strain was $2\cdot10^{-2}$ by the static measurement, and below 10^{-5} by the dynamic one. The static strain is much higher than the dynamic one, and nonlinear elasticity could explain the difference between the static and the dynamic value.

B. Young's modulus E_3

The sample had a cross-section area of $100\cdot100$ mm^2 perpendicular to the Z axis in the glass wool. Its length was 31 mm. Figure 7 shows the result for E_3 for the sample of glass wool. The data show that the real and imaginary parts are constants. The best graphical fit of the data was $E_3=12+0.6i$ kPa$=12(1+0.05i)$ kPa.

The real part of E_3 is more than 100 times smaller than the one of E_1. The strain used for Fig. 7 was below 10^{-4} to avoid elastic nonlinearity. A higher strain would have reduced to the electronic noise.

Equtions (12) and (13) with an airflow resistivity $=8$ kPa s m^{-2} were used to correct for the influence from airflow in the sample. Wave movements in the fiber skeleton were taken into account by Eqs. (18) and (19).

Wilson and Cummings[10] reported dynamic measurements for glass wool of density 24 kg/m^3. They found an approximately constant $E_3=3.3+0.2i$ kPa$=3.3(1+0.06i)$ kPa in the frequency range 40–200 Hz. The real part is four times smaller than the one found here, but the imaginary

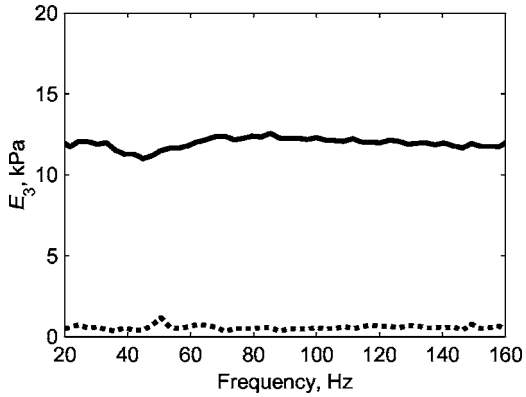

FIG. 7. The resulting Young's module $E_3=12+0.6i$ kPa. The solid line shows the real part and the dotted one the imaginary part. Both the real and imaginary parts are constant.

parts divided by the real ones, the loss factors, are approximately equal. For the glass wool Telwolle of density 71 kg/m^3 and fiber diameter 5–7 μm, Pritz[7] reported a constant complex Young's modulus $E_3=78.4(1+0.02\cdot i)$ kPa in the frequency range 100–3 000 Hz.

C. Shear modulus *G*

The sample had dimensions $100\cdot100\cdot31$ mm^3 in the X, Y, Z direction of the glass wool. The setup in Fig. 4 was used with 31 mm between plates B and C. The direction of displacement was along the 100 mm edges in the X direction. The result is shown in Fig. 8. The data are only reliable for frequencies below 100 Hz, because of resonance in the mechanical structure. In the frequency range 20–100 Hz the shear modulus is constant and equal to $40+2i$ kPa.

Only static measurements of this module have been published. Rice and Göransson[7] reported 13.7 kPa for glass wool of density 14 kg/m^3.

D. Poisson's ratios

Rice and Göransson[8] stated, based on static measurements, that the Poisson's ratios are zero for glass wool of mass density 15 and 11 kg/m^3. This means that $C_{12}=C_{13}=0$ from Jones.[13]

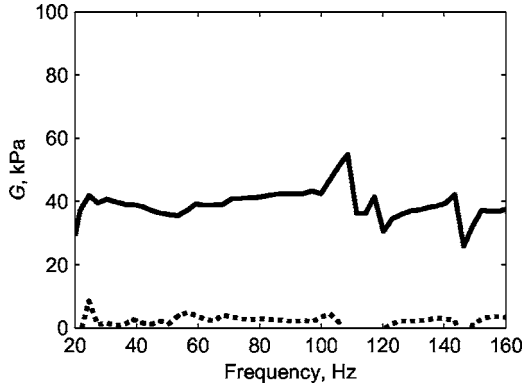

FIG. 8. The resulting shear module $G=40+2i$ kPa. The solid line shows the real part and the dotted one the imaginary part. Both the real and imaginary part are constant. For frequencies above 100 Hz the result is not accurate due to mechanical resonance.

It was attempted to measure the Poisson's ratios dynamically. A sample of glass wool was placed between two parallel aluminum plates. An electrodynamic shaker moved one of the plates. To detect the movement of the sides of the sample, aluminum foils 20 μm thick were glued on the sides of the sample, and a preamplifier for a condenser microphone was used to detect lateral movements of the sample. However, the scattering of the data made it impossible to detect movements of the sides of the sample.

Another attempt was made to measure Poisson's ratios. The apparent Young's modulus was found for samples of different lengths by the method in Sec. II. When the sample length is small compared to the dimensions of the aluminum plates, the deformation of the sample is perpendicular to the aluminum plates, because they prevent lateral movement. In this case one would find a high value of the Young's modulus. If the sample is long, there is lateral movement depending on the size of Poisson's constants, and this lateral movement would decrease the apparent Young's module. No such dependence on length was found, but the data were scattered due to inhomogeneity of the samples. Therefore the Poisson's ratios are assumed to be zero.

V. CONCLUSION

A new mechanical design for measuring the elastic constants of glass has been developed. Correction for viscous drag on fibers from airflow in the sample is presented, and correction for mechanical waves in the structure is described. The measurement showed that the Young's module E_1 depended on frequency, at 20 Hz it was $1.5+0.01i$ MPa, and at 160 Hz it was $2.6+0.06i$ MPa. Young's module $E_3=12+0.6i$ kPa did not depend on frequency. The shear module $G=40+2i$ kPa did not depend on frequency. Attempts to measure the Poisson's ratios did not give conclusive results, and they were assumed to be zero.

ACKNOWLEDGMENT

Myhrwold's fund, Denmark, supported the work reported here.

[1] T. E. Vigran, L. Kelders, W. Lauriks, P. Leclaire, and T. F. Johansen, "Prediction and measurements of the influence of boundary conditions in a standing wave tube," Acust. Acta Acust. **83**, 419–423 (1997).
[2] B. H. Song and J. S. Bolton, "Effect of circumferential edge constraint on the acoustic properties of glass fiber materials," J. Acoust. Soc. Am. **110**, 1902–2916 (2001).
[3] B. H. Song and J. S. Bolton, "Investigation of the vibrational modes of edge-constrained fibrous samples placed in standing wave tube," J. Acoust. Soc. Am. **113**, 1833–1849 (2003).
[4] V. Tarnow, "Fiber movements and sound attenuation in glass wool," J. Acoust. Soc. Am. **105**, 234–240 (1999).
[5] M. A. Biot, "Theory of Propagation of Elastic Waves in a Fluid-Saturated Porous Solid. I. Low-Frequency Range," J. Acoust. Soc. Am. **28**, 168–178 (1956).
[6] T. Pritz, "Transfer function method for investigating the complex modulus of acoustic materials: spring-like specimen," J. Sound Vib. **72**, 317–341 (1980).
[7] T. Pritz, "Frequency dependence of the frame dynamic characteristics of mineral and glass wool materials," J. Sound Vib. **106**, 161–169 (1986).
[8] H. J. Rice and P. Göransson, "A dynamical model of light fibrous materials," Int. J. Mech. Sci. **41**, 561–579 (1999).
[9] K. U. Ingard, *Notes on Sound Absorption Technology* (Noise Control Foundation, Poughkeepsie, New York, 1994).

[10]R. Wilson and A. Cummings, "An impedance technique for determining the dynamic structural properties of a porous material," Proceedings of the 1996 International Congress on Noise Control Engineering, Liverpool, UK, pp. 269–272.
[11]C. Langlois, R. Panneton, and N. Atalla, "Polynominal relations for quasi-static mechanical characterization of isotropic poroelatic materials," J. Acoust. Soc. Am. **110**, 3032–3040 (2001).
[12]L. Cremer, M. Heckl, and E. E. Ungard, *Structure-Borne Sound* (Springer, Berlin, 1973), p. 198.
[13]R. M. Jones, *Mechanics of Composite Materials* (Hemisphere, New York, 1975), pp. 32–33, 35.
[14]V. Tarnow, "Measurements of anisotropic sound propagation in of glass wool," J. Acoust. Soc. Am. **101**, 2243–2247 (2000).

The development of a Component Mode Synthesis (CMS) model for three-dimensional fluid–structure interaction

M. D. C. Magalhaes[a)]
Department of Materials Engineering and Construction, Federal University of Minas Gerais, Belo Horizonte, 31710 350 Brazil

N. S. Ferguson
Institute of Sound and Vibration Research (ISVR), University of Southampton, Highfield, Southampton—United Kingdom

(Received 13 October 2004; revised 5 August 2005; accepted 14 September 2005)

Our main aim in this paper is to develop analytically the three-dimensional Component Mode Synthesis method and to use it on fluid–structure interaction problems, such as sound transmission between coupled volumes. This will be shown for simple volume geometries, but, in principle, the same procedure can be applied when the component modes are obtained from numerical techniques, such as the Finite Element Model (FEM) or Boundary Element Method (BEM). The modal behavior of acoustic volumes and a partition is implemented in two steps. The first extension here is based on a one-dimensional model where the transverse acoustic modes of the volumes are incorporated into the formulation. The second extension, which is more general, considers not only the transverse acoustic modes of the volumes, but also structural modes of the partition. A comparison is made with predictions based on a modal model using the normal modes of rigid walled enclosures separated by a simply supported partition. For the latter modal model, particle velocity continuity was not incorporated in the formulation.
 [DOI: 10.1121/1.2114567]

PACS number(s): 43.55.Ka, 43.55.Rg [JBS] Pages: 3679–3690

I. INTRODUCTION

In the literature, significant studies have concentrated on analyzing sound transmission using uncoupled "rigid-walled" acoustic modes for the acoustic volumes.[1–3] In this case the boundary condition at the interface between the acoustic volumes, which is due to the velocity of the partition, cannot be reproduced. The acoustic and the structural response fields are typically expressed in terms of their uncoupled normal modes by means of coupled differential equations for each mode. The structural motion is expressed as a summation over the response of the *in vacuo* natural modes driven by fluid loading. The acoustic fields in the volumes are determined by a summation of the rigid-walled acoustic modes. According to Fahy,[3] the correct convergence of the modal pressure on the structural interface is obtained due to Gibb's phenomenon, which is an overshoot that occurs whenever basis functions (for instance, acoustic mode shapes) are used to represent spatial distributions containing discontinuities, e.g., in the derivatives of the response.

Our aim in this paper is to develop an alternative model that incorporates interface particle velocity continuity in the formulation for the prediction of noise transmission between two volumes. The Component Mode Synthesis (CMS) method[4] was used for the development of this alternative model. Subsequently, the CMS model implemented was then compared with a Modal Model[1] implemented previously.

The CMS approach was initially developed and applied to acoustic-structural coupled volumes possessing one-dimensional wave propagation through a limp partition to verify the accuracy and applicability of the approach.[5] Most sound transmission problems in buildings require a three-dimensional model for a better representation of the sound field distribution. Likewise, the application of the "limp" mass description is not entirely appropriate in frequency bands higher than the one that includes the fundamental resonance frequency of a partition, and so both requirements need to be considered herein. Another development is the extension of the one-dimensional CMS model[5] to the three-dimensional case (3-D-CMS model). This will be shown for simple volume geometries, but, in principle, the same procedure can be developed when the component modes are obtained from numerical techniques, such as FE, and then applied in the described CMS methodology.

The modal behavior of acoustic volumes and structural interface is implemented in two steps. The first extension is an extension of the one-dimensional model where the transverse acoustic modes of the volumes are incorporated into the formulation. The further extension incorporates a modal description for the structural interface and only requires the normal *in vacuo* structural modes with the relevant boundary conditions.

The CMS method requires the user to model separate components of a problem in terms of a summation over constraint modes and component normal modes and has previously been applied in structural dynamics. A constraint mode is defined as the static deformation of a subsystem when a

[a)]Author for correspondence. Electronic mail: maxdcm@ig.com.br

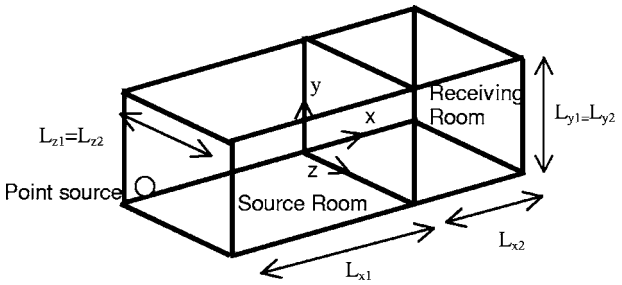

FIG. 1. Volume coordinates. A monopole source with volume velocity equal to 3×10^{-5} m^3/s was located at the corner of the source volume.

unit displacement or velocity is applied to one coordinate of a specific set of "interface" coordinates. Usually the number of constraint modes considered is equal in number to the number of redundant interface degrees of freedom. The acoustic constraint modes used corresponded to rigid walled conditions on all boundaries other than at the interface with the structure, which was specified as a free surface for these modes. They provide convergence to a better result, so that the particle velocity continuity at the interface can be replicated.

The component normal modes may be classified according to their boundary conditions either as fixed-interface or free-interface modes. The acoustic normal modes adopted are taken to be those of the volumes with a fixed interface (i.e., a rigid wall at the interface and on all other boundaries). The number of normal modes chosen depends upon the frequency range of the calculations and convergence requirements.

II. THE COMPONENT MODE SYNTHESIS METHOD FOR THE THREE-DIMENSIONAL CASE-MATRIX FORMULATION AND IMPLEMENTATION OF THE MODEL

As in the one-dimensional case,[1] the implementation of the CMS method for the 3-D case is also based on the selection of the sets of modes, definition of the constraint equations, and system synthesis.

A. The definition of sets of component modes

Two rigid-walled rectangular cross section volumes with a common elastic partition at the interface, as shown in Fig. 1, are considered as three distinct CMS components. The first consists of the acoustic fluid volume, being defined for $x=-L_{x1}$ to $x=0$. The second component is the receiving acoustic fluid volume, which is defined as varying from $x=0$ to $x=L_{x2}$. Both components have been considered with the same cross section, but the extension to other volumes is also straightforward. The third CMS component is an elastic simply supported partition, which separates the two volumes and is represented dynamically by its flexural modes. A harmonic constant amplitude volume velocity source is placed in one corner of the source volume, so that all acoustic modes can be excited. It is assumed that the fluid velocity function $\varepsilon(x,y,z,t)$ can be written in terms of the generalized velocity potential $\bar{\Phi}$ (scalar quantity) by the modal transformation[3]

$$\varepsilon = (\Psi_x i + \Psi_y j + \Psi_z k)\bar{\Phi}, \tag{1}$$

where Ψ_x, Ψ_y, and Ψ_z are matrices that consist of preselected normal velocity modes for a rigid-walled volume plus constraint modes, representing the fluid velocity distribution in the x, y, and z directions, respectively; The fluid velocity function and the generalized velocity potential are defined as $\varepsilon(x,y,z,t)=\partial\varepsilon(x,y,z,t)/\partial t$ and $\varepsilon=(u,v,w)=\nabla(\Phi)$, respectively.

The modal matrices for the source component are given by

$$\Psi_{x1} = s_{x1}[\Psi_{n_1} \quad \Psi_{c_{x1}}], \tag{2}$$

$$\Psi_{y1} = s_{y1}[\Psi_{l_1} \quad \Psi_{c_{y1}}], \tag{3}$$

$$\Psi_{z1} = s_{z1}[\Psi_{q_1} \quad \Psi_{c_{z1}}], \tag{4}$$

where the subscript c_{x1} represents the constraint mode number; c_{y1} and c_{z1} are the modal numbers for the set of modes $\Psi_{c_{y1}}$ and $\Psi_{c_{z1}}$, respectively. The subscripts n, l, and q denote the normal mode number of a particular mode in the x, y, and z directions, respectively. s_{x1}, s_{y1}, and s_{z1} represent scale constants whose units are such that Ψ_{x1}, Ψ_{y1}, and Ψ_{z1} have dimensions of $(\text{mass})^{-0.5}$. The matrix Ψ_{x1} consists of a set of fixed-fixed interface normal modes (Ψ_{n_1}) plus a set of fixed-free constraint modes ($\Psi_{c_{x1}}$) in the x direction. The matrix Ψ_{y1} is comprised of a set of fixed-fixed interface modes (Ψ_{l_1}) plus another set of fixed–fixed modes ($\Psi_{c_{y1}}$) in the y direction, which is due to the contribution of the constraint modes $\Psi_{c_{x1}}$ to the fluid particle velocity in the y direction. Likewise, matrix Ψ_{z1} consists of a set of fixed–fixed interface normal modes (Ψ_{q_1}) plus the set of modes $\Psi_{c_{z1}}$, which is due to the contribution of the constraint modes $\Psi_{c_{x1}}$ to the fluid particle velocity in the z direction.

Although the set of constraint modes $\Psi_{c_{x1}}$ contributes to the fluid particle velocity distribution in both y and z directions, there is no need to have any other set of constraint modes. This is justified by the fact that the interface between components is only in the constant plane $x=0$. The selected orthogonal and constraint modes were defined as shape functions satisfying the geometric boundary conditions for each acoustic component. By an application of the well-known relationship between velocity potential and particle velocity,[3] the orthogonal modes Ψ_{n_1} (in the x direction) and their contributions to the fluid particle velocity in the y and z directions (Ψ_{l_1} and Ψ_{q_1}) can be expressed by

$$\Psi_{n_1}(x,y,z,t) = -k_{n_1}\sin(k_{n_1}x)\cos(k_{l_1}y)\cos(k_{q_1}z), \quad \text{for } -L_{x_1} \leqslant x \leqslant 0, \tag{5}$$

$$\Psi_{l_1}(x,y,z,t) = -k_{l_1}\cos(k_{n_1}x)\sin(k_{l_1}y)\cos(k_{q_1}z), \quad \text{for } 0 \leqslant y \leqslant L_{y_1}, \tag{6}$$

$$\Psi_{q_1}(x,y,z,t) = -k_{q_1}\cos(k_{n_1}x)\cos(k_{l_1}y)\sin(k_{q_1}z), \quad \text{for } 0 \leqslant z \leqslant L_{z_1}, \tag{7}$$

where k_{n_1}, k_{l_1}, and k_{q_1} are equal to $n_1\pi/(L_{x1})$, $l_1\pi/L_{y1}$, and $q_1\pi/L_{z1}$, respectively. It is seen that the natural modes given by Eqs. (5)–(7) have units equal to (m^{-1}).

An additional set of constraint modes Ψ_c, which satisfies zero velocity on $x=-L_{x1}$ and unit velocity in the x direction on $x=0$ over the partition area, is used for the source room. In principle, the elastic partition can either cover the whole of the common boundary ($x=0$) or only part of the common interface. For the source room component, the constraint modes $\Psi_{c_{x1}}$ (in the x direction) and their contributions to the fluid particle velocity in the y and z directions ($\Psi_{c_{y1}}$ and $\Psi_{c_{z1}}$) are then given by

$$\Psi_{c_{x1}}(x,y,z,t) = \left(1 + \frac{x}{L_{x1}}\right)\cos(k_{c_{y1}}y)\cos(k_{c_{z1}}z), \tag{8}$$

$$\Psi_{c_{y1}}(x,y,z,t) = -\left(x + \frac{x^2}{2L_{x1}}\right)k_{c_{y1}}\sin(k_{c_{y1}}y)\cos(k_{c_{z1}}z), \tag{9}$$

$$\Psi_{c_{z1}}(x,y,z,t) = -\left(x + \frac{x^2}{2L_{x1}}\right)k_{c_{z1}}\cos(k_{c_{y1}}y)\sin(k_{c_{z1}}z), \tag{10}$$

where $k_{c_{y1}}$ and $k_{c_{z1}}$ are equal to $c_{y1}\pi/L_{y1}$ and $c_{z1}\pi/L_{z1}$, respectively. Equations (8)–(10) apply over the area of the partition, even if it might only cover a partial area of the whole interface (common wall).

It is seen that this set of equations (8)–(10) do not have the same dimensions of those equations defined previously (5)–(7). However, all original mode shape vectors defined above the natural and constraint modes were normalized to the more useful mass-normalized mode shape vectors.[4] It should be noted that the natural modes have units equal to (m^{-1}) and the constraint modes are dimensionless, while after normalization,[4] the mass-normalized vectors defined in Eqs. (2)–(4) have dimensions of $(\text{mass})^{-0.5}$.

According to Eq. (8), it is observed that the number of constraint modes $\Psi_{c_{x1}}$ is directly related to the number of different modal orders c_{y1} and c_{z1}. In addition, a linear function was chosen to represent the particle velocity distribution in the x direction, as higher-order functions did not provide better convergence. As the particle velocity of a fluid is defined by the first-order derivative of its velocity potential, a sine function appears in Eqs. (9) and (10), which represent the *constraint* mode velocity contributions in the y and z directions respectively.

Additionally, it is assumed that the set of normal structural modes ϕ_p are the flexural vibration mode shapes of a simply supported isotropic rectangular thin plate.[4] No constraint modes are necessary for the structural component and other structural boundary conditions could similarly be considered.

The modal matrices for the receiving component can be expressed as

$$\Psi_{x2} = s_{x2}[\Psi_{n_2} \quad \Psi_{c_{x2}}], \tag{11}$$

$$\Psi_{y2} = s_{y2}[\Psi_{l_2} \quad \Psi_{c_{y2}}], \tag{12}$$

$$\Psi_{z2} = s_{z2}[\Psi_{q_2} \quad \Psi_{c_{z2}}]. \tag{13}$$

Likewise, for the source component, s_{x2}, s_{y2}, and s_{z2} represent scale constants whose units are such that Ψ_{x2}, Ψ_{y2}, and Ψ_{z2} have dimensions of $(\text{mass})^{-0.5}$. The matrix Ψ_{x2} is comprised of a set of fixed–fixed interface normal modes (Ψ_{n_2}) plus a set of free–fixed constraint modes ($\Psi_{c_{x2}}$) in the x direction. The matrix Ψ_{y2} is composed of a set of fixed–fixed interface normal modes (Ψ_{l_2}) plus another set of fixed–fixed modes ($\Psi_{c_{y2}}$) in the y direction, which is due to the contribution of the constraint modes $\Psi_{c_{x2}}$ to the fluid particle velocity in the y direction. In the same way, matrix Ψ_{z2} comprises a set of fixed–fixed interface normal modes (Ψ_{q_2}) plus a set of modes $\Psi_{c_{z2}}$, which is due to the contribution of the constraint modes $\Psi_{c_{x2}}$ to the fluid particle velocity distribution in the z direction. As for the source room, the set of free-fixed constraint modes $\Psi_{c_{x2}}$ is sufficient for the formulation of the problem.

Additionally, the (x,y,z) particle velocity Cartesian components for the receiving volume are given, respectively, by

$$\Psi_{n_2}(x,y,z,t) = -k_{n_2}\sin(k_{n_2}x)\cos(k_{l_2}y)\cos(k_{q_2}z), \quad \text{for } 0 \leqslant x \leqslant L_{x_2}, \tag{14}$$

$$\Psi_{l_2}(x,y,z,t) = -k_{l_2}\cos(k_{n_2}x)\sin(k_{l_2}y)\cos(k_{q_2}z), \quad \text{for } 0 \leqslant y \leqslant L_{y_2}, \tag{15}$$

$$\Psi_{q_2}(x,y,z,t) = -k_{q_2}\cos(k_{n_2}x)\cos(k_{l_2}y)\sin(k_{q_2}z), \quad \text{for } 0 \leqslant z \leqslant L_{z_2}, \tag{16}$$

where k_{n_2}, k_{l_2}, and k_{q_2} are equal to $n_2\pi/L_{x2}$, $l_2\pi/L_{y2}$, and $q_2\pi/L_{z2}$, respectively.

The constraint modes c_2 in the x, y, and z directions have velocity components then given by

$$\Psi_{c_{x2}}(x,y,z,t) = \left(1 - \frac{x}{L_{x2}}\right)\cos(k_{c_{y2}}y)\cos(k_{c_{z2}}z), \tag{17}$$

$$\Psi_{c_{y2}}(x,y,z,t) = -\left(x - \frac{x^2}{2L_{x2}}\right)k_{c_{y2}}\sin(k_{c_{y2}}y)\cos(k_{c_{z2}}z), \tag{18}$$

$$\Psi_{c_{z2}}(x,y,z,t) = -\left(x - \frac{x^2}{2L_{x2}}\right)k_{c_{z2}}\cos(k_{c_{y2}}y)\sin(k_{c_{z2}}z), \tag{19}$$

where $k_{c_{y2}}$ and $k_{c_{z2}}$ are equal to $c_{y2}\pi/L_{y2}$ and $c_{z2}\pi/L_{z2}$, respectively.

It is also seen that for the receiving component the constraint modes given by Eqs. (17)–(19) are dimensionless while the natural modes defined by Eqs. (14)–(16) have units (1/m).

B. Constraint equations

Although the fluid particle velocity is considered in all directions [see Eq. (1)], for calculating the dynamic response of the acoustic components 1 and 2 the compatibility equations describing velocity continuity are only formulated in terms for the x direction normal to the partition or interface. Hence, although the fluid velocity function is equal to $\varepsilon = (\varepsilon_x, \varepsilon_y, \varepsilon_z)$, one only needs ε_x for the formulation of the constraint equations at the interface. When the structural partition is considered as an extra modal system, sufficient compatibility or constraint functions are given by

$$C_1 = \int_S \left[\left(\frac{\partial \varepsilon_{x,1}}{\partial t} \right)\Big|_{x=0} - \left(\frac{\partial w}{\partial t} \right)\Big|_{x=0} \right]^2 dS = \int_S [(\varepsilon_{x,1})|_{x=0} - (w)|_{x=0}]^2 \, dS, \tag{20}$$

$$C_2 = \int_S \left[\left(\frac{\partial \varepsilon_{x,2}}{\partial t} \right)\Big|_{x=0} - \left(\frac{\partial w}{\partial t} \right)\Big|_{x=0} \right]^2 dS = \int_S [(\varepsilon_{x,2})|_{x=0} - (w)|_{x=0}]^2 \, dS, \tag{21}$$

where $\varepsilon_{x,1}$ and $\varepsilon_{x,2}$ are the fluid particle displacements in the x direction for volumes 1 and 2, respectively, w is the normal displacement of the partition (in the x direction) due to its flexural elastic deformation, and S is the surface area of the interface.

These equations are used to determine a reduced set of generalized coordinates equal to the difference between the number of component coordinates and the number of constraint conditions. In situations where a partition covers only a part of the common boundary the integrals in the constraint equations are evaluated only over the partition area.

It is implicit in Eqs. (20) and (21) that the same reference coordinate is used for all components. It is not a linear problem in the generalized coordinates to set the constraint functions C_1 and C_2 to zero; instead one tries to minimize the error in a least squares sense by minimizing the functions. Hence, the following matrix form for the constraint equations can be obtained:

$$\frac{\partial C_1}{\partial \varepsilon_{x,1}} = \frac{\partial C_1}{\partial w_p} = \frac{\partial C_2}{\partial \varepsilon_{x,2}} = \frac{\partial C_2}{\partial w_p} = 0,$$

$$\text{or } \mathbf{R_c} \bar{G} = 0, \tag{22}$$

where

$$\bar{G} = [\bar{\Phi}_{c1} \; w_p \; \bar{\Phi}_{c2}]^T \text{ and } \mathbf{R_c} = [\mathbf{R_1} \; \mathbf{R_p} \; \mathbf{R_2}] \tag{23}$$

and

$$\mathbf{R_1} = \begin{bmatrix} 0 & R_{11} \\ 0 & R_{1p}^T \\ 0 & 0 \\ 0 & 0 \end{bmatrix}; \quad \mathbf{R_p} = \begin{bmatrix} -R_{1p} \\ -R_{pq} \\ -R_{pq} \\ -R_{2p} \end{bmatrix}; \quad \mathbf{R_2} = \begin{bmatrix} 0 & 0 \\ 0 & 0 \\ 0 & R_{2p}^T \\ 0 & R_{22} \end{bmatrix}. \tag{24}$$

The column vector $\bar{G}$ and the matrix $\mathbf{R_c}$ contain the system generalized coordinates and the geometrical coupling coefficients, respectively.

The submatrices R_{11}, R_{1p}, R_{pq}, R_{2p}, and R_{22} defining the geometrical coupling, are given by

$$R_{11} = \int_S (\Psi_{c_{x1}})^T (\Psi_{c_{x1}}) dS, \tag{25}$$

$$R_{1p} = \int_S (\Psi_{c_{x1}})^T \phi_p \, dS, \tag{26}$$

$$R_{pq} = \int_S \phi_p^T \phi_q \, dS, \tag{27}$$

$$R_{2p} = \int_S (\Psi_{c_{x2}})^T \phi_p \, dS, \tag{28}$$

$$R_{22} = \int_S (\Psi_{c_{x2}})^T (\Psi_{c_{x2}}) dS. \tag{29}$$

The analytical mode shape $\phi_{p,q}$ for a simply supported rectangular plate *in vacuo* is exactly described by $\phi_{p,q}(r,s) = \sin(k_{r_Y}) \sin(k_{s_Z})$, where $k_{r_Y} = r\pi/L_{y_p}$ and $k_{s_Z} = s\pi/L_{z_p}$ are the plate modal wave numbers in the y and z directions, respectively. The acoustic modal matrices Ψ_{x1} and Ψ_{x2} are defined in Eqs. (2) and (11), respectively.

No terms exist in coupling between the normal modes of the volumes (Ψ_{n_1} or Ψ_{n_2}) and the partition modes (ϕ_p), as the former have zero velocity at the interface ($x=0$). The matrix R_{pq} is also a diagonal matrix due to orthogonality for the structural modes.

C. Derivation of the general dynamic properties of the component mode synthesis acoustic components

In this section the dynamic properties of an acoustic component driven by a volume velocity source are derived using the direct application of Lagrange's equations.[4] It is necessary to formulate the scalar potential and kinetic energy quantities. The kinetic energy T_A for an acoustic volume V_1 can be expressed as[2]

$$T_A = \frac{1}{2} \rho_0 \int_{V_1} [(\varepsilon)^*]^T (\varepsilon) dV. \tag{30}$$

Substituting Eq. (1) into Eq. (30), the expression for the total kinetic energy using all of the modes employed in the formulation then becomes

$$T_A = \frac{1}{2}(\bar{\Phi}^T)^* \rho_0 \left(\int_{V_1} [(\Psi_x)^T \Psi_x] dV_1 + \int_{V_1} [(\Psi_y)^T \Psi_y] dV_1 + \int_{V_1} [(\Psi_z)^T \Psi_z] dV \right) (\bar{\Phi}). \quad (31)$$

The potential energy of a fluid inside a volume V_1 is defined in terms of a velocity potential function Φ as[2]

$$V_A = \frac{1}{2} \int_{V_1} \left(\kappa \rho_0^2 \frac{\partial (\Phi^T)^*}{\partial t} \frac{\partial \Phi}{\partial t} \right) dV_1, \quad (32)$$

where

$$\kappa = \frac{1}{\rho_0 c_0^2} \quad (33)$$

is the compressibility of the fluid.

Using the relationship between sound pressure and velocity potential,[2] the potential energy can then be expressed in terms of pressure as

$$V_A = \frac{1}{2} \int_{V_1} [\kappa (p^*)^T p] dV_1. \quad (34)$$

Assuming that the acoustic disturbances in each component are sufficiently small, a linear relationship between pressure and the fluid velocity $\varepsilon(x,y,z,t)$ can be written as[2]

$$p = \frac{1}{j\omega\kappa} div(\varepsilon) \quad (35)$$

and

$$div(\varepsilon) = \nabla \cdot \varepsilon = \left(\frac{\partial \Psi_x}{\partial x} + \frac{\partial \Psi_y}{\partial y} + \frac{\partial \Psi_z}{\partial z} \right) \bar{\Phi}, \quad (36)$$

where κ is defined in Eq. (33) and $\bar{\Phi}$ is the velocity potential of the fluid.

Substituting Eqs. (35) and (36) into Eq. (34), the expression for potential energy becomes

$$V_A = \frac{1}{2\kappa} (\bar{\Phi}^T)^* \left[\int_{V_1} \left(\frac{\partial (\Psi_x)^T}{\partial x} \frac{\partial \Psi_x}{\partial x} \right) dV_1 + \int_{V_1} \left(\frac{\partial (\Psi_y)^T}{\partial y} \frac{\partial \Psi_y}{\partial y} \right) dV_1 + \int_{V_1} \left(\frac{\partial (\Psi_z)^T}{\partial z} \frac{\partial \Psi_z}{\partial z} \right) dV_1 \right] \times (\bar{\Phi}). \quad (37)$$

For nonconservative systems, a dissipation function[6,7] must be included. For an acoustic component, it can be expressed as

$$\mathrm{D} = \frac{1}{2} (\bar{\Phi}^T)^* \rho_0 \left\{ \int_{V_1} [(\Psi_x)^T 2\omega_N \zeta_N \Psi_x] dV_1 + \int_{V_1} [(\Psi_y)^T 2\omega_N \zeta_N \Psi_y] dV_1 + \int_{V_1} [(\Psi_z)^T 2\omega_N \zeta_N \Psi_z] dV_1 \right\} \bar{\Phi}, \quad (38)$$

where ζ_N is the viscous modal damping ratio matrix for the components and ω_N is the modal matrix of natural frequencies. The damping matrix can then be derived from the above expression. Linear viscous damping was adopted for the purpose of simplification, as this is a reasonable choice for highly reverberant acoustic spaces.[3]

The system equations of motion can be obtained for a damped system by using Lagrange's equation of motion[4] as follows:

$$\frac{\partial}{\partial t} \left(\frac{\partial L}{\partial q_i} \right) - \frac{\partial L}{\partial q_i} + \frac{\partial \mathrm{D}}{\partial q_i} = Q_i, \quad i = 1,2, \ldots, n, \quad (39)$$

where L is the Lagrangian for the system of coupled components described below, D is the damping dissipation function, and q_i are the elements of the generalized coordinate $\bar{\Phi}$. In addition, it is assumed that the modes are real. Q_i is the time-dependent generalized volume velocity source strength in the case of a source within an acoustic volume or generalized force for a general system. The Lagrangian is defined by[4]

$$L = T_A - V_A + \lambda^T \mathbf{R_c} \bar{G}, \quad (40)$$

where λ is a Lagrange multiplier vector that enforces interface compatibility. It has the dimension of force.

The dynamic properties of a separate acoustic component 1 may be determined via Lagrange's equations [Eq. (39)], which lead to the following equations of motion:

$$M_1^{3\text{-D}} \ddot{\bar{\Phi}}_1 + C_1^{3\text{-D}} \dot{\bar{\Phi}}_1 + K_1^{3\text{-D}} \bar{\Phi}_1 - (R_1)^T \lambda_1 = Q_1^{3\text{-D}}, \quad (41)$$

where

$$M_1^{3\text{-D}} = \rho_0 \left(\int_{V_1} [(\Psi_{x1})^T \Psi_{x1}] dV_1 + \int_{V_1} [(\Psi_{y1})^T \Psi_{y1}] dV_1 + \int_{V_1} [(\Psi_{z1})^T \Psi_{z1}] dV_1 \right), \quad (42)$$

$$K_1^{3\text{-D}} = \rho_0 c^2 \int_{V_1} \left(\frac{\partial (\Psi_{x1})^T}{\partial x} \frac{\partial \Psi_{x1}}{\partial x} \right) dV_1 + \int_{V_1} \left(\frac{\partial (\Psi_{y1})^T}{\partial y} \frac{\partial \Psi_{y1}}{\partial y} \right) dV_1 + \int_{V_1} \left(\frac{\partial (\Psi_{z1})^T}{\partial z} \frac{\partial \Psi_{z1}}{\partial z} \right) dV_1, \quad (43)$$

$$C_1^{3\text{-D}} = 2\omega_N \rho \left(\int_{V_1} [(\Psi_{x1})^T \zeta_N \Psi_{x1}] dV_1 + \int_{V_1} [(\Psi_{y1})^T \zeta_N \Psi_{y1}] dV_1 + \int_{V_1} [(\Psi_{z1})^T \zeta_N \Psi_{z1}] dV_1 \right) \quad (44)$$

$$Q_1^{3\text{-D}} = j\omega\rho_0 Q_0 \int \Psi_{x1}\delta_0(x-x_0, y-y_0, z-z_0)dx. \quad (45)$$

$\delta_0(x-x_0, y-y_0, z-z_0)$ is the three-dimensional Dirac delta function representing a point volume velocity source at (x_0, y_0, z_0), and $\mathbf{M_1^{3\text{-D}}}$, $\mathbf{K_1^{3\text{-D}}}$, and $\mathbf{C_1^{3\text{-D}}}$ are scalar quantities representing the modal mass, stiffness, and damping matrices for the fluid volume, respectively. $Q_1^{3\text{-D}}$ is the column matrix of generalized volume velocity source strength where the individual terms relate to the excitation of individual model components. $\mathbf{R_1}$ is the matrix defined in Eq. (24). λ_1 is a column vector with a number of rows equal to the total number of constraint modes in component 1, plus the total number of panel modes and the total number of constraint modes in component 2.

As a consequence of classifying the modes into two categories, namely constraint modes and normal modes, the mass, stiffness, and damping matrices are partitioned into submatrices as follows:

$$M_1^{3\text{-D}} = \begin{bmatrix} m_{NN} & m_{NC} \\ m_{NC}^T & m_{CC} \end{bmatrix}; \quad K_1^{3\text{-D}} = \begin{bmatrix} k_{NN} & k_{NC} \\ k_{NC}^T & k_{CC} \end{bmatrix}; \quad (46)$$

$$C_1^{3\text{-D}} = \begin{bmatrix} c_{NN} & c_{NC} \\ c_{NC}^T & c_{CC} \end{bmatrix}.$$

The submatrix m_{NN}, k_{NN}, and c_{NN} are diagonal matrices. This is true due to the orthogonality property of these component modes. The order of these matrices depends upon the number of modes chosen for the analysis. The submatrices m_{CC}, k_{CC}, and c_{CC} are square matrices associated with the constraint modes; their orders are equal to the number of constraints. Finally, the rectangular matrices m_{NC}, k_{NC}, and c_{NC} are associated with the coupling between the normal and constraint modes, as these are generally not orthogonal, and cross-terms exist in the potential and kinetic energy expressions as well as in the dissipation function.

D. System synthesis

The equations of motion for the source volume (acoustic component 1), the structural partition (component p), and the receiving volume (acoustic component 2) are expressed in terms of their generalized coordinates $\bar{\Phi}$ as

$$M_1^{3\text{-D}}\ddot{\bar{\Phi}}_1 + C_1^{3\text{-D}}\dot{\bar{\Phi}}_1 + K_1^{3\text{-D}}\bar{\Phi}_1 - R_1^T\lambda_1 = Q_1^{3\text{-D}}, \quad (47)$$

$$M_p\ddot{w}_p + C_p\dot{w}_p + K_p w_p - R_p^T\lambda_p = 0, \quad (48)$$

$$M_2^{3\text{-D}}\ddot{\bar{\Phi}}_2 + C_2^{3\text{-D}}\dot{\bar{\Phi}}_2 + K_2^{3\text{-D}}\bar{\Phi}_2 - R_2^T\lambda_2 = 0, \quad (49)$$

where λ_1, λ_p, and λ_2 are column vectors of Lagrange multipliers for components 1, p and 2, respectively. The set of equations presented previously as well as the dynamic properties of the acoustic components $M^{3\text{-D}}$, $C^{3\text{-D}}$, and $K^{3\text{-D}}$ and the generalized volume velocity source strength $Q^{3\text{-D}}$ can all be derived, as shown in Sec. II C using Lagrange's equations of motion. The dynamic properties of the structural component (M_p, C_p, and K_p) are derived in Ref. 4

The coupled set of equations for the entire system is then given by

$$\mu\ddot{\bar{G}} + \varsigma\dot{\bar{G}} + \chi\bar{G} - \lambda R_c = Q_s \quad (50)$$

and

$$R_c\bar{G} = 0, \quad (51)$$

where

$$\lambda = \begin{Bmatrix} \lambda_1 \\ \lambda_p \\ \lambda_2 \end{Bmatrix}; \quad \mu = \begin{bmatrix} M_1^{3\text{-D}} & 0 & 0 \\ 0 & M_p & 0 \\ 0 & 0 & M_2^{3\text{-D}} \end{bmatrix};$$

$$\varsigma = \begin{bmatrix} C_1^{3\text{-D}} & 0 & 0 \\ 0 & C_p & 0 \\ 0 & 0 & C_2^{3\text{-D}} \end{bmatrix}; \quad \chi = \begin{bmatrix} K_1^{3\text{-D}} & 0 & 0 \\ 0 & K_p & 0 \\ 0 & 0 & K_2^{3\text{-D}} \end{bmatrix};$$

and $Q_s = [Q_1^{3\text{-D}}\ 0\ 0]^T$. The matrices μ, ς, and χ are the modal mass, damping, and stiffness matrices, respectively. Q_s is a column vector containing the generalized "forces" exerted on the components. It can also be shown that the coordinates $\bar{G}$ are not linearly independent in the set of equations (50), due to the constraint equations (51).

The matrix of generalized coordinates $\bar{G}$ cannot easily be rearranged and partitioned into dependent and linearly independent coordinates as in the one-dimensional case.[1]

Alternatively, Eqs. (50) and (51) may be written in the partitioned form [7]

$$\begin{bmatrix} (\chi - \omega^2\mu + j\omega\varsigma) & -R_c \\ R_c^T & 0 \end{bmatrix} \begin{Bmatrix} \bar{G} \\ \lambda \end{Bmatrix} = \begin{Bmatrix} Q_s \\ 0 \end{Bmatrix}. \quad (52)$$

The use of the Lagrange's Multiplier technique for the present situation, while more tedious than the transformation matrix technique,[1] permits the incorporation of the constraint equations in a systematic manner.[8] Equation (52) can be solved numerically by the application of a pseudoinversion technique, e.g., using Singular Value Decomposition.[9] One decision that has to be made by the analyst who uses component modes is how many modes to use. In order to prevent the matrices becoming singular, the number of constraint modes should be equal in number to the number of redundant constraints. In this case, the set of equations in (52) is overdetermined.

III. NUMERICAL RESULTS

All numerical simulations and results are presented for the three-dimensional problem, which also includes the modal contribution of the partition. A flexible partition with dimensions equal to 2 m $\times$ 1.8 m was considered over the whole common interface. The source and receiving volume dimensions were equal to (5 m $\times$ 2 m $\times$ 1.8 m) and (3 m $\times$ 2 m $\times$ 1.8 m), respectively (depth by height by width). A constant viscous modal damping equal to $\varsigma = 0.005$ was used for both the normal and constraint modes. Figure 1 shows that a monopole source with constant volume velocity equal to 3×10^{-5} m^3/s was placed at one corner of the source volume $(-5, 0, 0)$.

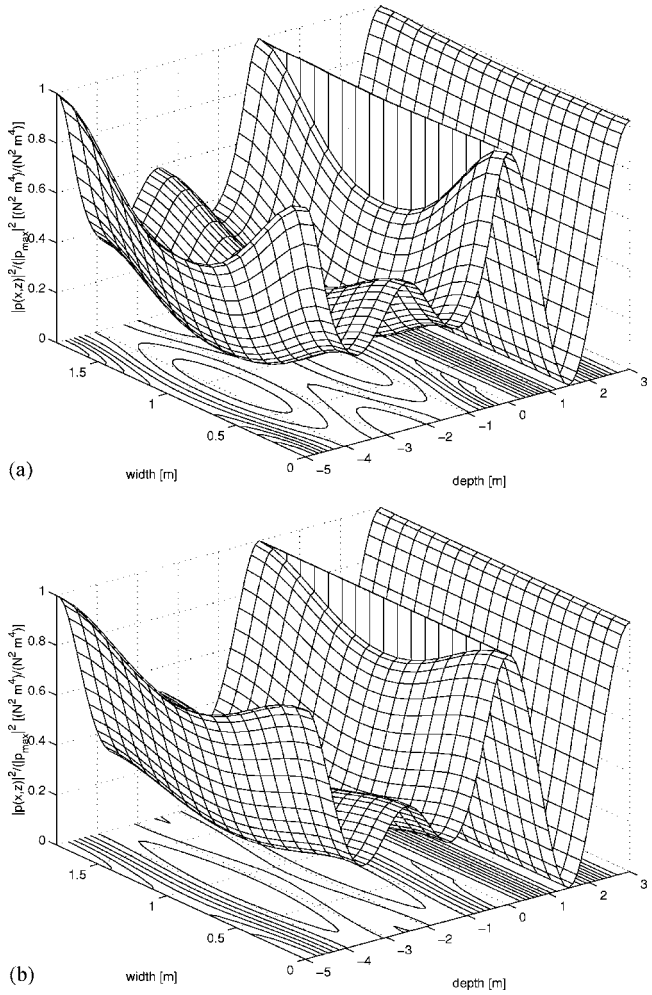

FIG. 2. Normalized mean square pressure distribution with respect to the horizontal plane $y=1$ m at 55 Hz. The elastic partition has dimensions, mass per unit area, and Young's Modulus equal to 2 m $\times$ 1.8 m, $\rho h=8.06$ kg/m^2, and $E=2.12\times10^9$ N/m^2, respectively. (a) The CMS model and (b) the Modal model in relative pressure levels to the maximum in the plane.

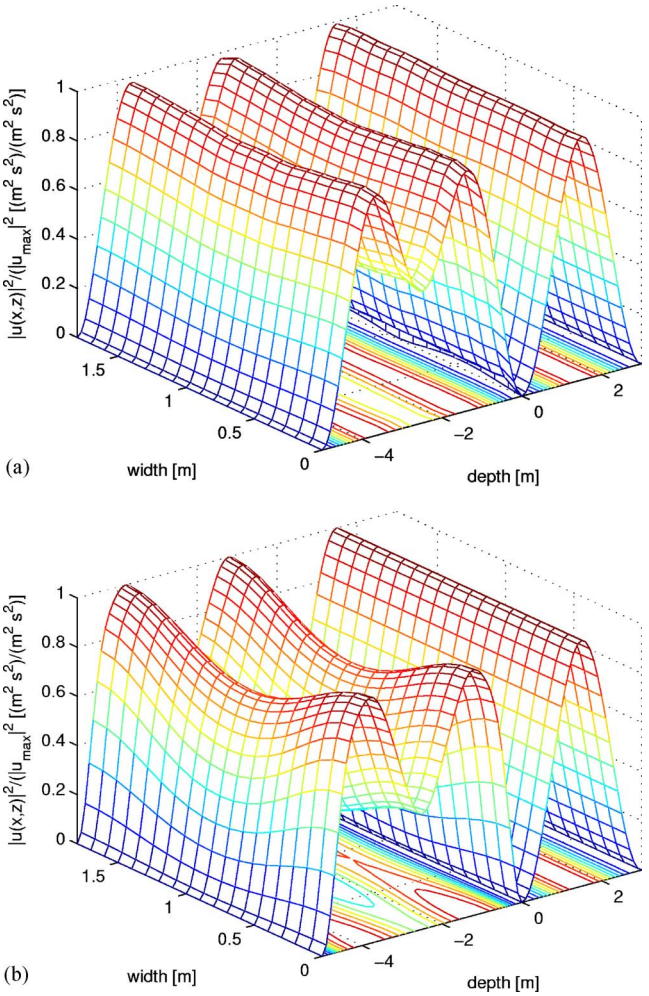

FIG. 3. (Color online) Normalized mean square velocity distribution with respect to the horizontal plane $y=1$ m at 55 Hz. The elastic partition has dimensions, mass per unit area, and Young's Modulus equal to 2 m $\times$ 1.8 m, $\rho h=8.06$ kg/m^2, and $E=2.12\times10^9$ N/m^2, respectively. (a) The CMS model and (b) the Modal model in relative velocity levels to the maximum in the plane.

The spatial results are presented in terms of the normalized mean square pressure distribution at 55 Hz and 140 Hz over certain positions (planes) that have been specified *a priori*. These particular frequencies, which do not necessarily coincide with the fundamental room modes, were arbitrarily chosen below and above the lowest natural frequency of the receiving room, above which tangential and oblique acoustic modes are generated in the receiving room. The mean square values are normalized to their maximum value in the plane. The mean square pressure distributions were symmetric with respect to the principal axes of both volumes.

Figures 2 and 3 show the normalized mean square pressure distribution in the horizontal midplane ($y=1$ m) at 55 and at 140 Hz, respectively. The elastic partition has a mass per unit area equal to 8.06 kg/m^2 and it's thickness, Young's modulus and Poisson's ratio are 0.01 m, 2.12×10^{-9} N/m^2, and 0.24, respectively. The partition fundamental natural frequency is 4.2 Hz. The maximum pressure at the end wall $x=-5$ m, corresponded to the source location.

An alternative model, namely a Modal model, was used to calculate a reference solution to compare with the one obtained using the CMS model. The analytical Modal model developed and implemented here is an extension of the set of integro-differential equations presented in Ref. 3 to a system comprising two coupled rooms and a simply supported partition. Thus, the problem involving sound transmission between two connected rooms can be tackled.

For the Modal model, the acoustic and the structural response fields are expressed in terms of their uncoupled normal modes by means of differential equations for each mode. Therefore, the structural motion is expressed as a summation over the response of the *in vacuo* natural modes driven by fluid loading. The acoustic field of rigid-walled rectangular components has been determined by the summation of the acoustic modes over the fluid volume. In fact, these acoustic modes in the source room were excited by a generalized volume velocity source. According to Fahy,[3] the correct convergence of the modal pressure on the partition surface is obtained due to the Gibb's phenomenon, which is an overshoot that occurs whenever basis functions (for instance, acoustic mode shapes) are used to represent spatial distributions containing the discontinuity of slope.

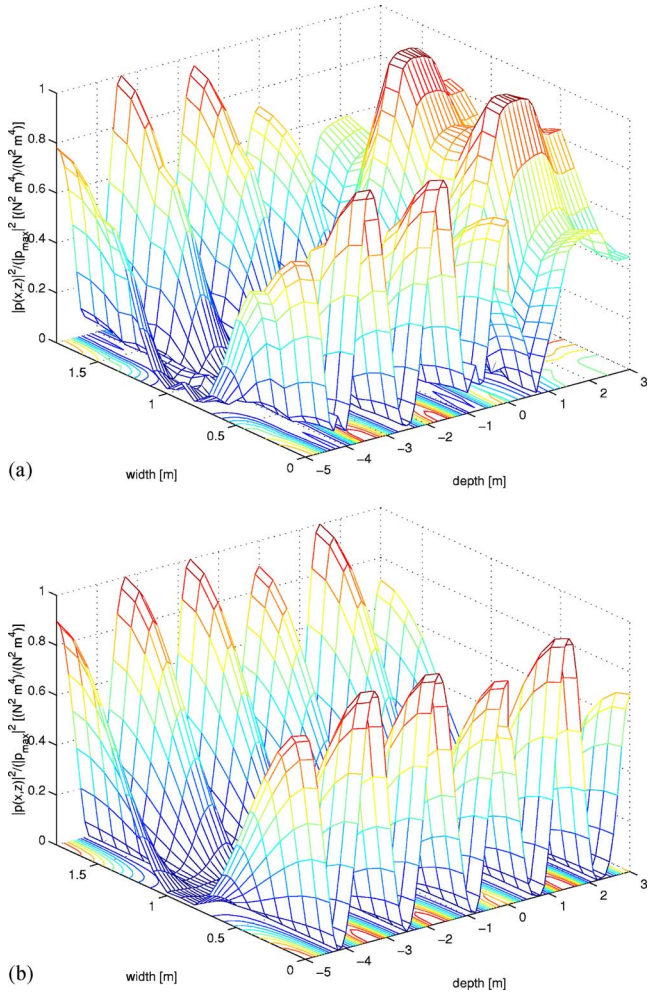

FIG. 4. (Color online) Normalized mean square pressure distribution with respect to the horizontal plane $y=1$ m at 140 Hz. The elastic partition has dimensions, mass per unit area, and Young's Modulus equal to 2 m $\times 1.8$ m, $\rho h=8.06$ kg/m^2, and $E=2.12\times 10^9$ N/m^2, respectively. (a) The CMS model and (b) the Modal model in relative pressure levels to the maximum in the plane.

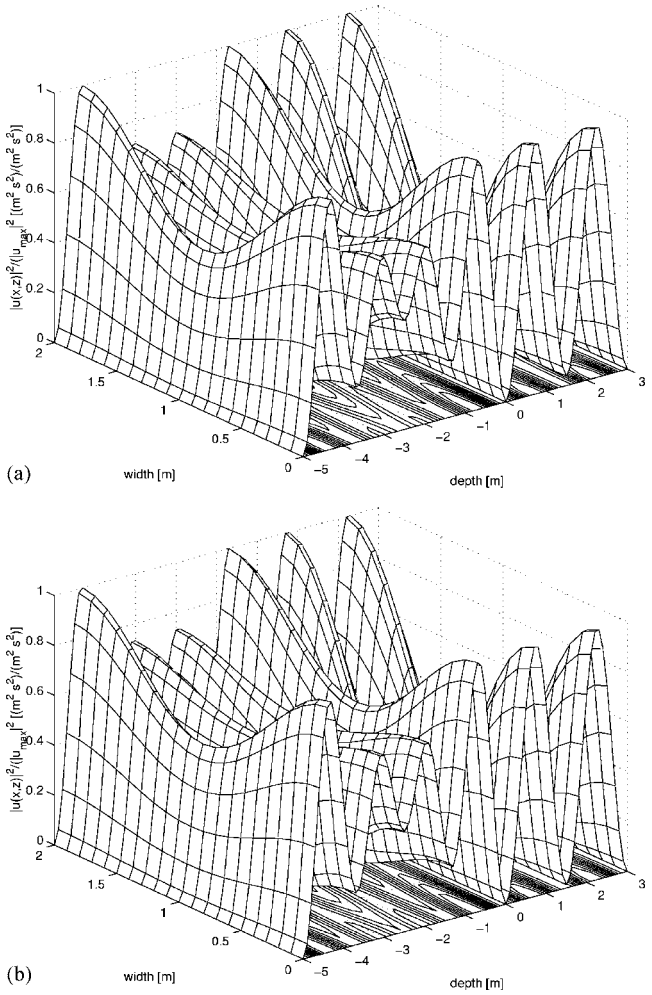

FIG. 5. Normalized mean square velocity distribution with respect to the horizontal plane $y=1$ m at 140 Hz. The elastic partition has dimensions, mass per unit area, and Young's Modulus equal to 2 m $\times 1.8$ m, $\rho h=8.06$ kg/m^2, and $E=2.12\times 10^9$ N/m^2, respectively. (a) The CMS model and (b) the Modal model in relative velocity levels to the maximum in the plane.

Figures 2(a) and 2(b) show the variation of mean square pressure using the CMS and Modal models, respectively. It is seen that the pressure variation in the horizontal midplane of the source and receiving rooms is symmetric for both models. It is plane across the width of the receiving room. This can be explained by the fact that the first tangential mode in the receiving room occurs at about 57 Hz. There is also pressure discontinuity at $x=0$.

Figures 3(a) and 3(b) show the normalized mean square particle velocity distribution in the x direction with respect to the horizontal midplane $y=1$ m at a frequency equal to 55 Hz. At the partition location the particle velocity is close to zero.

Figure 4 shows that the pressure variation in the horizontal midplane of the receiving room is symmetric across the width of the room but not plane, as tangential modes are excited at 140 Hz. It is also seen that fairly good agreement was found between the Modal and CMS model for the mean square pressure distributions in the source room. This indicates that the results are close to particular modes. For instance, the natural frequency at 139 Hz corresponds to the modes (3,0,1) and (1,1,1) for the source and receiving rooms, respectively. Nevertheless, in terms of mean square pressure distribution the results obtained via the Modal and CMS models present some slight differences for the receiving room. This is due to the presence of different modes that exist in one approach compared to the other. It shows the effect of these differences in terms of the absolute pressure levels at 140 Hz.

Figures 5(a) and 5(b) show the normalized mean square velocity distribution with respect to the vertical plane x-z along the center line length of the room ($y=1$ m) for the CMS and Modal model at 140 Hz. There is good agreement for the mean square particle velocity distribution. The results are close to particular modes of both rooms.

Figures 6(a) and 6(b) show a comparison of the overall spatially averaged mean square pressure between the same CMS and the modal model[1] for both source and receiving volumes, respectively. For the CMS model, a total of 96 modes (83 normal modes and 13 constraint modes) were used for the source volume and 67 modes (54 normal modes and 13 constraint modes) for the receiving volume. For the

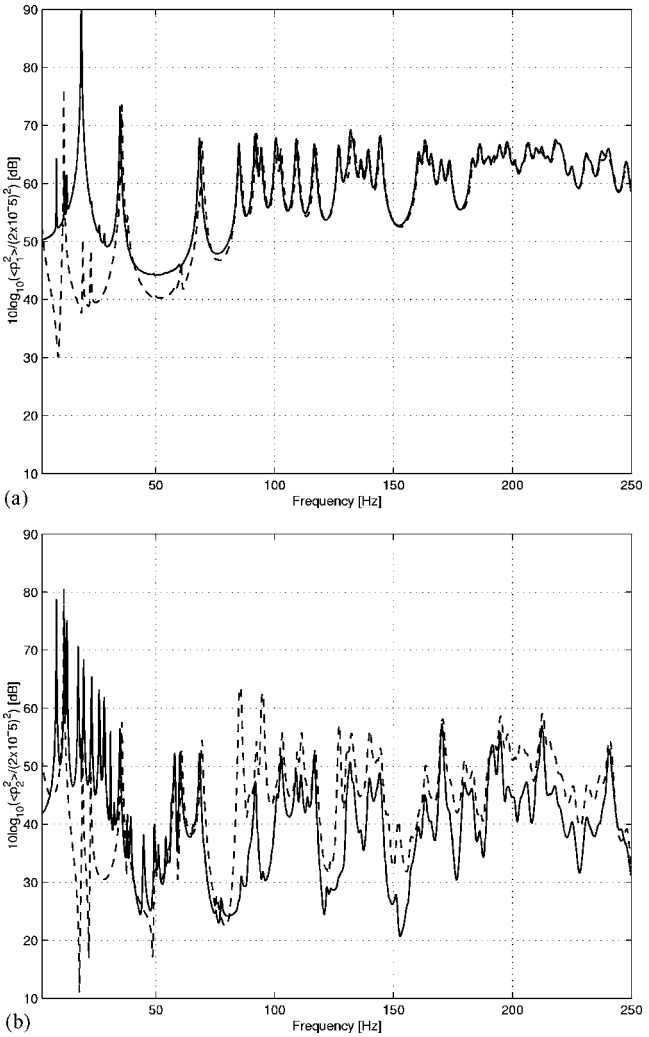

FIG. 6. A comparison between the CMS and a Modal model in terms of spatial-average mean square sound pressure (in narrow bands). The panel mass per unit area is equal to $\rho h = 8.06$ kg/m^2 and $E = 2.12 \times 10^9$ N/m^2. (a) source: $10 \log_{10}(\langle \bar{p}_1^2 \rangle / p_0^2)$(dB *re* 2×10^{-5} Pa); (b) receiver: $10 \log_{10}(\langle \bar{p}_2^2 \rangle / p_0^2)$(dB *re* 2×10^{-5} Pa). The subscripts 1 and 2 indicate source and receiving volumes, respectively; —, CMS model; ---, Modal model.

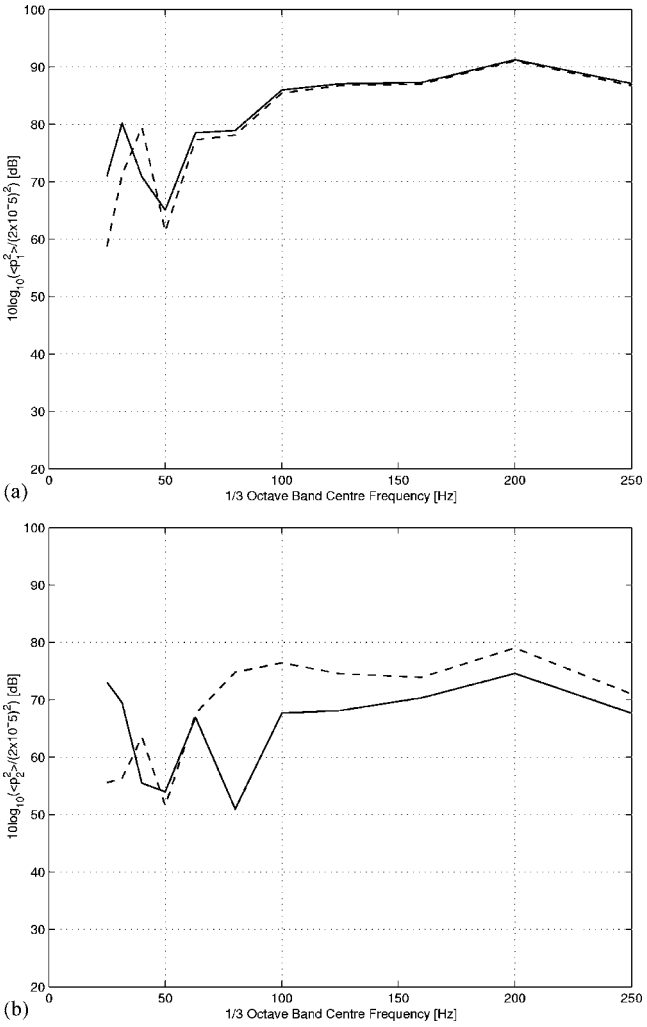

FIG. 7. A comparison between the CMS and the Modal model in terms of the variation of spatial-average mean square sound pressure in 1/3 octave bands. The panel mass per unit area is equal to $\rho h = 8.06$ kg/m^2 and $E = 2.12 \times 10^9$ N/m^2. (a) $10 \log_{10}(\langle \bar{p}_1^2 \rangle / p_0^2)$(dB *re* 2×10^{-5} Pa); (b) $10 \log_{10}(\langle \bar{p}_2^2 \rangle / p_0^2)$(dB *re* 2×10^{-5} Pa). The subscripts 1 and 2 indicate source and receiving volumes respectively; —, CMS model; ----, Modal model.

Modal model a total of 83 and 54 acoustic normal modes were considered for the source and receiving volumes, respectively. For both models a total of 100 structural modes were considered.

The effect of the inclusion of the 0 Hz bulk elastic mode in the Modal model has been checked by eliminating it from the calculations (not shown). As a result, the variation of sound pressure in the source and receiving volumes for the CMS model tended to zero at frequencies below their first "dynamic" modes. The latter are observed at 34 and 57 Hz in Fig. 4(a) for the source and receiving volume, respectively. Peaks at 34 and 68 Hz can be seen in the response of both the source and receiving volumes. However, there are some extra peaks in the response for the receiving volume, which correspond to coupled modes of the complete system. This is because the receiving volume controlled modes are weakly excited by the source volume. For example, the peak at about 19 Hz corresponds to the coupled mode 19.3 Hz that has been identified from an eigenvalue analysis.

Figure 7 shows a comparison between the models in terms of variation of the spatial-average mean square sound pressure in 1/3 octave frequency bands. Figure 7(a) presents the results for the source volume It is seen that a difference of less than 2 dB occurs between the models for frequencies above 100 Hz. Below 100 Hz there are differences of up to approximately 15 dB. For the receiving volume, Fig. 7(b) shows differences of up to 25 dB for frequencies below 100 Hz. This might be explained by the fact that few acoustic modes are excited at frequencies below 100 Hz in the receiving volume. For the CMS model the results are approximately 5 dB lower than those for the Modal model in the 1/3 octave bands with center frequencies greater than 160 Hz. This might be explained by the fact that for a lightweight partition the effect of considering particle velocity continuity at the interface is significant.

Figure 8(a) shows the Noise Reduction (NR) values in narrow and 1/3 octave bands. The difference in the NR between the CMS and Modal models in 1/3 octave bands tends to be less than about 6 dB at center frequencies greater than

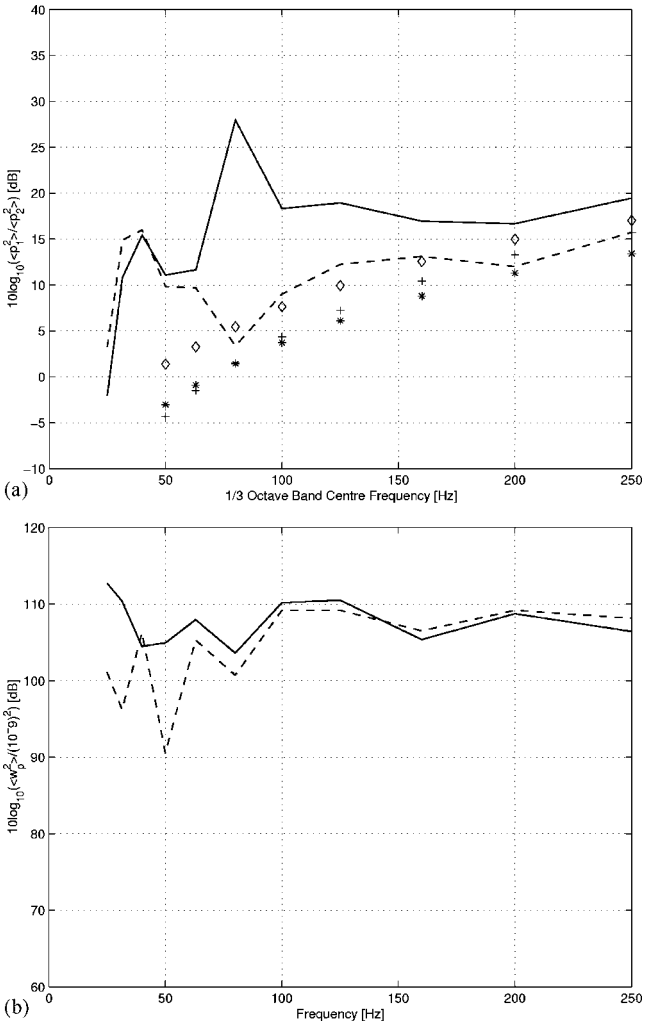

FIG. 8. Comparison between the CMS and the Modal model. (a) The variation of the Noise Reduction NR$=10\log_{10}(\langle\bar{p}_1^2\rangle/\langle\bar{p}_2^2\rangle)$(dB *re* 1 in 1/3 octave bands normalized to the system power input. (b) The variation of the spatially averaged mean square normal velocity of the partition (dB *re* 10^{-9} m/s). The subscripts 1 and 2 indicates source and receiving volumes, respectively; —, CMS model; ---, Modal model; ***, diffuse incidence Mass Law; +, Field incidence Mass Law; ◇, Leppington's prediction.

150 Hz. Below 150 Hz, the results show poor agreement. An alternative comparison shows that there is fair agreement between the CMS model and Leppington's approach[10] as frequency increases. However, in the 1/3 octave bands with center frequencies below 150 Hz, the values obtained using the Modal Model seems to be closer to those using Leppington's approach. The calculated "Schroeder" frequencies[2] were 442 and 571 Hz for the source and receiving rooms, respectively. They were greater than the highest 1/3 octave band center frequency considered in the model configuration. Thus, the predicted system response was strongly influenced by individual modes of the rooms. The NR results obtained using the models may not be appropriate, for the acoustic fields involved are not diffuse. Figure 8(b) shows a comparison of the spatially averaged mean square normal velocity of a lightweight partition calculated using both the CMS and the Modal models. A difference of about 18 dB between the

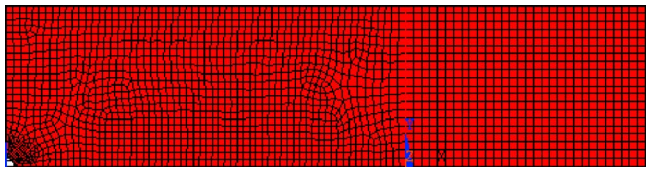

FIG. 9. (Color online) Finite Element Model used on the direct sound transmission analysis.

models occurs at very low frequencies. Nevertheless, a difference of less than 2 dB is found at frequencies greater than 100 Hz.

The frequency responses for a Finite Element (FE) model were obtained using a grid of points inside both the source and receiving components. For the source and receiving components, three-dimensional (3-D) fluid elements were considered on the analysis. For the partition, structural plate elements were adopted. A minimum of six elements per wavelength was considered on the model. Figure 9 shows the FE mesh used for the geometric model.

Figure 10 shows the results obtained when a *monopole* source excites the coupled system. A comparison between the CMS, the Modal, and the FE model is made in terms of spatial-average mean square sound pressure (in narrow bands). It can be seen that the results obtained for the FEM and the Modal models show a good agreement, especially at low frequencies. At certain frequencies, it is difficult to make a comparison between the models. Most coupled frequencies calculated for the CMS and FEM models were fairly similar. This might be explained by the fact that for the CMS model, additional modes (constraint modes) were also included in the summation, and the responses at particular frequencies corresponded to the coupled modes of the system. For higher frequencies (above 100 Hz), the FEM model predicted some significant oscillations in the sound pressure levels in the receiving room.

IV. CONCLUSIONS

The CMS approach for the one-dimensional problem[1] has been extended in this paper to the more general three-dimensional case. The application described the coupling of two, in general, dissimilar rectangular volumes separated by an elastic partition that might form only partial coverage of a common interface, with all of the rest being rigid. In principle, apart from the choice of the component and constraint modes, which for irregular volumes may require numerical (e.g., FE) calculations, the approach is very general and could be implemented within existing commercial software.

For the present examples considered, it has been possible to use existing analytical expressions for the modes under certain assumptions, e.g., simply supported edges for the partition, and then rapid numerical calculations for the coupled systems have been possible. As previously seen in the one-dimensional case,[5] there is a slight change in the detailed pressure spatial variations when correct velocity continuity is included, especially at very low frequencies, but that is not so important if the spatially averaged quantities or higher frequencies are considered. The most important findings from the simulations performed are when a comparison

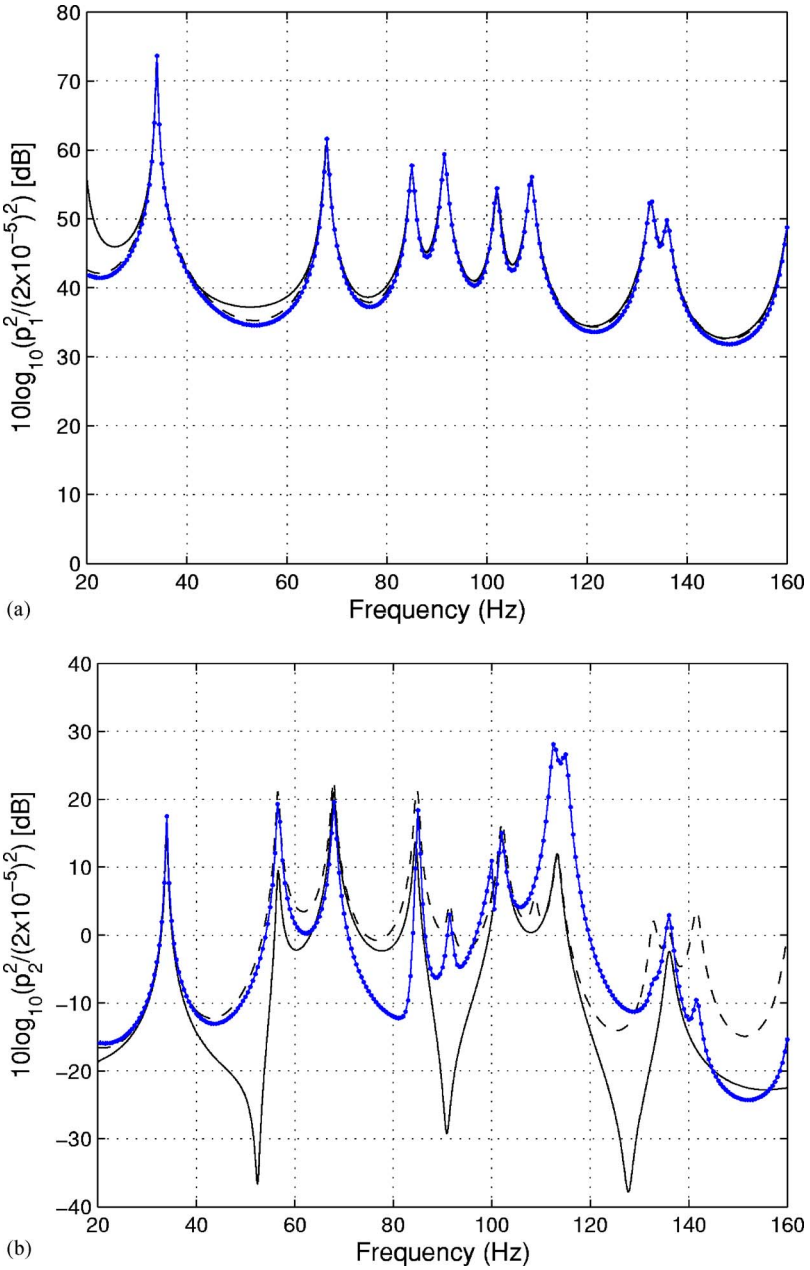

FIG. 10. (Color online) A comparison between the CMS, the Modal, and the Finite Element (FE) model in terms of spatial-average mean square sound pressure (in narrow bands). The panel mass per unit area is equal to $\rho h = 161.2$ kg/m^2 and $E = 2.12 \times 10^9$ N/m^2. (a) source: $10\log_{10}(\langle \bar{p}_1^2 \rangle / p_0^2)$(dB *re* 2×10^{-5} Pa); (b) receiver: $10\log_{10}(\langle \bar{p}_2^2 \rangle / p_0^2)$(dB *re* 2×10^{-5} Pa). The subscripts 1 and 2 indicate source and receiving volumes, respectively; —, CMS model; ---, Modal model; -*-, FE model.

is made between the CMS and the original Modal Model approach. It is seen that the spatial distribution of sound pressure in the volumes are very complex, depending on several factors such as source position, volume and partition dimensions, frequency, etc. For the cases presented herein the response in the receiving volume was directly related to the degree of coupling between the structural and the transverse acoustic modes.

An elastic partition was incorporated and considered as another modal component. The results have shown fairly good agreement between the CMS and the Modal model in terms of spatially averaged mean square pressure. Similarly, reasonably good agreement between the models was obtained at higher frequencies. One possible explanation is that the modal model, which considers rigid-walled modes, is more representative at higher frequencies, where the system boundary conditions are much less important. Nevertheless, it still cannot reproduce exactly the partition velocity compared to the CMS method.

In summary, the number of modes, and hence the order of the equations, increases significantly, and for practical computational and numerical reasons the CMS approach is primarily useful for low-frequency predictions. This comment is also applicable to the existing Modal methods and is a consequence of the high modal density with increasing frequency for acoustic volumes and is a reason why statistical approaches (e.g., SEA) have been developed. In principle, the constraint equations could also be used for the application of further conditions based on the impedance of the walls, for example, if one requires the distribution of absorbing material characterized as locally reacting and quantified by a normal impedance.

For irregular volumes the more general approximate methods, such as the numerical FE/BEM and the Trefftz techniques,[11,12] might be more appropriate unless the normal modes are found numerically in advance of applying the

CMS method. The incorporation of the approach into existing software packages for acoustics would be worth an investigation in future studies.

In conclusion, for certain practical problems where the description of sound pressure and particle velocity spatial distributions is considerably important, especially at very low frequencies, the CMS model is usually more appropriate than the Modal model. On the other hand, if for a specific problem the spatial-average mean square sound pressure is the most important parameter to be determined, the modal model can be an alternative solution.

[1]M. D. C. Magalhaes and N. S. Ferguson, "Low frequency airborne sound transmission," *Proceedings of Inter Noise*, The Hague, 2001, p. 4.

[2]P. M. Morse and K. U. Ingard, *Theoretical Acoustics* (McGraw-Hill, Princeton, NJ, 1986).

[3]F. J. Fahy, *Sound and Structural Vibration* (Academic Press, United Kingdom, 1985).

[4]R. R. Craig, Jr., *Structural Dynamics—An Introduction to Computer Methods* (Wiley, New York, 1981).

[5]M. D. C. Magalhaes and N. S. Ferguson, "Acoustic-structural interaction analysis using the component mode synthesis method," Appl. Acoust. **64**, 1049–1067 (2003).

[6]K. H. Ghlaim and K. F. Martin, "Reduced component modes in a damped system," *Proc. Int. Conf. On Modal Analysis*, Schenectady, N. Y. Union College, 1986, pp. 683–689.

[7]L. R. Klein and E. H. Dowell, "Analysis of modal damping by component modes method using Lagrange multipliers," J. Appl. Mech. **41**, 527–528 (1974).

[8]L. Meirovitch, *Analytical Methods in Vibrations* (Macmillan, New York, 1967).

[9]T. P. Gialamas, D. T. Tsahalis, D. Otte, H. Van Der Auwaraer, and D. A. Manolas, "Substructuring technique: Improvement by means of singular value decomposition (SVD)," J. Appl. Mech. **62**, 1211–1219 (2001).

[10]F. G. Leppington, "The transmission of randomly incident sound through an elastic panel," Proc. R. Soc. London, Ser. A **426**, 153–165 (1989).

[11]B. Pluymers, W. Desmet, D. Vandepitte, and P. Sas, "Application of the wave based prediction technique for the analysis of the coupled vibro-acoustic behaviour of a 3D cavity," *Proc. of ISMA*, International Conference on Noise and Vibration Engineering, KUL, Belgium, 2002, pp. 891–900.

[12]W. Desmet, B. Van Hal, P. Sas, and D. Vandepitte, "A computationally efficient prediction technique for the steady-state dynamic analysis of coupled vibroacoustic systems," *Advances in Engineering Software* (Elsevier, New York, 2002), Vol. 33, pp. 527–540.

A three-dimensional sound intensity measurement system for sound source identification and sound power determination by ln models[a)]

Shiho Nagata, Kenji Furihata,[b)] and Tomohiro Wada
Department of Electrical and Electronic Engineering, Faculty of Engineering, Shinshu University, 4-17-1 Wakasato, Nagano, 380-8533 Japan

David K. Asano
Department of Information Engineering, Faculty of Engineering, Shinshu University, 4-17-1 Wakasato, Nagano, 380-8533 Japan

Takesaburo Yanagisawa[c)]
Faculty of Engineering, Shinshu University, 4-17-1 Wakasato, Nagano, 380-8533 Japan

(Received 21 December 2004; revised 26 September 2005; accepted 27 September 2005)

This paper describes a full vector intensity probe which advances the field of sound intensity and sound source direction estimation using six matched rotating and variable directional microphones. The probe has three pairs of microphones at an equal spacing of 30 mm that are set up in each of the x, y, and z directions and share the same observation point. The calibration method using the rotating microphone system is effective to correct position errors in the y- and z-axes microphone pairs. Sound intensity measurements using the variable directional microphone method can locate with accuracy a sound source, i.e., the structure parts radiating most acoustic energy. The system can find the maximum sound intensity level and beamwidth of the major lobe, and the peak sound intensity levels of the minor lobes. Therefore, a procedure for sound power determination based on minimum measurement data is theoretically and experimentally discussed. Consequently, it is possible to reconstruct only parts of the system emitting the most noise and measure efficiently the sound power level. © *2005 Acoustical Society of America.* [DOI: 10.1121/1.2126929]

PACS number(s): 43.58.Fm, 43.55.Nd [AJZ] Pages: 3691–3705

I. INTRODUCTION

Sound intensity is a measure of the flow of energy passing through a unit area per unit time and is measured in W/m^2.[1] It is well known that the two-microphone method is very useful to determine the sound intensity vector in a sound field. A commonly used intensity probe consists of two closely spaced identical microphones, which are placed face to face.[2,3] However, there are three problems with this probe: (1) if there exists an intrinsic phase mismatch between microphones and/or channels, a so-called phase mismatch appears and the measurement error increases as the frequency decreases, (2) in the conventional technique based on deriving the particle velocity from the sound pressure gradient, if the two-microphone axis is not directed correctly toward the sound source, further errors result, and (3) from the probe's directional characteristics, this method is unable to separate the vectors precisely.

To solve problem (1), even a very small deviation between the phase responses of the two microphones, i.e., phase mismatch, has an adverse effect on the measurement accuracy with this technique,[4,5] so much effort has been spent on improving the transducers,[6] and on developing measurement procedures that ensure that the influence of the remaining phase mismatch is within acceptable limits.[7,8] One method of correcting such phase errors makes use of a switching technique that essentially performs measurements twice, the second time with the microphones interchanged.[9] Others methods make use of an initial calibration measurement where the two microphones are subjected to the same sound pressure, as in a small cavity.[10] Once the ratio for residual intensity to sound pressure used in determining the residual intensity has been determined, errors due to phase mismatch in subsequent intensity measurements can be corrected, provided that the mean square pressure is determined concurrently with the intensity.[11] In our proposed rotating microphone method,[12] which solves problems (1) and (2), the microphones are rotated around the measuring point in certain planes, and the data are processed numerically with use of periodic functions of the angles of rotation.

Some microphones allow us to vary the directional characteristics by selecting omnidirectional, cardioid, subcardioid, supercardioid, bidirectional, or shotgun patterns. In our variable directional microphone method,[13] which solves problem (3), the sound pressure spectrum of the microphone

[a)]Portions of this work were presented in "Three-dimensional sound intensity vector using a variable directional microphone system for identifying effective center of sound sources directly," Proceedings of Inter-Noise 2003, The 32nd International Congress and Exposition on Noise Control Engineering, Jeju, Korea, August 2003(N238), and "Fundamental study of the number of discrete measurement points on the sound power level using sound intensity method, " The 32nd International Congress and Exposition on Noise Control Engineering, Jeju, Korea, August 2003(N786).

[b)]Electronic-mail: kennfur@gipwc.shinshu-u.ac.jp

[c)]Professor Emeritus.

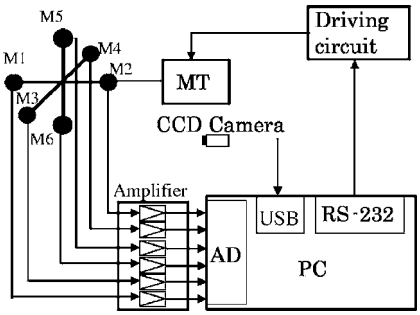

FIG. 1. Block diagram of our three-dimensional sound intensity measurement system.

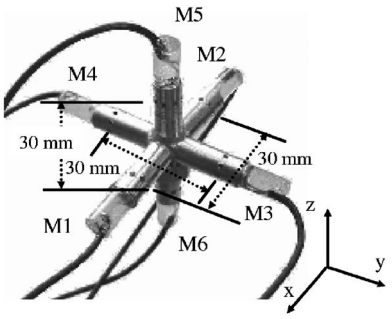

FIG. 2. Photo of our handmade three-dimensional sound intensity probe.

itself and the sound pressure gradient of the microphone pair are measured, the spectral amplitudes of both are compared, and only the sound incident from the desired direction is selected.

ISO 9614 governs sound power determination based on sound intensity. It is divided into two parts, one which makes use of point measurements (ISO 9614-1),[8] and one which makes use of swept or scanned measurements (ISO 9614-2).[14] The intention underlying the approach adopted in the ISO standard for sound power determination is to ensure that errors due to phase mismatch are within acceptable limits when some requirement is met, and to indicate actions to be taken in order to improve the situation when this is not the case. The switching technique and the rotating microphone method give in principle nearly perfect compensation for phase errors, but repeating the entire measurement is rather inconvenient. The calibration technique has never come into general use either, because of improvements in the available microphones, and partly because it seems to be surprisingly difficult to generate exactly the same sound pressure on the two microphones even in a very small coupler.[15]

The purpose of this paper is to discuss and demonstrate a three-dimensional sound intensity measurement system using six matched rotating and variable directional microphones in a symmetrical arrangement.[16] This system can measure the maximum sound intensity level and beamwidth of the major lobe, and the peak sound intensity levels of the minor lobes without the error sources of problems (1), (2), and (3). We also describe a sound power determination method based on minimum measurement data that seems to be surprisingly effective.

II. EQUIPMENT AND OPERATION PRINCIPLES

The following describes the operating principles of the proposed system. Figure 1 shows the block diagram of this system. It consists of a rotating intensity probe which has six microphones (M1–M6). The microphone outputs are amplified with six preamplifiers (gain: 60 dB) and the data are gathered using an eight-channel AD converter (Interface, PCI-3120, AD12P8D-79) and a personal computer (PC). MT is a stepping motor with a driving circuit, which is connected to the PC via an RS-232 interface. Sound intensity measurements offer several ways to locate and identify parts of devices and machines radiating the most acoustic energy. To identify visually each sound source, the proposed system is equipped with a small CCD (charge-coupled device) camera connected via a USB (universal serial bus) port.

A. Design of three-dimensional sound intensity probe

Figure 2 shows a photo of our handmade three-dimensional sound intensity probe. The probe has three pairs of microphones that are set up in each of the x, y, and z directions and share the same observation point. The microphones placed face to face in each pair are 30 mm apart. Each microphone is an electret condenser microphone (Star, MAA-06A-P, 6 mm in diameter). The frequency responses of these microphones are almost the same, and their sensitivity is about −43.0 dB(0 dB=1 V/Pa) from 100 Hz to 10 kHz.

LMS International SYSNOISE is effective for estimating the sound field around the probe structure. Figure 3 shows the diffraction effect in the sound field of our probe. From this figure, we see that the effect is less than 0.5 dB from 100 Hz to 2 kHz.

Thompson and Tree[17] considered the errors due to developmental finite difference approximations in the two-microphone acoustic intensity measurement technique. The best procedure would be to select measurement parameters based on the quadrupole nondimensional analysis as a worst-case design. Therefore, the parameter limits $0.1 \leqslant k\Delta r \leqslant 1.3$ and $0 \leqslant \Delta r/r \leqslant 0.5$ (k is the acoustic wave number, Δr is the microphone separation, and r is the distance between a source and the measurement point) would be useful guidelines for maximum inaccuracy for ±1.5 dB. Therefore, a microphone separation of 30 mm can cover frequencies from 182 Hz to 2.37 kHz.

For a sound field generated by a simple source, it can be shown that $|I_r|/|I_\infty| \approx \sin(k\Delta r)/k\Delta r$ in the far field, where I_∞

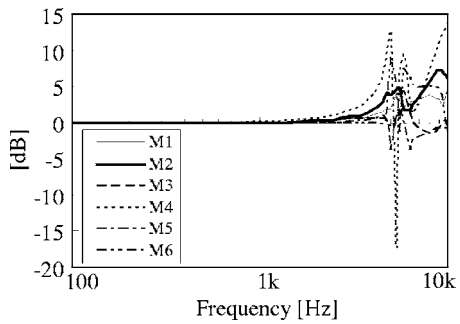

FIG. 3. Diffraction effect in the sound field of our probe predicted with LMS SYSNOISE.

indicates the magnitude of the far-field intensity. The magnitude of the far-field intensity is measured using the conventional mean-squared-pressure measurement, i.e., $|I_\infty| = \overline{p^2}/\rho c$, where $\overline{p^2}$ is the mean squared pressure, ρ is the air density, c is the speed of sound, and I_r is the radial intensity, which is measured at the same location in the direction pointing from the source to the measurement location. This expression shows that for $k\Delta r \leqslant 1$ ($k\Delta r = 1$ corresponds to 1.8 kHz, since $\Delta r = 30$ mm in this case) the deviation of $|I_r|$ from $|I_\infty|$ is less than 1 dB.[9]

B. Calibration of the rotating microphone system

The calculation of the sound intensity in the two-microphone method is very sensitive to any phase mismatch between the two microphones. However, in general, there are phase mismatches between each pair of microphones in our system. Therefore, a sound-pressure phase-difference calibrator is necessary to make the probes easy to use. Because our initial acoustic intensity measurement searches for the maximum sound intensity level of the major lobe, its beamwidth, and the peak sound intensity levels of the minor lobes, our three-dimensional sound intensity measurement system makes use of an initial calibration measurement where the three pairs of microphones are subjected to the same sound pressure.

To meet the most stringent requirements for measurement accuracy, calibration of the sound intensity probe and sound intensity level was done in our faculty's anechoic room ($3 \times 4 \times 5 = 60$ m^3). The loudspeaker used as the simple source was a dynamic type with a diameter of 16 cm. The back was sealed with clay. A sampling frequency of 32 kHz was used for the sound intensity measurements which gives us a Nyquist frequency of 16 kHz. Depending on the measurement accuracy,[18] the FFT sizes of 1024, 2048, and 4096 were used yielding 512, 1024, and 2048 frequency data points, respectively. Therefore, the complex transfer functions were measured using the above-noted FFT sizes.

Consider one pair of microphones. A sound wave front that reaches microphone M1 will reach microphone M2 after a certain time delay. The difference in time is used to calculate the sound intensity component on the microphone axis and to judge the direction of the sound as either backward or forward. Assuming the sound pressure at M1 is $p_1(t)$ and that at M2 is $p_2(t)$, then the average value of the sound pressure $p(t)$ and the particle velocity $v(t)$ is

$$p(t) = \frac{p_1(t) + p_2(t)}{2}, \tag{1}$$

$$v(t) = -\frac{1}{\rho} \int \frac{\{p_2(t) - p_1(t)\}}{\Delta r} dt, \tag{2}$$

where Δr is the distance between the two microphones and ρ is the air density. The sound intensity can be determined by multiplying $p(t)$ by $v(t)$ and calculating the time average for this product.[19]

Figure 4 shows the configuration of a sound source and the microphone orientation (four microphones) in Cartesian coordinates. When we direct the x-axis probe toward the sound source, the sound intensity I is given by[12]

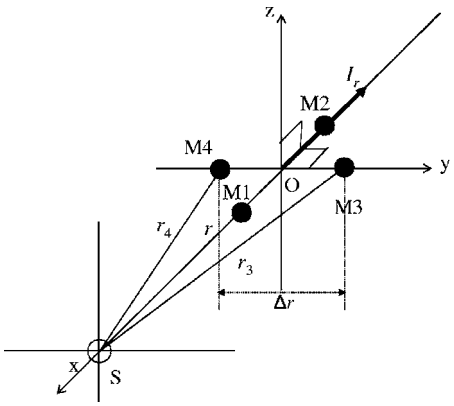

FIG. 4. Configuration of a sound source S and four microphones in Cartesian coordinates. O is the observation point (the center of our probe), M1, M2, M3, and M4 are the locations of the measuring microphones, r is the distance from O to S, r_3 is the distance from M3 to S, r_4 is the distance from M4 to S, and Δr denotes the microphone separation.

$$I = I_x = \frac{\overline{p^2}}{\rho c}\left(1 + \frac{\phi_{12}}{k\Delta r}\right), \tag{3}$$

where ρc is the specific acoustic impedance, k is the wave number, and ϕ_{12} is the phase mismatch between M1 and M2.

First, sound intensity levels were measured using this system (I_x) and an intensity level measuring system (I_r) by the cross-spectral method (RION Co., SA-74),[2,3] consisting of an intensity microphone (RION Co., SI-21, which has a maximum intrinsic phase mismatch of 0.25° at 150 Hz), a pistonphone (NC-72), and a FFT analyzer (SA-74). The two intensity probes were set 4 m away from the front of the loudspeaker.

From the results, the bias error $\phi_{12}/k\Delta r$ is given by

$$\frac{\phi_{12}}{k\Delta r} = \left|\frac{I_x}{I_r}\right| - 1. \tag{4}$$

Therefore, it can be seen that once the bias error $\phi_{12}/k\Delta r$ has been determined, errors due to phase mismatch in subsequent intensity measurements can be corrected. Figure 5 shows the bias error $\phi_{12}/k\Delta r$ (solid line) as a function of frequency (FFT size: 1024). From this figure, we see that

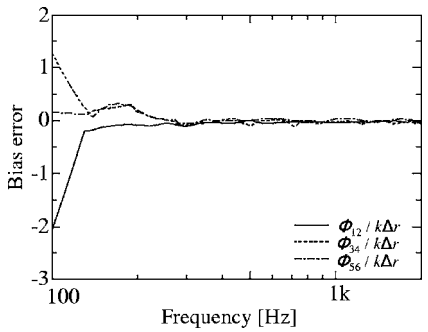

FIG. 5. Bias errors $\phi_{12}/k\Delta r$, $\phi_{34}/k\Delta r$, and $\phi_{56}/k\Delta r$ as a function of frequency.

the bias error is −2.1 at 100 Hz, and ±0.1 or less from 200 Hz to 2 kHz.

Second, the sound intensity I_y with a bias error due to the phase error ϕ_{34} between microphones M3 and M4 can be written as

$$I_y = \frac{\overline{p^2}}{\rho c} \cdot \frac{\phi_{34}}{k\Delta r}. \tag{5}$$

Similarly, the sound intensity I_z with a bias error due to the phase error ϕ_{56} between microphones M5 and M6 can be written as

$$I_z = \frac{\overline{p^2}}{\rho c} \cdot \frac{\phi_{56}}{k\Delta r}. \tag{6}$$

Consequently, if the y-axis and z-axis probes were to be rotated around the x-axis probe in the y-z plane, the sound intensity components given by Eqs. (5) and (6) would be obtained as functions of the rotation angle $\theta = 2\pi(i-1)/N$.[12] These would be periodic functions of the angle of rotation, containing the bias errors.

Accordingly, to cancel the bias errors from Eqs. (5) and (6), one can multiply them by the periodic function $e^{j\theta}$ and then integrate the results over the period of rotation, resulting in

$$\frac{1}{\pi}\int_0^{2\pi} I_y e^{j\theta} d\theta = \lim_{N\to\infty} \sum_{i=1}^{N} \frac{2}{N} I_y \exp\left(j\frac{2\pi}{N}(i-1)\right)$$

$$= \sum_{i=1}^{3} \frac{2}{3} I_y \exp\left(j\frac{2\pi}{3}(i-1)\right) = 0, \tag{7}$$

$$\frac{1}{\pi}\int_0^{2\pi} I_z e^{j\theta} d\theta = \lim_{N\to\infty} \sum_{i=1}^{N} \frac{2}{N} I_z \exp\left(j\frac{2\pi}{N}(i-1)\right)$$

$$= \sum_{i=1}^{3} \frac{2}{3} I_z \exp\left(j\frac{2\pi}{3}(i-1)\right) = 0. \tag{8}$$

From Eqs. (7) and (8), it is clear that when the components along each axis are zero, the x-axis probe is correctly directed toward the sound source, and the sound intensity I_r is given by Eq. (3). In this way, when our probe was set with the components along each axis equal to zero, the bias errors of Eqs. (5) and (6) can be determined. Figure 5 shows the bias errors of $\phi_{34}/k\Delta r$ (dashed line) and $\phi_{56}/k\Delta r$ (dash-dot line). From this figure, it can be seen that the bias errors of the sound intensities I_y and I_z have been determined, too. Therefore, the bias errors of our probe due to phase mismatches in subsequent intensity measurements can be corrected.

C. Variable directional microphone method (Ref. 13)

A complicated structure may radiate sound from several sources and absorb sound in other places. To evaluate the effectiveness of noise reduction methods we need to know how much noise is being radiated by the individual components of machines. The directivity characteristics for the sound intensity analysis system looks (two-dimensionally) like a figure-eight pattern, known as a cosine characteristic. This is due to the probe and the calculations done by the analyzer. For sound incident at an arbitrary angle α to an axis, the intensity component along the axis will be reduced by a factor of $\cos\alpha$. For sound incident at 90° to an axis, there is no component along the axis, as there will be no difference in the pressure signals. Hence there will be zero particle velocity and zero intensity. The full vector is made up of three mutually perpendicular components (at 90° to each other); one for each coordinate direction. Therefore, there is a change in direction for only a small change in the incident angle. The position of the measurement probe where the sound intensity direction alternates rapidly between positive- and negative-going intensities defines the point where the sound source must be incident on the probe at 90° to its axis. In this way, a technique using a variable directional microphone system that is able to separate a sound intensity vector is proposed.

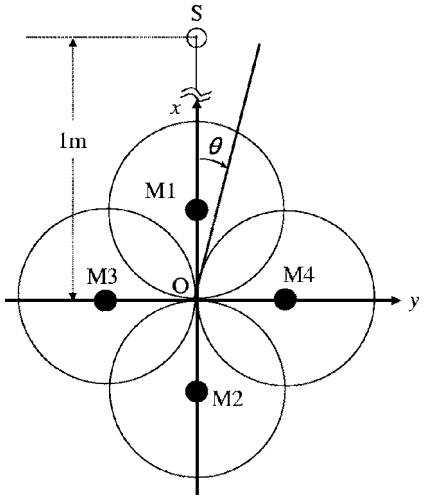

FIG. 6. Relationship between the directional separation angle θ and the microphone orientation. S is a sound source, r is the distance from O to S, and M1, M2, M3, and M4 are the locations of the measuring microphones.

Figure 6 shows the relationship between the separation angle and the microphone orientation (four microphones: M1, M2, M3, and M4) in the two-dimensional x-y sound field. In this figure, a directional separation angle θ is set on the x-y plane. When the intrinsic phase mismatches between each pair of microphones are zero, the sound intensity components I_x and I_y in the θ direction are given by

$$I_x = \frac{\overline{p^2}}{\rho c}\cos\theta, \tag{9}$$

$$I_y = \frac{\overline{p^2}}{\rho c}\cos(\theta - 90°). \tag{10}$$

Therefore, the relationship of the sound intensity level difference LD between I_x and I_y to the directional separation angle θ can be written as

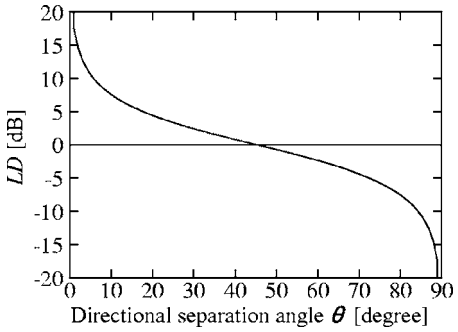

FIG. 7. Relationship between the level difference LD and the directional separation angle θ.

$$\mathrm{LD} = 10\log_{10}\left|\frac{I_x}{I_y}\right| = 10\log_{10}\left|\frac{\cos\theta}{\cos(\theta-90^\circ)}\right| (\mathrm{dB}). \quad (11)$$

Figure 7 shows the relationship between the level difference LD and the directional separation angle θ. From this figure, it can be found that when θ=5.7°, 10°, and 15°, LD =10.0, 7.5, and 5.7 dB, respectively.

1. Variation of the directional separation angle and its effectiveness

First, verification of the directional separation angle of the microphone system by Eq. (11) was carried out. In the experiment, a speaker S (a distance r=1 m from the sound source to the center of our probe) in the direction θ=0° was driven by a 1 kHz pure tone in our faculty's anechoic room. The sound intensity was measured while the probe was rotated in 1.8° steps at directional separation angles θ of 5.4°, 16.2°, and 30.6° (LD=10.24, 5.37, and 2.28 dB, respectively).

The measured results for the directional separation angles shown in Fig. 8 are normalized by the intensity level at the direction of the sound source (θ=0°). From Figs. 8, we see that the measured results, indicated by closed triangles, and the theoretical directional separation angles (θ =5.4°, 16.2°, and 30.6°), indicated by the solid lines, agree well, because the bias errors are zero. Therefore, it can be verified experimentally that the directional separation angle θ can be set arbitrarily.

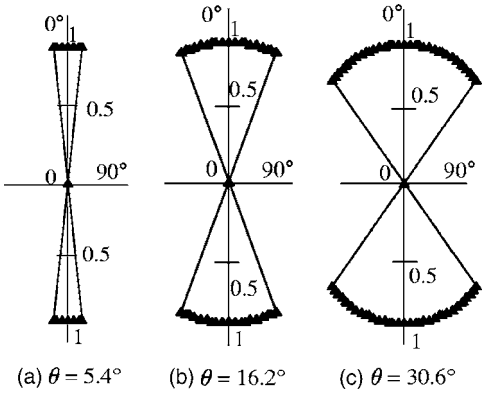

FIG. 8. Measured separation angle using our variable directional microphone method when the sound source was driven by a 1 kHz sine wave. Solid lines: theoretical value, and closed triangles: measured value.

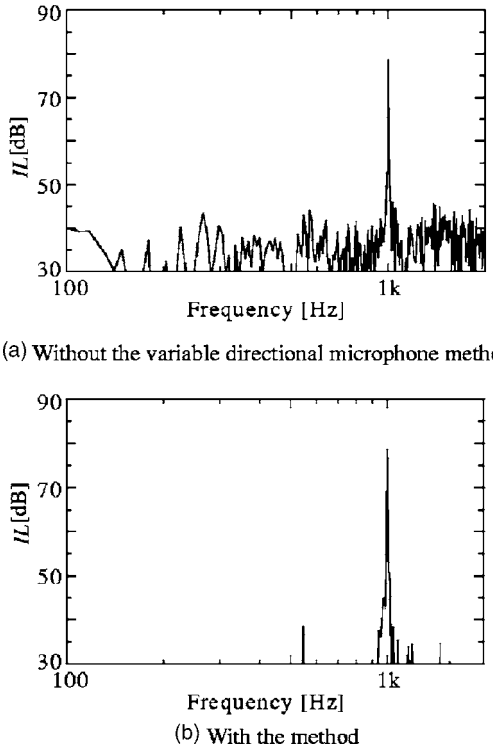

FIG. 9. Comparison of the measured results (a) without and (b) with the variable directional microphone method when the directional separation angle θ=5.7°, S_1 (1 kHz sine wave, and θ_1=0°), and S_2 (band noise from 128 Hz to 2 kHz, and θ_2=30°).

Second, the experiment on the signal from the desired sound source direction was carried out by simultaneously driving speaker $S_1(\theta_1=0^\circ)$ with a 1 kHz pure tone and speaker $S_2(\theta_2=30^\circ)$ with passband noise (128 Hz to 2 kHz) in our faculty's anechoic room. To separate the signals from S_1 and S_2, the directional separation angle θ was set 5.4°.

Figure 9(a) shows the sound intensity measured without the variable directional microphone method and Fig. 9(b) with the method. From Fig. 9(b), we see that the desired sound intensity spectrum (1 kHz) was separated from the sound intensity spectrum due to passband noise. Consequently, it can be said that the proposed method can separate sound intensity vectors of sound sources with different spectra.

2. Sound source identification

Figure 10 shows a block diagram of our equipment used to identify sound sources in a vacuum cleaner. The vacuum cleaner was rotated by a handmade turntable (0.04° / pulse) with a pulse motor and pulse motor control system. The distribution of each sound source was measured by our system at a distance of 10 cm from the vacuum cleaner at heights of 10, 20, 30, and 40 cm from the mesh floor in our faculty's anechoic room. The directional separation angle θ was set to 16.2°.

Contour and three-dimensional plots give a more detailed picture of the sound field generated by a sound source. Figure 11 shows contour plots of several sound sources in

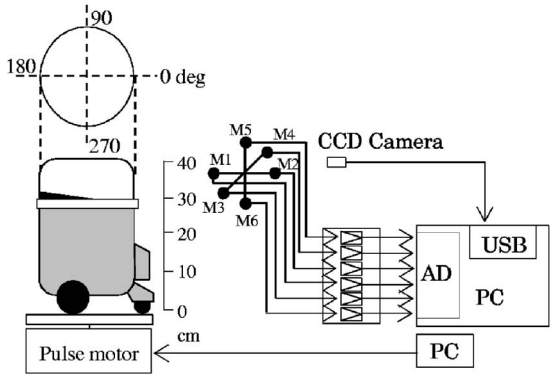

FIG. 10. Block diagram of the equipment used to identify the sound sources in a vacuum cleaner.

the vacuum cleaner at (a) 601 Hz and (b) 1828 Hz. From Fig. 11, it can be found that the sources and/or sinks can be identified with accuracy.

3. Source location—The null search method on the y-z plane

As a quick and easy test we can make use of the probe's directional characteristics. Sound incident at 85° to the axis will be recorded as positive-going intensity, whereas sound at 95° will give negative-going intensity. Therefore there is a change in direction for only a small change in angle. For example, Fig. 12 shows a three-dimensional intensity display of our sound intensity measuring system. Measurements (the sampling frequency; 32 kHz, FFT size; 1024 points) were

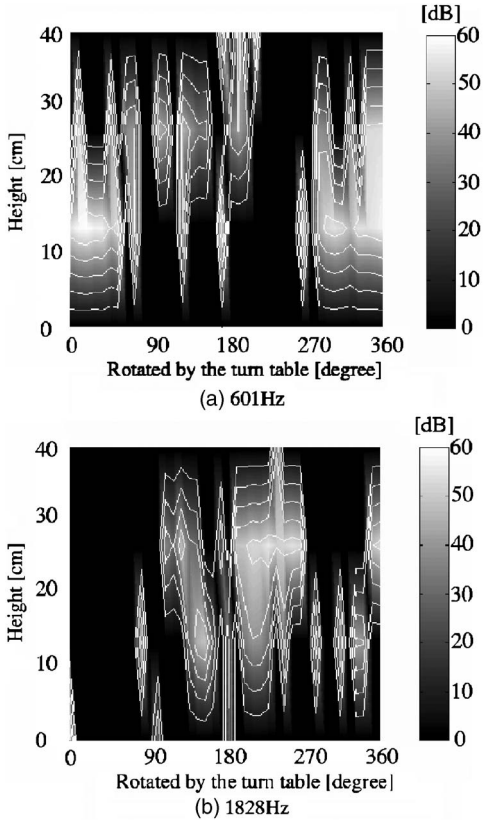

FIG. 11. Contour plots of the sound intensity distribution of the vacuum cleaner.

done every 0.113 s. While we watched the display, the probe was swept so that its axis followed a line parallel to the *y-z* plane on which the source was located. At some point, the direction suddenly changed as shown in the center figure $[\mathbf{I}_y(\mathrm{dB})]$ in Fig. 12. Here the sound must be incident on the *x*-axis probe at 90° to the *y* axis and thus identifies the source position. Figure 13 shows a picture taken by the CCD camera at the sound source identified visually as shown in Fig. 11.

Consequently, it can be said that this technique is effective to determine the location of sound sources and the amount of noise being radiated by the individual components of machines.

III. SOUND POWER DETERMINATION PROCEDURE

Requirements for sound power determination as part of a more general product noise measurements are becoming more and more widespread. One reason for this is the increasing amount of legislation regarding noise emissions. Sound intensity is a vector and is a measure of acoustic energy flow. It has a fundamental advantage in sound power determination since there is a direct connection between sound power and sound intensity. In theory, all that is required to measure the sound power of a source is to integrate the sound intensity over a surface totally enclosing the source based on Gauss's theorem.[20] Because of the vector nature of intensity, the effects of any noise sources external to the surface will cancel out. In practice, however, imperfections in the measuring equipment and measuring technique make the procedure rather complicated.

ISO 9614 governs sound power determination based on sound intensity. It is divided into two parts, one which makes use of point measurements (ISO 9614-1),[8] and one which makes use of swept or scanned measurements (ISO 9614-2).[14] Point measurements can be used for precision, engineering, and survey grade determination of sound power. The number of measurement points used in these methods tends to increase, i.e., the sound power level PWL can be calculated using the sound intensity method with the following:

$$\mathrm{IL}_i = 10 \log_{10} I_{ni}/I_0 \ (\mathrm{dB}), \quad I_{ni} = I_0 \cdot 10^{IL_i/10} \ (\mathrm{W/m^2}), \tag{12}$$

$$W \cong \sum_{i=1}^{N} I_{ni} \Delta S_i \ (\mathrm{W}), \tag{13}$$

$$\mathrm{PWL} = 10 \log_{10} W/W_0 \ (\mathrm{dB}), \tag{14}$$

where IL is the sound intensity level in dB, I_n is the normal sound intensity, $I_0 = 10^{-12}$ W/m^2, and $W_0 = 10^{-12}$ W.

ISO 9614-1 recommends starting with ten measurement positions. The number of measurement points N is determined from the nonuniformity field indicator F_4 using

$$F_4 = \frac{1}{\bar{I}_n} \sqrt{\frac{1}{N-1} \sum_{i=1}^{N} \left(I_{ni} - \bar{I}_n\right)^2}, \tag{15}$$

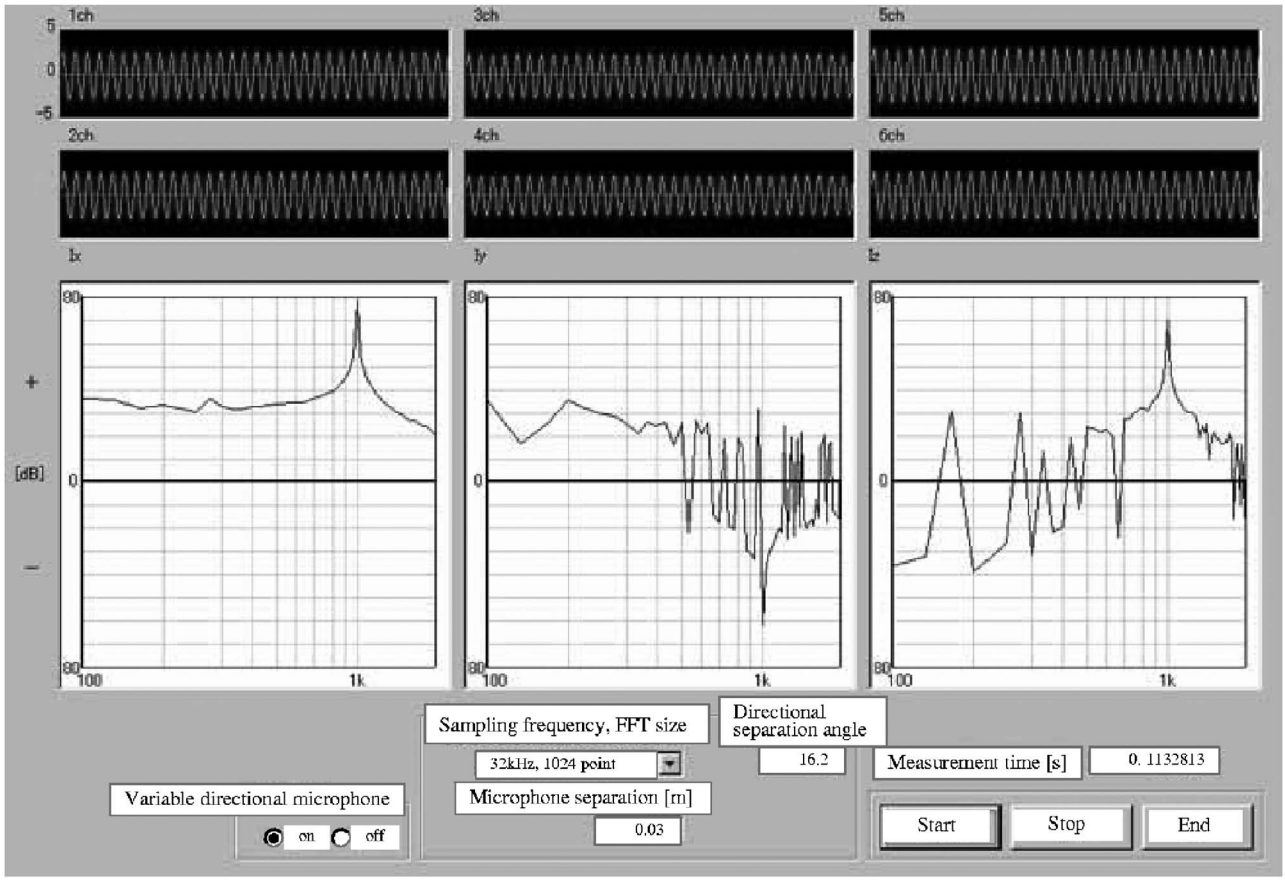

FIG. 12. An example of the three-dimensional intensity display of our sound intensity measuring system. Measurements (sampling frequency: 32 kHz, FFT size: 1024 points) were done every 0.113 s.

$$N > CF_4^2, \tag{16}$$

where $\bar{I}_n$ is the average normal sound intensity, and C is a constant depending on the required measurement accuracy. The values for C are: 11 when the 1/3 octave band center frequency is 100–160 Hz, 19 when the center frequency is 200–630 Hz; and 29 when the center frequency is 800 Hz to 5 kHz. ISO 9614-1 yields accuracy in the mid-frequency range (800–5000 Hz) of 1.0 dB for precision grade and 1.5 dB for engineering grade. From Eqs. (15) and (16), the number of measurement points is decided according to the variation in the sound intensity on the measurement surface. Therefore, many measurement points are required when the value of F_4 is large.

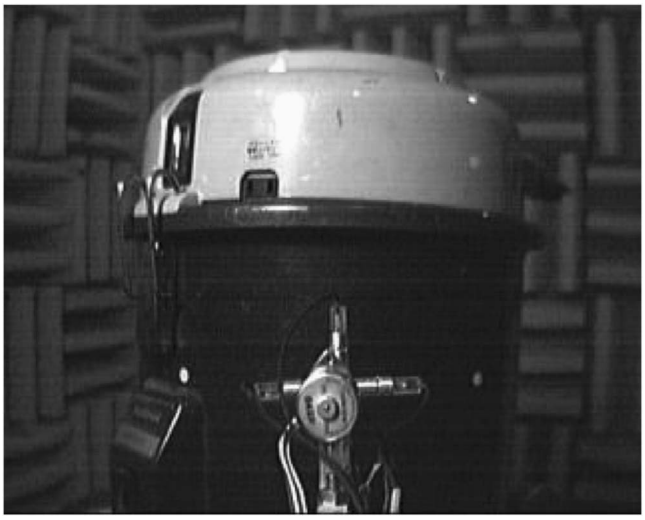

FIG. 13. Picture taken by the CCD camera at the position of the maximum sound intensity of the sound source.

A. Theory of sound power determination based on minimum measurement data

In general, sound waves produced by most sources have pronounced directional effects known as the directivity of the source. The number of measurement points is influenced by the directivity of the sources.

The sound power level of an omnidirectional sound source is given by

$$W = 4\pi r^2 I \ (\mathrm{W}),$$

$$\begin{aligned} \mathrm{PWL} &= \mathrm{IL} + 10\log_{10} 4\pi + 10\log_{10} r^2 \\ &= \mathrm{IL} + 10.99 + 20\log_{10} r \ (\mathrm{dB}), \end{aligned} \tag{17}$$

where r is the distance from the sound source to the measurement point. In this case, it is necessary to measure value of IL, which is the same in any direction.

The sound power level taking into account the directivity of the source is given by

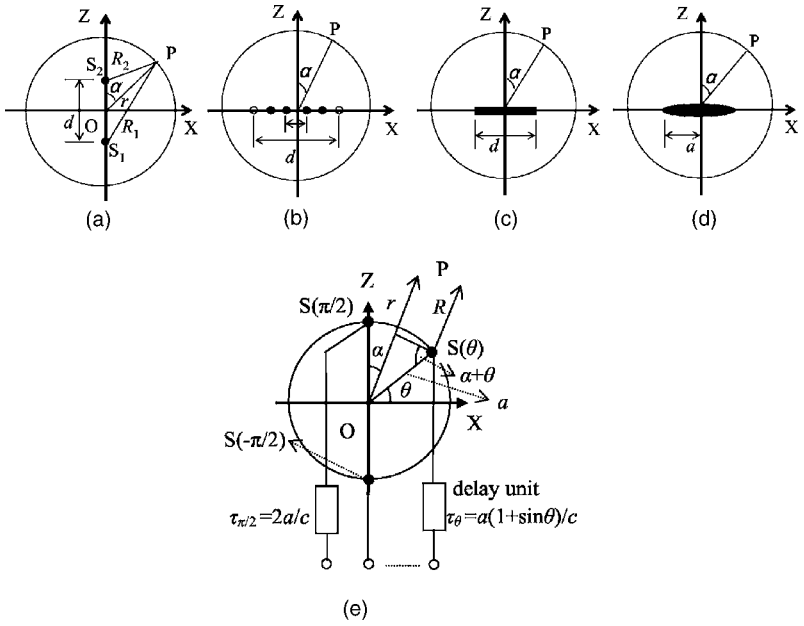

FIG. 14. Sound source location of each model: (a) a dipole source, (b) a model sound source with $n=2$ and 6 point sources of the same phase, (c) a line sound source, (d) a circular diaphragm, and (e) a circular array source with delay units.

$$\begin{aligned}\mathrm{PWL\_}D_i &= \mathrm{IL_{peak}} + 10\log_{10} 4\pi + 10\log_{10} r^2 + D_i \\ &= \mathrm{IL_{peak}} + 10.99 + 20\log_{10} r + D_i \ (\mathrm{dB}),\end{aligned} \tag{18}$$

where D_i is the directivity index.[21–23] The directivity index $D_i = 10\log_{10}(D_r)$ (dB) is simply the decibel expression for the directivity ratio D_r. In general, D_r is calculated from the directivity factor $D(\alpha)$ using

$$D_r = \frac{1}{4\pi}\int_0^{4\pi} D^2(\alpha)d\alpha. \tag{19}$$

When the directivity factor $D(\alpha)$ is symmetrical to a reference axis, Eq. (19) can be written as

$$D_r = \frac{1}{2}\int_0^{\pi} D^2(\alpha)\sin\alpha d\alpha. \tag{20}$$

Therefore, the sound power level can be calculated from the peak sound intensity level, the distance from the observation point to the source, and the directivity index.

This section discusses whether the directivity index can be theoretically calculated from the maximum directivity ratio, the beamwidth, and the surface area of minor lobes.

1. The directivity factor of model sound sources

This paragraph discusses the directivity factor of some model sound sources. Model sound sources are (a) a dipole source, (b) a model sound source with two or six point sources (two monopole sources of equal strength and same phase, and six monopole sources), (c) a line sound source, (d) a circular diaphragm, (e) a bidirectional sound source, (f) a cardioid sound source, (g) an end fired line source, and (h) a circular array source with delay units.

a. A dipole source (Refs. 24 and 25). A typical kind of source is a dipole source consisting of two monopole sources (S_1 and S_2) of equal strength but opposite phase and separated by a small distance compared with the sound wavelength as shown in Fig. 14(a). In this figure, d is the distance between two monopole sources, r is the distance from the origin O to P, α is the angle made by the line segment OP and the z axis, R_1 is the distance from the monopole source S_1 to P, and R_2 is the distance from the monopole source S_2 to P. The instantaneous value of the volume velocity of S_1 is $-\sqrt{2}\dot{U}e^{j\omega t}$, and the instantaneous value of the volume velocity S_2 is $\sqrt{2}\dot{U}e^{j\omega t}$, where $\dot{U}$ is the root mean square complex volume velocity.

The directivity factor is given by

$$D(\alpha) = \left|\sin\left(\frac{kd}{2}\cos\alpha\right)\right|, \tag{21}$$

where $k=\omega/c$ is the wave number and c is the speed of sound. The directivity has a rotational symmetry, and the characteristic changes with kd.

An expression for the theoretical sound intensity I is given by

$$I = \mathrm{Re}\left[\frac{1}{2}pv^*\right] = \frac{k^2\rho c|\dot{U}|^2}{(2\pi r)^2}\sin^2\left(\frac{kd}{2}\cos\alpha\right), \tag{22}$$

where v^* is the complex conjugate of the particle velocity, ρ is the air density. In this case, the theoretical sound power radiated is given by

$$\begin{aligned}W &= \int_s IdS = r^2\int_0^{\pi} I\sin\alpha d\alpha\int_0^{2\pi} d\beta = 2\pi r^2\int_0^{\pi} I\sin\alpha d\alpha \\ &= \frac{2|\dot{U}|^2\rho\omega^2}{4\pi c}\left(1-\frac{\sin kd}{kd}\right),\end{aligned} \tag{23}$$

where β is the directional angle from the x axis on the x-y plane.

b. A model sound source with n point sources (Ref. 21). The directivity factor is given by

$$D(\alpha) = \left| \frac{\sin nx}{n \sin x} \right|, \tag{24}$$

where n is the number of sound sources, and $x = (kd/2)\sin\alpha$.

Figure 14(b) shows a model sound source with two or six point sources in a line.

c. A line sound source (Ref. 21). Figure 14(c) shows a line sound source. The directivity factor is given by

$$D(\alpha) = \left| \frac{\sin x}{x} \right|, \tag{25}$$

where $x = (kd/2)\sin\alpha$.

d. A circular diaphragm (Refs. 21,23,25). The radiation pattern of sound intensity was calculated using the directivity factor of a circular diaphragm which was fitted into a rigid wall and vibrated like the piston. Figure 14(d) shows a circular diaphragm. The directivity factor is given by

$$D(\alpha) = \left| \frac{2J_1(ka \sin\alpha)}{ka \sin\alpha} \right|, \tag{26}$$

where J_1 is the Bessel function of the first kind of order one, and a is the radius of the circular diaphragm.

The radiation of sound is zero at certain angles from the axial direction of the source, and also has local maximi. The second local maximum, called the minor lobe, is usually much weaker than the first maximum (the major lobe) at a smaller angle. The beamwidth[23] is defined as the angle at which the sound intensity drops to one half of its value at the axial direction to the source.

e. A bidirectional sound source (Ref. 22). For a typical sound source, the bidirectional directivity factor is defined as

$$D(\alpha) = |\cos\alpha|. \tag{27}$$

Because the directivity can be made sharper by multiplying Eq. (27) by itself, a more general directivity factor is given by

$$D(\alpha) = |\cos^m \alpha|. \tag{28}$$

The values of m used are integers from 1 to 11.

f. A cardioid sound source (Ref. 22). For a typical sound source, the directivity factor of cardioid is defined as

$$D(\alpha) = |(1 + \cos\alpha)/2|. \tag{29}$$

Because the directivity can be made sharper by multiplying Eq. (29) by itself, a more general directivity factor is given by

$$D(\alpha) = |[(1 + \cos\alpha)/2]^m|. \tag{30}$$

The values of m used are 1/8, 1/7, 1/6, 1/5, 1/4, 1/3, 1/2, and integers from 1 to 11.

g. An end fired line source (Ref. 21). An end fired line source is one in which there is progressive phase delay between the elements arranged in a line. When the excitation time delay between the elements corresponds to the wave propagation time in space for this distance, the maximum directivity occurs in the direction corresponding to the line joining the elements. The directivity factor of this type of end fired line and of uniform strength is given by

$$D(\alpha) = \left| \sin\left[\frac{k}{2}(d - d\cos\alpha) \right] \Big/ \frac{k}{2}(d - d\cos\alpha) \right|, \tag{31}$$

where d is the length of the line.

h. A circular array source with delay units (Ref. 26). The direction and shape of the wave front produced by a circular array of sound sources may be altered by the introduction of a delay pattern in the excitation of the sources as shown in Fig. 14(e). In the system shown Fig. 14(e), a is the radius, θ is the angle made by the line segment $OS(\theta)$ and the x axis, $S(\theta)$ is a monopole source at the angle θ, r is the distance from the origin O to the observation point P, α is the angle made by the line segment OP and the z axis, and R is the distance from the monopole source $S(\theta)$ to P.

A theoretical model of a circular array source is a ring source in combination with a delay system, where the delay pattern is given by $\tau_\theta = a(1+\sin\theta)/c$. When the volume velocity per an unit arc Δs of the ring source is $\dot{Q}e^{j\omega t}$, the velocity potential $\phi(\alpha)$ at the observation point P caused by the ring source is given by

$$\phi(\alpha) = \frac{a\dot{Q}}{4\pi r} e^{j\{\omega t - k(r+a)\}} \int_0^{2\pi} e^{j2ka \sin(\alpha/2)\cos x} dx$$

$$= \frac{a\dot{Q}}{2r} e^{j\{\omega t - k(r+a)\}} J_0\left(2ka \sin\frac{\alpha}{2}\right), \tag{32}$$

where J_0 is the zero-order Bessel function.

The directivity factor is given by

$$D(\alpha) = \left| \frac{\phi(\alpha)}{\phi(0)} \right| = \left| J_0\left(2ka \sin\frac{\alpha}{2}\right) \right|. \tag{33}$$

2. The directivity index classified

From a practical viewpoint for the theoretical sound power level, a surface enclosing the source is a sphere of radius 1 m. The segments of the sphere can be calculated using

$$\Delta S_i = r^2 \int \sin\alpha d\alpha \int d\beta, \tag{34}$$

where $r = 1$ m is the radius of the sphere, α is the directional angle from the z axis ($0 \leqslant \alpha \leqslant \pi$) and β is the directional angle from the orthogonal projection of the x-y plane onto the x axis ($0 \leqslant \beta \leqslant 2\pi$).

Therefore, the dimensions of each model are (a) a dipole source ($d = 0.5$ m), (b) a model sound source with two point sources ($d = 0.5$ m), (c) a model sound source with six point sources ($d = 0.1$ m), (d) a line source ($d = 0.5$ m), (e) a circular diaphragm ($a = 0.5$ m), (f) an end fired line source ($d = 0.5$ m), and (g) a circular array source with delay units ($a = 0.5$ m). For the dipole source, the power of each monopole source is set to 1 W. For the other models, the sound intensity level is set to IL = 120 dB at $\alpha = 0°$.

a. Relationship between the directivity index and the decibel expression for the maximum directivity ratio ($D_r > 1/2$). There is no angle at which the fall-off in sound intensity from the axial direction is as great as 3 dB (D_r

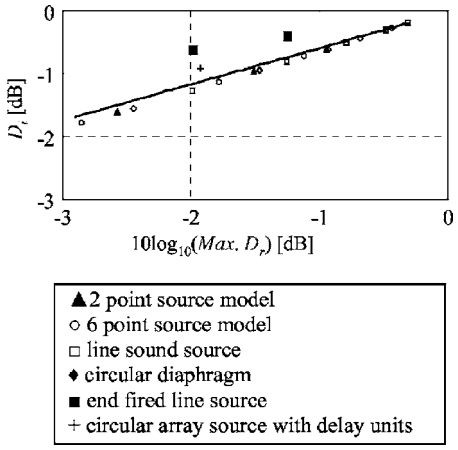

FIG. 15. Relationship between the directivity index D_i and the decibel expression for the maximum directivity ratio ($D_r > 1/2$).

$>1/2$). Figure 15 shows the relationship between the directivity index D_i and the decibel expression for the maximum directivity ratio ($D_r > 1/2$). From this figure, the relationship between the directivity index and the decibel expression for the maximum directivity ratio ($D_r > 1/2$) is analyzed by fitting coefficients in the following log model through simple regression analysis:

$$D_i = 0.574 \times 10 \log(\text{Max } D_r) - 0.021, \tag{35}$$

where the correlation coefficient is 0.9247.

b. Relationship between the directivity index and the beamwidth ($D_r \leqslant 1/2$). The beamwidth is measured as the angle in degrees between the 3 dB half power points. Figure 16 shows the relationship between the directivity index D_i and the beamwidth ($D_r \leqslant 1/2$). From this figure, the relationship between the directivity index D_i and the beamwidth ($D_r \leqslant 1/2$) is analyzed by fitting coefficients in the following natural log (ln) model through simple regression analysis:

$$D_i = 7.243 \ln(\text{Beamwidth}) - 32.279, \tag{36}$$

where the correlation coefficient is 0.9305.

Here, for a dipole source, the error in the sound power level when $r=1$ m relative to the theoretical value of the sound power level calculated from Eq. (23) is less than 0.01 dB.

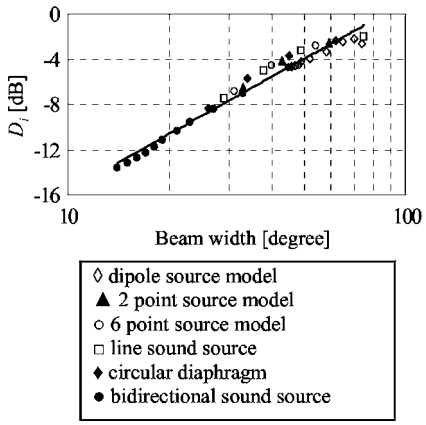

FIG. 16. Relationship between the directivity index D_i and the beamwidth ($D_r \leqslant 1/2$).

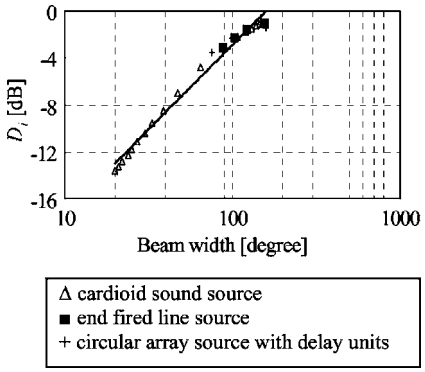

FIG. 17. Relationship between the directivity index D_i and the beamwidth of the cardioid pattern.

c. Relationship between the directivity index and the beamwidth for the cardioid pattern. Figure 17 shows the relationship between the directivity index D_i and the beamwidth for the cardioid pattern. From this figure, the relationship between the directivity index D_i and the beamwidth for the cardioid pattern is analyzed by fitting coefficients in the following ln model through simple regression analysis:

$$D_i = 6.250 \ln(\text{Beamwidth}) - 31.679, \tag{37}$$

where the correlation coefficient is 0.9384.

d. Relationship between the partial directivity index ΔD_i *and the beamwidth of major lobes.* The directivity factor becomes more pronounced at higher frequencies, and minor lobes develop in addition to major lobes. The radiation of sound is zero at certain angles from the axial direction of the source, and also has local maximi. The minor lobes are usually much weaker than the major lobe. Therefore, we only consider the major lobes here, and define the partial sound power for the major lobe. The sharpness of the major lobe is determined by the beamwidth. Figure 18 shows the relationship between the partial directivity index ΔD_i and the beamwidth of major lobes.

From this figure, the relationship between the partial di-

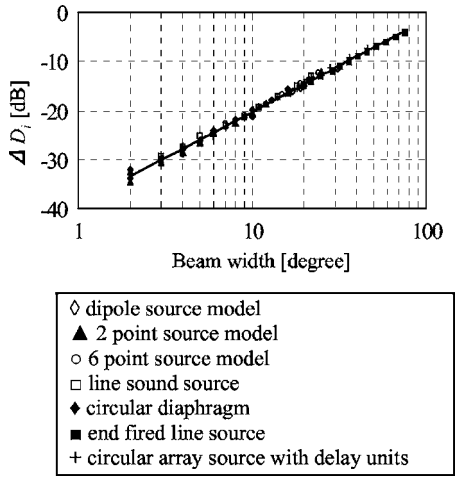

FIG. 18. Relationship between the partial directivity index ΔD_i and the beamwidth of the major lobes.

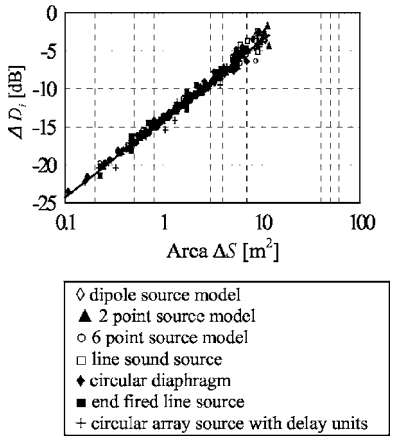

FIG. 19. Relationship between the partial directivity index ΔD_i and the surface area of the minor lobes.

rectivity index ΔD_i and the beamwidth of the major lobes is analyzed by fitting coefficients in the following ln model through simple regression analysis:

$$\Delta D_i = 8.190 \ln(\text{Beamwidth}) - 39.147, \tag{38}$$

where the correlation coefficient is 0.8812.

e. Relationship between the partial directivity index ΔD_i *and the surface area of the minor lobes.* In general, the larger the extent of the radiator, the sharper the major lobe and the greater the number of minor lobes will be. The partial sound power of the minor lobes is determined by the peak sound intensity level and the partial directivity index ΔD_i. The partial directivity index ΔD_i of the minor lobes is correlated with each surface area. The radiation of sound has a dip in the sound intensity level at a certain angle α_1 from the axial direction of the source. The next dip in sound intensity level is at α_2. Therefore, the surface area ΔS of minor lobes can be calculated with Eq. (34) integrated from α_1 to α_2, i.e., the partial sound power of only one minor lobe is considered. Since the surface enclosing the source is a sphere, the influence on the partial sound power of minor lobes by the surface area is large.

Figure 19 shows the relationship between the partial directivity index ΔD_i and the surface area of the minor lobes. From this figure, the relationship between the partial directivity index ΔD_i and the surface area of minor lobes is analyzed by fitting coefficients in the following ln model through simple regression analysis:

$$\Delta D_i = 4.487 \ln(\text{Area}) - 13.981, \tag{39}$$

where the correlation coefficient is 0.8874.

Having completed the measurements, the sound power is determined by summing the partial powers for the major lobe and the minor lobes, that is, if $\text{IL}_{\text{peak}n}$ is the intensity in W/m^2 of the nth measurement ($n=1$: IL_{peak} of the major lobe and $n \geqslant 2$: IL_{peak} of the minor lobes), and ΔD_{in} is the partial directivity index predicted from the beamwidth of the major lobe [$n=1$; Eq. (38)] and from the surface area of the minor lobes [$n \geqslant 2$; Eq. (39)], then:

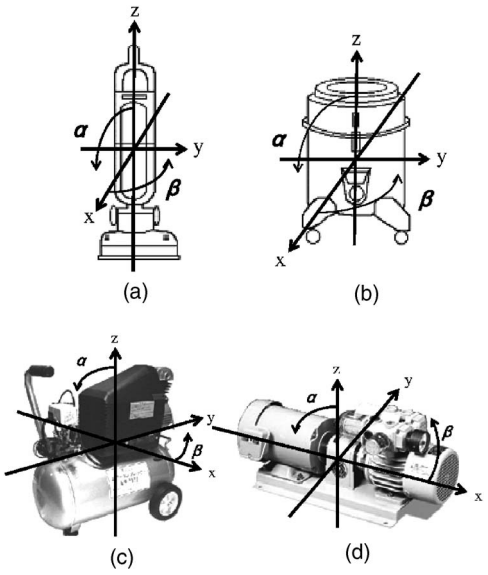

FIG. 20. Spherical coordinates in a three-dimensional system: $0 \leqslant \alpha \leqslant \pi$, and $0 \leqslant \beta < 2\pi$. (a) Broom type vacuum cleaner, (b) industrial vacuum cleaner, (c) air compressor, and (d) dry pump.

$$\text{PWL\_}D_i = \sum_{n=1}^{N} (\text{IL}_{\text{peak}n} + 10 \log_{10} 4\pi + \Delta D_{in}), \tag{40}$$

where N is the number of peaks.

B. Experiment

Practically all sound radiators have pronounced directional effects. This is particularly true when the source is radiating sound waves at high frequencies.

The following discusses experimentally whether sound power can be measured from the ln models of the preceding section.

1. Measurement procedure

The following four machines were selected

(a) A broom type vacuum cleaner (National MC-u30p, $W \times D \times H = 0.3 \times 0.28 \times 0.6$ m^3, electric power consumption: 430 W, number of fans: 6, a single-phase series ac commutator motor), as shown in Fig. 20(a). A rotational frequency of 3033 rpm was used.

(b) An industrial vacuum cleaner (National MC-G250, $W \times D \times H = 0.3 \times 0.3 \times 0.4$ m^3, electric power consumption: 1050 W, number of fans: 6, a single-phase series ac commutator motor), as shown in Fig. 20(b). A rotational frequency of 1910 rpm was used.

(c) An air compressor (TRUSCO ER-1525, $W \times D \times H = 0.55 \times 0.33 \times 0.6$ m^3, electric power consumption: 1200 W), as shown in Fig. 20(c). A discharge rate of 106 l/min was used.

(d) A dry pump[27] (ORION KRX3-SS-4002-G1, $W \times D \times H = 0.5 \times 0.27 \times 0.27$ m^3, electric power consumption: 400 W), as shown in Fig. 20(d). A rotational frequency of 1730 rpm, a discharge pressure of 40 kPa, a throughput of 280 l/min, and a flow rate of 685 l/min were used.

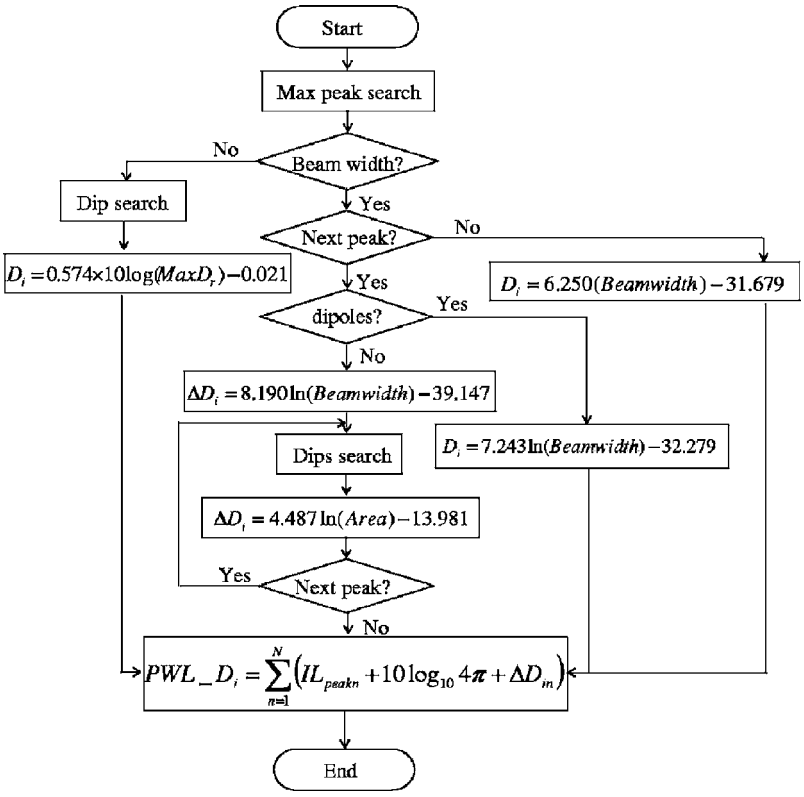

FIG. 21. Flowchart of the proposed measurement procedure.

The objective is to arrive at the total sound intensity passing through the measurement surface. The experiment was done in an anechoic room (Shinshu University; 60 m^3). Our three-dimensional sound intensity probe was set up in a hemisphere of radius 1 m with a handmade turntable. Each product was rotated by the turntable (0.04°/pulse) with a pulse motor and pulse motor control system (see Fig. 10). Figure 20 shows the three-dimensional spherical coordinates, where α is the angle from the positive z axis ($0 \leqslant \alpha \leqslant \pi$) and β is the angle from the x axis in the x-y plane ($0 \leqslant \beta < 2\pi$). To determine the sound power (PWL_D_i) of each machine, the procedure shown in the flowchart in Fig. 21 was used. The procedure is as follows.

(a) Find the local maximum peak sound intensity level as a function of frequency from 200 Hz to 2 kHz.
(b) Check whether the directivity has symmetry. Determine the beamwidth. If there is no beamwidth, the directivity index is found using Eq. (35) from the decibel expression for the maximum directivity ratio ($D_r > 1/2$).
(c) Determine whether there is a beamwidth and no other sound intensity peak. The directivity index is found using Eq. (37) from the beamwidth of the cardioid pattern.
(d) Determine whether there is another sound intensity peak and beamwidth. The directivity index is found using Eq. (36) from the beamwidth ($D_r \leqslant 1/2$).
(e) Determine whether there is another sound intensity peak, i.e., minor lobe. The partial directivity index for the major lobe is found using Eq. (38) from the maximum sound intensity peak and the beamwidth.
(f) Find the second sound intensity peak, i.e., minor lobe, and the side dips which are used to calculate the surface area (m^2). The partial directivity index for the minor lobe is found using Eq. (39) from the surface area ΔS calculated with Eq. (34) integrated from α_1 to α_2.
(g) Repeat (e) and (f) until the desired result has been achieved. Finally, calculate the sound power using Eq. (40).

The sound power level based on ISO 9614-1[8] was measured for comparison. For this standard sound power determination, the intensity passing through the measurement surface was integrated by measuring at a sufficient number of points on the surface. In an anechoic room (Research Institute of Nagano Pref.; 215.6 m^3), the intensity probe microphone (B&K 3545, 1/2 in. microphones, gap: 12 mm, bias error[12] from 200 Hz to 5 kHz: 0.2 dB) was set up on a robot arm (NITTOBO MT-3000 TYPE2). A dual channel real-time analyzer (B&K 2133A) was used for sound power determination. The number of measurement points required to satisfy Eqs. (15) and (16) were: 96 for the two kinds of vacuum cleaners,[28] 110 for the air compressor, and 63 for the dry pump.

2. Results and discussion

Table I shows the level differences (engineering grade) from 200 Hz to 2 kHz between ISO 9614-1[8] (PWL: 96 points) and the sound power determined from the proposed minimum measurement data for the broom type vacuum cleaner. From Table I, it can be found that the minimum number of measurement points is from 2 to 8 for engineering grade sound power determination. For the industrial vacuum cleaner, the minimum number of measurement points is 2 from 200 Hz to 1.25 kHz as shown in Table II. However, the number of points is 8 at 1.6 kHz, and because the number of

TABLE I. Level difference (engineering grade) between ISO 9614-1 (PWL: 96 points) and the sound power determined from the proposed minimum measurement data for a broom type vacuum cleaner.

Frequency (Hz)	200	250	315	400	500	630	800	1000	1250	1600	2000
PWL: 96 points (dB)	52.8	53.3	54.9	59.6	62.8	61.4	63.3	67.4	70.1	69.3	68.0
PWL_D_i (dB)	51.3	52.2	53.0	59.9	61.1	60.5	61.9	66.6	70.3	70.3	67.8
Difference (dB)	1.46	1.18	1.86	0.28	1.70	0.90	1.42	0.75	0.22	1.03	0.14
Number of data	5	8	2	2	2	8	2	2	2	2	2
IL_{peak1} (dB)	44.8	46.3	47.4	52.7	55.7	54.8	56.7	61.8	66.3	64.7	60.1
Beamwidth (°)	14	31	67	86	65	29	63	59	52	67	94
D_i *or* ΔD_i (dB)	−17.5	−11.0	−5.40	−3.84	−5.59	−11.6	−5.78	−6.19	−6.98	−5.40	−3.28
ln model	Eq. (38)	Eq. (38)	Eq. (37)	Eq. (37)	Eq. (37)	Eq. (38)	Eq. (37)	Eq. (37)	Eq. (37)	Eq. (37)	Eq. (37)
IL_{peak2} (dB)	43.4	43.2				51.5					
ΔS (m^2)	10.9	8.44				10.6					
D_i *or* ΔD_i (dB)	−3.26	−4.38				−3.39					
IL_{peak3} (dB)		42.5				48.9					
ΔS (m^2)		2.92				0.98					
D_i *or* ΔD_i (dB)		−9.20				−14.0					
ln model	Eq. (39)	Eq. (39)				Eq. (39)					

TABLE II. Level difference (engineering grade) between ISO 9614-1 (PWL: 96 points) and the sound power determined from the proposed minimum measurement data for an industrial vacuum cleaner.

Frequency (Hz)	200	250	315	400	500	630	800	1000	1250	1600	2000
PWL: 96 points (dB)	54.1	57.3	61.0	57.2	58.1	63.2	64.7	61.9	58.1	59.4	61.2
PWL_D_i (dB)	53.4	57.0	61.6	57.9	59.4	63.4	65.6	61.1	59.0	59.7	62.5
Difference (dB)	0.72	0.32	0.64	0.67	1.23	0.22	0.93	0.82	0.88	0.33	1.33
Number of data	2	2	2	2	2	2	2	2	2	8	17
IL_{peak1} (dB)	47.2	50.1	56.0	51.0	52.5	58.0	59.0	57.6	51.5	53.0	56.0
Beamwidth (°)	74	82	67	82	82	65	79	48	91	29	20
D_i *or* ΔD_i (dB)	−4.78	−4.14	−5.40	−4.14	−4.14	−5.59	−4.37	−7.48	−3.48	−11.6	−14.6
ln model	Eq. (37)	Eq. (37)	Eq. (37)	Eq. (37)	Eq. (37)	Eq. (37)	Eq. (37)	Eq. (37)	Eq. (37)	Eq. (38)	Eq. (38)
IL_{peak2} (dB)										52.0	55.5
ΔS (m^2)										6.92	3.55
D_i *or* ΔD_i (dB)										−5.31	−8.30
IL_{peak3} (dB)										52.0	55.5
ΔS (m^2)										2.13	0.48
D_i *or* ΔD_i (dB)										−10.7	−17.3
IL_{peak4} (dB)											55.0
ΔS (m^2)											2.71
D_i *or* ΔD_i (dB)											−9.51
IL_{peak5} (dB)											53.0
ΔS (m^2)											2.36
D_i *or* ΔD_i (dB)											−10.1
IL_{peak6} (dB)											52.5
ΔS (m^2)											1.84
D_i *or* ΔD_i (dB)											−11.3
ln model										Eq. (39)	Eq. (39)

TABLE III. Level difference (engineering grade) between ISO 9614-1 (PWL: 110 points) and the sound power determined from the proposed minimum measurement data for an air compressor.

Frequency (Hz)	200	250	315	400	500	630	800	1000	1250	1600	2000
PWL: 110 points (dB)	71.6	75.8	83.3	80.5	73.6	72.2	69.2	65.5	65.2	65.6	70.6
PWL_D_i (dB)	72.6	75.4	84.5	80.6	74.7	71.4	69.0	65.8	65.8	66.3	71.1
Difference (dB)	0.98	0.40	1.22	0.15	1.02	0.84	0.20	0.28	0.55	0.65	0.56
Number of data	2	2	2	2	2	2	2	2	2	2	2
IL_{peak1} (dB)	69.5	73.0	80.1	74.8	68.4	67.6	65.3	63.4	62.6	62.5	67.4
Beamwidth (°)	45	40	55	70	75	50	50	40	45	50	50
D_i (dB)	−7.89	−8.62	−6.63	−5.12	−4.69	−7.23	−7.23	−8.62	−7.89	−7.23	−7.23
ln model	Eq. (37)	Eq. (37)	Eq. (37)	Eq. (37)	Eq. (37)	Eq. (37)	Eq. (37)	Eq. (37)	Eq. (37)	Eq. (37)	Eq. (37)

minor lobes is 5 at 2 kHz, the number of points increases to 17. For the air compressor, the minimum number of measurement points is 2 from 200 Hz to 2 kHz as shown in Table III. For the dry pump, the minimum number of measurement points is from 2 to 5 as shown in Table IV.

From the results, it can be seen that sound power determination based on the proposed minimum measurement data yields an accuracy in the low-frequency range (200–630 Hz) of under 1.99 dB, and an accuracy in the midfrequency range (800 Hz to 2 kHz) of under 1.49 dB.

Consequently, it can be said that the proposed searching techniques are effective for sound power determination based on minimum measurement data.

IV. CONCLUSIONS

Because sound intensity measurements offer several ways to locate and identify parts of devices and machines radiating the most acoustic energy, first, a full vector intensity probe with a rotating and variable directional microphone system was developed for canceling both phase mismatch and position errors.

(a) The probe has three pairs of microphones at an equal spacing of 30 mm that are set up on the x, y, and z axes and share the same observation point.
(b) The symmetrical arrangement of the proposed system with six microphones is effective to calibrate both the intrinsic phase mismatch and the position errors by rotating four microphones on the y-z plane.
(c) Variation of the directional separation angle is effective for source location using the null search method on the y-z plane.
(d) The system can identify the maximum sound intensity level and beamwidth of the major lobe, and the peak sound intensity levels of minor lobes.

Second, a procedure for sound power determination based on minimum measurement data was proposed. Results show the following.

(e) The sound power level and directivity of the sound source can be used to calculate the maximum sound intensity level of the major lobe, the distance r from the sound source to the measuring point, the directivity index, and the peak sound intensity levels of the minor lobes.
(f) The directivity indices can be obtained from five curves: (1) the relationship between the directivity index and the decibel expression for the maximum directivity ratio ($D_r > 1/2$), (2) the relationship between the directivity index and the beamwidth ($D_r \leqslant 1/2$), (3) the relationship between D_i and the beamwidth of the cardioid pattern, (4) the relationship between the partial D_i and the beamwidth of major lobes, and (5) the relationship between the partial D_i and the surface area of the minor lobes.

TABLE IV. Level difference (engineering grade) between ISO 9614-1 (PWL: 63 points) and the sound power determined from the proposed minimum measurement data for a dry pump.

Frequency (Hz)	200	250	315	400	500	630	800	1000	1250	1600	2000
PWL: 63 points (dB)	71.0	79.9	74.7	70.9	69.4	70.7	70.4	71.6	70.6	64.2	64.3
PWL_D_i (dB)	69.2	80.6	72.7	69.4	70.6	69.9	68.9	72.3	71.2	63.9	63.1
Difference (dB)	1.88	0.70	1.99	1.57	1.28	0.77	1.49	0.66	0.57	0.30	1.20
Number of data	2	2	5	5	2	2	5	2	2	2	2
IL_{peak1} (dB)	66.8	76.8	73.1	66.1	65.2	64.5	67.0	66.6	62.8	58.0	59.3
Beamwidth [°]	40	50	20	30	40	40	30	70	60	70	50
D_i *or* ΔD_i (dB)	−8.62	−7.23	−14.6	−11.3	−5.56	−5.56	−11.3	−5.12	−2.62	−5.12	−7.23
ln model	Eq. (37)	Eq. (37)	Eq. (38)	Eq. (38)	Eq. (36)	Eq. (36)	Eq. (38)	Eq. (37)	Eq. (36)	Eq. (37)	Eq. (37)
IL_{peak2} (dB)			65.4	62.9			62.6				
ΔS (m^2)			5.16	4.71			3.14				
D_i *or* ΔD_i (dB)			−6.58	−7.04			−8.85				
ln model			Eq. (39)	Eq. (39)			Eq. (39)				

(g) From 200 Hz to 2 kHz each level difference (engineering grade) between ISO 9614-1 (PWL: 96 points) and the sound power determined from the proposed minimum measurement data of four practical sound sources yields an accuracy in the low-frequency range (200–630 Hz) of under 1.99 dB, and an accuracy in the mid-frequency range (800 Hz to 2 kHz) of under 1.49 dB.
(h) The minimum number of measurement points is from 2 to 17 for engineering grade sound power determination.

Consequently, it can be said that the proposed intensity measurement system is effective for sound power determination based on minimum measurement data.

[1]T. J. Schultz, "Acoustic wattmeter," J. Acoust. Soc. Am. **28**, 693–699 (1956).
[2]F. J. Fahy, "Measurement of acoustics intensity using the cross-spectral density of two microphone signals," J. Acoust. Soc. Am. **62**, 1057–1059 (1977).
[3]M. P. Waser and M. J. Crocker, "Introduction to the two-microphones cross-spectral method of determining sound intensity," Noise Control Eng. J. **22**, 76–85 (1984).
[4]G. Pavic, "Measurement of sound intensity," J. Sound Vib. **51**, 533–545 (1977).
[5]P. S. Watkinson, "The practical assessment of errors in sound intensity measurement," J. Sound Vib. **105**, 255–263 (1986).
[6]E. Frederiksen and O. Schultz, "Pressure microphones for intensity measurements with significantly improved phase properties," Brüel & Kjaer Tech. Rev. **4**, 11–23 (1986).
[7]G. Hübner, "Sound intensity measurement method–Errors in determining the sound power levels of machines and its correlation with sound field indicators," in *Proceedings of Inter-Noise*, 1987, pp. 1227–1230.
[8]ISO 9614-1, *Acoustics–Determination of Sound Power Levels of Noise Sources Using Sound Intensity–Part 1: Measurement at Discrete Points*. (ISO, Geneva, Switzerland, 1990).
[9]J. Y. Chung, "Cross-spectral method of measuring acoustic intensity without error caused by instrument phase mismatch," J. Acoust. Soc. Am. **64**, 1613–1616 (1978).
[10]G. Krishnappa, "Cross-spectral method of measuring acoustic intensity by correcting phase and gain mismatch errors by microphone calibration," J. Acoust. Soc. Am. **69**, 307–310 (1981).
[11]F. Jacobsen, "A simple and effective correction for phase mismatch in intensity probes," Appl. Acoust. **33**, 165–180 (1991).
[12]T. Yanagisawa and N. Koike, "Cancellation of both phase mismatch and position errors with rotating microphones in sound intensity measurements," J. Sound Vib. **113**, 117–126 (1987).
[13]N. Koike and T. Yanagisawa, "Separation of sound intensity vector using variable directional microphone," *Proceedings of Inter-Noise 1994*, pp. 1761–1764.
[14]ISO 9614-2, "Acoustics - determination of sound power levels of noise sources using sound intensity - part 2: Measurement by scanning, (ISO, Geneva, Switzerland, 1996).
[15]F. J. Fahy, *Sound Intensity* (Elsevier Applied Science, London, 1989), Secs. 6.3.1, 6.9.2, 6.9.4, and 8.2.
[16]F. J. Fahy, in Ref. 15, Sec. 6.2.2.
[17]J. K. Thompson and D. R. Tree, "Finite difference approximation errors in acoustic intensity measurements," J. Sound Vib. **75**, 229–238 (1981).
[18]T. Wada, K. Furihata, T. Yanagisawa, and N. Koike, "Measurement of vector sound intensity of moving vehicles for automatic supervision," *Proceedings of Inter-Noise* 2002, p. N375.
[19]F. J. Fahy, in Ref. 15, Sec. 5.2.2.
[20]F. J. Fahy, in Ref. 15, Sec. 9.2.
[21]H. F. Olson, *Acoustical Engineering* (Van Nostrand, Princeton, 1957), Chaps. 2–6, pp. 30–211.
[22]L. L. Beranek, *Acoustics* (McGraw-Hill, New York, 1954), Chaps. 4–6, pp. 91–182.
[23]L. E. Kinsler and A. R. Frey, *Fundamentals of Acoustics* (Wiley, New York, 1950), Chap. 7, pp. 162–197.
[24]P. M. Morse, *Vibration and Sound*, 2nd ed. (McGraw-Hill, New York, 1948), Chap. 7, pp. 294–380.
[25]M. Kawamura, *Introduction to Electro-acoustic Engineering*, 25th ed. (Shokodo, Tokyo, 1995), Chap. 3, pp. 39–53.
[26]T. Hayasaka and S. Yoshikawa, *Theory of Sound and Vibration* (Maruzen, Tokyo, 1974), Chap. 18, pp. 569–602.
[27]T. Shimada, T. Yanagisawa, and K. Tagawa, "Characterization of noise generated by a dry pump by using a vane vacuum pump and noise reduction methods," Noise Control Eng. J. **35**, 95–101 (1990).
[28]S. Nagata, K. Furihata, and T. Yanagisawa, "Relation between close curved surface and measurement points of sound power levels for electric cleaners using sound intensity method," *Proceedings of Inter-Noise* 2000, pp. 3793–3797.

An improved acoustic microimaging technique with learning overcomplete representation

Guang-Ming Zhang and David M. Harvey
General Engineering Research Institute, Liverpool John Moores University, Byrom Street, Liverpool, L3 3AF, United Kingdom

Derek R. Braden
Delphi Electronics & Safety, Kirkby, Liverpool, L33 7XL, United Kingdom

(Received 1 August 2005; revised 28 September 2005; accepted 29 September 2005)

Advancements in integrated circuit (IC) package technology are increasingly leading to size shrinkage of modern microelectronic packages. This size reduction presents a challenge for the detection and location of the internal features/defects in the packages, which have approached the resolution limit of conventional acoustic microimaging, an important nondestructive inspection technique in the semiconductor industry. In this paper, to meet the challenge the learning overcomplete representation technique is pursued to decompose an ultrasonic A-scan signal into overcomplete representations over a learned overcomplete dictionary. Ultrasonic echo separation and reflectivity function estimation are then performed by exploiting the sparse representability of ultrasonic pulses. An improved acoustic microimaging technique is proposed by integrating these operations into the conventional acoustic microimaging technique. Its performance is quantitatively evaluated by elaborated experiments on ultrasonic A-scan signals using acoustic microimaging (AMI) error criteria. Results obtained both from simulated and measured A-scans are presented to demonstrate the superior axial resolution and robustness of the proposed technique. © *2005 Acoustical Society of America.* [DOI: 10.1121/1.2126935]

PACS number(s): 43.60.Hj, 43.60.Lq, 43.60.Np [EJS] Pages: 3706–3720

I. INTRODUCTION

High-frequency ultrasound has become one of the most powerful tools for material evaluation since its invention.[1,2] Acoustic microimaging (AMI) [also known as scanning acoustic microscopy (SAM)] is widely employed in the nondestructive inspection of microelectronic packages for cracks, delaminations, porosity, and package integrity. Modern packages are often multilayer structures, creating a difficult challenge for acoustical imaging. When the layer thickness is less than or comparable to the wavelength of the ultrasound, the reflected echoes from the front and the back surface of the layer overlap. The interference between the two echoes results in pulse distortion, degrading ultrasonic C-scan images. In addition, the different propagation modes, diffraction, and dispersive attenuation make the interpretation of ultrasonic signals/images even more complex. Evidently, the development of new AMI techniques is required to keep pace with the continued miniaturization of advanced IC package technologies such as BGA, Flip-Chip, and 3D packages. A traditional method to meet the challenge is to develop higher resolution transducers with more sample-specific features in order to derive the optimum performance from the transducer.[3] For example, a transducer can be optimized to correct for edge effects and improve resolution. Recently, acoustic frequency domain imaging (FDAMI) was developed to increase the contrast of C-scan images.[4] More recently, acoustic time-frequency domain imaging and sparse signal representations were pursued to solve the problem.[5–7] In this paper, an improved AMI technique based on learning overcomplete representation is explored to improve the axial resolution of conventional AMI techniques without increasing the acoustic frequencies.

II. GENERAL FORMULATION

A. Modeling of the AMI signals

In AMI analysis of IC packages, most AMI systems employed in the IC packaging industry operate in a broadband, pulse excitation mode. For pulse-echo ultrasonic testing, the reflected echo $s(t)$ from a flat surface reflector can be modeled as

$$s(t) = c\,\exp(-\alpha(t-\tau)^2]\cos[2\pi f_c(t-\tau)+w], \tag{1}$$

where $\theta=[c,\alpha,f_c,\tau,w]$ denotes the parameter vector. The parameters of this model are closely related to the physical properties of the ultrasonic signal propagating through the material. The time of flight τ is related to location of the reflector as the distance between the transducer and the reflector. The amplitude of the echo c is primarily governed by the acoustical impedance values of the materials involved, the attenuation of the original signal, and the size and orientation of the reflector. The parameters f_c and α are the center frequency and bandwidth factor, respectively. These parameters are governed by the transducer frequency characteristics and the propagation path. The phase of the echo w accounts for the distance, impedance, size, and orientation of the reflector.

For a die-attach assembly, multiple interfaces are present. At each interface part of the incident pulse energy is

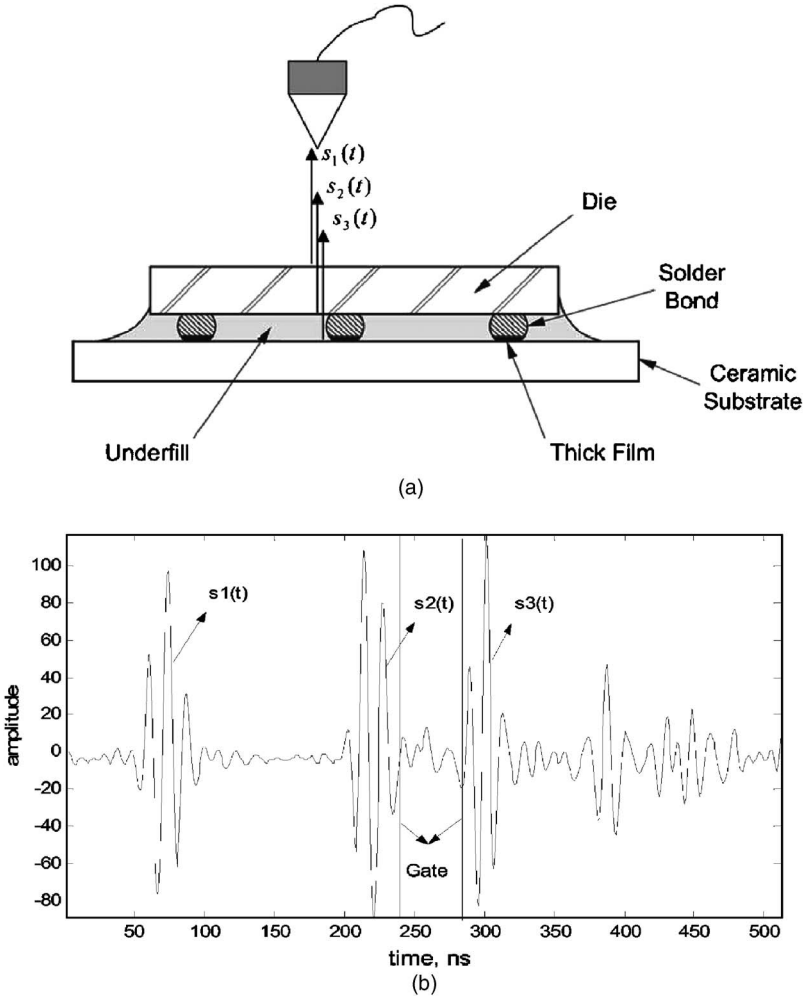

FIG. 1. AMI echoes at typical boundaries in Flip-Chip package mounted on ceramic substrate (a) and an Ascan obtained using a 230-MHz transducer (b). $s_1(t)$, $s_2(t)$, and $s_3(t)$ are ultrasonic echoes reflected at water–die, die–solder bond, and solder bond–ceramic substrate interfaces, respectively.

reflected, generating an echo signal. Figure 1(a) shows AMI echo components at typical boundaries in a flip-chip package mounted on ceramic substrate, where $s_1(t)$, $s_2(t)$, and $s_3(t)$ are ultrasonic echoes reflected at water–die, die–solder bond, and solder bond–ceramic substrate interfaces, respectively. The ultrasonic A-scan signal acquired from a die-attach assembly can then be represented as a superposition of M-reflected echoes as shown in Fig. 1(b)

$$y(t) = \sum_{i=1}^{M} s_i(t) + \xi(t). \tag{2}$$

The term $\xi(t)$ accounts for the measurement noise and can be characterized as white Gaussian noise (WGN). If the M echoes are the time-shifted, amplitude-scaled replica of a reference echo, Eq. (2) can be rewritten as a convolution format

$$y(t) = \sum_{i=1}^{M} c_i x(t-\tau_i) + \xi(t) = x(t) * \left\{ \sum_{i=1}^{M} c_i \delta(t-\tau_i) \right\} + \xi(t), \tag{3}$$

where the bracketed term denotes the reflectivity function. The problem of recovering the reflectivity function and estimating the ultrasonic pulse $x(t)$ can be reformulated as a *blind deconvolution* problem.

For microelectronic package inspection, the received echo often undergoes a shape distortion due to the focusing effects and dispersive attenuation. Thus, the deconvolution model in Eq. (3) is not applicable. In this case, Eq. (2) becomes

$$y(t) = \sum_{i=1}^{M} c_i x_i(t) + \xi(t), \tag{4}$$

where $x_i(t)$ is the "quasi" incident pulse impinged to the ith interface. Here, quasi means $x_i(t)$ is not a real incident pulse because it is a pulse which includes dual-way transmission and attenuation. The problem of ultrasonic signal interpretation is then formulated as the problem of *blind source separation* that separates a set of linear mixtures onto a number of unknown source signals,[8] inferring both the reflectivity function c_i, which can be considered as the virtual ultrasonic sources, and the ultrasonic incident pulses x_i from the observed signal y. In matrix format, Eq. (4) becomes

$$y = \Phi c + \xi. \tag{5}$$

Furthermore, an ultrasonic A-scan signal acquired from a die-attach assembly generally consists of limited echoes due to the layer structure of the microelectronic package containing a limited number of abrupt impedance change, i.e., M is very small. So, the ultrasonic signal can be assumed to have a very sparse representation in a proper signal dictionary, though not in the time domain.

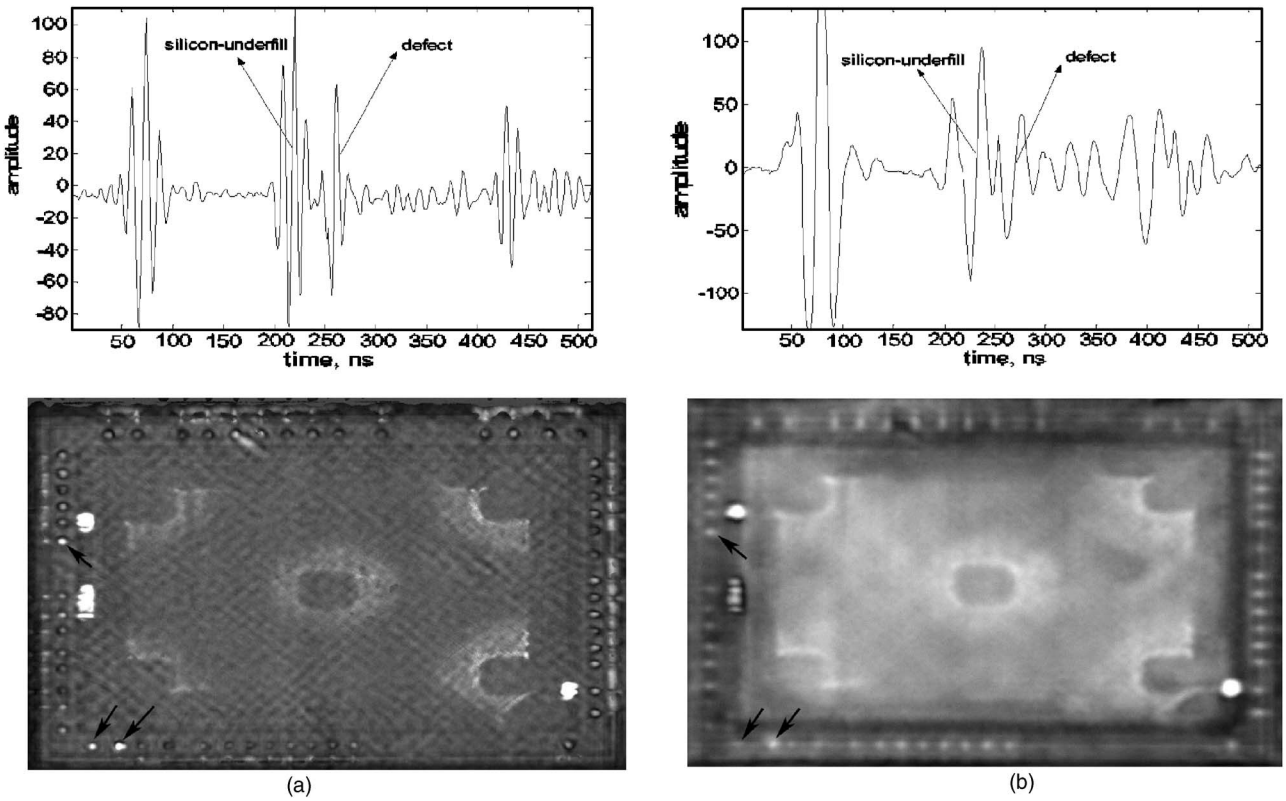

FIG. 2. Resolution limitation of acoustic time domain imaging with different acoustic frequencies: (a) 230 MHz; (b) 50 MHz. Upper: Ascans; lower: C scan images. The defective solder bumps are indicated by arrows in C-scan images.

B. Resolution analysis of conventional AMI techniques

The basic principle of conventional time-domain AMI technique (TDAMI) is that a focused ultrasonic transducer alternatively sends pulses into and receives reflected echoes from discontinuities within the sample. An electronic gate as depicted in Fig. 1(b) corresponding to a time window is used to select a specific interface to view. A mechanical scanner moves the transducer over the sample, producing C-scan images. At each *x*-*y* position the peak intensity value and the polarity of the echo within the electronic gate are displayed in the C-scan image. When there is a thin layer in the sample, pulse distortion might occur as described previously. In this case, no matter how the electronic gate is set, the gated signal is corrupted. As a consequence, the contrast of resulting images is corrupted and probably gives false indications of defects. Figure 2 shows such an example. The solder bumps of a flip chip are imaged by 230- and 50-MHz transducers, respectively. The two Ascans in Fig. 2 are from the same *x*-*y* position of a defective solder bump. Due to the low resolution of the 50-MHz transducer, echo overlap is observed in Fig. 2(b) and the corresponding C-scan image is contaminated, where three defective solder bumps indicated by arrows are difficult to identify. However, these defective solder bumps are very clear in the C-scan image produced by the 230-MHz transducer.

In FDAMI, at each *x*-*y* position the gated A-scan signal is decomposed into the frequency domain by the fast Fourier transform (FFT), and the amplitude of a single frequency at its spectrum is displayed as a pixel of C-scan image. The result will be some dozens of individual FFT images, each showing what that interface looks like at a single frequency.[4] Suppose that a gated signal is comprised of two echoes which are overlapped in the time domain, and the spectra of the two echoes are separated partly in the frequency domain. Due to phase change, some frequencies of an echo undergo constructive interference while others undergo destructive interference. At a fixed frequency, the frequency strength might come mainly from the expected echo, with the interfering echo making a minor contribution. In this case, frequency imaging still gives a high-contrast FFT image at this frequency, though the time-domain image is poor due to the echo superposition. Figure 3 demonstrates the features of FDAMI. Figures 3(b), 3(c), and 3(d) are the amplitude spectrum of the echoes 1, 2, and 3 in Fig. 3(a), respectively. It can be seen that the peak frequencies of these echoes are far less than the transducer frequency of 230 MHz due to the dispersive attenuation in water and packaging materials. Figure 3(e) displays the spectrum of the gated signal in Fig. 3(a), which consists of echo 3 and part of echo 2. Comparing Fig. 3(e) with Fig. 3(d), it is observed that the spectrum of the defect echo 3 suffers interference from echo 2. Some frequencies are enhanced while some are weakened. Therefore, at some frequencies the FFT images would have poor performance in terms of resolution and contrast. Additionally, it is hard, using quantitative analysis, to give the values of the frequencies where high contrast can be achieved in practical applications. A further limitation of frequency imaging is that, if a gated signal includes more than two echoes, the

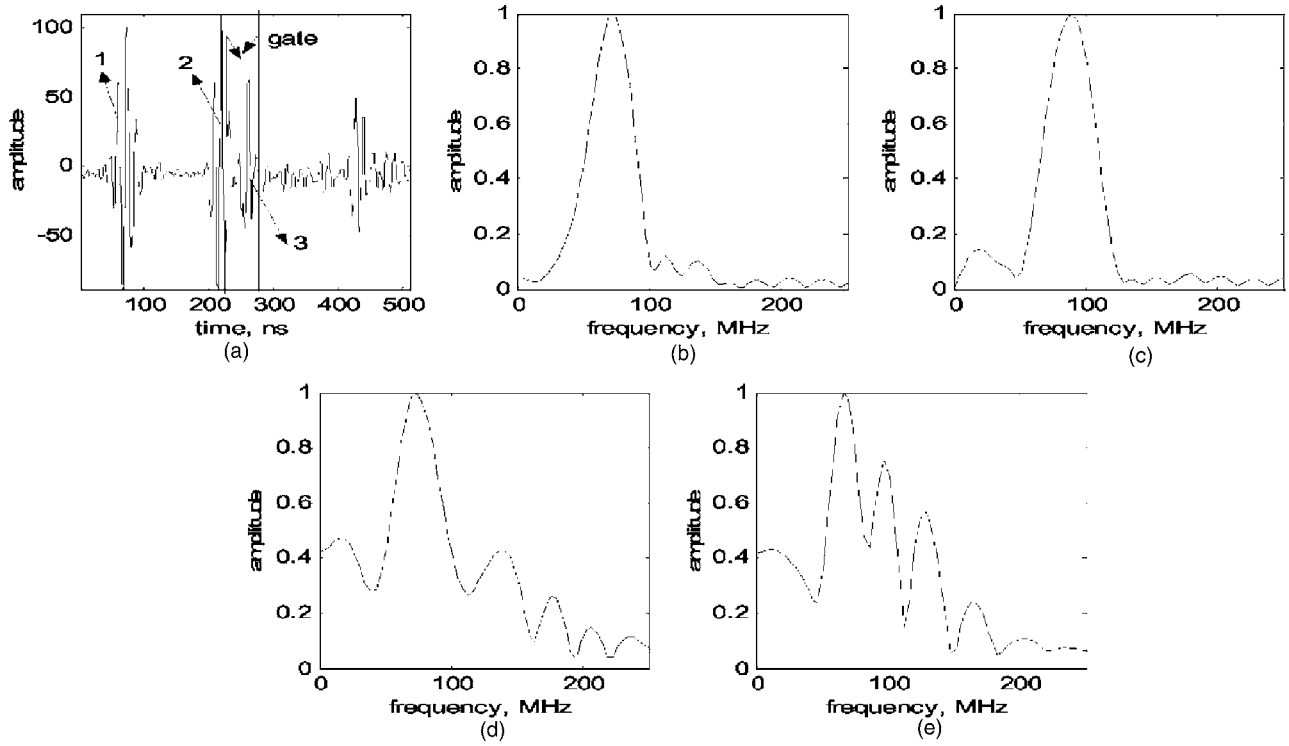

FIG. 3. Resolution limitation of acoustic frequency domain imaging. (a) Ascan; (b), (c), and (d) spectrum of the first, second, and third echoes, respectively; (e) spectrum of the gated signal in (a).

spectrum is more complicated, and the FFT images are difficult to interpret because they have no time resolution.

However, if echoes in the acquired Ascan can be separated accurately by digital signal processing, the imaging performance in terms of resolution and contrast can be improved by generating an image using only the echo corresponding to the interrogated interface, as suggested in Ref. 7. From the AMI signal model above, echo separation can be formulated as the problem of *blind source separation*.

C. Review of sparse signal representation-based AMI (SSRAMI)

In Ref. 7, an improved AMI technique, SSRAMI, was proposed by the authors. Super-resolution and high robustness were achieved by three processes—choosing an overcomplete signal dictionary, separating the incident pulses by exploiting their sparse representability, and selecting an appropriate echo and producing a C-scan output. Suppose that there exists an overcomplete dictionary Φ, an $N \times L$ matrix whose columns are the overcomplete basis vectors $\{\phi_i\}_{i=1}^{L}$ and $L > N$. Then, the problem of echo separation is formulated as follows:

(P_0) Given the observed Ascan y and the overcomplete dictionary Φ, find the vector of coefficients $c=\{c_i\}$ in Eq. (4) such that $y=\Phi c$ and c is as sparse as possible.

Under certain conditions (P_0) can be considered equivalent to the constrained optimization problem:

$$(P_1) \qquad \text{Minimize } \|c\|_1 \quad \text{subject to} \quad y = \Phi c,$$

which can be solved by the *basis pursuit* (BP) decomposition.[9]

After performing the echo separation, the third process of selecting the proper echo and producing the C-scan image in SSRAMI was carried out as follows. First, a time-frequency window as depicted by the dotted line in Fig. 4 was determined in terms of the frequency of transducer and the interface to be investigated in the microelectronic package. Suppose the time-frequency window centers at position (u_c, v_c) with time width Δu_c and frequency width Δv_c. Second, in the given time-frequency window we searched for the time-frequency atoms whose centers were lying in the window, and among them picked up the one with the biggest decomposed coefficient. The time-frequency atom selected

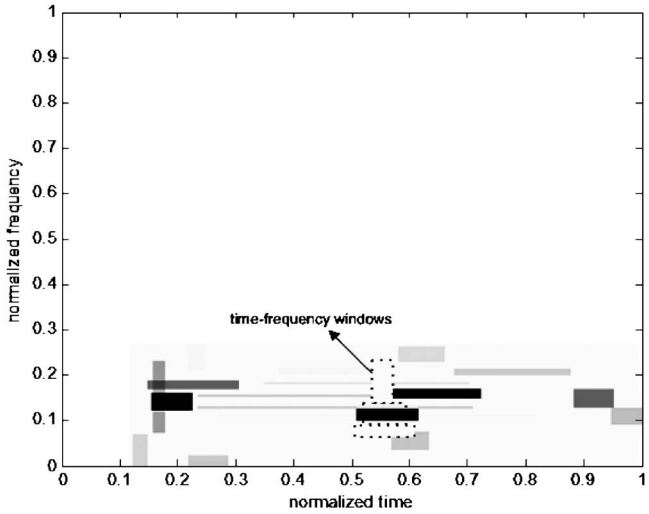

FIG. 4. The echo separation result of an Ascan shown in phase plane and a succession of time-frequency windows. The darkness of the time-frequency image increases with the energy value, and each time-frequency atom selected by the BP method is represented by a Heisenberg box.

and its coefficient were used as the approximation of the expected incident pulse x_i and reflection coefficient c_i, respectively. Third, the reflection coefficient AMI was carried out by directly displaying these selected coefficients at their corresponding position of the C-scan image.

The construction of Φ is a crucial step, on which the success of echo separation depends in great degree. Several overcomplete dictionaries such as the Gabor dictionary and wavelet packet dictionary were examined by both simulated and real AMI signals in Ref. 7. Experimental results demonstrated the great impact of overcomplete dictionary on AMI performance. The Gabor dictionary was the best of the existing overcomplete dictionaries.

Apart from the BP approach, there are several other popular approaches searching for a sparse solution of Eq. (4) in overcomplete dictionaries, including matching pursuit (MP)[10] and the best orthogonal basis (BOB).[11] Hence, several different implementation methods of SSRAMI: BP-based AMI (BPAMI), MP-based AMI (MPAMI), and BOB-based AMI (BOBAMI), were investigated in Ref. 7. BPAMI demonstrated better performance than MPAMI and BOBAMI when the same dictionary was used.

III. LEARNING OVERCOMPLETE REPRESENTATION (LOR)

The problem of learning overcomplete representation is that of representing some data $y \in R^N$ (e.g., the observed AMI signal) using a small number of nonzero components in a source vector $c \in R^L$ under the linear model in Eq. (5) so that

$$\log p(y|\Phi,c) \propto -\frac{1}{2\sigma^2}(y-\Phi c)^2,$$

where the dictionary $\Phi \in R^{N\times L}$ is overcomplete, and the additive noise ξ is assumed to be Gaussian, $p_\xi = N(0,\sigma^2)$. By assuming that the sources c_i are mutually independent, so that the joint probability distribution has the form $p(c) = \prod_{i=1}^{N} p(c_i)$, and assuming that the prior distribution of the source c is Laplacian distributed $p(c_i) \propto \exp(-\theta|c_i|)$, an extended independent component analysis (ICA) method to infer both the overcomplete dictionary Φ and source vector c given the observed signal y, has been proposed in Ref. 12.

A. Inferring the ultrasonic sources

Due to the fact that the additive noise is unknown and that the dictionary Φ is overcomplete, the problem of determining the sources c in Eq. (5) cannot be solved by the pseudoinverse $c = \Phi^+ y$. A probabilistic approach to estimating the sources is based on finding the maximum *a posteriori* value of c

$$\hat{c} = \max_c p(c|\Phi,y) = \max_c p(y|\Phi,c)p(c). \tag{6}$$

Given the dictionary Φ and observation y, Eq. (6) can be optimized by gradient ascent on the log posterior distribution.[12,13]

B. Learning the overcomplete dictionary

Learning the overcomplete dictionary is done using the learning algorithm based on the maximum likelihood (ML) principle with log-likelihood of the data

$$L = \log p(y|\Phi). \tag{7}$$

To obtain the ML estimate of Φ, the likelihood requires marginalizing over all possible sources:

$$p(y|\Phi) = \int p(y|\Phi,c)p(c)dc. \tag{8}$$

This integral is in general analytically intractable. For the special case of zero noise and Φ invertible (a complete basis), the integral is solvable and leads to the standard ICA learning algorithm.[14] Equation (8) is approximated by fitting a multivariate Gaussian around c as follows:

$$\log p(y|\Phi) \approx \frac{N}{2}\log\frac{\lambda}{2\pi} + \frac{L}{2}\log(2\pi) + \log p(c) - \frac{\lambda}{2}(y-\Phi c)^2 - \frac{1}{2}\log\det H, \tag{9}$$

where $\lambda = 1/\sigma^2$, and H is the Hessian of the log posterior at c, $H = \lambda\Phi^T\Phi - \nabla\nabla\log p(c)$. The dictionary is learned by performing gradient ascent on the likelihood of Eq. (7) using the approximation in Eq. (9). The learning rule is

$$\Delta\Phi \propto \Phi\Phi^T\frac{\partial}{\partial\Phi}\log p(y|\Phi) \approx -\Phi(z\hat{c}^T + I),$$

where $z(\hat{c}_i) = \partial\log p(\hat{c}_i)/\partial\hat{c}_i$ is called the score function, and I is the identity matrix. The prefactor $\Phi\Phi^T$ produces the natural gradient extension, which speeds convergence. Note that each gradient step requires the computation of $\hat{c}$ as in Eq. (6).

IV. LEARNING OVERCOMPLETE REPRESENTATION-BASED AMI (LORAMI)

Our earlier work[7] showed that sparse signal representations of AMI signals improved the AMI resolution and robustness greatly. The selection of nonadapted overcomplete dictionary was very important. Although the Gabor dictionary was well-matched to AMI signals in the experiments, the performance is expected to be further improved using learned basis vectors that are adapted to the signal statistics of the inputs. The real ultrasonic echoes inevitably deviate from the idealized Gabor model in Eq. (1). The adapted basis vectors could represent the activities of incident pulses x_i in Eq. (4) much closer than the existing model, and then the reflection coefficients c_i could be inferred more accurately. Therefore, a four-stage process for LORAMI is proposed as follows to further improve the SSRAMI technique by using learned basis vectors instead of fixed basis vectors.

A. Dictionary learning

The significant structure of AMI signals is patterns of ultrasonic echoes. Ideally, an overcomplete dictionary is learned so that each basis vector approximates a pattern of a

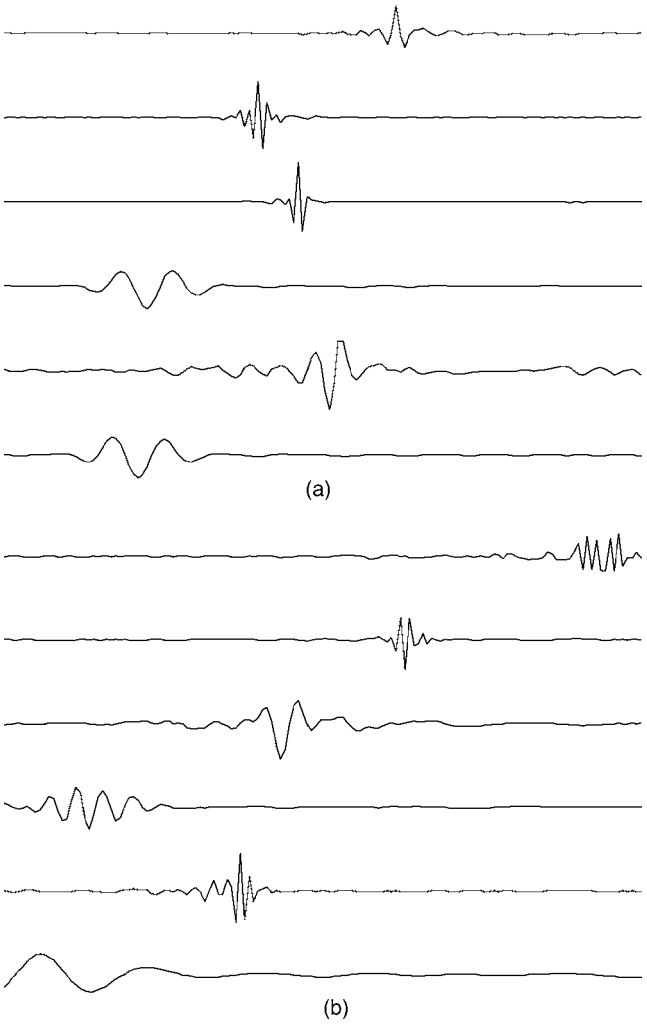

FIG. 5. A sample of learned basis vectors. (a) From the 2×-overcomplete dictionary learned for 230-MHz transducer; (b) from the 2×-overcomplete dictionary learned for 50-MHz transducer.

possible ultrasonic echo as accurately as possible. For AMI, a universal overcomplete dictionary could be learned from the AMI signal samples that are acquired by different transducers and for different types of packages. However, the dictionary performance could be improved by learning a unique overcomplete dictionary for each transducer and certain type of packages. Additionally, note that each Ascan segment is preprocessed by subtraction of its mean and further normalizing it before being used as training data.

B. Dictionary preprocessing

Once a dictionary has been learned, preprocessing is performed. First, each basis vector in the dictionary is normalized with $\|\phi_i\|=1$. Figure 5 shows a sample of the normalized basis vectors from learned 2×-overcomplete dictionaries. (The number of basis vectors L is two times the number of complete basis vectors N.) As expected, the basis vectors in an overcomplete dictionary learned from AMI signals are echo-type vectors, i.e., each basis vector approximates a pattern of a single ultrasonic echo. Notice that very few noise-type vectors might exist in a learned overcomplete dictionary. In the second step of preprocessing, we go through the dictionary to calculate the Heisenberg cell of each basis vector, i.e., its centers and widths in the time- and frequency domains.

To calculate the Heisenberg cell of each basis vector more accurately, median filtering is first performed on these basis vectors in our experiments. The center of the Heisenberg cell in the time domain is then simply determined as the peak position of the basis vector in the time axis. Then, the time width is computed as the total number of samples whose amplitudes are no less than half of the peak amplitude. After transforming the basis vector to the frequency domain by FFT, the frequency center and width are determined in a similar way to that in the time domain, i.e., the frequency with peak amplitude of spectrum is used as the frequency center, and the frequency width is the number of points whose spectrum amplitudes are no less than half of the peak amplitude of the spectrum. Advanced techniques need to be developed in the future to accurately define the Heisenberg cell for each basis vector.

C. Echo separation

Echo separation is carried out by inferring the sparse representations of ultrasonic Ascans using the method described in Sec. III. Similar to SSRAMI, the learning overcomplete representation can be displayed in the phase plane (namely, time-frequency plane), and each basis vector is represented by its Heisenberg cell.

D. Echo selection and image generation

The final step is the same as the one in SSRAMI, which is briefly described in Sec. II C.

V. SIMULATION STUDY

A. AMI signal generation

The performance of LORAMI was evaluated through simulation. Acoustical signals were produced according to the model of signal formation in Eqs. (2) and (4). To make the simulation as close to practice as possible, the incident pulses x_i in Eq. (4) was simulated by three measured ultrasonic pulses obtained from a planar reflector in a water tank using, respectively, 230, 50, and 30-MHz transducers on a commercial AMI system. To reduce the signal length, a downsampling operator with scale 2 was carried out on the measured pulses, which then truncated them to a length of 61 samples. The truncated pulses were then normalized, implying that $\|x_i\|=1$. The resulting pulses and corresponding amplitude spectrum were illustrated in Fig. 6.

Each echo s_i in an Ascan was then generated according to Eq. (4), where the reflection coefficient which determined the amplitude of each echo was changed to simulate different reflectivity properties of the interrogated interfaces/features. Each echo was translated along the time axis to various time positions to simulate a wide diversity of interfaces at different depths. The simulated Ascan was the superposition of several echoes according to Eq. (2).

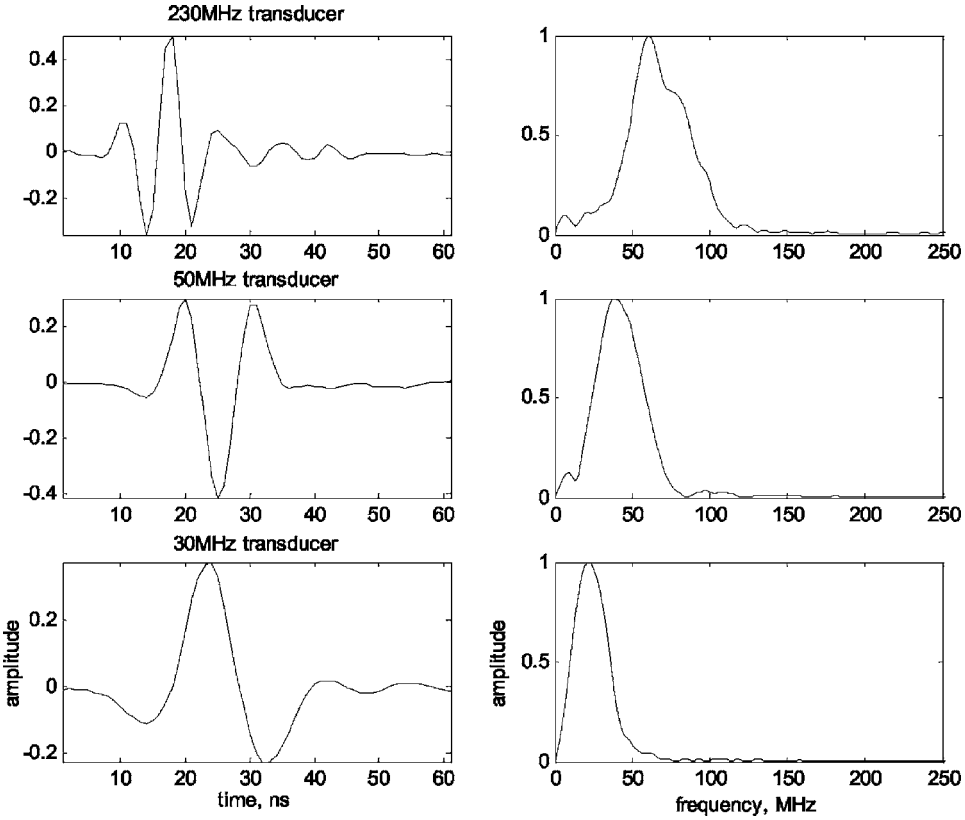

FIG. 6. Simulated incident ultrasonic pulses (left) and their amplitude spectrum (right).

B. Learning dictionaries

A training data set consisted of 43 200 simulated A-scans was generated by the following steps:

(1) Each Ascan was set to 144 samples in length, and assumed that two ultrasonic echoes were present in an Ascan;
(2) A random time position was set for each echo within the Ascan;
(3) Randomly picked up two of three simulated ultrasonic pulses shown in Fig. 6. Then, translated each pulse along the time axis so that its center was located in the setting position of step 2;
(4) Superposed the two translated pulses, resulting in an Ascan;
(5) Subtracted the mean of the resulting Ascan and normalized it; and
(6) Repeating steps 1–5 until all Ascans had been generated.

A complete (144 basis vectors) dictionary, a 2×-overcomplete (288 basis vectors) dictionary, a 3×-overcomplete (432 basis vectors) dictionary, and a 4×-overcomplete (576 basis vectors) dictionary were learned from the training data set. The dictionaries were initialized by Gaussian-modulated random vectors during the learning process.

C. Performance comparison between complete and overcomplete signal representations

Under an overcomplete dictionary the decomposition of a signal is not unique, but this can offer some advantages.[9,12] One is that there is greater flexibility in capturing structure in the data. Instead of a small set of general basis vectors, there is a larger set of more specialized basis vectors such that relatively few are required to represent any particular signal. An additional advantage of overcomplete representations is increased stability of the representation in response to small perturbations of the signal.

An experiment using simulation data was performed to examine the efficiency of overcomplete representations for LORAMI. The performance of AMI was measured quantitatively by the AMI error, which was defined as

$$\mathrm{Err} = \frac{|\tilde{c}_i| - k_j \cdot |c_i|}{k_j \cdot |c_i|} \times 100\% \tag{10}$$

where c_i was the original reflection coefficient, $\tilde{c}_i$ the estimated reflection coefficient in LORAMI and SSRAMI, and k_j ($j=1$, 2, and 3) was the correction factor. A simulated incident pulse shown in Fig. 6 was extended to the length of 144 samples by zero padding. Then, we decomposed it in the overcomplete dictionary. The absolute value of the reflection coefficient estimated from the incident pulse was set to k_j, where $j=1$, 2, and 3 was the index of the simulated incident pulses and was chosen according to the interrogated echo. Because the basis vectors from an overcomplete dictionary did not match the measured ultrasonic pulse exactly, $\tilde{c}_i$ never reached its theoretical value c_i. In the time-frequency domain, $k_j \cdot c_i$ was the corrected theoretical limitation value of $\tilde{c}_i$, which was only reachable in the situation where the interrogated echo did not interfere with the other echoes. Note that Eq. (5) is a linear model, so Err is good to measure the distortion caused by the echo overlap and imaging performance.

TABLE I. Performance comparison of complete and overcomplete dictionaries. The AMI error is presented.

		AMI error (%)			
	No.	Complete basis	2× overcomplete basis	3× overcomplete basis	4× overcomplete basis
A scan	#1	−80.35	−5.76	−2.86	−1.85
	#2	−83.02	−2.67	2.07	−17.91
	#3	33.67	4.08	−5.28	−12.82
	#4	70.32	−21.22	−20.07	−26.88
	#5	−89.72	2.10	22.99	1.66
	#6	−34.04	7.59	20.91	16.46
	#7	−72.76	−8.43	−5.11	−3.63
	#8	40.77	−5.57	13.75	−10.51
	#9	−23.45	11.38	15.96	6.57

Various Ascans had been simulated using the method described in Sec. V A. Each Ascan was simulated to contain two echoes, which were made to have different reflection coefficients, and different degrees of overlap in the time- and frequency domain. The overlap degree in the frequency domain was achieved by combining the simulated incident ultrasonic pulses in different order. For example, putting 230- and 30-MHz pulses together produces less overlap than the combination of 50- and 30-MHz pulses in the frequency domain. The overlap degree in the time domain can be easily tuned by translating these pulses along the time axis.

The complete and overcomplete learned dictionaries in Sec. V B were used to perform LORAMI on these simulated Ascans. The time-frequency window was set to the Heisenberg cell of the first echo. The results for nine simulated Ascans are listed in Table I. The table shows the learned overcomplete dictionaries perform significantly better than the complete dictionary.

An example of overcomplete and complete representations is shown in Fig. 7. The overcomplete and complete representations of the Ascan plotted in Fig. 7(a) are displayed in Figs. 7(b) and 7(c), respectively. The corresponding echoes recovered in LORAMI using 2×-overcomplete and complete learned dictionaries are plotted in Figs. 7(e) and 7(f), respectively, in comparison with the original echo shown in Fig. 7(d). It can be seen that the overcomplete basis vectors approximate the ultrasonic echo components much closer than the complete basis vectors, as a result improving the AMI performance. It is also observed that the overcomplete representations locate the echoes very well.

However, the 3×-overcomplete and 4×-overcomplete dictionaries did not show greater performance than the 2×-overcomplete dictionary, and in fact were even poorer. Similar results were observed in Ref. 12. One possible reason is that the assumptions of the prior distribution for the coefficients are inaccurate. A Laplacian is not sparse enough

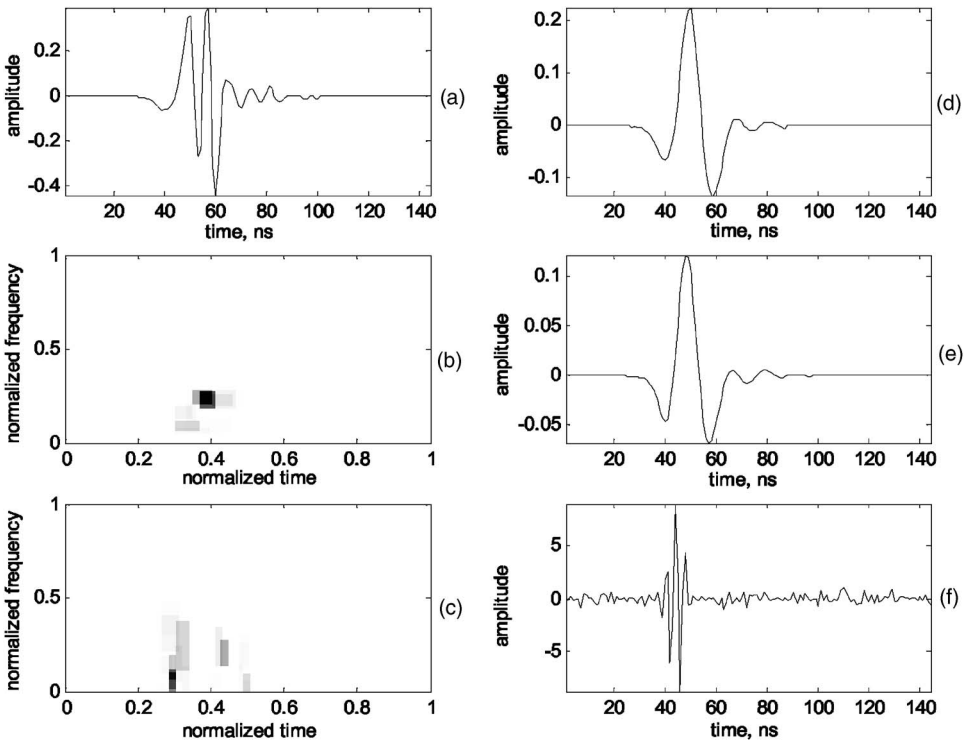

FIG. 7. The overcomplete representation and complete representation of a simulated ultrasonic Ascan. (a) The simulated Ascan; (b) the learning overcomplete representation; (c) the learning complete representation; (d) the original echo [the first echo in (a)]; (e) the recovered echo by the overcomplete representation; (f) the recovered echo by the complete representation.

TABLE II. Performance comparison of adapted and nonadapted dictionaries. The AMI error is presented.

		AMI error (%)			
	No.	LORAMI (2×-overcomplete)	BPAMI+WP (8×-overcomplete)	MPAMI+Gabor (2×-overcomplete)	MPAMI+Gabor (8×-overcomplete)
Ascan	#1	−5.76	−5.60	−1.98	−0.0023
	#2	−2.67	−7.52	0.77	0.77
	#3	4.08	36.53	−1.02	−0.89
	#4	−21.22	23.56	−57.58	51.59
	#5	2.10	10.44	56.68	−23.85
	#6	7.59	−27.26	1.58	−11.26
	#7	−8.43	13.84	−9.85	−20.86
	#8	−5.57	−9.26	−45.06	16.18
	#9	11.38	42.87	−68.18	−20.90

to reflect the practical coefficient distribution, especially for our simulations where the coefficient distribution is far sparser than predicted by the Laplace distribution. Another possible reason is that the approximation in Eq. (9) becomes increasingly inaccurate for higher degrees of overcompleteness. In addition, the fundamental assumption that the coefficients are statistically independent might not be true for AMI signals.

D. Performance comparison between adapted LORAMI and nonadapted SSRAMI

This experiment was carried out to quantitatively evaluate the performance of the proposed LORAMI in comparison with nonadapted SSRAMI. The 2×-overcomplete learned dictionary was used to perform LORAMI. For the simplification of implementation, the simulated Ascan was zero padded to a length of 256 samples to perform SSRAMI. Two implementation methods of SSRAMI, BPAMI with wavelet packet (WP) dictionary, and MPAMI with discrete Gabor dictionary were compared. In previous work,[7] it has been shown that the WP dictionary with *Symmlet 8* is superior to other WP dictionaries. So, the *Symmlet 8* was chosen as the mother wavelet in this paper. The WP dictionary[11] contains $N\log 2(N)$ basis vectors. With a signal length $N=256$, the WP dictionary is 8×-overcomplete. The real Gabor dictionary is defined by $D_R=\{g_{(r,w)}:(r,w)\in\Gamma\times[0,2\pi]\}$,[15] where $r=(s,u,v)$ and

$$g_{(r,w)}=\frac{K_{(r,w)}}{\sqrt{s}}g\left(\frac{t-u}{s}\right)\cos(vt+w), \tag{11}$$

where s is the scale of the function, u its translation, and v its frequency modulation; window function $g(t)$ is the Gaussian function $g(t)=e^{-\pi t^2}$, constant and factor $K_{(r,w)}/\sqrt{s}$ normalize $g_{(r,w)}$, and w is the phase of the real Gabor vectors. In practical applications, signal decomposition is performed in the discrete Gabor dictionary D_α, where Γ_α is composed of all $r=(a^j,pa^j du,ka^{-j}dv)$ with $du=dv/2\pi$ and $du\cdot dv<2\pi$. The parameter $r=(s,u,v)$ was discretized in the paper as follows:

(i) $s[j]=a^j$, for $1\leqslant j\leqslant n$, where n is the biggest integer power of a such that $a^n\leqslant N$, and the discretized scale parameter a can be selected in an arbitrary way.
(ii) $du[j]=s[j]/2$ and $dv[j]=\pi/s[j]$.
(iii) $u\in\{pdu\,|\,p\in Z,0\leqslant p,pdu\leqslant N-1\}$.
(iv) $v\in\{kdv\,|\,k\in Z,0\leqslant k,kdv<rmv\}$, where $rmv=2\pi$.

With this parameter discretization, the discrete Gabor dictionary contains $N\log 2(N)/\log 2(a)$ basis vectors. The smaller the scale a, the higher the overcompleteness. It is 8× overcomplete when parameter $a=2$ and 2× overcomplete with $a=16$.

The interface for C-scan imaging was set to the first echo by setting the time-frequency window to the Heisenberg cell of the first echo. Some results are presented in Table II. Table II shows the proposed LORAMI does improve the AMI performance by using the adapted dictionary instead of the nonadapted dictionary when comparing LORAMI with BPAMI and MPAMI. The AMI performance by learned 2×-overcomplete dictionary is even better than the nonadapted 8×-overcomplete dictionaries. In most cases, MPAMI with Gabor dictionaries have high performance. However, in certain cases MP fails to super-resolve[9] so that the MPAMI results in a big AMI error. From Table II, the LORAMI are more consistent and achieve better performance overall.

Figure 8 illustrates the overcomplete representations of an example Ascan plotted in Fig. 8(a). The adapted overcomplete representation of the Ascan by LORAMI with the learned 2×-overcomplete dictionary is displayed in Fig. 8(b). Figures 8(d), 8(e), and 8(f) show the nonadapted overcomplete representations of the zero-padded Ascan plotted in Fig. 8(c), respectively, by BPAMI with WP, MPAMI with 8×-overcomplete Gabor dictionary, and MPAMI with 2×-overcomplete Gabor dictionary. Figures 9(a) and 9(d) show two original echoes in Fig. 8(a). The recovered corresponding echoes in LORAMI are plotted in Figs. 9(b) and 9(e). The recovered echoes in SSRAMI are plotted in Figs. 9(c) and 9(f). Comparing the recovered echoes with the corresponding original echoes, it can be seen that the learned basis vectors approximate the ultrasonic echo components

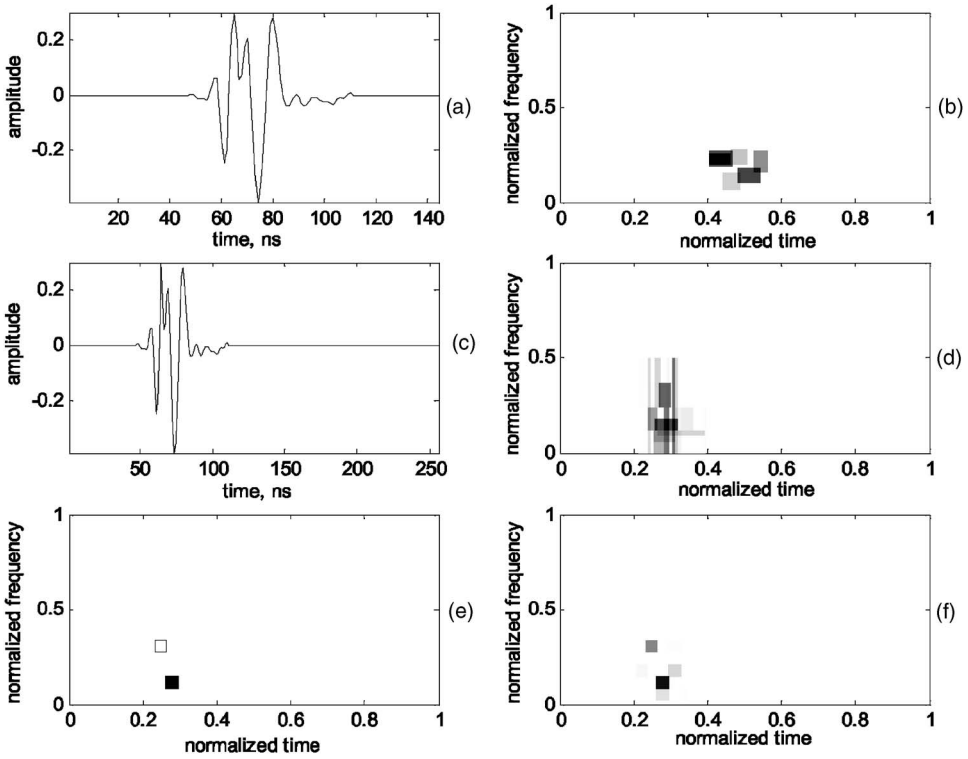

FIG. 8. Comparison of learning overcomplete representation-based AMI (LORAMI) and sparse signal representation-based AMI (SSRAMI): (a) A simulated Ascan; (b) adapted overcomplete representation of (a) by LORAMI with the learned 2×-overcomplete dictionary; (c) the extension of (a) by zero padding; (d) nonadapted overcomplete representation of (c) by basis pursuit-based AMI (BPAMI) with wavelet packet dictionary (WP); (e) matching pursuit-based AMI (MPAMI) with 8×-overcomplete Gabor dictionary; (f) MPAMI with 2 ×-overcomplete Gabor dictionary.

much closer than the Gabor basis vectors in terms of waveforms, giving more details of the original echoes.

A limitation of the LOR algorithm is also observed here. The amplitude of a recovered echo from LORAMI is far lower than the original amplitude. One possible reason for the results is that the assumptions of the prior distribution for the coefficients in LOR are inaccurate. For the probability distribution of the coefficients is much sparser than the Laplacian distribution and LOR seek global optimization, the Laplace prior of the decomposed coefficients might force the simulated Ascan is approximated by more basis vectors.

E. Performance comparison between LORAMI and conventional AMI techniques

This experiment was carried out to quantitatively evaluate the performance of the proposed LORAMI in comparison with conventional AMI techniques. The imaging perfor-

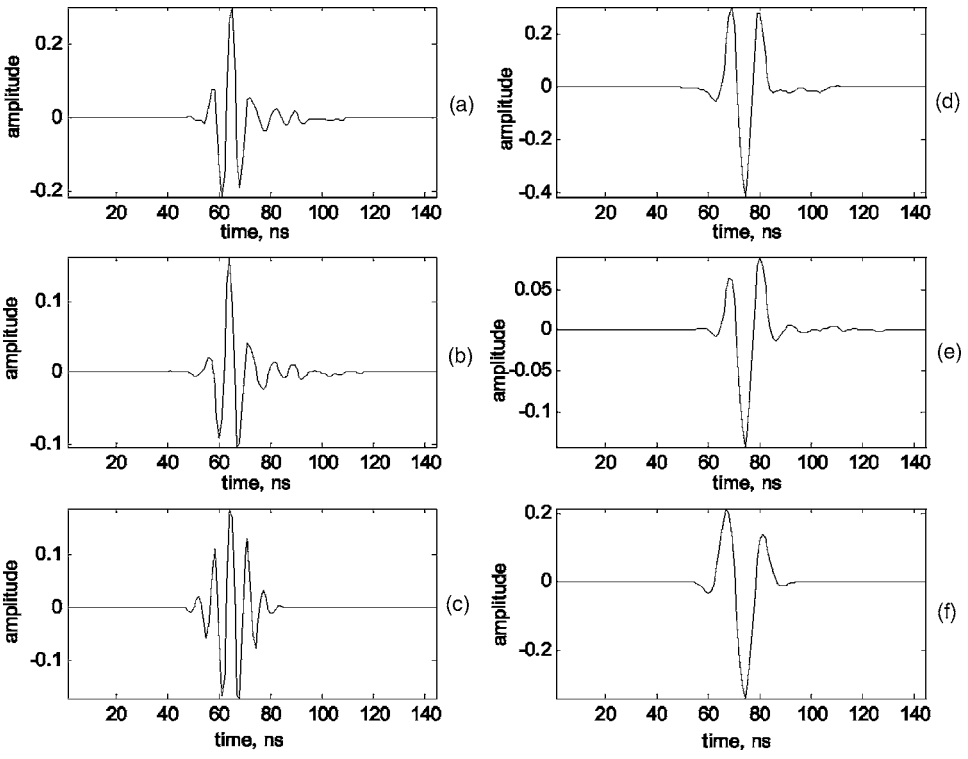

FIG. 9. Recovered echoes by LORAMI and SSRAMI. (a) The first echo in Fig. 8(a); (b) the recovered echo by LORAMI with the learned 2 ×-overcomplete dictionary; (c) the recovered echo by MPAMI with 8×-overcomplete Gabor dictionary; (d) the second echo in Fig. 8(a); (e) the recovered echo by LORAMI with the learned 2×-overcomplete dictionary; (f) the recovered echo by MPAMI with 8×-overcomplete Gabor dictionary.

TABLE III. Performance comparison of LORAMI and conventional AMI techniques.

		Parameters			AMI error(%)			
	No.	$A1/A2$	$u2$-$u1$ (Sample number)	$v2$-$v1$ (MHz)	LORAMI (2×-overcomplete)	FDAMI (f_c)	FDAMI (f_o)	TDAMI
Ascan	#1	1	22	39.06	1.27	8.96	5.51	0
	#2	0.8	12	39.06	2.39	−28.13	−24.17	3.23
	#3	0.5	12	39.06	15.99	−58.06	−53.90	93.37
	#4	1	6	39.06	−14.76	−3.33	−6.19	31.08
	#5	1	31	21.48	−5.76	−33.14	19.72	0
	#6	1/1.5	11	21.48	−8.15	86.51	14.84	−7.10
	#7	1	20	17.58	−0.48	41.55	−25.06	0
	#8	0.8	10	17.58	17.86	5.86	158.78	52.85
Ascan + noise (SNR in dB)	#9 (9.63)	1	22	39.06	14.61	14.58	22.54	14.45
	#10 (8.64)	0.8	12	39.06	9.04	−24.18	−38	22.13
	#11 (6.43)	0.5	12	39.06	38.48	−69.19	−71.59	102.98
	#12 (8.35)	1	6	39.06	−4.65	−6.30	−13.12	24.24
	#13 (9.22)	1	31	21.48	5.59	23.91	4.2	11.09
	#14 (8.86)	1	11	21.48	7.76	88.90	53.10	−2.33
	#15 (9.54)	1	20	17.58	2.70	29.93	−37.55	−18.11
	#16 (10.18)	0.8	10	17.58	21.55	18.01	169.79	58.33

mance of LORAMI was measured using the AMI error in Eq. (10) while TDAMI and FDAMI was evaluated by the AMI error, which is defined as

$$\mathrm{Err} = \frac{(\tilde{A}_i - A_i)}{A_i} \times 100\,\%\ ,$$

where for TDAMI, A_i is the peak intensity of the original echo, and $\tilde{A}_i$ is the measured value during the imaging process; for FDAMI, A_i and $\tilde{A}_i$ are the spectrum amplitude at a given frequency of original and measured, respectively. Some results of quantitative evaluation are listed in the upper part of Table III, where parameters $A1$ and $A2$ are the amplitudes of two echoes separately, $v2$-$v1$ is the frequency separation of two echoes, and $u2$-$u1$ is the time separation (in sample number) of two echoes. The interface for C-scan imaging was set to the first echo by choosing gates as follows: for TDAMI, the gate was chosen to center at $u1$, with width equal to 20 samples, which is the narrowest gate available in our commercial AMI system. The time-frequency window was set to the Heisenberg box of the first echo. For FDAMI, two FFT images were evaluated. One was at the center frequency of the first echo, and another one at off-center frequency in the overlapped interval. They are denoted by f_c and f_o, respectively. The learned 2×-overcomplete dictionary was used to perform LORAMI.

Table III shows that the proposed LORAMI perform significantly better than the conventional AMI techniques. When two echoes are overlapped the in time- and frequency domain, the conventional AMI techniques give a large error, but LORAMI still gives stable and accurate results. This implies the resolution improvement is achieved by LORAMI.

The robustness of LORAMI was examined by adding zero-mean Gaussian white noise into the simulated Ascans. The lower part of Table III tabulates some test results, where the Ascans #9 to #16 were obtained by adding noise into the Ascans #1 to #8, respectively. It is seen that LORAMI is more robust than the conventional AMI techniques. Figure 10 shows an example where SNR=3.88 dB. We can clearly see TDAMI and FDAMI are susceptible to noise. For LOR, the background noise usually cannot match any dictionary elements. Consequently, the technique tends to ignore the noise part of the signal.

F. Ascan with multiple echoes overlapped

In preceding experiments, the superior performance of LORAMI in dealing with acoustic microimaging with two echoes overlapped has been demonstrated. An extended experiment where each Ascan contained multiple echoes was further carried out in this work. The experimental results are in accordance with the foregoing simulation results. The LORAMI performed significantly better than the conventional TDAMI and FDAMI, and surpassed SSRAMI. Figure 11 demonstrates an example where an Ascan contains three overlapped echoes, as shown in Fig. 11(a). Figure 11(b) shows the learning overcomplete representation decomposed in the learned 2×-overcomplete dictionary. From Fig. 11(b),

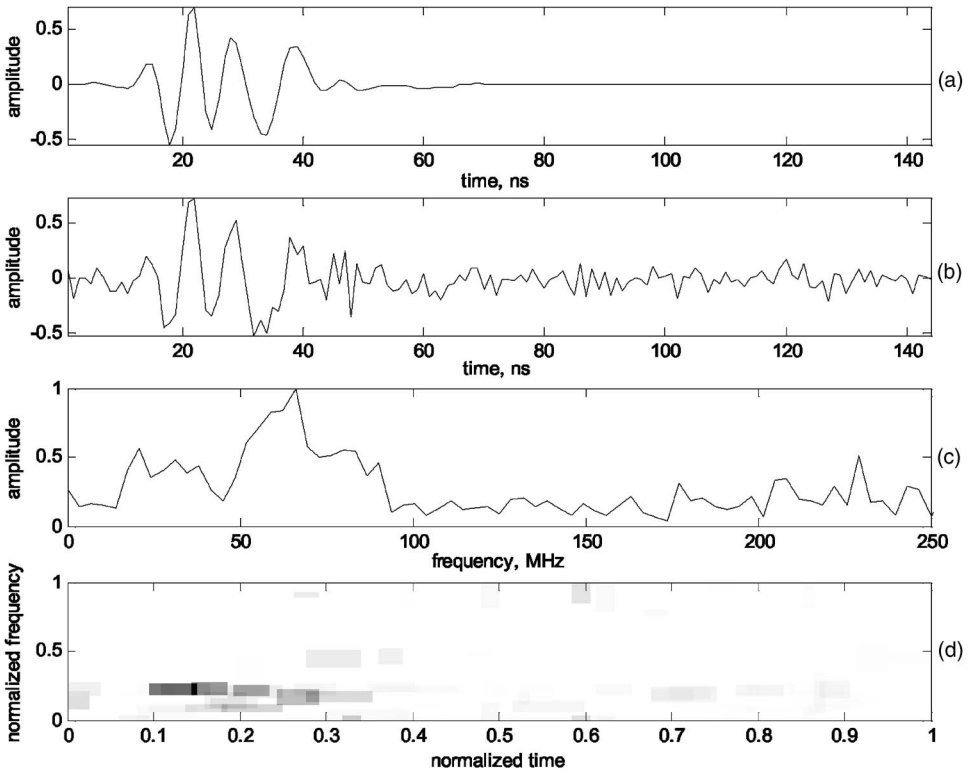

FIG. 10. The AMI results of a simulated Ascan: (a) Noise-free Ascan; (b) noisy Ascan with SNR=3.88 dB, produced by adding white noise into (a); (c) amplitude spectrum of (b); (d) sparse representations with learned overcomplete basis.

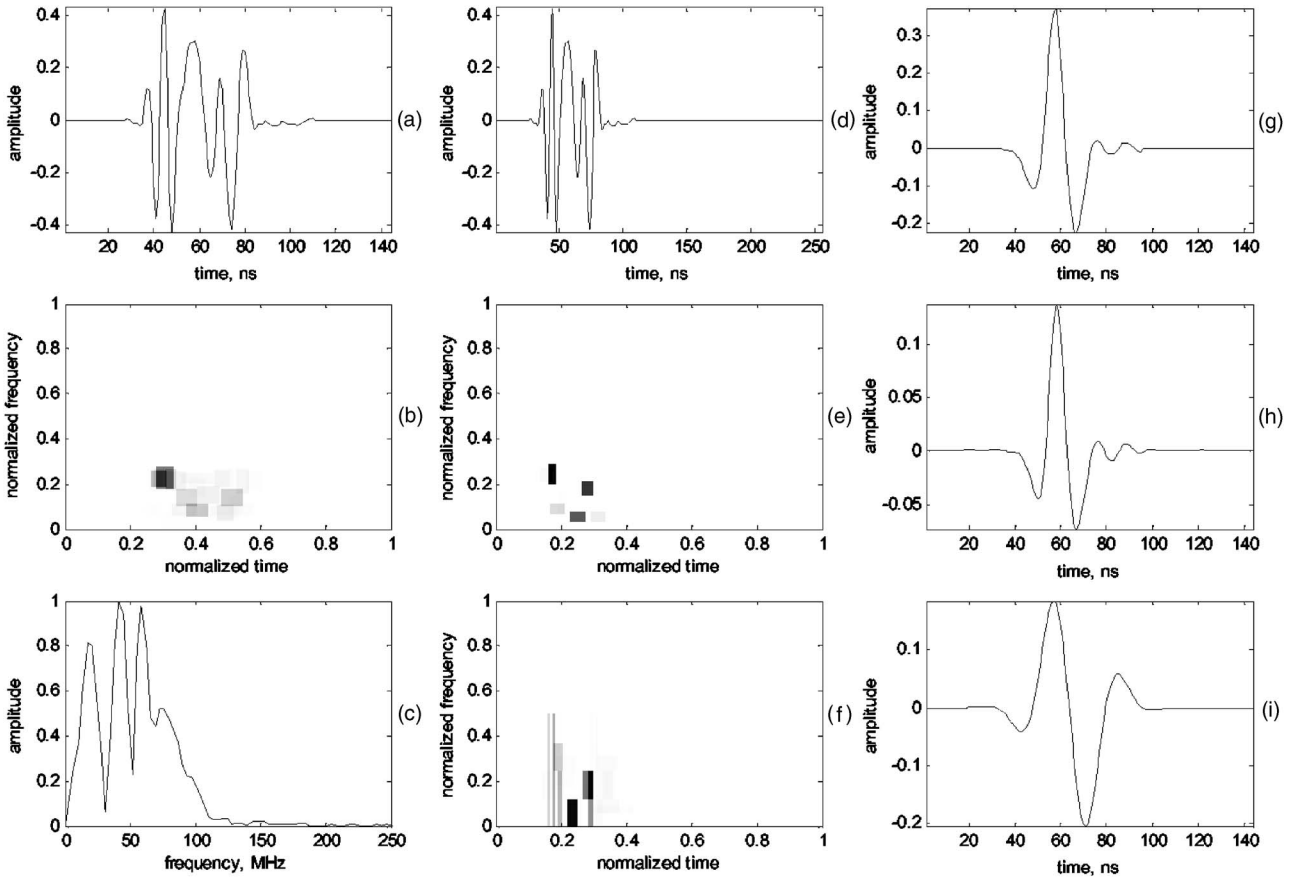

FIG. 11. Ascan with three echoes overlapped. (a) Original Ascan; (b) learning overcomplete representations of (a) by LORAMI; (c) amplitude spectrum of (a); (d) the extension of (a) by zero padding; (e) sparse overcomplete representations of (d) by MPAMI with 8×-overcomplete Gabor dictionary; (f) BPAMI +WP; (g) the middle echo in Fig. 11(a); (h) the recovered middle echo by LORAMI; (i) the recovered middle echo by MPAMI with 8×-overcomplete Gabor dictionary.

it is observed that the proposed LORAMI works very well. Figure 11(d) is formed by zero padding of Fig. 11(a). The corresponding sparse signal representations, obtained by MPAMI with 8×-overcomplete Gabor dictionary and BPAMI with WP dictionary, are displayed in Figs. 11(e) and 11(f). Figures 11(h) and 11(i) plot the middle echo recovered by LORAMI and MPAMI, respectively. Comparing the recovered echoes with the original middle echo plotted in Fig. 11(g), it is seen that the LORAMI recovers the ultrasonic echo much better than SSRAMI in terms of the waveform, time position, and frequency position of the echo. In addition, from Figs. 11(a) and 11(c) the middle echo is interfered with by both the front echo and the back echo in the time- and frequency domain, so TDAMI and FDAMI are more difficult to interpret provided the echo of interest is the middle echo.

VI. EXPERIMENT WITH MEASURED DATA

The proposed technique was further validated by experiments with measured data. Several real automotive electronic circuit boards (ceramic thick-film hybrid circuit) from a manufacturing line were used as test boards. For the thick-film hybrid circuitry, multiple layers (tracks, conductors, dielectric layers, etc.) were printed on one ceramic substrate. This work focused on the quality and reliability testing of flip-chip solder bonds. So, ultrasonic Ascans were acquired from various flip-chip packages mounted on these boards, as illustrated in Fig. 1. On each package, 16 Ascans from different positions were saved. Selected position points are the representatives of typical structures such as solder bonds with and without defects, and nonsolder bond area. At each point we captured Ascans starting from the package top with a signal length of 512 samples using both a 230-MHz transducer and a 50-MHz transducer.

A. Learning dictionaries

A training data set was made to consist of AMI segments. Each AMI segment was randomly extracted from the acquired Ascans, having 144 samples in length. The mean value of a segment was subtracted from it for each segment. Then, these resulting segments were normalized. In order that each learned basis vector models only a single echo pattern, extracting segments randomly is very important. Otherwise, the learned basis vector might be a pattern with multiple echoes inside, which is demonstrated in Fig. 12.

Two training data sets were constructed in the experiment. One is for the 50-MHz transducer, and another one is for the 230-MHz transducer. Each training data set was comprised of 25 200 segments. For each transducer, a 2×-overcomplete dictionary was learned. The dictionaries were initialized by Gaussian-modulated random vectors during the learning process. Several learned basis vectors are shown in Fig. 5.

B. Learning sparse representations of AMI data

Figure 13 shows example Ascans from a defective solder bond. Figure 13(a) is acquired by the 230-MHz transducer, in which the first echo is from the die-solder bond (C-B) interface, the second echo is reflected from the defect. At the same point, the measured Ascan using a 50-MHz transducer is displayed in Fig. 13(b), where two echoes cannot be resolved due to the lower resolution of the 50-MHz transducer. Figures 13(c) and 13(d) display the learning overcomplete representations of Figs. 13(a) and 13(b), respectively. Comparing Fig. 13(a) with the resulting LORAMI results in Fig. 13(d), it is observed that LORAMI resolves these echoes in the low-resolution 50-MHz Ascan. Thus, LORAMI can image the individual interfaces, improving the AMI resolution.

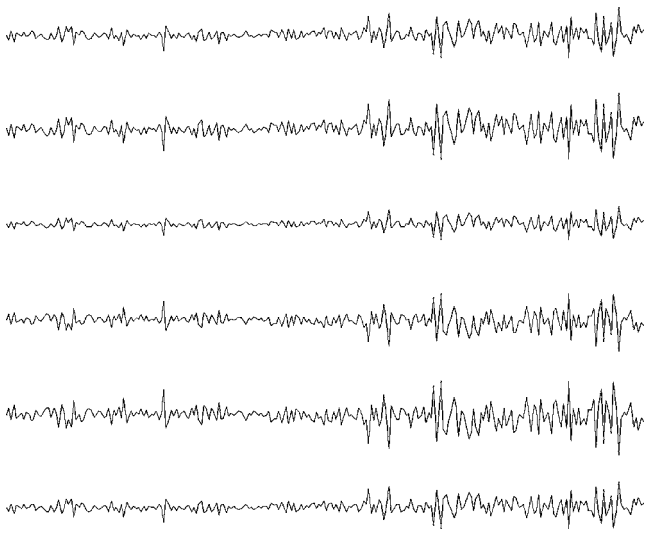

FIG. 12. The learned basis vectors with multiple echo patterns.

Figure 14 shows another case of example Ascans from a different circuit board. The result in Fig. 14 further confirms the effectiveness of LORAMI.

C. Effect of time-frequency windows

The determination of time-frequency window is a crucial step in LORAMI, on which the image quality depends in great degree. Some *a priori* information such as the center frequency of the transducer in use, and its fundamental bandwidth and package structure should be incorporated. In a broadband AMI system there is frequency downshifting due to frequency-dependent attenuation. Moreover, even at the same interface, there are minor differences in center frequency for the incident pulses at different x-y positions. Hence, calibration is usually carried out preceding the processing. The average center frequency is utilized as the center frequency position v_c of window. A reasonable selection for the window width Δu_c and Δv_c is the width of the Heisenberg box of the expected echo multiplied by a constant factor. The factor given empirically is to compensate for the changes of center frequency, and to reduce the loss of the interested echoes reflected in the interface to be investigated. If a small window is used, a clear image would be expected, but some features existing in the practical interface may not be displayed. On the contrary, the acoustic image might be a little blurred.

An alternative to the above method is to examine the internal features and possible defects by a succession of C

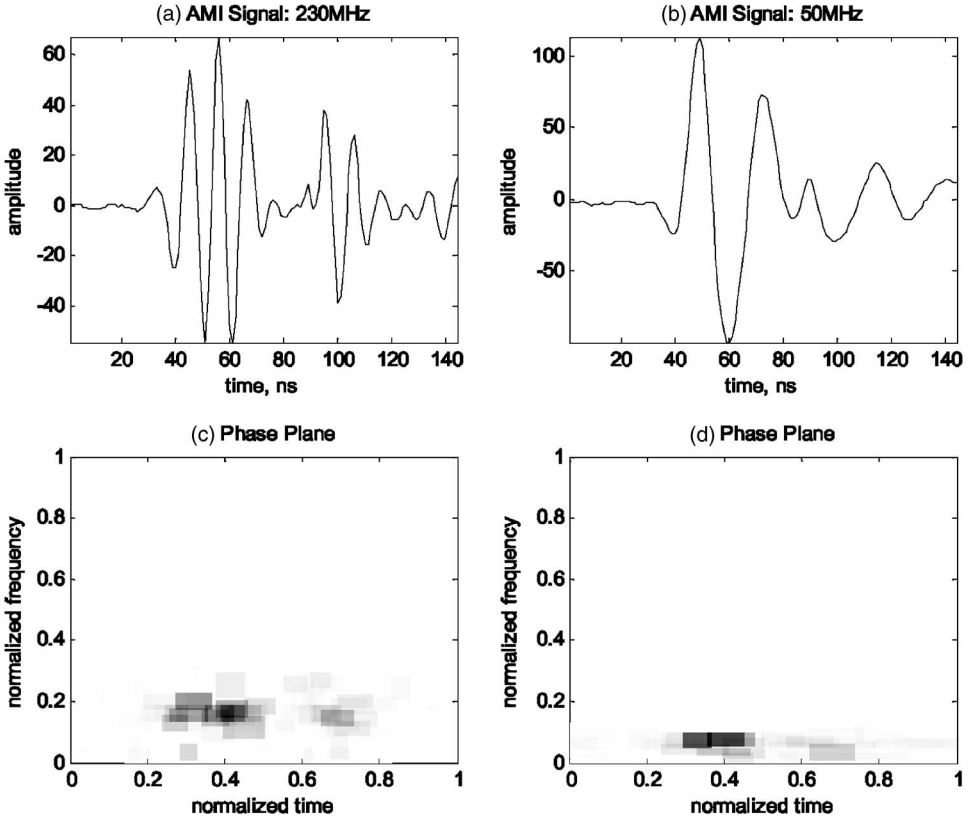

FIG. 13. Example Ascans from the first circuit board acquired by (a) the 230-MHz transducer and (b) the 50-MHz transducer. (c) The learning overcomplete representation of (a). (d) The learning overcomplete representation of (b).

scans produced by a succession of time-frequency windows as shown in Fig. 4, where small Δv_c is chosen when v_c becomes low. Specific features may yield more information at one time-frequency window rather than another. Therefore, LORAMI can bring out image details that might not be visible with conventional TDAMI and FDAMI.

An experiment was performed to examine the effect of time-frequency windows on LORAMI. Sixteen Ascans from

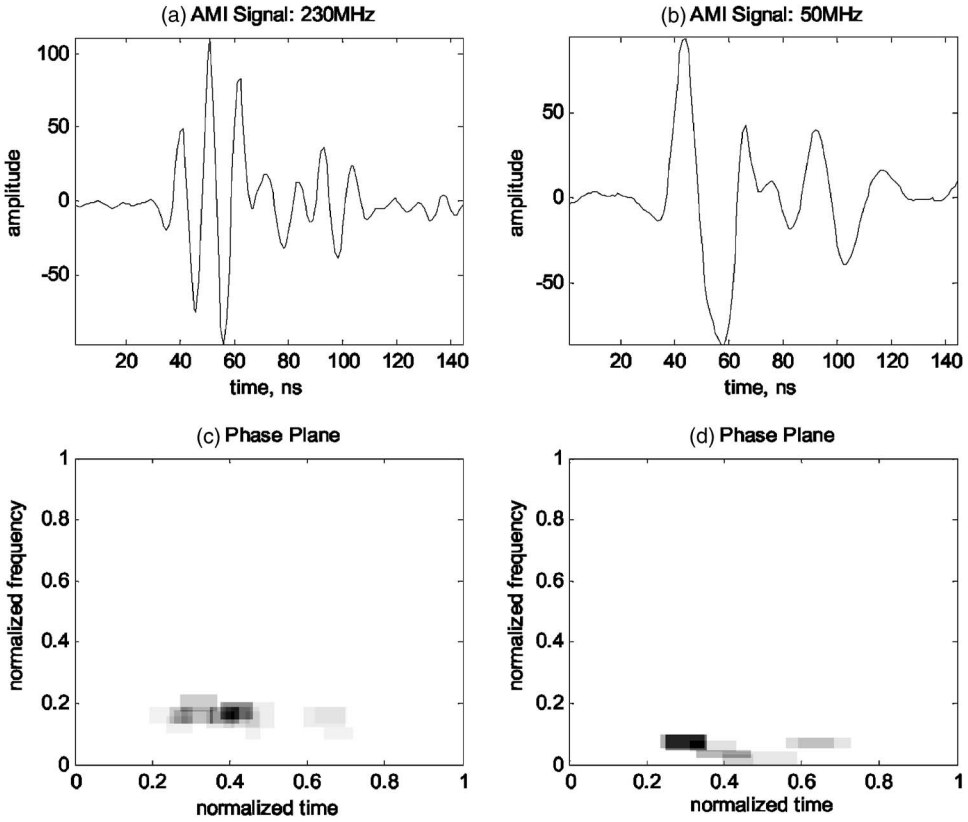

FIG. 14. Example Ascans from the second circuit board acquired by (a) the 230-MHz transducer and (b) the 50-MHz transducer. (c) The learning overcomplete representation of (a). (d) The learning overcomplete representation of (b).

a single flip-chip package acquired by the 50-MHz transducer were decomposed into sparse representations by LOR with the learned 2×-overcomplete dictionary. The interrogated interface was set to the die–solder bond interface. The Heisenberg box of the echo reflected from the interrogated interface in a typical Ascan was used as the time-frequency window. This was then applied to the 16 A-scans. For all Ascans, the window worked perfectly, choosing the proper atoms.

VII. DISCUSSION AND CONCLUSION

In this paper an improved acoustic microimaging technique has been presented, which integrated the learning overcomplete representation algorithm into conventional AMI techniques. The results obtained from computer simulation and measured data have demonstrated the advantages of the novel technique. Its performance was compared with that of SSRAMI and conventional TDAMI and FDAMI. Without increasing ultrasonic frequencies, both LORAMI and SSRAMI improve the axial resolution and robustness of traditional AMI systems by employing acoustical time-frequency domain imaging techniques with overcomplete representations of ultrasonic signals. The performance of LORAMI was further improved by using the learned dictionary instead of the nonadapted dictionary.

From Sec. IV B, it can be seen that development of advanced techniques, which can identify the noise-type basis vectors and echo-type basis vectors, and accurately define the Heisenberg cell for each echo-type basis vector, could be useful in improving the proposed technique.

Although the attenuation in the coupling medium and package materials is not incorporated explicitly into the AMI model in Sec. II A, it has been considered throughout this paper implicitly. The frequency-dependent attenuation in materials affects the frequency, phase, and amplitude of each incident pulse x_i and reflected echo s_i in Eqs. (1) and (2). Unlike conventional deconvolution techniques, where either the reflected echoes were assumed to have similar waveforms or the exact attenuation had to be considered, arbitrary attenuation is assumed in this paper because each reflected echo is assumed to be any frequency, phase, and amplitude. For the proposed LORAMI, its performance is affected by the overlap degree of two echoes in the time-frequency domain. If two echoes have very small differences in both time position and center frequency, the proposed techniques could not resolve them. The resolution limitation of LORAMI is determined by the sparse signal representation algorithm.

The simulation study in Sec. V reveals the limitation of the LOR algorithm used in this paper for AMI applications. One possible reason is that the assumptions of the probabilistic model in Sec. III are inaccurate. The observed coefficient distribution for the AMI data is much sparser than that of the Laplacian assumed by the model. Also, the fundamental assumption that the coefficients are statistically independent might not be true for AMI data. Another possibility is that the approximations in Eq. (9) are inaccurate. An improved LOR algorithm will lead to greater AMI performance and higher accuracy of ultrasonic echo estimation. A recently developed dictionary learning algorithm[16] might be a good alternative to the one used in this paper. In addition, once a dictionary has been learned for a certain application, a different algorithm can be used to choose the basis vectors to form an accurate, sparse representation. The Sparse Bayesian Learning[17] developed recently might lead to a better result, improving the performance of LORAMI technique. These new algorithms were developed on the basis of a more flexible assumption of coefficient distribution rather than the Laplacian prior.

Finally, further work performed on 3D rf ultrasonic data (i.e., the collection of Ascans along with the acoustical image) will be very useful for the practical applications. In this case, one can visually compare the C-scan images of the package before and after the use of LORAMI. Unfortunately, the commercial AMI system used in the work cannot produce these kinds of data.

ACKNOWLEDGMENTS

This work has been supported by The Engineering and Physical Sciences Research Council (EPSRC) of UK.

[1] K. Raum, "Scanning acoustic microscopy on bone—status and perspectives," J. Acoust. Soc. Am. **116**, 4, 2490 (2004).
[2] L. Wang, "The contrast mechanism of bond defects with the scanning acoustics microscopy," J. Acoust. Soc. Am. **104**, 5, 2750–2755 (1998).
[3] J. E. Semmens, "Flip-chips and acoustic micro imaging: An overview of past applications, present status, and roadmap for the future," Microelectron. Reliab. **40**, 1539–1543 (2000).
[4] J. E. Semmens and L. W. Kessler, "Application of acoustic frequency domain imaging for the evaluation of advanced micro electronic packages," Microelectron. Reliab. **42**, 1735–1740 (2002).
[5] G.-M. Zhang, D. M. Harvey, and D. R. Braden, "High-resolution AMI technique for evaluation of microelectronic packages," Electron. Lett. **40**, no. 6, 399–400 (2004).
[6] G.-M. Zhang, D. M. Harvey, and D. R. Braden, "Acoustic time-frequency domain imaging for the evaluation of microelectronic packages," in Proc. IEEE 6th International Conference on Electronic Materials and Packaging, Penang, Malaysia, 2004, pp. 355–360.
[7] G.-M. Zhang, D. M. Harvey, and D. R. Braden, "Advanced acoustic micro imaging using sparse signal representation for the evaluation of microelectronic packages," IEEE Trans. Adv. Packag. (in press).
[8] M. Zibulevsky and B. A. Pearlmutter, "Blind source separation by sparse decomposition in a signal dictionary," Neural Comput. **13**, no. 4, 863–882 (2001).
[9] S. Chen, D. L. Donoho, and M. A. Saunders, "Atomic decomposition by basis pursuit," SIAM Rev. **43**, no. 1, 33–61 (2001).
[10] S. G. Mallat, and Z. Zhang, "Matching pursuit with time-frequency dictionaries," IEEE Trans. Signal Process. **41**, 3397–3415 (1993).
[11] R. R. Coifman and M. V. Wickerhauser, "Entropy-based algorithms for best-basis selection," IEEE Trans. Inf. Theory **38**, 713–718 (1992).
[12] M. S. Lewicki and T. J. Sejnowski, "Learning overcomplete representations," Neural Comput. **12**, 337–365 (2000).
[13] M. S. Lewicki and B. A. Olshausen, "Probabilistic framework for the adaptation and comparison of image codes," J. Opt. Soc. Am. A **16**, no. 7, 1587–1601 (1999).
[14] A. J. Bell and T. J. Sejnowski, "An information-maximization approach to blind separation and blind deconvolution," Neural Comput. **7**, 1129–1159 (1995).
[15] S. E. Ferrando, L. A. Kolasa, and N. Kovacevic, "A flexible implementation of matching pursuit for Gabor dictionaries," ACM Trans. Math. Softw. **28**, no. 3, 337–353 (2002).
[16] K. Kreutz-Delgado, J. F. Murray, B. D. Rao, K. Engan, T.-W Lee, and T. J. Sejnowski, "Dictionary learning algorithms for sparse representation," Neural Comput. **15**, 349–396 (2003).
[17] D. P. Wipf and B. D. Rao, "Sparse Bayesian learning for basis selection," IEEE Trans. Signal Process. **52**, no. 8, 2153–2164 (2004).

Patch near-field acoustical holography in cylindrical geometry

Moohyung Lee[a] and J. Stuart Bolton[b]
Ray W. Herrick Laboratories, School of Mechanical Engineering, Purdue University, 140 South Intramural Drive, West Lafayette, Indiana 47907-2031

(Received 12 February 2005; revised 5 August 2005; accepted 9 August 2005)

Spatial discrete Fourier transform-based near-field acoustical holography is known to suffer from windowing effects since the measurement aperture is necessarily finite. The latter effect can be mitigated by using patch holography, in which the measured field is extended beyond the measurement aperture based on successive smoothing operations. In this article, the application of a patch holography algorithm to cylindrical geometries is described. In planar geometry, initial zero-padding can be applied to the hologram pressure to an arbitrary degree in both in-plane directions since the pressure magnitude is expected to limit ultimately towards zero in both directions. In a cylindrical geometry, zero-padding can be implemented axially in the same way, but the number of zeros added in the circumferential direction is necessarily determined by the angular sample spacing owing to the periodic nature of the field in this direction. By using both numerical simulation and experimental results, it is shown that the patch extrapolation procedure works well in the cylindrical case, and a discussion of rigid reflecting boundaries is also included. Finally, reconstruction results obtained by the combined use of pressures measured in the finite aperture and two different regularization parameter selection techniques are compared, and the effect of projection distance is discussed. [DOI: 10.1121/1.2047267]

PACS number(s): 43.60.Sx, 43.60.Pt, 43.20.Ye [EGW] Pages: 3721–3732

I. INTRODUCTION

When performing near-field acoustical holography (NAH) measurements, the measurement aperture must extend to a region in which the sound level drops to a low level in order to avoid undue truncation of the sound field. However, it is sometimes impossible in practice to measure the sound pressure over a sufficiently large aperture, and, even when it is possible in principle, this requirement may present an obstacle to the use of NAH, especially when the source is very large. If it is not possible to measure the sound pressure over a sufficiently large aperture, reconstruction results can be degraded by the inevitable windowing, or truncation, of the pressure field. Of the two principal approaches to NAH (i.e., discrete Fourier transform (DFT)- and singular value decomposition (SVD)-based NAH), DFT-based NAH is more efficient in terms of computation time but is more significantly affected by the effects of a finite measurement aperture.[1]

In DFT-based NAH, the projection of acoustical properties (e.g., sound pressure or particle velocity) from one surface to another is performed by multiplying the wave number spectrum of the pressure measured on the hologram surface by an appropriate propagator. The first result of spatial windowing is a wrap-around error that is caused by the implied periodicity of the data in the spatial domain. The latter problem can be easily dealt with by zero-padding the measured data; however, in that case, if the pressure magnitude is not zero at the aperture boundary, the resulting discontinuity causes spurious reconstruction results. That is, the reconstruction results on the source surface are corrupted by a spatially oscillatory field that results from the convolution of the wave number spectrum of the complete sound field with the transform of the spatial window function. The effect of the latter kind of error is observed locally, especially beneath the edge of the measurement aperture.

Various approaches have been developed to mitigate the distorting effects of the finite measurement aperture. These methods allow NAH measurements to be made over a limited region of interest, thus saving measurement effort. Saijyou and Yoshikawa proposed a sound field extrapolation procedure to reduce the inherent windowing problem of DFT-based NAH.[2] Their procedure, here referred to as "patch" NAH, allows the pressure measured in a finite measurement aperture, possibly smaller than the source, to be extended, or "continued," into the region exterior to the measurement patch by an iterative smoothing process, thus alleviating the pressure discontinuity at the edge of the measurement aperture. This method has also been applied to SVD-based NAH[3,4] and has been extended by the addition of regularization procedures.[3–6]

In the Helmholtz equation least-squares (HELS) procedure proposed by Wang and Wu,[7] the sound field is expressed in terms of an orthonormal expansion of spheroidal functions that satisfy the Helmholtz equation, and the Helmholtz equation is solved directly in a least-squares sense. This method works well compared with patch NAH, particularly in the low-frequency region,[8] and was further developed into the combined HELS (CHELS) method that combined the advantages of the HELS and SVD-based NAH.[9]

In statistically optimized NAH (SONAH), a plane-to-plane propagation in the spatial domain is performed by

[a]Author to whom correspondence should be addressed. Electronic mail: leemoohy@ecn.purdue.edu
[b]Electronic mail: bolton@purdue.edu

evaluating a two-dimensional convolution with a propagation kernel. Since no Fourier transforms are involved in this procedure, the effects of sound field truncation are avoided. SONAH was first described for a planar geometry by Steiner and Hald,[10,11] and its formulation was recently extended to cylindrical geometries.[12]

In the so-called method of superposition, the sound field is approximated as the superposition of fields produced by a number of simple sources.[13,14] The latter method can be used either to enlarge a finite measurement aperture (extrapolation) or to fill in gaps within the measurement aperture (interpolation).

Finally, in a wavelet-based method, the sound field is decomposed by using multiresolution analysis (MRA),[15] and spatial filtering is then performed in a selective way before the wave number spectrum is calculated.[16]

In the present study, patch NAH was applied to DFT-based NAH in a cylindrical geometry. In Sec. II, an iterative data extrapolation algorithm and its implementation in cylindrical coordinates will be described. In Sec. III, numerical simulation results obtained by using a two-dipole model with a rigid reflecting boundary will be presented to validate the applicability of a patch NAH to the cylindrical case. The effect of the finite measurement aperture in conjunction with various regularization parameter selection techniques on the reconstruction results, the treatment of a rigid boundary, and the effect of projection distance will also be discussed. In Sec. IV, experimental results related to a refrigeration compressor will be presented. Conclusions will be presented in the final section.

II. THE ITERATIVE PATCH EXTENSION ALGORITHM

Patch holography is in essence an extrapolation procedure that extends the sound field measured over a finite measurement aperture, possibly smaller than the source region, into the region exterior and tangential to the measurement patch. The extension of the sound field is achieved by a successive smoothing procedure that suppresses the high wave number components introduced by the sharp transition of the sound field at the aperture edge.

The flow chart of the complete extrapolation process is presented in Fig. 1. The extrapolation algorithm in cylindrical geometry is basically the same as that in planar geometry[2,5] except for the way in which the zero-padding is implemented in the first step. There, Ω_m and Ω_0 represent the measurement aperture and the exterior region created by an initial zero-padding on the hologram surface, respectively, Γ_m and Γ_0 represent the projected regions below Ω_m and Ω_0 on the source surface, respectively, and $\vec{r}$ is the position vector defining a point on the hologram surface, as shown in Fig. 2(a). In addition, $\hat{\mathbf{p}}^{(j)}$ represents the input pressure distribution at the jth iteration while $\hat{\mathbf{p}}^{\alpha(j)}$ represents the smoothed pressure resulting from the jth iteration, and $\bar{\mathbf{U}}^{\mathrm{H}}$ and $\bar{\mathbf{U}}$ represent the forward and inverse two-dimensional spatial discrete Fourier transform (DFT) operators, respectively. Note that terms denoted with a ^ represent spatially coherent sound fields. That is, when NAH measurements are

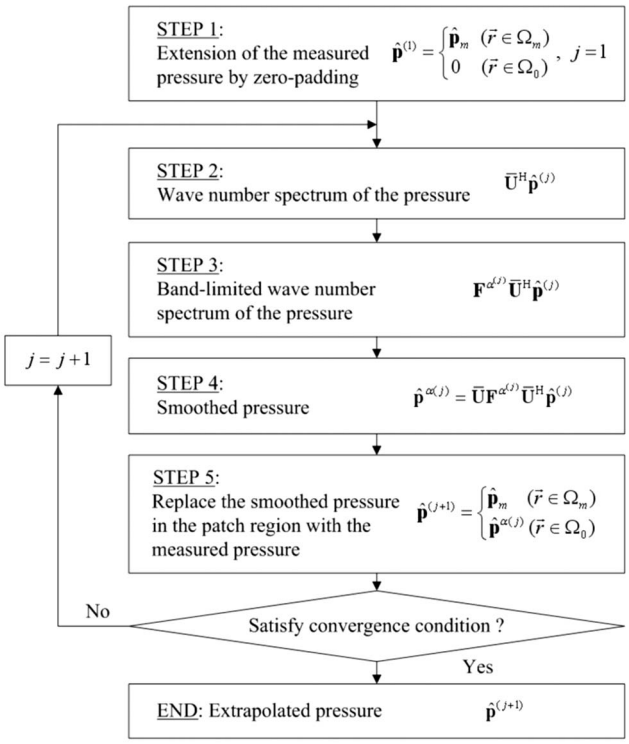

FIG. 1. Extrapolation algorithm.

performed based on a multireference, cross-spectral approach, $\hat{\mathbf{p}}^{(j)}$ represents each of the decomposed partial fields.[17]

In the first step, the initial pressure, $\hat{\mathbf{p}}^{(1)}$, comprises the measured pressure, $\hat{\mathbf{p}}_m$, in Ω_m, and zeros in Ω_0, as in the planar case, but the way in which the zero-padding is applied

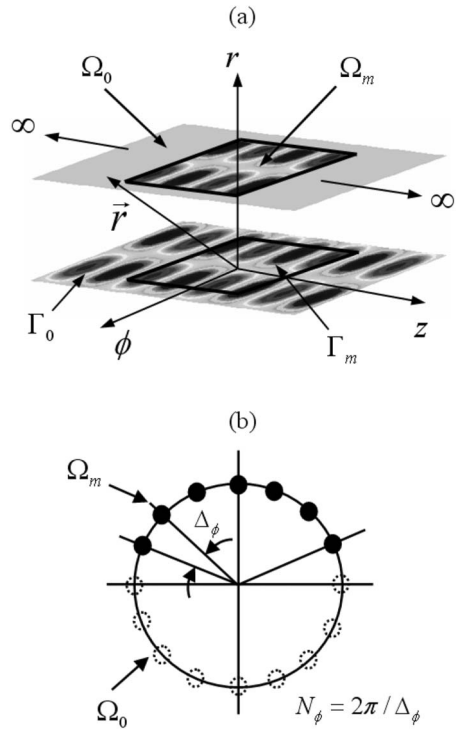

FIG. 2. Extension of the measurement aperture by zero-padding in the cylindrical case: (a) unwrapped view and (b) circumferential section.

distinguishes patch NAH in cylindrical geometry from that in planar geometry. The transformation of the sound field in the spatial domain into the wave number domain is implemented by taking the DFT of the spatial pressure distribution. Due to the implicit periodicity of the DFT representation of finite-length, discrete data sequences, an artificial field, i.e., a replica of the sound field measured in the finite region, is assumed to appear periodically in the region outside the measurement aperture. It is the latter characteristic of the DFT that leads to unwanted results. That error, referred to as a wrap-around error, can be avoided by applying a sufficient amount of zero-padding to the finite-length data. Thus, in the extrapolation process, zero-padding plays a role in giving initial values to the data to be recovered while also suppressing the wrap-around error. In the case of planar geometry, the sound fields in the two tangential directions to the measurement aperture decay gradually to zero in the direction away from the source region without exhibiting spatial periodicity. Therefore, the degree of zero-padding can be chosen arbitrarily in the two tangential directions so long as wrap-around error can be avoided. In contrast, in cylindrical geometry, the sound field in the circumferential direction is periodic in nature. That is, a periodically repeating data sequence with period N_ϕ (where N_ϕ is the number of data points in the whole circumference) is observed as the circumference of the cylinder is traversed repeatedly. Due to the latter periodicity, the data sequence in the circumferential direction is represented by a Fourier series corresponding to a sum of complex exponentials with frequencies that are integer multiples of the fundamental frequency, $2\pi/N_\phi$. Thus, the number of zeros to be added in the circumferential direction should be determined so that the total number of data after zero-padding is equal to N_ϕ associated with the angular sampling interval, Δ_ϕ (i.e., $N_\phi=2\pi/\Delta_\phi$). Zero-padding can still be applied arbitrarily in the axial direction since the sound field in this direction is aperiodic. Note that, in the case of SVD-based NAH, the number of zeros added is not necessarily determined by the angular sampling interval since measurement positions do not need to be equally spaced. Nevertheless, that number is also finite in effect since the use of a large number of zeros would cause the zeros in the region outside the measurement aperture to be located close to each other, which is computationally redundant.

The pressure discontinuity at the edge of the measurement aperture resulting from the zero-padding is first smoothed by low-pass filtering the high wave number components introduced by that discontinuity. In step 3, $\mathbf{F}^{\alpha^{(j)}}$ is a low-pass filter in the wave number domain obtained by implementing a regularization procedure. In this study, the modified Tikhonov regularization method was used to construct $\mathbf{F}^{\alpha^{(j)}}$, i.e.,[18]

$$\mathbf{F}^{\alpha^{(j)}} = \mathrm{diag}\left(\cdots |\lambda_i|^2 \Big/ \left(|\lambda_i|^2 + \alpha^{(j)}\left(\frac{\alpha^{(j)}}{\alpha^{(j)} + |\lambda_i|^2}\right)^2\right)\cdots\right), \quad 1 \leqslant i \leqslant M, \tag{1}$$

where $\alpha^{(j)}$ is the regularization parameter that is applied at the jth iteration, the λ_i's are the eigenvalues of the transfer matrix that relates the pressure on the hologram surface and the surface normal velocity on the source surface (its inverse is defined as the velocity propagator), and M is the total number of points after zero-padding. The value of the regularization parameter at each iteration was determined based on the use of the Mozorov discrepancy principle (MDP).[18,19] A more detailed description of this process in cylindrical geometry can be found in Ref. 20.

The smoothed pressure, $\hat{\mathbf{p}}^{\alpha(j)}$, is then obtained by evaluating the inverse DFT of the band-limited wave number spectrum (step 4), and the input pressure for the next iteration, $\hat{\mathbf{p}}^{(j+1)}$, is created by replacing the smoothed pressure, $\hat{\mathbf{p}}^{\alpha(j)}$, in the measurement aperture by the pressure originally measured over the aperture (step 5). This procedure is then repeated until the following convergence condition is satisfied, i.e.,[3,5]

$$\|\hat{\mathbf{p}}^{\alpha(j)} - \hat{\mathbf{p}}^{\alpha(j-1)}\|_2 < \varepsilon\sigma^{(j)}\sqrt{M}, \quad \text{when } j \geqslant 2, \tag{2}$$

where $\|\ \|_2$ represents the vector L2-norm, $\sigma^{(j)}$ is the standard deviation of the noise included in $\hat{\mathbf{p}}^{(j)}$, and ε is an *ad hoc* factor having a "small" value. As yet, there are no clear guidelines for determining the value of ε since, in any particular case, its value depends on a combination of factors, e.g., the level of measurement noise, the distance between the hologram and the reconstruction surfaces, the patch size, and so on.

In this way, the truncated pressure can be extended smoothly into the region outside the measurement aperture while the pressure in the measurement aperture is maintained at its original value, and the resulting, extended sound field can be used for holographic projection.

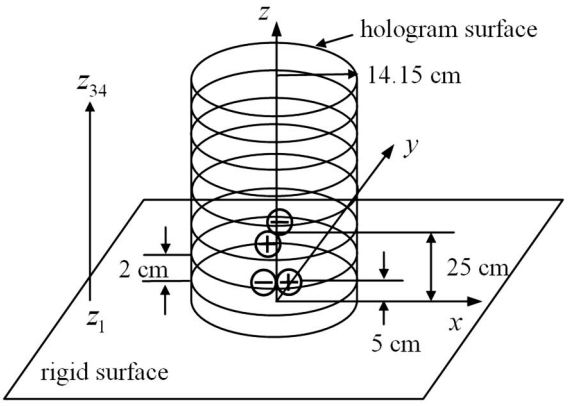

FIG. 3. Numerical simulation model (two orthogonally oriented coherent dipoles are located 5 and 25 cm above a rigid boundary).

III. NUMERICAL SIMULATION

The procedure described above was first verified by performing numerical simulations. The sound field was created by two orthogonally oriented coherent dipoles that were located 5 and 25 cm above an infinitely extended, rigid surface, operating at a frequency of 1 kHz (see Fig. 3). The sound pressure on the cylindrical hologram surface with a radius of 14.15 cm was sampled at 34-by-32 points in the axial and circumferential directions, respectively. Adjacent sampling grids were separated by 2 cm in the axial direction,

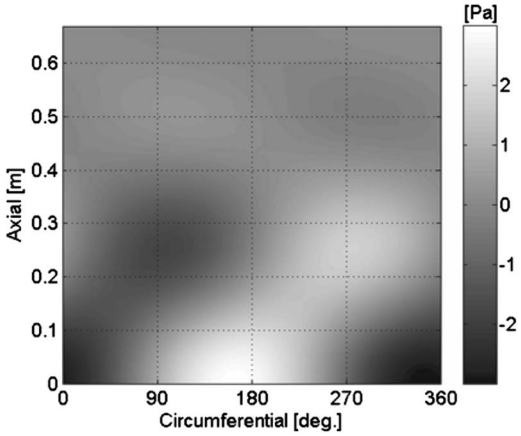

FIG. 4. Spatial distribution of the pressure radiated by two dipoles on the hologram surface ($r=14.15$ cm) at 1 kHz (20 dB SNR). Real part is plotted.

and the first axial sampling position (i.e., z_1) was located half the axial spacing (i.e., 1 cm) above the rigid surface because of the presence of the rigid boundary. In this model, spatially random noise with a signal-to-noise ratio of 20 dB was added to the pressure on the hologram surface.

The "measured" pressure on the cylindrical surface with the additive noise described above is shown in Fig. 4, and from it the following four patches were selected (see Fig. 5): patch 1 consisted of 11-by-32 points, and included the whole circumference and extended axially from the first to the 11th measurement position; patch 2 was 17-by-11 points, and patch 3 was 11-by-16 points, and, in contrast with patch 1, neither of the latter two patches extended over the full circumference. Patch 4 was the same as patch 1, but extended to the 17th axial measurement position.

The sound field in the presence of a rigid boundary can be modeled as an equivalent field that is extended symmetrically about the rigid surface including the mirror image of the sound field above the rigid surface. When implemented in patch NAH, the existence of a rigid boundary can be dealt with in two ways. The first way is simply to apply zero-

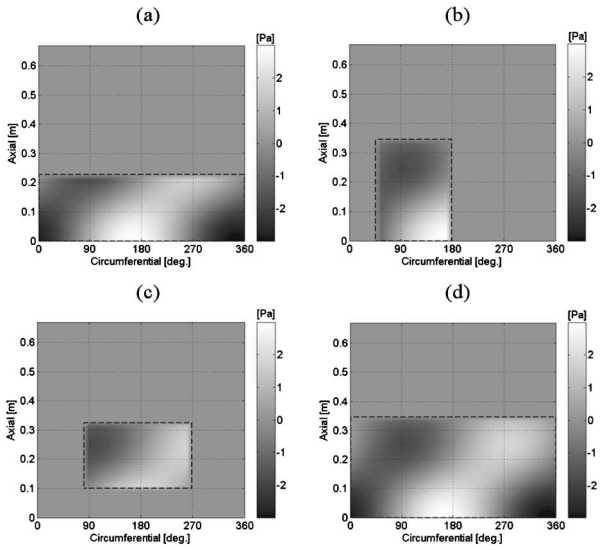

FIG. 5. Patch selection (real parts are plotted): (a) patch 1, (b) patch 2, (c) patch 3, and (d) patch 4.

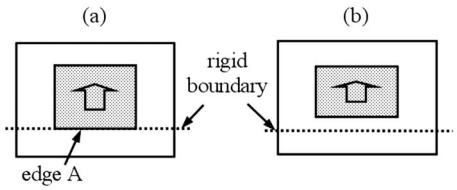

FIG. 6. Implementation of zero-padding in the presence of a rigid boundary (the first case): (a) when the measurement aperture extends from a rigid boundary and (b) when the measurement aperture is located above a rigid boundary.

padding to the pressure in the measurement aperture as shown in Fig. 6. The second way is to use a patch that is doubled in size by including the mirrored pressure as shown in Fig. 7. The three cases shown in Figs. 6(a), 6(b), and 7(a) are the same as the case in the absence of a rigid boundary (i.e., zeros around the truncated pressure). In contrast, in the case shown in Fig. 7(b) (i.e., when the measurement aperture does not extend from the first axial measurement position), the patch consists of two discrete subpatches. So long as the projection distance is small, either of the two procedures described above can be used to construct the initial input pressure since the influence of an image source on the sound field above a rigid boundary is expected to be small in that case. However, the use of the pressure doubled by mirroring is generally advantageous. For example, when comparing the cases shown in Figs. 6(a) and 7(a), the latter approach results in better reconstruction results near the edge A since that region is then located at the center of the doubled patch. When comparing the cases shown in Figs. 6(b) and 7(b), the advantage just mentioned is not observed, but the use of the doubled pressure is still advantageous as the projection distance becomes larger. Note that, when the presence of a rigid boundary is accounted for by using either of the approaches just described, the ergenvalues in Eq. (1) are obtained in the same way as in the absence of a rigid boundary.

When the numerical simulations discussed in this section were performed, the input pressure was created by including the mirror image. In effect, the sizes of the four patches became 22-by-32, 34-by-11, 22-by-16, and 34-by-32 points, respectively. In particular, patch 3 consisted of two discrete 11-by-16 subpatches after mirroring. The number of points after zero-padding was always made to be 32 in the circumferential direction and 128 in the axial direction. Note that 32 circumferential points were chosen since two adjacent points were separated by 11.25° (i.e., 360/32) in that

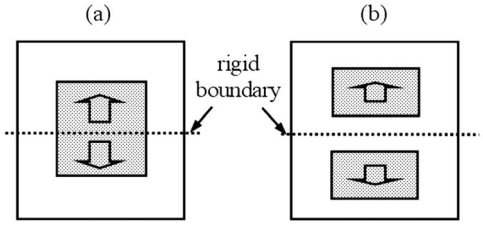

FIG. 7. Implementation of zero-padding in the presence of a rigid boundary (the second case): (a) when the measurement aperture extends from a rigid boundary and (b) when the measurement aperture is located above a rigid boundary.

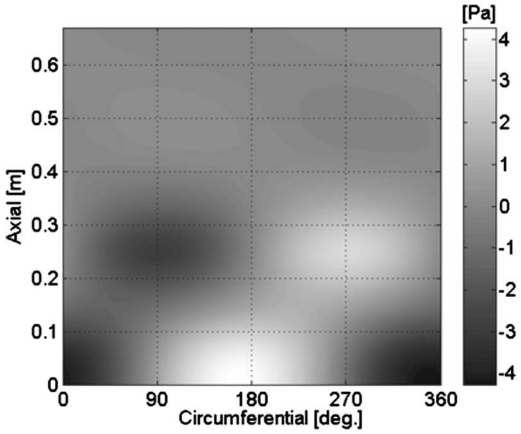

FIG. 8. Exact pressure on the surface at a radius of 9 cm. Real part is plotted.

case. In all figures presented here, results only in one-half of the computational domain (i.e., the sound fields above the rigid surface) are shown.

As will be shown below, the extrapolated pressure obtained by using two discrete subpatches showed good agreement with the actual pressure. The latter observation suggests the possibility of multi-patch measurements. That is, if the sound fields over several parts of a source are of interest, measurements can be performed over several patch regions, and the extended pressure can then be obtained by a single run of the extrapolation process. This subject, however, is beyond the scope of the present article.

A. Effect of the finite measurement aperture discussed in conjunction with regularization parameter selection techniques

In this subsection, the effect of the finite measurement aperture is demonstrated along with a comparison between

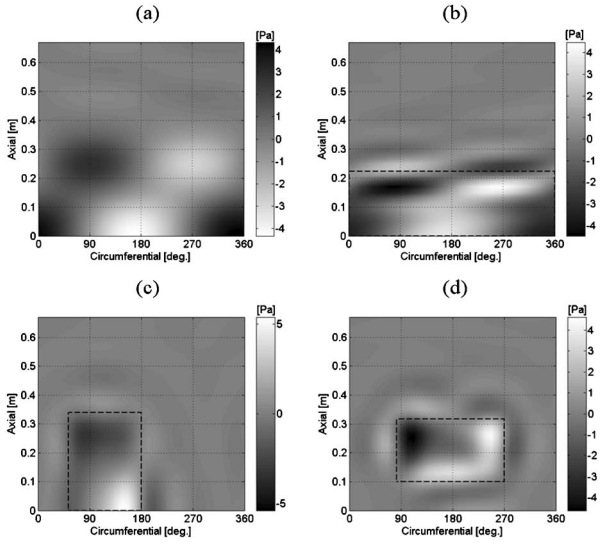

FIG. 9. Reconstructed pressures at a radius of 9 cm when the MDP was used (real parts are plotted): (a) obtained by using the pressure measured over the complete aperture, (b) obtained by using the pressure measured over patch 1, (c) obtained by using the pressure measured over patch 2, and (d) obtained by using the pressure measured over patch 3.

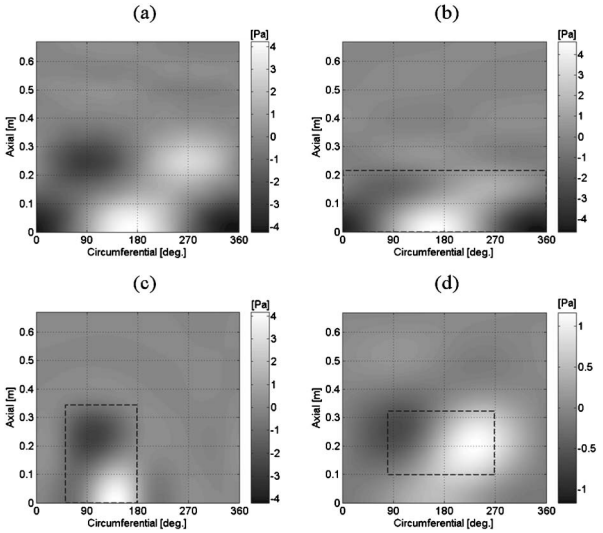

FIG. 10. Reconstructed pressures at a radius of 9 cm when the L-curve criterion was used (real parts are plotted): (a) obtained by using the pressure measured over the complete aperture, (b) obtained by using the pressure measured over patch 1, (c) obtained by using the pressure measured over patch 2, and (d) obtained by using the pressure measured over patch 3.

the results obtained by using two different regularization parameter selection techniques. The exact pressure at a radius of 9 cm (see Fig. 8) was compared to the pressures reconstructed by using the hologram pressures measured over the first three patches (see Figs. 9 and 10). When the pressures shown in Figs. 9 and 10 were calculated, the Mozorov discrepancy principle and the L-curve criterion[19,21] were used, respectively, to determine the value of the regularization parameter appearing in Eq. (1), and the pressures were tapered in the axial direction near the patch edges by using an eight-point Tukey window before holographic projection in order to mitigate the effect of a sharp pressure transition; such a taper represents normal NAH practice.

When the hologram pressure measured over the complete aperture (i.e., 34-by-32 points) was used, the results obtained by using either of the regularization parameter selection techniques showed good agreement with the exact pressure [compare Figs. 9(a) and 10(a) with Fig. 8]. In these cases, the errors defined as

$$\text{error}(\%) = \frac{\|\hat{\mathbf{p}}_{(\text{reconstructed})} - \hat{\mathbf{p}}_{(\text{exact})}\|_2}{\|\hat{\mathbf{p}}_{(\text{exact})}\|_2} \times 100 \tag{3}$$

were 6.4% when the MDP was used and 7.3% when the L-curve criterion was used (see Fig. 11).

When the pressures measured over the various patch regions were used, the reconstructed results were degraded significantly (see the results in Figs. 9 and 10, and the errors plotted in Fig. 11). Note that the errors in Fig. 11 were evaluated by using only the pressures in the region directly under the measurement patches (i.e., Γ_m). Of the two regularization parameter selection techniques used here, the L-curve criterion yielded smaller errors than did the MDP (compare the errors in Fig. 11), so at first glance it appeared that the L-curve criterion performed better than did the MDP. However, the error defined above is not necessarily suitable for judging this point, as will be shown next.

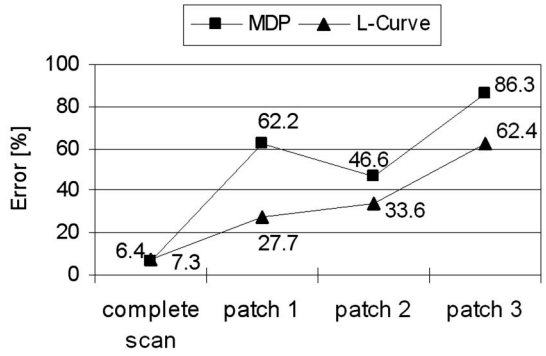

FIG. 11. Reconstruction errors with respect to the various patches (the error was evaluated by using pressures in the region directly under the corresponding patch regions).

When the measurement patch is smaller than the entire sound field, the convolution of the window function with the infinite-aperture wave number spectrum causes energy to be spread, thus creating "systematic" high wave number components. In the latter case, regularization parameter selection techniques may fail to provide the optimal value of $\alpha^{(j)}$. For example, the MDP is based on the assumption that the noise has zero mean and a standard deviation of σ;[19] as a result, this method is likely to undersmooth the pressure. In contrast, the L-curve criterion determines the optimal value of the regularization parameter by finding the best compromise between the residual and smoothing norms without any assumption as to the nature of the noise.[19] In the case of a patch measurement, the shape of the L-curve may not exhibit a clear "L-shaped" characteristic, thus making its "corner" difficult to identify, and the regularization parameter given by this method is likely to oversmooth the pressure.

The latter can be observed clearly in Fig. 12, in which the reconstructed pressures obtained by using the complete aperture and patch 1 at the section defined by $\phi=90°$ as a function of z are shown. At this circumferential position, a peak is located near the edge of patch 1. It can be observed that the pressure reconstructed when using the MDP was corrupted by an oscillatory field having a large amplitude near the aperture edge as a result of the relatively weak filtering of the high wave number components. In contrast, the results reconstructed when using the L-curve criterion had relatively smooth shapes and smaller amplitudes than the exact one as a result of the relatively heavy filtering of the high wave number components [see Fig. 12(b)]. In addition, the oversmoothing resulted in the failure to locate the peak position correctly, i.e., the peak located near the aperture edge was shifted towards the inner patch region.

However, when a peak was located in the central region of the measurement aperture, the reconstruction of a peak was accurate in terms of position (see Fig. 13, which compares the results at a section defined by $\phi=180°$ as a function of z. Recall that the initial input pressure was created by including a mirror image, so only half of the effective patch region is shown in Figs. 12–14). In Fig. 13(b), in particular, the results were still in error near the aperture edge, but the peak was reconstructed with reasonable accuracy irrespective of the regularization parameter selection techniques used.

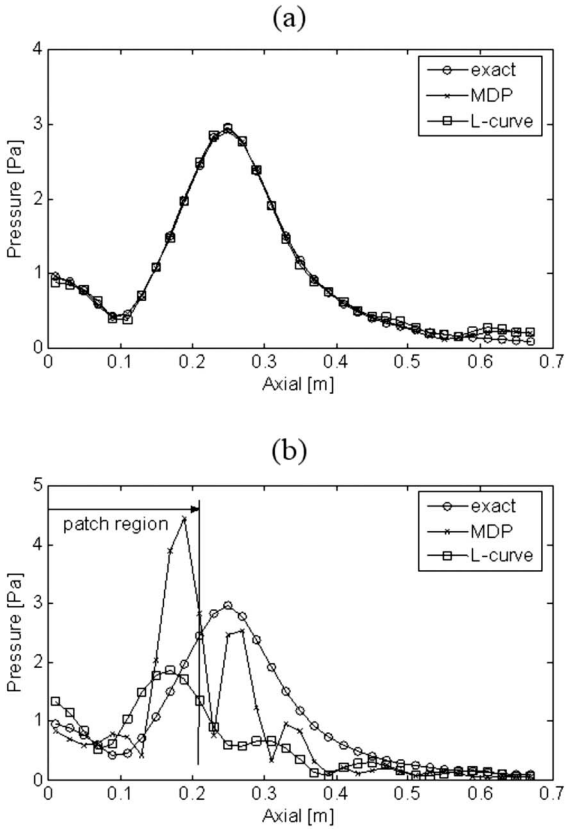

FIG. 12. Comparisons of the reconstructed pressures at a radius of 9 cm and at a section defined by $\phi=90°$ as a function of z: (a) when the complete aperture was used and (b) when patch 1 was used.

Thus, it can be concluded that the effect of the finite measurement aperture corrupts the reconstruction results particularly near the aperture edge.

The results shown in Fig. 14 confirm the latter observation. In that figure, the horizontal axis represents the number of axial measurement positions used (i.e., the region was expanded from the first measurement position) when the error was evaluated. When the complete aperture was used [see Fig. 14(a)], use of either the MDP or the L-curve criterion yielded good results in the region between the first and the 25th measurement positions (the errors were about 2%), and the errors then increased near the aperture edge. Although the 34-by-32 measurement region was termed the "complete" aperture, there still existed a transition to zero before spatial windowing was applied, even though the transition was small. The latter caused the error to increase, but the errors still remained reasonably small since the truncation of the pressure was not very significant. In contrast, in the case of patch 1, the errors increased rapidly near the aperture edge (i.e., the 11th axial measurement position) and converged to a nearly constant value. Thus, it could be concluded that the errors were concentrated mainly near the aperture edge region.

When the complete aperture was used, the error resulting when the MDP was used was smaller than that when the L-curve criterion was used [see Fig. 14(a)]. The latter possibly resulted from the fact that, in ideal cases (e.g., when the nature of noise is similar to the assumption described ear-

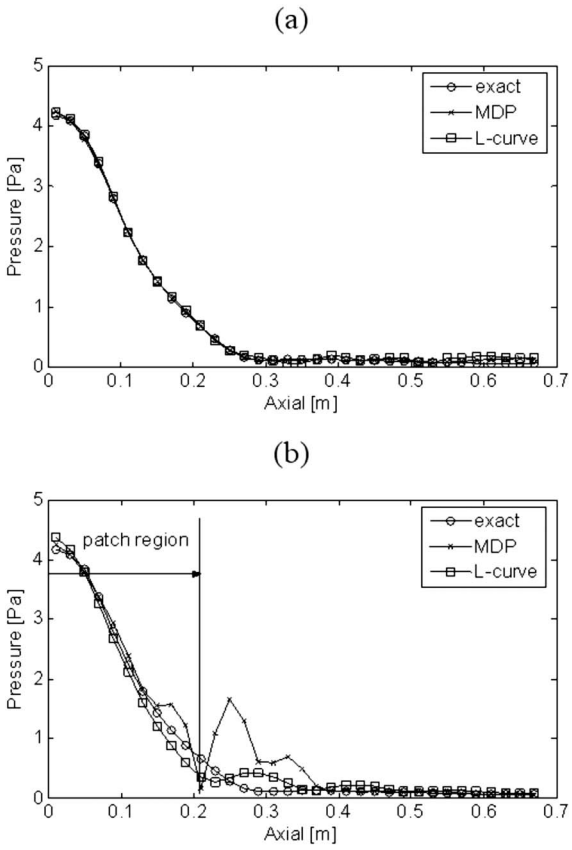

FIG. 13. Comparisons of the reconstructed pressures at a radius of 9 cm and at a section defined by $\phi=180°$ as a function of z: (a) when the complete aperture was used and (b) when patch 1 was used.

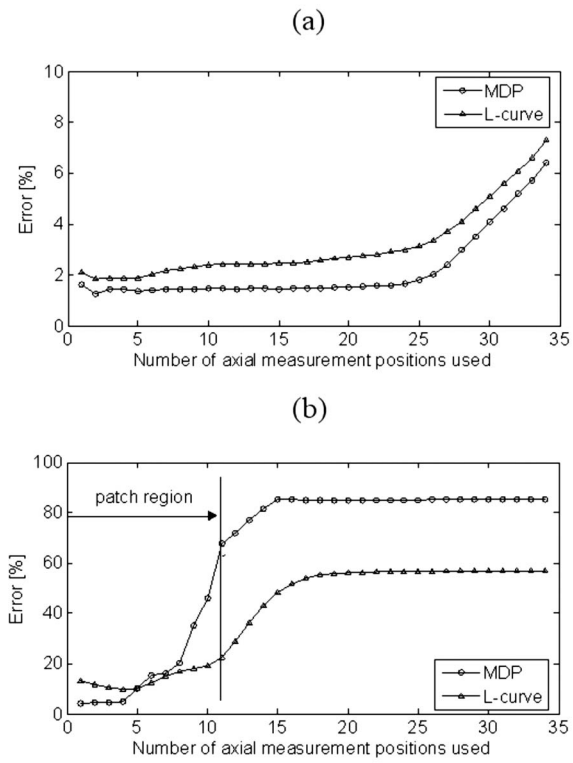

FIG. 14. Comparisons of the reconstruction error when the MDP and the L-curve criterion were used: (a) when the complete aperture was used and (b) when patch 1 was used.

lier), the regularization parameter provided by the MDP lies on the L-curve slightly to the right of the corner (i.e., in the more heavily filtered direction).[19] Recall, however, that, when patch pressures were used, the regularization parameters provided by the MDP lay to the left of the L-curve's corner. When patch 1 was used, it can be seen that the error in the region between the first and fifth axial measurement positions when using the MDP was smaller than that when using the L-curve criterion although the MDP resulted in larger errors than the L-curve criterion when the whole patch region was used for evaluating that error [see Fig. 14(b)]. Thus, from this point of view, it can be said that the MDP is a better choice than the L-curve criterion although the region where accurate reconstruction is ensured is limited to the central region of the measurement patch. However, the optimal value of the regularization parameter provided by the various techniques depends on the nature of the additive noise so that the best choice of techniques may differ from case to case.

In summary, when the measurement aperture size is limited, backward-projection results are significantly corrupted by the windowing effect, but the latter effect is concentrated near the aperture edge region.[3] Thus, the pressure measured in a finite aperture can still be used to perform a backward-projection so long as the region of interest in the reconstructed results is limited to the central region of the patch. However, as the distance between the hologram and reconstruction surfaces becomes large, the results over most of the patch region are likely to be corrupted. The latter problem can be addressed by using patch NAH as implemented in this work, thus increasing the size of the region where good results are ensured.

B. Extension of pressure

The extended hologram pressures corresponding to various numbers of iterations are presented in Figs. 15–17. It

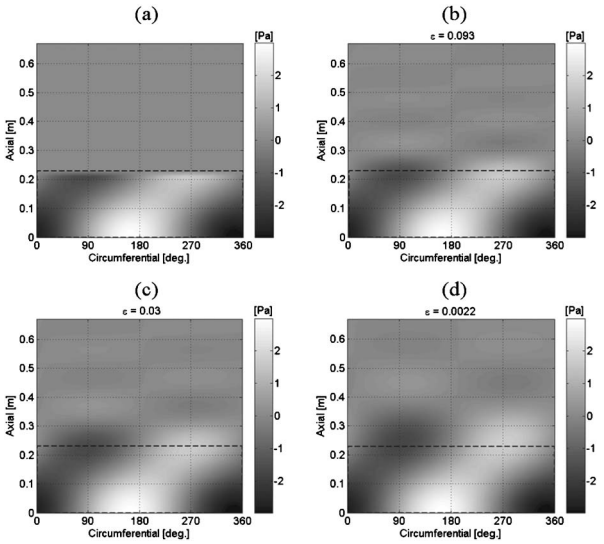

FIG. 15. Patch 1 extended pressure on the hologram surface with respect to the number of iterations (real parts are plotted): (a) without extrapolation, (b) 100 iterations, (c) 800 iterations, and (d) 8000 iterations.

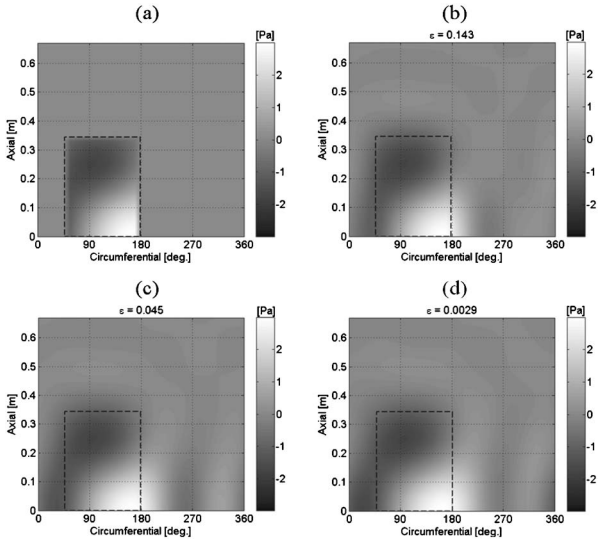

FIG. 16. Patch 2 extended pressure on the hologram surface with respect to the number of iterations (real parts are plotted): (a) without extrapolation, (b) 100 iterations, (c) 300 iterations, and (d) 8000 iterations.

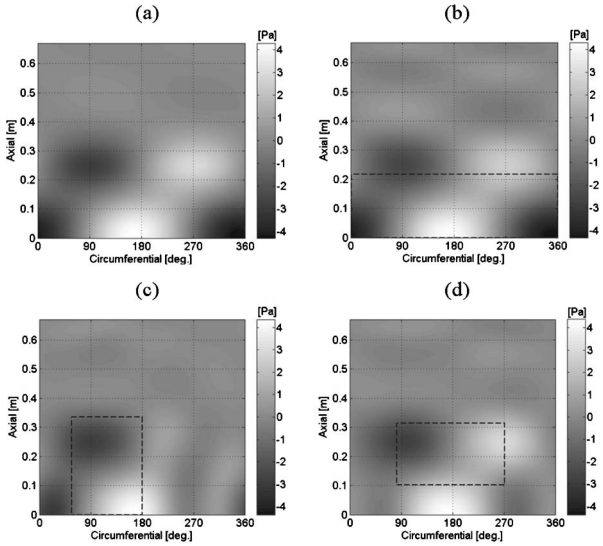

FIG. 18. Reconstructed pressures at a radius of 9 cm (real parts are plotted): (a) exact, (b) obtained by using the patch 1 extended pressure after 8000 iterations, (c) obtained by using the patch 2 extended pressure after 8000 iterations, and (d) obtained by using the patch 3 extended pressure after 3000 iterations.

was observed that the extended pressures near the patch regions approached the actual pressure in all cases as the number of iterations increased (compare with Fig. 4). However, the region into which the pressure could be extended accurately was limited.[5] The latter was evident, in particular, in the patch 2 and 3 cases (i.e., when the size of the patch was small compared to the entire sound field).

In Fig. 18, the pressures reconstructed at a radius of 9 cm by using the extended hologram pressures are shown. When reconstructing the pressures, the MDP was used to determine the value of the regularization parameter. In all cases, the results on the surface directly under the patches (i.e., Γ_m) showed good agreement with the actual pressure at that location. The errors corresponding to the various numbers of iterations are presented in Fig. 19. Errors were calculated over three regions: error_1 was calculated in a region

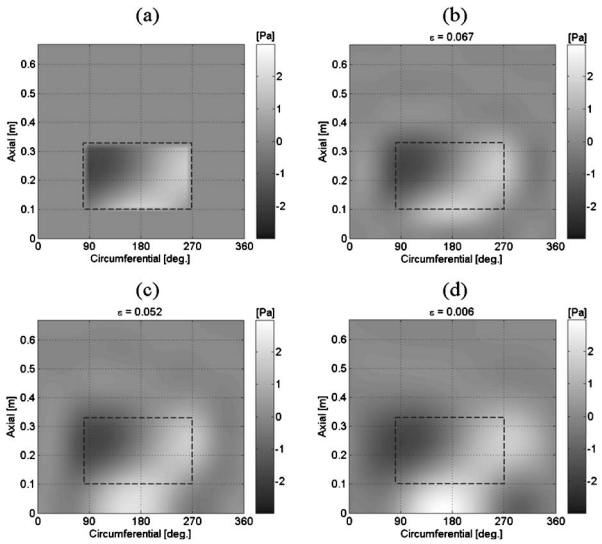

FIG. 17. Patch 3 extended pressure on the hologram surface with respect to the number of iterations (real parts are plotted): (a) without extrapolation, (b) 100 iterations, (c) 800 iterations, and (d) 8000 iterations.

larger than the measurement aperture by five measurement positions, error_2 was calculated only over the patch region, and error_3 was evaluated for a region smaller than the measurement aperture by two measurement positions. It can be seen that the patch 1 and 2 errors decreased monotonically as the number of iterations increased. In the case of patch 1, error_2 was ultimately reduced to 4.2% and, in the case of patch 2, to 3.6% after 10 000 iterations. Beyond a certain number of iterations, the rate of error decrease slowed and only a very slight degree of continuing improvement was observed. After 3000 and 1000 iterations based on patches 1 and 2, respectively, the value of error_2 for each case was smaller than 5%. In the case of patch 3, error_2 decreased to 2.6% after 3000 iterations but then began to increase slightly [see Fig. 19(c)]. The increase in error is caused by the effects of noise and the poorly determined cut-off of the band-limiting, low-pass filter. The latter problem can be addressed by an early termination of the interation procedure. In Fig. 19, the *ad hoc* convergence factor, ε, corresponding to the number of iterations is shown. In this simulation, good results were obtained by setting ε to be in the range 0.005 to 0.01.

Consider now the accuracy of the extrapolation. It can be seen that error_1 (which was evaluated over a region extending beyond the original patch) for patch 1 decreased to a low value. Thus, in this case, it was possible for the pressure outside the patch to be reconstructed to a reasonable degree of accuracy, but that is not always guaranteed (see error_1 for patches 2 and 3). The value of error_3, which was calculated including regions only inside the patch, was smaller than that of error_2 in all cases. From the latter result, it can again be concluded that the reconstruction error still arises near the edge of the patch region. However, compared with the results calculated by simply using truncated pressures without extrapolation, a significant improvement can be observed, e.g., the errors evaluated over the patch region reduced from

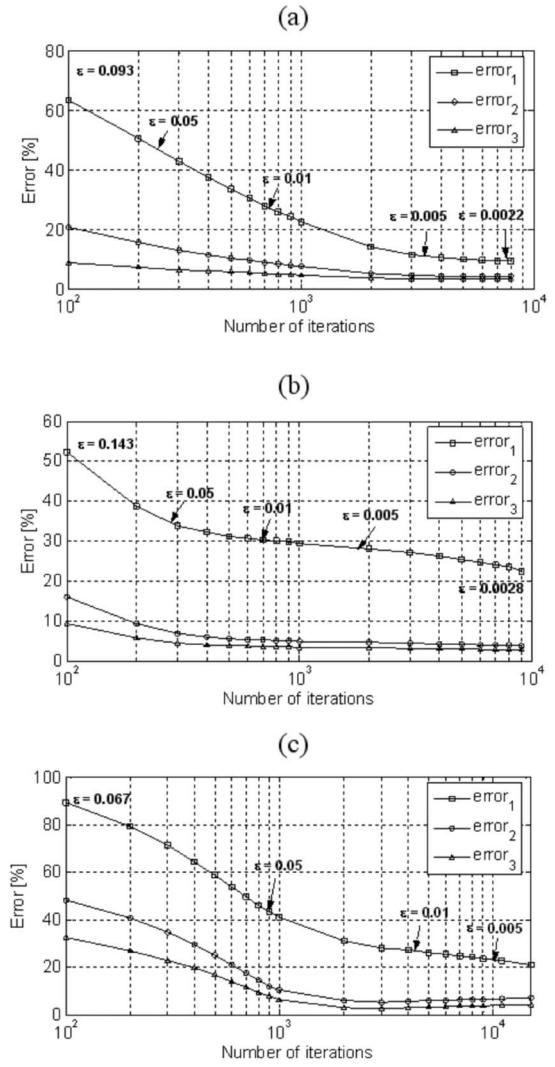

FIG. 19. Reconstruction errors with respect to the number of iterations (simulation): (a) patch 1, (b) patch 2, and (c) patch 3.

62.2%, 46.6%, and 86.3% to below 10% in all three cases. Even the errors evaluated over a region larger than the patch region were smaller than the errors shown above (compare Fig. 19 with Fig. 11). It can thus be claimed that the extrapolation procedure described here helps reduce the effect of pressure windowing, and, in practical measurements, it is recommended that the size of the measurement aperture should be made larger (but not significantly) than the region of interest whenever possible.

C. Effect of projection distance

In Fig. 20, errors calculated over the patch region (i.e., error_2) are plotted with respect to the distance between the hologram and reconstruction surfaces. Negative and positive distances represent backward- and forward-projections, respectively, and the MDP was used to determine the value of the regularization parameter. Comparisons were made for four cases: patch 1 pressure, patch 1 extended pressure (after 10 000 iterations), patch 4 pressure, and patch 4 extended pressure (after 2000 iterations).

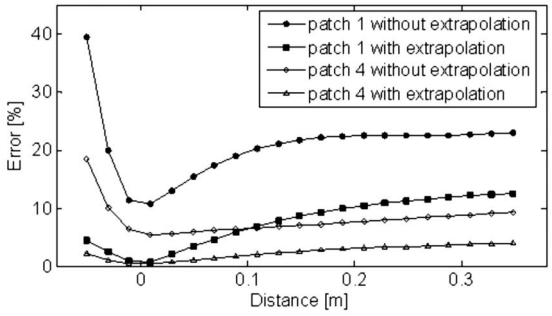

FIG. 20. Comparison of the reconstruction errors with respect to the distance between the hologram and reconstruction surfaces.

In all cases, the errors increased as the projection distance increased. The benefit of patch extension was apparent when backward-projection was performed. When the patch pressures were used, it can be seen that errors increased more rapidly as the distance increased than when the extended pressures were used. In the forward-projection region, the errors in all cases increased as well, but the rate of increase was much slower than in the backward-projection region when the patch pressures were used. In the backward-projection region, error results mainly from the amplification of the high wave number components near the edge area. In contrast, forward-projection rarely suffers from the latter effect; instead, the results are degraded by the contributions of sources located outside the patch region. When comparing results obtained by using patches 1 and 4, errors calculated for patch 4 were smaller than those for patch 1 with or without application of the extrapolation procedure. Compared with patch 1, the peak of the sound field radiated by the dipole located at $z=25$ cm was sensed in patch 4, thus resulting in a smaller error in the forward-projection region. A comparison of results obtained by using the pressures with and without the extrapolation procedure shows that the extrapolation procedure can improve the forward-projection results as well as the backward-projection results. The latter is to be expected since the extrapolation procedure can recover the pressure outside the patch region to some extent, thus including more subsources. Thus, it can be concluded that patch NAH can also be beneficial when farfield prediction is attempted.

However, the requirements are stricter in the farfield projection case than in the backward-projection case, i.e., the sound field (preferably the peaks) radiated from all subsources should be sensed in the patch region for the pressure to be reconstructed accurately in a complete region since the patch NAH procedure does not guarantee that the region in which recovery is possible extends to a sufficiently large region beyond the patch, and since the latter procedure requires at least a part of the sound field radiated by a source to be captured in order to recover the missing part. In the case of backward-projection, the patch size is not restricted by the latter condition, in principle, but depends on the region of interest since the backward-projection distance is usually small in practical NAH. In Figs. 21 and 22, the sound fields reconstructed by using the various pressures are compared with the exact pressure on the planes defined by $\phi=0°$ and

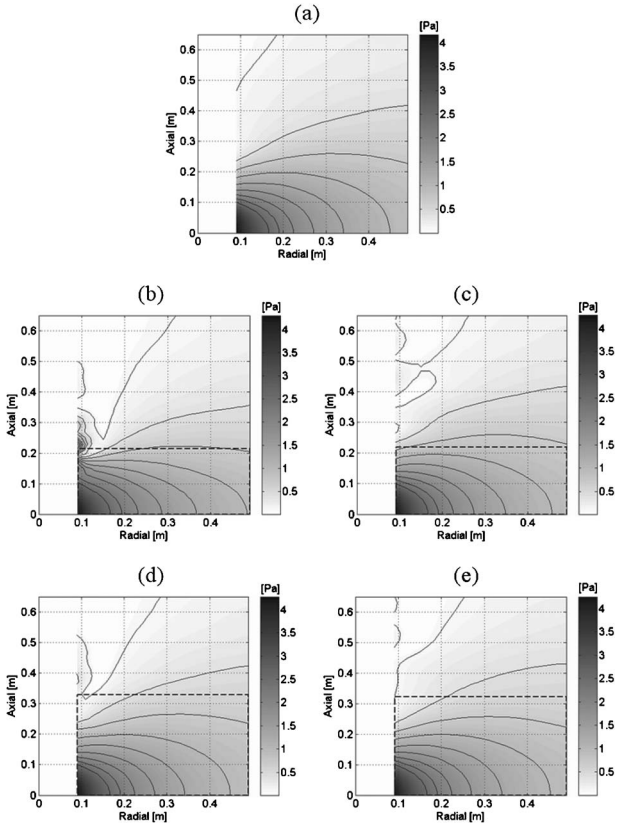

FIG. 21. Reconstructed pressures on the plane defined by $\phi=0°$: (a) exact, (b) obtained by using the patch 1 pressure, (c) obtained by using the patch 1 extended pressure after 8000 iterations, (d) obtained by using the patch 4 pressure, and (e) obtained by using the patch 4 extended pressure after 2000 iterations.

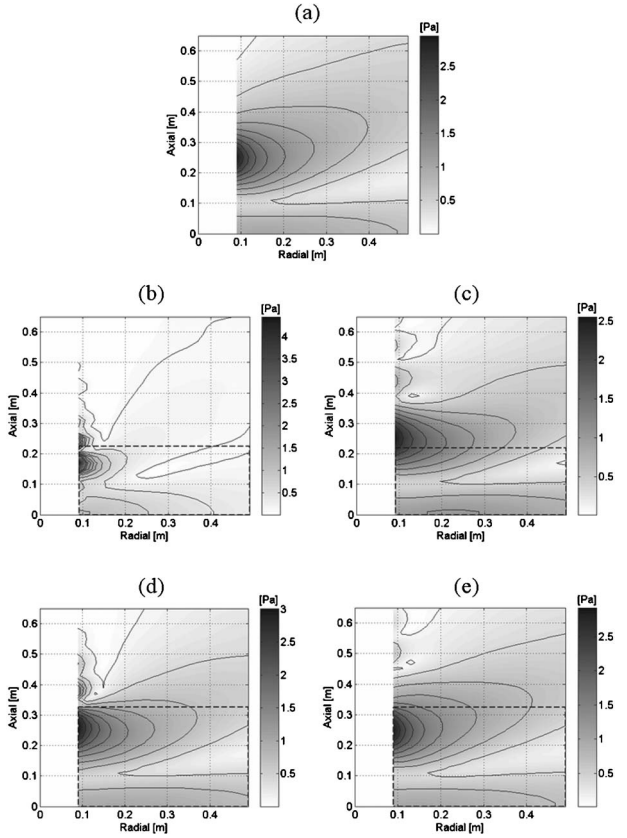

FIG. 22. Reconstructed pressures on the plane defined by $\phi=90°$: (a) exact, (b) obtained by using the patch 1 pressure, (c) obtained by using the patch 1 extended pressure after 8000 iterations, (d) obtained by using the patch 4 pressure, and (e) obtained by using the patch 4 extended pressure after 2000 iterations.

90°. It can be observed that the results on the plane defined by $\phi=90°$ were significantly affected by the finite measurement aperture while those on the plane defined by $\phi=0°$ were not. The latter observation confirms that the sources located outside the patch region degrade the reconstruction results on a plane far away from the hologram surface. Therefore, when the pressure in the farfield is to be reconstructed, the patch size should usually be larger than in the case when results only on the source surface are of interest.

IV. EXPERIMENTAL RESULTS

The same procedure was applied to the measurement of the sound field radiated by a refrigeration compressor that was 40 cm in height and 18 cm in diameter (see Fig. 23). The details of the measurements were the same as those used for the numerical simulation except for the frequency: results are presented at frequencies of 882 and 1293 Hz. The pressures on the hologram surface and the patches are shown in Fig. 24. The patches at the two frequencies consisted of 17-by-13 and 12-by-13 points, respectively. The extended hologram pressures are shown in Figs. 25 and 26, and those pressures were used to reconstruct the normal (i.e., radial) velocities on the compressor surface ($r=9$ cm). The error defined in Eq. (3), but based on surface normal velocity (see Fig. 27) instead of the pressure in this case, is presented in Fig. 28. When the error was evaluated, it was assumed that

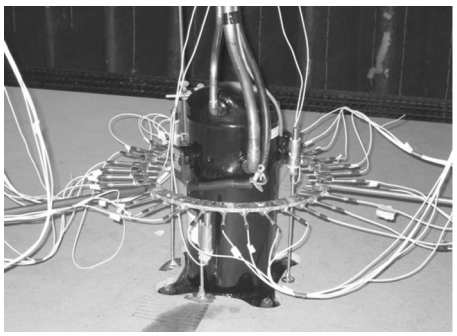

FIG. 23. Experimental setup.

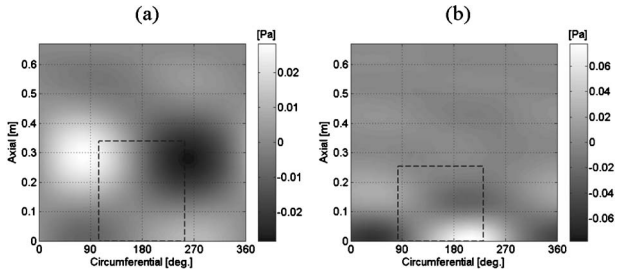

FIG. 24. Hologram pressures and selected patches (real parts are plotted): (a) at 882 Hz and (b) at 1293 Hz.

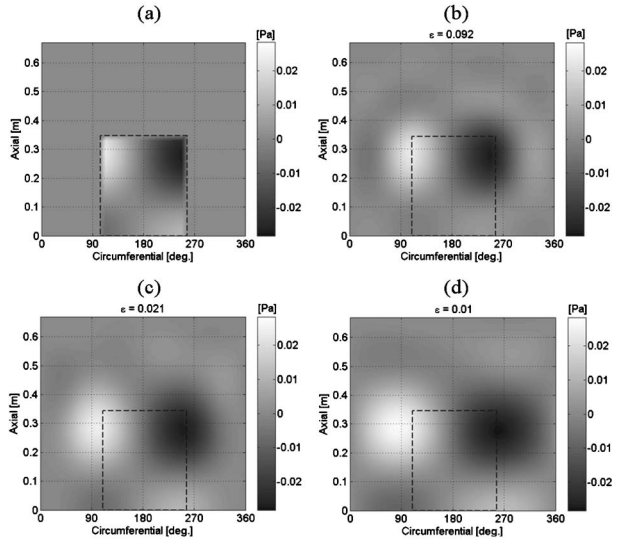

FIG. 25. Extended pressure with respect to the number of iterations at 882 Hz (real parts are plotted): (a) without extrapolation, (b) 100 iterations, (c) 3000 iterations, and (d) 9000 iterations.

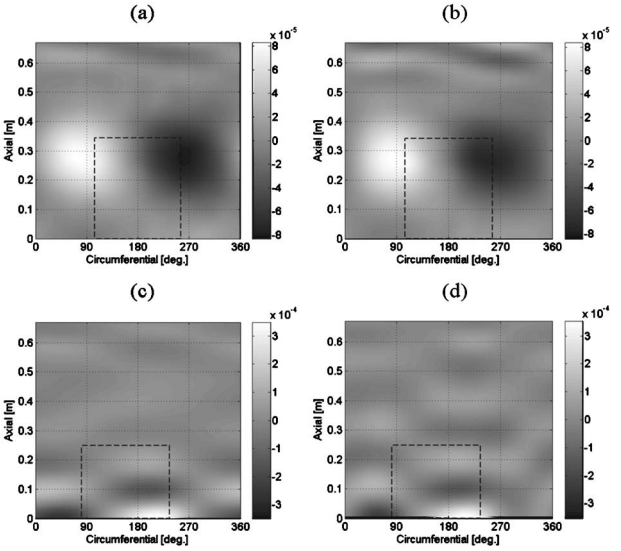

FIG. 27. Reconstructed surface normal velocities at a radius of 9 cm (real parts are plotted): (a) obtained by using the complete aperture at 882 Hz, (b) obtained by using the extended pressure at 882 Hz, (c) obtained by using the complete aperture at 1293 Hz, and (d) obtained by using the extended pressure at 1293 Hz.

the results reconstructed by using the pressure measured over the complete aperture were "exact." The reconstructed surface normal velocities directly under the patch regions showed good agreement with those calculated using the complete data set, and the reconstruction errors over the patch region at both frequencies were ultimately smaller than 10%. It was, however, observed that a larger number of iterations were required to ensure that the error dropped to a small value at 882 Hz compared to the 1293-Hz case. At 882 Hz, the pressure peaks were not included within the patch region, and the magnitude of the pressure was increasing at the edge of the patch region. In contrast, the main peak at 1293 Hz was included within the patch, which resulted in faster convergence. Thus, it can be concluded that by including the main peaks of the sound field within the patch it is more likely that good results will be obtained and that convergence will be relatively fast.

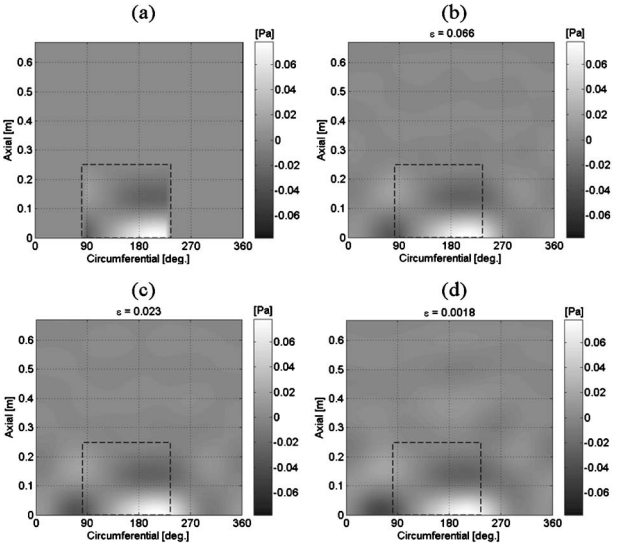

FIG. 26. Extended pressure with respect to the number of iterations at 1293 Hz (real parts are plotted): (a) without extrapolation, (b) 100 iterations, (c) 300 iterations, and (d) 9000 iterations.

V. CONCLUSIONS

In the present study, a DFT-based patch NAH procedure was implemented in cylindrical geometry. In this case, the truncated sound field can be extended to an arbitrary degree in the axial direction by zero-padding, as in the planar case,

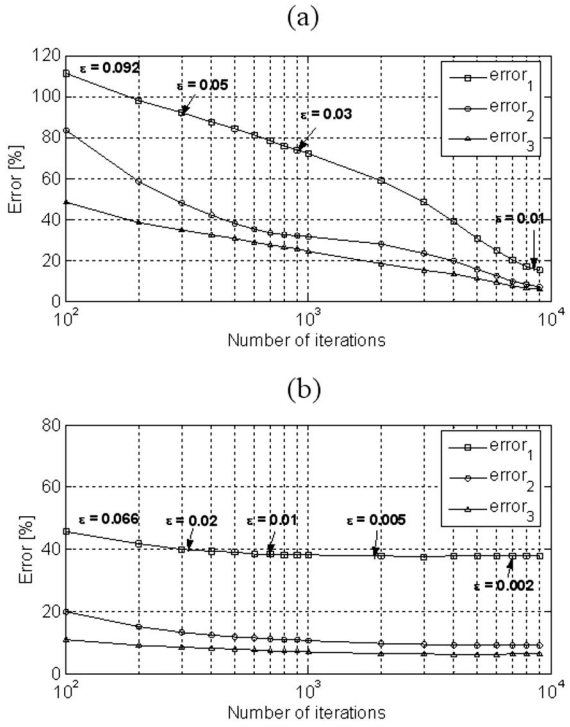

FIG. 28. Reconstruction errors with respect to the number of iterations (experiment): (a) at 882 Hz and (b) at 1293 Hz.

but the number of zeros added in the circumferential direction is necessarily limited by the fact that the sound field is periodic in this direction. Thus, when DFT-based NAH is used (i.e., when the angular sample spacing between measurement positions is constant), the number of points after zero-padding in the circumferential direction should be equal to 2π divided by the angular sample spacing to account for the periodic nature of the sound field in that direction. Both numerical simulation results performed by using a two-dipole model with a rigid boundary and experimental results related to the visualization of the sound field radiated by a refrigeration compressor were presented, and it was shown that the patch NAH algorithm can be successfully used in the cylindrical case and in the presence of a rigid boundary. Based on the results presented in this study, some practical conclusions were drawn: first, it is desirable to use a larger aperture size (which can, however, be smaller than in the case without extrapolation) than the region of interest since the reconstruction results in the central region of the aperture are less corrupted by errors, and second, it is desirable to include pressure peaks in the patch area since the reconstruction error converges relatively quickly to a low value in that case, thus saving computation time.

[1]E. G. Williams, "Comparison of SVD and DFT approaches for NAH," *Proceedings of INTER-NOISE 2002*, No. 415 (2002).

[2]K. Saijyou and S. Yoshikawa, "Reduction methods of the reconstruction error for large-scale implementation of near-field acoustical holography," J. Acoust. Soc. Am. **110**, 2007–2023 (2001).

[3]E. G. Williams, B. H. Houston, and P. C. Herdic, "Fast Fourier transform and singular value decomposition formulations for patch nearfield acoustical holography," J. Acoust. Soc. Am. **114**, 1322–1333 (2003).

[4]K. Saijyou and H. Uchida, "Data extrapolation method for boundary element method-based near-field acoustical holography," J. Acoust. Soc. Am. **115**, 785–796 (2004).

[5]E. G. Williams, "Continuation of acoustic near-fields," J. Acoust. Soc. Am. **113**, 1273–1281 (2003).

[6]K. Saijyou, "Regularization method for the application of K-space data extrapolation to near-field acoustical holography," J. Acoust. Soc. Am. **116**, 396–404 (2004).

[7]Z. Wang and S. F. Wu, "Helmholtz equation–least-squares method for reconstructing the acoustic pressure field," J. Acoust. Soc. Am. **102**, 2020–2032 (1997).

[8]E. G. Williams, "Approaches to patch NAH," *Proceedings of INTER-NOISE 2003*, No. 288 (2003).

[9]S. F. Wu and X. Zhao, "Combined Helmholtz equation–least-squares method for reconstructing acoustic radiation from arbitrarily shaped objects," J. Acoust. Soc. Am. **112**, 179–188 (2002).

[10]R. Steiner and J. Hald, "Near-field acoustical holography without the errors and limitations caused by the use of spatial DFT," *Proceedings of 6th International Congress on Sound and Vibration* (1999).

[11]J. Hald, "Patch near-field acoustical holography using a new statistically optimal method," *Proceedings of INTER-NOISE 2003*, No. 975 (2003).

[12]Y.-T. Cho, J. S. Bolton, and J. Hald, "Source visualization by using statistically optimized nearfield acoustical holography in cylindrical coordinates," J. Acoust. Soc. Am. **118**, 2355–2364 (2005).

[13]A. Sarkissian, "Extension of measurement surface in near-field acoustic holography," J. Acoust. Soc. Am. **115**, 1593–1596 (2004).

[14]A. Sarkissian, "Method of superposition applied to patch near-field acoustic holography," J. Acoust. Soc. Am. **118**, 671–678 (2005).

[15]S. G. Mallat, "A theory for multiresolution signal decomposition: the wavelet representation," IEEE Trans. Pattern Anal. Mach. Intell. **11**, 674–693 (1989).

[16]J.-H. Thomas and J.-C. Pascal, "Wavelet preprocessing for lessening truncation effects in nearfield acoustical holography," J. Acoust. Soc. Am. **118**, 851–860 (2005).

[17]M. Lee and J. S. Bolton, "Scan-based near-field acoustical holography and partial field decomposition in the presence of noise and source level variation," J. Acoust. Soc. Am., 2006 (unpublished).

[18]E. G. Williams, "Regularization methods for near-field acoustical holography," J. Acoust. Soc. Am. **110**, 1976–1988 (2001).

[19]P. C. Hansen, *Rank-Deficient and Discrete Ill-Posed Problems* (SIAM, Philadelphia, PA, 1998).

[20]M. Lee, J. S. Bolton, and L. Mongeau, "Application of cylindrical near-field acoustical holography to the visualization of aeroacoustic sources," J. Acoust. Soc. Am. **114**, 842–858 (2003).

[21]P. C. Hansen, "Analysis of discrete ill posed problems by means of the L-curve," SIAM Rev. **34**, 561–580 (1992).

Focused nonlinear phase-conjugate waves generated by a solid parametric amplifier

Andrew P. Brysev, Fedor V. Bunkin, and Leonid M. Krutyansky[a)]
Wave Research Center, A.M. Prokhorov General Physics Institute, Russian Academy of Sciences, 38 Vavilov Street, Moscow 119991, Russia

Xiang Yan and Mark F. Hamilton
Department of Mechanical Engineering, The University of Texas at Austin, 1 University Station C2200, Austin, Texas 78712-0292

(Received 16 May 2004; revised 29 September 2005; accepted 8 October 2005)

An experimental and numerical study is reported on focused, phase-conjugated sound beams of finite amplitude produced in water by a solid-state parametric amplifier, referred to as the conjugator. The sound beams incident on the conjugator were radiated by a focused circular source. Field distributions were measured along the beam axis and in the focal plane of the source. Both linear and nonlinear propagation were investigated. Apertures of different diameters were placed in front of the conjugator to demonstrate diffraction effects associated with size of the active surface of the conjugator. Peak-to-peak acoustic pressures of 8 MPa and strongly distorted, asymmetric waveforms were measured at the focus of conjugate beams having a fundamental frequency of 5 MHz. Numerical simulations of harmonic generation in the conjugate beams are in agreement with the measurements. The study reveals that the conjugate beams accurately reproduce the focal region of the incident beams when a sufficiently large aperture is used, even when substantial waveform distortion due to nonlinear propagation effects are observed in the conjugate beams. [DOI: 10.1121/1.2130965]

PACS number(s): 43.60.Tj, 43.25.Jh [DRD] Pages: 3733–3736

I. INTRODUCTION

Perfectly phase-conjugated (PC) or time-reversed (TR) acoustic waves reproduce the spatial distribution of an incident wave field, but they propagate in the opposite direction. Phase conjugation is known for its ability to compensate for phase aberrations created in the incident wave due to propagation through inhomogeneous media. The aberrations are removed as the conjugate wave propagates back to the source through the inhomogeneous medium.

Applications of phase conjugate waves include systems for acoustic imaging through inhomogeneous media, such as C-scan imaging.[1] Implementation of supercritical parametric magnetoacoustic interaction in ceramics provides a means of generating PC waves with strong amplification.[2,3] This method allows generation of PC beams in water exhibiting strong nonlinear behavior. Nonlinear properties of intense, focused PC beams have been used to advantage in a prototype C-scan harmonic imaging system.[4] The tighter focus and lower sidelobes associated with the harmonics generated nonlinearly in the fluid, combined with the special features of phase conjugation, substantially improve resolution of objects situated in strongly aberrating media.

Even with a conjugation device that accomplishes perfect transformation of the wave field inside, there remain factors that may adversely affect reproduction of the wave field incident on the conjugator. One is the finite size of the conjugator aperture. In principal, the aperture must completely enclose the incident wave field in order for the conjugator to perfectly reproduce that field. Apertures of finite extent introduce diffraction effects not present in the incident field. Another factor arises when the conjugator provides amplification so large that finite-amplitude propagation effects occur in the PC wave field.

Specifically of interest in the present paper are the combined effects of nonlinearity and diffraction on the harmonic components in the PC beam, and ultimately on the fundamental component. During propagation of the PC wave field, harmonics are generated that extract energy from the fundamental in a way that alters its spatial distribution. Because these effects cannot be filtered out electronically at the receiver, they should be properly modeled and understood. The effects of nonlinearity and diffraction in the conjugate beam were modeled numerically by Cunningham *et al.*,[5] and the same approach is used in the present paper to make comparisons with experiments. Other papers modeling nonlinear effects in the conjugate beam, by Hallaj *et al.*[6] and Tanter *et al.*,[7,8] did not take diffraction into account in the numerical simulations. However, inclusion of diffraction is essential to predicting variations in focal beamwidth that are caused by nonlinearity in the conjugate beam. Beamwidth, in turn, is directly related to resolution of acoustic imaging systems.

There has also been no experimental study devoted to altering the relative influence of nonlinearity and diffraction in order to examine parametrically their combined effect on the fundamental component in the conjugate beam and to compare observations with theory. The closest investigations

a)Author to whom correspondence should be addressed. Electronic mail: krut@orc.ru

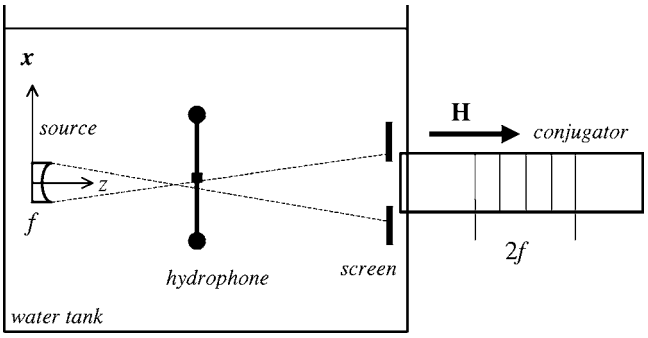

FIG. 1. Experimental setup and geometry, where **H** designates the dc magnetic bias field, x,z are coordinate axes, and $f,2f$ are frequencies of the electrical inputs to the source and the conjugator, respectively. Dashed lines outline the approximate region of propagation of the acoustic beams, both incident and phase conjugate.

in this regard, by Brysev *et al.*,[9,10] report measurements of harmonic components generated in a conjugate beam propagating through an inhomogeneous layer. The emphasis was on compensation of phase aberration due to the inhomogeneity, rather than on variation of parameters influencing diffraction, and there were no comparisons with theory. Earlier experiments on nonlinearity in time-reversed beams by Tanter *et al.*[7,8] were designed specifically to avoid diffraction by working only in the extreme nearfield of the source. These experiments were based on a simulation of time reversal accomplished with reflection from a pressure release surface. The reverse nonlinear distortion observed under these conditions was also reported in earlier experiments by Van Buren *et al.*[11] and by Muir *et al.*[12]

The present paper reports detailed measurements demonstrating the relative effects of nonlinearity and diffraction on the spatial distribution of the harmonic components in a PC beam of finite amplitude. Low and high conjugator gains were used to produce small-signal and finite-amplitude PC wave fields, respectively, to investigate the effect of nonlinearity. The influence of diffraction was varied by using conjugators with apertures of different sizes. Measurements of time waveforms, harmonic propagation curves, and beam patterns in the conjugate beam are compared with numerical simulations. Overall, measurements are found to be in reasonable quantitative agreement with theory. They also confirm earlier predictions[5] that increasing conjugator gain, or reducing the conjugator aperture size, reduces focal quality of the conjugate beam at the source frequency.

II. EXPERIMENTAL SETUP AND PROCEDURES

A schematic diagram of the experimental configuration is shown in Fig. 1. A focused circular Panametrics M-307 source with diameter 27 mm and geometrical focal length 84 mm was placed in a water tank in front of the active element of a parametric conjugator located a distance 206 mm away. The active element of the conjugator was made from magnetostrictive ceramics in the shape of a cylindrical rod 150 mm long and 36 mm in diameter. The rod was placed in a dc bias magnetic field. The end of the rod, which serves as the aperture that collects the incident acoustic field, was inserted into the tank through a hole in a side wall, coaxial with the source. In order to improve the performance of the conjugator, the end of the rod was etched with concentric circular grooves 1.5 mm in depth.[10] The purpose of this corrugation is to allow more uniform transmission of the angular spectrum of the incident beam from the water into the rod. The beam propagated through the focal region to the conjugator. The amplitude of the incident beam was sufficiently small that linear propagation could be assumed. After the incident beam entered the conjugator, a magnetic field in the form of a 10-MHz pulse (referred to as the pump) was applied to the rod via an inductance coil surrounding the rod. The magnetic field caused the sound speed in the magnetostrictive element to be modulated at twice the frequency of the incident sound beam. Due to parametric magnetoacoustic interaction in the ceramic, a phase conjugate beam is generated at frequency 5 MHz. When the pump exceeds the threshold of absolute parametric instability, the amplitude of the conjugate wave increases exponentially with time. By varying the duration of the pump, one can obtain a conjugate beam with low or very high amplitude with respect to the incident wave (see Ref. 3 for more details of supercritical parametric wave-phase conjugation). The amplified conjugate beam propagated back through the focal region to the source. Just after leaving the conjugator, the wave was nearly monochromatic because of the resonant nature of the parametric interaction.

In order to study the influence of the size of the conjugator aperture on reproduction of the incident field, the surface area exposed to the incident field was reduced by placing an acoustically opaque rubber screen with a round hole through it in front of the aperture. The influence of nonlinearity was studied by varying the amplification of the conjugator, which in turn varied the amplitude of the conjugate wave.

The wave fields of the incident and conjugate beams were measured with a wideband Marconi PVDF membrane hydrophone in the focal plane of the source and along the propagation axis. The diameter of the hydrophone membrane was 100 mm, large enough that there was no significant influence of diffraction off its edge. The size of the active element was 0.5 mm. The hydrophone was moved with a 2D automated positioning system having an accuracy of 0.2 mm. At each location in space, 32 waveforms were averaged, FFT frequency spectra were obtained using a Tektronix TDS 340A oscilloscope, and data for the first four harmonic amplitudes were stored.

Numerical simulations of both the incident and phase conjugate beam were performed using the KZK equation,[5] which accounts for nonlinear distortion, thermoviscous absorption, and diffraction. The incident beam was modeled as small-signal radiation from a focused circular source with uniform amplitude. Time reversal was applied in the plane of the front surface of the conjugator, the field was truncated in space according to the finite aperture, and amplification was introduced to match the measured pressure in the conjugate beam. Nonlinearity was taken into account in calculations for the conjugate beam.

Calibration of the hydrophone in the range 5–20 MHz was based on a series of auxiliary measurements of the inci-

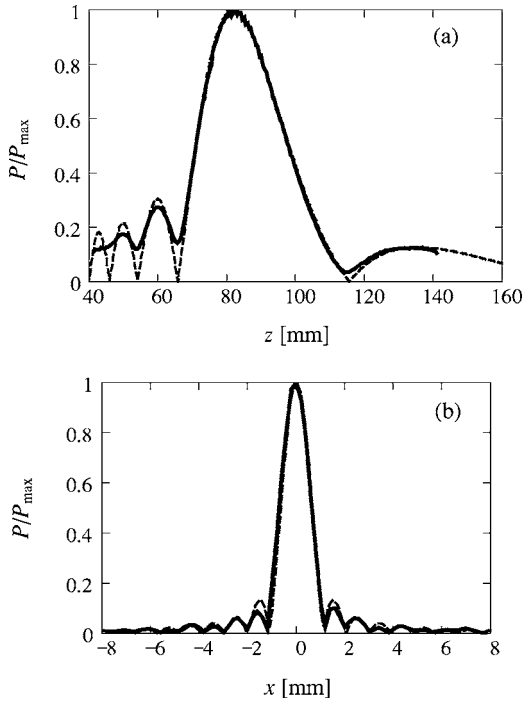

FIG. 2. Pressure amplitude of incident beam, normalized by its maximum value, (a) along the beam axis and (b) in the focal plane (z=84 mm). Solid lines are measurements and dashed lines are simulations.

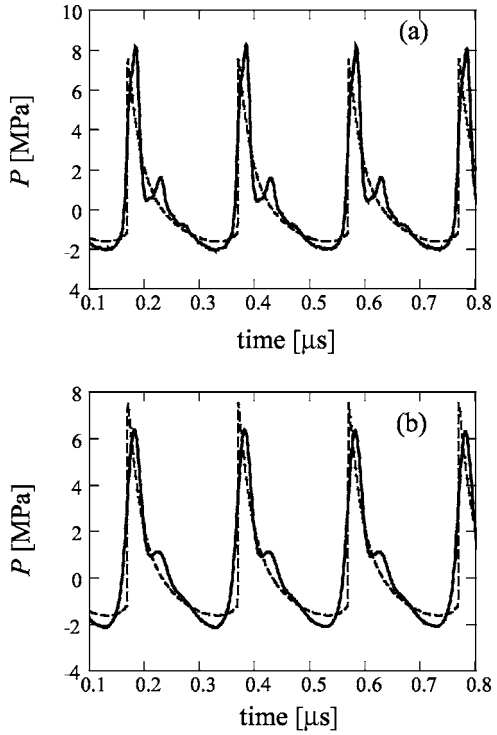

FIG. 3. Pressure waveform at the focus. Solid lines are measurements, dashed lines are simulations. In (a), the measurement corresponds to the electrical signal obtained directly from the hydrophone. In (b), the measured signal in (a) was adjusted according to the calibration data for the hydrophone.

dent beam at high amplitude. The measured distributions of the first four harmonics of the finite-amplitude beam were matched with calculations of the field obtained from the KZK equation for a focused piston source. For the frequencies 5, 10, 15, and 20 MHz the coefficients 1, 1.05, 1.33, and 1.61, respectively, were obtained for the calibration factors normalized to the sensitivity at 5 MHz.

III. RESULTS

The pressure amplitude in the incident beam is shown in Fig. 2, (a) along the axis of propagation and (b) in the focal plane of the source. The curves are normalized by their maximum values. The pressure at the focus was 0.2 MPa, and no significant nonlinear effects were observed in the incident beam. Solid lines are the measurements and dashed lines are the simulations (the same convention is used in all subsequent figures). This simulation is used to calculate the sound field incident on the conjugator for all cases discussed below.

In contrast, the wave radiated by the conjugator may be finite amplitude. A conjugate waveform at the focus is shown in Fig. 3(a). The calculation predicts strongly nonlinear behavior with shock formation. To perform this calculation, the radiated pressure amplitude at the face of the conjugator had to be determined. This was accomplished by matching the amplitudes of the predicted and measured fundamental (5 MHz) components at the focus. The measured waveform is in reasonable agreement with the resulting calculation. The secondary peak following each shock is due to the nonideal frequency response of the hydrophone, and especially its bandwidth. The measured waveform in Fig. 3(a) corresponds to the unfiltered signal obtained from the hydrophone. In Fig. 3(b), the signal from the hydrophone was transformed into the frequency domain, corrections were made according to the hydrophone calibration curve, and the resulting spectrum was transformed back into the time domain, yielding the solid line in Fig. 3(b). Although imperfect, we believe the measured waveform in Fig. 3(b) is closer to reality than the measurement shown in Fig. 3(a). According to the measurement in Fig. 3(b), the peak-to-peak acoustic pressure was about 8 MPa, and the intensity calculated for that waveform corresponds to 360 W/cm^2.

The main results are presented in Fig. 4. The left column corresponds to use of the conjugator with its entire 36-mm aperture exposed, the right column to use of a screen that creates a 20-mm aperture at the face of the conjugator. Axial propagation curves versus coordinate z are presented in the first and third rows. Focal plane beam profiles versus transverse coordinate x are presented in the second and fourth rows. In the upper two rows the pressure amplitude in the conjugate beam is sufficiently weak that propagation may be considered linear. In the lower two rows the conjugate beam has experienced strong nonlinear distortion.

Overall agreement between measurements and calculations is quite good. Reproduction of the incident wave field at the source frequency, as determined by comparison with Fig. 2, is much better for the conjugate beams produced using the large aperture, even in the presence of strong nonlinear distortion. The right column in Fig. 4 reveals that diffraction effects introduced by the small aperture, due to greater truncation of the incident beam, significantly impair repro-

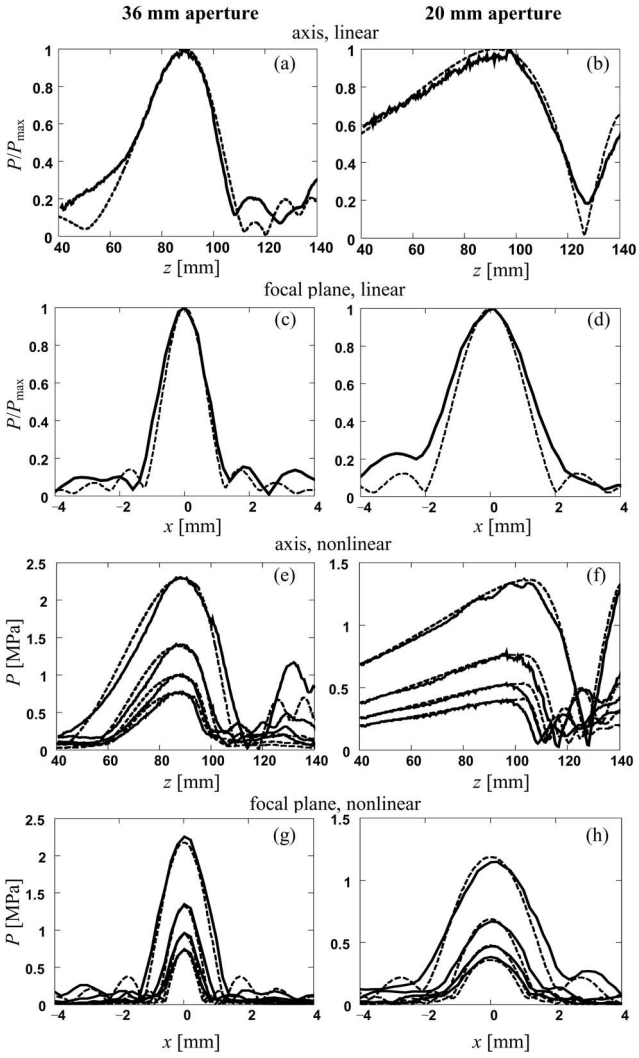

FIG. 4. Influence of aperture size and conjugator gain on the conjugate beam structure. Diameter of aperture is 36 mm for the left column and 20 mm for the right column. The first two rows correspond to low amplitude, and the last two rows correspond to finite amplitude. In the latter, the four curves in each frame represent pressure amplitudes of the first four harmonics (f, $2f$, $3f$, and $4f$). Rows 1 and 3 show propagation curves versus the axial coordinate z, and rows 2 and 4 show beam patterns in the focal plane versus the transverse coordinate x. Solid lines are measurements, dashed lines are simulations.

duction of the incident beam. Therefore, nonlinearity alone does not substantially impair reconstruction of the incident beam by the conjugate beam.

IV. CONCLUSION

Measurements and corresponding simulations have been presented for phase-conjugate sound beams that develop shocks as they propagate back toward the source. The sound beams incident on the conjugator were small-signal waves, and it was the large amplification during phase conjugation that produced conjugate beams of finite amplitude. Attention was focused on the effects of diffraction and nonlinearity on reproduction of the incident field distribution in the focal region. Reduction in the size of the conjugator aperture, and increase in the gain of the conjugator at finite amplitude, each diminish the ability to replicate the incident field with the conjugate beam. The stronger of these two effects is diffraction associated with conjugator size. With a sufficiently large conjugator aperture, it is demonstrated that good reproduction of an incident sound field, and thus automatic refocusing based on phase conjugation, can be achieved even with conjugate beams that are sufficiently nonlinear to develop shocks.

ACKNOWLEDGMENTS

Professor Vladimir Preobrazhensky is thanked for many fruitful discussions. The research described in this publication was made possible in part by Award No. RP-2367-MO-02 of the U.S. Civilian Research & Development Foundation for the Independent States of the Former Soviet Union (CRDF), Grant No. 1553.2003.2 of the President of RF, and the U.S. Office of Naval Research. A version of Fig. 4 appeared previously in Ref. 13 and is repeated here with permission.

[1] M. Ohno, K. Yamamoto, A. Kokubo, K. Sakai, and K. Takagi, "Acoustic phase conjugation by nonlinear piezoelectricity. II. Visualization and application to imaging systems," J. Acoust. Soc. Am. **106**, 1339–1345 (1999).

[2] A. P. Brysev, F. V. Bunkin, D. V. Vlasov, L. M. Krutyansky, V. L. Preobrazhensky, and A. D. Stakhovsky, "Regenerative amplification of acoustic waves with phase conjugation in a ferrite," Sov. Phys. Acoust. **34**, 567–569 (1988).

[3] A. P. Brysev, L. M. Krutyanskii, and V. L. Preobrazhenskii, "Wave phase conjugation of ultrasonic beams," Phys. Usp. **41**, 793–805 (1998).

[4] Yu. Pyl'nov, P. Pernod, and V. Preobrazhensky, "Acoustic imaging by second harmonic of phase conjugate wave in inhomogeneous medium," Appl. Phys. Lett. **78**, 553–555 (2001).

[5] K. B. Cunningham, M. F. Hamilton, A. P. Brysev, and L. M. Krutyansky, "Time-reversed sound beams of finite amplitude," J. Acoust. Soc. Am. **109**, 2668–2674 (2001).

[6] I. M. Hallaj, R. O. Cleveland, P. E. Barbone, S. G. Kargl, and R. R. Roy, "Amplitude degradation of time-reversed pulses in nonlinear absorbing thermoviscous fluids," Ultrasonics **38**, 885–889 (2000).

[7] M. Tanter, J.-L. Thomas, F. Coulouvrat, and M. Fink, "Acoustic time reversal experiments in nonlinear regime," in *Nonlinear Acoustics at the Turn of the Millennium, ISNA 15*, edited by W. Lauterborn and T. Kurz (AIP, New York, 2000), pp. 137–140.

[8] M. Tanter, J.-L. Thomas, F. Coulouvrat, and M. Fink, "Breaking of time reversal invariance in nonlinear acoustics," Phys. Rev. E **64**, 016602-1–016602-7 (2001).

[9] A. P. Brysev, F. V. Bunkin, R. V. Klopotov, L. M. Krutyanskii, and V. L. Preobrazhenskii, "Focusing of a nonlinear phase-conjugate ultrasound wave transmitted through a phase-inhomogeneous layer," JETP Lett. **73**, 389–392 (2001).

[10] A. Brysev, R. Klopotov, and L. Krutyansky, "A quality of parametric wave phase conjugation of ultrasound," Ultrasonics **40**, 329–332 (2002).

[11] A. L. Van Buren and M. A. Breazeale, "Reflection of finite-amplitude ultrasonic waves. I. Phase shift," J. Acoust. Soc. Am. **44**, 1014–1020 (1968).

[12] T. G. Muir, L. L. Mellenbruch, and J. C. Lockwood, "Reflection of finite-amplitude waves in a parametric array," J. Acoust. Soc. Am. **62**, 271–276 (1977).

[13] A. P. Brysev, K. B. Cunningham, M. F. Hamilton, L. M. Krutyansky, and X. Yan, "Influence of conjugator size and nonlinearity on focused, phase-conjugate sound beams in water," 17th International Congress on Acoustics, Rome, Italy, 2001, Book of Abstracts, p. 297, Paper 6P.03. Extended abstract published on CD-ROM, Vol. I, file 1.02, pp. 30–31, ISBN 88-88387-00-5.

Effect of voltage-dependent membrane properties on active force generation in cochlear outer hair cell

Zhijie Liao[a] and Aleksander S. Popel
Department of Biomedical Engineering, Johns Hopkins University, Baltimore, Maryland 21205

William E. Brownell
Bobby R. Alford Department of Otorhinolaryngology and Communicative Sciences, Baylor College of Medicine, Houston, Texas 77030

Alexander A. Spector
Department of Biomedical Engineering, Johns Hopkins University, Baltimore, Maryland 21205

(Received 13 June 2005; revised 7 September 2005; accepted 20 September 2005)

A computational model is proposed to analyze the active force production in an individual outer hair cell (OHC) under high-frequency conditions. The model takes into account important biophysical properties of the cell as well as constraints imposed by the surrounding environment. The biophysical properties include the elastic, piezoelectric, and viscous characteristics of the cell wall. The effect of the environment is associated with the stiffness of the constraint and the drag forces acting on the cell due to the interaction with the external and internal viscous fluids. The study concentrated on a combined effect of the transmembrane potential, frequency, and stiffness of the constraints. The effect of the voltage-dependent stiffness of the cell was particularly investigated and it was found to be twofold. First, it results in higher sensitivity and nonlinearity of the OHC active force production in the physiological range. Second, it determines smaller active forces in the hyperpolarization range. The resonant properties of the active force as functions of voltage and the constraint stiffness were also analyzed. The obtained results can be important for a better understanding of the OHC active force production and the contribution of cell electromotility to the cochlear amplification, sensitivity, and nonlinearity. © *2005 Acoustical Society of America.* [DOI: 10.1121/1.2118387]

PACS number(s): 43.64.Ld, 43.64.Kc, 43.64.Bt, 43.64.Nf [WPS] Pages: 3737–3746

I. INTRODUCTION

Outer hair cells (OHCs) are critically important for active hearing in mammals. These cells have a unique form of motility, named electromotility, responding to changes in the cell's transmembrane potential (Brownell *et al.*, 1985, 2001). The major features of electromotility are the cell's length changes, nonlinear capacitance, and active force production. All three features remain effective within a broad frequency range (Frank *et al.*, 1999; Gale and Ashmore, 1997a). The voltage dependence of the OHC characteristics has been known since the original discovery of electromotility when it was demonstrated that depolarized cells shorten and hyperpolarized cells elongate (Brownell *et al.*, 1985). After that, the voltage dependence of length's changes and that of nonlinear capacitance was studied extensively (Santos-Sacchi and Dilger, 1998; Santos-Sacchi, 1989; Iwasa, 1994; Santos-Sacchi and Navarette, 2002; Gale and Ashmore, 1994, 1997b). The important parameters of the voltage-dependent characteristics of OHC include the position and magnitude of the maximal value, the level of nonlinearity, slopes, etc. Moreover, these characteristics have been measured under hyper- and hypo-osmotic conditions as well as under the action of various agents known to affect hearing (Shehata *et al.*, 1991; Hallworth, 1995, 1997; Lue *et al.*, 2001; Ulfendahl, 1997). The voltage dependence of the active force was studied under low- and moderate-frequency conditions (Adachi and Iwasa, 1997; Iwasa and Adachi, 1997; Spector *et al.*, 1999; He and Dallos, 2000).

To explain the voltage dependence of the major features of OHC electromotility, a model of molecular motors in the cell's lateral wall has been proposed (Dallos *et al.*, 1991; Iwasa, 1994, 2001). In this theory, the voltage dependence of the cell's length changes, nonlinear capacitance, and active force was associated with the effect of the applied electric field on the probability of the motor being in different conformational states. Recently, the membrane protein, prestin, necessary for hearing and closely associated with outer hair cell electromotility, has been discovered (Zheng *et al.*, 2000; Oliver *et al.*, 2001; Liberman *et al.*, 2002). The native electromotility of human embryonic kidney cells is enhanced when they are transfected with prestin and acquire a greatly enhanced voltage-dependent capacitance showing an association between the voltage dependence of OHC electromotility and the properties of the membrane protein prestin. The information on the voltage-dependent properties of OHC electromotility, on the other hand, can be used to characterize the properties of the motor mechanism and to extract its parameters.

The main phenomenon of electromotility, similar to the converse piezoelectric effect, is associated with a mechanical

[a]Electronic mail: zliao@jhu.edu

response to the application of an electric field (Brownell *et al.*, 1985). The reciprocal phenomenon, the transfer of a charge across a part of the membrane in response to a mechanical perturbation of the membrane, which is similar to the direct piezoelectric effect, has also been demonstrated (Gale and Ashmore, 1997b; Zhao and Santos-Sacchi, 1999; Dong *et al.*, 2002). This level of coupling was successfully described by linear and nonlinear piezoelectric-type relationships (Mountain and Hubbard, 1994; Tolomeo and Steele, 1998; Spector, 2000, 2001). However, it is likely that the electromechanical coupling in the outer hair cell lateral wall has additional modes. It has recently been shown that the stiffness of the cell as a whole, which was earlier considered as a purely passive characteristic, is also voltage-dependent (He and Dallos, 1999). This effect has been demonstrated for both low and moderate (up to 2 kHz) frequencies (He and Dallos, 2000). He *et al.* (2003) showed that the replacement of intracellular chloride required for the motor mechanism abolishes the voltage dependence of the cell stiffness (as well as the cellular electromotile response). In a possible explanation of the voltage dependence of the cellular stiffness, it has been proposed that the motor protein has an intrinsic finite stiffness that contributes to the stiffness of the whole cell (He and Dallos, 2000; Deo and Grosh, 2004). According to this model, the motor-related stiffness is different depending on what conformational state the motor takes.

Other voltage-dependent modes of electromechanical coupling in the cell wall can also be important for the outer hair cell performance under various conditions. Oghalai *et al.* (2000) have found that the lateral diffusion in the outer hair cell plasma membrane is voltage-dependent following a voltage profile similar to that of the voltage-dependent displacement. The piezoelectricity of the cell wall can enhance high-frequency receptor potential in the cell (Spector *et al.*, 2003). Also, the strain-rate sensitivity of the cell wall that could be related to its viscoelastic properties can result in an increase in the cell's receptor potential in the moderate-frequency range (Spector *et al.*, 2005).

The OHC provides a positive feedback amplifying vibration of the basilar and tectorial membranes (Geisler, 1998; Dallos, 1996). This amplification ("cochlear amplifier") is based on the active force and active energy produced by the cell and pumped into the vibrating basilar and tectorial membranes. Somatic motility is a key contributor to the OHC-related active characteristics. The voltage sensitivity of the active force in the physiological range of the cell's transmembrane potential is important for the feedback provided by the OHC. In addition to the active amplification, hair cells are critical to the cochlear nonlinearities (Patuzzi, 1996). Voltage dependence and sensitivity of the OHC active force contribute to the nonlinearities of the cochlea as a whole. This contribution becomes more significant if a combination of two intrinsic OHC-related nonlinearities, length change versus voltage and stiffness versus voltage, are taken into account.

In the present paper, we extend our computational model (Liao *et al.*, 2005) and apply it to the analysis of the active force production in a constrained OHC under high-frequency conditions. Here, we study the voltage dependence of the active force and concentrate on a combined effect of three factors, the transmembrane potential, frequency, and stiffness of the constraint. In terms of voltage dependence, we assume that the potential driving the cell's electromotile response is significantly smaller than the resting (equilibrium) potential. This is a reasonable approximation of both physiological and experimental conditions where the cell is studied under high-frequency conditions. We start with general electrically nonlinear relationships and, on the basis of our assumption, linearize them about the point of the resting potential. In our model, the driving potential is a relatively small harmonic function with constant amplitude. In this approach, we mainly deal with the active force per unit transmembrane voltage. The resting potential enters our model in two ways. First, our model includes the coefficients that express the cell's length and radius changes estimated under special conditions of no constraints and low frequencies; these coefficients are voltage-dependent. Second, the local elastic moduli of the cell wall depend on the whole cell stiffness, and the latter also depends on voltage. The frequency effect is mainly related to the viscous losses inside the cell wall and the wall interaction with the fluids inside and outside the cell. In our model, the stiffness of the constraints is associated with two springs attached to the ends of the cell (Fig. 1). These springs represent the effects of both the basilar and tectorial membrane complex *in vivo* and the attached AFM lever or glass fiber measuring the active force generation *in vitro*. We estimated the OHC active force within broad ranges of resting potential, frequency, and the stiffness of the constraint. We found that the effect of the constraint on the voltage dependence of the active force is significant. At any value of voltage, the active force decreases with frequency if the stiffness of the constraint is relatively low. It becomes reversed, and the active force increases with frequency if the stiffness of the constraint is high. Our model also shows that the effect of the voltage-dependent cell stiffness is important. We found that this effect results in a shift of the point of the highest voltage sensitivity of the active force toward the physiological value of the cell's membrane potential. The obtained results can be important for a better understanding of the cochlear amplifier and nonlinearities associated with OHCs.

II. MODEL

Figure 1 presents the main features of our model. Panels (a) and (b) demonstrate applications of our model of the constrained cell to physiological and experimental conditions, and panel (c) shows how the constraints are treated in the model. Finally, panel (d) presents an element of the cell wall with the external tractions and internal resultants. In our model, the cell wall is considered as viscoelastic and piezoelectric material described by the following equations:

$$\begin{bmatrix} N_x \\ N_\theta \end{bmatrix} = \begin{bmatrix} C_{11} & C_{12} \\ C_{12} & C_{22} \end{bmatrix} \begin{bmatrix} \varepsilon_x \\ \varepsilon_\theta \end{bmatrix} + 2\eta \begin{bmatrix} s_x \\ s_\theta \end{bmatrix} + \begin{bmatrix} f_x^a \\ f_\theta^a \end{bmatrix}, \tag{1}$$

where N_x and N_θ are the components of the stress resultant (i.e., the product of the stress and cell wall thickness) generated in the cell wall; the subscripts x and θ indicate the axial

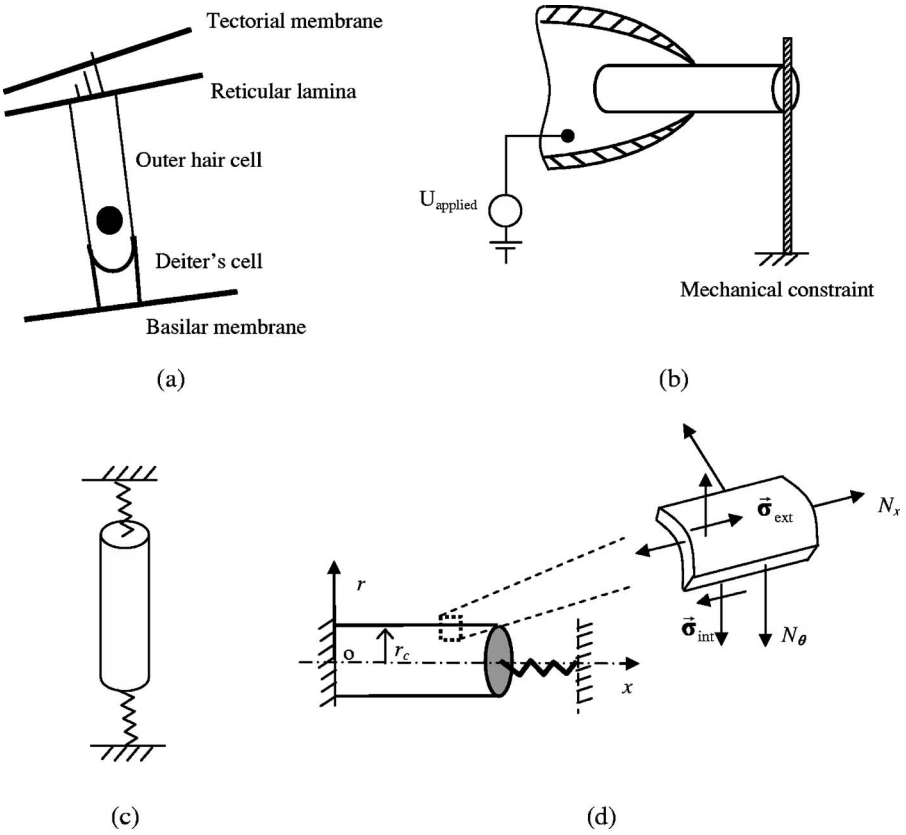

FIG. 1. Major features of the proposed model of the constrained OHC. (a) Sketch of the constraints imposed on the OHC *in vivo*; (b) sketch of the microchamber experiment used to measure the OHC high-frequency active force where the cell is held by the micropipette and bends an AFM lever or glass fiber; (c) sketch of cylindrical OHC with attached elastic springs that represents the constraints imposed on the cell; and (d) sketch of the apical half of an outer hair cell which allows consideration of the symmetry conditions. A portion of the lateral wall is shown on the upper right. $\boldsymbol{\sigma}_{ext}$ and $\boldsymbol{\sigma}_{int}$ are the tractions acting on the cell wall surface due to the interaction with the external and internal fluids, respectively, and N_x and N_θ are the components of the stress resultants.

and circumferential directions, respectively; C_{ij} are the orthotropic elastic moduli of the cell wall; ε_x and ε_θ are two components of the total (observable) strain, η is the cell wall viscosity; s_x and s_θ are the components of the deviatoric part of the strain rate (e.g., Evans and Skalak, 1980); and f_x^a and f_θ^a are the longitudinal and circumferential components of the active force corresponding to low-frequency conditions. The latter forces are associated with the converse piezoelectric effect in the cell wall.

By relating the components of the strain rate (s_x and s_θ) to the components of the velocity (time derivative of the wall displacement), we obtain the constitutive relations in their final form (Tolomeo, 1995; Ratnanather *et al.*, 1996; Tolomeo and Steele, 1998; Spector *et al.*, 1998, 1999; Spector and Jean, 2003; Liao *et al.*, 2005):

$$\begin{bmatrix} N_x \\ N_\theta \end{bmatrix} = \begin{bmatrix} C_{11} & C_{12} \\ C_{12} & C_{22} \end{bmatrix} \begin{bmatrix} \dfrac{\partial u_x}{\partial x} \\ \dfrac{u_r}{r_c} \end{bmatrix} + \begin{bmatrix} \eta & -\eta \\ -\eta & \eta \end{bmatrix} \begin{bmatrix} \dfrac{\partial^2 u_x}{\partial x \partial t} \\ \dfrac{\partial u_r}{r_c \partial t} \end{bmatrix} + \begin{bmatrix} f_x^a \\ f_\theta^a \end{bmatrix}, \tag{2}$$

where r denotes the radial (normal to the cell wall) direction, r_c is the cell radius, and u_x and u_θ are two components of the wall displacement;

The functions f_x^a and f_θ^a are given by the equations (e.g., Spector *et al.*, 1999)

$$\begin{aligned} f_x^a &= -(C_{11}\varepsilon_x^a + C_{12}\varepsilon_\theta^a), \\ f_\theta^a &= -(C_{12}\varepsilon_x^a + C_{22}\varepsilon_\theta^a), \end{aligned} \tag{3}$$

where ε_x^a and ε_θ^a are the components of the active strain determined in the microchamber experiment under low-frequency conditions (Dallos *et al.*, 1993).

In our model, the local moduli C_{ij} are voltage-dependent because they are functions of the whole cell stiffness, and the cell stiffness depends on the cell's membrane potential. The dependence of moduli C_{ij} on the cell's stiffness is described by the following equations (Spector *et al.*, 1999):

$$\begin{aligned} C_{11} &= 0.25C_{22} + 2.08\gamma, \\ C_{12} &= 0.5C_{22} + 1.08\gamma, \\ C_{22} &= 0.2 + 0.8 \times 10^{-3}/\gamma, \end{aligned} \tag{4}$$

where both C_{ij} and the whole cell stiffness γ are in the units of N/m. The voltage dependence of cell stiffness $\gamma(V_0)$ can be approximated as (He and Dallos, 2000)

$$\gamma = 10^{-3}\left\{ \frac{k_1}{1 + e^{(-k_2 V_c + k_3)}\left[1 + e^{(-k_4 V_c + k_5)}\right]} + k_6 \right\}, \tag{5}$$

where γ is in the unit of N/m; V_c is the command voltage (mV); and k_1=8.2, k_2=−0.0005, k_3=−0.46, k_4=−0.013, k_5=0.4, k_6=2.38. We adjusted parameter k_6 to make the moduli C_{ij} estimated at the reference point (*in vitro* normal resting potential) consistent with our previous data (Spector *et al.*, 1999; Liao *et al.*, 2005).

The proposed model can be applied to the analysis of the OHC high-frequency performance both in the microchamber experiment and under physiological conditions. In the former case, the cell's transmembrane potential is the sum of the cell's resting potential and a sinusoidal driving potential. The driving potential is determined by the AC component of command voltage generated in the microchamber. In the latter (physiological) case, the transmembrane potential of the cell is the sum of the cell's resting potential and the receptor potential. Normally, the receptor potential is a few millivolts, much smaller than the resting potential of about −70 mV. In the analysis of the high-frequency microchamber experiment, Frank *et al.* (1999) did not report explicitly the amplitude of the driving potential; instead they presented their results in a normalized form. Our interpretation of the Frank *et al.* (1999) results is that their driving potential was small compared to the resting (equilibrium) potential. Otherwise, the corresponding amplitudes would have been reported since the cellular characteristics involved in the experiment are voltage-dependent.

Thus, in our analysis below, we linearize the original nonlinear Eq. (2) about the point of the resting potential assuming that the driving (receptor) potential is much smaller. Also, to simplify the discussion, we will refer to the two potentials involved in the analysis as the resting and driving potentials. In the physiological case, these two potentials should be interpreted as the resting and receptor potentials, respectively. As a result of the introduced linearization, Eq. (2) takes the following form

$$\begin{bmatrix} N_x \\ N_\theta \end{bmatrix} = \begin{bmatrix} C_{11}(V_0) & C_{12}(V_0) \\ C_{12}(V_0) & C_{22}(V_0) \end{bmatrix} \begin{bmatrix} \dfrac{\partial u_x}{\partial x} \\ \dfrac{u_r}{r_c} \end{bmatrix} + \begin{bmatrix} \eta & -\eta \\ -\eta & \eta \end{bmatrix} \begin{bmatrix} \dfrac{\partial^2 u_x}{\partial x \partial t} \\ \dfrac{\partial u_r}{r_c \partial t} \end{bmatrix} + V \begin{bmatrix} \dfrac{\partial f_x^a(V_0)}{\partial V} \\ \dfrac{\partial f_\theta^a(V_0)}{\partial V} \end{bmatrix}, \tag{6}$$

where V_0 is the resting potential and V is the driving potential. According to Eq. (3), we have

$$\begin{aligned} f_x^a &= \frac{\partial f_x^a}{\partial V} V = -\left[\frac{\partial C_{11}(V_0)}{\partial V} \varepsilon_x^a(V_0) + C_{11}(V_0) \frac{\partial \varepsilon_x^a(V_0)}{\partial V} + \frac{\partial C_{12}(V_0)}{\partial V} \varepsilon_\theta^a(V_0) + C_{12}(V_0) \frac{\partial \varepsilon_\theta^a(V_0)}{\partial V} \right] V, \\ f_\theta^a &= \frac{\partial f_\theta^a}{\partial V} V = -\left[\frac{\partial C_{12}(V_0)}{\partial V} \varepsilon_x^a(V_0) + C_{12}(V_0) \frac{\partial \varepsilon_x^a(V_0)}{\partial V} + \frac{\partial C_{22}(V_0)}{\partial V} \varepsilon_\theta^a(V_0) + C_{22}(V_0) \frac{\partial \varepsilon_\theta^a(V_0)}{\partial V} \right] V, \end{aligned} \tag{7}$$

where the voltage derivatives of the local moduli are derived by using the chain rule applied to Eqs. (4) and (5).

The stress and displacement in Eq. (1) can be expressed in terms of Fourier series in the cell wall domain and fluid domain. Then, the Fourier series are substituted into the governing equations for the corresponding domain, and the boundary conditions are taken into account. Finally, the cell end displacement u_{end} can be calculated. The force acting on the constraint is obtained as

$$F_{\text{end}} = k_{\text{constr}} u_{\text{end}}, \tag{8}$$

where k_{constr} is the stiffness of the cell constraint, represented by a spring attached at the cell's end. The force calculated by this equation is equal to the active force generated by the cell as a result of its electrical stimulation. Other details of the model can be found in the Appendix.

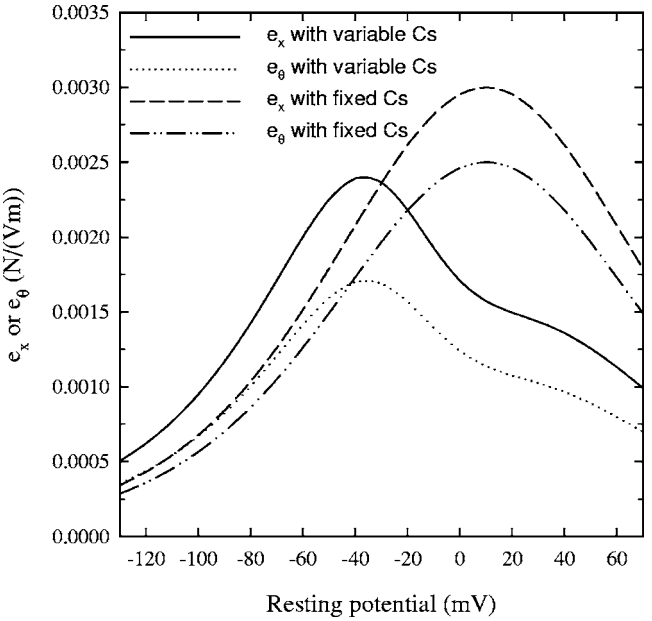

FIG. 2. The coefficients e_x and e_θ, the components of the active force per unit transmembrane potential as functions of the resting potential in the microchamber experiment. The *in vitro* normal resting potential (without electrical stimulation) in the isolated OHC in the microchamber is around −30 mV (Ashmore and Meech, 1986; He and Dallos, 2000). The *in vivo* OHC normal resting potential is around −70 mV. The solid (e_x) and dotted (e_θ) lines correspond to the general case of the moduli C_{ij} being variable with the cell stiffness and, therefore, voltage dependent. The dashed (e_x) and dash-dotted (e_θ) lines correspond to the case of the fixed (voltage-independent) moduli C_{ij}.

III. RESULTS

The presentation of the results in Figs. 2–5 is organized as follows. To emphasize the effect of the voltage-dependent stiffness, each parameter of the cell is presented for fixed C_{ij} (stiffness of the cell is fixed and voltage-independent) and for variable C_{ij} (voltage-dependent stiffness is taken into account). Besides that, Figs. 3–5 are meant to show the active force per unit transmembrane potential as a function of three parameters, resting potential, frequency, and the stiffness of the constraint. In order to do that, each of the Figs. 3–5 corresponds to one of the values of the constraint stiffness, and it is presented in a three-panel format. The panels (a) in Figs. 3–5 emonstrate 3-D surfaces of the force as a function of frequency and resting potential. In each figure, the panels (b) and (c) present 2-D cross sections of the 3-D surface shown in the panel (a), and these cross sections correspond

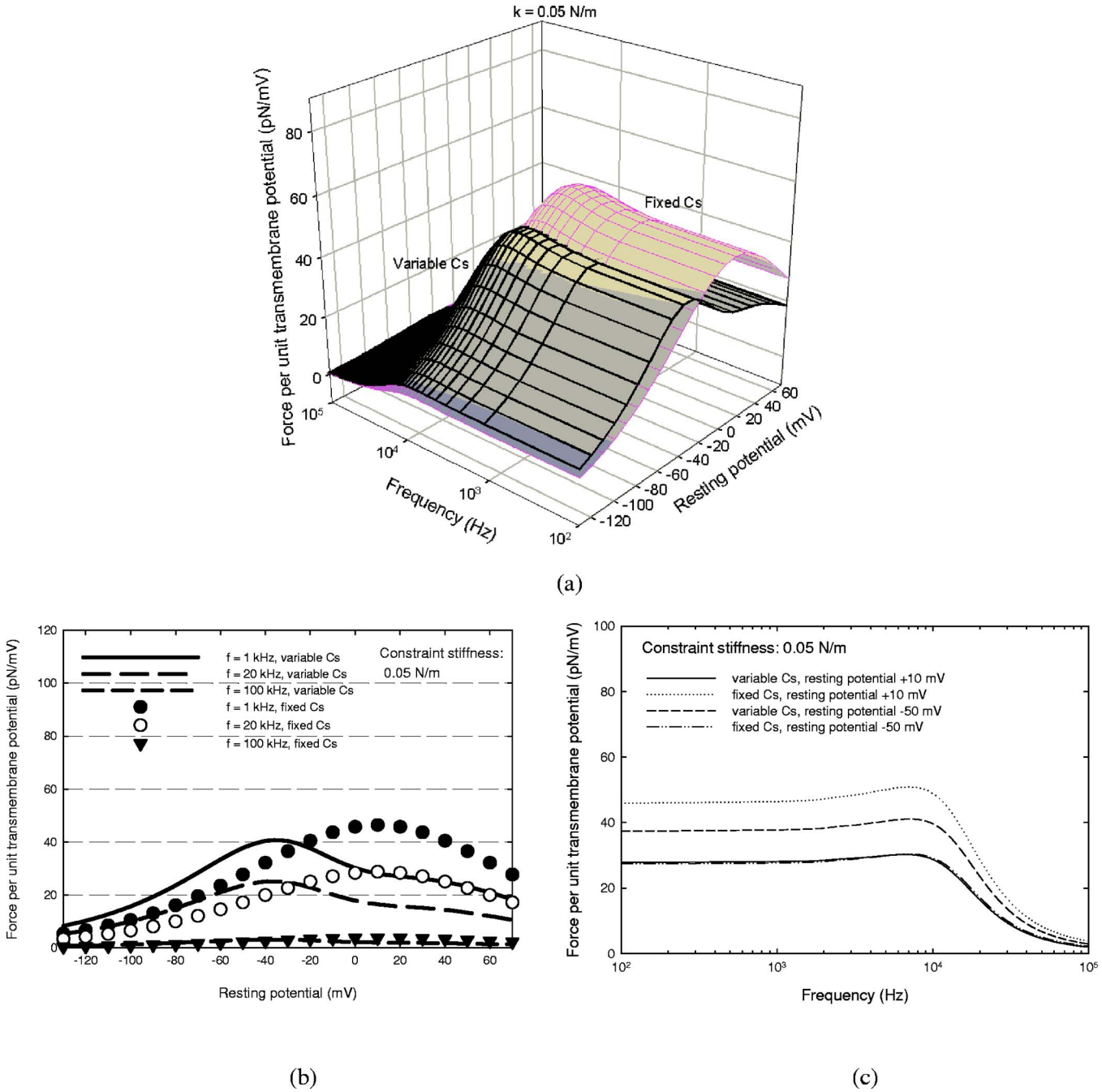

FIG. 3. The OHC active force per unit transmembrane potential as a function of frequency and resting potential in the microchamber experiment, and the value of the constraint stiffness is fixed and equal to 0.05 N/m. The *in vitro* normal resting potential (without electrical stimulation) in the isolated OHC in the microchamber is around −30 mV (Ashmore and Meech, 1986; He and Dallos, 2000). The *in vivo* OHC normal resting potential is around −70 mV. (a) 3-D surfaces (darker and lighter shades correspond to the variable and fixed moduli C_{ij}, respectively. (b) 2-D cross sections corresponding to three values of frequency. The solid, long-dashed, and short-dashed lines correspond to the cases of 1, 20, and 100 kHz (the moduli C_{ij} are variable and voltage-dependent). The filled circles, open circles, and black triangles correspond to the cases of 1, 20, and 100 kHz (the moduli C_{ij} are fixed and voltage-independent). (c) 2-D cross section corresponding to two values of the resting potential. The solid and dashed lines correspond to 10 and −50 mV when the moduli C_{ij} are variable and voltage-dependent. The dotted and dashed-dotted lines correspond to 10 and −50 mV when the moduli C_{ij} are fixed and voltage-independent.

to fixed frequency and fixed resting potential, respectively. Also, the panels (b) present the results for three, low (1 kHz), high (20 kHz), and very high (100 kHz) frequencies, and the panels (c) show the data for two values of the resting potential, one for −50 mV and the other for 10 mV.

In Fig. 2, we show two coefficients $e_x = \partial f_x^a / \partial V$ and $e_\theta = \partial f_\theta^a / \partial V$ given by Eq. (7) that express the active force production per unit transmembrane potential under low-frequency conditions. Figure 3 presents the active force per unit transmembrane potential as a function of frequency and resting potential for the stiffness of the constraint of 0.05 N/m. Such stiffness is close to that of the tectorial membrane (Zwislocki and Cefaratti, 1989), and it is also close to the lower limit of the stiffness of the reticular lamina overlying the OHCs (Scherer and Gummer, 2004). The data in Fig. 4 are presented for the value of the stiffness of the constraint (0.2 N/m), which is close to the upper limit of that of the reticular lamina. Finally, Fig. 5 shows the results

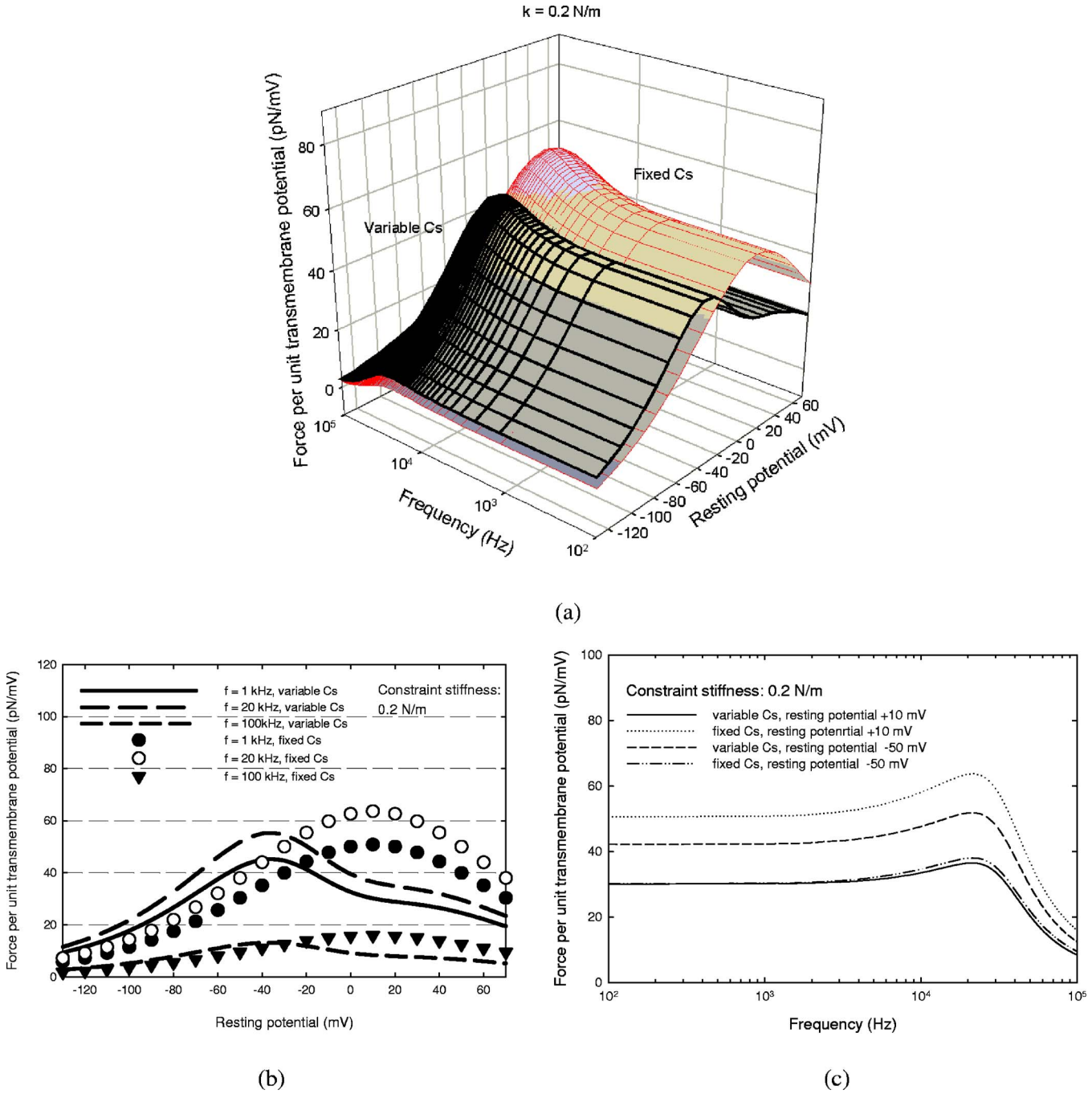

FIG. 4. The OHC active force per unit transmembrane potential as a function of frequency and resting potential in the microchamber experiment, and the value of the constraint stiffness is fixed and equal to 0.2 N/m. The *in vitro* normal resting potential (without electrical stimulation) in the isolated OHC in the microchamber is around −30 mV (Ashmore and Meech, 1986; He and Dallos, 2000). The *in vivo* OHC normal resting potential is around −70 mV. (a) 3-D surfaces (darker and lighter shades correspond to the variable, and fixed moduli C_{ij}, respectively. (b) 2-D cross sections corresponding to three values of frequency. The solid, long-dashed, and short-dashed lines correspond to the cases of 1, 20, and 100 kHz (the moduli C_{ij} are variable and voltage-dependent). The filled circles, open circles, and black triangles correspond to the cases of 1, 20, and 100 kHz (the moduli C_{ij} are fixed and voltage-independent). (c) 2-D cross section corresponding to two values of the resting potential. The solid and dashed lines correspond to 10 and −50 mV when the moduli C_{ij} are variable and voltage-dependent. The dotted and dashed-dotted lines correspond to 10 and −50 mV when the moduli C_{ij} are fixed and voltage-independent.

for the stiffness of the constraint (1.25 N/m) close to the stiffness of the basilar membrane in the cochlear basal turn (Gummer *et al.*, 1981).

IV. DISCUSSION

We developed here a computational model to estimate the OHC's active force, and our model explicitly incorporates a number of important factors associated with the biophysical properties of the cell and the environment around the cell. The biophysical factors include the orthotropic elastic moduli, piezoelectric parameters, and the viscosity of the cell wall. The effect of the environment is associated with the cell's interaction with the surrounding fluids and with the constraints imposed on the cell. The proposed scheme can be applied to both physiological and experimental conditions, and it covers two types of constraints imposed on the outer

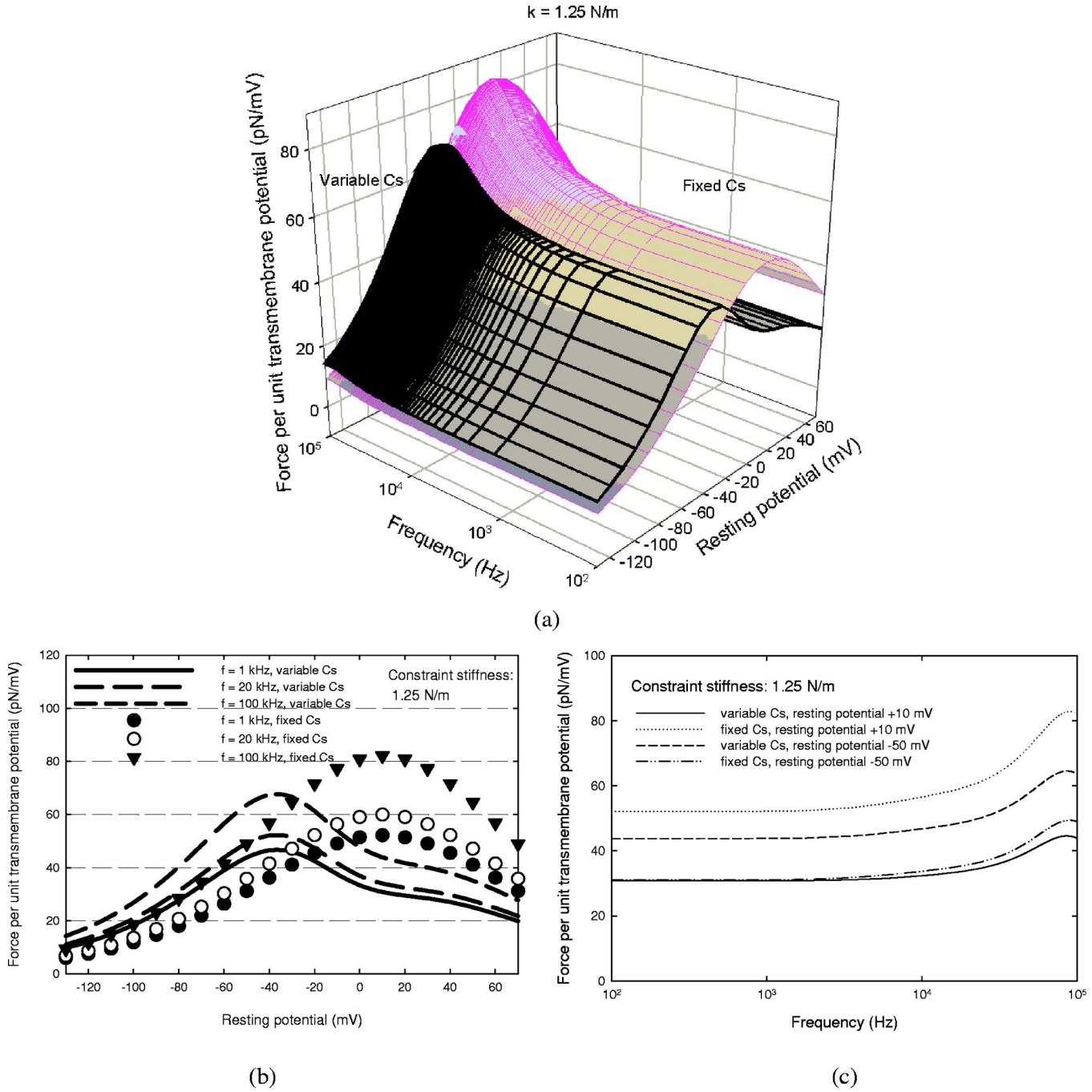

FIG. 5. The OHC active force per unit transmembrane potential as a function of frequency and resting potential in the microchamber experiment, and the value of the constraint stiffness is fixed and equal to 1.25 N/m. The *in vitro* normal resting potential (without electrical stimulation) in the isolated OHC in the microchamber is around −30 mV (Ashmore and Meech, 1986; He and Dallos, 2000). The *in vivo* OHC normal resting potential is around −70 mV. (a) 3-D surfaces (darker and lighter shades correspond to the variable, and fixed moduli C_{ij}, respectively. (b) 2-D cross sections corresponding to three values of frequency. The solid, long-dashed, and short-dashed lines correspond to the cases of 1, 20, and 100 kHz (the moduli C_{ij} are variable and voltage-dependent). The filled circles, open circles, and black triangles correspond to the cases of 1, 20, and 100 kHz (the moduli C_{ij} are fixed and voltage-independent). (c) 2-D cross section corresponding to two values of the resting potential. The solid and dashed lines correspond to 10 and −50 mV when the moduli C_{ij} are variable and voltage-dependent. The dotted and dashed-dotted lines correspond to 10 and −50 mV when the moduli C_{ij} are fixed and voltage-independent.

hair cell, the basilar and tectorial membrane complex and the AFM lever or glass fiber attached to the cell. The cases considered in Figs. 3–5 correspond to the stiffness of the springs, which are attached to the cell's ends, equal to that of the basilar membrane, tectorial membrane, and reticular lamina. Here the stiffness of two springs is the same, and to fully represent the effect of the *in vivo* constraints, future versions of the model will include the case of two springs with different properties.

The main focus of the present model is the voltage dependence of the OHC active force and the combined effect of the transmembrane potential, frequency, and constraint. The voltage dependence of the active force is associated with several voltage-dependent parameters that enter the constitutive relations given by Eqs. (1) and (2). First, the components of the active strain, ε_x^a and ε_θ^a, which express the relative length and radius changes under special, no-resultant and low-frequency conditions, vary with voltage (Dallos *et al.*,

1993). Second, the local elastic moduli, C_{ij}, depend on the whole cell stiffness [Eq. (5)], which is voltage-dependent (He and Dallos, 1999, 2000; He *et al.*, 2003). We have previously estimated (Spector *et al.*, 1998; Spector and Jean, 2003) the local moduli C_{ij} by using a combination of the data from three experiments, the osmotic challenge, axial loading, and micropipette aspiration. In those experiments, the membrane potential was not clamped and the data for different voltages were not collected. A comprehensive analysis of the voltage dependence of the local elastic moduli can be done if the three mentioned experiments are redone under the conditions of controlled voltage. However, the overall cell stiffness is a key parameter of the OHC physiology whose voltage dependence has been extensively studied in recent papers (He and Dallos, 1999, 2000; He *et al.*, 2003; Deo and Grosh, 2004). Thus, we concentrate here on the voltage dependence of the local moduli associated with the voltage-dependent cell stiffness.

In Figs. 3–5, the active force changes significantly within the considered broad ranges of the resting potential, constraint stiffness, and frequency. However, the results corresponding to low-frequency range can be compared with estimates obtained earlier. The stiffness of the glass fibers attached to the cell in the low-frequency experiments of Hallworth (1995) and Iwasa and Adachi (1997) is much smaller than that in our modeling (Figs. 3–5). Iwasa and Adachi (1997) combined their experimental measurements with a model to estimate the isometric active force per unit transmembrane potential, and they obtained the value of about 100 pN/mV. The low frequency data in Fig. 5 corresponding to the highest value of the constraint stiffness (about 60 pN/mV) are probably close to the isometric force. Thus, these data are consistent with the corresponding results of Iwasa and Adachi (1997).

The shape of the two surfaces in Figs. 3–5 corresponding to three different values of the stiffness of the constraint is similar. The surfaces obtained for fixed values of the local moduli C_{ij} (without the effect of the voltage-dependent stiffness) are bell shaped in each cross section corresponding to a certain frequency. In the general case, when the voltage dependence of the cell stiffness is taken into account, these cross sections have an inflection point in the depolarization range. The cross sections of the surfaces along the frequency axis are almost flat after that inflection point. The value and position of the peaks depend on the stiffness of constraint (see also more discussion below).

We found a significant effect of the voltage-dependent stiffness on the active force production. First, this effect causes a shift of the range of the highest sensitivity of the force from the area of depolarization to that of hyperpolarization [Figs. 3(a), 4(a), 5(a), 3(b), 4(b), and 5(b)]. The highest sensitivity of the force generation corresponds to the maximum of the force per unit transmembrane potential. In Figs. 3(b), 4(b), and 5(b) the resting potential corresponding to the maximum of the force per unit transmembrane potential shifts from about 10 mV to about −40 mV. The *in vitro* normal resting potential (without electrical stimulation) in the isolated OHC in the microchamber is around −30 mV (Ashmore and Meech, 1986; He and Dallos, 2000). The *in vivo* OHC normal resting potential is around −70 mV. Thus, due to the effect of the voltage-dependent stiffness, the point of the highest sensitivity of the active force generation becomes quite close to the physiological range of the resting potential. As a result of such shift, the sensitivity of the active force estimated at the point of the physiological potential is higher. The case of 20 kHz in Figs. 3(b), 4(b), and 5(b) is probably the most important to the analysis of the cochlear amplifier. Comparing the curves that correspond to the voltage-dependent and constant C_{ij}, we can estimate the effect of the shift of the force per unit transmembrane potential on the magnitude of this force within the physiological range. In the case of the 20-kHz frequency and for all considered values of the stiffness of the constraint, we found that the effect of the voltage-dependent cell stiffness causes an increase in the value of the force per unit transmembrane potential of around 50% in the physiological range. Another aspect of the discussed shift is associated with an increase in the nonlinearity of the active force per unit transmembrane potential as a function of voltage in the physiological range. At the beginning of the hyperpolarization area near the physiological range of the potential, Figs. 3(b), 4(b), and 5(b), the force function enters a "linear" range of almost constant slope in the cases of constant stiffness of the cell. In contrast, the slopes change significantly if the voltage-dependent stiffness is taken into account. This is because the maximal value of the force is reached at a potential of about −40 mV, instead of the value of about 10 mV observed in the case of the voltage-independent cell stiffness. Thus, the voltage-dependent stiffness causes an increase in both the sensitivity and nonlinearity of the active force as a function of voltage, and it can have important implications for the mechanics of the cochlea as a whole. We also found an additional effect of the voltage-dependent stiffness: a decrease in the force per unit transmembrane potential in the depolarization area. The values of these forces are about two times smaller than those corresponding to the case of the constant (voltage-independent) cell stiffness. This result obtained in a broader range of the transmembrane potential can be important for the analysis of the properties of the motor mechanism.

Here, we consider a number of physiologically meaningful values of the stiffness of the constraint (see Sec. III). The main effect of that stiffness is on the corner frequency and the maximum (resonance) value of the active force. In the case of relatively low values of stiffness, such as 0.05 N/m, there is a minimal resonance, and the force begins to decrease after the corner frequency of about 10 kHz. For higher values of the stiffness (0.2 N/m), a resonance appears at around 20 kHz with the ratio of the maximal value to the plateau value of about 1.2. When the constraint stiffness is high (1.25 N/m), the resonance becomes quite significant with the peak point close to 100 kHz and the maximum-to-plateau values ratio of about 1.6. The frequency roll-off in all cases is associated with the viscous losses in the cell wall and the fluids.

Here it is assumed that the viscosity of the extracellular fluid is similar to that of water. We also chose 1×10^{-7} Ns/m for the cell wall viscosity and 6

$\times 10^{-3}$ Ns/m^2 for intracellular fluid viscosity. The detailed discussion of the viscous properties of the cell wall and of two fluids can be found in Liao *et al.* (2005).

The level of the stiffness of the constraint has an interesting effect on the voltage dependence of the active force computed for different frequencies (Figs. 3–5). In the case of the stiffness equal to 0.05 N/m the highest force corresponds to the frequency of 1 kHz followed by those for 20 and 100 kHz. However, in the case of the stiffness 0.2 N/m, the highest force corresponds to the frequency of 20 kHz followed by the forces for 1 kHz and then by 100 kHz. Finally, when the stiffness of the constraint is equal to 1.25 N/m, the highest force is observed for the frequency of 100 kHz with those for 20 and 1 kHz in the second and third places, respectively. The electromechanical characteristics of the dynamic cochlea have their resonant properties that drew significant attention in recent papers. Weitzel *et al.* (2003) have analyzed a one-dimensional model of the cell with assigned inertial and piezoelectric properties, and the authors have found ultrasound resonances in the system's admittance. Grosh *et al.* (2004) have applied an electrical stimulation to the cochlea and observed high-frequency resonances in the movement of the cochlear partition. Scherer and Gummer (2004) found resonances in the electromechanical force measured at the top of the organ of Corti, and the observed resonant frequency is located within the acoustic range. In the present work, we discuss the resonant properties of the active force per unit transmembrane potential, the function described by the dynamical system of the Navier-Stokes equations for the fluids (discussed in Liao *et al.*, 2005) and the equation of the cell's wall [Eq. (2)]. These resonant properties are determined by the mechanical parameters: the stiffness of the constraint, the mass of the fluids involved in vibration of the cell, the viscosity of the fluids and the cell's wall as well as parameters of the piezoelectric nature (active strain and voltage-dependent stiffness).

We proposed here a model to analyze the active force production in an individual OHC that takes into account important biophysical properties of the cell as well as constraints imposed on the cell by the surrounding environment. We concentrated on a combined effect of the resting potential, frequency, and stiffness of the constraint. We particularly investigated the effect of the voltage-dependent stiffness of the cell and found it twofold. First, it results in higher sensitivity and nonlinearity of the OHC active force production in the physiological range. Second, it determines smaller active force in the hyperpolarization range. We have also analyzed the resonant properties of the active force as a function of voltage and the constraint stiffness. The obtained results can be important for a better understanding of the mechanism of the active force associated with somatic motility of outer hair cell and its contribution to the cochlear amplifier.

APPENDIX: MODEL EQUATIONS

The stress generated in the cross section of the cell wall is balanced by the tractions on the cell wall surface due to the surrounding fluids. The viscous intracellular and extracellular fluids are governed by linearized Navier-Stokes equations. The cell wall is considered as viscoelastic and piezoelectric material.

The equilibrium equations for the cell wall are

$$N_\theta = \sigma_r r_c, \tag{A1}$$

$$N_x = -\int_a^x \sigma_x d\bar{x} + N_{\text{end}} + N_{\text{spring}}, \tag{A2}$$

where σ_x and σ_r are two components of traction acting on the cell wall surface, and N_{end} and N_{spring} are the stress resultants generated at the cell end by the closed end and constraint, respectively. The constraint is treated as a spring, and therefore

$$N_{\text{spring}} = -\frac{k_{\text{spring}}}{2\pi r_c} u_{\text{end}}, \tag{A3}$$

where r_c is the cell radius. The closed end is treated as an oscillatory rigid plate and is subject to fluid resistance, which is transmitted and applied to the cell wall. This force is calculated by

$$N_{\text{end}} = -\frac{k_{\text{end}}}{2\pi r_c} u_{\text{end}}, \tag{A4}$$

where

$$k_{\text{end}} = 16\left[\frac{i\lambda^2}{6} + (1.32e^{i0.27\pi}\lambda)\right]\mu r_c (i\omega) e^{i\omega t}, \tag{A5}$$

and $\lambda^2 = \rho\omega r_c^2/\mu$, μ is fluid dynamic viscosity, ρ is fluid density, ω is circle frequency, and i is $\sqrt{-1}$ (Zhang and Stone, 1998). It should be mentioned that the method we use does not include the complete interaction of the fluid flow, the cell's wall, and the cell's closed ends, such as an additional radial stress in the cell wall as a consequence of the cell ends pushing back and forth the intracellular fluid. However, Tolomeo (1995) did consider the effect of the cell's closed ends and, on the basis of his theoretical approach, found this effect insignificant. By using a simplified approach, our previous paper (Liao *et al.*, 2005) compared the difference between the results for the closed-end and open-end conditions, and also found it to be insignificant.

Finally, the solution in terms of the Fourier coefficient of the cell wall displacement is obtained by this equation:

$$\mathbf{u}_{\text{cell}} = [\mathbf{k}_{\text{cell}} + \mathbf{k}_{\text{fluid}} + \mathbf{k}_{\text{end}} + \mathbf{k}_{\text{spring}}]^{-1}(-\boldsymbol{\sigma}_{\text{piez}}), \tag{A6}$$

where $\mathbf{u}_{\text{cell}}$ and $\boldsymbol{\sigma}_{\text{piez}}$ are, respectively, the vectors of the Fourier coefficients of the cell wall displacement and the stress due to electrical stimulation of the cell. Also, $\mathbf{k}_{\text{cell}}$, $\mathbf{k}_{\text{fluid}}$, $\mathbf{k}_{\text{end}}$, and $\mathbf{k}_{\text{spring}}$ are the matrices that determine the stiffness associated with the cell wall, fluids, closed end, and constraint, respectively (Liao *et al.*, 2005).

Adachi, M., and Iwasa, K. H. (**1997**). "Effect of diamide on force generation and axial stiffness of the cochlear outer hair cell," Biophys. J. **73**, 2809–2818.

Ashmore, J. F., and Meech, R. W. (**1986**). "Ionic basis of membrane potential in outer hair cells of guinea pig cochlea," Nature (London) **322**, 368–371.

Brownell, W. E., Bader, C. D., Bertrand, D., and de Ribaupierre, Y. (**1985**). "Evoked mechanical responses of isolated cochlear outer hair cells," Science **224**, 194–196.
Brownell, W. E., Spector, A. A., Raphael, R. M., and Popel, A. S. (**2001**). "Micro- and Nanomechanics of the Cochlear Outer Hair Cell," Annu. Rev. Biomed. Eng. **3**, 169–194.
Dallos, P. (**1996**). "Overview: cochlear neurobiology," in *The Cochlear*, edited by P. Dallos, A. N. Popper, and R. R. Fay, (Springer-Verlag, New York), pp. 1–43.
Dallos, P., Evans, B. N., and Hallworth, R. (**1991**). "Nature of the motor element in electrokinetic shape changes of cochlear outer hair cells," Nature (London) **350**, 155–157.
Dallos, P., Hallworth, R., and Evans, B. N. (**1993**). "Theory of electrically driven shape changes of cochlear outer hair cells," J. Neurophysiol. **70**, 299–323.
Deo, N., and Grosh, K. (**2004**). "Two-state model for outer hair cell stiffness and motility," Biophys. J. **86**, 3519–3528.
Dong, X. X., Ospeck, M., and Iwasa, K. H. (**2002**). "Piezoelectric reciprocal relationship of the membrane motor in the cochlear outer hair cell," Biophys. J. **82**, 1254–1259.
Evans, E. A., and Skalak, R. (**1980**). *Mechanics and Thermodynamics of Biomembranes* (CRC, Boca Raton, FL).
Frank, G., Hemmer, W., and Gummer, A. W. (**1999**). "Limiting dynamics of high-frequency electromechanical transduction of outer hair cells," Proc. Natl. Acad. Sci. U.S.A. **96**, 4420–4425.
Gale, J. E., and Ashmore, J. F. (**1994**). "Charge displacement induced by rapid stretch in the basolateral membrane of the guinea-pig outer hair cell," Proc. R. Soc. London **255**, 243–249.
Gale, J. E., and Ashmore, J. F. (**1997a**). "An intrinsic frequency limit to the cochlear amplifier," Nature (London) **389**, 63–66.
Gale, J. E., and Ashmore, J. F. (**1997b**). "The outer hair cell motor in membrane patches," Pfluegers Arch. **434**, 267–271.
Geisler, C. D. (**1998**). *From Sound to Synapse: Physiology of the Mammalian Ear* (Oxford U. P., Oxford, England).
Grosh, K., Zheng, J., Zou, Y., de Boer, E., and Nuttall, A. L. (**2004**). "High-frequency electromotile responses in the cochlea," J. Acoust. Soc. Am. **115**, 2178–2184.
Gummer, A. W., Johnstone, B. M., and Armstrong, N. J. (**1981**). "Direct measurement of basilar membrane stiffness in the guinea pig," J. Acoust. Soc. Am. **70**, 1298–1309.
Hallworth, R. (**1995**). "Passive compliance and active force generation in the guinea pig outer hair cell," J. Neurophysiol. **74**, 2319–2328.
Hallworth, R. (**1997**). "Modulation of OHC force generation and stiffness by agents known to affect hearing," in *Diversity in Auditory Mechanics*, edited by E. R. Lewis, G. R. Long, R. F. Lyon, P. M. Narins, C. R. Steele, and E. Hecht-Poinar (World Scientific, Singapore), pp. 524–530.
He, D. Z., and Dallos, P. (**1999**). "Somatic stiffness of cochlear outer hair cells is voltage-dependent." Proc. Natl. Acad. Sci. U.S.A. **96**, 8223–8228.
He, D. Z., and Dallos, P. (**2000**). "Properties of voltage-dependent somatic stiffness of cochlear outer hair cells," J. Assoc. Res. Otolaryngol. **1**, 64–81.
He, D. Z., Jia, S., and Dallos, P. (**2003**). "Prestin and the dynamic stiffness of cochlear outer hair cells," J. Neurosci. **23**, 9089–9096.
Iwasa, K. H. (**1994**). "A membrane motor model for the fast motility of the outer hair cell," J. Acoust. Soc. Am. **96**, 2216–2224.
Iwasa, K. H. (**2001**). "A two-state piezoelectric model for outer hair cell motility," Biophys. J. **81**, 2495–2506.
Iwasa, K. H., and Adachi, M. (**1997**). "Force generation in the outer hair cell of the cochlea," Biophys. J. **73**, 546–555.
Liao, Z., Popel, A. S., Brownell, W. E., and Spector, A. A. (**2005**). "Modeling high-frequency electromotility of cochlear outer hair cell in microchamber experiment," J. Acoust. Soc. Am. **117**, 2147–2157.
Liberman, M. C., Gao, J., He, D. Z., Wu, X., Jia, S., and Zuo, J. (**2002**). "Prestin is required for electromotility of the outer hair cell and for the cochlear amplifier," Nature **419**, 300–304.
Lue, A. J., Zhao, H. B., and Brownell, W. E. (**2001**). "Chlorpromazine alters outer hair cell electromotility," Otolaryngol.-Head Neck Surg. **125**, 71–76.
Mountain, D. C., and Hubbard, A. E. (**1994**). "A piezoelectric model of outer hair cell function," J. Acoust. Soc. Am. **95**, 350–354.
Oghalai, J. S., Zhao, H.-B., Kutz, W. J., and Brownell, W. E. (**2000**). "Voltage- and tension-dependent lipid mobility in the outer hair cell plasma membrane," Science **287**, 658–661.
Oliver, M., He, D. Z., Klocker, N., Ludwig, J., Schulte, U., Waldegger, J. P., Ruppenberg, P., Dallos, P., and Fakler, B. (**2001**). "Intracellular anions as the voltage sensor of Prestin, the outer hair cell motor protein," Science **292**, 2340–2343.
Patuzzi, R. (**1996**). "Cochlear micromechanics and macromechanics," in *The Cochlear*, edited by P. Dallos, A. N. Popper, and R. R. Fay (Springer-Verlag, New York), pp. 186–257.
Ratnanather, J. T., Spector, A. A., Popel, A. S., and Brownell, W. E. (**1996**). "Is the outer hair cell wall viscoelastic?" in *Proceedings of the Congress in Diversity in Auditory Mechanics*, edited by E. R. Lewis, G. R. Long, R. F. Lyon, P. M. Narins, C. R. Steele, and E. Hecht-Poinar (World Scientific, Singapore), pp. 601–607.
Santos-Sacchi, J. (**1989**). "Asymmetry in voltage-dependent movements of isolated outer hair cells from the organ of Corti," J. Neurosci. **9**, 2954–2962.
Santos-Sacchi, J., and Dilger, J. P. (**1998**). "Whole cell currents and mechanical responses of isolated outer hair cells," Hear. Res. **35**, 143–150.
Santos-Sacchi, J., and Navarrete, E. (**2002**). "Voltage-dependent changes in specific membrane capacitance caused by prestin, the outer hair cell lateral membrane motor," Pfluegers Arch. **444**, 99–106.
Scherer, M. M., and Gummer, A. W. (**2004**). "Impedance analysis of the organ of Corti with magnetically actuated probes," Biophys. J. **87**, 1378–1391.
Shehata, W. E., Brownell, W. E., and Dieler, R. (**1991**). "Effects of salicylate on shape, electromotility and membrane characteristics of isolated outer hair cells from guinea pig cochlea," Acta Oto-Laryngol. **111**, 707–718.
Spector, A. A. (**2000**). "Thermodynamic potentials and constitutive relations for a nonlinear electroelastic biological membrane," in *Symposium on the Mechanics and Electromagnetic Materials and Structures*, edited by J. Yang and G. A. Maugin (IOS, Amsterdam).
Spector, A. A. (**2001**). "A nonlinear electroelastic model of the auditory outer hair cell," Int. J. Solids Struct. **38**, 2115–2129.
Spector, A. A., and Jean, R. P. (**2003**). "Elastic moduli of the piezoelectric cochlear outer hair cell membrane," Exp. Mech. **43**, 355–360.
Spector, A. A., Brownell, W. E., and Popel, A. S. (**1998**). "Estimation of elastic moduli and bending stiffness of the anisotropic outer hair cell wall," J. Acoust. Soc. Am. **103**, 1007–1011.
Spector, A. A., Brownell, W. E., and Popel, A. S. (**1999**). "Nonlinear active force generation by cochlear outer hair cell," J. Acoust. Soc. Am. **105**, 2414–2420.
Spector, A. A., Brownell, W. E., and Popel, A. S. (**2003**). "Effect of outer hair cell piezoelectricity on high-frequency receptor potentials," J. Acoust. Soc. Am. **113**, 453–461.
Spector, A. A., Popel, A. S., Eatock, R. A., and Brownell, W. E. (**2005**). "Mechanosensitive channels in the lateral wall can enhance the cochlear outer hair cell frequency response," Ann. Biomed. Eng. **33**, 991–1002.
Tolomeo, J. A. (1995). "Models of the structure and motility of the auditory outer hair cell," Ph.D. thesis, Stanford University.
Tolomeo, J. A., and Steele, C. R. (**1998**). "A dynamic model of outer hair cell motility including intracellular and extracellular viscosity," J. Acoust. Soc. Am. **103**, 524–534.
Ulfendahl, M. (**1997**). "Mechanical responses of the mammalian cochlea," Prog. Neurobiol. **53**, 331–80.
Weitzel, E. K., Tasker, R., and Brownell, W. E. (**2003**). "Outer hair cell piezoelectricity: Frequency response enhancement and resonance behavior," J. Acoust. Soc. Am. **114**, 1462–1466.
Zhang, W., and Stone, H. A. (**1998**). "Oscillatory motions of circular disks and nearly spherical particles in viscous flows," J. Fluid Mech. **367**, 329–358.
Zhao, H. B., and Santos-Sacchi, J. (**1999**). "Auditory collusion and a coupled couple of outer hair cells," Nature (London) **399**, 359–362.
Zheng, J., Shen, W., He, D. Z., Long, K. B., Madison, L. D., and Dallos, P. (**2000**). "Prestin is the motor protein of cochlear outer hair cell," Nature (London) **405**, 149–155.
Zwislocki, J. J., and Cefaratti, J. K. (**1989**). "Tectorial membrane II: Stiffness measurements in vivo," Hear. Res. **42**, 211–227.

Evidence for a bipolar change in distortion product otoacoustic emissions during contralateral acoustic stimulation in humans

Jörg Müller and Thomas Janssen[a)]
Hals-Nasen-Ohrenklinik, Technische Universität München, Ismaningerstraße 22, D-81675 Munich, Germany

Guido Heppelmann and Wolfgang Wagner
Hals-Nasen-Ohrenklinik, Eberhard-Karls-Universität Tübingen, Elfriede-Aulhorn-Str. 5, D-72076 Tübingen, Germany

(Received 31 March 2005; revised 6 September 2005; accepted 9 September 2005)

The aim of this study was to investigate the activity of the medial olivocochlear (MOC) efferents during contralateral (CAS) and ipsilateral acoustic stimulation (IAS) by recording distortion product otoacoustic emission (DPOAE) suppression and DPOAE adaptation in humans. The main question was: do large bipolar changes in DPOAE level (transition from enhancement to suppression) also occur in humans when changing the primary tone level within a small range as described by Maison and Liberman for guinea pigs [J. Neurosci. **20**, 4701–4707 (2000)]? In the present study, large bipolar changes in DPOAE level (14 dB on average across subjects) were found during CAS predominantly at frequencies where dips in the DPOAE fine structure occurred. Thus, effects of the second DPOAE source might be responsible for the observed bipolar effect. In contrast, comparable effects were not found during IAS as was reported in guinea pigs. Reproducibility of CAS DPOAEs was better than that for IAS DPOAEs. Thus, contralateral DPOAE suppression is suggested to be superior to ipsilateral DPOAE adaptation with regard to measuring the MOC reflex strength and for evaluating the vulnerability of the cochlea to acoustic overexposure in a clinical context. © *2005 Acoustical Society of America.* [DOI: 10.1121/1.2109127]

PACS number(s): 43.64.Jb, 43.64.Kc [BLM] Pages: 3747–3756

I. INTRODUCTION

Distortion product otoacoustic emissions (DPOAEs) are sound emissions apparently produced by the outer hair cell (OHC) system in response to a two-tone stimulation (Kemp, 1986; Brownell, 1990). DPOAEs are supposed to primarily reflect OHC activity at the f_2 place when stimulated with an adequate primary tone paradigm (Kummer *et al.*, 1995). However, there is evidence that DPOAEs are generated by two distinct cochlear sources (Whitehead *et al.*, 1992; Brown *et al.*, 1996; Shera and Guinan, 1999). The first source is located at the region of overlap of the traveling waves of the two primary tones near the f_2 place and is due to intermodulation distortion. The second source, which is unwantedly adding to the first source emission, is located at the $2f_1-f_2$ place and is suggested to reflect energy that has traveled apically from the overlap region near f_2. Thus, energy from both interacting sources yields the composite DPOAE signal. The influence of the second DPOAE source may be observed when recording DPOAEs with high frequency resolution (DPOAE fine structure). In normal-hearing subjects a pattern of dips and peaks was found in the DPOAE fine structure, which may be due to either destructive or constructive superposition of the two DPOAE sources (He and Schmiedt, 1993; Heitmann *et al.*, 1998; Talmadge *et al.*, 1999; Mauermann and Kollmeier, 2004).

OHC amplification seems to be directly influenced by the efferent medial olivocochlear (MOC) system, which originates from the medial nuclei of the superior olivary complex and is comprised of fibers that almost exclusively synapse on the base of the OHCs (Mountain, 1980; Guinan *et al.*, 1984; Brownell *et al.*, 1985; Guinan, 1996). The MOC system consists of the crossed and the uncrossed feedback loops, both of which project onto the ipsilateral OHCs. The crossed MOC fibers are stimulated ipsilaterally while the uncrossed fibers are stimulated contralaterally (see Fig. 1 in Liberman *et al.*, 1996). There are several assumptions concerning the physiological function of the MOC system, i.e., improvement of detection of transient low-level stimuli in the presence of background noise (Winslow and Sachs, 1987; Liberman and Guinan, 1998) or protection from acoustic overexposure (Cody and Johnstone, 1982; Reiter and Liberman, 1995; Maison and Liberman, 2000; Luebke and Foster, 2002).

The function of the MOC system (MOC reflex) can be assessed by monitoring changes in DPOAE amplitude. There are two different recording methods, which quantify either the effect induced by the contralaterally or by the ipsilaterally stimulated pathway. The contralateral pathway can be examined by comparing the DPOAE steady-state level mea-

[a)]Author to whom correspondence should be addressed. Electronic mail: t.janssen@lrz.tum.de

sured in the presence and in the absence of contralateral acoustic stimulation (CAS). This recording technique is commonly referred to as contralateral DPOAE suppression (e.g., Collet *et al.*, 1990). The ipsilateral pathway can be examined by measuring the post-onset time course of the DPOAE level during ipsilateral acoustic stimulation (IAS) by the primary tones. The difference between the DPOAE level at onset and the level at steady state provides a measure for the adaptation magnitude. This recording technique is commonly referred to as ipsilateral DPOAE adaptation (e.g., Liberman *et al.*, 1996). Both DPOAE suppression and adaptation are suggested to be a means for evaluating the MOC system's reflex strength (e.g., Collet *et al.*, 1990; Maison and Liberman, 2000).

The effect of CAS on DPOAEs has been extensively studied in animals (e.g., Puel and Rebillard, 1990; Puria *et al.*, 1996) and humans (e.g., Collet *et al.*, 1990; Moulin *et al.*, 1993; Williams and Brown, 1995; Maison *et al.*, 2000). The observed change in DPOAE level due to CAS was found to be more commonly a decreasing effect (suppression) than an increasing effect (enhancement) and amounted to only some dB, depending on the type of the contralateral stimulus and the primary tone level setting. In general, with increasing contralateral stimulus bandwidth and level, and with decreasing primary tone level, the suppression effect increased (e.g., Janssen *et al.*, 2003). However, in the literature there are no data concerning systematic $L_2|L_1$ variation across a major primary tone level range for contralateral DPOAE suppression in humans.

Compared to contralateral DPOAE suppression there is little data concerning ipsilateral DPOAE adaptation in the literature. Ipsilateral DPOAE adaptation, first measured by Liberman *et al.* (1996) in cats, was reported to exhibit a decrease in steady-state DPOAE level of up to 6 dB. In humans, however, DPOAE adaptation was observed to be lower than 1 dB on average across subjects (Agrama *et al.*, 1998; Kim *et al.*, 2001; Bassim *et al.*, 2003).

Due to the rather small contralateral DPOAE suppression and ipsilateral DPOAE adaptation effects in humans the clinical applicability of DPOAEs for investigating the function of the MOC efferents seems to be restricted. Maison and Liberman (2000) paved the way for getting higher DPOAE adaptation effects. They showed that in guinea pigs at particular $L_2|L_1$ level combinations, predominantly in notched regions of DPOAE input/output (I/O) functions, a small shift in primary tone level could yield a large bipolar change in adaptation magnitude, typically progressing from an increasing (enhancement) to a decreasing (suppression) post-onset time course. The difference between maximum suppression and maximum enhancement amounted up to 30 dB. Until now, bipolar changes of that amount have not been found in humans even though in some studies DPOAE adaptation behavior was examined when changing primary tone levels within a wide range (Kim *et al.*, 2001; Meinke *et al.*, 2004).

The purpose of the present study was to further investigate DPOAE suppression and adaptation in order to find out whether large bipolar changes in DPOAE level also occur in humans when changing the primary tone level in small steps as described by Maison and Liberman (2000) for guinea pigs. In our study, DPOAE suppression and DPOAE adaptation were measured at particular frequencies, i.e., when the DPOAE fine structure exhibited pronounced dips. This was done because the second DPOAE source is suggested to generate the dips and peaks in the fine structure (e.g., Mauermann and Kollmeier, 2004) and to be the reason for the observed bipolar change in DPOAE level (Kujawa and Liberman, 2001). Also, in view of a clinical application for assessing MOC reflex strength and with that presumably cochlear vulnerability, this study investigated the reproducibility of the DPOAE measures.

II. METHODS

A. Subjects

Seven subjects (ten ears) with normal hearing participated in the study. The subjects (four male, three female) were aged between 19 and 30 years. Clinical audiometry showed that hearing thresholds were 15 dB HL or lower at audiometric frequencies between 500 and 8000 Hz. For all subjects tympanometry showed normal middle ear function. A brief medical history was taken from each subject documenting the absence of ear-related complaints, ear infections, ear surgery, and ototoxic medication use. Moreover, ipsilateral and contralateral stapedius reflex thresholds were measured at 4 kHz. The median stapedius reflex threshold amounted to 90 dB SPL, while the minimum reflex threshold was 75 dB SPL. All measurements were conducted in a sound-attenuated cabin while subjects were seated in a comfortable recliner.

B. Stimulus generation and DPOAE recording

DPOAE measurements were implemented on the basis of a PCMCIA DSP card (Communication Automation Corporation). Ipsilateral stimuli were presented and DPOAEs were recorded using an ER-10C (Etymotic Research) ear probe. For contralateral acoustic stimulation an FZ-PRC1 (Fischer-Zoth) sound probe was used. Measurement and evaluation software was custom-made using MATLAB (Mathworks). Primary tone levels were adjusted according to an in-the-ear-calibration strategy. Contralateral noise signals were calibrated *a priori* in an ear simulator (Brüel & Kjær Type 4157).

DPOAEs were elicited in response to a stimulation with two primary tones presented simultaneously at the frequencies f_1 and f_2. The frequency ratio was set to $f_2/f_1=1.2$ for all experimental conditions. The distortion component at $2f_1-f_2$ was exclusively evaluated. DPOAEs were accepted as valid for signal-to-noise ratios (SNRs) exceeding 6 dB. The noise floor level was computed by averaging the levels at six frequencies located around the DPOAE frequency. During the measurement, if a DPOAE value failed to fulfill this criterion or if the noise level between two consecutive measurements increased by more than 5 dB, the measurement of the DPOAE was repeated with the current parameter setting at least twice or until the emission was accepted as valid. Moreover, a technical distortion criterion was implemented. Technically distorted data were discarded when the levels of at least seven out of ten frequency bins at other

distortion product components (e.g., $2f_2-f_1$) around the DPOAE component at $2f_1-f_2$ exceeded an SNR of 10 dB. The SNR criterion was not checked at single DPOAE adaptation measurements since the measurement time was, especially in cases of responses with low emission levels, too short for sufficient time domain averaging.

C. DPOAE fine structure measurement procedure

The DPOAE fine structure [DPOAE level $L_{dp}(f_2)$] was measured between $f_2=3000$ and 5016 Hz with a frequency resolution of $\Delta f=47$ Hz. The primary tone level L_2 was set to 40, 30, and 20 dB SPL, whereas L_1 was set according to the equation $L_1=0.4\,L_2+39$ dB SPL (Janssen *et al.*, 1995; Kummer *et al.*, 2000). This level setting was used to account for the nonlinear interaction of the two primaries at the DPOAE generation site at the f_2 place (Boege and Janssen, 2002). The averaging time for recording DPOAEs was set to 4.5 s and the pause time between two measurement settings to 1 s. The total measuring duration amounted to about 15 min.

For further evaluation, the dip depth $d_{\mathrm{dip},L2}(f_2)$ was calculated by adding up the DPOAE level differences between f_2 and both neighboring frequencies for a constant L_2. The total dip depth $d_{\mathrm{dip}}(f_2)$ was defined as the average across $d_{\mathrm{dip},L2}(f_2)$ for the three L_2 level settings ($L_2=40,30,20$ dB SPL). Equation (1) illustrates the calculation of the dip depth values:

$$d_{\mathrm{dip},L2}(f_2)=[L_{dp}(L_2,f_2)-L_{dp}(L_2,f_2-\Delta f)]+[L_{dp}(L_2,f_2)-L_{dp}(L_2,f_2+\Delta f)],$$
$$d_{\mathrm{dip}}(f_2)=[d_{\mathrm{dip},40}(f_2)+d_{\mathrm{dip},30}(f_2)+d_{\mathrm{dip},20}(f_2)]/3. \quad (1)$$

Please note that in the following the term dip depth is used synonymously with the total dip depth d_{dip}. The standard deviation of d_{dip} across the entire frequency range was used as a measure for quantifying the roughness of the DPOAE fine structure.

For reproducibility examinations, DPOAE fine structure was measured for one subject (J.M.) with the parameter setting described above, ten times on different days and eight times on one day with constant and varying ear probe position, respectively.

D. Contralateral DPOAE suppression measurement procedure

Contralateral DPOAE suppression was measured at two frequencies, depending on the results of the DPOAE fine structure. The first frequency $f_{2,\mathrm{dip}}$ was located at the deepest dip in the DPOAE fine structure. The second frequency $f_{2,\mathrm{flat}}$ was at a location where there was no major change of L_{dp} across frequency. If there was no completely flat region, a point at a peak in the fine structure was chosen [$d_{\mathrm{dip}}(f_2)>-0.2$ dB].

The effect of CAS on DPOAEs was investigated at different $L_2|L_1$ combinations. L_2 was shifted from 60 down to 20 dB SPL in steps of 5 dB. For each L_2, L_1 was changed symmetrically around the center level $L_{1,\mathrm{center}}=0.4\,L_2+39$ dB SPL. The offset $L_{1,\mathrm{offset}}$ around the center level was changed from -10 to $+10$ dB in steps of 2 dB. Thus, altogether 99 $L_2|L_1$ combinations were examined. The averaging time for recording DPOAEs was set to 4.5 s and the pause time between two consecutive DPOAE measurements to 1 s as it was done for recording DPOAE fine structure. For each level setting, DPOAEs were recorded first in the absence and then in the presence of CAS. The contralateral stimulus was started 0.5 s before the onset of the ipsilateral primary tones and ended 0.5 s after their termination. The contralateral stimulus consisted of broadband noise (100 Hz to 10 kHz), which was presented with a stimulus level of 60 dB SPL. The total measuring duration for each frequency amounted to about 25 min.

Please note that the DPOAE level difference between measurements with and without CAS is in the following labelled ΔL_{dp}. Positive values of ΔL_{dp} mean enhancement, negative values mean suppression. For evaluating the MOC reflex strength, corresponding to the definition of Maison and Liberman (2000), a value was defined, which in the following is referred to as the ΔL_{dp} range. It was defined as the difference between maximum enhancement and maximum suppression. In the very few cases where no enhancement occurred, it was defined as the difference between minimum and maximum suppression.

For reproducibility examinations, the CAS effect on DPOAEs was measured for one subject (J.M.) at one frequency ($f_{2,\mathrm{dip}}$) ten times on different days and eight times on one day with constant and varying ear probe position, respectively.

E. Ipsilateral DPOAE adaptation measurement procedure

Corresponding to contralateral DPOAE suppression measurements, ipsilateral DPOAE adaptation was measured at frequencies $f_{2,\mathrm{dip}}$ and $f_{2,\mathrm{flat}}$. At least three different $L_2|L_1$ combinations were selected for each frequency. The first level combination was that one in the primary tone level matrix that resulted in maximum DPOAE suppression during CAS, while the second level combination was that one leading to maximum DPOAE enhancement during CAS. These two level combinations were chosen based on the assumption that for ipsilateral adaptation a distinct change in DPOAE level should appear if there is a similar behavior for CAS and IAS effects. However, the DPOAE level and hence the SNR at level combinations leading to maximum suppression or enhancement, respectively, were usually low. As a consequence, depending on how much time the subject could spare, additional measurements were carried out at one to four other level combinations with varying but normally rather low suppression or enhancement during CAS but with high emission levels. The DPOAE adaptation measurements were conducted immediately after DPOAE suppression measurements with the same sound probe position in order to attain best possible comparability.

DPOAE adaptation was measured using monaural primary tone stimulation in order to exclusively assess the function of the crossed MOC system. The rise/fall times of the

stimuli were zero. The measurement time for recording the DPOAE time course as well as the pause time between two measurements were set to 2 s. The number of consecutive measurements for time domain averaging was set to 100. The total measuring duration for one level combination and for one frequency amounted to about 7 min.

In order to check the adaptation behavior in notched regions of DPOAE I/O functions, as suggested by Maison and Liberman (2000), for three subjects adaptation was measured at seven primary tone level combinations (constant L_2 and varying L_1) around a distinct notch in the DPOAE I/O function. L_2 was chosen taking into account all cross sections of the suppression matrix with L_2 held constant while L_1 was varied, resulting in DPOAE I/O functions with L_{dp} plotted above L_1. L_2 was selected depending on which of the I/O functions showed (*i*) the most pronounced notch and (*ii*) a major bipolar change of ΔL_{dp} from suppression to enhancement. L_1 was varied from −3 to +3 dB in steps of 1 dB around the deepest point of the notch.

For reproducibility examinations, DPOAE adaptation was measured for one subject (J.M.) at one frequency (f_2 =4219 Hz) and one level combination ($L_2|L_1$=60|67 dB SPL) eight times on one day with constant and varying ear probe position, respectively. The level combination was chosen since reliable DPOAE adaptation measurements were only possible at high primary tone levels.

For evaluating DPOAE adaptation, the DPOAE post-onset time course was calculated using the heterodyne technique described by Kim *et al.* (2001). A Blackman shaped filter with a limiting frequency of 120 Hz was applied. An exponential fitting function was calculated on the basis of the DPOAE level time course. Following Kim *et al.* (2001) a nonlinear simplex fitting procedure was used to obtain the least-squared difference between the DPOAE envelope level and the exponential fitting function. For this step, a short offset period (30 ms) of the DPOAE envelope level at the beginning and the same period at the end of the stimulus were excluded in order to remove transients at the two ends. The following fitting function shown in Eq. (2) was applied:

$$L_{dp}(t) = L_{ss} - m \exp(-t/\tau). \tag{2}$$

$L_{dp}(t)$ is the fit for the DPOAE envelope level as a function of time t. L_{ss} represents the steady-state DPOAE level, m the magnitude, and τ the time constant of adaptation. Please note that a positive m means an increasing (enhancement) and a negative m a decreasing (suppression) adaptation time course. The initial estimate for L_{ss} was calculated from the average level of the last second of the time course signal. The initial estimate for m was set to 0.7 dB and for τ to 70 ms. The values were chosen to be within the margins of the results of other studies of DPOAE adaptation in humans (Kim *et al.*, 2001; Bassim *et al.*, 2003). The quality of the fit is given as "the variance accounted for" (VAF), which is defined as shown in Eq. (3):

$$\mathrm{VAF} = 1 - r, \tag{3}$$

where r is the ratio of (*i*) the mean-squared difference between the fitting function and the DPOAE envelope level and (*ii*) the variance of the DPOAE level. The value of VAF ranges from 0 (poor fit) to 1 (perfect fit). In this study, fitting functions were regarded as valid for VAF values exceeding 0.1.

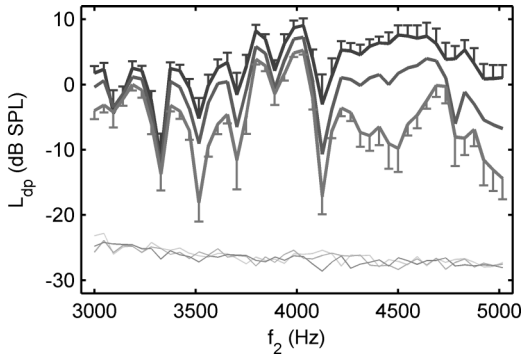

FIG. 1. DPOAE fine structure reproducibility for one subject. Data were averaged across ten measurements conducted on different days. The three top lines show from top to bottom mean L_{dp} plotted across frequency for L_2=40, 30, and 20 dB SPL. The standard deviation is given for data measured at L_2=40 dB SPL and L_2=20 dB SPL. The three bottom lines represent the particular mean noise floor levels.

III. RESULTS

A. DPOAE fine structure

1. Dips and their reproducibility in a single subject

DPOAE fine structure across frequency and its reproducibility was examined in one subject (J.M.) for three different test conditions. Measurements were conducted over several days (n=10), and on one day with varying (n=8) and constant (n=8) sound probe position, respectively. The result for the worst test condition, i.e., the measurement of the DPOAE fine structure on ten different days, is shown in Fig. 1.

The standard deviation of DPOAE level L_{dp} was on average across frequency 1.8 dB and was highest in the dip regions of the DPOAE fine structure. The maximum standard deviation amounted to 4.6 dB at 4125 Hz. In general, all major dips were present in all repetition measurements, whereas their dip depth fluctuated across measurements. The dip depth and its variability was examined at the three deepest dips of the averaged DPOAE fine structure data with d_{dip} [see Eq. (1)] amounting to −21.0±8.1 dB at f_2=3328 Hz, −18.0±4.5 dB at 4125 Hz, and −13.6±4.0 dB at 3516 Hz. The average roughness of DPOAE fine structure (see Sec. II C) amounted to 7.2±1.0 dB.

The variability of the measures obtained on one day with varying and fixed sound probe position was lower than that obtained on several days.

2. Distribution of dips and dip depth across subjects

DPOAE fine structure was examined in all ten ears of the seven subjects. The distribution of major dips (d_{dip} < −4 dB) is shown in Fig. 2 with d_{dip} plotted across the corresponding $f_{2,\mathrm{dip}}$. The open circle and error bar show mean and standard deviation along both axes (d_{dip}=−9.2±4.4 dB, $f_{2,\mathrm{dip}}$=3735±516 Hz).

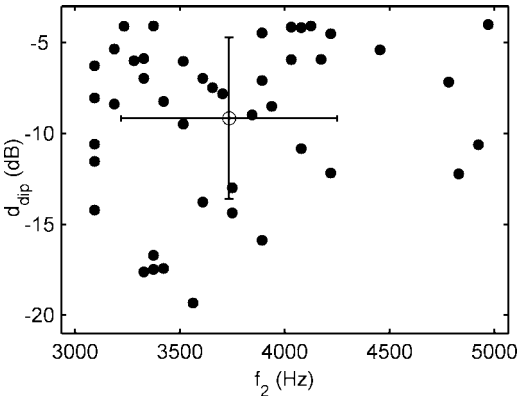

FIG. 2. Distribution of DPOAE fine-structure dips with dip depth d_{dip} [see Eq. (1)] <−4 dB for all ten ears. The mean and standard deviation are indicated by the open circle and error bars.

The average roughness of the DPOAE fine structure across subjects amounted to 4.2±1.6 dB. Splitting the frequency range at 4000 Hz, the roughness below 4000 Hz was 5.6±2.2 dB while the roughness above 4000 Hz was 2.5±1.5 dB. Thus, the fine structure was more pronounced and deeper dips occurred in the lower frequency region. Furthermore, the roughness increased with decreasing L_2 (4.0 dB at L_2=40 dB SPL, 4.7 dB at L_2=30 dB SPL, and 6.2 dB at L_2=20 dB SPL).

B. DPOAEs during contralateral acoustic stimulation (CAS)

1. Enhancement and suppression and its reproducibility in a single subject

The change in DPOAE level during CAS and its reproducibility was examined in one subject (J.M.) for three different test conditions: on several days (n=10), and on one day with varying (n=8) and constant (n=8) sound probe position, respectively. The measurements were conducted at f_2=4125 Hz, a frequency at which in the DPOAE fine structure a distinct dip occurred (see Fig. 1).

The results for the worst test condition, i.e., the measurement on ten different days, is shown in Fig. 3. Figure 3(A) shows mean L_{dp} obtained in the absence (black lines) and in the presence of CAS (gray lines) for all tested primary tone level combinations (see Sec. II D). Light gray lines at the bottom represent the average noise floor level. Cross-sections of Fig. 3(A) are shown in Figs. 3 Ca-Ci for constant L_2 (Ca: L_2=60 dB SPL, …, Ci: L_2=20 dB SPL) and in Figs. 3 Ea–Ek for constant $L_{1,\text{offset}}$ with $L_{1,\text{offset}}$ being the level offset from the center level $L_{1,\text{center}}$=0.4 L_2+39 dB SPL (Ea: $L_{1,\text{offset}}$=−10 dB, …, Ek: $L_{1,\text{offset}}$=+10 dB).

DPOAE I/O-functions (L_{dp} plotted across the primary tone level of the varied parameter L_2 or $L_{1,\text{offset}}$) featured notched regions when L_2 was fixed and L_1 varied (e.g., Figs. 3 Cg, Ch, and Ci), while this phenomenon did not occur for the opposite case of fixed $L_{1,\text{offset}}$ and L_2 being varied (Figs. 3 Ea–Ek).

The change in DPOAE level ΔL_{dp} due to CAS is shown in Fig. 3(B) for all tested primary tone level combinations. Negative ΔL_{dp} values represent suppressive (L_{dp} decreases due to CAS), positive values represent enhancing (L_{dp} increases due to CAS) effects. The cross sections of Fig. 3(B) are shown in Figs. 3 Da–Di for constant L_2 and in Figs. 3 Fa–Fk for constant $L_{1,\text{offset}}$. Please note that a small change in L_1 in the region around the center level (i.e., $L_{1,\text{offset}}$=0 dB) caused pronounced changes in ΔL_{dp} from enhancement to suppression (e.g., Figs. 3 Dg, Dh, and Di) while there were rather smooth ΔL_{dp} changes, which stretched across a wider level range, when varying L_2 (Figs. 3 Fa–Fk). It should be emphasized that the bipolar effect (transition from enhancement to suppression) was more pronounced at low L_2 and occurred when varying L_1 within a small level range. Regarding all cross sections, the maximum bipolar effect occurred at the cross section with L_2=30 dB SPL and amounted to 7.9 dB (Fig. 3 Dg).

This finding is important because it shows that also in humans a bipolar change in DPOAE level from enhancement to suppression is present. However, it should be emphasized that the bipolar change occurred during CAS. Please remember that in guinea pigs the large bipolar effect was observed for ipsilateral DPOAE adaptation (see Maison and Liberman, 2000).

For the repetition measurements (n=10), the mean standard deviation of L_{dp} was 3.6 dB and there were no pronounced level regions of particularly high L_{dp} variability. The average standard deviation of ΔL_{dp} amounted to 1.6 dB. The standard deviation increased in regions around DPOAE I/O function notches where CAS effects shifted from enhancement to suppression (e.g., Fig. 3 Dh) and increased with increasing $|\Delta L_{dp}|$. The maximum suppression amounted on average to −5.8±1.9 dB and the maximum enhancement to 9.6±2.3 dB. The resultant ΔL_{dp} range (difference between maximum suppression and maximum enhancement) was on average 15.4±3.4 dB.

The variability of the measures obtained on one day with varying and fixed sound probe position was lower than that obtained on several days as it was observed for DPOAE fine structure data.

2. Enhancement and suppression across subjects

The effect of CAS on DPOAEs was examined across all ten ears at frequencies $f_{2,\text{dip}}$ where a pronounced dip occurred in the DPOAE fine structure, and for comparison at frequencies $f_{2,\text{flat}}$ where the DPOAE fine structure was flat.

In general, for both frequencies, suppression rather than enhancement was more common. At $f_{2,\text{dip}}$ on average 67 (69%) and at $f_{2,\text{flat}}$ 80 (82%) out of 97 valid data points for each ear showed suppressive effects. Please note that in one ear no enhancement occurred at $f_{2,\text{flat}}$. Figure 4 shows the mean and standard deviation for maximum suppression and enhancement at $f_{2,\text{dip}}$ (black) and $f_{2,\text{flat}}$ (gray). At $f_{2,\text{dip}}$, the average maximum suppression was −7.3±3.2 dB and the average maximum enhancement 6.8±5.7 dB. Thus, the resulting ΔL_{dp} range amounted to 14.1±6.6 dB. In comparison to DPOAE level changes of only 1–2 dB reported in the literature when using conventional stimulus settings (e.g., Collet *et al.*, 1990) this is an extremely large effect. In contrast, at $f_{2,\text{flat}}$, the average maximum suppression was −4.1±1.9 dB, and the average maximum enhancement 1.7±1.7 dB, resulting in a ΔL_{dp} range of only 5.7±2.9 dB. Comparing mea-

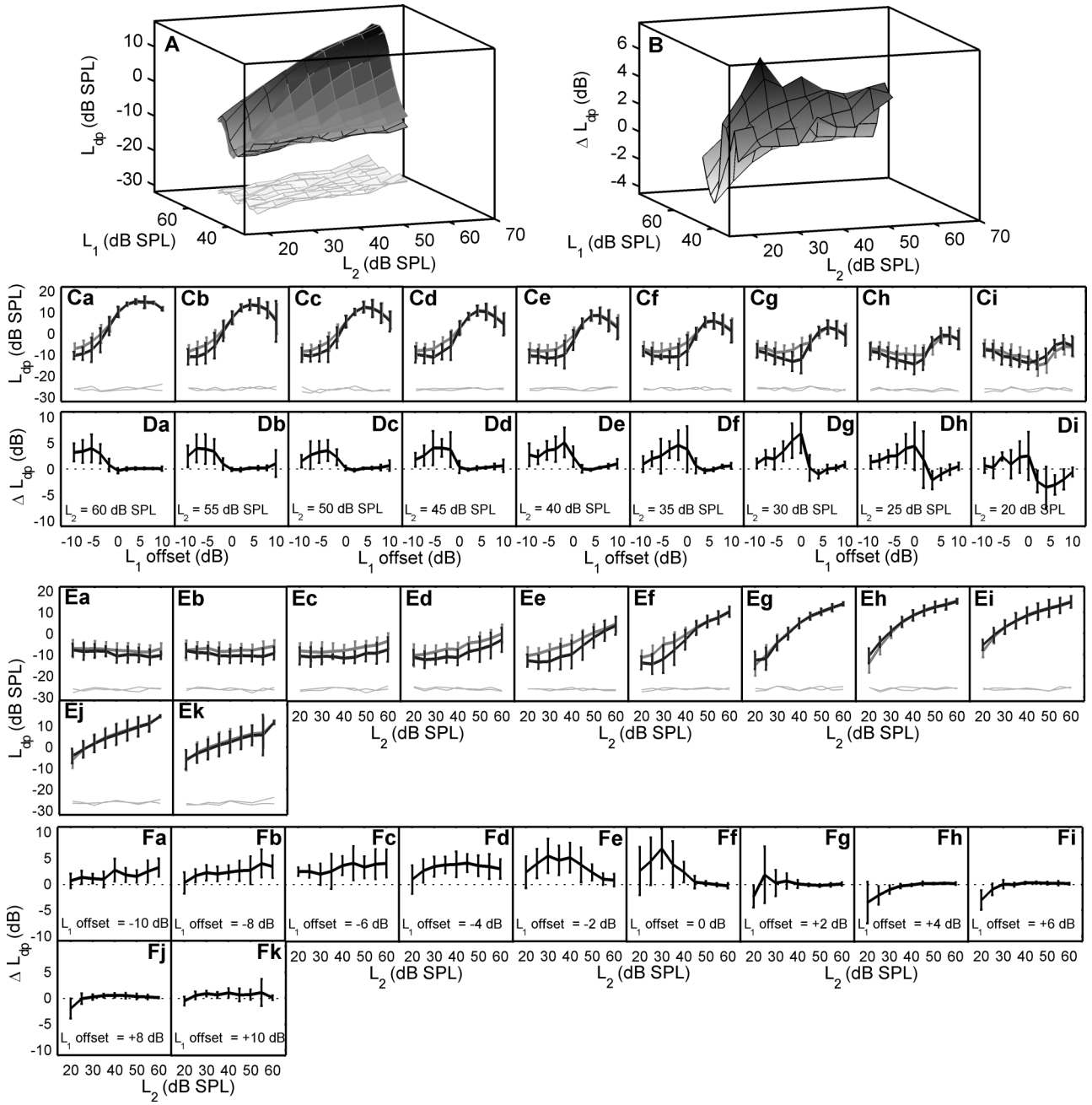

FIG. 3. Contralateral acoustic stimulation (CAS) effect on DPOAEs and its reproducibility at f_2=4125 Hz for one subject. Data were averaged across ten measurements conducted on different days. Panel A shows mean L_{dp} plotted above L_2 and L_1 for the condition without (black lines) and with (gray lines) CAS. The light gray area at the bottom represents the noise floor level. Panel B shows the DPOAE level difference ΔL_{dp} between measurements with and without CAS. Negative values mean suppressive, positive values enhancing behavior due to CAS. Panels C and E show cross sections of panel A. Panel C represents cross sections with constant L_2 and varying $L_{1,\text{offset}}$ (Ca: L_2=60 dB SPL, …, Ci: L_2=20 dB SPL) while panel E pictures cross sections with constant $L_{1,\text{offset}}$ (level offset from the center level L_1=0.4 L_2+39 dB SPL) and varying L_2 (Ea: $L_{1,\text{offset}}$=−10 dB, …, Ek: $L_{1,\text{offset}}$=+10 dB). Panels D (constant L_2, varying $L_{1,\text{offset}}$) and F (constant $L_{1,\text{offset}}$, varying L_2) show cross sections of panel B. The dotted lines mark the turning point from suppression to enhancement at ΔL_{dp}=0 dB. All cross-section plots show mean and standard deviation of the repetition measurements.

surement data at $f_{2,\text{dip}}$ and at $f_{2,\text{flat}}$ both maximum suppression and maximum enhancement were significantly different ($\alpha<0.05$). Moreover, the ΔL_{dp} range differed highly significantly ($\alpha<0.01$) between the two frequencies. Thus, the bipolar change in DPOAE level was considerably higher at dip frequencies than at frequencies where the fine structure was flat.

Figure 5 shows the level combinations $L_2|L_1$ at which maximum suppression (black dots) or maximum enhancement (gray squares) occurred in each ear. Panel (A) shows data for measurements at $f_{2,\text{dip}}$ and panel (B) for measurements at $f_{2,\text{flat}}$ across all ten ears. In both panels the applied L_1 range and the L_1 center level are shown by dashed light gray lines. Regarding data obtained at $f_{2,\text{dip}}$ [Fig. 5(A)], L_2 at which maximum suppression or enhancement occurred varied across the entire L_2 range. However, a majority of points were in the low L_2 region $\leqslant$30 dB SPL [60% of all points in Fig. 5(A)]. Maxima were more commonly at negative $L_{1,\text{offset}}$ values. Regarding data obtained at $f_{2,\text{flat}}$ [Fig. 5(B)], both maximum suppression and enhancement occurred almost ex-

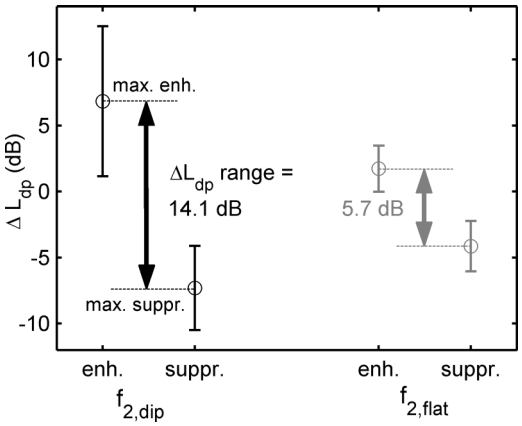

FIG. 4. Mean and standard deviation of maximum suppression (suppr.) and maximum enhancement (enh.) due to CAS for measurements at $f_{2,\mathrm{dip}}$ (black) and $f_{2,\mathrm{flat}}$ (gray) across all ten ears. The arrows show the corresponding average ΔL_{dp} range.

clusively in the low L_2 region $\leqslant$30 dB SPL [89% of all points in Fig. 5(B)] with L_1 values distributed nearly in equal shares around $L_{1,\mathrm{center}}$.

C. DPOAEs during ipsilateral acoustic stimulation (IAS)

1. Adaptation and its reproducibility in a single subject

DPOAE adaptation and its reproducibility were examined in one subject (J.M.) for two different test conditions.

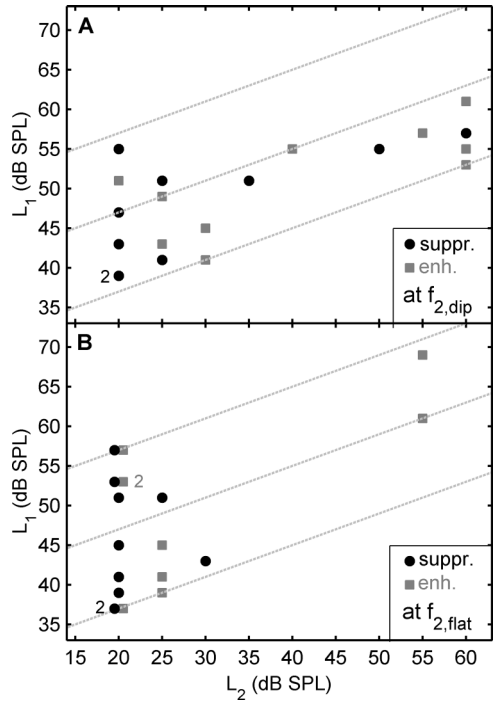

FIG. 5. Distribution of maximum suppression (suppr.) and maximum enhancement (enh.) due to CAS across their corresponding level combinations $L_2|L_1$ for all ten ears. Panel (A) includes data measured at dip frequencies ($f_{2,\mathrm{dip}}$) and panel (B) data measured at flat frequency regions ($f_{2,\mathrm{flat}}$) of the DPOAE fine structure. Black dots show level combinations $L_2|L_1$ for maximum suppression, gray squares for maximum enhancement. If more than one measurement resulted in the same $L_2|L_1$ combination, the respective number of similar measurement results is given. The dashed light gray lines show the L_1 center level $L_{1,\mathrm{center}}$=0.4 L_2+39 dB SPL and the range in which L_1 was varied around $L_{1,\mathrm{center}}$.

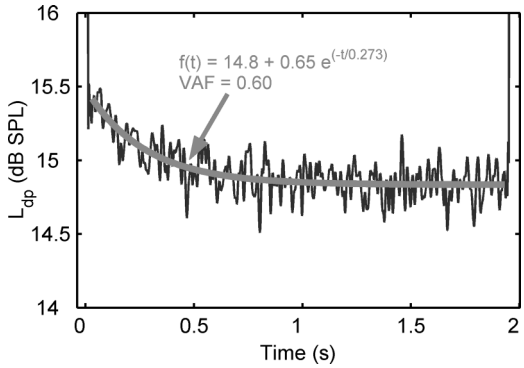

FIG. 6. DPOAE adaptation example taken from the repetition measurements at f_2=4219 Hz and $L_2|L_1$=60|67 dB SPL. The gray line shows the one-exponential fit f(t). The VAF [see Eq. (3)] of the fitting function was 0.60.

Measurements were conducted eight times on one day with varying and constant sound probe position, respectively. DPOAE adaptation was quite inconsistent when measured on different days. It happened that on one day a distinct adaptation was present and on the other day not. No reproducibilty measurements were therefore conducted on different days. In the following data from measurements with varying sound probe position are presented.

Figure 6 shows an example of one measurement with the L_{dp} time course (black line) and the one-exponential fitting function (gray line). For evaluating the reproducibility of DPOAE adaptation, the steady-state level L_{ss}, the adaptation magnitude m, and the adaptation time constant τ were averaged. L_{ss} amounted on average to 14.6±0.5 dB, m to −0.47±0.12 dB, and τ to 0.372±0.128 s. The average VAF (see Sec. II E) was 0.41. For constant sound probe position the variability of the measures was lower.

2. Adaptation in DPOAE I/O function notches

Ipsilateral DPOAE adaptation was measured in three subjects in DPOAE I/O function notches that occurred when varying L_2 at a fixed $L_{1,\mathrm{offset}}$. For each subject seven adaptation measurements were conducted with L_2 being varied around the deepest point of the notch. Subject L.J. yielded three, subject T.R. one, and subject J.M. no valid adaptation time courses (VAF$>$0.1). Regarding these results only decreasing adaptation time courses occurred with an average m of −1.2±0.4 dB. All in all, even when regarding fitting functions with lower VAF values, no bipolar adaptation effect was found.

3. Adaptation across subjects

Ipsilateral DPOAE adaptation was investigated in all ten ears at $f_{2,\mathrm{dip}}$ and at $f_{2,\mathrm{flat}}$ for a total of 49 ($f_{2,\mathrm{dip}}$) and 38 ($f_{2,\mathrm{flat}}$) level combinations. For each group there were 20 valid measurements (VAF$>$0.1). The mean VAF across all valid measurements amounted to 0.36±0.19. The mean DPOAE steady-state level L_{ss} was 11.2±5.3 dB SPL ($f_{2,\mathrm{dip}}$) and 12.6±5.3 dB SPL ($f_{2,\mathrm{flat}}$). The average adaptation time constant τ was 0.426±0.493 s ($f_{2,\mathrm{dip}}$) and 0.345±0.154 s ($f_{2,\mathrm{flat}}$). The mean adaptation magnitude m amounted to only −0.55±0.79 dB ($f_{2,\mathrm{dip}}$) and −0.65±0.20 dB ($f_{2,\mathrm{flat}}$). Thus, in

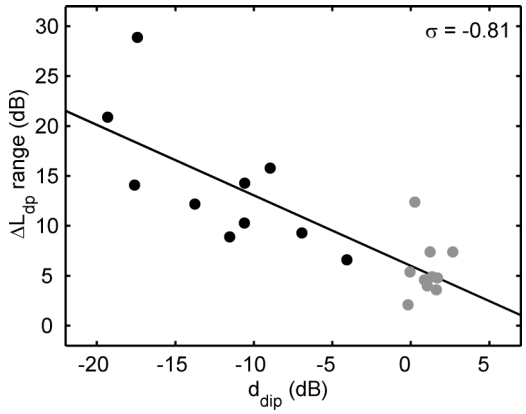

FIG. 7. Relationship between DPOAE fine structure and DPOAE suppression data across subjects. ΔL_{dp} range is plotted above the corresponding dip depth d_{dip} for all ten ears. Black dots show data for measurements at $f_{2,\mathrm{dip}}$, gray dots for measurements at $f_{2,\mathrm{flat}}$. The regression line and the correlation σ was calculated on the basis of all data points.

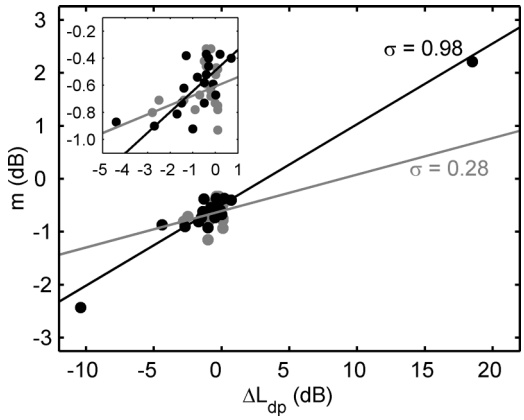

FIG. 8. Relationship between DPOAE suppression and DPOAE adaptation data across subjects. Adaptation magnitude m is plotted across ΔL_{dp} for all ten ears. Black dots show data for measurements at $f_{2,\mathrm{dip}}$, gray dots for measurements at $f_{2,\mathrm{flat}}$. Regression lines and correlations are shown for each frequency group. The insert figure displays a magnification of ΔL_{dp} data between −5 and +1 dB.

our human data the adaptation magnitude was very small compared to that observed in cats (6 dB, Liberman *et al.*, 1996). A bipolar change in adaptation magnitude could be found in only one subject and amounted to 4.6 dB (−2.4 dB at $L_2|L_1=25|51$ dB SPL, 2.2 dB at $L_2|L_1=60|61$ dB SPL). In all other subjects no bipolar effect was observed. Compared to Maison and Liberman (2000), who found in guinea pigs a bipolar change in adaptation magnitude of up to 30 dB, the effect in our human data is very small.

D. Correlations between DPOAE measures

The relationship between DPOAE fine structure and the change in DPOAE level ΔL_{dp} due to CAS, in particular the relationship between the dip depth d_{dip} of the DPOAE fine structure and the corresponding ΔL_{dp} range, is shown in Fig. 7. Black dots show data for measurements at $f_{2,\mathrm{dip}}$, gray points for measurements at $f_{2,\mathrm{flat}}$. With increasing dip depth (negative values) the ΔL_{dp} range increased, the two measures being closely correlated ($\sigma=-0.81$). The observation that bipolar effects were most prominent in the deepest dips is important with regard to a clinical application of DPOAEs for assessing MOC reflex strength. Due to time restrictions in a clinical context, the bipolar effect cannot be explored at all test frequencies. Therefore it is necessary to choose critical frequencies (e.g., $f_{2,\mathrm{dip}}$).

In Fig. 8 the DPOAE level change ΔL_{dp} due to CAS is plotted over the adaptation magnitude m. Black dots represent data for measurements at $f_{2,\mathrm{dip}}$, gray points for measurements at $f_{2,\mathrm{flat}}$. The insert figure shows a magnification of ΔL_{dp} data between −5 and +1 dB. It could be observed that the change in DPOAE level was in general lower during IAS (m varied between −2.4 and 2.2 dB) compared to that during CAS (ΔL_{dp} varied between −10.4 and 18.5 dB). It was striking that only in one subject enhancement could be observed in both measures (see $\Delta L_{dp}=18.5$ dB in Fig. 8). The correlation between m and ΔL_{dp} was 0.98 for measurements at $f_{2,\mathrm{dip}}$. However, the high correlation coefficient was mainly influenced by the two single data points at the left and right margin of Fig. 8, representing adaptation data from one subject at ΔL_{dp} with maximum suppression and maximum enhancement, respectively. When the two data points were excluded the correlation decreased to 0.66. In contrast, the correlation for measurements at $f_{2,\mathrm{flat}}$ was only 0.28. As a consequence, the data suggests a poor correlation between contralateral DPOAE suppression and ipsilateral DPOAE adaptation.

IV. DISCUSSION

The aim of the present study was to investigate whether large bipolar changes in DPOAE level, which were reported for guinea pigs (Maison and Liberman, 2000), are also present in humans. Actually, we found large bipolar changes in our human data, but, in contrast to the findings in guinea pigs, the bipolar effect was present for contralateral DPOAE suppression and not for ipsilateral DPOAE adaptation. The bipolar effect was largest at the deepest dips of the DPOAE fine structure and amounted on average to 14 dB across subjects. This effect is much larger than that observed for conventional contralateral DPOAE suppression measurements, in which DPOAEs were measured not at critical frequencies ($f_{2,\mathrm{dip}}$) and not at different $L_2|L_1$ combinations (e.g., Collet *et al.*, 1990). With respect to a clinical application for assessing the MOC reflex strength, a large change in DPOAE level is needed in order to assure that the obtained effect exceeds L_{dp} variability (in our data between 1.8 and 3.6 dB). Therefore, our approach and not the conventional contralateral DPOAE suppression measurement seems to be more suitable for assessing the MOC reflex strength in a clinical context. However, it is important to note that a large bipolar effect seems to be present at particular frequencies and $L_2|L_1$ combinations only. The magnitude of the bipolar effect was correlated with the dip depth of DPOAE fine structure (Fig. 7). Thus, for clinical application, the bipolar effect needs to be examined at only some frequencies, specifically frequencies at which the DPOAE fine structure exhibits distinct dips.

The main findings in detail were the following. (*i*) DPOAE measurements showed a good reproducibility even for the worst test condition (measurements on several days). (*ii*) DPOAE fine structure showed most pronounced dips and

was roughest between 3 and 4 kHz. (*iii*) Contralateral DPOAE suppression data exhibited the bipolar effect (transition from suppression to enhancement) with the ΔL_{dp} range being significantly higher when measured at $f_{2,\mathrm{dip}}$ compared to measurements at $f_{2,\mathrm{flat}}$. (*iv*) Maximum suppression and enhancement at $f_{2,\mathrm{dip}}$ occurred for contralateral DPOAE suppression across the entire primary tone level range, but predominantly at lower L_2 and at negative $L_{1,\mathrm{offset}}$. (*v*) The dip depth and the corresponding ΔL_{dp} range were closely correlated across subjects. (*vi*) No bipolar DPOAE adaptation effect was observed in DPOAE I/O function notches. (*vii*) Finally, the correlation between the change in DPOAE level ΔL_{dp} due to CAS and the DPOAE adaptation magnitude m due to IAS cannot be evaluated due to a lack of valid adaptation data.

The worst test condition was supposed to be the one with measurements on several days, which is a test situation that is nearest to clinical practice. As expected, for this test condition the highest variability was present. However, the standard deviation of the ΔL_{dp} range was only 3.4 dB for one person on different days ($n=10$) and thus was considerably lower than the average ΔL_{dp} range observed across subjects, which was 14.1 dB (see Fig. 4). Due to the large bipolar effect and the relatively small variability of the measure a good test performance of our approach for assessing the MOC reflex strength during CAS is suggested.

In comparison, the reproducibility of DPOAE adaptation magnitude was insufficient, especially when considering that adaptation measured on consecutive days was on one day present and on the next day not. This and the fact that no distinct bipolar effects were present during IAS suggests DPOAE adaptation not to be a suited tool for investigating MOC reflex strength in humans.

In our data, major dips occurred predominantly in the lower frequency region of the DPOAE fine structure below 4 kHz (see Fig. 2). In the literature, dips and peaks of the DPOAE fine structure are thought to be due to second DPOAE source effects (He and Schmiedt, 1993; Heitmann *et al.*, 1998; Talmadge *et al.*, 1999; Mauermann and Kollmeier, 2004). Thus, the impact of the second source seems to be higher at lower frequencies. However, we have no explanation for this observation. Another observation in the literature is that the roughness of the fine structure increases with decreasing L_2 (Mauermann and Kollmeier, 2004). This finding is consistent with our data (Fig. 1) and suggests the influence of the second source to be higher at near-to-threshold stimulus levels. Furthermore, the high interindividual variability of the roughness found in our data may be attributed to morphological differences among subjects.

Typically, distinct transitions from enhancement to suppression during CAS occurred in notched regions of DPOAE I/O functions (see, e.g., Figs. 3 Ch and Dh). As shown by Maison and Liberman (2000), also in our data large bipolar changes were present for a small shift in primary tone level. However, primary tone level combinations eliciting maximum suppression and maximum enhancement for a single subject were not always located close to each other in the primary tone level matrix. In contrast to Maison and Liberman (2000), in our data transitions from enhancement to suppression occurred when varying L_1 with fixed L_2 and not the other way round.

Supposing that notches in DPOAE I/O functions and with that also the bipolar effect is due to the second source (Kujawa and Liberman, 2001), the observed difference could be attributed to a different impact of the primaries on the second source. Since in our data the magnitude of the bipolar effect is correlated with the dip depth of the DPOAE fine structure (see Fig. 7), the second source is suggested to be the underlying mechanism for the bipolar effect. The fact that maximum suppression and enhancement during CAS occurred predominantly at lower primary tone levels (see Fig. 5) and the observation that the roughness of the DPOAE fine structure increases with decreasing primary tone level (Mauermann and Kollmeier, 2004) supports the idea that the second source influences the magnitude of CAS effects.

To further investigate the relationship between DPOAE fine structure, second DPOAE source, and bipolar changes in DPOAE level, additional studies are necessary. The question whether and to what extent the second DPOAE source is influencing CAS effects might be answered by performing contralateral DPOAE suppression measurements while presenting simultaneously an additional ipsilateral tone near $2f_1-f_2$, which may suppress the second DPOAE source (Heitmann *et al.*, 1998).

Another cause for changes in DPOAE level might be the stapedius muscle reflex, which is known to be activated by acoustic stimulation from either the ipsilateral or contralateral ear. The activation of the stapedius reflex changes the middle ear impedance and with that the DPOAE level. In this study, the stapedius muscle reflex threshold for a 4-kHz pure tone was on average at about 90 dB SPL across subjects. Since the maximum primary tone level was set to 75 dB SPL, the influence of the stapedius muscle on the DPOAE level is suggested to be not relevant during IAS. However, reflex thresholds could be lower for broadband noise stimulation. Therefore, an impact of the stapedius muscle reflex on DPOAEs during CAS cannot be excluded. However, assuming that the middle ear is a linear system, it is unlikely that the observed bipolar effect, which occured when shifting the primary tone level by only 2 dB, can be achieved by the activation of the stapedius muscle.

Contralateral DPOAE suppression and ipsilateral DPOAE adaptation effects were closely correlated when including, and poorly correlated when excluding, the outliers, which represent data from only one ear (see Fig. 8). The small number of valid adaptation measurements makes it impossible to evaluate the correlation between the two measures. Further studies are therefore necessary to investigate the impact of the uncrossed and crossed MOC efferents on OHC motility.

V. CONCLUSIONS

Large bipolar changes in DPOAE level also occur in humans when measuring DPOAEs at frequencies where the DPOAE fine structure exhibits the deepest dips. However, in

contrast to the findings in guinea pigs the bipolar effect occurs during contralateral acoustic stimulation (CAS), i.e., when activating the *uncrossed* MOC fibers, and not during ipsilateral acoustic stimulation (IAS), i.e., when activating the *crossed* MOC fibers. It is unclear which intrinsic mechanisms (e.g., second DPOAE source) are responsible for the observed bipolar effect. Moreover, it remains unknown why in humans the bipolar effect is stronger during CAS than during IAS, which is contrary to the findings in animals. Contralateral DPOAE suppression, when measured at dip frequencies and varying the primary tone level in small steps, provides a suited tool for assessing the reflex strength of the MOC efferents. Further studies, which have to compare contralateral DPOAE suppression with temporary or permanent pure-tone threshold shifts in noise-exposed humans, are required to answer the question whether the MOC reflex strength measured during CAS could provide a reliable measure for detecting the vulnerability of the cochlea to noise overexposure.

ACKNOWLEDGMENTS

This work was supported by Deutsche Forschungsgemeinschaft (Ja 597/7, Wa1677/2). We thank the reviewers for their valuable comments on the manuscript.

Agrama, M. T., Waxman, G. M., Stagner, B. B., Martin, G. K., and Lonsbury-Martin, B. L. (**1998**). "Effects of efferent activation on distortion-product otoacoustic emissions in normal humans using ipsilateral acoustic stimulation," Abst. Assoc. Res. Otolaryngol. **21**, 152.

Bassim, M. K., Miller, R. L., Buss, E., and Smith, D. W. (**2003**). "Rapid adaptation of the $2f_1-f_2$ DPOAE in humans: Binaural and contralateral stimulation effects," Hear. Res. **182**, 140–152.

Boege, P., and Janssen, T. (**2002**). "Pure-tone threshold estimation from extrapolated distortion product otoacoustic emission I/O-functions in normal and cochlear hearing loss ears," J. Acoust. Soc. Am. **111**, 1810–1818.

Brown, A. M., Harris, F. P., and Beveridge, H. A. (**1996**). "Two sources of acoustic distortion products from the human cochlea," J. Acoust. Soc. Am. **100**, 3260–3267.

Brownell, W. E. (**1990**). "Outer hair cell electromotility and otoacoustic emissions," Ear Hear. **11**, 82–92.

Brownell, W. E., Bader, C. R., Bertrand, D., and Ribaupierre, Y. (**1985**). "Evoked mechanical responses of isolated cochlear hair cells," Science **227**, 194–196.

Cody, A. R., and Johnstone, B. M. (**1982**). "Temporary threshold shift modified by binaural acoustic stimulation," Hear. Res. **6**, 199–205.

Collet, L., Kemp, D. T., Veuillet, E., Duclaux, R., Moulin, A., and Morgon, A. (**1990**). "Effect of contralateral auditory stimuli on active cochlear micro-mechanical properties in human subjects," Hear. Res. **43**, 251–261.

Guinan, J. J., Jr. (**1996**). "Physiology of olivocochlear efferents," in *The Cochlea*, edited by P. Dallos, A. Popper, and R. Fay (Springer, New York), pp. 435–502.

Guinan, J. J., Jr., Warr, W. B., and Norris, B. E. (**1984**). "Topographic organization of the olivocochlear projections from lateral and medial zones of the superior olivocochlear complex," J. Comp. Neurol. **226**, 21–27.

He, N., and Schmiedt, R. A. (**1993**). "Fine structure of the $2f_1-f_2$ acoustic distortion product: changes with primary levels," J. Acoust. Soc. Am. **94**, 2659–2669.

Heitmann, J., Waldmann, B., Schnitzler, H. U., Plinkert, P. K., and Zenner, H. P. (**1998**). "Suppression of distortion product otoacoustic emissions (DPOAE) near $2f_1-f_2$ removes DP-gram fine structure—Evidence for a secondary generator," J. Acoust. Soc. Am. **103**, 1527–1531.

Janssen, T., Gehr, D. D., and Kevanishvili, Z. (**2003**). "Contralateral DPOAE suppression in humans at very low sound intensities," in *Biophysics of the Cochlea: from Molecules to Models*, edited by A. W. Gummer (World Scientific, London), pp. 498–505.

Janssen, T., Kummer, P., and Arnold, W. (**1995**). "Wachstumsverhalten der Distorsionproduktemissionen bei kochleären Hörstörungen," Otorhinolaryngol. NOVA **5**, 34–46 (in German).

Kemp, D. T. (**1986**). "Otoacoustic emissions, travelling waves and cochlear mechanisms," Hear. Res. **22**, 95–104.

Kim, D. O., Dorn, P. A., Neely, S. T., and Gorga, M. P. (**2001**). "Adaptation of Distortion Product Otoacoustic Emissions in Humans," J. Assoc. Res. Otolaryngol. **2**, 31–40.

Kujawa, S. G., and Liberman, M. C. (**2001**). "Effects of Olivocochlear Feedback on Distortion Product Otoacoustic Emissions in Guinea Pig," J. Assoc. Res. Otolaryngol. **2**, 268–278.

Kummer, P., Janssen, T., and Arnold, W. (**1995**). "Suppression tuning characteristics of the $2f_1-f_2$ distortion-product otoacoustic emissions in humans," J. Acoust. Soc. Am. **98**, 197–210.

Kummer, P., Janssen, T., Hulin, P., and Arnold, W. (**2000**). "Optimal L_1-L_2 primary tone level separation remains independent of test frequency in humans," Hear. Res. **146**, 47–56.

Liberman, M. C., and Guinan, J. J., Jr. (**1998**). "Feedback control of the auditory periphery: anti-masking effects of middle ear muscle vs. olivocochlear efferents," J. Commun. Disord. **31**, 471–483.

Liberman, M. C., Puria, S., and Guinan, J. J., Jr. (**1996**). "The ipsilaterally evoked olivocochlear reflex causes rapid adaptation of the $2f_1-f_2$ distortion product otoacoustic emission," J. Acoust. Soc. Am. **99**, 3572–3584.

Luebke, A. E., and Foster, P. K. (**2002**). "Variation in Inter-Animal Susceptibility to Noise Damage Is Associated with α9 Acetylcholine Receptor Subunit Expression Level," J. Neurosci. **22**, 4241–4247.

Maison, S. F., and Liberman, M. C. (**2000**). "Predicting Vulnerability to Acoustic Injury with a Noninvasive Assay of Olivocochlear Reflex Strength," J. Neurosci. **20**, 4701–4707.

Maison, S., Micheyl, C., Andeol, G., Gallego, S., and Collet, L. (**2000**). "Activation of medial olivocochlear efferent system in humans: influence of stimulus bandwidth," Hear. Res. **140**, 111–125.

Mauermann, M., and Kollmeier, B. (**2004**). "Distortion product otoacoustic emission (DPOAE) input/output functions and the influence of the second DPOAE source," J. Acoust. Soc. Am. **116**, 2199–2212.

Meinke, D. K., Stagner, B. B., Martin, G. K., and Lonsbury-Martin, B. L. (**2004**). "Human Efferent Adaptation of DPOAEs in the L_1, L_2 space," Am. Auditory Society Bulletin **29/1**, 39.

Moulin, A., Collet, L., and Duclaux, R. (**1993**). "Contralateral auditory stimulation alters acoustic distortion products in humans," Hear. Res. **65**, 193–210.

Mountain, D. C. (**1980**). "Changes in endolymphatic potential and crossed olivocochlear bundle stimulation alter cochlear mechanics," Science **210**, 71–72.

Puel, J. L., and Rebillard, G. (**1990**). "Effects of contralateral sound stimulation on the distortion product $2f_1-f_2$: Evidence that the medial efferent system is involved," J. Acoust. Soc. Am. **87**, 1630–1635.

Puria, S., Guinan, J. J., and Liberman, M. C. (**1996**). "Olivocochlear reflex assays: Effects of contralateral sound on compound action potentials versus ear-canal distortion products," J. Acoust. Soc. Am. **99**, 500–507.

Reiter, E. R., and Liberman, M. C. (**1995**). "Efferent-mediated protection from acoustic overexposure: relation to slow effects of olivocochlear stimulation," J. Neurophysiol. **73**, 506–514.

Shera, C. A., and Guinan, J. J., Jr. (**1999**). "Evoked otoacoustic emissions arise by two fundamentally different mechanisms: a taxonomy for mammalian OAEs," J. Acoust. Soc. Am. **105**, 782–798.

Talmadge, C. L., Long, G. R., Tubis, A., and Dhar, S. (**1999**). "Experimental confirmation of the two-source interference model for the fine structure of distortion product otoacoustic emissions," J. Acoust. Soc. Am. **105**, 275–292.

Whitehead, M. L., Lonsbury-Martin, B. L., and Martin, G. K. (**1992**). "Evidence for two discrete sources of $2f_1-f_2$ distortion-product otoacoustic emission in rabbit. I. Differential dependence on stimulus parameters," J. Acoust. Soc. Am. **91**, 1587–1607.

Williams, D. M., and Brown, A. M. (**1995**). "Contralateral and ipsilateral suppression of the $2f_1-f_2$ distortion product in human subjects," J. Acoust. Soc. Am. **97**, 1130–1140.

Winslow, R. L., and Sachs, M. B. (**1987**) "Effect of electrical stimulation of the crossed olivocochlear bundle on auditory nerve response to tones in noise," J. Neurophysiol. **57**, 1002–1021.

Perception of the envelope-beat frequency of inharmonic complex temporal envelopes

Christian Füllgrabe[a] and Christian Lorenzi[b]
Laboratoire de Psychologie Expérimentale, UMR CNRS 8581, Institut de Psychologie, Université René Descartes, Paris 5, 71 Av. Edouard Vaillant, 92774 Boulogne-Billancourt, France

(Received 18 June 2004; revised 19 September 2005; accepted 23 September 2005)

Listeners can hear slow sinusoidal variations in the depth of sinusoidally amplitude-modulated (SAM) stimuli. Here, the SAM stimulus of frequency f_m acts as the carrier, and the slow variation in depth of frequency f'_m (referred to as "second-order" amplitude modulation) corresponds to a beat in the temporal envelope. Recent studies have suggested that second-order amplitude modulation perception is based on a modulation-distortion component or the "venelope" (the Hilbert envelope of the ac-coupled Hilbert envelope), both occurring at the envelope-beat frequency f'_m. This was tested by transposing to the modulation domain the matching paradigm used by Schouten *et al.* [J. Acoust. Soc. Am. **34**, 1418–1424 (1962)]. Listeners estimated the envelope-beat frequency evoked by a 5-Hz, second-order SAM white noise with f_m either an integer multiple of f'_m or shifted in frequency to make the complex envelope inharmonic. The results indicate that the perception of the envelope-beat frequency was affected by these shifts when $f_m \leqslant 20$ Hz. This suggests that, at least at low modulation frequencies, the perceived envelope beat is not determined by a modulation-distortion or venelope component, but rather relies on the time intervals between the main peaks of the first-order envelope. © *2005 Acoustical Society of America.* [DOI: 10.1121/1.2126824]

PACS number(s): 43.66.Ba, 43.66.Mk [JHG] Pages: 3757–3765

I. INTRODUCTION

The perception of behaviorally relevant acoustic signals, such as speech, depends at least partially on the temporal envelopes of the signals, i.e., their slow fluctuations in amplitude over time (e.g., Shannon *et al.*, 1995; Smith *et al.*, 2002). Auditory sensitivity to temporal envelope cues has been extensively investigated using single-component (i.e., sinusoidal) amplitude modulation (AM) (e.g., Viemeister, 1979; Dau *et al.*, 1997a). This psychoacoustical approach of temporal-envelope perception was recently extended by studies (e.g., Lorenzi *et al.*, 2001a, b; Füllgrabe *et al.*, 2004) suggesting a distinction between so-called first-order envelope cues (i.e., temporal variations in the sound's amplitude) and second-order envelope cues (i.e., temporal variations in the sound's *AM depth*, such as found in multi-component temporal envelopes).

Within this new framework, a first-order sinusoidally amplitude-modulated (SAM) stimulus corresponds to sinusoidal modulation of the amplitude of a pure-tone or a noise stimulus (the "audio" carrier) with frequency f_m and depth m. A second-order SAM stimulus, illustrated in Fig. 1 (top row), is obtained by applying a slow, sinusoidal modulation of frequency f'_m and depth m' to the depth m of a first-order AM [cf. Eq. (1) in Sec. III A 2]. Figure 1 shows that, in the time domain, the sinusoidal modulation of the depth of the SAM stimulus corresponds to a beat, i.e., a slow, cyclic increase and decrease in modulation depth of the temporal envelope at a frequency equal to f'_m. In the modulation spectrum, this sinusoidal modulation in AM depth generates two additional components (i.e., sidebands) at $f_m - f'_m$ and $f_m + f'_m$, but there is no energy at the envelope-beat frequency f'_m.

Psychoacoustical studies have assessed the auditory sensitivity to second-order AM by measuring second-order temporal modulation transfer functions that relate detection thresholds for second-order AM (i.e., m' at threshold) to f'_m, the frequency of the second-order AM (Lorenzi *et al.*, 2001a, b; Füllgrabe and Lorenzi, 2003; Füllgrabe *et al.*, 2004). It was shown that, under certain stimulus conditions, second-order AM may be perceptually as salient as first-order AM (Lorenzi *et al.*, 2001b; Füllgrabe and Lorenzi, 2003). Additional psychoacoustical measurements revealed that second-order AM-detection thresholds were degraded when first-order masking modulations were introduced near the envelope-beat frequency (e.g., Lorenzi *et al.*, 2001b), and conversely detection performance of a first-order AM probe was degraded when second-order masker modulations beating at the probe frequency were introduced (e.g., Füllgrabe *et al.*, 2005b). In all these experiments, the physical modulation components of the first- and second-order AM were too far away to yield modulation-masking effects as shown by Bacon and Grantham (1989), Houtgast (1989), and Strickland and Viemeister (1996). Together with psychoacoustical and electrophysiological data obtained with two-component modulators (Shofner *et al.*, 1996; Sheft and Yost, 1997; Moore *et al.*, 1999; Ewert *et al.*, 2002; Verhey *et al.*, 2003; Sek and Moore, 2004), these results support the idea that detection of spectral energy at the envelope-beat frequency

[a]Current address: Department of Experimental Psychology, University of Cambridge, Downing Street, Cambridge CB2 3EB, United Kingdom. Electronic mail: c.fullgrabe@psychol.cam.ac.uk
[b]Also affiliated with the Institut Universitaire de France.

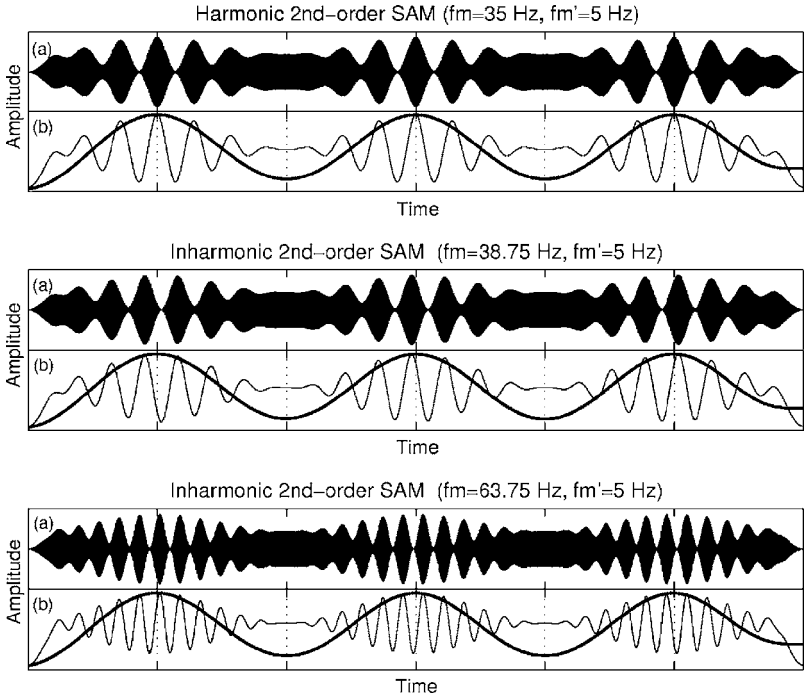

FIG. 1. Waveform (a), first-order envelope (b, thin line), and second-order envelope (b, thick line) of a harmonic second-order SAM stimulus with f_m=35 Hz (i.e., n=7) and f'_m=5 Hz are depicted in the top panel. Note that the main first-order envelope peaks and the second-order envelope peaks coincide. The middle panel shows the same stimulus after applying a frequency shift Δf_m of +3.75 Hz to the carrier modulation frequency. The inharmonicity of such a frequency-shifted stimulus is revealed by the mismatch between the main first-order envelope peaks and the second-order envelope peaks. The bottom panel shows an inharmonic second-order SAM stimulus with f_m =63.75 Hz (i.e., n=12 and Δf_m=+3.75 Hz) and f'_m =5 Hz.

f'_m contributes to the detection of second-order modulation. In other words, envelope-beat information seems to be converted into a first-order component via peripheral and/or central auditory mechanism(s) (Füllgrabe *et al.*, 2005b). Since there is no energy at the envelope-beat frequency in the modulation spectrum of the physical stimulus, it has been argued that some nonlinear mechanism(s) along the auditory pathway must generate an audible *modulation-distortion component* at the envelope-beat frequency in the internal modulation spectrum of complex temporal envelopes (e.g., Shofner *et al.*, 1996; Moore *et al.*, 1999). This idea has been recently implemented in a computational model of temporal-envelope processing (Ewert *et al.*, 2002). This model initially computes the so-called "venelope" of the stimulus (i.e., the Hilbert envelope of the ac-coupled Hilbert envelope) within a separate processing route, and then combines both venelope and envelope information into a single internal representation before feeding it to an array of selective modulation channels [i.e., a modulation filterbank as proposed by Dau *et al.* (1997a, b)].

The notion that a modulation-distortion or venelope component is entirely responsible for second-order AM perception is however contradicted by the fact that its magnitude seems to be relatively weak (Moore *et al.*, 1999, Ewert *et al.*, 2002; Verhey *et al.*, 2003; Sek and Moore, 2004; Füllgrabe *et al.*, 2005b), whereas second-order AM is perceptually salient in a number of stimulus conditions (e.g., Lorenzi *et al.*, 2001b). Moreover, in the two modulation-masking studies conducted by Lorenzi *et al.* (2001b) and Millman *et al.* (2003), second-order AM detection was not abolished when first-order masking modulations were introduced near the envelope-beat frequency f'_m. This suggests that additional cues were used by listeners when detecting second-order AM, such as the dynamic information at the output of the modulation channel tuned to or near the modulation components (Ewert *et al.*, 2002, Füllgrabe and Lorenzi, 2003; Millman *et al.*, 2003; Sek and Moore, 2003; Verhey *et al.*, 2003).

Further experiments are therefore warranted to determine what cues listeners use when perceiving the envelope beat of second-order AM. The goal of the present study was to address this issue by transposing to the temporal-envelope domain the paradigm originally used by Schouten *et al.* (1962) to study pitch perception of inharmonic SAM tones. Listeners were asked to estimate the envelope-beat frequency evoked by a second-order SAM white noise using a matching procedure. The second-order modulation frequency f'_m was fixed at 5 Hz. The first-order modulation frequency f_m corresponded to 15, 20, 35, or 60 Hz (i.e., the 3rd, 4th, 7th, or 12th harmonic of f'_m), or was shifted in frequency by Δf_m (ranging from ±25 to 100% of f'_m) relative to these frequencies, making the complex envelope inharmonic in most conditions. Figure 1 illustrates the waveforms (a) and first- and second-order envelopes (i.e., the envelope beat) (b) of harmonic (top panel) and inharmonic (middle panel) SAM stimuli, for f_m=35 Hz and f'_m=5 Hz, when Δf_m=0 or +3.75 Hz (i.e., shifts by 0 or +75% of f'_m). As shown in the middle panel of Fig. 1, the period of the second-order envelope remains constant despite the shift applied to the first-order modulation frequency, while the time interval between the main peaks of the first-order envelope (i.e., the largest first-order envelope peaks per second-order cycle) is affected (this is also true for all other values of f_m used in the present study). It was thus reasoned that the perceived envelope-beat frequency should be unaffected by shifts in modulation frequency if listeners mainly use a modulation-distortion component or compute explicitly the venelope. In contrast, the perceived envelope-beat frequency should be systematically shifted if listeners compute the envelope-beat frequency from the time intervals between the main peaks of the first-

order envelope. More specifically, the perceived shift should be proportional to the frequency shift Δf_m and inversely proportional to the harmonic rank n of the first-order (carrier) modulation component in the unshifted complex envelope ($n=3$, 4, 7, or 12). As illustrated in the bottommost panel of Fig. 1 for $f_m=63.75$ Hz and $f'_m=5$ Hz (i.e., for $n=12$ and $\Delta f_m=+3.75$ Hz), increasing n, and therefore the number of first-order envelope cycles within a given second-order modulation cycle, yields a smaller disparity between time intervals in the venelope and time intervals between the main peaks of the first-order envelope.

However, other potential cues may be used by the listeners to perform the matching task leading to shifts in the listeners' responses. Given the subjective nature of the adjustment procedure, it is possible that listeners, despite instructions to listen for the slow envelope beat, attempt to match the time intervals related to the carrier modulation frequencies of the standard and matching stimuli. In addition, Moore and Moore (2003) have recently shown that the pitch shifts described by Schouten *et al.* (1962) may be explained by the match of spectral centers of gravity of excitation patterns. The concept of excitation pattern may also hold in the temporal-envelope domain. Indeed, recent data by Füllgrabe *et al.* (2005a) are consistent with the notion that, under certain conditions, listeners use variations in "modulation excitation pattern" (i.e., compare levels of excitation at the output of modulation channels) when detecting changes in modulation frequency. Therefore, in the present study, shifts in the carrier modulation frequency should be accompanied by changes in the modulation excitation pattern, and shifts in matching f'_m may thus (partly) reflect the listeners' matching of the centroids or any part of the evoked modulation excitation patterns. To preclude the use of these additional cues, a second envelope-beat matching task was conducted using first-order AM as the matching stimulus.

II. EXPERIMENT 1: FIRST-ORDER AM-FREQUENCY DISCRIMINATION THRESHOLDS

A. Rationale

Before conducting the matching experiments, just-noticeable differences in modulation frequency were assessed for the AM used as carriers in the subsequent experiments. This appeared necessary because the magnitude of the frequency shifts Δf_m applied to the first-order (carrier) modulation frequency f_m in the matching experiments should be greater than first-order AM-frequency discrimination thresholds to allow us to observe any shift in the perceived envelope-beat frequency.

B. Method

1. Listeners

Five listeners with normal hearing were tested. Their ages ranged from 21 to 26 years. All listeners had audiometric thresholds less than 20 dB HL between 0.25 and 8 kHz and no history of hearing difficulty. All listeners were university students who were paid for their services. They were given practice at each reference modulation frequency prior to data collection.

2. Stimuli and procedure

All stimuli were generated with a PC using a 16-bit D/A converter operating at a sampling frequency of 44.1 kHz, and delivered diotically via Sennheiser HD 565 earphones at 70 dB SPL. The audio carrier consisted of statistically independent realizations of white noise. Listeners were tested individually in a sound-attenuating booth.

A two-interval, two-alternative forced-choice procedure with feedback was used to assess the just-noticeable difference in modulation frequency of first-order AM. On each trial, a standard stimulus having a fixed modulation frequency (referred to as the reference modulation frequency f_m) and target stimulus having a variable modulation frequency ($f_m+\Delta f_m$) were successively presented in random order. The listeners' task was to indicate the interval with the higher modulation frequency. For a given threshold run, the reference modulation frequency was fixed at 15, 20, 35, or 60 Hz. The starting phase of the AM was randomized in each interval. The modulation depth m was held constant at 0.5. In each interval, the AM was applied over the full stimulus duration chosen at random between 1 and 1.5 s, including 100-ms rise/fall times shaped using a raised-cosine function. The randomization of the duration of the stimuli, carrying always an integer number of modulation cycles, was used to prevent listeners from performing the discrimination task by counting the number of modulation cycles. All stimuli were equated in energy (rms). The interstimulus interval (ISI) was fixed at 1 s.

At the beginning of a given threshold run, the modulation frequency of the target stimulus always corresponded to 1.41 times the reference modulation frequency. In other words, the modulation frequency of the target stimulus was 21.2, 28.1, 49.5, and 84.8 Hz for reference modulation frequencies of 15, 20, 35, and 60 Hz, respectively. The target modulation frequency was then varied using a two-down one-up stepping rule that estimates the AM-frequency discrimination threshold Δf_m (in Hz) necessary for 70.7% correct discrimination (Levitt, 1971). The size of the Δf_m variation corresponded initially to a factor of 1.59 and was reduced to 1.26 after the first two reversals. The geometric mean of the values of Δf_m at the last 10 reversals in a series of 16 reversals was taken as the threshold estimate for that run. For each combination of listener and reference modulation frequency, thresholds presented here are based upon three estimates.

C. Results

Figure 2 shows individual and mean AM-frequency discrimination thresholds Δf_m ($\pm$ one standard deviation) plotted as a function of the reference modulation frequency f_m. Overall, Δf_m worsens from 0.7 to 3.3 Hz when f_m increases from 15 to 60 Hz. These results are roughly in agreement with previous data on the discrimination of AM frequencies using tonal (Lee, 1994; Füllgrabe and Lorenzi, 2003) or broadband-noise carriers (Formby, 1985; Hanna, 1992; Füllgrabe *et al.*, 2005a). A repeated-measures analysis of variance (ANOVA) conducted on the AM-frequency discrimination data (expressed as log Δf_m) confirmed the global

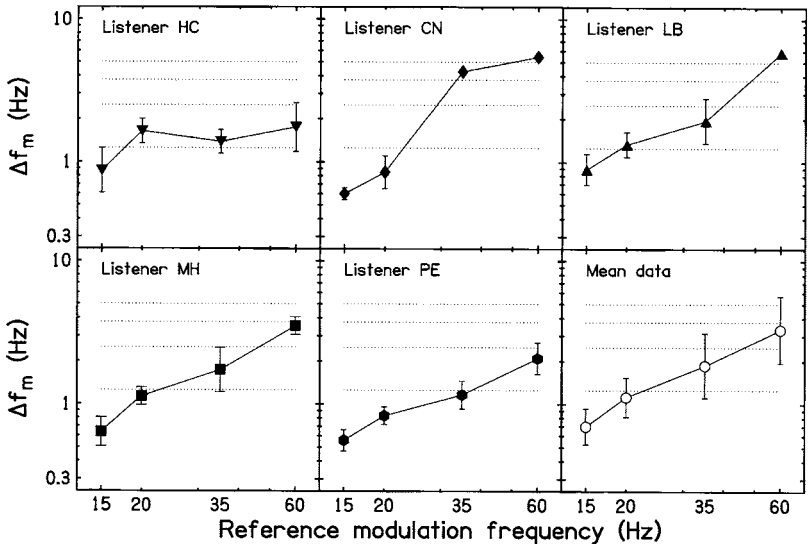

FIG. 2. Individual and mean AM-frequency discrimination thresholds for five listeners. Difference limens Δf_m (in Hz) are plotted as a function of the reference modulation frequency f_m. Error bars represent ± one standard deviation across repeated measures or across listeners. Horizontal dotted lines indicate the four frequency shifts used in the envelope-beat matching experiments.

visual impression by showing a significant main effect of reference modulation frequency $[F(3,12)=16.56, p<0.001]$. In addition, the individual data reveal that, out of the five listeners, three (HC, CN, LB) do not show constant Weber fractions over the range of reference modulation frequencies under study. Such a deviation from a Weber relationship is also seen in previous studies using a larger modulation depth (Formby, 1985; Hanna, 1992; Lee, 1994).

III. EXPERIMENT 2: SECOND-ORDER AM-FREQUENCY MATCHING WITH SECOND-ORDER AM

A. Method

The apparatus and experimental setup used in the matching experiment were identical to that used in the discrimination experiment. Stimulus duration was chosen at random from two values (1 or 1.5 s) and the ISI was fixed at 990 ms.

1. Listeners

The same five listeners who participated in the AM-frequency discrimination experiment took part in the first matching experiment conducted with harmonic second-order AM matching stimuli. Listeners were given between 1 and 2 h of practice prior to data collection in order to familiarize them with the adjustment procedure.

2. Stimuli and procedure

In each matching run, listeners were asked to adjust the second-order modulation frequency of a second-order SAM stimulus to match the perceived envelope-beat frequency of a second-order SAM standard stimulus. The equation of the envelope of the standard and matching stimuli is given by

$$Env(t) = 1 + [m + m' \sin(2\pi f'_m t + \phi)]\sin(2\pi f_m t + \phi), \quad (1)$$

where f_m and f'_m correspond to the first- and second-order modulation frequencies, respectively, and m and m' correspond to the first- and the second-order modulation depths, respectively, which were both set to 0.5. The starting phases ϕ of the first- and second-order modulations were identical and randomized for each stimulus.

The matching stimulus was always harmonic in the modulation domain: the first-order modulation frequency f_m was a multiple integer of the second-order modulation frequency f'_m as shown by the following equation:

$$f_m = nf'_m, \quad (2)$$

where n corresponds to the harmonic rank of f'_m. Within a matching run, n was fixed at 3, 4, 7, or 12.

The second-order modulation frequency f'_m of the standard stimulus was fixed at a nominal value of 5 Hz. At the beginning of each matching run, f'_m was randomized within a range of 20% above or below this nominal value of 5 Hz to prevent listeners from storing an estimate of f'_m in long-term memory. The first-order modulation frequency f_m was then computed according to the following equation:

$$f_m = nf'_m + \Delta f_m, \quad (3)$$

where Δf_m corresponds to a frequency shift. f_m was either fixed at a nominal value of 15, 20, 35, or 60 Hz when $\Delta f_m = 0\%$ or was shifted in frequency by Δf_m (ranging from ±25% to ±100% of the standard f'_m) relative to these nominal frequencies, making the complex envelope inharmonic for values of Δf_m different from ±100%. Thus, this shift was $\pm 1.25, \pm 2.5, \pm 3.75$, or ±5 Hz when f'_m was strictly equal to 5 Hz (its nominal value).

The starting value of f'_m of the matching stimulus was randomized within a range of 50%–60% above or below f'_m of the standard stimulus used for the current run. The listener used mouse clicks on two buttons displayed on the computer screen to raise f'_m of the matching stimulus by 1% or 10% and two other buttons to lower f'_m by 1% or 10%. Since its carrier modulation frequency was an integer multiple of f'_m, the matching stimulus always showed a harmonic structure. There was no limit on the number of adjustments within a matching run; a matching run was ended by the listener when he/she was satisfied with the envelope-beat match by clicking on a fifth button. No feedback was provided. Listeners were asked to listen for the slow, cyclic fluctuation in modulation depth and were encouraged to use a bracketing strategy. For each of the experimental conditions completed

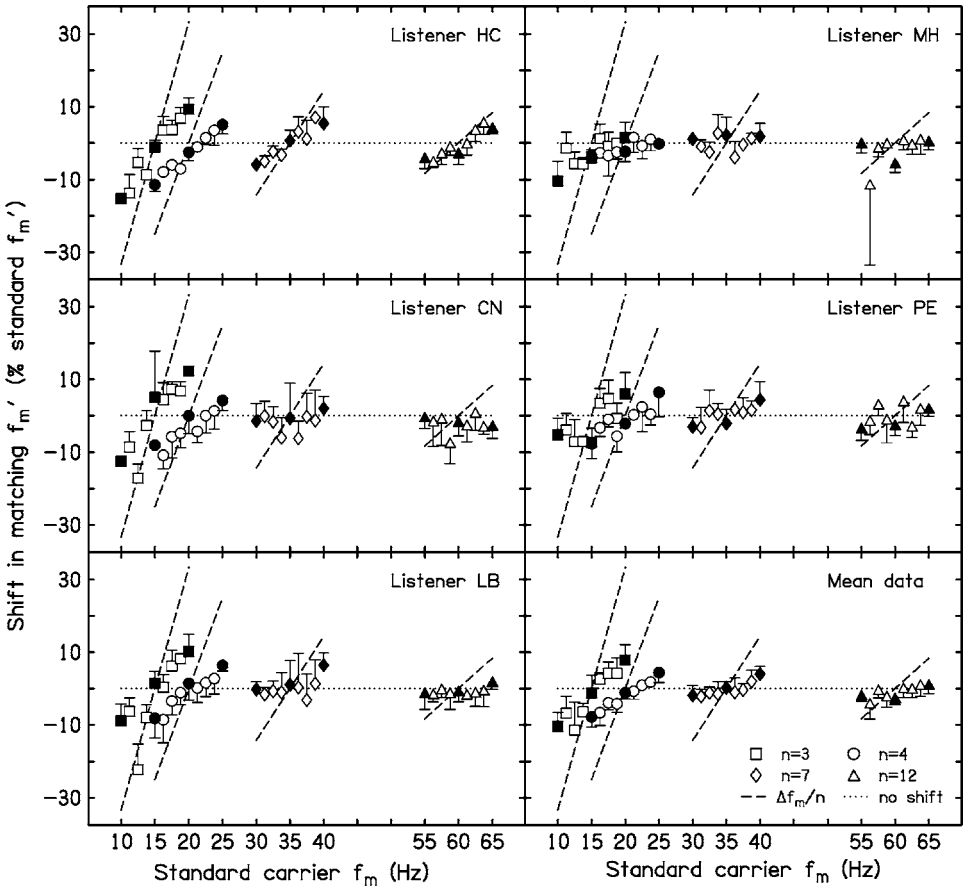

FIG. 3. Individual and mean results for the envelope-beat matching task, using harmonic second-order SAM matching stimuli. In each panel, the observed shift in matching f'_m (expressed as a percentage of the standard f'_m) is plotted as a function of the shift in carrier modulation frequency f_m for each harmonic number [$n=3$ (squares), 4 (circles), 7 (diamonds), or 12 (triangles)]. Open and filled symbols correspond to cases where the standard stimulus had an inharmonic and a harmonic structure, respectively. The dotted line indicates adjustments to the standard f'_m, while the straight broken lines show predictions based on $\Delta f_m/n$, with n corresponding to the harmonic rank of the carrier modulation. To avoid cluttering, error bars represent only + or − one standard deviation across repeated adjustments or across listeners.

in random order, the final estimate of the standard second-order modulation frequency was based on four estimates per listener.

B. Results

Mean and individual results obtained using harmonic second-order SAM matching stimuli are given in Fig. 3. The observed shifts in matching f'_m (expressed as a percentage of the standard f'_m) are plotted as a function of the (shifted or unshifted) standard carrier modulation frequency f_m for each harmonic rank ($n=3$, 4, 7, or 12). Straight broken lines illustrate predictions based on the ratio $\Delta f_m/n$, i.e., a transposition to the modulation-frequency domain of the "first effect of pitch shift" observed by Schouten *et al.* (1962). In other words, the shift in perceived f'_m should be proportional to the frequency shift of the carrier modulation and inversely proportional to the harmonic rank of the carrier modulation component if listeners estimate the beat frequency from the time intervals between the main first-order envelope peaks. Here, predictions are calculated using the harmonic rank of the carrier modulation. Filled symbols correspond to cases where harmonic second-order SAM standard stimuli were used, while open symbols denote the use of inharmonic second-order SAM standard stimuli.

The inspection of the AM-frequency discrimination data obtained in experiment 1 reveals that the different frequency shifts Δf_m used in the matching experiment (cf. horizontal dotted lines in Fig. 1) were not always detectable (as defined by the used stepping rule) by all listeners. For $f_m \leqslant 35$ Hz, shifts of at least +2.5 Hz (i.e., +50% when $f'_m=5$ Hz) were above threshold for four out of the five listeners (on average by a factor of 1.7 to 7), while listener CN detected shifts of the same magnitude only for $f_m \leqslant 20$ Hz. When $f_m=60$ Hz, two listeners (CN, LB) were not able to perceive any frequency shifts. By contrast, frequency shifts of at least +3.75 Hz (i.e., +75%) were still supra-threshold, even though less perceptible (on average twice the threshold), for the remaining three listeners. This finding somewhat limits the interpretation of the adjustment data obtained for the highest carrier modulation frequency, since the absence of a systematic shift in matching f'_m would be compatible with all the different hypotheses listed in the introduction (i.e., modulation-distortion or venelope component, temporal mechanism, modulation excitation-pattern cues).

Overall, the results indicate that listeners are able to adjust accurately the matching f'_m to the second-order modulation frequency of unshifted harmonic standard stimuli, but under- or overestimate the envelope-beat frequency of frequency-shifted standard stimuli. In that case, prominent systematic shifts in matching f'_m are observed mainly for the two lowest values of n, i.e., when the nominal carrier modulation frequency was 15 or 20 Hz. Here, shifts in matching f'_m range on average from −10% to +8% and from −8% to +4% of the standard f'_m when $n=3$ and 4, respectively. These overall trends represent well the shifts observed in individual data of three out of the five listeners (HC, CN, LB). For the remaining two listeners (MH, PE), shifts in matching f'_m are less pronounced or less systematic. Listener MH shows a general underestimation (i.e., mainly negative shifts) of the

TABLE I. Observed mean and predicted slopes as a function of matching-stimulus type and harmonic rank n. The goodness-of-fit of linear best-fitting lines for mean shifts in matching f_m or f'_m is given by r^2. Predictions are based on the ratio $\Delta f_m/n$, with n corresponding to the harmonic rank of the first-order (carrier) modulation of the standard stimulus. The last two columns indicate if the predicted and/or zero slopes fall inside (−) or outside (×) the 95% confidence interval ($CI_{.95}$) around the observed slope.

Type of SAM matching stimuli	Harmonic rank n	r^2	Observed slope [$CI_{.95}$]	Predicted slope	Difference from predicted	Difference from zero
first-order	3	0.99	1.76 [−0.56; 4.08]	6.67	×	−
first-order (without PE)	3	0.99	2.39 [0.22; 4.57]	6.67	×	×
first-order	12	0.68	0.49 [−0.53; 1.50]	1.67	×	−
second-order	3	0.89	1.95 [0.92; 3]	6.67	×	×
second-order	4	0.97	1.16 [0.62; 1.72]	5	×	×
second-order	7	0.74	0.51 [−0.07; 1.08]	2.86	×	−
second-order	12	0.59	0.40 [−0.13; 0.93]	1.67	×	−

second-order modulation frequency. For the higher nominal carrier modulation frequencies under study (when $n=7$ or 12), introducing frequency shifts does not systematically affect the perception of the envelope-beat frequency in four out of the five listeners. However, systematic shifts are also apparent at these higher harmonic ranks in listener HC. It is noteworthy that the individual standard deviations of matching f'_m stay constant across the different harmonic ranks.

In all listeners, when shifts in matching f'_m occurred, the magnitudes of these shifts tend to decrease as a function of harmonic rank, thereby following qualitatively the predictions. However, shifts are consistently smaller than what can be expected based on $\Delta f_m/n$.

Best-fitting lines (not shown) were calculated for the data obtained at each harmonic rank to compare slopes of predicted and observed shift lines. Table I shows goodness-of-fit measures (r^2) of the linear model adjusted to the mean data. For all harmonic ranks, the data points are well fitted by the linear model (all $r^2 \geqslant 0.59$). The inspection of best-fitting lines for individual adjustment data reveals that, when shifts are observed, the linear model provides a good fit for each listener (all $r^2 \geqslant 0.55$), and the observed slopes are approximately two to four times shallower than those predicted by the ratio $\Delta f_m/n$.

To test if the slopes of the observed shifts in perceived envelope-beat frequency are significantly different from zero, the 95% confidence intervals for the slopes of the best-fitting lines were calculated. Zero slopes would be predicted if a modulation-distortion or venelope component rather than the first-order envelope determined the perceived envelope-beat frequency. Table I shows predictions and observed mean slopes for all experimental conditions (type of matching stimulus × harmonic rank). The last two columns indicate if the predicted and/or zero slopes fall within (−) or outside (×) the 95% confidence interval ($CI_{.95}$; the lower and upper limits of the interval are given in parentheses).

The results in Table I reveal that, for second-order SAM matching stimuli, all observed slopes differ significantly from predicted shift lines, confirming the visual impression that the observed shifts are always smaller than $\Delta f_m/n$. However, the statistical analysis indicates that the observed slopes are significantly different from zero when $n=3$ and 4, only.

IV. EXPERIMENT 3: SECOND-ORDER AM-FREQUENCY MATCHING WITH FIRST-ORDER AM

A. Method

In the second matching experiment, listeners were asked to adjust the modulation frequency of a first-order SAM matching stimulus to be equal to the perceived envelope-beat frequency of a second-order SAM standard stimulus. The apparatus, experimental setup, matching procedure, and stimulus parameters were otherwise identical to those used in the first matching experiment. However, measurements conducted with this type of matching stimulus were restricted to conditions where $n=3$ and 12 and the standard stimulus was frequency-shifted only by 0%, ±50%, or ±100% of the standard f'_m.

Four out of the initial five listeners took part in this matching experiment. All listeners initially had difficulty performing the matching task, leading to poor consistency across repeated adjustments. Informal questioning of the listeners revealed that this difficulty was due to the different percepts evoked by the second-order SAM standard and first-order SAM matching stimuli [it is noteworthy that similar difficulties were already mentioned by Schouten *et al.* (1962) when SAM tones had to be matched with unmodulated pure tones]. Thus, listeners received at least three practice runs in each experimental condition prior to data collection. This lasted approximately 4 h.

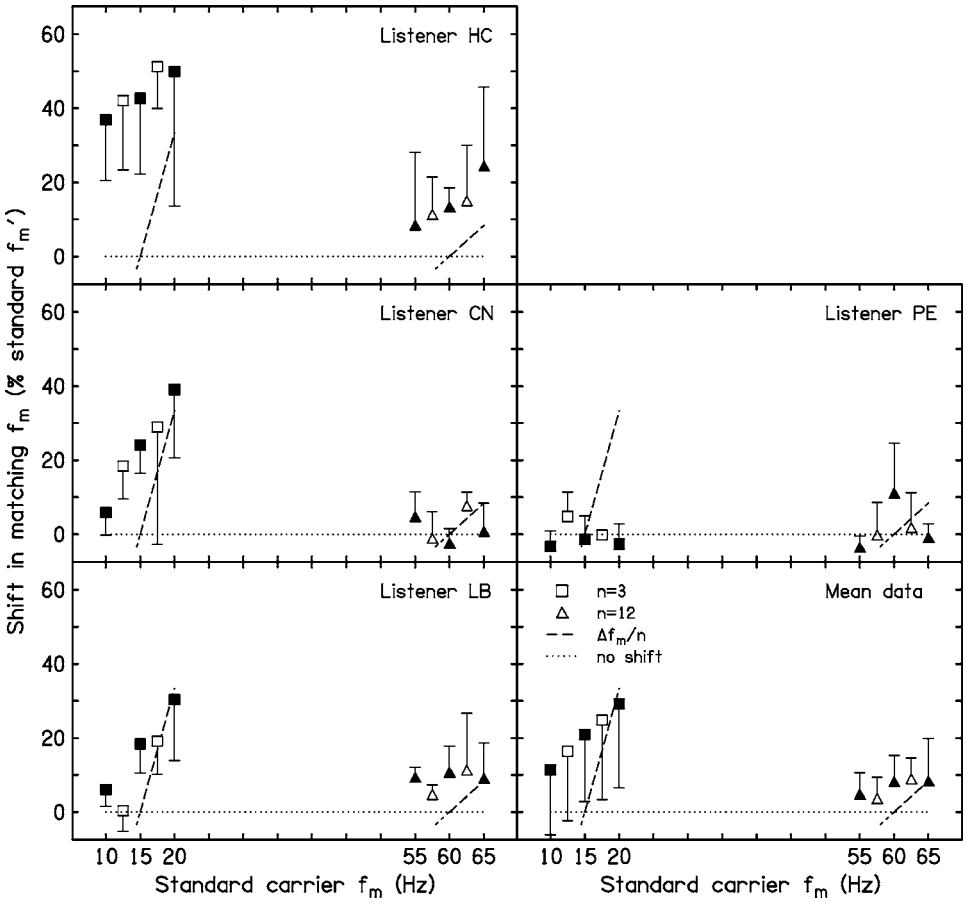

FIG. 4. Individual and mean results for the envelope-beat matching task, using first-order SAM matching stimuli. Otherwise as in Fig. 3. Note that the ordinate only shows positive shifts in matching f_m. Predictions (broken lines) continue below zero as indicated by the short dashes.

B. Results

Mean and individual results obtained using a first-order SAM matching stimulus are plotted in Fig. 4. For $n=3$, systematic shifts in matching f_m (expressed as a percentage of the standard f_m') are apparent in all listeners, except for listener PE, who already showed less pronounced shifts in the previous matching task. For the highest harmonic rank tested here ($n=12$), a systematic change in perceived envelope-beat frequency with shifts in carrier modulation frequency is only apparent in listener HC, who was the only listener showing a shift in the same harmonic rank condition using a second-order SAM matching stimulus. The steepness of the observed individual shift lines is similar to that obtained with second-order SAM matching stimuli. In contrast to the first matching experiment, all listeners systematically overestimated the second-order AM frequency of the standard stimulus (on average, by about 21% and 7% of the standard f_m' when $n=3$ and 12, respectively). In addition, the listeners' adjustments were more variable over the four repeated measures when a first-order SAM matching stimulus was used than when the standard and matching stimuli consisted of second-order AM.

As shown in Table I, both observed slopes for first-order SAM matching stimuli differ significantly from predicted shift lines, but none is significantly different from zero despite the apparent systematic shifts in three listeners with $n=3$. However, when listener PE, who shows no systematic shift in this condition, is excluded from the analysis, the slope is significantly different from zero. The comparison of slopes observed in the two matching experiments for identical harmonic ranks shows no significant difference due to the type of SAM matching stimuli used.

V. GENERAL DISCUSSION

Previous studies reviewed in the Introduction section provided evidence that the perception of the envelope beat of two- or three-component modulators is based on a modulation-distortion or venelope component at the envelope-beat frequency. This assumption was tested in two envelope-beat matching experiments. The present results showed that audible frequency shifts applied to the carrier modulation frequency of a second-order SAM stimulus had a systematic effect on the perception of its envelope beat; an increase (or decrease) in carrier modulation frequency by Δf_m led to an overestimation (or underestimation) of the envelope-beat frequency by an amount that was roughly proportional to Δf_m. Such shifts in perceived envelope-beat frequency occurred mainly at the lowest carrier modulation frequencies (at harmonic ranks 3 and 4), although one listener showed a systematic effect of Δf_m at all harmonic ranks under study (i.e., 3–12). This observation indicates that, at least at these low carrier modulation frequencies, the perceived slow envelope beat is not determined by a modulation-distortion or venelope component, both of which should have led to adjustments to the envelope-beat frequency independently of the harmonicity of the modulation components. Instead, the data are in line with the idea that it is the first-order envelope that provides crucial information for envelope-beat

perception. According to this interpretation, the observed shifts in perceived f_m' are due to changes in the time intervals between prominent peaks in the first-order envelope. The present results therefore appear consistent with the existence of a purely temporal mechanism computing the time intervals between the main peaks of the first-order envelope. At first sight, it may be assumed that the current matching data (shallower-than-predicted frequency-shift functions and effect of increasing n) reflect the effect of internal noise and coding variance that increases with the first-order modulation frequency. This notion is consistent with the general form of the modulation-frequency discrimination functions reported in experiment 1. However, in experiments 2 and 3, this added noise should increase the variance among matches in any condition without changing the average value. Thus, such an interpretation must be discarded. A more plausible interpretation may be that listeners do not maintain consistent use among the possible first-order envelope peaks that can estimate the second-order envelope period during a single (and relatively long) observation interval. As a consequence, the final judgment of the second-order envelope period may correspond to an average of the various estimates. With increasing n, this average converges on the period of the second-order modulator leading to a reduction of the shift in estimated envelope-beat frequency.

In the framework of currently proposed AM-processing schemes, the temporal mechanism should operate at the output of the envelope detector (i.e., a bank of modulation channels or a temporal integrator). This view contrasts with the parallel (i.e., dual-route) architecture (proposed for venelope extraction) since it suggests distinct, but sequentially coordinated processing stages for the extraction of auditory first- and second-order temporal-envelope information.

Though the present set of data does not necessarily preclude the existence of a (weak) modulation-distortion or venelope component, it clearly minimizes the role played by such a component in temporal-envelope-beat perception. Indeed, the smaller-than-expected shifts in matching f_m or f_m' may indicate that listeners have access to both high-frequency carrier modulation information and low-frequency modulation-distortion or venelope information and the perceived envelope-beat frequency corresponds to some form of trade-off or competition between these two sources of information. However, in contrast with the "competition hypothesis," detailed inspection of individual data reveals that listeners did not adjust the matching f_m or f_m' alternatively to f_m or f_m' of the standard stimulus across successive adjustments.

Since the second-order SAM standard and matching stimuli used in experiment 2 had identical harmonic ranks, listeners might have matched excitation patterns evoked by these stimuli in the modulation-frequency domain, rather than the low-frequency envelope beat. For instance, listeners might have matched the centroids or any part of the modulation excitation patterns. Given the poor selectivity of the auditory system in the modulation-frequency domain (e.g., Ewert and Dau, 2000), this would be possible at the lowest carrier modulation frequencies (i.e., when $n=3$ or 4), only. Thus, the observed shifts in matching f_m' at $n=3$ and 4 may (partly) reflect variations in modulation excitation patterns. Biases of this type were reported by Moore and Moore (2003) in the audio-frequency domain for pitch perception of inharmonic SAM tones. In the modulation-frequency domain, shifts due to changes in modulation excitation patterns are not expected when the matching stimulus is a first-order AM. However, shifts in matching f_m with similar slopes to those obtained with second-order SAM matching stimuli were observed in three out of four listeners at $n=3$. Thus, it appears that modulation excitation-pattern cues were not used in the first matching task. Nevertheless, when first-order SAM matching stimuli were used, most listeners largely overestimated the envelope-beat frequency of standard stimuli, suggesting that the high-frequency information of the carrier and/or sideband components contributed to the listeners' estimates. In other words, the more rapid first-order fluctuations acted somewhat like a perceptual anchor, positively biasing the perceived second-order modulation frequency of the standard stimuli. However, several observations invalidate the idea that the listeners solely relied on this high modulation-frequency cue. Firstly, shifts in matching f_m rarely exceeded 50% of the standard f_m' (i.e., about 2.5 Hz) and, secondly, the magnitude of the shifts did not increase but in fact decreased with carrier modulation frequency.

Finally, an alternative (albeit more speculative) interpretation is that different mechanisms operate in the low and high modulation-frequency regions; slow envelope fluctuations may be coded by temporal response patterns while fast envelope fluctuations may be coded by discharge rate. Such a dual AM-coding scheme has been supported by recent physiological (Schulze and Langner, 1997; Lu *et al.*, 2001a, b) and modeling studies (Sheft and Yost, 2005). As a consequence, envelope-beat information may be processed via a temporal mechanism when carried by low-frequency modulations, whereas a weak, but audible, modulation-distortion or venelope component would become (more) important when higher modulation components are used. Given the intrinsic limitations of the present experimental setting, it is not possible to determine which of the two approaches (distortion/venelope component versus temporal mechanisms) is responsible for the fact that shifts in matching f_m or f_m' disappear when the modulation components are above 30 Hz.

VI. SUMMARY AND CONCLUSIONS

Taken together, the results indicate the following.

(1) The perception of the low-frequency envelope beat of complex temporal envelopes with modulation components below 30 Hz is not determined by a modulation-distortion or venelope component. Instead, it relies at least partially on first-order envelope information, suggesting that current models of complex temporal-envelope perception should be revised to incorporate a contribution of first-order envelope information.
(2) The perceived slow envelope beat of complex temporal envelopes with modulation components below 25 Hz is not influenced by changes in modulation excitation-pattern cues evoked by those stimuli.

(3) The perception of low-frequency envelope beats presumably results from the operation of a purely temporal mechanism estimating the time intervals between the most prominent peaks in the first-order envelope. Such a mechanism operates at the output of either type of envelope processor: a modulation filterbank or a temporal integrator. Alternatively, the reported results of smaller-than-predicted shifts may be consistent with a combination of a modulation-distortion or venelope component and first-order timing information.

ACKNOWLEDGMENTS

This research was supported by a MENRT grant to C. Füllgrabe and a grant from the Institut Universitaire de France to C. Lorenzi. We wish to thank B. C. J. Moore for having suggested the second matching experiment and for his helpful comments during the course of this research. We also thank Neal Viemeister for helpful discussions and Stan Sheft and an anonymous reviewer for valuable suggestions on previous versions of this manuscript.

Bacon, S. P., and Grantham, D. W. (**1989**). "Modulation masking patterns: Effects of modulation frequency, depth, and phase," J. Acoust. Soc. Am. **85**, 2575–2580.

Dau, T., Kollmeier, B., and Kohlrausch, A. (**1997a**). "Modeling auditory processing of amplitude modulation. I. Modulation detection and masking with narrow-band carriers," J. Acoust. Soc. Am. **102**, 2892–2905.

Dau, T., Kollmeier, B., and Kohlrausch, A. (**1997b**). "Modeling auditory processing of amplitude modulation. II. Spectral and temporal integration in modulation detection," J. Acoust. Soc. Am. **102**, 2906–2919.

Ewert, S. D., and Dau, T. (**2000**). "Characterizing frequency selectivity for envelope fluctuations," J. Acoust. Soc. Am. **108**, 1181–1196.

Ewert, S. D., Verhey, J. L., and Dau, T. (**2002**). "Spectro-temporal processing in the envelope-frequency domain," J. Acoust. Soc. Am. **112**, 2921–2931.

Formby, C. (**1985**). "Differential sensitivity to tonal frequency and to the rate of amplitude modulation of broadband noise by normally hearing listeners," J. Acoust. Soc. Am. **78**, 70–77.

Füllgrabe, C., and Lorenzi, C. (**2003**). "The role of envelope beat cues in the detection and discrimination of second-order amplitude modulation," J. Acoust. Soc. Am. **113**, 49–52.

Füllgrabe, C., Demany, L., and Lorenzi, C. (**2005a**). "Detecting changes in amplitude-modulation frequency: A test of the concept of excitation pattern in the temporal-envelope domain," in *Auditory Signal Processing: Physiology, Psychoacoustics, and Models*, edited by D. Pressnitzer, A. de Cheveigné, S. McAdams, and L. Collet (Springer, New York), pp. 230–236.

Füllgrabe, C., Maillet, D., Moroni, C., Belin, C., and Lorenzi, C. (**2004**). "Detection of 1st- and 2nd-order temporal envelope cues in a patient with left superior cortical damage," Neurocase **10**, 189–197.

Füllgrabe, C., Moore, B. C. J., Demany, L., Ewert, S. D., Sheft, S., and Lorenzi, C. (**2005b**). "Modulation masking with 2nd-order modulators," J. Acoust. Soc. Am. **117**, 2158–2168.

Hanna, T. E. (**1992**). "Discrimination and identification of modulation rate using noise carrier," J. Acoust. Soc. Am. **91**, 2122–2128.

Houtgast, T. (**1989**). "Frequency selectivity in amplitude-modulation detection," J. Acoust. Soc. Am. **85**, 1676–1680.

Lee, J. (**1994**). "Amplitude modulation rate discrimination with sinusoidal carriers," J. Acoust. Soc. Am. **96**, 2140–2147.

Levitt, H. (**1971**). "Transformed up-down methods in psychoacoustics," J. Acoust. Soc. Am. **49**, 467–477.

Lorenzi, C., Soares, C., and Vonner, T. (**2001a**). "Second-order temporal modulation transfer functions," J. Acoust. Soc. Am. **110**, 1030–1038.

Lorenzi, C., Simpson, M. I. G., Millman, R. E., Griffiths, T. D., Woods, W. P., Rees, A., and Green, G. G. R. (**2001b**). "Second-order modulation detection thresholds for pure-tone and narrow-band noise carriers," J. Acoust. Soc. Am. **110**, 2470–2478.

Lu, T., Liang, L., and Wang, X. (**2001a**). "Neural representations of temporally asymmetric stimuli in the auditory cortex of awake primates," J. Neurophysiol. **85**, 2364–2380.

Lu, T., Liang, L., and Wang, X. (**2001b**). "Temporal and rate representations of time-varying signals in the auditory cortex of awake primates," Nat. Neurosci. **4**, 1131–1138.

Millman, R. E., Green, G. G. R, Lorenzi, C., and Rees, A. (**2003**). "Effect of a modulation noise masker on the detection of second-order amplitude modulation," Hear. Res. **178**, 1–11.

Moore, B. C. J., Sek, A., and Glasberg, B. R. (**1999**). "Modulation masking produced by beating modulators," J. Acoust. Soc. Am. **106**, 908–918.

Moore, G. A., and Moore, B. C. J. (**2003**). "Perception of the low pitch of frequency-shifted complexes," J. Acoust. Soc. Am. **113**, 977–985.

Schouten, J. F., Ritsma, R. J., and Cardozo, B. L. (**1962**). "Pitch of the residue," J. Acoust. Soc. Am. **34**, 1418–1424.

Schulze, H., and Langner, G. (**1997**). "Periodicity coding in the primary auditory cortex of the Mongolian gerbil (*Meriones unguiculatus*): two different coding strategies for pitch and rhythm?," J. Comp. Physiol., A **181**, 651–663.

Sek, A., and Moore, B. C. J. (**2003**). "Testing the concept of a modulation filter bank: The audibility of component modulation and detection of phase change in three-component modulators," J. Acoust. Soc. Am. **113**, 2801–2811.

Sek, A., and Moore, B. C. J. (**2004**). "Estimation of the level and phase of the simple distortion tone in the modulation domain," J. Acoust. Soc. Am. **116**, 3031–3037.

Shannon, R. V., Zeng, F., Kamath, V., Wygonski, J., and Ekelid, M. (**1995**). "Speech recognition with primarily temporal cues," Science **270**, 303–304.

Sheft, S., and Yost, W. A. (**1997**). "Modulation detection interference with two-component masker modulators," J. Acoust. Soc. Am. **102**, 1106–1112.

Sheft, S., and Yost, W. A. (**2005**). "Minimum integration times for processing of amplitude modulation," in *Auditory Signal Processing: Physiology, Psychoacoustics, and Models*, edited by D. Pressnitzer, A. de Cheveigné, S. McAdams, and L. Collet (Springer, New York), pp. 244–250.

Shofner, W. P., Sheft, S., and Guzman, S. J. (**1996**). "Responses of ventral cochlear nucleus units in the chinchilla to amplitude modulation by low-frequency, two-tone complexes," J. Acoust. Soc. Am. **99**, 3592–3605.

Smith, Z. M., Delgutte, B., and Oxenham, A. J. (**2002**). "Chimaeric sounds reveal dichotomies in auditory perception," Nature (London) **416**, 87–90.

Strickland, E. A., and Viemeister, N. F. (**1996**). "Cues for discrimination of envelopes," J. Acoust. Soc. Am. **99**, 3638–3646.

Verhey, J. L., Ewert, S. D., and Dau, T. (**2003**). "Modulation masking produced by complex tone modulators," J. Acoust. Soc. Am. **114**, 2135–2146.

Viemeister, N. F. (**1979**). "Temporal modulation transfer functions based upon modulation thresholds," J. Acoust. Soc. Am. **66**, 1364–1380.

Spatial unmasking of birdsong in human listeners: Energetic and informational factors[a)]

Virginia Best, Erol Ozmeral, Frederick J. Gallun,
Kamal Sen, and Barbara G. Shinn-Cunningham[b)]
Hearing Research Center, Boston University, 677 Beacon Street Boston, Massachusetts 02215

(Received 21 April 2005; revised 29 July 2005; accepted 7 October 2005)

Spatial unmasking describes the improvement in the detection or identification of a target sound afforded by separating it spatially from simultaneous masking sounds. This effect has been studied extensively for speech intelligibility in the presence of interfering sounds. In the current study, listeners identified zebra finch song, which shares many acoustic properties with speech but lacks semantic and linguistic content. Three maskers with the same long-term spectral content but different short-term statistics were used: (1) chorus (combinations of unfamiliar zebra finch songs), (2) song-shaped noise (broadband noise with the average spectrum of chorus), and (3) chorus-modulated noise (song-shaped noise multiplied by the broadband envelope from a chorus masker). The amount of masking and spatial unmasking depended on the masker and there was evidence of release from both energetic and informational masking. Spatial unmasking was greatest for the statistically similar chorus masker. For the two noise maskers, there was less spatial unmasking and it was wholly accounted for by the relative target and masker levels at the acoustically better ear. The results share many features with analogous results using speech targets, suggesting that spatial separation aids in the segregation of complex natural sounds through mechanisms that are not specific to speech. © *2005 Acoustical Society of America.*
[DOI: 10.1121/1.2130949]

PACS number(s): 43.66.Dc, 43.66.Pn [RAL] Pages: 3766–3773

I. INTRODUCTION

In natural environments, sound sources of interest often must be extracted from a background of noise and other distracting sounds. There is a rich history of studies addressing this problem in the context of speech intelligibility, where a listener must extract the content of one source (a "target") in the presence of competing sources ["maskers;" see Bronkhorst (2000) for a recent review]. Masking is thought to have two main forms. The first is "energetic masking," in which the masker reduces the audibility of components of the target due to interference in peripheral frequency channels. The classic illustration of energetic masking is the disruption of speech intelligibility caused by the presence of broadband noise. However, a different kind of masking can occur in addition to energetic masking, or even in the absence of frequency overlap between target and masker. If a competing signal has similar spectro-temporal characteristics, it can interfere with the perception of a target at a more central perceptual level (so-called "informational masking;" Pollack, 1975; Watson, 1987; Durlach *et al.*, 2003). For example, this kind of masking is thought to be a factor in the masking of speech by other talkers with similar voices (Carhart *et al.*, 1969; Brungart *et al.*, 2001).

In most masking situations, spatial separation of the target from the masker(s) improves performance. For primarily energetic maskers, this "spatial unmasking" has two components. First, the relative energy of the target and masker reaching the ears changes with target and masker location. Usually, spatial separation of target and masker increases the audibility of the target in each frequency band at one of the ears. Second, binaural processing increases the audibility of a target in a particular band if the target and masker contain different interaural time and/or level differences (Zurek, 1993; Bronkhorst, 2000). For primarily informational maskers, the benefit of spatial separation can be much greater than for energetic maskers. In these conditions it is thought that the differences in perceived location strengthen the formation of distinct objects and reduce confusion between the two sources (Freyman *et al.*, 1999; Arbogast *et al.*, 2002; Kidd *et al.*, 2005).

Many studies have attempted to unravel the contribution of these various factors to speech-on-speech masking and spatial unmasking. Energetic effects are examined by using a noise masker that is matched in its magnitude spectrum to the long-term average spectrum of speech ("speech-shaped noise"). As speech maskers contain large fluctuations in energy which may allow subjects to "listen in the gaps," a more appropriate energetic masking control for actual speech is a noise masker modulated by the envelope of a speech signal. Although informational masking is somewhat more difficult to isolate using natural stimuli, it is often assumed to include any additional masking seen with a speech-on-speech masker that cannot be explained by energetic effects in the peripheral auditory representation. Several recent studies adopted a powerful paradigm to minimize energetic masking and em-

[a)]Portions of this work were presented at the 2005 Mid-Winter meeting of the Association for Research in Otolaryngology.
[b)]Author to whom correspondence should be addressed. Electronic mail: shinn@cns.bu.edu

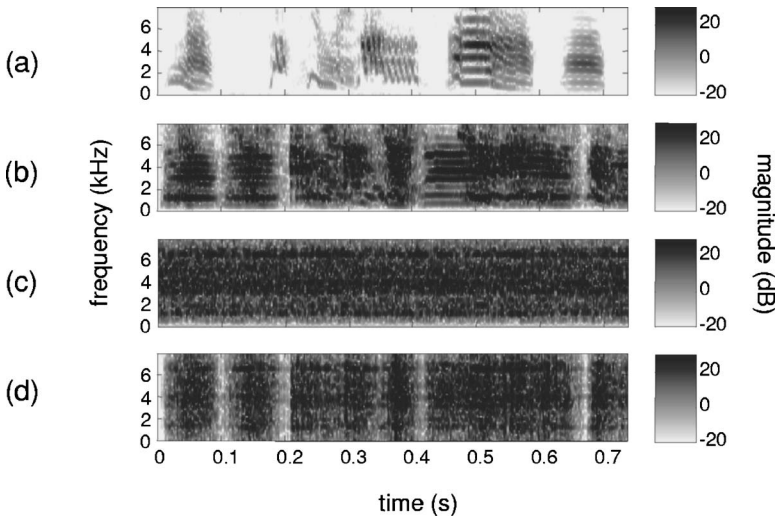

FIG. 1. Spectrograms of (a) an example target song, (b) a chorus masker, (c) a song-shaped noise masker, and (d) a chorus-modulated noise masker.

phasize informational masking by processing competing speech signals to have very little masking due to spectral overlap (e.g., see Arbogast *et al.*, 2002). These studies suggest that fundamentally different mechanisms underlie spatial release from energetic and informational masking. For instance, one important feature of spatial release from informational masking is that it appears to be robust to reverberation, unlike spatial release from energetic masking (Kidd *et al.*, 2005).

In natural environments, both energetic and informational masking undoubtedly influence the perception of sound sources (e.g., see Oh and Lutfi, 1999). Interestingly, few studies have examined spatial unmasking with complex natural sounds other than speech. In the current study, zebra finch songs were used to replace human speech in some of the classic masking conditions described above. One reason for using zebra finch song as a stimulus is that it has a structure that is similar to speech: both are spectro-temporally complex but relatively sparse, both have clear harmonic structure, and both possess dynamic features such as frequency modulation and comodulation across frequency (Doupe and Kuhl, 1999). By using these songs as stimuli in human experiments we can uncouple the influences of complex spectro-temporal sound structure from top-down linguistic and semantic effects that may affect masked speech perception. In previous studies this goal has been met using reversed speech, which is strongly speechlike but is not intelligible (e.g., see Freyman *et al.*, 2001). However, if spatial unmasking follows similar patterns for zebra finch song, it strongly suggests that the brain has general mechanisms for dealing with complex structured stimuli that are not specific to speech.

II. METHODS

A. Stimuli

1. Target songs

Songs from five male zebra finches (*Taeniopygia guttata*) were used as target stimuli. Between 5 and 30 songs were recorded from each of the five birds. Recordings were conducted in a single-walled sound-treated both (Industrial Acoustics Company, New York) using a single microphone (Audio-Technica AT3031) placed 7 in. above the caged bird. Often, to entice singing, a female bird was placed temporarily in a neighboring cage in the booth. Four of the birds were recorded with a sampling rate of 32 kHz and one with a rate of 41.1 kHz.

Recorded songs consisted of many smaller elements (syllables) arranged into repeated patterns (motifs). Five similar motifs were selected from each bird's repertoire. Each motif was highly stereotypical for a particular bird but quite distinct from those of the other birds. For example, each bird's motif generally consists of a particular pattern of syllables repeated in a fixed order with nearly identical rhythm. Motifs vary across birds in the exact syllables making up the motif as well as the number and rhythm of the syllables. Overall duration of the motifs varied from 750 to 1000 ms across the five birds. For uniformity, all were low-pass filtered at 8 kHz before use in this experiment. The 25 motifs were used both for the identification training and for the masking experiment (see Sec. II B). A spectrogram representation of a sample target motif is shown in Fig. 1(a).

2. Masker stimuli

Three types of masker were used, all with the same long-term spectral characteristics but different short-term statistics. All maskers were generated with duration 1 s to ensure that all target motifs could be fully masked in time. Figure 1 (panels b–d) shows spectrogram representations of examples of each of the three maskers.

Chorus maskers: To make maskers that could easily be mistaken for targets, chorus maskers were generated by adding three song motifs from unfamiliar birds together. Six such mixtures were generated by using all possible combinations of three unfamiliar motifs drawn randomly from a set of five. These unfamiliar motifs were obtained in a previous experiment from five unfamiliar birds. Before adding the unfamiliar motifs to create the chorus, each was looped as necessary to create a 1-s long signal. An example of a chorus masker is shown in Fig. 1(b).

Song-shaped noise maskers: Song-shaped noise maskers were created by generating broadband noise that had a spec-

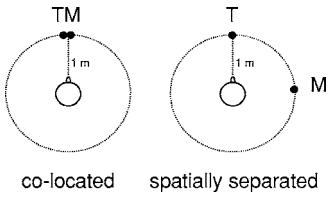

FIG. 2. The two spatial configurations examined. The target (T) was always located directly in front of the listener. The masker (M) was either co-located with the target (left panel) or spatially separated at 90° to the right (right panel).

tral profile matching that of the average of the set of chorus maskers. Twelve independent maskers were generated and an example is shown in Fig. 1(c).

Chorus-modulated noise maskers: Chorus-modulated noise maskers were generated by modulating a song-shaped noise with the envelope from a random chorus masker. Six such maskers were created, using the six chorus envelopes and six different song-shaped noises. These maskers are more similar to the song targets than the song-shaped noise maskers as they contain broad fluctuations in energy over time. An example is shown in Fig. 1(d).

On each trial, one target and one masker were presented simultaneously at one of seven randomly selected target-to-masker ratios (TMRs). TMR was calculated using the broadband rms levels of the two signals. The target level was varied to produce TMRs evenly spaced between −40 and 8 dB. These TMRs were chosen on the basis of preliminary testing to span the sloping portions of psychometric functions relating identification performance to TMR. The overall presentation level of the stimulus was set by individual subjects such that the masker level (which remains fixed on every trial) was at a comfortable listening level and the highest TMR was not uncomfortable.

3. Spatialization

For the masking experiment, stimuli were first processed to create binaural signals containing realistic spatial cues, then presented over headphones. The stimuli were processed with pseudo-anechoic head-related transfer functions (HRTFs) measured on a KEMAR manikin at a distance of 1 m (Shinn-Cunningham *et al.*, 2005) in the horizontal plane at the level of the ears (0° elevation). In all trials the target was processed by the HRTFs from straight ahead (0° azimuth). The masker was processed with either the same HRTFs at 0° azimuth ("co-located") or with HRTFs at 90° azimuth ("spatially separated"), as depicted in Fig. 2.

The resulting spatialized target and masker signals were then added to simulate two sources with the desired spatial cues. To create a realistic, externalized percept, the left and right ear binaural signals for target and masker were summed ("spatial" presentation). In control trials, the energetically "better ear" (the one with the highest target-to-masker ratio) was presented to both ears simultaneously ("diotic" control). This condition exactly reproduced the TMR at the better ear caused by the spatial configuration of target and masker, but removed any differences in perceived location of target and masker.

Casual listening confirmed that the recorded zebra finch songs signals were very "dry" (i.e., not strongly affected by reverberation). Furthermore, because each signal was processed through anechoic HRTFs to generate the spatialized stimuli, any reverberant energy present in the recorded songs could not have caused any interaural decorrelation which might reduce spatial unmasking.

B. Experimental procedures

1. Subjects

Five listeners (one male, four female, aged 22–27) were paid for their participation in the experiment, which included both training and testing (see below). Listeners were screened to ensure that they had normal hearing (within 10 dB) for frequencies between 250 Hz and 8 kHz.

2. Environment

Presentation of the stimuli was controlled by a PC, which selected the stimulus to play on a given trial. Digital stimuli were resampled to 50 kHz and sent to Tucker-Davis Technologies hardware for D/A conversion and attenuation before presentation over headphones (Sennheiser HD-580). Subjects were seated in a sound-treated booth in front of the PC terminal displaying a graphical user interface (GUI). Following each presentation, subjects identified which target bird they heard by clicking on the GUI with a mouse, allowing the PC to store their responses. MATLAB software (Mathworks Inc.) was used to generate the stimuli (offline), to control stimulus presentation, and to collect responses for later analysis.

3. Identification training

Subjects were trained to identify the five target birds on the basis of their unique song motifs. Each target bird was given a name ("Uno," "Junior," "Moe," "Toro," and "Nibbles") that subjects were trained to associate with the specific motifs. Training began with a familiarization session in which subjects could press one of five labeled buttons on the GUI and hear the song of the corresponding bird. This session continued for as long as the subject desired. Subjects became familiar with the birds relatively quickly and reported anecdotally that the different birds were distinguishable on the basis of (a) particular syllables having a unique pitch or structure as well as (b) the temporal arrangement of syllables.

After familiarization, subjects initiated an identification test of 100 trials. In this test, a target was presented in quiet (with no masker) and the subject was required to identify the bird by clicking on the appropriate button. Correct response feedback was provided in written form on the screen. Subjects were required to achieve a score of at least 90% on this test before moving on to the masking experiment, and all subjects met this criterion on their first attempt.

4. Masking experiment

The format of the masking tests was similar to that of the identification test, but a masking stimulus was present and no feedback was provided. In a single test, the masker

type (chorus, modulated-noise, or noise), spatial configuration (co-located or separated), and presentation mode (spatial or diotic) were fixed. Each test consisted of 35 trials (five repetitions at each of the seven TMRs, randomly interleaved). Subjects were instructed to listen for the target stimulus, which was always simulated as coming from directly in front, and to identify it by clicking on the GUI.

All combinations of masker type, spatial configuration, and presentation mode were tested in a single session, for a total of 12 tests per session. The tests were presented in a different random order for each subject. In order to ensure that subjects maintained their ability to identify the target birds in quiet during the experiment, short identification tests were interleaved with the masking tests. At the beginning of a new session, subjects were required to make 24 correct identifications in a 25-trial test in order to commence the masking test. Within a session, subjects were required to make 10 correct identifications on a 10-trial test before every masking test.

Each subject completed six sessions in total, corresponding to 30 trials at every TMR in every condition. No subject completed more than one session on any given day.

5. Generation of psychometric functions

Data were sorted by subject, masker type, and presentation condition, and psychometric functions were plotted for each case. Raw psychometric functions were generated by plotting performance (in percent correct) as a function of TMR (see Fig. 3). To enable the estimation of slope and threshold parameters, logistic functions were fit to each raw psychometric function.

III. RESULTS

A. Performance as a function of target-to-masker ratio

Figure 3 shows the mean raw psychometric functions across subjects for both co-located and spatially separated configurations (error bars indicate the across-subject standard deviation). The top, center, and bottom panels show data for the song-shaped noise masker, chorus-modulated noise masker, and chorus masker, respectively. For all conditions, performance improved with increasing TMR, from chance levels (20% correct) to near perfect identification. Furthermore, for all maskers, there was a large advantage to having target and masker spatially separated (compare squares to circles). For song-shaped and chorus-modulated noise maskers, spatial and diotic presentations gave similar results (compare filled and open symbols in top and center panels). However, for the chorus masker, spatial performance was superior to diotic performance, but only when the sources were spatially separated (compare filled and open symbols in bottom panel).

An additional observation that can be made about the psychometric functions is that their slopes vary with masker type. To quantify this effect, slopes of the logistic functions fit to the raw data were examined for each subject. Figure 4 shows the mean and standard deviation of these slope values

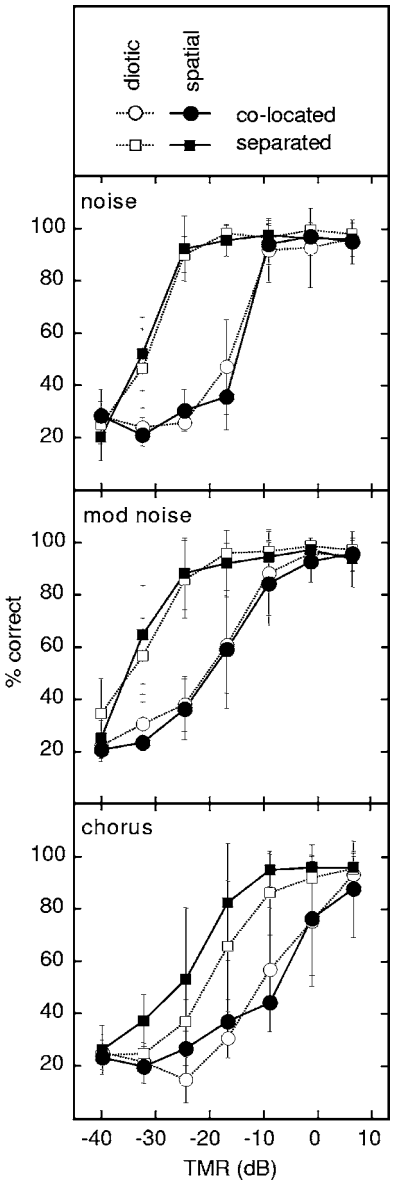

FIG. 3. Mean psychometric functions showing percentage correct for different TMRs. Data points represent the mean across subjects and error bars show standard deviations. Each panel shows results for one masking condition, and the four curves in a panel represent the different presentation conditions. Symbol type indicates spatial configuration (circles: co-located, squares: spatially separated). Symbol shading indicates listening condition (filled: spatial, open: diotic).

for each masker type (pooled across subjects and psychometric functions). On average, slopes were steepest for the song-shaped noise masker, but were similar for the other two maskers. An ANOVA revealed a significant effect of masker condition on slope [$F(2,57)=6.3$, $p=0.0034$], and *posthoc* analysis (Tukey HSD, $p=0.05$) confirmed that the song-shaped noise masker produced steeper slopes than the other two maskers.

B. Individual masked thresholds

In order to compare performance across the various conditions, thresholds were extracted from the individual logistic functions. Threshold was defined as the TMR giving 60% accuracy, which represents a performance level half-way be-

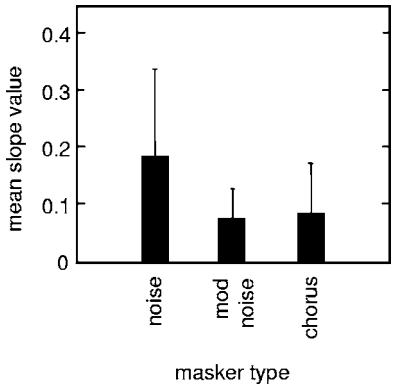

FIG. 4. Mean slopes of psychometric functions for each masker condition. Slope values were extracted from logistic fits to the raw data. Bars represent the mean across subjects and psychometric functions for a particular masker, and the error bars represent standard deviations across the pooled values.

tween chance (20%) and perfect performance (100%). Thresholds can be seen for the three maskers in the three panels of Fig. 5. In each panel, the five columns represent the five subjects with thresholds plotted in dB (note that a lower value indicates less masking).

This figure demonstrates that there were large individual differences, but also highlights several main effects. First, the chorus masker was a more effective masker than the two noise maskers. In general, thresholds are higher for the chorus masker than the noise maskers, i.e., the target had to be presented at a higher intensity to reach threshold performance. An ANOVA showed a significant effect of masker type $[F(2,57)=8.74,\ p=0.0005]$ and *posthoc* analysis (Tukey HSD, $p=0.05$) confirmed that thresholds for the chorus masker were significantly larger than for the two noise maskers. Second, spatial separation resulted in a reduction in masking for all subjects in all conditions (compare squares and circles). A third important result is seen in the difference between the spatial (filled symbols) and the diotic (open symbols) presentation conditions. For the two noise maskers, thresholds are essentially the same for spatial and diotic presentations. For the chorus masker, the spatial and diotic conditions produced similar thresholds in the co-located configuration. However, for the spatially separated configuration the spatial condition consistently produced less masking than

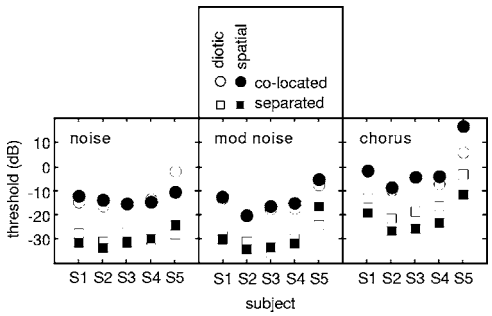

FIG. 5. Thresholds measured from fits to individual psychometric functions. The three panels show thresholds for the three masking conditions. For all panels, the five subjects are represented along the abscissa. Symbol type indicates spatial configuration (circles: co-located, squares: spatially separated). Symbol shading indicates listening condition (filled: spatial, open: diotic). Note that a lower threshold indicates better performance.

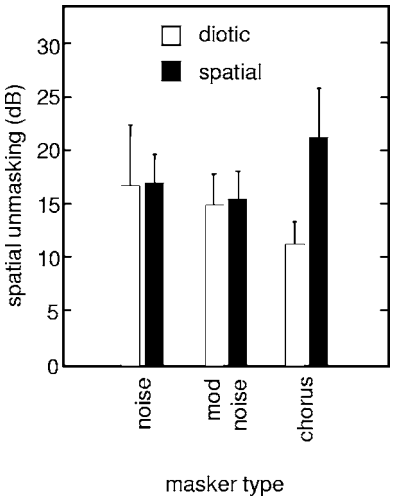

FIG. 6. Mean spatial unmasking (threshold for separated configuration minus threshold for co-located configuration). The three masking conditions are represented along the abscissa, and the bars represent the mean across subjects (filled: spatial, open: diotic). Note that a higher value represents a larger benefit of spatial separation. Error bars show standard deviations.

the diotic condition. These latter effects are quantified and examined more closely in the following section.

C. Spatial release from masking

Spatial unmasking was calculated by taking the difference in threshold between the co-located and spatially separated configurations for each subject and each condition. Mean spatial unmasking values, averaged across the five subjects, are plotted in Fig. 6 (error bars show across-subject standard deviations).

Spatial release from masking in the spatial listening condition was similar for the song-shaped noise and chorus-modulated noise maskers (means of 16.8 and 15.3 dB, respectively). For these noise maskers, spatial unmasking in the diotic listening condition was also substantial (means of 16.5 and 14.8 dB) and not significantly different from the spatial condition (paired t tests; $p=0.5, 0.4$, respectively). In contrast, for the chorus masker, there was a large advantage in the spatial listening condition (mean 21.1 dB compared to 11.1 dB for the diotic control), a difference that was highly significant (paired t test, $p=0.001$).

IV. DISCUSSION

A. Spatial unmasking of birdsong and speech in human listeners

For the two noise maskers (song-shaped noise and chorus-modulated noise), benefits of around 17 and 15 dB (respectively) were observed with spatial separation of the target and masker. These values are quite large compared to spatial benefits reported for the intelligibility of speech masked by speech-shaped noise. In his comprehensive review, Bronkhorst (2000) reported between 6 and 10 dB of spatial release from masking for various types of speech material in this configuration (target in front, masker in front or

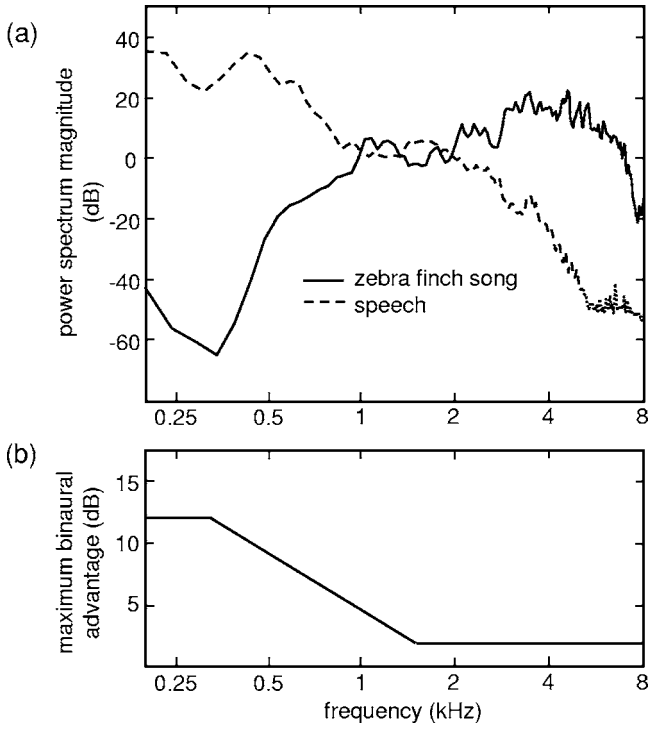

FIG. 7. (a) Mean power spectral density plots of zebra finch song and speech (see text for details of the samples used). (b) Maximum binaural advantage predicted by the model of Zurek (1993) as a function of frequency. This maximum corresponds to the detection of an interaurally out-of-phase signal in diotic noise (figure adapted from Zurek, 1993).

to the side). One likely explanation for this difference is that zebra finch song contains more high-frequency energy (above 2 kHz) than speech.

Figure 7(a) compares the power spectral density of zebra finch song and speech (calculated using the MATLAB function "psd"). The zebra finch song curve is based on the 25 target tokens used in the current experiment, and the speech curve is based on a sample of similar size from a well-known speech corpus (Bolia *et al.*, 2000). While the speech signals contain significant low-frequency energy and have spectral levels that drop off gradually above 1 kHz, the songs have most of their energy between 2 and 5 kHz (see also Zann, 1996). Given the small wavelengths at these frequencies and the size of the human head, the head-shadow effect for zebra finch song is large and greatly improves the target-to-masker ratio in the better ear when sources are spatially separated. Indeed, analysis of the long-term broadband TMR at the better ear showed an increase of approximately 18 dB with spatial separation, which can fully account for the benefits observed for the noise maskers. The idea that advantageous energy in the better ear is driving much of the observed spatial unmasking is consistent with the observation that the unmasking was equal in the spatial and diotic conditions for these maskers. In other words, for the noise maskers, the benefit of moving the masker to the side can be entirely explained by the change in energy at the better ear.

The fact that no additional spatial unmasking was observed with spatial presentation relative to diotic presentation for the noise maskers implies that ITD processing did not provide any release from masking for these stimuli. In contrast, for speech, additional advantages of binaural processing of up to 7 dB are typically observed (Carhart *et al.*, 1967; Dirks and Wilson, 1969). Models of binaural unmasking show that ITD effects are dominant for frequencies up to 500 Hz and essentially disappear for frequencies above 2 kHz [Zurek, 1993, see Fig. 7(b)]. Thus, this apparent discrepancy between spatial unmasking of zebra finch song and speech presumably reflects the different amounts of low-frequency energy present in the stimuli. Unlike speech, the zebra finch songs used in this study have very little energy below 2 kHz [Fig. 7(a)]. It may also be that the information below 2 kHz is less important for the identification of zebra finch song than for the identification of speech.

For the chorus masker, the better ear advantage was roughly 11 dB (i.e., diotic thresholds for the spatially separated configuration were 11 dB lower than for the co-located configuration). This benefit is smaller than that found for the noise maskers, presumably because the chorus masker is spectro-temporally sparser and therefore a less effective energetic masker than the noise maskers. However, in contrast to the noise maskers, the spatial release from masking in the spatial condition was greater than in the diotic condition for all subjects. It can be assumed that this extra spatial unmasking (approximately 10 dB) is not due to binaural processing, as it did not occur for the noise maskers (which have more energetic overlap and hence are more likely to gain an advantage from such within-channel processing). We attribute the large extra spatial unmasking seen with the chorus masker to a reduction in informational masking due to perceived differences in target song and chorus locations.

The mean spatial release from masking of 21.1 dB in the chorus condition of this study is large when compared to the spatial release reported in past speech studies. For studies of speech intelligibility against a background of same-talker speech, reported spatial unmasking values range up to 14 dB (e.g., see Freyman *et al.*, 1999). As discussed already, head-shadow contributes much more to spatial unmasking for zebra finch song than it does for speech. This large contribution of better-ear TMR benefit at least partially accounts for the large amounts of spatial unmasking observed in the current study. The 10 dB of extra unmasking that we attribute to informational unmasking (although remarkable) is within the range observed in speech tasks dominated by informational masking. In situations where informational masking dominates, release from masking can reach up to 18 dB (Arbogast *et al.*, 2002; Kidd *et al.*, 2005).

B. Evidence for different forms of masking

To summarize, the different maskers in the current experiment resulted in different patterns of masking and of spatial unmasking. A clear indication that the chorus masker produced the most informational masking is the fact that subjects made substantial identification errors even when the target was clearly audible in a chorus background (Fig. 3, TMRs of 0 and 8 dB). However, perhaps the most important finding was that the benefit of spatial separation for the chorus masker was much *greater* than for the noise maskers, even though the energetic gain due to separation was

smaller. This is consistent with the idea that spatial separation can act to reduce informational masking in situations where the target and masker have similar short-term spectrotemporal characteristics and are easily confused with one another (Durlach *et al.*, 2003). For this experiment, the spatial percept helped listeners group target segments together (and segregate them from masker segments), improving identification performance.

Secondary support for these different kinds of masking comes from the psychometric functions described in Sec. III A. It has been noted previously that more "informational" maskers tend to give rise to shallower psychometric functions than more "energetic" maskers (Festen and Plomp, 1990; Kidd *et al.*, 1998; Lutfi *et al.*, 2003). One reason that has been put forward for this is that informational maskers are generally less homogeneous than energetic maskers. If the different maskers in the inhomogeneous set are differentially effective (and give rise to psychometric functions with different thresholds), then averaging across these maskers will give rise to a shallower slope even if each masker-specific psychometric function is equally steep (see Durlach *et al.*, 2005). A second explanation for shallower slopes in informational masking is that the masking is due to confusion and thus depends less directly on target-to-masker ratio than energetic masking.

In the current study (Figs. 3 and 4) the psychometric functions were steepest for the song-shaped noise masker, the masker that was most homogeneous from trial-to-trial and which caused little informational masking. The chorus masker gave rise to shallower psychometric functions, consistent with both factors: the individual maskers were drawn from a highly inhomogeneous set, and the chorus masker may interfere with target song identification in a way that is only weakly dependent on TMR. The fact that the chorus-modulated noise masker (which had a similar amount of inhomogeneity) produced equally shallow psychometric functions suggests that masker inhomogeneity was a dominant factor affecting slope values in the current study. Interestingly, however, an analysis of the average performance level for the different masker tokens in the current study revealed no greater variability across chorus maskers and chorus-modulated noise maskers than across song-shaped noise maskers. Furthermore, there appeared to be no specific interaction between particular targets and particular chorus or chorus-modulated noise masker tokens. It remains to be seen whether this is a result of the heavy data reduction required for this analysis; perhaps a larger data set might reveal such effects.

It was interesting to find (as discussed in the previous section) that, in general, the contributions of energetic and informational masking and the relative benefits of spatial separation follow very similar patterns for zebra finch song and speech. Although there are differences in the extent to which spatial separation improves identification of these two natural stimuli, most of these differences can be attributed to differences in the acoustics of the stimuli (e.g., differences in which frequency range contains information about the speech or song content). In particular, it seems that identifying a bird in a chorus poses a problem similar to understanding a talker in the presence of other talkers. Such fundamental similarities suggest that there are general mechanisms for segregating complex sounds that are not unique to speech.

Traditional models of spatial unmasking (such as those estimating speech intelligibility in the presence of interference) cannot predict the effects of informational unmasking or the benefits of spatially separating target and masker when informational masking is dominant. Traditional models consider energy effects at the ears as well as binaural processing [see Colburn (1996) for a review], operating on each frequency channel independently. Thus, such models only explain within-channel masking effects. In the current study, as well as in the speech studies discussed earlier, benefits of spatial separation have been observed that (a) do not depend on frequency overlap and (b) are much larger than traditional "energetic" unmasking effects. Extensions of existing models are required to explain these effects and produce a complete picture of spatial unmasking with complex stimuli. Some modeling efforts have had success in predicting the effect of masker uncertainty on tone detection (e.g., Lutfi, 1993; Oh and Lutfi, 1999). However, some aspects of informational masking, such as confusion between target and masker components, have not yet been modeled. Furthermore, no models have been applied to explain performance in more complex tasks such as understanding speech in a mixture of similar maskers.

C. Final comments

This study demonstrated that for the human listener, spatial separation enhances the identification of a familiar zebra finch song in the presence of different kinds of interference. The results give insight into what kinds of masking can occur with these signals, and what factors can provide release from masking in humans. However, it is not known how relevant this situation is to the birds that use these signals for communication in real environments. While there is evidence that songbirds are capable of segregating mixtures of signals [see Hulse (2002) for a review], spatial factors have not yet been examined. Furthermore, some evidence suggests that spatial cues are not as salient for small birds as they are for humans (Park and Dooling, 1991; Dent and Dooling, 2004; however see Nelson and Suthers, 2004). It would be interesting to test zebra finches on the same stimuli used in this experiment, to address whether spatial unmasking enhances song identification in these birds.

V. CONCLUSIONS

Spatial separation enhanced the ability of human listeners to identify familiar zebra finch songs in the presence of interfering sounds with identical long-term spectra, but the nature of the benefit varied with the short-term statistics of the interference. All maskers showed a large benefit due to energetic advantages at the acoustically "better ear." For noise maskers this advantage could fully explain the observed spatial unmasking. However, for maskers made up of unfamiliar songs, there was an additional advantage of spatial separation that could not be solely explained by energetic effects. It appears that when the target and masker had simi-

lar short-term spectro-temporal characteristics, differences in perceived location helped listeners segregate the sources, leading to large reductions in informational masking. The data are consistent with previous studies examining speech recognition in the presence of noise and competing speech sources and provide further evidence that both energetic and informational masking influence behavior in natural acoustic settings.

ACKNOWLEDGMENTS

This work was supported by a grant from the Air Force Office of Scientific Research to BGSC (Grant No. FA9550-04-1-0260).

Arbogast, T. L., Mason, C. R., and Kidd, G. (**2002**). "The effect of spatial separation on informational and energetic masking of speech," J. Acoust. Soc. Am. **112**, 2086–2098.

Bolia, R. S., Nelson, W. T., Ericson, M. A., and Simpson, B. D. (**2000**). "A speech corpus for multitalker communications research," J. Acoust. Soc. Am. **107**, 1065–1066.

Bronkhorst, A. W. (**2000**). "The cocktail party phenomenon: A review of research on speech intelligibility in multiple-talker conditions," Acust. Acta Acust. **86**, 117–128.

Brungart, D. S., Simpson, B. D., Ericson, M. A., and Scott, K. R. (**2001**). "Informational and energetic masking effects on the perception of multiple simultaneous talkers," J. Acoust. Soc. Am. **110**, 2527–2538.

Carhart, R., Tillman, T. W., and Greetis, E. S. (**1969**). "Perceptual masking in multiple sound backgrounds," J. Acoust. Soc. Am. **45**, 694–703.

Carhart, R., Tillman, T. W., and Johnson, K. R. (**1967**). "Release of masking for speech through interaural time delay," J. Acoust. Soc. Am. **42**, 124–138.

Colburn, H. S. (**1996**). "Computational models of binaural processing," in *Auditory Computation*, edited by H. L. Hawkins, T. A. McMullen, A. N. Popper, and R. R. Fay (Springer-Verlag, New York).

Dent, M. L., and Dooling, R. J. (**2004**). "The precedence effect in three species of birds (*Melopsittacus undulatus, Serinus canaria, and Taeniopygia guttata*)," J. Comp. Psychol. **118**(3), 325–331.

Dirks, D. D., and Wilson, R. H. (**1969**). "The effect of spatially separated sound sources on speech intelligibility," J. Speech Hear. Res. **12**, 5–38.

Doupe, A., and Kuhl, P. K. (**1999**). "Birdsong and speech: Common themes and mechanisms," Annu. Rev. Neurosci. **22**, 567–631.

Durlach, N. I., Mason, C. R., Gallun, F. J., Shinn-Cunningham, B. G., Colburn, H. S., and Kidd, G. (**2005**). "Psychometric functions for fixed and randomly mixed maskers," J. Acoust. Soc. Am. **118**, 2482–2497.

Durlach, N. I., Mason, C. R., Kidd, G., Arbogast, T. L., Colburn, H. S., and Shinn-Cunningham, B. G. (**2003**). "Note on informational masking," J. Acoust. Soc. Am. **113**, 2984–2987.

Festen, J. M., and Plomp, R. (**1990**). "Effects of fluctuating noise and interfering speech on the speech-reception threshold for impaired and normal hearing," J. Acoust. Soc. Am. **88**, 1725–1736.

Freyman, R. L., Helfer, K. S., McCall, D. D., and Clifton, R. K. (**1999**). "The role of perceived spatial separation in the unmasking of speech," J. Acoust. Soc. Am. **106**, 3578–3588.

Hulse, S. H. (**2002**). "Auditory scene analysis in animal communication," in *Advances in the Study of Behavior, 31*, edited by P. Slater, J. Rosenblatt, C. Snowdon, and T. Roper (Academic, New York).

Kidd, G., Mason, C. R., Brughera, A., and Hartmann, W. M. (**2005**). "The role of reverberation in release from masking due to spatial separation of sources for speech identification," Acust. Acta Acust. **114**, 526–536.

Kidd, G., Mason, C. R., Rohtla, T. L., and Deliwala, P. S. (**1998**). "Release from masking due to spatial separation of sources in the identification of nonspeech auditory patterns," J. Acoust. Soc. Am. **104**, 422–431.

Lutfi, R. A. (**1993**). "A model of auditory pattern analysis based on component-relative entropy," J. Acoust. Soc. Am. **94**, 748–758.

Lutfi, R. A., Kistler, D. J., Callahan, M. R., and Wightman, F. L. (**2003**). "Psychometric functions for informational masking," J. Acoust. Soc. Am. **114**, 3273–3282.

Nelson, B. S., and Suthers, R. A. (**2004**). "Sound localization in a small passerine bird: Discrimination of azimuth as a function of head orientation and sound frequency," J. Exp. Biol. **207**, 4121–4133.

Oh, E. L., and Lutfi, R. A. (**1999**). "Informational masking by everyday sounds," J. Acoust. Soc. Am. **106**, 3521–3528.

Park, T. J., and Dooling, R. J. (**1991**). "Sound localization in small birds: Absolute localization in azimuth," J. Comp. Psychol. **105**, 125–133.

Pollack, I. (**1975**). "Auditory informational masking," J. Acoust. Soc. Am. **57**, S5.

Shinn-Cunningham, B. G., Kopco, N., and Martin, T. (**2005**). "Localizing nearby sound sources in a classroom: binaural room impulse responses," J. Acoust. Soc. Am. **117**, 3100–3115.

Watson, C. S. (**1987**). "Uncertainty, informational masking and the capacity of immediate auditory memory," in *Auditory Processing of Complex Sounds*, edited by W. A. Yost and C. S. Watson (Erlbaum, Hillsdale, NJ), pp. 267–277.

Zann, R. A. (**1996**). *The Zebra Finch: A Synthesis of Field and Laboratory Studies* (Oxford U. P., New York).

Zurek, P. M. (**1993**). "Binaural advantages and directional effects in speech intelligibility," in *Acoustical Factors Affecting Hearing Aid Performance*, edited by G. A. Studebaker and I. Hochberg (Allyn and Bacon, Boston), pp. 255–276.

Detection of spectrally complex signals in comodulated maskers: Effect of temporal fringe

John H. Grose,[a] Joseph W. Hall III, Emily Buss, and Debora R. Hatch
Department Otolaryngology/Head and Neck Surgery, University of North Carolina at Chapel Hill, Chapel Hill, North Carolina 27599-7070

(Received 19 August 2004; revised 1 September 2005; accepted 2 September 2005)

This study tested the hypothesis that masking release for a complex signal under conditions where signal energy is present in all frequency regions occupied by the masker is attributable to an across-frequency-channel comodulation masking release (CMR) process. The approach was to identify a signature CMR trait, and to then determine if that trait was associated with the detection advantage for complex signals. The selected trait was the decline of CMR in the presence of a random temporal fringe. In experiment 1, a masking release was observed for a four-component harmonic signal presented in a comodulated masker, and this masking release was diminished by the random temporal fringe. A similar effect was observed in experiment 2 for a four-component inharmonic signal. These results support the hypothesis that a CMR can be measured for a complex signal even when there is substantial spectral overlap between the signal and its comodulated masker. This finding has consequences for CMR models since it demonstrates that the presence of "signal-free" cue bands is not a prerequisite for CMR, and that the presence of comodulation during the signal window is not sufficient to result in CMR. © *2005 Acoustical Society of America.* [DOI: 10.1121/1.2108958]

PACS number(s): 43.66.Dc, 43.66.Mk [RAL] Pages: 3774–3782

I. INTRODUCTION

Comodulation masking release (CMR) refers to the detection advantage conferred on a masked signal when the masker exhibits a coherent amplitude fluctuation pattern across frequency channels relative to when the fluctuation pattern is independent across frequency channels. The operational phrase here is "across frequency channel" since, as will be discussed in more detail later, the term CMR is not applicable to those situations where a masking release is observed for stimuli confined to a single auditory filter ("within frequency channel"). In most realizations of CMR, the comodulated masker occupies frequency regions that are relatively free of signal energy, and which therefore provide information about the waveform statistics that are unique to the masker. This configuration lends itself to models of CMR wherein frequency regions containing masker energy alone facilitate the identification of low-energy epochs of the masker where the instantaneous signal-to-noise ratio is relatively high (for review, see Hall *et al.*, 1995; van de Par and Kohlrausch, 1998; Verhey *et al.*, 2003). In physiological implementations of this approach, such signal enhancement effects can be realized by inhibitory neural circuits activated by frequency regions of the masker that are devoid of signal energy (Pressnitzer *et al.*, 2001). Models such as these are not designed to deal with stimulus configurations where there is substantial spectral overlap between a complex signal and its comodulated masker.

The purpose of this study is to determine whether mechanisms underlying CMR play a role in auditory environments where signal energy exists in every frequency region where comodulated masking energy is present. This is an important question because, whereas most laboratory demonstrations of CMR involve a pure-tone signal, ecologically significant signals are typically more complex. In a configuration where each component of a complex tonal signal is masked by a narrow band of noise centered at the component frequency, threshold for the complex signal will likely be lower if all masker bands are comodulated than if they are all independent (Hall *et al.*, 1988; Bacon *et al.*, 2002). However, this detection advantage does not necessarily represent an authentic CMR. Consider the study of Bacon *et al.* (2002) in which maskers were constructed of 100-Hz-wide bands of noise that were either unmodulated or were sinusoidally modulated at a low rate. For any single 100-Hz-wide band presented alone, threshold for a tone centered in that band was lower in the modulated case than in the unmodulated case—a detection advantage that was within-frequency-channel in nature. When the masker consisted of three widely spaced bands of noise and the signal was a three-tone complex centered in those bands, a detection advantage was similarly observed for the complex signal in the comodulated masker relative to the unmodulated masker. However, because a signal threshold reduction had been demonstrated for each individual modulated masker band alone, the detection advantage measured for the complex signal masked by the comodulated noise-bands could not be attributed unambiguously to CMR. Rather, it could be argued that the signal component in each frequency channel was detected on a within-channel basis, and that threshold for the signal complex as a whole was determined by the spectral integration of the "individually extracted" components. Herein lies the quandary: Given that threshold for a complex signal will likely be lower if all masker bands cen-

[a]Electronic mail: jhg@med.unc.edu

tered on the signal components are comodulated than if they are all independent, how can it be determined whether the detection advantage reflects a veridical across-frequency-channel CMR?

One approach to this issue is to identify a signature characteristic of CMR and to determine whether this trait can be observed in the detection advantage measured for the complex signals. To illustrate this approach, two examples will be described: the first deals with pure-tone signals (Dau *et al.*, 2004); the second deals with complex-tone signals (Grose and Hall, 1992). Dau *et al.* (2004) measured pure-tone detection in maskers made up of 20-Hz-wide bands of noise that were either closely spaced in frequency to fall within a single frequency channel or were widely spaced to fall into relatively independent frequency channels. In each composite masker, the constituent noise-bands were either comodulated or random. For both the closely-spaced and widely-spaced composite maskers, detection threshold for a pure tone centered in the masker was lower in the comodulated masker than in the random masker. Based on the premise that CMR represents an across-frequency-channel process, it is likely that the detection advantage associated with the widely-spaced masker reflected an authentic CMR. However, by the same token, it is not likely that the detection advantage associated with the closely-spaced masker was an authentic CMR. The challenge faced by Dau *et al.* (2004) was distinguishing between the underlying mechanisms contributing to the observed detection advantages in the two cases. They noted that an authentic across-frequency-channel CMR was subject to auditory grouping effects, such that perceptual segregation of the flanking cue bands from the on-signal noise-band in the comodulated masker undermined CMR (cf. Grose and Hall, 1993). Based on this signature CMR trait, they reasoned that exposing both the closely-spaced and widely-spaced comodulated maskers to such manipulations should differentiate between the underlying mechanisms of masking release. Using asynchronies on the flanking cue bands to promote perceptual segregation, they demonstrated that the masking release was obliterated for the widely-spaced masker but not for the closely-spaced masker. Thus, they concluded that the signal detection advantage associated with the widely-spaced masker reflected an authentic CMR, whereas that for the closely-spaced masker did not.

The second example, using complex-tone signals, comes from the study of Grose and Hall (1992). They noted that the magnitude of CMR is sensitive to the number of comodulated noise-bands present, such that CMR increases asymptotically as the number of bands increases (Carlyon *et al.*, 1989; Schooneveldt and Moore, 1989; Haggard *et al.*, 1990; Hall *et al.*, 1990; Hatch *et al.*, 1995). Taking this as a signature CMR trait, they demonstrated that the detection advantage measured for a three-tone signal masked by three comodulated noise-bands was enhanced by the addition of (12) further comodulated noise-bands. They therefore concluded that the original detection advantage was likely due to CMR.

Both of these studies employed the logic that, (a) if a signature CMR trait can be identified, and (b) if this trait can be shown to be associated with the detection advantage observed for a particular signal, then (c) the observed detection advantage represents an authentic CMR. The same reasoning was used here to further investigate CMR under conditions where signal energy exists in every frequency region where comodulated masker energy is present. However, the manipulation of onset/offset synchrony used by Dau *et al.* (2004) was not well-suited to the present study because the concepts of "on-signal band" and "cue band" lose their distinction in the multi-component signal paradigm employed here. Similarly, the use of additional (signal-free) cue bands implemented by Grose and Hall (1992) was poorly suited to the present paradigm because this manipulation undermines the goal of assessing masking release in conditions where substantial spectral overlap exists between signal and masker energy. Instead, it was decided to pursue an effect first reported by Mendoza *et al.* (1998), but not formally published. In that study, it was noted that the magnitude of CMR for a pure-tone signal was highly sensitive to the characteristics of the noise that temporally bracketed the observation intervals containing the comodulated noise-bands. Specifically, when only the gated comodulated masker was present, a substantial CMR was observed; however, when the gated comodulated masker was embedded in a temporal fringe that consisted of narrow bands of noise that were in all respects similar to the masker except that their envelopes were random across frequency (not comodulated), CMR declined markedly. The sensitivity of CMR to the random noise-bands temporally bracketing the comodulated maskers was concluded to be a signature trait of CMR processing. In the context of this investigation, the attraction of this CMR trait is that it does not require the inclusion of additional masker energy at other frequencies, and does not require gating asynchronies across the comodulated noise-bands.

In summary, the purpose of this investigation was to determine whether mechanisms underlying CMR are applicable to situations where signal energy exists in every frequency region where comodulated masking energy is present. The detectability of individual signal components was equated, and the effect of a temporal fringe comprised of random noise-bands was taken as an indication of whether any detection advantage observed could be attributed to a valid CMR process. The hypothesis was that a masking release would be observed for complex signals in a comodulated masker, and that this would reflect an authentic CMR process as demonstrated by the sensitivity of the masking release to a random temporal fringe. Two experiments were undertaken. The first experiment incorporated harmonic maskers and referenced CMR to detection thresholds in a single narrow band of noise. The second experiment incorporated inharmonic maskers and referenced CMR to detection thresholds in random maskers.

II. EXPERIMENT 1: EFFECT OF A RANDOM TEMPORAL FRINGE ON COMPLEX SIGNAL DETECTION IN COMODULATED HARMONIC MASKERS

The purpose of experiment 1 was to demonstrate that a masking release could be observed for a complex signal masked by a set of comodulated narrow bands of noise, where each band of noise was centered at a signal component

and where the detectability of each signal component was equated. The hypothesis was that this masking release is due to CMR mechanisms as evidenced by the reduction in the magnitude of masking release due to the presence of a random temporal fringe. A four-component complex signal was employed and, hence, the on-component masker consisted of four narrow bands of noise. As a supplementary test of CMR, a ten-band masker was also included since, as noted earlier, the magnitude of CMR is known to increase with the number of comodulated noise-bands.

A. Method

1. Subjects

Eight listeners ranging in age from 19 to 46 years (mean=28.3 years) participated. All had normal hearing, with audiometric thresholds below 20 dB HL across the octave frequencies 250–8000 Hz (ANSI, 1996). All listeners practiced the task until thresholds appeared stable; this typically took less than 1 h.

2. Stimuli

The signals were pure tones having frequencies of 1600, 2000, 2400, or 2800 Hz, as well as a complex tone consisting of all four frequencies. Each signal was 400 ms in duration, including 50-ms cosine-squared rise/fall ramps. Three maskers were constructed. The first masker consisted of a single 20-Hz-wide band of noise centered at 2000 Hz. The second masker consisted of four 20-Hz-wide, comodulated bands of noise centered at 1600, 2000, 2400, and 2800 Hz. Complementing this masker was a set of four 20-Hz-wide, independent bands of noise centered at the same frequencies. The third masker consisted of ten comodulated bands of noise, each 20-Hz-wide, centered at the first ten harmonics of 400 Hz (400–4000 Hz). Again, complementing this masker was a set of ten independent 20-Hz-wide bands of noise centered at the same frequencies. The frequency region of the signal and the harmonic structure of the stimuli followed from the earlier work of Mendoza *et al.* (1998). All bands of noise were generated by an inverse fast Fourier transform (FFT) technique using a long buffer size that resulted in a temporal waveform approximately 6.6 s in duration that wrapped seamlessly because all noise components consisted of an integer number of cycles. For any particular condition, the appropriate comodulated masker (four-band or ten-band) was played continuously out of one channel of a DAC (TDT PD1), while its complementary set of random bands was played continuously out of a separate DAC channel. The noise-band sets were gated on and off as needed using electronic switches which imposed 50-ms cosine-squared rise/fall ramps (TDT SW2). All stimuli were generated at a sampling rate of 20 kHz and were antialias filtered at 8 kHz (Kemo VBF8). The maskers were presented at a spectrum level of 52 dB/Hz SPL (65 dB SPL per noise-band) through the left phone of a Sennheiser HD580 headset.

3. Procedure

Signal detection threshold was measured using a three-alternative, forced-choice (3AFC) procedure incorporating a three-down, one-up stepping rule that estimated the 79.4% correct point on the psychometric function. The observation intervals were marked with light emitting diodes on a hand-held response box and the listeners entered their interval selection by means of a corresponding button on the same box. The initial step-size of signal level adjustment was 4 dB and, following each of the first two reversals in signal level direction, the step-size was halved. A threshold estimation track was terminated after eight reversals in level direction, and threshold was computed as the mean of the final six reversal levels. For each condition, four estimates of threshold were obtained, and the final threshold value was taken as the mean of all four estimates.

There were three masking conditions that formed the core of the experiment: (1) a baseline condition against which masking release was referenced; (2) a gated comodulated condition where each of the four components of the complex signal was masked by an on-component comodulated noise-band; and (3) a temporal fringe condition where the gated comodulated masker of (2) was bracketed by its complementary set of four random noise-bands. In addition to these three main conditions, other conditions were implemented where the number of noise-bands (four or ten) and the nature of the temporal fringe (random or comodulated) were varied to test aspects of the hypothesis. The rationale for these manipulations will be noted at the relevant points in the discussion later.

The choice of baseline for this experiment was the threshold of the 2000-Hz pure-tone signal masked by the single 20-Hz-wide band of noise centered at 2000 Hz [in this context, termed the on-signal band (OSB)]. In CMR experiments where the signal consists of a pure tone, this baseline is an accepted reference against which to measure masking release, and the derived release is sometimes termed the reference-comodulated (*R-C*) measure of CMR (Schooneveldt and Moore, 1987). The use of this baseline here rests partly on the assumption that the threshold of the 2000-Hz signal masked by its OSB is representative of the thresholds that would have been measured for the other pure-tone signals masked by their respective on-signal bands. This assumption is valid since it has been shown that pure-tone thresholds in narrow on-signal masker bands do not vary significantly with frequency (Bos and de Boer, 1966). However, the validity of using this baseline in an experiment where the main signal of interest is a four-component complex requires further support because of the expected reduction in signal threshold due to spectral integration. As expanded on in the footnote, the reduction in signal threshold due to spectral integration under the conditions of this experiment is countered by an increase in threshold due to across-channel masking.[1] Thus the OSB baseline provides a viable reference. The OSB masker was gated on for 500 ms in each observation interval of the 3AFC trial, and the 2000-Hz signal was gated on in the temporal center of one of the observation intervals at random. The inter-stimulus interval within each 3AFC trial was 500 ms.

The second main condition consisted of the four-band comodulated masker, which was gated on with the same timing as in the baseline condition. Detection thresholds were

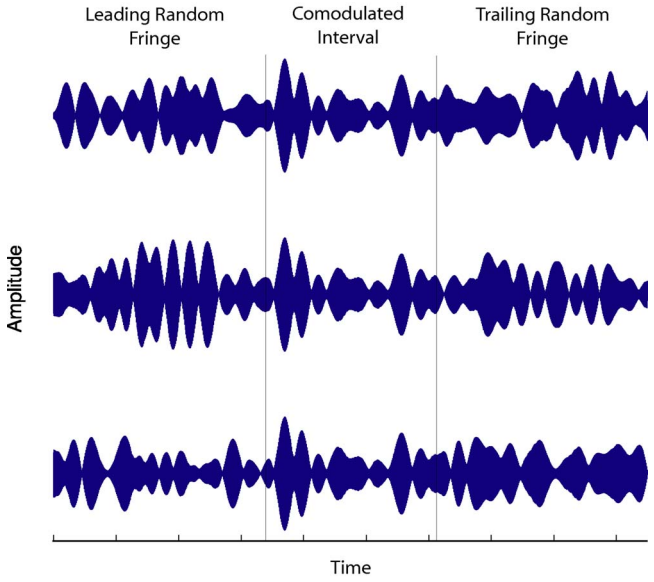

FIG. 1. (Color online) Schematic of a comodulated observation interval with a random temporal fringe. Three noise-bands are depicted whose envelopes are uncorrelated before and after the observation interval, but whose envelopes are comodulated during the observation interval.

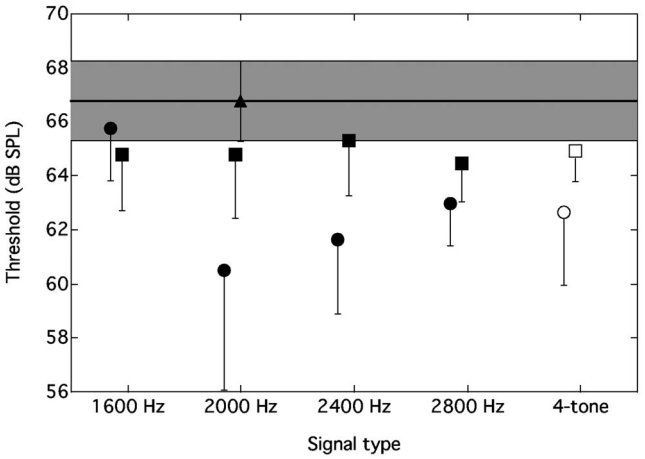

FIG. 2. Group mean detection thresholds for three masking conditions of experiment 1: 2000-Hz OSB (triangle and horizontal line, with hatched area = ±1 standard deviation); four-band comodulated masker (circles); four-band comodulated masker with random temporal fringe (squares). Thresholds for the complex signal are highlighted as unfilled symbols. Error bars indicate −1 standard deviation.

measured first for the four individual pure-tone signals. Once threshold levels for these signals had been determined for a given listener, a complex-tone signal was constructed that was tailored to that listener's thresholds. The levels of the individual components within the four-tone complex were adjusted to provide equal detectability. This was accomplished by attenuating components relative to the component with the highest masked pure-tone threshold by an amount that corresponded to the respective pure-tone threshold difference between them. For example, if the highest masked threshold was 63 dB SPL for the 1600-Hz tone, whereas the threshold for the 2000-Hz tone was 61 dB SPL, then within the four-tone complex the 2000-Hz component would be fixed at 2-dB down from the 1600-Hz component. Threshold for the complex signal was then referenced to the level of the most intense component. Note that in the complex signal, component starting phase was randomized across components.

In the third main condition, a temporal fringe was added to the gated comodulated masker. The temporal fringe consisted of a continuous presentation of the four random noise-bands except during the observation intervals of the 3AFC trial where the comodulated masker was gated on. The transition between the surrounding random noise and the gated comodulated masker consisted of overlapping 50-ms rise/fall ramps; i.e., the surrounding noise was gated off as the comodulated masker was gated on at the beginning of an observation interval, and the surrounding noise was gated on as the comodulated masker was gated off at the termination of the observation interval. This is illustrated in Fig. 1. The overlapping switching yielded perceptually seamless transitions between the two noise sources. For the temporal fringe condition, detection thresholds were measured first for the four separate pure-tone signals followed by threshold for an individually tailored complex-tone signal. (Note that an individually tailored complex signal was made separately for the gated comodulated condition and the temporal fringe condition.)

In addition to these three main conditions, data were also collected for other conditions where either the number of noise-bands (4 or 10) or the characteristics of the temporal fringe (random or comodulated) were varied. In all these conditions, the gating patterns were the same as described above. Again, for any masking condition that involved the complex signal, the relative levels of the four components were individually tailored for each listener for that masker; i.e., for each masker the pure-tone thresholds were measured first and the complex signal then individually constructed. For each listener, the conditions were blocked, but the order of conditions was random across listeners.

B. Results and discussion

The basic pattern of results was similar across the eight listeners and so the group means are representative of all listeners' performance. The mean results for the three main masking conditions are shown in Fig. 2. To highlight the effect first reported by Mendoza *et al.* (1998), consider first the data pattern associated with the 2000-Hz signal. The average threshold in the baseline OSB masker was about 67 dB SPL (triangle). Detection threshold decreased to about 61 dB SPL in the four-band comodulated masker (circle), yielding a CMR of about 6 dB. When the comodulated masker was presented within its complementary random temporal fringe, thresholds rose to about 65 dB SPL (square), reducing CMR to 2 dB. The purpose of experiment 1 was to determine whether this pattern was real and present for all signals, particularly the complex signal (highlighted by unfilled symbols in Fig. 2). The first step in the analysis was to determine whether a masking release was associated with signal detection in the four-band comodulated masker. With reference to Fig. 2, this analysis sought to determine whether the thresholds represented by the circles were significantly lower than

the reference threshold shown by the horizontal bar (the threshold for the 2000-Hz signal masked by its OSB, with the shaded region indicating ±1 standard deviation). A repeated-measures analysis of variance (ANOVA) was undertaken that included thresholds for the five signal types tested with this masker, as well as the reference threshold. The analysis revealed a significant effect of condition ($F_{5,35}=7.943; p<0.0001$), and post-hoc simple contrasts indicated that detection thresholds for all signal types in the four-band comodulated masker differed significantly from the OSB reference, except for the 1600-Hz signal. Thus, a masking release was observed in the four-band comodulated masker for all signals, including the complex signal, with the exception of the 1600-Hz signal. Failure to observe a significant CMR for the 1600-Hz signal is likely due to its spectral position on the lower edge of the stimulus complex. Hall *et al.* (1988) have shown that, for a set of comodulated narrowband maskers, CMR is minimal for a signal centered in the lowest frequency band. For the remaining signals, the magnitude of masking release ranged from 3.8 dB for the 2800-Hz signal to 6.3 dB for the 2000-Hz signal.

The key experimental question was whether this masking release diminished in the presence of the random temporal fringe, particularly for the complex signal. To assess this, a repeated-measures ANOVA was undertaken that compared the thresholds in the four-band gated comodulated masker to those obtained in the condition where the four-band gated comodulated masker was embedded in a temporal fringe consisting of four random noise-bands. With reference to Fig. 2, this analysis sought to determine whether the thresholds represented by the squares were significantly higher than the thresholds represented by the circles. Data for the 1600-Hz pure-tone signal were excluded from this analysis since no masking release was observed for this signal. The analysis incorporated two within-subjects factors: masker configuration (comodulated versus comodulated+fringe) and signal type. The analysis indicated a significant reduction in masking release in the presence of the random temporal fringe ($F_{1,7}=11.88$; $p=0.011$) with no effect of signal type and no interaction between these factors. Thus, the effect noted by Mendoza *et al.* (1998) held for all signal types for which a masking release had been observed, including the complex signal.

The motivation of this study was to determine whether the detection advantage for the complex signal in the comodulated masker represented an authentic CMR. The experimental approach was to demonstrate the sensitivity of the masking release to the presence of a random temporal fringe, a manipulation known to be detrimental to CMR. The results therefore support the interpretation that the masking release measured for the complex signal is the product of CMR mechanisms. In order to further substantiate this interpretation, two supplementary tests were undertaken, each testing another specific feature of CMR: (1) the effect of the number of cue bands; and (2) the effect of continuous versus gated presentation of the comodulated noise-bands.

As noted earlier, it is known that the magnitude of CMR is sensitive to the number of comodulated noise-bands (Carlyon *et al.*, 1989; Schooneveldt and Moore, 1989; Haggard *et al.*, 1990; Hall *et al.*, 1990; Hatch *et al.*, 1995). If the threshold reduction for the complex signal in the four-band comodulated masker is due to CMR, then threshold should be reduced still further upon an increase in the number of comodulated noise-bands. This trait was tested for here by measuring the change in threshold for the complex signal in the four-band comodulated masker when six additional cue bands were added. The average threshold in the four-band masker was 62.7 dB SPL and this was reduced to a mean of 58.4 dB SPL in the ten-band comodulated masker. A paired *t*-test indicated that this reduction was significant ($t_7=2.579$; $p=0.037$).

In terms of gating effects, it has been shown that for a 2000-Hz signal masked by a relatively few number of comodulated noise-bands (3–5), detection thresholds improve by about 6 dB when the masker is presented continuously rather than gated synchronously with the signal (Hatch *et al.*, 1995). In the present context, this is equivalent to presenting the gated four-band comodulated masker in a temporal fringe consisting of the same four comodulated noise-bands. As noted earlier, the average threshold for the complex signal in the four-band gated masker was 62.7 dB SPL and this decreased to 58.5 dB SPL in the continuous masker. A paired *t*-test showed this reduction to be significant ($t_7=4.174$; $p=0.004$). These two supplementary tests therefore add further support to the notion that the masking release observed for the complex signal in the four-band gated comodulated masker is a product of CMR mechanisms.

In summary, the results of this experiment support the notion that CMR can play a role in auditory environments where signal energy exists in every frequency region where comodulated masking energy is present. The sensitivity of CMR to the characteristics of the noise bracketing the comodulated observation intervals corroborates existing findings that show relatively long-term effects of stimulus coherence. For example, introducing an onset asynchrony between the OSB masker and the comodulated flanking bands reduces CMR despite the fact that all maskers are present and comodulated during the observation intervals (Grose and Hall, 1993). Such long-term effects of stimulus coherence have been demonstrated over a wide range of stimuli and phenomena (Hall and Grose, 1990; Grose and Hall, 1993; Oxenham and Dau, 2001; Dau *et al.*, 2004). In terms of CMR, they are likely to represent a general characteristic of the phenomenon.

As noted earlier, there are traditionally two methods of deriving CMR. The method used in this experiment, the *R-C* derivation, uses the threshold of a pure-tone signal masked by its OSB as the reference. The second method of deriving CMR, known as the *U-C* derivation, uses as the baseline the signal threshold in the full complement of random noise-bands making up the masker (Schooneveldt and Moore, 1987). Because the use of a complex signal makes the optimum choice for baseline less straightforward, as discussed in the footnote, a second experiment was undertaken that employed the *U-C* method of deriving CMR.

III. EXPERIMENT 2: EFFECT OF A RANDOM TEMPORAL FRINGE ON COMPLEX SIGNAL DETECTION IN COMODULATED INHARMONIC MASKERS

The purpose of experiment 2 was again to demonstrate that a masking release could be observed for a complex signal masked by a set of comodulated narrow bands of noise under conditions where there was one noise-band per signal component and where the detectability of each signal component was equated. The hypothesis was that this masking release is due to CMR mechanisms as evidenced by the reduction in the magnitude of masking release due to the presence of a random temporal fringe. A four-component complex signal was employed and, hence, the on-component masker consisted of four narrow bands of noise. In addition to employing the *U-C* method of deriving CMR, experiment 2 made use of inharmonic spacings between signal components. Because harmonicity is a strong auditory grouping cue (e.g., Bregman *et al.*, 1990; Darwin *et al.*, 1991), the motivation was to undermine the contribution of this cue to the perceptual organization of the comodulated noise-bands; i.e., it was desired that the primary grouping cue for the noise-bands would be their temporal envelope coherence.

A. Method

1. Subjects

Seven listeners ranging in age from 19 to 47 years (mean=30.4 years) participated in the second experiment. All had normal hearing, with audiometric thresholds below 20 dB HL across the octave frequencies 250–8000 Hz (ANSI, 1996). All listeners practiced the task using a pure-tone signal until thresholds appeared stable; this typically took less than 1 h.

2. Stimuli

The signals were pure tones having frequencies of 804, 1200, 1747, or 2503 Hz, as well as a complex tone consisting of all four frequencies. These frequencies were selected as being the center frequencies of equivalent rectangular bandwidths (ERBs) (Moore and Glasberg, 1987) that formed a series in which two non-overlapping ERBs intervened between each selected ERB. The frequencies thus activated relatively discrete regions of the basilar membrane. As in experiment 1, signals were 400 ms in duration, including 50-ms cosine-squared rise/fall ramps. The masker consisted of four 20-Hz-wide narrow bands of noise centered at these frequencies; the bands were either comodulated or random with respect to each other. Each four-band masker (comodulated or random) was generated by the same inverse FFT technique described earlier. The comodulated masker was output continuously through one channel of the DAC (TDT PD1) whereas the random masker was output through the second channel. The noise-band sets were gated on and off as needed using electronic switches which imposed 50-ms cosine-squared rise/fall ramps (TDT SW2). Whereas the maskers in experiment 1 were presented at a level of 65 dB SPL per noise-band, here the overall level of the four-band masker was 65 dB SPL (c. 46 dB/Hz).

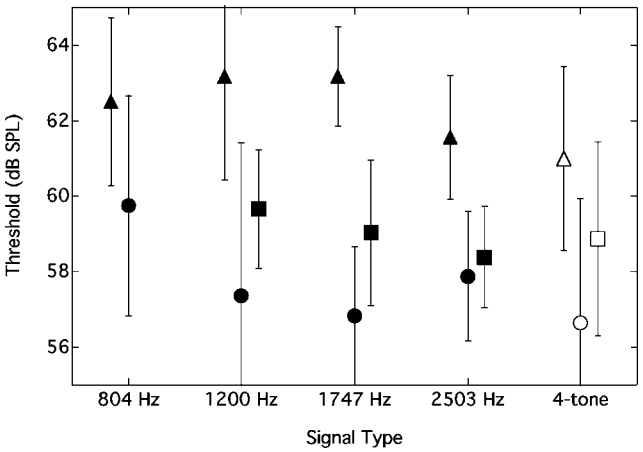

FIG. 3. Group mean detection thresholds for three masking conditions of experiment 2: four-band random masker (triangles); four-band comodulated masker (circles); four-band comodulated masker with random temporal fringe (squares). Thresholds for the complex signal are highlighted as unfilled symbols. Error bars indicate ±1 standard deviation.

3. Procedure

The procedure for measuring signal detection threshold was the same as that in experiment 1 except that five estimates of threshold were obtained for each condition. Final threshold value was taken as the mean of all five estimates. Threshold for each signal type was measured in three masking conditions: (1) the gated random masker (baseline); (2) the gated comodulated masker; and (3) the gated comodulated masker bracketed by a temporal fringe consisting of the random noise bands. For each of these maskers, thresholds for the pure-tone signals were measured first and then the complex signal was individually tailored for each listener based on the pure-tone thresholds. For the masking condition with the temporal fringe, the transition between the surrounding random noise and the gated comodulated masker consisted of overlapping 50-ms rise/fall ramps as in experiment 1. For each listener, the conditions were blocked, but the order of conditions was random across listeners, with the proviso that for any particular masker condition the pure-tone thresholds were measured prior to the complex-tone thresholds.

B. Results and discussion

The basic pattern of results was similar across the seven listeners and so the group means are representative of all listeners' performance. The mean results for each signal and masking condition are shown in Fig. 3. Thresholds for the gated, random masker (triangles) were higher than thresholds for the gated, comodulated masker (circles), although the magnitude of the difference appeared to depend on signal type. (Again, results for the complex signal are highlighted as unfilled symbols.) To test this observation, a repeated-measures ANOVA was undertaken on the gated thresholds using two within-subjects factors: signal type (five levels) and masker type (two levels). The analysis indicated that the main effect of signal type was significant ($F_{4,24}=2.965$; $p=0.04$), as was the effect of masker type ($F_{1,6}=48.619$; $p<0.001$); however, the interaction between signal type and

masker type was also significant ($F_{4,24}=4.45$; $p=0.008$). To interpret the interaction between signal and masker types, pair-wise comparisons between the signal thresholds obtained in the two types of masker were undertaken for each signal type using paired *t*-tests with Bonferroni correction. The results of the pair-wise analysis indicated that thresholds were reliably lower in the comodulated masker for all signal types except for the 804-Hz pure tone signal. As with the 1600-Hz signal of experiment 1, the failure to observe a masking release for the 804-Hz signal here is probably due to its spectral position on the low-frequency edge of the stimulus configuration. The magnitude of the masking release for the remaining signals ranged from 3.7 dB for the 2503-Hz signal to 6.3 dB for the 1747-Hz signal. Note that a significant threshold reduction of about 4.4 dB was apparent also for the complex-tone signal.

The key issue was the effect of a random temporal fringe on the masking release observed for the gated comodulated conditions. The results of this condition are shown as squares in Fig. 3. To determine the effect of this condition, a repeated-measures ANOVA was undertaken that incorporated two within-subjects factors: masker configuration (comodulated versus comodulated+fringe) and signal type. Only the four signal types that were associated with a masking release were included in the analysis; i.e., the 804-Hz data were excluded. The analysis revealed that the effect of masker configuration was significant ($F_{1,6}=7.498$; $p=0.034$). There was no effect of signal type, nor was the interaction between signal type and masker configuration significant. The results of this analysis therefore indicate that the presence of a random temporal fringe significantly elevated signal threshold (reduced CMR) in those configurations where the gated comodulated noise-bands initially led to a masking release. Because this occurred also for the masking release observed for the complex signal, it can be concluded that this masking release reflects the contributions of CMR mechanisms.

Whereas the pattern of results supports an interpretation in terms of the role of CMR processing, it does not rule out accounts framed in terms of spectral integration. However, such accounts would require that spectral integration be sensitive to the temporal fringe of the masker. Evidence against this can be gleaned from two supplementary conditions tested on a subset of listeners in experiment 2. These two conditions examined the effect of a temporal fringe on a masker configuration that is not conducive to CMR, i.e., a gated random masker. Three of the listeners were tested with a comodulated temporal fringe bracketing the gated random masker, and four of the listeners were tested with a random temporal fringe bracketing the gated random masker (equivalent to a continuous random masker). Neither of these conditions resulted in a significant change in threshold relative to that measured in the gated random masker alone. This supports the notion that spectral integration is not sensitive to temporal fringe. In turn, this interpretation reinforces the contention that the effect of the random temporal fringe on thresholds for the complex signal in comodulated noise indicates the involvement of CMR mechanisms.

IV. GENERAL DISCUSSION

Confirmation that CMR processing can take place even when signal and masker spectra substantially overlap is informative as to the nature of CMR. As noted by Hall *et al.* (1988), the fact that the presence of "signal-free" cue bands is not a prerequisite for the occurrence of CMR does not appear at first sight to be compatible with dip-listening strategies. A number of studies have provided evidence that the underpinning of CMR is the ability to preferentially monitor the epochs of low masker energy (i.e., "dips") where the signal-to-noise ratio is relatively optimal (Buus, 1985; Grose and Hall, 1989; Moore *et al.*, 1990; Hall and Grose, 1991; Hicks and Bacon, 1995; Buus *et al.*, 1996). Phenomenologically, this benefit is described in terms of a process wherein the comodulated flanking bands cue the auditory system as to when to "listen" for the signal. Such a description implies the necessity of signal-free cue bands. However, signal enhancement, or increased weighting of the stimulus energy during the masker dips, will result from any process in which the envelope information associated with comodulated cue bands is used to account for the envelope information originating from the masker in the signal channel. Physiologically, Pressnitzer *et al.* (2001) have modeled this as a neural circuit in which the output of a cell with a wide-band receptive field responding to all the cue bands leads to a fast-acting inhibition of a cell with a narrow-band receptive field that responds to only the signal frequency. If a compressive function is added to the circuit to institute some degree of equalization between the inhibitory and excitatory inputs to the narrow-band cell, then this circuit provides a simple equalization/cancellation mechanism that can result in CMR-like behavior. A further feature of an equalization/cancellation mechanism, of which the Pressnitzer model is a particular example, is that even if a signal component exists in every frequency channel conveying comodulated masker information, such a mechanism could potentially have a higher output when the signal was present than when just the comodulated masker alone was present. That is, a higher residue would remain at the output of the cancellation stage when a signal was present than when a signal was absent because, with the random starting phases of the individual signal components, the envelopes of the signal+masker waveforms in the various frequency channels would not be identical. This higher output may in turn constitute a detection cue. Such a mechanism would be of no benefit for a random masker since it would have a significant output whether or not the signal was present. In this sense, the mechanism is informative only when the auditory system is anticipating coherent fluctuations across frequency. Perhaps this is why the presence of an independent temporal fringe reduces the benefit of comodulation, as observed here and in the Mendoza *et al.* (1998) study: the on-going random noise puts the system in a state where comodulation is not expected, and therefore potential cueing mechanisms (perhaps based on grouping by common modulation) are not activated. In line with this, Grose and Hall (1993) have shown that the presence of comodulation during the signal epoch is, in itself, insufficient to result in a CMR.

Although this study was not motivated to examine the characteristics of spectral integration under conditions of comodulation, the results are relevant to the findings of Bacon *et al.* (2002). That study specifically examined spectral integration for complex signals presented in narrow (100-Hz wide) bands of frozen noise that were either unmodulated, or were sinusoidally modulated at 8 Hz. They found that for unmodulated noise-bands, or for widely-spaced comodulated noise-bands, spectral integration reflected the expected $10 \log \sqrt{N}$ rule, where N is the number of equally-detectable signal components. However, for noise-band spacings that were an octave or less, "super-integration" was observed; i.e., amounts of spectral integration in excess of that predicted by the $10 \log \sqrt{N}$ rule. They conjectured that, under these conditions, a CMR mechanism may act in tandem with a spectral integration process, although it is not clear how these additive effects would come about.

In order to compare the pattern of spectral integration observed in this study with that of Bacon *et al.* (2002), measures of spectral integration were derived for the multi-component signals used here. Because threshold level for the multi-component signal was referenced to the component with the highest pure-tone threshold, the derivation of spectral integration consists of a simple subtraction of the multi-component signal threshold from the highest pure-tone signal threshold for that masker set. Note that a $10 \log \sqrt{N}$ rule would predict a 3-dB improvement in threshold between a pure-tone signal and a four-component signal. From the data of experiment 1, spectral integration was computed for the two main conditions (four-band gated comodulated masker and the four-band gated comodulated masker presented in a random temporal fringe), as well as the two supplementary conditions (ten-band gated comodulated masker and the four-band continuous comodulated masker). From the data of experiment 2, spectral integration was computed for the gated random masker, the gated comodulated masker, and the gated comodulated masker with the random temporal fringe. The results are shown in Fig. 4, and it can be seen that, on average, a 3-dB spectral integration was observed for three of the conditions, with less than this amount observed for the other conditions. However, individual variability was pronounced. Nevertheless, the present results do not appear to be in line with Bacon *et al.* (2002) in that no super-integration was seen across all listeners for the comodulated bands that were separated by less than an octave from each other. It is possible that the marked differences in masker stimuli across the two studies may underlie this disparity. Here, the comodulation was dictated by the common inherent fluctuations across frequency in the envelopes of the 20-Hz-wide bands of noise, whereas in the Bacon *et al.* (2002) study the comodulation was dictated by the imposed 8-Hz sinusoidal modulation of the 100-Hz-wide bands of frozen noise. Further work is required to clarify this issue.

V. CONCLUSIONS

The purpose of this investigation was to test the hypothesis that a masking release would be observed for a complex signal in a comodulated masker, and that this masking release is attributable to a CMR process as demonstrated by the sensitivity of the masking release to a random temporal fringe. In both experiments 1 and 2, a masking release was observed for a complex signal, and this release was shown to be sensitive to the presence of a random temporal fringe. This finding provides support for the hypothesis that the masking release for the complex signal is associated with CMR processing. This conclusion has consequences for models of CMR since (a) it is demonstrated that the presence of signal-free cue bands is not a prerequisite for the occurrence of CMR, and (b) the presence of comodulation during the signal window is not sufficient to result in a CMR.

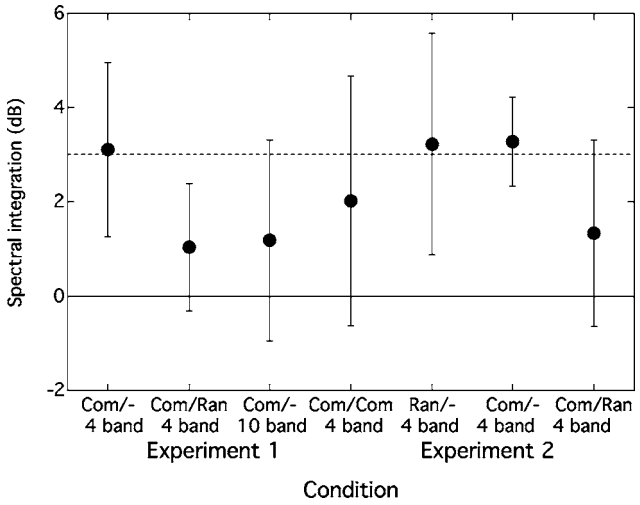

FIG. 4. Group mean magnitudes of spectral integration, ±1 standard deviation, for seven masking conditions. From experiment 1, four-band comodulated, gated (com/-); four-band comodulated with random fringe (com/ran); ten-band comodulated, gated (com/-); and four-band comodulated, continuous (com/com). From experiment 2, four-band random, gated (ran/-); four-band comodulated, gated (com/-); four-band comodulated with random surround (com/ran). Lower solid line references no spectral integration; upper dashed line references expected spectral integration using $10 \log \sqrt{N}$ rule.

ACKNOWLEDGMENTS

This work was supported by NIH NIDCD (#R01-DC01507).

[1]With regard to the complex signal, a valid objection to the *R-C* method of deriving CMR in experiment 1 is that it potentially overestimates the CMR magnitude by ignoring any effect of spectral integration due to the presence of multiple signal components. That is, if the reference for the complex signal had been its threshold in a masker composed of independent bands of noise (one band centered on each signal component), rather than a single tone masked by a single band of noise, then the reference threshold might have been lower due to spectral integration. A lower reference threshold would have resulted in a smaller derived measure of CMR. Whereas this objection is sound, it fails to take into account any increase in the reference threshold for the pure-tone signals due to across-channel masking associated with the multiple masker bands (Hall *et al.*, 1984; McFadden, 1986; Cohen and Schubert, 1987; Schooneveldt and Moore, 1987; Eddins and Wright, 1994). That is, failure to incorporate potential effects of across-channel masking in defining the reference threshold in experiment 1 would have resulted in an underestimation of the CMR magnitude. To illustrate this, additional data were collected from two listeners where the reference masker consisted of the four independent bands of noise centered at the signal component frequencies. Thresholds for the 2000-Hz pure-tone signal measured in the masker were, on average, 2.1 dB higher for the two listeners than their thresholds for the 2000-Hz signal masked by its on-signal

band alone (the reference used in experiment 1). Spectral integration was indeed observed for the complex signal in the random reference masker (on average, 3.1 dB for the two listeners), but the threshold reduction due to spectral integration was largely offset by the threshold elevation due to across-channel masking. Thus, the actual reference used in experiment 1 is a viable baseline against which to measure CMR, even for the complex signal. In any case, the results of experiment 1 are substantiated by experiment 2 which did use the multiple random noise bands as the reference for masking release.

ANSI. (**1996**). *American National Standards Specification for Audiometers (ANSI S3-1996)*. American National Standards Institute.

Bacon, S. R., Grimault, N., and Lee, J. (**2002**). "Spectral integration in bands of modulated or unmodulated noise," J. Acoust. Soc. Am. **112**, 219–226.

Bos, C. E., and de Boer, E. (**1966**). "Masking and discrimination," J. Acoust. Soc. Am. **39**, 708–715.

Bregman, A. S., Levitan, R., and Liao, C. (**1990**). "Fusion of auditory components: Effects of the frequency of amplitude modulation," Percept. Psychophys. **47**, 68–73.

Buus, S. (**1985**). "Release from masking caused by envelope fluctuations," J. Acoust. Soc. Am. **78**, 1958–1965.

Buus, S., Zhang, L., and Florentine, M. (**1996**). "Stimulus-driven, time-varying weights for Comodulation Masking Release," J. Acoust. Soc. Am. **99**, 2288–2297.

Carlyon, R. P., Buus, S., and Florentine, M. (**1989**). "Comodulation masking release for three types of modulators as a function of modulation rate," Hear. Res. **42**, 37–46.

Cohen, M. F., and Schubert, E. D. (**1987**). "Influence of place synchrony on detection of a sinusoid," J. Acoust. Soc. Am. **81**, 452–458.

Darwin, C. J., Buffa, A., Williams, D., and Ciocca, V. (**1991**). "Pitch of dichotic complex tones with a mistuned frequency component," in *Auditory Physiology and Perception*, edited by Y. Cazals, L. Demany, and K. Horner (Pergamon, Oxford).

Dau, T., Ewert, S. D., and Oxenham, A. J. (**2004**). "Effects of concurrent and sequential streaming in comodulation masking release," in *Auditory Signal Processing: Physiology, Psychoacoustics, and Models*, edited by D. Pressnitzer, A. de Cheveigne, S. McAdams, and L. Collet (Springer-Verlag, Berlin).

Eddins, D. A., and Wright, B. A. (**1994**). "Comodulation masking release for single and multiple rates of envelope fluctuation," J. Acoust. Soc. Am. **96**, 3432–3442.

Grose, J. H., and Hall, J. W. (**1989**). "Comodulation masking release using SAM tonal complex maskers: Effects of modulation depth and signal position," J. Acoust. Soc. Am. **85**, 1276–1284.

Grose, J. H., and Hall, J. W. (**1992**). "Comodulation masking release for speech stimuli," J. Acoust. Soc. Am. **91**, 1042–1050.

Grose, J. H., and Hall, J. W., III. (**1993**). "Comodulation masking release: Is comodulation sufficient?" J. Acoust. Soc. Am. **93**, 2896–2902.

Haggard, M. P., Hall, J. W., and Grose, J. H. (**1990**). "Comodulation masking release as a function of bandwidth and test frequency," J. Acoust. Soc. Am. **88**, 113–118.

Hall, J. W., and Grose, J. H. (**1990**). "Consequences of onset asynchrony for modulation detection interference," J. Acoust. Soc. Am. **88**, S145.

Hall, J. W., and Grose, J. H. (**1991**). "Relative contributions of envelope maxima and minima to comodulation masking release," Q. J. Exp. Psychol. A **43**, 349–372.

Hall, J. W., Grose, J. H., and Haggard, M. P. (**1988**). "Comodulation masking release for multi-component signals," J. Acoust. Soc. Am. **83**, 677–686.

Hall, J. W., Grose, J. H., and Haggard, M. P. (**1990**). "Effects of flanking band proximity, number, and modulation pattern on comodulation masking release," J. Acoust. Soc. Am. **87**, 269–283.

Hall, J. W., Grose, J. H., and Mendoza, L. (**1995**). "Across-channel processes in masking," in *Handbook of Perception and Cognition Vol VI: Hearing*, edited by B. C. J. Moore (Academic, San Diego).

Hall, J. W., Haggard, M. P., and Fernandes, M. A. (**1984**). "Detection in noise by spectro-temporal pattern analysis," J. Acoust. Soc. Am. **76**, 50–56.

Hatch, D. R., Arne, B. C., and Hall, J. W. (**1995**). "Comodulation masking release (CMR): Effects of gating as a function of number of flanking bands and masker bandwidth," J. Acoust. Soc. Am. **97**, 3768–3774.

Hicks, M. L., and Bacon, S. P. (**1995**). "Some factors influencing comodulation masking release and across-channel masking," J. Acoust. Soc. Am. **98**, 2504–2514.

McFadden, D. (**1986**). "Comodulation masking release: Effects of varying the level, duration, and time delay of the cue band," J. Acoust. Soc. Am. **80**, 1658–1667.

Mendoza, L., Hall, J. W., III, and Grose, J. H. (**1998**). "Comodulation masking release: the effect of the characteristics of noisebands presented before and after a signal," J. Acoust. Soc. Am. **103**, 2843.

Moore, B. C. J., and Glasberg, B. R. (**1987**). "Formulae describing frequency selectivity as a function of frequency and level and their use in calculating excitation patterns," Hear. Res. **28**, 209–225.

Moore, B. C. J., Glasberg, B. R., and Schooneveldt, G. P. (**1990**). "Across-channel masking and comodulation masking release," J. Acoust. Soc. Am. **87**, 1683–1694.

Oxenham, A. J., and Dau, T. (**2001**). "Modulation detection interference: effects of concurrent and sequential streaming," J. Acoust. Soc. Am. **110**, 402–408.

Pressnitzer, D., Meddis, R., Delahaye, R., and Winter, I. M. (**2001**). "Physiological correlates of comodulation masking release in the mammalian ventral cochlear nucleus," J. Neurosci. **21**, 6377–6386.

Schooneveldt, G. P., and Moore, B. C. J. (**1987**). "Comodulation masking release (CMR): Effects of signal frequency, flanking band frequency, masker bandwidth, flanking band level, and monotic vs dichotic presentation flanking bands.," J. Acoust. Soc. Am. **82**, 1944–1956.

Schooneveldt, G. P., and Moore, B. C. J. (**1989**). "Comodulation masking release (CMR) for various monaural and binaural combinations of the signal, on-frequency, and flanking bands," J. Acoust. Soc. Am. **85**, 262–272.

van de Par, S., and Kohlrausch, A. (**1998**). "Comparison of monaural (CMR) and binaural (BMLD) masking release," J. Acoust. Soc. Am. **103**, 1573–1579.

Verhey, J. L., Pressnitzer, D., and Winter, I. M. (**2003**). "The psychophysics and physiology of comodulation masking release," Exp. Brain Res. **153**, 405–417.

Reduced contribution of a nonsimultaneous mistuned harmonic to residue pitch[a)]

Hedwig Gockel[b)]
MRC Cognition and Brain Sciences Unit, 15 Chaucer Road, Cambridge CB2 2EF, United Kingdom

Christopher J. Plack
Department of Psychology, Lancaster University, Lancaster LA1 4YF, United Kingdom

Robert P. Carlyon
MRC Cognition and Brain Sciences Unit, 15 Chaucer Road, Cambridge CB2 2EF, United Kingdom

(Received 2 June 2005; revised 19 September 2005; accepted 23 September 2005)

Ciocca and Darwin [V. Ciocca and C. J. Darwin, J. Acoust. Soc. Am. **105**, 2421–2430 (1999)] reported that the shift in residue pitch caused by mistuning a single harmonic (the fourth out of the first 12) was the same when the mistuned harmonic was presented after the remainder of the complex as when it was simultaneous, even though subjects were asked to ignore the pure-tone percept. The present study tried to replicate this result, and investigated the role of the presence of the nominally mistuned harmonic in the matching sound. Subjects adjusted a "matching" sound so that its pitch equaled that of a subsequent 90-ms complex tone (12 harmonics of a 155-Hz F0), whose mistuned (±3%) third harmonic was presented either simultaneously with or after the remaining harmonics. In experiment 1, the matching sound was a harmonic complex whose third harmonic was either present or absent. In experiments 2A and 2B, the target and matching sound had nonoverlapping spectra. Pitch shifts were reduced both when the mistuned component was nonsimultaneous, and when the third harmonic was absent in the matching sound. The results indicate a shorter than originally estimated time window for *obligatory* integration of nonsimultaneous components into a virtual pitch. © *2005 Acoustical Society of America.* [DOI: 10.1121/1.2126823]

PACS number(s): 43.66.Hg, 43.66.Mk, 43.66.Ba [JHG] Pages: 3783–3793

I. INTRODUCTION

Several studies have provided evidence that listeners can perceive a virtual pitch based on the upper harmonics of a complex tone even when the harmonics are presented nonsimultaneously. The extent to which this is true has fundamental implications for theories of pitch perception, which either explicitly specify the time constant over which pitch is calculated (Moore, 1982; Meddis and Hewitt, 1991a; b) or which do not make predictions about pitch derived from nonsimultaneous components (Goldstein, 1973; Terhardt *et al.*, 1982). Hall and Peters (1981) found that the integration of nonsimultaneous components into a single virtual pitch took place only when the harmonics were presented at a low signal-to-noise ratio (6 dB above masked threshold). When they presented the harmonics in quiet, the spectral pitch of individual harmonics was perceived rather than the residue pitch. The basic stimulus used by Hall and Peters (1981) was a three-tone sequence consisting of three short consecutive harmonics; the harmonics had a duration of 40 ms (including 10-ms rise and fall times) and were separated by a 10-ms silent gap. For similar stimuli, Houtsma (1984) reported that one out of five subjects could extract virtual pitch even in quiet. However, this corresponds to a minority of his subjects, and, in contrast to Hall and Peters, performance was worse for two subjects when tested additionally at a low signal-to-noise ratio. No virtual pitch was perceived for a two-tone sequence employing a considerably longer tone duration of 200 ms when the two tones were separated by a silent interval of 100 ms (Houtsma and Goldstein, 1972).

More recently, Grose *et al.* (2002) presented a study designed to estimate the integration time with regard to virtual pitch extraction. They measured fundamental frequency (F0) discrimination thresholds for virtual pitch based on a sequence of four nonsimultaneous 40-ms harmonics separated by silent gaps of various durations. Their results indicated that subjects were able to extract a virtual pitch from three consecutive 40-ms harmonics that were separated by silent intervals of up to about 45 ms and presented against a noise background. This was taken as evidence that the pitch integration period was at least 210 ms long. However, Grose *et al.* (2002) also pointed out an alternative explanation. Subjects might have gleaned some virtual pitch information by treating the tone sequence as arpeggio and internally constructing the F0 that would give the best fit to a given arpeggio. In Grose *et al.*'s (2002) study, it was advantageous for subjects to integrate information over time as this would result in lower thresholds. Also, subjects received feedback and were especially trained.

[a)]Parts of this work were presented at the 149th meeting of the Acoustical Society of America, Vancouver, Canada, 16–20 May 2005 [J. Acoust. Soc.**117**, 2539 (2005)]

[b)]Electronic mail: hedwig.gockel@mrc-cbu.cam.ac.uk

In an earlier study by Ciocca and Darwin (1999), the integration of nonsimultaneous components was investigated using the pitch matching paradigm developed by Moore *et al.* (1985). Subjects were presented with the first 12 components of an equal-amplitude harmonic complex tone with an F0 of 155 Hz and duration of 90 ms. The frequency of the fourth component was increased or decreased by various amounts from its harmonic value. All components were presented simultaneously, except the mistuned one which could be presented immediately after (or in a different condition, before) the remainder of the complex. Especially when the mistuned harmonic was presented nonsimultaneously, it would "pop out," i.e., it could be heard as an individual pure tone in addition to the richer percept evoked by the complex tone. Subjects were asked to ignore the pure tone and to focus their attention on matching the pitch of the complex tone (the target) with that of a perfectly harmonic complex (the matching sound). The matching sound consisted of the first 12 harmonics of an F0 that could be adjusted in the range 155±4 Hz and had all harmonics presented simultaneously. The results showed that the pitch shift caused by the mistuned harmonic when presented after the target did not differ significantly from that observed when the mistuned harmonic was presented simultaneously with the target. In contrast, when the mistuned harmonic was presented before the target, the pitch shifts were significantly smaller than when it was presented simultaneously. In further experiments, a silent gap of various durations was introduced between the target and the mistuned harmonic. No significant difference was observed between pitch shifts obtained with simultaneous presentation of the mistuned harmonic and presentation following the target, for silent interval durations of up to 80 ms. These findings were taken as indicative of the duration of the pitch integration period (starting with the onset of the target complex) and led to an estimated duration of about 170 to 250 ms. The results are somewhat surprising, as the subjects in Ciocca and Darwin's (1999) study were asked to ignore the mistuned component that popped out. Thus, the results seem to indicate an *obligatory* integration of a nonsimultaneous post-target component into the residue pitch. The term "obligatory" was not used by Ciocca and Darwin. It is introduced here in order to contrast their task, where subjects were asked to ignore the pure tone, with that used by Grose *et al.* (2002), where subjects tried to integrate nonsimultaneous components to derive a virtual pitch.[1]

The first objective of the present study was to try to replicate Ciocca and Darwin's (1999) findings on the effect of a nonsimultaneous mistuned component on the residue pitch but with the third harmonic mistuned rather than the fourth; the fourth harmonic might have a somewhat special status because its frequency is a double octave above the F0. The second objective was to investigate the role of the presence of the nominally mistuned harmonic in the *matching* sound. Ciocca and Darwin discussed and, for several reasons, rejected the idea that subjects matched the spectral pitch of the mistuned component with the corresponding harmonic of the harmonic matching sound, instead of matching to the virtual pitch of the target. One of the reasons for rejecting this idea was that matching the spectral pitch of the mistuned component with that of the corresponding harmonic in the matching sound would lead to a monotonic increase in pitch shifts with increasing mistuning. The latter generally was not observed, either when the mistuned component was presented simultaneously (see also Moore *et al.*, 1985) or, and more importantly in the current context, when it followed the target. However, subjects may have pursued a somewhat different, analytical listening-and-matching strategy that would not require integration of the mistuned component into the residue pitch of the target. Gockel *et al.* (2005) suggested that, in situations like the above when the mistuned component follows the target, subjects may compare the harmonic matching complex with the two distinct percepts of the mistuned component and the "remainder" of the mistuned complex (the target). They could then try to minimize simultaneously the overall discrepancy between the harmonic matching complex and these two distinct percepts. On the one hand, for the mistuned component, this would imply that subjects compare the mistuned component with the corresponding harmonic in the matching sound. Also, to a certain degree, subjects might be able to compare how the mistuned harmonic fits in with the harmonic matching sound. On the other hand, for the remainder of the mistuned complex, subjects would compare the pitch of the remainder of the target with that of the matching complex. This strategy would not predict a monotonic increase in pitch shift with increasing mistuning. If such a strategy were used, pitch shifts should be smaller when the component corresponding to the nominally mistuned harmonic is absent rather than present in the matching sound.

II. GENERAL METHOD AND STIMULI

As in Ciocca and Darwin (1999), the target was a complex tone with an F0 of 155 Hz, containing the first 12 harmonics (except when stated otherwise) added in sine phase, with equal amplitude. The duration of the tone was, as in Ciocca and Darwin's study, 90 ms, including 5-ms raised-cosine onset and offset ramps. The third harmonic was mistuned by ±3%, and it was presented either immediately after the remainder of the target complex (condition Post-target) or simultaneously with the remainder of the target complex. In one control experiment (experiment 1B), the mistuned component could be presented immediately before the target complex (condition Pre-target). In the present study, the third harmonic was mistuned rather than the fourth to test the generality of Ciocca and Darwin's findings.

Ciocca and Darwin's (1999) subjects used a roller-ball to adjust the frequency of the matching sound. Here, a two-interval, two-alternative adaptive procedure was used to obtain pitch matches between a 90-ms matching sound (the characteristics of which will be described individually for each experiment) and the target complex; the F0 (or frequency) of the former was adjusted to obtain the match. In all experiments, the matching sound with the variable F0 was presented in the first interval, except in experiment 1B, where the matching sound was presented in the second interval. This order was adopted following Ciocca and Darwin's

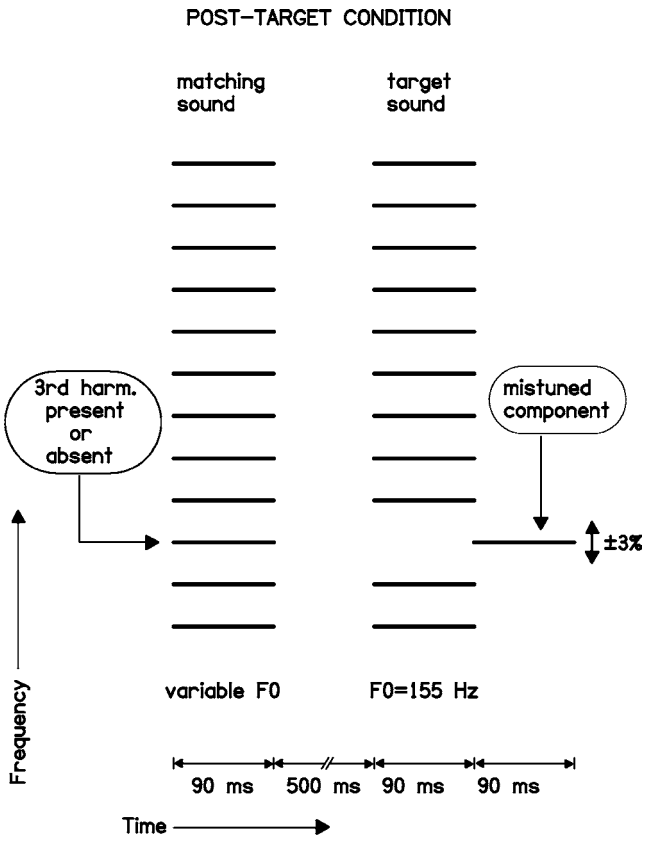

FIG. 1. Schematic spectrogram of the stimuli used in experiment 1A when the mistuned component was presented after the target complex (Post-target condition).

method: In experiments with Post-target conditions, the matching sound was first (see Fig. 1), while in experiments with Pre-target conditions, the matching sound was second. The following description of events applies to all experiments containing Post-target conditions (in experiment 1B the order was reversed). Following the matching sound and an interstimulus interval of 500 ms, the target tone, including or followed by the mistuned partial, was presented. Each interval was marked by a light. Subjects were required to indicate the interval containing the sound with the higher pitch. They were explicitly instructed to ignore the pure-tone percept in the interval containing the target sound and to match the pitch of the matching sound to that of the target complex.

A two-down, two-up rule was used to adjust the F0 or the frequency of the matching sound. Subjects were told that after two consecutive answers of the same type, the pitch of the matching sound was increased if the second interval was judged higher and decreased if the first interval was judged higher. When there were no two successive answers of the same type, the matching sound was unchanged. This procedure tracks the point corresponding to 50% "higher" (or "lower") judgments of the adjustable matching sound.

The starting step size was 5 Hz. Following each of the first six turnpoints (a change in the direction of the F0 change), the step size was halved. After the seventh turnpoint, the step size was set to its minimum of 0.0775 Hz, corresponding to 0.05% of the F0 of the target. Two buttons on a response box, marked 1 and 2, respectively, were used to indicate the interval with the higher pitch. By pressing a third button (underneath a red LED), subjects initiated the presentation of the same stimulus pair again. By pressing a fourth button (underneath a green LED) subjects indicated when they were satisfied with the pitch match. Subjects were encouraged to "bracket" the overall pitch of the target sound with the pitch of the matching sound several times, by making the variable matching sound clearly lower than the target sound and then clearly higher, before using the buttons to make the sounds equal in pitch. They were also encouraged to listen a few times to the same stimulus pair before indicating the interval with the higher pitch. Only after they reached the minimum step size was their response "Pitch of the two tones is the same" accepted. If a subject pressed the fourth button before the minimum step size was reached, the response was ignored and the same stimulus pair was presented again. Subjects were informed about the procedure and the stimuli, but no feedback was provided.

The starting F0 (or frequency) of the matching sound was varied quasi-randomly in the range 155 ± 30 Hz. Except in experiment 3, in which all conditions were presented in a randomized order, there were always four runs in a sequence for each condition; in two, the third component in the target sound was mistuned upwards and in two it was mistuned downwards. One of the two runs for each mistuning direction had a starting F0 of the matching sound higher than 155 Hz, and one had an F0 lower than 155 Hz. The two levels "present" and "absent" of the factor "presence of the third harmonic in the matching sound," were tested in alternating order. The two levels, "simultaneous" and "nonsimultaneous"of the factor "timing of the mistuned harmonic relative to the remainder of the target sound," were tested in a blocked design in each session. In a given session, conditions which had the mistuned harmonic presented simultaneously were tested during the first half of the session, while conditions which had the mistuned harmonic presented nonsimultaneously with the target sound were tested during the second half of the session; in the next session, the order of the two was reversed.

The matching pitch was defined as the F0 or frequency of the matching sound presented immediately before the subject indicated that the pitch in the two intervals was equal. At least ten pitch matches were obtained for each condition and subject. The data reported are the means of these ten (or more) pitch matches. The total duration of a single session was about 2 h, including rest times. To familiarize subjects with the procedure and equipment, they were given about 2–3 h of practice before data collection proper was started.

The target sounds were presented at a level of 58 dB SPL per component in a continuous pink background noise that had a spectrum level of 9 dB at 1 kHz (*re* 20 μPa). The pink noise was used so that the individual components would have approximately equal sensation levels. It would also have reduced the audibility of f2-f1 combination tones. The tones were generated digitally and were played out using a 16-bit digital-to-analog converter (CED 1401 plus), with a sampling rate of 10 kHz. Stimuli were passed through an antialiasing filter (Kemo 21C30) with a cutoff frequency of

4.3 kHz (slope of 96 dB/oct) and presented using one earpiece of Sennheiser HD250 headphones. Subjects were seated individually in an IAC double-walled sound-attenuating booth.

III. EXPERIMENT 1: MATCHING SOUND WITH AND WITHOUT THIRD HARMONIC

The first two experiments compared the pitch shifts obtained with a matching sound consisting of the first 12 harmonics of a variable F0, i.e., identical to the one used by Ciocca and Darwin (1999), to those obtained with a matching sound containing harmonics 1–2 and 4–12. If subjects use an analytical listening and matching strategy (see above), then pitch shifts would be expected to be smaller when the nominally mistuned third harmonic was absent in the matching sound. The reasoning for this is that, in the absence of the nominally mistuned harmonic in the matching sound, subjects cannot compare the pitch of the mistuned third harmonic in the target sound with the pitch of the corresponding harmonic in the matching sound. Also, as noted in the Introduction, to a certain degree subjects might be able to compare the pitch of the mistuned harmonic with the residue pitch of the matching sound and assess whether they are in tune and/or whether the mistuned harmonic fits as a subharmonic. The influence of this strategy would be expected to be strongest when the mistuned component was clearly audible as a pure tone separate from the richer percept evoked by the remainder of the target complex, i.e., when it "popped out." Although a mistuning of 3% can lead to some pop out, this would be reduced for tones of short duration (Moore *et al.*, 1986). The popping out of the mistuned component was clearest and most obvious when it was presented nonsimultaneously with the remainder of the target complex. Thus, differences between the pitch shifts obtained in the presence and in the absence of the third harmonic in the matching sound would be expected to be largest for nonsimultaneous presentation of the mistuned component.

The effects of the absence of the third harmonic from the matching sound were investigated in two separate experiments, for target sounds that were followed by the mistuned third component and for target sounds that were preceded by the mistuned third component. In each of the two experiments, the mistuned third component could also be presented simultaneously. Simultaneous and nonsimultaneous conditions were run in a blocked design (see Sec. II) in order to enhance possible learning effects. The matching complexes were, like the target complexes, presented at a level of 58 dB SPL per component.

A. Experiment 1A: Post-target

1. Stimuli and subjects

Subjects adjusted the pitch of the matching complex with variable F0 (either components 1–12, or components 1–2 and 4–12) to match that of the subsequent target complex with an F0 of 155 Hz and a mistuned third harmonic (either components 1–12 simultaneously, or components 1–2 and 4–12 followed by the mistuned third component).

TABLE I. Mean pitch matches (in Hz), averaged across positive and negative mistunings of the third component, and the corresponding standard errors across subjects. The mistuned component was presented either simultaneously or nonsimultaneously with the remainder of the target complex (immediately after in experiments 1A, 2A, 2B, and 3; immediately before in experiment 1B). The third harmonic could either be absent from or present in the matching sound. See text for details of the experiments.

	Condition				
	Simultaneous		Nonsimultaneous		
Experiment	Absent	Present	Absent	Present	Mean
1A	154.85	154.96	154.92	154.95	154.92
	(0.17)	(0.08)	(0.07)	(0.05)	(0.07)
1B	155.30	155.13	155.20	154.85	155.12
	(0.15)	(0.08)	(0.08)	(0.17)	(0.08)
2A	154.72	⋯	154.69	⋯	154.71
	(0.34)		(0.31)		(0.31)
2B	156.32	⋯	156.76	⋯	156.54[2]
	(1.21)		(1.46)		(1.33)
3	155.17	154.83	154.86	154.44	154.83
	(0.17)	(0.25)	(0.19)	(0.24)	(0.21)

Eight subjects participated in all conditions. They ranged in age from 17 to 34 years, and their quiet thresholds at octave frequencies between 250 and 4000 Hz were within 15 dB of the ANSI (2004) standard. Stimuli were presented monaurally to the left ear for six subjects and to the right ear for the other two. All of them had considerable musical experience.

2. Results

The results are based on 10 to 15 matches for each subject in each condition (and for each direction of mistuning). The number of pitch matches collected was varied slightly across subjects in order to compensate somewhat for differences in the variability of the matches across subjects. Typically 12 matches were collected, and the standard error of matches within a given condition and subject was about 0.06–0.07 Hz.

Initially, in this and all following experiments, the pitch matches were averaged across negative and positive mistuning of the third component to see whether there were any overall differences in pitch between target and matching sound. These possible "biases" were not the topic of the present paper, but are given for completeness. The mean pitch matches (averaged across negative and positive mistuning and across subjects) are shown in Table I for each experiment. The corresponding standard errors across subjects are given in brackets. In none of the experiments reported did the grand mean differ significantly from 155 Hz, i.e., there was no overall difference between the pitch of the target and the matching sound. Furthermore, for each experiment a repeated measures ANOVA that used the mean pitch matches for each subject and condition as input tested whether there were differences between the mean matches across conditions. There were never any significant differences, except in experiment 3. These will be described when the results of the third experiment are presented.

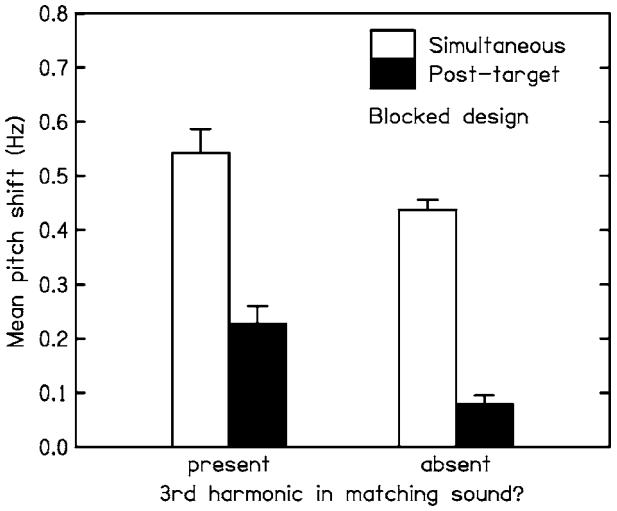

FIG. 2. Mean pitch shifts and the corresponding standard errors across eight subjects observed in experiment 1A. The left-hand group of two bars shows pitch shifts obtained for a matching complex that included the third harmonic. The right-hand group of two bars shows the pitch shifts obtained when the third harmonic was absent from the matching complex. The white and the black bars show results for simultaneous and post-target presentation of the mistuned component, respectively.

The data of principal interest with regard to the objectives of the current experiments—the differences between the pitch matches to positive and negative mistunings of the third harmonic—will be considered next. The results are presented [following Moore *et al.* (1985) and Ciocca and Darwin (1999)] as the mean *absolute* pitch shift, which is calculated as half the difference between pitch matches for corresponding positive and negative mistunings. Figure 2 shows the means and standard errors of the pitch shifts across subjects.

Pitch shifts were largest (about 0.54 Hz) when the mistuned component was presented simultaneously with the target complex and the third harmonic was present in the matching complex. The size of this pitch shift is at the lower end of the range of values observed by Ciocca and Darwin (1999) for the same condition (except that in their experiments the fourth instead of the third component was mistuned). Pitch shifts were second largest for simultaneous presentation of the mistuned component in the absence of the third harmonic in the matching complex (about 0.44 Hz). Pitch shifts were generally smaller when the mistuned component was presented after the target complex (filled bars).

To determine the statistical significance of these effects, a repeated measures two-way ANOVA (with factors timing of the mistuned component and presence of the third harmonic in the matching sound) was calculated, using the mean pitch shift for each subject and condition as input. The ANOVA showed significant main effects of timing of the mistuned component [$F(1,7)=318.3$, $p<0.001$] and presence of the third harmonic [$F(1,7)=8.7$, $p<0.05$], but no significant interaction. *Planned contrasts* (paired samples *t*-test) showed that for simultaneous presentation of the mistuned harmonic, the effect of the presence of the third harmonic in the matching sound was of borderline insignificance ($p=0.053$, one-tailed), while in the post-target conditions, the absence of the third harmonic in the matching sound led to a highly significant reduction in the size of the mean pitch shifts ($p=0.001$, one-tailed). The small pitch shift of 0.08 Hz in the post-target condition in the absence of the third harmonic in the matching sound was significantly larger than zero ($p=0.002$, one-tailed).

In summary, in contrast to the results of Ciocca and Darwin (1999), the present data showed a marked reduction in the size of the pitch shifts caused by a mistuned component when the mistuned component was presented after the remainder of the target complex instead of simultaneously with it. In addition, the pitch shifts were reduced (especially in the post-target condition) when the nominally mistuned harmonic was absent rather than present in the matching sound. The latter finding might indicate some role of an analytical listening and matching strategy.

B. Experiment 1B:Pre-target

1. Stimuli and listeners

Subjects matched the pitch of the matching complex (either components 1–12, or components 1–2 and 4–12) to that of the preceding target complex with an F0 of 155 Hz and a mistuned third harmonic. The mistuned component was presented either simultaneously with or immediately before the remainder of the target complex (Pre-target conditions).

Seven subjects participated in all conditions. Four of them had also taken part in experiment 1A. They ranged in age from 17 to 44 years, and their quiet thresholds at octave frequencies between 250 and 4000 Hz were within 15 dB of the ANSI (2004) standard. Stimuli were presented monaurally to the left ear for six subjects and to the right ear for one. All subjects had considerable musical experience.

2. Results

The results are based on about 12 to 32 matches for each subject in each condition; more matches were collected for some subjects than for others, because the variability of their matches was larger. Typically 16 matches were collected, and the standard error of matches within a given condition and subject was about 0.06–0.07 Hz. Figure 3 shows the pitch shifts and standard errors over all subjects.

Pitch shifts were largest when the mistuned component was presented simultaneously with the target complex. When the mistuned component was presented before the target complex, pitch shifts were smaller, about 0.23 and 0.14 Hz in the presence and in the absence of the nominally mistuned harmonic in the matching sound, respectively.

A repeated measures two-way ANOVA (with factors timing of the mistuned component and presence of the third harmonic in the matching sound) showed a highly significant main effect of timing of the mistuned component [$F(1,6)=74.4$, $p<0.001$] but no main effect of the presence of the third harmonic nor an interaction. *Planned contrasts* (paired samples *t* test) showed that the effect of the presence of the third harmonic in the matching sound was not significant when the mistuned harmonic was presented simultaneously with the remainder of the target. In contrast, in the pre-target conditions, removing the third harmonic from the matching

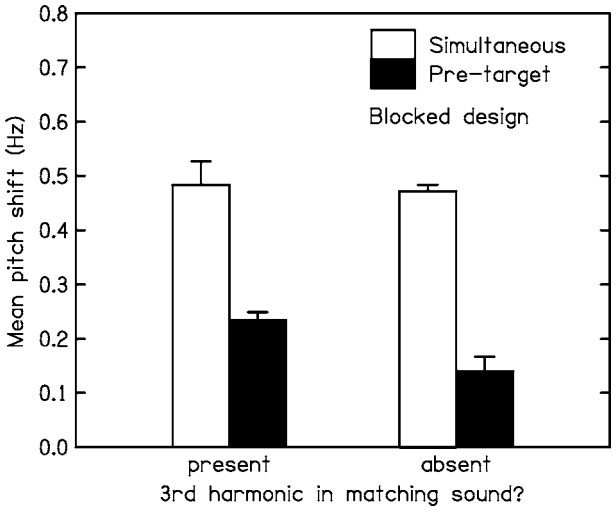

FIG. 3. Results for experiment 1B. Error bars indicate the standard error across seven subjects. The white and the black bars show results for simultaneous and pre-target presentation of the mistuned component, respectively. Otherwise, as in Fig. 2.

sound led to a significant reduction in the size of the pitch shifts ($p=0.016$, one-tailed).

Overall, the present data replicated the finding of Ciocca and Darwin (1999) for the pre-target conditions, i.e., the pitch shifts caused by a mistuned component were significantly smaller when the mistuned component was presented before the remainder of the target complex rather than simultaneously with it. In addition, the present results showed that, when the mistuned component was presented before the remainder of the target complex, pitch shifts were reduced even more when the third harmonic was absent than when it was present in the matching sound. Thus, for nonsimultaneous presentation of the mistuned component, both experiment 1A with post-target presentation and experiment 1B with pre-target presentation of the mistuned component showed smaller pitch shifts in the absence than in the presence of the nominally mistuned harmonic in the matching sound. This finding is consistent with the hypothesis that, when the mistuned component was presented nonsimultaneously, an analytical listening and matching strategy played some role in the task.

IV. EXPERIMENT 2: NONOVERLAPPING SPECTRA

In the following two experiments, pitch shifts caused by a mistuned harmonic were measured using matching sounds and target complexes that had nonoverlapping spectra. The use of such stimuli was intended to prevent subjects from using an analytical listening strategy. Subjects would have to concentrate on the residue pitch and try to ignore spectral differences. Due to the large differences in timbre of the matching and target sounds, it was expected that the task would be harder. A second objective was to test whether the spectral gap, produced by the absence of the third harmonic in the matching sound in some conditions in the first experiment, somehow increased the segregation of the mistuned third harmonic from the target complex. This in turn might have led to a reduction in the size of the pitch shifts.

In each of the following two experiments, the mistuned third component was either presented simultaneously with or after the remainder of the target complex, which was presented at a level of 58 dB SPL per component. As in experiment 1, simultaneous and post-target conditions were run in a blocked design.

A. Experiment 2A: Nonoverlapping harmonics

1. Stimuli and listeners

The target and matching complexes consisted of nonoverlapping harmonics, following a design that was originally used by Moore and Glasberg (1990) when determining F0 difference limens. The target complex contained harmonics number 2, 3, 6, 7, 10, and 11. The third harmonic was mistuned by ±3% and was presented either simultaneously with or immediately after the remainder of the target complex. The matching complex contained harmonics 1, 4, 5, 8, 9, and 12.

Four subjects participated. They ranged in age from 19 to 34 years. Initially, two more subjects were screened for their ability to give reliable pitch estimates and were rejected. All (screened) subjects also took part in experiment 1A. Stimuli were presented monaurally to the left ear for three subjects and to the right ear for the remaining one.

2. Results

As expected, the variability of the matches was larger than in experiment 1A. Therefore, a larger number of pitch matches was collected. The results are based on about 60 to 80 matches for each subject in each condition. For three subjects, the typical standard error of matches within a given condition was about 0.06–0.07 Hz, i.e., comparable (after increasing the number of matches) to that for experiment 1A. For one subject, the standard errors were about 0.12 Hz. The increase in the number of collected matches by a factor of about 6–7, necessary in order to keep the standard error approximately constant, corresponds to an increase of the standard deviation of the pitch matches by a factor of about 2.6 ($\sqrt{7}$). This is compatible with the finding of Moore and Glasberg (1990) that F0 difference limens increased by a factor of about 3 when listeners had to compare complex tones with no harmonic in common, relative to when they compared tones with identical harmonics. Figure 4(a) shows the mean and the standard errors of the pitch shifts across the four subjects.

The sizes of the pitch shifts were about 0.46 and 0.09 Hz when the mistuned component was presented simultaneously and after the target complex, respectively. The difference was highly significant ($p=0.001$, one-tailed, paired samples t test with df=3). The small pitch shift of 0.09 Hz in the post-target condition was significantly larger than zero ($p=0.012$, one-tailed). The shifts were very similar to those observed in experiment 1A in the absence of the third harmonic in the matching complex.

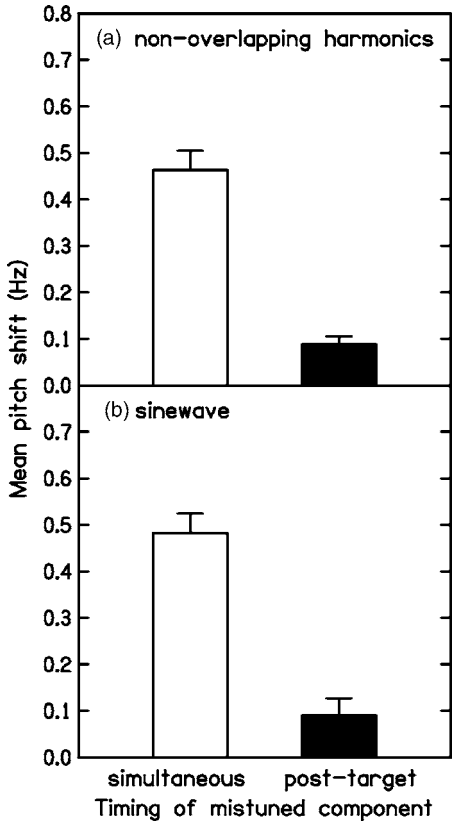

FIG. 4. Mean pitch shifts and standard errors across four subjects observed in experiment 2 with non-overlapping spectra of matching sound and target complex. Panel (a) shows results when the matching sound consisted of six harmonics that were non-overlapping with those of the target complex (experiment 2A). Panel (b) shows results when the matching sound was a sinewave (experiment 2B). The white and the black bars show results for simultaneous and post-target presentation of the mistuned component, respectively.

B. Experiment 2B: Sinewave as matching sound

1. Stimuli and listeners

As another way of preventing subjects from matching individual components, in experiment 2B, subjects matched the pitch of a sinewave, presented at a level of 68 dB SPL, to that of the target complex. The target complex was identical to that used in experiment 1A, except that the first harmonic was missing.

Four subjects, ranging in age from 17 to 34 years, participated. One more subject was screened for his ability to give reliable pitch matches with a sinewave. However, even though he participated in experiment 2A, he was not able to do the present task. All four subjects also participated in experiment 1A, and two of them also took part in experiment 2A. Stimuli were presented monaurally to the left ear for two subjects and to the right ear for the other two.

2. Results

The results are based on about 30, 60, 75, and 120 matches in each condition for the four subjects. For three subjects, the typical standard error of matches within a given condition was about 0.13–0.19 Hz, i.e., somewhat larger than in experiment 2A. For the subject for whom only 30 matches could be collected, because she was not available for longer, the typical standard error was 0.25 Hz. Clearly, the task in experiment 2B was the most difficult one. Figure 4(b) shows the results. The difference between pitch matches with post-target and with simultaneous presentation of the mistuned component was statistically significant ($p=0.003$, one-tailed, paired samples t test with df=3). The small pitch shift of 0.09 Hz in the post-target condition was not significantly larger than zero ($p=0.06$, one-tailed). The mean pitch shifts were virtually identical to those observed when the matching complex and target complex consisted of nonoverlapping harmonics. Both sets of shifts were very similar to those observed in experiment 1A when the third harmonic was not present in the matching complex.

In summary, although the differences in timbre and quality of the matching sound and target complex made it more difficult to match the pitch of the two sounds in experiments 2A and 2B, (most) musically trained subjects were able to do so. The stimuli in experiment 2 were chosen in such a way that spectral characteristics differed across matching and target sound and subjects had to match the overall pitch of the two sounds. Under these conditions, the results of experiment 1A were replicated. In contrast to Ciocca and Darwin's finding, when the mistuned component was presented after the target complex, mean pitch shifts were significantly smaller (about a fifth) than when the mistuned component was presented simultaneously. Furthermore, the pitch shifts observed in experiment 2 were very similar to those observed in experiment 1A in the absence of the third harmonic in the matching sound. The latter finding indicates that the results of experiment 1A were not caused by perceptual segregation of the mistuned component from the target complex due to the absence of that single specific component in the matching sound.

V. EXPERIMENT 3: RANDOMIZED DESIGN

None of the above experiments replicated Ciocca and Darwin's finding of equal-sized pitch shifts caused by a simultaneous and by a post-target mistuned component. In the present experiments, simultaneous and post-target conditions were tested in a blocked design, i.e., half a session each, with the order changed around across sessions. In Ciocca and Darwin's experiment, these conditions were run in a quasi-random order within each experimental session. (Note, however, that post- and pre-target conditions were not run in the same session.) The objective of the third experiment was to test whether the blocked design used here might have been the reason for the failure to replicate Ciocca and Darwin's findings.

A. Stimuli and listeners

The target complex and the matching complex were identical to those in experiment 1A. All conditions (upwards and downwards mistuning, starting F0 above and below 155 Hz, presence and absence of the third harmonic in the matching sound, simultaneous and post-target presentation of the mistuned component relative to the remainder of the target complex) were presented in a quasi-randomized order; a

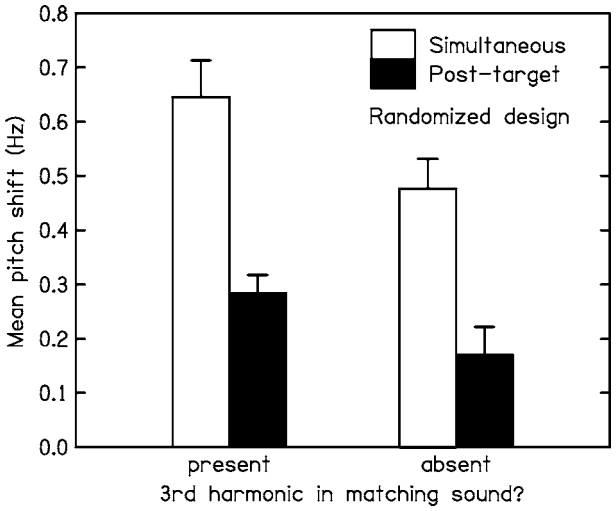

FIG. 5. Results of experiment 3. Error bars indicate the standard error across six subjects. As in Fig. 2 (experiment 1A) except that conditions were presented in a randomized instead of in a blocked design.

pitch match was collected in each condition, before additional matches in any condition were collected.

Six subjects participated, ranging in age from 18 to 44 years. None of them had participated before in any of the other experiments and their quiet thresholds at octave frequencies between 250 and 4000 Hz were within 15 dB of the ANSI (2004) standard. All of them had considerable musical experience. New subjects were chosen deliberately to avoid a possible influence of learning effects that might have resulted from the blocked conditions. Stimuli were presented monaurally to the left ear for four subjects and to the right ear for the remaining two.

B. Results

The results are based on between 10 and 50 matches in each condition for the six subjects, with a typical standard error for a given condition and subject of 0.06–0.07 Hz. As mentioned before, it was only in this experiment that the mean pitch matches (averaged across negative and positive mistuning) differed across conditions (see Table I). A repeated-measures two-way ANOVA with factors "timing of the mistuned component" and "presence of the third harmonic in the matching sound" showed that both main effects were significant [$F(1,5)=20.47$, $p<0.01$ and $F(1,5)=17.62$, $p<0.01$]. In the post-target conditions, the matched F0 was significantly lower than in the simultaneous conditions. When the third harmonic was present in the matching sound, the matched F0 was significantly lower than when it was absent. Both of these main effects seem to indicate that when the third harmonic (mistuned or not) was presented simultaneously within a complex (matching complex or target complex) the pitch of that complex was somewhat higher than when it was missing. The interaction was not significant.

Figure 5 shows the pitch shifts. As in experiment 1A, pitch shifts were largest for simultaneous presentation of the mistuned component in the presence of the third harmonic in the matching sound and were similar to Ciocca and Darwin's observed values for the corresponding condition (but with the fourth rather than the third component mistuned). They were somewhat smaller in the absence of the third harmonic in the matching complex and markedly reduced in the post-target conditions. A repeated measures two-way ANOVA showed a highly significant main effect of time of presentation of the mistuned component [$F(1,5)=72.57$, $p<0.001$] and a significant effect of the presence of the third harmonic [$F(1,5)=8.97$, $p<0.05$], but no significant interaction. *Planned contrasts* (paired samples t test) showed that for both simultaneous conditions and post-target conditions, the effect of the presence of the third harmonic in the matching sound was significant at the 5% level (one-tailed).

Overall, the mean pitch shifts were somewhat larger than those observed in experiment 1A. This could be due either to the randomized design in the present experiment or to differences between the two groups of subjects. Importantly, the pattern of results across conditions observed with the randomized design was the same as that observed with the blocked design in experiment 1A. Therefore, this difference in the design cannot explain the failure to replicate the results of Ciocca and Darwin (1999) for the corresponding post-target condition.

VI. GENERAL DISCUSSION

In several experiments, the pitch shift caused by a mistuned harmonic in an otherwise harmonic 90-ms complex tone with an F0 of 155 Hz was measured. When the mistuned harmonic was presented simultaneously with the target complex and the nominally mistuned harmonic was present in the matching complex, pitch shifts were between 0.48 and 0.65 Hz. When the mistuned harmonic was presented immediately before the target complex, the pitch shifts were significantly smaller than when it was presented simultaneously. These two results replicate Ciocca and Darwin's (1999) findings and show that they apply when the third harmonic is mistuned as well as when the fourth is mistuned. However, in contrast to Ciocca and Darwin's findings, the present experiments showed significantly smaller pitch shifts when the mistuned harmonic was presented after the remainder of the target complex than when presented simultaneously. This was true not only when the third harmonic was absent from the matching sound, but also when it was present. The former condition was not tested by Ciocca and Darwin, but the latter was.

In addition, the present results showed that pitch matches were smaller when the third harmonic was not present in the matching sound, especially when the mistuned third component followed or preceded the remainder of the target complex. This indicates that an analytical listening and matching strategy may have some influence on the pitch matches, especially for nonsimultaneous components that pop out. The strategy considered does not imply that subjects matched *only* the mistuned component to the corresponding harmonic in the matching sound. Such a strategy is not supported by the pitch matches observed [as noted earlier by Ciocca and Darwin (1999)], as the shifts were generally much smaller than 3%. However, the present data do support

the use of a different analytical listening-and-matching strategy that was suggested by Gockel *et al.* (2005). This strategy does not require integration of the nonsimultaneous mistuned component into the residue pitch of the target and it would not predict a monotonic increase in pitch shift with increasing mistuning. Subjects may have compared the harmonic matching complex with the two distinct percepts of the mistuned component and the "remainder" of the target complex and tried to minimize the overall discrepancy between the matching complex and these two distinct percepts. On the one hand, for the mistuned component, this would imply that subjects compare the mistuned component with the corresponding harmonic in the matching sound. However, even if the nominally mistuned component is absent in the matching sound, to a certain degree subjects might also be able to compare how the mistuned harmonic "fits with the harmonic matching sound." There are two ways how this could happen: (1) by assessing how well the pitch of the mistuned component fits as a harmonic of the harmonic matching complex and (2) under certain circumstances (for an octave relationship between mistuned harmonic and residue pitch of the matching sound, see below) by comparing the pitch (chroma) of the mistuned component with the residue pitch of the harmonic matching sound. On the other hand, for the remainder of the mistuned complex, subjects may compare the pitch of the remainder of the target with that of the matching complex. We will come back to this point below, as the use of this strategy might help to explain the differences between the current results and those of Ciocca and Darwin (1999).

In the first experiment, pitch shifts were smaller when the mistuned harmonic was presented after the remainder of the target complex than when presented simultaneously. This contrasted with the findings of Ciocca and Darwin, and the following experiments assessed possible reasons for this. In experiment 2, the spectra of matching sound and target were varied greatly, to check whether the use of the matching sound with harmonics 1–2 plus 4–12 somehow led to perceptual segregation of the mistuned third harmonic from the remainder of the target complex. Under those conditions pitch shifts were as small as those in experiment 1, and so this explanation was rejected. Also rejected as the cause for the difference was the use of a blocked versus randomized design; this factor did not influence the general pattern of results (see experiment 3).

The only difference between the stimuli across the two studies (for the common conditions) was that, in the present experiments, the third rather than the fourth harmonic was mistuned. As mentioned in the Introduction, the fourth harmonic might have a special status in pitch-matching tasks, as its frequency is two octaves above the F0. There is evidence that a single isolated partial with an octave relationship to the fundamental (two, four, eight times the F0) is typically judged to have the same pitch as the harmonic complex (Houtsma, 1979). This could lead to larger pitch shifts for the fourth than for the third harmonic, when presented nonsimultaneously with the target, in two different ways.

Firstly, when subjects use an analytical listening and matching strategy, the pitch of a slightly mistuned fourth harmonic following the remainder of the target can be matched with the residue pitch of the harmonic matching sound without the matching sound having a pitch very different from that of the remainder of the target. Thus, for the fourth harmonic, it would be possible to adjust the matching sound so that its pitch was more similar to that of the mistuned component, without decreasing markedly its similarity to the pitch of the remainder of the target. In contrast, attempts to match the pitch of a slightly mistuned third harmonic with the residue pitch of the harmonic matching sound would lead to a large discrepancy between the residue pitch of the matching sound and that of the remainder of the target. In this situation, subjects may abandon any attempt to make the mistuned harmonic "fit with the harmonic matching sound" (see above). Therefore, if subjects used an analytical listening and matching strategy, a mistuned third harmonic would have less influence on pitch matches than a mistuned fourth harmonic, when presented after the target.

Secondly, a (near) octave relationship between the pitch of the mistuned harmonic, presented after the remainder of the target, and the residue pitch of the remainder of the target might lead to larger pitch shifts. Carlyon (1996) found that F0 discrimination between two sequentially presented 200-ms complex-tone targets was markedly impaired in the presence of temporal fringes (a complex tone with fixed F0 that was presented before and after each target). He discussed this in terms of "overintegration" of information about the fringes' F0 when estimating that of the target. Later studies showed that this impairment depended on the similarity of the F0s (and spectral region) of the temporal fringes and the target (Micheyl and Carlyon, 1998), and on perceiving the stimuli in one perceptual stream (Micheyl and Carlyon, 1998; Gockel *et al.*, 1999). In a similar way, the influence of the mistuned post-target component on the pitch of the target could depend on the similarity of the pitch of the mistuned component and that of the remainder of the target. This could account for why the fourth harmonic had a large effect and the third had only a small effect. Although the effect of temporal fringes on F0 discrimination were originally discussed in terms of overintegration of information about the fringes' F0 when estimating that of the target (Carlyon, 1996), the exact stage where this interference arises (encoding or retrieval of pitch) is not clear.

In summary, we can think of two reasons why a mistuned fourth harmonic, that is presented after the remainder of the target, could lead to larger pitch shifts than a mistuned third. One does not rely on temporal integration of the mistuned harmonic into the residue pitch of the remainder of the target, although the other might.

In addition to the difference between the stimuli (mistuned harmonic number) there is one more, but maybe less likely, candidate that might explain the different findings in the corresponding conditions of Ciocca and Darwin's (1999) and of the present study. All of the present subjects, but only six out of eight of Ciocca and Darwin's subjects, were musically trained. The two studies used somewhat different methods for pitch matching. Ciocca and Darwin's subjects used a roller-ball to adjust the F0 within a permitted range of 155 ± 4 Hz. The present subjects had to indicate the higher of the two sounds in a trial and the F0 (or frequency in experi-

ment 2B) of the matching sound could vary over a much wider range of 155±30 Hz. The latter means that the present subjects had to be very good "pitch matchers" in order to do the task. If they had not been good pitch matchers, the matched pitches would have varied over a wide range and they would not have been accepted as subjects. The same is not true for the subjects in Ciocca and Darwin's study, i.e., the possible pitch matches were much more restricted. Another, related, point is the size of the standard errors within subjects and conditions. In the present study, standard errors were small (typically around 0.06–0.07 Hz). Ciocca and Darwin did not specify the size of the standard errors within subjects, except for experiment 2. For this, they mentioned that "The criterion for stopping after five matches was a standard error smaller than 0.4 Hz in all conditions." However, in a personal communication they pointed out that the subjects' standard errors were typically around 0.1 Hz, which is nevertheless still slightly larger than observed here. It could be that the reason for the discrepancy across studies is connected to the restricted range of permitted pitch matches and the slightly larger variability in Ciocca and Darwin's study.

Whatever the reason for the discrepancy, the present results show that obligatory integration into the residue pitch of a component presented after the remainder of a 90-ms target complex is much weaker than estimated by Ciocca and Darwin (1999).

Ciocca and Darwin (1999) found no significant difference between the pitch shifts caused by a simultaneously presented mistuned component and one that was presented after the target complex, even when it was separated from the remainder by up to 80 ms of silence. Thus, their results implied that pitch processes always integrate acoustic energy over a period of a few hundred milliseconds for virtual pitch. They argued that this poses a major problem for models of pitch perception that estimate virtual pitch by combining autocorrelation functions of the activity of individual nerve fibres. Models like the summary autocorrelation model (Meddis and Hewitt, 1991a, b) have "time constants" of about 3–20 milliseconds which determine the time period over which information is integrated; the time period considered in these models corresponds to three times the "time constant." Ciocca and Darwin argued that these time constants are too short to accommodate their results.

In contrast, the pitch shifts observed in the present study, in the absence of the nominally mistuned harmonic in the matching sound, were generally very small. The present results do *not* imply that pitch processes always integrate information over a period of a few hundred milliseconds for calculating virtual pitch. Therefore, the results do not seem to pose a major problem for models like the summary autocorrelation model. Also note that it has been shown that for changing stimuli, the end of a stimulus receives more weight in the overall calculation of pitch (Nábělek *et al.*, 1970). Thus, a relatively short integration time would seem sufficient to explain the small shifts in pitch observed when the mistuned harmonic is presented after the remainder of the complex tone.

A shorter obligatory integration time would be more useful with regard to the perception of the pitch of auditory objects in a changing acoustic environment. It is hard to see the advantage of a system that integrates energy in an obligatory way *across* events clearly segregated in time for the purpose of pitch calculation. Indeed, temporal discontinuities of only a few milliseconds may be sufficient to cause the pitch mechanism to "reset" and to start a new pitch estimate (Nábělek, 1996; Plack and White, 2000). This suggests that the auditory system is able to keep temporally segregated events distinct for the purpose of pitch extraction, even over short time periods. Note, however, that for events overlapping in time, even though they might be perceptually segregated, effects on pitch perception have been observed (Darwin and Ciocca, 1992; Hukin and Darwin, 1995; Gockel *et al.*, 2004).

The situation might be different altogether, when sounds are presented at a relatively low sensation level in background noise. Hall and Peters (1981) found that integration of nonsimultaneous components into a single virtual pitch took place only when the harmonics were presented at a low signal-to-noise ratio (see the Introduction). As pointed out by Hall and Peters, this might be related to an effect known as continuity effect (Elfner and Homick, 1967) or auditory induction (Warren *et al.*, 1972), where listeners restore missing parts of a signal that might have been masked by a noise.

In Ciocca and Darwin's (1999) study and here, subjects were asked to ignore the pure-tone percept caused by the mistuned component that followed the remainder of the target. This is why the term "obligatory integration" was used here to describe the effects of the mistuned component on the residue pitch of the remainder of the target. In contrast, if the task explicitly requires subjects to integrate information over several events, as in Grose *et al.*'s (2002) study (see the Introduction), then a different ability is assessed which might lead to subjects using different strategies. Grose *et al.*'s subjects were able to extract a virtual pitch from three consecutive 40-ms harmonics that were separated by silent intervals of up to about 45 ms. This *might* indicate that a pitch integrator can cope with nonsimultaneous components within a certain time range. However, as Grose *et al.* (2002) pointed out, their subjects might have gleaned some virtual pitch information by treating the tone sequence as arpeggio and internally constructing the F0 that would give the best fit to a given arpeggio. This might be easier when the silent intervals between the tones are short rather than long, which would be an alternative explanation for their finding.

VII. SUMMARY AND CONCLUSIONS

Pitch shifts were measured for a 90-ms complex tone with an F0 of 155 Hz. The third harmonic was mistuned by ±3%, and pitch shifts were measured for three times of presentation (before, simultaneous, after) of the mistuned harmonic relative to the remainder of the target complex. Subjects were instructed to ignore the percept of a pure tone, i.e., to ignore any mistuned component that popped out, especially when it was presented nonsimultaneously with the target. The experimental findings were as follows:

(1) When the mistuned component was presented nonsimultaneously with the remainder of the target complex,

shifts in residue pitch were significantly smaller than when it was presented simultaneously. The marked reduction in pitch shifts for the post-target conditions contrasts with Ciocca and Darwin's (1999) results.

(2) Pitch shifts were significantly smaller when the matching complex did not contain the third harmonic.

(3) When the matching sound was a sinewave (experiment 2B) or when target and matching sound had nonoverlapping harmonics (experiment 2A), pitch shifts were similar to those observed with a matching sound that consisted of harmonics 1–2 plus 4–12 (experiment 1A).

(4) A randomized design (experiment 3) produced the same pattern of results as when simultaneous and post-target conditions were presented in a blocked design.

The results indicate the following:

(a) An analytical listening and matching strategy contributed to the pitch shifts measured, especially when the mistuned component was presented nonsimultaneously.

(b) Obligatory integration of nonsimultaneous components for the purpose of determining the residue pitch of a complex tone seems to take place over a much shorter time period than originally estimated by Ciocca and Darwin (1999).

ACKNOWLEDGMENTS

This work was supported by EPSRC Grant No. GR/R65794/01. We thank Brian Moore, Chris Darwin, an anonymous reviewer, and John Grose for helpful comments.

[1]Note, however, that the use of this term rests on the assumption that the subjects in the Ciocca and Darwin study and in the present study tried to obey the instruction to ignore the pure tone.

[2]Walliser (1969) and Terhardt (1971) found that when listeners matched the pitch of a complex tone with that of a sinusoid, the frequency of the latter was often below that of the F0 of the complex. This finding was not observed in the results of experiment 2B, as the grand mean was not significantly different from 155 Hz. Note, however, that there were also considerable individual differences in Walliser's and Terhardt's data.

ANSI (**2004**). ANSI S3.6-2004, Specification of Audiometers (American National Standards Institute, New York).

Carlyon, R. P. (**1996**). "Masker asynchrony impairs the fundamental-frequency discrimination of unresolved harmonics," J. Acoust. Soc. Am. **99**, 525–533.

Ciocca, V., and Darwin, C. J. (**1999**). "The integration of nonsimultaneous frequency components into a single virtual pitch," J. Acoust. Soc. Am. **105**, 2421–2430.

Darwin, C. J., and Ciocca, V. (**1992**). "Grouping in pitch perception: Effects of onset asynchrony and ear of presentation of a mistuned component," J. Acoust. Soc. Am. **91**, 3381–3390.

Elfner, L. F., and Homick, J. L. (**1967**). "Auditory continuity effects as a function of the duration and temporal location of the interpolated signal," J. Acoust. Soc. Am. **42**, 576–579.

Gockel, H., Carlyon, R. P., and Micheyl, C. (**1999**). "Context dependence of fundamental-frequency discrimination: Lateralized temporal fringes," J. Acoust. Soc. Am. **106**, 3553–3563.

Gockel, H., Carlyon, R. P., and Plack, C. J. (**2004**). "Across-frequency interference effects in fundamental frequency discrimination: Questioning evidence for two pitch mechanisms," J. Acoust. Soc. Am. **116**, 1092–1104.

Gockel, H., Carlyon, R. P., and Plack, C. J. (**2005**). "Dominance region for pitch: Effects of duration and dichotic presentation," J. Acoust. Soc. Am. **117**, 1326–1336.

Goldstein, J. L. (**1973**). "An optimum processor theory for the central formation of the pitch of complex tones," J. Acoust. Soc. Am. **54**, 1496–1516.

Grose, J. H., Hall, J. W., and Buss, E. (**2002**). "Virtual pitch integration for asynchronous harmonics," J. Acoust. Soc. Am. **112**, 2956–2961.

Hall, J. W., and Peters, R. W. (**1981**). "Pitch for nonsimultaneous successive harmonics in quiet and noise," J. Acoust. Soc. Am. **69**, 509–513.

Houtsma, A. J. M. (**1979**). "Musical pitch of two-tone complexes and predictions by modern pitch theories," J. Acoust. Soc. Am. **66**, 87–99.

Houtsma, A. J. M. (**1984**). "Pitch salience of various complex sounds," Music Percept. **1**, 296–307.

Houtsma, A. J. M., and Goldstein, J. L. (**1972**). "The central origin of the pitch of pure tones: Evidence from musical interval recognition," J. Acoust. Soc. Am. **51**, 520–529.

Hukin, R. W., and Darwin, C. J. (**1995**). "Comparison of the effect of onset asynchrony on auditory grouping in pitch matching and vowel identification," Percept. Psychophys. **57**, 191–196.

Meddis, R., and Hewitt, M. (**1991a**). "Virtual pitch and phase sensitivity studied using a computer model of the auditory periphery. I: Pitch identification," J. Acoust. Soc. Am. **89**, 2866–2882.

Meddis, R., and Hewitt, M. (**1991b**). "Virtual pitch and phase sensitivity studied using a computer model of the auditory periphery. II: Phase sensitivity," J. Acoust. Soc. Am. **89**, 2883–2894.

Micheyl, C., and Carlyon, R. P. (**1998**). "Effects of temporal fringes on fundamental-frequency discrimination," J. Acoust. Soc. Am. **104**, 3006–3018.

Moore, B. C. J. (**1982**). *An Introduction to the Psychology of Hearing*, 2nd ed. (Academic, London).

Moore, B. C. J., and Glasberg, B. R. (**1990**). "Frequency discrimination of complex tones with overlapping and non-overlapping harmonics," J. Acoust. Soc. Am. **87**, 2163–2177.

Moore, B. C. J., Glasberg, B. R., and Peters, R. W. (**1985**). "Relative dominance of individual partials in determining the pitch of complex tones," J. Acoust. Soc. Am. **77**, 1853–1860.

Moore, B. C. J., Glasberg, B. R., and Peters, R. W. (**1986**). "Thresholds for hearing mistuned partials as separate tones in harmonic complexes," J. Acoust. Soc. Am. **80**, 479–483.

Nábêlek, I. V. (**1996**). "Pitch of a sequence of two short tones and the critical pause duration," Acust. Acta Acust. 82, 531–539.

Nábêlek, I. V., Nábêlek, A. K., and Hirsh, I. J. (**1970**). "Pitch of tone bursts of changing frequency," J. Acoust. Soc. Am. **48**, 536–553.

Plack, C. J., and White, L. J. (**2000**). "Pitch matches between unresolved complex tones differing by a single interpulse interval," J. Acoust. Soc. Am. **108**, 696–705.

Terhardt, E. (**1971**). "Die Tonhöhe harmonischer Klänge und das Oktavintervall," Acustica **24**, 126–136.

Terhardt, E., Stoll, G., and Seewann, M. (**1982**). "Algorithm for extraction of pitch salience from complex tonal signals," J. Acoust. Soc. Am. **71**, 679–688.

Walliser, K. (**1969**). "Zusammenhänge zwischen dem Schallreiz und der Periodentonhöhe," Acustica **21**, 319–329.

Warren, R. M., Obusek, C. J., and Ackroff, J. M. (**1972**). "Auditory induction: Perceptual synthesis of absent sounds," Science **176**, 1149–1151.

A perceptual learning investigation of the pitch elicited by amplitude-modulated noise[a)]

Matthew B. Fitzgerald[b)] and Beverly A. Wright[c)]
Department of Communication Sciences and Disorders and Northwestern University Institute for Neuroscience, Northwestern University, 2240 Campus Drive, Evanston, Illinois 60208-3550

(Received 24 January 2005; revised 11 July 2005; accepted 26 August 2005)

Noise that is amplitude modulated at rates ranging from 40 to 850 Hz can elicit a sensation of pitch. Here, the processing of this temporally based pitch was investigated using a perceptual-learning paradigm. Nine listeners were trained (1 hour per day for 6–8 days) to discriminate a standard rate of sinusoidal amplitude modulation (SAM) from a faster rate in a single condition (150 Hz SAM rate, 5 kHz low-pass carrier). All trained listeners improved significantly on that condition. These trained listeners subsequently showed no more improvement than nine untrained controls on pure-tone and rippled-noise discrimination with the same pitch, and on SAM-rate discrimination with a 30 Hz rate, although they did show some improvement with a 300 Hz rate. In addition, most trained, but not control, listeners were worse at detecting SAM at 150 Hz after, compared to before training. These results indicate that listeners can learn to improve their ability to discriminate SAM rate with multiple-hour training and that the mechanism that is modified by learning encodes (1) the pitch of SAM noise but not that of pure tones and rippled noise, (2) different SAM rates separately, and (3) differences in SAM rate more effectively than cues for SAM detection. © *2005 Acoustical Society of America.* [DOI: 10.1121/1.2074687]

PACS number(s): 43.66.Hg, 43.66.Mk [NFV] Pages: 3794–3803

I. INTRODUCTION

Pitch is one of the most salient perceptual qualities of sound and is perceived with a variety of different waveform types. Of interest here is the pitch of amplitude-modulated noise. The strongest evidence that amplitude-modulated noise can elicit pitch comes from demonstrations that musically trained listeners can identify musical intervals and melodies, as well as transcribe unfamiliar melodies, produced by varying the modulation rate within the range of 40–850 Hz [Burns and Viemeister (1976) (1981)]. Aside from evidence that this pitch is temporally based, arising from the amplitude envelope of the sound [e.g., Miller and Taylor (1948); Pollack (1969); Burns and Viemeister (1976), (1981)], relatively little is known about it. Here we investigated the relationship between the encoding of the pitch of sinusoidally amplitude modulated (SAM) noise with a given modulation rate to that of the pitch of other stimulus types, other modulation rates, and the detection of modulation. We did so by examining the generalization of learning on a SAM-rate-discrimination task. Like others [Grimault *et al.* (2003); Hall *et al.* (2003)], we inferred that listeners made these discriminations based on pitch.

A. The pitches of SAM noise, pure tones, and rippled noise

Our first question was whether the pitch of SAM noise is processed separately from, or together with, the pitches of pure tones or rippled noise. There are data to support both options. At least three pieces of evidence indicate that the processing of the pitch of SAM noise is at least partially independent from that of these other stimulus types. First, the pitch of SAM noise arises from a different stimulus cue than that underlying the pitches of pure tones or rippled noise. The pitch elicited by SAM noise is carried by the temporal envelope of the stimulus and is not likely influenced by spectral cues [e.g., Miller and Taylor (1948); Small (1955); Pollack (1969); Burns and Viemeister, (1976), (1981)]. In contrast, the temporal fine structure of the stimulus, and perhaps even spectral cues, can convey pure-tone and rippled-noise pitches [pure tones, for a review see Moore (1997); rippled-noise, see Bilsen and Ritsma (1969/70); Raatgever and Bilsen (1992); Cohen *et al.* (1995); Patterson *et al.* (1996); Yost *et al.* (1998)]. Second, the discrimination thresholds for the cues that elicit pitch for each of these three stimulus types differ across them. For example, for highly trained listeners, thresholds at 150 Hz are highest for SAM-rate discrimination [~12 Hz; Formby (1985)], intermediate for rippled-noise delay-time discrimination [~4 Hz; Yost *et al.* (1978)], and lowest for pure-tone frequency discrimination [~1 Hz; Formby (1985)]. Finally, SAM stimuli are processed by different neurons than pure tones or rippled noises at several levels of the auditory system. For example, there are periodotopic representations of modulation rate that are largely separate from and orthogonal to the tonotopic representation of pure-tone frequency in both the inferior colliculus and auditory cortex [Schreiner and Langner (1988); Langner *et al.* (1997); Schulze and Langner (1997)]. Similarly, chopper units in the cochlear nucleus appear to be well suited for encoding the stimulus envelope, the cue for the

[a)]Portions of this work were presented in "Specificity of learning for the discrimination for sinusoidal-amplitude-modulation rate," 139th Meeting of the Acoustical Society of America, Atlanta, Georgia, June 2000.
[b)]Electronic mail: matthew.fitzgerald@med.nyu.edu
[c)]Electronic mail: b-wright@northwestern.edu

pitch of SAM noise [Greenberg and Rhode (1987); Frisina *et al.* (1990); Shofner (1999)], while primary-like units may best represent the fine structure, the cue for the pitch of rippled noise [Shofner (1991), (1999)].

Other evidence, however, suggests that the pitches of SAM noise, pure tones, and rippled noise may be processed together. Despite the differences in the stimulus cues thought to underlie these three pitch types, an autocorrelation-based model that extracts periodic information from the stimulus waveform can predict the pitch of all of them [Meddis and Hewitt (1991a, b); Meddis and O'Mard (1997)]. This model also predicts differences in pitch saliency that correspond to the differences in the pitch-cue discrimination thresholds observed across these three stimulus types [Meddis and Hewitt (1991b)]. Further, physiologically, it appears that both the stimulus-envelope and the fine-structure cues that elicit pitch for these three stimulus types can be conveyed by chopper units in the cochlear nucleus [Winter *et al.* (2001); Wiegrebe and Winter (2001); Wiegrebe and Meddis (2004)].

B. Different SAM rates

Our second question was whether different SAM rates, both those that do and do not elicit pitch, are processed separately or together. Again, there is some support for both modulation-rate specific processing and for shared processing of different modulation rates. However, most of the relevant psychophysical data come from investigations of SAM detection, rather than discrimination, in which the employed SAM rates were too slow, and the modulation depths too shallow, to elicit pitch. The majority of this evidence indicates that different modulation rates are processed separately. First, when a target modulation rate is presented with a second, masking, modulation rate, the target rate is most difficult to detect or discriminate when the masker is modulated at the same rate as the target. The amount of impairment decreases as the difference in the target and masker rate increases, both when the target and masker modulate the same [e.g., Bacon and Grantham (1989); Houtgast (1989)] or different [e.g., Yost and Sheft (1989); Yost *et al.* (1989)] carriers. Second, the ability to detect modulation at a target rate is more impaired after exposure to 100% modulation at the target rate than at other modulation rates [Richards *et al.* (1997); Sheft (2000); Wojtczak and Viemeister (2003)]. Third, different modulation rates generate different percepts, ranging from resolvable fluctuations ($<\sim 20$ Hz), to roughness (strongest at 70 Hz), to pitch ($\sim$40–850 Hz; Terhardt (1974); Burns and Viemeister (1976); Fastl (1977)], and listeners appear to focus on different percepts at different rates when trying to detect SAM [Wright and Dai (1998)]. Fourth, a psychophysical model based on modulation-rate-specific processing can predict the ability of listeners to detect a single modulation rate in isolation and in the presence of a second modulation rate [Dau *et al.* (1997a, b); Ewert and Dau (2000)]. Finally, there is physiological evidence that different modulation rates are processed separately from each other, either at different stages along the auditory pathway, or at different sites within a given stage. Most neurons in auditory cortex preferentially respond to slow modulation rates [Schreiner and Urbas (1988); Eggermont (1994); Giraud *et al.* (2000)], while a majority of neurons in inferior colliculus and cochlear nucleus respond best to fast rates [e.g., Moller (1974); Langner and Schreiner (1988); Schreiner and Langner (1988); Giraud *et al.* (2000)]. Periodotopic representations of modulation rate also have been observed in both the inferior colliculus [Langner and Schreiner (1988); Schreiner and Langner (1988)] and the auditory cortex [Langner *et al.* (1997); Schulze and Langner (1997)].

In contrast, there is also reason to think that different modulation rates may be processed together. For example, a psychophysical model that assumes shared processing for different modulation rates can predict, in most instances, the ability of listeners to detect a single modulation rate in isolation and, given an appropriate decision strategy, in the presence of a second modulation rate [Viemeister (1979); Strickland and Viemeister (1996)]. In addition, there are neurons that respond to multiple modulation rates below an upper cutoff rate at many processing levels [see Joris *et al.* (2004) for a review].

C. SAM-rate discrimination and SAM detection

Our third question was to what extent the processing involved in SAM-rate discrimination with a stimulus that elicits pitch is shared with that involved in SAM detection. Suggesting that there is a relationship between the two, thresholds for both modulation-rate discrimination and modulation detection increase approximately in parallel, rather than divergently, with increasing modulation rate [Burns and Viemeister (1976); Patterson *et al.* (1978); Formby (1985); Grant *et al.* (1998)]. However, indicating that these abilities may engage different mechanisms at some stage of processing, the correlation between modulation-detection and SAM-rate-discrimination thresholds in individual listeners is minimal [Grant *et al.* (1998)], and modulation can be detected at shallower modulation depths than are necessary for modulation-rate discrimination [Burns and Viemeister (1976); Patterson and Johnson-Davies (1977)].

D. Perceptual-learning paradigm

To investigate these three questions, we examined patterns of learning and generalization on a SAM-rate discrimination task. We gave nine listeners multiple-hour practice on a single SAM-rate discrimination condition, and examined whether, relative to nine untrained controls, this training improved the ability of the trained listeners to discriminate the frequency of a pure tone or the delay time of a rippled noise that elicited the same pitch as the trained standard rate (150 Hz), to discriminate SAM of slower (30 Hz) or faster (300 Hz) standard rates, or to detect SAM at the trained rate. We assumed that learning on the trained condition would generalize to an untrained condition only if the processing affected by learning on the trained condition also was involved in the processing of the untrained condition. Given this assumption, we reasoned that the pattern of generalization would indicate whether the processing affected by learning encodes: (1) only the pitch elicited by SAM noise (no generalization to the pure-tone or rippled-noise stimuli) or the pitch elicited by

multiple stimulus types (generalization), (2) only the trained SAM rate (no generalization to untrained SAM rates) or multiple modulation rates (generalization), (3) SAM only for discrimination (no generalization to SAM detection) or for SAM detection as well (generalization).

Others have also used learning paradigms to investigate pitch-encoding mechanisms [e.g., Irvine *et al.* (2000); Demany and Semal (2002); Grimault *et al.* (2002)], but we are aware of only one instance in which learning on SAM-rate discrimination was used to do so. As part of their investigation of the mechanisms underlying the pitches of resolved and unresolved harmonic complexes, Grimault *et al.* (2003) gave two groups of listeners training on SAM-rate discrimination twelve two-hour sessions spread over four weeks; one group was trained at 88 Hz and the other at 250 Hz. Addressing one of their primary questions, they reported that learning to discriminate SAM rate generalized to fundamental-frequency discrimination with resolved and unresolved harmonic complexes. More closely related to the current project, they also reported that learning on pure-tone frequency discrimination did not generalize to SAM-rate discrimination. However, their results as to whether learning on SAM-rate discrimination generalized to pure-tone frequency discrimination (one of the current questions) were ambiguous. On one hand, listeners trained on SAM-rate discrimination improved just as much on pure-tone frequency discrimination as did listeners trained with pure tones, indicating generalization. On the other hand, listeners trained on SAM-rate discrimination showed rapid learning in pure-tone frequency discrimination that was not seen in listeners trained with pure tones, suggesting that the apparent generalization from SAM-rate to pure tones may actually have resulted from this rapid learning and, by implication, through procedural as opposed to perceptual learning. Finally, they state in passing that learning on SAM-rate discrimination generalized to untrained SAM rates (another of the current questions) and to untrained carriers.

While the results of Grimault *et al.* (2003) are relevant to the present experiment, additional examination is still warranted for the two current questions that overlap with their investigation. Their results regarding the generalization from SAM-rate discrimination to pure-tone frequency discrimination were inconclusive and their comment that learning generalized across different modulation rates was not substantiated by statistical analyses. It is also worth noting that, in their experiment, there were only three listeners in each trained group, and listeners trained with different SAM rates were apparently treated as a single trained group in the statistical analyses, just as they were in the figures. This collapsing across trained groups may have obscured differences in the amount of learning at the two trained rates; the time course of learning has been observed to be slower at faster modulation rates [Schulz and Scheich (1999)].

II. METHODS

A. Listeners

Eighteen listeners (10 females) between the ages of 18 and 31 years (mean 19.8 years) participated in this experiment. None of the listeners reported any history of hearing disorder. We paid all listeners an hourly wage, and gave the trained listeners a 20% bonus upon completing the experiment. None of the listeners had any previous experience with psychoacoustic tasks.

B. Procedure and conditions

We used the same paradigm as in a previous experiment on auditory perceptual learning [Wright and Fitzgerald (2001)]. Listeners were divided into two groups of equal size: a trained group and a control group. The trained group completed a pre-test, a training phase, and a post-test. The control group completed only the pre- and post-tests.

On both the pre- and post-tests, all listeners performed the same six conditions: three on SAM-rate discrimination, and one each on pure-tone frequency discrimination, rippled-noise discrimination, and SAM detection. We randomized the condition order across listeners, but each listener used the same order in the pre- and post-tests. For each condition in these tests, listeners completed five blocks of 60 two-interval forced-choice trials (300 total trials). In one interval of each trial, we presented a standard sound, and in the other a target sound. Listeners were asked to indicate which interval contained the target sound. In the *30, 150, and 300 Hz SAM-rate-discrimination conditions*, the standard sound was a SAM noise with a modulation rate of 30, 150, or 300 Hz and the target sound a SAM noise with a faster modulation rate. The dependent variable was the SAM rate of the target sound (in Hz). In the *150 Hz pure-tone frequency-discrimination condition*, the standard sound was a 150 Hz pure tone and the target sound a tone of higher frequency. The dependent variable was the frequency of the target sound (in Hz). In the *150 Hz rippled-noise-discrimination condition*, the standard sound was a cos+rippled noise with a delay time of 6.67 ms [corresponding to a pitch value of 150 Hz; Bilsen (1966); Bilsen and Ritsma (1969/70); Yost *et al.* (1978)] and the target sound a cos+rippled noise with a shorter delay time (corresponding to a higher pitch value). The dependent variable was the delay time of the target sound (in ms). Finally, in the *150 Hz SAM-detection condition*, the standard sound was an unmodulated noise and the target sound a SAM noise. The dependent variable was the modulation depth of the target sound (converted to dB). The pre- and post-tests were separated by an average of 10.2 days for the trained listeners and 11.3 days for the controls.

During the training phase, which occurred between the pre- and post-tests, trained listeners completed twelve blocks (720 trials) of practice per day for six to eight days on only the 150 Hz SAM-rate-discrimination condition. The control listeners received no training.

In all conditions we manipulated the dependent variable to determine the discrimination or detection threshold for each listener. This threshold was obtained by decreasing the dependent variable after three consecutive correct responses, and by increasing it after each incorrect response. When the dependent variable changed from decreasing to increasing, or vice versa, its value was noted. We discarded the first three of these reversal values in each 60-trial block, and then

averaged the remaining reversal values to obtain the discrimination or detection threshold. This threshold corresponded to the 79.4% correct point on the psychometric function [Levitt (1971)]. To ensure accuracy, no threshold was computed if there were fewer than four remaining reversal values. Only 2.1% of all 60-trial blocks were omitted for this reason. For the three SAM-rate-discrimination conditions, the starting difference between the standard and target was typically 6 Hz for the 30 Hz standard rate, 20 Hz for the 150 Hz standard rate, and 90 Hz for the 300 Hz standard rate. The step size was 0.018 of the standard rate until the third reversal, and was 0.006 of the standard rate thereafter. For the pure-tone frequency-discrimination condition, the starting difference was typically 6 Hz, and the two step sizes were 0.75 and 0.15 Hz. For the rippled-noise-discrimination condition, the starting difference was generally 0.338 ms, and the step sizes were 0.157 and 0.026 ms. In the five discrimination conditions, if the adaptive procedure called for the target sound to have a lower modulation rate, lower pure-tone frequency, or a longer delay time than the standard, the target sound was made to be equal to the standard sound and the track continued. This situation never occurred for any of the SAM-rate-discrimination conditions, occurred on 0.8% of trials for the pure-tone frequency-discrimination condition, and on 2.1% of the trials for the rippled-noise-discrimination condition. Finally, for the SAM-detection condition, the starting modulation depth (m) was 1 (100% modulation) and the step sizes in units of 20 $\log(m)$ were 4 and 2 dB. We provided feedback after each trial in all measurement phases.

C. Stimuli

All stimuli were generated digitally (Tucker Davis Technologies APOS). The pure tones had a starting phase of zero degrees. The standard SAM noises were created by multiplying an unmodulated broadband Gaussian noise with a DC-shifted sinusoid of either 30, 150, or 300 Hz. The SAM noises were low-pass filtered at 5000 Hz after modulation and the modulation had a starting phase of zero degrees. In the SAM-rate-discrimination task, the modulation depth was always 100%. The amplitude of all SAM noises was reduced by $1+m^2/2$ (m=modulation depth) to cancel out the increase in power resulting from amplitude modulation [e.g., Viemeister (1979)].

The cos+rippled-noise sounds were created by duplicating an unmodulated broadband Gaussian noise, delaying the duplicated noise, and adding the delayed noise back to the original noise. For the standard sound in the 150 Hz rippled-noise-discrimination condition, the delay time was 6.667 ms. Only one iteration of the duplication-delay-addition process was performed, with a gain of 1.0, to obtain a pitch strength for the rippled noise that was slightly stronger than, but comparable to, that of SAM noise [Fastl and Stoll (1979)]. The cos+rippled noise were low-pass filtered at 5000 Hz.

All noise stimuli were presented at a spectrum level of 40 dB SPL (overall level of 77 dB SPL). The sinusoids in the pure-tone frequency-discrimination task were presented at an overall level of 70 dB SPL. Each sound was shaped with cosine-squared 10 ms rise/fall envelopes and had a duration of 400 ms, measured from onset to offset. The interstimulus interval was 600 ms for all conditions.

The stimuli were played through a 16-bit digital-to-analog converter (TDT DD1) at a sampling rate of 25 kHz, followed by an anti-aliasing filter set to low-pass at 8500 Hz (TDT FT6-2), a programmable attenuator (TDT PA4), a sound mixer (TDT SM3), and a headphone driver (TDT HB6). The stimuli were then presented through the left earpiece of Sennheiser HD265 headphones. All listeners were tested in a sound-treated room.

III. RESULTS

A. Learning on the trained condition: 150 Hz SAM-rate discrimination

Multiple-hour training improved performance on the trained 150 Hz SAM-rate-discrimination condition. Figure 1(a) shows that the grand mean SAM-rate-discrimination threshold of the nine trained listeners decreased from 25 to 12 Hz between the pre- and post-tests (filled squares), and from 22 to 13 Hz between the first and last training session (open squares). A one-way analysis of variance (ANOVA) with repeated measures on the mean thresholds of the individual listeners revealed significant changes in performance over sessions both with ($F_{7,56}=33.72$, $p<0.001$) and without ($F_{5,40}=32.97$, $p<0.001$) the pre- and post-test data, indicating learning. The post-test thresholds are consistent with previous reports of SAM-rate-discrimination thresholds at rates near 150 Hz using well-trained listeners [Formby (1985); Hanna (1992); Grant *et al.* (1998)]. All trained listeners reported using a pitch cue to perform the trained condition.

Consistent with the mean data, each individual listener learned on the trained condition during the training phase [Fig. 1(b)]. We completed a two-step process to determine whether an individual listener showed training-phase learning. First, for each listener, we performed a one-way ANOVA on the thresholds measured in each training session. Second, we fitted a regression line to the same data. If a listener showed a significant change in performance ($p<0.05$) across the training sessions according to the ANOVA, and if the regression line showed a significant negative slope ($p<0.05$), we said that listener had learned significantly on the trained condition during the training phase [Wright *et al.* (1997); Wright and Fitzgerald (2001)]. All nine trained listeners met these criteria.

B. Generalization of learning to untrained conditions

1. Mean performance

We examined the mean pre- and post-test data to determine whether the trained listeners generalized their training-phase learning on the trained condition to (1) the two untrained stimulus types, (2) the two untrained SAM rates, and (3) the untrained SAM-detection task. Because the six pre- and post-test conditions employed a variety of measurement scales and the rate-discrimination thresholds varied markedly across the different SAM rates, we normalized the raw thresholds for each listener on each condition by converting them to z scores [see also, Wright and Fitzgerald (2001)]. In

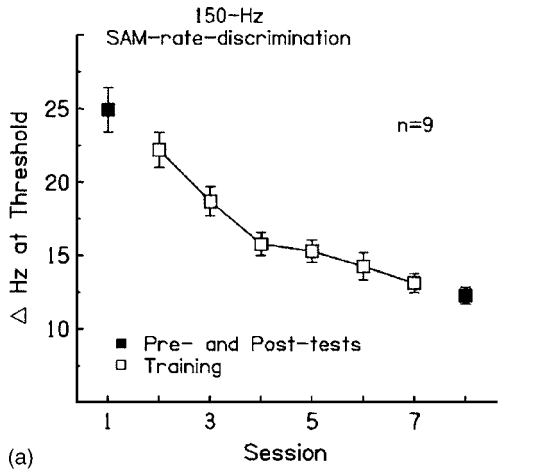

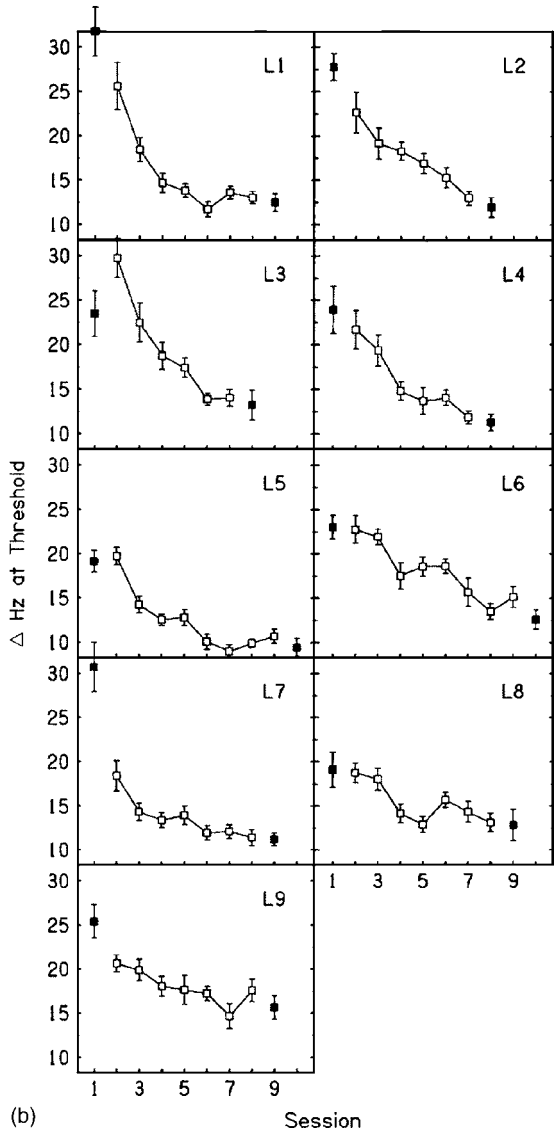

FIG. 1. *Learning on the trained 150 Hz SAM-rate-discrimination condition*. The group mean [panel (a)] and individual [panel (b)] thresholds of the nine trained listeners are shown for each testing session. Results are plotted separately for the pre- and post-tests (filled squares) and the training phase (open squares). The error bars indicate ± one standard error of the mean across listeners [panel (a)] or within listeners [panel (b)]. The threshold is the difference in SAM rate (in Hz) needed to discriminate a faster SAM rate from the standard 150 Hz SAM rate on 79% of trials. Note that the mean training-phase data include only the six days of training that all trained listeners completed, and that the ordinate differs slightly between panels (a) and (b).

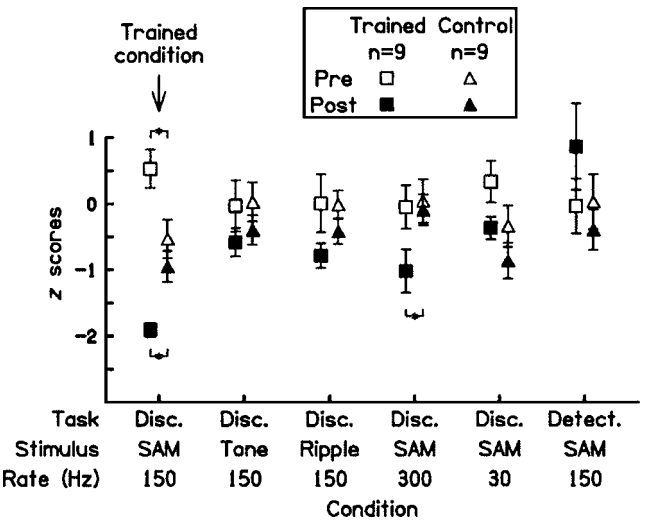

FIG. 2. *Generalization to untrained conditions*. Mean pre-test (open symbols) and post-test (filled symbols) z scores are shown for the nine trained (squares) and nine control (triangles) listeners in each of the six conditions. The error bars indicate ± one standard error of the mean across listeners. Asterisks and short horizontal brackets denote significant differences ($p < 0.05$) between the z scores of the trained and control listeners on the pre- or post-tests. The presence of these differences only for the trained and one untrained condition indicate that the training-induced learning of SAM-rate discrimination was largely specific to the trained SAM-rate-discrimination condition. In each condition, both the pre- and post-test z scores were computed from the mean and standard deviation of the pre-test thresholds of the trained and control listeners combined ($n=18$).

each condition, we combined the pre-test data from the trained and control listeners to calculate a mean threshold and standard deviation, and then used these values to compute the pre- and post-test z scores. Note that in all conditions, the more negative the z score, the lower the threshold, and thus, the better the performance on that condition. We analyzed the pre- and post-test z scores with a $2\times2\times6$ ANOVA on group (trained versus control), time (pre-versus post-test), and condition, with repeated measures on both time and condition. There was a significant main effect of time ($F_{1,16}=42.36$, $p<0.001$), a significant time × condition interaction ($F_{5,80}=9.59$, $p<0.001$), and a significant three-way interaction ($F_{5,80}=10.10$, $p<0.001$). We subsequently analyzed the three-way interaction with 2×2 ANOVAs on group and time (repeated on time) for each of the six conditions, and followed those analyses with t-tests, to assess generalization.

The training-phase learning did not generalize to the untrained stimulus types. On the pure-tone frequency-discrimination and rippled-noise-discrimination conditions, the trained (Fig. 2, squares) and control (triangles) listeners improved by the same amount between the pre- and post-tests (open and filled symbols, respectively). The 2×2 ANOVAs showed main effects of time for both conditions ($p=0.002$ in each case) but revealed no significant time × group interaction for either condition ($p\geqslant0.259$ in each case).

The training-phase learning generalized partially to the untrained 300 Hz rate, but not at all to the 30 Hz rate. On the SAM-rate-discrimination conditions, the control listeners learned at the 30 and 150 Hz rates. The trained listeners

learned more than controls at the trained 150 Hz rate as well as at the untrained 300 Hz rate, but not at the 30 Hz rate (Fig. 2). The 2×2 ANOVAs revealed main effects of time for all three rates ($p\leqslant0.012$ in each case) but showed significant time $\times$ group interactions only for the 150 Hz ($p<0.001$) and the 300 Hz ($p=0.047$) rates (30 Hz rate, $p=0.582$). Subsequent *t*-tests on these significant interactions revealed that the trained listeners improved between the pre- and post-tests on both the 150 and 300 Hz rates ($p\leqslant0.002$ in each case), while the controls showed nearly significant improvements only for the 150 Hz rate ($p=0.054$; 300 Hz, $p=0.681$). Further, the post-test z scores were significantly *lower* for the trained than the control listeners at the 150 Hz ($t_{16}=-3.68$, $p=0.002$) and 300 Hz ($t_{16}=-2.78$, $p=0.013$) rates, while the pre-test z scores were either similar between the groups (300 Hz rate; $p=0.85$) or significantly *higher* for the trained than the control listeners (150 Hz rate; $t_{16}=2.60$, $p=0.019$) (Fig. 2, short horizontal brackets and asterisks). Taken together, these results indicate that the control listeners learned at 30 and 150 Hz, but not at 300 Hz (see the main effect of time at 30 Hz, *t*-tests at 150 and 300 Hz). More notably, the trained listeners learned more than controls on the trained 150 Hz and untrained 300 Hz rates (significant 2×2 interactions and *t*-tests), but learned the same amount as controls on the untrained 30 Hz rate (significant effect for time, but no interaction). However, it appears that the trained listeners learned more at 150 than 300 Hz because the post-test thresholds of the trained listeners at 150 Hz were equivalent to those previously obtained from well-trained listeners near that rate [Formby (1985); Hanna (1992); Grant *et al.* (1998)], whereas at 300 Hz, the present thresholds were higher [Formby (1985); Grant *et al.* (1998)]. Thus, the trained listeners appear to have reached asymptotic performance at 150 Hz, but not at 300 Hz, suggesting that the generalization of their training-phase learning was incomplete.

Finally, the training-phase learning of SAM-rate-discrimination generalized negatively to the 150 Hz SAM-detection condition (Fig. 2). The 2×2 ANOVA on this condition only revealed a significant time $\times$ group interaction ($p=0.047$). Here, neither the pre- nor the post-test z scores differed significantly between the trained and control listeners. However, the post-test z scores of the trained listeners were almost significantly *higher* than their pre-test z scores ($t_8=-2.23$, $p=0.056$), while the control listeners scores did not differ between those two tests ($t_8=-1.65$, $p=0.137$). Thus, training on SAM-rate discrimination appeared to have actually impaired the ability to detect SAM at the trained rate.

2. Individual performance

We used linear regression to analyze the relationship between the individual raw pre- and post-test thresholds because this relationship is not illustrated in the mean z-score data [see also, Wright and Fitzgerald (2001)]. In each condition, we computed the linear regression of the post-test on the pre-test thresholds separately for the trained and control listeners, excluding data values for which the pre-test threshold was greater than two standard deviations from the mean of all listeners.

In all five discrimination conditions (Fig. 3, top five rows), listeners with the highest pre-test thresholds showed the most improvement. In these conditions, the data points of both the trained (left column) and control (right column) listeners were generally below the solid diagonal line, indicating that listeners improved between the pre- and post-tests. Regression lines fitted to these data points had slopes that were less than 1.0 (dashed lines), demonstrating that listeners with the worst initial thresholds improved the most. The performance of the trained listeners on the trained condition shows this pattern most dramatically (top left panel). The slope of that regression line was nearly flat (0.05), indicating that regardless of the pre-test value, the trained listeners all finished with a similar post-test value. In reasonable accord with the conclusion that learning was most marked on the trained condition, tests of the homogeneity of regression revealed significant differences in the regression-line slopes between trained and control listeners only in that condition (top row: $F_{1,14}=5.50$, $p=0.034$; all others $p>0.29$). Finally, consistent with the conclusion that learning generalized partially to the 300 Hz SAM rate (4th row), while the regression-line slopes did not differ significantly between the two groups on that condition ($p=0.29$), the y-intercepts of the regression lines clearly did.

Supporting the idea that listeners became worse at SAM detection after training on SAM-rate discrimination, six of the nine data points of the trained listeners were above the diagonal line in the SAM-detection condition, compared to only one of the nine points of the control listeners (Fig. 3, bottom row). The slope of the regression line for the trained listeners was 1.29, suggesting that the trained listeners with the highest pre-test thresholds showed the largest decrements in performance. It should be noted, however, that three of the listeners whose pre-test thresholds spanned the observed range all showed the same large decrement.

C. Preservation of learning

The trained listeners maintained their post-test performance on both the trained and untrained conditions for at least one month after training. Five of the nine trained listeners completed a second post-test one month after the original post-test. Figure 4 shows the z scores for the original (filled squares) and for the one-month (filled hourglasses) post-tests. A 2×6 ANOVA repeated on both time (original versus one-month post-test) and condition revealed a significant main effect of condition ($F_{5,20}=5.94$, $p=0.002$), but no main effect of time and no significant interaction. Thus, the pattern of learning and generalization did not change from the original to the one-month post-test.

IV. DISCUSSION

It is clear from the present results that listeners can improve their ability to discriminate SAM rate with multiple-hour practice. Given the inference that listeners used a pitch cue to make these discriminations, and the assumptions about the interpretation of the generalization of learning, the present results provide insight into the encoding of the pitch of SAM noise.

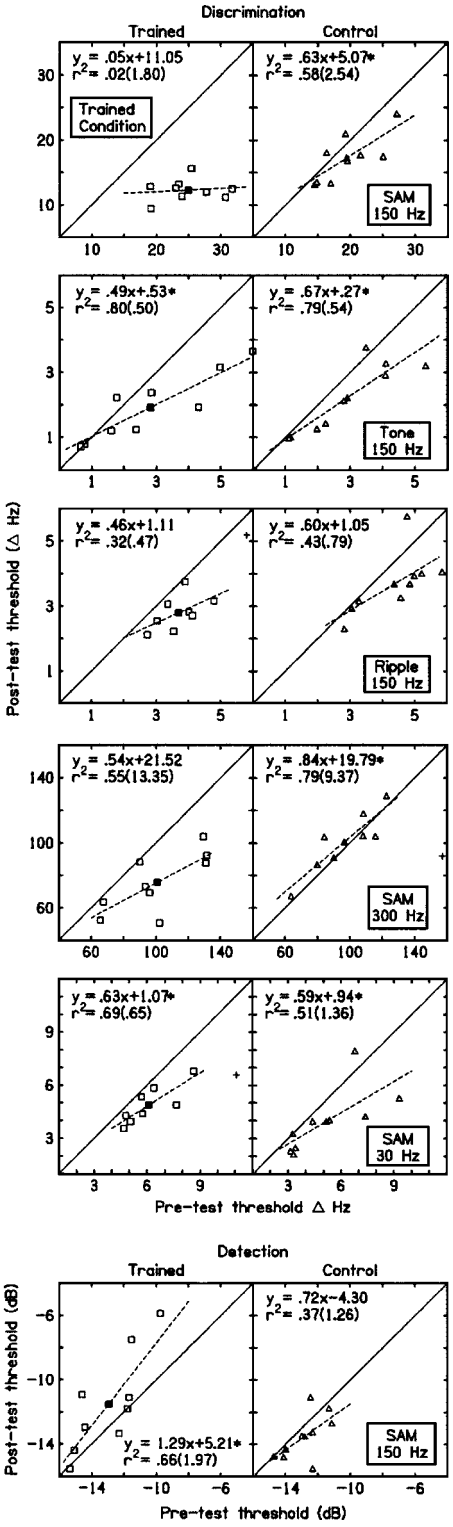

FIG. 3. *Relationship between individual pre- and post-test thresholds*. Pre-test (x axis) and post-test (y axis) thresholds are shown for the individual listeners (open symbols) and their group means (filled symbols) in each of the six conditions (rows). Thresholds are plotted separately for the nine trained (squares, left column) and nine control (triangles, right column) listeners. The linear regression of the post-test on the pre-test thresholds was determined for each data set (dashed lines), excluding values (plus signs) for which the pre-test threshold was more than two standard deviations above or below the mean of all listeners ($n=18$). Listed in each panel, are the regression equation, the r^2, and the standard error of the estimate (in parentheses). Asterisks indicate regression-line slopes that were significantly different from zero ($p<0.05$). The solid diagonal line in each panel indicates a regression-line slope of 1. Points beneath this line indicate improvement between the pre- and post-test.

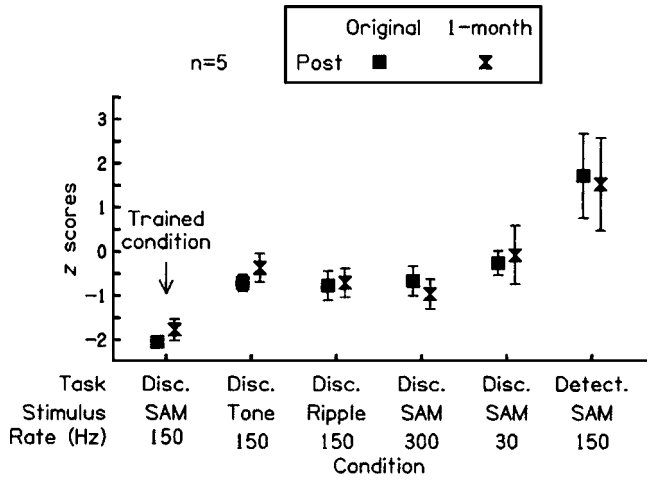

FIG. 4. *Retention of learning*. Mean post-test (squares) and one-month return post-test (hourglasses) z scores are shown for the trained listeners in each condition. Error bars indicate ± one standard error of the mean across listeners. Only the data of the five listeners who completed the one-month return post-test are included in this figure.

A. The pitches of SAM noise, pure tones and rippled noise

The lack of generalization to the discrimination of pure-tone frequency and rippled-noise delay time suggests that the mechanism affected by learning on SAM-rate discrimination is not involved in the processing of the pitches elicited by these other stimulus types. This result is in accord with the differences in stimulus cue, discrimination threshold, and physiological encoding that distinguish the pitch of SAM noise from that of pure tones and rippled noise (see Introduction). It also agrees with Grimault *et al.'s* (2003) report of no generalization of learning from pure-tone frequency discrimination to SAM-rate discrimination, and supports the view that their ambiguous results regarding generalization in the opposite direction, from SAM rate to pure-tone frequency, most likely reflect no generalization.

The present data are consistent with two trends suggesting that pitch-cue based discrimination learning induced by multiple-hour training typically affects processing specific to the trained stimulus type. First, pitch-cue discrimination learning often fails to generalize to untrained stimulus types. Learning generalized only partially or not at all: from a SAM noise to a pure tone or rippled noise (present results), from a pure tone to SAM noise [Grimault *et al.* (2003)] or an unresolved harmonic complex [Grimault *et al.* (2003)], from an unresolved to a resolved harmonic complex [Grimault *et al.* (2002)], and from a resolved harmonic complex to a pure tone [Demany and Semal (2002)] or unresolved harmonic complex [Grimault *et al.* (2002)]. Second, the learning rate differs for different stimulus types. Listeners reached asymptotic performance after approximately two hours of practice with unresolved harmonic complexes [Grimault *et al.* (2002)], four hours with pure tones [e.g., Campbell and Small (1963); Loeb and Holding (1975); Watson (1980); Irvine *et al.* (2000); Demany and Semal (2002)], six hours with SAM noise (present results) and more than ten hours with resolved harmonic complexes [Demany and Semal (2002); Grimault *et al.* (2002)]. There are, however, excep-

tions to these trends illustrating that multiple-hour training on pitch-cue discrimination can affect processing common to different stimulus types. These cases include the generalization of learning from a SAM noise to both resolved and unresolved harmonic complexes [Grimault *et al.* (2003)], from a pure tone to a resolved harmonic complex [Grimault *et al.* (2003)], and perhaps from a SAM noise to a pure tone (ambiguous, see preceding paragraph).

B. Different SAM rates

The current observation that learning on SAM-rate discrimination generalized only partially to one untrained rate, and not at all to another, suggests that the mechanism affected by this learning is tuned, albeit perhaps broadly, to particular modulation rates. This outcome is in agreement with the previous evidence for rate-specific processing of amplitude modulation including the rate-specific masking and adaptation of modulation, the different percepts associated with different rates, the predictive power of a rate-specific psychophysical model, and the separation of the neurological representations of different modulation rates (see Introduction). That there was some generalization to the untrained 300 Hz rate, but none to the 30 Hz rate, may indicate that the clearest separation of processing of different rates is between those that do (300 Hz) and those that do not (30 Hz) elicit pitch. This scenario could also account for the brief statement by Grimault *et al.* (2003) that rate-discrimination learning generalized between 88 and 250 Hz, because both of those rates were within the pitch range.

Taken together with data from other perceptual-learning experiments, it appears that multiple-hour training on stimulus discrimination based on pitch cues affects mechanisms that process different pitch values separately for some stimulus types, but not others. For both pure tones and SAM noises, learning generalized only partially, or not at all, from trained to untrained pitch values, suggesting that different pitch values are processed separately for these stimulus types [Wright (1998); Irvine *et al.* (2000); Demany and Semal (2002); present data]. In contrast, learning generalized to untrained pitch values for both resolved and unresolved harmonic complexes [Grimault *et al.* (2002)], implying common processing of multiple pitch values within these two stimulus types. However, in these cases, the generalization may have resulted from procedural learning [Grimault *et al.* (2002)]. Given the current evidence, it seems that future experiments on perceptual learning of pitch-cue discrimination are more likely to reveal specificity to the trained stimulus type than to the trained pitch value.

C. SAM-rate discrimination and SAM detection

The decrease in the ability to detect SAM following training on SAM-rate discrimination most likely indicates that the mechanism modified by learning was separate from that ideally used for SAM detection. According to this idea, a mechanism specialized for SAM detection precedes a separate mechanism that is specialized for SAM-rate discrimination, but can also be used, sub-optimally, for detection. This scenario is consistent with the evidence for both separate and shared processing for these two abilities described in the Introduction. That the ability of listeners to detect modulation affects their ability to discriminate modulation rate [Burns and Viemeister (1976); Patterson *et al.* (1978); Formby (1985); Grant *et al.* (1998)], but does not predict SAM-rate discrimination thresholds in individual listeners [Grant *et al.* (1998)] supports the idea of separate, serial, mechanisms for detection and rate discrimination. That greater modulation depths are required to discriminate SAM rate than to detect the SAM itself [Burns and Viemeister (1976); Patterson and Johnson-Davies (1977)] suggests that a rate-discrimination mechanism could be used suboptimally for modulation detection. By this account, the six of nine trained listeners who became worse at detecting SAM after learning to discriminate between different SAM rates (Fig. 3) did so because they had become accustomed to monitoring the rate-discrimination mechanism, and so presumably adopted a suboptimal pitch cue, provided by that mechanism, to perform the SAM-detection condition on the post-test.

A less likely explanation for the decrement in SAM-detection performance is that it resulted from adaptation to modulation [e.g., Tansley and Suffield (1983); Richards *et al.* (1997); Sheft (2000); Wojtczak and Viemeister (2003)] induced by the exposure to modulation in the SAM-rate-discrimination conditions. According to this idea, the 6–8 h of exposure to 100% modulation at 150 Hz during the training on SAM-rate discrimination led to a reduction in the perceived depth of the modulation in that stimulus. This reduction, in turn, made that modulation more difficult to detect. This explanation is consistent with the observation that the decrement in modulation-detection performance occurred in many more trained listeners, who had received multiple-hour exposure to modulation, than in controls, who had not received this extensive exposure. The strongest argument against this proposal is that the effects of adaptation only appear to last for approximately one minute after the end of the adapting stimulus [Tansley and Suffield (1983)]. Thus, even taking into account the longer total exposure time to the adapting stimulus in the present experiment, the adaptation would have to have lasted for at least 24 h (time from the last training session to the post-test) and in some instances for one month (time between the original and one-month post-tests) after the end of the training exposure to account for the decrements in SAM-detection performance seen on the original and one-month post-tests here.

Finally, it is worth noting that the decrement in SAM-detection performance associated with training on SAM-rate discrimination appears to be temporary. Listeners L2 and L5 returned to complete the same post-test 15 months after the original post-test. Both listeners displayed decrements in performance between the pre- and the original post-test on the SAM-detection condition (decrements of 3.9 and 1.4 dB, respectively). In contrast, their thresholds were nearly identical on the pre- and the 15 month post-test on the SAM-detection condition (differences of 0.1 and 0.2 dB, respectively). This return to initial performance could be accounted for by either proposed explanation. Listeners may revert to their original listening strategy in the detection task after long periods without practice on rate discrimination. Alternatively, even

long-lasting effects of adaptation could fail to extend over many months. Contrasting the temporary influence of SAM-rate-discrimination training on SAM-detection performance, these same two listeners, on average, preserved 9 Hz of their original 13 Hz improvement at the 15 month post-test on the trained SAM-rate-discrimination condition, indicating that training yields long lasting learning on SAM-rate discrimination.

ACKNOWLEDGMENTS

We thank Dr. Stan Sheft for his helpful advice. We also thank Karen Banai, Tessa Bent, Julia Huyck, Julia Mossbridge, Jeanette Ortiz, Yuxuan Zhang, associate editor Neal Viemeister and two anonymous reviewers for providing helpful comments on earlier drafts of this paper. This work was supported by the National Institutes of Health/National Institute for Deafness and Other Communication Disorders (F31-DC05093-01 awarded to M.B.F.; R29-DC02997 and R01 DC04453 awarded to B.A.W.) and by Northwestern University (Graduate Research Grant awarded to M.B.F.).

Bacon, S. P., and Grantham, D. W. (**1989**). "Modulation masking patterns: Effects of modulation frequency, depth, and phase," J. Acoust. Soc. Am. **85**, 2575–2580.

Bilsen, F. A. (**1966**). "Repetition pitch: Monaural interaction of a sound with the repetition of the same, but phase shifted, sound," Acustica **17**, 295–300.

Bilsen, F. A., and Ritsma, R. J. (**1969/70**). "Repetition pitch and its implication for hearing theory," Acustica **22**, 63–73.

Burns, E. M., and Viemeister, N. F. (**1976**). "Nonspectral pitch," J. Acoust. Soc. Am. **60**, 863–869.

Burns, E. M., and Viemeister, N. F. (**1981**). "Played-again SAM: Further observations on the pitch of amplitude-modulated noise," J. Acoust. Soc. Am. **70**, 1655–1659.

Campbell, R. A., and Small, A. M. (**1963**). "Effect of practice and feedback on frequency discrimination," J. Acoust. Soc. Am. **35**, 1511–1514.

Cohen, M. A., Grossberg, S., and Wyse, L. L. (**1995**). "A spectral network model of pitch perception," J. Acoust. Soc. Am. **98**, 862–879.

Dau, T., Kollmeier, B., and Kohlrausch, A. (**1997a**). "Modeling auditory processing of amplitude modulation. I. Detection and masking with narrow-band carriers," J. Acoust. Soc. Am. **102**, 2892–2905.

Dau, T., Kollmeier, B., and Kohlrausch, A. (**1997b**). "Modeling auditory processing of amplitude modulation. II. Spectral and temporal integration," J. Acoust. Soc. Am. **102**, 2905–2919.

Demany. L., and Semal, C. (**2002**). "Learning to perceive pitch differences," J. Acoust. Soc. Am. **111**, 1377–1387.

Eggermont, J. J. (**1994**). "Temporal modulation transfer functions for AM and FM stimuli in cat auditory cortex. Effects of carrier type, modulating waveform, and intensity," Hear. Res. **74**, 51–66.

Ewert, S. D., and Dau, T. (**2000**). "Characterizing frequency selectivity for envelope fluctuations," J. Acoust. Soc. Am. **108**, 1181–1196.

Fastl, H. (**1977**). "Roughness and temporal masking patterns of sinusoidally amplitude modulated broadband noise," in *Psychophysics and Physiology of Hearing*, edited by E. F. Evans and J. P. Wilson (Academic, London), pp. 403–414.

Fastl, H., and Stoll, G. (**1979**). "Scaling of pitch strength," Hear. Res. **1**, 293–301.

Formby, C. (**1985**). "Differential sensitivity to tonal frequency and to the rate of amplitude modulation of broadband noise by normally hearing listeners," J. Acoust. Soc. Am. **78**, 70–77.

Frisina, R. D., Smith, R. L., and Chamberlain, S. C. (**1990**). "Encoding of amplitude modulation in the gerbil cochlear nucleus: I. A hierarchy of enhancement," Hear. Res. **44**, 99–122.

Giraud, A. L., Lorenzi, C., Ashburner, J., Wable, J., Johnsrude, I., Frackowiak, R., and Kleinshmidt, A. (**2000**). "Representation of the temporal envelope of sounds in the human brain," J. Neurophysiol. **84**, 1588–1598.

Grant, K. W., Summers, V., and Leek, M. R. (**1998**). "Modulation rate detection and discrimination by normal-hearing and hearing-impaired listeners," J. Acoust. Soc. Am. **104**, 1051–1060.

Greenberg, S., and Rhode, W. S. (**1987**). "Periodicity coding in cochlear nerve and ventral cochlear nucleus," in *Auditory Processing of Complex Sounds*, edited by W. A. Yost and C. S. Watson (Erlbaum, Hillsdale, NJ), pp. 225–236.

Grimault, N., Micheyl, C., Carlyon, R. P., and Collet, L. (**2002**). "Evidence for two pitch encoding mechanisms using a selective auditory training paradigm," Percept. Psychophys. **64**, 189–197.

Grimault, N., Micheyl, C., Carlyon, R. P., Bacon, S. P., and Collet, L. (**2003**). "Learning in discrimination of frequency or modulation rate: generalization to fundamental frequency discrimination," Hear. Res. **184**, 41–50.

Hall, J. W. III., Buss, E., and Grose, J. H. (**2003**). "Modulation-rate discrimination for unresolved components: Temporal cues related to fine structure and envelope," J. Acoust. Soc. Am. **113**, 986–993.

Hanna, T. E. (**1992**). "Discrimination and identification of modulation rate using a noise carrier," J. Acoust. Soc. Am. **91**, 2122–2128.

Houtgast, T. (**1989**). "Frequency selectivity in amplitude-modulation detection," J. Acoust. Soc. Am. **85**, 1676–1680.

Irvine, D. R. F., Martin, R., Klimkeit, E., and Smith, R. (**2000**). "Specificity of perceptual learning in a frequency-discrimination task," J. Acoust. Soc. Am. **108**, 2964–2968.

Joris, P. X., Schreiner, C. E., and Rees, A. (**2004**). "Neural processing of amplitude-modulated sounds," Physiol. Rev. **84**, 541–577.

Langner, G., and Schreiner, C. E. (**1988**). "Periodicity coding in the inferior colliculus of the cat. I. Neuronal mechanisms," J. Neurophysiol. **60**, 1799–1822.

Langner, G., Sams, M., Heil, P., and Schulze, H. (**1997**). "Frequency and periodicity are represented in orthogonal maps in the human auditory cortex: evidence from magnetoencephalography," J. Comp. Physiol. **181**, 665–676.

Levitt, H. (**1971**). "Transformed up-down procedures in psychoacoustics," J. Acoust. Soc. Am. **49**, 467–477.

Loeb, M., and Holding, D. H. (**1975**). "Backward interference by tones or noise in pitch perception as a function of practice," Percept. Psychophys. **18**, 205–208.

Meddis, R., and Hewitt, M. J. (**1991a**). "Virtual pitch and phase sensitivity of a computer model of the auditory periphery. I: Pitch identification," J. Acoust. Soc. Am. **89**, 2866–2882.

Meddis, R., and Hewitt, M. J. (**1991b**). "Virtual pitch and phase sensitivity of a computer model of the auditory periphery. II: Phase sensitivity," J. Acoust. Soc. Am. **89**, 2883–2894.

Meddis, R., and O'Mard, L. (**1997**). "A unitary model of pitch perception," J. Acoust. Soc. Am. **102**, 1811–1820.

Miller, G. A., and Taylor, W. G. (**1948**). "The perception of repeated bursts of noise," J. Acoust. Soc. Am. **20**, 171–182.

Moller, A. R. (**1974**). "Responses of units in the cochlear nucleus to sinusoidally amplitude modulated tones," Exp. Neurol., **45**, 104–117.

Moore, B. C. J. (**1997**). "Pitch perception," in *An Introduction to the Psychology of Hearing* (Academic, London), pp. 177–212.

Patterson, R. D., and Johnson-Davies, D. (**1977**). "Detection of a change in the pitch of AM noise," in *Psychophysics and Physiology of Hearing*, edited by E. F. Evans and J. P. Wilson (Academic, London), pp. 363–371.

Patterson, R. D., Johnson-Davies, D., and Milroy, R. (**1978**). "Amplitude-modulated noise: The detection of modulation versus the detection of modulation rate," J. Acoust. Soc. Am. **63**, 1904–1911.

Patterson, R. D. Handel, S. Yost, W. A., and Datta, A. J. (**1996**). "The relative strength of the tone and noise components in iterated rippled noise," J. Acoust. Soc. Am. **100**, 3286–3294.

Pollack, J. (**1969**). "Periodicity pitch for interrupted white noise-fact or artifact?" J. Acoust. Soc. Am. **45**, 237–238.

Raatgever, J., and Bilsen, F. A. (**1992**). "The pitch of anharmonic comb filtered noise reconsidered," in *Auditory Physiology and Perception*, edited by Y. Cazals, L. Demany, and K. Horner (Pergamon, Oxford), pp. 215–222.

Richards, V. M., Buss, E., and Tian, L. (**1997**). "Effects of modulator phase for comodulation masking release and modulation detection interference," J. Acoust. Soc. Am. **102**, 468–476.

Schreiner, C. E., and Langner, G. (**1988**). "Periodicity coding in the inferior colliculus of the cat. II. Topographical organization," J. Neurophysiol. **60**, 1823–1840.

Schreiner, C. E., and Urbas, J. V. (**1988**). "Representation of amplitude modulation in the auditory cortex of the cat. II. Comparison between cortical fields," Hear. Res. **32**, 49–63.

Schulze, H., and Langner, G. (**1997**). "Periodicity coding in the primary auditory cortex of the Mongolian gerbil: Two different coding strategies for pitch and rhythm?" J. Comp. Physiol., A **181**, 651–663.
Schulze, H., and Scheich, H. (**1999**). "Discrimination learning of amplitude modulated tones in Mongolian gerbils," Neurosci. Lett. **261**, 13–16.
Sheft, S. (2000). "Adaptation to amplitude modulation," *Parmly Annual Report.* 29–32.
Shofner, W. P. (**1991**). "Temporal representation of rippled noise in the anteroventral cochlear nucleus of the chinchilla," J. Acoust. Soc. Am. **90**, 2450–2466.
Shofner, W. P. (**1999**). "Responses of cochlear nucleus units in the chinchilla to iterated rippled noises: Quantitative analysis of neural autocorrelograms of primarylike and chopper units," J. Neurophysiol. **81**, 2662–2674.
Small, A. M. (**1955**). "Some parameters influencing the pitch of amplitude modulated signals," J. Acoust. Soc. Am. **27**, 751–760.
Strickland, E. A., and Viemeister, N. F. (**1996**). "Cues for discrimination of envelopes," J. Acoust. Soc. Am. **99**, 3638–3646.
Tansley, B. W., and Suffield, J. B. (**1983**). "Time course of adaptation and recovery of channels selectively sensitive to frequency and amplitude modulation," J. Acoust. Soc. Am. **74**, 765–775.
Terhardt, E. (**1974**). "On the perception of periodic sound fluctuations," Acustica **30**, 201–213.
Viemeister, N. F. (**1979**). "Temporal modulation transfer functions based upon modulation thresholds," J. Acoust. Soc. Am. **66**, 1364–1380.
Watson, C. S. (**1980**). "Time course of auditory perceptual learning," Ann. Otol. Rhinol. Laryngol. **89**, Suppl. 74, 96–102.
Wiegrebe, L., and Winter, I. M. (**2001**). "Temporal representation of iterated rippled noise as a function of delay and sound level in the ventral cochlear nucleus," J. Neurophysiol. **85**, 1206–1219.
Wiegrebe, L., and Meddis, R. (**2004**). "The representation of periodic sounds in simulated sustained chopper units of the ventral cochlear nucleus," J. Acoust. Soc. Am. **115**, 1207–1218.
Winter, I. M., Wiegrebe, L., and Patterson, R. D. (**2001**). "The temporal representation of the delay of iterated rippled noise in the ventral cochlear nucleus of the guinea pig," J. Physiol. **537**, 553–566.
Wojtczak, M., and Viemeister, N. F. (**2003**). "Suprathreshold effects of adaptation produced by amplitude modulation," J. Acoust. Soc. Am. **114**, 991–997.
Wright, B. A. (**1998**). "Generalization of auditory-discrimination learning." Assoc. Res. Otolaryngol. Abs., Abs. 413, **21**, 104.
Wright, B. A., and Dai, H. (**1998**). "Detection of sinusoidal amplitude modulation at unexpected rates," J. Acoust. Soc. Am. **104**, 2991–2996.
Wright, B. A., and Fitzgerald, M. B. (**2001**). "Different patterns of human discrimination learning for two interaural cues to sound-source location," Proc. Natl. Acad. Sci. U.S.A. **98**, 12307–12312.
Wright, B. A., Buonomano, D. V., Mahncke, H. W., and Merzenich, M. M. (**1997**). "Learning and generalization of auditory temporal-interval discrimination learning in humans," J. Neurosci. **17**, 3956–3963.
Yost, W. A., Hill, R., and Perez-Falcon, T. (**1978**). "Pitch and pitch discrimination of broadband signals with rippled power spectra," J. Acoust. Soc. Am. **63**, 1166–1173.
Yost, W. A., and Sheft, S. (**1989**). "Across-critical-band processing of amplitude-modulated tones," J. Acoust. Soc. Am. **85**, 848–857.
Yost, W. A., Sheft, S., and Opie, J. (**1989**). "Modulation interference in detection and discrimination of amplitude modulation," J. Acoust. Soc. Am. **86**, 2138–2147.
Yost, W. A., Patterson, R., and Sheft, S. (**1998**). "The role of the envelope in processing iterated rippled noise," J. Acoust. Soc. Am. **104**, 2349–2361.

The advantage of knowing where to listen[a)]

Gerald Kidd, Jr.,[b)] Tanya L. Arbogast, Christine R. Mason, and Frederick J. Gallun
Department of Speech, Language and Hearing Sciences and Hearing Research Center, Boston University, 635 Commonwealth Avenue, Boston, Massachusetts 02215

(Received 31 May 2005; revised 9 September 2005; accepted 12 September 2005)

This study examined the role of focused attention along the spatial (azimuthal) dimension in a highly uncertain multitalker listening situation. The task of the listener was to identify key words from a target talker in the presence of two other talkers simultaneously uttering similar sentences. When the listener had no *a priori* knowledge about target location, or which of the three sentences was the target sentence, performance was relatively poor—near the value expected simply from choosing to focus attention on only one of the three locations. When the target sentence was cued before the trial, but location was uncertain, performance improved significantly relative to the uncued case. When spatial location information was provided before the trial, performance improved significantly for both cued and uncued conditions. If the location of the target was certain, proportion correct identification performance was higher than 0.9 independent of whether the target was cued beforehand. In contrast to studies in which known versus unknown spatial locations were compared for relatively simple stimuli and tasks, the results of the current experiments suggest that the focus of attention along the spatial dimension can play a very significant role in solving the "cocktail party" problem. © *2005 Acoustical Society of America.* [DOI: 10.1121/1.2109187]

PACS number(s): 43.66.Lj, 43.66.Dc, 43.66.Pn [AJO] Pages: 3804–3815

I. INTRODUCTION

There are many factors that can interfere with a listener attempting to comprehend the speech of one particular talker in the presence of competing talkers. The speech of the target talker can be masked by other sounds, obscuring portions of the message, leaving it so incomplete as to be meaningless or misunderstood. The target speech stream can be embedded in other speech streams to the point where the listener is unable to segregate it from the others and cannot connect the elements of the target message that belong together. The listener can be uncertain or confused about which talker to attend to and thereby direct attention to the wrong source of speech. There are other acoustic and perceptual factors that come into play as well. The target speech, competing speech, and other sounds usually reflect off of the various surfaces of the sound field, creating echoes that arrive at the ears delayed in time and from various directions and that interact with the direct sources of sound. Also, there is the normal, fundamental use of the sense of hearing to continually monitor the auditory scene for important changes and rapidly evaluate them when they occur, potentially interrupting and diverting processing resources away from the target. Despite the daunting complexity of this task, humans are normally quite successful at selecting and comprehending the speech of one talker among many talkers or other distracting and competing sources of sound. However, this complexity—comprised of acoustic, perceptual, and cognitive factors—makes it extremely difficult to completely describe the processes involved and how they interact. Despite the fact that this capability has been studied extensively since Cherry (1953) published his famous article describing the "cocktail party problem" (for recent reviews see Yost, 1997; Bronkhorst, 2000; and Ebata, 2003), a number of important questions remain.

Among the questions about the cocktail party problem for which we are lacking a satisfactory answer is that of the importance of the ability to focus attention at a point along the spatial dimension.[1] Clearly, attention must be focused on the target source of speech if it is to be fully understood, but there are many ways to segregate the target speech stream from other sounds and the importance of the focus of attention along the spatial dimension, *per se*, is not well understood. Scharf (1998), for example, in his review of attention in the auditory modality, notes that most of the evidence regarding the role of spatial focus of attention does not indicate large effects. Generally, cuing uncertain locations results in relatively small improvements in response time and, in some cases, in accuracy (e.g., Spence and Driver, 1994; Mondor and Zattore, 1995; Mondor *et al.*, 1998; Sach *et al.*, 2000; Woods *et al.*, 2001). However, very little of this work has used speech as the stimulus. The question addressed in the current study is: if the speech of the target talker is not appreciably masked by competing sounds, and the sounds and their sources are easily segregated into distinct auditory objects, what is the benefit of directing attention toward the target source?

Determining the role of focused attention in the spatial dimension is closely related to understanding how binaural information is processed in the auditory system. There is an extensive and compelling body of evidence in support of the important role that binaural cues provide in hearing out a target source among masking sources. However, binaural

[a)]Portions of this work were presented at the 149th meeting of the Acoustical of America in Vancouver, BC, Canada, May 2005.
[b)]Electronic mail: gkidd@bu.edu

cues may be used in different ways at different stages of processing in the auditory system to produce a selective listening advantage. The most extensively studied binaural cues improve the effective target-to-masker ratio (T/M) of the input from the auditory periphery to higher neural levels. These include the "better-ear advantage" in which the spatial separation of target and masker improves the acoustical T/M in one ear relative to the case in which target and masker emanate from the same location. Spatial separation of sources also causes interaural differences which are processed by neurons in the binaural portions of the ascending auditory pathway to improve the effective T/M of the stimulus (cf. Durlach, 1972; Colburn, 1996; Colburn and Durlach, 1978). Binaural interaction is usually thought of as occurring automatically (i.e., not under voluntary control) according to the stimulus-driven properties of these neurons. The maximum advantage of spatial separation of a speech target and a speech-shaped noise masker in a sound field is about 8–10 dB (larger advantages may be obtained for sources very near the listener, e.g., Shinn-Cunningham *et al.*, 2001) and is roughly equally attributable to contributions of the better-ear advantage and binaural interaction (Zurek, 1993; see also Plomp, 1976; Bronkhorst and Plomp, 1988; Culling *et al.*, 2004).

When a speech target is masked by a noise, better-ear listening and binaural interaction may almost completely account for the advantage afforded the listener by spatial separation of sound sources. However, when the target is the speech of one talker and the masker is the speech of another talker(s), the problem is more complex and other factors must be considered. First of all, perceptual segregation of a human voice from a Gaussian noise is a trivial problem—they differ in nearly every important way that might cause them to be erroneously grouped together. Normally, a listener has little difficulty distinguishing which object is noise and which is speech and focusing attention on one or the other is a simple matter. When the masker is another speech source, however, the segregation task *may* be simple, but then again it may not be, depending on how different the two talkers are with respect to segregation cues such as fundamental frequency, intonation patterns, envelope coherence across frequency, timbre, etc. In such cases, segregating and directing attention to the correct source may be difficult indeed. Furthermore, similar voices are easily confused and lead to errors in speech recognition even for clearly segregated sources particularly when the listener is uncertain about which source is the target (e.g., Brungart *et al.*, 2001; Arbogast *et al.*, 2002). In selective listening tasks involving multiple talkers, it is often unclear whether the interference observed in target speech recognition is a result of masking, failure to segregate the target, confusion and misdirected attention, or some combination of factors.

In attempting to determine the role played by selective attention, manipulating the expectation of the observer is often key. Greenberg and Larkin (1968) demonstrated that listeners exhibit a high degree of selectivity in the frequency domain using the "probe-signal" method in which the signal (target) frequency had a much higher likelihood of occurrence than several surrounding probe frequencies. Although both target and probe tones were equally detectable when presented alone, detectability was higher in the mixed case for the more likely target tone than for the less likely probe tones, with performance (as a function of frequency) resembling the attenuation characteristics of a bandpass filter. Since the initial report by Greenberg and Larkin (1968), the technique has been used by many other investigators to demonstrate attentional tuning in frequency (e.g., MacMillan and Schwartz, 1975; Scharf *et al.*, 1987; Schlauch and Hafter, 1991; Green and McKeown, 2001); time (Wright and Dai, 1994); spectral shape (Hill *et al.*, 1998); and modulation frequency (Wright and Dai, 1998).

Arbogast and Kidd (2000) found evidence for "tuning" in spatial azimuth for both accuracy and response time measures in a probe-signal frequency pattern identification task, but the effects were relatively small and occurred when the acoustic environment was very complex and uncertain. In fact, most of the recent work on spatial attention has used simple stimuli and tasks such as detection of the presence of a tone in quiet or in noise and thus does not bear a close correspondence to the complex multitalker problem posed early on by Cherry (1953).

Erickson *et al.* (2004) compared speech identification performance for conditions in which the location (simulated under headphones using head-related transfer functions, HRTFs) of a target talker was chosen at random from among four possible locations to conditions in which the location of the talker was held constant. They measured identification performance for a target talker in the presence of one to three other talkers uttering similarly constructed sentences. For a known target talker (same voice across trials in a block of trials), the performance advantage obtained by providing a fixed location was significant when either two or three competing talkers were present. The size of the advantage was nearly 20 percentage points for the two-masker condition. Recently, Brungart and Simpson (2005) extended these findings to conditions where target location changed probabilistically across trials within a run. As the probability of a location transition increased, speech identification performance decreased.

The results of the Erickson *et al.* (2004) and Brungart and Simpson (2005) studies suggest that attending to a particular location along the spatial dimension, at least when the listener knows the talker and/or has *a priori* knowledge about the target sentence, can provide a significant advantage in recognizing the speech of a target talker in the presence of competing talkers. This effect appears to be principally due to directed attention rather than a "better ear" advantage or binaural analysis. An important factor in the Erickson *et al.* and Brungart and Simpson studies, as well as the Arbogast and Kidd (2000) study mentioned earlier, was the presence of a high degree of uncertainty. Perhaps the role of spatial focus of attention is revealed more readily when the listening task is very demanding and produces a heavy processing load on the observer.

The present study is similar to that discussed above by Erickson *et al.* (2004) but also has some important methodological differences. First, a condition was tested in which there was no *a priori* knowledge provided to the listener

(within the context of the range of uncertainty in the experiment) about the target. In that condition, the callsign that identifies the target sentence was only provided after the stimulus. This manipulation was intended to produce a very high load on both the attention and the memory of the listener and is essentially a divided attention task. Second, uncertainty about target location was varied probabilistically over a range of values in order to produce a function relating performance to degree of uncertainty.

II. METHODS

A. Listeners

The listeners were four normal-hearing college students ranging in age from 19 to 22 years. Listeners were paid for their participation.

B. Stimuli

The stimuli were sentences from the Coordinate Response Measure (CRM) corpus (Bolia *et al.*, 2000). The four male talkers were used. Sentences have the format: "Ready [callsign] go to [color] [number] now." For each talker, the corpus contains sentences with all possible combinations of eight callsigns, four colors, and eight numbers.

C. Procedures

The data were collected in a 12×13 ft soundfield enclosed by a single-walled IAC booth. The walls and ceiling were perforated metal panels and the floor was carpeted. The acoustic characteristics of this room are described in Kidd *et al.* (2005; room condition "BARE"). The stimuli were presented via three Acoustic Research 215PS loudspeakers located 5 ft. from the listener and positioned at 0° and ±60° where 0° is directly in front of the listener and +60° is to the listener's right. The height of the loudspeakers was approximately the same as the height of the listener's head when seated. These loudspeakers were calibrated and matched in terms of overall level at the location of the listener's head. Each sentence was played through a separate channel of Tucker-Davis Technologies hardware. Sentences were converted at a rate of 40 kHz by a 16-bit, eight-channel D/A converter (DA8), low-pass filtered at 20 kHz (FT6), attenuated (PA4), and passed through power amplifiers (Tascam) that were connected to the three loudspeakers.

On each trial, three sentences were presented simultaneously, one to each of the three loudspeakers. Each sentence was played at 60 dB SPL. The three sentences were randomly chosen on each trial with the requirement that the talkers, callsigns, colors, and numbers of the three sentences were all mutually exclusive. One sentence of the three was randomly designated as the target sentence by providing the listener with its callsign while the other two were considered maskers. The listener's task was to identify the color and number from the target sentence in a 4×8-alternative forced-choice procedure. A handheld keypad/LCD display (Q-term) was used to relay messages to the listener in the booth and to register the listener's responses. A warning on the Q-term display preceded each trial. Data were collected in blocks of 30 trials each. At the end of each block percent correct feedback was provided for that block. Listeners participated in the experiment in sessions of $1\frac{1}{2}$ to 2 h each, including several breaks. The listeners' heads were not restrained, but they were instructed to face directly ahead (0° azimuth) during stimulus presentation.

There were two main variables in the experiment. First, the callsign indicating the target sentence could be provided to the listener (by visual display on the Q-term) either a minimum of 1 s before ("callsign before") or immediately after ("callsign after") stimulus presentation. In both cases the callsign display remained on the screen until after the listener's response was recorded and response feedback was provided. Second, the *a priori* probabilities associated with target occurrence at each location were varied. When one loudspeaker was more likely to be the source of the target the probabilities tested were 1, 0.8, and 0.6 and the probabilities assigned to both of the other two loudspeakers were 0, 0.1, and 0.2, respectively. Each callsign by probability condition was tested separately for each of the three locations. There was also a condition in which the target source was equally likely among all three locations (i.e., $p=\frac{1}{3}$) that is referred to as "random." The probabilities assigned the three locations were held constant across a block of 30 trials. The listener was reminded of the probabilities associated with each location at the start of every trial. The warning message that preceded each stimulus presentation indicated the expected percentage of trials for which the signal sentence would be presented from each location. For example, "80-10-10" indicated that the target sentence would be expected to be played from −60° approximately 80% of the time and from the 0° and +60° locations approximately 10% of the time each for that block of trials. The sampling that determined target location on any given trial was with replacement so that the actual frequency of occurrence varied.

The combination of these variables yielded 24 conditions (2 callsigns $\times$ 3 locations $\times$ 4 probabilities). Data were collected in two-block pairs of the same condition. After every pair of blocks the callsign condition (callsign before or callsign after) was changed with the initial callsign condition chosen randomly for each listener. For every two blocks of data for a given callsign before or callsign after condition, the probability/location condition was chosen randomly without replacement from among the 12 possible conditions available (3 locations $\times$ 4 probabilities). A minimum of 16 blocks (480 trials) were collected for each callsign, location, and probability condition. In the random probability condition, because there was no location subcondition, three times as many blocks were collected for a minimum of 48 blocks (1440 trials) or the same number as in the other conditions when summed across location. Listeners were minimally trained in the task with a single block of 30 trials in which the target sentence was played alone at 0° azimuth.

III. RESULTS

A. Accuracy

Performance was specified as proportion correct identification where a response was counted correct only if both

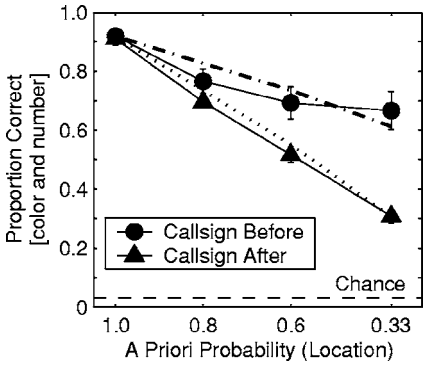

FIG. 1. Group mean proportion correct identification scores, and standard deviations of the means, plotted as a function of increasing uncertainty about target location (*a priori* probability of occurrence). The circles represent performance in the "callsign before" condition and triangles indicate performance in the "callsign after" condition (see text). The dashed line at the bottom represents chance performance. The lines near the data points indicate the performance predicted by a simple single-source listener strategy for callsign before (dash-dot) and callsign after (dot) conditions.

the color and number of the target sentence were identified. Chance performance was about 0.03 (1/32; 4 colors by 8 numbers). The four listeners were very similar in their performance, therefore the results are displayed as group means and standard deviations. Figure 1 shows proportion correct identification (symbols) as a function of the probability of occurrence of the target at a specific location for the callsign before (circles) and callsign after (triangles) conditions. For both callsign before and callsign after, performance declined as target location uncertainty increased. For the callsign after condition, performance decreased from a proportion correct of about 0.91 when the target location was certain (i.e., $p=1$) to about 0.31 when the target location was randomly chosen among the three locations. For callsign before, proportion correct identification performance was about the same as for callsign after when the location was certain (0.92) and decreased to about 0.67 when the location of the target was chosen at random. The dashed line at the bottom indicates chance performance and the other two lines with no symbols (dotted and dash-dot) will be discussed later.

In order to determine whether the trends apparent in Fig. 1 were statistically significant, the data were transformed into arcsine units and then submitted to a repeated-measures ANOVA with three within-subjects factors: callsign, location (−60°, 0°, +60°), and probability of occurrence at a given location. All three main factors were significant: callsign $[F(1,3)=59.3, p<0.01]$, location $[F(2,6)=75.5, p<0.001]$, and probability $[F(3,9)=998.1, p<0.001]$. In addition, the interaction of callsign and probability was significant $[F(3,9)=95.5, p<0.001]$ as were the interactions of location and probability $[F(6,18)=9.95, p<0.001]$ and callsign and location $[F(2,6)=6.2, p<0.05]$. The three-way interaction was not significant $[p>0.05]$.

Knowing the callsign in advance potentially allowed the listener to identify the target voice early in the stimulus and either find and focus on the location of the target talker or simply follow the voice of the target talker until the test items occurred, or both. However, it appears that knowing the callsign beforehand without knowledge about location was less useful as a cue than the converse. The proportion correct identification for the condition in which callsign was certain (callsign before) paired with uncertain location ($p=0.33$, random) was on average about 0.67 whereas the certain location condition ($p=1$) paired with uncertain callsign (callsign after) was about 0.91. When $p=1$ and the callsign was given in advance, no additional improvement was noted (0.92). The callsign-before random-location condition resulted in roughly the same performance as the callsign-after $p=0.8$ condition.

Not only are the main effects of callsign before versus after and of probability of occurrence apparent in Fig. 1, the significant interaction between the two factors is also obvious. There was essentially no difference between callsign after and callsign before at $p=1$, but the difference between the two increased systematically as uncertainty increased until, in the random condition, the proportion correct in the callsign before condition was about 0.36 higher than in the callsign after condition. The main effect of location noted above was significant because, overall, presenting the target from the location of +60° (to the right) resulted in a higher proportion correct (0.76) than for the locations of −60° (0.65) or 0° (0.66). However, as the significant interaction between location and probability of occurrence indicates, the effect of location also depended on uncertainty and was mainly due to the random condition. This effect may be seen in Fig. 2, which displays proportion correct identification as a function of the target location uncertainty. The circles are

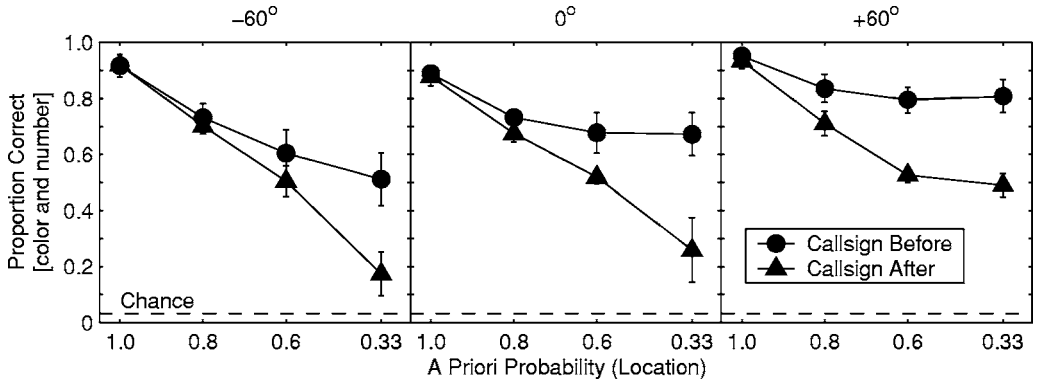

FIG. 2. Group mean proportion correct identification scores, and standard deviations of the means, subdivided according to the location from which the target was presented.

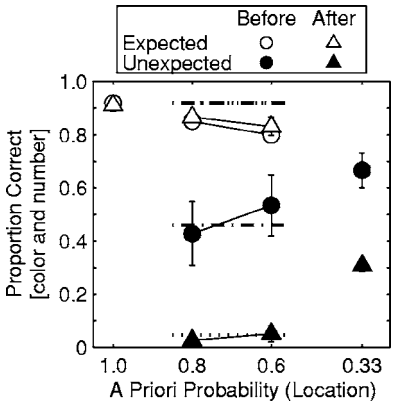

FIG. 3. Group mean proportion correct identification scores (ordinate), and standard deviations of the means, subdivided according to whether the target was presented at the expected (more likely; open symbols) or an unexpected (less likely; filled symbols) location. The abscissa is target location uncertainty. The circles represent performance for the callsign before condition while the triangles represent performance for the callsign after condition. The horizontal lines not connecting data points are the predictions of the single-source listener strategy discussed in the text.

for the callsign before condition and the triangles are for the callsign after condition. Each panel is for a different location. In the $p=1$ case, no additional data sorting was required. However, for the $p<1$ cases the data were sorted according to actual location (that is, the proportion correct is for all trials in which the target was presented from that particular location as opposed to proportion correct for all trials in the nominal location condition). The error bars are ±1 standard deviation of the mean. The effect of location increases with increasing location uncertainty with the greatest difference in performance, as noted above, for the two random conditions, where proportion correct identification was about 0.3 higher for target at +60° than at −60°.

It is also of interest to determine how well listeners performed when the target actually occurred at the expected location versus when it occurred at an unexpected location. This can be examined in the two intermediate probability conditions. It might be expected, for example, that the listeners always focused attention at the more likely location. In that case, performance should equal that found in the $p=1$ condition (i.e., about 0.92 correct) on the trials when the target was presented from that location. Figure 3 displays proportion correct performance as a function of expected and unexpected target locations. Expected location means that the target sentence was played at the most likely location, while unexpected location means that the target sentence was played at one of the other two less likely locations. Circles are for the callsign before condition and triangles are for the callsign after condition. Unfilled symbols indicate target presentation at the expected location and filled symbols are for target presentation at unexpected locations. Data are means and standard deviations computed across listeners for all locations. The results from $p=1$ and $p=0.33$ are included here for comparison (same as in Fig. 1) although there is no "unexpected" case for $p=1$ or "expected" case for $p=0.33$. The horizontal lines will be discussed later.

When the target was presented at the expected location, proportion correct identification performance was 0.8 or greater in all conditions. In that case, the callsign condition did not matter and the degree of uncertainty had a relatively minor effect, decreasing from around 0.92 for $p=1$ to around 0.80 for $p=0.6$. The decline in observed performance with decreasing p undoubtedly reflects a cost associated with the greater uncertainty about location and could indicate some attempt by the listeners to increasingly divide or distribute attention among locations. However, the small effect suggests that this had only a minor influence on performance for trials at the expected location.

In contrast to the results obtained when the target was presented at the expected location, target presentation from an unexpected location led to much poorer performance with large differences observed between callsign before and callsign after conditions. For callsign before, performance actually *improved* as uncertainty increased from a proportion correct of about 0.43 for $p=0.8$ to about 0.67 for $p=0.33$. The improvement in performance with increasing target-location uncertainty is a reasonable outcome if one assumes that there is a substantial penalty associated with attending to the wrong location.

Perhaps the most striking result shown in Fig. 3 is that, for the callsign after condition and $p=0.8$ or 0.6, listeners were almost never correct (0.02 and 0.05, respectively) when the target occurred at an unexpected location. Even the knowledge that the target would occur in the more likely location only 60% of the time still did not improve performance for the unexpected locations. Therefore, for callsign after, the listeners appeared to focus attention almost entirely at the expected location.

For the callsign before $p=0.8$ and 0.6 conditions, listeners were correct nearly half the time (0.43 and 0.53, respectively) when the location was unexpected. This implies that listeners used a combination of expected location and target callsign to perform the task. They probably were not using target callsign alone because performance for expected locations was significantly better than for unexpected locations. Obviously, they did not use location alone either because they were correct for unexpected locations fairly often.

B. Predictions of a simple single-source listener strategy

There are a number of strategies potentially available to the listener in attempting to solve this task. It is not possible from the data obtained in the current experiments, however, to evaluate and decide among all of the alternative strategies or observer models. On the other hand, it can be very useful and informative to take a single, simple strategy and follow through its assumptions and predictions. In this section, we consider the predictions of one such strategy and make comparisons to the results described above.

There are three initial assumptions that define this listener strategy. First, it is assumed that the sources are perfectly segregated and that errors occur because attention is directed to the incorrect source. It is already known, however, from the results discussed above, that performance was not perfect even for the $p=1$ case. Accordingly, the predictions of listener performance that follow are scaled by a multiplier of 0.92 (the observed proportion correct in the certain

location case) to reflect some (unspecified) limitations on the ability to identify targets at attended locations. Second, it is assumed that the listener attends to only one source at any given moment in time. While this is a strong assumption that excludes models based on divided attention, it also is straightforward to evaluate and provides a means for determining whether interpretations based on divided attention are necessary. The results described above for targets occurring at unexpected locations for the callsign after conditions provide some degree of support for this assumption. Third, it is assumed that the listener always attends to the more likely location. In the case of callsign before presentation, this provides an opportunity for the listener to switch attention to another location if it is determined that that location does not contain the target. This would happen whenever a nontarget callsign is presented from the location initially attended, i.e., the expected location. In those instances, it is assumed that the listener randomly chooses to focus on one of the other two sources because at the time switching occurs the other callsigns would have already been presented and are assumed not to be useful to the listener.

In determining the performance of this hypothetical listener, certain conditional probabilities may be defined. First, for callsign after, performance should simply be the probability of occurrence scaled by the $p=1$ value of 0.92. So, the predicted performance for callsign after is

$$PC_a = p\ PC_{max}, \tag{1}$$

where PC_a is the predicted proportion correct for the callsign after condition, p is the *a priori* probability of occurrence at one location, and PC_{max} is the highest proportion correct possible for an attended location (based on the $p=1$ results). The predictions of listener performance from this equation are shown as the dotted line in Fig. 1.

The predictions for the callsign before condition include PC_a as a term, but also include a term representing the increase in performance expected by switching attention after determining that the attended location is not the target location. In that case

$$PC_b = PC_a + 0.5[(1-p)PC_{max}], \tag{2}$$

where PC_b is the predicted performance for the callsign before condition. The predictions for performance based on this equation are also shown in Fig. 1 as a dash-dotted line. As a first approximation, this simple strategy accounts for the group-mean accuracy results fairly well (comparison of group mean data and lines in Fig. 1).

It is also possible to compare the predictions associated with this strategy to the results shown in Fig. 3, where the listener responses are computed according to target presentation at expected and unexpected locations for the target probabilities of 0.8 and 0.6. The predictions of this listener strategy are straightforward. Based on the assumption that the listener attends to the most likely location, performance should equal PC_{max} whenever the target is actually presented from that location for both the callsign before and callsign after conditions. This prediction is shown on Fig. 3 as horizontal lines (dash-dotted and dotted for the two callsign conditions) both at a proportion correct value of 0.92. As noted earlier, performance is slightly below the prediction, possibly reflecting a cost associated with target location uncertainty. When the target occurs at unexpected locations, the predictions of this listener strategy differ markedly for callsign after and callsign before conditions. For callsign after, the only information available to the listener is from the masker at the expected location, so optimal performance would be to choose a color/number combination from among the remaining alternatives after eliminating the ones known to be inaccurate. Thus, performance should be at around 0.05 proportion correct (3 colors $\times$ 7 numbers, with a small correction for guessing on 1-PC_{max} proportion of the trials, shown by the horizontal dotted line). In fact, the observed performance is close to that prediction. In the random condition, we assume the listener simply attends to one arbitrarily chosen location and thus should obtain a proportion correct of p times PC_{max}, or about 0.31 which, as noted above in Fig. 1, is quite close to the data point.

For the callsign before conditions, once the masker callsign is heard from the expected location, the hypothetical listener switches the focus of attention to one of the other locations. The choice would be arbitrary because it is assumed that only the callsign from the attended—and incorrect—location was processed, so the listener would have a 0.5 probability of selecting the correct source. Thus, performance should be equal to PC_{max} times 0.5, or about 0.46 proportion correct (shown as the dash-dotted line at that value). Inspection of Fig. 3 suggests that, again, this listener strategy predicts performance reasonably well with the obtained performance for callsign before at unexpected locations near the predicted values.

Overall, this simple listener strategy was fairly successful at predicting the proportion correct obtained from actual listeners in most conditions. However, there were some effects that it cannot capture, such as the difference between locations revealed in Fig. 2. Also, the results in Fig. 3 indicate small but understandable differences between the 0.8 and 0.6 probability conditions that are not accounted for in this simplified strategy. The results from the 0.6 condition suggest a slightly greater tendency to distribute attention with lower scores at the expected locations and higher scores at unexpected locations.

C. Error analysis

It is also informative to examine the errors in identification made by listeners as uncertainty varied. This analysis is of interest both for attempting to understand actual listener performance and for evaluating the listener strategy considered above which makes strong predictions about the types of errors that should occur. We should consider four broad categories of errors that are possible. First, the listener could confuse the target and a masker so that the color and number that are reported correspond to those of one of the two maskers. That type of error could be considered misdirection of attention due to focusing on the wrong source. This would form the great majority of errors predicted by the listener strategy discussed above. A second type of error would be due to random guessing from among the alternatives or per-

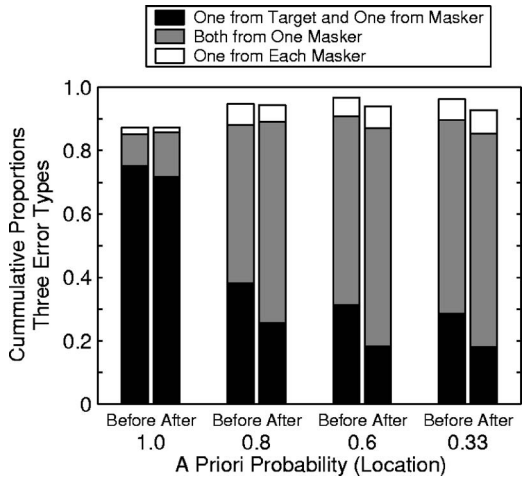

FIG. 4. This bar graph indicates the proportions of various types of errors in the speech identification task. The ordinate is the proportion of errors and the abscissa is the degree of target location uncertainty. The different shadings designate the types of errors (see legend and text).

haps guessing after eliminating one color and one number as hypothesized above for some callsign after conditions. Errors from random guessing might occur if performance were limited by energetic masking, where the test words (colors and numbers) were obscured and guessing was the only option available. Third, the errors could take the form of mixing colors and numbers from among the three sources, either one word from the target and one from a masker or one each from the two different maskers. This type of error might occur due to a breakdown in stream segregation. That is, the words are available but the listener is unable to properly connect the callsign, color, and number. And, finally, the errors could contain words not presented during the trial. This type of error could result in a mixture of words including one target or masker word and one word not presented on the trial (i.e., guessed from among the other alternatives). This type of error is not as easily interpreted as the other three types because there is a fairly high chance that it could occur due to random guessing (9 of the 32 alternatives are presented on each trial). The frequency of occurrence of each of these error types can be determined by analyzing the errors found in the experiment.

Figure 4 shows the proportions of incorrect responses obtained in the experiment subdivided according to the three main types of errors that were made. These data are plotted as a function of location uncertainty, and, because the patterns of errors were very similar across listeners, are shown as group means. The different types of errors are indicated by the black, gray, and white portions of the stacked bars. First, the overall height of the bars represents the proportion of all errors in which both of the responses (color and number) matched *any* of the six key words spoken on a given trial. For $p=1$, this accounted for a proportion of the errors equal to 0.87 while for the other values of p this accounted for proportions between 0.93 and 0.97 regardless of callsign condition. What this means is that there was very little guessing that occurred in any of these conditions—the key words were confused or mixed together but they appear to have been available to the listener. By way of comparison, the expected proportion of errors due to random guessing in which both responses were from the words spoken on a given trial is 0.26 (8 of the 9 possible combinations of words presented on a trial are errors out of 31 total possible error combinations). The obtained proportion of errors of this type overall was 0.94 (same as average of the total heights of bars in Fig. 4). These findings, along with the $p=1$ results, suggest that very little energetic masking was present in any of these conditions and support the conclusion that the second type of error discussed above (random guessing) had a negligible effect on performance.

The different shadings indicate a finer-grain analysis of these errors. The black lower portions of the bars represent the proportion of errors in which one of the words reported was from the target sentence and the other word was from one of the two masker sentences. This type of error was by far the most common for $p=1$ (keeping in mind that there were very few errors overall in this condition) but was less frequent for the other values of p. The occurrence of this error would be consistent with a breakdown in the process of speech stream segregation: the target and masker sentences were not held separate, but were mixed. To the extent that stream segregation involves perceptually connecting a sequence of sound elements that belong together, these "mixing" errors reveal a failure of that process and dominated the $p=1$ condition (0.75 and 0.72 proportion of errors for callsign before and after, respectively). It also accounted for substantial proportions of errors (ranging from about 0.18 to 0.38) in the more uncertain location conditions. For these $p<1$ conditions, the proportion of errors of this type were somewhat higher for callsign before than callsign after.

The intermediate gray bars indicate the proportions of errors in which *both* key words reported corresponded to the key words from one of the two masker sentences. This was the first category of error discussed above. When the listener was certain about where to listen ($p=1$), confusions with masker talkers rarely occurred (0.10 to 0.14 proportion of errors). For the conditions containing location uncertainty, however, masker confusions formed the most common type of error (with overall proportions of errors ranging from 0.50 to 0.69, with higher proportions for callsign after than for callsign before). This could occur if the spatial focus of attention was directed to the wrong location and the listener reported the color and number from that location. Finally, the white bars at the top indicate the proportions of errors when one word was from one masker and the other word was from the other masker. That type of error was infrequent in all conditions, did not differ with callsign knowledge, and was least frequent for the $p=1$ case.

The remaining errors not plotted in Fig. 4 are cases in which at least one word reported did not correspond to any of the words spoken (one target word and one unspoken word; one masker word and one unspoken word; both words unspoken). The probability from random guessing for one word spoken and one word unspoken is 0.58 (18 of 31), whereas the obtained proportion of errors of that type was 0.055. The expected proportion of errors due to guessing when both words reported were unspoken would be 0.16 (5 of 31), but the obtained proportion was only 0.005.

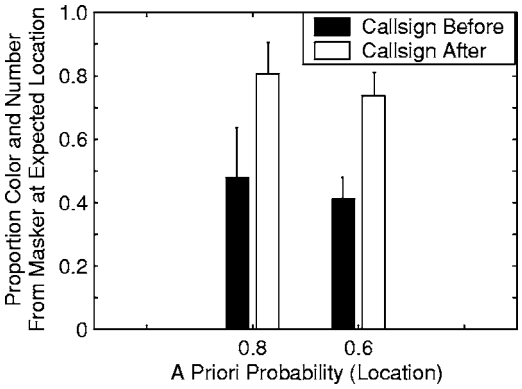

FIG. 5. The proportions of incorrect responses that matched the color and number of the masker sentence presented at the expected (more likely) location when the target was presented at an unexpected (less likely) location. The values plotted are group means and standard deviations for the callsign before (black bars) and callsign after (white bars) conditions.

As discussed above, the most common type of error for the $p<1$ conditions was a masker confusion error. To what extent does this error reflect focusing attention at the wrong location? An analysis of errors that is relevant to this issue involves determining the extent to which incorrect responses in uncertain location conditions corresponded to the masker sentence that was presented at the expected target location. That is, the listener knew that the target was more likely at one particular location and incorrectly reported the (masker) color and number from that location. This analysis is only possible for the 0.8 and 0.6 probability conditions. Figure 5 shows the proportion of incorrect responses that matched the color and number from the masker sentence presented at the expected location (when the target was actually presented at an unexpected location). The data are intersubject means and standard deviations (combined over the three locations). The black bars are for callsign before and the white bars are for the callsign after condition. In the callsign before condition, the proportion of errors corresponding to the masker sentence presented at the expected target location was between 0.4 and 0.5. For the callsign after condition, the corresponding proportions of errors were much higher (0.74 and 0.81).

These data, along with those presented in Fig. 4, are inconsistent with the simple listener strategy described in Sec. III B above. Although that strategy was generally successful in accounting for the group-mean accuracy results in the various conditions, the patterns of errors obtained were not consistent with that strategy. The listener strategy examined above predicts that all of the errors (except perhaps those errors equal to 1-PC_{max}) should be confusions with one of the two maskers. That prediction was not supported by the results. The proportions of errors for $p<1$ cases that were *not* from one specific masker ranged from about 0.3–0.5 and increased to almost 0.9 when $p=1$. Thus, a substantial proportion of errors occurred that could not be attributed to confusing a masker with the target or simply reporting the sentence from the wrong location. Furthermore, the callsign before results shown in Fig. 5 are incompatible with the predictions of a switching strategy because nearly one-half of the errors corresponded to reporting a masker presented at the expected location. While these proportions are smaller than those seen in the callsign after condition in which this strategy is not possible, the switching strategy predicts that *none* of the errors should correspond to that location. This suggests a fairly strong tendency to report the content from the expected location and not shift attention away from that location during stimulus presentation. For callsign before, that result is surprising because the listener should realize that the expected location does not contain the target as soon as the inaccurate callsign is heard. We do not have a good explanation for this nonoptimal listener behavior and can only speculate that the results reflect a strong bias in favor of *a priori* information regarding location. The tendency to rely on expected target location is even more strongly apparent for the callsign after condition in which the proportions of errors from the expected location were greater than 0.74. In that case, if it were assumed that only the callsign, color, and number from one location—the attended location—were remembered, then a more effective strategy would be simply to guess from among the color and number alternatives after *excluding* those from that masker. In that case, again, none of the errors would correspond to the most likely target location. The results in Fig. 5 reveal that listeners tended not to adopt that strategy.

IV. DISCUSSION

The first point to be made concerns the degree to which the findings here answer the question posed in the Introduction regarding the role of spatial focus of attention in solving the cocktail party problem. The results of the current study support the conclusion that focusing attention toward a target sound source in the presence of spatially distributed maskers can provide a very significant advantage in speech identification performance. However, this prominent role of spatial focus of attention may depend on other factors such as the complexity of the listening environment and the processing load placed on the observer.

In order to conclude that the listening advantages found in this study may be attributed to spatial focus of attention, we must consider the possible role of other factors such as masking and perceptual segregation of sounds. In contrast to studies in which the spatial separation between sources was varied in an attempt to reveal listening advantages due to binaural interaction and better ear listening, the spatial location of the sources in the present study did not vary across conditions. Thus, the binaural cues of interaural time and level differences allowed the listener to locate the sources within the environment, but did not differ across test conditions and whatever amount of masking was present did not influence the main variables of interest. The only case where acoustic differences may have played a factor is in the comparison of performance across fixed locations. For example, an acoustically "better ear" would occur when the target was presented through either the left or right loudspeaker compared to the center loudspeaker. As shown in Fig. 2, some differences in performance were observed favoring the right location in the random condition. However, this is not likely to be an indication of binaural masking release because it was not present consistently across conditions nor was it

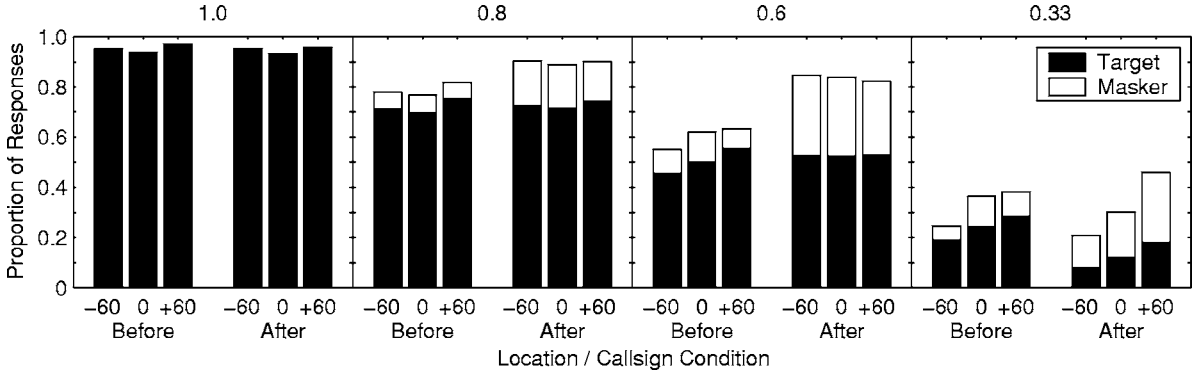

FIG. 6. The proportion of all words (single words or pairs) reported from the more likely location. This includes both words from the target (correct responses—lower black portion of bars) and from a masker (incorrect responses—upper white portion of bars). In each panel both callsign before and after responses are shown at each loudspeaker location. In the random condition (right-most panel) these are just proportions of responses by location because there was no "more likely" location.

present for left location presentation, which would be expected to produce roughly the same binaural cues as the symmetrically placed right location.

It is not clear from Fig. 2 whether the difference in performance across loudspeaker locations reflects a genuine perceptual effect or a bias on the part of the listeners to attend to the location on the right.[2] There is a long history of study of "right-ear advantages" in dichotic listening and, although the effect has been attributed primarily to differences in the processing of speech in the two hemispheres of the brain (e.g., Kimura, 1967; Zatorre, 1989), there is also evidence that the effect is labile and susceptible to attentional focus (e.g., Asbjornsen and Hugdahl, 1995; Asbjornsen and Bryden, 1996). A further analysis of the data was undertaken to help understand this effect in the current experiment. The results of this analysis are shown in Fig. 6. This figure shows the proportions of all words reported from the more likely location regardless of whether the words were from targets (lower black portions of bars) or from maskers (upper white portions of bars). Note that for the random condition, there was no "more likely location" so the bars represent all responses to words from each location.

Inspection of Fig. 6 indicates that a strong asymmetry between right- and left-side locations is only clearly evident in the random condition. In that condition, not only was there a tendency to report target words more often when they were presented from the right side, but there was also a tendency to report masker words more often when presented from the right side (primarily for the callsign after condition but in both callsign conditions both target and masker words were reported less often when located to the left). Thus, the words presented from the right loudspeaker were chosen more often than those from (in particular) the left loudspeaker regardless of whether they were correct or incorrect. This response pattern clearly reflects bias on the part of the listeners because the expected probability of occurrence from the three locations in the random condition was equal. This bias largely disappears when uncertainty about target location is decreased. Whether there is also a genuine processing difference, and whether that is in some way related to the observed bias, cannot be ascertained from these data. Another relevant point is that, because the stimuli were presented via loudspeakers, the speech from all three talkers was present in both ears on every trial. Thus, the differences in performance must be related to the differences in acoustics as target position varied. The acoustic differences between target and masker talkers, though, are much less than in dichotic listening tasks where the stimuli are presented separately to the two ears. It is not clear how the effect found here is related to these acoustic differences. It should be noted that both Bolia *et al.* (2001) and Brungart and Simpson (2005) have reported right hemifield identification performance advantages using the CRM test for earphone-based stimuli processed by HRTFs.

The analysis presented in Fig. 6 also provides insight into another issue. There is an extensive literature concerning the tendency of subjects to adjust their response strategy to match the *a priori* probabilities of different response alternatives being correct, or having different payoffs, even if that strategy is nonoptimal (called "probability matching;" e.g., Shanks *et al.*, 2002; West and Stanovich, 2003; also, review by Vulkan, 2000). In the current experiments, evidence for probability matching might be found by comparing the proportions of responses to stimuli from expected locations to the *a priori* probabilities of target presentation from those locations. For callsign before, there is indeed a reasonably close correspondence between overall response rates and the assigned probabilities (Fig. 6). However, because the callsign was provided in addition to location probabilities, it cannot be determined if this correspondence truly reflects matching responses to probabilities of occurrence at the different locations or is a by-product of a combined callsign-location weighting strategy. Furthermore, the opportunity for switching the attended location based on callsign also could produce the proportions of responses shown in Fig. 6. For callsign after for $p=0.8$ and, especially, $p=0.6$, little support for a probability matching interpretation is apparent. The obtained proportions of responses from the expected locations for those two conditions are greater than 0.9 and 0.8, respectively, which are substantially above the corresponding probabilities of occurrence.

The finding that identification performance was so accurate when $p=1$ provides support for the conclusion that, generally, masking was minimal and the sound sources could be

successfully segregated. This conclusion is based on the assumption that both factors are necessary for successful identification to occur. However, errors attributed to a breakdown in the perceptual segregation of the speech streams were present in all conditions. Although these "mixing errors" were the most common type of error for the certain-location conditions, the errors were still very infrequent with proportion correct scores over 0.9 found for both callsign conditions. The success of the listeners in those conditions indicates that the speech streams *can* be segregated, but the maintenance of separate streams is vulnerable to increasing uncertainty about target location. Here, when attention is focused at the wrong location, performance suffers with increased uncertainty and errors consistent both with misdirected attention and loss of stream segregation were found. Furthermore, because identification performance was not perfect even when the most *a priori* information was provided to the listener (about 0.92 proportion correct for the callsign before, $p=1$ condition), some interference caused by nontarget sound sources clearly was present (proportion correct identification performance for a single-talker baseline condition was nearly perfect). Thus, the two more common types of errors were confusions between target and masker, which we believe indicate misdirection of attention, and mixing target and masker words, which probably indicates a breakdown in maintaining speech stream segregation.

The present results also imply that surprisingly little shifting or redirecting of attention occurred during trials. When the callsign *was* provided before trials, but the target occurred at an unexpected location ($p=0.6$ and 0.8), nearly one-half of the errors corresponded to the masker at the target's most likely location. These conditions indicate a rivalry of cues: target talker versus location. In this case, directing attention to the wrong location clearly diminished the ability of the listener to follow the speech of the target talker from the callsign to the test words. These scores are worse, in fact, than in the random case where proportion correct performance was about 0.7. Thus, when the target talker was indicated beforehand there was a penalty of directing attention to the wrong location.

Comparison of performance in the callsign before and callsign after conditions overall indicates the interaction between the processing load imposed by the task and the importance of spatial focus of attention. Ideally, if an observer were capable of remembering all three simultaneous sentences, specifically, associating and remembering the three key words from each source—the callsign, color, and number, then spatial information would be unnecessary and performance in both callsign before and callsign after conditions would be equivalent. Clearly, this was not possible when there were three simultaneous talkers. According to the "load theory of attention" proposed by Lavie *et al.* (2004), when observers are faced with a very demanding perceptual task—segregating one element of an array of similar elements, for example—the nontarget elements produce little interference in the selection and processing of the target. This is because of the assumption that all available perceptual resources are occupied at any given point in time. If the resources required to process the target occupy the entire pool of resources available, none are left to allocate to distracting sources, so little or no interference occurs. However, if the perceptual task is not demanding but the subsequent cognitive control load is, as would be the case if a high load were placed on working memory, much greater interference from distracters is predicted. In the current conditions, despite the fact that the three sources are male talkers, the segregation task is relatively easy. This conclusion is based on the high identification scores in the certain-location conditions. However, particularly in the callsign after case, the cognitive load—the demands on working memory that would be sufficient to solve the task—are very high. Furthermore, when uncertainty about location increased, errors in perceptual segregation—mixing errors—increased as well (note that here we are referring to the combination of number of errors as in Fig. 1 *and* the error type as in Fig. 4). If we assume that increasing uncertainty mainly affects cognitive load, then increasing errors from distracters—either misdirected attention or loss of stream segregation—would be expected. Thus, although the evidence in support of the load theory usually takes the form of response times (as do most data concerned with auditory attention, with some exceptions, cf. Sach *et al.*, 2000; Erickson *et al.*, 2004), our results appear to be qualitatively consistent with that theory.

We do not have data for other numbers of talkers (except for the control case of one talker) but speculate that equally strong spatial effects could be observed for four or more talkers. This is because the three-talker condition has already degraded performance to near the limiting case imposed by the number of potential target sources. Assuming that each source may be segregated from the others and that only one message can be remembered, then performance in the callsign after-random condition should at best be equal to the reciprocal of the number of sources, if each is equally likely to be the target. That is, the listener chooses one to attend to and does so perfectly and completely to the exclusion of the others. For callsign after, performance in the random condition was near that which would be expected based on this strategy. An interesting case, then, is for two simultaneous sources. At present, we have some indications that performance in the two-talker callsign after condition may exceed the reciprocal of the number-of-sources limit (Gallun *et al.*, 2005).

Recently, the two- vs three-source comparison for multitalker speech identification has been considered by Brungart and Simpson (2002). In their study, the task was the same as here—reporting the color and number for a designated callsign in the CRM task—and there were either one or two other talkers also uttering sentences from the CRM task. However, the stimuli were presented via earphones. When the target, which was presented to the "ipsilateral" ear, was mixed with one masker in the same ear, performance varied predictably according to T/M. When one masker was presented to the contralateral ear, no interference in target identification was observed; i.e., identification performance approached 100% correct. When both maskers—one ipsilateral and one contralateral—were presented, target identification performance was as much as 40 percentage points poorer than the single (ipsilateral) masker condition. Brungart and

Simpson (2002) attributed this large decline in performance to the much greater difficulty in ignoring two sources, rather than one source, when there was a difficult segregation task to perform in the target ear. Kidd *et al.* (2003) found a parallel effect using complex nonspeech stimuli. The greater difficulty in three-talker conditions than in two-talker conditions has been noted by Yost *et al.* (1996) and Hawley *et al.* (2004). In the current study, we speculate that the high processing load caused by three simultaneous talkers contributed to the large beneficial effect of *a priori* information, especially that of the most likely target location.

V. SUMMARY AND CONCLUSIONS

A priori knowledge about where to direct attention provided significant advantages in speech identification in highly uncertain multitalker listening conditions. This result was found for both cued and uncued target sentence presentation. The differences in performance found across the various conditions could not be attributed to binaural analysis, masking, or perceptual segregation, but rather appear to be uniquely related to focus of attention. The pattern of errors suggested a high degree of spatial selectivity with very little processing of speech originating from unattended locations. A simple single-source listener strategy was found to predict accuracy fairly well in most conditions but failed to account for the observed patterns of errors. The current results support the view that spatial focus of attention can be a very important factor in complex and uncertain multisource listening environments and may play a crucial role in solving the "cocktail party problem."

ACKNOWLEDGMENTS

The authors are grateful to Kelly Egan for her assistance. They would also like to thank Nathaniel I. Durlach and Barbara Shinn-Cunningham for comments on an earlier version of the manuscript. This work was supported by Grants Nos. DC00100, DC04545, and DC04663 from NIH/NIDCD and by AFOSR Award No. FA9550-05-1-2005. Frederick Gallun was supported by F32 DC006526 from NIDCD.

[1]The use of the term "spatial dimension" in this article is confined to variations in sound source azimuth. A complete description of sound source location includes distance from the listener and elevation, which are not considered here.

[2]Preferential selection of objects or events on the right side has been observed in many tasks other than speech recognition (e.g., Nisbett and Wilson, 1977).

Arbogast, T. L., and Kidd, G., Jr. (**2000**). "Evidence for spatial tuning in informational masking using the probe-signal method," J. Acoust. Soc. Am. **108**, 1803–1810.

Arbogast, T. L., Mason, C. R., and Kidd, G., Jr. (**2002**). "The effect of spatial separation on informational and energetic masking of speech," J. Acoust. Soc. Am. **112**, 2086–2098.

Asbjornsen, A. E., and Bryden, M. P. (**1996**). "Biased attention and the fused dichotic words test," Neuropsychologia **34**, 407–411.

Asbjornsen, A., and Hugdahl, K. (**1995**). "Attentional effects in dichotic listening," Brain Lang **49**, 189–201.

Bolia, R. S., Nelson, T. W., and Morley, R. M. (**2001**). "Asymmetric performance in the cocktail party effect: Implications for the design of spatial audio displays," Hum. Factors **43**, 208–216.

Bolia, R. S., Nelson, W. T., Ericson, M. A., and Simpson, B. D. (**2000**). "A speech corpus for multitalker communications research," J. Acoust. Soc. Am. **107**, 1065–1066.

Bronkhorst, A. W. (**2000**). "The cocktail party phenomenon: A review of research on speech intelligibility in multiple-talker conditions," Acust. Acta Acust. **86**, 117–128.

Bronkhorst, A. W., and Plomp, R. (**1988**). "The effect of head-induced interaural time and level differences on speech intelligibility in noise," J. Acoust. Soc. Am. **83**, 1508–1516.

Brungart, D. S., and Simpson, B. D. (**2002**). "Within-ear and across-ear interference in a cocktail-party listening task," J. Acoust. Soc. Am. **112**, 2985–2995.

Brungart, D. S., and Simpson, B. D. (**2005**). "Cocktail party listening in a dynamic multitalker environment," (unpublished).

Brungart, D. S., Simpson, B. D., Ericson, M. A., and Scott, K. R. (**2001**). "Informational and energetic masking effects in the perception of multiple simultaneous talkers," J. Acoust. Soc. Am. **110**, 2527–2538.

Cherry, E. C. (**1953**). "Some experiments on the recognition of speech, with one and two ears," J. Acoust. Soc. Am. **25**, 975–979.

Colburn, H. S. (**1996**). "Computational models of binaural processing," in *Auditory Computation*, edited by H. Hawkins, T. McMullin, A. N. Popper, and R. R. Fay (Springer-Verlag, New York), pp. 332–400.

Colburn, H. S., and Durlach, N. I. (**1978**). "Models of binaural interaction," in *Handbook of Perception, Vol. IV, Hearing*, edited by E. C. Carterette and M. P. Friedman (Academic, New York).

Culling, J. F., Hawley, M. L., and Litovsky, R. Y. (**2004**). "The role of head-induced interaural time and level differences in the speech reception threshold for multiple interfering sound sources," J. Acoust. Soc. Am. **116**, 1057.

Durlach, N. I. (**1972**). "Binaural signal detection: Equalization and cancellation theory," in *Foundations of Modern Auditory Theory, Vol. II*, edited by J. V. Tobias (Academic, New York).

Ebata, M. (**2003**). "Spatial unmasking and attention related to the cocktail party problem," Acoust. Sci. Tech. **24**, 208–219.

Erickson, M. A., Brungart, D. S., and Simpson, B. D. (**2004**). "Factors that influence intelligibility in multitalker speech displays," J. Aviation Psych. **14**, 311–332.

Gallun, F. J., Mason, C. R., and Kidd, G., Jr. (**2005**). "Task-dependent costs in processing two simultaneous auditory stimuli," (unpublished).

Green, T. J., and McKeown, J. D. (**2001**). "Capture of attention in selective frequency listening," J. Exp. Psychol. Hum. Percept. Perform. **27**, 1197–1210.

Greenberg, G. S., and Larkin, W. D. (**1968**). "Frequency-response characteristic of auditory observers detecting signals of a single frequency in noise: The probe-signal method," J. Acoust. Soc. Am. **44**, 1513–1523.

Hawley, M. L., Litovsky, R. Y., and Culling, J. F. (**2004**). "The benefit of binaural hearing in a cocktail party: Effect of location and type of interferer," J. Acoust. Soc. Am. **115**, 833–843.

Hill, N. I., Bailey, P. J., and Hodgson, P. (**1998**). "A probe-signal study of auditory discrimination of complex tones," J. Acoust. Soc. Am. **102**, 2291–2296.

Kidd, G., Jr., Mason, C. R., Brughera, A., and Hartmann, W. M. (**2005**). "The role of reverberation in release from masking due to spatial separation of sources for speech identification," Acust. Acta Acust. **91**, 526–536.

Kidd, G., Jr., Mason, C. R., Arbogast, T. L., Brungart, D., and Simpson, B. (**2003**). "Informational masking caused by contralateral stimulation," J. Acoust. Soc. Am. **113**, 1594–1603.

Kimura, D. (**1967**). "Functional asymmetry of the brain in dichotic listening," Cortex **22**, 163–178.

Lavie, N., Hirst, A., de Fockert, J. W., and Viding, E. (**2004**). "Load theory of selective attention and cognitive control," J. Exp. Psychol. Gen. **133**, 339–354.

Macmillan, N. A., and Schwartz, M. (**1975**). "A probe-signal investigation of uncertain-frequency detection," J. Acoust. Soc. Am. **58**, 1051–1058.

Mondor, T. A., and Zatorre, R. J. (**1995**). "Shifting and focusing auditory spatial attention," J. Exp. Psychol. Hum. Percept. Perform. **21**, 397–409.

Mondor, T. A., Zattore, R. J., and Terrio, N. A. (**1998**). "Constraints on the selection of auditory information," J. Exp. Psychol. Hum. Percept. Perform. **24**, 66–79.

Nisbett, R. E., and Wilson, T. C. (**1977**). "Telling more than we know: Verbal reports on mental processes," Psychol. Rev. **84**, 231–259.

Plomp, R. (**1976**). "Binaural and monaural speech intelligibility of connected discourse in reverberation as a function of azimuth of a single

competing sound source (speech or noise)," Acustica **34**, 200–211.
Sach, A. J., Hill, N. I., and Bailey, P. J. (**2000**). "Auditory spatial attention using interaural time differences," J. Exp. Psychol. Hum. Percept. Perform. **26**, 717–729.
Scharf, B. (**1998**). "Auditory attention: The psychoacoustical approach," in *Attention*, edited by H. Pashler (Psychology Press, East Sussex, UK), pp. 75–117.
Scharf, B., Quigley, S., Aoki, C., Peachey, N., and Reeves, A. (**1987**). "Focused auditory attention and frequency selectivity," Percept. Psychophys. **42**, 215–223.
Schlauch, R. S., and Hafter, E. R. (**1991**). "Listening bandwidths and frequency uncertainty in pure-tone signal detection," J. Acoust. Soc. Am. **90**, 1332–1339.
Shanks, D. R., Tunney, R. J., and McCarthy, J. D. (**2002**). "A re-examination of probability matching and rational choice," J. Behav. Dec. Making **15**, 233–250.
Shinn-Cunningham, B. G., Schickler, J., Kopco, N., and Litovsky, R. Y. (**2001**). "Spatial unmasking of nearby speech sources in a simulated anechoic environment," J. Acoust. Soc. Am. **110**, 1118–1129.
Spence, C. J., and Driver, J. (**1994**). "Covert spatial orienting in audition: Exogenous and endogenous mechanisms," J. Exp. Psychol. Hum. Percept. Perform. **20**, 555–574.
Vulkan, N. (**2000**). "An economist's perspective on probability matching," J. Econ. Surveys **14**, 101–118.
West, R. F., and Stanovich, K. E. (**2003**). "Is probability matching smart? Associations between probabilistic choices and cognitive ability," Mem. Cognit. **31**, 243–251.
Woods, D. L., Alain, C., Diaz, R., Rhodes, D., and Ogawa, K. H. (**2001**). "Location and frequency cues in auditory selective attention," J. Exp. Psychol. Hum. Percept. Perform. **27**, 65–74.
Wright, B. A., and Dai, H. (**1994**). "Detection of unexpected tones with short and long durations," J. Acoust. Soc. Am. **95**, 931–938.
Wright, B. A., and Dai, H. (**1998**). "Detection of sinusoidal amplitude modulation at unexpected rates," J. Acoust. Soc. Am. **104**, 2991–2997.
Yost, W. A. (**1997**). "The cocktail party problem: Forty years later," in *Binaural and Spatial Hearing in Real and Virtual Environments*, edited by R. A. Gilkey and T. R. Anderson (Erlbaum, Hillsdale, NJ), pp. 329–348.
Yost, W. A., Dye, R. H., and Sheft, S. (**1996**). "A simulated 'cocktail party' with up to three sound sources," Percept. Psychophys. **58**, 1026–1036.
Zattore, R. J. (**1989**). "Perceptual asymmetry on the dichotic fused words test and cerebral speech lateralization determined by the carotoid sodium amytal test," Neuropsychologia **27**, 1207–1219.
Zurek, P. M. (**1993**). "Binaural advantages and directional effects in speech intelligibility," in *Acoustical Factors Affecting Hearing Aid Performance*, edited by G. A. Studebaker and I. Hochberg (Allyn and Bacon, Boston), pp. 255–276.

Discrimination of speaker size from syllable phrases[a)]

D. Timothy Ives, David R. R. Smith, and Roy D. Patterson
Centre for the Neural Basis of Hearing, Physiology Department, University of Cambridge, Downing Street, Cambridge, CB2 3EG, United Kingdom

(Received 29 March 2005; revised 14 September 2005; accepted 20 September 2005)

The length of the vocal tract is correlated with speaker size and, so, speech sounds have information about the size of the speaker in a form that is interpretable by the listener. A wide range of different vocal tract lengths exist in the population and humans are able to distinguish speaker size from the speech. Smith *et al.* [J. Acoust. Soc. Am. **117**, 305–318 (2005)] presented vowel sounds to listeners and showed that the ability to discriminate speaker size extends beyond the normal range of speaker sizes which suggests that information about the size and shape of the vocal tract is segregated automatically at an early stage in the processing. This paper reports an extension of the size discrimination research using a much larger set of speech sounds, namely, 180 consonant-vowel and vowel-consonant syllables. Despite the pronounced increase in stimulus variability, there was actually an improvement in discrimination performance over that supported by vowel sounds alone. Performance with vowel-consonant syllables was slightly better than with consonant-vowel syllables. These results support the hypothesis that information about the length of the vocal tract is segregated at an early stage in auditory processing. © *2005 Acoustical Society of America.* [DOI: 10.1121/1.2118427]

PACS number(s): 43.66.Lj, 43.66.Ba, 43.71.Bp [RAL] Pages: 3816–3822

I. INTRODUCTION

Animal communication sounds contain information about the size (or scale) of the source. Recent work has shown that this scale information is present in the calls of birds (Mergell *et al.*, 1999; Fitch, 1999; Fitch and Kelley, 2000), cats (Hast, 1989), dogs (Riede and Fitch, 1999), and primates (Fitch, 1997). In humans (like all mammals), communication sounds are produced by the resonance of a modulated stream of air. The air is forced up from the lungs and passes through the vocal folds. The vocal folds open and close rapidly, which modulates the stream of air producing a stream of glottal pulses. This modulated stream of air travels up through the pharyngeal and oral cavities (vocal tract) where it resonates in accordance with the shape and length of the vocal tract. Finally the air radiates out through the mouth as speech. Information about the size of the speaker is conveyed to the listener by the frequencies of the resonances (or formants) and their decay rates and by the glottal pulse rate (GPR). As humans grow, their vocal folds grow, becoming longer and heavier (Titze, 1989), which results in a lowering of GPR. The value decreases from about 260 Hz for small children to about 90 Hz for large adult males. Vocal tract length (VTL) is largely determined by height (Fitch and Giedd, 1999) and it increases from about 9 cm for young children to about 17 cm for large adults. The center frequencies of the resonances are inversely proportional to its length (Fant, 1970), while their decay rates are proportional to VTL; so, in general, taller people have lower formant frequencies than shorter people and their resonances ring longer. This relationship has also been demonstrated in macaques (Fitch, 1997) where the height, weight, VTL, and formant frequencies were all measured in the same individuals. Unfortunately, there are no equivalent studies for humans in which VTL was measured and compared with the formant frequencies of the speaker.

Speakers can modify their VTL a little by lip rounding and by raising or lowering the larynx. Both effects change the positions of the formant frequencies and so alter the perceived size of the speaker. The variability introduced by these factors reduces the correlation between formant frequency and height in adults, and when the range of heights is limited and/or the sample size is relatively small, the correlation can be unreliable. Thus we find that Gonzalez (2004) found a weak relationship between formant frequency and height that was stronger for women than for men, whereas Rendall *et al.* (2005) found a weak relationship between formant frequency and height that was stronger for men than for women. It is also the case that speakers can lower or raise the average pitch of their voice, and thereby increase or decrease their apparent size and/or age, and Kunzel (1989) found that GPR is not significantly correlated with speaker size in adults when other variables like age and sex are controlled. So, although it is easy to distinguish children from adults on the basis of a few syllables, one cannot readily estimate the height of adults accurately from their speech alone, and research in this area has been hampered by the complexity of the interaction of the variables (Owren and Anderson, 2005).

Recently, two high-quality vocoders have been developed that make it possible to manipulate VTL and GPR in isolation, or in arbitrary combinations, while at the same time avoiding concomitant changes in secondary factors such as lip rounding and larynx lowering. The vocoders are re-

[a)]Portions of this work were presented in "Size discrimination in CV and VC English syllables," British Society of Audiology, London, United Kingdom, 2004.

ferred to as STRAIGHT (Kawahara *et al.*, 1999; Kawahara and Irino, 2004) and PRAAT (Boersma, 2001). When GPR is changed keeping the VTL constant, we hear one person's voice changing in pitch; when the VTL is changed keeping GPR constant, we hear two different-sized people speaking on the same pitch. Demonstrations are provided on the web page[1] of the Centre for Neural Basis of Hearing. The vocoder STRAIGHT has been used to investigate the effect of VTL variability on vowel recognition and to measure the just noticeable difference (jnd) in VTL. Assmann and Nearey (2003) scaled vowels with STRAIGHT and measured vowel recognition performance for combinations of GPR and VTL in the range normally encountered in human speech and somewhat beyond. They found that good performance extends beyond the normal range but that it falls off as the GPR rises beyond 800 Hz, and it falls off faster for longer VTLs. They proposed a model of vowel recognition consisting of a neural network that learns the associations between vowel type, GPR, and formant frequencies in natural speech. Smith *et al.* (2005) scaled vowels with STRAIGHT over a much wider range and showed that vowel recognition was still possible even though the range of GPRs and VTLs was much greater than that experienced in natural speech. Irino and Patterson (2002) have argued that the auditory system segregates the acoustic features in speech sounds associated with the shape of the vocal tract from those associated with its length at an early stage in auditory processing. Turner *et al.* (2005) and Smith *et al.* (2005) argued that good recognition performance outside the normal speech range favors the hypothesis of Irino and Patterson (2002) that there is a size normalization process in the early stages of auditory processing. Smith *et al.* (2005) also measured size discrimination using vowel sounds. They showed that discrimination was possible over a large range of VTLs and GPRs, including combinations well beyond the natural human range. The data support the hypothesis of Cohen (1993) that scale is a dimension of speech sounds, and the hypothesis of Irino and Patterson (2002) that there is a scale normalization process at an early stage in the auditory system.

In this paper, the vowel experiments of Smith *et al.* (2005) were extended to determine how size discrimination performance is affected when the variability of the set of speech sounds is increased to be more like that experienced in everyday speech. The number of speech tokens in the experiment was increased from 5 vowels to 180 syllables. The number of combinations of GPR and VTL in the experiment was reduced from 17 to 5.

II. METHOD

To expand the domain of size perception from vowels to more speechlike utterances, we created a large database of CV and VC syllables which were scaled in GPR and VTL using STRAIGHT. In the experiment listeners were presented with two phrases of four syllables, which were selected at random, with replacement, from a specific category of the syllable database. The only consistent difference between the two phrases was vocal tract length; the listener's task was to identify the interval with the smaller speaker.

The stimuli consisted of syllables that were analyzed, manipulated, and resynthesized by STRAIGHT, which is a high-quality vocoder developed by Kawahara and Irino (2004). Liu and Kewley-Port (2004) have reviewed STRAIGHT and commented favorably on the quality of its production of resynthesized speech. Assmann and Katz (2005) have also shown that a listener's ability to identify vowels is not adversely affected when they are manipulated by STRAIGHT over a reasonable range of GPR and VTL. STRAIGHT allows one to the separate the VTL and GPR information in speech sounds and resynthesize the same utterance with different VTL and/or GPR values. STRAIGHT performs a "pitch synchronous" spectral analysis with a high-resolution FFT, and then the envelope is smoothed to remove the zeros introduced by the FFT. The resultant sequence of spectral envelopes describes the resonance behavior of the vocal tract in a form that is largely independent of pitch. The GPR vector can be scaled to change the pitch of the syllable, and the frequency dimension of the sequence of spectral envelopes can be scaled to vary the VTL of the speaker; then the syllable can be resynthesized with its new GPR and VTL values.

The speech in this experiment was taken from a database created at the CNBH for brain imaging experiments; it contains 180 unique syllables. Versions of the syllables were analyzed with STRAIGHT and then resynthesized with many different combinations of GPR and VTL. The syllables were divided into 6 groups: three consonant-vowel (CV) groups and three vowel-consonant (VC) groups. Within the CV and VC categories, the groups were distinguished by consonant category: sonorants, stops, and fricatives. The full set of syllables is shown in Table I. The syllables were recorded from one speaker (author RP) in a quiet room with a Shure SM58-LCE microphone. The microphone was held approximately 5 cm from the lips to ensure a high signal-to-noise ratio and to minimize the effect of reverberation. A high-quality PC sound card (Sound Blaster Audigy II, Creative Labs) was used with 16-bit quantization and a sampling frequency of 48 kHz. The syllables were normalized by setting the rms value in the region of the vowel to a common value so that they were all perceived to have about the same loudness. We also wanted to ensure that, when any combination of the syllables was played in a sequence, they would be perceived to proceed at a regular pace; an irregular sequence of syllables causes an unwanted distraction. Accordingly, the positions of the syllables within their files were adjusted so that their perceptual-centers (P-centers) all occurred at the same time relative to file onset. The algorithm for finding the P-centers was based on procedures described by Marcus (1981) and Scott (1993), and it focuses on vowel onsets. Vowel onset time was taken to be the time at which the syllable first rises to 50% of its maximum value over the frequency range of 300–3000 Hz. To optimize the estimation of vowel onset time, the syllable was filtered with a gammatone filterbank (Patterson *et al.*, 1992) having 30 channels spaced quasi-logarithmically over the frequency range of 300–3000 Hz. The 30 channels were sorted in descending order based on their maximum output value and the ten highest were selected. The Hilbert envelope was calcu-

TABLE I. Stimulus set showing categories of CVs, VCs, sonorant, stops, and fricatives. Pronunciation details are described in the text.

	Sonorants						Stops						Fricatives					
CV's	ma	na	la	ra	wa	ya	ba	da	ga	pa	ta	ka	sa	fa	va	za	sha	ha
	me	ne	le	re	we	ye	be	de	ge	pe	te	ke	se	fe	ve	ze	she	he
	mi	ni	li	ri	wi	yi	bi	di	gi	pi	ti	ki	si	fi	vi	zi	shi	hi
	mo	no	lo	ro	wo	yo	bo	do	go	po	to	ko	so	fo	vo	zo	sho	ho
	mu	nu	lu	ru	wu	yu	bu	du	gu	pu	tu	ku	su	fu	vu	zu	shu	hu
VC's	am	an	al	ar	aw	ay	ab	ad	ag	ap	at	ak	as	af	av	az	ash	ah
	em	en	el	er	ew	ey	eb	ed	eg	ep	et	ek	es	ef	ev	ez	esh	eh
	im	in	il	ir	iw	iy	ib	id	ig	ip	it	ik	is	if	iv	iz	ish	ih
	om	on	ol	or	ow	oy	ob	od	og	op	ot	ok	os	of	ov	oz	osh	oh
	um	un	ul	ur	uw	uy	ub	ud	ug	up	ut	uk	us	uf	uv	uz	ush	uh

lated for these ten channels and, for each, the time at which the level first rose to 50% of the maximum was determined; the vowel onset time was taken to be the mean of these ten time values. The P-center was determined from the vowel onset time and the duration of the signal as described by Marcus (1981). The P-center adjustment was achieved by the simple expedient of inserting silence before and/or after the sound. After P-center correction the length of each syllable, including the silence, was 683 ms.

With regard to the pronunciation of the syllables, the listeners were not required to recognize the syllables or specify their phonetic content, so the precise pronunciation of the syllables is not an issue for the current experiments. As a matter of record, the sounds were intended to be two-phoneme sequences of the most common speech sounds in balanced, cv-vc pairs, rather than a representative sample of syllables from English. The vowels were pronounced as they are in most five vowel languages like Japanese and Spanish so that they could be used with a wide range of listeners; thus the pronunciation was /a/ as in "fa," /e/ as in "bay," /i/ as in "bee," /o/ as in "toe," and /u/ as in "zoo." Syllables involving a sonorant consonant, which would be diphthongs in English (e.g., oy), were pronounced more like two distinct phonemes than diphthongs so that the duration of the components would be similar in cv-vc pairs.

Once the recordings were edited and standardized as described above, STRAIGHT was used to generate all the different versions of each syllable with the specific combinations of VTL and GPR values required for the experiment. In STRAIGHT, the VTL is varied simply by dilating or contracting the spectral envelope of the recorded syllable. The change in VTL is described in terms of the ratio of the width of the new spectral envelope to that of the original spectral envelope. This spectral envelope ratio (SER) is inversely proportional to the change in the length of the vocal tract. SER values less than unity mean that the vocal tract has been made longer to synthesize a larger person; the process shifts all of the vocal tract resonances to lower frequencies. Figure 1 shows the five combinations of SER and GPR that were used as standards in the experiment; they were chosen to be characteristic of five speaker types. The SER value is also shown as a VTL in Fig. 1. The VTL is estimated from the data in Fitch and Giedd (1999). The height of the speaker (RP) was 173 cm and, for a person of this height, Fitch and Giedd give a VTL of 15.2 cm. This value was used as the reference and has an SER of 1.0. For the experimental stimuli, combination 1 has a low GPR of 80 Hz and a long VTL of 16.5 cm, which is characteristic of a large male. Combination 2 has a high GPR of 320 Hz and a long VTL of 16.5 cm, which is highly unusual for a human. Nevertheless, the syllables are readily recognized as speech from a tall person with a high pitch. For convenience in the paper, these speakers will be referred to as a "castrati." Combination 3 has a GPR of 160 Hz and a VTL of 12.5 cm, which is characteristic of an average-sized person somewhere between the average adult male and the average adult female. Combination 4 has a low GPR of 80 Hz and a short VTL of 9.2 cm, which is also highly unusual for a human. Again, the syllables are obviously speech but this time from a short person with a low pitch. For convenience in the paper, these speakers will be referred to as a "dwarves." Finally, combination 5 has a high GPR of 320 Hz and a short VTL of 9.2 cm, which is characteristic of a small child, either male or female.

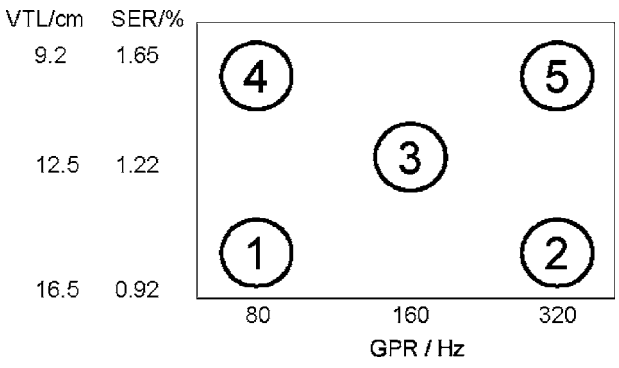

FIG. 1. The GPR-VTL combinations for the five reference speakers in the experiment. These speakers are typically heard as a large male (1), a castrato (2), a small male or a large female (3), a dwarf (4), and a small child (5).

The listeners were presented with two phrases of four syllables each; the one consistent difference between the phrases was the VTL of the speaker. The syllables were selected randomly, with replacement, from one of six groups within the database (e.g. CV-sonorants, CV-stops, CV-fricatives, VC-sonorants, VC-stops, or VC-fricatives). The level of the syllables in each phrase was roved between phrases over a 6-dB range. The GPR of each of the syllables within the phrase was varied along one of four pitch contours: rising, falling, up-down, and down-up. In the rising contour, the GPR of each successive syllable increased linearly such that the GPR of the last syllable was 10% higher than that of the first syllable. The falling contour was the reverse of the rising contour, i.e., the GPR of each successive syllable decreased linearly such that the first syllable had a GPR 10% higher than the last syllable. In the up-down contour the first and the last syllables had the same GPR values which were 10% lower than the GPR values of the second and third syllables. Finally, for the down-up contour, the first and last syllables had the same GPR values which were 10% higher than the second and third syllables. The starting value for the GPR contour was also varied over a 10% range. Thus, the only consistent difference between the two phrases was the VTL. One of the phrases, chosen at random, had one of the reference VTLs, that is, one of the five combinations shown in Fig. 1; the other phrase had a test VTL which was varied over trials to measure VTL discrimination. For each reference VTL, there were six test VTLs, three of which were longer and three of which were shorter. The three longer VTLs had lengths of 106%, 122%, and 143% relative to the reference, except for the castrato speech (point 2 in Fig. 1) for which the test VTLs had lengths of 103%, 110%, and 118% relative to the reference, and the small male/large female speech (point 3 in Fig. 1) for which the test VTLs had lengths of 103%, 112%, and 125% relative to the reference. The reduction in the range of VTLs for the castrato speech was due to difficulty in resynthesizing longer VTLs; F0 rises to values above the first formant in which case the vowel is ill defined (see Smith *et al.*, 2005; top panel of Fig. 3). The reduction in the range of VTLs for the small male/large female speech was due to pilot data showing that discrimination performance was improved for this range of VTLs. The three shorter VTLs had lengths of 77%, 85%, and 94% relative to the reference except for the small male/large female speech for which the test VTLs had lengths of 83%, 89%, and 96% relative to the reference. The change in the range of VTLs was again due to pilot data showing an improvement in discrimination performance for this reference VTL.

Discrimination performance was measured separately at each of the five points shown on Fig. 1, using a two-alternative, forced-choice paradigm (2AFC). The listener was asked to choose the phrase spoken by the smaller person, and to indicate their choice by clicking on the appropriate interval box on a computer screen. The subject had to discriminate between the reference value (taken from Fig. 1) and one of the three longer or three shorter VTLs. The data from the six VTL comparisons were combined to produce a psychometric function for one specific reference value. There were six listeners (three male and three female between 21 and 35 years of age); they all had normal hearing thresholds at 0.5, 1, 2, 4, and 8 kHz. There was a brief training session in which the listener was presented with about 20 trials with different VTLs chosen at random from the six test values. During this training session, feedback was provided to the listeners as to whether they had correctly identified the smaller speaker. Discrimination performance was then measured for that reference point with approximately 40 trails per reference point. During the discrimination measurement there was no feedback. This procedure was repeated for each of the six syllable groups in a random order which was selected individually for each listener. The sounds were presented at a level of 70 dB diotically over AKG K240DF headphones while seated in a double-walled IAC sound attenuating booth.

III. RESULTS

The results for each of the five reference speakers are shown in Fig. 2 as a set of psychometric functions, where the layout mirrors that for the reference conditions presented in Fig. 1. That is, the positions of psychometric functions reflect the position of the reference condition on the GPR-VTL plane; the small child is at the top right and the large man is at the bottom left. The data have been averaged across listeners because there was very little difference between listeners. They have also been averaged over syllable type, because the data for individual syllable types showed very similar patterns and levels of performance. The abscissa for the psychometric functions is VTL expressed as a ratio of the reference VTL; the ordinate is the percentage of trials on which the test interval was identified as having the smaller speaker. The error bars show ±2 standard deviations over all listeners and syllable types. A cumulative Gaussian function has been fitted to the data for each psychometric function and used to calculate the jnd. The jnd was defined as the difference in VTL for a 26% increase in performance from 50% to 76% performance; it is shown on each graph at the top left corner, and the error shows 2 standard deviations of the fitted Gaussian function. Figure 2 shows that size discrimination is possible for each of the five speaker types; performance is best for the small-male/large-female speaker type and poorest for the dwarf speaker type. The jnd values for the individual syllable groups are summarized in Table II.

A summary of the jnd values is shown in Fig. 3, which has the same layout as Figs. 1 and 2. The jnd's for the six syllable groups are shown separately for each speaker type. The jnd for both the large male speaker type and the small-male/large-female speaker type is stable at around 4% for all syllable types. The jnd for the castrato speaker type is slightly worse, particularly for syllables containing stop consonants for which the jnd is 5%–6%. The jnd's for the dwarf speaker type and the small child speaker type are around 7% and 6% respectively, and again it is worst for syllables with stop consonants.

IV. DISCUSSION

The jnd's for speaker size measured by Smith *et al.* (2005) with vowel sounds are included in the bottom row of

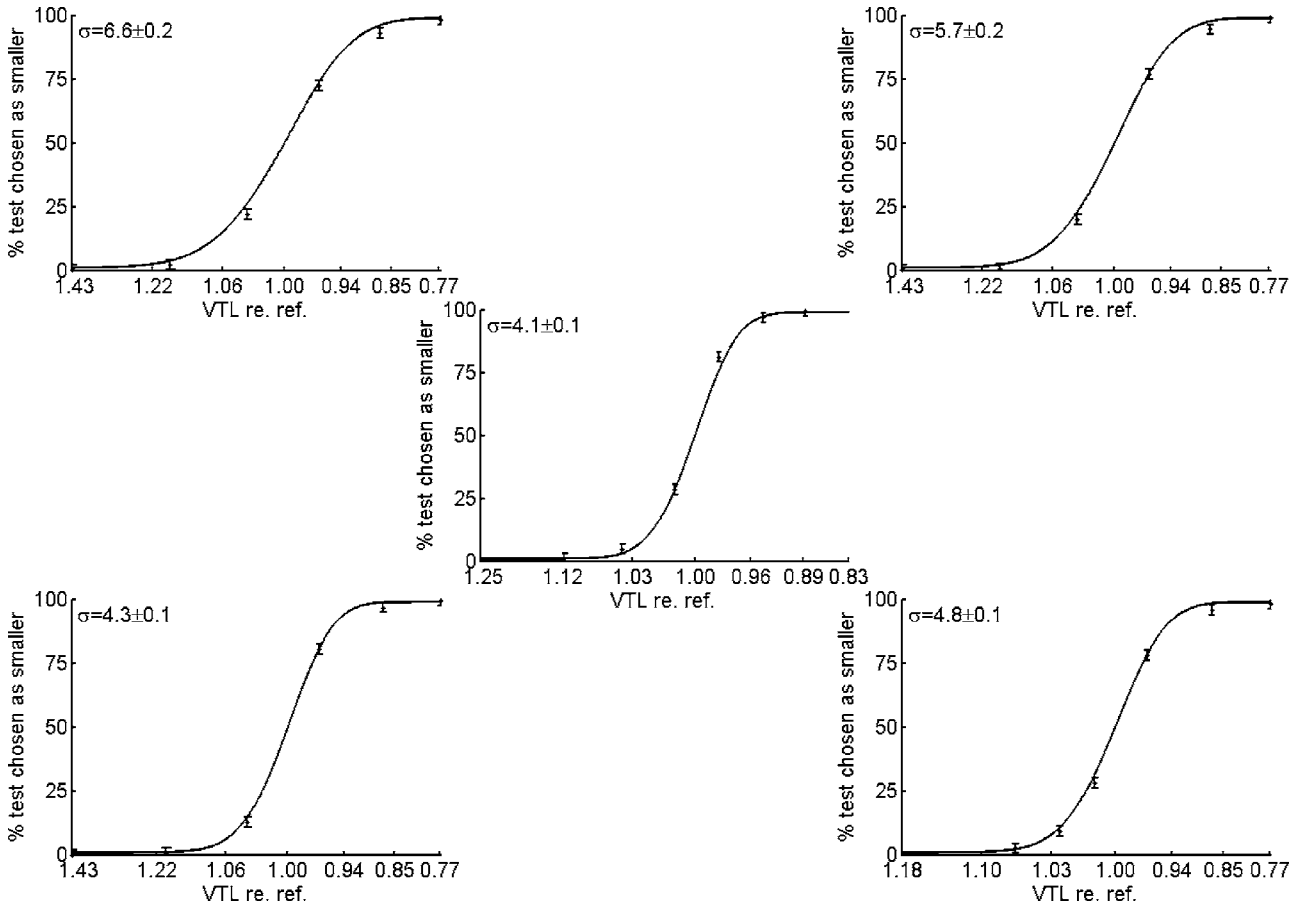

FIG. 2. Psychometric functions for the five reference speakers, averaged over all listeners, all syllables within group and all syllable groups (approximately 1400 trials per point on each psychometric function). The jnd value is the difference between 76% and 50% performance as estimated by the fitted Gaussian function. The jnd value is shown on each graph in the top left corner; the error bars represent 2 standard deviations.

Table II. When compared with the data of the current experiment, they show that discrimination performance is much better when syllables are used rather than just vowels, despite the increase in stimulus variability in the syllable version of the experiment. For the small-male/large-female, dwarf, and small child, the jnd for syllables is about 30% less than with isolated vowels. For the large male, the jnd has decreased by about 60%, and for the castrato the jnd value has decreased by about 70%. This improvement in performance may be due to the increased naturalness of the speech. Although Smith *et al.* (2005) used natural vowels, they applied an artificial amplitude envelope to the onset; the natural onset of the syllable was preserved in the current study. There was one other difference between the vowel and syllable experiments, which is the duration of the silence between the vowels or syllables: in the vowel experiment, the duration of the silence was a constant 40 ms; in the syllable experiment, due to the P-centering, the duration of the silence was much longer (between about 100 and 300 ms). This may have provided more time to process the individual syllables.

The content for each syllable type can be categorized into three components, namely, a voiced component (including any vowel information), a vowel component, and finally

TABLE II. The jnd values for all syllable groups averaged over all listeners.

Stimuli group	VTL-GPR condition 1	2	3	4	5
All	4.3±0.1	4.8±0.1	4.1±0.1	6.6±0.2	5.7±0.2
CV	4.0±0.2	5.0±0.2	4.0±0.2	5.9±0.2	5.3±0.2
VC	4.5±0.2	4.7±0.2	4.4±0.2	7.6±0.3	6.3±0.2
Sonorant	4.1±0.2	4.2±0.2	4.1±0.2	5.9±0.3	5.1±0.3
Stop	4.6±0.3	6.3±0.3	4.3±0.2	8.4±0.3	6.5±0.3
Fricative	4.2±0.2	4.4±0.2	3.8±0.2	5.7±0.3	5.3±0.3
Smith *et al.* (2005)	*10.5*	*17.2*	*6.6*	*10.6*	*9.3*

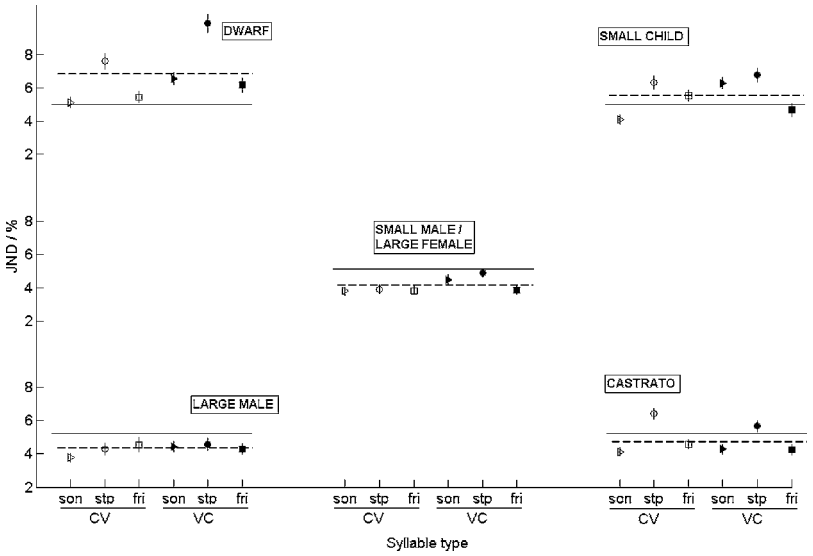

FIG. 3. The jnd values for the six syllable groups plotted separately for the five speaker types. The layout of speaker types is the same as in Figs. 2 and 3, i.e., large male at the bottom left and small child at the top right. The dotted line is the average jnd across syllable category for that specific speaker type. The solid, thin line is grand average jnd for the experiment plotted in each subfigure for comparison with the local average.

any other component which contains information about the vocal tract length which is not included by either of the two previous components (this is mainly noise from the fricatives and will be termed the noise component). Figure 4 shows the duration of each of these components for each of the six speech groups together with a summary for CVs and VCs. CV syllables have longer voiced components than VC syllables and significantly longer vowel components. The average length of the periodic component for a CV syllable is about 450 ms, whereas for a VC syllable, this is about 350 ms. The average vowel duration for CV syllables is about 400 ms, and for VC syllables this reduces to about 260 ms. Sonorants have the longest voiced and vowel components followed by stops and then fricatives, however this difference is only really apparent in the VC versions of the syllables. The increased amount of voiced/vowel content in the CV syllables may improve CV size discrimination when compared to VC syllables. There is only a small variation in the duration of the noise component of all speech sounds when compared to the much longer voiced and vowel components.

Assmann *et al.* (2002) and Assmann and Nearey (2003) argued that listeners can recognize scaled vowels because they have extensive experience with speech that has included examples of most syllables with many combinations of GPR and VTL. They showed that a neural network could learn the variability of the vowels in their experiment and suggested that the brain has a similar learning mechanism. However, Smith and Patterson (2004) and Smith *et al.* showed that vowel recognition is possible over a range of VTL and GPR values that extends far beyond that normally encountered during everyday experience. They argue that the auditory system uses a scale normalization process like that suggested by Irino and Patterson (2002) and that this avoids the need for an elaborate learning mechanism. Figure 5 shows the distribution of men, women, and children speaker types in

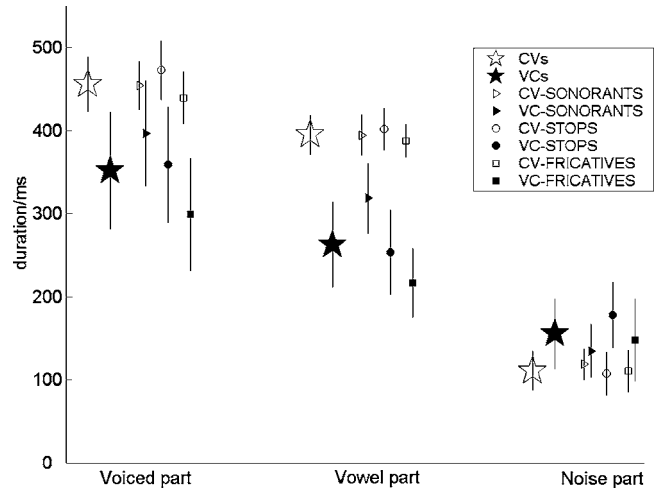

FIG. 4. The small symbols show the duration of the "voiced," "vowel," and "noise" components for each of the six syllable classes with error bars showing ±2 standard deviations. The large star symbols show the average values for all of the CV syllables (open) and all of the VC syllables (filled).

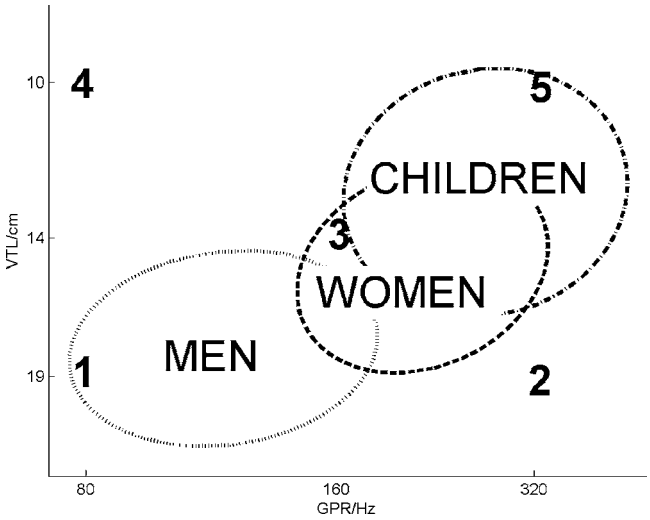

FIG. 5. Ellipses showing the distribution of vocal tract lengths and glottal pulse rates for men, women and children, based on the data of Peterson and Barney (1952). The ellipses encompass 96% of the data for each group. The numbered points show the reference speakers used in the experiment.

the GPR-VTL space. The three ellipses were derived from the classic data ofPeterson and Barney (1952) and each ellipse encompasses 96% of the population for that speaker group, which represents the vast majority of VTLs and GPRs that one would encounter in everyday life. The numbered points show the GPR-VTL conditions that were used in the experiment. Conditions 1 and 5, large man and small child, lie just within the extremities of their respective ellipses. Conditions 2 and 4 (castrato and dwarf) lie well outside these ellipses. Thus, the range of VTL-GPR combinations includes the full range of normal human speech and well beyond. The ability to discriminate size to such a fine resolution over this entire range supports the argument of Irino and Patterson (2002) that the auditory system includes a scale normalization process.

V. CONCLUSIONS

A series of VTL discrimination experiments has shown that it is possible to make fine discriminations about a person's size by listening to their speech. This shows that the size information in speech is available to the listener and changes in VTL alone produce reliable differences in perceived size. The average jnd values for VTL discrimination measured with phrases of syllables are between 4% and 6% depending on the location in the GPR-VTL space. These jnd's are considerably smaller than those obtained with vowels by Smith *et al.* (2005), despite the increase in the variability of the stimulus set. There is a small difference in the jnd between CV syllables and VC syllables with the former having the smaller jnd.

ACKNOWLEDGMENTS

Research supported by the U.K. Medical Research Council (G9901257) and the German Volkswagen Foundation (VWF 1/79 783). The authors would like to thank Peter Assmann and an anonymous reviewer for helpful comments on an earlier version of the manuscript.

[1]http://www.mrc-cbu.cam.ac.uk/cnbh/web2002/bodyframes/sounds_movies/ra_demo_16_06_04_files/slide0304.htm. (last updated 14 September 2005)

Assmann, P. F., and Katz, W. F. (**2005**). "Synthesis fidelity and time-varying spectral change in vowels," J. Acoust. Soc. Am. **117**, 886–895.

Assmann, P. F., and Nearey, T. M. (**2003**). "Frequency shifts and vowel identification," in Proceedings of the 15th Int. Congress of Phonetic Sciences, Barcelona ICPhS.

Assmann, P. F., Nearey, T. M., and Scott, J. M. (**2002**). "Modeling the perception of frequency-shifted vowels," in Proceedings of the 7th Int. Conference on Spoken Language Perception, ICSLP, pp. 425–428.

Boersma, P. (**2001**). "Praat, a system for doing phonetics by computer," Glot. Int. **5**(9/10), 341–345.

Cohen, L. (**1993**). "The scale transform," IEEE Trans. Acoust., Speech, Signal Process. **41**, 3275–3292.

Fant, G. (**1970**). *Acoustic Theory of Speech Production*, 2nd ed. (Mouton, Paris).

Fitch, W. T. (**1997**). "Vocal tract length and formant frequency dispersion correlate with body size in rhesus macaques," J. Acoust. Soc. Am. **102**, 1213–1222.

Fitch, W. T. (**1999**). "Acoustic exaggeration of size in birds by tracheal elongation: Comparative and theoretical analyses," J. Zool. **248**, 31–49 [discussed in "News & Views," Nature (London) **399**, 109 (**1999**)].

Fitch, W. T., and Giedd, J. (**1999**). "Morphology and development of the human vocal tract: A study using magnetic resonance imaging," J. Acoust. Soc. Am. **106**, 1511–1522.

Fitch, W. T., and Kelley, J. P. (**2000**). "Perception of vocal tract resonances by whooping cranes, *Grus Americana*," Ethology **106**(6), 559–574.

González, J. (**2004**). "Formant frequencies and body size of speaker: A weak relationship in adult humans," J. Phonetics **32**, 277–287.

Hast, M. (**1989**). "The larynx of roaring and non-roaring cats," J. Anat. **163**, 117–121.

Irino, T., and Patterson, R. D. (**2002**). "Segregating information about the size and shape of the vocal tract using a time-domain auditory model: The stabilized wavelet-Mellin transform," Speech Commun. **36**, 181–203.

Kawahara, H., and Irino, T. (**2004**). "Underlying principles of a high-quality speech manipulation system STRAIGHT and its application to speech segregation," in *Speech Segregation by Humans and Machines*, edited by P. Divenyi (Kluwer Academic, Boston), pp. 167–180.

Kawahara, H., Masuda-Kasuse, I., and de Cheveigne, A. (**1999**). "Restructuring speech representations using pitch-adaptive time-frequency smoothing and instantaneous-frequency-based *F*0 extraction: Possible role of repetitive structure in sounds," Speech Commun. **27**(3-4), 187–207.

Kunzel, H. (**1989**). "How well does average fundamental frequency correlate with speaker height and weight?" Phonetica **46**, 117–125.

Liu, C., and Kewley-Port, D. (**2004**). "STRAIGHT: a new speech synthesizer for vowel formant discrimination," ARLO **5**, 31–36.

Marcus, S. M. (**1981**). "Acoustic determinants of perceptual centre (P-centre) location," Percept. Psychophys. **30**, 247–256.

Mergell, P., Fitch, W. T., and Herzel, H. (**1999**). "Modelling the role of non-human vocal membranes in phonation," J. Acoust. Soc. Am. **105**, 2020–2028.

Owren, M. J., and Anderson, J. D., IV (**2005**). "Voices of athletes reveal only modest acoustic correlates of stature," J. Acoust. Soc. Am. **117**, 2375.

Patterson, R. D., Allerhand, M., and Giguere, C. (**1995**). "Time domain modeling of peripheral auditory processing: A modular architecture and a software platform," J. Acoust. Soc. Am. **98**, 1890–1894.

Patterson, R. D., Robinson, K., Holdsworth, J., McKeown, D., Zhang, C., and Allerhand, M. H. (**1992**). "Complex sounds and auditory images," in *Auditory Physiology and Perception, Proceedings of the 9th International Symposium on Hearing*, edited by Y. Cazals, L. Demany, and K. Horner (Pergamon, Oxford), pp. 429–446.

Peterson, G. E., and Barney, H. L. (**1952**). "Control methods used in the study of vowels," J. Acoust. Soc. Am. **24**, 175–184.

Rendall, D., Vokey, J. R., Nemeth, C., and Ney, C. (**2005**). "Reliable but weak voice-formant cues to body size in men but not women," J. Acoust. Soc. Am. **117**, 2372.

Riede, T., and Fitch, W. T. (**1999**). "Vocal tract length and acoustics of vocalization in the domestic dog *Canis familiaris*," J. Exp. Biol. **202**, 2859–2867.

Scott, S. K. (**1993**). "P-centres in speech an acoustic analysis," Ph.D thesis, University College, London.

Smith, D. R. R., and Patterson, R. D. (**2004**). "The existence region for scaled vowels in pitch-VTL space," 18th Int. Conference on Acoustics, Kyoto, Japan, Vol. **I**, pp. 453–456.

Smith, D. R. R., Patterson, R. D., and Jefferis, J. (**2003**). "The perception of scale in vowel sounds," British Society of Audiology, Nottingham, P35.

Smith, D. R. R., Patterson, R. D., Turner, R., Kawahara, H., and Irino, T. (**2005**). "The processing and perception of size information in speech sounds," J. Acoust. Soc. Am. **117**, 305–318.

Titze, I. R. (**1989**). "Physiologic and acoustic differences between male and female voices," J. Acoust. Soc. Am. **85**, 1699–1707.

Turner, R. E., Al-Hames, M. A., Smith, D. R. R., Kawahara, H., Irino, T., and Patterson, R. D. (**2005**). "Vowel normalisation: Time-domain processing of the internal dynamics of speech," in *Dynamics of Speech Production and Perception*, edited by P. Divenyi (IOS Press) (in press).

Psychophysical estimates of nonlinear cochlear processing in younger and older listeners

René H. Gifford[a] and Sid P. Bacon
Psychoacoustics Laboratory, Department of Speech and Hearing Science, P.O. Box 870102, Arizona State University, Tempe, Arizona 85287-0102

(Received 25 October 2004; revised 27 September 2005; accepted 28 September 2005)

The primary goal of this project was to compare the performance of younger and older listeners on a number of psychophysical measures thought to be influenced by nonlinear cochlear processing. Younger (mean of 25.6 years) and older (mean of 63.8 years) listeners with normal hearing were matched (within 5 dB) according to their quiet thresholds at the two test frequencies of 1200 and 2400 Hz. They were similarly matched at the adjacent octave frequencies of 600 and 4800 Hz (within 5 dB at one and 9 dB at the other). Performance was compared on measures of auditory filter shape, psychophysical suppression, and growth of forward masking. There was no difference between the two age groups on these psychophysical estimates reflecting nonlinear processing, suggesting that aging *per se* does not affect the cochlear nonlinearity, at least for the ages sampled here. The results did, however, consistently demonstrate an age-related increase in the susceptibility to forward masking. © *2005 Acoustical Society of America.* [DOI: 10.1121/1.2126933]

PACS number(s): 43.66.−x, 43.66.Ba, 43.66.Dc [AJO] Pages: 3823–3833

I. INTRODUCTION

Older listeners often experience poorer speech intelligibility than younger listeners, particularly in the presence of noise (e.g., Plomp and Mimpen, 1979; Duquesnoy and Plomp, 1980). Age-related hearing loss is the most likely cause of the difficulties in speech recognition exhibited by older listeners. The articulation index (AI), more recently referred to as the speech intelligibility index (SII), predicts that speech intelligibility performance will systematically decrease as increasing segments of the speech spectrum become inaudible to the listener (ANSI, 1997). Recent studies, however, have shown that substantial threshold elevation need not be present for older listeners to exhibit significant performance deficits on measures of speech intelligibility (Dubno *et al.*, 2002, 2003).

Aside from the effects of reduced audibility on speech recognition is the relationship between suprathreshold processing, especially temporal resolution, and aging. Temporal resolution has been found to be impaired in older listeners both with and without clinically significant hearing loss (e.g., Humes and Christopherson, 1991; Gordon-Salant and Fitzgibbons, 1999; Schneider *et al.*, 1994; Snell, 1997). Although impaired temporal resolution likely contributes to age-related deficits in speech intelligibility, it cannot account entirely for the reduced intelligibility (e.g., Humes and Christopherson, 1991).

Another potential contributor to reduced speech understanding among older listeners is a reduced cochlear nonlinearity. Nonlinear cochlear processing is responsible for, among other things, high sensitivity, sharp tuning, and enhanced spectral contrasts via suppression. It is well known that healthy outer hair cells (OHCs) are responsible for this nonlinearity (e.g., Liberman and Dodds, 1984). Several studies have examined the effects of aging on OHC function using evoked otoacoustic emissions (OAEs). Examining distortion product otoacoustic emissions (DPOAEs) as an index of outer hair cell (OHC) functioning, McFadden *et al.* (1997a) reported significant differences between younger and older chinchillas in terms of DPOAE thresholds and amplitudes. Similar findings have also been observed in the CBA mouse (Parham *et al.*, 1999). These comparisons between the younger and older animals, however, may not have isolated changes in aging alone, because the older animals had auditory thresholds that were higher than the thresholds for the younger animals (McFadden *et al.*, 1997a; Parham *et al.*, 1999). Thus, it is possible that elevated thresholds may have influenced the results.

McFadden *et al.* (1997b) conducted another study examining suprathreshold measures of auditory functioning as a function of age in the chinchilla auditory system. All testing was completed at frequencies (1) that were within the limits of normal hearing in even the aged chinchillas and (2) where no significant age differences in quiet thresholds were observed. They obtained measures of frequency selectivity, including evoked potential tuning curves and DPOAEs following acoustic overstimulation. Results showed that the evoked potential tuning curves measured from the aged animals were more broadly tuned than those measured from the young, control animals. Inasmuch as we can attribute broadened tuning to a loss of OHC-driven nonlinearity (e.g., Liberman and Dodds, 1984), one may conclude that the older animals exhibited a decrease in cochlear nonlinearity independent of hearing loss. In addition, the post-acoustic-overstimulation DPOAE data showed that the older animals had a greater initial reduction in DPOAE amplitude following the noise, as well as a greater overall reduction in DPOAE amplitude with time. Thus it appears that the ability of the OHCs to recover following intense acoustic stimula-

[a]Author to whom correspondence should be addressed; Electronic mail: Rene.Gifford@asu.edu

tion is reduced in older as compared to younger animals. These age-induced changes were observed in the absence of hearing loss in the frequency range tested.

Research examining DPOAEs (Dorn *et al.*, 1998) and transient-evoked otoacoustic emissions (TEOAEs) (e.g., Satoh *et al.*, 1998) in humans has revealed findings similar to the animal studies. Specifically, older subjects have been shown to exhibit higher OAE thresholds and lower amplitudes than younger subjects. A potentially critical problem with the interpretation of these OAE studies in humans is that no attempt has been made to match younger and older subjects on the basis of auditory thresholds. Simply requiring that thresholds not exceed 15 or 20 dB HL could yield comparisons between subjects with threshold differences of 20 dB or more in a range considered *clinically normal*.

Aside from the issue of potentially elevated thresholds in older subjects, another difficulty with the interpretation of all OAE data is that significant changes in middle ear stiffness have been found in aged mice (Doan *et al.*, 1996). Thus, one cannot discount middle ear changes as contributing to the age-related changes in OAEs. However, in support of compromised OHC functioning are reports of histopathologic changes in aged cochleae, particularly in the stria vascularis which plays a critical role in maintaining OHC function (e.g., McFadden *et al.*, 1997a).

There are a number of psychophysical measures that are thought to depend upon normally functioning OHCs, including frequency selectivity and the nonlinear phenomena of suppression and basilar membrane compression. If age affects OHC function, then one might expect to see differences between younger and older listeners on these measures. For example, if OHCs are compromised by aging, auditory filters (AFs) should be broader in older than in younger listeners. However, the research on the effects of age on AF shapes is equivocal. Patterson *et al.* (1982) found that older subjects exhibited wider AF bandwidths for all signal frequencies tested (even for those frequencies where age-related threshold differences were minimal), whereas others have not (Peters and Moore, 1992; Sommers and Humes, 1993; Peters and Hall, 1994; Sommers and Gehr, 1998). The generalizability of these results to the nature of the cochlear nonlinearity in older listeners may be limited. For example, Peters and Moore (1992) completed all testing at signal frequencies below 1000 Hz, where nonlinear cochlear processing may be less frequency selective than at higher frequencies (Plack and Drga., 2003), and thus where the effects of age may be less clear. Further, a potential problem with all of these studies is that the filter shapes have been derived with the assumption that the masker level determines the shape of the filter. Rosen and Baker (1994) and Rosen *et al.* (1998) have shown that the AF shape is more likely determined by signal level. Thus, it may be more appropriate either to analyze results using a fixed masker level differently [using the PolyFit procedure (Rosen and Baker, 1994)] or to employ a fixed, low-level signal (Oxenham and Shera, 2003).

If advanced age adversely affects OHCs, then one would expect to observe less suppression in older than in younger listeners. Few have examined the relationship between psychophysical suppression and aging. However, what research has been done suggests that suppression is reduced in older listeners (Sommers and Gehr, 1998; Dubno and Ahlstrom, 2001b, c). However, Dubno and Ahlstrom (2001b, c) included older normal-hearing listeners whose audiometric thresholds were higher than those of the younger normal-hearing listeners. Thus, as of yet, there is not a clear picture of the relationship between aging and suppression, independent of hearing loss.

The growth of response of the basilar membrane is highly compressive for a tone equal to or near the characteristic frequency (CF) of the measurement site (e.g., Ruggero *et al.*, 1997), although it is linear for a tone much lower in frequency than CF (though this may not be the case at low CFs—see Plack *et al.*, 2004; Lopez-Poveda *et al.*, 2005; Williams and Bacon, 2005). One way to estimate basilar membrane compression psychophysically is with a masking experiment, in which the masker frequency (f_m) is well below the signal frequency (f_s) (for a recent review, see Oxenham and Bacon, 2004). In young listeners with normal hearing, the masking function has a slope quite different from 1.0 (i.e., from linearity), being much greater than 1.0 when signal level is plotted as a function of masker level (e.g., Bacon *et al.*, 1998) and much less than 1.0 when masker level is plotted as a function of signal level (e.g., Oxenham and Plack, 1997). The slope of the masking function is linear, or at least closer to linear, when the OHCs are compromised by either permanent (Oxenham and Plack, 1997) or temporary aspirin-induced hearing loss (Hicks and Bacon, 2000). If age adversely affects OHCs, then the masking functions in older listeners would be expected to be more linear than they are in younger listeners. There are, however, no published data examining the effects of age on masking functions designed to estimate basilar membrane compression.

Psychophysical studies examining nonlinear cochlear processing in normal-hearing listeners following a course of aspirin ingestion have demonstrated broader AFs, reduced or eliminated two-tone suppression, and less compression on psychophysical masking experiments where $f_m < f_s$ (Hicks and Bacon, 1999, 2000). These effects were observed even for frequencies where minimal shifts in quiet threshold were observed (as low as 5 dB). Thus, it appears that even mild disturbances of OHC function (Hicks and Bacon, 1999, 2000)—that may or may not yield a significant elevation of quiet threshold—can translate to significant functional effects on psychophysical measures of auditory function. It follows that subtle changes in active cochlear mechanics that may be attributable to age might also yield considerable functional deficits on measures of nonlinear cochlear processing.

In summary, although there is histopathological and physiological evidence that aging adversely affects OHC functioning, possibly independent of hearing loss, there have been few studies designed to examine the relationship between aging and psychophysical estimates of nonlinear processing. Further, the collective results of these studies are equivocal. There is a need for such studies given the importance of normally functioning OHCs on the perception of sound, and the fact that many older listeners often experience

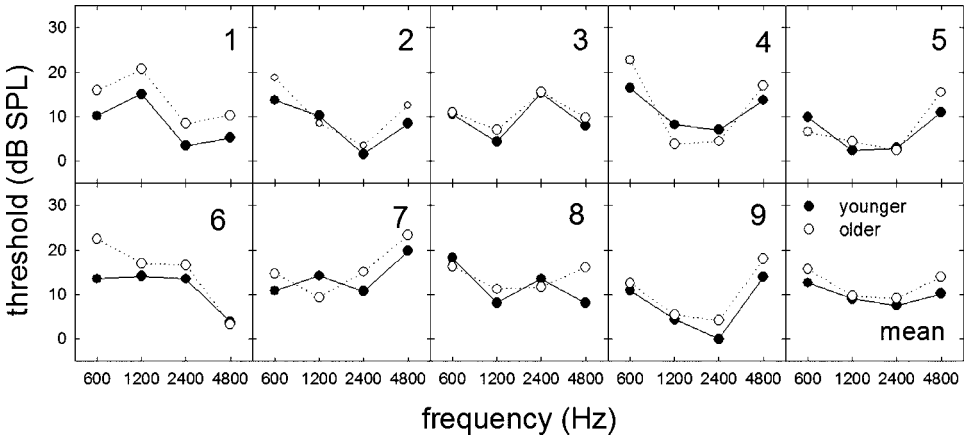

FIG. 1. Individual and mean quiet thresholds for a 200-ms signal for the younger (filled symbols) and older (unfilled symbols) listeners.

more difficulty understanding speech than would be expected from their pure-tone hearing loss. Thus, the goal of this project was to compare the performance of younger and older listeners on three psychophysical measures thought to depend upon normally functioning OHCs, to determine whether an age-related decline in nonlinear cochlear processing exists.

II. METHODS

A. Subjects

All three experiments were designed to examine measures at two signal frequencies, 1200 and 2400 Hz. These frequencies were chosen so that it was possible to obtain older subjects with normal hearing in the range of frequencies from one octave below to one octave above f_s. The reason that hearing was required to be normal above the test frequency is that the cochlear location of the nonlinearity ranges from $\frac{1}{3}$ to $\frac{1}{2}$ of an octave above that of the cochlear place corresponding to the CF of the test stimulus (e.g., Davis, 1983). Thus, it is important to control for hearing thresholds located above the signal frequencies. The reason for controlling hearing thresholds below the test frequency was to control audibility of maskers that were lower in frequency than the signal.

Nine younger and nine older subjects with normal hearing were recruited from Arizona State University and the surrounding communities. With the exception of the ninth younger/older subject pair, the same subjects in each group completed all three experiments. The subjects included in the *younger* age category were 30 years of age or younger and the *older* subjects were 60 years of age or older. All older listeners were considered as "high functioning" with respect to mental alertness and intellect. For example, one of the older listeners was a graduate student in the Audiology program, one was a practicing oral surgeon, one was a retired college professor fluent in multiple languages, three were retired schoolteachers, and one was a recently retired engineer. The other two were both retired from a business-like working environment. The mean age of the younger subject group was 25.6 years with a range of 19 to 30 years. The mean age of the older subject group was 63.8 years with a range of 60 to 75 years. The criterion for inclusion was hearing thresholds $\leqslant$15 dB HL at audiometric test frequencies from 250 to 6000 Hz. The younger and older subjects were matched according to their quiet thresholds for 200-ms signals. The original criterion required less than a 5-dB difference in quiet thresholds at 600, 1200, 2400, and 4800 Hz. Given the difficulty in obtaining older subjects with normal hearing and then matching a younger subject to those thresholds, however, the criterion was relaxed such that quiet thresholds needed to match within 5 dB for the two test frequencies (1200 and 2400 Hz) and one of the other two frequencies, but that differences of up to 9 dB were acceptable at the fourth frequency. The subjects were classified such that younger subject 1 (Y1) was matched to older subject 1 (O1), and so on. Figure 1 displays the individual and mean quiet thresholds for the 200-ms signals for all subjects enrolled in the study. The thresholds for the 1200- and 2400-Hz signals are also given in Table I, along with thresholds for 10- and 20-ms signals at those frequencies.

TABLE I. Quiet thresholds (in dB SPL) at 1200 and 2400 Hz for signal durations of 10, 20, and 200 ms. Subject matching was achieved on the basis of the thresholds for the 200-ms signals.

	1200 Hz			2400 Hz		
Subject	10 ms	20 ms	200 ms	10 ms	20 ms	200 ms
Y1	19.6	20.1	15.1	20.1	17.9	3.4
Y2	26.1	26.2	10.2	12.8	12.6	1.5
Y3	15.2	14.9	4.3	28.2	27.8	15.3
Y4	26.0	20.5	8.2	30.4	16.5	7.0
Y5	23.2	16.5	2.4	19.3	13.4	2.9
Y6	24.2	21.5	14.1	19.5	16.0	13.5
Y7	34.3	24.6	14.2	31.3	23.2	10.8
Y8	18.5	17.2	8.1	23.5	21.2	13.5
Y9	23.1	21.4	4.4	25.3	14.2	–0.1
Mean	23.4	20.3	9.0	23.4	18.1	7.5
O1	30.9	27.6	20.0	21.9	19.4	8.4
O2	26.9	23.4	8.5	21.5	15.6	3.5
O3	25.3	23.8	7.0	28.8	24.7	15.5
O4	22.2	15.5	3.8	20.7	17.2	4.4
O5	23.3	20.1	4.3	18.4	13.9	2.3
O6	34.3	30.7	17.0	24.9	23.5	16.7
O7	22.7	20.6	9.4	27.9	26.7	15.1
O8	25.0	22.3	11.2	27.3	21.8	11.7
O9	20.1	19.0	5.4	22.9	17.7	4.2
Mean	25.6	22.6	9.6	23.8	20.1	9.1

With the exception of subject Y8 (the first author), all subjects were paid an hourly wage for their participation. Subjects Y3, Y6, and Y8 were experienced listeners in psychoacoustic experiments similar to those in the present study. Regardless of past listening experience, all subjects were provided with training prior to data collection (specifics are given below).

B. General procedures

Thresholds for all experiments were measured in an adaptive, two-interval, forced-choice paradigm with a decision rule to track 79.4% correct (Levitt, 1971). That is, after three consecutive correct responses, the task was made more difficult and after one incorrect response, the task was made easier. Each reported threshold is based on at least three runs typically obtained over at least two different test sessions. For any given experiment, test sessions lasted approximately 2 h. Subjects were typically scheduled for one to two sessions per week. On average, subjects were able to complete data collection in approximately four to five sessions (including training). Since all three experiments involved forward masking, which some subjects may find somewhat difficult, all subjects were trained for at least 1.5 h on conditions from experiment 1, with an average training time of approximately 2.5 h. Data collection commenced once threshold estimates appeared stable.

Tonal stimuli were generated and produced digitally at a 20-kHz sampling rate. The noise masker in experiments 1 and 2 was produced by an analog random noise generator (General Radio 1381). All gated stimuli were shaped with $\cos^2$ rise/fall times. In all three experiments, the sinusoidal signal was output through one channel of a 16-bit digital-to-analog converter (DAC), whereas the masker was output through the second channel of the DAC (TDT DA1). The output of each channel was low-pass filtered at 8 kHz (Kemo, VBF.25.01, 135 dB/oct), attenuated by separate programmable attenuators (Wilsonics PATT), ultimately added together, and routed monaurally to one channel of Sony MDR-7506 stereo headphones via a headphone buffer (TDT HB6). To avoid electrical crosstalk, the headphone of the nontest ear was disconnected by means of a custom-made switchbox.

Subjects were tested in a double-walled, sound-attenuating booth. The interstimulus interval was 500 ms. The observation intervals were indicated by lights on a response box. For experiments 1 (AF shapes) and 3 (masking functions), forward-masked thresholds were measured by fixing the signal level and varying the masker level. For experiment 2 (suppression), thresholds were measured by fixing the level of the masker and varying the level of the signal. The maximum level for the dynamically varying stimulus was 95 dB SPL for tonal stimuli and 45 dB SPL (spectrum level) for the notched-noise stimuli. During a run, it was permissible for the threshold track to reach the ceiling value; however, if the tracking procedure called for a higher level, that run was discarded. If two runs for a particular condition were discarded on this basis, it was concluded that a masked threshold for that individual condition could not be achieved.

The tonal signal was presented randomly in one of two intervals. Subjects responded by pressing a button on the response box corresponding to what they believed to be the signal interval. Visual correct-answer feedback was provided. A run consisted of 50 trials. The first two (or three) reversals were discarded and the threshold estimate was determined using the average signal or masker level at the remaining even number of reversal points. All threshold estimates are based on the average of at least six reversals. If a run produced an estimate based on the average of less than six reversals, that particular run was discarded. The initial step size of 5 dB was decreased to 2 dB after the second reversal. On the rare occasion that an estimate had a standard deviation greater than 5 dB, that run was discarded. All reported thresholds represent the mean of at least three estimates. If the standard deviation of the mean of those estimates was greater than 3 dB, one additional run was completed and averaged. Out of the 738 thresholds obtained, 697 (94.4%) had standard deviations less than 3 dB and 540 (73.2%) had standard deviations less than 2 dB.

III. EXPERIMENT 1: AUDITORY FILTER (AF) SHAPE

A. Stimuli and conditions

AF shapes were derived using the notched-noise method (Patterson *et al.*, 1982) in a forward-masking paradigm to avoid any masking by suppression. This would be of critical importance given that psychophysical suppression—which would effectively broaden AF bandwidth—may be influenced by age independent of hearing loss. The notched-noise maskers were produced by low-pass filtering (Kemo VBF 25.01, 135 dB/oct) random noise from two independent analog noise generators (General Radio 1381) and multiplying each low-pass noise by a sinusoid (HP 8904 A synthesizer). This method produced a noise masker that was comprised of two noise bands each having a bandwidth that was twice the cutoff frequency of the low-pass filter and a center frequency that was equivalent to the sinusoidal frequency.

Each band of noise ($0.4f_s$ wide) was placed symmetrically or asymmetrically around f_s. Given that it is possible to obtain accurate (and time-efficient) estimates of the AF shape with just five notch widths (e.g., Stone *et al.*, 1992), the following five notch widths, expressed as a proportion of f_s, were used: symmetric—0.0 (no notch), 0.1, and 0.2 f_s; asymmetric—closer edge 0.1 f_s, farther edge 0.2 f_s (in one case the lower frequency band was closer, and in the other the higher frequency band was closer).[1] The signal was fixed at a level of 10 dB sensation level (SL), and the masker level was varied adaptively. The masker and signal were 300 and 20 ms in duration, respectively. All durations include a 10-ms $\cos^2$ rise/fall time. The onset of the signal was delayed 5 ms following the offset of the masker to minimize confusion effects (Neff, 1985).

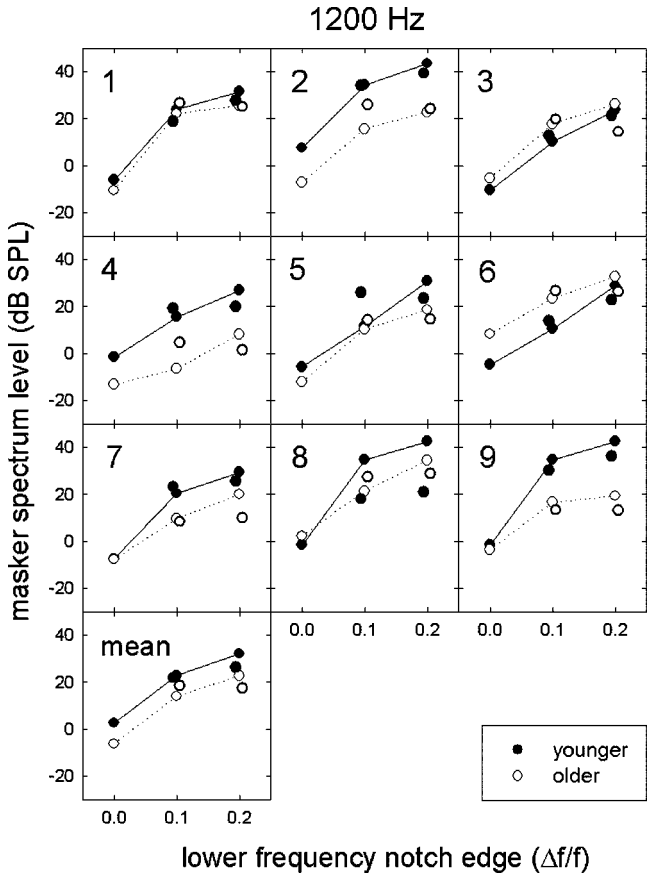

FIG. 2. Masker spectrum levels required to mask the 10-dB-SL, 1200-Hz signal for the younger (filled symbols) and older (unfilled symbols) subjects. Thresholds for the asymmetric notch width conditions are offset for clarity.

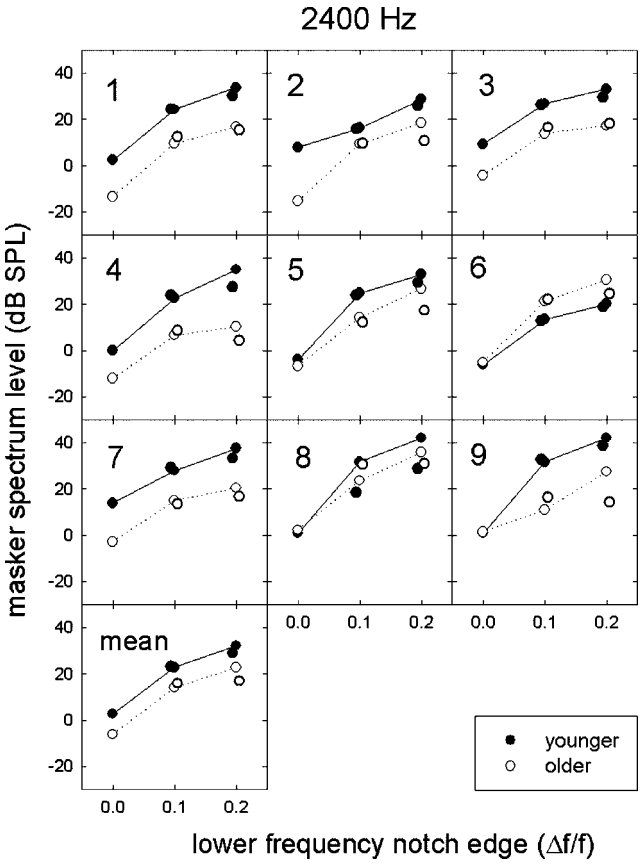

FIG. 3. As Fig. 2, but for the 2400-Hz signal.

B. Results and discussion

Figures 2 and 3 display the masker spectrum levels required to mask the 10-dB-SL signal for the younger (filled circles) and older (unfilled circles) subjects at 1200 and 2400 Hz, respectively. The data for the asymmetrical conditions are offset slightly relative to the symmetrical conditions, and not connected by a line. For both f_s, the masker level at threshold generally increased with increasing notch width. The masker levels at threshold, however, were generally lower for the older subjects, indicating a greater susceptibility to forward masking. A two-way repeated-measures analysis of variance (ANOVA) of masker levels at threshold for the 1200-Hz signal condition revealed no effect of age [$F(1,16)=2.4$, $p=0.14$], a significant effect of notch width [$F(1,4)=225.1$, $p<0.001$], and no interaction between age and notch width [$F(1,16)=3.3$, $p=0.06$]. The same analysis was computed for 2400 Hz revealing a significant effect of age [$F(1,16)=11.7$, $p=0.004$], a significant effect of notch width [$F(1,4)=222.6$, $p<0.001$], and no interaction between age and notch width [$F(1,16)=1.4$, $p=0.24$]. Comparing average thresholds (collapsed across notch width) across the age groups, the masker levels at threshold were 5.3 dB lower for the older listeners at 1200 Hz and 9.4 dB lower for the older listeners at 2400 Hz. Thus, although the age effect did not reach significance at 1200 Hz, there is still a trend for masker levels at threshold to be lower for the older listeners—indicating a greater susceptibility to forward masking for the older listeners.

Although the subjects were carefully matched for quiet thresholds using 200-ms signals, subject pairs were not matched as well for the 20-ms signals (see Table I). The group mean thresholds for the 20-ms thresholds, however, were closely matched. Moreover, a two-way repeated-measures ANOVA revealed no significant effect of age [$F(1.16)=2.0$, $p=0.17$] or frequency [$F(1,16)=2.5$, $p=0.13$] on the 20-ms thresholds. Thus, the differences in masker levels between the groups in Figs. 2 and 3 cannot be accounted for by differences in quiet thresholds for the 20-ms signal.

The masker levels at threshold were used to derive filter shapes using the roex (p,k) model (Patterson *et al.*, 1982). The parameter p represents the slope of the filter skirts, and k represents the processing efficiency—or the signal-to-masker ratio at threshold. This model set the upper and lower skirts of the filter symmetrically about f_s. The results of the fitting procedure are displayed in Table II.

The equivalent rectangular bandwidth [(ERB_n), Glasberg and Moore, 1990] values are similar for the younger and older subject pairs. These values, however, are generally lower than most reported in the literature. There are several possible reasons for this finding. First, many of the ERB_n values in the literature were obtained in simultaneous masking and at masker spectrum levels in the range of 40 to 60 dB SPL. Given that AF bandwidths are broader in

TABLE II. ERB_n (Hz), p, k (dB), and rms (dB) values for the individual younger and older subjects (and the mean values) for the 1200- and 2400-Hz tonal signals. The roex (p,k) filter model of Patterson *et al.* (1982) was used to derive the filter shapes. The mean estimates represent filters fitted to the mean thresholds and not the mean of the individual parameters.

	Younger subjects					Older subjects			
	ERB_n	p	k	rms		ERB_n	p	k	rms
				1200 Hz					
Y1	91	53	10	5	O1	99	48	14	6
Y2	91	53	4	4	O2	93	52	19	7
Y3	94	51	12	3	O3	97	50	16	4
Y4	116	42	10	2	O4	113	43	18	2
Y5	91	53	10	4	O5	103	47	17	4
Y6	94	51	16	5	O6	131	37	12	2
Y7	90	54	17	5	O7	118	40	16	2
Y8	90	53	9	5	O8	98	49	7	3
Y9	84	57	5	6	O9	141	34	8	4
Mean	91	53	9	3	Mean	108	44	16	3
				2400 Hz					
Y1	193	50	−1	3	O1	202	48	15	4
Y2	216	45	−8	2	O2	194	49	14	5
Y3	246	39	2	2	O3	219	44	11	4
Y4	184	52	2	3	O4	246	39	12	4
Y5	181	53	−2	5	O5	188	51	6	2
Y6	204	47	6	3	O6	182	53	14	4
Y7	241	40	−6	1	O7	252	38	13	3
Y8	236	41	5	3	O8	189	51	3	3
Y9	173	55	−6	5	O9	247	39	5	1
Mean	198	49	−1	2	Mean	226	42	10	3

simultaneous masking (Sommers and Gehr, 1998) and at high levels (e.g., Hicks and Bacon, 1999), it is reasonable to assume that the narrower bandwidths in the current study are a result of the forward-masking paradigm and the relatively low signal and masker levels employed. Consistent with this are the recent results of Oxenham and Shera (2003), who used a 10-dB-SL signal in a forward-masking paradigm and observed AF bandwidths similar to those reported here.

A two-way repeated-measures ANOVA revealed no effect of age $[F(1,16)=3.1,\ p=0.1]$ and a significant effect of frequency on the ERB_n values $[F(1,16)=119.6,\ p<0.001]$. There was no interaction between age and frequency $[F(1,16)=0.4,\ p=0.6]$. Thus, there was no difference between the younger and older subjects in terms of frequency selectivity as measured here.

IV. EXPERIMENT 2: SUPPRESSION

A. Stimuli and conditions

It is possible to measure suppression with a band-widening procedure. As the bandwidth of the noise masker is increased beyond a critical band, the noise components outside the critical band may suppress those within the critical band, resulting in a decrease in forward masking (e.g., Houtgast, 1974). Using several different band-widening methods, Dubno and Ahlstrom (2001a, b) have shown that fixing the upper cutoff frequency of the masker and subsequently increasing the bandwidth below that cutoff produces the greatest amount of suppression. Thus, experiment 2 used a similar band-widening procedure. Forward-masked thresholds were obtained as a function of masker bandwidth. The noise masker was produced by low-pass filtering (Kemo VBF 25.01, 135 dB/oct) random noise (General Radio 1381) and multiplying that noise by a sinusoid (HP 8904 A synthesizer).

TABLE III. Masker bandwidths and lower and upper cutoff frequencies of the masker for each signal frequency used for the measurement of suppression (in experiment 2).

Signal frequency (Hz)	
1200 Hz masker BW, spectral range	2400 Hz masker BW, spectral range
134 Hz, 1133–1267 Hz	246 Hz, 2277–2523 Hz
398 Hz, 869–1267 Hz	731 Hz, 1792–2523 Hz
610 Hz, 657–1267 Hz	1122 Hz, 1401–2523 Hz
782 Hz, 485–1267 Hz	1438 Hz, 1085–2523 Hz
920 Hz, 347–1267 Hz	1692 Hz, 831–2523 Hz
1031 Hz, 236–1267 Hz	1897 Hz, 626–2523 Hz

The masker had an initial bandwidth of one ERB_n, and was centered at the signal frequency.[2] Six masker bandwidths, increasing in 2-ERB_n steps relative to the lower frequency edge of the 1-ERB_n masker, were tested for each f_s. Table III displays the six bandwidths used for each f_s, as well as the frequency ranges of each masker bandwidth. The masker and signal were 300 and 20 ms in duration, respectively (including 10-ms $\cos^2$ rise/fall times). The signal onset was delayed 5 ms following the offset of the masker in an attempt to minimize confusion effects (Neff, 1985). The masker level was fixed at a spectrum level of 45 dB SPL, and the signal level was varied adaptively. This relatively high masker level was chosen because suppression tends to increase with level and it was shown previously to reveal differences in suppression between younger and older listeners (Dubno and Ahlstrom, 2001a, b).

B. Results and discussion

Figure 4 displays the results for the younger (filled symbols) and older (unfilled symbols) listeners. Circles represent thresholds for the 1200-Hz signal and triangles represent the thresholds for the 2400-Hz signal. For the majority of the conditions, the thresholds for the older subjects were higher than those of the younger subjects. This trend for greater forward masking was also observed in experiment 1.

A reduction in threshold with increasing masker bandwidth beyond the 1-ERB_n condition provides evidence of suppression. The maximum amount of suppression for each subject was calculated by subtracting the lowest threshold (usually at the widest BW) from the threshold for the 1-ERB_n condition (see Table IV). On average, the amount of suppression exhibited by the younger and older listeners was essentially equivalent. The average amount of maximum suppression for the younger subjects was 21.7 dB at 1200 Hz and 23.1 dB at 2400 Hz. The average amount of maximum suppression for the older subjects was 21.3 dB at 1200 Hz and 20.9 dB at 2400 Hz. A two-way repeated-measures ANOVA revealed that there was no significant effect of age

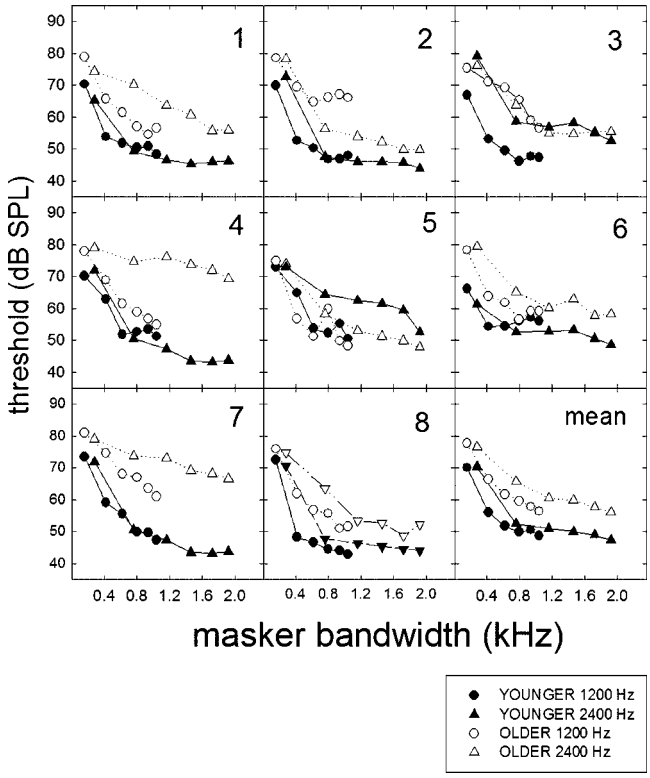

FIG. 4. Masked thresholds for the younger (filled symbols) and older (unfilled symbols) listeners for both the 1200-(circles) and 2400-Hz (triangles) signals. The thresholds are plotted as a function of masker bandwidth.

$[F(1,14)=0.4,\ p=0.5]$ on the amount of maximum suppression, nor was there a significant effect of frequency $[F(1,14)=0.07,\ p=0.8]$ or an interaction between age and frequency $[F(1,14)=0.4,\ p=0.5]$. However, statistical analysis performed on the thresholds revealed an effect of age $[F(1,14)=19.8,\ p<0.001]$, with no effect of frequency $[F(1,14)=0.5,\ p=0.5]$ and no interaction between age and frequency $[F(1,14)=0.03,\ p=0.9]$. The effect of age resulted from the thresholds being 9.1 dB higher, on average, for the older subjects.

Dubno *et al.* (2003) observed 3 to 7 dB higher forward-masked thresholds in their older listeners compared to their younger listeners, although the two groups revealed similar amounts of masking. In the present study, the older subjects exhibited higher forward-masked thresholds (9.1 dB on average) and greater amounts of forward masking (7 dB on average) than their younger counterparts.

V. EXPERIMENT 3: MASKING FUNCTIONS ($f_m<f_s$)

A. Stimuli and conditions

Masking functions were measured for tonal maskers and signals. The signal level was fixed from 40 to 90 dB SPL (or the highest level possible such that the level of the masker did not exceed 95 dB SPL), in 5-dB steps. The masker level was varied adaptively. The corresponding f_m was 3 ERBs below each f_s. Thus, the f_m was 806 Hz for the 1200-Hz signal and 1675 Hz for the 2400-Hz signal. The masker duration was 300 ms and the signal duration was 10 ms (including 10- and 5-ms $\cos^2$ rise/fall times for the masker and signal, respectively). A delay of 5 ms between the masker offset and the signal onset was incorporated to minimize any temporal overlap between the masker and signal due to ringing in the auditory filter (see Oxenham and Plack, 1997) and confusion effects (Neff, 1985). To reduce the possibility of off-frequency listening, a high-pass noise, with a cutoff frequency of $1.12f_s$, was presented continuously at a spectrum level that was 55 dB below the level of the signal (Oxenham and Plack, 1997).

TABLE IV. Individual estimates of maximum suppression. Suppression has been calculated as the difference between the masked threshold for the 1-ERN_n masker and the lowest masked threshold obtained—which typically occurred for the broadest masker bandwidth condition.

Younger subjects	Suppression estimate (dB)	Older subjects	Suppression estimate (dB)
	1200 Hz		
YN1	21.9	ON1	22.5
YN2	22.0	ON2	13.7
YN3	20.8	ON3	18.5
YN4	18.9	ON4	22.9
YN5	22.4	ON5	26.2
YN6	12.0	ON6	21.3
YN7	26.0	ON7	20.0
YN8	29.7	ON8	25.0
Mean	21.7	Mean	21.3
	2400 Hz		
YN1	20.0	ON1	19.1
YN2	29.1	ON2	28.3
YN3	24.9	ON3	23.0
YN4	22.9	ON4	9.7
YN5	20.5	ON5	27.1
YN6	12.7	ON6	21.7
YN7	28.1	ON7	12.5
YN8	26.5	ON8	26.0
Mean	23.1	Mean	20.9

B. Results and discussion

Results are shown in Fig. 5. The filled and unfilled symbols represent the younger and older subjects, respectively. Circles represent the results for the 1200-Hz signal and triangles represent the results for the 2400-Hz signal. Given that the masking functions extended over different signal levels for the different subjects, group mean results were not calculated. To obtain an estimate of compression, the slopes of the masking functions were derived via linear regression analysis for the data points corresponding to signal levels in the range of 50 to 75 dB SPL. All estimates of compression for the masking functions are shown in Table V. These estimates were generally similar across the groups. The average compression estimates at 1200 Hz were 0.46 for both the younger and older listeners, whereas the average compression estimates at 2400 Hz were 0.36 for the younger and 0.40 for the older subjects. These estimates are somewhat less compressive than previously reported physiological (e.g., Ruggero *et al.*, 1997) and psychophysical (e.g., Oxenham and Plack, 1997) estimates of BM compression. One possible reason for this is that the frequency of the masker

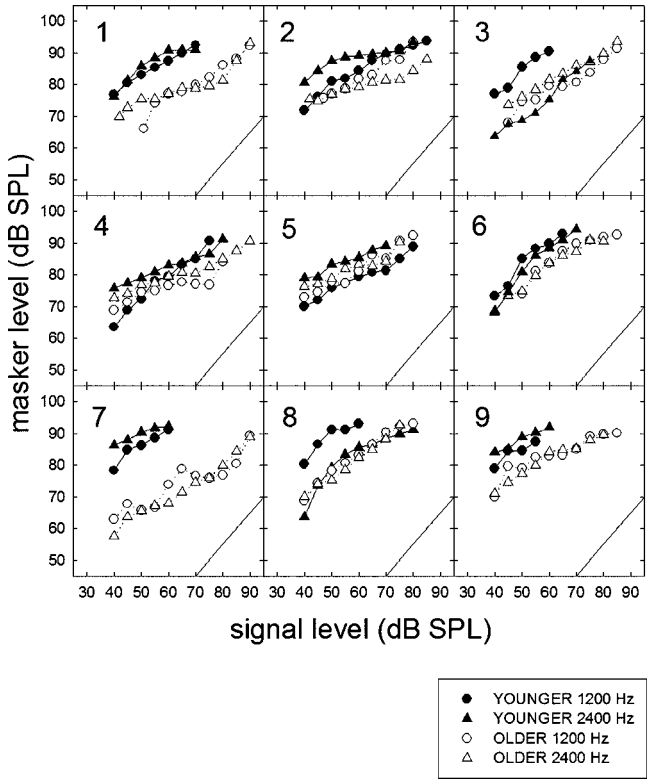

FIG. 5. Masker levels at threshold for signals ranging from 40 to 55–90 dB SPL for the younger (filled symbols) and older (unfilled symbols) listeners at 1200 (circles) and 2400 Hz (triangles). The reference line in the lower right-hand corner of each panel provides a linear slope reference.

TABLE V. Psychophysical estimates of basilar membrane compression. The compression estimates represent the slope of the function for signal levels ranging from 50 to 75 dB SPL (see text for details).

Younger subjects	Compression estimate	Older subjects	Compression estimate
	1200 Hz		
YN1	0.47	ON1	0.56
YN2	0.44	ON2	0.47
YN3	0.50	ON3	0.35
YN4	0.65	ON4	0.11
YN5	0.34	ON5	0.53
YN6	0.50	ON6	0.65
YN7	0.50	ON7	0.49
YN8	0.18	ON8	0.59
YN9	0.55	ON9	0.35
Mean	0.46	Mean	0.46
	2400 Hz		
YN1	0.25	ON1	0.20
YN2	0.12	ON2	0.19
YN3	0.80	ON3	0.46
YN4	0.26	ON4	0.22
YN5	0.30	ON5	0.36
YN6	0.64	ON6	0.60
YN7	0.19	ON7	0.45
YN8	0.40	ON8	0.68
YN9	0.30	ON9	0.43
Mean	0.36	Mean	0.40

may not have been placed far enough below the frequency of the signal to evoke a completely linear response at the cochlear place corresponding to f_s. Physiological (e.g., Ruggero *et al.*, 1997) and psychophysical (e.g., Hicks and Bacon, 2000; Nelson *et al.*, 2001) research has demonstrated that a f_s/f_m ratio of approximately 1.8 may be required to observe maximum compression. In the current study, the masker was 3 ERBs below f_s, resulting in an f_s/f_m ratio of about 1.4 to 1.5. Nevertheless, the estimates of compression reported here provide a reasonable comparison across the age groups. The estimate of compression was not significantly affected by age [$F(1,16)=0.2$, $p=0.6$] or frequency [$F(1,16)=1.4$, $p=0.3$]. There was, however, a significant effect of age on the masker level at threshold, as revealed by a two-way repeated-measures ANOVA [$F(1,16)=9.9$, $p=0.007$]. There was no effect of frequency [$F(1,16)=0.3$, $p=0.6$] and no interaction between age and frequency [$F(1,16)=0.4$, $p=0.6$]. On average, the masker levels at threshold were 5.8 dB lower for the older listeners (see Fig. 5), suggesting a greater susceptibility to forward masking in the older listeners (also see experiments 1 and 2).

VI. GENERAL DISCUSSSION

The results of the present study clearly demonstrate that three measures thought to be influenced by OHCs (frequency selectivity, suppression, and compression) were not different in younger and older listeners.[3] The lack of an age effect on AF bandwidth is consistent with some past research with similar signal frequencies (e.g., Peters and Moore, 1992; Sommers and Gehr, 1998), though inconsistent with the results of Patterson *et al.* (1982), who demonstrated an effect of age on AF bandwidth across a wide range of signal frequencies.

The lack of an age effect on psychophysical estimates of suppression is in contrast with relatively recent studies in this area. Sommers and Gehr (1998) reported significantly reduced suppression in older listeners. Suppression was quantified as the difference in AF bandwidth (in ERBs) obtained in simultaneous versus forward masking. Although the ERB_n values between the younger and older subjects were not significantly different within a given masking paradigm, the *difference* between the ERB_n values obtained in simultaneous versus forward masking (which can be used as an indirect estimate of suppression) was significantly affected by age. Dubno and Ahlstrom (2001a, b, c) also examined the effects of age on psychophysical suppression. They reported that the older subjects with normal hearing exhibited significantly less suppression than their younger counterparts. The discrepancy in findings between the current study and those of Dubno and Ahlstrom (2001b, c) may relate to how well younger and older subjects were matched in the studies. Dubno and Ahlstrom (2001b, c) included older subjects with clinically normal hearing, but their thresholds were on average 7.5 dB higher than those of the younger subjects (collapsed across frequency).

There are no other data in the literature examining the effects of age on estimates of BM compression. The lack of an age effect observed here, however, is consistent with the other results of the present study.

A consistent finding in the present study was that the older subjects demonstrated greater susceptibility to forward masking than their younger counterparts. There are other reports of age-related increases in forward-masked thresholds (Sommers and Gehr, 1998; Dubno and Ahlstrom, 2001a, b; Dubno *et al.*, 2002, 2003). Indeed, Dubno *et al.* (2002, 2003) reported significantly higher forward-masked thresholds for older subjects with normal hearing; however, due to the higher quiet thresholds for these listeners, the amount of masking was found to be essentially identical across the age groups. Sommers and Gehr (1998) did not report their subjects' quiet thresholds for the 20-ms signals used for testing so it is unclear whether their older subjects exhibited greater masking. In the present study, the older subjects, on average, exhibited greater amounts of masking as well as greater forward-masked thresholds. Our results are consistent with evidence from vision research showing that older subjects are more susceptible to forward masking by visual noise (e.g., Coyne, 1981).

The finding of an age-related increase in susceptibility to forward masking is somewhat enigmatic given the lack of an age effect in the estimates of cochlear nonlinearity. It is thought that forward masking is influenced by nonlinear cochlear processing (e.g., Oxenham and Plack, 1997), as revealed within the context of the temporal window model. The temporal window model is one of several popular models describing the temporal resolving capabilities of the auditory system (e.g., Moore *et al.*, 1988; Oxenham, 2001). The model incorporates bandpass filtering, level-dependent, instantaneous compression, a temporal window centered over the signal presentation, and a decision device. The essentially identical compression estimates for the younger and older listeners (Table V) suggest that the elevated forward-masked thresholds in the older subjects are not due to differences in peripheral processing. Thus it would appear that the origin of the aging differences in forward masking may be more centrally located. One possibility is that the temporal window may be wider in the older listeners.

Another possible explanation for the increased forward masking, and one that could co-exist with a broader temporal window, is that the older listeners have poorer auditory processing efficiency. Processing efficiency, which represents one's ability to detect a signal in noise, is calculated as the signal-to-noise ratio at threshold. Auditory processing efficiency is thought to be influenced not only by auditory processing but by general cognitive factors such as attention, memory, and learning (Patterson *et al.*, 1982; Hartley and Moore, 2002). The current study provides some information about the effects of aging on auditory processing efficiency. Comparing the fitting parameters of the derived AFs in the current study, the values of k (which provide an estimate of detection efficiency) were generally higher for the older listeners.[4] The signal-to-masker ratio required at threshold was on average 9 dB higher for the older listeners than for the younger listeners. A two-way repeated-measures ANOVA computed on the values of k as a function of age and frequency revealed a significant effect of age on k $[F(1,16)=16.3,\ p<0.001]$, a significant effect of frequency $[F(1,16)=50.1,\ p<0.001]$, and an interaction between age and frequency $[F(1,16)=12.4,\ p=0.003]$. That is, there was a much larger difference in k values between the age groups for 2400 Hz (11.0-dB difference) than for 1200 Hz (7.0-dB difference). This effect of age is not surprising given that, on average, the younger and older listeners had essentially equivalent AF bandwidths, yet the masker levels at threshold were consistently lower for the older listeners. Thus, it is likely that some degree of an age-related deficit in processing efficiency exists.

VII. SUMMARY AND CONCLUSIONS

The goal of this study was to compare the performance of younger and older listeners on three psychophysical measures thought to depend upon normally functioning OHCs, to determine whether an age-related decline in nonlinear cochlear processing exists independent of hearing loss. The first step was to closely match older and younger listeners for quiet thresholds across a broad frequency range. The second step was to examine whether an effect of age could be observed on three psychophysical measures thought to be influenced by nonlinear cochlear processing: (1) AF bandwidth, (2) suppression, and (3) estimates of basilar membrane compression. There were no significant differences between the age groups on any of the metrics. There was, however, a highly consistent and significant effect of age on the susceptibility to forward masking in all three experiments. Given that this was not due to an age-induced reduction in peripheral nonlinear processing, it more likely reflects an age-related change in central processing (Dubno and Schaefer, 1991; Gifford and Bacon, 2004; Henry and Grantham, 2000; Leek and Sommers, 1993; Moore *et al.*, 1997, 1999).

ACKNOWLEDGMENTS

This work was supported by NIDCD Grant Nos. DC005085 (RHG) and DC01376 (SPB). We thank Chris Plack and an anonymous reviewer for their comments on a previous version of this manuscript.

[1]The notch widths used in this experiment were not as wide as those used by Stone *et al.* (1992) because the signal could not be masked by some subjects at the maximum masker level at the wider notch widths.

[2]The individual ERB_n values obtained for each subject in experiment 1 were not used for this experiment because this experiment was conducted at a much higher level (masker spectrum level of 45 dB SPL) than that of experiment 1 (signal level of 10 dB SL). Past research has shown that the width of the auditory filter increases with level (Hicks and Bacon, 1999). Thus, the initial 1-ERB_n condition (in experiment 2) was based on estimates with moderate-level maskers provided by Glasberg and Moore (1990).

[3]Pearson product moment correlations were computed comparing all three metrics of nonlinear cochlear processing as observed in the younger and older listeners—auditory filter bandwidth, suppression, and compression. Given that no age or frequency effects had been found, the correlation analyses were collapsed across subject age and signal frequency. Moreover, ERB_n values were normalized (by dividing by f_s) so that both age and frequency could be factored out of the analysis. No significant correlations were found between any two psychophysical measures of nonlinear cochlear processing. Correlation coefficients and associated p values were $r=0.01$, $p=0.32$ for maximum suppression (in dB) versus normalized ERB_n, $r=-0.30$, $p=0.07$ for compression versus normalized ERB_n, and $r=-0.18$, $p=0.32$ for compression versus maximum suppression (in dB). Thus, no

significant correlations were observed for any of the comparisons between the psychophsycial estimates of nonlinear cochlear processing.

[4]In the context of forward masking, a change in the value of k could reflect a change in processing or a change in temporal window shape. Here, the filters were fitted assuming a rectangular temporal window shape for all listeners. If the window shape differed for the two groups, the differences in k would not necessarily reflect differences in processing efficiency.

ANSI (**1997**). ANSI S3.5–1997, "American National Standard Methods for Calculation of the Speech Intelligibility Index" (American National Standards Institute, New York).

Bacon, S. P., Opie, J. M., and Montoya, D. Y. (**1998**). "The effects of hearing loss and noise masking on the masking release for speech in temporally complex backgrounds," J. Speech Lang. Hear. Res. **41**, 549–563.

Coyne, A. C. (**1981**). "Age differences and practice in forward visual masking," J. Gerontol. **36**, 730–732.

Davis, H. (**1983**). "An active process in cochlear mechanics," Hear. Res. **9**, 79–90.

Doan, D. E., Erulkar, J. S., and Saunders, J. C. (**1996**). "Functional changes in the aging mouse middle ear," Hear. Res. **97**, 174–177.

Dorn, P. A., Piskorski, P., Keefe, D. H., Neely, S. T., and Gorga, M. P. (**1998**). "On the existence of an age/threshold/frequency interaction in distortion product otoacoustic emissions," J. Acoust. Soc. Am. **104**, 964–971.

Dubno, J. R., and Ahlstrom, J. B. (**2001a**). "Forward- and simultaneous-masked thresholds in bandlimited maskers in subjects with normal hearing and cochlear hearing loss," J. Acoust. Soc. Am. **110**, 1049–1057.

Dubno, J. R., and Ahlstrom, J. B. (**2001b**). "Psychophysical suppression measured with bandlimited noise extended below and/or above the signal: effects of age and hearing loss," J. Acoust. Soc. Am. **110**, 1058–1066.

Dubno, J. R., and Ahlstrom, J. B. (**2001c**). "Psychophysical suppression effects for tonal and speech signals," J. Acoust. Soc. Am. **110**, 2108–2119.

Dubno, J. R., and Schaefer, A. B. (**1991**). "Frequency selectivity for hearing-impaired and broadband-noise-masked normal listeners," Q. J. Exp. Psychol. A **43**, 543–564.

Dubno, J. R., Horwitz, A. R., and Ahlstrom, J. B. (**2002**). "Benefit of modulated maskers for speech recognition by younger and older adults with normal hearing," J. Acoust. Soc. Am. **111**, 2897–2907.

Dubno, J. R., Horwitz, A. R., and Ahlstrom, J. B. (**2003**). "Recovery from prior stimulation: Masking of speech by interrupted noise for younger and older adults with normal hearing," J. Acoust. Soc. Am. **113**, 2084–2094.

Duquesnoy, A. J., and Plomp, R. (**1980**). "Effect of reverberation and noise on the intelligibility of sentences in cases of presbyacusis," J. Acoust. Soc. Am. **68**, 537–544.

Gifford, R. H., and Bacon, S. P. (**2004**). "Recovery from forward masking in a continuous broadband noise," American Auditory Society Meeting, Scottsdale, AZ, March.

Glasberg, B. R., and Moore, B. C. J. (**1990**). "Derivation of auditory filter shapes from notched-noise data," Hear. Res. **47**, 103–138.

Gordon-Salant, S., and Fitzgibbons, P. J. (**1999**). "Profile of auditory temporal processing in older listeners," J. Speech Lang. Hear. Res. **42**, 300–311.

Hartley, D. E., and Moore, D. R. (**2002**). "Auditory processing efficiency deficits in children with developmental language impairments," J. Acoust. Soc. Am. **112**, 2962–2966.

Henry, P. P., and Grantham, D. W. (**2000**). "Forward masking in normal-hearing, hearing-impaired, and noise-masked normal listeners," J. Acoust. Soc. Am. **107**, 2915.

Hicks, M. L., and Bacon, S. P. (**1999**). "Psychophysical measures of auditory nonlinearities as a function of frequency in individuals with normal hearing," J. Acoust. Soc. Am. **105**, 326–338.

Hicks, M. L., and Bacon, S. P. (**2000**). "The effects of aspirin on a psychophysical estimate of basilar membrane compression," J. Acoust. Soc. Am. **107**, 2914.

Houtgast, T. (**1974**). "Lateral suppression in hearing," Ph. D. thesis, Free University of Amsterdam.

Humes, L. E., and Christopherson, L. A. (**1991**). "Speech identification difficulties of hearing-impaired older persons: The contributions of auditory processing deficits," J. Speech Hear. Res. **34**, 686–693.

Leek, M. R., and Summers, V. (**1993**). "Auditory filter shapes of normal-hearing and hearing-impaired listeners in continuous broadband noise," J. Acoust. Soc. Am. **94**, 3127–3137.

Levitt, H. (**1971**). "Transformed up-down methods in psychoacoustics," J. Acoust. Soc. Am. **49**, 467–477.

Liberman, M. C., and Dodds, L. W. (**1984**). "Single-neuron labeling and chronic cochlear pathology. III. Stereocilia damage and alterations of threshold tuning curves," Hear. Res. **16**, 55–74.

Lopez-Poveda, E. A., Plack, C. J., Meddis, R., and Blanco, J. L. (**2005**). "Cochlear compression in listeners with moderate sensorineural hearing loss," Hear. Res. **205**, 172–183.

McFadden, S. L., Campo, P., Quaranta, N., and Henderson, D. (**1997a**). "Age-related decline of auditory function in the chinchilla (Chinchilla laniger)," Hear. Res. **111**, 114–126.

McFadden, S. L., Quaranta, N., and Henderson, D. (**1997b**). "Suprathreshold measures of auditory function in the aging chinchilla," Hear. Res. **111**, 127–135.

Moore, B. C. J., Glasberg, B. R., Plack, C. J., and Biswas, A. K. (**1988**). "The shape of the ear's temporal window," J. Acoust. Soc. Am. **83**, 1102–1116.

Moore, B. C. J., Vickers, D. A., Glasberg, B. R., and Baer, T. (**1997**). "Comparison of real and simulated hearing impairment in subjects with unilateral and bilateral cochlear hearing loss," Br. J. Audiol. **31**, 227–245.

Moore, B. C. J., Vickers, D. A., Plack, C. J., and Oxenham, A. J. (**1999**). "Interrelationship between different psychoacoustic measures assumed to be related to the cochlear active mechanism," J. Acoust. Soc. Am. **106**, 2761–2778.

Neff, D. L. (**1985**). "Stimulus parameters governing confusion effects in forward masking," J. Acoust. Soc. Am. **78**, 1966–1976.

Nelson, D. A., Schroder, A. C., and Wojtczak, M. (**2001**). "A new procedure for measuring peripheral compression in normal-hearing and hearing-impaired listeners," J. Acoust. Soc. Am. **110**, 2045–2064.

Oxenham, A. J. (**2001**). "Forward masking: adaptation or integration?" J. Acoust. Soc. Am. **109**, 732–741.

Oxenham, A. J., and Bacon, S. P. (**2004**). "Psychophysical manifestations of compression: normal-hearing listeners," in *Compression: From Cochlea to Cochlear Implants*, edited by S. P. Bacon, R. R. Fay, and A. N. Popper (Springer, New York).

Oxenham, A. J., and Plack, C. J. (**1997**). "A behavioral measure of basilar-membrane nonlinearity in listeners with normal and impaired hearing," J. Acoust. Soc. Am. **101**, 3666–3675.

Oxenham, A. J., and Shera, C. A. (**2003**). "Estimates of human cochlear tuning at low levels using forward and simultaneous masking," J. Assoc. Res. Otolaryngol. **4**, 541–554.

Parham, K., Sun, X. M., and Kim, D. O. (**1999**). "Distortion product otoacoustic emissions in the CBA/J mouse model of presbycusis," Hear. Res. **134**, 29–38.

Patterson, R. D., Nimmo-Smith, I., Weber, D. L., and Milroy, R. (**1982**). "The deterioration of hearing with age: Frequency selectivity, the critical ratio, the audiogram, and speech threshold," J. Acoust. Soc. Am. **72**, 1788–1803.

Peters, R. W., and Hall, J. W. (**1994**). "Comodulation masking release for elderly listeners with relatively normal audiograms," J. Acoust. Soc. Am. **96**, 2674–2682.

Peters, R. W., and Moore, B. C. J. (**1992**). "Auditory filter shapes at low center frequencies in young and older hearing-impaired subjects," J. Acoust. Soc. Am. **91**, 256–266.

Plack, C. J., and Drga, V. (**2003**). "Psychophysical evidence for auditory compression at low characteristic frequencies," J. Acoust. Soc. Am. **113**, 1574–1586.

Plack, C. J., and Drga, V., and Lopez-Poveda, E. A. (**2004**). "Inferred basilar-membrane response functions for listeners with mild to moderate sensorineural hearing loss," J. Acoust. Soc. Am. **115**, 1684–1695.

Plomp, R., and Mimpen, A. M. (**1979**). "Speech-reception threshold for sentences as a function of age and noise level," J. Acoust. Soc. Am. **66**, 1333–1342.

Rosen, S., and Baker, R. J. (**1994**). "Characterising auditory filter nonlinearity," Hear. Res. **73**, 231–243.

Rosen, S., Baker, R. J., and Darling, A. (**1998**). "Auditory filter nonlinearity at 2 kHz in normal hearing listeners," J. Acoust. Soc. Am. **103**, 2539–2550.

Ruggero, M. A., Rich, N. C., Recio, A., Narayan, S. S., and Robles, L. (**1997**). "Basilar-membrane responses to tones at the base of the chinchilla cochlea," J. Acoust. Soc. Am. **101**, 2151–2163.

Satoh, Y., Kanzaki, J., O-Uchi, T., and Yoshihara, S. (**1998**). "Age-related changes in transiently evoked otoacoustic emissions and distortion product otoacoustic emissions in normal-hearing ears," Auris Nasus Larynx **25**, 121–130.

Schneider, B. A., Pichora-Fuller, M. K., Kowalchuk, D., and Lamb, M. (**1994**). "Gap detection and the precedence effect in young and old adults," J. Acoust. Soc. Am. **95**, 980–991.

Snell, K. B. (**1997**). "Age-related changes in temporal gap detection," J. Acoust. Soc. Am. **101**, 2214–2220.

Sommers, M. S., and Gehr, S. E. (**1998**). "Auditory suppression and frequency selectivity in older and younger adults," J. Acoust. Soc. Am. **103**, 1067–1074.

Sommers, M. S., and Humes, L. E. (**1993**). "Auditory filter shapes in normal hearing, noise-masked normal, and older listeners," J. Acoust. Soc. Am. **93**, 2903–2914.

Stone, M. A., Glasberg, B. R., and Moore, B. C. J. (**1992**). "Simplified measurement of impaired auditory filter shapes using the notched-noise method," Br. J. Audiol. **26**, 329–334.

Williams, E. J., and Bacon, S. P. (**2005**). "Compression estimates using behavioral and otoacoustic emission measures," Hear. Res. **201**, 44–54.

Synergistic modes of vocal tract articulation for American English vowels[a)]

Brad H. Story[b)]
Speech Acoustics Laboratory, Department of Speech and Hearing Sciences, University of Arizona, Tucson, Arizona 85721

(Received 6 June 2005; revised 19 September 2005; accepted 20 September 2005)

The purpose of this study was to investigate the spatial similarity of vocal tract shaping patterns across speakers and the similarity of their acoustic effects. Vocal tract area functions for 11 American English vowels were obtained from six speakers, three female and three male, using magnetic resonance imaging (MRI). Each speaker's set of area functions was then decomposed into mean area vectors and representative modes (eigenvectors) using principal components analysis (PCA). Three modes accounted for more than 90% of the variance in the original data sets for each speaker. The general shapes of the first two modes were found to be highly correlated across all six speakers. To demonstrate the acoustic effects of each mode, both in isolation and combined, a mapping between the mode scaling coefficients and [F1, F2] pairs was generated for each speaker. The mappings were unique for all six speakers in terms of the exact shape of the [F1, F2] vowel space, but the general effect of the modes was the same in each case. The results support the idea that the modes provide a common system for perturbing a unique underlying neutral vocal tract shape. [DOI: 10.1121/1.2118367]

PACS number(s): 43.70.−h, 43.70.Bk, 43.70.Gr [AL] Pages: 3834–3859

I. INTRODUCTION

The upper airway in humans, extending from the larynx to the lips, is utilized as a conduit for the physiologic processes of respiration, deglutition, and sound production. Each physiologic function requires specific types of coordinated articulatory movement involving the larynx, tongue soft palate, lips, and jaw to accomplish a particular goal. For respiration, the vocal folds must be abducted and, depending on the amount of oxygen needed, the jaw may be lowered and the tongue moved anteriorly and inferiorly to allow a high volume of air to flow into the lungs. A typical swallow proceeds as a sequence of distinct "phases" in which movements of articulatory structures, and their generated forces are precisely orchestrated to propel a bolus of food or liquid through the oral cavity, the pharynx, and eventually into the esophagus and stomach (e.g., Logeman, 1983). For both respiration and deglutition, the goals of the process are to achieve the efficient transport of fluids and solids to a destination (i.e., lungs and stomach). In contrast, the goals of speech production require that the articulatory system not only *transport* sound waves from the larynx to the lips, but also *transform* them into highly structured, linguistically relevant sounds.

The transformation of sounds, produced by vocal fold vibration or other sources, into speech is accomplished through specific shapes and shape changes of the tubelike structure formed collectively by the epilarynx, pharynx, and oral cavity (henceforth referred to as the "vocal tract"). This vocal tract tube creates an acoustic filter whose resonances generate enhanced regions of amplitude (i.e., formant frequencies) that are observable in the spectrum of a speech signal. The relation between vocal tract shape and the acoustic characteristics it generates, especially formant frequencies, is known to be nonlinear (e.g., Fant, 1960; Stevens and House, 1955) and, theoretically, many-to-one (Schroeder, 1967; Mermelstein, 1967). But even though many possible vocal tract shapes can support the same pattern of formant frequencies, speakers easily coordinate the actions of the articulators, efficiently modifying the vocal tract shape over time, to produce a coarticulated stream of intelligible speech sounds. Thus, part of understanding speech production is to know how the vocal tract shape, represented as a tubular entity, may be systematically controlled to specify and simplify its relation to the formant frequencies.

While all of the articulators potentially contribute to any particular vocal tract shape, it is largely dominated by the configuration of the tongue. This is evidenced by common use of the high/low and front/back descriptors for tongue position in vowel production and implies a simple relation to formant frequencies. Quantitative studies tend to support a view that the tongue shape can be described by underlying patterns of spatial deformation. Harshman *et al.* (1977) statistically decomposed tongue profiles of ten English vowels taken from midsagittal x-ray pictures into basic displacement patterns called "factors." They found that only two factors were needed to reconstruct the profiles within a small error of the originals. Furthermore, the factors had an apparent articulatory phonetic interpretation. The first indicated a forward movement of the tongue root along with an elevation of the front of the tongue; this was suggested to correspond to the action of the genioglossus muscle. The second factor produced an upward and backward movement of the tongue

[a)]Portions of this paper were presented at the 144th Meeting of the Acoustical Society of America.
[b)]Electronic mail: bstory@u.arizona.edu

which was compared to the action of the styloglossus muscle. Nearly parallel to this work was research reported by Shirai and Honda (1977), who also represented midsagittal tongue shapes with two empirically determined displacement patterns. The shapes were generally similar to those of Harshman *et al.* (1977). Using tongue shapes obtained from cineradiographic tracings for Icelandic speakers, Jackson (1988) reported that *three* factors were necessary to describe Icelandic vowels, where the second factor was of significantly different shape than that reported by Harshman *et al.* (1977). A reanalysis of these data by Nix *et al.* (1996), however, showed that two factors could, in fact, describe the Icelandic tongue shapes too. More recently, Zheng *et al.* (2003) have applied a factor analysis to tongue shapes determined from 3-D image sets based on MRI. While their results were not identical to previous studies, they suggest that a large percentage of the variance in tongue shape for vowels can be described with two shaping factors.

Although in a strict sense "factors" are only a statistical description of tongue shape, a physiologic basis for them was reported by Maeda and Honda (1994). During vowel production, the electromyographic activity of two antagonistic muscle pairs, hyoglossus (HG)-genioglossus posterior (GGp) and styloglossus (SG)-genioglossus anterior (GGa), was observed to coincide with the spatial tongue shaping characteristics of two factors that had been derived from midsagittal images of the vocal tract. The vowel-dependent differential activity of each antagonistic pair was also shown to form a vowel triangle much like that of the first two formant frequencies (Kusakawa *et al.*, 1993). To further investigate the relation between muscle activity patterns, vocal tract shape, and formant frequencies, Maeda and Honda (1994) used the analyzed EMG activities (of the HG-GGp and SG-GGa pairs) as the driving input to an articulatory model based primarily on two tongue shaping patterns [similar to the factors derived by Harshman *et al.* (1977)]. The results were F1-F2 patterns that corresponded closely to measured formant values and led them to state: "We speculate the brain optimally exploits the morphology of the vocal tract and the kinematic functions of the tongue muscles so that the mappings from the muscle activities (production) to the acoustic patterns (perception) are simple and robust."

The results of these experiments suggest that tongue shaping patterns obtained from statistical analyses may capture the spatial, and perhaps kinematic, representation of a coordinated pattern of individual articulator positions or movements that is directly related to the acoustic characteristics of speech. This is similar to the concept of "coordinative structures" or "synergies" that has been proposed as the means by which a potentially large number of articulatory degrees of freedom can be significantly reduced to enable the efficient production of phonetically relevant gestures (e.g., Kelso *et al.*, 1986; Fowler and Saltzman, 1993). In a review of movement control and speech production literature, Löfqvist (1997) defines coordinative structures as "…linkages between muscles that are set up for the execution of specific tasks," and further that they are "…a set of constraints between muscles that are set up to make the set of muscles behave as a unit." Thus, the observed relation between tongue shaping patterns (e.g., factors) and muscle activations appears to represent some underlying synergy of muscles controlled as a functional unit for the production of speech. Whether or not the nature of such functional units is specific to speech is still an open question, however. Perrier *et al.* (2000) proposed that the two degrees of freedom expressed by factor analyses of the tongue have an anatomical and biomechanical basis. Using a model of the tongue that included a representation of the lingual musculature, they showed that much of the variation in tongue shape (84%) allowed by the model could be described by two factors with shapes similar to those reported by Nix *et al.* (1996). Thus, biomechanical constraints, as well as task-specific constraints, may play a role in reducing the degrees of articulatory freedom.

While tongue shape for vowel production apparently has a consistent, systematic description, similar analyses of area functions (i.e., cross-sectional area of the upper airway as a function of distance from the glottis) have indicated that control of the vocal tract shape may also be characterized by a small set of spatial deformation patterns that extend over the entire length of the vocal tract. Story and Titze (1998) applied a principal components analysis (PCA) to a set of MRI-based area functions for ten vowels from an adult male speaker. The two most significant orthogonal components accounted for nearly 88% of the total variance in the set of area functions. When the first component was superimposed on the mean area function in isolation and weighted with its minimum (negative) coefficient, the area function approximated an [i] vowel and produced widely spaced F1 and F2 formant frequencies. Conversely, when weighted with its maximum coefficient, an [ɑ]-like shape and closely spaced F1 and F2 frequencies were produced. Similar isolated weightings of the second component showed that it specified area functions and formants approximately representative of [æ] and [o]. Combinations of incremental coefficient weights for both components led to development of an area function model that can generate a wide variety of vocal tract shapes that were not included in the original set of area functions, and produce a nearly one-to-one mapping between component coefficients (weights) and the F1-F2 vowel space (Story and Titze, 1998; Story, 2005). Other studies based on principal components analysis of area functions derived from sagittal x-ray images (Meyer *et al.*, 1989; Yehia *et al.*, 1996) have also shown that two to five components account for the majority of the variance in their respective data sets.

It is noteworthy that a similar system of spatial shaping patterns has been determined for hand postures. Santello *et al.* (1998) recorded spatial coordinates from sensors on subjects' hands while they grasped 57 different objects with wide variations in shape (analogous to speakers producing a variety of vowel sounds in an MRI scanner). A PCA performed on the coordinates indicated that, for each subject, two principal components could account for greater than 80% of the variance in hand posture. A model for controlling the general shape of the hand was developed based on superimposing coefficient weighted components, either in isolation or combination, on the mean hand shape. In this manner, many hand shapes not in the original set could be produced.

Santello *et al.* note that if control of the general shape of the hand were based on the principal components, the number of degrees of freedom would be significantly reduced. Drawing on the concepts of Macpherson (1991), they further suggested that each component represents a postural "synergy" between individual muscles of the hand that can be utilized alone or in combination with other synergies (i.e., another principal component).

An area function representation of the vocal tract is, strictly, only a description of the nonuniform shape of a tubular structure and cannot necessarily be considered an "articulatory" representation. Based on definitions of coordinative structures (e.g., Löfqvist, 1997), and also by analogy to Santello *et al.* (1998), however, it is conceivable that the principal components derived from a set of vowel area functions (e.g., Story and Titze, 1998) could represent some form of synergy of muscles associated with individual articulators, that facilitates the production of predictable patterns of formant frequencies (cf. Story, 2004). While speculative at this point, the idea is consistent with Gracco's (1992) statement that speech motor control is apparently "organized at a functional level according to sound-producing vocal tract actions." Story and Titze (1998) referred to the principal components in their model as "modes" to emphasize a similarity to a modal decomposition of a dynamical system into natural modes. Hence, to the degree that they capture some aspect of possible muscle synergies, the modes may be conceptualized as "synergistic modes."

To date, modes or principal components reported for area functions measured with 3-D imaging techniques (e.g., MRI) have been based on only one adult male speaker's area function set (Story *et al.*, 1996). While they provide an efficient parametric representation of the vocal tract area function under both normal and perturbed conditions (Story, 2004, 2005), it is necessary to obtain mode shapes for additional speakers to determine if the concept of area function modes can be generalized. This study was motivated by a simple question: Are synergistic modes, based on area functions, similar across speakers? The specific aims of the project were to (1) acquire area functions for vocal tract shapes of vowels from six speakers (three adult males and three adult females) using magnetic resonance imaging (MRI), (2) compare formant frequencies extracted from acoustic recordings to those calculated for each area function, (3) determine mode shapes and coefficient weights for each speaker's area function set and compare across speakers, and (4) calculate the effects of the modes on the first two formant frequencies (F1 and F2) for each speaker.

II. ACQUISITION AND ANALYSIS OF IMAGES AND AUDIO SAMPLES

A. Image collection

Magnetic resonance imaging (MRI) was used to obtain volumetric image sets for a variety of vocal tract shapes from three male and three female speakers. The vocal tract shapes corresponded to each speaker's production of the American English vowels [i, ɪ, e, ɛ, æ, ʌ, ɑ, ɔ, o, ʊ, u]. Image sets for [l], [ɝ], the nasal tract, and trachea were also obtained but will not be reported in this article.

TABLE I. The age of each speaker at the time of MR scanning and the geographic area they reported as being most representative of their "growing up" years. The female speakers are denoted by "SF" and the male speakers by "SM."

Speaker	Age (years)	Region
SF1	29	N. Carolina, USA
SF2	25	Oklahoma, USA
SF3	23	Manitoba, Canada
SM1	33	N. Carolina, USA
SM2	41	New York (Long Island), USA
SM3	30	Los Angeles, CA, USA

The six speakers were recruited from the student, faculty, and staff population at the University of Arizona. They will be identified in this article as SF1, SF2, SF3, SM1, SM2, and SM3, where the "F" denotes *female* and "M" *male*. None of the speakers had any specialized voice or speech training (e.g., singing, acting, etc.), although it may be noted that all three female speakers were students in the Department of Speech, Language, and Hearing Sciences. Five of the speakers had no history of speech, language, or hearing disorders. SM2 reported a cleft of his soft palate that had been surgically repaired at approximately 2.5 years of age. At the time of image collection his speech was judged to be normal. The age of each speaker is shown in Table I, along with the geographic area they reported as being most representative of their "growing up" years.

Prior to image collection, each speaker participated in three practice/training sessions. The purpose was to present the speakers with some of the conditions that are experienced in the MR scanner and to provide them with ample time to practice producing the set of speech sounds under these conditions. They were first given earplugs to partially simulate the limited auditory feedback conditions in the MR scanner. Then while lying supine on a cushioned table in a sound treated room, they practiced sustaining each speech sound. Throughout each session an emphasis was placed on the concentration required to maintain a steady vocal tract shape. A high-quality digital audio tape recording of the third session was made and later used for formant frequency analysis.

The MR images were acquired with a General Electric Signa 1.5-T scanner at the University of Arizona Medical Center. The data acquisition mode was fast spin echo and the scanning parameters were set to TE=13 ms, TR=4000 ms, ETL=16 ms, and NEX=2. During each speaker's production of a particular vocal tract shape, a 24–30 slice series was collected with an interleaved acquisition sequence. Each image set consisted of contiguous, parallel, axial sections (slices) extending from a location just superior of the hard palate to an inferior location near the first tracheal ring. The field of view (slice dimensions) for each slice was 24 cm $\times$ 24 cm which, with a pixel matrix of 256$\times$256, provided an in-plane spatial resolution of 0.938 mm/pixel. Image collection for the female speakers was performed in late 2001 and early 2002, and at that time only a flexible anterior neck

coil was available. By the time that the male speakers were imaged in the summer of 2003, a new rigid, anterior/posterior neck coil had been obtained and was used for the acquisition of their image data. The newer coil produced slightly better image quality and allowed thinner slices to be obtained. Thus, the image slice thickness was 5 mm for all of the female data and 4 mm for the male data.

After the subject had been positioned in the MR scanner [see Story *et al.* (1996, 1998) for more details], the image acquisition protocol proceeded as follows. For a specific vocal tract shape, a corresponding example word (hVd context for each vowel, "luck" and "earth" for [l] and [ɜ˞], respectively) was spoken to the subject over the intercom. The subject was then asked to produce a sustained version of the particular speech sound that the investigator verified before beginning the actual image acquisition. When the subject was ready he/she began phonation and the MR technologist followed by initiating the scan. After 8 s the scan was paused to allow time for the subject to breathe. The scanning was continued when the subject resumed phonation. The scanning time required for each image set (i.e., for one complete tract shape) was 4 min and 16 s which required approximately 30 repetitions. With pauses for respiration between repetitions, each image set was completed in about 10–15 min. Because of the potential for vocal and general physical fatigue, the image collection for each speaker was separated into at least two sessions which occurred different days.

B. Image analysis

The first step in the image analysis procedure was the application of an airway segmentation technique and was followed by shape-based interpolation to generate a 3-D reconstruction of each vocal tract shape [identical to methods reported in Story *et al.* (1996, 1998)]. Based on raw images and 3-D reconstructions, the location of the glottis was determined, and a point just above it was identified as the inlet to the vocal tract. Cross-sectional areas between this point and the lip termination were obtained by first finding the centerline through the 3-D reconstruction with an iterative bisection algorithm (see Story *et al.*, 1996, p. 542). Areas were then measured from oblique sections calculated to be locally perpendicular to the centerline. The collection of these areas extending from just above the glottis to the lips, along with the distance of each cross section from the glottis, comprises the area function. Each area function was subsequently resampled with a cubic spline from which 44 area sections[1] were obtained at equal length increments. A smoothing filter was also applied to remove small discontinuities assumed to be imaging artifacts (see Story *et al.*, 2001, p. 1653).

The piriform sinuses were segmented in each image set and included in the shape-based interpolation. Their shapes and sizes, however, were not generally consistent across the vowels of a given speaker and were, in many cases, discontinuous with the main vocal tract. While the vowel dependency of the piriform sinuses may be an interesting study in itself, including this component was considered to be beyond the scope of the present study. Hence, their cross-sectional areas are not reported here.

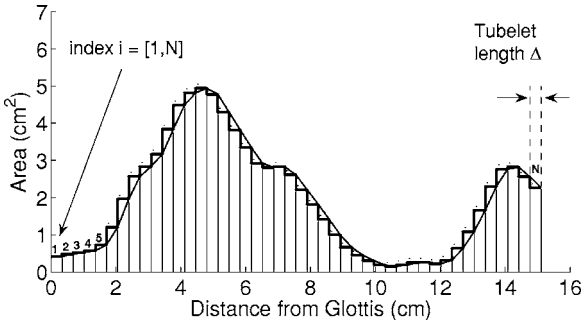

FIG. 1. Example of an area function ([i] vowel produced by SF1) shown as a succession of tubelets, denoted by the index i, extending from just above the glottis to the lips. The tubelet length is Δ and is shown at the rightmost section.

An area *function* can be considered to be comprised of two components, an area vector and a length vector. The area *vector* $A(i)$ contains the $N=44$ cross-sectional areas, assumed to represent a concatenation of "tubelets" ordered consecutively from glottis to lips. The index i denotes this ordering and extends from 1 to N. Similarly, a length vector $L(i)$ contains $N=44$ elements representing the length Δ of each tubelet (i.e., distance increment between consecutive x-sect. areas).[2] A cumulative length vector $\mathcal{X}(i)$ representing the actual distance from the glottis can be derived from L as

$$\chi(i) = \sum_{z=1}^{i} L(z), \quad i = [1,N]. \tag{1}$$

An area function can be shown graphically by plotting $A(i)$ versus $\mathcal{X}(i)$. An example is given in Fig. 1 for speaker SF1's [i] vowel where the "stair-step" plot indicates the discretization of the vocal tract shape into consecutive tubelets, each of length Δ. For graphical clarity in subsequent plots, the area functions will be shown with a smooth curve rather than in stair-step fashion (e.g., see the thin, smooth line in Fig. 1).

C. Audio recording, analysis, and theoretical calculation of formants

As stated in Sec. II A, the third practice session for each speaker was recorded onto digital audio tape and served as the high-quality recording used for formant frequency analysis. The audio signal was transduced with an AKG CK92 microphone that was positioned 30 cm from the speaker and off-axis at 45°. An electroglottographic (Glottal Enterprises, EG-2) signal was simultaneously recorded on the second channel of the digital tape. This signal was intended to be used in later studies for the accurate extraction of fundamental frequency and detection of voicing.

The recordings were transferred to digital files and then downsampled from 44.1 to 22.05 kHz. Formant frequencies were obtained with a LPC algorithm (autocorrelation method) written in Matlab that first estimated the frequency response over a 25-ms window and then found the formants with a peak-picking technique. For the vowels of the female speakers, 16–20 LPC coefficients were used, whereas, for

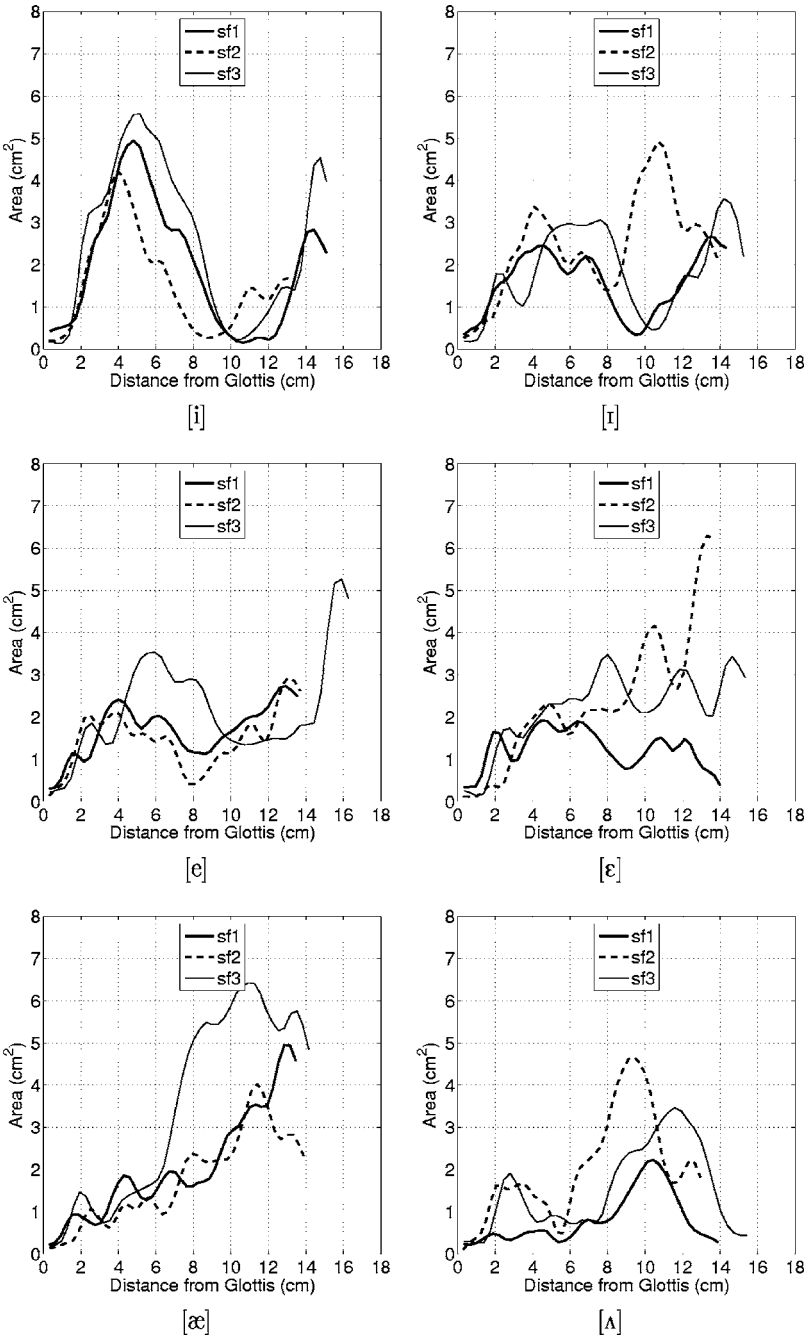

FIG. 2. Area functions for the six vowels, [i, ɪ, e, ɛ, æ, ʌ], produced by three female speakers. Each plot shows one of the vowels for all three speakers and is identified with the corresponding IPA symbol. The thick solid line represents SF1, the dashed line represents SF2, and the thin solid line is for SF3.

the male vowels 26 coefficients were used. This technique was applied to consecutive 25-ms windows (with 12.5-ms overlap) over the time course of each vowel sample which ranged from 4 to 8 s. Thus, with more than 150 sets of formant values obtained for each vowel, the standard deviations reported in Sec. III refer to the variability of a given formant over the time course of a sustained vowel. For each vowel, the mean fundamental frequency was also estimated.

Frequency response functions were calculated for each area function with a frequency-domain technique based on cascaded "ABCD" matrices (Sondhi and Schroeter, 1987; but specifically as presented in Story *et al.*, 2000). This calculation included energy losses due to yielding walls, viscosity, heat conduction, and radiation. Formant frequencies were determined by finding the peaks in the frequency response functions.

III. AREA FUNCTIONS AND FORMANT FREQUENCIES

Area functions for vowels produced by the six speakers are presented in Figs. 2–5. Within each figure panel, three area functions are plotted that correspond to a particular vowel for either the three female speakers (Figs. 2 and 3) or the three male speakers (Figs. 4 and 5). These data are tabulated numerically in vector form in Appendix A.

A. Female speakers

A general observation that can be made from Figs. 2 and 3 is that the vocal tract length for SF2 was consistently shorter than the other two speakers. She, in fact, had a mean tract length of 13.8 cm, whereas for SF1 and SF3 the mean lengths were 14.4 and 15.4 cm, respectively. Taking the length differences into account, the gross shape of each

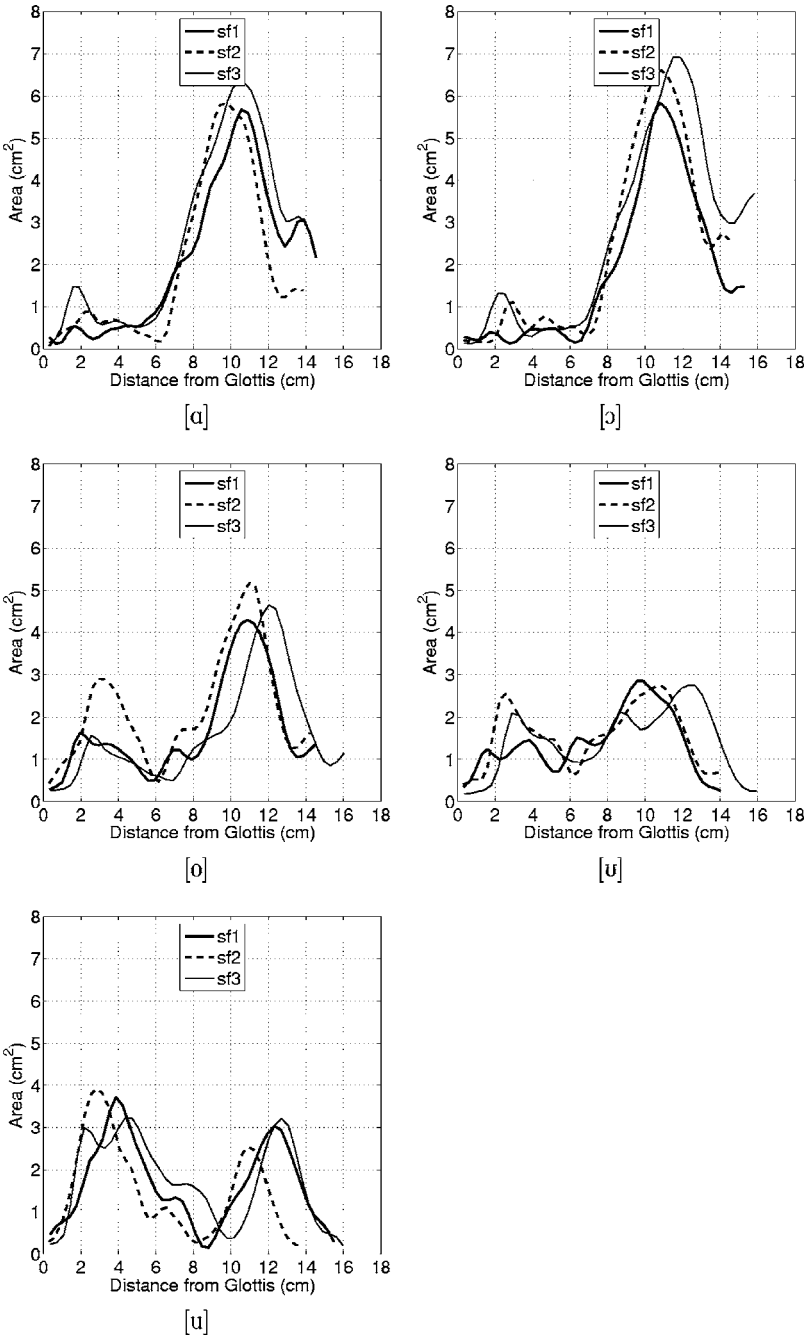

FIG. 3. Area functions for the five vowels, [ɑ, ɔ, o, ʊ, u], produced by three female speakers. Each plot shows one of the vowels for all three speakers and is identified with the corresponding IPA symbol. The line-type assignments are the same as in Fig. 2.

vowel, in terms of the location of major constrictions and expansions, is fairly similar across the three speakers. Some notable exceptions are the wide opening at the lips for SF3's [e] and SF2's [ɛ], the large oral cavity areas for SF3's [æ], and the wide lower pharyngeal space of SF2's [o]. The shape of area functions for the corner vowels, [i, æ, ɑ, u], all reasonably fit expected, prototypical vocal tract configurations of high/low and front/back vowels. The area functions for vowels that exist between the "corners" tend to be somewhat more unique to the speaker.

All three female speakers produced relatively small areas just superior to the glottis. Often referred to as the epilaryngeal space or tube, cross-sectional areas in this region averaged about 0.25 cm^2. The artificial speaking conditions imposed by the MR scanner (e.g., supine position, highly restricted movement, interfering sounds) likely affect the configuration in this part of the vocal tract because they force the speaker to produce "loud" speech (Story *et al.*, 1998). But a constricted epilarynx has also been theoretically implicated as a means by which phonation threshold pressure may be reduced (Titze and Story, 1997). Thus, it is possible that speakers may constrict this part of the vocal tract to a similar degree during normal speech production.

Comparisons of measured and calculated formant frequencies for the female speakers are given in Tables II–IV. The first row in each table contains the mean fundamental frequency produced during the sustained production of a particular vowel. Measurements of the first three formant frequencies and their respective standard deviations are shown in the next six rows. Each formant is labeled with the superscript *N* to denote "natural" speech. In the next three rows are the calculated formant frequencies based on the area

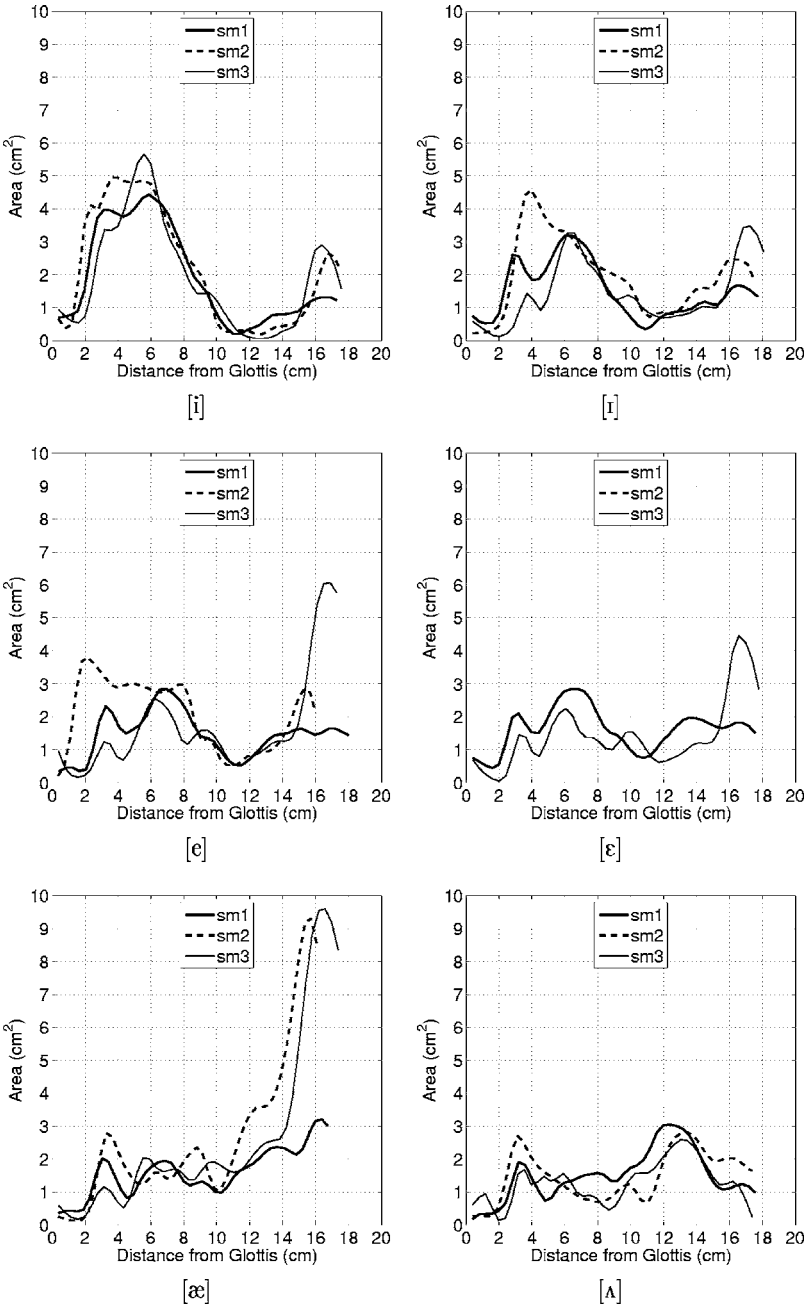

FIG. 4. Area functions for the six vowels, [i, ɪ, e, ɛ, æ, ʌ], produced by three male speakers. Each plot shows one of the vowels for all three speakers and is identified with the corresponding IPA symbol. The thick solid line represents SM1, the dashed line represents SM2, and the thin solid line is for SM3. For reasons explained in the text, an area function for SM2's [ɛ] is not shown.

functions; a superscript *C* is used to denote that they are "calculated." Finally, the percentage errors between measured and calculated formants are given in the bottom three rows. Positive errors indicate that a calculated formant was an overestimation of its measured counterpart, whereas negative errors suggest the opposite.

Across the three speakers, the tabulated errors range from an absolute minimum of −0.1% for the second formant of SF2's [ɛ] vowel to a maximum of 31.4% for the third formant of SF3's [i]. While a large error such as 30% or more is undesirable, it is noted that over half of the errors shown in the tables are less than 10%, and more than a third are less than 5%. It is also noted that the smallest combined error occurs for each speaker's [æ] vowel. This may be coincidental but perhaps there is some characteristic of [æ], either acoustic or articulatory, that facilitates a more consistent production than other vowels.

B. Male speakers

The area functions for the three male speakers are shown in Figs. 4 and 5. Consistent with the plots for the females, each figure panel contains three area functions corresponding to a particular vowel, except for the [ɛ] in Fig. 4, where area functions are shown only for speakers SM1 and SM3. Because of movement artifact, the 3-D reconstruction of SM2's [ɛ] vowel produced a discontinuous air space, and hence an area function could not be determined.

The [i] vowel was produced by all three male speakers with similar vocal tract configurations, both in terms of cross-sectional area distribution and vocal tract length. The expanded pharynx and constricted oral cavity are prototypical for an [i] vowel. There were, however, slight differences in the location and extent of the oral cavity constrictions which, because of their small cross-sectional areas, could

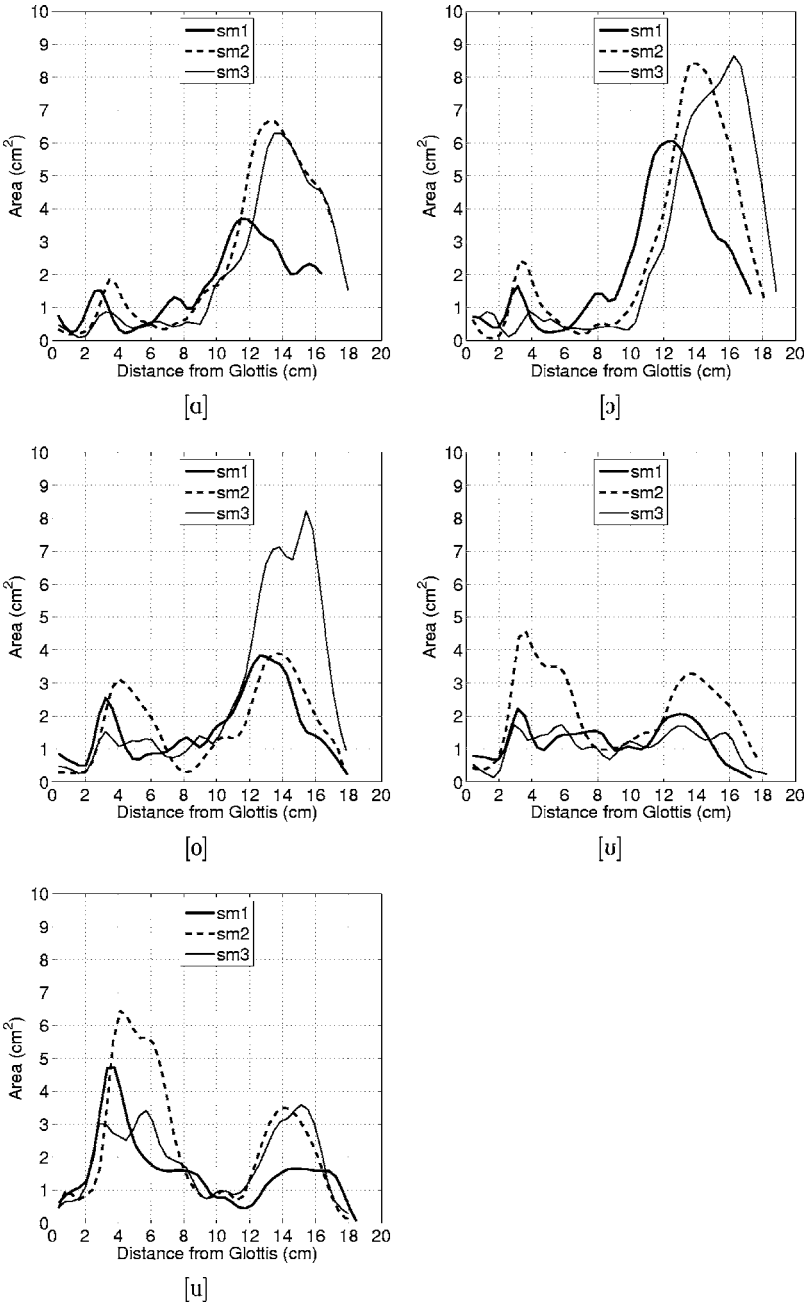

FIG. 5. Area functions for the five vowels, [ɑ, ɔ, o, ʊ, u], produced by three male speakers. Each plot shows one of the vowels for all three speakers and is identified with the corresponding IPA symbol. The line-type assignments are the same as in Fig. 4.

have significant effects on the acoustic characteristics. The gross shape of the area functions for the other corner vowels, [æ, ɑ, u], were also fairly prototypical, but were produced quite differently by each speaker. In particular, the cross-sectional area within the oral cavity for SM1's version of these vowels, as well as for [ɔ], is considerably smaller than in those of the other two speakers. SM1 also exhibited a comparatively shorter tract length for both the [ɑ] and [o] vowels. The vowels [i], [e], [ɛ], and [ʌ] were similarly shaped for each speaker, although SM2 does maintain slightly larger areas in the lower pharyngeal portion for these vowels. For the [ʊ] vowel, SM2 produced a tract shape with an expansion in the pharynx and oral cavity somewhat like an [u], whereas SM1 and SM3 kept the cross-sectional area nearly constant except at the glottal and lip ends.

Similar to the females, the cross-sectional areas representing the epilaryngeal portion of the vocal tract were less than 1 cm^2 for all of the vowels produced by each speaker. The mean area in this region, however, was roughly 0.5 cm^2, which is about twice that measured for the female speakers. Also in comparison to the females, the epilarynx for each male was more distinctly shaped like a tube. This was true for most of vowels where the area remained on the order of 0.5 cm^2 over a distance of about 1.5–2 cm from the glottis. Beyond this point, the cross-sectional area tended to increase rapidly.

Comparisons of measured and calculated formant frequencies are shown in Tables V–VII. The data are arranged in exactly the same format as they were for the female speakers. The absolute minimum error is −0.1% for the first formant in SM2's [e] and [ɔ] vowels. The maximum error of 48.5% occurs in the second formant for SM3's [u]; the next largest error is −28.8% for the third formant of SM3's [e]. Notwithstanding these largest errors, the match between

TABLE II. Fundamental frequencies F_0 and measured and calculated formants for the 11 vowels of speaker SF1. Each measured formant (denoted by superscript "*N*") is the mean across several seconds of recording and *sd* is the standard deviation. The calculated formant values are denoted by "*C*." The Δ's represent the percent error of the computed formants relative to the mean value of the natural speech formants (e.g., $\Delta 1 = 100(F1^C - F1^N)/F1^N$).

	i	ɪ	e	ɛ	æ	ʌ	ɑ	ɔ	o	ʊ	u
F_0	280	276	278	275	267	264	245	251	266	268	286
$F1^N$	391	654	704	770	903	843	917	811	773	721	391
sd	±16	±11	±8	±8	±9	±7	±9	±11	±9	±24	±16
$F2^N$	2720	2269	2404	2240	2087	1574	1484	1242	1326	1602	1163
sd	±13	±44	±46	±26	±25	±10	±8	±9	±6	±12	±23
$F3^N$	3332	3264	3383	3152	3157	3129	3366	2985	2977	3549	2855
sd	±17	±23	±107	±59	±102	±33	±57	±26	±38	±97	±79
$F1^C$	340	537	706	555	901	655	842	737	663	511	417
$F2^C$	2757	2311	2156	1838	2044	1461	1679	1247	1296	1452	1081
$F3^C$	4235	2849	3247	2852	3114	3228	3077	2932	3290	3221	3167
Δ1	−13.0	−18.0	0.2	−28.0	−0.2	−22.3	−8.1	−9.1	−14.2	−29.1	6.5
Δ2	1.3	1.8	−10.3	−18.0	−2.0	−7.2	13.1	0.4	−2.3	−9.3	−7.1
Δ3	27.1	−12.7	−4.0	−9.5	−1.4	3.2	−8.6	−1.8	10.5	−9.2	10.9

TABLE III. Fundamental frequencies F_0 and measured and calculated formants for the 11 vowels of speaker SF2.

	i	ɪ	e	ɛ	æ	ʌ	ɑ	ɔ	o	ʊ	u
F_0	249	249	249	247	248	246	248	249	247	247	250
$F1^N$	446	599	639	718	892	741	862	842	643	666	460
sd	±6	±4	±11	±13	±7	±17	±7	±10	±9	±20	±10
$F2^N$	2875	2261	2445	2156	2004	1616	1337	1184	1240	1483	1319
sd	±60	±13	±13	±36	±16	±32	±17	±15	±11	±5	±34
$F3^N$	4452	3209	3193	3159	3080	3437	3266	3230	3082	3252	3012
sd	±31	±10	±25	±29	±31	±59	±28	±13	±32	±34	±36
$F1^C$	457	710	622	910	878	773	711	839	619	569	412
$F2^C$	2512	1721	2152	2155	1828	1588	1166	1324	1295	1442	1235
$F3^C$	3591	3549	3255	3703	3137	3926	4000	3650	3570	3472	3310
Δ1	2.6	18.6	−2.6	26.8	−1.6	4.3	−17.6	−0.4	−3.7	−14.5	−10.5
Δ2	−12.6	−23.9	−12.0	−0.1	−8.8	−1.7	−12.8	11.8	4.4	−2.8	−6.3
Δ3	−19.3	10.6	2.0	17.2	1.8	14.2	22.5	13.0	15.8	6.8	9.9

TABLE IV. Fundamental frequencies F_0 and measured and calculated formants for the 11 vowels of speaker SF3.

	i	ɪ	e	ɛ	æ	ʌ	ɑ	ɔ	o	ʊ	u
F_0	280	272	280	275	277	279	273	273	270	274	267
$F1^N$	368	557	694	771	820	617	708	683	603	631	433
sd	±5	±14	±14	±19	±44	±25	±37	±37	±5	±15	±16
$F2^N$	2828	2180	2277	2024	1712	1432	1329	1231	1017	1353	1144
sd	±47	±45	±22	±38	±55	±25	±36	±29	±9	±18	±46
$F3^N$	3552	3270	3213	3221	3253	3117	3299	3299	3086	3162	2881
sd	±46	±45	±23	±60	±62	±41	±21	±34	±43	±62	±25
$F1^C$	371	536	563	672	877	773	848	775	614	458	391
$F2^C$	2914	2152	2094	1914	1747	1588	1366	1216	1190	1331	1153
$F3^C$	4666	2525	2801	2906	3049	3926	3365	3015	3036	2845	2976
Δ1	0.7	−3.8	−18.9	−12.8	6.9	25.3	19.8	13.5	1.9	−27.4	−9.5
Δ2	3.0	−1.3	−8.0	−5.4	2.1	10.9	2.8	−1.2	17.1	−1.7	0.7
Δ3	31.4	−22.8	−12.8	−9.8	−6.3	25.9	2.0	−8.6	−1.6	−10.0	−7.1

TABLE V. Fundamental frequencies F_0 and measured and calculated formants for the 11 vowels of speaker SM1.

	i	ɪ	e	ɛ	æ	ʌ	ɑ	ɔ	o	ʊ	u
F_0	122	126	125	126	124	125	125	123	124	123	126
$F1^N$	311	449	495	496	566	521	640	631	493	463	326
sd	±5	±5	±4	±4	±4	±4	±6	±6	±3	±5	±3
$F2^N$	2086	1765	1729	1693	1598	1236	1105	925	912	1137	928
sd	±20	±19	±18	±38	±7	±8	±26	±12	±20	±24	±13
$F3^N$	2570	2299	2278	2272	2172	2246	2465	2513	2356	2277	2282
sd	±23	±29	±30	±33	±12	±11	±29	±20	±16	±32	±13
$F1^C$	327	414	470	503	638	552	701	636	442	390	314
$F2^C$	2032	1771	1650	1599	1671	1361	1184	984	1047	1211	954
$F3^C$	2514	2418	2356	2400	2497	2605	2596	2596	2488	2366	2235
Δ1	5.2	−7.7	−5.0	1.4	12.7	5.9	9.5	0.9	−10.3	−15.8	−3.8
Δ2	−2.6	0.3	−4.6	−5.5	4.6	10.1	7.1	6.4	14.8	6.5	2.8
Δ3	−2.2	5.2	3.4	5.7	15.0	16.0	5.3	3.3	5.6	3.9	−2.1

TABLE VI. Fundamental frequencies F_0 and measured and calculated formants for the 11 vowels of speaker SM2.

	i	ɪ	e	ɛ	æ	ʌ	ɑ	ɔ	o	ʊ	u
F_0	144	145	144	143	141	142	139	138	135	137	135
$F1^N$	289	428	425	547	606	568	659	569	406	515	352
sd	±1	±2	±4	±3	±4	±3	±4	±2	±11	±10	±11
$F2^N$	2215	1866	1983	1740	1719	1329	1180	875	799	974	818
sd	±17	±6	±13	±12	±10	±19	±11	±9	±21	±19	±6
$F3^N$	2729	2429	2454	2664	2606	2675	2678	2924	2867	2892	2424
sd	±45	±7	±10	±14	±12	±22	±24	±22	±14	±45	±24
$F1^C$	294	446	425		748	559	742	568	462	457	286
$F2^C$	2317	1845	2013		1816	1340	1170	837	942	1185	864
$F3^C$	2651	2577	2624		2648	2691	2928	2338	2979	2870	2934
Δ1	1.6	4.2	−0.1		23.5	−1.6	12.6	−0.1	13.7	−11.3	−18.8
Δ2	4.6	−1.1	1.5		5.6	0.8	−0.9	−4.4	17.9	21.7	5.6
Δ3	−2.9	6.1	6.9		1.6	0.6	9.4	−20.0	3.9	−0.8	21.1

TABLE VII. Fundamental frequencies F_0 and measured and calculated formants for the 11 vowels of speaker SM3.

	i	ɪ	e	ɛ	æ	ʌ	ɑ	ɔ	o	ʊ	u
F_0	134	129	129	131	126	122	122	122	123	124	125
$F1^N$	307	499	519	538	652	619	678	627	498	514	355
sd	±7	±3	±1	±4	±7	±3	±4	±3	±3	±9	±5
$F2^N$	2171	1773	1720	1723	1595	1244	1041	866	845	1044	696
sd	±8	±17	±12	±28	±6	±7	±23	±4	±12	±27	±14
$F3^N$	3224	2322	3311	2367	2345	2142	2134	2276	2413	2319	2338
sd	±45	±18	±11	±24	±35	±16	±15	±14	±29	±69	±32
$F1^C$	265	503	567	563	758	495	722	637	611	429	404
$F2^C$	2428	1897	1903	1662	1753	1134	1089	875	1068	1207	1034
$F3^C$	3328	2187	2356	2020	2304	2122	2489	2044	2591	2503	2618
Δ1	−13.6	0.7	9.2	4.6	16.3	−20.0	6.5	1.6	22.7	−16.6	13.9
Δ2	11.9	7.0	10.7	−3.6	9.9	−8.8	4.6	1.1	26.4	15.6	48.5
Δ3	3.2	−5.8	−28.8	−14.6	−1.7	−0.9	16.6	−10.2	7.4	8.0	12.0

measured and calculated formants for all of the vowels produced by each of the three speakers is reasonably accurate. Nearly two-thirds of the errors were calculated to be less than 10% and more than a third were less than 5%.

IV. "SYNERGISTIC" MODES

Based on visual inspection, and comparison of calculated and measured formant frequencies, it was assumed that the six sets of area functions provide a reasonable "sampling" of possible vocal tract configurations used by each speaker to produce these vowels. From this "sampling," a set of *modes*, as defined in the Introduction, are reported for *each* speaker. The similarity of the modes across speakers was assessed visually, with correlation analysis and with an acoustic mapping technique.

A. Principal components analysis

The collection of area vectors for a given speaker (i.e., Tables XI–XVI) can be represented in matrix form as $A(i,j)$, where i is the area index as defined in Sec. II B, and j denotes the particular vowel in the left-to-right order used in the tables in Appendix A (i.e., $j=1$ for [i], $j=2$ for [ɪ]…, $j=11$ for [u]). A principal components analysis (PCA) was used to derive, for each of the six $A(i,j)$'s, a set of orthogonal eigenvectors representing the prominent vocal tract shaping features utilized by each speaker. Following Story and Titze (1998), the PCA was performed on the equivalent diameters of the cross-sectional areas rather than on the areas themselves.[3] Thus, an area matrix $A(i,j)$ was first converted to a diameter matrix $D(i,j)$ by

$$D(i,j) = \sqrt{\frac{4}{\pi}A(i,j)}. \tag{2}$$

The square root operation has the effect of compressing and expanding the portions of a vocal tract shape with the largest and smallest areas, respectively, and has been shown to produce somewhat more accurate reconstructions of vowel configurations than a PCA performed on areas alone (Story and Titze, 1998).

The next step was to assume that a speaker's $D(i,j)$ can be represented by a mean and variable part,

$$D(i,j) = \Omega(i) + \alpha(i,j), \tag{3}$$

where $\Omega(i)$ is the mean diameter vector across $D(i,j)$, and $\alpha(i,j)$ is the variation superimposed on $\Omega(i)$ to produce a specific diameter vector. The PCA was then carried out by calculating the eigenvectors of a covariance matrix formed with $\alpha(i,j)$. The specific implementation was essentially the same method as reported in Story and Titze (1998), and results in the following parametric representation of the original *area* matrix,

$$A(i,j) = \frac{\pi}{4}\left(\Omega(i) + \sum_{i=1}^{N} q_k(j)\phi_k(i)\right)^2,$$
$$i=[1,N] \quad j=[1,11], \quad k=[1,N] \tag{4}$$

where the $\phi_k(i)$'s are 44-element eigenvectors that, when multiplied by the appropriate scaling coefficients $q_k(j)$, will reconstruct each area vector in $A(i,j)$. As explained in the Introduction, the eigenvectors or principal components obtained from the area vector matrices have been called *modes* and will henceforth be referred to as such.

This particular implementation of the PCA effectively normalizes the vocal tract lengths for each speaker's vowels by excluding the length data in the analysis. That is, for each speaker's $A(i,j)$, and subsequent $D(i,j)$, the ith section was assumed to correspond to the same location within the vocal tract. This is not strictly true because each area function in Tables XI–XV has its own unique length increment Δ, thus the distance of the ith tubelet from the glottis is vowel dependent. Comparisons of the formant frequencies calculated with the actual lengths of each area function to those based on the normalized length showed approximately a 5% shift upward for the longest area function in each speaker's set and a 5% downward shift for the shortest. Whereas this approach somewhat limits the interpretation of the results, especially with regard to rounded vowels which typically have long vocal tract lengths, it simplified the execution of the PCA and facilitated the comparison of modes across speakers.

To further aid interspeaker comparison, the three modes that accounted for most of the variance in each speaker's $D(i,j)$ [referred to as $\phi_1(i), \phi_2(i), \phi_3(i)$] have been smoothed by fitting them with eighth-order polynomials. This simplified the visual comparison of the modes but maintained their gross characteristics. The amount of variance in each speaker's diameter matrix that is accounted for by each mode was calculated based on these smoothed modes.

TABLE VIII. Percentage of the total variance in each speaker's diameter matrix $D(i,j)$ accounted for by the most significant modes (in their smoothed form).

Mode	SF1	SF2	SF3	SM1	SM2	SM3
ϕ_1	63.6	61.1	63.0	76.2	67.4	63.7
ϕ_2	21.5	22.0	28.7	12.3	20.5	25.2
ϕ_3	7.7	7.4	3.0	4.5	4.7	8.4
Total	92.8	90.5	94.7	93.0	92.6	97.3

B. Modes and mean area functions for six speakers

Percentages of the total variance in each speaker's diameter matrix $D(i,j)$ that are accounted for by the three most significant modes are shown in Table VIII. Together, the three modes accounted for more than 90% of the variance for each speaker. The first mode, ϕ_1, accounted for variance of over 60%, while ϕ_2 typically accounted for 20% or more. The exception was SM2 whose second mode accounted for only 12.3% of the variance in his diameter matrix, but was balanced by the high 76.2% that was attributed to his first mode. The first two modes combined accounted for a minimum of 83% of the variance for SF2 and a maximum of 91.7% for SF3. The amount of variance accounted for by ϕ_3

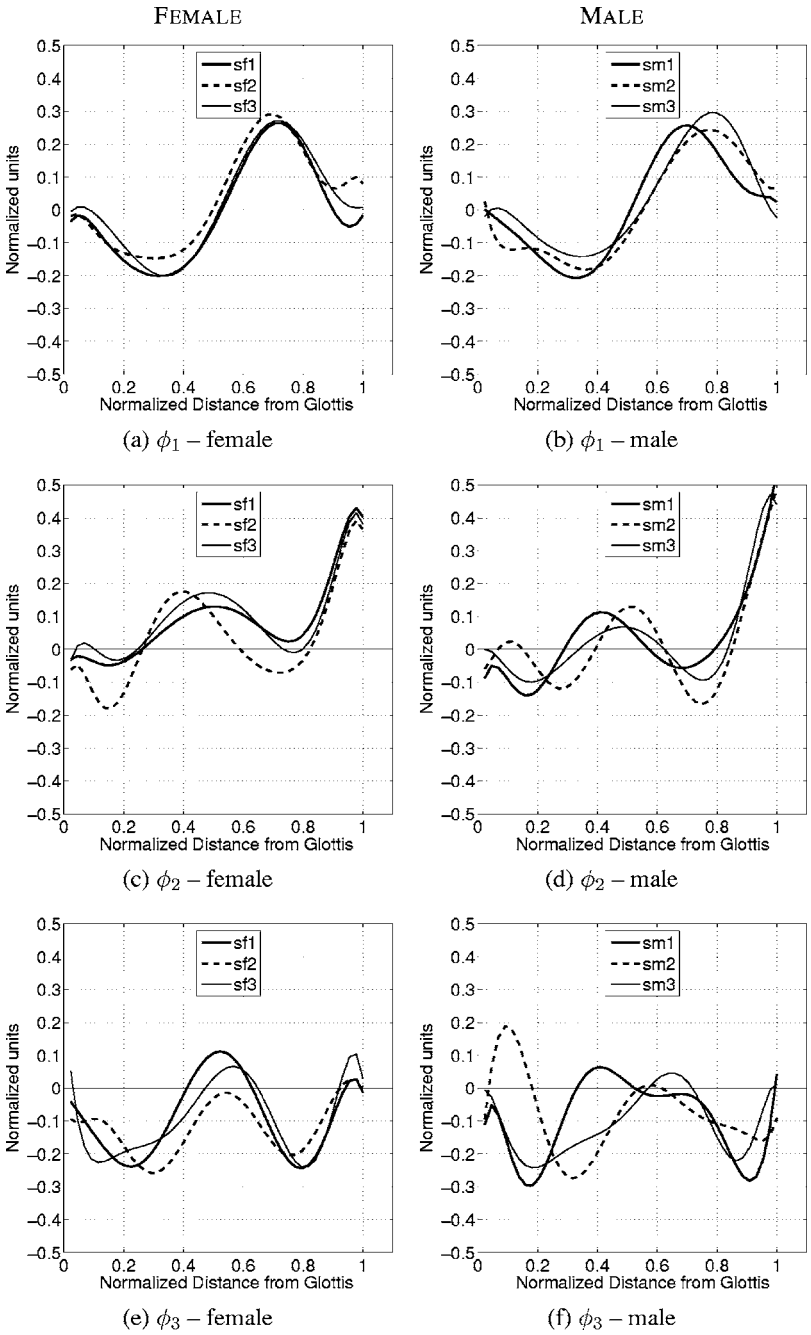

FIG. 6. Three modes obtained from the area function data of the three female and three male speakers. The left column shows plots corresponding to the females (a, c, and e) and the right corresponds to the males (b, d, and f). Each row of the plot is associated with mode ϕ_1, ϕ_2, or ϕ_3.

was no greater than 8.4% for any of the speakers. Thus, the third mode is much less significant than either ϕ_1 or ϕ_2.

The three modes are shown graphically in Fig. 6 and, for reference, are numerically tabulated in Appendix B. This figure is arranged so that the left and right columns of plots correspond to the three female and three male speakers, respectively. Each row corresponds to one of the three modes ϕ_1, ϕ_2, or ϕ_3. Note that the x axis of each plot ranges from 0 to 1.0 to indicate a normalized distance from the glottis. An approximate actual distance could be obtained for each speaker by scaling the x axis with their respective mean vocal tract lengths. Associated with the plots of the three modes are their respective scaling coefficients that correspond to each speaker's vowels. These are given in Table IX, where the minimum and maximum values along each row are shown in boldface.

The first mode, shown in Figs. 6(a) and 6(b), presents similar characteristics for all of the speakers. The amplitude is near zero at both the glottal and lip ends, a zero crossing occurs at approximately the mid-point of the vocal tract, and negative and positive maxima occur at normalized distances of about 0.35 and 0.75, respectively. When scaled with a positive coefficient and superimposed on a mean vocal tract shape, as specified by Eq. (4), this mode would have the effect of constricting the pharyngeal portion of the tract while expanding the oral cavity; the glottal and lip ends would be minimally affected. Such a shape would be characteristic of a low-back vowel. A negative scaling coefficient would impose the opposite changes in vocal tract shape and would be suggestive of a high-front vowel. It is not surprising then that the scaling coefficient for the first mode, q_1, shown in Table IX, is maximally positive for the [ɔ] vowel

TABLE IX. Scaling coefficients of the three modes that will reconstruct each of the 11 vowels. Coefficients are given for all six speakers. The minimum and maximum values along each row are shown in boldface type.

Subject	Coefficient	i	ɪ	e	ɛ	æ	ʌ	ɑ	ɔ	o	ʊ	u
SF1	q_1	**−4.667**	−2.456	−1.206	−1.275	0.359	1.168	3.170	**3.790**	1.572	0.756	−1.211
	q_2	0.770	0.610	0.894	−1.119	**2.455**	**−2.108**	1.619	0.342	−0.485	−1.500	−1.478
	q_3	0.496	0.330	−0.135	0.690	−0.222	**1.406**	0.197	0.250	−1.044	−0.018	**−1.949**
SF2	q_1	**−4.025**	0.070	−2.213	0.930	0.821	1.263	2.969	**3.457**	0.563	−0.692	−3.142
	q_2	0.859	**1.059**	0.761	2.833	0.789	−0.355	−1.311	−0.123	−1.075	−1.485	**−1.952**
	q_3	0.357	**−1.728**	0.852	−0.150	**1.067**	−0.244	0.734	0.332	−1.270	0.230	−0.180
SF3	q_1	**−4.927**	−2.506	−2.228	−0.591	2.999	0.961	3.460	**3.761**	1.378	−0.179	−2.128
	q_2	1.503	0.825	1.618	1.000	**2.842**	−2.290	0.546	0.715	−1.942	**−2.467**	−2.351
	q_3	−0.249	**0.702**	0.384	0.233	−0.608	0.549	−0.347	0.178	0.168	0.499	**−1.508**
SM1	q_1	**−3.860**	−2.192	−1.334	−0.956	0.295	1.169	2.659	**4.260**	1.761	−0.120	−1.683
	q_2	0.131	0.510	0.636	0.717	**1.437**	−0.251	0.542	0.294	−1.206	**−1.448**	−1.360
	q_3	−0.410	0.242	0.400	0.138	−0.184	0.658	0.038	−0.687	−0.001	**0.895**	**−1.090**
SM2	q_1	**−4.777**	−2.109	−3.115	⋯	1.864	0.396	4.175	**4.816**	0.915	−0.449	−1.715
	q_2	0.879	0.529	1.276	⋯	**3.209**	−0.142	0.694	−0.727	−1.621	−1.242	**−2.854**
	q_3	0.298	−0.670	1.039	⋯	**−1.300**	**1.254**	0.084	0.461	0.332	−0.214	−1.285
SM3	q_1	**−5.047**	−2.349	−1.740	−1.682	0.916	−0.235	3.409	**5.066**	3.725	−1.350	−0.714
	q_2	−0.079	0.851	2.176	1.184	**3.531**	−1.979	−0.213	0.298	−0.656	**−2.657**	−2.457
	q_3	−1.551	0.812	0.584	0.901	−0.801	**1.453**	0.709	−0.012	−1.246	0.999	**−1.849**

across all six speakers. Likewise, for every speaker, q_1 has the largest negative value for the vowel [i]. It is also noted that q_1 generally increases stepwise from this most negative value toward the most positive as the vowel changes in the order given in the table. This ordering of vowels follows a counter-clockwise rotation through a articulation-based vowel quadrilateral (e.g., Shriberg and Kent, 2003; p. 28), or clockwise through a typical F1-F2 vowel space plot.

Collections of the second mode, ϕ_2, for the six speakers are shown in Figs. 6(c) and 6(d). Though the similarity across speakers is perhaps not as visually apparent as for the first mode, the ϕ_2's do possess some common features. The lip end of these modes is uniformly of high amplitude, suggesting that it would expand or constrict the mouth opening with positive and negative scaling coefficients, respectively. Moving posteriorly from the lips, each ϕ_2 drops sharply in amplitude and, for five speakers, crosses zero at a normalized distance from the glottis of about 0.8. SF1's second mode does not have a zero crossing at this point but does maintain a shape that is similar to the other speakers. The amplitude then drops further until a local minima is reached at a location ranging from 0.68 to 0.78 across the speakers. Continuing toward the glottal end, a local maxima is encountered for each speaker at a normalized distance between 0.4 and 0.5. As the amplitude drops again, the second mode for each of the females has a zero crossing at a distance of about 0.25. The ϕ_2 amplitudes for the males also drop but their subsequent zero crossings are not as closely aligned as they are for the females. Finally, for all speakers, the ϕ_2 amplitudes dip down to another local minima before returning to nearly zero amplitude at the glottal end. In general, the primary effect of the second mode on vocal tract shape is to expand or constrict both the lip end and the middle portion, depending on whether the scaling coefficient q_2 is positive or negative. From Table IX, it is apparent that the largest positive value of q_2 occurred for the [æ] vowel of every speaker except SF2. Also, with the exception of SF2, the most negative value of q_2 is associated with either the vowel [ʊ] or [u]. Notwithstanding the results for SF2, this suggests that the second mode roughly corresponds to a continuum from low-front to high-back vowels.

The primary features contributed to the vocal tract shape by the third mode, shown in Figs. 6(e) and 6(f) are complementary expansive or constrictive effects in both the pharyngeal and oral cavities. This is most apparent for the female speakers, but approximately true for the male speakers as well. Although only a small percentage of the variance is accounted for by this mode (see Table VIII), the simultaneous expansive effects in the pharyngeal and oral cavities, obtained with a negative scaling coefficient, would seem to be useful for enhancing vocal tract shapes with a mid-tract constriction. This is supported by Table IX where, for four of the six speakers, the largest negative value of q_3 occurred for the [u] vowel.

To provide a numerical assessment of the similarity of the mode shapes, a correlation coefficient was calculated for each speaker's modes relative to those of the other five speakers. The calculation was performed by dividing the covariance of a given pair of modes (e.g., ϕ_1 from SF1 and SF2) by the product of their standard deviations (e.g., Taylor, 1982). Note that because normalized vocal tract length is assumed for all correlation calculations, female modes can be compared to male modes. The correlation coefficients are presented in Table X and are arranged so that female-female, female-male, and male-male comparisons within each mode can be readily observed. The upper part of the table indicates that the shape of the first mode is highly correlated among all of the speakers, which supports the visual comparisons dis-

TABLE X. Matrix of correlation coefficients quantifying the similarity of ϕ_1, ϕ_2, ϕ_3, and $(\pi/4)\Omega^2$ across the six speakers. The table is divided into sections showing female-female, male-male, and female-male comparisons.

		Female			Male		
Quantity	Subject	SF1	SF2	SF3	SM1	SM2	SM3
ϕ_1	SF1	1.00	0.97	0.99	0.98	0.90	0.91
$\bar{R}_1=0.94$	SF2		1.00	0.96	0.99	0.91	0.87
	SF3			1.00	0.99	0.92	0.93
	SM1				1.00	0.93	0.90
	SM2					1.00	0.97
	SM3						1.00
ϕ_2	SF1	1.00	0.90	0.97	0.94	0.86	0.97
$\bar{R}_2=0.91$	SF2		1.00	0.93	0.95	0.74	0.89
	SF3			1.00	0.93	0.90	0.96
	SM1				1.00	0.82	0.94
	SM2					1.00	0.92
	SM3						1.00
ϕ_3	SF1	1.00	0.74	0.90	0.53	0.11	0.59
$\bar{R}_3=0.44$	SF2		1.00	0.74	−0.06	0.41	0.43
	SF3			1.00	0.39	−0.04	0.69
	SM1				1.00	−0.18	0.60
	SM2					1.00	0.25
	SM3						1.00
	SF1	1.00	0.93	0.92	0.64	0.66	0.70
$\frac{\pi}{4}\Omega^2$	SF2		1.00	0.89	0.69	0.74	0.68
	SF3			1.00	0.64	0.57	0.67
$\bar{R}=0.71$	SM1				1.00	0.72	0.52
	SM2					1.00	0.73
	SM3						1.00

cussed previously. The highest correlation coefficients were $R=0.99$ for the comparisons of SF1-SF2, SF2-SM1, and SF3-SM1. The lowest correlation for the first mode was $R=0.87$ resulting from the comparison of SF2-SM3; this was the only R below 0.90. The mean correlation coefficient across all comparisons of the first mode was $\bar{R}_1=0.94$ and is shown in the far left-hand column of the table. The correlation across speakers for the second mode was also fairly high as indicated by the mean coefficient of $\bar{R}_2=0.91$. In addition, 11 of the 15 coefficients were greater than 0.90, while the low was 0.74. As expected from visual inspection, the shape of the third mode is less well correlated across speakers with $\bar{R}_3=0.44$. The female-female comparisons did have R values that were 0.74 or greater, but any of the correlations involving male speakers were typically much lower than 0.70.

Correlation coefficients are also presented in Table X for the mean area vectors of the six speakers. These vectors were generated from Eq. (4), but with the mode coefficients set to zero [i.e., $\pi/4\Omega^2(i)$]. For female-female comparisons, the correlation coefficients ranged from 0.89 to 0.93. These are fairly high, but somewhat less so than their correlations for either ϕ_1 or ϕ_2. The correlations for male-male mean area vectors are comparatively low, and the female-male correlations are lower yet. The mean correlation coefficient across all of the comparisons is $R=0.71$.

The low correlation for the mean area vectors across speakers suggests that they are somewhat more speaker-specific than either of the ϕ_1 or ϕ_2 modes. They are plotted for each female speaker in Fig. 7(a) and for the male speakers in Fig. 7(b). Visually, the three female area vectors are similar to each other, but they also possess some idiosyncratic features such as differences in maximum cross-sectional area and shape of the mid-portion of the vocal tract. For the male speakers, the mean area vectors appear more idiosyncratic than those of the females, as expected from the correlation analysis. For example, the cross-sectional areas within the pharyngeal portion of the vocal tract (i.e., between about 0.2 and 0.4) are similar for SM1 and SM3, but they differ in the oral cavity. In contrast, the oral cavity areas are similar for SM2 and SM3, but their pharyngeal areas differ by about 1.5–2.0 cm^2.

Frequency response functions for the six mean area *functions* were calculated and are plotted in Figs. 7(c) and 7(d). This calculation was performed with the methods described in Sec. II C and with the tubelet length set to the mean of a given speaker's set of Δ's as given in the next to last row of Tables XI–XVI. As indicated by Fig. 7(c), the first two formant frequencies were closely aligned for the female speakers, where F1 ranged from 684 to 744 Hz and F2 from 1675 to 1741 Hz. F1 and F2 were also similar for the male speakers [Fig. 7(d)]. Their F1 values ranged from 536 to 626 Hz, while F2 ranged from 1430 to 1553 Hz. The

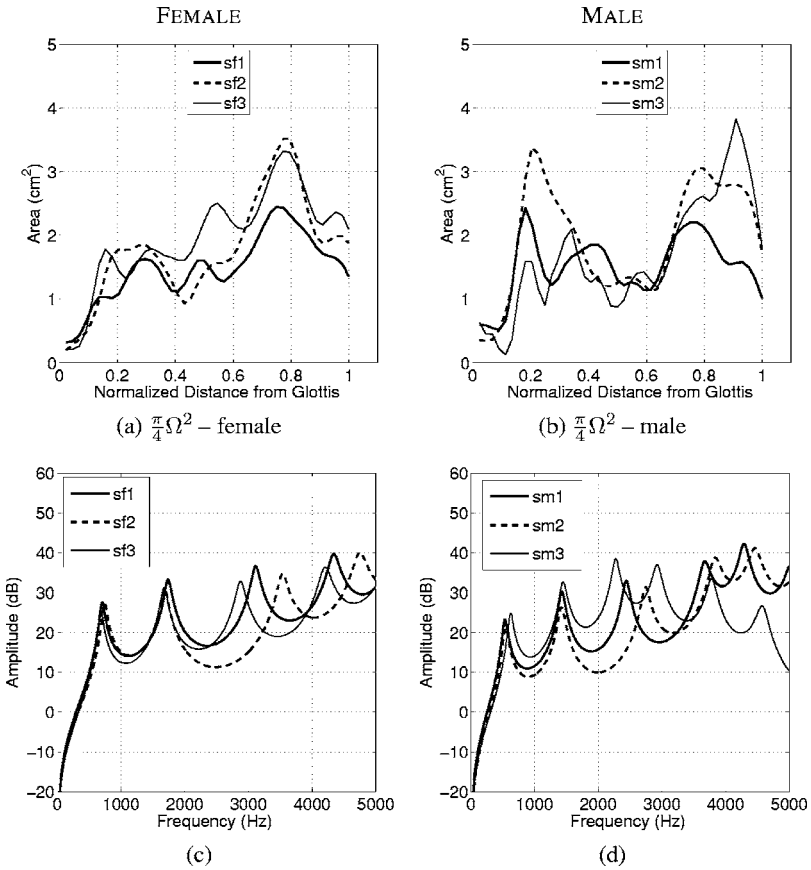

FIG. 7. Mean area vectors and calculated frequency response functions for six speakers. (a) Area vectors for SF1 (thick), SF2 (dashed), and SF3 (thin); (b) area vectors for SM1 (thick), SM2 (dashed), and SM3 (thin); (c) frequency response functions corresponding the female area vectors in (a); and (d) frequency response functions corresponding the male area vectors in (b).

values of F1 and F2 for both female and male speakers are approximately representative of a "neutral" vowel. That is, they are similar to those expected from a uniform tube with length appropriate for each speaker. There were, however, large differences in the locations of the upper formants, a frequency range where the idiosyncratic differences of the area vectors seem to exert their largest effect on the acoustic characteristics. Thus, each speaker's mean area vector could be considered to be a phonetically neutral vocal tract shape with regard to F1 and F2, but speaker-specific for higher frequency formants.

C. Mode coefficient-to-formant mapping

In the previous section, the spatial similarity of the mode shapes across speakers was assessed by visual inspection and with correlation analysis. To a large degree, the vocal tract shape changes imposed by the modes were found to be similar regardless of the speaker. It follows that the modes should also similarly affect the formant frequencies supported by area functions generated with Eq. (4), but perhaps with speaker-specific characteristics due to the underlying neutral shape on which the modes are superimposed.

To demonstrate the acoustic effects of the modes, a mapping was generated for each speaker that linked the three scaling coefficients (q_1, q_2, and q_3) to the first two formant frequencies (F1 and F2). This was motivated by a similar approach used by Story and Titze (1998) for two modes and is capable of producing thousands of area function configurations that did not exist in a given speaker's original area function set. The first step was to generate an equal increment continuum for each mode coefficient that ranged from their respective minimum to maximum values (see Table IX). The increments were specified as

$$\Delta q_1 = \frac{q_1^{\max} - q_1^{\min}}{M-1}, \tag{5a}$$

$$\Delta q_2 = \frac{q_2^{\max} - q_2^{\min}}{N-1}, \tag{5b}$$

$$\Delta q_3 = \frac{q_3^{\max} - q_3^{\min}}{K-1}, \tag{5c}$$

where M, N, and K were the number of increments along each coefficient dimension. Since the first two modes accounted for most of the variance in the original data sets (i.e., Table VIII), it was assumed that they would have the largest acoustic effects. Hence, the sampling along the q_1 and q_2 continua was chosen to be more dense than for q_3, such that M, N, and K were set to 60, 60, and 5, respectively. The coefficient continua were then generated by

$$q_{1m} = q_1^{\min} + m\Delta q_1, \quad m = 0, \ldots, M-1, \tag{6a}$$

$$q_{2n} = q_2^{\min} + n\Delta q_2, \quad n = 0, \ldots, N-1, \tag{6b}$$

$$q_{3k} = q_3^{\min} + k\Delta q_3, \quad k = 0, \ldots, K-1, \tag{6c}$$

with m, n, and k serving as indexes along each continuum.

By modifying Eq. (4) to contain only three modes and to eliminate the dependency on a specific vowel (i.e., jth vowel), an area vector can be generated with

TABLE XI. Area vectors for the 11 vowels of speaker SF1. Each original area function has been segmented to consist of 44 area sections; the length of each section is given by Δ. The glottal end of each area vector is at section 1 and the lip end at section 44. The total vocal tract length (VTL) is computed as 44Δ.

Section i	i	ɪ	e	ɛ	æ	ʌ	ɑ	ɔ	o	ʊ	u
1	0.42	0.34	0.29	0.34	0.22	0.24	0.27	0.28	0.28	0.41	0.46
2	0.48	0.45	0.33	0.35	0.26	0.23	0.12	0.24	0.35	0.47	0.67
3	0.53	0.53	0.51	0.35	0.44	0.25	0.16	0.20	0.46	0.77	0.77
4	0.58	0.66	0.89	0.63	0.72	0.34	0.39	0.27	0.83	1.11	0.88
5	0.74	1.01	1.14	1.21	0.94	0.42	0.55	0.40	1.39	1.24	1.14
6	1.21	1.39	1.08	1.65	0.94	0.49	0.47	0.36	1.63	1.11	1.67
7	1.97	1.57	0.94	1.61	0.85	0.45	0.31	0.21	1.51	0.99	2.21
8	2.58	1.64	1.03	1.26	0.76	0.36	0.23	0.13	1.36	1.05	2.41
9	2.84	1.83	1.39	0.96	0.69	0.34	0.28	0.17	1.33	1.19	2.73
10	3.16	2.15	1.82	0.98	0.73	0.40	0.40	0.33	1.37	1.31	3.38
11	3.84	2.29	2.16	1.29	0.99	0.48	0.47	0.45	1.34	1.41	3.72
12	4.49	2.32	2.34	1.59	1.37	0.53	0.49	0.46	1.26	1.46	3.52
13	4.82	2.43	2.41	1.80	1.68	0.54	0.53	0.45	1.14	1.32	3.06
14	4.94	2.46	2.34	1.92	1.86	0.56	0.56	0.48	1.02	1.08	2.60
15	4.78	2.36	2.14	1.90	1.82	0.54	0.52	0.48	0.85	0.85	2.23
16	4.30	2.17	1.86	1.76	1.56	0.40	0.59	0.36	0.64	0.70	1.85
17	3.82	1.91	1.72	1.65	1.34	0.28	0.73	0.22	0.50	0.71	1.49
18	3.35	1.77	1.84	1.68	1.28	0.31	0.85	0.15	0.51	0.95	1.28
19	2.92	1.87	2.00	1.79	1.36	0.41	1.06	0.20	0.71	1.31	1.28
20	2.82	2.07	2.03	1.90	1.58	0.55	1.39	0.53	1.01	1.51	1.34
21	2.84	2.20	1.96	1.87	1.82	0.73	1.78	1.07	1.22	1.47	1.25
22	2.62	2.14	1.81	1.73	1.96	0.82	2.05	1.47	1.22	1.37	0.93
23	2.22	1.90	1.59	1.59	1.94	0.77	2.15	1.67	1.08	1.33	0.50
24	1.83	1.56	1.35	1.41	1.76	0.74	2.29	1.91	0.99	1.38	0.18
25	1.42	1.20	1.20	1.21	1.60	0.76	2.64	2.26	1.10	1.53	0.15
26	1.00	0.88	1.17	1.05	1.60	0.85	3.29	2.75	1.36	1.78	0.40
27	0.67	0.63	1.16	0.90	1.69	1.03	3.85	3.31	1.75	2.09	0.75
28	0.46	0.45	1.12	0.77	1.72	1.25	4.13	3.91	2.32	2.39	1.07
29	0.31	0.34	1.19	0.79	1.79	1.49	4.41	4.72	2.95	2.67	1.33
30	0.19	0.35	1.37	0.92	2.05	1.74	4.86	5.53	3.48	2.84	1.54
31	0.15	0.54	1.51	1.07	2.44	1.99	5.37	5.84	3.93	2.84	1.81
32	0.19	0.84	1.61	1.27	2.79	2.19	5.67	5.70	4.22	2.72	2.20
33	0.26	1.05	1.70	1.45	2.93	2.23	5.60	5.42	4.30	2.58	2.59
34	0.27	1.11	1.82	1.51	3.03	2.12	5.15	4.97	4.21	2.44	2.87
35	0.22	1.16	1.95	1.37	3.26	1.93	4.44	4.36	3.98	2.33	3.03
36	0.32	1.35	2.01	1.20	3.48	1.65	3.72	3.79	3.62	2.17	2.94
37	0.64	1.61	2.03	1.30	3.54	1.33	3.17	3.33	3.10	1.83	2.56
38	1.09	1.84	2.10	1.48	3.49	1.01	2.69	2.89	2.42	1.44	2.10
39	1.67	2.10	2.26	1.34	3.52	0.72	2.43	2.37	1.71	1.06	1.64
40	2.31	2.42	2.50	1.02	3.92	0.57	2.64	1.82	1.23	0.70	1.20
41	2.77	2.66	2.70	0.80	4.55	0.48	3.00	1.41	1.05	0.46	0.91
42	2.83	2.64	2.73	0.71	4.95	0.43	3.07	1.33	1.08	0.36	0.75
43	2.57	2.48	2.63	0.62	4.94	0.37	2.75	1.46	1.21	0.31	0.58
44	2.28	2.40	2.49	0.38	4.57	0.27	2.15	1.48	1.35	0.26	0.29
Δ	0.343	0.326	0.308	0.318	0.306	0.316	0.330	0.348	0.330	0.319	0.352
VTL	15.11	14.32	13.55	14.01	13.46	13.90	14.53	15.29	14.51	14.02	15.51

$$A_{mnk}(i) = \frac{\pi}{4}[\Omega(i) + q_{1m}\phi_1(i) + q_{2n}\phi_2(i) + q_{3k}\phi_3(i)]^2, \quad i = [1,44]. \tag{7}$$

This suggests that the three continua [Eq. (6)] form a parametric "articulation" space in the sense that any combination of the coefficients produces a vocal tract shape. With q_3 held constant at zero, the continua for the first two modes can be viewed as a 60×60 two-dimensional space consisting of all possible combinations of q_{1m} and q_{2n}. An example, based on SF1's coefficient set, is shown in Fig. 8(a), where every intersection point in the grid represents a $[q_1, q_2]$ pair. The thick solid and dashed lines indicate the continua for the first and second modes, respectively, when the other coefficient is zero. These represent the isolated spatial effect of each mode on the vocal tract shape, while all other lines (vertical or horizontal) in the grid are comprised of a nonzero contribu-

TABLE XII. Area vectors for SF2.

Section i	i	ɪ	e	ɛ	æ	ʌ	ɑ	ɔ	o	ʊ	u
1	0.19	0.27	0.13	0.12	0.15	0.10	0.07	0.20	0.44	0.34	0.29
2	0.19	0.33	0.27	0.11	0.16	0.26	0.24	0.17	0.66	0.51	0.42
3	0.25	0.44	0.39	0.11	0.22	0.36	0.38	0.17	0.88	0.52	0.70
4	0.34	0.59	0.59	0.17	0.27	0.45	0.46	0.17	1.04	0.50	1.15
5	0.53	0.68	0.97	0.33	0.33	0.71	0.53	0.16	1.15	0.82	1.72
6	0.94	0.77	1.52	0.41	0.55	1.23	0.68	0.21	1.40	1.66	2.49
7	1.58	1.10	1.98	0.34	0.90	1.63	0.88	0.59	2.03	2.42	3.28
8	2.19	1.67	2.05	0.42	1.07	1.62	0.88	1.07	2.65	2.55	3.77
9	2.55	2.13	1.87	0.87	0.96	1.53	0.70	1.11	2.90	2.34	3.91
10	2.84	2.31	1.82	1.38	0.74	1.57	0.63	0.84	2.89	2.08	3.83
11	3.38	2.58	1.98	1.67	0.63	1.65	0.67	0.58	2.77	1.83	3.52
12	3.95	3.08	2.11	1.84	0.78	1.67	0.69	0.50	2.61	1.72	2.99
13	4.21	3.38	2.08	1.98	1.06	1.54	0.66	0.66	2.29	1.65	2.49
14	4.09	3.26	1.84	2.13	1.18	1.35	0.57	0.77	1.91	1.53	2.23
15	3.72	3.06	1.58	2.28	1.09	1.28	0.47	0.69	1.66	1.49	2.02
16	3.28	2.83	1.55	2.31	1.10	1.19	0.39	0.55	1.39	1.47	1.58
17	2.75	2.48	1.61	2.18	1.29	0.89	0.34	0.50	0.98	1.28	1.08
18	2.25	2.11	1.54	1.88	1.34	0.52	0.29	0.53	0.59	0.91	0.84
19	2.06	2.00	1.42	1.59	1.13	0.49	0.19	0.51	0.48	0.61	0.89
20	2.11	2.19	1.48	1.64	0.94	0.97	0.17	0.40	0.72	0.69	1.05
21	2.04	2.30	1.55	1.94	1.01	1.62	0.43	0.32	1.16	1.09	1.10
22	1.70	2.14	1.39	2.13	1.31	2.01	1.12	0.46	1.55	1.41	0.95
23	1.32	1.88	1.03	2.17	1.78	2.15	1.92	0.95	1.71	1.52	0.78
24	1.02	1.59	0.64	2.18	2.20	2.26	2.48	1.75	1.71	1.56	0.59
25	0.76	1.40	0.42	2.19	2.39	2.39	2.98	2.53	1.72	1.61	0.35
26	0.53	1.41	0.43	2.15	2.33	2.56	3.55	3.20	1.86	1.71	0.27
27	0.38	1.55	0.54	2.14	2.20	2.96	4.19	3.89	2.20	1.87	0.33
28	0.29	1.99	0.69	2.19	2.16	3.57	4.90	4.59	2.75	2.09	0.41
29	0.26	2.83	0.89	2.35	2.21	4.04	5.48	5.19	3.35	2.33	0.53
30	0.28	3.69	1.09	2.66	2.24	4.37	5.78	5.69	3.81	2.48	0.72
31	0.34	4.14	1.15	3.17	2.24	4.62	5.82	6.14	4.15	2.57	0.99
32	0.40	4.34	1.13	3.72	2.41	4.67	5.70	6.48	4.53	2.65	1.41
33	0.53	4.66	1.27	4.07	2.81	4.53	5.57	6.61	4.93	2.72	1.97
34	0.78	4.91	1.55	4.16	3.34	4.26	5.35	6.49	5.18	2.72	2.40
35	1.15	4.79	1.78	3.91	3.86	3.80	4.80	6.18	5.07	2.62	2.54
36	1.43	4.22	1.82	3.32	4.03	3.08	3.98	5.74	4.44	2.33	2.46
37	1.44	3.40	1.56	2.79	3.83	2.36	3.04	5.12	3.49	1.95	2.14
38	1.29	2.85	1.39	2.67	3.39	1.91	2.17	4.19	2.68	1.58	1.70
39	1.17	2.81	1.72	3.05	2.90	1.68	1.56	3.22	2.02	1.19	1.28
40	1.20	2.96	2.32	3.95	2.71	1.71	1.24	2.58	1.50	0.85	0.88
41	1.43	2.93	2.77	5.10	2.82	1.98	1.23	2.37	1.26	0.68	0.54
42	1.64	2.73	2.94	5.96	2.83	2.21	1.37	2.57	1.28	0.65	0.32
43	1.67	2.48	2.85	6.30	2.61	2.16	1.44	2.74	1.46	0.68	0.22
44	1.63	2.17	2.61	6.23	2.27	1.82	1.38	2.58	1.63	0.69	0.20
Δ	0.303	0.315	0.311	0.309	0.317	0.294	0.315	0.329	0.323	0.321	0.313
VTL	13.32	13.84	13.71	13.60	13.93	12.94	13.85	14.47	14.22	14.11	13.76

tion from both coefficients. The inset plots within Fig. 8(a)demonstrate the area vector shapes generated at the end points of the ϕ_1 and ϕ_2 lines.

When q_3 is nonzero a third dimension is added to the articulation space. The q_2 vs q_1 grid will be the same as in Fig. 8(a), but can be considered to be shifted along the q_3 dimension. This is demonstrated in Fig. 8(b), again based on SF1's coefficients, where the dark grid in the middle is the case when $q_3=0$, and the other two lighter grids are positioned at the minimum and maximum values of q_3, respectively. Although $K=5$, only three grids are shown along the q_3 dimension to preserve the visual clarity of the figure.

To complete the mapping for a given speaker (e.g., SF1), Eq. (7) was used to generate an area vector for every coefficient combination within that speaker's three-dimensional coefficient space. A length vector was also generated in which the tubelet length (and consequently vocal tract length) was held constant for each speaker at the same mean values used to calculate frequency responses of the mean area functions in Sec. IV B. Finally, for each newly created area function, a set of formant frequencies was calculated.

Results for each of the six speakers are shown in the vowel space plots of Fig. 9. Within each figure panel is a dark, solid-lined grid of 3600 [F1, F2] pairs that corresponds

TABLE XIII. Area vectors for SF3.

Section i	i	ɪ	e	ɛ	æ	ʌ	ɑ	ɔ	o	ʊ	u
1	0.21	0.20	0.21	0.25	0.22	0.30	0.15	0.14	0.26	0.18	0.23
2	0.13	0.18	0.27	0.20	0.22	0.29	0.23	0.12	0.27	0.19	0.28
3	0.15	0.22	0.31	0.12	0.31	0.26	0.49	0.18	0.30	0.23	0.46
4	0.33	0.49	0.56	0.19	0.63	0.28	1.04	0.47	0.39	0.28	1.18
5	1.17	1.17	1.16	0.62	1.13	0.54	1.47	0.96	0.67	0.39	2.34
6	2.47	1.79	1.72	1.27	1.47	1.15	1.46	1.33	1.19	0.79	2.99
7	3.20	1.78	1.85	1.70	1.37	1.76	1.17	1.30	1.57	1.54	2.88
8	3.33	1.44	1.62	1.73	1.07	1.92	0.84	0.98	1.47	2.09	2.60
9	3.42	1.13	1.35	1.54	0.86	1.66	0.63	0.58	1.23	2.05	2.51
10	3.72	1.02	1.39	1.51	0.74	1.29	0.58	0.32	1.12	1.78	2.67
11	4.34	1.29	1.86	1.73	0.79	0.95	0.62	0.29	1.06	1.59	2.98
12	4.95	1.86	2.51	1.92	1.04	0.76	0.66	0.40	1.00	1.51	3.22
13	5.29	2.40	3.04	2.12	1.26	0.78	0.65	0.49	0.92	1.49	3.22
14	5.56	2.72	3.38	2.31	1.38	0.90	0.58	0.48	0.82	1.37	2.97
15	5.57	2.86	3.51	2.31	1.45	0.92	0.53	0.46	0.71	1.16	2.58
16	5.25	2.93	3.54	2.31	1.51	0.84	0.52	0.48	0.63	1.01	2.27
17	5.10	2.97	3.42	2.43	1.59	0.73	0.55	0.53	0.60	0.94	2.03
18	4.93	2.95	3.08	2.44	1.66	0.72	0.62	0.57	0.52	0.93	1.78
19	4.45	2.93	2.82	2.38	1.77	0.81	0.74	0.70	0.50	0.98	1.64
20	3.99	2.94	2.83	2.53	2.10	0.79	0.98	1.11	0.70	1.05	1.64
21	3.69	3.01	2.90	2.94	2.73	0.71	1.32	1.66	1.02	1.21	1.67
22	3.46	3.06	2.88	3.35	3.49	0.94	1.74	2.24	1.25	1.52	1.61
23	3.19	2.94	2.65	3.47	4.19	1.48	2.29	2.80	1.37	1.90	1.49
24	2.74	2.55	2.22	3.26	4.75	1.95	2.88	3.19	1.47	2.12	1.29
25	2.05	2.02	1.82	2.91	5.10	2.22	3.45	3.51	1.57	2.06	0.93
26	1.36	1.52	1.57	2.53	5.35	2.39	3.92	3.96	1.64	1.84	0.56
27	0.85	1.10	1.45	2.24	5.49	2.45	4.24	4.58	1.80	1.70	0.37
28	0.51	0.78	1.38	2.10	5.43	2.48	4.53	5.17	2.11	1.75	0.39
29	0.30	0.56	1.34	2.11	5.44	2.63	4.90	5.54	2.66	1.91	0.60
30	0.22	0.45	1.35	2.18	5.60	2.92	5.35	5.98	3.36	2.05	0.98
31	0.25	0.49	1.39	2.33	5.87	3.17	5.86	6.54	3.95	2.23	1.49
32	0.35	0.72	1.44	2.60	6.18	3.35	6.21	6.92	4.40	2.50	2.11
33	0.49	1.09	1.49	2.92	6.37	3.47	6.29	6.91	4.65	2.68	2.69
34	0.68	1.51	1.48	3.13	6.43	3.38	6.29	6.65	4.56	2.75	3.06
35	0.90	1.76	1.48	3.10	6.41	3.17	6.13	6.20	4.07	2.74	3.22
36	1.18	1.73	1.60	2.80	6.16	2.97	5.76	5.34	3.33	2.53	3.04
37	1.44	1.70	1.80	2.39	5.77	2.67	5.29	4.28	2.67	2.16	2.46
38	1.46	2.02	1.82	2.04	5.49	2.15	4.67	3.55	2.19	1.74	1.77
39	1.38	2.69	1.86	2.02	5.29	1.55	3.91	3.19	1.74	1.29	1.18
40	1.88	3.32	2.56	2.55	5.36	1.03	3.28	3.00	1.29	0.87	0.75
41	3.17	3.56	4.02	3.22	5.69	0.67	3.01	2.97	0.97	0.54	0.54
42	4.36	3.47	5.17	3.43	5.76	0.50	3.06	3.21	0.85	0.34	0.48
43	4.53	3.06	5.27	3.23	5.42	0.45	3.14	3.52	0.95	0.25	0.41
44	3.97	2.20	4.81	2.93	4.84	0.45	3.00	3.69	1.14	0.25	0.20
Δ	0.343	0.346	0.370	0.349	0.322	0.351	0.316	0.360	0.364	0.362	0.363
VTL	15.10	15.24	16.27	15.34	14.15	15.44	13.92	15.83	16.03	15.92	15.97

to a particular speaker's $[q_1, q_2]$ grid when $q_3=0$. The thick white lines (solid and dashed) indicate the formant frequency pairs that are produced in this same grid when either q_1 or q_2 are zero, thus demonstrating the acoustic effect of ϕ_1 or ϕ_2 by itself. The intersection point of these two lines gives the values of F1 and F2 when all three scaling coefficients are zero (i.e., the "neutral" location). There are five lighter, dashed grids "underneath" the dark one that are [F1, F2] pairs associated with the $[q_1, q_2]$ grids as they are shifted along the q_3 dimension. It is not intended that their separation be visible, but rather it is the extension of the vowel space around the dark grid provided by the third mode that is of interest. The four white dots (outlined in black) in each panel, plotted in clockwise order starting at the upper left corner, are the [F1, F2] pairs *measured* from the audio recording of each speaker's [i], [æ], [ɑ], and [u] vowels (see Tables II–VII).

Taking SF1 as an example, the solid white line in Fig. 9(a) represents the acoustic mapping of the q_1 coefficient continuum shown previously as the black, horizontal line in Fig. 8(a). This demonstrates that the primary acoustic effect of ϕ_1 is to generate a low F1 and high F2 when its scaling

TABLE XIV. Area vectors for SM1.

Section i	i	ɪ	e	ɛ	æ	ʌ	ɑ	ɔ	o	ʊ	u
1	0.70	0.75	0.34	0.75	0.36	0.18	0.77	0.73	0.86	0.79	0.62
2	0.73	0.58	0.45	0.64	0.43	0.33	0.43	0.70	0.71	0.77	0.85
3	0.78	0.52	0.46	0.52	0.44	0.34	0.25	0.56	0.60	0.75	0.99
4	0.90	0.53	0.36	0.45	0.41	0.35	0.30	0.41	0.50	0.69	1.08
5	1.54	0.83	0.40	0.55	0.46	0.44	0.62	0.39	0.49	0.68	1.29
6	2.77	1.75	0.96	1.18	0.83	0.66	1.10	0.72	1.05	0.99	2.02
7	3.73	2.60	1.87	1.97	1.53	1.31	1.50	1.37	2.05	1.69	3.49
8	3.98	2.56	2.33	2.10	2.02	1.91	1.52	1.65	2.55	2.22	4.70
9	3.95	2.09	2.09	1.79	1.92	1.81	1.12	1.21	2.23	2.03	4.74
10	3.86	1.84	1.66	1.53	1.49	1.43	0.62	0.67	1.58	1.45	3.98
11	3.77	1.88	1.50	1.50	1.07	1.05	0.32	0.39	1.03	1.04	3.05
12	3.86	2.14	1.61	1.78	0.82	0.74	0.23	0.27	0.71	0.96	2.38
13	4.08	2.55	1.76	2.20	0.93	0.83	0.28	0.24	0.69	1.16	2.06
14	4.33	2.97	2.04	2.56	1.32	1.14	0.39	0.28	0.82	1.36	1.83
15	4.44	3.20	2.52	2.78	1.61	1.29	0.43	0.31	0.87	1.43	1.67
16	4.29	3.18	2.83	2.85	1.79	1.33	0.49	0.40	0.87	1.43	1.60
17	4.11	3.06	2.85	2.85	1.91	1.43	0.67	0.60	0.91	1.45	1.57
18	3.82	2.88	2.70	2.78	1.95	1.51	0.91	0.85	1.05	1.50	1.60
19	3.36	2.57	2.50	2.52	1.89	1.54	1.15	1.16	1.25	1.54	1.59
20	2.88	2.14	2.19	2.09	1.63	1.58	1.32	1.43	1.35	1.56	1.55
21	2.37	1.66	1.74	1.69	1.33	1.52	1.23	1.42	1.22	1.46	1.47
22	1.93	1.35	1.42	1.52	1.21	1.35	0.98	1.20	1.05	1.17	1.19
23	1.70	1.15	1.36	1.45	1.27	1.34	0.99	1.25	1.22	0.95	0.86
24	1.43	0.91	1.26	1.27	1.32	1.56	1.31	1.73	1.56	1.00	0.77
25	0.99	0.66	0.97	0.99	1.21	1.74	1.63	2.30	1.76	1.09	0.77
26	0.63	0.45	0.70	0.81	1.02	1.82	1.82	2.86	1.87	1.02	0.63
27	0.38	0.34	0.55	0.75	0.97	1.97	2.11	3.72	2.13	0.99	0.48
28	0.20	0.44	0.52	0.81	1.17	2.35	2.63	4.84	2.58	1.11	0.44
29	0.19	0.65	0.65	1.03	1.46	2.80	3.18	5.63	3.09	1.39	0.55
30	0.30	0.79	0.86	1.30	1.65	3.03	3.56	5.91	3.57	1.74	0.83
31	0.39	0.85	1.07	1.50	1.75	3.05	3.71	6.04	3.83	1.95	1.16
32	0.46	0.89	1.29	1.72	1.85	3.01	3.67	6.06	3.78	2.03	1.37
33	0.62	0.91	1.44	1.91	2.02	2.92	3.51	5.87	3.65	2.07	1.50
34	0.77	0.97	1.47	1.97	2.22	2.71	3.27	5.50	3.56	2.04	1.63
35	0.80	1.11	1.51	1.95	2.34	2.34	3.12	5.01	3.24	1.92	1.66
36	0.80	1.18	1.61	1.90	2.37	1.92	3.03	4.46	2.56	1.73	1.64
37	0.83	1.11	1.64	1.80	2.34	1.50	2.75	3.89	1.84	1.45	1.63
38	0.89	1.09	1.54	1.70	2.23	1.19	2.31	3.36	1.50	1.11	1.58
39	1.04	1.32	1.46	1.65	2.14	1.07	2.01	3.09	1.43	0.78	1.58
40	1.20	1.60	1.52	1.72	2.31	1.10	2.04	2.99	1.30	0.54	1.58
41	1.28	1.69	1.63	1.82	2.76	1.19	2.23	2.71	1.09	0.42	1.42
42	1.33	1.63	1.64	1.83	3.15	1.25	2.33	2.26	0.83	0.33	0.99
43	1.32	1.50	1.55	1.72	3.22	1.16	2.25	1.85	0.53	0.23	0.47
44	1.22	1.34	1.44	1.50	3.01	0.98	2.03	1.42	0.22	0.12	0.05
Δ	0.393	0.403	0.409	0.399	0.381	0.400	0.372	0.393	0.408	0.394	0.420
VTL	17.28	17.73	18.02	17.56	16.75	17.58	16.35	17.31	17.94	17.34	18.48

coefficient q_1 is large and negative, and produces a fairly high F1 and low F2 when q_1 is large and positive. Such a result is not unexpected based on the mode coefficient table (Table IX) which suggests that ϕ_1 roughly represents vowels along the high-front to low-back continuum. The acoustic effect of ϕ_2, shown by the dashed white line, is to increase both F1 and F2 as the q_2 coefficient is increased from its most negative to most positive values. This result is also suggested by the mode coefficients in Table IX, where the largest negative and positive values of q_2 were typically associated with high-back and low-front vowels, respectively.

The dark grid in Fig. 9(a) shows how the entire rectangular $[q_1, q_2]$ coefficient space of Fig. 8(a) becomes deformed when mapped to the acoustic space. For the most part the characteristic shape of the ϕ_1 and ϕ_2 mappings (white lines) are retained throughout the grid and appear to influence its overall shape. This grid also demonstrates that the mapping between formant frequencies and mode coefficients is essentially one-to-one. That is, one [F1, F2] pair corresponds to one $[q_1, q_2]$ pair in Fig. 8(a). A similar one-to-one mapping of this type was reported by Story and Titze (1998).

TABLE XV. Area vectors for SM2. An area function for [ɛ] could not be obtained from this speaker.

Section i	i	ɪ	e	ɛ	æ	ʌ	ɑ	ɔ	o	ʊ	u
1	0.66	0.21	0.21	⋯	0.25	0.27	0.34	0.64	0.29	0.42	0.45
2	0.37	0.24	0.48	⋯	0.19	0.29	0.23	0.27	0.28	0.37	0.99
3	0.49	0.25	1.34	⋯	0.14	0.26	0.18	0.09	0.28	0.40	0.85
4	1.79	0.30	2.74	⋯	0.12	0.28	0.20	0.07	0.26	0.50	0.72
5	3.63	0.44	3.69	⋯	0.16	0.54	0.26	0.17	0.32	0.77	0.84
6	4.11	0.86	3.81	⋯	0.37	1.24	0.40	0.69	0.58	1.51	1.02
7	3.96	1.93	3.60	⋯	1.05	2.22	0.78	1.70	1.18	3.01	1.65
8	4.48	3.42	3.37	⋯	2.11	2.71	1.41	2.43	2.08	4.38	3.40
9	4.94	4.42	3.15	⋯	2.79	2.45	1.85	2.31	2.84	4.57	5.54
10	4.95	4.58	2.96	⋯	2.69	2.07	1.72	1.66	3.12	4.09	6.45
11	4.84	4.20	2.88	⋯	2.21	1.80	1.29	1.10	3.00	3.68	6.27
12	4.80	3.77	2.95	⋯	1.80	1.61	0.96	0.86	2.76	3.49	5.87
13	4.82	3.49	3.01	⋯	1.51	1.48	0.75	0.70	2.49	3.50	5.61
14	4.87	3.36	2.99	⋯	1.29	1.33	0.60	0.49	2.21	3.50	5.63
15	4.77	3.33	2.94	⋯	1.23	1.19	0.53	0.35	1.94	3.25	5.43
16	4.39	3.15	2.86	⋯	1.38	1.05	0.44	0.26	1.56	2.66	4.71
17	3.90	2.85	2.79	⋯	1.59	0.91	0.33	0.18	1.08	1.96	3.66
18	3.39	2.60	2.75	⋯	1.59	0.81	0.36	0.23	0.66	1.45	2.58
19	2.95	2.40	2.76	⋯	1.41	0.76	0.48	0.44	0.40	1.13	1.82
20	2.66	2.25	2.84	⋯	1.43	0.69	0.56	0.55	0.30	0.98	1.34
21	2.42	2.16	2.97	⋯	1.70	0.70	0.64	0.47	0.34	0.98	1.00
22	2.19	2.07	2.99	⋯	1.97	0.80	0.87	0.49	0.52	1.03	0.83
23	1.90	1.95	2.50	⋯	2.20	0.96	1.19	0.68	0.77	1.06	0.77
24	1.29	1.86	1.62	⋯	2.36	1.17	1.47	0.92	1.04	1.15	0.84
25	0.60	1.70	1.26	⋯	2.15	1.24	1.62	1.28	1.29	1.28	0.97
26	0.28	1.30	1.37	⋯	1.55	1.05	1.68	1.86	1.40	1.39	0.90
27	0.26	0.86	1.14	⋯	1.08	0.74	1.95	2.53	1.33	1.49	0.69
28	0.30	0.72	0.73	⋯	1.09	0.68	2.46	3.06	1.37	1.52	0.80
29	0.31	0.81	0.55	⋯	1.45	1.06	3.12	3.74	1.74	1.58	1.29
30	0.28	0.86	0.51	⋯	1.96	1.71	4.11	4.82	2.35	2.01	1.90
31	0.20	0.81	0.57	⋯	2.55	2.31	5.29	6.22	3.05	2.60	2.53
32	0.19	0.83	0.73	⋯	3.06	2.64	6.14	7.67	3.59	3.00	3.06
33	0.30	1.02	0.85	⋯	3.40	2.79	6.52	8.40	3.83	3.21	3.37
34	0.41	1.31	0.90	⋯	3.57	2.82	6.67	8.41	3.89	3.29	3.50
35	0.44	1.54	0.93	⋯	3.59	2.72	6.65	8.28	3.84	3.23	3.45
36	0.47	1.62	0.95	⋯	3.65	2.46	6.42	7.93	3.59	3.04	3.22
37	0.53	1.58	1.03	⋯	3.96	2.14	6.10	7.22	3.17	2.84	2.89
38	0.72	1.71	1.24	⋯	4.57	1.95	5.75	6.52	2.73	2.66	2.51
39	1.03	2.13	1.55	⋯	5.50	1.95	5.38	5.87	2.29	2.45	2.01
40	1.49	2.45	2.00	⋯	6.77	2.03	5.06	4.88	1.86	2.26	1.42
41	2.18	2.46	2.52	⋯	8.15	2.04	4.84	3.78	1.56	1.96	0.84
42	2.66	2.45	2.85	⋯	9.20	1.95	4.61	2.86	1.35	1.49	0.40
43	2.54	2.32	2.74	⋯	9.30	1.78	4.22	2.06	1.00	1.06	0.16
44	2.11	1.84	2.11	⋯	8.49	1.63	3.59	1.26	0.35	0.69	0.06
Δ	0.398	0.398	0.364	⋯	0.366	0.395	0.387	0.411	0.404	0.403	0.414
VTL	17.53	17.50	16.03	⋯	16.10	17.37	17.02	18.10	17.76	17.71	18.20

Also observable in Fig. 9(a) are the effects of the third mode on the acoustic mapping. Denoted by the light grids are the [F1, F2] pairs corresponding to the $[q_1, q_2]$ grids in Fig. 8(b) that have been shifted along the q_3 dimension. The most negative values of q_3 tend to lower both F1 and F2, extending the formant space to a region more representative of an [u] vowel. Large positive values of q_3 generally have the opposite effect of increasing F1 and F2. It is noted that all of the formant pairs for the measured vowels lie outside the dark grid, although [i] and [ɑ] are located just at the edge. This suggests that, for this speaker, the third mode is necessary to adequately represent her vowel space, especially for [u] and [æ].

The characteristics of the acoustic mappings for the other speakers shown in Fig. 9 are similar to those of SF1. It is evident that the independent effect of ϕ_1 on the vowel space (thick white lines) is to generate low F1 and high F2 frequencies at one end of the q_1 continuum and high F1 and low F2 frequencies at the other. Likewise, for all speakers, ϕ_2's effect (dashed white lines) is to produce F1s and F2s

TABLE XVI. Area vectors for SM3.

Section i	i	ɪ	e	ɛ	æ	ʌ	ɑ	ɔ	o	ʊ	u
1	0.95	0.58	0.96	0.69	0.60	0.61	0.47	0.69	0.47	0.53	0.50
2	0.73	0.44	0.45	0.44	0.38	0.84	0.34	0.73	0.44	0.37	0.65
3	0.58	0.29	0.22	0.25	0.23	0.95	0.20	0.87	0.36	0.25	0.66
4	0.54	0.15	0.17	0.11	0.17	0.53	0.10	0.78	0.26	0.14	0.75
5	0.73	0.13	0.21	0.05	0.25	0.15	0.14	0.35	0.28	0.35	1.11
6	1.48	0.21	0.41	0.21	0.55	0.19	0.42	0.12	0.64	1.11	2.05
7	2.70	0.41	0.83	0.83	0.96	0.73	0.75	0.23	1.24	1.73	3.00
8	3.37	0.96	1.24	1.46	1.16	1.55	0.87	0.57	1.53	1.58	3.01
9	3.34	1.43	1.17	1.38	1.03	1.68	0.82	0.89	1.32	1.26	2.75
10	3.48	1.23	0.80	0.92	0.72	1.24	0.66	0.74	1.08	1.33	2.63
11	3.98	0.92	0.68	0.81	0.52	1.31	0.46	0.57	1.16	1.41	2.51
12	4.71	1.22	0.96	1.21	0.82	1.48	0.37	0.65	1.25	1.45	2.82
13	5.38	1.94	1.41	1.76	1.55	1.33	0.44	0.52	1.23	1.66	3.26
14	5.67	2.69	1.93	2.11	2.04	1.43	0.52	0.37	1.31	1.74	3.42
15	5.37	3.26	2.37	2.25	2.01	1.57	0.57	0.38	1.27	1.47	3.07
16	4.50	3.28	2.55	2.03	1.75	1.33	0.58	0.36	0.98	1.13	2.40
17	3.59	2.80	2.42	1.57	1.61	1.00	0.48	0.33	0.77	0.98	2.02
18	3.04	2.35	2.20	1.38	1.66	0.88	0.41	0.35	0.74	1.06	1.91
19	2.68	2.16	1.84	1.38	1.72	0.91	0.45	0.40	0.79	1.05	1.82
20	2.24	1.86	1.30	1.24	1.58	0.83	0.56	0.43	0.92	0.81	1.67
21	1.74	1.41	1.16	1.04	1.36	0.59	0.54	0.42	1.15	0.68	1.27
22	1.44	1.22	1.41	1.01	1.39	0.46	0.49	0.36	1.39	0.88	0.83
23	1.42	1.30	1.58	1.23	1.66	0.59	0.89	0.31	1.32	1.15	0.74
24	1.45	1.39	1.60	1.52	1.89	0.93	1.54	0.54	1.16	1.25	0.87
25	1.24	1.27	1.45	1.55	1.92	1.34	1.89	1.25	1.39	1.16	0.99
26	0.91	1.01	1.15	1.33	1.80	1.56	2.03	2.01	1.85	1.06	0.95
27	0.60	0.85	0.79	1.03	1.66	1.58	2.20	2.40	2.27	1.06	0.86
28	0.33	0.75	0.54	0.74	1.59	1.58	2.47	2.83	2.69	1.17	0.92
29	0.17	0.69	0.51	0.62	1.66	1.73	2.92	3.79	3.30	1.37	1.16
30	0.10	0.70	0.65	0.66	1.87	1.98	3.73	5.08	4.37	1.58	1.49
31	0.07	0.74	0.79	0.74	2.15	2.23	4.86	6.19	5.68	1.70	1.88
32	0.06	0.78	0.91	0.84	2.38	2.44	5.84	6.82	6.62	1.69	2.34
33	0.08	0.83	1.03	0.98	2.51	2.58	6.29	7.14	7.05	1.55	2.82
34	0.15	0.94	1.19	1.14	2.56	2.56	6.30	7.38	7.12	1.38	3.09
35	0.28	1.04	1.27	1.21	2.60	2.39	6.10	7.59	6.85	1.27	3.18
36	0.35	1.01	1.25	1.18	2.95	2.12	5.75	7.83	6.74	1.30	3.40
37	0.45	1.00	1.34	1.23	3.92	1.78	5.27	8.26	7.45	1.44	3.60
38	0.96	1.21	1.72	1.58	5.52	1.44	4.82	8.65	8.22	1.50	3.46
39	1.95	1.82	2.65	2.58	7.35	1.23	4.64	8.35	7.67	1.26	3.01
40	2.75	2.78	4.11	3.92	8.82	1.25	4.54	7.26	6.07	0.78	2.20
41	2.91	3.43	5.41	4.45	9.54	1.33	4.13	5.99	4.34	0.44	1.25
42	2.71	3.48	6.03	4.25	9.61	1.17	3.39	4.65	2.78	0.34	0.66
43	2.28	3.23	6.06	3.74	9.18	0.75	2.43	3.07	1.67	0.29	0.44
44	1.57	2.70	5.76	2.84	8.34	0.25	1.52	1.49	0.96	0.24	0.29
Δ	0.399	0.411	0.393	0.404	0.395	0.395	0.409	0.428	0.406	0.415	0.409
VTL	17.57	18.07	17.28	17.79	17.38	17.38	17.98	18.84	17.87	18.28	17.98

that are both low in frequency at the negative end of the q_2 continuum and both high in frequency at the positive end. There are, however, speaker-specific differences. For example, the ϕ_1 line for SF2 has a relatively shallow slope and lacks the distinct curvature near the endpoints exhibited by the other speakers. This contrasts most apparently with the steepness of SM3's ϕ_1 line as well as with the curved portions at both the upper left and lower right ends of the line. For each speaker, the characteristic shape of their ϕ_1 and ϕ_2 lines is essentially retained throughout the entire vowel space mapping and influences its overall shape. Furthermore, the dark grids, representing the cases when $q_3=0$, all represent nearly one-to-one mappings between the $[q_1,q_2]$ coefficient space and the [F1, F2] acoustic space. The exception is for SM3 [Fig. 9(f)] where the upper left portion of his [F1, F2] grid indicates that multiple coefficient pairs correspond to the same [F1, F2] pair. This seems to be due in part to the steepness of ϕ_1 line.

When the q_3 dimension is included, the formant space for all speakers is slightly expanded. A consequence of this expansion is that, with the exception of the [u] vowel for SM1, all of the measured formant pairs for the four vowels

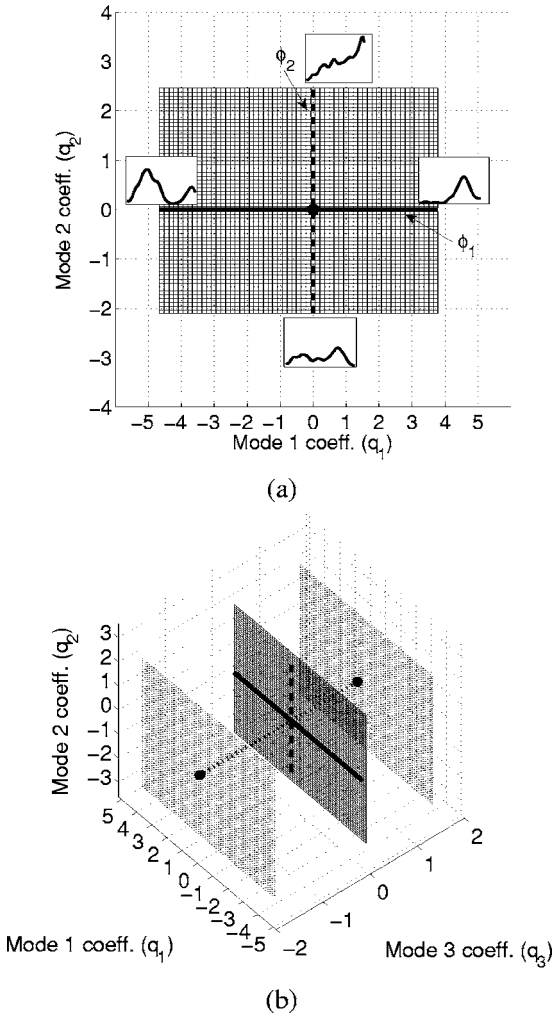

FIG. 8. (a) Grid of q_1 and q_2 scaling coefficients based on speaker SF1. The thick solid and dashed lines represent the continua for q_1 and q_2, respectively, when the other coefficient is equal to zero and are labeled with ϕ_1 and ϕ_2. The inset plots demonstrate the area vector shapes generated at the end points of the ϕ_1 and ϕ_2 lines. (b) Extension of the coefficient space to account for three modes. The (q_1,q_2) grid located at $q_3=0$ is identical to the grid shown in (a). The other two grids include the same collection of (q_1,q_2) values but are shifted along the q_3 dimension.

are included within each speaker's producible formant space. The mapping between the three-dimensional coefficient space and [F1, F2] formant space, however, is not one-to-one because many $[q_1,q_2,q_3]$ triplets may correspond to the same [F1, F2] pair. It is apparent though, from all of the speakers, that the primary effect of ϕ_3 is to slightly extend the edges of the vowel space relative to the $q_3=0$ condition. Thus, based on these figures, as well as on the calculated variances for each mode (see Table VIII), it seems reasonable to suggest that the nearly one-to-one mappings based on ϕ_1 and ϕ_2 capture most of a speaker's vowel production, while ϕ_3 may be "activated" to tune the vocal tract for the extreme vowels.

V. DISCUSSION

The main goal of this study was to determine whether vocal tract shaping patterns, obtained from sets of area functions, were similar across speakers. Toward this goal, area functions for 11 vowels were obtained from six speakers, three female and three male, using MRI. From each speaker's set of area functions, eigenvectors or *modes* were determined with principal components analysis (PCA).

The spatial similarity of each mode was assessed by visual comparison across all of the speakers as well as with correlation analysis. In both cases, the spatial features present in the first and second modes, ϕ_1 and ϕ_2, were highly correlated within the female and male groups, and across sex. The average correlation coefficient across all six speakers was 0.94 for the first mode and 0.91 for the second mode. The shape of third mode, ϕ_3, was fairly similar across the female speakers, but less so for the males. It is also noted that the mean area vectors, upon which the modes are superimposed to reconstruct specific vowels, contained more idiosyncratic features than did the modes. Acoustically, these idiosyncratic features primarily influenced the frequencies of the upper formants, while leaving F1 and F2 at locations representative of a neutral vowel. Thus, at this stage, the modes appeared to provide roughly a *common* system for perturbing a *unique* underlying neutral vocal tract shape.

This idea was further supported by the mappings generated between the scaling coefficients of the modes $[q_1,q_2,q_3]$ and the [F1, F2] frequencies of the resulting area functions. The mappings were unique for all six speakers in terms of the exact shape of the [F1, F2] vowel space, but the general effect of the modes was the same in each case. Vocal tract configurations produced by the first modes gave rise to a continuum of formant pairs over which F1 and F2 monotonically increased and decreased, respectively. In contrast, the second mode produced a continuum of formants over which both F1 and F2 monotonically increased. In addition, these mappings were essentially one-to-one when just the first two modes were considered. This means that an [F1, F2] pair in a given speaker's vowel space could be associated with one pair of $[q_1,q_2]$ coefficients.

A similar one-to-one mapping, based on the calculated modes of a male speaker, was reported by Story and Titze (1998). They later used the mapping in the "reverse" direction to transform time-varying formant frequencies obtained from recorded speech into time-varying mode coefficients. These were then used to generate area functions for synthesis of the original speech. Presumably the mappings presented in Fig. 9 could be similarly used to map formants to coefficients and ultimately to area functions. With regard to understanding how the vocal tract airspace is utilized for speech production, however, perhaps it is of more interest to note that the magnitudes of the mode scaling coefficients for the speakers in the present study (see Table IX) as well as in Story and Titze (1998) are of nearly the same range. This means that a transformation of formant frequencies of some utterance for a given speaker may yield scaling coefficients that could potentially generalize across all of the speakers. Likewise, "forward" specification of a sequence of coefficients that vary in time would, for all speakers, generate the same vowel-to-vowel transition but with different absolute formant frequencies.

Whereas the modes seem to capture some type of common shaping patterns of the vocal tract airspace, they cannot

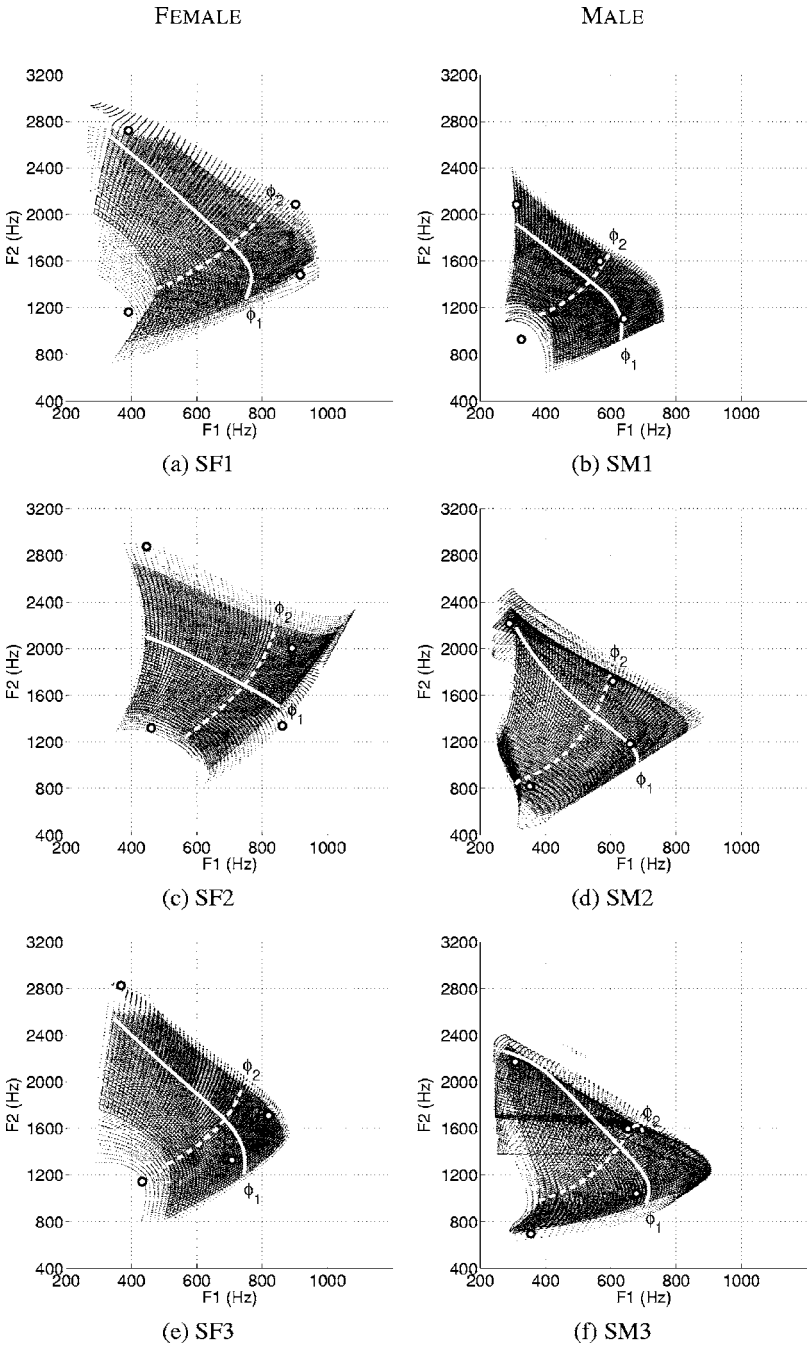

FIG. 9. Coefficient-to-formant mappings for each of the six speakers based the area functions generated with Eq. (7). The left column of plots corresponds to the female speakers and the right column to the males. Within each figure panel, the dark grid is the mapping obtained when $q_3=0$, the white lines (solid and dashed) represent the effect of each mode in isolation, the four white dots are the [F1, F2] pairs *measured* from each speaker's audio recording of the [i, æ, ɑ, u] vowels, and the light grids indicate the effect of ϕ_3.

be directly related to specific articulators. This may be regarded as a limitation of the study because little can be said about the actual articulatory coordination used for speech production. The data and subsequent analyses presented here, however, imply the existence of a common system for deforming the vocal tract shape that facilitates production of predictable patterns of formant frequencies, an essential component of efficient speech production. In this sense, perhaps the modes or combinations thereof prescribe a "goal" that some collective coordination of the articulators must achieve. Thus, even though variable positions and movement of articulators may be utilized during speech production, the goal would be achieved if the common deformation patterns, of the type predicted by the modes, are indeed generated by their collective effect. Although no information concerning muscle activity was presented in this study, the mode shapes apparently must represent some level of muscle orchestration that influences the shape of the vocal tract. To a degree consistent with the concept of coordinative structures or synergies in which muscles are organized into functional units, each of the modes may be thought to represent some abstract synergy of articulatory muscle activations that produce a desired acoustic effect.

Further investigation of the mode-based approach to vowel articulation needs to include vocal tract information based on languages other than American English. The results presented here may be inadvertently biased toward vocal tract configurations with expanded palatal regions (i.e., only 4 of the 11 vowels have significant constrictions in this region). It is possible that speakers of a language that includes the same American English vowels used in this study, as well as additional vowels with constricted front cavities (e.g.,

TABLE XVII. Mode and mean diameter vectors for the three female speakers. The glottal end of each area vector is at section 1 and the lip end at section 44. Each speaker's data are grouped into four consecutive columns within the table.

	SF1				SF2				SF3			
Section i	$\Omega(i)$	$\phi_1(i)$	$\phi_2(i)$	$\phi_3(i)$	$\Omega(i)$	$\phi_1(i)$	$\phi_2(i)$	$\phi_3(i)$	$\Omega(i)$	$\phi_1(i)$	$\phi_2(i)$	$\phi_3(i)$
1	0.638	−0.035	−0.030	−0.040	0.499	−0.018	−0.062	−0.093	0.518	−0.005	−0.035	0.053
2	0.661	−0.016	−0.021	−0.070	0.600	−0.012	−0.046	−0.107	0.520	0.008	0.011	−0.096
3	0.739	−0.022	−0.025	−0.099	0.688	−0.027	−0.075	−0.101	0.580	0.008	0.019	−0.177
4	0.901	−0.041	−0.034	−0.128	0.781	−0.051	−0.119	−0.093	0.792	−0.003	0.009	−0.215
5	1.065	−0.066	−0.042	−0.157	0.918	−0.076	−0.156	−0.093	1.128	−0.020	−0.008	−0.226
6	1.147	−0.092	−0.047	−0.184	1.120	−0.097	−0.177	−0.103	1.406	−0.041	−0.023	−0.222
7	1.151	−0.117	−0.048	−0.207	1.335	−0.113	−0.178	−0.123	1.508	−0.065	−0.032	−0.213
8	1.136	−0.139	−0.044	−0.226	1.467	−0.125	−0.159	−0.151	1.457	−0.090	−0.034	−0.202
9	1.174	−0.158	−0.035	−0.237	1.506	−0.133	−0.125	−0.182	1.355	−0.114	−0.028	−0.193
10	1.274	−0.173	−0.023	−0.239	1.503	−0.139	−0.079	−0.211	1.302	−0.138	−0.015	−0.186
11	1.374	−0.185	−0.008	−0.233	1.508	−0.142	−0.027	−0.236	1.344	−0.159	0.003	−0.179
12	1.428	−0.194	0.009	−0.218	1.531	−0.145	0.025	−0.252	1.427	−0.176	0.025	−0.173
13	1.440	−0.200	0.027	−0.194	1.539	−0.146	0.073	−0.259	1.491	−0.190	0.049	−0.166
14	1.428	−0.202	0.045	−0.163	1.502	−0.146	0.114	−0.254	1.512	−0.198	0.073	−0.157
15	1.375	−0.200	0.062	−0.127	1.443	−0.144	0.145	−0.239	1.491	−0.201	0.096	−0.143
16	1.282	−0.194	0.078	−0.086	1.375	−0.139	0.166	−0.216	1.464	−0.197	0.117	−0.126
17	1.202	−0.183	0.093	−0.044	1.283	−0.130	0.176	−0.185	1.450	−0.187	0.135	−0.104
18	1.193	−0.167	0.105	−0.003	1.163	−0.115	0.175	−0.150	1.431	−0.169	0.150	−0.079
19	1.255	−0.146	0.116	0.035	1.091	−0.094	0.165	−0.115	1.430	−0.145	0.162	−0.051
20	1.356	−0.119	0.123	0.067	1.142	−0.067	0.149	−0.081	1.488	−0.115	0.169	−0.022
21	1.430	−0.087	0.128	0.091	1.256	−0.034	0.126	−0.052	1.580	−0.079	0.172	0.005
22	1.428	−0.050	0.131	0.107	1.345	0.004	0.101	−0.030	1.684	−0.038	0.171	0.030
23	1.366	−0.010	0.130	0.112	1.394	0.047	0.074	−0.017	1.766	0.006	0.166	0.050
24	1.296	0.034	0.126	0.106	1.410	0.092	0.047	−0.014	1.786	0.051	0.157	0.062
25	1.275	0.078	0.119	0.090	1.411	0.138	0.021	−0.020	1.748	0.096	0.145	0.066
26	1.316	0.122	0.109	0.063	1.439	0.182	−0.003	−0.036	1.688	0.140	0.129	0.060
27	1.371	0.163	0.096	0.028	1.509	0.222	−0.023	−0.059	1.645	0.180	0.110	0.044
28	1.419	0.200	0.082	−0.013	1.612	0.255	−0.041	−0.087	1.634	0.214	0.088	0.018
29	1.482	0.230	0.066	−0.059	1.731	0.278	−0.054	−0.117	1.664	0.242	0.065	−0.017
30	1.565	0.252	0.051	−0.105	1.834	0.290	−0.065	−0.147	1.731	0.261	0.043	−0.059
31	1.653	0.264	0.038	−0.150	1.913	0.291	−0.071	−0.174	1.825	0.271	0.022	−0.105
32	1.729	0.264	0.028	−0.189	1.981	0.279	−0.072	−0.193	1.931	0.271	0.004	−0.150
33	1.768	0.254	0.023	−0.220	2.055	0.257	−0.068	−0.203	2.014	0.261	−0.007	−0.191
34	1.760	0.232	0.027	−0.239	2.114	0.226	−0.057	−0.203	2.056	0.243	−0.010	−0.222
35	1.721	0.200	0.040	−0.244	2.116	0.189	−0.038	−0.191	2.051	0.216	−0.002	−0.240
36	1.678	0.160	0.064	−0.234	2.029	0.150	−0.008	−0.168	1.992	0.184	0.020	−0.239
37	1.640	0.114	0.101	−0.209	1.866	0.114	0.032	−0.135	1.894	0.148	0.056	−0.218
38	1.588	0.067	0.151	−0.170	1.701	0.085	0.085	−0.096	1.784	0.111	0.108	−0.175
39	1.523	0.023	0.212	−0.120	1.590	0.069	0.150	−0.056	1.687	0.076	0.173	−0.113
40	1.478	−0.015	0.280	−0.066	1.548	0.065	0.222	−0.018	1.661	0.047	0.248	−0.038
41	1.460	−0.041	0.348	−0.015	1.564	0.074	0.297	0.011	1.701	0.024	0.324	0.037
42	1.446	−0.051	0.404	0.021	1.594	0.090	0.360	0.026	1.736	0.011	0.386	0.094
43	1.405	−0.043	0.430	0.028	1.591	0.100	0.392	0.025	1.716	0.006	0.415	0.104
44	1.313	−0.016	0.403	−0.014	1.545	0.081	0.362	0.005	1.633	0.008	0.380	0.028

Swedish) may produce somewhat different mode shapes than those reported here. In addition, the vocal tract length differences across vowels should be more adequately accounted for in the PCA, as well as in subsequent models for generating area functions.

ACKNOWLEDGMENTS

The author would like to thank Ted Trouard for consulting on image acquisition, Jennifer Johnson for operating the MR scanner, Kristen Bencala and Kang Li for assisting in the image analysis, and Wolfgang Golser for assistance with acoustic analysis. This work was supported by NIH Grant No. R01-DC04789.

APPENDIX A—Area Vectors and Vocal Tract Lengths

Area vectors for the three female and three male speakers are presented numerically in Tables XI–XVI. The first column in each table is the index i, which denotes successive sections or "tubelets" along the length of the vocal tract. Tubelet I is located just above the glottis and tubelet 44 at the

TABLE XVIII. Mode and mean diameter vectors for the three male speakers. The glottal end of each area vector is at section 1 and the lip end at section 44. Each speaker's data are grouped into four consecutive columns within the table.

	SM1				SM2				SM3			
Section i	$\Omega(i)$	$\phi_1(i)$	$\phi_2(i)$	$\phi_3(i)$	$\Omega(i)$	$\phi_1(i)$	$\phi_2(i)$	$\phi_3(i)$	$\Omega(i)$	$\phi_1(i)$	$\phi_2(i)$	$\phi_3(i)$
1	0.873	0.002	−0.089	−0.112	0.676	0.025	−0.059	0.094	0.897	−0.019	0.000	−0.005
2	0.867	−0.014	−0.050	−0.052	0.666	−0.060	−0.029	−0.063	0.762	0.002	−0.006	−0.027
3	0.835	−0.031	−0.056	−0.081	0.683	−0.102	0.001	−0.154	0.753	0.006	−0.027	−0.076
4	0.815	−0.047	−0.080	−0.146	0.811	−0.118	0.020	−0.189	0.529	−0.002	−0.051	−0.131
5	0.917	−0.065	−0.108	−0.215	1.004	−0.121	0.023	−0.179	0.405	−0.016	−0.073	−0.179
6	1.242	−0.083	−0.130	−0.267	1.251	−0.119	0.013	−0.136	0.698	−0.034	−0.089	−0.214
7	1.610	−0.102	−0.139	−0.295	1.589	−0.117	−0.010	−0.073	1.195	−0.052	−0.098	−0.235
8	1.759	−0.121	−0.136	−0.296	1.921	−0.117	−0.038	0.001	1.425	−0.071	−0.100	−0.243
9	1.662	−0.141	−0.120	−0.274	2.075	−0.122	−0.068	0.075	1.420	−0.088	−0.095	−0.240
10	1.470	−0.159	−0.094	−0.233	2.041	−0.130	−0.093	0.143	1.206	−0.103	−0.085	−0.231
11	1.312	−0.176	−0.061	−0.181	1.932	−0.140	−0.112	0.200	1.072	−0.116	−0.070	−0.217
12	1.247	−0.191	−0.025	−0.125	1.841	−0.152	−0.120	0.241	1.322	−0.127	−0.053	−0.203
13	1.299	−0.201	0.011	−0.071	1.778	−0.164	−0.117	0.266	1.437	−0.135	−0.034	−0.189
14	1.398	−0.207	0.045	−0.022	1.722	−0.173	−0.102	0.274	1.575	−0.140	−0.016	−0.176
15	1.456	−0.207	0.073	0.016	1.666	−0.180	−0.078	0.267	1.632	−0.142	0.003	−0.165
16	1.482	−0.200	0.094	0.044	1.578	−0.182	−0.046	0.248	1.471	−0.141	0.020	−0.156
17	1.512	−0.186	0.108	0.059	1.455	−0.179	−0.009	0.218	1.312	−0.137	0.035	−0.146
18	1.536	−0.165	0.113	0.064	1.351	−0.170	0.029	0.181	1.268	−0.129	0.047	−0.136
19	1.538	−0.138	0.111	0.060	1.286	−0.155	0.065	0.142	1.317	−0.118	0.057	−0.124
20	1.499	−0.104	0.102	0.048	1.244	−0.135	0.095	0.103	1.219	−0.103	0.064	−0.110
21	1.400	−0.064	0.087	0.033	1.235	−0.109	0.117	0.067	1.066	−0.084	0.067	−0.092
22	1.284	−0.021	0.068	0.017	1.266	−0.079	0.129	0.037	1.058	−0.061	0.067	−0.072
23	1.246	0.025	0.047	0.001	1.300	−0.046	0.130	0.013	1.123	−0.034	0.063	−0.049
24	1.270	0.071	0.025	−0.012	1.306	−0.010	0.118	−0.002	1.276	−0.004	0.055	−0.025
25	1.256	0.115	0.003	−0.020	1.291	0.027	0.095	−0.009	1.338	0.029	0.043	−0.001
26	1.207	0.157	−0.017	−0.024	1.250	0.064	0.062	−0.008	1.347	0.065	0.027	0.020
27	1.204	0.193	−0.033	−0.025	1.197	0.100	0.023	0.000	1.289	0.102	0.009	0.036
28	1.282	0.222	−0.046	−0.022	1.212	0.134	−0.021	0.012	1.229	0.139	−0.012	0.045
29	1.415	0.243	−0.054	−0.019	1.337	0.165	−0.065	0.028	1.311	0.176	−0.034	0.046
30	1.536	0.255	−0.057	−0.018	1.516	0.192	−0.105	0.045	1.451	0.210	−0.055	0.036
31	1.609	0.257	−0.054	−0.020	1.689	0.214	−0.138	0.062	1.616	0.241	−0.074	0.016
32	1.650	0.250	−0.047	−0.029	1.828	0.230	−0.159	0.078	1.709	0.266	−0.088	−0.015
33	1.675	0.234	−0.035	−0.046	1.922	0.241	−0.166	0.090	1.763	0.285	−0.094	−0.053
34	1.678	0.210	−0.018	−0.072	1.968	0.244	−0.157	0.100	1.806	0.295	−0.090	−0.097
35	1.653	0.182	0.004	−0.107	1.973	0.241	−0.131	0.107	1.824	0.296	−0.072	−0.141
36	1.600	0.151	0.031	−0.149	1.940	0.232	−0.088	0.112	1.798	0.287	−0.038	−0.180
37	1.519	0.120	0.063	−0.193	1.894	0.216	−0.030	0.118	1.836	0.266	0.013	−0.209
38	1.437	0.092	0.102	−0.236	1.875	0.194	0.039	0.125	1.965	0.235	0.081	−0.221
39	1.402	0.069	0.148	−0.268	1.885	0.168	0.116	0.134	2.076	0.195	0.165	−0.212
40	1.411	0.053	0.203	−0.283	1.889	0.139	0.197	0.145	2.207	0.147	0.258	−0.180
41	1.419	0.045	0.268	−0.268	1.875	0.110	0.276	0.155	2.121	0.096	0.352	−0.127
42	1.381	0.041	0.346	−0.215	1.824	0.084	0.351	0.159	1.983	0.045	0.431	−0.062
43	1.288	0.038	0.436	−0.114	1.701	0.067	0.421	0.144	1.801	0.003	0.471	−0.005
44	1.136	0.025	0.541	0.043	1.483	0.065	0.490	0.091	1.521	−0.023	0.441	0.012

lips. The other columns are the area data for the vowels in the order: [i, ɪ, e, ɛ,æ, ʌ, ɑ, ɔ, o, ʊ, u]. For reasons noted in the main text, the [ɛ] vowel for SM2 cannot be made available. The bottom two rows in each table indicate the length Δ of each successive section and the total vocal tract length (VTL=44Δ).

APPENDIX B—Mean Diameter and Mode Vectors

Numerical versions of the mode vectors, $\phi_1(i)$, $\phi_2(i)$, and $\phi_3(i)$, along with the mean diameter vectors $\Omega(i)$ are presented in Table XVII for the female speakers and in Table XVIII for the males. As with the area vectors in Appendix A, the first column of each table shows the index i which denotes successive sections along the length of the vocal tract.

[1]The use of 44 sections derives from the approximate spatial resolution obtained in MRI-based reconstructions of vocal tract shape. It is also convenient to use 44 elements for simulating male speech with acoustic waveguide models because it allows for a sampling frequency of 44.1 kHz when the tract length is approximately 17.5 cm (typical adult male). The female

area functions have also been segmented into 44 sections to simplify the management of the data.

[2]For this study, the length of each tubelet in a given area function is equal to the Δ shown in the area functions tables in Appendix A. Hence, $L(i)=\Delta$ for every tubelet within an area function. The form of the length vector used here, however, would generalize to cases where the tubelet length may be unequal (e.g., see Story, 2005).

[3]Story and Titze (1998) performed the PCA on the square root of the areas. In this study, the scaling factor of $4/\pi$ within the square root operation generates equivalent diameters which are a more intuitively appealing quantity and are more convenient to use for explanation and discussion.

Fant, G. (**1960**). *Acoustic Theory of Speech Production* (Mouton, The Hague).

Fowler, C. A., and Saltzman, E. L. (**1993**). "Coordination and coarticulation in speech production," Lang Speech **36**(2,3), 171–195.

Gracco, V. L. (**1992**). "Some organizational characteristics of speech movement control," J. Speech Hear. Res. **37**, 4–27.

Harshman, R., Ladefoged, P., and Goldstein, L. (**1977**). "Factor analysis of tongue shapes," J. Acoust. Soc. Am. **62**, 693–707.

Jackson, M. T. T. (**1988**). "Analysis of tongue positions: Language-specific and cross-linguistic models," J. Acoust. Soc. Am. **84**, 124–143.

Kelso, J. A. S., Saltzman, E. L., and Tuller, B. (**1986**). "The dynamical perspective on speech production: Data and theory," J. Phonetics **14**, 29–59.

Kusakawa, N., Honda, K., and Kakita, Y. (1993). "Construction of articulatory trajectories in the space of tongue muscle contraction force," ATR Technical Report, TR-A-0717 (in Japanese).

Löfqvist, A. (**1997**). "Theories and models of speech production," in *The Handbook of Phonetic Sciences*, edited by W. J. Hardcastle and J. Laver (Blackwell, Oxford), pp. 405–426.

Logeman, J. (**1983**). *Evaluation and Treatment of Swallowing Disorders* (College-Hill, San Diego, CA).

Macpherson, J. M. (**1991**). "How flexible are muscle synergies?" in *Motor Control: Concepts and Issues*, edited by D. R. Humphrey and H.-J. Freund (Wiley, Chichester), pp. 33–47.

Maeda, S., and Honda, K. (**1994**). "From EMG to formant patterns of vowels: the implication of vowel spaces," Phonetica **51**, 17–29.

Mermelstein, P. (**1967**). "Determination of the vocal-tract shape from measured formant frequencies," J. Acoust. Soc. Am. **41**, 1283–1294.

Meyer, P., Wilhelms, R., and Strube, H. W. (**1989**). "A quasiarticulatory speech synthesizer for German language running in real time," J. Acoust. Soc. Am. **86**, 523–539.

Nix, D. A., Papcun, G., Hogden, J., and Zlokarnik, I. (**1996**). "Two cross-linguistic factors underlying tongue shapes for vowels," J. Acoust. Soc. Am. **99**, 3707–3717.

Perrier, P., Perkell, J., Payan, Y., Zandipour, M., Guenther, F., and Khalighi, A. (**2000**). "Degrees of freedom of tongue movements in speech may be constrained by biomechanics," in Proc. of the Sixth Intl. Conf. on Spoken Lang. Proc., ICSLP-2000, Vol. **2**, pp. 162–165.

Santello, M., Flanders, M., and Soechting, J. F. (**1998**). "Postural hand synergies for tool use," J. Neurosci. **18**(23), 10105–10115.

Schroeder, M. R. (**1967**). "Determination of the geometry of the human vocal tract by acoustic measurements," J. Acoust. Soc. Am. **41**, 1002–1010.

Shirai, K., and Honda, M. (**1977**). "Estimation of articulatory motion," in *Dynamic Aspects of Speech Production*, edited by M. Sawashima and F. Cooper (Univ. of Tokyo, Tokyo), pp. 279–302.

Shriberg, L. D., and Kent, R. D. (**2003**). *Clinical Phonetics*, 3rd ed. (Allyn and Bacon, Boston).

Sondhi, M. M., and Schroeter, J. (**1987**). "A hybrid time-frequency domain articulatory speech synthesizer," IEEE Trans. Acoust., Speech, Signal Process. **ASSP-35**(7), 955–967.

Stevens, K. N., and House, A. S. (**1955**). "Development of a quantitative description of vowel articulation," J. Acoust. Soc. Am. **27**, 484–493.

Story, B. H. (**2004**). "On the ability of a physiologically-constrained area function model of the vocal tract to produce normal formant patterns under perturbed conditions," J. Acoust. Soc. Am. **115**, 1760–1770.

Story, B. H. (**2005**). "A parametric model of the vocal tract area function for vowel and consonant simulation," J. Acoust. Soc. Am. **117**, 3231–3254.

Story, B. H., and Titze, I. R. (**1998**). "Parameterization of vocal tract area functions by empirical orthogonal modes," J. Phonetics **26**(3), 223–260.

Story, B. H., Titze, I. R., and Hoffman, E. A. (**1996**). "Vocal tract area functions from magnetic resonance imaging," J. Acoust. Soc. Am. **100**, 537–554.

Story, B. H., Titze, I. R., and Hoffman, E. A. (**1998**). "Vocal tract area functions for an adult female speaker based on volumetric imaging," J. Acoust. Soc. Am. **104**, 471–487.

Story, B.H., Laukkanen, A.M., and Titze, I.R. (**2000**). Acoustic impedance of an artificially lengthened and constricted vocal tract, J. Voice **14**(4), 455–469.

Story, B. H., Titze, I. R., and Hoffman, E. A. (**2001**). "The relationship of vocal tract shape to three voice qualities," J. Acoust. Soc. Am. **109**, 1651–1667.

Taylor, J. R. (**1982**). *An Introduction to Error Analysis* (University Science Books, Mill Valley, CA).

Titze, I. R., and Story, B. H. (**1997**). "Acoustic interactions of the voice source with the lower vocal tract," J. Acoust. Soc. Am. **101**, 2234–2243.

Yehia, H. C., Takeda, K., and Itakura, F. (**1996**). "An acoustically oriented vocal-tract model," IEICE Trans. Inf. Syst. **E79-D**(8), 1198–1208.

Zheng, Y., Hasegawa-Johnson, M., and Pizza, S. (**2003**). "Analysis of the three-dimensional tongue shape using a three-factor analysis model," J. Acoust. Soc. Am. **113**, 478–486.

Interacting effects of syllable and phrase position on consonant articulation[a)]

Dani Byrd[b)]
Department of Linguistics, USC College, Los Angeles, California 90089-1693

Sungbok Lee
Department of Linguistics, USC College and Department of Electrical Engineering-Systems, USC Viterbi School of Engineering, Los Angeles, California

Daylen Riggs
Department of Linguistics, USC College, Los Angeles, California

Jason Adams
Department of Computer Science, USC Viterbi School of Engineering, Los Angeles, California

(Received 9 February 2005; revised 6 October 2005; accepted 7 October 2005)

The complexities of how prosodic structure, both at the phrasal and syllable levels, shapes speech production have begun to be illuminated through studies of articulatory behavior. The present study contributes to an understanding of prosodic signatures on articulation by examining the joint effects of phrasal and syllable position on the production of consonants. Articulatory kinematic data were collected for five subjects using electromagnetic articulography (EMA) to record target consonants (labial, labiodental, and tongue tip), located in (1) either syllable final or initial position and (2) either at a phrase edge or phrase medially. Spatial and temporal characteristics of the consonantal constriction formation and release were determined based on kinematic landmarks in the articulator velocity profiles. The results indicate that syllable and phrasal position consistently affect the movement duration; however, effects on displacement were more variable. For most subjects, the boundary-adjacent portions of the movement (constriction release for a preboundary coda and constriction formation for a postboundary onset) are not differentially affected in terms of phrasal lengthening—both lengthen comparably. © *2005 Acoustical Society of America.* [DOI: 10.1121/1.2130950]

PACS number(s): 43.70.−h, 43.70.Bk [AL] Pages: 3860–3873

I. INTRODUCTION

Syllable and phrasal structure, as well as focal accent, have been highlighted as linguistic factors responsible for variation in the articulatory characteristics of consonants. This variation has been explored in terms of the spatial or magnitude properties of the articulatory movements and in terms of the gestures' temporal or durational properties. However, a comprehensive understanding of positionally conditioned spatiotemporal variation of articulatory gestures is still being built, particularly in terms of how the influences of different levels of linguistic structure, from syllabic to phrasal, combine in their effects on the performance of articulatory gestures.

A. Positional effects on articulation

Setting aside focal accent as a source of articulatory variation, studies of *positional* effects on articulation have largely focused on word edges and phrase edges, that is, the effect of syllable and phrasal boundaries. A diagram showing an example of the hierarchical relations among segments, syllables, and phrases is shown in Fig. 1.

A number of studies using both electropalatography (EPG) and movement tracking have reported more constricted articulatory postures for consonants in syllable onsets as compared to those in syllable codas (e.g., Browman and Goldstein, 1995; Byrd, 1996; Fougeron and Keating, 1997). For example, in EPG studies by Byrd (1996) and Keating *et al.* (1999), certain consonants were shown to have more linguapalatal contact word-(syllable-) initially than word-(syllable-) finally (/t/ and /d/ in the Keating study and /d/ and /g/ in the Byrd study). Similar patterns obtain for duration such that coda articulations are shorter than onset articulations (e.g., Byrd, 1996—an EPG study). (We note that it is not clear whether syllable and word boundaries are differentiated in English, since the relevant experiments generally use a word boundary condition to ensure a certain syllable edge.)

Other articulatory studies have examined the effects of phrase boundaries identifying longer constriction formation and release durations at phrase edges as compared to phrase medially [e.g., the articulatory point-tracking studies of Byrd *et al.* (2000), Byrd and Saltzman (1998), and Cho (in press), and the earlier seminal work on the jaw (Edwards *et al.*,

[a)]Portions of this work were presented in "Interacting effects of phrasal and syllable position on consonant production" Acoustical Society of America meeting, San Diego, CA, November 2004.
[b)]Electronic mail: dbyrd@usc.edu

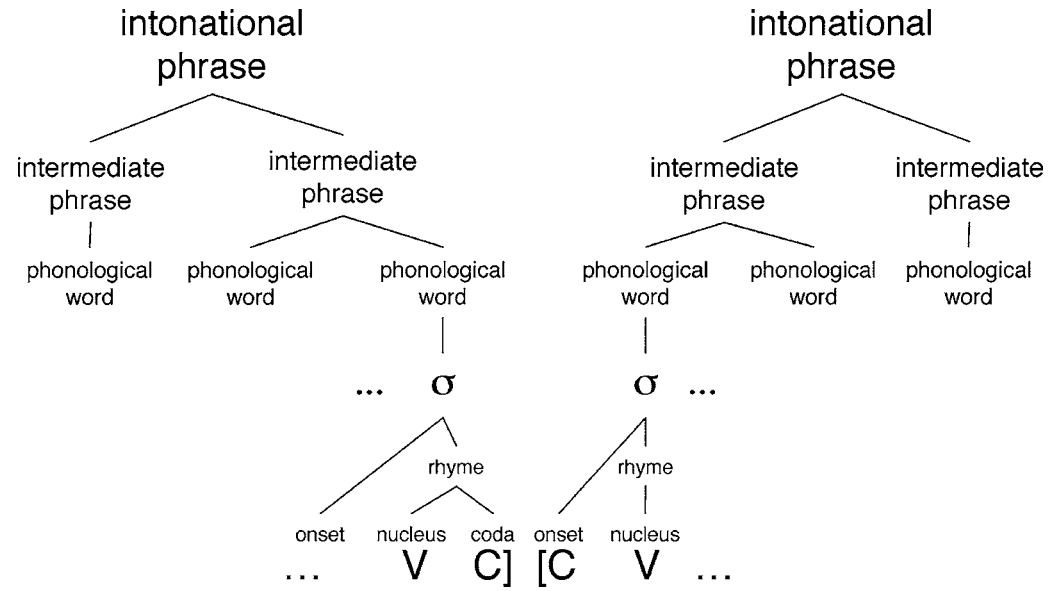

FIG. 1. A diagram showing a partial example of the hierarchical relations among segments syllables and phrases for a phrase ending in [VC] and a following phrase beginning with [CV].

1991; Beckman and Edwards, 1992)]. Additionally, larger movement displacements and greater linguapalatal contact have also been identified at the edges of strong phrasal domains [e.g., using magnetometry in Byrd and Saltzman (1998) and Tabain (2003), and EPG in Keating *et al.* (2003)]. Finally, there is some indication that phrase initial edges show more of this behavior than phrase-final edges (e.g., Byrd and Saltzman, 1998; Keating *et al.*, 1999). For example, Keating *et al.* (1999) showed that significantly more peak linguapalatal contact occurred in phrase-initial positions than in phrase-final positions. Additionally, in an EPG case study of Korean, Cho and Keating (2001) found that a range of consonants (specifically, /n/, /t/ /t^h/, and /t^*/) located in domain-initial position at large boundaries had both more extreme and longer articulations than consonants located initially in lower prosodic domains and those located domain medially. However, it is not at all clear that phrase-*final* edges are not also larger/longer than their phase-medial consonant counterparts (see, e.g., Hacopian, 2003; Keating *et al.*, 1999). In Keating *et al.* (1999), the authors found that consonants located phrase finally indeed received a significant articulatory "boost" in linguopalatal contact as compared to those located phrase medially. Additionally, the magnetometer study of Cho (in press) found evidence of articulatory lengthening of labial consonants in a CV##CV sequence spanning a boundary; the articulations were longer in duration and exhibited longer time-to-peak-velocities when at a phrase boundary. Finally, Keating *et al.*'s (1999) EPG data indicate that "Averaged across consonants and speakers, the most contact is seen for consonants which are utterance-initial and word-initial; the next-most contact is seen for consonants which are word-initial but utterance-medial; the next for consonants which are utterance-final and word-final; and the least contact is seen for consonants which are word-final but utterance-medial… exactly how [utterance-medial word initial and utterance-final word-final] pattern…and which differences are statistically significant, depend on the consonant."

As an understanding of articulatory modifications in particular prosodic positions has been acquired over past years, studies have focused primarily on *either* the syllable or the phrasal effect. (Similarly, studies on focal accent have also generally been specific only to focus, but we address the positional effects here.) Likewise, some experiments (often because of instrumentation) have attended more to spatial characteristics of consonant articulations, and others have focused more on temporal characteristics. And, finally, some studies (for example, those done with EPG) are limited to lingual consonants. The present experiment offers several contributions to the body of knowledge of positional effects on articulation. It examines both spatial and temporal variations as a function of both syllable and phrasal position for both lingual and labial consonants. Specifically, it evaluates the *interaction* of syllable and phrasal position on consonant articulation. We consider whether the effects of syllable and phrase position on the magnitude and length of consonant articulation are independent or interact to yield even greater prominence in certain circumstances. The experiment presented will allow us to address the question of the relative articulatory robustness (constriction magnitude and duration) of consonants as they occur as codas phrase medially, as codas phrase finally, as onsets phrase medially, and as onsets phrase initially.

B. The prosodic gesture model

The prosodic (π-) gesture model (Byrd and Saltzman, 2003; Byrd *et al.*, 2000) views phrase boundaries as extending over an interval at a juncture and slowing the time course of articulatory gestures that are active during that interval. Thus, the π-gesture model extends to the suprasegmental level the notion, forwarded within Articulatory Phonology (e.g., Browman and Goldstein, 1992), that phonological ges-

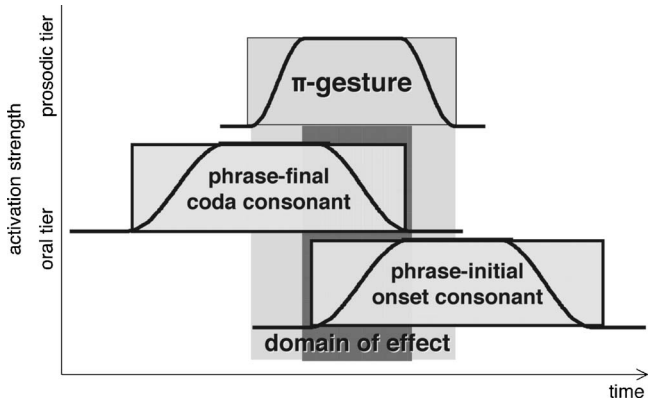

FIG. 2. A schema of the π-gesture model indicating two constriction gestures overlapping one another and a prosodic boundary (π) gesture.

tures are inherently temporal, that is, that gestures are active over a temporal interval and that the activation intervals of gestures are patterned or choreographed in an overlapping fashion. Figure 2 shows a representative partial gestural score schematizing the overlapping arrangement of a prosodic gesture, whose activation waxes and wanes, with two co-active constriction gestures.

This model of phrasal juncture predicts the same qualitative effect of a boundary on the articulatory behavior both preceding and following the boundary. For example, both phrase-final and phrase-initial constriction activation trajectories are predicted to be lengthened. This lengthening of the activation trajectories is quantitatively indexed by a longer acceleration duration (i.e., time-to-peak-velocity) in the movement trajectory. [This interval reflects the stiffness parameter of a gesture within a Task Dynamics model of speech production (Saltzman and Munhall, 1989), i.e., the parameter shaping the internal temporal properties of an articulatory gesture. A longer acceleration duration is associated with lower stiffness.] Many of the empirical findings on intra- and intergestural timing at phrase boundaries have been successfully simulated using a π gesture that slows the central clock controlling the pace at which constriction gestures unfold (see Byrd and Saltzman, 2003). The activation strength of the π gesture, and therefore the degree of local slowing, is viewed as directly corresponding to the strength of a phrasal juncture (captured in many phonological theories as depth of embedding in a prosodic hierarchy).

The π gesture model does allow for asymmetric quantitative effects around a boundary. That is, the magnitude of effect on the constriction gestures overlapping the boundary interval may differ before and after the juncture. The π gesture may be skewed rightward (yielding larger effects phrase initially) or leftward (yielding larger effects phrase finally) depending on the alignment of the π gesture with the constriction gestures or depending on the activation wave shape of the π gesture itself. [See Byrd and Saltzman (2003) for detailed modeling of these sorts of π-gesture effects on articulation.] The present experiment will evaluate the degree of symmetry in prosodic slowing at phrase boundaries by examining whether an intonational phrase boundary equivalently affects a preceding coda and a following onset consonant. In addition to the primary goal of addressing a deficit in our empirical knowledge of the interaction of phrase and syllable position on articulatory behavior, this work will help inform future prosodic modeling generally.

C. Experimental hypotheses: Temporal lengthening and spatial strengthening

Below we present an articulatory study on consonant production conducted using movement tracking (magnetometry). First, this study investigates the nature of the articulatory lengthening at phrase and syllable edges. Based on early work, longer articulations are expected at initial phrase and syllable (word) edges. Second, the present study also considers whether spatial changes in articulation pattern in the same way as temporal changes pattern. Several of the studies reviewed above have observed spatially larger articulations in phrase and syllable initial positions, but it is unclear whether spatial strengthening is limited to this position. Some previous research showing that larger displacements occur with longer durations (Kelso *et al.*, 1985; Ostry and Munhall, 1985) would suggest that spatial strengthening and lengthening should co-occur. Alternatively, the attention paid to strengthening in phrasal onset position (e.g., Keating *et al.*, 2003) might suggest that only phrase-initial onset consonants strengthen relative to phrase-medial consonants, with no comparable change found for codas at phrase edges (e.g., see Keating *et al.*, 2003). Last, and most importantly in terms of new investigation, the present study examines the *interaction* of syllable and phrase boundaries on the spatial and temporal characteristics of consonant articulation. Five subjects and both lingual and labial consonants are included.

II. METHOD

Electromagnetic articulography (the Carstens AG200 EMA system) was used to record the motion of transducers placed on the lips (at the vermillion border) and tongue tip (approximately 5 mm from the endpoint of the protruded tongue). Articulatory data were sampled at 200 Hz and simultaneous audio data at 10 kHz. Data were corrected for head movement using reference transducers adhered to the maxilla and bridge of the nose and were rotated to the sampled occlusal plane of each subject.

A. Subjects and stimuli

The consonants under examination in this study were [f], [t], and [p]. Consonants appeared in each of four positions: (1) phrase-medial coda, (2) coda at an phrase edge, (3) phrase-medial onset, and (4) onset at an phrase edge. For consonants in coda, the following phrase started with an [h] to ensure that no resyllabification occurred. The segment preceding the target consonant was controlled for not in the sense of being identical for all target consonants, but in the sense of always having a different primary articulator from each target consonant. This was done to minimize potential coarticulatory effects. The stimuli are shown in Table I.

Five subjects, denoted below as speakers A, E, M, N, and R, read the 12 sentences in eight randomized blocks. (For speaker E only two phrase boundary tokens for [t] were available for analysis due to unreliability of the tongue tip

TABLE I. Stimuli material.

	/f/
/f/: coda, phrase medial	"The doctor brought the scar**f** home for the holidays."
/f/: coda, phrase edge	"The doctor brought the scar**f**. Home weather was cold."
/f/: onset, phrase medial	"The doctor made the scar **f**oam with antiseptic."
/f/: onset, phrase edge	"The doctor made the scar. **F**oam antiseptic didn't help."
	/t/
/t/: coda, phrase medial	"The doctor had a very def**t** hand at all sorts of things."
/t/: coda, phrase edge	"The doctor was quite def**t**. Handiness was a big help."
/t/: onset, phrase medial	"That made being deaf **t**antamount to isolation."
/t/: onset, phrase edge	"It's hard being very deaf. **T**antamount to isolation."
	/p/
/p/: coda, phrase medial	"The puppy might yel**p** hideously due to its sore paw."
/p/: coda, phrase edge	"The puppy might yel**p**. Hideous illness it was not."
/p/: onset, phrase medial	"The mother might yell **p**itifully at that two-year-old."
/p/: onset, phrase edge	"The mother might yell. **P**itiful discipline had failed."

receiver at this point in the experiment; for this reason, only [f] and [p] tokens are included in the analysis for speaker E, so that the full-interaction model could still be run.) Total tokens for each subject and consonant are shown in Table II.

B. Data analysis

1. Kinematic landmarks

Movement trajectories and accompanying first-order derivatives (velocity trajectories) were smoothed with a 15-Hz low-pass filter (ninth-order Butterworth). Different signals were used for measurement of each consonant. For consonant [t], the *y* position and velocity of the transducer on the tongue tip (TT*y*) were used. For the two other consonants, a derived signal was created. For [p], the Euclidean distance between the lower and upper lip (lip aperture, LA) and its accompanying velocity trajectory were used. For [f], the Euclidean distance between the transducer on the lower lip and the stationary transducer on the maxilla (lower lip aperture, LLA) and its accompanying velocity trajectory were used.

TABLE II. Total tokens analyzed for each subject and for each consonant.

Speaker	/f/	/t/	/p/	Total
A	32	32	30	94
E	32	0	32	64
M	32	32	32	96
N	29	32	31	92
R	32	31	32	95
Total	157	127	157	441

In order to identify the articulatory magnitude and duration of the consonant articulations, kinematic landmarks were algorithmically identified in *y*-velocity trajectory and recorded automatically. Time and position for consonant onset, target, and end were defined by zero-crossings of the velocity trajectory. Additionally, the time of peak velocity for

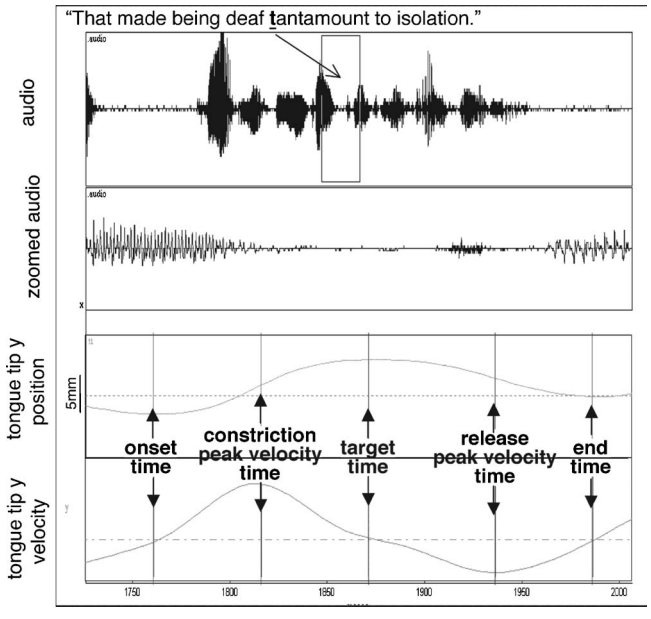

FIG. 3. An example token (speaker A) showing the audio signal (top panel), the zoomed audio signal (second panel), the smoothed tongue tip *y* position trajectory (third panel), and tongue tip *y* velocity trajectory (bottom panel). In the trajectories, the algorithmically defined timepoints of onset, target, and end (determined by velocity zero crossings) and of constriction and release peak velocities (determined by velocity extrema) are shown.

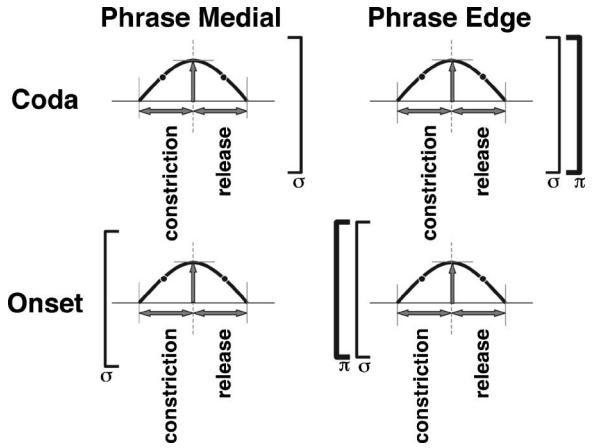

FIG. 4. A schema showing the measurements and conditions for the experiment. $]_\sigma$ and $_\sigma[$ refer to final and initial syllable edges, respectively, and $]_\pi$ and $_\pi[$ to final and initial phrase edges, respectively.

both the constriction and release of the consonant were recorded. (In the occasional case of multiple peak velocities, the highest peak velocity point was the landmark selected.)[1] Figure 3 shows an example data token with the kinematic landmarks marked.

The kinematically defined timepoints and positions of movement onset, target, and end and constriction and release time-peak-velocity (acceleration duration) were used to calculate several dependent measures of gestural magnitude and duration:

Temporal variables

(i) Total duration (end timepoint − onset timepoint)
(ii) Constriction duration (target timepoint − onset timepoint)
(iii) Release duration (end timepoint − target timepoint)
(iv) Constriction time-to-peak-velocity (constriction peak velocity timepoint − onset timepoint)
(v) Release time-to-peak-velocity (release peak velocity timepoint − target timepoint)

Spatial variables

(i) Extremum position (position at target timepoint)
(ii) Constriction displacement [|position at target timepoint − position at onset timepoint|]
(iii) Release displacement [|position at target timepoint − position at end timepoint|]

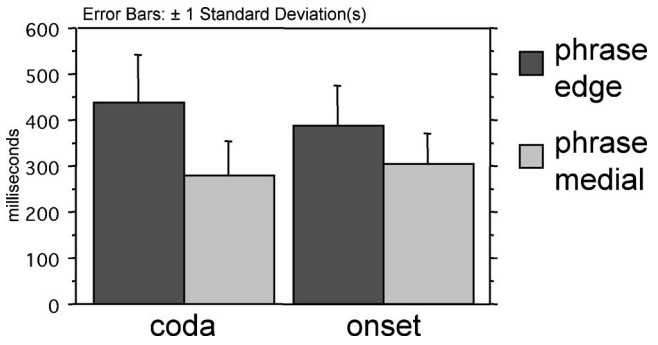

FIG. 5. Total duration (constriction duration plus release duration) (all subjects pooled).

The schema shown in Fig. 4 serves to orient the reader to the measurements and conditions in the experiment.

2. Statistical testing

A three-factor full interaction ANOVA (Statview by SAS) was used to test, separately for each subject, the effects of consonant ([f], [t], [p]), syllable position (onset/coda), phrase position (edge/final), and their interactions on the temporal and spatial dependent variables listed above. A criterial p value was set at $p<0.05$. For all speakers and dependent variables, main effects of the consonant factor were predicted and observed. This main effect will not be reported below, as it is not relevant to addressing the hypotheses concerning syllable and phrasal position effects. Interesting significant crossover interactions of the consonant factor with the syllable or phrase factors will, however, be identified.

III. RESULTS

A. Duration

1. Total duration

As predicted, all subjects shared a main effect of phrasal position on total duration; consonants were longer at phrase edges than phrase medially. The result, pooled across subjects and consonants, is shown in Fig. 5.

The main effect of syllable position on the total duration variable was significant for two out of the five subjects (speakers E and R), and three subjects (A, E, and R) also had a significant interaction between syllable and phrase position such that phrasal lengthening was greater for codas than it was for onsets. Statistical results are shown in Table III.

TABLE III. Total duration effects statistical results (consonants pooled).

Total duration	Syllable main effect	Phrase main effect	Two-way interaction effect
Speaker A	n.s. coda 372 ms; onset 356 ms	$F(1,83)=94.05$, $p<0.0001$ edge 428 ms; medial 298 ms	$F(1,83)=22.920$, $p<0.0001$
Speaker E	$F(1,56)=13.697$, $p=0.0005$ coda 381 ms; onset 331 ms	$F(1,56)=54.223$, $p<0.0001$ edge 436 ms; medial 299 ms	$F(1,56)=28.335$, $p<0.0001$
Speaker M	n.s. coda 329 ms; onset 348 ms	$F(1,84)=29.170$, $p<0.0001$ edge 374 ms; medial 302 ms	n.s.
Speaker N	n.s. coda 334 ms; onset 343 ms	$F(1,80)=77.236$, $p<0.0001$ edge 403 ms; medial 279 ms	n.s.
Speaker R	$F(1,83)=11.1$, $p=0.0013$ coda 366 ms; onset 333 ms	$F(1,83)=231.731$, $p<0.0001$ edge 424 ms; medial 276 ms	$F(1,83)=23.902$, $p<0.0001$

TABLE IV. Constriction duration effects statistical results (consonants pooled).

Constriction duration	Syllable main effect	Phrase main effect	Two-way interaction effect
Speaker A	$F(1,83)=24.443$, $p<0.0001$ coda 169 ms; onset 226 ms	$F(1,83)=24.833$, $p<0.0001$ edge 226 ms; medial 168 ms	n.s.
Speaker E	$F(1,56)=6.673$, $p=0.0124$ coda 181 ms; onset 208 ms	n.s. ($p=0.0515$) edge 205 ms; medial 184 ms	n.s.
Speaker M	$F(1,84)=11.515$, $p=0.0011$ coda 163 ms; onset 200 ms	$F(1,84)=16.301$, $p=0.0001$ edge 204 ms; medial 159 ms	$F(1,84)=6.494$, $p=0.0126$
Speaker N	$F(1,80)=39.173$, $p<0.0001$ coda 172 ms; onset 231 ms	$F(1,80)=91.294$, $p<0.0001$ edge 251 ms; medial 159 ms	$F(1,80)=4.193$, $p=0.0439$
Speaker R	$F(1,83)=135.494$, $p<0.0001$ coda 118 ms; onset 197 ms	$F(1,83)=142.475$, $p<0.0001$ edge 198 ms; medial 117 ms	$F(1,83)=54.223$, $p<0.0001$

2. Constriction formation

It is important to note that the total duration measure does not consider the intervals of constriction formation and release separately. When constriction duration in particular is examined (see Table IV), four of the subjects had a main effect of phrase position on constriction duration. The fifth (E) had a near significant effect ($p=0.0515$) (recall that only [f] and [p] tokens could be included for E), and an interaction with consonant indicates that her [p]'s did not lengthen. The constriction durations for consonants at phrase edges were longer than for those located phrase medially. Additionally, syllable onset constrictions were longer than those for syllable codas, as indicated by a significant main effect of syllable position for all subjects. The mean constriction durations are shown in Fig. 6 for consonants separately (speakers A, M, N, and R pooled, i.e., the speakers with a significant phrasal effect). Three subjects (M, N, and R) had an interaction between syllable and phrase position such that longer constriction durations occurred for onsets located phrase initially than for codas located phrase finally.

The temporal properties of consonant release immediately preceding a boundary (i.e., the coda release) will be analyzed in the next section, but, for the sake of completeness, the release durations for the onset consonants show no effect of a preceding phrase boundary for speakers A, N, and M; for speaker E the releases lengthen slightly in the phrase boundary condition [$F(1,30)=4.498$, $p=0.0423$] and for speaker R the reverse obtains [$F(1,45)=12.301$, $p=0.001$].

In order to further investigate the mechanism of the positional lengthening, time-to-peak-velocity (i.e., the acceleration interval) for the constriction formation was examined (see Table V). Four of the five subjects showed main effects of both syllable and phrase position on constriction time-to-peak-velocity. For all speakers, onset time-to-peak-velocities were longer than in codas. For the four speakers with a significant main effect of phrase position, consonants located at phrase edges had longer time-to-peak-velocities than their counterparts located phrase medially. The fifth subject, who did not have a main effect for phrase boundary (again E), had an interaction with consonant as above, namely the majority pattern is reversed for her [p]. The majority pattern did not show any interaction of syllable and phrase position. Only two of the subjects (M and R) had such an interaction, and it was not consistent across consonants. For subject M, coda [p]s (only) did not lengthen at phrase edges, thereby contributing to the shorter means for codas at phrase edges. For subject R, onsets lengthened much more than codas. The constriction duration and time-to-peak-velocity patterns are shown in Fig. 7 with the speakers pooled.

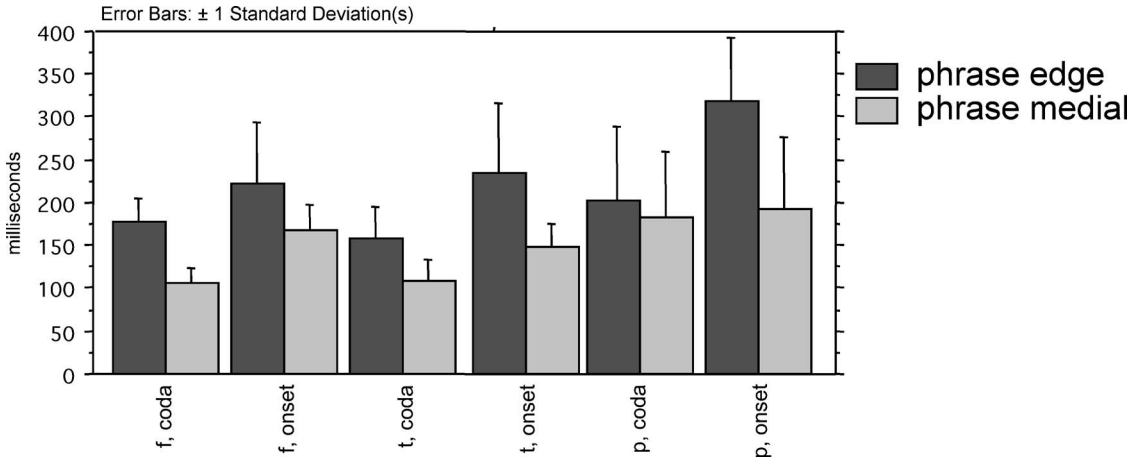

FIG. 6. Constriction duration (subject E excluded).

TABLE V. Constriction time-to-peak-velocity effects statistical results (consonants pooled).

Constriction time-to-peak-velocity	Syllable main effect	Phrase main effect	Two-way interaction effect
Speaker A	$F(1,83)=27.104$, $p<0.0001$ coda 104 ms; onset 163 ms	$F(1,83)=20.968$, $p<0.0001$ edge 160 ms; medial 108 ms	n.s.
Speaker E	$F(1,56)=6.552$, $p=0.0132$ coda 106 ms; onset 134 ms	n.s. edge 118 ms; medial 122 ms	n.s.
Speaker M	$F(1,84)=7.847$, $p=0.0063$ coda 108 ms; onset 137 ms	$F(1,84)=8.387$, $p=0.0048$ edge 137 ms; medial 108 ms	$F(1,84)=7.191$, $p=0.0088$
Speaker N	$F(1,80)=5.238$, $p=0.0247$ coda 103 ms; onset 131 ms	$F(1,80)=18.472$, $p<0.0001$ edge 143 ms; medial 95 ms	n.s.
Speaker R	$F(1,83)=73.480$, $p<0.0001$ coda 59 ms; onset 110 ms	$F(1,83)=90.001$, $p<0.0001$ edge 113 ms; medial 56 ms	$F(1,56)=38.309$, $p<0.0001$

3. Local duration

The final and initial consonants' constrictions intervals are not, however, equivalently "close" to the boundary. The onset consonant's constriction immediately follows the boundary, but, for the coda consonant, it is the release interval, rather than the constriction interval, that is immediately adjacent to the boundary. For this reason, an additional temporal analysis was conducted on what we term local duration—this is the duration of the consonant articulation interval (either constriction formation or release) located immediately adjacent to the phrase boundary. For codas, this is the constriction release phase (the time that elapses during the motion of the articulator from its target to the end of the articulation) and, for onsets, this is the constriction formation phase (the time that elapses from when the constriction starts until the time that the target is reached). The local duration measurement is shown schematically in Fig. 8. This analysis is particularly useful in examining a phrase boundary by syllable position interaction to determine the degree of symmetry in phrasal lengthening to the left and right of the boundary. (Syllable position main effects are expected in this case since release durations are being compared to constriction durations.) Results are given in Table VI.

For all subjects local durations for consonants located at phrase boundaries were significantly and robustly longer than local durations for consonants located phrase medially. The pooled average local duration for consonants phrase medially was approximately 160 ms, and the average local duration for consonants located at phrase boundary was approximately 256 ms. Most (3/5) subjects had no interaction effect—local durations at phrase edges were affected similarly for codas and onsets. The two subjects with an interaction effect (A and E) displayed greater lengthening for codas than for onsets.

For local time-to-peak-velocity, all subjects showed patterns similar to that for local duration (see Table VII). The portion of the consonant immediately local to the phrase boundary had a longer time-to-peak-velocity than the like portion phrase medially. Pooled across subjects and consonants there was a difference between the two phrasal conditions of 59 ms for onsets and 37 ms for codas. An asymmetry between codas and onsets exists for three subjects (M, N, and R) as indicated by a significant interaction effect of phrase and syllable position. For these subjects, the lengthening effect on time-to-peak-velocity was greater for onsets than it was for codas. A fourth subject with an interaction effect (E) had the asymmetry in the other direction. However, this only occurred due to a lack of effect in her onset

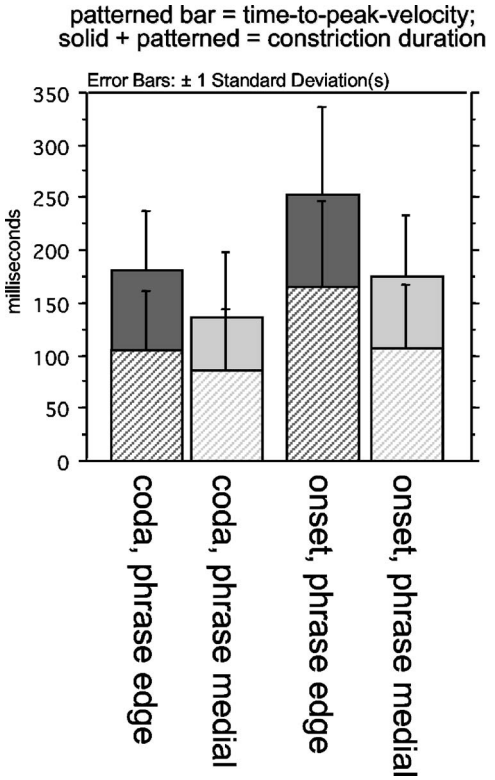

FIG. 7. Constriction duration (solid+patterned) and time-to-peak-velocity (patterned) (all subjects pooled).

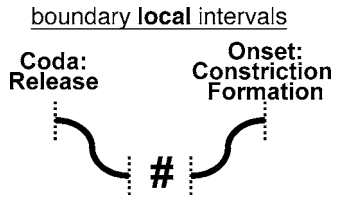

FIG. 8. A schema showing the local duration measure (i.e., release duration for codas and constriction duration for onsets).

TABLE VI. Local duration effects statistical results (consonants pooled).

Local duration	Syllable main effect	Phrase main effect	Two-way interaction effect
Speaker A	$F(1,83)=4.789$, $p=0.0315$ coda 203 ms; onset 226 ms	$F(1,83)=71.670$, $p<0.0001$ edge 261 ms; medial 167 ms	$F(1,83)=12.025$, $p=0.0008$
Speaker E	n.s. coda 228 ms; onset 208 ms	$F(1,56)=51.755$, $p<0.0001$ edge 266 ms; medial 170 ms	$F(1,56)=36.749$, $p<0.0001$
Speaker M	$F(1,84)=8.597$, $p=0.0043$ coda 166 ms; onset 200 ms	$F(1,84)=30.803$, $p<0.0001$ edge 215 ms; medial 151 ms	n.s
Speaker N	$F(1,80)=27.094$, $p<0.0001$ coda 162 ms; onset 231 ms	$F(1,80)=44.604$, $p<0.0001$ edge 244 ms; medial 155 ms	n.s
Speaker R	$F(1,83)=28.268$, $p<0.0001$ coda 248 ms; onset 197 ms	$F(1,83)=209.982$, $p<0.0001$ edge 291 ms; medial 156 ms	n.s

[p]s (recall from above that speaker E's [p]s behaved aberrantly); her onset and coda [f]s lengthen comparably, not showing any asymmetry. The overall means for local duration and local time-to-peak-velocity are shown in Fig. 9.

4. Summary for temporal patterning results

Generally, constriction formation was longer for consonants located in syllable onsets than for codas, and constriction formation was longer in duration for both onsets and codas at phrase boundaries. This effect of lengthening was most robust for consonant intervals most local to the boundary; that is, the constriction release for codas and the constriction formation for onsets. As expected based on previous work (e.g., Byrd *et al.*, 2000; Cho, in press), these portions exhibited a longer total duration and a longer time-to-peak-velocity when they occurred at phrasal boundaries.

The overall pattern of lengthening is shown in Fig. 10. Generally, the interval of boundary effect, i.e., the span over which temporal lengthening is exhibited, includes the constriction formation of phrase-final codas, their release, and the constriction formation (but not release) of onsets. Specifically, the most lengthening occurs for the releases of the preboundary codas and the constrictions of the postboundary onsets. These lengthen comparably as indicated by the lack of interaction effect in Table VI for the majority of subjects (3/5)—the mean amount of lengthening for these three subjects was 101 ms for onset constrictions and 90 ms for coda releases. (The other two subjects had more lengthening for coda releases.) In turn, the postboundary onset constriction lengthens more than the preboundary coda constriction for the majority of subjects, as indicated by the significant interaction effect for three of five subjects in Table IV. The amount of lengthening for onset constrictions at a phrase boundary was 73 ms (sp. M), 106 ms (sp. N), and 120 ms (sp. R), as compared to 17 ms (sp. M), 71 ms (sp. N), and 46 ms (sp. R) for coda constrictions preceding the boundary. Finally, recall from Sec. III A 2 that there was no lengthening of the onset consonant release after a phrase boundary for three of five speakers. (The other two show opposite directions of effect, such that one lengthens and one shortens the release following the phrase boundary.) Thus we conclude that the general pattern for consonant articulation adjacent to a phrase boundary is a great deal of lengthening in the immediate neighborhood of the boundary, lesser lengthening more remotely preceding the boundary, and no lengthening more remotely after a boundary.

B. Spatial results

The results concerning spatial characteristics of consonants at different syllable and phrase positions are not as consistent or conclusive as the results concerning temporal lengthening. Unlike the temporal domain, spatial strengthening is not exhibited consistently across subjects, consonants, or syllable position.

This may indeed reflect speaker variability, however, it is also possible that the EMA technique introduces limitations. Whereas EPG, for example, can evaluate changes in extrema positions due to tissue compression after the active and passive articulator have come into contact, EMA is not suited to such evaluation. In the case of the consonants /f/,

TABLE VII. Local interval (release for codas and constriction formation for onsets) time-to-peak-velocity effects statistical results (consonants pooled).

Local TPV	Syllable main effect	Phrase main effect	Two-way interaction effect
Speaker A	$F(1,83)=21.942$, $p<0.0001$ coda 110 ms; onset 163 ms	$F(1,83)=36.988$, $p<0.0001$ edge 171 ms; medial 102 ms	n.s.
Speaker E	$F(1,56)=20.676$, $p<0.0001$ coda 90 ms; onset 134 ms	$F(1,56)=9.931$, $p=0.0026$ edge 127 ms; medial 96 ms	$F(1,56)=6.567$, $p=0.0131$
Speaker M	$F(1,84)=57.859$, $p<0.0001$ coda 68 ms; onset 137 ms	$F(1,84)=13.825$ $p=0.0004$ edge 119 ms; medial 86 ms	$F(1,84)=6.980$, $p=0.0098$
Speaker N	$F(1,80)=53.848$, $p<0.0001$ coda 58 ms; onset 131 ms	$F(1,80)=7.976$, $p=0.0060$ edge 112 ms; medial 81 ms	$F(1,80)=10.448$, $p=0.0018$
Speaker R	n.s. coda 95 ms; onset 110 ms	$F(1,83)=54.018$, $p<0.0001$ edge 137 ms; medial 69 ms	$F(1,83)=8.498$, $p=0.0046$

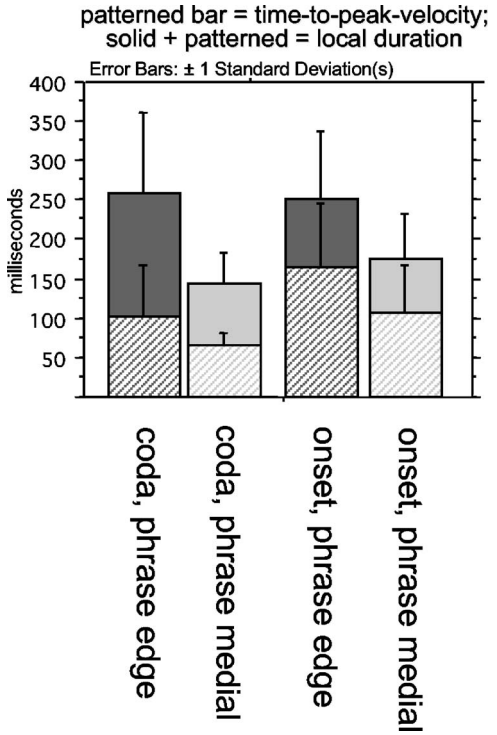

FIG. 9. Local duration (solid) and local time-to-peak-velocity (patterned) (all subjects pooled).

/p/, and /t/ here, lip aperture for /p/ and, possibly, lower lip aperture for /f/ might continue to show small effects of tissue compression as the lip receivers are on soft tissue at the vermillion border. For /t/, such effects would not be observed as the tongue tip receiver contacts the hard palate. Also, as for any point-tracking technology, the point (i.e., receiver) under examination might not be optimally located to reflect the maximal constriction location. However, because point tracking is a widespread technology often used in prosody investigations, we will, with these limitations in mind, examine constriction displacement and extremum position to determine, at least for magnetometry studies, whether the spatial variables pattern in the same way as the temporal variables. One might want to be conservative about the degree to which these spatial results are directly comparable to results using other methodology.

Because of the different nature of the consonant measures, each consonant's spatial behavior will be analyzed in separate two-factor ANOVAS, with syllable position and phrase boundary being the independent variables. The means for displacement and extremum position are given in Table VIII, though of course not every cell for each subject represents significant differences. (When a subject had no significant effects for a consonant, those means are omitted for brevity.) The significant ANOVA results are shown in Table IX.

1. /p/ spatial results

For the consonant /p/, four of the five subjects (excepting M) showed an effect of syllable position on displace-

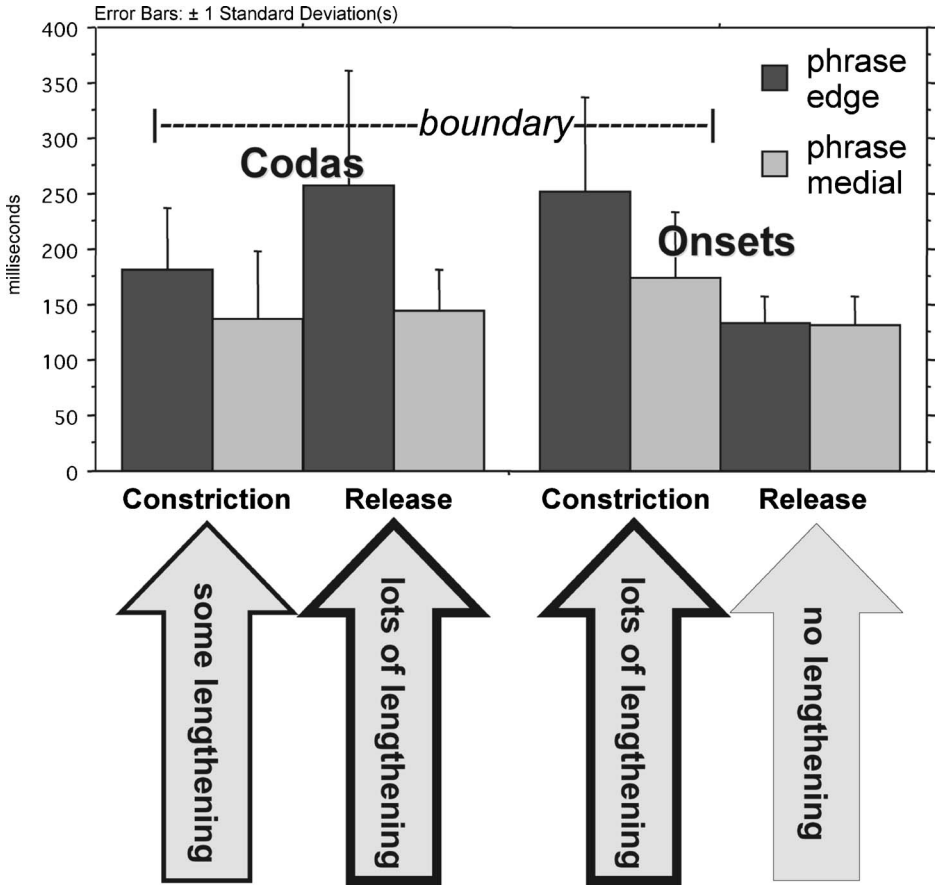

FIG. 10. Overview of temporal lengthening effects at phrase edge for codas and onsets (all subjects pooled).

TABLE VIII. Constriction displacement and extremum means. (Speaker A's /f/s do not appear because there were no significant effects; likewise Speaker M's displacement means for /p/ and /t/ and N's for /f/ were not significantly different.)

Consonant	Speaker	Syllable position	Phrasal position	Displacement value (mm)	Extremum value[a]
f	E	coda	phrase edge	3.2	22.6
f	E	coda	phrase medial	4.0	21.2
f	E	onset	phrase edge	6.5	20.2
f	E	onset	phrase medial	4.6	20.5
f	M	coda	phrase edge	4.4	24.2
f	M	coda	phrase medial	3.2	24.0
f	M	onset	phrase edge	5.2	24.5
f	M	onset	phrase medial	4.9	22.6
f	N	coda	phrase edge	n.s.	18.1
f	N	coda	phrase medial	n.s	19.5
f	N	onset	phrase edge	n.s.	17.5
f	N	onset	phrase medial	n.s.	18.3
f	R	coda	phrase edge	11.1	21.7
f	R	coda	phrase medial	9.6	23.2
f	R	onset	phrase edge	12.4	20.2
f	R	onset	phrase medial	12.3	20.7
t	A	coda	phrase edge	8.2	2.0
t	A	coda	phrase medial	4.0	0.5
t	A	onset	phrase edge	10.0	3.2
t	A	onset	phrase medial	8.5	2.3
t	M	coda	phrase edge	n.s.	2.0
t	M	coda	phrase medial	n.s.	−0.8
t	M	onset	phrase edge	n.s.	3.9
t	M	onset	phrase medial	n.s.	−1.7
t	N	coda	phrase edge	5.6	−0.8
t	N	coda	phrase medial	3.8	−0.8
t	N	onset	phrase edge	5.9	−0.3
t	N	onset	phrase medial	5.7	−0.3
t	R	coda	phrase edge	15.1	−7.5
t	R	coda	phrase medial	13.9	−7.1
t	R	onset	phrase edge	15.0	−6.0
t	R	onset	phrase medial	16.2	−6.6
p	A	coda	phrase edge	9.6	17.0
p	A	coda	phrase medial	9.7	17.8
p	A	onset	phrase edge	10.7	16.5
p	A	onset	phrase medial	11.2	17.8
p	E	coda	phrase edge	11.0	16.3
p	E	coda	phrase medial	11.7	15.3
p	E	onset	phrase edge	8.1	16.1
p	E	onset	phrase medial	12.1	15.2
p	M	coda	phrase edge	n.s.	17.4
p	M	coda	phrase medial	n.s.	16.4
p	M	onset	phrase edge	n.s.	17.4
p	M	onset	phrase medial	n.s.	17.5
p	N	coda	phrase edge	10.5	14.9
p	N	coda	phrase medial	9.8	14.6
p	N	onset	phrase edge	12.4	13.9
p	N	onset	phrase medial	10.2	13.9
p	R	coda	phrase edge	15.1	18.9
p	R	coda	phrase medial	14.6	18.7
p	R	onset	phrase edge	16.3	16.7
p	R	onset	phrase medial	16.4	18.0

[a]For extremum position /f/ and /p/ aperture in mm; /t/ position in mm in head-based coordinates where increasingly positive numbers indicate increasingly high vertical positions in the mouth.

TABLE IX. Spatial effects statistical results.

Subject	Consonant	Syllable effect	Phrase effect	Interaction
		Displacement		
A	p	$F(1,27)=7.938$, $p=0.0089$		
	t	$F(1,28)=137.6$, $p<0.0001$	$F(1,28)=111.7$, $p<0.0001$	$F(1,28)=25.346$, $p<0.0001$
	f			
E	p	$F(1,28)=7.953$, $p=0.0087$	$F(1,28)=30.139$, $p<0.0001$	$F(1,28)=15.396$, $p=0.0005$
	f	*		*
M	p			
	t			
	f	$F(1,28)=20.177$, $p<0.0001$	$F(1,28)=7.341$, $p=0.0114$	
N	p	$F(1,27)=5.633$, $p=0.025$	$F(1,27)=8.817$, $p=0.0062$	
	t	$F(1,28)=11.073$, $p=0.0025$	$F(1,28)=9.944$, $p=0.0038$	$F(1,28)=5.773$, $p=0.0231$
	f			
R	p	$F(1,28)=6.84$, $p=0.0142$		
	t	$F(1,27)=8.182$, $p=0.0081$		$F(1,27)=9.391$, $p=0.0049$
	f	$F(1,28)=47.192$, $p<0.0001$	$F(1,28)=8.02$, $p=0.0085$	$F(1,28)=5.960$, $p=0.0212$
		Extremum Position		
A	p		$F(1,27)=30.645$, $p<0.0001$	
	t	$F(1,28)=83.103$, $p<0.0001$	$F(1,28)=54.499$, $p<0.0001$	
	f			
E	p		$F(1,28)=16.108$, $p=0.0004$	
	f	$F(1,28)=20.809$, $p<0.0001$		$F(1,28)=6.902$, $p=0.0138$
M	p	$F(1,28)=5.028$, $p=0.033$		$F(1,28)=5.19$, $p=0.0306$
	t		$F(1,28)=12.743$, $p=0.0013$	
	f		$F(1,28)=8.156$, $p=0.008$	$F(1,28)=4.873$, $p=0.0356$
N	p	$F(1,27)=10.064$, $p=0.0037$		
	t	$F(1,28)=4.7$, $p=0.0388$		
	f	$F(1,25)=13.291$, $p=0.0012$	$F(1,25)=19.951$, $p=0.0001$	
R	p	$F(1,28)=18.794$, $p=0.0002$		$F(1,28)=4.932$, $p=0.0346$
	t	$F(1,27)=21.771$, $p<0.0001$		$F(1,27)=4.663$, $p<0.0399$
	f	$F(1,28)=176.5$, $p<0.0001$	$F(1,28)=45.12$, $p<0.0001$	$F(1,28)=12.095$, $p=0.0017$

ment; three of these had larger displacements in onset position. Only two subjects (E, N) showed an effect of phrase position on /p/ displacement, and they differed in direction of effect. An interaction for speaker E indicated that the displacement difference for phrase position is mostly limited to her onsets, with onset /p/ having a large phrase medial and small phrase edge displacement.

Results for lip aperture extremum values for /p/ indicate that three subjects (M, N, R) had a syllable effect such that onsets were more constricted than codas; however, two of these (M, R) had an interaction with phrase position. Speaker M exhibited a phrasal aperture difference for coda /p/s (smaller aperture phrase medially than at edges) but not for onset /p/. Speaker R's phrasal difference were only seen for onsets, where phrase edge coda /p/s had smaller apertures (i.e., were more constricted) than phrase medial coda /p/s. Two other subjects had a phrasal effect (A, E), in opposite directions of one another.

2. /f/ spatial results

For the consonant /f/, three of the five subjects (E, M, R) had a significant effect of syllable position on displacement, and two (M, R) had a phrasal effect on /f/ displacement. Speakers E and R, however, had an interaction effect. For speaker M (who lacked an interaction), phrase edge /f/ had larger displacements than phrase medial ones, and onsets had larger displacements than codas. Both speakers R and E, like speaker M, exhibited larger onset than coda displacements for /f/. For speaker R, only coda /f/ exhibited a phrasal difference such that phrase edge codas had larger displacements. For speaker E, the larger displacement at phrase edges as compared to phrase medial position was found for onsets, but codas were little different in the two phrasal contexts.

For /f/ extremum position, three of five subjects (E, N, R) had a syllable effect with onset /f/s having smaller apertures (more constricted) than coda /f/s, but speaker E and R also had a significant interaction with phrase position, as did speaker M. Speakers M, N, and R had a significant main effect of phrase position. Speaker N, who lacked an interaction effect, had smaller /f/ extremum aperture (i.e., were more constricted) for onsets than codas and for phrase edges than for phrase medially. The other speakers with interactions patterned as follows. For speaker M, only onsets showed an extremum aperture difference as a function of phrasal position with edges being less constricted than medial position. For speaker E, only codas showed an extremum aperture difference as a function of phrasal position with edges being less constricted than medial position. For speaker R, the phrasal effect was found for coda /f/s such that phrase edges are more constricted than phrase-medial codas.

3. /t/ spatial results

For the consonant /t/, displacement was significantly affected by syllable position for three of four subjects (A, N, R) and was significantly affected by phrase position for two subjects (N, R). (Recall that for the consonant /t/, speaker E was not represented.) However, all of these three speakers had a significant interaction effect as well. All three exhibited greater displacements for onsets than codas, though for speaker R this was limited to phrase medial position. Speaker A exhibited a large displacement for phrase edge codas, as compared to medial codas. The same direction of effect existed for onsets but was smaller in magnitude. Speaker N exhibited larger phrase edge as compared to medial displacements for coda /t/s but only a negligible effect, albeit in the same direction, for onset /t/s. Speaker R similarly exhibited large displacements for coda /t/s at phrase edges but no phrasal effect on onset /t/s.

Vertical extremum tongue tip position for /t/ was significantly affected by syllable position for three speakers (A, N, and R), just as with displacement, such that /t/ was more constricted in onset than in codas. Speakers A and M also had a phrasal main effect such that phrase edges had a higher (more constricted) extremum position. Speaker R exhibited an interaction effect such that phrase-edge onsets have a higher (more constricted) extremum position than phrase-medial onsets, thereby accentuating the coda versus onset distinction at phrase edges. Speakers A and N showed higher (more constricted) extremum positions for onsets than codas in both phrasal positions.

4. Summary of spatial patterning results

The spatial data were highly inconsistent both within and across subjects and within and across consonants. At best, the following generalizations can be distilled for the majority of subjects. With regard to syllable position effects, most speakers (three subjects) exhibited larger displacements in onset than in coda position for all three consonants. For most speakers for /f/ and /t/ and for two speakers for /p/, consonants also showed more constricted extrema in onsets than in codas, in line with previous studies. With regard to phrase position effects, for /f/ and /t/, most speakers exhibited larger displacements at phrase edges than phrase medially, though this pattern is not limited to only coda or onset consonants. Similarly for /f/ and /t/, consonants at a phrase edge generally showed more constricted extrema positions than when they occurred medially.

In sum, the above results on spatial strengthening lacked consistency across subjects, consonant locations, and consonants, though there were tendencies to strengthen at onsets and phrase edges. When phrasal strengthening did occur, it was *not* limited to onsets; phrase-final codas likewise could exhibit spatial strengthening patterns.

IV. DISCUSSION

The above results on spatiotemporal syllable position effects are consistent with those of previous articulatory studies (e.g., Browman and Goldstein, 1995; Keating *et al.*, 1999). Generally, consonants occurring syllable initially had longer total durations, constriction durations, and time-to-peak-velocities than those that occurred syllable finally. The notion that consonants are more prominent in word- or syllable-initial positions holds on a temporal level, as they exhibit significant amounts of lengthening when located in this position. With regard to the effect of syllable position on the spatial characteristics of consonant articulation, most subjects showed increased ranges of movement for the constriction formation portion of consonants located syllable initially than for those located syllable finally. Additionally, most showed this same spatial difference in terms of articulator extremum position—onsets had more extreme positions of articulator target achievements than codas. These results support previous studies, such as Byrd (1996) and Keating *et al.* (1999), that found similar strengthened articulation of onsets as compared to codas using electropalatography.

As for the phrasal influences on consonant articulation, the present results are likewise generally consistent with previous experiments when the temporal domain is considered (e.g., Byrd *et al.*, 2000; Cho and Keating, 2001). For all subjects, consonants that occurred at phrase-initial or phrase-final boundaries were longer in duration than those located phrase medially. They were longer in total duration, constriction duration, and time-to-peak-velocity. However, spatial strengthening of articulation of consonants occurring at phrase boundaries did not always occur, nor was it consistent across subjects or consonants. For constriction displacement, strengthening did not occur for the majority of subjects. However, when it did occur, consonants located at phrase edges had larger ranges of displacement than their phrase-medial counterparts. The majority of the speakers also showed greater articulator extrema positions for consonants located at phrase boundaries. This pattern of strengthening (when it did occur) is similar to that found in EPG (and other) studies reporting increased strengthening of consonants occurring at domain-initial boundaries, such as Keating *et al.* (2003). However, the strengthening that the subjects exhibited in the current study differs from what previous research has suggested in that strengthening was not limited to domain-initial positions. Consonants in phrase-final coda positions also showed the strengthening pattern, as suggested by an examination of strengthening of the consonantal portions adjacent to the phrasal boundary. Such behavior is preliminarily reported in Keating *et al.* (1999), and similar effects have been observed for vowels (e.g., Byrd *et al.*, 2000; Cho, 2005; Tabain, 2003).

Crucially, the present study sought to examine the *interaction* of syllable and phrasal position on the articulation of consonants, a phenomenon that has not been much explored. The results indicate that generally spatiotemporal phrasal effects exist comparably preceding and following a boundary. When constriction formation is examined, three of five subjects showed a larger phrasal lengthening effect on onsets, but this is not surprising when one considers that the constriction formation of the onset is immediately adjacent to the phrase edge whereas that interval for the coda is slightly farther removed (it is the constriction release that is the interval immediately preceding the phrase edge). When the intervals immediately local to the phrase edge are compared,

most subjects (3/5) did not show an interaction of syllable position with phrasal position; that is, leftward and rightward phrasal lengthening were comparable. For those speakers that do show an asymmetry in the temporal effect, coda releases lengthened more but onset constrictions' time-to-peak-velocity lengthened more. Finally, with regard to syllable and phrase position interactions in the spatial domain, strengthening does not exactly pattern similarly to lengthening, nor is it limited to onsets, as previous research has suggested. Consonant codas at phrase boundaries may strengthen equally to onsets. Overall, temporal lengthening is consistent and its presence for a consonant can be predicted depending on the consonant's location within the syllable and within the phrase. However, spatial strengthening in terms of articulator displacement is not as consistent, nor is its presence as predictable as lengthening. In sum, strengthening does not necessarily pattern like lengthening.

Recall that that our research agenda included an examination of the relative spatiotemporal strength of codas phrase medially, codas phrase finally, onsets phrase medially, and onsets phrase initially. This ranking was examined with consonants for four speakers for constriction duration and local duration (with speaker E excluded since her data did not include [t], and her [p]s were seen to be aberrant from the general pattern). Speakers do not always agree in the positional rankings, but some generalizations do emerge. For constriction duration, onsets at phrase edges are consistently the longest and phrase medial codas consistently the shortest, but speakers varied in whether they differentiated the medial onsets from the medial or phrase edge codas. For local duration, subjects consistently had longer durations at phrase edges than medially but were not in agreement on if or how initial (i.e., onset) constriction duration and final (i.e., coda) release duration patterned. Most subjects (3/4) also had longer medial onset constriction durations than medial coda release durations. With regard to spatial prominence, the great variability between subjects and consonants and the small size of many effects makes it impossible to rank these positions in the spatial domain.

The results concerning temporal lengthening of consonants give support for the π gesture model (Byrd and Saltzman, 2003). Qualitatively, the local edges of both codas and onsets are lengthened similarly for most subjects at a phrase boundary. This supports the conception of the π gesture spanning the boundary interval, overlapping the portion of the consonant most local to the boundary, and the prediction of like leftward and rightward qualitative effects. Quantitatively, the effect on gestural stiffness is seen on both left and right sides of the π gesture. However, for three subjects there is some evidence to suggest that the quantitative effect of the π gesture is more robust rightward. That is, the effect on gestural stiffness is more readily seen and more robust for phrase-initial edges than for phrase-final edges. This suggests that in further modeling work of prosodic boundary effects within this framework the activation trajectory or the phasing of the π gesture might have a rightward skew for some speakers (see Byrd and Saltzman, 2003). In general, across prosodic modeling frameworks the possibility of subtle speaker-specific differences in a common mechanism of boundary-adjacent lengthening will need to be accommodated.

V. CONCLUSION

The present study contributes to an understanding of prosodic signatures on articulation by examining the effects of phrasal and syllable position on the constriction formation and release of consonants. Spatial effects on the consonant articulations were quite variable, differing among speakers and consonants. Phrasal strengthening was possible for both coda and onset consonants at phrase edges. Onsets were generally spatially strengthened in comparison to codas in equivalent phrasal position. The temporal results were quite consistent and indicate that syllable and phrasal position both affect the movement duration. Syllable-initial consonants had longer articulatory durations as compared to like consonants syllable-finally. Articulations at phrase edges were also consistently longer than those phrase medially. For most subjects, the boundary-adjacent portion of the movement (constriction release for a preboundary coda and constriction formation for a postboundary onset) are not differentially affected in terms of phrasal lengthening—both lengthen comparably. This indicates that the boundary-adjacent articulatory lengthening is roughly symmetrical in the immediate vicinity of the boundary.

ACKNOWLEDGMENTS

The authors are grateful for the support of NIH's NIDCD and of the USC Undergraduate Research Program and for the assistance and advice of Professors James Mah and Shri Narayanan. The authors also thank Marija Tabain and an anonymous reviewer for their helpful comments.

[1]A couple of tokens for each subject showed multiple velocity zero-crossings at target attainment, due to a plateaued shape for the position trajectory. In these cases, the middle crossing was generally selected.

Beckman, M. E., and Edwards, J. (**1992**). "Intonational categories and the articulatory control of duration," in *Speech Perception, Production, and Linguistic Structure*, edited by Y. Tohkura, E. Vatikiotis-Bateson, and Y. Sagisaka (Ohmasha, Tokyo), pp. 359–375.

Browman, C., and Goldstein, L. (**1992**). "Articulatory phonology: An overview," Phonetica **49**, 155–180.

Browman, C., and Goldstein, L. (**1995**). "Gestural syllable position effects in American English," in *Producing Speech: Contemporary Issues. For Katherine Safford Harris*, edited by F. Bell-Berti and L. Raphael (AIP, Woodbury, NY), pp. 19–34.

Byrd, D. (**1996**). "Influences on articulatory timing in consonant sequences," J. Phonetics **24**, 209–244.

Byrd, D., and Saltzman, E. (**1998**). "Intragestural dynamics of multiple prosodic boundaries," J. Phonetics **26**, 173–199.

Byrd, D., and Saltzman, E. (**2003**). "The elastic phrase: Modeling the dynamics of boundary-adjacent lengthening," J. Phonetics **31**, 149–180.

Byrd, D., Kaun, A., Narayanan, S., and Saltzman, E. (**2000**). "Phrasal signatures in articulation," in *Papers in Laboratory Phonology V*, edited by M. B. Broe and J. B. Pierrehumbert (Cambridge U.P., London), pp. 70–87.

Cho, T. (in press). "Manifestation of prosodic structure in articulatory variation: Evidence from lip kinematics in English," in *Laboratory Phonology 8: Varieties of Phonological Competence*, edited by L. M. Goldstein, D. H. Whalen, and C. T. Best (Mouton de Gruyter, Berlin).

Cho, T. (**2005**). "Prosodic strengthening and featural enhancement: Evidence from acoustic and articulatory realizations of /a, i/ in English," J.

Acoust. Soc. Am. **117**, 3867–3878.
Cho, T., and Keating, P. (**2001**). "Articulatory and acoustic studies on domain-initial strengthening in Korean," J. Phonetics **29**, 155–190.
Edwards, J., Beckman, M. E., and Fletcher, J. (**1991**). "The articulatory kinematics of final lengthening," J. Acoust. Soc. Am. **89**, 369–382.
Fougeron, C., and Keating, P. (**1997**). "Articulatory strengthening at edges of prosodic domains," J. Acoust. Soc. Am. **101**, 3728–3740.
Hacopian, N. (**2003**). "A three-way VOT contrast in final position: Data from Armenian," J. Int. Phonetic Assoc. **33**, 51–80.
Keating, P., Wright, R., and Zhang, J. (1999). "Word-level asymmetries in consonant articulation" UCLA Working Papers in Phonetics 97.
Keating, P., Cho, T., Fougeron, C., and Hsu, C. (**2003**). "Domain-initial strengthening in four languages,"in *Papers in Laboratory Phonology 6*, edited by J. Local, R. Ogden, and R. Temple (Cambridge U.P., London), pp. 143–161.
Kelso, J. A. S., Vatikiotis-Bateson, E., Saltzman, E., and Kay, B. (**1985**). "A qualitative dynamic analysis of speech production: phase portraits, kinematics, and dynamic modeling," J. Acoust. Soc. Am. **77**, 226–280.
Ostry, D. J., and Munhall, K. (**1985**). "Control of rate and duration of speech movements," J. Acoust. Soc. Am. **77**, 640–648.
Saltzman, E. L., and Munhall, K. G. (**1989**). "A dynamical approach to gestural patterning in speech production," Ecological Psychol. 1, 333–382.
Tabain, M. (**2003**). "Effects of prosodic boundary on /aC/ sequences: articulatory results," J. Acoust. Soc. Am. **113**, 2834–2849.

The influence of noise on vowel and consonant cues

Gaurang Parikh and Philipos C. Loizou[a)]
Department of Electrical Engineering, University of Texas at Dallas, Richardson, Texas 75083-0688

(Received 29 April 2005; revised 19 September 2005; accepted 20 September 2005)

This study assessed the acoustic and perceptual effect of noise on vowel and stop-consonant spectra. Multi-talker babble and speech-shaped noise were added to vowel and stop stimuli at −5 to +10 dB S/N, and the effect of noise was quantified in terms of (a) spectral envelope differences between the noisy and clean spectra in three frequency bands, (b) presence of reliable F1 and F2 information in noise, and (c) changes in burst frequency and slope. Acoustic analysis indicated that F1 was detected more reliably than F2 and the largest spectral envelope differences between the noisy and clean vowel spectra occurred in the mid-frequency band. This finding suggests that in extremely noisy conditions listeners must be relying on relatively accurate F1 frequency information along with partial F2 information to identify vowels. Stop consonant recognition remained high even at −5 dB despite the disruption of burst cues due to additive noise, suggesting that listeners must be relying on other cues, perhaps formant transitions, to identify stops. © *2005 Acoustical Society of America.* [DOI: 10.1121/1.2118407]

PACS number(s): 43.71.Es, 43.71.Ky [ALF] Pages: 3874–3888

I. INTRODUCTION

Since the classic study by Peterson and Barney (1952) on the distribution of the vowel formant frequencies on the F1-F2 plane, many studies were conducted in quiet on vowel perception (see reviews by Strange, 1989, 1999), estimation of difference limens for formant discrimination (Flanagan, 1955; Hawks, 1994; Liu and Kewley-Port, 2001), vowel modeling (e.g., Syrdal and Gopal, 1986; Molis, 2005), and other aspects of vowel discrimination. Many factors were found to be important for vowel identification including formant frequencies (Peterson and Barney, 1952), vowel duration (e.g., Ainsworth, 1972), F0 (e.g., Lehiste and Meltzer, 1973), spectral contrast (Leek *et al.*, 1987; Loizou and Poroy, 2001), formant contour (Hillenbrand and Gayvert, 1993; Hillenbrand and Nearey, 1999), spectral shape (e.g., Zahorian and Jaghargi, 1986; Ito *et al.*, 2001), and spectral change (e.g., Strange *et al.*, 1983). Of these factors, the formant frequencies and spectral shape, in particular, have been found to be major cues to vowel perception. The contribution of these cues to vowel perception has been the subject of a longstanding debate between a formant-based and a spectral-shape-based theory of vowel perception (see review in Ito *et al.*, 2001).

Evidence in support of a formant theory comes from studies in which speech synthesized from formant frequencies was found to be highly intelligible despite removal of detailed spectral shape information (e.g., Remez *et al.*, 1981). There is also ample evidence from animal neurophysiological studies that suggests that the formant frequencies are encoded in the temporal discharge patterns of the auditory nerve fibers (e.g., Young and Sachs, 1979). Discharge rates of large populations of auditory nerve fibers when plotted as a function of the characteristic frequency showed distinct peaks corresponding to the formants of the vowels, suggesting a place-code representation of vowel formants, at least for low sound intensities. Formants are also coded in the time pattern of the auditory fiber's discharges over a large range of sound intensities, suggesting a temporal-code representation (Young and Sachs, 1979). Scalp-recorded frequency-following responses (FFRs) from humans showed clearly discernible peaks at harmonics adjacent to the first two formant frequencies (Krishnan, 1999, 2002). The FFR data led Krishnan (2002) to conclude that the neural coding of formants based on phase locking is preserved even at high levels in the human brainstem.

Despite its simplicity, the formant theory does not account for the outcomes of several psychophysical and modeling studies, leading some researchers to a spectral-shape or whole-spectrum theory. Advocates of the whole-spectrum theory describe the vowels in terms of the properties of the spectrum as a whole rather than in terms of the individual formant frequency values. Several arguments were offered against a formant representation (e.g., Bladon, 1982). First, automatic formant frequency detection tends to be unreliable particularly in noise and in situations in which the harmonics are spaced widely apart (e.g., in children's speech). Errors made by formant tracking algorithms (e.g., formants merging) are not consistent with those made by human listeners. Second, formant-based models do not incorporate any characteristics of the peripheral auditory system such as critical band filtering. The whole-spectrum model proposed by Bladon and Lindblohm (1981) incorporated several aspects of auditory processing including critical-band filtering and loudness and yielded a high correlation with normal-hearing listener's judgments of vowel quality. Third, cues other than formant frequencies can affect vowel perception. Several researchers have demonstrated that the relative amplitude of adjacent formants can affect the perceived vowel quality (Chistovich and Lublinskaja, 1979; Ito *et al.*, 2001). Ito *et al.*, for instance, demonstrated that the formant amplitude

[a)]Author to whom correspondence should be addressed. Electronic-mail: loizou@utdallas.edu

ratio is equally or more effective than F2 as cue to place of articulation (front/back). Ito *et al.* (2001) concluded that the formant frequency cues are not the exclusive cues to vowel perception and that spectral shape could be crucial.

In most of the above studies the formant frequencies and spectral shape were varied independently of one another. In noise, however, both formant frequencies and spectral envelope (shape) will be affected to some degree, but it is not known which of the two will be affected the most. Also, it is not known how and to what degree the formant frequencies will be affected or to what degree the spectral envelope will be altered by the noise. These questions have not been addressed in previous studies on recognition of vowels in noise as those studies concentrated primarily on identification errors (e.g., Pickett, 1957; Nebalek and Dagenais, 1986) and on the relationship between vowel identification, hearing loss, and age (e.g., Nebalek, 1988), rather than on factors that might potentially be responsible for the identification errors.

The present study takes the first step in quantifying the effect of noise (multi-talker babble and continuous speech-shaped noise) on the spectrum of vowels. Given the importance of formant frequencies and spectral shape on vowel identification, we focus primarily on analyzing acoustic measurements of formant frequencies and spectral envelopes. Since we are ultimately interested in knowing whether listeners use formant frequency information to identify vowels in noise, we seek to establish first if there exists reliable and relatively accurate formant-frequency information in noise. More specifically, we measure how often there exists reliable F1 and/or F2 information in noise. This measure will tell us whether listeners have access to reliable and coherent formant frequency (F1 and F2) information in noise and, if so, to what degree. If there is no reliable formant information, then perhaps listeners make use of spectral shape information. To examine that, we evaluate the differences between the critical-band spectra of the clean and noisy vowels and correlate those differences with vowel identification scores. If the correlation analysis reveals that large critical-band spectral differences are associated with lower identification scores, then that would suggest that listeners are making use of spectral shape cues. The vowel representation based on critical-band spectra is chosen for two reasons. First, the critical-band spectra contain only gross peak information and no irrelevant harmonic details and can therefore be used to assess whether listeners make use of spectral-shape cues to identify vowels. Second, the critical-band vowel representation incorporates characteristics of the peripheral auditory system, such as critical-band filtering, and has been used by some as approximation to the "auditory excitation patterns" (Plomp, 1970; Klatt, 1982).

Parallel to examining the effect of noise on the vowel spectra, we also analyze the effect of noise on the consonant spectra, and particularly the stop consonants which have been studied extensively in the literature (see review in Kent and Read, 1992). The acoustic cues used for stop perception differ from those for vowel perception, hence different acoustic parameters are extracted and analyzed for the stop consonants. These parameters are based on theories and models proposed for understanding the cues to stop-consonant place of articulation. It is has long been recognized, since the Pattern Playback days at Haskins Labs (see Liberman *et al.*, 1952; Cooper *et al.*, 1952), that the spectrum of the stop burst is a major cue to place of articulation. Labial stops typically have low-frequency dominance, alveolars have high-frequency dominance, and velars are associated with a mid-frequency burst. Stevens and Blumstein (1978) explored the idea of constructing a spectral template that could be associated with each place of stop articulation. In these templates, the bilabials had a flat or a falling spectrum, the alveolars had a rising spectrum, and the velars had a compact (with a peak in mid-frequencies) spectrum. Using these templates, Blumstein and Stevens (1980) were able to classify stops with 85% accuracy. After several reevaluations of the spectral-template theory (e.g., Blumstein *et al.*, 1982; Walley and Carrell, 1983), research on place of articulation shifted toward the dynamic spectral change following the first tens of ms of the release. Other cues found in later studies to be important for place for articulation were the spectral change from the burst to voicing onset (e.g., Kewley-Port, 1983; Lahiri *et al.*, 1984) and formant transitions (e.g., Delattre *et al.*, 1955; Dorman and Loizou, 1996; Smits *et al.*, 1996).

In summary, the burst spectrum and formant transitions have been found to be major cues to stop-place of articulation. The effect of noise on these place cues, however, is not clear and has not been investigated. It is not known, for instance, how noise affects the tilt of the burst spectrum, and consequently whether a change in the spectral tilt would be accompanied by a shift in phonetic category. Similarly, it is also not known whether a change in burst frequency will be associated with low identification scores. While several studies (e.g., Dorman *et al.*, 1977; Dorman and Loizou, 1996; Smits *et al.*, 1996) used a conflicting-cue paradigm to probe the above questions, those studies were done in quiet. To answer the above questions, we will measure the slope and frequency of the burst spectrum in quiet and in noise and correlate these measurements with identification scores. We chose those two acoustic parameters because they are relatively simple to estimate in noise.

Previous studies examining stop consonant recognition in noise (e.g., Miller and Nicely, 1955; Wang and Bilger, 1973; Pickett, 1957) have not addressed the above questions. The studies by Pickett (1957) and Miller and Nicely (1955) on consonant identification in noise assessed the effect of noise on vowel/consonant perception, but only indirectly by analyzing the confusion errors. Such an analysis, however, leaves many questions unanswered and does not tell us specifically what caused the confusion errors. Only white noise was used in the studies of Miller and Nicely (1955) and Wang and Bilger (1973), making it difficult to generalize their findings to more realistic types of noise (e.g., multi-talker babble).

In summary, not many studies have assessed or quantified the perceptual effect of noise on vowel and consonant perception. In this study, we take the first step in quantifying the effect of multi-talker babble and continuous speech-shaped noise on the spectra of vowels and stop consonants. This paper attempts to answer several questions and has two

TABLE I. Mean F1 and F2 frequencies (in Hz) of the vowels used in this study.

		Had	Hod	Head	Hayed	Heard	Hid	Heed	Hoed	Hood	Hud	Who'd
F1	Male	627	786	555	438	466	384	331	500	424	629	319
	Female	666	883	693	492	518	486	428	538	494	809	435
F2	Male	1910	1341	1851	2196	1377	2039	2311	868	992	1146	938
	Female	2370	1682	1991	2437	1604	2332	2767	998	1102	1391	1384

interrelated aims. The first aim is to quantify the effect of noise by means of acoustic analysis of the vowel and consonant spectra. A subset of the aforementioned factors, known to be important for vowel and stop-consonant identification, will be assessed by comparing the acoustic parameters (e.g., spectral tilt, etc.) estimated in quiet with those estimated in noise. The acoustic parameter comparisons are meant to answer several questions, including the following. (1) How are the vowel spectral envelopes (critical-band spectra) affected? (2) How are the two formant frequencies (F1 and F2), known to be major cues to vowel recognition, affected? (3) How are the spectral tilt and frequency of the burst spectra affected? The above, and other, questions will be answered quantitatively by performing acoustic analysis of vowels and stop consonants embedded in −5 to 10 dB noise.

The second aim of this paper is to assess the perceptual effect of noise on vowel and stop-consonant identification. This will be done by performing correlation analysis between the acoustic parameter values and the vowel/stop-consonant identification scores. The second aim will be addressed in experiment 1. The results from the acoustic analysis and experiment 1 taken together will provide valuable insights on the cues used by listeners to understand speech in noise. Knowing how noise affects the spectrum of speech is important for several reasons. For one, such knowledge could help us design better noise reduction algorithms that could potentially improve hearing-impaired listeners' speech understanding in noise. Secondly, it could help us better understand which speech features are perceptually robust in additive noise, and consequently which features listeners attend to when identifying vowels or consonants in noise.

II. ACOUSTIC ANALYSIS

A. Method

1. Speech material

The vowel material consisted of the vowels in the words: "heed, hid, hayed, head, had, hod, hud, hood, hoed, who'd, heard." The stimuli were drawn from a large multi-talker vowel set used by Hillenbrand *et al.* (1995). A total of 66 vowel tokens were used for acoustic analysis: 33 vowels produced by male speakers and 33 vowels produced by female speakers. There were 6 tokens for each of the 11 vowels, 3 produced by male speakers and 3 by female speakers. A total of 20 different male speakers and 23 female speakers produced the 66 vowel tokens. Each speaker produced only a subset of the 11 vowels. The vowels were sampled at 16 kHz. Table I gives the steady-state F1 and F2 values of the vowel stimuli used in this study. The F1 and F2 values were sampled at the steady-state portion of the vowel and averaged across all speakers. The steady-state F1 and F2 values (Table I) of the vowel stimuli used in this study were provided by Hillenbrand *et al.* (1995).

Consonant material consisted of the stop consonants in VCV context, where V=/i a,u/ and C=/b d g p t k/. The stimuli were drawn from recordings made by Shannon *et al.* (1999). A total of 36 consonant tokens were used for acoustic analysis: 18 consonants (6 stops×3 vowel contexts) produced by a male speaker and 18 consonants produced by a female speaker. The consonants were sampled at 44.1 kHz.

2. Noise

Two types of noise were used, multi-talker babble (two male and two female talkers) and speech-shaped noise. The babble was taken from the AudiTEC CD (St. Louis) and was sampled at 16 kHz. The speech-shaped noise (sampled at 20 kHz) was constructed by filtering white noise through a 60-tap FIR filter with a frequency response that matched the long-term spectrum of the 11 male and 11 female vowels. Noise was first up-sampled to the sampling frequency of the vowel/consonant materials and then added to the vowels at −5, 0, 5, and 10 dB. Figure 1 shows the averaged long-term spectra of the multi-talker babble and speech-shaped noise.

3. Acoustic analysis of vowels

Prior to the acoustic analysis, the complete vowel data set was manually segmented to [h Vowel d]. The starting and ending times of the vocalic nuclei were measured by hand

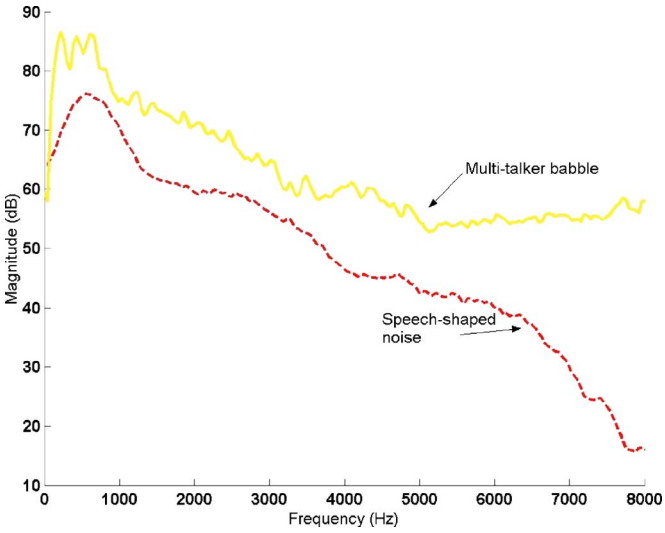

FIG. 1. (Color online) The long-term spectra of the multi-talker babble and continuous speech-shaped noise used in this study as maskers.

TABLE II. Lower and upper-edge edge (−3 dB) frequencies of the critical band filters.

Critical band	Lower edge frequencies (Hz)	Upper edge frequencies (Hz)	Center frequency (Hz)	Bandwidth (Hz)
1	0	100	50	100
2	100	200	150	100
3	200	300	250	100
4	300	400	350	100
5	400	510	450	110
6	510	630	570	120
7	630	770	700	140
8	770	920	840	150
9	920	1080	1000	160
10	1080	1270	1170	190
11	1270	1480	1370	210
12	1480	1720	1600	240
13	1720	2000	1850	280
14	2000	2320	2150	320
15	2320	2700	2500	380
16	2700	3150	2900	450
17	3150	3700	3400	550
18	3700	4400	4000	700
19	4400	53000	4800	900
20	5300	6400	5800	1100
21	6400	7700	7000	1300

from high-resolution digital spectrograms. To minimize the effect of formant movements due to /h/ and /d/, acoustic measurements were made starting from 20% of the vowel duration and ending at 80% of the vowel duration.

a. Critical-band spectral difference measurements. In order to quantify the effect of noise on different regions of the spectrum, we measured the critical-band spectral difference between the clean and noisy vowels in two different bands corresponding to the F1 and F2 regions. The measurements were based on a critical-band vowel representation. The critical-band spectra representation was chosen as it approximates the auditory "excitation patterns" (Plomp, 1970) of the vowels. The critical-band spectra were computed as follows.

The vocalic segment of the vowels (containing 20%–80% of the vowel duration) was first filtered through a 21-channel filterbank implemented using sixth-order Butterworth filters. The center frequencies of the filterbank were chosen according to critical-band spacing (Zwicker and Fastl, 1990) and are given in Table II. Estimates of the vowel spectra were then made by computing the root-mean-square (rms) energy of the 21-filterbank outputs within 10-ms windows. The 21-filterbank outputs provide approximations to the auditory excitation patterns (Plomp, 1970; Klatt, 1982).

The spectral difference between the clean and noisy vowels was then computed for two different frequency bands spanning the 0–8 kHz bandwidth, using a normalized Euclidean distance metric of the filterbank energies. This metric is similar to that used by Plomp (1970) based on third-octave bands and is used in our study for two reasons: (1) to quantify the effect of noise in individual frequency bands and (2) to assess the importance of spectral shape cues on vowel identification, since the critical-band spectra contain only gross peak information and no harmonic details. For the purposes of this study, the Euclidean distance metric was normalized by the energy of the clean spectrum within the specified frequency band. We found this normalization necessary due to the inherent differences in spectral magnitude levels at the low and high frequencies.

The two bands considered include a low-frequency (LF) band spanning the 0–1 kHz region and a middle-frequency (MF) band spanning the 1–2.7 kHz region. F1 typically resides in the LF band, and F2 resides in the MF band. Two spectral difference measurements were made, one for each band, every 10 ms:

$$\mathrm{LF} = \frac{\sqrt{\sum_{i=1}^{9} (F_i^c - F_i^n)^2}}{\sqrt{\sum_{i=1}^{9} (F_i^c)^2}}, \tag{1a}$$

$$\mathrm{MF} = \frac{\sqrt{\sum_{i=10}^{15} (F_i^c - F_i^n)^2}}{\sqrt{\sum_{i=10}^{15} (F_i^c)^2}}, \tag{1b}$$

where F_i^c denotes the ith filterbank energy of the clean vowel and F_i^n denotes the ith filterbank energy of the noisy vowel.

b. Measurements of formant frequency (F1 and F2) presence. Formant frequency measurements were made based on a 22-pole LPC spectrum computed over 20-ms Hamming-windowed segments. The LPC spectrum was obtained using a 2048-point FFT, yielding a 7.8-Hz frequency resolution. The frequencies of the first seven spectral peaks were extracted from the LPC spectrum every 20 ms. In order to get reliable F1 and F2 frequency estimates, we estimated the formant frequencies manually rather than using a peak-picking algorithm. An interactive MATLAB program was used that allowed the user to select among multiple spectral peaks the peaks corresponding to F1 and F2. This was done successively for each 20-ms segment of the vowel. The clean vowel spectrum was overlaid to the noisy vowel spectrum in order to get a rough estimate on the location of the F1/F2 frequencies of the noisy vowel spectra. Knowledge of acoustic phonetics played a role in the editing process, particularly knowledge about the close proximity of F1 and F2 for vowels such as /a/ and /u/.

Although it is relatively easy to identify (at least manually) F1 and F2 in quiet or relatively high S/N conditions, it is extremely difficult to identify F1 and F2 in extremely low S/N conditions. For that reason, F1 and F2 measurements were made only when the user felt confident that the selected peaks represented F1/F2 and not noise. For consistency purposes, several rules were adopted which classified each frame into four categories: (1) F1 not present, (2) F2 not present, (3) neither F1 nor F2 present, and (4) F1 and F2 reliably present. The percentage of frames that fell in each of the four categories was recorded for further analysis.

A frame was classified into category 1 (F1 not detected) whenever two or more peaks were present in the proximity[1] of the F1 region of the noisy vowel spectrum. A frame was classified into category 2 (F2 not detected) if either of the following two conditions were satisfied: (a) two or more

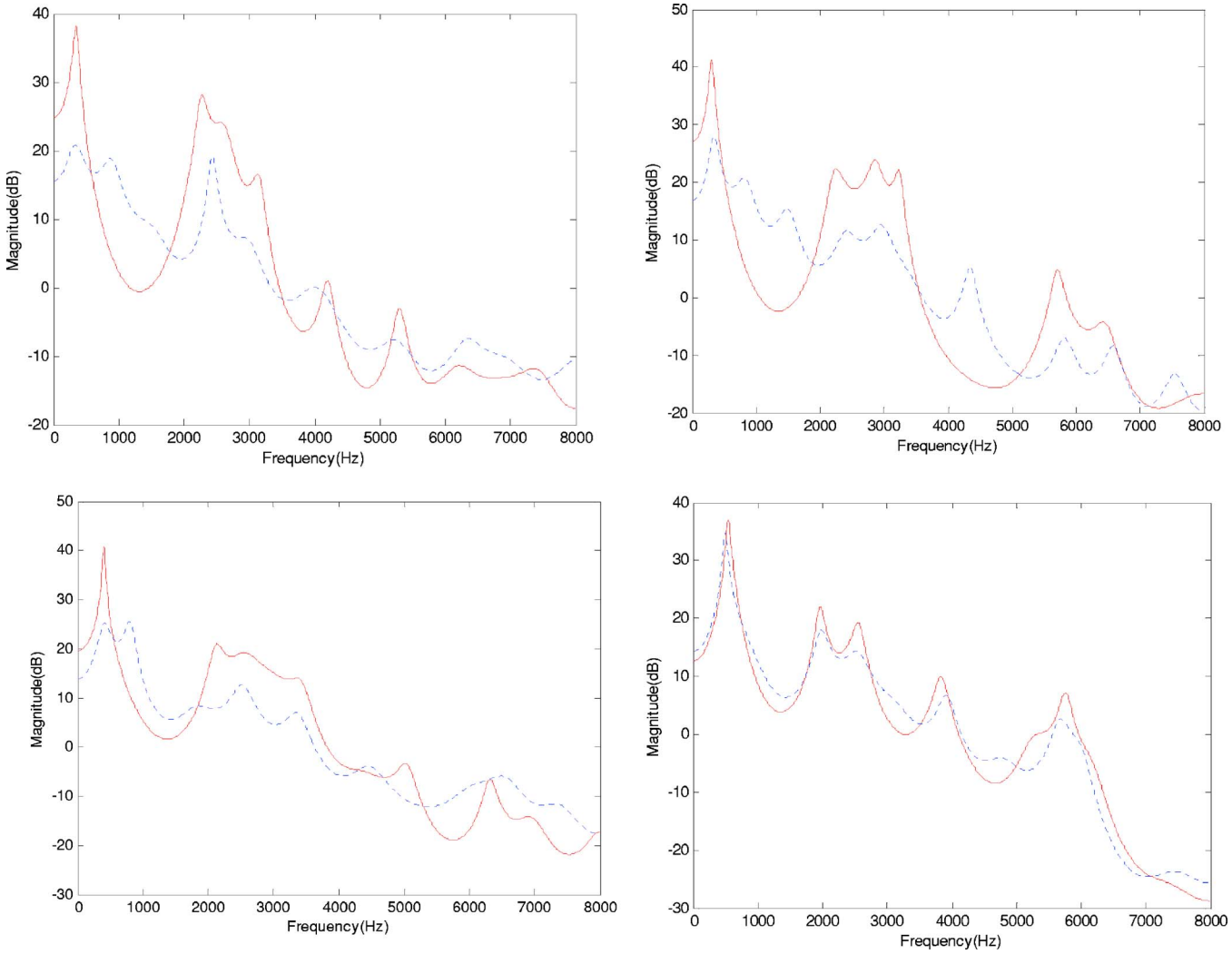

FIG. 2. (Color online) Example LPC spectra showing the four different categories used to label detection of F1 and F2. Solid lines indicate the clean spectra, and dashed lines indicate the corrupted vowel spectra. (Top left) Category 1: F1 not reliably detected because of multiple peaks in the proximity of F1 region. (Top right) Category 2: F2 not reliably detected because multiple peaks were present in the F1-F2 region. (Lower left) Category 3: Neither F1 nor F2 reliably detected. (lower right) Category 4: Both F1 and F2 reliably detected.

peaks were present in the proximity of the F2 region of the noisy vowel spectrum and (b) multiple peaks were present in the F1-F2 frequency range. A frame was classified into category 4 whenever a single peak was found near the F1 and F2 regions. Figure 2 shows example spectra from each category.

For the frames in which both F1 and F2 formants were reliably detected, we performed additional analysis to compare the formant frequencies estimated in noise with those estimated in quiet. We computed the absolute difference between the formant frequencies as follows:

$$\Delta F_1 = |F_1^q - F_1^n|, \qquad \Delta F_2 = |F_2^q - F_2^n|, \tag{2}$$

where the superscript q indicates the formant frequency estimated in quiet and the superscript n indicates the corresponding formant frequency estimated in noise.

4. Acoustic analysis of consonants

Prior to analysis, the complete VCV consonant data set was manually segmented to [Vowel Consonant Vowel]. The starting and ending times of the burst were measured by hand from high-resolution digital spectrograms and displays of the time waveform. Only the first 10 ms of the release burst was considered, or the whole burst if smaller than 10 ms.

a. Burst frequency measurements. The burst frequency is defined as the frequency corresponding to the largest spectral magnitude of the burst spectrum (Liberman *et al.*, 1952). Burst frequency measurements were made using a 20-pole LPC spectrum. A Hamming window of 20 ms was used centered at the onset of the burst. In effect, only the latter half of the Hamming window was multiplied with the 10 ms of the release burst samples. The LPC spectrum was obtained using a 512-point FFT.

The frequency of the maximum amplitude of spectral peak was extracted from LPC spectra using a global peak-picking algorithm. Table III gives the consonant burst fre-

TABLE III. Burst frequencies (in Hz) of stop-consonants in three vowel contexts.

Vowel context	Stop consonant					
	/p/	/b/	/t/	/d/	/g/	/k/
/i/	3575	1938	7321	6675	3252	3208
/a/	1357	711	5103	5190	1852	1873
/U/	797	840	4522	3811	1701	1701

quencies estimated in quiet. The differences in burst frequencies between the clean and noisy burst spectra were computed and recorded.

b. Spectral tilt measurements. Spectral tilt measurements were made based on a four-pole LPC spectrum estimated using a 512-point FFT (fast Fourier transform). A low-order LPC was chosen to capture the trend of the burst spectrum while avoiding unnecessary details (e.g., peaks and valleys) in the spectrum. The spectral tilt was computed by evaluating the LPC magnitude spectrum at two frequencies, at 1000 and 5000 Hz. Spectral tilt was calculated as the difference between the spectral magnitudes (in dB) at 1000 and 5000 Hz. This frequency range was chosen to ensure that F2 was included in the spectral tilt computation[2] (Smits *et al.*, 1996). The dB difference values can be easily converted into slopes (in dB/Hz) by dividing the difference values by 4000 Hz (=5000−1000). A positive slope is indicated by a positive difference (rising spectrum), a negative slope is indicated by a negative difference (falling spectrum), and a slope close to zero (diffuse spectrum) is indicated by difference values close to zero. Figure 3 shows example LPC spectra of /p/ and /t/ along with their corresponding spectral tilt measurements.

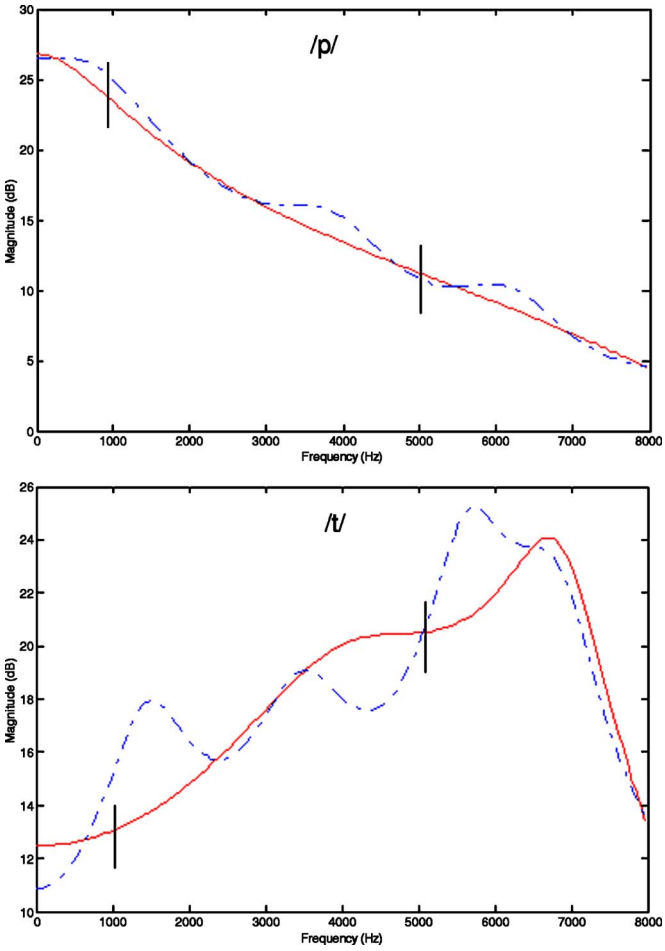

FIG. 3. (Color online) Example estimation of burst spectral slopes of /p/ and /t/. The dashed lines show the four-pole LPC spectra used for estimating the spectral slope, and the solid lines show the original burst spectra of /p/ and /t/. The vertical lines indicate the points (1000 and 5000 Hz) used to estimate the dB differences.

B. Results

1. Vowels

The acoustic measurements of the critical-band difference metric and number of formants reliably detected are shown in Figs. 4 and 5, respectively.

a. Critical-band spectral difference metric. Figure 4 shows the average critical-band spectral differences between clean and noisy spectra for each of the two frequency bands considered and for vowels embedded in speech-shaped noise (top panel) and multi-talker babble (bottom panel). Repeated measures ANOVA of the mean spectral difference (between noisy and clean vowels) of each vowel using noise type (multi-talker babble and speech-shaped noise), S/N level, and frequency band (low- and middle-frequency bands) as factors indicated a significant effect of noise type [$F(1,10)=7.18$, $p=0.023$], a significant effect of S/N level [$F(3,30)=11.7$, $p<0.005$], and a nonsignificant effect of frequency band [$F(1,10)=4.3$, $p=0.065$]. All the interactions between the within-subject factors were found to be significant ($p<0.05$). The interactions were partly caused by the fact that noise (babble and steady-speech-shaped) affected the two frequency bands of the vowel spectra differently depending on the S/N level. These interactions are probed in more detail below.

As shown in Fig. 4, the critical-band spectral difference between clean and noisy vowels decreased as the S/N increased. The largest spectral difference between the noisy and clean vowel spectra occurred in the mid-frequency band (1–2.7 kHz). This suggests that the F2 region was heavily masked by the noise. The F2 region was masked significantly ($p=0.049$) more than the F1 region (low frequency band) only for vowels corrupted by multi-talker babble at −5 dB S/N. For vowels corrupted by speech-shaped noise, the difference between the spectral distance measurements obtained for the low- and mid-frequency bands was not significant at any S/N level. Further *t* tests, with Bonferroni correction, indicated no statistically significant differences between the corresponding critical-band difference metrics for the two types of noise at any S/N level, suggesting that the two types of noise examined in this study affected the spectrum in the same way, at least for S/N levels higher than −5 dB.

b. Counts of formant frequencies. For reliability purposes, a second experimenter worked independently and remeasured 20% of the vowels embedded in the various S/N conditions. The second experimenter made use of the same software used by the first experimenter and the same rules for classifying the frames into one of the four categories.

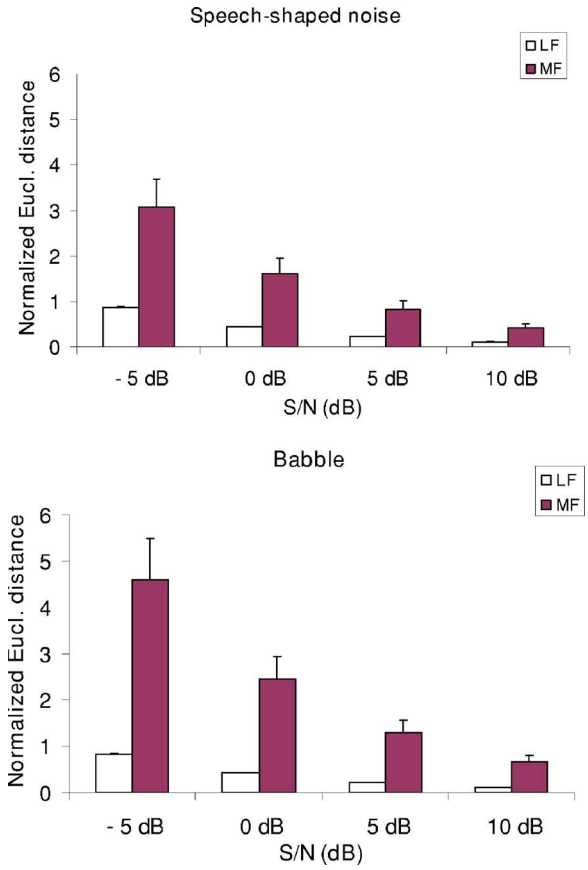

FIG. 4. (Color online) Mean spectral envelope differences (based on the Euclidean distance metric) between the clean vowel spectra and noisy vowel spectra in the low (LF) and middle (MF) frequency regions. Error bars indicate standard errors of the mean.

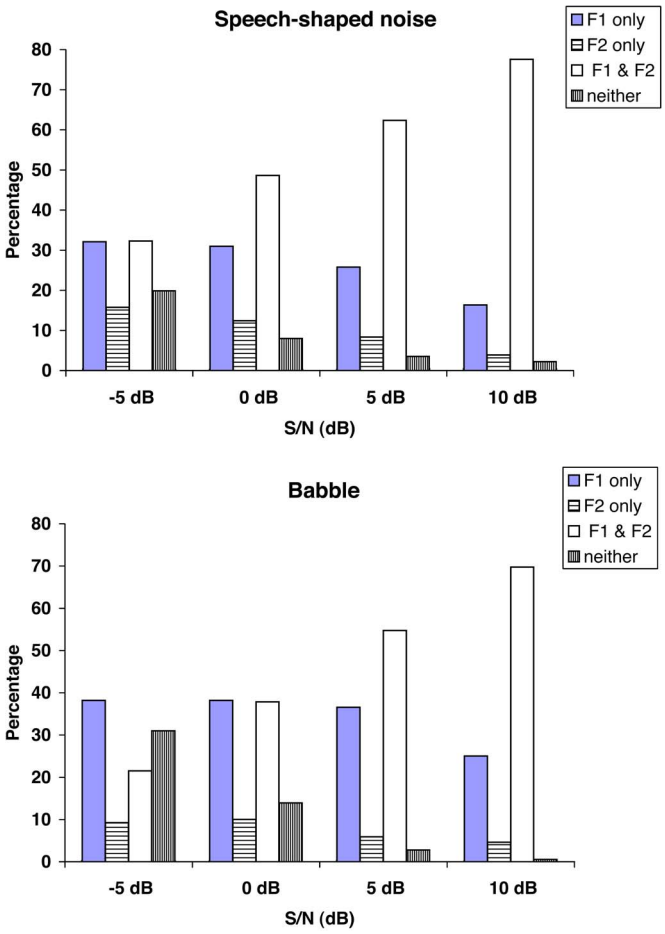

FIG. 5. (Color online) Percentage of vowel frames in which the F1 and/or F2 formants were reliably detected in various noise conditions.

Results from recounting the number of F1 and F2 peaks detected reliably in noise indicated an average difference of less than 1% (across all S/N conditions) between the measurements of the two experimenters.

Figure 5 shows the percentage of frames (out of a total of 539 frames) in which F1 and/or F2 were reliably identified for vowels embedded in speech-shaped noise (top panel) and for vowels embedded in multi-talker babble (bottom panel) at various S/N levels. For the low S/N conditions, the first formant (F1) was reliably identified more often compared to the second formant (F2). According to nonparametric tests (Mann-Whitney test), F1 was identified significantly ($p < 0.05$) more often than F2 in both types of noise.

F1 and F2 formants were identified significantly ($p = 0.036$) more often (according to Mann-Whitney tests) in −5 dB S/N speech-shaped noise than in −5 dB S/N multi-talker babble. No significant difference was found between the number of the two formants (F1 and F2) identified in babble and speech-shaped noise in other S/N conditions. F1 and F2 formants were reliably identified more than 50% of the time only for S/N values of 5 dB and higher. In multi-talker babble (5 dB S/N), the F1 and F2 formants were identified 54.6% of the time, while in speech-shaped noise the two formants were identified 62% of the time.

For the frames in which both formants were reliably identified, we computed the differences [ΔFs as per Eq. (2)] between the true (estimated in quiet) formant frequencies and the estimated formant frequencies in noise, averaged across all vowels. The results are tabulated in Table IV for +5 and +10 dB S/N. As can be seen from Table IV, the differences in formant frequencies (ΔF's) were extremely small. In fact, the ΔF values were close to the difference limens (DLs) of formant frequencies, known to be in the order of 1%–2% of the formant frequencies (Flanagan, 1955; Hawks, 1994).

2. Consonants

Acoustic measurements of the burst frequency and slope are shown in Figs. 6 and 7, respectively.

a. Burst frequency measurements. Figure 6 shows the burst frequency differences between measurements made in noise and in quite, averaged across all stop consonants for

TABLE IV. Mean absolute differences in F1 and F2 values between formant frequencies estimated in quite and those corrupted in +5 and +10 dB S/N. These differences were estimated only for frames which contained reliable F1 and F2 information.

Noise type	S/N level (dB)	ΔF1 (Hz)	ΔF2 (Hz)
Multi-talker	5	19.3	27.6
Speech shaped		15.8	22.8
Multi-talker	10	12.4	20.0
Speech shaped		11.1	16.9

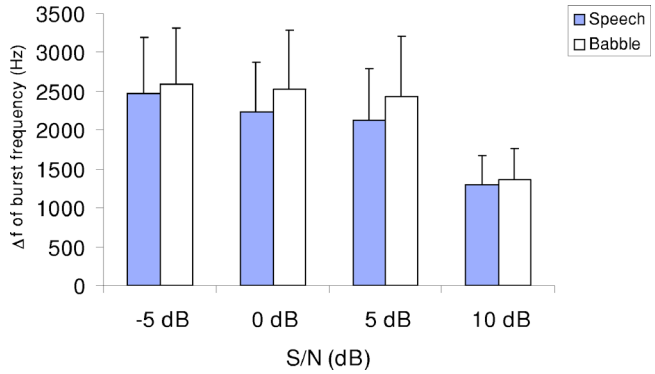

FIG. 6. (Color online) Mean shift in burst frequency of noisy stops relative to the burst frequency estimated in quiet. Error bars indicate standard deviations

different S/N levels and noise conditions. Repeated measures ANOVA of the burst frequency deviation (difference) of each stop consonant using noise type (multi-talker babble and speech-shaped noise) and S/N level as factors indicated a significant effect of noise type [$F(1,5)=10.48$, $p=0.023$], a significant effect of S/N level [$F(3,15)=5.26$, $p=0.011$], and a nonsignificant interaction between noise type and S/N [$F(3,15)=2.59$, $p=0.091$]. Posthoc comparisons indicated a significantly ($p=0.016$) larger deviation of the burst frequency for multi-talker babble at 5 dB S/N. No significant differences were found at the other S/N levels between the deviations of the burst frequencies for the two types of noise.

b. Spectral slope measurements. Figure 7 shows the mean spectral slopes of the labial and alveolar consonant bursts at various S/N levels for speech-shaped noise (top panel) and multi-talker babble (bottom panel). The slopes were given in terms of dB differences of the burst spectra sampled at 5000 and 1000 Hz. The dB difference values can be easily converted into slopes (in dB/Hz) by dividing the difference values by 4000 (=5000−1000) Hz. A rising spectrum is indicated by a positive difference (positive slope), a falling spectrum is indicated by a negative difference (negative slope), and a diffuse spectrum is indicated by difference values close to zero. Repeated measures ANOVA of the burst spectral slope of the stop consonants /b d p t/, using noise type (multi-talker babble and speech-shaped noise) and S/N level as factors, indicated a nonsignificant effect of noise type [$F(1,3)=0.0001$, $p=0.99$], a significant effect of S/N level [$F(3,9)=50.1$, $p<0.0005$], and a nonsignificant interaction between noise type and S/N [$F(3,9)=0.087$, $p=0.96$]. The effect of noise type was nonsignificant, suggesting that both types of noise affected the slope of the burst spectra the same way. This can be partly explained by the fact that both types of noise—babble and continuous speech-shaped noise—had low-frequency dominance (Fig. 1) and consequently affected the slope of the burst spectra the same way.

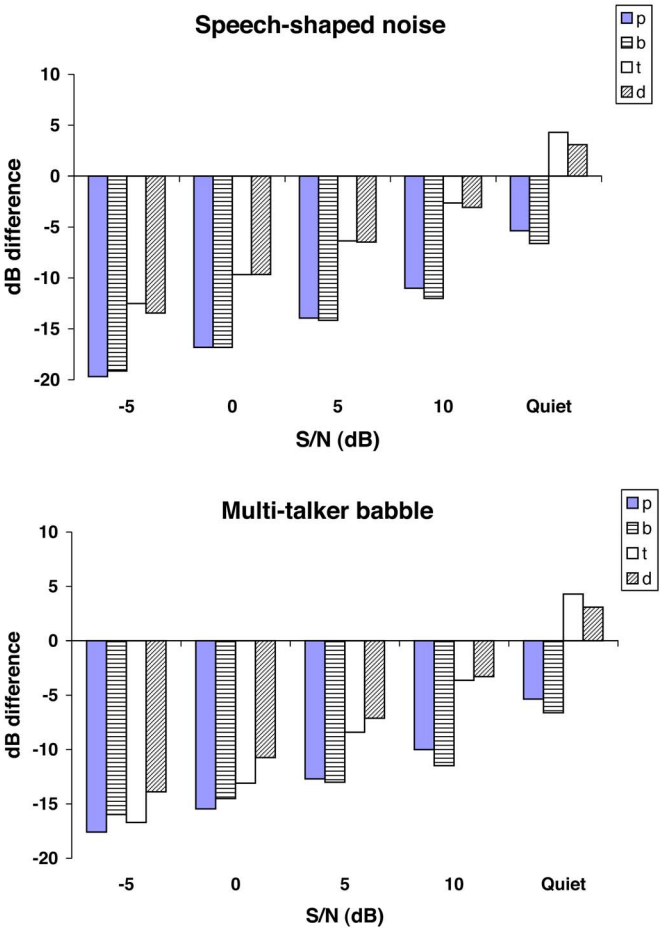

FIG. 7. (Color online) Spectral slope measurements of the burst spectra in terms of differences between the spectral magnitudes (in dB) at 1000 and 5000 Hz. A positive dB difference indicates a rising spectrum and a negative dB difference indicates a falling spectrum.

C. Discussion

Acoustic analysis indicated that the two types of noise (multi-talker babble and speech-shaped noise) examined in this study affected the vowel and stop-consonant spectra in a similar way. The differences between babble and speech-shaped noise were only prominent in extremely low S/N (−5 dB) conditions. This was found to be true for nearly all the acoustic parameters examined.

The vowel spectral difference measurements indicated a nonuniform effect of noise in the various frequency bands, as expected. The F2 region (1–2 kHz) was affected the most (at least in −5 dB S/N), suggesting that the second formant was heavily masked by the noise. This conclusion is also supported by the formant frequency data (Fig. 5) which indicated that F2 was not detected as reliably as F1. In contrast, F1 was detected more reliably and a smaller spectral difference between noisy and clean vowels was obtained for the F1 region. This outcome is consistent with the findings of the study by Diehl *et al.* (2003), i.e., the F1 peak is more resistant to noise than the F2 peak. These findings suggest that in noise listeners must be identifying vowels with a good F1 representation but a poor F2 representation. The question of whether this will impair vowel recognition will be investigated in experiment 1.

The data from the spectral difference measurements are not only important for understanding vowel perception in noise, but are also important for the development of noise-reduction algorithms. These findings point to a multi-band approach for noise reduction in which individual frequency

bands are treated differently by taking into account the non-uniform effect of noise. In spectral-subtractive-type algorithms (e.g., Boll, 1979), for instance, different rules could be applied to the low-, middle-, or high-frequency regions of the spectrum. Such an approach was proposed in Kamath and Loizou (2002) (see also Kamath, 2001) and could easily be extended to multi-channel hearing aids and multi-channel cochlear implants.

The formant frequency measurements indicated that F1 was identified reliably more often than F2. In multi-talker babble at −5 dB S/N, F1 was identified 60% of the time while F2 was identified only 30% of the time (these values were obtained by summing the percentages of "F1 only" and "F1&F2" in Fig. 5). In speech-shaped noise at −5 dB S/N, F1 was detected 64% of time, while F2 was detected 48% of the time. There were substantial differences in reliable detection of F1 and F2 across vowels. In multi-talker babble (−5 dB S/N), for instance, the F1 of the vowel /ɝ/ was identified most reliably (89%), while the F1 of the vowel /ɑ/ was identified least reliably (34%). F1 was generally identified more reliably in vowels with low F1 values (e.g., /i/, /e/). No clear pattern emerged for F2 identification. The F2 of the vowel /ɑ/ was identified most reliably (47%), while the F2 of the vowel /u/ was identified least reliably (11%). Significant differences between the two types of noise in percentage of formants identified were noted only for the extremely low S/N level, −5 dB. These findings are also supported by the critical-band spectral difference measurements—noise affected the F2 region more than the F1 region. Since the first two formants are known to be the primary cues to vowel identification, one would expect to find a strong correlation between presence of reliable F1 and F2 information and vowel identification, and this is investigated in experiment 1.

As shown in Fig. 7, the spectral tilt was severely affected. The spectral tilt of the alveolar stops (/t/, /d/), which is typically positive (see Fig. 3), became negative for S/N levels lower than 10 dB. Because of the low-pass nature of the noise (Fig. 1), the alveolar stops had now a falling spectrum. The spectral tilt of the labial stops (/b/, /p/) was not affected; the labial spectra remained falling, but had a more negative slope. It is questionable whether the change in spectral tilt alone will affect stop-consonant identification in noise, and this is investigated in experiment 1.

Consistent with the large changes in spectral tilt, the burst frequencies were also greatly affected. The average shift in burst frequency was 2500 Hz for S/N=−5, 0, and 5 dB, and 1500 Hz for S/N=10 dB. Particularly large shifts of about 5000 Hz were observed for the alveolar stops, consistent again with the reversal of the direction (sign) of the spectral slope. Even a small amount of noise (S/N=10 dB) produced a large shift in burst frequency, suggesting that the burst frequency might not be a robust cue to place of articulation, at least in noisy conditions.

III. EXPERIMENT 1: VOWEL AND STOP-CONSONANT IDENTIFICATION IN NOISE

The acoustic analysis quantified the effect of noise on the vowel and stop-consonant spectra. Several acoustic parameters such as the Euclidean distance metric between the noisy and clean critical-band spectra, the number of formants reliably detected, the spectral tilt, and so on, were extracted and analyzed. But, to what degree do these parameters correlate with perceptual data? This question is addressed in the present experiment.

A. Subjects

Nine normal-hearing listeners (20 to 30 years of age) participated in this experiment. All subjects were native speakers of American English. The subjects were paid for their participation. The subjects were undergraduate students (not trained in phonetics) from the University of Texas at Dallas.

B. Speech material

The same speech materials from acoustic analysis were used.

C. Procedure

The experiments were performed on a PC equipped with a Creative Labs SoundBlaster 16 soundcard. Stimuli were played to the listeners at a comfortable level through Sennheiser's HD 250 Linear II circumaural headphones. A graphical user interface was used that enabled the subjects to indicate their response by clicking a button corresponding to the word played.

The tests were conducted in two separate sessions, one for the vowels and one for the consonants. Prior to each test the subjects were presented with a practice session in which the identity of the test syllables (vowels or consonants) was displayed on the screen. In the practice session, the vowels and consonants were presented in quiet. In the test session, the vowels and consonants were completely randomized and presented in noise (−5, 0, 5, 10 dB S/N) and in quiet with no feedback. The order of the various S/N conditions was counterbalanced among subjects. Six repetitions per speaker group (female and male) were used for the vowel test, for a total of 12 repetitions per vowel. Three repetitions per vowel context and per speaker group were used for the consonant test, for a total of 18 repetitions (=3×2 speaker groups×3 vowel contexts) per consonant.

D. Results

The mean percent scores on vowel and stop-consonant identification are shown in Fig. 8 for different S/N levels and in quiet. Repeated measures ANOVA of the vowel scores, using noise type (multi-talker babble and speech-shaped noise) and S/N level as factors, indicated a significant effect of noise type [$F(1,8)=17.51$, $p=0.003$], a significant effect of S/N level [$F(2,16)=62.2$, $p<0.0005$], and a significant interaction between noise type and S/N level [$F(2,16)=11.04$, $p=0.001$]. Identification scores of vowels corrupted by multi-talker babble at −5 dB S/N were found to be significantly ($p=0.003$) lower than the scores of the vowels corrupted by speech-shaped noise. There was no statistically significant difference in vowel identification scores for the 0

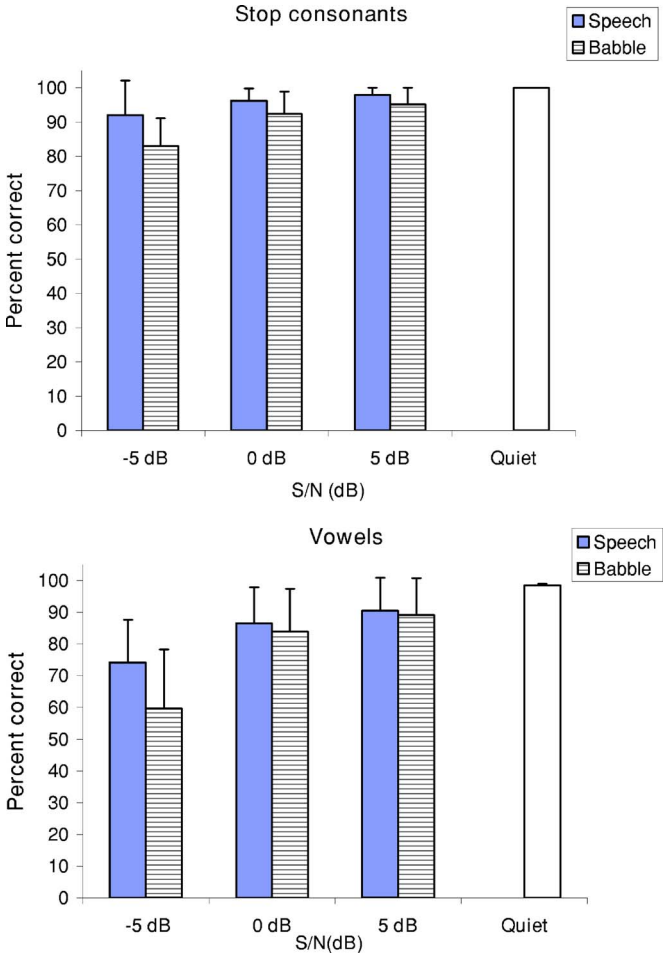

FIG. 8. (Color online) Mean stop-consonant and vowel recognition in noise and in quiet. Error bars indicate standard deviations.

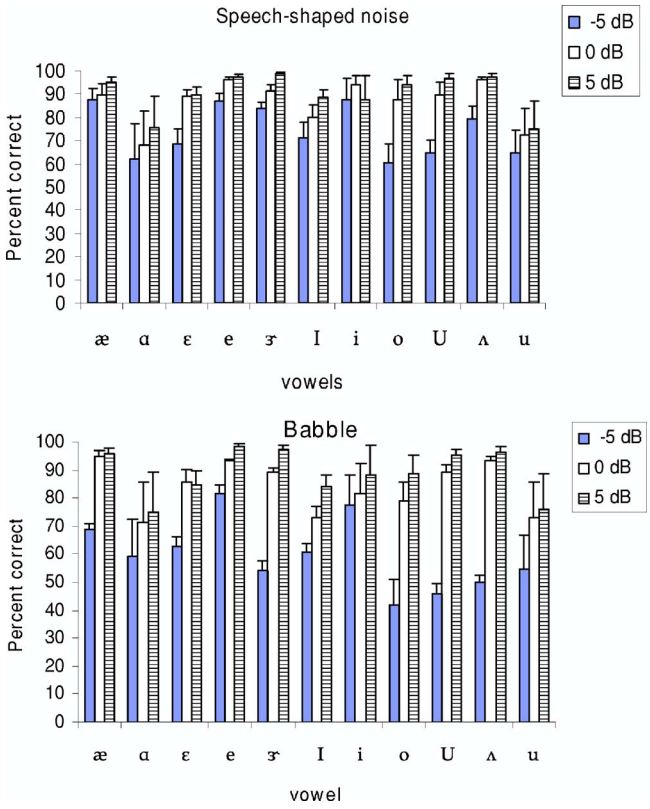

FIG. 9. (Color line) Individual vowel identification in noise. Error bars indicate standard deviations.

and 5 dB conditions between the two types of noise. In quiet, the vowels were identified with 98.5% accuracy,[3] while the stop-consonants were identified perfectly (100% correct) by all listeners.

The individual vowel identification scores are given in Fig. 9. Vowel identification remained high (90% correct) at 0 and 5 dB S/N levels, and dropped to 74% and 60% correct at −5 dB S/N for speech-shaped noise and babble respectively. At −5 dB S/N, the lowest score was obtained for the vowel /o/ and the highest score was obtained for the vowel /i/. The aggregate confusion matrix (compiled across all subjects) for the −5 dB condition is given in Table V. The vowels in the matrices are arranged in order of increasing F1. Adjacent vowels have therefore similar F1. The vowels in Table V are further arranged in four groups, enclosed in rectangles, according to whether they have generally low, medium, high, or very high F1 frequency. Most of the vowel confusions were along the main diagonal. The confusions which fell near the main diagonal and within the individual rectangles (groups) were caused by vowels with similar F1 but different F2. This suggests that listeners were using primarily F1 information to identify vowels, since the F2 region was heavily corrupted, but not necessarily obscured, by the noise (see Fig. 4; more on this in Sec. III E). The most dominant confusions between vowels with similar F1 included the pairs /o/-/ɝ/, /o/-/e/, /ɝ/-/U/, /I/-/U/, and /ɛ/-/ʌ/. Confusions that fell off the main diagonal and outside the rectangles indicated that the first formant was not perceived correctly. These included the confusions between the vowel pairs /ɑ/-/æ/, /U/-/u/, /I/-/ɛ/, /ʌ/-/ɑ/, and /ɛ/-/æ/. Note that the vowels in the pairs /U/-/u/, /I/-/ɛ/, and /ʌ/-/ɑ/ had similar F2.

ANOVA performed on the consonant scores indicated a significant effect of noise type [$F(1,8)=9.36$, $p=0.016$], a significant effect of S/N level [$F(2,16)=7.17$, $p=0.06$], and a significant interaction between noise type and S/N level [$F(2,16)=7.09$, $p=0.006$]. Identification scores of stop-consonants corrupted by multi-talker babble at −5 dB S/N were found to be significantly ($p=0.002$) lower than the scores of consonants corrupted by speech-shaped noise. There was no statistically significant difference in consonant identification between the two types of noise for the 0 or 5 dB conditions.

The individual stop-consonant identification scores are given in Fig. 10. Stop-consonant identification was impaired only at −5 dB S/N. At −5 dB, the lowest scores were obtained for the labial consonants /b/ and /p/. We suspect that this is because the babble noise (and speech-shaped noise) masks the low frequencies more than the high frequencies. The alveolar consonants have a spectral prominence in the mid to high frequencies and are therefore less susceptible to masking by the type of noise used in this study (Fig. 1). The aggregate confusion matrix (compiled across all subjects) for the −5 dB condition is given in Table VI. As can be seen, most of the confusions were place errors, consistent with the findings of Miller and Nicely (1955).

TABLE V. Aggregate confusion matrices obtained in identification of vowels corrupted with noise at −5 dB S/N.

Speech-shaped noise (S/N=-5 dB)

	/u/	/i/	/ɪ/	/ʊ/	/e/	/ɝ/	/o/	/ɛ/	/æ/	/ʌ/	/ɑ/
/u/	65	4	2	22	1	3	2			1	
/i/		88	11					1			
/ɪ/	2		88	2				8			
/ʊ/	2		6	65		7	5	4	2	8	1
/e/	1	1	6	2	87		1	1	1		
/ɝ/	2			11		84	2		1		
/o/	5		1	12	2	15	60	1	1	1	2
/ɛ/			6	2		5		69	10	8	
/æ/				1	1	1		6	87		4
/ʌ/				1		1	1	7	5	79	6
/ɑ/			10		5			2	19	2	62

Babble (S/N=-5 dB)

	/u/	/i/	/ɪ/	/ʊ/	/e/	/ɝ/	/o/	/ɛ/	/æ/	/ʌ/	/ɑ/
/u/	55	5	4	23	4	4	4			1	
/i/	2	77	14		3	1	1	1		1	
/ɪ/		1	60	16		3	1	13	3	2	1
/ʊ/	4		11	46	3	9	2	9	5	7	4
/e/	2	1	5		82	1	3	4	1	1	
/ɝ/	6	1	6	12	5	54	8	1	2	3	2
/o/	5	1	2	8	11	23	42	3		2	3
/ɛ/	1	2	4	1	2	2	1	63	6	17	1
/æ/		2	2	1	2	2	1	5	69	3	13
/ʌ/	1	1	5	4	3	2	2	10	6	50	16
/ɑ/		2	5	2	3	3	1		20	5	59

Correlation analysis (see Table VII) was performed between the vowel identification scores and the corresponding acoustic parameter values. For the critical-band difference metric, separate analysis was performed for the low-frequency (LF) band, the middle-frequency (MF) band, the low- and middle-frequency bands (LF+MF) combined and the whole spectrum (indicated as WF in Table VII). In the whole-spectrum analysis, the normalized Euclidean metric [Eq. (1)] was computed between the clean and noisy vowel spectra taking the whole bandwidth (0–8 kHz) into consideration, i.e., all 21 critical bands were included in the summation in Eq. (1). For the formant-frequency count data, separate correlation analysis was performed between the percentage of F1 identified and vowel identification scores, between the percentage of F2 identified and vowel scores, and between the percentage of both F1 and F2 (F1+F2) identified and vowel scores. Pearson's correlation analysis was used for the critical-band difference metric, and nonparametric Spearman's correlation analysis was used for the formant-frequency count data. Multiple-linear regression analysis was used for the LF+MF and F1+F2 data. The correlation coefficients (r) along with the corresponding p values are tabulated in Table VII for both speech-shaped noise and multi-talker babble at −5 and 0 dB S/N. No correlation was performed for the 5 dB condition because of ceiling effects.

A modestly high correlation (r=0.724) was found between the critical-band difference metric of the low frequency band [LF; Eq. (1a)] and vowel identification in multi-talker babble at −5 dB S/N (see Table VII). The correlation coefficient (r=0.558) for the LF band obtained for vowels in speech-shaped noise was not significant (p=0.07). A significant correlation was also found between the critical-band difference metric of the combined LF+MF bands and vowel

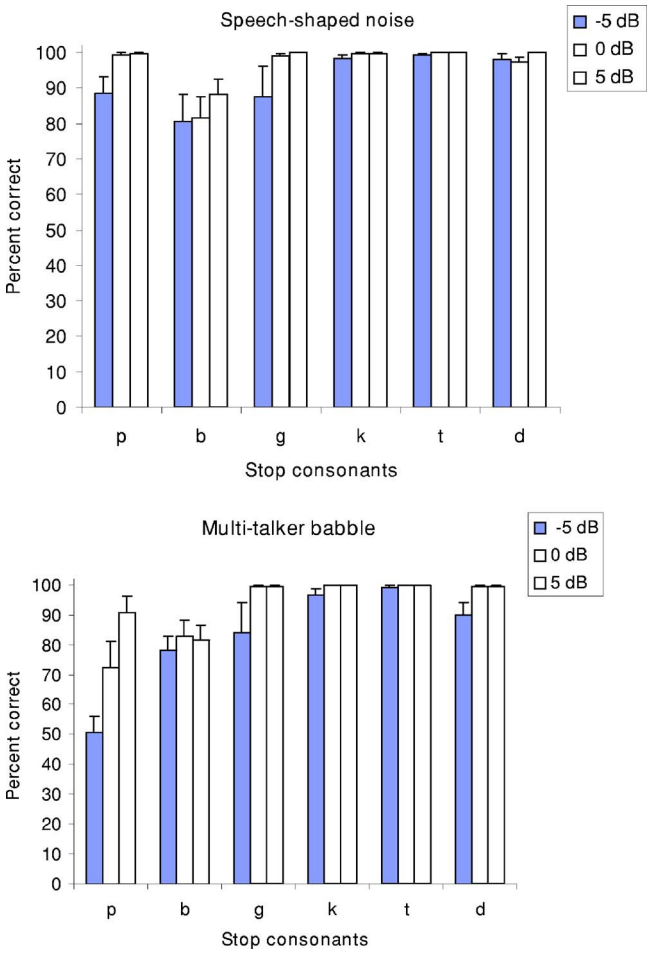

FIG. 10. (Color online) Individual stop-consonant identification in noise. Error bars indicate standard deviations.

TABLE VI. Aggregate confusion matrices obtained in identification of stop-consonants corrupted with noise at −5 dB S/N.

	Speech-shaped noise (S/N=−5 dB)					
	/b/	/d/	/g/	/k/	/p/	/t/
/b/	80	17	1		1	1
/d/	1	98				1
/g/		1	87	10		1
/k/			1	98	1	
/p/				11	88	
/t/						99
	Babble (S/N=−5 dB)					
/b/	78	6	2		2	12
/d/		90	9			
/g/		6	84	8		1
/k/				97	1	1
/p/	1	1	3	33	50	13
/t/		1				99

identification in −5 dB S/N for both multi-talker babble and speech-shaped noise conditions. No other significant correlations were found at −5 and 0 dB S/N in either babble or speech-shaped conditions. No significant correlations were found between the count of formant frequencies (F1, F2, F1+F2) and vowel identification at −5 and 0 dB S/N for either babble or speech-shaped noise conditions.

E. Discussion

One of the main goals of this study was to understand the cues used by listeners for vowel and stop-consonant recognition in noise. The good identification performance in vowel and stop recognition at −5 dB S/N challenged some of the traditional cues (e.g., formant frequencies, release burst, etc.) known to be important for vowel and stop perception, at least in quiet.

Vowel identification scores remained moderately high (75% correct in speech-shaped noise and 60% correct in babble) at −5 dB S/N despite the absence of clear and coherent F1 and F2 information. We exclude the possibility that listeners utilized exclusively formant frequency cues (F1 and F2 frequencies) for the main reason that the F2 region was heavily masked by the noise and F2 was not reliably identified (see Fig. 5). Only access to F1 information was reliable as evidenced by the formant frequency count data (Fig. 5). We also rule out the possibility that listeners utilized exclusively whole-spectrum shape cues to identify vowels because vowels with dissimilar spectral shapes were not identified correctly (Table V). This is illustrated in the example shown in Fig. 11 which compares the excitation patterns of the vowels /ɛ/ and /ʌ/ embedded in −5 dB babble. The excitation pattern of the vowel /ɛ/ is distinctly different from that of the vowel /ʌ/ as it is characterized by two peaks in the F2 region. In contrast, the excitation pattern of the vowel /ʌ/ has no peak in the F2 region, as it has a low F2 frequency. Yet, the vowel /ɛ/ was confused with the vowel /ʌ/ 17% of the time in babble noise (S/N=−5 dB). Similarly, the confusion of /o/ with /e/ cannot be explained by a pattern matching mechanism which relies on spectral shape information, since the excitation patterns of these vowels differ greatly in the F2 region (the difference between the F2 frequencies of these two vowels is larger than 1000 Hz). Further evidence is provided by the absence of correlation between the whole-spectrum difference metric (WF) and vowel identification scores (see Table VII).

TABLE VII. Correlation analysis between critical-band spectral differences of noisy and clean vowels for four different frequency regions (LF =0−1 kHz, MF=1−2.7 kHz, LF+MF=0−2.7 kHz, and WF=0−8 kHz) and vowel identification scores (top). Correlation analysis between presence of F1/F2 frequency information in noisy vowels and vowel identification scores (bottom). Correlation coefficients (r) with the corresponding p values are given in the two rightmost columns. Sample size for the correlation analysis was $n=11$.

Noise type	S/N (dB)	Independent variable	r	p
Speech shaped	−5 dB	LF	0.558	0.075
		MF	−0.491	0.125
		LF+MF	**0.733**	0.046
		WF	0.358	0.280
	0 dB	LF	0.183	0.589
		MF	−0.169	0.620
		LF+MF	0.251	0.770
		WF	0.135	0.692
Multi-talker babble	−5 dB	LF	**0.724**	0.012
		MF	−0.468	0.146
		LF+MF	**0.850**	0.006
		WF	0.474	0.141
	0 dB	LF	0.006	0.985
		MF	−0.355	0.285
		LF+MF	0.355	0.584
		WF	−0.090	0.791
Speech shaped	−5 dB	F1	−0.351	0.290
		F2	0.486	0.129
		F1+F2	0.369	0.264
	0 dB	F1	0.064	0.854
		F2	0.073	0.830
		F1+f2	0.021	0.950
Multi-talker babble	−5 dB	F1	−0.282	0.401
		F2	0.032	0.926
		F1+F2	0.100	0.770
	0 dB	F1	0.027	0.936
		F2	0.016	0.962
		F1+F2	0.279	0.406

The data from Figs. 4 and 5 taken together suggest that noise (babble and speech-shaped) produced vowels that have a poor (but not necessarily obscure) F2 representation, but a reasonably good F1 representation. Listeners must therefore be relying primarily on F1 frequency information to identify vowels in noise. Evidence of this is provided by the pattern of the vowel confusion errors (Table V). The most dominant confusions occurred along the main diagonal, i.e., between vowels that had similar F1 but different F2 (recall that the vowels in Table V are arranged in increasing F1, hence adjacent vowels have similar F1). Among the most dominant

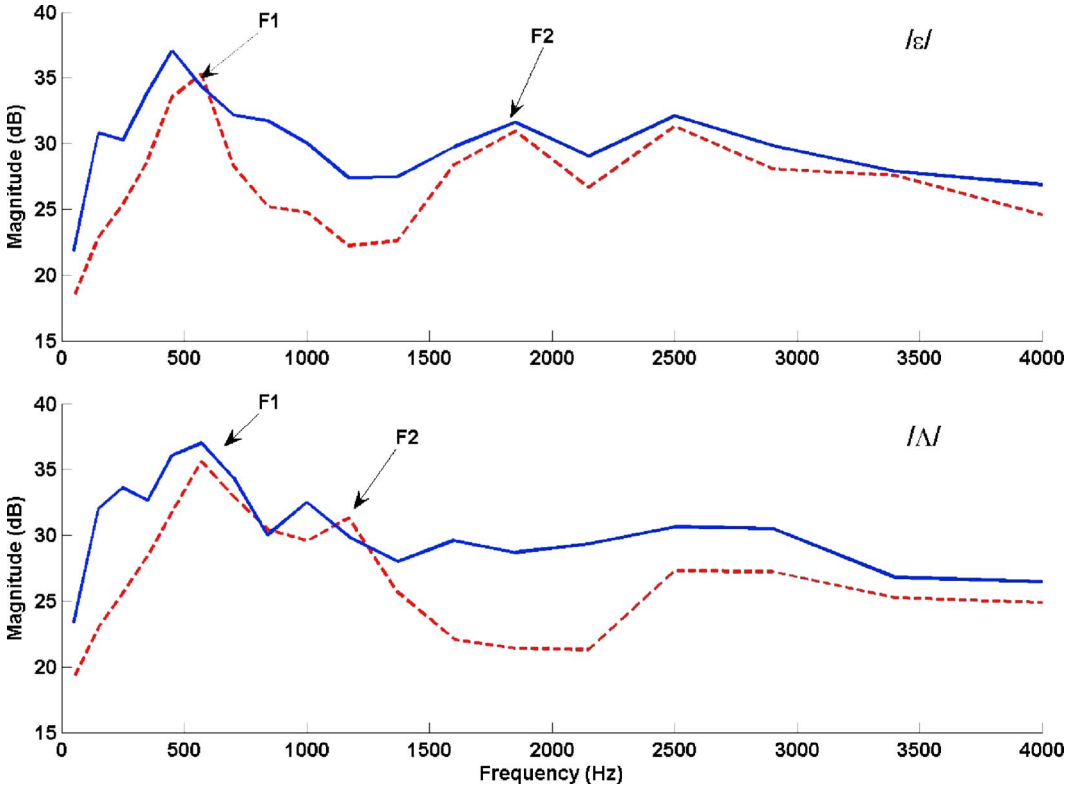

FIG. 11. (Color online) Excitation patterns of the vowel /ɛ/ (top panel) and vowel /ʌ/ (bottom panel) estimated in quiet (dashed lines) and in −5 dB S/N babble noise (solid lines). These patterns were computed based on a 20-ms segment of the vowels extracted from the steady-state portion of the words "head" and "hud" produced by a male speaker. Arrows show the locations of the F1 and F2 formants in quiet.

confusions included the pairs /o/-/ɜ˞/,/o/-/e/,/ɜ˞/-/U/,/I/-/U/, /ɛ/-/ʌ/. Hence, although listeners might not have a coherent idea on the location of *both* F1 and F2 frequencies, they had a good indication about the location of F1 and only a vague idea about the location of F2. Previous studies (e.g., Dubno and Dorman, 1987) have shown that that alone is sufficient for vowel identification. In the study by Dubno and Dorman (1987), for instance, listeners identified with greater than 95% accuracy six (synthetic) front vowels which had a normal F1 but higher frequency formants represented by a broad spectral plateau ranging from 1600 to 3500 Hz (i.e., F2 and F3 were flattened). We find it unlikely that a spectral-shape pattern matching mechanism based on the F1-region alone is responsible for the confusion patterns shown in Table V. We base this assertion on prior evidence from the study by Beddor and Hawkins (1990) where they showed that the perceived quality of vowels with prominent F1 peak is dominated primarily by the frequency of F1 rather than the spectral envelope. Our data from the critical-band difference metric (Fig. 4) suggest that the F1 peak remained prominent in noise.

The critical-band difference metric and the counts of F2 detection suggest a poor F2 representation due to the relatively heavy masking of the F2 region by noise. Despite that, the F2 region seems to contain some useful information. Evidence of this is given by the lack of confusion errors between the vowels /i/ and /u/. These vowels have nearly identical F1 but markedly different F2 frequencies (as much as 1300 Hz). We would therefore expect a large number of confusions between these two vowels if noise had completely obscured all information in the F2 region. But, the vowels /i/ and /u/ were rarely confused with each other by the listeners (Table V). Hence, listeners must be utilizing, in addition to F1 frequency information, some other form of information about F2. One possibility is that listeners are making use of partial spectral shape information contained in the F1-F2 region. This observation is collaborated with the data from the correlation analysis of the critical-band difference metric and the identification scores. A significant correlation was found between spectral envelope differences of noisy and clean vowels in the low-to-mid frequencies (based on the composite LF+MF difference metric) and vowel identification at −5 dB S/N. In the absence of enough formant frequency information listeners must be relying on other cues to identify vowels in extremely low S/N conditions. Other cues probably used by listeners (but not examined in this study) include vowel duration, spectral change, and formant contours. The salience of spectral change and formant contour cues in extremely low S/N conditions, however, is questionable and needs further investigation.

Stop-consonant identification remained high (80%–90% correct) even at −5 dB S/N. This was achieved despite the fact that both spectral tilt and burst frequency were significantly altered by the noise. The tilt of the alveolar burst spectra became negative after adding noise. Yet, the alveolar stops were identified perfectly (see Fig. 10) even at −5 dB. Previous studies (e.g., Smits *et al.*, 1996) have shown that the velar bursts are efficient cues to place of articulation, at least in quiet. In our study, the velar burst spectra were severely altered by noise, yet the identification of /k/ remained

at near 100%, and the identification of /g/ was only modestly affected at −5 dB. In summary, changes to the burst spectra did not impair stop-consonant identification. This suggests that in the presence of noise, the burst cues become unreliable and listeners must be relying on other cues, perhaps formant transitions and/or spectral change, to identify stops.

The present study assessed the perceptual and acoustic differences between babble and continuous speech-shaped noise. The data from acoustic analysis indicate no significant differences in the way the two types of noise affected the speech spectra, at least for S/N levels higher than and including 0 dB. Consistent with the data from acoustic analysis, listeners identified vowels and stop-consonants corrupted by babble and speech-shaped noise with the same accuracy at 0, 5, and 10 dB S/N. Identification scores were significantly lower only for multi-talker babble at −5 dB S/N. In brief, the data from this study indicate that the two types of noise examined are perceptually and acoustically equivalent, at least for low to moderate S/N levels (0–10 dB) and for single words presented in isolation.

IV. SUMMARY AND CONCLUSIONS

This study assessed the perceptual and acoustic effects of multi-talker babble and continuous speech-shaped noise on the vowel and stop-consonant spectra. Noise was added to vowel and stop-consonant stimuli at −5 to +10 dB S/N, and the spectra were examined by means of acoustic analysis. Acoustic analysis indicated the following.

(i) At −5 dB S/N, the largest spectral envelope difference between the noisy and clean vowel spectra occurred in the mid-frequency band (1–2.7 kHz) for both types of noise. This suggests that the second formant is heavily masked by noise at very low S/N levels.
(ii) The first formant (F1) was reliably detected in noise more often than F2, suggesting that listeners had access to correct F1 information but vague information about F2.
(iii) There was a large shift (of about 2500 Hz) of the apparent burst frequency of the stop consonants with the addition of noise.
(iv) The spectral slope of the consonant burst spectra was severely affected by noise. The alveolar stops (/d t/) which originally had a positive slope (rising spectrum) had now a negative slope (falling spectrum) for all S/N levels except for +10 dB S/N. This pattern was consistent with both types of noise.

The above acoustic parameters were subjected to correlation analysis with vowel and stop-consonant identification scores collected in experiment 1. The perception study and correlation analysis indicated the following.

(i) Vowel identification scores remained moderately high (75% correct in speech-shaped noise and 60% correct in babble) at −5 dB S/N despite the absence of clear and coherent F1 and F2 information. Based on acoustic analysis data (Figs. 4 and 5), we infer that at low S/N conditions listeners must be relying on relatively accurate F1 frequency information along with partial F2 information to identify vowels in noise.
(ii) Identification scores of vowels and consonants corrupted by multi-talker babble at −5 dB S/N were significantly lower than the corresponding scores obtained in speech-shaped noise. No significant differences were observed between identification scores of vowels (and consonants) corrupted by multi-talker babble and speech-shaped noise at S/N levels higher than −5 dB.
(iii) Stop-consonant identification remained high (80%–90% correct) even at −5 dB S/N, despite the fact that both the spectral tilt and burst frequency were significantly altered by the noise. This suggests that listeners must be relying on other cues, perhaps formant transitions, to identify stops.

ACKNOWLEDGMENTS

This research was supported by Grant No. R01 DC03421 from the National Institute of Deafness and other Communication Disorders, NIH. This project was the basis for the Master's thesis of the first author (G.P.) in the Department of Electrical Engineering at the University of Texas—Dallas. We would like to thank Kalyan Kasturi for all his help with the listening tests. Many thanks to Dr. Alexander Francis and the anonymous reviewers for their comments.

[1]We define F1 proximity as the frequency region that extends from F1 to the mid-point between F1 and F2, i.e., from F1 to F1+(F1+F2)/2. Similarly F2 proximity is defined as the frequency region encompassing F2±(F1+F2)/2.
[2]A similar procedure was used in Lahiri *et al.* (1984) to measure the spectral tilt. In their study, spectral tilt was obtained by drawing a straight line by hand through the F2 and F4 peaks in the LPC spectrum.
[3]The normal-hearing listeners in the Hillenbrand *et al.* (1995) study identified a large set of vowels with 95.4% accuracy (our study included a subset of those vowels). In their study, however, listeners were also presented with vowels produced by children and the test vowel set included the vowel /ɔ/, which was excluded from the present study. The vowel /ɔ/ was excluded because many speakers of American English do not maintain the /ɑ/-/ɔ/ distinction.

Ainsworth, W. A. (**1972**). "Duration as a cue in the recognition of synthetic vowels," J. Acoust. Soc. Am. **51**, 648–651.
Beddor, P., and Hawkins, S. (**1990**). "The influence of spectral prominence on perceived vowel quality," J. Acoust. Soc. Am. **87**, 2684–2704.
Bladon, R. (**1982**). "Arguments against formants in the auditory representation of speech," in *The Representation of Speech in the Peripheral Auditory System*, edited by R. Carlson and B. Grandstrom (Elsevier Biomedical, Amsterdam), pp. 95–102.
Bladon, R., and Lindbhlom, B. (**1981**). "Modeling the judgment of vowel quality differences," J. Acoust. Soc. Am. **69**, 1414–1422.
Blumstein, S., and Stevens, K. (**1980**). "Perceptual invariance and onset spectra for stop consonants in different vowel environments," J. Acoust. Soc. Am. **67**, 648–662.
Blumstein, S., Issacs, E., and Mertus, J. (**1982**). "The role of gross spectral shape as a perceptual cue to place of articulation in initial stop consonants," J. Acoust. Soc. Am. **72**, 43–50.
Boll, S. (**1979**). "Suppression of acoustic noise in speech using spectral subtraction," IEEE Trans. Acoust., Speech, Signal Process. **ASSP-27**, 113–120.
Chistovich, L., and Lublinskaja, V. (**1979**). "The center of gravity effect in vowel spectra and critical distance between the formants," Hear. Res. **1**, 185–195.
Cooper, F., Delattre, P., Liberman, A., Borst, J., and Gerstman, L. (**1952**).

"Some experiments on perception of synthetic speech sounds," J. Acoust. Soc. Am. **24**, 597–606.
Delattre, P., Liberman, A., and Cooper, F. (**1955**). "Acoustic loci and transitional cues for consonants," J. Acoust. Soc. Am. **27**, 769–774.
Diehl, R., Lindblom, B., and Creeger, C. (**2003**). "Increasing realism of auditory representations yields further insights into vowel phonetics," *Proc. 5th Intl Congress Phonetic Sciences*.
Dorman, M., and Loizou, P. (**1996**). "Relative spectral change and formant transitions as cues to labial and alveolar place of articulation," J. Acoust. Soc. Am. **100**, 3825–3830.
Dorman, M., Studdert-Kennedy, M., and Ralphael, L. (**1977**). "Stop consonant recognition: Release bursts and formant transitions as functionally equivalent context-dependent cues," Percept. Psychophys. **22**, 109–122.
Dubno, J., and Dorman, M. (**1987**). "Effects of spectral flattening on vowel identification," J. Acoust. Soc. Am. **82**, 1503–1511.
Flanagan, J. (**1955**). "A difference limens for vowel formant frequency," J. Acoust. Soc. Am. **27**, 288–291.
Hawks, J. (**1994**). "Difference limens for formant patterns of vowel sounds," J. Acoust. Soc. Am. **95**, 1074–1084.
Hillenbrand, J., and Gayvert, R. (**1993**). "Identification of steady-state vowels synthesized from the Peterson and Barney measurements," J. Acoust. Soc. Am. **94**, 668–674.
Hillenbrand, J., and Neary, T. (**1999**). "Identification of resynthesized /hVd/ utterances: Effects of formant contour," J. Acoust. Soc. Am. **105**, 3509–3523.
Hillenbrand, J., Getty, L., Clark, M., and Wheeler, K. (**1995**). "Acoustic characteristics of American English vowels," J. Acoust. Soc. Am. **97**, 3099–3111.
Ito, M., Tsuchida, J., and Yano, M. (**2001**). "On the effectiveness of whole spectral shape for vowel perception," J. Acoust. Soc. Am. **110**, 1141–1149.
Kamath, S. (**2001**). "A multi-band spectral subtraction method for speech enhancement," Masters thesis, Dept. of Electrical Engineering, University of Texas—Dallas.
Kamath, S., and Loizou, P. (**2002**). "A multi-band spectral subtraction method for enhancing speech corrupted by colored noise," *Proc. ICASSP*, Orlando, FL.
Kent, R., and Read, C. (**1992**). *The Acoustic Analysis of Speech* (Singular, San Diego, CA), Chap. 6.
Kewley-Port, D. (**1983**). "Time varying features as correlates of place of articulation in stop consonants," J. Acoust. Soc. Am. **73**, 322–335.
Klatt, D. (**1982**). "Prediction of perceived phonetic distance from critical band spectra: A first step," *IEEE ICASSP*, pp. 1278–1281.
Krishnan, A. (**1999**). "Human frequency-following responses to two-tone approximations of steady-state vowels," Audiol. Neuro-Otol. **4**, 95–103.
Krishnan, A. (**2002**). "Human frequency-following responses: representation of steady-state synthetic vowels," Hear. Res. **166**, 192–201.
Lahiri, A., Gerwirth, L., and Blumstein, S. (**1984**). "A reconsideration of acoustic invariance for place of articulation in diffuse stop consonants. Evidence from a cross-language study," J. Acoust. Soc. Am. **76**, 391–404.
Leek, M., Dorman, M., and Summerfield, Q. (**1987**). "Minimum spectral contrast for vowel identification by normal-hearing and hearing-impaired listeners," J. Acoust. Soc. Am. **81**, 148–154.
Lehiste, I., and Meltzer, D. (**1973**). "Vowel and speaker identification in natural and synthetic speech," Lang Speech **16**, 356–364.
Liberman, A., Delattre, P., and Cooper, F. (**1952**). "The role of selected stimulus variables in the perception of unvoiced stop consonants," Am. J. Psychol. **65**, 497–516.
Liu, C., and Kewley-Port, D. (**2001**). "Vowel formant discrimination for high-fidelity speech," J. Acoust. Soc. Am. **116**, 1224–1233.
Loizou, P., and Poroy, O. (**2001**). "Minimum spectral contrast needed for vowel identification by normal hearing and cochlear implant listeners," J. Acoust. Soc. Am. **110**, 1619–1627.
Miller, G. A., and Nicely, P. E. (**1955**). "An analysis of perceptual confusions among some English consonants," J. Acoust. Soc. Am. **27**, 338–352.
Molis, M. (**2005**). "Evaluating models of vowel perception," J. Acoust. Soc. Am. **118**, 1062–1071.
Nebalek, A. (**1988**). "Identification of vowels in quiet, noise and reverberation: Relationships with age and hearing loss," J. Acoust. Soc. Am. **84**, 476–484.
Nebalek, A., and Dagenais, P. (**1986**). "Vowel errors in noise and in reverberation by hearing-impaired listeners," J. Acoust. Soc. Am. **80**, 741–748.
Peterson, G., and Barney, H. (**1952**). "Control methods used in a study of the vowels," J. Acoust. Soc. Am. **24**, 175–184.
Pickett, J. (**1957**). "Perception of vowels heard in noises of various spectra," J. Acoust. Soc. Am. **29**, 613–620.
Plomp, R. (**1970**). "Timbre as a multidimensional attribute of complex tones," in *Frequency Analysis and Periodicity Detection in Hearing*, edited by R. Plomp and G. Smoorenbburg (Sijthoff, Leiden), pp. 397–414.
Remez, R., Rubin, P., Pisoni, D., and Carrell, T. (**1981**). "Speech perception without traditional speech cues," Science **212**, 947–950.
Shannon, R., Jensvold, A., Padilla, M., Robert, M., and Wang, X. (**1999**). "Consonant recording for speech testing," J. Acoust. Soc. Am. **106**, L71–L74.
Smits, R., Bosch, L., and Collier, R. (**1996**). "Evaluation of various sets of acoustic cues for the perception of prevocalic stop consonants: I. Perception experiment," J. Acoust. Soc. Am. **100**, 3852–3864.
Stevens, K., and Blumstein, S. (**1978**). "Invariant cues for the place of articulation in stop consonants," J. Acoust. Soc. Am. **64**, 1358–1368.
Strange, W. (**1989**). "Evolving theories of vowel perception," J. Acoust. Soc. Am. **85**, 2081–2081.
Strange, W. (**1999**). "Perception of vowels: Dynamic constancy," in *The Acoustics of Speech Communication*, edited by J. Pickett, (Allyn and Bacon, Needham Heights) 153–166.
Strange, W., Jenkins, J. J., and Johnson, T. L. (**1983**). "Dynamic specification of coarticulated vowels," J. Acoust. Soc. Am. **74**, 695–705.
Syrdal, A., and Gopal, H. (**1986**). "A perceptual model of vowel recognition based on the auditory representation of American English vowels," J. Acoust. Soc. Am. **79**, 1086–1100.
Walley, A., and Carrell, T. (**1983**). "Onset spectra and formant transitions in the adult's and children's perception of place of articulation in stop consonants," J. Acoust. Soc. Am. **73**, 1011–1022.
Wang, M., and Bilger, R. (**1973**). "Consonant confusions in noise: A study of perceptual features," J. Acoust. Soc. Am. **54**, 1248–1266.
Young, E., and Sachs, M. (**1979**). "Representation of steady-state vowels in the temporal aspects of the discharge patterns of populations of auditory nerve fibers," J. Acoust. Soc. Am. **66**, 1381–1403.
Zahorian, S. A., and Jagharghi, A. J. (**1993**). "Spectral-shape features versus formants as acoustic correlates for vowels," J. Acoust. Soc. Am. **94**, 1966–1982.
Zwicker, E., and Fastl, H. (**1990**). *Psychoacoustics, Facts and Models*, (Springer Verlag, Berlin).

Interference from audio distracters during speechreading

Douglas S. Brungart[a] and Brian D. Simpson
Air Force Research Laboratory, WPAFB, Ohio 45433

(Received 13 August 2004; revised 27 September 2005; accepted 28 September 2005)

Although many audio-visual speech experiments have focused on situations where the presence of an incongruent visual speech signal influences the perceived utterance heard by an observer, there are also documented examples of a related effect in which the presence of an incongruent audio speech signal influences the perceived utterance seen by an observer. This study examined the effects that different distracting audio signals had on performance in a color and number keyword speechreading task. When the distracting sound was noise, time-reversed speech, or continuous speech, it had no effect on speechreading. However, when the distracting audio signal consisted of speech that started at the same time as the visual stimulus, speechreading performance was substantially degraded. This degradation did not depend on the semantic similarity between the target and masker speech, but it was substantially reduced when the onset of the audio speech was shifted relative to that of the visual stimulus. Overall, these results suggest that visual speech perception is impaired by the presence of a simultaneous mismatched audio speech signal, but that other types of audio distracters have little effect on speechreading performance.
[DOI: 10.1121/1.2126932]

PACS number(s): 43.71.Ma, 43.66.Mk [KWG] Pages: 3889–3902

I. INTRODUCTION

Although speech is often considered to be an auditory stimulus, there are many situations where visual cues have a strong influence on the perception of spoken utterances. The contributions that visual cues make to speech perception are most noticeable in environments where the audio portion of the speech is degraded by noise, room reverberation, or hearing impairment. In these adverse listening situations, the visual cues provided by the movements of the talker's face can improve speech intelligibility by as much as a 12-dB increase in the signal-to-noise ratio (SNR) of the audible speech signal (Sumby and Pollack, 1954; Grant and Walden, 1996; Summerfield, 1992). Visual cues can also improve intelligibility in quiet listening situations when the utterances are difficult to understand because they are spoken in a foreign language or by a talker with a heavy accent (Reisberg, 1978). And, in extreme cases where the audio signal is completely absent or the listener is profoundly deaf, speechreading cues alone can be used to extract a substantial amount of information from visual-only speech stimuli (Summerfield, 1987).

While it is clear that visual speech cues influence speech perception when the audio signal is degraded, it is also true that normal-hearing listeners in quiet environments can usually achieve 100% intelligibility with audio-only speech stimuli. This makes it tempting to assume that visual speech cues provide purely redundant phonetic information that is used only when the audio signal is somehow corrupted. However, experiments conducted with *mismatched* audio-visual (AV) speech stimuli have shown that vision can influence speech perception even when the audio portion of the stimulus is perfectly intelligible. The most compelling example of AV speech integration in a quiet listening environment is the "McGurk" effect, in which observers who are exposed to a visual representation of one word and an auditory representation of another word often report that they "hear" a third word that was not actually present in the stimulus (McGurk and McDonald, 1976). For example, listeners who see a talker saying "aga" and listen to a talker saying "aba" consistently report that they hear the talker saying "ada." This is an extremely robust effect which has been shown to occur in different languages (Fuster-Duran, 1996), in infants (Burnham and Dodd, 1996), and even in cases where there is an obvious mismatch between the gender of the visible face and the gender of the audible voice (Green, 1996) or between the spatial location of the visible face and the audible voice (Jones and Munhall, 1997).

The robustness of the McGurk effect across a wide range of laboratory conditions suggests that a similar kind of AV fusion may occur in real-word face-to-face conversations. The specific details of this fusion process are not yet clear, but there are indications in the literature that this fusion is, in part at least, a preattentive process that cannot be voluntarily controlled by the observer. Strong evidence for the involuntary nature of AV speech integration is provided by a series of experiments by Massaro (1987, 1998) in which subjects were presented with McGurk-like AV speech signals and instructed to pay attention only to the audio portions, both the audio and visual portions, or only to the visual portions of the stimuli. The results showed that listeners performed similarly in the "attend to the audio" and "attend to both audio and visual" conditions of the experiments, suggesting that the discrepant visual portion of a McGurk stimulus actually changes what the listener "hears" the talker say and that the listener cannot voluntarily ignore the visual cues and attend only to the auditory portion of the stimulus.[1]

[a]Electronic mail: douglas.brungart@wpafb.af.mil

In the third condition of the Massaro experiments, in which the subjects were instructed to attend only to the visual portions of the stimuli, the audio portion of the stimulus had less effect than it did in the "attend to both audio and visual" condition but still had a strong influence on the speechreading responses of the subjects. For example, in the 1998 experiment, Massaro instructed his subjects to focus on the visual portion of a spoken /ba/ or /da/ syllable and determine whether the visible face produced a /b/ or /d/, and he found that performance dropped from roughly 95% correct identifications of the visible syllable to roughly 70% correct responses when a mismatched audio signal was added to a visual-only speech stimulus. This indicates the existence of a cross-modal interference effect (Dekle *et al.*, 1992) in which an observer's ability to accurately speechread utterances spoken by a visible talker is impaired by the presence of an incongruent auditory stimulus.

Although Massaro's experiments were not directly focused on the cross-modal interference that an incongruent audio signal can cause during speechreading, at least two other experiments have been conducted for the express purpose of quantifying the magnitude of this effect. The first was an experiment by Easton and Basala (1982) in which subjects were asked to speechread visual speech stimuli that were either presented without sound or dubbed with a different audible monosyllable word than the one spoken by the visible talker (Easton and Basala, 1982). As in the Massaro experiment, the subjects were instructed to ignore the audio signal and focus on identifying the word spoken by the visible talker. The results showed that speechreading performance was substantially worse in the mismatched audio condition than in the no-sound condition, both in an open response word identification task (5% versus 19% correct responses) and in a multiple choice word identification task (42% versus 90% correct responses).

The interfering effect that incongruent audio speech has on visual speech perception was revisited in a 1992 experiment by Dekle *et al.* (1992), who observed that the stimuli used by Easton and Basala's 1982 experiment may have systematically overestimated the effect of the cross-modal interference effect by dubbing audio words onto the visual stimuli that were optically identical to the words spoken by the visible talker. For example, one of the mismatched AV stimuli in the Easton and Basala experiment combined the visible word "word" with the audible word "whirl." Because these two words have the same vowels and beginning and ending consonants with the same places of articulation, it is unlikely that they can be distinguished from one another visually (Summerfield, 1987). Thus, it is not surprising that a subject presented with the visual stimulus "word" and the visually identical audio stimulus "whirl" would respond with the word "whirl" both in a word identification test and in a multiple choice test containing both alternatives.

In order to address this potential confound, Dekle and her colleagues conducted an experiment with word pairs that were specifically chosen to have discrepant optically and acoustically signaled place-of-articulation information in an attempt to maximize the effect of visual information on the perception of the heard words. The subjects in this experiment were again instructed to ignore the audio signal and identify the word spoken by the visual talker from a three-item list containing the visual word, the audio word, and the expected McGurk fusion of the two. The result was a much smaller decrease in speechreading performance in the misdubbed condition relative to the no-audio condition (55% versus 69% correct identifications) than the one reported in the earlier experiment by Easton and Basala.

Although the Dekle *et al.* experiment found a smaller effect than the Easton and Basala experiment, both reported the same general result as the experiment by Massaro: namely, that it was significantly more difficult to speechread visual speech signals that were dubbed with mismatched audio speech signals than it was to speechread visual speech signals that were presented without an auditory stimulus. This begs the question of whether the presence of *any* arbitrary audio stimulus might also interfere with speechreading ability. Thus far, the results of studies examining this question have been inconclusive. Markides (1989) examined speechreading ability in three audio conditions (quiet, speech-shaped Gaussian noise, and classroom noise) and found that the addition of classroom noise resulted in a significant decrease in speechreading performance relative to the quiet condition, but that the addition of speech-shaped Gaussian noise did not. Lyxell and Ronnberg (1993) also examined speechreading performance in three audio conditions (quiet, continuous white noise, and continuous speech read from a newspaper) and found that neither of the two audio distracters produced any significant decrease in speechreading performance. Thus, although it is apparent that some sounds interfere with speechreading and some do not, the acoustic features that determine whether or not any particular audio signal will interfere with speechreading are not yet known. In this paper, we describe a series of experiments that used a sentence-based speechreading task to further explore the effects that interfering audio signals have on visual speech perception.

II. EXPERIMENT 1: SPEECHREADING PERFORMANCE WITH A DISTRACTING AUDIO SIGNAL

A. Methods

1. Subjects

Nine volunteer subjects, five males and four females, were paid to participate in the experiment. All had normal hearing (<15 dB HL from 500 Hz to 8 kHz), and their ages ranged from 21 to 55 years. All of the subjects were native speakers of US English, and all had participated in previous audio experiments that utilized audio speech materials similar to those used in this experiment, but none had previous experience in AV speech experiments.

2. Stimulus materials

The speech materials used in the experiment were based on the coordinate response measure (CRM), a call-sign-based measure of speech intelligibility with a limited vocabulary of color and number responses (Moore, 1981). The CRM stimuli used in this experiment consisted of phrases of the form "Ready (call sign) go to (color) (number) now"

FIG. 1. Example frames from the CRM AVIs recorded for the male and female talkers used in the experiments.

spoken with the call sign "Baron" and all possible combinations of four colors ("blue," "green," "red," "white,") and eight numbers (1–8). Thus, a typical example of a CRM sentence would be the phrase "Ready Baron go to blue five now."

AV recordings of these CRM phrases were made in the corner of a large anechoic chamber with a digital video camera (Sony Digital Handycam) located roughly 1.5 m in front of the talker. Two native speakers of US English, one male and one female, were recruited to serve as talkers. These talkers stood in front of a black, acoustically transparent background covering the wedges on the wall of the anechoic chamber and were instructed to repeat the CRM phrases at a monotone level while keeping their heads as still as possible. The audio track was recorded directly onto the digital videotape (16 bits, 22.05 kHz sampling rate) and breaks were inserted between the CRM phrases to avoid any effects of coarticulation between consecutive recordings. The resulting videotapes were digitally downloaded onto a PC where they were partitioned into different individual AVI files for each of the 128 recorded phrases. Note that the AVI format was selected because it uses a file structure that physically interleaves the audio and visual components of the data stream to minimize the possibility of any audio-visual asynchrony in the playback of the stimulus. After the video files were downloaded, a commercially available video editor (VirtualDub) was used to crop the frames of the AVI files around the locations of the talkers' heads, convert them from color to grayscale, and compress them with the Indeo 5.1 codec.[2] Figure 1 shows example frames from the CRM AVIs for the male and female talkers used in these experiments. The CRM utterances were approximately 2000 ms long, and the AVI files contained a short period of silence both before and after the actual utterance. Appendix A provides more details about the pacing of the CRM phrases, as well as an analysis of the variability in the onset of the color and number keywords within and across the two talkers used to collect the AV corpus.

3. Procedure

The experiments were conducted in a quiet listening room with the subject seated in front of the CRT of a control computer (Pentium III PC) while wearing stereo headphones (AKG K240DF). Prior to each trial of the experiment, a MATLAB script running on the control computer randomly selected one of the 32 AVI phrases in the corpus containing the call sign "Baron." The audio signal associated with this AVI file was then stripped off, processed in MATLAB, and redubbed onto the visual signal with a scripted call to the VirtualDub multimedia processing program. This redubbed AVI file was presented to the subject through a call to the Windows Multimedia Player. Finally, the listeners were asked to identify the color and number combination contained in the target phrase spoken by the visible target talker by using the mouse to select the appropriate digit from an array of colored numbers displayed on the CRT of the control computer.

A total of five different audio conditions were tested in the experiment:

(i) No audio, where no audio signal was presented;

(ii) Noise, where the audio signal was a random noise that was filtered to match the overall average spectrum of the phrases in the CRM corpus and rectangularly gated on and off to correspond to the beginning and end of the CRM phrase spoken by the visual target talker;

(iii) Miscued speech, where the video was redubbed with the audio signal from a phrase in the CRM corpus that was addressed to the call sign "Baron" but contained a different color and a different number than the visible target phrase. This miscued audio signal was time shifted to place the onset of the word "ready" at the same point as the onset of the word "ready" in the target AVI file (i.e., at the same time as the "ready" in the visual stimulus);

(iv) Irrelevant speech, in which the audio signal was a continuous narrative of a different prerecorded talker than the target talker reading from the children's story Danny the Champion of the World by Roald Dahl (1998). This story was recorded separately onto an audio CD that played continuously while the subject participated in the experiment. Prior to this condition, each subject was forced to listen to the entire prerecorded passage three times in order to prevent them from being distracted by the content of the irrelevant speech signal during actual data collection;

(v) Reversed speech, which was identical to the irrelevant speech condition except that the continuous audio speech file was time reversed prior to being played to the subject during the experiment.

The data were collected in blocks of 60 consecutive trials with the same target talker and the same audio condition. In the no-audio and noise conditions of the experiment, each of the nine subjects participated in two blocks of trials with the male target talker and two blocks with the female target talker. In the miscued, reversed, and irrelevant speech conditions of the experiment, two blocks were collected with each of the target talkers in a same-sex condition, where the dubbed audio signal was spoken by a talker who was the same sex as the visible talker, and two additional blocks were collected with each of the target talkers in a different-sex condition, where the dubbed audio signal was spoken by a talker who was different in sex than the visible talker.

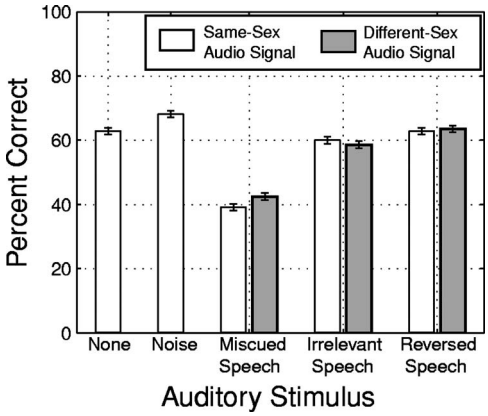

FIG. 2. Percentages of correct color *and* number identifications in each condition of experiment 1. In the conditions with a speech masker, the shaded bars show results with the dubbed audio voice that was spoken by a talker who was different in sex than the visible talker. The error bars show the 95% confidence intervals for each data point.

B. Results

Figure 2 shows the overall percentages of correct color and number identifications in each condition tested in experiment 1. The different groups of bars represent different audio conditions, and the shaded bars show the conditions where the audio stimulus was speech that was spoken by a talker who was of the opposite sex of the visual target talker. The arcsine-transformed[3] percentages of correct responses were also analyzed with a two-factor, within-subjects repeated measures ANOVA, with target talker sex (male or female) and audio condition (no audio, noise, same-sex miscued speech, different-sex miscued speech, same-sex irrelevant speech, different-sex irrelevant speech, same-sex reversed speech, and different-sex reversed speech) as the two factors. The results of this ANOVA indicated that there were significant main effects of both target talker ($F_{(1,8)}=31.87$, $p<0.001$) and audio condition ($F_{(7,56)}=16.38$, $p<0.0001$), and that there was a significant interaction between these two factors ($F_{(7,56)}=4.05$, $p<0.001$).

A *post-hoc* test (Tukey HSD) was then conducted to look for significant performance differences across the eight audio conditions tested in the experiment. The results of this test showed that performance in the two miscued speech conditions was significantly worse than in the no-audio, noise, irrelevant speech, and reversed speech conditions, but that there were no other significant differences across any of the audio conditions in the experiment.

C. Discussion

1. Overall speechreading performance

In the no-audio condition of the experiment, the subjects on average correctly identified both the color and the number in 63% of the stimulus presentations. Their ability to perform this well in a speechreading task without any training or feedback was probably the result of at least three contributing factors: (1) there were only four possible color and eight possible number response alternatives in the CRM corpus; (2) all of the color and number words contained at least one viseme that optically distinguished it from the other response alternatives in that response group; and (3) all of the possible response alternatives were common words that the subjects may have had some experience speechreading in adverse audio environments.

The speechreading task was not, however, equally difficult for the color and number words. Despite the smaller set of response alternatives, the subjects were substantially worse at identifying the color in the visual-only stimuli (67% correct responses) than they were at identifying the number in the visual-only stimuli (93% correct responses). This might be related to the earlier position of the color word within the CRM phrase, or it might indicate that the four color words in the CRM corpus were more difficult to distinguish optically than the eight number words.

Overall speechreading performance was also slightly better with the female target talker (61% correct responses) than it was with the male target talker (51% correct responses), which might reflect the fact that the male talker's face was partially obscured by facial hair. The overall pattern of responses across the different conditions was similar for both target talkers.

2. Miscued speech condition

The third group of bars in Fig. 2 shows performance in the miscued audio condition, where the visual stimuli were dubbed with an audio phrase from the CRM corpus that was time aligned with the visible target phrase but contained different color and number coordinates. Overall performance in this condition was roughly 20 percentage points lower than in the no-audio condition of the experiment, a difference that was statistically significant at the $p<0.001$ level (Tukey HSD *post-hoc* test). This result is consistent with the earlier results by Easton and Basala (1982), Dekle *et al.* (1992), and Massaro (1998) that showed that speechreading performance is impaired by the presence of a temporally overlapping audio word that is different from the visual stimulus. However, our results show that this result generalizes to the case where the visible and audible words are embedded within sentences rather than presented as isolated words.

A more detailed analysis of the results revealed that 54% of the incorrect color responses matched the color keyword in the mismatched audio stimulus and that 48% of the incorrect number responses matched the number keyword in the mismatched audio stimulus. The prevalent occurrence of these kinds of "audio errors" suggests that crossmodal interference, rather than AV integration, may have been the dominant factor behind the reduced speechreading performance that occurred in the miscued speech conditions of the experiment. However, there is also evidence that AV fusion effects were responsible for some of the additional errors that occurred in these conditions. A detailed analysis of the error patterns in the experiment, and their relation to possible fusion or combination effects, is presented in Sec. VII.

No difference was found between the same-sex and different-sex versions of the miscued speech audio condition of the experiment. Apparently a plausible consistency between the target face and interfering voice was not a necessary prerequisite for the audio signal to interfere with the speechreading process. In comparison, Easton and Basala

(1982) found that the addition of a different-sex voice interfered with speechreading performance when the audio word was optically similar to the visual word, but that a different-sex voice did not interfere when the audio and visual words were optically different. This suggests that the color and number words in this experiment were similar enough to generate AV interference even when the audio and visual voices clearly originated from different-sex talkers. Note that Green (1996) and Walker *et al.* (1995) found that the traditional McGurk effect also occurs when the target and masking faces originate from different-sex talkers.

3. Other audio conditions

None of the other interfering audio signals tested in the experiment had any significant effects on speechreading performance (Tukey HSD *post-hoc* test, $p > 0.05$). This is consistent with the results of Lyxell and Ronnberg (1993), who examined the effects of continuous white noise and speech read from a newspaper on speechreading performance and found that neither had any significant effect on visual speech perception. Together with those results, the results of our experiment strongly suggest that presence of an audio speech signal alone is not enough to cause interference in the speechreading process: the audio speech signal has to be related in some way to the visual speech for this cross-modal interference to occur. In the miscued audio conditions of this experiment, at least three factors may have played a role in establishing a link between the audio and visual portions of the stimuli that made it difficult for the listeners to ignore the distracting audio phrase: (1) the visible and audible phrases started and stopped at the same time; (2) the color and number keywords were embedded in a carrier phrase that was very similar in the visual and audio portions of the stimulus; and (3) the distracting audio phrase contained color and number keywords that were semantically similar to the keywords in the visual target phrase. The following sections describe a series of experiments that were conducted to explore these possibilities in more detail.

III. EXPERIMENT 2: AV SYNCHRONIZATION

One factor that has consistently been shown to influence AV integration in speech perception is the introduction of a temporal offset between the audible and visible portions of a bimodal speech stimulus. The intelligibility advantages that visual speech cues produce when they are presented in conjunction with distorted audio signals start to degrade when the sound is advanced more than 40 ms relative to the visual signal (Grant *et al.*, 2004a) or delayed by more than 120–240 ms relative to the visual signal (Pandey *et al.*, 1986; Grant *et al.*, 2004a). These AV advantages disappear altogether when the audio signal is advanced or delayed by more than 400 ms (Grant *et al.*, 2004a). AV asynchronies also influence the likelihood that McGurk fusions will occur with mismatched audio and visual stimuli. Such fusions start to become less frequent when the audio signal is advanced by more than 60–240 ms relative to the visual signal or delayed by more than 240–267 ms relative to the audio signal (Munhall *et al.*, 1996; Massaro *et al.* 1996). Experiments that have asked observers to detect AV asynchronies in a multimodal speech stimuli have also found that listeners are sensitive only to audio advances greater than 40–150 ms and audio delays greater than 240–258 ms (Dixon and Spitz, 1980; Grant *et al.*, 2004b; Conrey and Pisoni, 2003). All of these results indicate that AV integration is substantially less likely to occur when an AV asynchrony is introduced into a multimodal speech stimulus. To the extent that speechreading performance in the mismatched audio conditions of experiment 1 was impaired by the involuntary perceptual grouping of the visible target signals with the temporally overlapping audio distracters, one might expect performance in that condition to be improved by the introduction of a temporal offset in the audio portion of the stimulus. Experiment 2 was conducted to explicitly test this hypothesis.

A. Method

The stimuli in experiment 2 were derived from the miscued speech stimuli from experiment 1 that used the male talker for both the audio and visual portions of the stimuli. The primary difference was that the onset time of the miscued audio stimulus was delayed or advanced relative to the onset time of the video stimulus by inserting or deleting zeros prior to the start of the audio signal before redubbing the stimulus in VirtualDub. A total of 12 different delay values were tested in the experiment: −1500, −1000, −500, −250, −100, 0, 100, 250, 500, 750, 875, and 1000 ms (where negative values indicate that the onset of the word "ready" in the audio signal was time advanced relative to the onset of the word "ready" in the visual stimulus[4]). Note that, because of differences in the speaking rates of the different phrases in the CRM corpus, the actual alignment of the color and number keywords in the audio and visual potions of the stimuli varied from these nominal offset values by an average of 28 ms for the color keyword and 75 ms for the number keyword (see Appendix A for more details of this timing analysis). In addition to these 12 delay values, a control condition was included that duplicated the no-audio condition of experiment 1. These experimental conditions were presented in random order, with three repetitions of each condition within each 39-trial block of the experiment. As in experiment 1, the subjects were instructed to ignore the audio signal and use the mouse to select the colored digit corresponding to the color-number combination spoken by the visible talker. The same nine subjects who participated in experiment 1 also participated in experiment 2, with each subject participating in 32 blocks of trials for a total of 96 trials in each of the 13 conditions of the experiment.

B. Results

Figure 3 plots the overall mean percentage of correct color and number identifications in experiment 2 as a function of the temporal offset of the mismatched audio signal. Negative delay values indicate that the audio signal occurred before the video signal, and positive delay values indicate that the audio signal occurred after the video signal. The shaded region in the figure indicates the mean performance level in the no-audio condition of the experiment, plus or

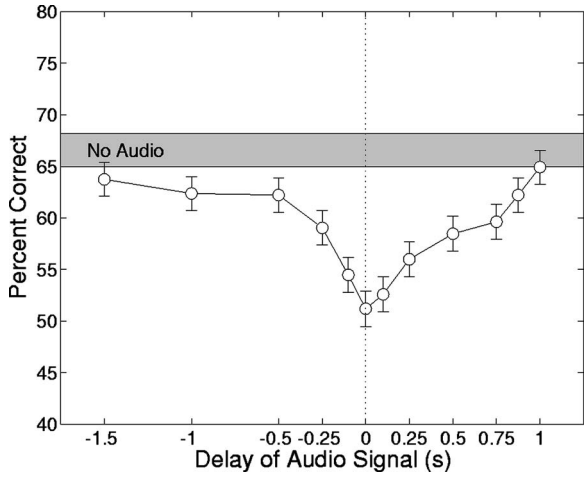

FIG. 3. Percentage of correct color *and* number identifications as a function of the offset between the audio and visual portions of the miscued stimuli in experiment 2. Negative delays indicate that the onset of the audio signal occurred before the onset of the video signal, and positive delays indicate that the onset of the audio signal occurred after the onset of the video signal. The shaded regions show the mean ±1 standard error for the no-audio conditions, and the error bars show ±1 standard error around each data point.

minus one standard error, and the error bars indicate plus or minus one standard error around each data point. These data clearly show that performance in the speechreading task varied systematically with the relative onset time of the audio distracter: performance was worst when the mismatched audio signal started at the same time as the visual stimulus (i.e., at an audio delay of 0 ms), and it improved systematically as the mismatched audio signal was advanced or delayed relative to the visual target. A one-factor within-subjects ANOVA on the arcsine-transformed mean scores for each subject in each audio condition (each of the 12 delay values plus the no-audio condition) confirmed that the main effect of audio condition was significant ($F_{(12,96)}=5.277$, $p<0.0001$). An additional *post-hoc* examination of the arcsine-transformed performance scores further indicated that a significant decrease in performance relative to the no-audio condition occurred for audio delay values ranging from −250 to +500 ms (Fisher LSD, $p<0.05$).

Although performance in the task was improved both by advancing and delaying the audio signal, the performance function was not symmetrical around the zero delay point. Performance improved much more rapidly when the audio signal was advanced relative to the video signal than when it was delayed relative to the video signal.

C. Discussion

The asymmetrical change in performance that occurred for positive and negative audio delays in this experiment is consistent with the results of previous AV speech perception studies that have shown that time advances in the audio signal are much more likely to interfere with AV integration than time delays in the audio signal. Because the visual-only speechreading task used in this experiment would be expected to be *impaired* by integration of the audio distracter with the visual stimulus, it is not surprising that performance was better when the audio signal was advanced than when it was delayed.

The range of advance and delay values that resulted in cross-modal interference in experiment 2 was also consistent with the results of previous studies examining the effects of asynchrony on AV speech perception. The range of delay values that showed a decrease in performance relative to the no-audio condition (−250 to +500 ms) was similar to the range of delay values where Grant *et al.* (2004a) found that listeners were able to obtain some benefit from AV integration in a speech intelligibility task with a badly distorted audio signal. Thus, the overall results of experiment 2 seem to be consistent with earlier experiments that have shown that AV integration decreases when stimulus onset asynchronies are introduced in the audio and visual portions of an AV speech stimulus.

IV. EXPERIMENT 3: TEMPORAL AND SEMANTIC SIMILARITY

The results of experiment 2 indicate that the temporal alignment of the visible and audible phrases in the miscued-speech conditions of experiment 1 contributed to the substantial cross-modal interference effects that occurred in those conditions. These results do not, however, address the question of whether the semantic similarities between the audio and visual color words and the audio and visual number words were critical in producing this cross-modal interference. Nor do they indicate what role the common carrier phrase might have played in making the visual portions of the AV stimuli more susceptible to interference from the audio distracter. Experiment 3 was conducted to explore these questions in more detail.

A. Methods

1. Subjects

A total of eight normal-hearing subjects, five females and three males ranging in age from 19 to 53, participated in the experiment. Four of the eight subjects were also participants in experiments 1 and 2.

2. Procedure

The procedures used in experiment 3 were similar to the ones used in experiments 1 and 2. The primary difference was that experiment 3 examined a wider range of audio conditions than the earlier experiments. Only the male target talker face was used in experiment 3. In all, a total of nine different audio conditions were tested, as illustrated in Table I:

(i) No audio, where no signal was presented. This condition was identical to no-audio conditions used in the first two experiments.
(ii) Miscued speech, which was identical to the same-sex miscue condition of experiment 1.
(iii) Female miscued speech, where the miscued audio signal began with the "Ready Baron go to" carrier phrase spoken by the male talker but abruptly switched to the female talker at the onset of the color keyword and

TABLE I. Experimental conditions tested in experiment 3. In all cases, the visible (target) talker was the male talker from the AV corpus. The boldface CRM phrase represents an example of a possible visual target phrase from a single trial in the experiment. The phrases in the center column show examples of the distracting audio signals that were used in each condition of the experiment, with italics indicating words that were spoken by a different-sex (female) talker and the bold text indicating the words spoken by the visible target talker. Note that many conditions modified the masking phrase only in the segment containing the color and number keywords: in these cases, the boundaries of this segment were determined from the hand-labeled reference points described in Appendix A. See text for details.

	Target Phrase		
Stimulus condition	**Ready Baron go to**	**blue six**	**now.**
No audio			
Miscued-speech (same-sex)	Ready Baron go to	red two	now.
Miscued-speech (different-sex)	Ready Baron go to	*red two*	*now.*
Keywords only		red two	
Swapped keywords	Ready Baron go to	two red	now.
Random keywords (same sex)	Ready Baron go to	maybe I could	now.
Random keywords (different sex)	Ready Baron go to	*maybe I could*	now.
Full-length random	had a brake pedal, a steering wheel, and a comfortable seat		
Carrier phrase only	Ready Baron go to		now.

remained that way until the end of the sentence. This condition was intended to determine whether a sudden change in the voice of the distracting talker at the onset of the keywords might either improve performance by helping the observer segregate the audio voice from the visual face or decrease performance by drawing attention towards the audio distracter.

(iv) Keywords only, which was identical to the standard miscue condition except that the carrier phrase was eliminated and only the color and number keywords were retained. Note that these color and number words still occurred at the same time within the AV stimulus, with their onset at approximately the same time as the color word in the visual stimulus. This condition was intended to determine whether the apparently synchronized carrier phrase that preceded the target keywords in the miscued speech conditions of experiment 1 played a critical role in the cross-modal interference that occurred in those conditions.

(v) Swapped keywords, where the order of the color and number words was reversed, i.e., "red two" was replaced with "two red." This condition was intended to help determine whether any cross-modal interference effects that might have occurred due to semantic similarity between the target and distracting keywords in the miscued speech condition of experiment 1 required perfect AV synchronization between the audio and visual keywords or whether it merely required the semantically similar words to be present at approximately the same position within the target sentence.

(vi) Random keywords, where the color and number keywords in the miscued audio phrase were replaced with an equal-length passage randomly chosen from the recording of a male talker reading *Danny the Champion of the World* that was used in the irrelevant-speech condition of experiment 1. The passage was chosen randomly from all the possible equal-length intervals within the entire recording of the story. No attempt was made to exactly align the randomly selected interval to begin or end at the same time as full words in the recorded speech, but each randomly selected interval was checked to ensure that it contained significant speech energy throughout its full duration (i.e., that it did not coincide with a long pause between words or sentences in the recorded story).

(vii) Female random keywords, where the color and number keywords in the miscued audio phrase were replaced with an equal-length passage randomly chosen from the recording of a female talker reading *Danny the Champion of the World*.

(viii) Full-length random, where the entire audio masking phrase was replaced with an equal-length passage that was randomly chosen from the recording of a male talker reading *Danny the Champion of the World*.

(ix) Carrier phrase only, which was identical to the standard miscue condition except that the color and number coordinates in the miscued audio phrase were replaced with silence.

Prior to data collection, each subject first participated in a training block of 70 trials of the no-audio condition in which they received correct-answer feedback after each response. They then participated in 20 blocks of trials, with each block containing 90 trials of the different audio conditions in random order. Thus each subject participated in a total of 200 trials in each of the nine audio conditions of the experiment. As in the earlier experiments, the subjects were instructed to ignore the audio signal and respond with the color-number combination spoken by the visible talker. Note that no performance feedback was provided during the data collection portion of the experiment.

B. Results and discussion

Figure 4 shows the percentage of correct color and number identifications in each of the nine conditions tested in the experiment. The arcsine-transformed results for the individual subjects were analyzed with a within-subjects

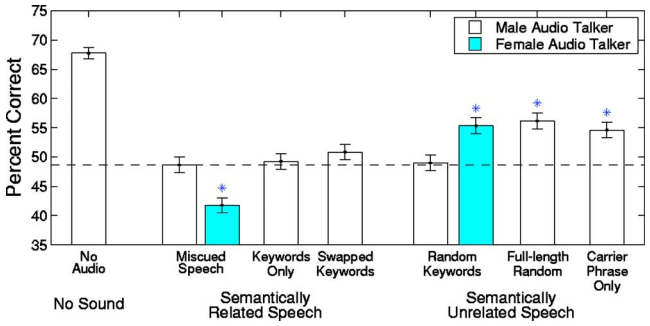

FIG. 4. Percentages of correct color *and* number identifications in each condition of experiment 3. The shaded bars show results with the dubbed audio voice that was spoken by a talker who was different in sex than the visible talker. The error bars show ±1 standard error for each data point, and the asterisks indicate data points that were significantly different from the baseline miscued speech condition, which is indicated by the horizontal dashed line (Fisher LSD *post-hoc* test, $p<0.05$).

ANOVA that showed that the main effect of audio condition was significant ($F_{(8,56)}=12.911$, $p<0.0001$). These results show that *every* audio signal produced a significant reduction in performance relative to the baseline no-audio condition (Fisher LSD *post-hoc* test, $p<0.0001$). This is in direct contrast to the results of experiment 1, which showed that continuously running unrelated speech had no effect on speechreading performance. The only difference between the full-length random condition of this experiment and the continuous unrelated speech condition in experiment 1 is that the random speech in this experiment was switched on and off at the start and end of the visual stimulus. This seems to indicate that even irrelevant speech signals can interfere with speechreading ability when they are presented concurrently with the visual speech signal. One possible explanation for this result is that the ability to selectively ignore a continuous talker is a gradual process that takes longer than the roughly 1-s delay that occurred between the onset of the audible speech and the onset of the visual keywords in the full-length random condition of this experiment (see Appendix A). This possibility is explored in more detail in experiment 4. It is interesting to note, however, that synchronous gating of any audio signal is not sufficient to cause interference: the distracting speech-shaped noise distracter in experiment 1 was switched on and off at exactly the same times as the full-length random speech signal in experiment 3, but it had no effect on performance.

Semantic similarity between the visible target and audible masking speech did not have a consistent effect on speechreading accuracy in the experiment. Although performance in the same-sex miscued-speech condition (horizontal dashed line in Fig. 4) was significantly worse than in the full-length-random and carrier-phrase-only conditions (Fisher LSD *post-hoc* test, $p<0.05$), it was not significantly different than performance in the same-sex random-keywords condition. The presence of a synchronized carrier phrase also had only a modest impact on the amount of cross-modal interference in the speechreading task. Performance in the standard miscued-speech condition, where the mismatched color-number keywords were embedded in a synchronized carrier phrase, was essentially identical to performance in the keywords-only condition, where no carrier phrase was used. Indeed, the only conditions where the carrier phrase influenced performance were the same-sex random-speech conditions, where the subjects were significantly more susceptible to interference from semantically unrelated speech embedded in a carrier phrase (random-keywords condition) than they were to semantically unrelated speech that was presented without a carrier phrase (full-length random condition) (Fisher LSD, $p<0.02$). Thus, it seems that most of the degradation in performance in the miscued-speech conditions of experiments 1 and 2 was simply due to the presence of a temporally synchronized masking speech signal, and the fact that the audible masker contained semantically similar keywords embedded in a synchronized carrier phrase had, at best, only a second-order effect on overall performance.

A final unexpected result from experiment 3 was the surprisingly large and inconsistent effect that a sudden change in the gender of the distracting audio voice had on overall performance. In the miscued speech conditions, the switch in gender caused a significant decrease in performance, while in the random keywords condition it caused a significant increase in performance. *A priori*, we expected such a change in voice to improve performance by making it easier to disassociate the interfering audio speech from the visual target speech. However, the results in the mismatched-speech condition suggest that the change may have made the distracting voice more salient and perhaps may have triggered some additional involuntary semantic processing of the audio signal. This effect is examined in more detail in experiment 5.

V. EXPERIMENT 4: LEADING RANDOM SPEECH

One unexpected result of experiment 3 was that the same irrelevant speech signal that had no impact on performance in experiment 1 caused a significant reduction in performance when it was rectangularly gated to match the onset and offset times of the visual speech signal. As stated before, this result could be explained by an attentional mechanism that allows listeners to gradually "tune out" an irrelevant audio speech signal. Such a mechanism might require several seconds to build up, which could explain why speechreading performance is impaired by synchronously windowed irrelevant speech but not by continuous irrelevant speech. Experiment 4 was conducted to determine whether performance could be improved by starting the irrelevant speech masker prior to the onset of the visual speech signal.

A. Methods

The experimental conditions tested in experiment 4 were derived from the full-length random audio condition of experiment 3. As in experiment 3, the distracting speech signals were selected randomly from the roughly 30-min-long passage from a children's story used in the irrelevant speech condition of experiment 1. In this experiment, the selected audio passage started either at the same time as the visual target speech (the full-length random condition of experiment 3) or 1, 2, 3, 4, or 5 s before the onset of the visual

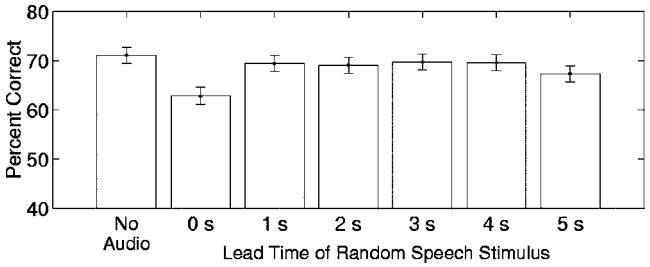

FIG. 5. Percentages of correct color *and* number identifications in each condition of experiment 4. The error bars show ±1 standard error for each data point.

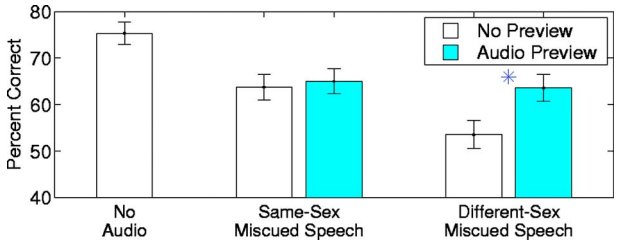

FIG. 6. Percentages of correct color *and* number identifications in each condition of experiment 5. The white bars show results in the conditions without an audio preview, and the shaded bars show results in conditions with an audio preview. The error bars show ±1 standard error for each data point, and the asterisks indicate where the audio preview produced a significant increase in performance (Fisher LSD *post-hoc* test, $p<0.05$).

speech. In all cases, the random speech passage continued playing until the end of the visual speech stimulus. An additional control condition replicating the no-audio condition of experiments 1–3 was also tested. The same eight subjects used in experiment 3 were used in experiment 4, with each subject participating in ten blocks of trials for a total of 50 trials in each of the seven conditions of the experiment.

B. Results and discussion

The results of experiment 4 are shown in Fig. 5. The arcsine-transformed data from the eight individual subjects were also subjected to a within-subjects repeated-measure ANOVA, which showed that the main effect of audio condition was statistically significant ($F_{(6,42)}=2.52$, $p<0.05$). As in experiment 3, the addition of the synchronized full-length random speech signal produced a significant decrease in overall lipreading performance relative to the no-audio condition (Fisher LSD *post-hoc* test, $p<0.05$). However, this decrease in performance disappeared in the conditions where the onset of the random audio signal occurred before the onset of the visual speech signal. None of the five leading-audio conditions produced performance levels that were significantly different from one another or from the no-audio condition, and all but the 5-s lead condition produced significant performance improvements relative to the synchronized (0 s) condition (Fisher LSD *post-hoc* tests, $p<0.05$). These results seem to confirm that the deleterious effects that irrelevant audio speech signals have on speechreading performance disappear when the listener is given the opportunity to listen to the irrelevant speech prior to the onset of the visual speech stimulus.

VI. EXPERIMENT 5: AUDITORY PREVIEW OF CHANGE IN TALKER GENDER

Another somewhat unexpected finding in experiment 3 was the large decrease in performance that occurred in the miscued speech condition when the gender of the distracting audio talker suddenly changed at the onset of the color keyword. This result suggests that sudden changes in voice characteristics can make speechreaders more susceptible to cross-modal interference from a synchronously presented audio distracter. However, it is not clear whether this increased susceptibility occurs because sudden changes in an ignored voice automatically trigger some kind of additional processing or simply because these changes are surprising and they encourage a momentary diversion of attention away from the primary speechreading task. In order to distinguish between these two possibilities, an experiment was conducted in which the subjects were given a preview of the distracting audio signal prior to their attempt to speechread the visual talker.

A. Methods

Experiment 5 was essentially a replication of three of the conditions from experiment 3: the *no-audio* condition, the same-sex *miscued speech* condition, and the different-sex *miscued speech* condition. The primary difference was that, in some of the miscued speech trials, the subjects heard a preview of the distracting audio signal prior to the start of the AV speechreading trial. In trials where this preview occurred, the subjects first listened to the entire audio portion of the trial, and then, after a break of approximately 1 s, they observed the combined AV stimulus. A second difference was that the subjects were provided with correct answer feedback after each trial in the experiment. Each of the 8 subjects from experiment 3 participated in five blocks of experiment 4, with each block containing ten no-audio trials and ten trials in each mismatched-speech condition with and without the audio preview. Thus, each subject participated in a total of 50 trials in each condition of the experiment.

B. Results and discussion

The results of experiment 4 are shown in Fig. 6. A within-subjects ANOVA on the arcsine transformed data from each subject indicated that the main effect of audio condition was significant ($F_{(4,28)}=7.83$, $p<0.0005$), and a *post-hoc* test (Fisher LSD) indicated that performance in all of the miscued audio conditions was significantly worse than in the no-audio condition. The *post-hoc* test also indicated that the availability of the audio preview in the different-sex mismatched speech condition significantly improved performance to a level that was not different than either of the same-sex miscued speech conditions. This indicates that the effect of the gender switch on performance in the different-sex mismatched speech condition of experiment 3 occurred primarily because the subjects were surprised by the sudden change in voice. When the subjects were given advance notice that such a change in voice would occur, performance was no worse than in the standard miscued speech condition.

VII. ERROR ANALYSIS

In the analysis of AV speech perception, valuable insights can often be obtained by looking beyond the overall error rates and carefully examining distribution of subject responses that occurred for each possible combination of audio and visual content used in the experiment. Analyses of this type require a great deal of data to obtain meaningful results, and none of the individual experiments presented in this paper included enough trials to support such a detailed analysis. However, four of these five experiments included some form of the miscued speech condition, and by compiling the results across all these conditions, it is possible to obtain a very detailed picture of how the specific audio and visual keywords in each stimulus influenced the subject responses in the CRM speechreading task.

In order to perform the error analysis, the data were pooled across the following four conditions:

(1) the same- and different-sex miscued speech conditions of experiment 1;
(2) the miscued speech conditions of experiment 2 with audio delays between −250 and +250 ms;
(3) the same- and different-sex full-sentence miscued speech conditions of experiment 3; and
(4) the four miscued speech conditions of experiment 4.

This pooling resulted in a total of 12 890 trials, distributed across the 16 possible AV color combinations and 64 possible AV number combinations tested in the experiment. These pooled trials were first used to determine the overall impact that each individual color or number word had on keyword identification performance in the speechreading task. The results of this analysis are shown in Fig. 7. The top left panel of the figure shows overall color identification performance as a function of the color keyword in the visual stimulus. The results show a large impact of individual keyword, with very good performance (≈90%) for the keyword "blue," very poor performance (≈20%) for the keyword "red," and intermediate performance in the other two conditions.

The top right panel shows overall number identification performance as a function of the number keyword in the visual stimulus. The results show less variation across number keywords than occurred for the color keywords, but still a fairly substantial difference between the worst two keywords ("one" and "six") and the other six keywords tested in the experiment.

The bottom two panels show the impact that the audio keywords in the miscued speech conditions had on speechreading performance in the CRM task. These results indicate that there were only relatively small differences in performance across the individual audio keywords tested in the experiment.

Many previous AV speech perception experiments have used an even finer-grain analysis to classify each individual response into one of three different categories: visual responses that exactly matched the visual portion of the stimulus (i.e., correct responses in our paradigm where the subjects were instructed to attend only to the visual stimulus);

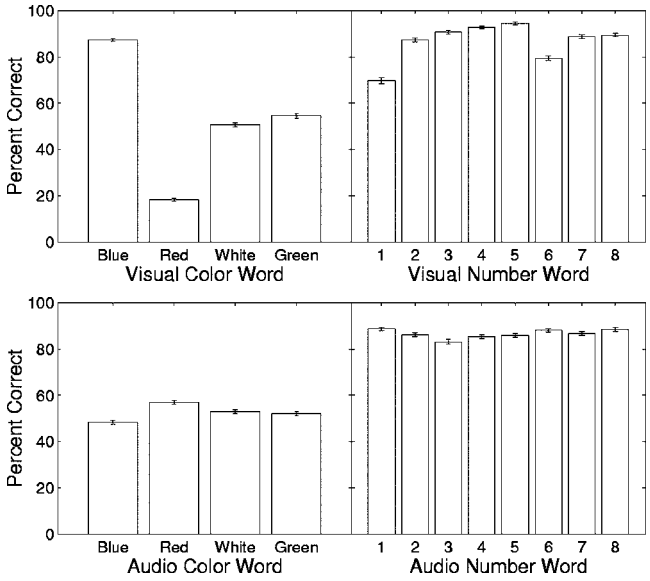

FIG. 7. Overall effect that each specific audio and visual keyword had on speechreading performance in the CRM task. The top left panel shows the percentage of correct color identifications for each possible color keyword in the visual target phrase. The top right panel shows the percentage of correct number identifications for each possible number keyword in the visual stimulus. The bottom left panel shows the influence that the audio color keyword had on color identification performance, and the bottom right panel shows the influence that the audio number keyword had on number identification performance. The error bars show the 95% confidence interval around each data point.

audio responses that exactly matched the audio portion of the stimulus; and "fusion" responses that consistently occurred in trials with the same AV stimuli but did not match either the auditory or visual portions of the stimulus. Fusion responses tend to be especially prevalent in studies examining the McGurk effect, because these studies typically incorporate small numbers of stimuli that have been specifically selected for their propensity to generate audiovisual fusions in human speech perception (for example, the visual /ga/ and auditory /ba/ that are known to create the fusion perception /da/).

However, the stimuli used in this experiment were selected on the basis of their semantic properties rather than their phonetic properties, and *a priori* there was no expectation that any particular combination of audio and visual keywords would consistently generate the perception of a different keyword within the CRM vocabulary. Rather, it was considered likely that any AV fusions that might occur would result in the perception of an ambiguous word not contained in the CRM response set, and that this would prompt the subjects to make a random selection from the four color words and/or eight number words available in the CRM vocabulary.

In order to determine if any unexpected fusion responses might have occurred in these experiments, the results for each combination of visual keyword and auditory keyword were examined to look for stimuli that elicited a consistent subject response that did not match either the auditory or visual portion of the stimulus. This analysis was conducted by using a conservative one-tailed t test ($p<0.0001$) to determine if there were any cases where one particular re-

sponse accounted for a disproportionately high percentage of all of the nonaudio and nonvisual responses that occurred for a particular AV stimulus combination.

In the color identification task, this analysis uncovered three possible AV fusion effects. The strongest of these effects occurred when the visual keyword was "red" and the auditory keyword was "blue." This stimulus combination, which occurred 1108 times, produced only 23% visual (correct) responses and only 12% audio responses. Fully 46% of the responses in this case were "white" responses, while the remaining 18% were "green" responses. Thus, it seems that the addition of the auditory keyword "blue" to the visual keyword "red" made the subjects substantially more likely to make a "white" response than when they were exposed to the visual keyword "red" in the visual-only condition of the experiment (where 47% of their responses were correct "red" responses, 35% were "white" responses, 18% were "green" responses and less than 1% were "blue" responses). This result seems to indicate that the combination of a visual "red" and an auditory "blue" produces the illusion of a word that is substantially more similar to the word "white" than to either of its two unimodal components.

The two other fusion effects that occurred with the color keywords were much less dramatic. The combination of a visual "green" and auditory "white" produced substantially more "red" responses (9.5%) than "blue" responses (4.0%), while the combination of a visual "white" and an auditory "red" produces significantly more "green" responses (9.6%) than "blue" responses (1.0%).

None of the combinations of auditory and visual number keywords presented in the experiment were found to produce reliable fusion effects. All produced responses either matched the audio portion of the keyword, matched the visual portion of the keyword, or were randomly distributed across the other possibilities in the response set.

Although these results suggest that a handful of stimulus combinations produced reliable fusion effects, these effects only accounted for a very small proportion of the overall responses in the experiment. In the color identification task, 56% of the responses correctly matched the visual keyword, 31% matched the audio keyword, 7% produced one of the three identifiable "fusion" responses described above, and the remaining 6% were distributed in a manner consistent with random guessing. In the number identification task, 89% of the trials correctly matched the visual keyword, 4% matched the audio keyword, and the remaining 7% were distributed in a manner consistent with random guessing.

VIII. SUMMARY AND CONCLUSIONS

Speechreading is primarily a visual task, but the results of these experiments, along with those of previous studies that have examined similar cross-modal interference effects, provide compelling evidence that certain types of audio distracters can substantially degrade speechreading performance. In experiment 1, we showed that speechreading performance in the CRM task was impaired by the presentation of a distracting audio phrase with the same onset time as the visual speech stimulus. In experiment 2, we showed that this audio distraction effect was highly dependent on the relative onset times of the audio and visual speech phrases, and in experiment 3 we showed that it could occur even with a random audio speech stimulus that started at the same time as the target speech. Finally, in experiment 4, we showed that the cross-modal interference effect of random distracting speech was reduced when its onset occurred one or more seconds prior to the onset of the visible target speech. Although these experiments reflect only a small number of the almost infinite number of possible audio distracting signals that could be tested, the results so far suggest that at least two conditions must be fulfilled in order for a sound to generate a significant amount of cross-modal interference during speechreading: (1) the audio distracter must be speech or a speechlike signal and (2) the audio distracter must be temporally synchronized with the visual speech stimulus. Apparently neither condition alone is sufficient to cause interference: continuous speech that is initiated even a few seconds before the visual keywords has very little impact on speechreading performance, while speech-shaped noise that starts and stops at the same time as the visual stimulus has no effect on speechreading.

At this point, it is helpful to place these results into the context of previous research that has examined AV integration effects in AV speech perception and in other kinds of multisensory integration tasks. In general, our finding that visual speech perception is impaired by the presence of a mismatched audio cue is consistent with most currently existing models of AV speech perception [see Schwartz *et al.* (1998) for a recent review of these models] and more general models of multisensory integration [see Ernst and Bülthoff (2004) or Gelder and Bertelson (2003) for recent reviews]. Most of these currently existing models would predict the existence of cross-modal interference effects that cannot be overcome by conscious direction of attention onto a single modality within a multimodal stimulus. The many studies that have been conducted to examine different aspects of the McGurk effect provide ample evidence that involuntary AV fusions can occur when certain combinations of phonemes and visemes are presented synchronously in an AV speech stimulus. Most models of AV speech perception would also predict the finding from experiment 2 that the introduction of a temporal asynchrony between the audio and visual portions of the mismatched AV stimulus decreased the amount of cross-modal interference in the speechreading task. However, we are unaware of any current AV perception models that could explain why an unrelated audio speech distracter that was switched on at the start of the carrier phrase in experiment 3 produced just as much cross-modal interference as random speech that started almost 1 s later at approximately the same time as the onset of the visible color keyword, or why the same random audio speech distracter produced little or no interference when it was turned on 1 s prior to the onset of the carrier phrase (in experiment 4) or when it was left running continuously over the course of the experiment (in experiment 1).

This decrease in cross-modal interference that occurred when the lead time of the random-speech masker was increased may be more closely related to the attentional adap-

tation effects that allow listeners to segregate disparate streams of sensory information after several seconds of exposure to a combined stimulus than to the short-term fusion effects typically associated with AV speech perception. One example of such an adaptation effect occurs in audio stream segregation, where listeners who are presented with a signal consisting of two logical streams of audio information initially hear a jumbled mess of random sound but after a few moments begin to hear two distinct sound sources. For example, McAdams and Bregman (1979) conducted an experiment where listeners heard a repeated six-tone pattern consisting of alternating high and low tones at a tempo of 10 tones per second. Initially, this stimulus sounded like a repeated six-tone pattern, but after a few 600 ms cycles of exposure, two distinct audio streams (one with three repeated high tones and one with three repeated low tones) seemed to emerge from the stimulus.

Under the right circumstances, this kind of adaptive stream segregation can greatly improve a listener's ability to extract information from an auditory stimulus. For example, Oxenham and Dau (2001) performed an experiment that examined how well listeners could extract amplitude modulation information from a target signal presented at one carrier frequency when a modulated masker was simultaneously presented at a different carrier frequency. Performance in this task was very poor when the target and masking signals had synchronized onsets and offsets, but it improved dramatically when the stimulus was preceded by four 250-ms long "precursor tones" at the same frequency as the masker. Again, the authors attributed this effect to stream segregation: the precursor tones caused the target and masker to be perceptually grouped into different streams, and this allowed the listeners to focus attention on the modulation properties of the target while ignoring the modulation properties of the masker.

McAdams and Bregman interpreted the results of their stream segregation experiment by hypothesizing that the auditory system "assumes things are coming from one source until it acquires enough information to suggest an alternate interpretation." Similarly, it might be the case that the AV speech perception mechanism assumes that concurrent audio and visual speech signals originate from the same source, and thus should be grouped together perceptually, until sufficient evidence is collected to indicate that the two speech signals are not originating from the same talker. Further research will be needed to more fully explore how the effects of cross-modal interference change over time when a listener is presented with an extended stimulus containing disjoint audio and visual information.

APPENDIX A: TEMPORAL ASPECTS OF THE AV SPEECH STIMULI

Figure 8 shows a timing analysis of the AV stimuli used in the experiments. The top and bottom panels of the figure show the waveforms of the male and female talkers speaking the typical phrase "Ready Baron go to Red Three Now." Within each panel, vertical lines have been used to mark five reference points in the utterance: (1) the start of the phrase (onset of the word "Ready"), (2) the start of the color word, (3) the end of the color word/start of the number word, (4) the end of the number word, and (5) the end of the phrase. The five reference points were hand-labeled with a MATLAB script that allowed the user to visually inspect the speech waveform, temporarily mark a reference point with the mouse, listen to the auditory stimulus before and after the reference point, and choose either to accept the break point or move it to a new location it and listen to it again. These five reference points were labeled in this manner for each of the 64 phrases in the corpus with the call sign "Baron," and numbers shown at each point on the figure represent the mean time $t\pm$ one standard deviation across all the 32 utterances spoken by that particular talker. These results show that the mean onset times of the color and number words were very consistent across the two talkers (within 100 ms) and that there was relatively little variation in onset of the two words within each talker (the largest standard deviation was 114 ms for the female talker). The male talker was particularly consistent, with a standard deviation in the onset time of the color word (24 ms) that was much smaller than the smallest desynchronization evaluated in experiment 2. In the same-sex miscued speech condition with the male talker, the time difference between the audio and visual onsets of the color keyword ranged from −120 to +120 ms, with mean absolute value of 28.7 ms. The time difference between the audio and visual onsets of the number keyword ranged from −220 to +220 ms, with a mean absolute value of 75.0 ms. In the different-sex miscued speech condition with the visible male talker, the AV onset asynchrony of the color keyword ranged from −433 to +433 ms, with a mean absolute value of 63 ms, and the AV onset asynchrony of the number keyword ranged from −508 to +508 ms, with a mean absolute value of 98.90 ms. Thus, although variations in the speaking rates of the different CRM phrases generally

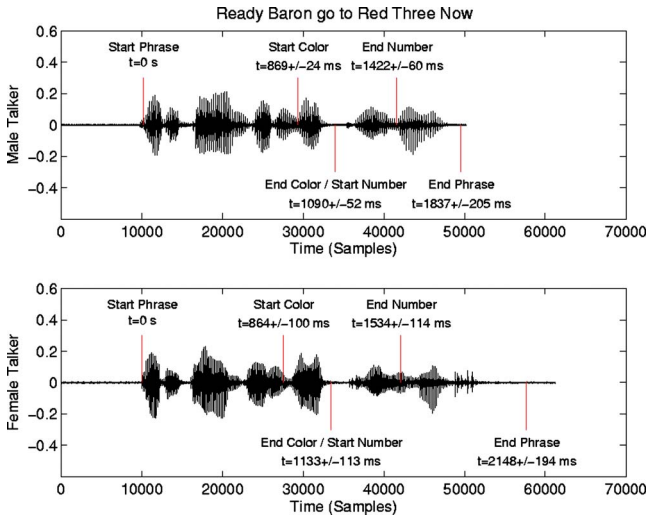

FIG. 8. Analysis of the timing of four key reference points within the AV CRM utterances used in the experiments. These reference points were hand labeled for each of the 32 phrases containing the call sign "Baron" spoken by each of the two talkers. The two panels show actual waveforms for the typical phrase "Ready Baron go to Red Three Now" and the vertical lines show the four reference points within that phrase for each talker. The numbers for t at each reference point show the mean ±1 standard deviation of that reference point across all the utterances spoken by that talker (note that the mean values do not necessarily correspond to the timing of these reference points for the example phrase shown in the figure).

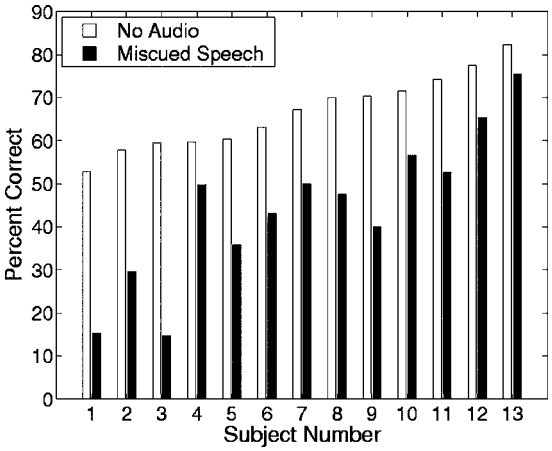

FIG. 9. Percentages of correct color *and* number identifications for each of the 13 unique subjects who participated in experiment 1 or 3. The white bars show performance in the no-audio condition, and the black bars show performance in the standard miscue condition. The data for the four subjects who participated in both experiments 1 and 3 have been averaged together across those two experiments.

prevented the onsets of the color and number words from being truly synchronous in the same tightly controlled way as the single-word or single syllable stimuli that have been used is most previous studies of AV speech perception, the CRM phrases were synchronized well enough to ensure that the key color and number words in the visible and audible CRM phrases generally overlapped in the miscued audio conditions of the experiment.

APPENDIX B: INDIVIDUAL DIFFERENCES

In the main body of the paper, all the data were discussed only in terms of the mean performance levels across all the subjects used in the experiments. However, it is also worth taking a moment to discuss how the different subjects varied in terms of their susceptibility to interference from an audio distracter. Although there were some individual differences, the overall patterns of performance across the different experimental conditions were similar for most of the participants. Figure 9 compares performance in the no-audio and miscued-speech conditions of experiments 1 and 3 for the 13 unique subjects who participated in at least one of those two experiments. The subjects have been sorted in ascending order according to their overall speechreading performance in the no-audio condition. Although there were some variations in susceptibility to cross-modal interference from the distracting speech signals, every subject tested showed some reduction in performance in the miscued-speech conditions of the experiment. Also note that there was a weak negative correlation ($r=-0.63$, $p<0.05$) between the percentage point reduction in performance that occurred in the mismatched speech conditions of the experiment and the overall percentage of correct identifications in the no-audio speechreading conditions of the experiment. This suggests that there is some tendency for poor speechreaders to be more susceptible to audio interference than proficient speechreaders.

[1]It is perhaps worth noting that, while it makes little difference whether observers direct their attention to the audio only or audio and visual portions of the stimulus, the frequency of McGurk fusions can be influenced by the extent to which they are focusing their visual attention directly on the talker's face. Tiipana *et al.* (2001) conducted an experiment where observers were asked to respond to McGurk stimuli while focusing their attention either directly at the talker or on a translucent visual distracter presented at the same location as the talker and found that the visual cues had a significantly greater impact on responses when attention was focused directly on the talker's face.

[2]The primary purpose of this processing was to compress the AVI files into a size that was more manageable for the real-time stimulus modifications that were implemented throughout the course of these experiments.

[3]The arcsine transformation was performed to normalize the percent correct scores prior to application of the ANOVA.

[4]Note that additional copies of the first and last frames were added to the beginning and end of each AVI file in order to ensure that the video signals were on long enough to accommodate the time-shifted audio signals.

Burnham, D., and Dodd, B. (**1996**). "Audio-visual speech perception as a direct process: the McGurk effect in infants and across languages," in *Speechreading by Man and Machine: Data, Models, and Systems*, edited by D. Stork and M. Hennecke (Springer-Verlag, New York), pp. 103–114.

Conrey, B., and Pisoni, D. (**2003**). "Audiovisual asynchrony detection for speech and nonspeech signals," in Proceedings of the 2003 Audio-Visual Speech Processing Workshop.

Dahl, R. (**1998**). *Danny the Champion of the World* (Puffin, New York).

Dekle, D., Fowler, C., and Funnell, M. (**1992**). "Audiovisual integration in the perception of real words," Percept. Psychophys. **51**, 335–362.

Dixon, N., and Spitz, L. (**1980**). "The detection of auditory visual desynchrony," Perception **9**, 719–721.

Easton, R., and Basala, M. (**1982**). "Perceptual dominance during lipreading," Percept. Psychophys. **32**, 562–570.

Ernst, M., and Bülthoff, H. (**2004**). "Merging the senses into a robust precept," Trends in Cognitive Science **8**, 162–169.

Fuster-Duran, A. (**1996**). "Perception of conflicting audio-visual speech: an examination across Spanish and German," in *Speechreading by Man and Machine: Data, Models, and Systems*, edited by D. Stork and M. Hennecke (Springer-Verlag, New York), pp. 135–143.

Gelder, B., and Bertlson, P. (**2003**). "Multisensory integration, perception and ecological validity," Trends in Cognitive Science **7**, 460–467.

Grant, K., and Walden, B. (**1996**). "Evaluating the articulation index for auditory-visual consonant recognition," J. Acoust. Soc. Am. **100**, 2415–2424.

Grant, K. W., Greenberg, S., Poeppel, D., and van Wassenhove, V. (**2004a**). "Effects of spectrotemporal asynchrony in auditory and auditory-visual speech processing," in Seminars in Hearing 25, pp. 241–255.

Grant, K. W., van Wassenhove, V., and Poeppel, D. (**2004b**). "Detection of auditory (crossspectral) and auditory-visual (cross-modal) synchrony," Speech Commun. Special Issue on Audio Visual Speech Processing, edited by J.-L. Schwartz, F. Bertommier, M.-A. Cathiard, and R. de Mori **44**, pp. 43–53.

Green, K. (**1996**). "The use of auditory an visual information in phonetic perception," *Speechreading by Man and Machine: Data, Models, and Systems*, edited by D. Stork and M. Hennecke (Springer-Verlag, New York), pp. 55–77.

Jones, J., and Munhall, K. (**1997**). "The effects of separating auditory and visual sources on audiovisual integration of speech," Can. Acoust. **25**, 13–19.

Lyxell, B., and Ronnberg, J. (**1993**). "The effects of background noise and working memory capacity on speechreading performance," Scand. Audiol. **22**, 67–70.

Markides, A. (**1989**). "Background noise and lip-reading ability," Br. J. Audiol. **23**, 251–253.

Massaro, D. (**1987**). *Hearing by Eye: A paradigm for Psychological Inquiry* (Erlbaum, Mahwah, NJ).

Massaro, D. (**1998**). *Perceiving Talking Faces: From speech perception to a Behavioral Principle* (MIT, Cambridge, MA).

Massaro, D., Cohen, M., and Smeele, P. (**1996**). "Evaluating the articulation index for auditory-visual consonant recognition," J. Acoust. Soc. Am. **100**, 1777–1786.

McAdams, S., and Bregman, A. (**1979**). "Hearing musical streams," J. Comput. Music **3**, 26–44.

McGurk, H., and McDonald, J. (**1976**). "Hearing lips and seeing voices,"

Nature (London) **264**, 746–748.
Moore, T. (**1981**). "Voice communication jamming research," in AGARD Conference Proceedings 331: Aural Communication in Aviation, Neuilly-Sur-Seine, France, pp. 2:1–2:6.
Munhall, K., Gribble, P., Sacco, L., and Ward, M. (**1996**). "Temporal constraints on the McGurk effect," Percept. Psychophys. **58**, 351–362.
Oxenham, A., and Dau, T. (**2001**). "Modulation detection interference: Effects of concurrent and sequential streaming," J. Acoust. Soc. Am. **110**, 402–408.
Pandey, P., Kunov, H., and Abel, S. (**1986**). "Disruptive effects of auditory signal delay on speechreading," J. Aud Res. **26**, 27–41.
Reisberg, D. (**1978**). "Looking where you listen: Visual cues and auditory attention," Acta Psychol. **42**, 331–341.
Schwartz, J.-L., Robert-Ribes, J., and Escudier, P. (**1998**). "Ten years after Summerfield: a taxonomy of models for audio-visual fusion in speech perception," in *Hearing by Eye (II): The Psychology of Speechreading and Auditory-visual Speech*, edited by B. D. R. Campbell and D. Burnham (Psychology, East Sussex, UK), pp. 85–108.
Sumby, W., and Pollack, I. (**1954**). "Visual contribution to speech intelligibility in noise," J. Acoust. Soc. Am. **26**, 212–215.
Summerfield, Q. (**1987**). "Some preliminaries to a comprehensive account of audio-visual speech perception," in *Hearing by Eye: The Psychology of Lipreading*, edited by B. Dodd and R. Campbell (Erlbaum, New York), pp. 3–51.
Summerfield, Q. (**1992**). "Lipreading and audio-visual speech perception," Philos. Trans. R. Soc. London **335**, 71–78.
Tiippana, K., Sams, M., and Andersen, T. S. (**2001**). Visual Attention Influences Audiovisual Speech Perception, in Proceedings of the 2001 Audio-Visual Speech Processing Workshop, pp. 167–171.
Walker, S., Bruce, V., and O'Malley, C. (**1995**). "Facial identity and facial speech processing: Familiar faces and voices in the McGurk effect," Percept. Psychophys. **57**, 1124–1133.

Self-to-other ratios measured in an opera chorus in performance

Sten Ternström
Department of Speech, Music and Hearing, Kungliga Tekniska Högskolan, Stockholm, Sweden

Densil Cabrera
School of Architecture, Design Science and Planning, University of Sydney, Sydney, Australia

Pamela Davis
School of Human Communication Sciences, La Trobe University, Victoria, Australia

(Received 17 November 2004; revised 12 September 2005; accepted 12 September 2005)

Four volunteer members of the chorus of Opera Australia, representing four different voice categories, wore binaural pairs of wireless microphones during a penultimate dress rehearsal on the Opera Theater stage of the Sydney Opera House. From the recordings, data were obtained on sound levels and on the self-to-other ratios (SORs). The sound levels were comparable to those found in loud music in chamber choir performance. The average SOR ranged from +10 to +15 dB. Compared to chamber choirs in other types of room, the SOR values were high. On a separate occasion, the stage support parameters ST1 (early reflections) and ST2 (late reflections) were measured over the whole stage area. ST1 was about −16 dB, which is typical for opera stages, and −20 dB for ST2, which is unusually low. It is concluded that the SOR in the opera chorus depends mostly on choir formation, which is highly variable, and that an opera chorus artist generally can hear his or her own voice very well, but little of the others and of the orchestra. This was confirmed by informal listening to the recordings. © *2005 Acoustical Society of America.* [DOI: 10.1121/1.2109212]

PACS number(s): 43.75.Rs, 43.55.Gx [NHF] Pages: 3903–3911

I. INTRODUCTION

For a choir singer it is important to be able to hear both one's own voice, called "Self," and the rest of the choir, "Other." The Self-to-Other ratio (SOR) is the level difference in decibels between Self and Other, with a stronger self signal represented by a positive SOR value. The SOR will increase with increased spacing between singers, because the direct sound from immediate neighbors becomes weaker with distance. The amount of reverberation in the room governs the intensity of the diffuse field, which is dominated by the other sound; hence, the SOR decreases with increasing reverberation. Earlier measurements on chamber choirs (Ternström, 1994, 1995) gave average SOR values of +4 dB for a 25-person choir standing in a single row in a congregational hall and +3 dB for a 30-person choir standing in two rows on the podium in a large broadcasting studio. There was a tendency for the SOR to be small at the center of the choir and larger at the ends, which may be expected, since singers at the center have more neighbors standing near. A production experiment was also carried out to determine the SOR that is preferred by choir singers if they are given control of this parameter (Ternström, 1999). The average preferred SOR was +6 dB, but the range of preferences across the 23 subjects was very large, ranging from about 0 dB to almost +15 dB. The subjects were, however, very consistent, and reproduced their own preferences to about ±2 dB over three replications.

The acoustical conditions on the opera stage can be expected to be very different from those in a rehearsal hall, a church, or a concert auditorium. In particular, there is little reflection from the sides, the opera chorus is often choreographed to spread out, and the orchestra may be tucked away in a pit. Furthermore, opera chorus artists, unlike most other choir singers, are often professionals employed on a full-time basis, so their working conditions are a more important issue than for choir singers who sing part time as amateurs. Therefore, it is of interest to try to assess the acoustics of the opera stage from the chorus artists' point of view.

In performance, the opera chorus formation can be close or spread out and can be changed frequently, even while singing. Also, the acoustics of the stage will be different depending on the given decor. The SOR in the opera chorus must therefore be very variable, and there would be little point in trying to account for it in great detail. The aim of this investigation was to obtain a set of representative SOR values for an opera chorus on the stage of the Opera Theatre at the Sydney Opera House, and at the same time to acquire a glimpse of the acoustic perspectives experienced by the chorus artists. The sound heard by four chorus artists was recorded binaurally in a dress rehearsal with orchestra, which is acoustically equivalent to the actual performance. The recordings were used to estimate the SOR and its range for each singer and serve also to document the work conditions of the chorus.

Although room acoustic data are available for the Sydney Opera Theatre (e.g., Jordan, 1980; Farina and Tronchin, 2004), we have not been able to find measurements of its typical podium acoustics when prepared for an opera performance. The podium sits at the boundary between two large-volume rooms, and its acoustics could vary greatly with the construction of the decor on the set. In order to examine the influence of reverberation on the stage area, some aspects of

the acoustics of the stage were measured, but on a separate occasion. The opera was recorded in July of 2002, and the stage measurements were made in February of 2005.

II. METHOD

A. Subjects

Four singers, a soprano, mezzosoprano, tenor, and baritone, aged 38 to 56, volunteered to wear the microphones and transmitter packs throughout a penultimate dress rehearsal with orchestra. This was a significant undertaking, in view of the possible stress of having one's own voice monitored, and also because of the close-fitting period costumes and wigs, which at one point were to be changed quickly between scenes.

Permission to record was obtained from the conductor, all members of the orchestra, most of the assembled soloists, and all the opera chorus. Where permission had not been granted, and as it was not possible to stop and start the recordings with sufficient precision, the recordings containing samples without permission were discarded electronically. Ethical approval was obtained from the institutional committee.

B. SOR estimation

The Self signal is the sum of the airborne sound (not counting room reflections) and the bone-conducted sound that the singer perceives of his or her own voice, while the Other signal is the sum of all external sounds perceived by the singer. A simple method for estimating the level ratio of Self-to-Other has been described earlier (Ternström, 1999, 1994). This method accounts only for the airborne sound. The implications of neglecting the bone-conducted component will be considered in Sec. IV. For the reader's convenience, the method is briefly recapitulated here.

The symbols *M* (middle) and *S* (sides) are conventionally used in sound recording to denote the sum and difference signals from a coincident pair of microphones. Here we use them for the same operation applied to binaural signals. The level of Self is estimated by adding the left and right channels from the binaural microphones to form a *M* signal. Because the singer's own voice will propagate equally and in phase to the left and right ears, this will give a 6-dB boost to Self (and to all other sounds incident in the vertical plane of symmetry). The Other signal, generally having low correlation or a level difference between the left and right channels, will gain only about 3 dB. Provided that Self already dominates the SPL, which is true in most situations, the level of *M* less 6 dB provides a good approximation of the level of Self.

The level of Other can be estimated by subtracting the right channel from the left channel to form a *S* signal. If Self is truly identical in left and right, it will be cancelled out entirely in *S*, while most Other sounds will add with low correlation, and their level will again increase by 3 dB. Hence, the level of Other can be approximated by the level of *S*, less 3 dB, and the Self-to-Other ratio can be estimated as

$$\mathrm{SOR} = L_M - L_S - 3 \ (\mathrm{dB}).$$

The dominant spectrum peak in the long time average spectrum (LTAS) of the recordings was at about 700 Hz, which is relevant to the SOR estimation. On the opera stage there is little reverberation (see below), and so the direct sounds from a nearby singer are still binaurally correlated; however, with many nearby singers in different directions, this correlation too would decrease. On occasion there may be chorus neighbors standing in one's plane of symmetry, and for those sources, no Self-Other separation will be obtained. However, it is typical for neighbors to be standing to the sides. The interaural level difference (ILD) for lateral incidence at 700 Hz is on the order of 3–4 dB, due to the shading of the head (Feddersen *et al.*, 1957), while the interaural time difference (ITD) is on the order of 0.7 ms. The ITD corresponds to half a wavelength at about 700 Hz. Hence there is a tendency for the left-right correlation in Other to be *negative*. For lateral incidence, these fortunate phase and amplitude relationships will reduce the component of Other in the *M* signal by some 15 dB, as compared to the case of symmetrical incidence. The LTAS level at 1400 Hz—a whole interaural wavelength—was typically about 10 dB lower than the main spectrum peak, and constructive interference at 0.7 ms delay may therefore be neglected.

If, in addition, the left-to-right cross-correlation of the Other signal can be estimated, which may be possible in laboratory conditions, then the SOR can be corrected to give useful values even when Self is weaker than Other, down to about −4 dB (Ternström, 1999). This was not possible in the present investigation, because the Self and Other signals were uncontrolled. Given that Self was always considerably stronger than Other, such correction would have made very little difference. Granqvist (2003) has elaborated on the frequency dependencies of the cancellation that are due to interaural delays and the shading of the head.

C. Recording equipment

Each singer wore two miniature omni-directional condenser microphones (Shure model DPA 4061, without resonator, see Fig. 1). The pocket-sized transmitters (Shure U1-MA) were worn on the back, attached with velcro hip belts. The signals from the radio receiver channels were connected to the eight inputs of a multichannel hard disk recorder (Yamaha AW2816 audio workstation). The eight channels were recorded in synchrony, at a sampling rate of 44.1 kHz and a word length of 16 bits per sample. After acquisition, the eight channels were copied out in stereo pairs onto stereo audio compact discs, one for each singer, using a CD recorder (Marantz CDR-631) connected to the S/P-DIF digital output of the hard disk recorder.

D. Calibration and accuracy issues

1. Sound pressure level

Calibrating all the microphones for sound pressure level (SPL) was a particular concern. The singers can be very loud (Cabrera *et al.*, 2002) and the microphone distance was

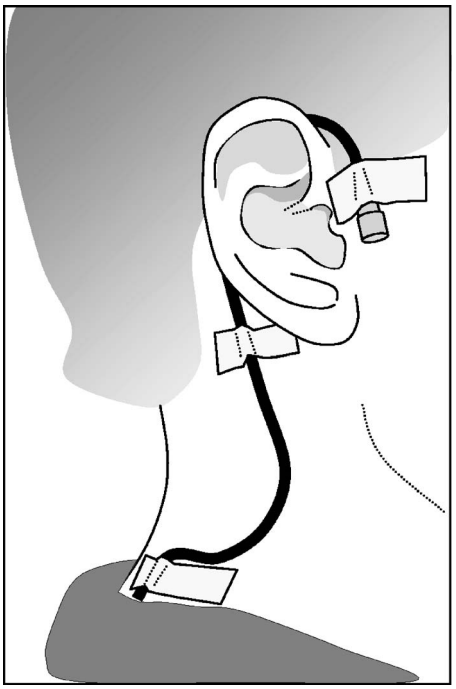

FIG. 1. Microphone placement, right-hand side.

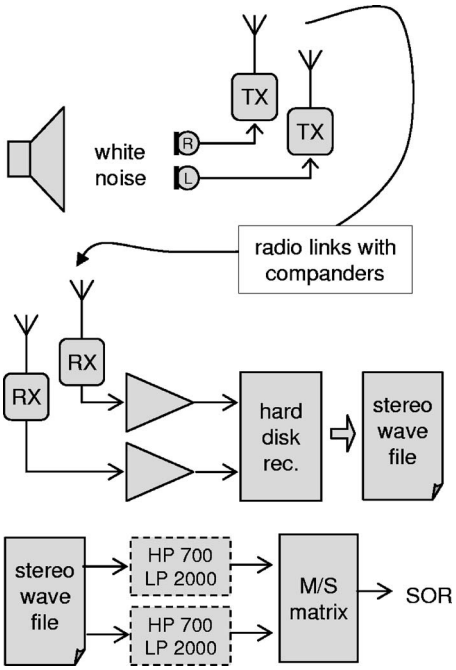

FIG. 2. Calibration setup. Only one of the four channel pairs is shown. The filters were used for channel matching, but not for the SPL calibration.

small, about 14 cm, so the risk for clipping was high. The microphone transmitters had a gain switch and a gain trim potentiometer; both were set to the minimum position. As an additional precaution prior to the experiment, an opera soprano with a powerful voice was recorded on all eight microphone channels at a voice effort level that was judged to be at least as loud as the maximum to be expected in the chorus on stage. The hard disk recorder had one input trim potentiometer only per channel, which was set to the physical minimum. All other gains in the recorder were under software control and could be stored and recalled. Gain settings that avoided clipping were established and then frozen until all recordings had been completed. Care was taken always to pair each microphone capsule with the same transmitter and receiver.

2. Channel matching

The M/S method for estimating the SOR will work well only if the left and right microphones and audio channels are accurately matched. Even small discrepancies in gain will reduce the effectiveness of the cancellation of the Self signal. In our earlier studies, the conditions were stationary and well controlled, and it was possible to use factory-matched microphones for the binaural pairs. For the present study, however, the equipment had to be rented off-the-shelf for a short time, and there was very little time for preparation, calibration, and placing the microphones on the singers. Precise matching of the left and right signal paths could not be achieved.

The noise level inherent in an analog wireless FM radio link is typically much higher than that of a cabled link. Most wireless microphone systems for stage use therefore incorporate a compander system that compresses the dynamic range of the audio prior to transmission and then expands it after reception. The accuracy in level of such companders does not necessarily meet laboratory standards. A 20-s white noise signal for level calibration was presented to the microphones from a loudspeaker at three different SPLs: 80, 90, and 100 dB(A). The microphones of each pair were placed less than 2 cm apart for this calibration (Fig. 2). The noise signals were recorded through the wireless links and onto the hard-disk recorder of the audio workstation. On later analysis, we found that the SPL of the recorded signals did not always increase by exactly 10 dB from one noise to the next. The differences between left and right in reproduced level were small, in the order of 1 dB, but this could still be a concern.

The main consequence of channel mismatches in frequency response, phase, and compander linearity would be to reduce the effectiveness of the cancellation of the Self signal, which would lead to SOR values being underestimated. Therefore, the recordings of the SPL calibration noise were reexamined *post hoc* to try to estimate the maximum SOR that could have been obtained with each pair of microphones. Because the left and right microphones were physically very close (2 cm) for the SPL calibration, the left and right signals should be very similar, like a Self signal, at low frequencies. The white noise that had been recorded via the radio link for the SPL calibrations was digitally filtered so as to be more similar to a vocal music spectrum: high pass at 700 Hz and low pass at 2000 Hz, 12 dB/oct. This gave the noise a spectral envelope with a peak in the vicinity of the first formant, and which was roughly similar to long-time average spectra of the actual recordings. The gain of the left channel relative to that of the right channel was ramped from −5 to +5 dB while the SOR was measured. An example of the results is shown in Fig. 3, for the pair of microphones that was used by the mezzo-soprano. The figure shows one noisy bell-shaped curve for each of the 80-, 90-, and 100-dB calibration noises. The maximum SOR in this ex-

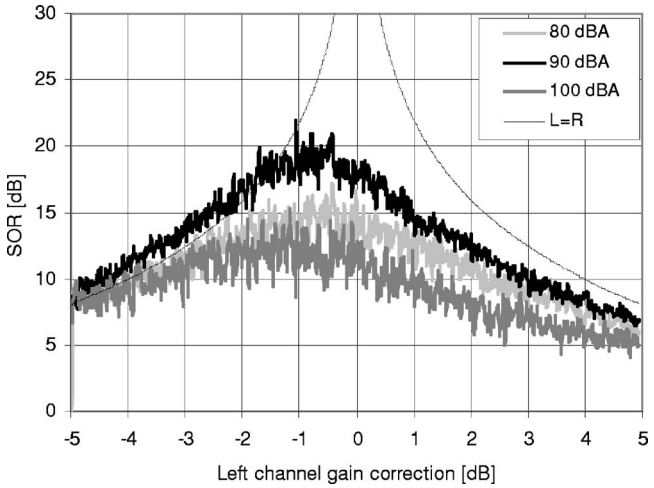

FIG. 3. Effect of channel gain mismatch on maximum SOR, obtained with white noise at the microphones and filtered noise at the M/S matrix, for one of the four pairs of microphones.

ample is 18–19 dB and it was obtained with the 90-dB noise. Somewhat disappointingly, the maximum SOR for the 80-dB noise is only about 15 dB, and for the 100-dB noise, only about 13 dB. The results for the three other microphone pairs were very similar, with the 90-dB noise always giving the highest SOR. This could be due to differences arising between the two compander channels.

It may be noted that white noise, while adequate for SPL calibration, was not an ideal signal for assessing the matching of the companders. The inevitable amplitude differences between the two separate microphone capsules will be larger for white noise than for musical signals, in which greater wavelengths dominate. Because the compander circuitry is sensitive to waveform transients, the left and right companders are more likely to regulate the dynamics differently for white noise than for vocal signals. With hindsight, it would have been better to use a pink or low-pass filtered noise in the speaker for the SPL calibration. As will be seen in Sec. III, higher SOR values than the maximum values estimated here were sometimes obtained from the singer recordings.

The smooth curve in Fig. 3 shows the SOR that is obtained when the two channels are identical and the relative gain of the left channel is changed. This curve was obtained by copying an identical noise signal to both channels. The smooth curve shows clearly the effect of channel gain mismatch: for example, a mismatch of 1 dB will limit the maximum SOR to 22 dB. It can be seen that for this microphone pair, in the calibration rig, the SOR peaked at a gain correction of about −0.8 dB.

For the purposes of this investigation, small nonlinearites in the compander dynamics would not be a problem if they were the exactly the same in the left and right channels. To check if this might be the case, correlation scatter plots were made of the left SPL versus right SPL in the live recordings, to assess the balance in channel gain. These showed that in some cases the compander nonlinearities were visible: the level was not consistently restored in precisely the same way in the left and right channels. These errors were in the order of 1 or 2 dB.

The spectral matching of the microphones in a free field was assessed by taking the long-time average spectrum (LTAS) of the calibration noise. The LTAS was computed as the average power spectrum based on overlapping 512-point Hamming-windowed FFTs at 22 050-Hz sampling rate. This showed that the agreement in frequency response for all microphone pairs was within ±1 dB over the voice frequency range 100–8000 Hz at matched gains. When taking the LTAS of the actual sung performances, there were discrepancies of up to 8 dB between channels in varying parts of the spectrum. These will have been caused partly by lateral Other sounds, and partly by channel mismatch in frequency response due to slight asymmetries in the mounting of the microphones.

In summary, differences in gain and phase between the left and right signal paths can be expected, especially from the two independent dynamic companding processes in either channel. This will reduce the effectiveness of the Self cancellation, and the SOR may therefore be underestimated with the setup that we used. The magnitude of this error will vary with the temporal and dynamic characteristics of the signal as it passes through the companders.

3. Noise level

The background noise in the recordings was dominated by the noise of the signal path, but included also the background noise in the auditorium. The background noise, measured on stage during a brief silence in the rehearsal, corresponded to 51 dB SPL linear weighting. This noise level was −73 dB relative to the maximum signal level of the 16-bit recordings (0 dB being a full scale sine wave), and more than 20 dB lower than Self in the softest portions for which the SOR was measured.

E. Acquisition setup

A recording desk was arranged in one of the theater's stall rows, where the experimenters had good overview of the stage, and the wireless microphones had unhindered line-of-sight conditions. Off-stage, most of the microphones were out of radio range, but this was of no concern. The radio channel frequencies were allocated so as not to interfere with the house system. Our recording equipment was completely independent of the house audio system and mixing desk. There was no audience present, except for a handful of persons directly involved in the dress rehearsal.

On each singer, the two microphones were taped down just in front of each ear, each about 14 cm circumferentially from the center of the mouth (Fig. 1). With the costume and wig in place, the arrangement was inconspicuous. The microphone placement was not ideal for making accurate binaural recordings, since the microphone membranes were not seated within the pinnae. This was not possible because of time constraints in the dressing rooms. For measuring the Self-to-Other ratio, however, the placement was adequate.

We had no control over what was being sung (*The Masked Ball*, Acts 1, 2, and 3, with some passages repeated). As it turned out, the male voices had a lot more singing time than did the female voices. The original recordings were ed-

ited so that only portions where the chorus was actually singing were retained. This resulted in a total of 200 s each of the two female voices and 800 s each of the two male voices.

During an unexpected mid-morning fire drill, when the entire ensemble had to assemble outdoors, the microphones were inspected and found to be still in place, except for the mezzo soprano's right-ear microphone, which was reattached.

F. SOR analysis

There were four sets of binaural recordings, one for each singer. The recordings were manually edited to obtain excerpts that covered only those bars in the score where the chorus had notes to sing. Each excerpt represented a particular musical passage in a particular chorus formation on stage. The formations were generally not regular as for ordinary choirs and because of the many changes in formation, there seemed to be little point in trying to track the positions of the four recorded singers in the ensemble. Each excerpt was labeled with a reference to its page number(s) in the vocal score (Verdi, 1859). For each singer, one file with all excerpts concatenated together was built. This was repeated for the three acts of the opera that had been recorded (two for the female parts).

To achieve matching of the channel gains, the equivalent level L_{eq} over each entire file was computed per channel. The gain of the right channel was normalized against that of the left channel, on the assumption that the L_{eq} over such a long interval should be the same at the two ears. The gain corrections thus obtained differed by no more than 0.8 dB from the results of the SPL calibration procedure, suggesting that the placements of the microphones on the singer heads had been practically symmetrical.

The M and S signals were computed as $(L+R)/2$ and $(L-R)/2$, respectively, and written to new two-channel M/S-files, with the labels copied from the stereo files. The M/S files were then submitted to a program that automatically sought out the labeled segments and computed the L_{eq} of M and S for each excerpt (the *Extract* utility in the Soundswell Signal Workstation 4.0, Hitech Development AB, Täby, Sweden). Finally, the SOR estimates were computed in a spreadsheet as

$$L_{eqM} - L_{eqS} - 3 \text{ (dB)}.$$

Using the L_{eq} is particularly convenient here, since this measure will be highly influenced by the portions when the signal level is high (i.e., when the singer carrying the microphones is singing), while weaker portions, when there is only background and no Self signal, will have little influence. We tried also using a threshold level for the voiced portions only, but this was fraught with difficulty.

A similar procedure was applied also to the original stereo files, yielding L_{eq} measures of the left and right channel signals for each excerpt. Level calibration was maintained throughout.

G. Measurements of the stage acoustics

The stage acoustics will of course be affected to some degree by the set of theatrical decor. During our recordings of *The Masked Ball* dress rehearsal, the set was changed between acts a couple of times, but was in all cases sparse, with little in the way of reflecting side walls. For one set, the floor was slightly elevated by sections toward the rear, so as to produce a wide staircase, the chorus mostly standing on its steps. For logistical reasons, the stage acoustics could not be measured with any of these sets. The stage measurements were made with a sparse set and flat floor with canvas "walls" along the sides. The stage was acoustically unobstructed in both cases.

Of the many room acoustic parameters available, the Early Stage Support (ST1) and Late Stage Support (ST2) were considered to be the most relevant for this investigation. These were developed by Gade (1989, 1992) for the measurement of acoustic support on orchestra platforms in auditoria. ST1 is the ratio in dB of the early reflected energy (within the 20–100-ms period) relative to the direct sound (taken as the first 10 ms of the impulse response). It relates to the ease of hearing other members of an ensemble. ST2 is the ratio of the reflected energy after the first 100 ms relative to the direct sound. Both are to be measured at a distance of 1 m from the acoustic center of an omni-directional sound source.

Stage support measurements were made using a Brüel & Kjær type 4296 dodecahedral loudspeaker and a Brüel & Kjær type 4190 microphone, both at a height of 1.5 m, deriving impulse responses from a 21st-order maximum length sequence signal with a 48-kHz sampling rate. The mean value for the octave bands from 250 Hz to 2 kHz inclusive was taken as the single number stage support rating.

Both the ST measures were obtained for 15 positions across the stage, as shown schematically in Fig. 4. For each position, four measurements were made in the four directions N, E, S, and W as shown in the figure, and the average of the four was computed.

The mid-frequency reverberation times (average of 500-Hz and 1-kHz octave band T30 values) were computed from impulse responses measured from positions A1 and B1 (Fig. 4) to seat number M19 in the 15th row in the middle of the stalls. This was done to check against more thorough measurements done previously. The same mid-frequency reverberation time was also measured on the stage, from the A-to-C impulse responses in each of the five rows in Fig. 4. This was done to obtain a measure of the "room" reverberation time in the stage area.

III. RESULTS

A. Self-to-other ratio

The SOR results are shown in Fig. 5. Each marker point represents the SOR as measured over one musical excerpt. The duration of the excerpts varied between 2 and 20 s. The average SOR was about +15 dB for the soprano, +10 dB for the mezzosoprano and tenor, and +14 dB for the baritone. It is possible that these SOR values are somewhat underestimated due to L-R channel mismatches in the rented equip-

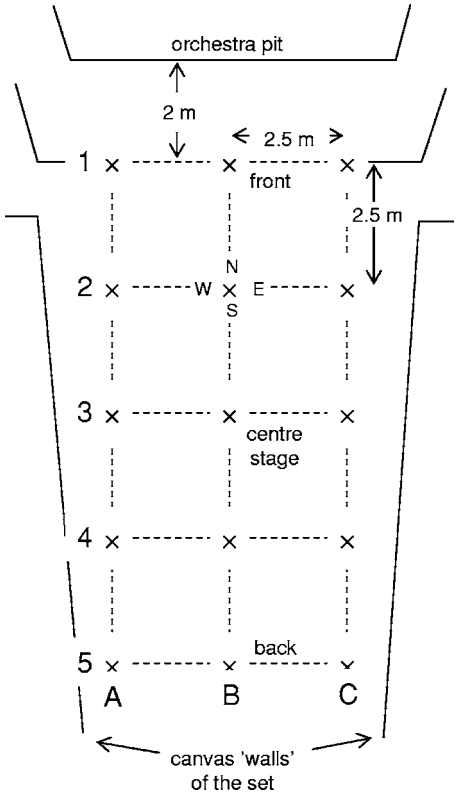

FIG. 4. Plan of positions in which the stage support parameters were measured on stage.

ment, as discussed earlier. Nevertheless, the SOR values found here are considerably higher than the 0 to +8 dB that was found for chamber choirs in more reverberant rooms and with accurate channel matching (Ternström, 1994, 1995).

Figure 5 also shows the range of sound pressure levels encountered by the singers, as measured by the microphone at the left ear. Most of this sound would be that of their own voice at close range (about 14 cm) to the microphones. The level of Self, estimated as M-6 dB, was typically 0–2 dB below the level of either channel. The level of Other ranged from 60 to 97 dB. The level of Other can also be estimated from Fig. 5, simply by subtracting the SOR from the corresponding SPL. The musical dynamic indicated in the score corresponded to the SPL as shown in Table I. A long *fortissimo* passage was rehearsed several times, which accounts for the large number of points above 100 dB SPL.

B. Acoustics of the stage

The results of the ST1 and ST2 measurements over the stage area are given in Table II. The mean ST1 is −16.2 dB under the proscenium arch (2 m from the front edge of the stage). By way of comparison, this value is within the low range encountered for orchestra platforms in concert halls. For example, Gade (1989) found a median ST1 of −10.9 dB in a survey of nine Danish, eight British, and six other European concert halls, with values ranging between −18.3 and −14.5 dB. In Beranek's (2004) survey of concert auditoria, the median ST1 for 24 halls is −14.8 dB, with values ranging between −18.1 and −12.2 dB. Chamber music halls tend to have greater early stage support: in a survey of 17 chamber

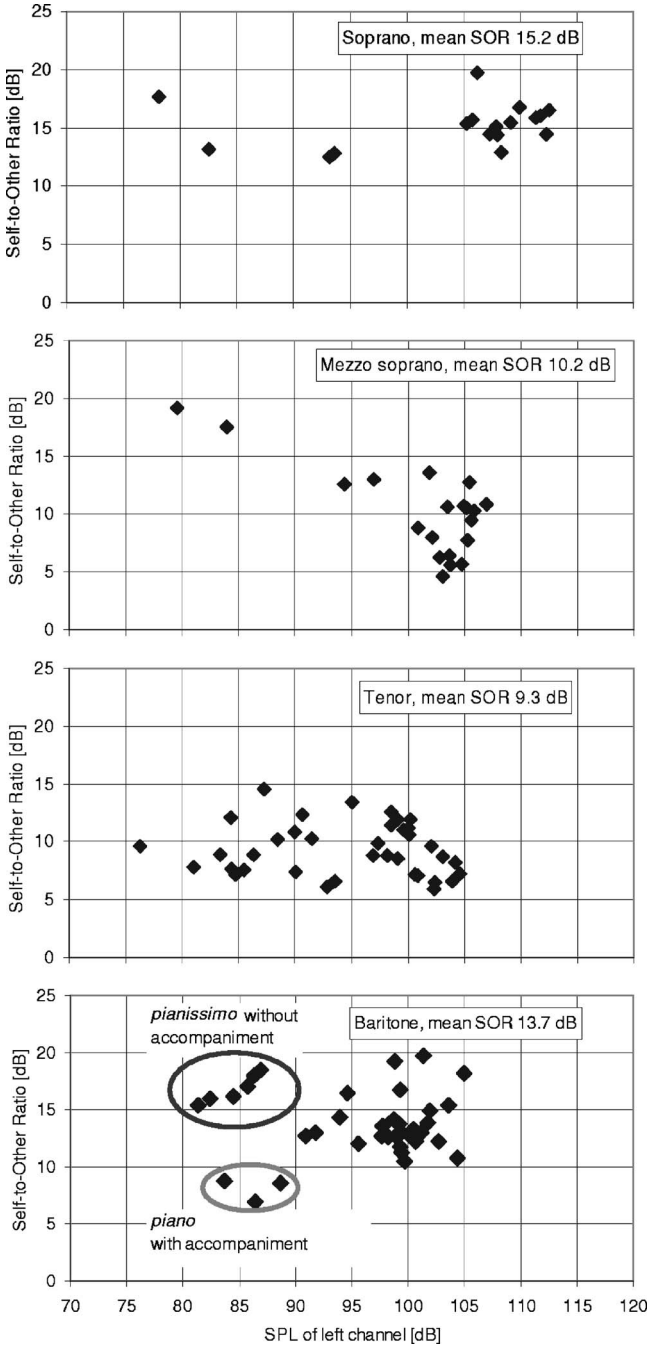

FIG. 5. Self-to-Other ratios (SORs) measured on stage for (top to bottom) the soprano, the mezzosoprano, the tenor, and the baritone singer. The horizontal axis represents the L_{eq} at the singer's left ear, and the vertical axis shows the SOR. The boxed inset shows the mean SOR. Each point corresponds to a musical phrase or passage of 2 to 20 s duration. Most points above 100 dB are from several repeats of a few loud *tutti* passages. The two leftmost points for the soprano and mezzo-soprano are from a soft passage with very little accompaniment and no male voices.

music halls, Hidaka and Nishihara (2004) found a median ST1 of −9.7 dB, with values ranging between −12.8 and −4.4 dB.

Studies by Gade (1989) and Jeon and Barron (2005) show that stage support can be varied in a given auditorium by changing the position of reflective surfaces above and around the stage. Since the stage support in opera theaters is likely to vary with the set, survey data for opera theaters are

TABLE I. Approximate relationship between the SPL (in the left channel) and the musical dynamic as indicated in the score. Values in dB (linear weighting). These SPL ranges cover the levels measured on all four singers.

Dynamic	SPL
ff	99–113
f	97–105
mf	93–100
p	85–95
pp	76–87

not currently published. However, the ST1 result of −16.2 dB under the proscenium arch appears to be typical for that encountered on opera theater stages, being equal to the median of measurements made for 20 opera theaters of the world (not including the Sydney Opera House) by Beranek and Hidaka (1999; personal communication). The opera houses surveyed by Beranek and Hidaka had ST1 values ranging between −21.4 and −11.9 dB.

The ST2 values in this theater are distinctive in that they are less than the ST1 values. Concert auditorium data from Gade (1989) and opera theater data from Beranek and Hidaka (1999; personal communication) both show ST2 to be typically 1.4 dB greater than ST1, with no cases of ST2 less than ST1. The median ST2 for Gade's concert halls is −12.6 dB (ranging between −16.8 and −10.1 dB), while that for Beranek and Hidaka's opera theaters is −15.0 dB (ranging between −19.3 and −11.0 dB). Hence, the measurements indicate that relatively little reverberation would be audible to a singer in this theater because of its distinctively high sound absorption. Beranek and Hidaka find similarly low levels of late stage support in much larger opera theaters. As shown in Table II, early stage support increases a little towards the back of the stage, while late stage support declines.

The mid-frequency reverberation time, measured from the front of the stage to the seat 15 rows back and near the middle (seat M19), was 1.15 s. This is consistent with measurements made on a previous occasion by the researchers in the unoccupied auditorium, showing an average mid-frequency reverberation time of 1.15 s (standard deviation of 0.05 s, 34 measurement positions throughout the audience area with the source on stage). It is also consistent with recent results of Farina and Tronchin (2004), but substantially less than early measurements by Jordan (1980) made when the seats had leather upholstery instead of the current porous upholstery (unoccupied auditorium mid-frequency reverberation time of about 2 s). Hence, the acoustical conditions during the stage support measurements appear to be consistent with those normally encountered for this unoccupied auditorium, which was the situation for the dress rehearsal during which the SOR measurements were obtained.

On the stage, the mid-frequency reverberation time was very close to 1.0 s in four of the five positions, and somewhat longer at the very front of the stage, where the auditorium's longer reverberation would have some influence (Table II).

TABLE II. Results of the stage support and reverberation time measurements. All ST values are in dB. Positions A1–C5 are those given in Fig. 4.

ST1 (early)	A	B	C	Average		RTmid (s)
1	−16,8	−15,3	−16,3	−16,2	Front	1.04
2	−16,3	−14,7	−14,5	−15,1		0.99
3	−16,9	−14,9	−15,0	−15,6		1.00
4	−14,5	−13,9	−15,4	−14,6		0.98
5	−15,6	−13,4	−15,9	−15,0	Back	0.98
	Side	Centre	Side			
ST2 (late)	A	B	C	Average		
1	−19,6	−19,2	−19,3	−19,4	Front	
2	−19,5	−19,1	−19,0	−19,2		
3	−19,6	−19,3	−19,0	−19,3		
4	−19,3	−20,1	−21,0	−20,2		
5	−21,5	−20,1	−21,4	−21,0	Back	
	Side	Centre	Side			

TABLE III. Room and choir data for this study (opera stage) and the ones in Ternström (1995) (studio, hall). Values marked with asterisks follow from the assumed effective volume of the opera stage area.

Room data	Unit	Opera stage	Studio	Hall
Room volume V	m^3	7000*	3100	480
Reverberation time T at 500 Hz	s	1.0	1.3	1.2
Equivalent absorption area A	m^2	1140*	390	65
Reverberation radius r_r	m	4.7*	2.7	1.1
Relative intensity level of the diffuse field	dB	0	+4.7*	+12.4*
Choir data				
No. of singers	⋯	up to 30	32	25
Singer rows	⋯	variable	2	1
Singer spacing	m	variable	0.7	0.7
Average SOR overall	dB	12.1	2.5	3.9

IV. DISCUSSION

A. Comparison to chamber choirs

The two earlier studies on chamber choirs were done in a congregational hall and on the podium of a large broadcasting studio with 200 audience seats. Both rooms were of a rectangular "shoe-box" shape. It is not straightforward to compare those rooms to the opera house theater, because while the opera stage area reverberation time T is now known, the acoustically effective volume of the "room" in the opera stage area is not known. The volume V of the auditorium alone is given by Jordan (1980) as 8200 m^3. Some basic acoustic data for the three venues and choirs are given in Table III, where V for the opera stage area has simply been guessed to be 7000 m^3. The asterisks in Table III indicate the values affected by that guess. The equivalent absorption area A has been derived from T and V using Sabine's formula, $T=0.163V/A$, which should be valid for the studio and hall, but may be inappropriate for the guessed volume. Since the intensity of the diffuse field with a given source is inversely proportional to A, we can also estimate the relative intensities of the diffuse field for a given source in the three venues. With the opera stage as a reference, the

level of the diffuse field would have been about 5 dB higher in the studio and 12 dB higher in the hall (again, these values will depend on the set and on the effective room volume of the stage). With a strong diffuse field, the SOR will generally be low and dependent on the total number of singers. With a weak diffuse field, which is the case for the opera stage, the SOR will depend more on the number of singer neighbors that are closer than the reverberation radius. Here, the choreography on stage made the spacing between the four recorded singers and their neighbors highly variable, and no record was kept of their positions or of the directions they were facing. In Table III, the reverberation radius r_r has been computed as $0.056(V/T)^{0.5}$.

The sound levels of Other found here are similar to those found earlier in choral music performed by chamber choirs (good amateur or semi-professional) in reverberant rooms, when the person wearing the binaural microphones remained silent inside the choirs (Ternström and Sundberg, 1988). This suggests that, on the opera stage, the greater room absorption and often wider spacing was offset by the more powerful and operatic voices of the vocally skilled chorus artists, which also would be consistent with the higher SOR values. Note that while a louder voice for a particular singer will increase that singer's SOR, the SOR will remain constant if all singers sing louder by the same number of decibels.

While the SOR differences between the four singers in this investigation appear to be systematic, we cannot generalize these differences to apply to the voice *categories* that the singers represent (i.e., soprano, mezzo-soprano, tenor, baritone), since there was only one individual in each category. In the chamber choirs, the individual SOR averages tended to be larger for sopranos and smaller for basses, with altos and tenors in between. Except for the baritone, the opera chorus data are similar in this regard.

B. Subjective impressions

It was clear from listening to the recordings that the opera chorus artists at times can hear the orchestra only incidentally, and that the soloists and the rest of the ensemble often sound distant. This is to be expected on any large stage and is not to be construed as a problem specific to the given opera house.

The recordings were played to two other opera chorus singers, unconnected with this investigation, who commented anecdotally that the recordings felt quite realistic, and that the sensations of being rather alone on the stage and singing as a soloist rather than inside a choir were familiar. For time-keeping, they said, one must rely on visual contact with the conductor, or, failing that, simply on "dead reckoning." Timing cues from other ensemble members were said to be often absent or unreliable.

With regard to the issue of channel matching, it was noted on listening to the singer recordings that the Self signal always appeared to be stable in the center of the stereo image. It was noted also that a correct playback level was important to realism. A good quality headphone amplifier (Nyvalla DSP Audio Interface Box, Hitech Development) was required in order to achieve the correct sound pressure levels; a consumer sound card output would not suffice. When heard out of context (that is, in the laboratory rather than on the opera stage), the recordings were perceived as very loud. Readers who are interested in the possible hearing hazards of opera chorus singing may wish to refer to Steurer *et al.* (1998).

C. Bone conduction

The level of the bone-conducted component of Self is complicated to account for (Howell, 1985). The pronounced low-pass characteristic of bone transmission relative to air conduction means that the ratio of airborne to bone-conducted sound will vary with the vowel and with the mode of voice production, such as breathy-pressed. The reader can easily test this by occluding the ears and singing "aah-ooh:" the "ooh" will sound louder by bone conduction. Pörschmann (2000) found through masking experiments that the perceived level of the bone-conducted sound *in speech* can be up to 4 dB higher than the level of the airborne sound, for frequencies in the octave 700–1400 Hz. This is an important octave, since it may contain the dominant first formant peak of the voice spectrum. On average, both the first formant frequency and the relative level of the high end of the spectrum are higher in singing than in speech (the mouth is more open), so it is likely that the airborne-to-bone-conduction ratio would be higher in singing, although this has not been shown. Neglecting the bone conduction, as we have done here, means that the effective SOR may be underestimated by a few decibels, but the error may depend on both the vowel and the mode of phonation. This should apply equally to chamber choirs (Ternström, 1994) and opera choruses.

ACKNOWLEDGMENTS

We are very grateful to the four opera chorus artists from Opera Australia who volunteered to wear the microphones and to the conductor Simone Young and the other artists in the opera company and in the Opera and Ballet Orchestra who gave their permission for the recordings. We are especially indebted to Opera Australia for consenting to and supporting these unusual recordings, and to Ian McMahon in particular for his many efforts in making the recordings possible. We thank Jenni Oates who made many of the preparations in obtaining the artists' consent. The management of the Sydney Opera House is gratefully acknowledged for providing access and assistance for the measurements. We thank Leo Beranek and Takayuki Hidaka for making available their survey data on opera theater stage support. Thanks also to Coda Audio of Sydney for their helpfulness and competence in providing the equipment rentals. Karin Carlsson assisted in editing the recordings. Ternström's travel was funded by a grant from Australian Research Council Strategic Partnerships with Industry Research and Training (SPIRT) and by two full-day voice workshops produced by Alison Winkworth.

Beranek, L. (**2004**). *Concert Halls and Opera Houses* (Springer-Verlag, New York).

Beranek, L., and Hidaka, T. (**1999**). "New subjective and objective data on

20 opera houses of the world," J. Acoust. Soc. Am. **105**, 929.
Cabrera, D., Davis, P., Barnes, J., Jacobs, M., and Bell, D. (**2002**). "Recording the operatic voice for acoustic analysis," Acoust. Aust. **30**(3), 103–108.
Farina, A., and Tronchin, L. (**2004**). "Advanced techniques for measuring and reproducing spatial sound properties of auditoria," *Proc Int'l Symp on Room Acoustics—Design and Science*, Hyogo, Japan.
Feddersen, W. E., Sandel, T. T., Teas, D. C., and Jeffress, L. A. (**1957**). Localization of high-frequency tones, J. Acoust. Soc. Am. **29**, 988–991.
Gade, A. C. (**1989**). "Investigations of musicians' room acoustic conditions in concert halls. II. Field experiments and synthesis of results," Acustica **69**, 249–262.
Gade, A. C. (**1992**). "Practical aspects of room acoustic measurements on orchestra platforms," *Proc Int'l Congress on Acoustics*, Beijing, F3-5.
Granqvist, S. (**2003**). "The self-to-other ratio applied as a phonation detector for voice accumulation," Logopedics Phoniatrics Vocology **28**, 71–80.
Hidaka, T., and Nishihara, N. (**2004**). "Objective evaluation of chamber-music halls in Europe and Japan," J. Acoust. Soc. Am. **116**, 357–372.
Howell, P. (**1985**). "Auditory feedback of the voice in singing," *Musical Structure and Cognition*, edited by P. Howell, I. Cross, and R. West (Academic, London), pp. 259–286.
Jeon, J. Y., and Barron, M. (**2005**). "Evaluation of stage acoustics in the Seoul Arts Center Concert Hall by measuring stage support," J. Acoust. Soc. Am. **117**, 232–239.
Jordan, V. L. (**1980**). *Acoustical Design of Concert Halls and Theatres* (Applied Science, London).
Pörschmann, C. (**2000**). "Influences of bone conduction and air conduction on one's own voice," Acust. Acta Acust. 86(6), 1038–1045.
Steurer, M., Simak, S., Denk, D. M., and Kautzky, M. (**1998**). "Does choir singing cause noise-induced hearing loss?" Audiology **37**, 38–51.
Ternström, S. (**1994**). "Hearing myself with the others—sound levels in choral performance measured with separation of the own voice from the rest of the choir," J. Voice **8**(4), 293–302.
Ternström, S. (**1995**). "Self-to-other ratios measured in choral performance," *Proc 15th Int'l Congress on Acoustics*, ICA 95, Trondheim, Norway, June 1995/II, pp. 681–684.
Ternström, S. (**1999**). "Preferred self-to-other ratios in choir singing," J. Acoust. Soc. Am. **105**, 3563–3574.
Ternström, S., and Sundberg, J. (**1988**). "Intonation precision of choir singers," J. Acoust. Soc. Am. **84**, 59–69.
Verdi, G. (**1859**). *Una Ballo in Maschera* (vocal score) (Editions Ricordi, Rome, Italy), no. 48180.

Kramers-Kronig analysis of attenuation and dispersion in trabecular bone[a)]

Kendall R. Waters[b)]
Materials Reliability Division, National Institute of Standards and Technology, Boulder, Colorado 80305

Brent K. Hoffmeister
Department of Physics, Rhodes College, Memphis, Tennessee 38112

(Received 31 May 2005; revised 29 September 2005; accepted 29 September 2005)

A restricted-bandwidth form of the Kramers-Kronig dispersion relations is applied to *in vitro* measurements of ultrasonic attenuation and dispersion properties of trabecular bone specimens from bovine tibia. The Kramers-Kronig analysis utilizes only experimentally measured properties and avoids extrapolation of ultrasonic properties beyond the known bandwidth. Compensation for the portions of the Kramers-Kronig integrals over the unknown bandwidth is partially achieved by the method of subtractions, where a subtraction frequency acts as an adjustable parameter. Good agreement is found between experimentally measured and Kramers-Kronig reconstructed dispersions. The restricted-bandwidth approach improves upon other forms of the Kramers-Kronig relations and may provide further insight into how ultrasound interacts with trabecular bone. [DOI: 10.1121/1.2126934]

PACS number(s): 43.80.Cs, 43.20.Hq [FD] Pages: 3912–3920

I. INTRODUCTION

There has been considerable interest in the measurement and modeling of ultrasonic propagation and scattering properties of trabecular bone in an effort to better understand the mechanisms and effects of the skeletal disorder osteoporosis.[1–11] These efforts have assisted the development of clinical bone sonometers for evaluation of osteoporosis based on measurements related to the speed of sound and the slope of attenuation with respect to frequency.[4] The slope of attenuation is a parameter that is widely used to characterize biological materials and is appropriate for cases where attenuation is approximately proportional to frequency. Researchers who study the ultrasonic properties of bone often refer to this parameter as normalized broadband ultrasonic attenuation (nBUA). Speed of sound is also often reported for biological materials and can be related to some mechanical property such as Young's modulus.[12]

The velocity at which ultrasound propagates in soft tissues is largely independent of the frequency. That is, soft tissues are only weakly dispersive. Because dispersion is negligible and attenuation is relatively small in soft tissues, there is little waveform distortion due to dispersion of a (linear) ultrasonic signal as it propagates over distances on the order of centimeters. Consequently, estimates of speed of sound that are based on times of flight can be determined easily. Furthermore, estimation of time of flight is not particularly sensitive to the estimation technique (e.g., envelope peak or percentage of envelope peak). In contrast, the phase velocity of ultrasound in trabecular (cancellous) bone can depend strongly on the frequency. Specifically, trabecular bone can exhibit both relatively high attenuation and strong dispersion. These two features lead to strong distortion of an ultrasonic signal as it propagates, which can make estimation of the speed of sound difficult. Furthermore, the variety of techniques that has been used to estimate times of flight has led to biases in estimates of speed of sound.[13]

Although dispersion has been experimentally observed,[5,14,15] it is generally ignored as a potential parameter for evaluation of structural properties of trabecular bone and changes due to osteoporosis. When dispersion has been studied, it is sometimes discussed in the context of *apparent* inconsistencies between experimental measurements and a form of Kramers-Kronig (K-K) analysis.[5] This paper examines the dispersive properties of trabecular bone and discusses an appropriate framework for the K-K analysis of attenuation and dispersion. In Sec. II, we briefly review the so-called nearly local approximation to the K-K dispersion relations as applied to measurements of biological materials. We then discuss an alternative approach to the K-K analysis that avoids some of the restrictive conditions of the nearly local approximation. This technique is based on a restricted-bandwidth integral approach and the method of subtractions. Methods for experimental measurement and analysis of the attenuation coefficient and phase velocity in bovine trabecular bone are reported in Sec. III. In Sec. IV, we compare measurements of phase velocity with reconstructions based on the K-K analysis of the attenuation coefficient. We close with a discussion of the potential role that K-K analysis can play in regard to experimental measurements and analytical models of ultrasonic propagation in trabecular bone.

[a)]Portions of this work were presented in "Application of the Kramers-Kronig relations to measurements of attenuation and dispersion in cancellous bone," in Proceedings of IEEE International Ultrasonics, Ferroelectrics, and Frequency Control 50th Anniversary Joint Conference, Montréal, Canada, August, 2004.

[b)]Current affiliation is Volcano Corp., Advanced Technology Laboratory, Cleveland, Ohio, 44195.

II. KRAMERS-KRONIG ANALYSIS OF MEASUREMENTS OF BIOLOGICAL MATERIALS

A. Historical perspective

The ultrasonic K-K relations are generally used to relate the phase velocity to the attenuation coefficient. Our present interest is application of the K-K relations to evaluate the consistency of experimental measurements of the propagation properties of trabecular bone. A standard form of the K-K relations as applied to ultrasonic measurements of biological materials is the nearly local approximation that relates the attenuation coefficient to a derivative of the phase velocity[16,17]

$$\alpha(\omega) - \alpha(0) \approx -\frac{\pi}{2}\omega^2 \frac{d}{d\omega}\left(\frac{1}{c(\omega)}\right). \tag{1}$$

This contrasts with the conventional K-K relations that involve infinite integrals.[18] The nearly local approximation to the K-K relations has been shown to be consistent with experimental measurements of materials whose attenuation is approximately proportional to frequency, including soft tissues. Some limitations of the original approximation were identified,[19] but have subsequently been addressed such that differential forms of the K-K relations are available for media with attenuation exhibiting an arbitrary frequency power law.[20] An unspoken assumption in the use of the nearly local approximation is that the form of the attenuation is *implicitly extrapolated* over the entire spectrum (or over a very broad frequency range, at the very least).[20] This assumption seems to be reasonable for soft tissue, but may not be valid for trabecular bone. The linear-with-frequency form of attenuation is sometimes attributed to a distribution of viscous and relaxation losses due to the liquid- and polymer-like nature of soft tissue.[21] These losses are weighted such that the resultant attenuation has the empirically observed linear-with-frequency form. In contrast, trabecular bone is known to be composed of a hard tissue structure (i.e., trabeculae) filled with soft tissue (i.e., bone marrow). Although the trabecular structure is not composed of regular-shaped objects, some success has been demonstrated by modeling the trabecular bone as a network of cylindrical objects.[22] The propagation and scattering properties (e.g., resonances) of cylindrical objects are known to depend on the ratio of the ultrasonic wavelength to scatterer size.[23] Trabeculae have diameters ranging typically from 400 μm down to 100 μm,[24] and can be smaller depending on age[25] as well as disease state. For clinically used ultrasonic frequencies (<2 MHz) and higher frequencies under investigation in laboratories (up to 5 MHz), the ultrasonic wavelength begins to approach the size of the trabecular diameter. In Sec. V we discuss in additional detail the validity of extrapolating ultrasonic properties beyond the experimentally measured bandwidth.

For cases when the attenuation increases linearly with frequency, the nearly local approximation to the K-K relations indicates that the phase velocity should increase logarithmically with frequency. In the case of trabecular bone, a linear-with-frequency attenuation has been observed for a range of bone mineral densities, but the form of the phase velocity is found to *decrease* with frequency for many cases. Based on experience with soft tissue (and linear-with-frequency attenuation), it is this behavior of the propagation properties of trabecular bone that appears to be inconsistent with the K-K analysis based on the nearly local approximation. To illustrate this apparent inconsistency, Fig. 1 compares experimentally measured phase velocity of trabecular bone from bovine tibia with the phase velocity reconstructed from measurements of the corresponding attenuation coefficient using the nearly local approximation. Experimental details are provided in Sec. III, and improved reconstruction results are shown in Sec. IV.

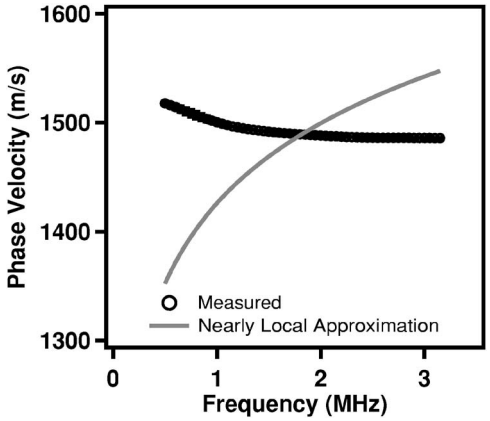

FIG. 1. Illustration of the apparent inconsistency between experimentally measured phase velocity (mean$\pm 2\sigma$) and Kramers-Kronig reconstructed phase velocity using the nearly local approximation for a trabecular bone specimen from the bovine tibia having a low mass density (180 kg/m^3) and oriented along the medial-lateral direction. The Kramers-Kronig reconstructed phase velocity was determined from the corresponding experimentally measured attenuation coefficient shown in Fig. 3.

We propose to use a restricted-bandwidth integral form of the K-K relations with a subtracted form of the ultrasonic quantities[26,27] in an effort to avoid the implicit extrapolation of the nearly local approximation technique. We first state the method of subtractions and its role in this approach. We then describe the restricted-bandwidth integral form of the K-K relations and how artifacts caused by truncation of the integrals can be suppressed.

B. Method of subtractions

The method of subtractions is a standard technique used in K-K analysis to improve the convergence of the integrals.[28] We start with a finite Taylor series expansion of the complex wave number $\kappa(\omega)$

$$\kappa(\omega) = \kappa(\omega_0) + (\omega - \omega_0)\kappa'(\omega_0) + \frac{1}{2!}(\omega - \omega_0)^2\kappa''(\omega_0) + \cdots + (\omega - \omega_0)^n D_n(\omega, \omega_0), \tag{2}$$

where $D_n(\omega, \omega_0)$ is a remainder function that can depend on the frequency of evaluation ω and the frequency of expansion ω_0, and we assume that the complex wave number is sufficiently well behaved at ω_0. The frequency of expansion ω_0 is often referred to as the *subtraction frequency*. If the high-frequency behavior of the complex wave number is such that it is not square integrable, the method of subtrac-

tions can be used to construct a subtracted form of the complex wave number that is indeed square integrable. For example, if the complex wave number grows proportional to frequency for high frequencies [i.e., $\kappa(\omega)=O(\omega)$ as $|\omega|\to\infty$], then the complex wave number with two subtractions $D_2(\omega,\omega_0)$

$$D_2(\omega,\omega_0)=\frac{\kappa(\omega)-\kappa(\omega_0)-(\omega-\omega_0)\kappa'(\omega_0)}{(\omega-\omega_0)^2}, \tag{3}$$

is square integrable and would consequently improve the convergence of the K-K relations. Here, $\kappa(\omega_0)$ and $\kappa'(\omega_0)$ are referred to as *subtraction constants*. A disadvantage to using a subtracted form of the complex wave number is that the value of the complex wave number (and its derivatives) must be known at a particular frequency, namely the subtraction frequency ω_0. In addition, calculation of derivatives can sometimes be problematic with experimental data that include the inherent noise of any experimental system. We note that the use of $\kappa(\omega)$ indicates that we treat the water-filled bone structure of our experiment as an effective medium. Such an approach for other composite media, including suspensions of solid polymer microspheres[26,27] and encapsulated microbubbles,[29] has demonstrated consistency between experimental measurement and K-K analysis.

C. Restricted-bandwidth form of the Kramers-Kronig dispersion relations

A standard form of the K-K relations in terms of the phase velocity $c(\omega)$ and attenuation coefficient $\alpha(\omega)$ can be written as Hilbert transforms

$$\frac{\omega}{c(\omega)}=\frac{1}{\pi}\int_{-\infty}^{\infty}\frac{\alpha(\omega')-\alpha(\omega)}{\omega'-\omega}d\omega' \tag{4}$$

and

$$\alpha(\omega)=-\frac{1}{\pi}\int_{-\infty}^{\infty}\frac{\omega'/c(\omega')-\omega/c(\omega)}{\omega'-\omega}d\omega'. \tag{5}$$

The second term in the numerator of the integrands [$\alpha(\omega)$ or $\omega/c(\omega)$] is constant with respect to the variable of integration and is the subtraction constant. The motivation and justification to subtract a constant in the integrand of the Hilbert transform has been discussed in detail elsewhere.[26,27] As is standard in K-K analysis, it is necessary to know the *absorptive part* $\alpha(\omega)$ over *all frequencies* in order to reconstruct the *dispersive part* $c(\omega)$ at a *single frequency*, and vice versa.

Ultrasonic properties are typically measured over only a limited bandwidth. One approach for handling this situation is to extrapolate the properties over the known bandwidth to the unknown bandwidth. However, it may not be evident how to best handle the *extrapolation problem*. The alternative approach that we consider here truncates the infinite integrals to only the known bandwidth. For example, the Hilbert transform of the attenuation coefficient can be written as five terms (three unknown and two known)

$$\begin{aligned}\frac{\omega}{c(\omega)}=&\underbrace{\frac{1}{\pi}\int_{-\infty}^{-\omega_{\text{high}}}\frac{\alpha(\omega')-\alpha(\omega)}{\omega'-\omega}d\omega'}_{unknown}\\&+\underbrace{\frac{1}{\pi}\int_{-\omega_{\text{high}}}^{-\omega_{\text{low}}}\frac{\alpha(\omega')-\alpha(\omega)}{\omega'-\omega}d\omega'}_{known}\\&+\underbrace{\frac{1}{\pi}\int_{-\omega_{\text{low}}}^{\omega_{\text{low}}}\frac{\alpha(\omega')-\alpha(\omega)}{\omega'-\omega}d\omega'}_{unknown}\\&+\underbrace{\frac{1}{\pi}\int_{\omega_{\text{low}}}^{\omega_{\text{high}}}\frac{\alpha(\omega')-\alpha(\omega)}{\omega'-\omega}d\omega'}_{known}\\&+\underbrace{\frac{1}{\pi}\int_{\omega_{\text{high}}}^{\infty}\frac{\alpha(\omega')-\alpha(\omega)}{\omega'-\omega}d\omega'}_{unknown},\end{aligned} \tag{6}$$

where the experimental bandwidth is restricted to those frequencies between ω_{low} and ω_{high} ($0\leqslant\omega_{\text{low}}\leqslant\omega_{\text{high}}$). Considering the symmetry properties of $\alpha(\omega)$ [i.e., $\alpha(-\omega)=\alpha(\omega)$], we can rewrite Eq. (6) over non-negative frequencies

$$\begin{aligned}\frac{\omega}{c(\omega)}=&\underbrace{\frac{1}{\pi}\int_{0}^{\omega_{\text{low}}}\left[\frac{\alpha(\omega')-\alpha(\omega)}{\omega'-\omega}-\frac{\alpha(\omega')-\alpha(\omega)}{\omega'+\omega}\right]d\omega'}_{unknown}\\&+\underbrace{\frac{1}{\pi}\int_{\omega_{\text{low}}}^{\omega_{\text{high}}}\left[\frac{\alpha(\omega')-\alpha(\omega)}{\omega'-\omega}-\frac{\alpha(\omega')-\alpha(\omega)}{\omega'+\omega}\right]d\omega'}_{known}\\&+\underbrace{\frac{1}{\pi}\int_{\omega_{\text{high}}}^{\infty}\left[\frac{\alpha(\omega')-\alpha(\omega)}{\omega'-\omega}-\frac{\alpha(\omega')-\alpha(\omega)}{\omega'+\omega}\right]d\omega'}_{unknown}.\end{aligned} \tag{7}$$

By truncating the Hilbert transform to be over only the known bandwidth

$$\begin{aligned}\frac{\omega}{c(\omega)}=&\frac{1}{\pi}\int_{\omega_{\text{low}}}^{\omega_{\text{high}}}\left[\frac{\alpha(\omega')-\alpha(\omega)}{\omega'-\omega}-\frac{\alpha(\omega')-\alpha(\omega)}{\omega'+\omega}\right]d\omega'\\&+A^{(0)}_{\alpha\to c}(\omega,\omega_{\text{low}},\omega_{\text{high}}),\end{aligned} \tag{8}$$

we introduce a term $A^{(0)}_{\alpha\to c}(\omega,\omega_{\text{low}},\omega_{\text{high}})$ to represent the unknown integrals in Eq. (7). For present purposes, we shall consider this term as an *artifact* due to the integral truncation that can depend on the frequency of evaluation ω and the limits of the experimental bandwidth ω_{low} and ω_{high}. The superscript (0) of $A^{(0)}_{\alpha\to c}$ indicates that the artifact term is for the complex wave number with zero subtractions, and the subscript $\alpha\to c$ indicates that the attenuation coefficient $\alpha(\omega)$ is integrated to reconstruct the phase velocity $c(\omega)$. Because there are no parameters in this form of the restricted-bandwidth K-K dispersion relation to adjust, there is no means to compensate for the effects of this

artifact. This leads us to consider the method of subtractions to reduce the impact of the artifact.

The ultrasonic complex wave number with two subtractions $[D_2(\omega,\omega_0)]$ appears to be sufficient for establishing the Hilbert transforms.[30] One form of the exact (so-called unrestricted bandwidth) Hilbert transform for the complex wave number with two subtractions can be written as

$$\mathrm{Re}\, D_2(\omega,\omega_0) = \frac{1}{\pi}\int_{-\infty}^{\infty} \frac{\mathrm{Im}\, D_2(\omega',\omega_0) - \mathrm{Im}\, D_2(\omega,\omega_0)}{\omega'-\omega} d\omega', \tag{9}$$

or substituting the phase velocity $c(\omega)$ and attenuation coefficient $\alpha(\omega)$ into the real and imaginary parts of $D_2(\omega,\omega_0)$, we find

$$\begin{aligned}\frac{\omega}{c(\omega)} = \frac{\omega_0}{c(\omega_0)} &+ (\omega-\omega_0)\frac{d}{d\omega}\frac{\omega}{c(\omega)}\bigg|_{\omega=\omega_0} + \frac{1}{\pi}(\omega-\omega_0)^2 \\ &\times \int_{-\infty}^{\infty}\left[\frac{\alpha(\omega')-\alpha(\omega_0)-(\omega'-\omega_0)\alpha'(\omega_0)}{(\omega'-\omega_0)^2}\right. \\ &\left. - \frac{\alpha(\omega)-\alpha(\omega_0)-(\omega-\omega_0)\alpha'(\omega_0)}{(\omega-\omega_0)^2}\right]\frac{d\omega'}{\omega'-\omega}. \end{aligned} \tag{10}$$

We next consider a restricted-bandwidth form of the Hilbert transform of the complex wave number with two subtractions written over non-negative frequencies

$$\begin{aligned}\frac{\omega}{c(\omega)} = \frac{\omega_0}{c(\omega_0)} &+ (\omega-\omega_0)\frac{d}{d\omega}\frac{\omega}{c(\omega)}\bigg|_{\omega=\omega_0} + \frac{(\omega-\omega_0)^2}{\pi} \\ &\times \int_{\omega_{\mathrm{low}}}^{\omega_{\mathrm{high}}}\left[\frac{\alpha(\omega')-\alpha(\omega_0)-(\omega'-\omega_0)\alpha'(\omega_0)}{(\omega'-\omega_0)^2}\right. \\ &\left. - \frac{\alpha(\omega)-\alpha(\omega_0)-(\omega-\omega_0)\alpha'(\omega_0)}{(\omega-\omega_0)^2}\right]\frac{d\omega'}{\omega'-\omega} \\ &- \frac{(\omega-\omega_0)^2}{\pi} \\ &\times \int_{\omega_{\mathrm{low}}}^{\omega_{\mathrm{high}}}\left[\frac{\alpha(\omega')-\alpha(\omega_0)+(\omega'+\omega_0)\alpha'(\omega_0)}{(\omega'+\omega_0)^2}\right. \\ &\left. - \frac{\alpha(\omega)-\alpha(\omega_0)-(\omega-\omega_0)\alpha'(\omega_0)}{(\omega-\omega_0)^2}\right]\frac{d\omega'}{\omega'+\omega} \\ &+ A^{(2)}_{\alpha\to c}(\omega,\omega_{\mathrm{low}},\omega_{\mathrm{high}},\omega_0), \end{aligned} \tag{11}$$

where our artifact term $A^{(2)}_{\alpha\to c}$ may now depend on the subtraction frequency ω_0 in addition to the limits of our experimental bandwidth (ω_{low} and ω_{high}) and the frequency of evaluation ω.

Following some algebraic manipulation, we can rewrite this in a so-called *expansion form* of the K-K relations[26,27] as

$$\begin{aligned}\frac{\omega}{c(\omega)} = \frac{\omega_0}{c(\omega_0)} &+ (\omega-\omega_0)\frac{d}{d\omega}\frac{\omega}{c(\omega)}\bigg|_{\omega=\omega_0} \\ &+ I_\alpha(\omega,\omega_{\mathrm{low}},\omega_{\mathrm{high}}) - I_\alpha(\omega_0,\omega_{\mathrm{low}},\omega_{\mathrm{high}}) - (\omega-\omega_0) \\ &\times \frac{d}{d\omega} I_\alpha(\omega,\omega_{\mathrm{low}},\omega_{\mathrm{high}})\bigg|_{\omega=\omega_0} \\ &+ A^{(2)}_{\alpha\to c}(\omega,\omega_{\mathrm{low}},\omega_{\mathrm{high}},\omega_0), \end{aligned} \tag{12}$$

where

$$\begin{aligned} I_\alpha(\omega,\omega_{\mathrm{low}},\omega_{\mathrm{high}}) = \frac{1}{\pi}\int_{\omega_{\mathrm{low}}}^{\omega_{\mathrm{high}}}&\left[\frac{\alpha(\omega')-\alpha(\omega)}{\omega'-\omega}\right. \\ &\left. - \frac{\alpha(\omega')-\alpha(\omega)}{\omega'+\omega}\right]d\omega'. \end{aligned} \tag{13}$$

The subtracted nature of this approach is apparent in the expansion form of the K-K relations. We remark that the local variations in $\omega/c(\omega)$ are determined in large part by the first integral on the right-hand side of Eq. (12) $[I_\alpha(\omega,\omega_{\mathrm{low}},\omega_{\mathrm{high}})]$. The remaining integral terms $I_\alpha(\omega_0,\omega_{\mathrm{low}},\omega_{\mathrm{high}})$ and $(\omega-\omega_0)(d/d\omega)I_\alpha(\omega,\omega_{\mathrm{low}},\omega_{\mathrm{high}})|_{\omega=\omega_0}$ define a linear contribution (with respect to ω) whose slope and intercept is a function of the subtraction frequency ω_0.

The present strategy is to compensate for the unknown term $A^{(2)}_{\alpha\to c}$ through a judicious choice of the subtraction frequency ω_0. The degree to which the unknown parts of the Hilbert transform are compensated will be evaluated based on statistical comparisons of the experimentally measured phase velocity with the reconstructed phase velocity. We remark that a similar development is available for reconstructing the attenuation coefficient in terms of the phase velocity.[26,27]

III. EXPERIMENTAL METHODS

A. Specimen preparation

Trabecular bone specimens ($n=10$) were obtained from the proximal end of four bovine tibia, cut into cubes (approximately 15-mm sides), and then prepared with the axis of measurement along the medial-lateral ($n_{\mathrm{ML}}=5$) and superior-inferior ($n_{\mathrm{SI}}=5$) directions. Although measurements in the medial-lateral direction are more clinically relevant than those in the superior-inferior direction, we include measurements in the superior-inferior direction because they provide a wider range of cases for which to examine the K-K analysis. Marrow was removed prior to measurement. Apparent densities were (96 to 534) kg/m^3. Further details of specimen preparation are available elsewhere.[31] For purposes of the present study, densities of approximately 250 kg/m^3 and lower are considered low density, between 250 and 500 kg/m^3 are considered medium density, and above 500 kg/m^3 are considered high density. These categories were selected based on common features of the time-domain and corresponding frequency-domain characteristics of the ultrasonic signals. Briefly, seven low-density specimens with medial-lateral and superior-inferior orientations exhibited little dispersion (or *spreading*) in the time-domain signal.

TABLE I. Summary of bone specimen details and experimental results (mean values only). The bone specimens are listed in order of increasing density. Specimens 1–7 correspond to the low-density category, specimens 8 and 9 correspond to the medium-density category, and specimen 10 corresponds to the high-density category. For each specimen, we report the density, the anatomical orientation [medial-lateral (ML) or superior-inferior (SI)], the type of wave [fast (F) or slow (S)], the peak-detected speed of sound (c_{pk}), the threshold-detected speed of sound (c_{th}), the −20-dB bandwidth, the normalized broadband ultrasonic attenuation (nBUA), the measured dispersion (Δc), the Kramers-Kronig (K-K) reconstructed dispersion (Δc_{KK}), and the subtraction frequency (f_0).

				Time-domain analysis		Frequency-domain analysis			K-K analysis	
Specimen	Density (kg/m^3)	Orientation	Wave type	c_{pk} (m/s)	c_{th} (m/s)	Bandwidth (MHz)	nBUA (dB/cm/MHz)	Δc (m/s)	Δc_{KK} (m/s)	f_0 (MHz)
1	96	ML	S	1491.5	1488.6	0.50–3.30	3.6	−11.7	−12.3	0.65
2	160	SI	S	1489.0	1486.1	0.50–3.30	2.6	6.3	8.1	1.85
3	180	ML	S	1476.9	1473.9	0.50–3.15	6.8	−31.7	−37.4	2.05
4	187	SI	S	1478.5	1472.1	0.50–3.20	4.9	−55.9	−55.9	1.20
5	193	SI	S	1478.1	1487.3	0.50–3.30	2.8	23.5	20.8	1.65
6	211	ML	S	1481.4	1481.4	0.50–3.15	5.4	−40.1	−43.9	0.65
7	251	SI	S	1475.0	1481.0	0.50–3.20	2.8	18.8	20.3	2.20
8	290	ML	S	1469.2	1685.4	0.50–3.00	14.1	−92.5	−110.8	1.25
9	300	ML	S	1469.7	1902.3	0.50–2.50	20.5	−115.7	−163.5	2.20
10	534	SI	F	1455.2	2830.5	0.50–2.50	20.3	247.4	226.1	1.25
			S			0.50–3.10	7.8	35.7	46.7	1.85

Two medium-density specimens with medial-lateral orientation exhibited a modest degree of dispersion and were more attenuating than the low-density specimens. One high-density specimen with superior-inferior orientation exhibited both a fast and slow wave in the time-domain signal.

B. Experimental setup and data acquisition

Measurements were performed in a water bath ($T \approx 23\ ^\circ$C) using a pair of planar transducers (2.25 MHz, 12.7-mm diameter) aligned coaxially. A broadband pulser/receiver was used to generate and detect electrical signals. Received signals were digitized at a sampling rate of 100 MHz with 8-bit resolution, temporally averaged 256 times, and then transferred to a personal computer for off-line analysis. Measurements were performed with both sides of a given specimen orientation toward the transmitting transducer (e.g., medial side and lateral side). Additional details of the experimental setup are available elsewhere.[8]

C. Frequency-domain analysis

The attenuation coefficient and phase velocity of the bone specimens were determined by spectral analysis[32] of the ultrasonic signals, as given by

$$\alpha(\omega) = 20 \log_{10}(|F_{ref}(\omega)|/|F_{bone}(\omega)|)/L, \tag{14}$$

and

$$c(\omega) = v_w/[1 - v_w \Delta\varphi(\omega)/\omega L], \tag{15}$$

where $F_{ref}(\omega)$ is the Fourier transform of the reference path signal, $F_{bone}(\omega)$ is the Fourier transform of the signal through bone, L is the thickness of the bone specimen, v_w is the speed of sound in water,[33] $\Delta\varphi(\omega)$ is the change in phase between the reference and bone measurements, and ω is angular frequency. The ultrasonic signals were temporally gated. In the case where a fast wave and a slow wave exist, we first applied a gate that included only the fast wave and then applied a gate that included only the slow wave. In cases where the fast and slow waves are suspected to exist but overlap in time (e.g., medium-density specimens), the time-domain signal was treated as a single wave.

D. Kramers-Kronig analysis

The reconstruction of phase velocity from measurements of the attenuation coefficient was performed using the expansion form of the restricted-bandwidth form of the K-K relations, Eqs. (12) and (13). The lower and upper limits of the experimental bandwidth (ω_{low} and ω_{high}) corresponded to the −20-dB level of the water-path reference and bone measurements. The subtraction frequency ω_0 was determined empirically by sweeping through the bandwidth and selecting the ω_0 that minimized the discrepancy (least-square error) between the experimentally measured phase velocity and K-K reconstructed phase velocity.

IV. RESULTS

Quantitative results of the time-domain, frequency-domain, and K-K analyses for all bone specimens are summarized in Table I. The bone specimens are listed in order of increasing density. The results for each specimen include density, anatomical orientation (medial-lateral or superior-inferior), wave type (fast or slow), speed of sound (peak and threshold techniques), bandwidth, normalized broadband ultrasonic attenuation (nBUA), measured dispersion, K-K reconstructed dispersion, and subtraction frequency. All reported ultrasonic parameters are mean values. We discuss these results in more detail below.

A. Time-domain analysis

Representative time-domain waveforms of the ultrasonic signals that have propagated through trabecular bone specimens are shown in Fig. 2. The ultrasound propagates with modest loss and dispersion in the low-density (medial-

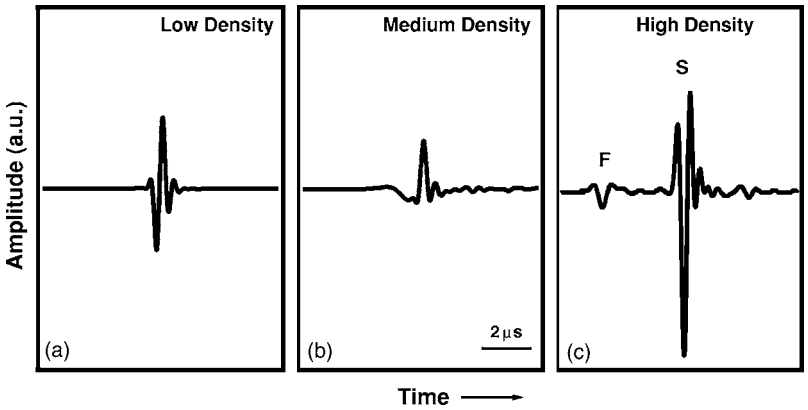

FIG. 2. Representative time-domain ultrasonic signals after having propagated through trabecular bone specimens from the bovine tibia having the following anatomical orientation and mass densities: (a) medial-lateral orientation, low mass density (180 kg/m^3); (b) medial-lateral orientation, medium mass density (290 kg/m^3); (c) superior-inferior orientation, high mass density (534 kg/m^3). These time-domain signals are indicative of the variation in attenuation and dispersion found in trabecular bone. The vertical scale for amplitude [in arbitrary units (a.u.)] is identical in each plot. A time scale bar of 2 μs is included.

lateral) specimen [Fig. 2(a)] and with moderate loss and dispersion in the medium-density (medial-lateral) specimen [Fig. 2(b)]. The high-density (superior-inferior) specimen [Fig. 2(c)] exhibits both a fast and slow wave. We list in Table I the corresponding speeds of sound as estimated by a peak-detected and threshold-detected (10% of peak) time of flight. Although the speeds of sound are not of primary interest for the present investigation, they do illustrate the discrepancy between the two techniques for specimens that are more lossy and dispersive. The implications of these discrepancies for bone characterization have been discussed in detail by Wear.[13]

B. Frequency-domain analysis

The phase velocities and attenuation coefficients corresponding to the waveforms in Figs. 2(a), 2(b), and 2(c) are shown in Figs. 3–5 respectively. Values reported are the mean of the measurements performed in both directions of a given orientation. The error bars represent 2 standard deviations. As expected from the time-domain waveforms, the medium-density (medial-lateral) specimen (Fig. 4) exhibits attenuation larger than that of the low-density (medial-lateral) specimen (Fig. 3). The fast wave of the high-density (superior-inferior) specimen is, however, the most lossy and dispersive (Fig. 5). Negative dispersion is observed for the low- and medium-density specimens, whereas positive dispersion is observed for the high-density (superior-inferior) specimen. Only the medium-density (medial-lateral) specimen exhibits attenuation that might not be considered linear with frequency. We discuss these results in the context of a poroelastic model in Sec. V. Quantitative values are listed in Table I for nBUA (in units of dB/cm/MHz) and dispersion across the −20-dB bandwidth for each specimen.

C. Kramers-Kronig analysis

The measured and K-K reconstructed phase velocities for each representative specimen are shown in Fig. 6. We observe good agreement in all cases. We remark that the reconstructed phase velocity of the low-density specimen using the restricted-bandwidth forms of the K-K relations [Fig. 6(a)] contrasts markedly with the reconstructed phase velocity using the nearly local approximation to the K-K relations (Fig. 1). The empirically determined subtraction frequencies for the low-, medium-, and (fast wave and slow wave) high-density specimens are, respectively, 2.05, 1.25, 1.25, and 1.85 MHz. The subtraction frequency and the K-K reconstructed dispersion for all specimens are listed in Table I.

The measured and K-K reconstructed dispersions across the experimental bandwidth for all specimens are compared in Fig. 7. We observe good agreement, which indicates that the measured attenuation coefficient and phase velocity are consistent with one another within the limits of the K-K

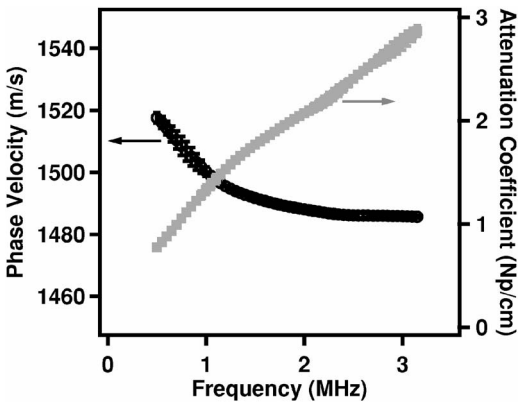

FIG. 3. Phase velocity and attenuation coefficient (mean$\pm 2\sigma$) for a trabecular bone specimen from the bovine tibia having a low mass density (180 kg/m^3) and oriented along the medial-lateral direction. The frequency dependence of both the phase velocity and attenuation is modest. This specimen exhibits a dispersion of approximately −30 m/s.

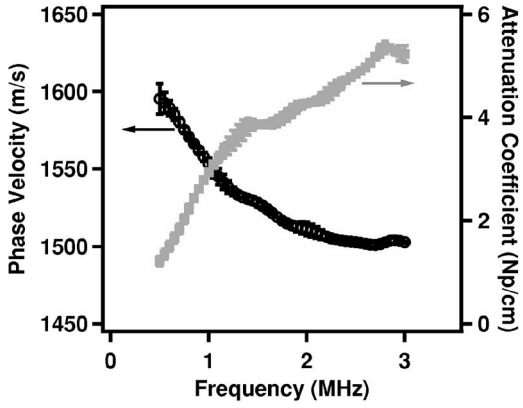

FIG. 4. Phase velocity and attenuation coefficient (mean$\pm 2\sigma$) for a trabecular bone specimen from the bovine tibia having a medium mass density (290 kg/m^3) and oriented along the medial-lateral direction. The frequency dependence of both the phase velocity and attenuation is appreciable. This specimen exhibits a dispersion of approximately −90 m/s.

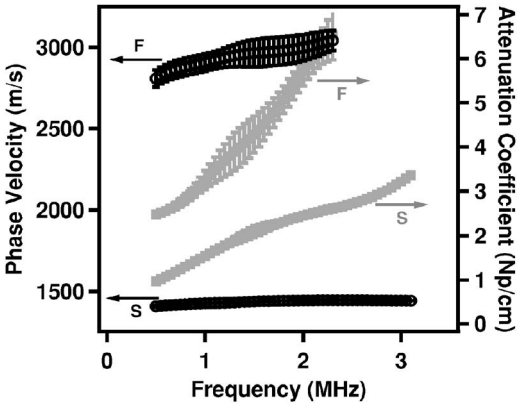

FIG. 5. Phase velocity and attenuation coefficient (mean$\pm 2\sigma$) for both the fast and slow propagation modes in a trabecular bone specimen from the bovine tibia having a high mass density (534 kg/m^3) and oriented along the superior-inferior direction. The frequency dependence of the phase velocity and attenuation for the fast mode is strong, exhibiting a dispersion of approximately +250 m/s. The frequency dependence of the phase velocity and attenuation for the slow mode is modest, exhibiting a dispersion of approximately +35 m/s.

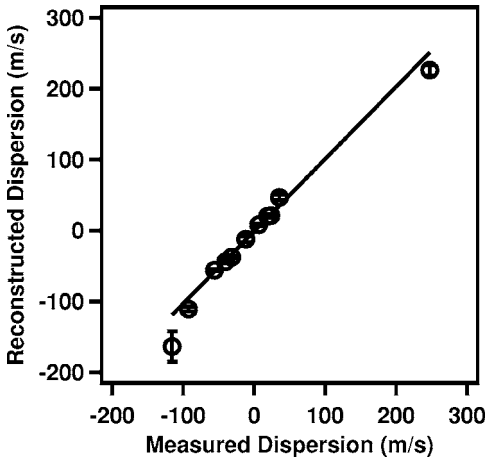

FIG. 7. Comparison of experimentally measured and Kramers-Kronig reconstructed dispersions (mean$\pm 2\sigma$) of trabecular bone specimens from the bovine tibia. A weighted least-squares regression linear fit has a slope of 1.0. The correlation coefficient is $R^2=0.61$.

analysis. The weighted least-squares regression linear fit has a correlation coefficient of $R^2=0.61$. It can be observed that absolute discrepancies are larger for the larger magnitudes of dispersion. Because we have a small population of specimens, it is difficult to say whether the modest correlation is indicative of a limitation of this technique for larger magnitudes of dispersion. However, there is no *a priori* reason based on the development of the K-K relations to expect such a limitation.

V. DISCUSSION

The K-K relations provide a useful tool for evaluating the consistency of measurements of attenuation and dispersion in trabecular bone. Furthermore, accurate reconstructions of the phase velocity are achieved without use of unmeasured or extrapolated parameters. In particular, this approach appears to be capable of reconstructing a phase velocity having either positive or negative dispersion. By use of a restricted-bandwidth form of the K-K relations, we have avoided extrapolation of the ultrasonic properties beyond the measured bandwidth. In contrast, the nearly local approximation to the K-K relations involves an implicit assumption that the same behavior exists outside the measured bandwidth. The reconstructed phase velocity using the nearly local approximation to the K-K relation exhibits a logarithmic increase with frequency, as shown in Fig. 1. This contrasts with the modest negative decrease of the measured phase velocity and reconstructed phase velocity using the restricted-bandwidth K-K relations as shown in Fig. 6(a). As mentioned in Sec. II, we expect that the forms of the propagation properties (attenuation and dispersion) of trabecular bone are sensitive to the ratio of the scatterer size to ultrasonic wavelength, particularly over ultrasound frequencies where the wavelength and size of trabeculae are of the same order. That is, we do not expect the same propagating and scattering behavior under the so-called Rayleigh regime when the ultrasonic wavelength is much greater than that of the mean scatterer size (e.g., 3-mm wavelength near 500 kHz for trabecular diameters less than 100 μm) compared to cases when the wavelength is the same order of scatterer size. Consequently, extrapolation of the propagation properties beyond the measured bandwidth is suspect. In addition, this type of erroneous extrapolation when using forms of the K-K relations that require unrestricted bandwidths could lead to artifacts in the reconstruction of the propagation properties, as we observed in Fig. 1. In future studies, it would be useful to have accompanying morphological information available from high-resolution imaging techniques such as microcomputed tomography that can achieve resolutions on the order of tens of microns.

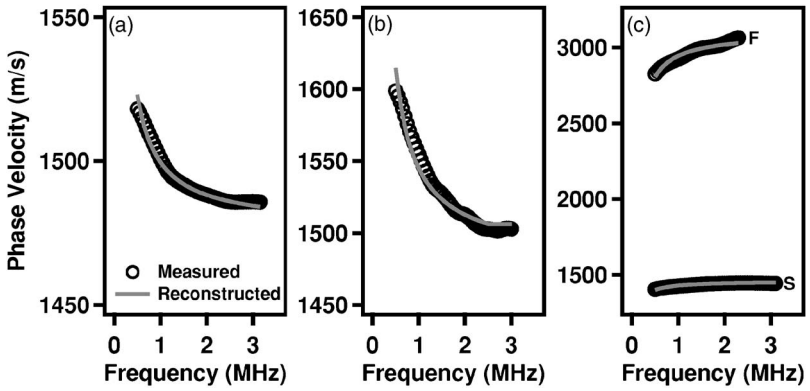

FIG. 6. Comparison of experimentally measured and Kramers-Kronig reconstructed phase velocities of trabecular bone specimens from the bovine tibia having the following anatomical orientation and mass densities: (a) medial-lateral orientation, low mass density (180 kg/m^3); (b) medial-lateral orientation, medium mass density (290 kg/m^3); (c) superior-inferior orientation, high mass density (534 kg/m^3). The Kramers-Kronig analysis was performed using a restricted-bandwidth form and the complex wave number with two subtractions. The subtraction frequencies for each measurement are: (a) 2.05 MHz; (b) 1.25 MHz; and (c) 1.25 and 1.85 MHz for the fast and slow modes, respectively.

Although we find good agreement between the measured and K-K reconstructed dispersions for trabecular bone specimens having a range of densities, the sensitivity of our present approach to the choice of subtraction frequency is somewhat unsatisfactory. In essence, the subtraction frequency is free to slide across our experimental bandwidth and is selected only on a statistical basis that minimized discrepancies between the K-K reconstruction and experimental measurement. Approximately 20% of frequencies within the experimental bandwidth result in K-K reconstructions that agree with experimental measurement. This sensitivity has previously been explored in some detail[26,27] for the case of resonant media. Subtraction frequencies that led to reconstructions that were inconsistent with experimental measurement generally introduced an artifact that grew linearly with frequency, as described in Sec. II C. It is a topic of continuing research to determine if some physical insight can be inferred from the choice of subtraction frequency. One could speculate that such an approach would be similar in spirit to techniques employed in high-energy physics that relate subtraction constants to coupling constants that characterize the physical system (e.g., the so-called scattering length).[34]

One can alternatively consider techniques that reduce or eliminate the impact of subtraction constants. Recent progress[29] indicates that a stricter test of the consistency between measured and K-K reconstructed ultrasonic properties can be found by examining the first derivative of the complex wave number, namely the group velocity and the first derivative of the attenuation coefficient (or slope of attenuation). For this approach, the subtraction frequency leads to only a constant offset in the reconstruction of the phase velocity, rather than a linear trend as discussed in Sec. II C. We have also shown that a *generalized* form of the K-K relations can be formulated without subtraction constants,[35] for which physical quantities such as the complex wave number are treated as generalized functions or distributions rather than point functions. The attraction of such an approach is that the sometimes cumbersome nature of the K-K relations with subtractions is avoided.

The restricted-bandwidth form of the K-K relations may also help improve analytical models of how ultrasound interacts with the trabecular bone structure. We emphasize that the K-K relations do not indicate whether a physical model is correct, only that consistency of a model or measurement indicates consistency with the assumptions of the K-K relations, namely causality and linearity. A promising theory is the Biot model as applied to poroelastic media[36,37] in which both fast and slow compressional waves are predicted to exist,[27] similar to the case shown in Fig. 2(c). The fast wave develops when the particle velocity in the fluid (water) is in phase with the particle velocity in the solid (trabecular bone structure). The slow wave develops when these two particle velocities are out of phase with one another. For our experimental setup, it is not yet clear how efficiently these modes are generated, and this issue of coupling is a topic of continuing study. Although the Biot model does account for the dispersive effects of a medium, these are often ignored in models applied to the interaction of ultrasound with trabecular bone.[38] The K-K relations could play a role in developing a form of the Biot model for trabecular bone similar to its role[39] in the use of the time-causal wave equation[40] for propagation in media with attenuation obeying a frequency power law. In the case of the time-causal wave equation, the form of the time-domain convolution loss operator depends on the relationship of the attenuation coefficient and phase velocity as determined by the time-domain representation of the Hilbert transform (or K-K relations).

VI. CONCLUDING REMARKS

We have applied a restricted-bandwidth form of the Kramers-Kronig dispersion relations with subtractions to *in vitro* measurements of trabecular bone from bovine tibial specimens in order to evaluate the causal consistency between the attenuation coefficient and phase velocity. The restricted-bandwidth form uses the subtraction frequency as a fitting parameter. The role of the subtraction frequency is, however, not yet completely understood. We found good agreement between the measured phase velocities and phase velocities reconstructed via Kramers-Kronig analysis of the measured attenuation coefficient. The restricted-bandwidth form improves upon previous applications of a nearly local approximation to the Kramers-Kronig dispersion relations without need for unmeasured or extrapolated properties. The application of these relations may provide further insight into how ultrasound interacts with trabecular bone and can lead to improved analytical models.

ACKNOWLEDGMENTS

The authors thank Dr. Joel Mobley (National Center for Physical Acoustics) for discussions regarding the Kramers-Kronig analysis. This research was performed while K. R. W. held a National Research Council Research Associateship Award at the National Institute of Standards and Technology.

[1] C. M. Langton, S. B. Palmer, and R. W. Porter, "The measurement of broadband ultrasonic attenuation in cancellous bone," Phys. Med. Biol. **30**, 98–99 (1985).
[2] C. C. Gluer, C. Y. Wu, M. Jergas, S. A. Goldstein, and H. K. Genant, "Three quantitative ultrasound parameters reflect bone structure," Calcif. Tissue Int. **55**, 46–52 (1994).
[3] P. H. F. Nicholson, M. J. Haddaway, and M. W. J. Davie, "The dependence of ultrasonic properties on orientation in human vertebral bone," Phys. Med. Biol. **39**, 1013–1024 (1994).
[4] S. Han, J. Rho, J. Medige, and I. Ziv, "Ultrasound velocity and broadband attenuation over a wide range of bone mineral density," Osteoporosis Int. **6**, 291–296 (1996).
[5] P. Droin, G. Berger, and P. Laugier, "Velocity dispersion of acoustic waves in cancellous bone," IEEE Trans. Ultrason. Ferroelectr. Freq. Control **45**, 581–592 (1998).
[6] A. Hosokawa and T. Otani, "Acoustic anisotropy in bovine cancellous bone," J. Acoust. Soc. Am. **103**, 2718–2722 (1998).
[7] K. A. Wear and B. S. Garra, "Assessment of bone density using ultrasonic backscatter," Ultrasound Med. Biol. **24**, 689–695 (1998).
[8] B. K. Hoffmeister, S. A. Whitten, and J. Y. Rho, "Low-megahertz ultrasonic properties of bovine cancellous bone," Bone (N.Y.) **26**, 635–642 (2000).
[9] K. A. Wear and D. W. Armstrong, "Relationships among calcaneal backscatter, attenuation, sound speed, hip bone mineral density, and age in normal adult women," J. Acoust. Soc. Am. **110**, 573–578 (2001).
[10] S. Chaffai, F. Peyrin, S. Nuzzo, R. Porcher, G. Berger, and P. Laugier, "Ultrasonic characterization of human cancellous bone using transmission and backscatter measurements: Relationships to density and microstruc-

ture," Bone (N.Y.) **30**, 229–237 (2002).
[11]C. Roux, V. Roberjot, R. Porcher, S. Kolta, M. Dougados, and P. Laugier, "Ultrasonic backscatter and transmission parameters at the os calcis in postmenopausal osteoporosis," J. Bone Miner. Res. **16**, 1353–1362 (2001).
[12]B. K. Hoffmeister, S. R. Smith, S. M. Handley, and J. Y. Rho, "Anisotropy of Young's modulus of human tibial cortical bone," Med. Biol. Eng. Comput. **38**, 333–338 (2000).
[13]K. A. Wear, "The effects of frequency-dependent attenuation and dispersion on sound speed measurements: Applications in human trabecular bone," IEEE Trans. Ultrason. Ferroelectr. Freq. Control **47**, 265–273 (2000).
[14]P. H. F. Nicholson, G. Lowet, C. M. Langton, J. Dequeker, and G. van der Perre, "A comparison of time-domain and frequency-domain approaches to ultrasonic velocity measurement in trabecular bone," Phys. Med. Biol. **41**, 2421–2435 (1996).
[15]K. A. Wear, "Measurements of phase velocity and group velocity in human calcaneus," Ultrasound Med. Biol. **26**, 641–646 (2000).
[16]M. O'Donnell, E. T. Jaynes, and J. G. Miller, "General relationships between ultrasonic attenuation and dispersion," J. Acoust. Soc. Am. **63**, 1935–1937 (1978).
[17]M. O'Donnell, E. T. Jaynes, and J. G. Miller, "Kramers-Kronig relationship between ultrasonic attenuation and phase velocity," J. Acoust. Soc. Am. **69**, 696–701 (1981).
[18]K. R. Waters, M. S. Hughes, J. Mobley, G. H. Brandenburger, and J. G. Miller, "On the applicability of Kramers-Kronig relations for media with attenuation obeying a frequency power law," J. Acoust. Soc. Am. **108**, 556–563 (2000).
[19]T. L. Szabo, "Causal theories and data for acoustic attenuation obeying a frequency power law," J. Acoust. Soc. Am. **97**, 14–24 (1995).
[20]K. R. Waters, M. S. Hughes, J. Mobley, and J. G. Miller, "Differential forms of the Kramers-Kronig dispersion relations," IEEE Trans. Ultrason. Ferroelectr. Freq. Control **50**, 68–76 (2003).
[21]F. Dunn and S. A. Goss, "Definition of Terms and Measurements of Acoustical Quantities," in *Tissue Characterization With Ultrasound. Volume I. Methods*, edited by J. F. Greenleaf (CRC Press, Boca Raton, 1986), Chap. 1, pp. 1–13.
[22]K. A. Wear, "Frequency dependence of ultrasonic backscatter from human trabecular bone: Theory and experiment," J. Acoust. Soc. Am. **106**, 3659–3664 (1999).
[23]J. J. Faran, "Sound scattering by solid cylinders and spheres," J. Acoust. Soc. Am. **23**, 405–418 (1951).
[24]H. K. Genant, C. Gordon, Y. Jiang, T. F. Lang, T. M. Link, and S. Majumdar, "Advanced imaging of bone macro and micro structure," Bone (N.Y.) **25**, 149–152 (1999).
[25]S. Chaffai, V. Roberjot, F. Peyrin, G. Berger, and P. Laugier, "Frequency dependence of ultrasonic backscattering in cancellous bone: Autocorrelation model and experimental results," J. Acoust. Soc. Am. **108**, 2403–2411 (2000).
[26]J. Mobley, K. R. Waters, M. S. Hughes, C. S. Hall, J. N. Marsh, G. H. Brandenburger, and J. G. Miller, "Kramers-Kronig relations in ultrasonics: Applications to finite-bandwidth data of encapsulated microbubbles," J. Acoust. Soc. Am. **108**, 2091–2106 (2000).
[27]J. Mobley, K. R. Waters, M. S. Hughes, C. S. Hall, J. N. Marsh, G. H. Brandenburger, and J. G. Miller, "Erratum: 'Kramers-Kronig relations applied to finite bandwidth data from suspensions of encapsulated microbubbles' [J. Acoust. Soc. Am. **108**, 2091–2106 (2000)]," J. Acoust. Soc. Am. **112**, 760–761 (2002).
[28]H. M. Nussenzveig, *Causality and Dispersion Relations*, 1st ed. (Academic, New York, 1972), pp. 28–33.
[29]J. Mobley, K. R. Waters, and J. G. Miller, "Causal determination of acoustic group velocity and frequency derivative of attenuation with finite-bandwidth Kramers-Kronig relations," Phys. Rev. E **72**, 016604 (2005).
[30]J. Mobley, K. R. Waters, and J. G. Miller, "Finite bandwidth effects on the causal prediction of ultrasonic attenuation of the power-law form," J. Acoust. Soc. Am. **114**, 2782–2790 (2003).
[31]B. K. Hoffmeister, J. A. Auwarter, and J. Y. Rho, "Effect of marrow on the high frequency ultrasonic properties of cancellous bone," Phys. Med. Biol. **47**, 3419–3429 (2002).
[32]W. Sachse and Y.-H. Pao, "On the determination of phase and group velocities of dispersive waves in solids," J. Appl. Phys. **49**, 4320–4327 (1978).
[33]M. Greenspan and C. E. Tschiegg, "Tables of the Speed of Sound in Water," J. Acoust. Soc. Am. **31**, 75–76 (1959).
[34]H. M. Nussenzveig, *Causality and Dispersion Relations*, 1st ed. (Academic, New York, 1972), pp. 127–131.
[35]K. R. Waters, J. Mobley, and J. G. Miller, "Causality-imposed (Kramers-Kronig) relationships between attenuation and dispersion," IEEE Trans. Ultrason. Ferroelectr. Freq. Control **52**, 822–833 (2005).
[36]M. A. Biot, "The theory of propagation of elastic waves in fluid-saturated porous solid. I. Low frequency range," J. Acoust. Soc. Am. **28**, 168–178 (1956).
[37]M. A. Biot, "The theory of propagation of elastic waves in fluid-saturated porous solid. II. Higher frequency range," J. Acoust. Soc. Am. **28**, 179–191 (1956).
[38]Z. E. A. Fellah, J. Y. Chapelon, S. Berger, W. Lauriks, and C. Depollier, "Ultrasonic wave propagation in human cancellous bone: Application of Biot theory," J. Acoust. Soc. Am. **116**, 61–73 (2004).
[39]K. R. Waters, M. S. Hughes, G. H. Brandenburger, and J. G. Miller, "On a time-domain representation of the Kramers-Kronig dispersion relations," J. Acoust. Soc. Am. **108**, 2114–2119 (2000).
[40]T. L. Szabo, "Time-domain wave equations for lossy media obeying a frequency power law," J. Acoust. Soc. Am. **96**, 491–500 (1994).

Localization of aerial pure tones by pinnipeds

Marla M. Holt, Ronald J. Schusterman, and David Kastak
Long Marine Laboratory, University of California, Santa Cruz, 100 Shaffer Road, Santa Cruz, California 95060

Brandon L. Southall
Long Marine Laboratory, University of California, Santa Cruz, 100 Shaffer Road, Santa Cruz, California 95060 and NOAA Acoustics Program, National Marine Fisheries Service, Office of Protected Resources, 1315 East-West Highway, SSMC3 13754, Silver Spring, Maryland 20910

(Received 11 July 2005; revised 21 September 2005; accepted 28 September 2005)

In this study, minimum audible angles (MAAs) of aerial pure tones were measured in and compared between a northern elephant seal (*Mirounga angustirostris*), a harbor seal (*Phoca vitulina*), and a California sea lion (*Zalophus californianus*). Testing was conducted between 0.8 and 16 kHz in the elephant seal and 0.8 and 20 kHz in the harbor seal and sea lion in a hemi-anechoic chamber using a left/right psychophysical procedure. Performance for the same frequencies was also quantified for discrete speaker separation of 5° from the mid-line. For all subjects, MAAs ranged from approximately 3° to 15° and were generally equal to or larger than those previously measured in the same subjects with a broadband signal. Performance at 5° ranged from chance to 97% correct, depending on frequency and subject. Poorest performance in the sea lion and harbor seal occurred at intermediate frequencies, which is consistent with the duplex theory of sound localization. In contrast, the elephant seal's poorest performance occurred at higher frequencies. The elephant seal's result suggests an inferior ability to utilize interaural level differences and is perhaps related to best hearing sensitivity shifted toward lower frequencies in this species relative to other pinnipeds. [DOI: 10.1121/1.2126931]

PACS number(s): 43.80.Lb, 43.66.Qp [WWA] Pages: 3921–3926

I. INTRODUCTION

Many pinnipeds produce loud, stereotyped, repetitive calls in air. In land breeding species, including elephant seals, sea lions, and fur seals, aerial vocalizations are produced regularly during the breeding season by all age classes. For example, mothers and pups exchange calls to facilitate contact and/or reunions during the lactation period (Insley *et al.*, 2003) while males produce threat vocalizations during male-male competitive behaviors (Bartholomew and Collias, 1962; Peterson and Bartholomew, 1969; Fernandez-Juricic *et al.*, 2001). Thus, detection and localization of conspecific aerial vocalizations in pinnipeds apparently have direct implications for reproductive success. Furthermore, these auditory processes are also likely important in detecting land predators (Stirling and Archibald, 1977) and may contribute to fitness by enhancing survival. Thus, the need to localize a variety of airborne acoustic signals has likely been a significant source of selective pressure in these marine mammals.

Most mammals rely on both monaural and binaural input for localizing sounds in a three-dimensional space. The auditory mechanisms involved in azimuth (horizontal plane) localization are best described by the duplex theory of sound localization (Strutt, 1907) which states that low frequencies are localized by interaural time differences (ITDs) while high frequencies are localized by interaural level differences (ILDs). The duplex theory has been supported by studies conducted with human subjects (Stevens and Newman, 1936; Mills, 1958; Wightman and Kistler, 1992; Macpherson and Middlebrooks, 2002) and several other terrestrial mammals (see Heffner and Heffner, 1992, for review). However, not all mammals have demonstrated the ability to utilize both of these binaural cues. For example, hedgehogs (*Paraechinus hypomelas*) have a limited ability to utilize ITDs (Masterton *et al.*, 1975) while horses (*Equus caballus*) have a limited ability to utilize ILDs (Heffner and Heffner, 1986). In pinnipeds, pure tones at intermediate frequencies (between 2 and 4 kHz) of the audible range were poorly localized by both a harbor seal (*Phoca vitulina*) listening in air (Terhune, 1974) and a California sea lion (*Zalophus californianus*) listening under water (Gentry, 1967; Moore and Au, 1975). The general interpretation of these results is that, according to the duplex theory, there are significantly reduced ITDs and ILDs for the intermediate frequencies, resulting in poorer localization ability.

Accordingly, there have been several attempts to predict the intermediate frequencies at which the auditory system of a given species might shift between the utilization of time-based to level-based interaural cues for localization in the horizontal plane. One consideration is phase ambiguity that occurs when a particular phase cycle of a sound does not reach the far ear before the next phase cycle reaches the near ear (Brown *et al.*, 1978). Assuming a simplified spherical head, the frequency of phase ambiguity for a given interaural distance, azimuth, and medium may be estimated by the following equation:

$$F = 1/[6(r/c)\sin\theta], \quad (1)$$

where r is the head radius, c is sound speed, and θ is azimuth in degrees (Kuhn, 1977; Brown *et al.*, 1978). This relationship predicts the upper frequency limit at which ITD cues are physically available for azimuth sound localization. The frequency of phase ambiguity will occur at higher frequencies as head size decreases. Neurophysiologically, ITD cues are also dictated by the limits of phase locking. Phase locking has typically not been found to be robust in the auditory nerve fibers of mammals at frequencies higher than 2500 Hz (Kuwada *et al.*, 1997; Taberner and Liberman, 2005).

Investigators have commonly measured sound localization ability using the minimum audible angle (MAA). The MAA is most often defined as half the angle between two sound sources bisected by an observer's midline that are acoustically discriminated as separate in space (Mills, 1958). By this definition, smaller MAAs indicate better sound localization performance. In mammals, horizontal plane MAAs for broadband signals range from a few degrees in humans (Mills, 1958), elephants (*Elephas maximus*; Heffner and Heffner, 1992), and dolphins (*Tursiops truncatus*; Renaud and Popper, 1975) to over 30° in cows (*Bos taurus*; Heffner and Heffner, 1992) and gophers (*Geomus bursarius*; Heffner and Heffner, 1990a).

MAAs are typically estimated by varying the angle of projection. However, according to Eq. (1), the frequency of phase ambiguity is not only dependent on the speed of sound and head size, but also on the azimuth relative to a listener. Thus, attempts to determine the frequencies in which neither ITDs nor ILDs are salient for sound localization using MAA estimates will vary depending on the test angles employed. This may lead to inconsistency in the data and nonmonotonic performance functions (e.g., see Brown *et al.*, 1978). To address this potential limitation, some investigators have opted to fix the angle of sound projection and measure performance across a number of frequencies of the audible range to determine at which frequencies performance declines. These frequencies are interpreted as the region in which the auditory system shifts from using ITDs at low frequencies to ILDs at high frequencies at the given test angle (e.g., Heffner *et al.*, 2001).

For this study, two experiments were conducted to measure and compare the abilities of three pinnipeds, a northern elephant seal (*Mirounga angustirostris*), a harbor seal, and a California sea lion, to localize a range of aerial pure tones. These species have anatomical, behavioral, and phylogenetic differences that are potentially relevant to sound localization. For example, the elephant seal and harbor seal are phocids (true seals) and lack external ears while the sea lion is an otariid and has vestigial external ears. Furthermore, the elephant seal and sea lion are land breeders and primarily call in air (Bartholomew and Collias, 1962; Peterson and Bartholomew, 1969) while the harbor seal is an aquatic breeder and adult males primarily call under water (Hanggi and Schusterman, 1994), although pups vocalize in air and water during their dependence period to maintain contact with their mothers (Renouf, 1984). These pinniped species have been shown to resolve the spatial location of aerial broadband signals within 5° from the midline (Terhune, 1974; Holt *et al.*, 2004). Previous studies on localization of airborne pure tones have been conducted on harbor seals between 0.5 and 8 kHz (Møhl, 1964; Terhune, 1974). MAAs measured in these studies ranged from approximately 5° at the lowest and highest frequencies to an undefined MAA estimate at the intermediate frequencies due to very poor performance (Møhl, 1964; Terhune, 1974).

In the first experiment of this study, MAAs were measured in the horizontal plane at frequencies ranging from 0.8 to 16 kHz in the elephant seal and from 0.8 to 20 kHz in the sea lion and harbor seal. MAAs across these frequencies were then compared within and between subjects and between previous pinniped results including MAAs measured with a broadband signal in the same subjects using the same methods (Holt *et al.*, 2004). It was expected that pure tone MAAs would be equal to or larger (i.e., performance would be worse) than MAAs for broadband signals because localization performance is typically better with a wider signal bandwidth that contains both ITD and ILD cues (Brown *et al.*, 1980). It was also expected that MAAs at the intermediate frequencies tested would be larger than those at the extreme frequencies. This is based on the observation that pinnipeds tested thus far have demonstrated evidence of utilizing both ITDs and ILDs and ambiguity of these two cues is expected to occur at intermediate frequencies (Terhune, 1974; Moore and Au, 1975).

In the second experiment, performance at a fixed angle of 5° at the same test frequencies and subjects as in experiment 1 was assessed to determine at which frequencies performance was reduced to chance and how this correlated with the predicted frequency of phase ambiguity given by Eq. (1) for each subject. Preliminary results from experiment 1 indicated that a relatively small test angle would be necessary to obtain chance performance at least at some of the test frequencies and thus a fixed angle of 5° was used. Equation (1) predicts that the highest frequency available for ITD cues will be lower for a larger head. Hence, the elephant seal was expected to show a shift between the two binaural cues at a lower frequency relative to both the sea lion and the harbor seal subjects.

This study extends the previous pure tone localization work on pinnipeds in the left/right plane (Møhl, 1964; Gentry, 1967; Terhune, 1974; Moore and Au, 1975). The results of this comparative investigation provide further information regarding the use of binaural cues for sound localization in air while considering physical and species-related factors that may influence this auditory ability in pinnipeds.

II. METHODS

A. Subjects

The subjects were an 11-years-old female Northern elephant seal (Burnyce), a 14-years-old male harbor seal (Sprouts), and a 17-years-old female California sea lion (Rio). All subjects were resident animals at Long Marine Laboratory in Santa Cruz, CA, and had experience performing sound localization tasks of a broadband signal in air (Holt *et al.*, 2004). For the current study, subjects received up

to 50% of their daily food totals (3–15 kg of mixed herring and capelin) during experimental sessions. This study followed the protocols approved by the University of California Chancellor's Animal Research Committee (CARC).

B. Experimental apparatus

Testing occurred in a custom-built $4.0 \times 2.8 \times 2.4$ m^3 double-walled hemi-anechoic chamber (Eckel Industries) as described in Holt *et al.* (2004). All surfaces of the test chamber were lined with acoustic foam wedges except the concrete floor and stainless steel door, which were covered with 2.6-cm neoprene mats. A stationing chin cup made of PVC was mounted to the floor and placed 1 m from the sound sources mounted to the wall in front of the chin cup. Two rectangular PVC response targets (11.4×8.9 cm) were also mounted to the floor and spaced equidistant (11.7 cm) from either side of the chin cup. All subjects were tested with stimuli projected at ear level. A small light, placed 1 m in front of the subjects, was used to ensure that the subject was attentive to the auditory signal during the trial interval.

All equipment was controlled by the experimenter in a $1.3 \times 2.8 \times 2.4$-m^3 control room adjacent to the test chamber. The signals were pure tones at 0.8, 1, 2, 4, 8, 16, and 20 kHz that were generated and triggered by the experimenter using custom-designed LabVIEW software and a National Instruments PXI-6070E multifunction I/O board. Due to limitations of the equipment and a lower sensitivity at higher frequencies, the elephant seal could not be tested above 16 kHz. The signal duration was 100 ms, which was short enough to minimize any performance improvement due to head motion during its presentation (Heffner *et al.*, 2001). Additionally, the signal was shaped with a linear rise and fall time of 10 ms and, when necessary, the signal was low-pass filtered (Krohn-Hite 3550 filter) to remove or reduce harmonics below the sensation level of the subject. The signal was routed to a speaker selector (Acoustic Research 1108) that allowed one of six connected speakers (Morel MDT37 horn tweeters) to be manually selected by the experimenter. In the case of testing the elephant seal at 16 kHz, an amplifier was connected from the output of the filter to the input of a 20-W amplifier (Radio Shack MPA 40). The output of the amplifier was fed to the input of the speaker selector. Background noise emitted from a selected speaker was maintained below the absolute detection threshold of all subjects. Each speaker was housed in a PVC cup and mounted on a 2.4-m linear track that was placed 1 m away from and at 0° elevation relative to the subject's ears. This allowed the speakers to be placed anywhere between 45° to the left and 45° to the right of the subject's midline (with ±0.5° of accuracy).

For experiment 1, three speakers were always placed to the right and the left of the subject's midline. The speaker positions were manually changed in azimuth relative to the subject's midline between experimental sessions using a modified method of constant stimuli to determine horizontal plane MAAs for each subject. In experiment 2, test speakers were placed at 5° to the left and the right of the subjects' midline, along with another pair of speakers placed at wider angles for "warm-up" and "cool-down" trials.

The average sound pressure level of the stimuli (dB_{RMS} *re*:20 μPa) was determined at a position corresponding to the center of the subject's head (with the subject removed) using a calibrated free-field microphone (C550H, Josephson Engineering, Santa Cruz, CA) and a spectrum analyzer (using LabVIEW software and National Instruments PXI-6070E multifunction I/O board) for each of the test angles at the beginning of each experimental session. Acoustic mapping was performed in which received signal levels were measured at every 2° within 10° of azimuth and at every 5° between 10° and 45° of azimuth. For each azimuth location, received levels were measured at ten separate positions within a $10 \times 10 \times 10$-cm^3 area surrounding the chin cup of the test apparatus. Differences of up to 10 dB in sound pressure levels were observed between stimuli projected from different speaker locations during acoustic mapping. Therefore, the stimulus level was randomly varied from trial to trial over a 10-dB range surrounding the average level so that the subjects could not use intensity discrimination between speakers or speaker positions to improve performance. Sound detection thresholds for the 100-ms signal at each frequency were determined prior to localization testing for each subject using methods described in Kastak and Schusterman (1998). The average signal level was 25–30 dB above threshold depending on the test frequency. Based on the results of studies involving terrestrial mammals, it has been shown that these differences in sensation levels have only marginal effects (within the average range of error) on the ability of some terrestrial mammals to localize the signal (Heffner *et al.*, 2001; Inoue, 2001; Su and Recanzone, 2001).

C. Procedure

For both experiments, the procedure was similar to those reported in Holt *et al.* (2004). Only one frequency was presented within an experimental session. Subject responses were monitored by the experimenter in the control room via a surveillance camera. A trial began when the animal stationed properly in the chin cup and the trial light was manually illuminated. A correct response was defined as pressing the left target when a left speaker was activated and pressing the right target when a right speaker was activated. If a correct response was made, a digitized "whistle" was played through a separate speaker (0° azimuth), the trial light was turned off, and an assistant in the control room delivered a fish reward via a PVC conduit to the subject. Both types of correct responses were given an equal proportion of fish. Additionally, one or two no-go trials in which the animal was reinforced for not responding to "blank" trials were randomly incorporated within each experimental session. Responses made before the stimulus presentation or to an incorrect target were not reinforced. The overall and first-order conditional probabilities of left and right trial presentations were 0.5 within a testing session (Holt and Schusterman, 2002). Approximately six warm-up and cool-down trials were given at the beginning and end of each experimental session in which the stimulus was projected at angles $\geqslant 25°$. These trials were incorporated to ensure good stimulus con-

TABLE I. Minimum audible angles (MAAs), standard errors, performance at 5° relative to the midline, and testing order for each subject at each test frequency.

Subject	Test frequency (kHz)	MAA (deg)	Standard error	Performance at 5°	Testing order
Harbor seal	0.8	4.3	0.25	97%	6
(*Phoca*)	1	4.1	0.23	84%	1
	2	5.4	0.19	92%	3
	4	7.9	0.18	67%	2
	8	12.7	0.23	52%	4
	16	3.8	0.20	83%	5
	20	6.9	0.18	74%	7
Sea lion	0.8	4.7	0.20	91%	6
(*Zalophus*)	1	6.0	0.19	84%	1
	2	11.9	0.21	92%	3
	4	8.0	0.19	58%	2
	8	11.1	0.20	63%	4
	16	3.9	0.17	75%	5
	20	8.7	0.23	70%	7
Elephant seal	0.8	3.3	0.19	83%	1
(*Mirounga*)	1	4.8	0.19	77%	2
	2	3.7	0.19	87%	4
	4	3.9	0.18	80%	3
	8	15.0	0.23	49%	5
	16	14.2	0.23	66%	6

trol over the subject's behavior but were not used for data analysis. An experimental session typically contained approximately 60 trials.

1. MAA estimates

For experiment 1, 30 trials for each left and right test angle were pooled across approximately 12 experimental sessions for each frequency tested. Performance for left and right angles were plotted separately rather than pooling performance across angles of symmetry (Mills, 1958). Based on previous work (Holt *et al.*, 2004), it was expected that data from the resulting plots would follow a sigmoidal psychometric function. Probit analysis (Finney, 1971) was used to transform the data linearly and interpolate MAAs from a linear regression analysis as the azimuth value corresponding to 75% correct performance averaged from both left and right angles (see Holt *et al.*, 2004).

2. Fixed angle performance

For experiment 2, the results of 50 trials collected at both 5° to the left and the right were pooled and used to quantify performance relative to chance. Based on preliminary results of experiment 1 and a previous investigation (Holt *et al.*, 2004), subjects may develop a bias toward one response within an experimental session, particularly as discrimination becomes more difficult. To address this potential bias and to justify pooling the data, only data from sessions in which there was no significant difference in performance (as determined using a Fisher's exact test and an alpha level of 0.05) across the two angles of symmetry were used in the analysis.

III. RESULTS

Localization data collected during experiment 1 for all subjects were best described as sigmoidal psychometric functions similar to those obtained with broadband signals for the same subjects (Holt *et al.*, 2004). MAAs, standard errors of the estimate, performance at 5°, and testing order for all three subjects at each frequency are given in Table I. MAAs were generally smaller and performance was better at the two lowest frequencies tested for all subjects and at 16 and 20 kHz for the harbor seal and sea lion (see Fig. 1).

In the elephant seal subject, MAAs ranged from 3.3° to 15.0° and were smallest below 4 kHz. In the harbor seal subject, MAAs ranged from 3.8° to 12.7° and increased with increasing frequency up to 8 kHz, beyond which perfor-

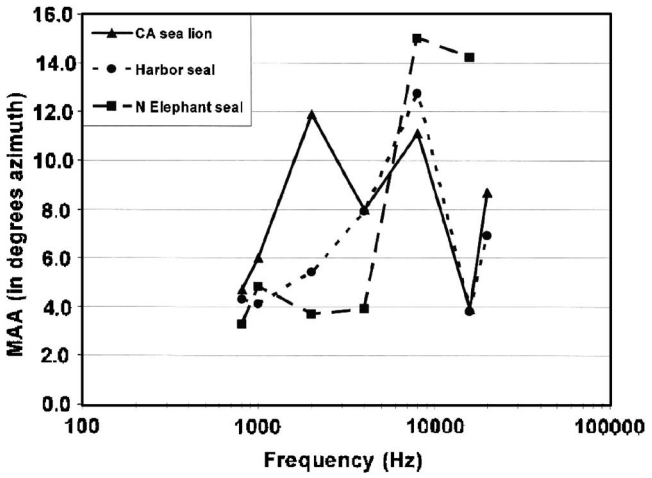

FIG. 1. Minimum audible angles for each subject at each test frequency of this study.

TABLE II. Head size and predicted frequency of phase ambiguity for each subject of this study at a test angle of 5° from the midline using the equation from Kuhn (1977).

Subject	Head radius (m)	Frequency of ambiguity (kHz)
Harbor seal	0.083	7.9
Sea lion	0.080	8.2
Elephant seal	0.154	4.3

mance improved at the two highest frequencies tested and resulted in smaller MAAs. In the sea lion subject, MAAs ranged from 3.9° to 11.9° and increased with increasing frequency up to 2 kHz. At 4 kHz, performance improved relative to the 2-kHz data point, declined at 8 kHz, and then improved at the two highest frequencies tested. The smallest MAAs measured for each subject of this study were within a degree of those previously measured for a broadband signal in the same subject (Holt *et al.*, 2004).

Head radius (m) for each subject and the predicted frequency of phase ambiguity for 5° angular separation are shown in Table II. Figure 2 shows performance at 5° for each subject along with the predicted frequency of phase ambiguity given by Eq. (1) and indicated by the coded legend. The shaded section of Fig. 2 indicates chance performance. For the elephant seal and harbor seal, performance was significantly above chance for all frequencies except 8 kHz. For the sea lion, performance was significantly above chance for all frequencies except 4 kHz, although performance at 8 kHz was only marginally above chance.

IV. DISCUSSION

As expected, pure tone MAAs were generally equal to or larger (i.e., performance was worse) than broadband MAAs within a subject (Holt *et al.*, 2004). MAAs for both the harbor seal and sea lion were largest at the intermediate frequencies tested, supporting the duplex theory of sound

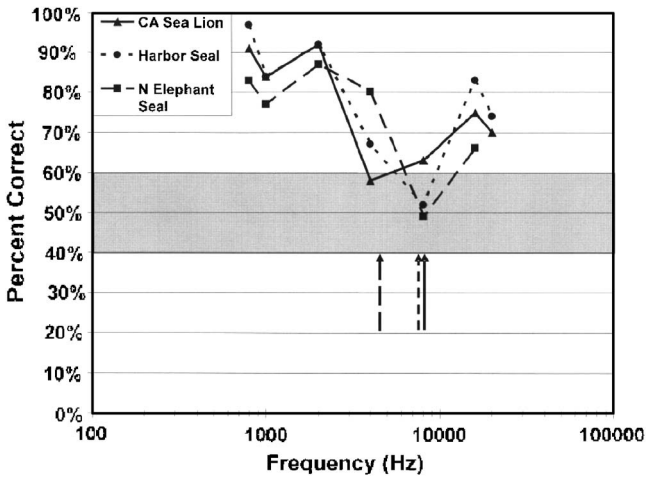

FIG. 2. Performance for each subject at 5° from the midline. Shaded section of the graph indicates chance performance using a binomial test and an alpha level of 0.05. Arrows indicate predicted frequency of phase ambiguity using the equation from Kuhn (1977) for each subject as indicated by the legend.

localization in these animals while the elephant seal MAAs were smallest at only the lowest frequencies tested.

The MAA of a harbor seal measured in air at 1 kHz by Terhune (1974) agreed closely with the MAA estimate at the same frequency for the harbor seal of this study. The worst performance of the harbor seal of this study was found at 8 kHz. The worst performance in the Terhune (1974) study was found between 2 and 4 kHz. It is likely that differences in testing environment, signal design, angles tested, and procedure contributed to the differences found between the two studies as well as the small sample sizes ($n=1$ for both studies).

Performance at a fixed angle (5°) for the harbor seal agreed well with the predictions based on Eq. (1). The highest frequency that phase cues should be available for this angle was 7.9 kHz and performance was at chance for only the 8-kHz data point. The MAAs for this subject measured in the first experiment agreed closely with these results. In the sea lion, the predicted frequency of phase ambiguity was at 8.2 kHz. In experiment 2, performance of the sea lion was at chance at 4 kHz and slightly above chance at 8 kHz. While these results are somewhat consistent with the prediction, it is possible that using a model that assumes a spherical head is not as accurate for a sea lion. Furthermore, in experiment 1, the worst performances (largest MAAs) of this subject occurred at 2 and 8 kHz (see Table II for a comparison of MAAs estimates and performance at 5°). Although the ITD cue by itself should be physically unambiguous at 4 kHz, the relatively poor performances of both the harbor seal and sea lion at this frequency is likely explained by the limits of phase locking. For experiment 2, the predicted frequency of phase ambiguity for the elephant seal was 4.3 kHz and this subject performed above chance at all frequencies except 8 kHz. Although this subject had a larger head size and interaural distance relative to the two other subjects, the frequency of chance performance did not occur at a lower frequency. The fixed angle performances of both true seals were in closer agreement to each other compared to those of the sea lion.

Results from this study demonstrate that these pinnipeds can localize both low- and high-frequency pure tone signals in air proficiently, although the elephant seal had more difficulty at higher frequencies. Neither the presence of external ears nor the medium in which acoustic displays occur correlated with this ability. Other large mammals such as the horse, elephant, pig (*Sus scrofa*), goat (*Capra hircus*), and cow have also shown relative difficulty localizing high-frequency pure tones (Heffner and Heffner, 1992). The elephant seal's range of best hearing sensitivity is shifted toward the lower frequencies relative to the other two pinniped subjects tested in this study, although, as in the other pinniped subjects of this study, the upper frequency cutoff of aerial hearing sensitivity (defined at 60 dB *re*:20 μPa) extends beyond 16 kHz (Kastak and Schusterman, 1999; Schusterman, unpublished data). Performance suggests that the elephant seal has a reduced ability to utilize ILDs for sound localization in the horizontal plane; the first and largest pinniped tested thus far that has not demonstrated an equal proficiency to localize both low- and high-frequency

tones, at least at the frequencies tested in this study. Heffner and Heffner (1990b) discuss the possibilities of why some large mammals have limited or absent abilities to localize high frequencies even though these mammals do possess high-frequency hearing abilities. They suggest that sensitivity to high frequencies is probably not a vestigial ability but necessary rather to utilize monaural cues for vertical plane and front/back sound localization (Heffner and Heffner, 1990b). These monaural cues are primarily created by the diffraction of sound around the pinna (Musicant and Butler, 1984; Heffner *et al.*, 1996) and hoofed mammals typically possess large, mobile pinnae. As with all true seals, northern elephant seals lack pinnae, and this does not adequately explain the retention of some high-frequency hearing in elephant seals. Other selective pressures placed on elephant seals such as the reception of communicative signals, specifically of pups and juveniles, may better explain the need to detect higher-frequency signals, although these animals most likely rely on the lower-frequency components of conspecific calls for localization.

ACKNOWLEDGMENTS

This study was conducted under U.S. Marine Mammal Permit No. 239-1481-00 of the U.S. National Marine Fisheries Service Office of Protected Resources. Funding from the Office of Naval Research (Grant No. N00014-02-0159) to RJS and the Myers' Oceanographic Trust Fund, the Friends of Long Marine Laboratory, University of California Regents Fellowship Program, and Graduate Assistance in Areas of National Need (GAANN) Doctoral Fellowship Program to MMH made this study possible. The authors thank the dedicated volunteers at Long Marine Laboratory in Santa Cruz, CA, Colleen Reichmuth Kastak for providing her assistance on animal training and procedure, as well as two anonymous reviewers for commenting on earlier versions of this manuscript.

Bartholomew, G. A., and Collias, N. E. (**1962**). "The role of vocalization in the social behavior of the northern elephant seal," Anim. Behav. **10**, 7–14.

Brown, C. H., Beecher, M. D., Moody, D. B., and Stebbins, W. C. (**1978**). "Localization of pure tones by old world monkeys," J. Acoust. Soc. Am. **63**, 1484–1492.

Brown, C. H., Beecher, M. D., Moody, D. B., and Stebbins, W. C. (**1980**). "Localization of noise bands by old world monkeys," J. Acoust. Soc. Am. **68**, 127–132.

Fernandez-Juricic, E., Campagna, C., Enriquez, V., and Ortiz, C. L. (**2001**). "Vocal rates and social context in male south American sea lions," Marine Mammal Sci. **17**, 387–396.

Finney, D. J. (**1971**). *Probit Analysis*, 3rd ed. (Cambridge U. P., Cambridge).

Gentry, R. L. (**1967**). "Underwater auditory localization in the California sea lion (*Zalophus californianus*)," J. Aud Res. **7**, 187–193.

Hanggi, E. B., and Schusterman, R. J. (**1994**). "Underwater acoustic displays and individual variation in male harbour seals, *Phoca vitulina*," Anim. Behav. **48**, 1275–1283.

Heffner, R. S., and Heffner, H. E. (**1986**). "Localization of tones by horses: Use of binaural cues and the role of the superior olivary complex," J. Acoust. Soc. Am. **100**, 93–103.

Heffner, R. S., and Heffner, H. E. (**1990a**). "Vestigial hearing in a fossorial mammal, the pocket gopher (*Geomys bursarius*)," Hear. Res. **46**, 239–252.

Heffner, R. S., and Heffner, H. E. (**1990b**). "Hearing in domestic pigs (*Sus scrofa*) and goats (*Capra hircus*)," Hear. Res. **48**, 231–240.

Heffner, R. S., and Heffner, H. E. (**1992**). "Evolution of sound localization in mammals," in *The Evolutionary Biology of Hearing*, edited by D. B. Webster, R. R. Fay, and A. N. Popper (Springer-Verlag, New York), pp. 691–715.

Heffner, R. S., Koay, G., and Heffner, H. E. (**1996**). "Sound localization in chinchillas III: Effect of pinna removal," Hear. Res. **99**, 13–21.

Heffner, R. S., Koay, G., and Heffner, H. E. (**2001**). "Sound localization in a new-world frugivorous bat, *Artibeus jamaicensis*: Acuity, use of binaural cues, and relationship to vision," J. Acoust. Soc. Am. **109**, 412–421.

Holt, M. M., and Schusterman, R. J. (**2002**). "Seals, sequences, and signal detection," Marine Mammal Sci. **18**, 208–212.

Holt, M. M., Schusterman, R. J., Southall, B. L., and Kastak, D. (**2004**). "Localization of aerial broadband noise by pinnipeds," J. Acoust. Soc. Am. **115**, 2339–2345.

Inoue, J. (**2001**). "Effects of stimulus intensity on sound localization in the horizontal and upper-hemispheric median plane," J. Univ. Occup. Environ. Health Jpn. **23**, 127–138.

Insley, S. J., Phillips, A. V., and Charrier, I. (**2003**). "A review of social recognition in pinnipeds," Aquat. Mammal **29**, 181–201.

Kastak, D., and Schusterman, R. J. (**1998**). "Low frequency amphibious hearing in pinnipeds: Methods, measurements, noise, and ecology," J. Acoust. Soc. Am. **103**, 2216–2228.

Kastak, D., and Schusterman, R. J. (**1999**). "In-air and underwater hearing sensitivity of a northern elephant seal (*Mirounga angustirostris*)," Can. J. Zool. **77**, 1751–1758.

Kuhn, G. F. (**1977**). "Model for the interaural time differences in the azimuthal plane," J. Acoust. Soc. Am. **62**, 157–167.

Kuwada, S., Batra, R., and Fitzpatrick, D. C. (**1997**). "Neural processing of binaural temporal cues," in *Binaural and Spatial Hearing in Real and Virtual Environments* edited by R. H. Gilkey and T. R. Anderson (Law Erlbaum, Mahwah, NJ), pp. 399–425.

Macpherson, E.A., and Middlebrook, J.C. (**2002**). "Listener weighting of cues for lateral angle: The duplex theory of sound localization revisited," J. Acoust. Soc. Am. **111**, 2219–2236.

Masterton, B., Thompson, G. C., Bechtold, J. K., and Robards, M. J. (**1975**). "Neuroanatomical basis of binaural phase-difference analysis for sound localization: A comparative study," J. Comp. Physiol. Psychol. **89**, 379–386.

Mills, A. W. (**1958**). "On the minimum audible angle," J. Acoust. Soc. Am. **30**, 237–246.

Møhl, B. (**1964**). "Preliminary studies and hearing in seals," Vidensk. Medd. Dansk. Naturh. Foren. **127**, 283–294.

Moore, P. W. B., and Au, W. W. L. (**1975**). "Underwater localization of pulsed pure tones by the California sea lion (*Zalophus californianus*)," J. Acoust. Soc. Am. **58**, 721–727.

Musicant, A. D., and Butler, R. A. (**1984**). "The influence of pinnae-based spectral cues on sound localization," J. Acoust. Soc. Am. **75**, 1195–1200.

Peterson, R. S., and Bartholomew, G. A. (**1969**). "Airborne vocal communication in the California sea lion," Anim. Behav. **17**, 17–24.

Renaud, D. L., and Popper, A. N. (**1975**). "Sound localization by the bottlenose porpoise, *Tursiops truncates*," J. Exp. Biol. **63**, 569–585.

Renouf, D. (**1984**). "The vocalization of the harbor seal pup (*Phoca vitulina*) and its role in the maintenance of contact with the mother," J. Zool. **202**, 583–590.

Stevens, S. S., and Newman, E. B. (**1936**). "The localization of actual sources of sound," Am. J. Psychol. **48**, 297–306.

Stirling, I., and Archibald, W. R. (**1977**). "Aspects of predation of seals by polar bears," J. Fish. Res. Board Can. **34**, 1126–1129.

Strutt, J. W. (**1907**). "On our perception of sound direction," Philos. Mag. **13**, 214–232.

Su, T. K., and Recanzone, G. H. (**2001**). "Differential effect of near-threshold stimulus intensities on sound localization performance in azimuth and elevation in normal human subjects," J. Assoc. Res. Otolaryngol. **2**, 246–256.

Taberner, A. M., and Liberman, M. C. (**2005**). "Response properties of single auditory nerve fibers in the mouse," J. Neurophysiol. **93**, 557–569.

Terhune, J. M. (**1974**). "Directional hearing of a harbor seal in air and water," J. Acoust. Soc. Am. **56**, 1862–1865.

Wightman, F. L., and Kistler, D. J. (**1992**). "The dominant role of low frequency interaural time differences in sound localization," J. Acoust. Soc. Am. **85**, 868–1661.

Doppler-shift compensation in the Taiwanese leaf-nosed bat (*Hipposideros terasensis*) recorded with a telemetry microphone system during flight

Shizuko Hiryu[a] and Koji Katsura
Department of Electrical Engineering, Doshisha University, Kyotanabe, 610-0321, Japan

Liang-Kong Lin[b]
Department of Biology, Tunghai University, Taichung, 407, Taiwan

Hiroshi Riquimaroux[c]
Department of Knowledge Engineering and Computer Sciences, Doshisha University, Kyotanabe, 610-0321, Japan

Yoshiaki Watanabe[d]
Department of Electrical Engineering, Doshisha University, Kyotanabe, 610-0321, Japan

(Received 21 March 2005; revised 5 August 2005; accepted 5 October 2005)

Biosonar behavior was examined in Taiwanese leaf-nosed bats (*Hipposideros terasensis*; CF-FM bats) during flight. Echolocation sounds were recorded using a telemetry microphone mounted on the bat's head. Flight speed and three-dimensional trajectory of the bat were reconstructed from images taken with a dual high-speed video camera system. Bats were observed to change the intensity and emission rate of pulses depending on the distance from the landing site. Frequencies of the dominant second harmonic constant frequency component (CF_2) of calls estimated from the bats' flight speed agreed strongly with observed values. Taiwanese leaf-nosed bats changed CF_2 frequencies depending on flight speed, which caused the CF_2 frequencies of the Doppler-shifted echoes to remain constant. Pulse frequencies were also estimated using echoes returning directly ahead of the bat and from its sides for two different flight conditions: landing and U-turn. Bats in flight may periodically alter their attended angles from the front to the side when emitting echolocation pulses. © *2005 Acoustical Society of America.* [DOI: 10.1121/1.2130940]

PACS number(s): 43.80.Ka, 43.80.Lb, 43.66.Gf [JAS] Pages: 3927–3933

I. INTRODUCTION

Echolocating bats have a highly developed biosonar system. By comparing emitted pulses with returning echoes, bats are capable of instantaneously recognizing the physical attributes of their environment. This enables them to catch insects or to avoid obstacles. Bats have evolved efficient echolocation techniques and are capable of adjusting the acoustical parameters of their calls to different echolocation requirements such as different target-background relationships (Novick and Vaisnys, 1964; Henson *et al.*, 1987; Lancaster *et al.*, 1992; Tian and Schnitzler, 1997; Moss and Surlykke, 2001; Ghose and Moss, 2003). Only the more recent studies have begun to quantify the acoustic parameters of bat calls and the corresponding echo signals while relating them to the spatio-temporal conditions under which the call-echo pairs were produced. Understanding these different echolocation strategies and their acoustical basis is particularly important for bat biosonar systems to serve as model systems for technological applications.

Hipposiderid (*Rhinolophus* spp.) and mustache bats (*Pteronotus parnellii*) produce echolocation calls in a very narrow frequency band (constant-frequency component, CF). During flight, the frequency of the CF component shifts due to Doppler effects. Horseshoe and mustache bats compensate for these Doppler shifts by adjusting their call frequency accordingly, thus maintaining the echo frequency within the narrow frequency range that the bats can hear best (Doppler-shift compensation, DSC) (Schnitzler, 1968; Schuller *et al.*, 1974; Simmons, 1974; Trappe and Schnitzler, 1982; Henson *et al.*, 1987; Gaioni *et al.*, 1990; Lancaster *et al.*, 1992; Keating *et al.*, 1994). In Hipposiderids, Gustafson and Schnitzler (1979) have first demonstrated that the bats in flight compensated for Doppler shifts caused by their own flight movement.

We examined changes in the dominant second harmonic CF component (CF_2) of echolocation calls emitted by Taiwanese leaf-nosed bats (*Hipposideros terasensis*) during different flight maneuvers in the laboratory (Riquimaroux and Watanabe, 2002). The echolocation sounds were recorded using a telemetry microphone (Telemike) mounted on the bat's head using previously reported radio telemetry techniques (Henson *et al.*, 1987; Lancaster *et al.*, 1992). Analysis of call frequency in response to the echo information the bat did hear enabled us to determine which target the bat paid attention to (e.g., target wall versus side walls). We estimated the position of the target listened to by the bat during flight

[a]Electronic mail: etd1101@mail4.doshisha.ac.jp
[b]Electronic mail: lklin@mail.thu.edu.tw
[c]Electronic mail: hrikimar@mail.doshisha.ac.jp
[d]Electronic mail: kwatanab@mail.doshisha.ac.jp

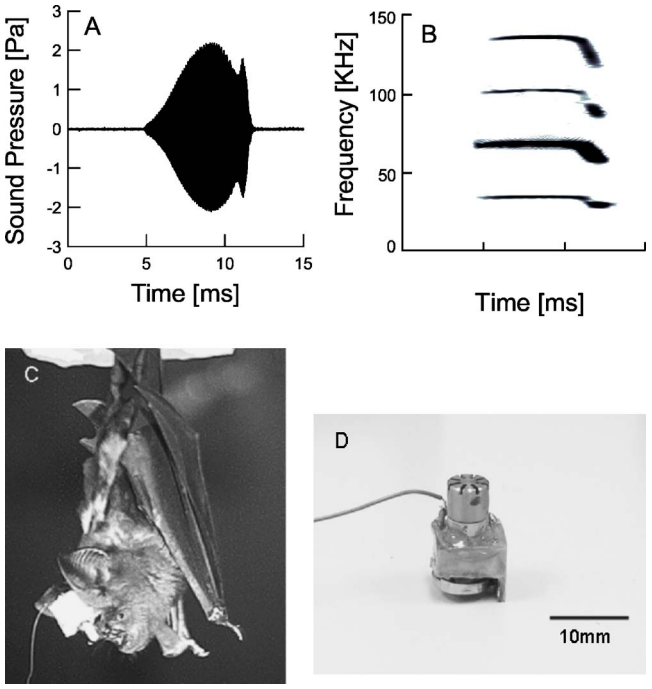

FIG. 1. Typical echolocation pulse in the Taiwanese leaf-nosed bat (*Hipposideros terasensis*) recorded from a Telemike mounted on the bat's head: (a) envelope and (b) sonagram. Calls usually contained four harmonics, with the second being dominant. Each call consisted of a long constant-frequency (CF) component followed by a short downward frequency-modulated (FM) component. Photographs of the Telemike: (c) stationary *Hipposideros terasensis* with the Telemike mounted on its head and (d) frontal view of the Telemike. Telemike consisted of a $\frac{1}{4}$-in. condenser microphone, transmitter, battery, and transmitting wire antenna.

by evaluating call parameters such as their CF_2 frequency and the interemission interval (IEI). By comparing these data with the three-dimensional coordinates of the flight path, we also checked whether bats altered the direction of attention during direct approaches to the target wall. The attended angle was the angle of this direction of attention relative to the flight path. This parameter provided important insights into the bat biosonar behavior, especially the direction towards which the bat directed its sonar beam. This then allowed us to study how the bat scanned the spatial characteristics of surrounding multiple targets while approaching its destination.

II. MATERIALS AND METHODS

A. Subjects

Three adult Taiwanese leaf-nosed bats (*Hipposideros terasensis*) were used in this study. The animals were captured in Taiwan and housed in a temperature- and humidity-controlled facility at Doshisha University, Japan. Body mass of the bats ranged from 50 to 60 g. Figure 1 shows the envelope (a) and sonagram (b) of a typical echolocation call. Taiwanese leaf-nosed bats use a compound signal consisting of an approximately 5-ms CF component followed by a short, 1-ms, downward frequency-modulated (FM) component. The frequency of the dominant second harmonic CF component of calls emitted at rest (resting frequency) is about 70 kHz. This frequency is emitted when the bat is not flying and experiencing flight-induced Doppler shifts.

B. Recording procedures

The experiments were conducted in a flight chamber 8 m(L) × 3 m(W) × 2 m(H). The chamber was made of steel plates painted black to avoid optical effects and minimize interference from external electromagnetic waves. The bats were released at one end of the chamber and allowed to fly freely to the opposite end of the flight chamber where a landing mesh [1 m(W) × 0.7 m(H)] was attached to the wall 1.8 m above the floor. This wall is referred to as the target wall. Flight behaviors were recorded as the flying bat approached the target wall and either landed on the net or returned to the starting point without landing. Echolocation sounds were recorded by a custom-made telemetry microphone (Telemike; Dia-medical, Tokyo, Japan) mounted on the head of the bat [Figs. 1(c) and 1(d)]. The Telemike was a $\frac{1}{4}$-in. electrets condenser microphone (RION, SCM-204E, Tokyo, Japan), a small custom-designed FM transmitter unit, a battery, and a transmitting antenna. The plastic surface of the FM transmitter unit was glued to the scalp of the bat. Since the Telemike weighed less than 3 g, it was light enough to be carried by the animals, and the bats did not exhibit any fatigue during the experiments. Experiment sessions were less than an hour. The Telemike was easily removed from the bat's head after each experiment using a parting agent without irritating the scalp. The Telemike transmitted signals with a carrier frequency between 90 and 100 MHz to a wire antenna attached to the ceiling of the flight chamber. Received signals were demodulated using a custom-made FM receiver, high-pass filtered (NF Corporation, model 3625, Yokohama, Japan), and then digitally recorded on a 16-bit, 384-kHz DAT recorder (SONY, SIR-1000W, Tokyo, Japan). The acoustical parameters of the echolocation pulses, such as frequency and interemission interval (IEI), were analyzed from the sonagram using a custom program of Matlab on a personal computer. Each pulse was extracted on the displayed sonagram, and then a fast Fourier transform (FFT) was performed over 4096 points from the onset of the pulse so that the frequency of the CF_2 component was determined with the resolution of ±46.9 Hz. Prior to the recording session, CF_2 frequency for each bat at rest was measured with the Telemike mounted on the bat's head for at least 20 s. A mean of the 30 pulses that were randomly selected was determined as the resting frequency. The resting frequency showed no particular change over the observation during the experiment limited less than several flights for each bat per day. In this study, IEI was defined as the time from the beginning of one call to the beginning of the subsequent call. Since echolocation sounds were recorded directly by the microphone on the head of the flying bat, the acoustic parameters could be precisely measured without interference from the movement of the bat's head or Doppler-induced errors.

Flight behaviors of the bats were recorded using a dual digital high-speed video camera system (NIPPON ROPER Co., Ltd., CR Imager model 2000s, Chiba, Japan). Cameras

were positioned along the edge of the flight chamber and did not interfere with the bat flight path. Video cameras recorded at 125 frames per second. Three-dimensional coordinates of the flying bats were reconstructed from these video images using commercial motion analysis software (DITECT, DippMotion 2D version 2.1). Prior to recording, a reference frame with known coordinates was positioned in the center of the flight chamber, and then filmed by two cameras. The analysis software calibrated the reconstruction system from the coordinate data of the reference frame. Based on direct linear transformation technique, the positions of the flying bat or other objects were reconstructed from 2-D coordinate data in the video images. The signal triggering the video cameras was digitally recorded using a DAT recorder so that flight coordinates could be synchronized with sound data. Using coordinate data, the flight trajectory, flight speed, and distance from the target wall (target distance) were calculated. The flight speed was determined along the flight path of the bat using three-dimensional coordinate data.

We confirmed that echo frequencies directly measured by the Telemike are usually about several tens of Hertz higher than the resting frequency. This suggests that the reference frequency of *H. terasensis* is estimated to be approximately several tens of Hertz higher than the resting frequency. For calculation presented here, we used the resting frequency instead of the reference frequency since the reference frequency of *H. terasensis* was not physiologically determined and, in addition, it was still difficult to observe echoes with enough amplitude by Telemike.

III. RESULTS

A. Echolocation pulses of bats during flight

The echolocation behavior of bats was examined for two different flight tasks. The first was a direct approach to the target wall followed by landing on the mesh of the target wall. The second scenario consisted of an initial approach of the target wall followed by a U-turn. Figure 2 shows representative echolocation pulses recorded with the Telemike and the flight trajectory in two scenarios for indicating spatio-temporal aspects of the echolocation behavior. When the bats flew in the middle of the flight chamber in the landing scenario, the maximum call intensity was as much as 120 dB SPL peak-to-peak. The bats started to gradually decrease pulse intensity at 3–4 m from the target wall. At the same time, the pulse emission rate increased from 20–30 pulses/s to 70–80 pulses/s. This suggested that the emission pattern for *H. terasensis* intending to land showed three flight phases, search, approach and terminal, as in other Hipposiderids (Gustafson and Schnitzler, 1979). After landing, the bats suddenly increased call intensity and decreased pulse emission rate as they appeared to familiarize themselves with their immediate surroundings.

In the U-turn scenario, pulse emission rate remained almost constant at 20–30 pulses/s. The animals seemed to fly using only the surveillance phase to assess their surroundings while making U-turns. The differences in pulse trains observed during these two different flight scenarios indicated

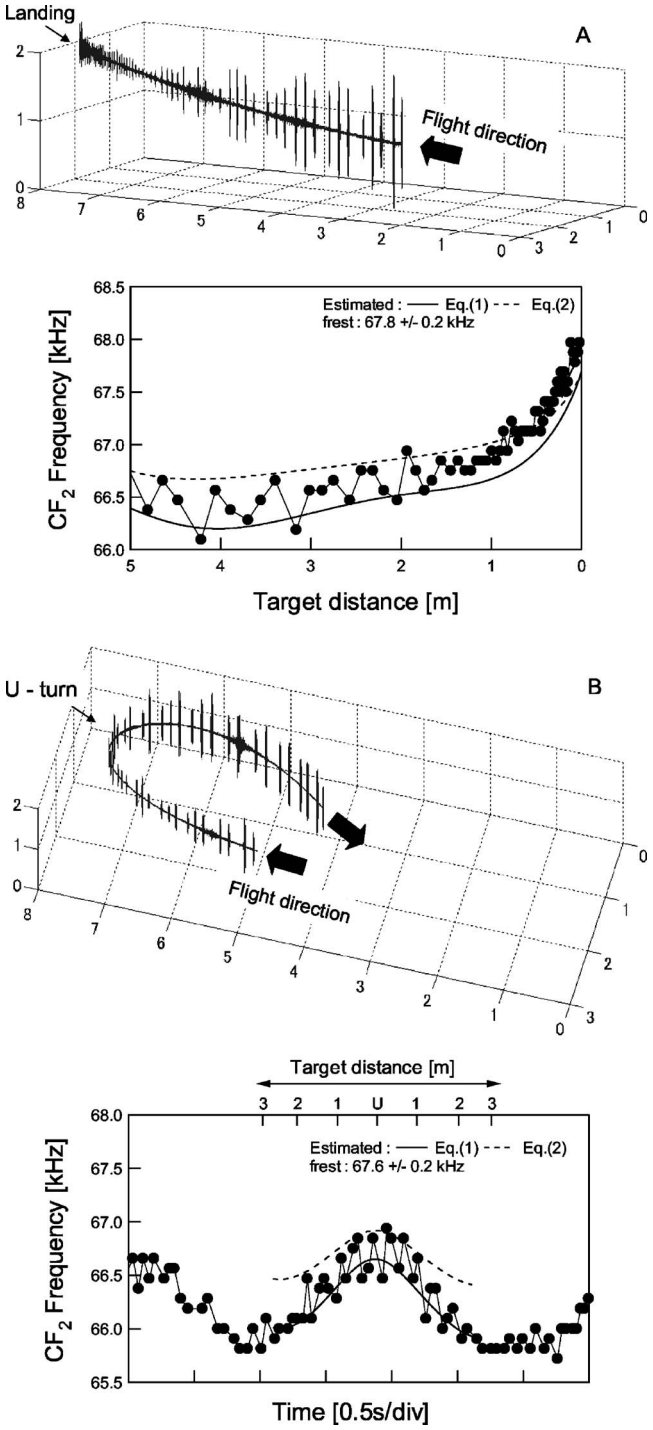

FIG. 2. Three-dimensional spatio-temporal reconstruction and changes in the call frequencies of *Hipposideros terasensis* echolocation behavior for two different flight scenarios: (a) landing and (b) U-turn. Upper graphs: Coordinate grids (1 m^2) show the dimensions of the flight chamber ($8 \times 3 \times 2$ m^3). Echolocation pulses recorded by a Telemike are placed alongside the flight trajectory. Lower graphs: Solid circles indicate call frequencies. Solid and dashed lines indicate estimated call frequencies calculated with Eqs. (1) and (2) (described in text), respectively.

that the bats used different echolocation strategies for different echolocation tasks as reported in earlier publications.

B. Doppler-shift compensation

When analyzing the CF_2 frequency of the calls, we found that in the landing scenario, *H. terasensis* systemati-

cally changed call frequencies as a function of distance to the target wall [solid circles in Fig. 2(a)]. In the center of the flight chamber, where the target distance was about 4 m, the CF_2 frequencies of the bat calls were almost 2 kHz below resting frequency. Such frequency changes were likely due to Doppler-shift compensation and dependent on flight speed. Therefore, we determined the relationship between amount of call frequency changes and flight speed using the 3D coordinate data taken from the high-speed video cameras. Equation (1) was used to estimate the compensated frequencies of the pulse CF_2.

$$f_{\text{pulse}} = \frac{c - V}{c + V} f_{\text{rest}} \tag{1}$$

where V is bat flight speed, c is sound velocity in air (344 m/s), and f_{rest} is resting frequency. The f_{pulse} indicates the compensated frequency of the call CF_2. This keeps the frequency of the returning echo constant at resting frequency. The reference frequency is thought of as slightly above resting frequency (Schuller *et al.*, 1974; Henson, *et al.*, 1982; Riquimaroux *et al.*, 1992; Keating *et al.*, 1994). However, we used values for the resting frequency instead of the reference frequency for calculations presented here because the reference frequency of *H. terasensis* was not determined. The compensated pulse frequency estimated by Eq. (1) is indicated by the solid line in Fig. 2(a). We found that frequency of call CF_2 agreed well with the estimated values. This strongly suggested that the bats did indeed perform DSC in the landing scenario. When we estimated the call frequencies in the U-turn scenario with Eq. (1), we found that they agreed well with the call frequencies measured by the Telemike [Fig. 2(b)]. These results are similar to these from other CF-FM bats such as *Asellia tridens* (Gustafson and Schnitzler, 1979), *Pteronotus parnellii* (Gaioni *et al.*, 1990; Lancaster *et al.*, 1992), and *Rhinolophus ferrumequinum* (Schnitzler, 1968; Simmons, 1974; Schuller *et al.*, 1974). *Hipposideros terasensis* compensated for flight-induced frequency shifts in the returning echo signal by exhibiting DSC behavior.

C. Changes in call frequency and interemission interval (IEI)

A closer examination of the call frequencies emitted in both scenarios (Fig. 2) revealed that the bats, in addition to performing DSC, typically switched between slightly higher and lower call frequencies. Although the difference was small and measured only a few hundred Hz, this pattern of frequency alterations prompted us to examine temporal call parameters in more detail. Figure 3 depicts the typical relationship between the call frequency and interemission intervals (IEI) for the three bats in the landing scenario. We found that the alternating pattern seen in the call frequencies was also reflected in IEIs. *Hipposideros terasensis* calls clearly switched between long and short IEIs. Lower call frequencies [see arrows in Fig. 3(a)] were usually emitted after longer IEIs [asterisks in Fig. 3(a)]. These vocalization patterns were most often observed in the search and approach phases in the landing scenario.

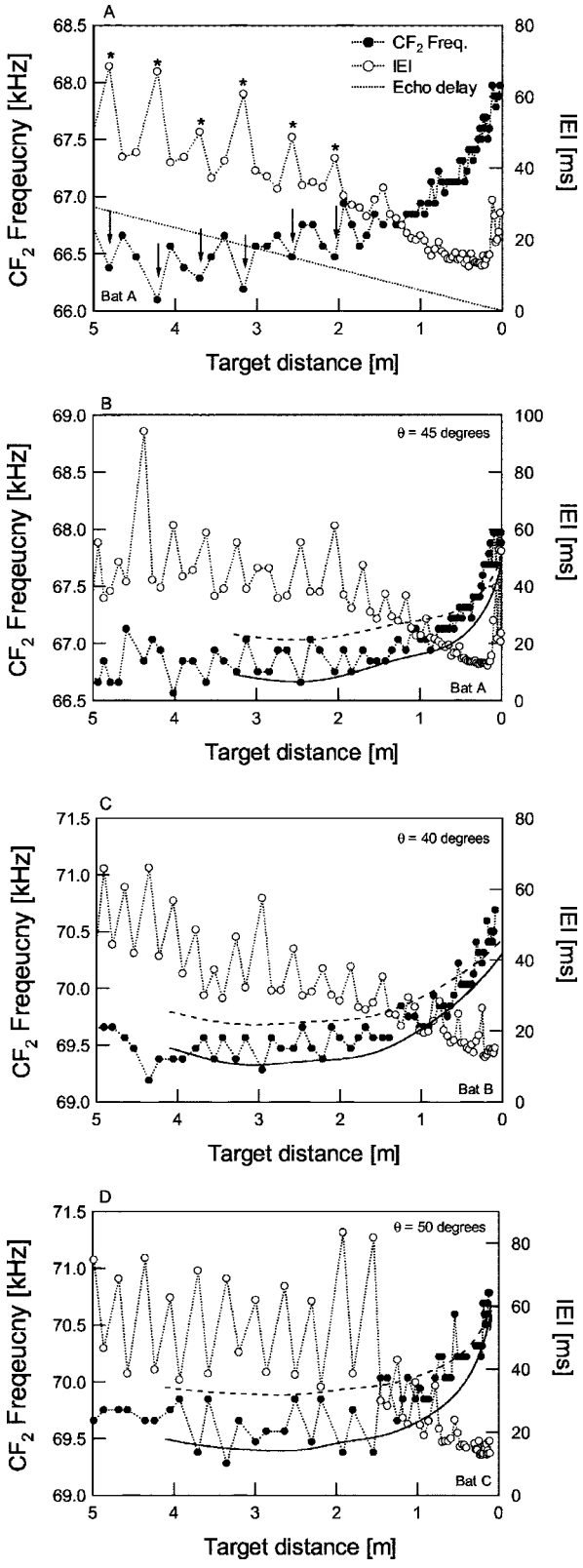

FIG. 3. Relationship between interemission intervals and call frequencies as a function of target distance for calls emitted by landing for three bats. Interemission interval is the time interval between the beginning of the pulse preceding the interval and the beginning of the current pulse. The dashed line in (a) indicates the echo delay from the target wall. Lower call frequencies (arrows) were usually emitted after long interemission interval (asterisks). Solid and dashed lines in (b)–(d) indicate estimated call frequencies calculated with Eqs. (1) and (2) (described in text), respectively. θ is estimated attended angle. (a) and (b) indicate the results of one individual for different flight sessions.

IV. DISCUSSIONS

A. Estimation of the attended angle from the call frequency

When comparing call frequencies estimated from Eq. (1) with those the bats actually emitted (Fig. 2), it becomes apparent that the call frequencies were somewhat underestimated; many calls were produced at frequencies above the estimated values. The values differed by as much as 500 Hz with a certain periodicity. The difference was three times larger than the standard deviation of the resting frequency. It also changed with the target distance, being greater for longer distances. In the U-turn scenario [Fig. 2(b)], the difference between estimated and measured call frequencies appeared to increase as the bats made the U-turn. Because these differences were larger than the standard deviations of the measured frequencies, the variations may have been intentional.

The frequencies estimated by Eq. (1) were assumed to be echoes from a target directly ahead of the bat. The bats flying in our flight chamber, however, were also likely to receive echoes from surrounding walls. If a bat emitted its call frequency based upon the echo reflected from an angle other than straight ahead, the different frequency of this echo might explain the periodic alterations observed in the call frequencies. This assumes that the bats switched their attention between the target wall and sidewalls. As a result, the angles at which the side wall echoes reached the bats' ears (attended angle) changed between call emissions. This would affect the amount of Doppler shift in the attended echo. Bats always adjusted their call frequency's response to previously heard echoes. Here we defined the angle between the direction of the attended echo and bat flight direction as attended angle. This angle can be estimated using the deviation observed in the call frequency. This deviation carried information about the direction of the previously attended echo. Equation (2) is based on Eq. (1) and includes the attended angle. The call frequency for a bat compensating for a Doppler-shifted sideways echo returning at an attended angle θ is

$$f_{\text{pulse}} = \frac{c - V\cos\theta}{c + V\cos\theta} f_{\text{rest}}. \tag{2}$$

The maximum attended angle is the angle where the upper values of the observed pulse frequency correspond to f_{pulse} estimated by Eq. (2). We used several values for the attended angles to estimate the maximum of the attended angle for the scenarios shown in Fig. 2. We found that f_{pulse} for an attended angle of 45° best fit the upper values of actually measured call frequencies for both landing and U-turn scenarios of this bat. Because the lower values of the measured call frequencies best matched the estimated call frequencies emitted in response to echoes returning at 0° [equivalent to Eq. (1)], we concluded that this bat switched between an attended angle of 0° and one of 45° based on periodic variations in call frequencies. Maximum attended angle for the three bats ranged from 40° to 50° (Fig. 3).

The alterations in attended angles were particularly obvious in the U-turn scenario [Fig. 2(b)]. The periodic frequency changes began at a target distance of about 2 m. This corresponded to where the U-turn began. The frequency changes continued throughout flight, presumably to avoid colliding with surrounding walls. Our data suggest that bats in flight were capable of perceiving the spatio-temporal structure of their surroundings by periodically adjusting the attended angle. In this study, the adjustments were between forward and sideways directions. We suggest that degree and rate of alterations in call frequency reflected the complexity of the echolocation task. Estimates for attended angles from measured pulse trains could indicate the way bats scan their surroundings.

When compensating for the highest occurring Doppler shift from straight ahead of the bat, echo frequencies from the side wall may occasionally fall into the tuning region below the resting frequency. This suggests that the bat may compensate for the negative frequency shift. Although further discussion should take into account the auditory abilities of this bat's species, DSC for negative shift has been demonstrated in other species (Metzner *et al.*, 2002). In addition, if a small negative shift never leads to compensation, echo frequencies even from slightly to the side will be out of the best auditory tuning of the bat during flight. We suppose that DSC for a small negative shift may be considered for a flying bat.

B. Relation between alterations in call frequency and IEI

How do alterations in call frequency, which presumably reflect changes in the attended angle, relate to the alterations in IEIs (see Fig. 3)? Figure 4 (left) schematically illustrates the conditions under which echo signals return to the bat at attended angles of 0° (E_{front} from the target wall) and 45° (E_{side} from the side walls). The echoes from the side walls, which we found to elicit higher call frequencies (Fig. 2), had shorter travel distances than the echoes returning from the target wall, which elicited lower call frequencies. This was especially clear during the early phases of DSC when the bat was still far from the target wall. Long travel distances of attended echoes would require the bat to wait longer before emitting the next call to avoid call-echo mismatches. Conversely, the bat called earlier if the echo returned sooner to maximize information gathered by call-echo pairs. Because bats always adjust call frequencies in response to echoes that corresponds to the previously emitted calls, lower calls frequencies are produced after longer IEIs (in response to E_{front}) and higher call frequencies after shorter IEIs (in response to E_{side}). This would explain the alterations of IEIs and call frequencies depicted in Fig. 3.

This interpretation of our results is schematically summarized in Fig. 4 (right). This figure shows how a bat would switch from short IEIs and less DSC [i.e., call frequencies higher than estimated by Eq. (1)] to longer IEIs and more DSC [corresponding to the frequencies estimated by Eq. (1)]. Based upon the spatial dimensions of our flight chamber, we suggest that the delays for E_{front} are longer than those for E_{side}, especially during early phases of DSC. Based on Eq. (2), the Doppler-shift experienced by the bat was larger for E_{front} than for E_{side}. Both echoes, E_{front} and E_{side}, were always

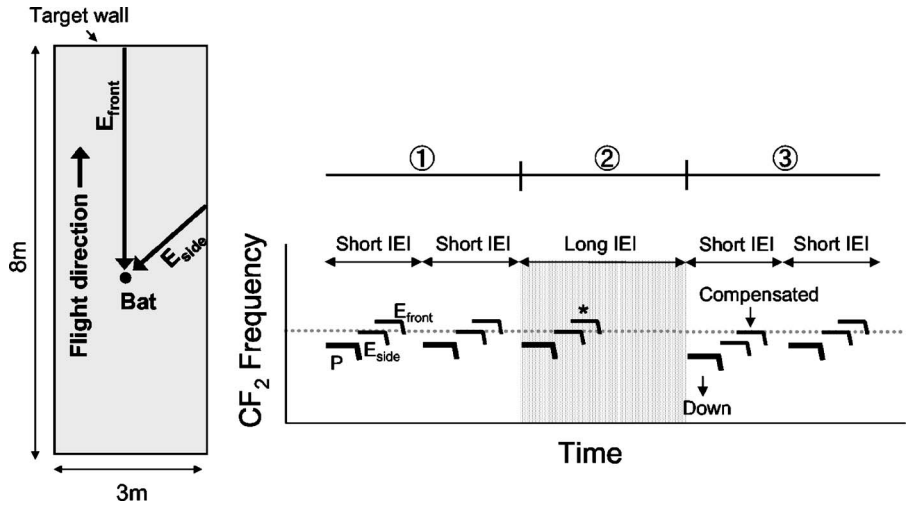

FIG. 4. Schematic diagram of *Hipposideros terasensis* calls and echoes. Left: The top view of the flight chamber indicating the directions and echoes from target wall (E_{front}) and side wall (E_{side}). The closed circle indicates the point at which the flying bat emitted the call producing the two echo signals shown here. Right: A sonagram of pulse-echo pairs for echoes returning from the front target and side walls. The dotted line indicates reference frequency. *P* indicates bat call and *E* indicates retuning echo. Numbered gray areas indicate the time period during which the bat shifts attention from side walls (1) to target wall (2) and back to side walls (3). The call marked "Down" is a low-frequency call emitted by the bat to ensure a return echo at reference frequency.

present. Since the bat switched its attention between the two echoes, it used different Doppler-shift information to adjust the frequency of the subsequent call. When the bat attended to echoes from the side walls (area "1" in Fig. 4), it lowered its call frequencies enough to make the E_{side} echo return at the reference frequency. The echo from the target wall had a longer delay and carried a larger Doppler shift. So, when the bat switched its attention to this echo (see E_{front} labeled by asterisk in gray area "2"), it emitted its next call after a longer IEI and a much lower frequency (see call marked "Down") to ensure the next echo returned at the reference frequency (see echo marked "Compensated"). This echolocation strategy might allow flying bats to perceive the spatial structure of their surroundings without constantly changing the direction of their flight path. In a detailed preliminary analysis of our video recordings, we found that *H. terasensis* exhibited intricate pinna movements closely timed to pulse emission. This phenomenon is common to hipposiderid and rhinolophoid bats. We did not, however, observe head turns. Pinna movements may be important for changing attended angle.

The long IEIs observed here and in other studies are thought to be related to bat respiratory rates and wing beat cycles (Suthers *et al.*, 1972; Schnitzler *et al.*, 1987; Lancaster *et al.*, 1992, 1995). For *H. terasensis*, our video analysis confirmed that wing beat cycle and changes in IEI are synchronized (unpublished observations). In the present study, therefore, we propose that bats may alternate between long and short IEIs when changing the attended angle from flight path target to targets on the side, synchronizing with wing beat cycles. This would be thought of as an effective maneuver for both flight and echolocation. Further investigation is be needed to confirm our hypothesis.

C. Call-echo overlap during DSC

In *Rhinolophus ferrumequinum*, the echo signal overlapped its outgoing pulse due to the long pulse duration (Tian and Schnitzler, 1997). Such call-echo overlap is considered a prerequisite for DSC (Schuller, 1974, 1977). When comparing IEI and echo travel time, however, we found that *H. terasensis* did not experience call-echo overlaps during flight because its call duration is so much shorter than in *Rhinolophus*. Nevertheless, *H. terasensis* compensated for flight-induced frequency shifts in the echo, suggesting that call-echo overlap was not a prerequisite to DSC. It also assumed a difference in signal processing mechanism for DSC between these two CF-FM bats. This difference probably depended on the acoustical characteristics of each species distinct calls.

In conclusion, the alterations in IEIs and amount of DSC observed in our flight scenarios suggested that the bats might use a series of short IEIs to investigate their immediate surroundings (presumably to avoid collisions with the side walls) and checked for distant targets ahead of the bat using longer IEIs. These alterations were caused by a change in the attended angle. By periodically focusing on different echoes (times sharing information), the bats were able to simultaneously perceive several targets. Such systematic variations in the attended angle may have important applications in the examination of other biosonar systems.

ACKNOWLEDGMENTS

We would like to thank Professor Walter Metzner for tremendous precious suggestions on this paper. We also thank Dr. Caralin Bridgmen for careful reading of the manuscript and helpful comments. This work was partly supported by a grant to RCAST at Doshisha University from MEXT of Japan: Special Research Grants for the Development of Characteristic Education from the Promotion and Mutual Aid Corporation for Private Schools Japan and the Innovative Cluster Creation Project.

Gaioni, S. J., Riquimarous, H., and Suga, N. (**1990**). "Biosonar behavior of mustached bats swung on a pendulum prior to cortical ablation," J. Neu-

rosci. **64**, 1801–1817.
Ghose, K., and Moss, C. F. (**2003**). "The sonar beam pattern of a flying bat as it tracks tethered insects," J. Acoust. Soc. Am. **114**, 1120–1131.
Gustafson, Y., and Schnitzler, H.-U. (**1979**). "Echolocation and obstacle avoidance in the hipposiderid bat *Assellia tridens*," J. Comp. Physiol. **131**, 161–167.
Henson, O. W., Jr., Pollak, G. D., Kobler, J. B., Henson, M. M., and Goldman, L. J. (**1982**). "Cochlear microphonic potentials elicited by biosonar signals in flying bats, *Pteronotus p. parnellii*," Hear. Res. **7**, 127–147.
Henson, O. W., Jr., Bishop, A., Keating, A., Kobler, J., Henson, M., Wilson, B., and Hansen, R. (**1987**). "Bisonar imaging of insects by *Pteronotus p. parnellii*, the mustached Bat," Nat. Geog. Res. **3**, 82–101.
Keating, A. W., Henson, O. W., Jr., Henson, M. M., Lancaster, W. C., and Xie, D. H. (**1994**). "Doppler-shift compensation by the mustached bat: quantitative data," J. Exp. Biol. **188**, 115–129.
Lancaster, W. C., Henson, O. W., Jr., and Keating, A. W. (**1995**). "Respiratory muscle activity in relation to vocalization in flying bats," J. Exp. Biol. **198**, 175–191.
Lancaster, W. C., Keating, A. W., and Henson, O. W., Jr. (**1992**). "Ultrasonic vocalizations of flying bats monitored by radiotelemetry," J. Exp. Biol. **173**, 43–58.
Metzner, W., Zhang, S., and Smotherman, M. (**2002**). "Doppler-shift compensation behavior in horseshoe bats revisited: auditory feedback controls both a decrease and an increase in call frequency," J. Exp. Biol. **205**, 1607–1616.
Moss, C. F., and Surlykke, A. (**2001**). "Auditory scene analysis by echolocation in bats," J. Acoust. Soc. Am. **110**, 2207–2226.
Novick, A., and Vaisnys, J. R. (**1964**). "Echolocation of flying insects by the bat, *Chilonycteris parnellii*," Biol. Bull. **127**, 478–488.
Riquimaroux, H., and Watanabe, Y. (**2002**). "Characteristics of bat sonar sounds recorded by a telemetry system and a fixed ground microphone," The seventh western pacific regional acoustics conference (WESTPRAC VII), 233–238.
Riquimaroux, H., Gaioni, S. J., and Suga, N. (**1992**). "Inactivation of the DSCF area of the auditory cortex with muscimol disrupts frequency discrimination in the mustached bat," J. Neurophysiol. **68**, 1613–1623.
Schnitzler, H.-U. (**1968**). "Die ultraschall-ortungslaute der Hufeisen-Fledermäuse (*Chiroptera-Rhinolophidae*) in verschiedenen orientierungssituationen," Z. Vergl. Physiol. **57**, 376–408.
Schnitzler, H.-U., Kalko, E., Miller, L., and Surlykke, A. (**1987**). "The echolocation and hunting behavior of the bat, *Pipistrellus kuhli*," J. Comp. Physiol., A **161**, 267–274.
Schuller, G. (**1974**). "The role of overlap of echo with outgoing echolocation sound in the bat *Rhinolophus ferrumequinum*," Naturwiss. **61**, 171–172.
Schuller, G. (**1977**). "Echo delay and overlap with emitted orientation sounds and Doppler-shift compensation in the bat, *Rhinolophus ferrumequinum*," J. Comp. Physiol. **114**, 103–114.
Schuller, G., Beuter, K., and Schnitzler, H.-U. (**1974**). "Response to frequency shifted artificial echoes in the bat *Rhinolophus ferrumequinum*," J. Comp. Physiol. **89**, 275–286.
Simmons, J. A. (**1974**). "Response of the Doppler echolocation system in the bat, *Rhinolophus ferrumequinum*," J. Acoust. Soc. Am. **56**, 672–682.
Suthers, R. A., Thomas, S. P., and Suthers, B. J. (**1972**). "Respiration, wingbeat and ultrasonic pulse emission in an echo-locating bat," J. Exp. Biol. **56**, 37–48.
Tian, B., and Schnitzler, H.-U. (**1997**). "Echolocation signals of the greater horseshoe bat (*Rhinolophus ferrumequinum*) in transfer flight and during landing," J. Acoust. Soc. Am. **101**, 2347–2364.
Trappe, M., and Schnitzler, H.-U. (**1982**). "Doppler-shift compensation in insect-catching horseshoe bats," Naturwiss. **69**, 193–194.

Origin of the double- and multi-pulse structure of echolocation signals in Yangtze finless porpoise (*Neophocaena phocaenoides asiaeorientialis*)

Songhai Li
Institute of Hydrobiology, The Chinese Academy of Sciences, Wuhan, 430072, People's Republic of China and Graduate School of the Chinese Academy of Sciences, Beijing, 100039, People's Republic of China

Kexiong Wang and Ding Wang[a)]
Institute of Hydrobiology, The Chinese Academy of Sciences, Wuhan, 430072, People's Republic of China

Tomonari Akamatsu
National Research Institute of Fisheries Engineering, Fisheries Research Agency, Ebidai, Hasaki, Kashima, Ibaraki 314-0421, Japan

(Received 20 April 2005; revised 8 August 2005; accepted 26 September 2005)

The signals of dolphins and porpoises often exhibit a multi-pulse structure. Here, echolocation signal recordings were made from four geometrically distinct positions of seven Yangtze finless porpoises temporarily housed in a relatively small, enclosed area. Some clicks demonstrated double-pulse, and others multi-pulse, structure. The interpulse intervals between the first and second pulse of the double- and multi-pulse clicks were significantly different among data from the four different positions ($p<0.01$, one-way ANOVA). These results indicate that the interpulse interval and structure of the double- and multi-pulse echolocation signals depend on the hydrophone geometry of the animal, and that the double- and multi-pulse structure of echolocation signals in Yangtze finless porpoise is not caused by the phonating porpoise itself, but by the multipath propagation of the signal. Time delays in the 180° phase-shifted surface reflection pulse and the nonphase-shifted bottom reflection pulse of the multi-pulse structures, relative to the direct signal, can be used to calculate the distance to a phonating animal. © *2005 Acoustical Society of America.* [DOI: 10.1121/1.2126919]

PACS number(s): 43.80.Ka, 43.80.Lb, 43.64.Tk, 43.30.Vh [WWA] Pages: 3934–3940

I. INTRODUCTION

Odontocetes possess highly developed echolocation sound production capabilities. Many theories exist on how, and where anatomically, odontocetes produce echolocation sounds (see reviews in Norris *et al.*, 1961; Norris, 1964, 1968, 1975; Mead, 1975; Popper, 1980; Amundin, 1991; Cranford, 2000; Cranford and Amundin, 2004). However, any tenable theory must account for the acoustical characteristics of the signals themselves in order to understand the sound-generation mechanism.

The phenomenon of the double- and multi-pulse structure of echolocation signals has been demonstrated in *Tursiops truncatus* (Norris *et al.*, 1966), *Inia geoffrensis* and *Sotalia fluviatilis* (Norris *et al.*, 1972), *Phocoena phocoena and Cephalorhynchus mersonii* (Kamminga and Wiersma, 1981), and *Cephalorhynchus hectori* (Dawson, 1988). However, because of the uncertainty of the animal's hydrophone geometry, it is difficult to discern whether double- and multi-pulse structures are emitted by the animals themselves, or if they are the result of multipath propagation or some other artifact (Au, 1993).

Vocalizations of the finless porpoise *Neophocaena phocaenoides*, a representative of the Phocoenidae family and a species that includes both marine and riverine populations inhabiting different environments, have been investigated over the past 40 years (Mizue *et al.*, 1968; Pilleri *et al.*, 1980; Kamminga *et al.*, 1986, 1996; Wang, 1996; Nakahara *et al.*, 1997; Akamatsu *et al.*, 1998; Goold and Jefferson, 2002; Li *et al.*, 2005). Li *et al.* (2005) illustrated the phenomenon of the double- and multi-pulse structure of echolocation signals in free-ranging Yangtze finless porpoise (*N. p. asiaeorientialis*). Again, however, because of the uncertainty of the hydrophone geometry of the animal, they could not determine the origin of the double- and multi-pulse structure.

In this study, we measured the interpulse intervals and analyzed the structures of double- and multi-pulse echolocation signals of relatively immobile porpoises from four geometrically distinct positions to determine whether the interpulse intervals and structures of the double- and multi-pulse clicks depend on changes in the animal's hydrophone geometry.

II. MATERIALS AND METHODS

A. Study site and animals

The experiment was conducted in an enclosure (approximately 30×60 m, with a maximum depth of 3.3 m), which

[a)]Author to whom correspondence should be addressed. Electronic mail: wangd@ihb.ac.cn

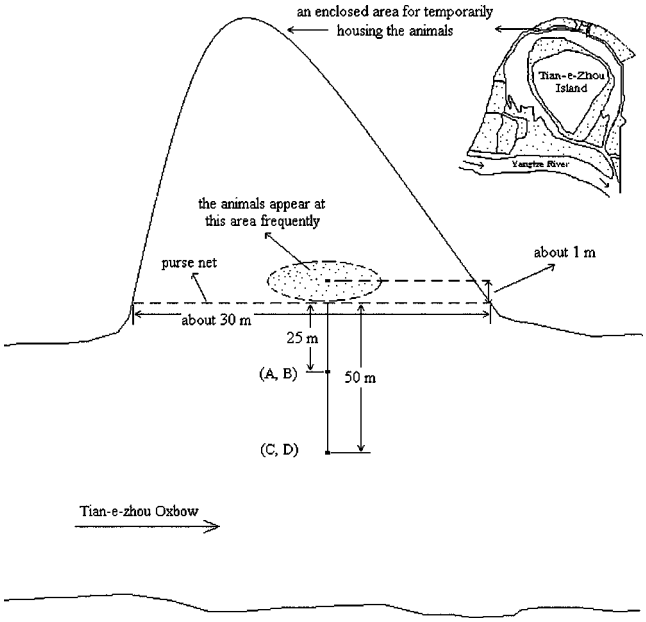

FIG. 1. Map of the study site, an enclosed area located at the top of the Tian-e-Zhou Oxbow. The oval dotted area indicates the range of frequently observed surface behaviors of the temporarily housed porpoise. A, B, C, and D indicate the underwater positions of the four recording hydrophones.

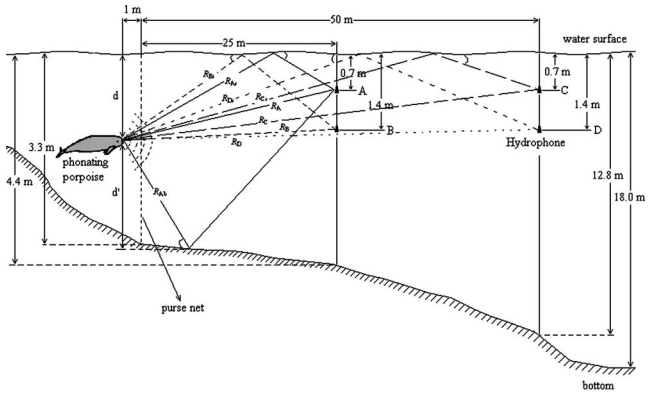

FIG. 2. Cross-sectional view of the experimental setup and multipath propagation of signals corresponding to the different positions A, B, C, and D. R_{As}, R_{Bs}, R_{Cs}, and R_{Ds} correspond to the propagation lengths for surface reflections to positions A, B, C, and D, respectively; R_A, R_B, R_C, and R_D correspond to the propagation lengths for direct signals to positions A, B, C, and D, respectively; R_{Ab} is the propagation length for bottom reflections to position A.

was established using a purse net in a small inlet of the Tian-e-zhou Oxbow (Fig. 1) to temporarily house porpoise. The oxbow (21-km length, 1–2-km width, 20-m maximum depth) is an old course of the Yangtze River in Shishou, Hubei, China, and was established as a reserve for baiji (*Lipotes vexillifer*) and Yangtze finless porpoise in 1992. In 2004, there were over 20 individuals of Yangtze finless porpoise living in this oxbow, including those introduced from the Yangtze River and those born in the oxbow. Wei *et al.* (2002) showed that the behavior and ecology of porpoises in the oxbow were similar and comparable to those of porpoises in the Yangtze River.

For this experiment, seven animals were caught in the oxbow on 13 October 2004 under a special permit from the Department of Fisheries Management, Hubei Province. No porpoise was injured during capture. After a basic medical examination (including measurements of weight and body length, an electrocardiogram, and collection of a blood sample), all animals were temporarily housed in the enclosure (Fig. 1). They were maintained undisturbed for several hours to allow acclimation before acoustic recordings were performed. During this phase, surface behaviors and respiration frequency were observed and recorded. The animals appeared frequently in an approximately oval area (the dotted area in Fig. 1). Depth measurements showed that this oval area was the deepest area of the enclosure (ca. 3.3 m; see Fig. 2).

B. Experimental setup and acoustic measurements

A hydrophone was presented in positions A, B, C, and D, directly in front of the oval area (Figs. 1 and 2) to record acoustic data from the porpoises on 13 and 14 October 2004 (Table I). Positions A and B were at a horizontal distance of 26 m to the center of the oval area and were at depths of 0.7 and 1.4 m, respectively. Positions C and D were at a horizontal distance of 51 m to the center of the oval area and were at depths of 0.7 and 1.4 m, respectively (Figs. 1 and 2). Distance was measured using a flexible measuring tape, and depth was measured using a handheld depth measure (PS-7 LCD Digital Sounder, Hondex, Japan).

The hydrophone was an OKI ST1020 (sensitivity, −180 dB *re*: 1 V μPa^{-1} +3/−12 dB, up to 150 kHz; the sensitivity declines with an increase in frequency from 100 to 150 kHz; when the frequency is 125 kHz, the sensitivity is approximately −185 dB *re*: 1 V μPa^{-1}). Recordings were made using a Sony PCHB244 digital data recorder, with a flat frequency response from dc to 147 kHz within 3 dB (Akamatsu *et al.*, 1998).

The analysis of echolocation signals was performed using PC-based SIGNAL/RTS™ software (Version 3.0, July 1996; American Engineering Design, USA). The recorded signals were replayed from the data recorder at half-speed and were digitized using a 12-bit Data Translation-2821G A/D board with a sampling frequency of 200 kHz (i.e., an equivalent real time sample rate of 400 kHz). Raw click trains were first reviewed to assess the signal-to-noise ratio, and then the individual clicks manually acquired using the built-in cursor option in high signal-to-noise ratio click trains were examined (see Li *et al.*, 2005 for details). Only click trains that had clicks with distinct double- or multi-pulse

TABLE I. Details of acoustic recordings.

Position	Date	Acoustic recording time	Details
A	13 October	19:41–20:42	7 animals recordings of 61 min
B	13 October	20:50–21:51	7 animals recordings of 61 min
C	14 October	7:50–8:34	7 animals recordings of 44 min
D	14 October	8:37–8:54, 9:02–9:43	7 animals recordings of 58 min

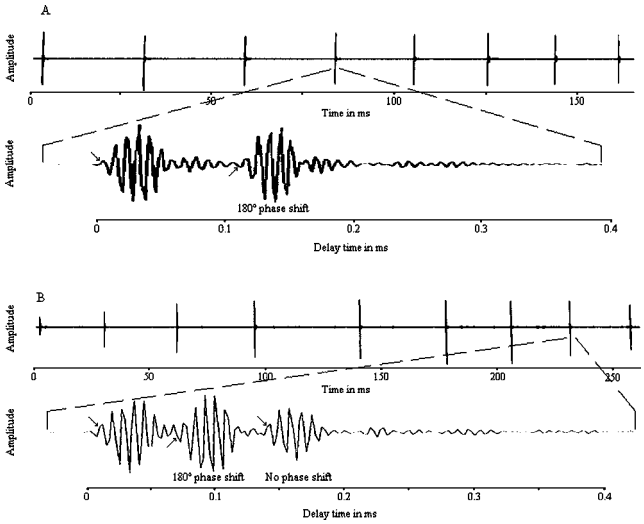

FIG. 3. Double-pulse (a) and multi-pulse (b) structure of echolocation signals in Yangtze finless porpoise.

structure were selected for subsequent interpulse interval (time between instantaneous peak pressure points within the pulses) and phase analysis. The waveform of each individual click in one train tends to be very repetitive and stereotyped (Li *et al.*, 2005). Thus, to maintain independent samples, only one click was chosen from each selected click train for acoustic measurement. For each click that exhibited a distinct double- or multi-pulse structure, the waveform, interpulse interval, and phase relation among pulses were documented. One-way analysis of variance (ANOVA) was used to examine the difference in interpulse interval between the first and second pulses of double- and multi-pulse echolocation signals among the four geometrically distinct positions. A p value of 0.05 was considered significant.

III. RESULTS

Recordings of 61, 61, 44, and 58 min were acquired from positions A, B, C, and D, respectively (Table I). Double- and multi-pulse structures in echolocation signals were detected from all four positions. In many cases, the second or third pulse had equal amplitude, and even higher amplitude than the first pulse. Among the data from all four positions, a total of 177 clicks from 177 different click trains with distinct double- or triple-pulse signal structure were measured acoustically. The waveform, interpulse interval, and phase relation among pulses were documented. The magnifications of click 4 in Fig. 3(a) and click 8 in Fig. 3(b) demonstrate the properties of interest for most of the measured clicks.

Recordings from position A included 49 click trains with distinct double-pulse echolocation clicks and 16 click trains with distinct triple-pulse echolocation clicks. Among the double- and triple-pulse clicks, 42 of 49 measured double-pulse clicks had a 180° phase shift between the first and second pulse [Fig. 3(a)], and all 16 triple-pulse clicks had a 180° phase shift between the first and second pulse, with no phase shift between the first and third pulse [Fig. 3(b)]. The interpulse interval between the first and second pulse of all measured double- and triple-pulse echolocation clicks ranged from 39 to 96 μs, with an average of 67±13 μs (Table II).

TABLE II. Summary statistics for the interpulse intervals between the first and second pulse of double- and multi-pulse echolocation signals in Yangtze finless porpoise recorded at four different positions A, B, C, and D (see Figs. 1 and 2). The highlighted area indicates significant differences (one-way ANOVA; $p<0.01$).

	Interpulse interval (μs)			
	Minimum	Maximum	Mean	Standard deviation
Position A (N=65)	39	96	**67**	13
Position B (N=66)	44	187	**114**	39
Position C (N=4)	34	41	**37**	3
Position D (N=42)	35	70	**55**	9

Recordings from position B included 60 click trains with distinct double-pulse clicks and only 6 click trains with distinct triple-pulse clicks. Among the 66 measured clicks from 66 different click trains, 46 of 60 double-pulse clicks had a 180° phase shift between the first and second pulse, while all 6 triple-pulse clicks had a 180° phase shift between the first and second pulse, with no phase shift between the first and third pulse. The interpulse interval between the first and second pulse of all measured double- and triple-pulse echolocation clicks ranged from 44 to 187 μs, with an average of 114±39 μs (Table II).

Recordings from position C included only 4 click trains with distinct double-pulse clicks, and no click trains with distinct triple- or multi-pulse echolocation clicks. Most of the click trains had clicks with overlapping pulse components and were not used in subsequent analyses. All selected double-pulse clicks had a 180° phase shift between the first and second pulse. The interpulse interval ranged from 34 to 41 μs, with an average of 37±3 μs (Table II).

In position D, recordings included 42 click trains with distinct double-pulse clicks. No distinct triple- or multi-pulse echolocation clicks were recorded. Of the measured clicks, 41 had a 180° phase shift between the first and second pulse. The interpulse interval ranged from 35 to 70 μs, with an average of 55±9 μs (Table II).

One-way ANOVA detected a significant difference in interpulse interval between the first and second pulses of double- and multi-pulse echolocation signals among the four positions (F=61.28, df=3, $p<0.01$; Table II).

Comparison of the percentage distributions for interpulse intervals between the first and second pulse of double- and multi-pulse echolocation signals among recordings from the four positions indicated that signals from all positions had interpulse intervals of <50 μs, but only signals from position B had interpulse intervals of >100 μs (64%; Fig. 4). All interpulse intervals from position C were <50 μs, all interpulse intervals from position D were <70 μs, and interpulse intervals from positions A and B ranged from <50 μs to >90 μs (Fig. 4).

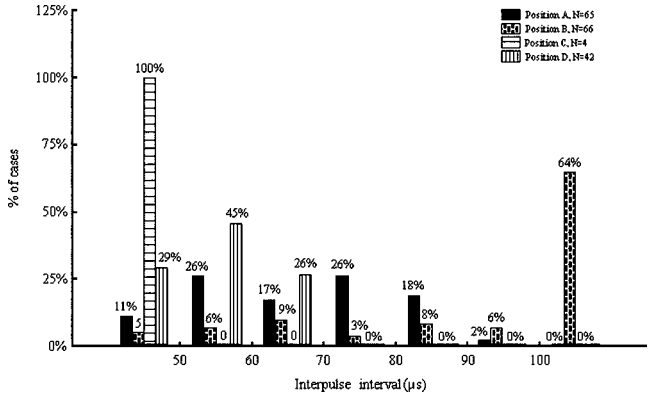

FIG. 4. Comparison of the percent distributions of interpulse intervals between the first and second pulses among positions A, B, C, and D.

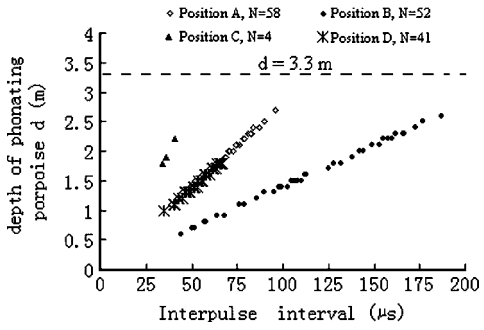

FIG. 6. Calculated porpoise depth versus interpulse interval from positions A, B, C, and D. The broken line represents the water depth in the area where frequent surface behaviors were observed.

IV. DISCUSSION AND CONCLUSIONS

A. Origin of the double- and multi-pulse echolocation signal structure

The interpulse interval and the structure of double- and multi-pulse echolocation signals varied among recordings from the four geometrically distinct positions (Table II, Fig. 4). Comparison of the percentage distributions of interpulse intervals with the animals' hydrophone geometry indicated that the differences were not caused by the animals themselves, but, rather, were related to their hydrophone geometry (Fig. 2).

Because of large differences in acoustic impedance at the air-water and water-bottom interfaces, sound would be reflected relatively well by these interfaces. Figure 5 shows the multipath reflection propagation of porpoise echolocation signals. When sound travels from a high to a much lower density medium, such as at the water-air interface, its reflection will exhibit a 180° phase shift, whereas when sound travels from a low to a higher density medium, such as at the water-bottom interface, its reflection will have a 0°–180° phase shift, depending on the angle of reflection [see Aubauer *et al.* (2000) for details]. Assuming that double- and multi-pulse echolocation signals from Yangtze finless porpoise were caused by multipath sound propagation, and not by the porpoise itself, the result that only a portion of the double-pulse echolocation signals had a 180° phase shift between the first and second pulse can be explained by a combination of double-pulse echolocation signals from surface and bottom reflections. Subsequently, porpoise depth can be determined by measuring the time delay τ_s of the pulse of a 180° phase-shifted surface reflection relative to the initial pulse (Aubauer *et al.*, 2000; Lammers *et al.*, 2004), using Eqs. (1) and (2). Two additional measures, the depth of the hydrophone h and the horizontal distance between the hydrophone and the phonating porpoise a, are required. The relatively limited territory (Fig. 1) of the animals facilitated the estimation of a. Here, variable a was assumed to be the distance between the hydrophone and the center of the oval area,

$$c\tau_s = \frac{h}{\sin\alpha} + \frac{d}{\sin\alpha} - \sqrt{a^2 + (d-h)^2}, \tag{1}$$

$$\frac{d}{\tan\alpha} + \frac{h}{\tan\alpha} = a, \tag{2}$$

where c is the sound velocity in water and α is the incident and reflected angle of the surface path. The depth of the porpoise d is given by

$$d = \sqrt{\frac{(c\tau_s)^4 - 4(a^2+h^2)(c\tau_s)^2}{4[(c\tau_s)^2 - 4h^2]}}. \tag{3}$$

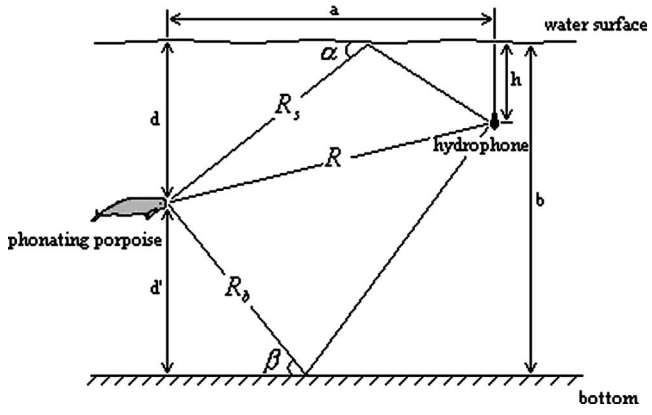

FIG. 5. Multipath propagation of porpoise clicks in shallow water, where a=the horizontal distance between the phonating animal and the hydrophone, h=hydrophone depth, b=water depth, R=the distance between the phonating animal and the hydrophone, d=the depth of the phonating animal, d'=the distance of the phonating animal from the bottom, R_s=the propagation length of a water surface reflection, and R_b=the propagation length of a bottom reflection.

The calculated depths of phonating porpoise are plotted in Fig. 6. Although there were large differences in the distribution of interpulse intervals between the initial pulse and the 180° phase-shifted surface reflection among signals from the four different positions, the depths of phonating porpoise were concentrated in the range from 0.5 to 2.5 m, and none were beyond the upper boundary of the water depth, 3.3 m, the maximum depth of the bottom in the area where the animals moved (Fig. 6). The range in calculated depths was congruous with the range of potential actual porpoise depths. In fact, there might be some difference between the assumed value of a and the actual distance from the hydrophone to the phonating animal (Fig. 1); however, this difference would not have caused considerable error in the conclusion that the calculated depth of the phonating animals was consistently

lower than the actual water depth of 3.3 m. This is because, according to the observation of surface behaviors, the porpoises were found to usually appear within an approximately oval area with a difference of only ±1 m between the assumed and actual distance (Fig. 1), which can be neglected in the depth estimate. Even though, a difference of ±5 m between the assumed and actual distance was conservatively assumed, the calculated depth of phonating animal will remain lower than the actual water depth of 3.3 m.

Relatively shallow water and a flat bottom surface are necessary for ideal bottom reflection (Aubauer *et al.*, 2000). The fact that there were distinct triple-pulse echolocation signal structures in positions A and B, but not in positions C and D, is related to the bottom conformation of the experimental site (Fig. 2); i.e., the bottom was relatively flat between the location of phonating animal and positions A and B, whereas the bottom was steep from positions A and B to C and D.

If we account for the loss of transmission caused by the spherical or cylindrical spread and absorption of signals in water, it is difficult to explain the phenomenon of equal or higher amplitude of the second or third pulse than of the initial pulse in double- and multi-pulse clicks. However, considering the transmission beam pattern of echolocation signals (Au, 1993), this phenomenon may have been caused by on-axis reflections and off-axis direct incidence.

In the past, the double- and multi-pulse structures of echolocation signals in dolphin and porpoise were interpreted as waveform characteristics emitted by the animals themselves (Norris, 1968; Kamminga and Wiersma, 1981). However, based on the direct and indirect evidence discussed in this paper, we conclude that the structure of double- and multi-pulse clicks in Yangtze finless porpoise depended on the animal's hydrophone geometry, and the double- and multi-pulse echolocation signals were in fact the result of multipath propagation (Figs. 2 and 5) and were not emitted by the porpoise.

Considerable indirect evidence (Cranford, 1992a, b, 2000; Cranford *et al.*, 1996) and some recent direct evidence (Cranford, 1999; Cranford *et al.*, 2000) exists for at least two separately controllable pulse generators in the heads of odontocetes. It is not currently clear whether both pulse generators are involved in the production of sonar pulse, although this seems a reasonable assumption. If the two separately controllable pulse generators produced sonar signal independently, our results would have indicated that the two sources were activated simultaneously without phase shift.

B. Estimation of distance to the animals

Because the double- and multi-pulse structures of echolocation signals are caused by multipath propagation of sounds (Fig. 5), and not by the porpoise itself, the distance of a phonating porpoise can be determined by measuring the arrival-time differences τ_s and τ_b, between the direct pulse, the 180° phase-shifted surface reflection pulse, and the nonphase-shifted bottom reflection pulse using Eqs. (4)–(7):

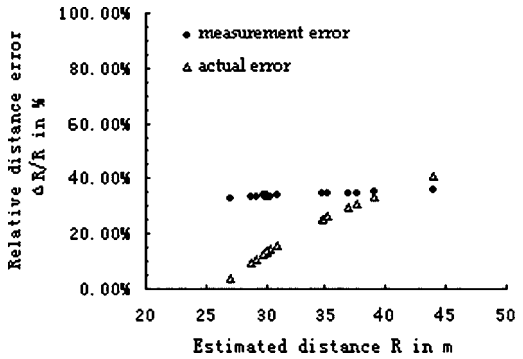

FIG. 7. Measurement error ($\Delta R/R$) and actual error ($\Delta R'/R$) for relative distance.

$$\frac{h}{\sin\alpha}+\frac{d}{\sin\alpha}-c\tau_s=R, \tag{4}$$

$$\cos(\pi-2\alpha)=\frac{[h/(\sin\alpha)]^2+[d/(\sin\alpha)]^2-R^2}{2\times[d/(\sin\alpha)]\times[h/(\sin\alpha)]}, \tag{5}$$

$$\frac{b-h}{\sin\beta}+\frac{b-d}{\sin\beta}-c\tau_b=R, \tag{6}$$

$$\cos(\pi-2\beta)=\frac{[(b-h)/(\sin\beta)]^2+[(b-d)/(\sin\beta)]^2-R^2}{2\times[(b-d)/(\sin\beta)]\times[(b-h)/(\sin\beta)]}, \tag{7}$$

where α is the incident and reflected angle of the surface path, β is the incident and reflected angle of the bottom path, c is the sound velocity in water, and b, d, and h are the bottom, phonating porpoise, and hydrophone depths, respectively (Fig. 5). The distance of the phonating animal (R) is given by

$$R=\frac{4bh(b-h)-(c\tau_s)^2(b-h)-h(c\tau_b)^2}{2c\tau_b h+2c\tau_s(b-h)}. \tag{8}$$

Sixteen distinct triple-pulse structure clicks from 16 click trains at position A were used to estimate the distance between the phonating animal and the hydrophone.

In the present study, because the value of $|d-h|\ll a$ (see Figs. 2 and 5), the distance between the phonating animal and the hydrophone (R) is approximate to the value of a, which was assumed to be 26 m in this case (Figs. 2 and 5). However, there is always some difference between the estimated and assumed distances, and the estimated distances are usually greater than the assumed distances (Fig. 7). One explanation may be that the phonating animal overstepped the range of the oval area (Fig. 1) and its actual distance to the hydrophone is greater than the assumed distance. Alternatively, a comparison of measurement and actual errors in the relative distance in Fig. 7 indicated that the measurement errors of the individual variables that were used in Eq. (8) could have caused the difference between the estimated and assumed distances. The measurement error for relative distance ($\Delta R/R$) is defined as the quotient of the total error differential of distance [the sum of the partial derivatives of

all variables multiplied by the error bounds of the individual measurements; see Eq. (9); Aubauer *et al.* 2000] and the estimated distance [Eq. (9)]. The actual error for relative distance ($\Delta R'/R$) is defined as the quotient of the difference between the estimated and assumed actual distances, and the estimated distance [Eq. (10)]:

$$\frac{\Delta R}{R} = \frac{|\partial R/\partial b| \cdot |\Delta b| + |\partial R/\partial h| \cdot |\Delta h| + |\partial R/\partial c| \cdot |\Delta c| + |\partial R/\partial \tau_s| \cdot |\Delta \tau_s| + |\partial R/\partial \tau_b| \cdot |\Delta \tau_b|}{R}. \quad (9)$$

$$\frac{\Delta R\prime}{R} = \frac{|R - 26|}{R}. \quad (10)$$

In the present analysis, the assumed individual measurement errors were $|\Delta b| = 0.5$ m for the bottom depth, $|\Delta h| = 0.1$ m for the hydrophone depth, $|\Delta c| = 5$ m s^{-1} for the sound velocity in water, and $|\Delta \tau| = 4$ μs for the time delays τ_s and τ_b.

Figure 7 shows that the measurement error for relative distance is less than 40% and is almost constant, and the actual error for relative distance is lower than the measurement error in all cases except one, indicating that the difference between the estimated and assumed distance may have resulted from the measurement errors of the individual variables used in Eq. (8). This result demonstrates again that the multi-pulse structure of the echolocation signals is caused by multipath propagation. Because the measurement error is less than 40% (Fig. 7), the time delays in detection of the trailing pulse relative to the initial pulse can be used to estimate the distance between the phonating porpoise and the hydrophone fairly accurately (Aubauer *et al.*, 2000).

ACKNOWLEDGMENTS

Dr. Jianqiang Xiao provided valuable feedback and encouragement. We especially acknowledge the staff at Baiji Aquarium and Tian-e-zhou Baiji National Natural Reserve for sharing time and resources, and for providing endless support. We would also like to express our appreciation to Dr. Peter T. Madsen and two reviewers for valuable comments on the manuscript. This research was supported by the Chinese Academy of Sciences (CAS) and the Institute of Hydrobiology, CAS (No. KSCX2-SW-118 and 220103) and the Program for Promotion of Basic Research Activities for Innovative Biosciences of Japan.

Akamatsu, T., Wang, D., Nakamura, K., and Wang, K. (**1998**). "Echolocation range of captive and free-ranging baiji (*Lipotes vexillifer*), finless porpoise (*Neophocaena phocaenoides*), and bottlenose dolphin (*Tursiops truncatus*)," J. Acoust. Soc. Am. **104**, 2511–2516.

Amundin, M. (**1991**). "Sound production in odontocetes with emphasis on the harbour porpoise *Phocoena phocoena*," Ph.D. dissertation, University of Stockholm, Sweden.

Au, W. W. L. (**1993**). *The Sonar of Dolphins* (Springer-Verlag, New York).

Aubauer, R., Lammers, M. O., and Au, W. W. L. (**2000**). "One-hydrophone method of estimating distance and depth of phonating dolphins in shallow water," J. Acoust. Soc. Am. **107**, 2744–2749.

Cranford, T. W. (**1992a**). "Directional asymmetry in odontocetes," Am. Zool. **32**, 140.

Cranford, T. W. (**1992b**). "Functional morphology of the odontocete forehead: Implications for sound generation," Ph.D. dissertation, Univ. of California, Santa Cruz.

Cranford, T. W. (**1999**). "Evidence for multiple sonar signal generators in odontocetes," in *Proceedings of the Thirteenth Biennial Conference on the Biology of Marine Mammals*. Marine Mammal Society, Mauri, HI, p. 40.

Cranford, T. W. (**2000**). "In search of impulse sound sources in odontocetes," in *Hearing by Whales and Dolphins*, edited by W. W. L. Au, A. N. Popper, and R. R. Fay (Springer-Verlag, New York), pp. 109–156.

Cranford, T. W., and Amundin, M. (**2004**). "Biosonar pulse production in odontocetes: the state of our knowledge," in *Echolocation in Bats and Dolphins*, edited by J. Thomas, C. F. Moss, and M. Vater (Univ. of Chicago, Chicago), pp. 27–35.

Cranford, T. W., Amundin, M., and Norris, K. S. (**1996**). "Functional morphology and homology in the odontocete nasal complex: Implications for sound generation," J. Morphol. **228**, 223–285.

Cranford, T. W., Elsberry, W. R., Blackwood, D. J., Carr, J. A., Kamolnick, T., Todd, M., Van Bonn, B. G., Carder, D. A., Ridgway, S. H., Bozlinski, D. M., and Decker, E. C. (**2000**). "Physiological evidence for two independent sonar signal generators in the bottlenose dolphin," J. Acoust. Soc. Am. **108**, 2613.

Dawson, S. M. (**1988**). "The high frequency sounds of free-ranging Hector's Dolphin, *Cephalorhynchus hectori*," Rep. Int. Whal. Comm. **9**, 339–341.

Goold, J. C., and Jefferson, T. A. (**2002**). "Acoustic signals from free-ranging Finless porpoises (*Neophocaena phocaenoides*) in the waters around Hong Kong," Raffles Bull. Zool., Suppl. **10**, 131–139.

Kamminga, C., and Wiersma, H. (**1981**). "Investigations on cetacean sonar II. Acoustical similarities and differences in odontocete sonar signals," Aquat. Mammal. **8**, 41–62.

Kamminga, C., Cohen Stuart, A. B., and Silber, G. K. (**1996**). "Investigations on cetacean sonar XI: Intrinsic comparison of the wave shapes of some members of the Phocoenidae family," Aquat. Mammal. **22**, 45–55.

Kamminga, C., Kataoka, T., and Engelsma, F. J. (**1986**). "Investigations on cetacean sonar VII: Underwater sounds of *Neophocaena phocaenoides* of the Japanese coastal population," Aquat. Mammal. **12**, 52–60.

Lammers, M. O., Au, W. W. L., Aubauer, R., and Nachtigall, P. E. (**2004**). "A comparative analysis of the pulsed emissions of free-ranging Hawaiian spinner dolphins," in *Echolocation in Bats and Dolphins*, edited by J. Thomas, C. F. Moss, and M. Vater (Univ. of Chicago, Chicago), pp. 414–419.

Li, S., Wang, K., Wang, D., and Akamatsu, T. (**2005**). "Echolocation signals of the free-ranging Yangtze finless porpoise (*Neophocaena phocaenoides asiaeorientialis*)," J. Acoust. Soc. Am. **117**, 3288–3296.

Mead, J. C. (**1975**). "Anatomy of the external nasal passages and facial complex in the Delphinidae (Mammalia: Cetacea)," Smithsonian Contrib. Zool. **207**, 1–72.

Mizue, K., Takemura, A., and Nakasai, K. (**1968**). "Studies on the little toothed whales in the west sea area of Kyusyu-XV. Underwater sound of the Chinese finless porpoise caught in the Japanese coastal sea," Bull. Faculty Fish. Nagasaki Univ. **25**, 25–32.

Nakahara, F., Takemura, A., Koido, T., and Hiruda, H. (**1997**). "Target discrimination by an echolocating Finless porpoise, *Neophocaena phocaenoides*," Marine Mammal Sci. **133**, 639–649.

Norris, K. S. (**1964**). "Some problems of echolocation in cetaceans," in *Marine Bio-Acoustics*, edited by W. N. Tavolga (Pergamon, New York), pp. 317–336.

Norris, K. S. (**1968**). "The echolocation of marine mammals," in *The Biology of Marine Mammals*, edited by T. H. Andersen (Academic, New York), pp. 391–423.

Norris, K. S. (**1975**). "Cetacean biosonar: Part 1—Anatomical and behav-

ioral studies," in *Biochemical and Biophysical Perspectives in Marine*, edited by D. C. Malins and J. R. Sargent (Academic, New York), pp. 215–234.
Norris, K. S., Evans, W. E., and Turner, R. N. (**1966**). "Echolocation in an Atlantic bottlenose porpoise during discrimination," in *Animal Sonar Systems*, edited by R.-G. Busnel (Plenum, New York), Vol. **I**, pp. 409–447.
Norris, K. S., Harvey, G. W., Burzell, L. A., and Krishna Kartha, T. D. (**1972**). "Sound production in the freshwater porpoises *Sotalia fluviatilis* Gervais and Deville and *Inia geoffrensis* Blainville, in the Rio Negro, Brazil," in *Investigations on cetacean*, edited by G. Pilleri, Bern, Vol. **IV**, pp. 251–262.
Norris, K. S., Prescott, J. H., Asa-Dorian, P. V., and Perkins, P. (**1961**). "An experimental demonstration of echolocation behavior in the porpoise, *Tursiops truncates* (Montagu)," Biol. Bull. **120**, 163–176.
Pilleri, G., Zbinden, K., and Kraus, C. (**1980**). "Characteristics of the sonar system of cetaceans with pterygoschis. Directional properties of the sonar system of *Neophocaena phocaenoides* and *Phocoena phocoena* (Phocoenidae)," Invest. Cetacea. **11**, 157–188.
Popper, A. N. (**1980**). "Sound emission and detection by delphinids," in *Cetacean Behavior: Mechanisms and Function*, edited by L. M. Herman (Wiley, New York), pp. 1–52.
Wang, D. (**1996**). "A preliminary study on sound and acoustic behavior of the Yangtze River finless porpoise, *Neophocaena phocaenoides*," Acta Hydrobiol. Sinica. **20**, 127–133.
Wei, Z., Wang, D., Kuang, X., Wang, K., Wang, X., Xiao, J., Zhao, Q., and Zhang, X. (**2002**). "Observations on behavior and ecology of the Yangtze finless porpoise (*Neophocaena phocaenoides asiaeorientalis*) group at Tian-e-Zhou oxbow of the Yangtze River," Raffles Bull. Zool., Suppl. **10**, 97–103.

Sei whale sounds recorded in the Antarctic

Mark A. McDonald
Whale Acoustics, 11430 Rist Canyon Road, Bellvue, Colorado 80512

John A. Hildebrand and Sean M. Wiggins
Scripps Institution of Oceanography, 9500 Gilman Drive, La Jolla, California 92093-0205

Deborah Thiele and Deb Glasgow
School of Ecology and Environment, Deakin University, P.O. Box 423, Warrnambool, Victoria 3280, Australia

Sue E. Moore
NOAA/Alaska Fisheries Science Center, 7600 Sand Point Way NE, Seattle, Washington 98115-6349

(Received 9 January 2005; revised 4 October 2005; accepted 5 October 2005)

Sei whales are the least well known acoustically of all the rorquals, with only two brief descriptions of their calls previously reported. Recordings of low-frequency tonal and frequency swept calls were made near a group of four or five sei whales in waters west of the Antarctic Peninsula on 19 February 2003. These whales also produced broadband sounds which can be described as growls or whooshes. Many of the tonal and frequency swept calls (30 out of 68) consist of multiple parts with a frequency step between the two parts, this being the most unique characteristic of the calls, allowing them to be distinguished from the calls of other whale species. The average duration of the tonal calls is 0.45 ± 0.3 s and the average frequency is 433 ± 192 Hz. Using a calibrated seafloor recorder to determine the absolute calibration of a sonobuoy system, the maximum source level of the tonal calls was 156 ± 3.6 dB *re* 1 μPa at 1 m. Each call had different character and there was no temporal pattern in the calling. © *2005 Acoustical Society of America.* [DOI: 10.1121/1.2130944]

PACS number(s): 43.80.Ka, 43.30.Sf [WWA] Pages: 3941–3945

I. INTRODUCTION

Sounds produced by the sei whale (*Balaenoptera borealis*) are perhaps the most poorly documented for any rorqual. The two extant descriptions (Thompson *et al.*, 1979; Knowlton *et al.*, 1991) are for sei whales encountered near Nova Scotia in the North Atlantic, where two-part stereotyped pulsive bursts in the 1.5 to 3.5 kHz frequency range were recorded.

The taxonomy of sei whales has a complex history, particularly in relation to Bryde's whales, these species sometimes being grouped as the sei/Bryde's complex (Dizon *et al.*, 1996, 2000). New species within this group continue to be described (Wada *et al.*, 2003). At-sea identification of these species is difficult, but fortunately the geographic location of the observations reported here minimized the potential confusion, with only southern hemisphere sei whales (*Balaenoptera borealis schlegellii*) presumed to occur at the recording site (Rice, 1998).

Sei whales found in the Antarctic are migratory, spending the summer at high latitudes for feeding and the winter at lower latitudes for calving and breeding (Horwood, 1987). Only large animals are observed south of the Antarctic convergence (Lockyer, 1977). More than 130 000 sei whales have been harvested from south of 40 degrees latitude, reducing this population from about 100 000 in 1930 to about 16 000 in 1979 when harvesting stopped (Horwood, 1987). From historic data, the most common group sizes for sei whales south of 60° are one to four with ten being a maximum (Lockyer, 1977).

We present recordings of sounds produced by sei whales at frequencies below 1 kHz, west of the Antarctic Peninsula. These low-frequency sounds are distinctly different from the sounds previously described for sei whales, and possible explanations for the differences are discussed.

II. METHODS

A. Visual observations

The initial sighting of the sei whales we later recorded acoustically occurred during the recovery of a seafloor acoustic recording package (ARP) (Wiggins, 2003) with the Research Vessel *Laurence M. Gould* on 19 February 2003 at 1329 in approximately 3000 m of water. This work was part of a long-term project for monitoring whales acoustically with seafloor recorders, as part of the Southern Ocean GLOBEC project (Hofmann *et al.*, 2002; Širović *et al.*, 2004). The wind speed was 20 to 26 kts with an average sustained wind of 23 kts. Three experienced observers (Thiele, Moore, and Glasgow) were on the bridge wings with binoculars and cameras. Numerous photos were taken of dorsal fins, heads, and backs, although not of the lateral ridges on the rostrum. All observations were noted in a logbook, and ship locations and meteorological measurements were recorded by the ship's automated data logging systems.

B. Recording equipment

Two sonobuoys were deployed, the first a type SSQ-53D DIFAR buoy which provides magnetic bearing information

to the whale calls (McDonald, 2004) and a type SSQ-57B omni directional broadband buoy. The recording system consisted of calibrated radios custom built by Greeneridge Sciences (Goleta, CA) and a Sony TCD-D8 digital recorder sampling at 48 kHz. Postcruise analysis of the data was done by digitally transferring the recordings to a computer hard drive with a Roland UA-30 external computer interface.

The frequency response of the radios is flat (±1 dB) across the 100 to 1000 Hz band where the whale calls occur, then rolls off 5 dB from 1 to 10 kHz. The frequency response of the 57B sonobuoy is considered usable from 20 Hz to 40 kHz and has slightly greater than 4.5 dB per octave greater sensitivity on the higher frequencies up to approximately 10 kHz. The 53D DIFAR sonobuoy has useful frequency response from 10 Hz to 4 kHz (McDonald, 2004) and has slightly greater than 6 dB/oct greater sensitivity on higher frequencies up to approximately 1200 Hz. The Sony D8 recorder has a flat frequency response (±1 dB) from 20 Hz to 20 kHz.

The seafloor ARP was calibrated at the U.S. Navy's Transducer Evaluation Center (TRANSDEC) in San Diego. The sampling rate for the ARP was 500 samples per second and recording was continuous throughout the deployment. The hydrophone is floated 10 m above the seafloor, except when the recorder is floating on the surface and the hydrophone is suspended 1 to 2 m below the surface.

III. RECORDINGS

When the seafloor ARP was spotted floating at the surface, a group of sei whales (four to five individuals) was seen near it at 63° 51.63′ S 67° 0.82′ W. The recorder was brought on board at 1350 while the whales remained within 1–2 nm of the vessel. A second group of four to five sei whales was subsequently seen within 4 km of the first group. Both groups exhibited active surface behaviors and very dynamic group composition—the whales appearing to split and merge in the short time we could observe them before steaming on.

We began deploying sonobuoys as we departed the ARP recovery site. Multiple groups of whales could be seen ahead of the ship at this time, with one group directly in the track of the ship. We deployed a DIFAR buoy at 1400 to a depth of 1000 ft (305 m) and an omnidirectional buoy at 1405 to a depth of 90 ft (27 m), while taking photos of a group of sei whales which passed directly off the starboard side of the vessel. These individuals could be seen within 200 m of the vessel, including from the starboard portholes while starting the recording system. The precise time of this observation was unfortunately not recorded, but it is presumed to have been just after 1401. There were four individuals in this group and side lunge feeding behavior was observed.

At 1413, the ship's 3.5-kHz sonar was secured to reduce acoustic interference with the recordings. At 1421 the R/V *Gould* was stopped at a distance of 5 to 6 km from the sonobuoys, well within radio range, and the propellers were declutched. Ship noise, which was apparent on the sonobuoys while the ship was underway, was thereby reduced to a nearly undetectable level when the ship was stopped. After the ship was stopped, three groups of surface active whales remained under observation: six animals, four animals, and four animals with one group within 2 km of the sonobuoys. The whales did not appear to react to the vessel, but continued with the feeding and surface-active behaviors as seen upon ship's approach. Overall, sei whale calls were recorded from 1408 until 1528 when radio reception for the sonobuoys became poor. No marine mammals of other species were sighted for many hours before or after the sei whale sightings.

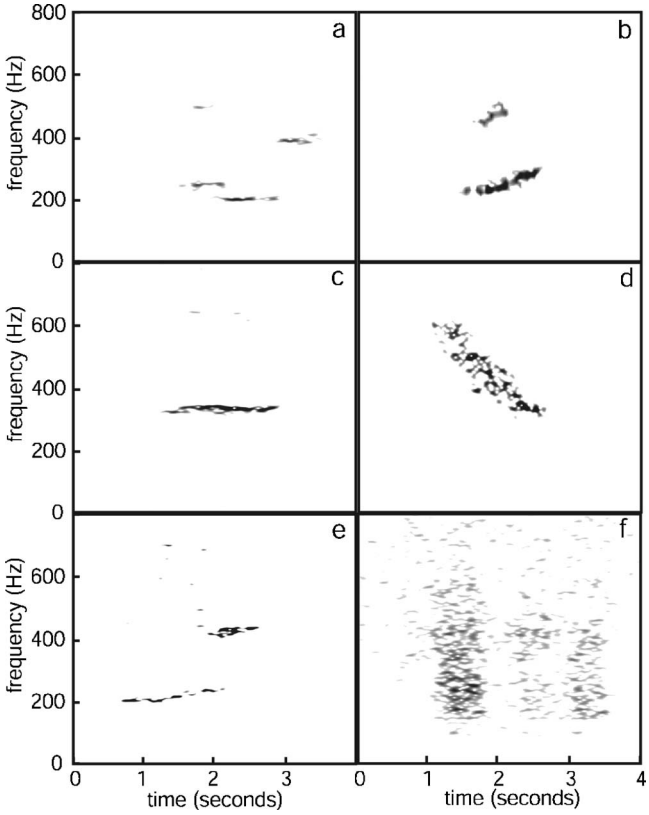

FIG. 1. Spectrograms are shown for an example in each call category: (a) multi-part frequency stepping tonals, (b) upsweep, (c) tonal, (d) downsweep, (e) upsweep stepping up, and (f) a series of three broadband calls. All spectrograms were made with a FFT length of 0.25 s, 95% overlap, and a Hanning window.

IV. ANALYSIS

A. Classification

We broadly categorize the calls into (1) tonal and frequency swept calls and (2) broadband calls (Fig. 1). The audible character of the tonal and frequency swept sounds can be described as "moans" while the broadband sounds have been variously described as "growls," "blows," or "whooshes" by different listeners hearing the same sounds. We recorded 68 distinct calls in the tonal and frequency swept category and some greater number of broadband calls. It is not possible to describe precisely how many sounds were produced by the whales because the signal-to-noise ratio of the calls becomes the determining factor in deciding if a sound should be counted as a whale call.

Of the 68 calls in the tonal and frequency swept category, we consider 18 to be frequency swept and 50 to be

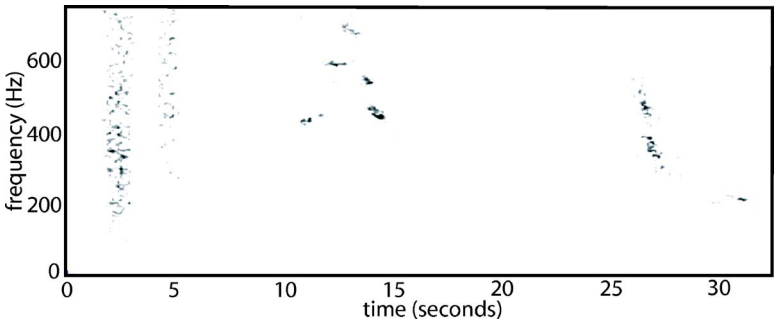

FIG. 2. A cluster of sei whale calls is illustrated, starting with two broadband calls at 2 and 4 s, followed by a five component call starting at 10 s, a broken or two part downsweep at 27 s and a weak downsweep at 31 s.

tonal sounds. Of the tonals, 28 were multi-part calls, stepping in frequency, though each part is of relatively constant frequency. Calls were judged to be multi-part only when the end of one part coincides with the beginning of another, without pause. Calls were clustered in time (Fig. 2), although this may be in part due to the location of the whales relative to the sonobuoys with the more distant calls not clearly recorded above the ambient noise.

B. Quantitative call descriptors

Duration and frequencies were measured for the 50 tonal calls. Of the 50 tonal calls, 22 consisted of one part, 16 of two parts, 9 of three parts, 2 of four parts, and 1 of five parts. There were 94 tones identified within the 50 tonal calls with durations [Fig. 3(a)] and frequencies [Fig. 3(b)] averaging 0.45 ± 0.30 s and 433 ± 192 Hz, respectively. The mean duration of the two-part calls was 0.9 s, very near twice the mean of the duration of the single-tonal sounds, suggesting tonal components are static components of multi-part calls.

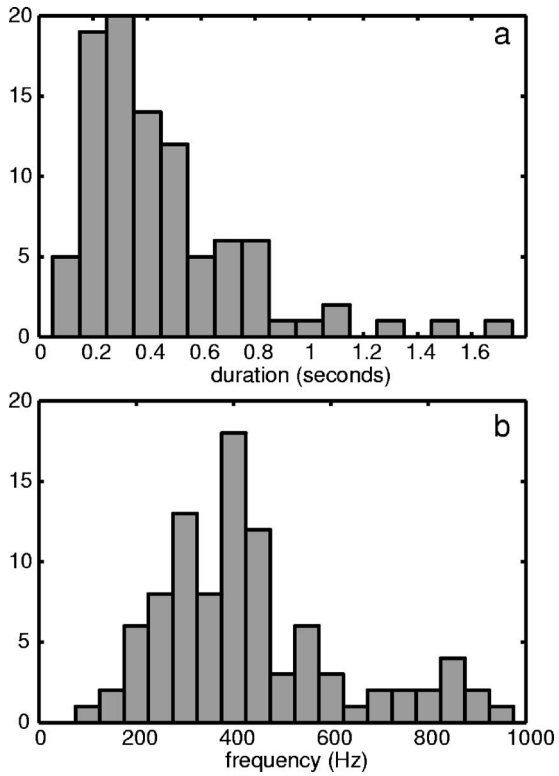

FIG. 3. Histograms of the (a) duration and (b) frequency of the 94 tonal call components from the 50 tonal calls.

The 18 frequency swept calls have an average midpoint (halfway in time from start to finish) frequency of 432 ± 151 Hz and an average duration of 1.1 ± 0.6 s. The average frequency sweep was 178 ± 141 Hz. Only two of the frequency swept calls also contained a frequency step, as illustrated in Figs. 1(e) and 2. The total durations of the two multipart calls containing sweeps were 1.9 and 3.7 s.

The frequency shifts in the sei whale calls range from less than one semitone to almost one octave or one harmonic. Note that none of the shifts are greater than one octave even though the frequency range of the calls covers more than two octaves. There is no apparent bias in frequency step size associated with the start frequency or the direction of the frequency step. Neither are there any dominant ratios in the frequency changes.

C. Acoustic localization of calls

Using the bearings to calls from the DIFAR sonobuoy together with the time difference of arrival (TDOA) of the sounds on the two sonobuoys, we compute locations for whale calls which had a sufficient signal-to-noise ratio on both sonobuoys (Fig. 4). The locations are at the intersection of the hyperbola resulting from the TDOA and the line from the DIFAR bearing. Errors in these locations can be roughly estimated from the previously established errors in similar DIFAR bearings to whale calls (McDonald, 2004) and an estimate of the errors in picking TDOA from the spectro-

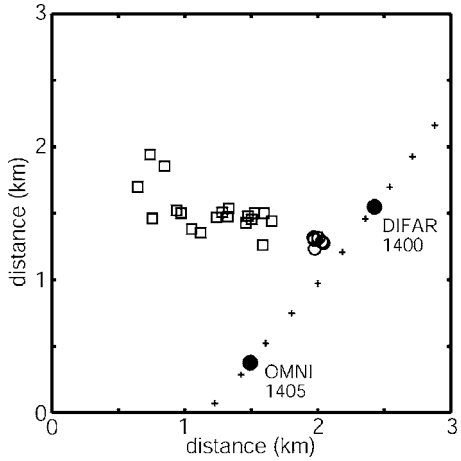

FIG. 4. The open squares indicate the locations of tonal and sweep calls, while the open circles indicate the location of broadband type calls. The plus symbols indicate the ship track at 1-min intervals and the filled circles indicate the sonobuoy locations.

grams. We consider the 95% confidence interval to be on the order of 500 m, primarily due to picking errors in TDOA. Tonal and frequency swept calls are most easily localized, while the signal-to-noise ratio prevents localization of broadband calls except at locations almost between the sonobuoys. The coincident locations and times of some of the broadband calls with the locations of tonal and frequency swept calls gives us confidence these calls were produced by the sei whales.

D. Source levels of calls

We cannot provide direct measurements of received sound pressure level for the sei whale calls because our sonobuoy recording system was not calibrated in absolute terms, but only in frequency response and as one sonobuoy relative to the other. However, the ARP was calibrated and gives an ambient background noise spectral density of 72.5 dB *re* 1 μPa^2/Hz at 220 Hz on the seafloor averaged over the hour before the ship arrived on location. For comparison purposes a one-week average level before the ship arrived in the area was determined by averaging 200-s windows, one every 4.4 min, yielding an average noise spectral density of 72.2 dB *re* 1 μPa^2/Hz at 220 Hz.

While the ARP was on the surface and distant from the ship, as it serendipitously was for 4 h in this case, the noise spectral density was 75 dB *re* 1 μPa^2/Hz at 220 Hz, as averaged from numerous 5-s intervals which were chosen to be in between obvious breaking wave noise and the greatest hydrophone movement noise. The average noise spectral density including all the hydrophone movement and breaking waves was 80 dB *re* 1 μPa^2/Hz at 220 Hz.

Based on our measured spectral densities at 220 Hz of 72.5 dB at depth when wind speed was 17 kts (9 m/s) and 75 dB at the surface when wind speed had increased to 23 kts (12 m/s) we estimate the 220-Hz noise spectral density at the sonobuoy hydrophone depths of 120 and 300 m to be 73±2 dB. Not all the hydrophone motion could be avoided in the measurements at the surface and we expect the surface noise to be slightly higher than the seafloor noise in an environment where the SOFAR channel is at the surface (Wagstaff, 1981; Bannister, 1986). We use the 73±2 dB ambient noise spectral density estimate at 220 Hz at the sonobuoy hydrophones as our basis and the known frequency response of each component in the recording system to estimate the received sound pressure levels of the whale calls. The ambient noise spectra calculated from the two sonobuoys agree within 2 dB across the frequency range 200 to 900 Hz, the frequency band important to the whale calls and the ambient noise reference, but diverge outside these frequencies. The divergence may be caused by the difference in deployment depths of the sonobuoy hydrophones (27 and 305 m) coupled with the high sea state and hydrophone suspension limitations.

The recorded sound pressure levels of the sei whale calls were measured in 10-Hz bands rather than as 1-Hz spectral densities because the duration of the calls were so short that a 1-Hz bin would have necessarily included times outside the call duration. Little or no correction is needed to reduce these sound pressure levels to the standard 1-Hz spectral density reference because the signals analyzed are all greater than 10 dB above the background noise level and are considered to be contained within a 1-Hz bandwidth. The calls analyzed were 12 to 22 dB above background noise at 0.9- to 1.8-km distances from the sonobuoys. Many calls detected were beyond these ranges, but could not be analyzed because they could not be localized. Assuming spherical spreading loss and no significant absorption, the propagation losses are 59 to 65 dB, respectively, for ranges 0.9 and 1.8 km. Calculated source levels are 147 to 156 dB rms *re* 1 μPa at 1 m using the aforementioned 73 dB background ambient level to calibrate the sonobuoy systems. The lower bound on source level is biased by the limits of our ability to measure the source level rather than an actual lower bound on call sound pressure levels, but the 156 dB rms *re* 1 μPa at 1 m is considered an approximate limit for the highest sound pressure levels recorded. Estimation of error for the 156 dB maximum call level is a combination of our 95% error estimate for the ambient noise spectral density of ±2 dB and the error in propagation loss due to error in call localization. The 95% confidence interval for the propagation loss error due to localization error (±500 m) averages 3 dB, more at shorter ranges and less at the furthest ranges. Combining the two errors as the square root of the sum of the errors squared gives a 95% error estimate of ±3.6 dB.

V. DISCUSSION

Sei whale calls recorded in the North Atlantic are stereotyped two part calls in the 1.5 to 3.5 kHz band, as reported by Knowlton *et al.* (1991) and Thompson *et al.* (1979). These mid-frequency calls are distinctly different from the low-frequency calls we report here for sei whales recorded west of the Antarctic Peninsula. All reported sei whale recordings, including our own, were made during late summer, which is believed to be the breeding season (Horwood, 1987; Budylenko, 1977). Knowlton *et al.* (1991) reports recording the 1.5 to 3.5 kHz sound on all 16 of the recording sessions during which sei whales were seen and on 6 of 16 sessions when sei whales were not seen. Our recordings covered the 10 Hz to 24 kHz band yet careful review detected no sounds resembling those of Knowltons' recordings. Undoubtedly habitat, season, location and specific activity influences the type of sounds produced by sei whales.

While reasons for differences between the North Atlantic and Antarctic sei whale calls are unclear, it may be that stereotyped high-frequency sounds reported for sei whales by Knowlton *et al.* (1991) and Thompson *et al.* (1979), represent a reproductive "song," while the lower-frequency sounds that we report represent feeding or social calls. Such a dichotomy may be analogous to minke whales which produce both relatively simple low frequency calls, and more complex high frequency stereotyped calls. The high frequency stereotyped calls appear to vary geographically and to be produced seasonally (Edds-Walton, 1997; Mellinger *et al.*, 2000; Gedamke *et al.* 2001, 2003; S. Rankin and J. Barlow, unpublished manuscript; Thompson and Friedl, 1982; authors, unpublished data).

The frequency stepping character of the tonal calls [e.g., Fig. 1(a)] make the sei whale calls reported here distinctive from any other known whale calls. While we cannot rule out the possibility that the two part calls were in fact made by two nearby animals interacting, the coincidence of the end of the previous part coinciding with the start of the next part at a different frequency suggests these are multipart calls made by one whale.

We find no temporal pattern in the recorded calls and each call shows different frequencies and character. Given the irregular nature of these calls, the relatively low source levels as compared to other baleen whale calls (Richardson *et al.*, 1995) and the offshore distribution of sei whales (Horwood, 1987; Gregr and Trites, 2001), perhaps it is not surprising that these calls have not been previously reported in the published literature.

The production of low frequency calls by sei whales is consistent with the behavior of all other rorquals. The low source levels of these calls suggest that they are intended for communication over limited distances of at most a few kilometers. Knowledge of these calls, however, may allow for monitoring of sei whale presence using long-term passive acoustic recordings (Clapham *et al.*, 1999).

ACKNOWLEDGMENTS

The authors would like to thank the Master, officers and crew of the R/V *Laurence M. Gould* and the staff at Raytheon Polar Services who ably handled logistics. This work was supported by NSF Office of Polar Programs Grant No. OPP 99-10007 as part of the SOGLOBEC program, with program guidance by Polly Penhale and the International Whaling Commission Southern Ocean Collaboration Working Group.

Bannister, R. W. (**1986**). "Deep sound channel noise from high latitude winds," J. Acoust. Soc. Am. **79**, 41–48.

Budylenko, G. A. (**1977**). "Distribution and composition of sei whale schools in the southern hemisphere," Rep. Int. Whal. Comm. (special issue 1), 121–123.

Clapham, P. J., Young, S. B., and Brownell, R. L., Jr. (**1999**). "Baleen whales: conservation issues and the status of the most endangered populations," Mammal Rev. **29**, 35–60.

Dizon, A., Baker, C. S., Cipriano, F., Lento, G., Palsboll, P., and Reeves, R. (eds.) (**2000**). *Molecular Genetic Identification of Whales, Dolphins, and Porpoises: Proceedings of a Workshop on the Forensic Use of Molecular Techniques to Identify Wildlife Products in the Marketplace*, La Jolla, CA, 14–16 June 1999, U. S. Department of Commerce, NOAA Technical Memorandum, NOAA-TM-NMFS-SWFSC-286.

Dizon, A. E., Lux, C. A., Le Duc, R. G., Urbon, R. J., Henshaw, M., Baker, C. S., Cipriano, E., and Brownell, R. L., Jr. (**1996**). "Molecular phylogeny of the Bryde's/Sei Whale Complex: Separate species for the pygmy Bryde's whale form?" IWC Meeting Document, IWCSC/48/027, unpublished.

Edds-Walton, P. L. (**1997**). Acoustic communication signals of mysticete whales, Bioacoustics **8**, 47–60

Gedamke, J., Costa, D. P., and Dunstan, A. (**2001**). "Localization and visual verification of a complex minke whale vocalization," J. Acoust. Soc. Am. **109**, 3038–3047.

Gedamke, J., Costa, D. P., Clark, C. W., Mellinger, D. K., and O'Neill, F. L. (**2003**). "Deciphering dwarf minke whale (*Balaenoptera acutorostrata*) song: results from passive acoustic tracking and active playback experiments," Society for Marine Mammalogy, 15th Biennial Conference on the Biology of Marine Mammals, 14–19 December, Greensboro, NC, abstract, pp. 58–59.

Gregr, E. J., and Trites, A. W. (**2001**). "Predictions of critical habitat for five whale species in the waters of coastal British Columbia," Can. J. Fish. Aquat. Sci. **58**, 1265–1285.

Hofmann, E. E., Klinck, J. M., Costa, D. P., Daly, K. L., Torres, J. J., and Fraser, W. R. (**2002**). "U. S. Southern Ocean Global Ocean Ecosystems Dynamics Program," Oceanogr. **15**, 64–71.

Horwood, J. (**1987**). *The Sei Whale: Population Biology, Ecology and Management* (Croom Helm, London).

Knowlton, A. R., Clark, C. W., and Kraus, S. D. (**1991**). "Sounds recorded in the presence of Sei whales, Balaenoptera borealis," in Proceedings of the Ninth Biennial Conference on the Biology of Marine Mammals, abstract, p. 40.

Lockyer, C. (**1977**). "Some possible factors affecting age distribution of the catch of sei whales in the Antarctic," Rep. Int. Whal. Comm. (special issue 1), 63–70.

McDonald, M. A. (**2004**). "DIFAR hydrophones applied to whale research," Can. Acoust. **32**, 155–160.

Mellinger, D. K., Carson, C., and Clark, C. W. (**2000**). "Characteristics of minke whale (*Balaenoptera acutorostrata*) pulse trains recorded near Puerto Rico," Marine Mammal Sci. **16**, 739–756.

Rice, D. W. (**1998**). Marine Mammals of the World—Systematics and Distribution, Special Publication Number 4 of The Society for Marine Mammalogy, edited by D. Wartzok, Lawrence, KS, pp. 231.

Richardson, W. J., Greene, C. R., Jr., Malme, C. I., and Thomson, D. H. (**1995**). *Marine Mammals and Noise* (Academic, San Diego).

Širović, A., Hildebrand, J. A., Wiggins, S. M., McDonald, M. A., Moore, S. M., and Thiele, D. (**2004**). "Seasonality of blue and fin whale calls west of the Antarctic Peninsula," Deep-Sea Res., Part II **51**, 2327–2344.

Thompson, P. O., and Friedl, W. A. (**1982**). "A long term study of low frequency sounds from several species of whales off Oahu, Hawaii," Cetology **45**, 1–19.

Thompson, T. J., Winn, H. E., and Perkins, P. J. (**1979**). "Mysticete sounds," in *Behavior of Marine Animals*, edited by H. E Winn and B. L. Olla (Perseus, Cambridge, MA), pp. 403–431.

Wada, S., Oishi, M., and Yamada, T. K. (**2003**). "A newly discovered species of living baleen whale," Nature (London) **426**, 278–281.

Wagstaff, R. A. (**1981**). "Low-frequency ambient noise in the deep sound channel—The missing component," J. Acoust. Soc. Am. **69**, 1009–1014.

Wiggins, S. M. (**2003**). "Autonomous Acoustic Recording Packages (ARPs) for long-term monitoring of whale sounds," Mar. Technol. Soc. J. **37**(2), 13–22.

Nonlinear resonant ultrasound spectroscopy (NRUS) applied to damage assessment in bone

Marie Muller[a)]
Laboratoire d'Imagerie Paramétrique, CNRS, Université Paris 6, 15 Rue de l'Ecole de Médecine, 75006 Paris, France

Alexander Sutin[b)]
Davidson Laboratory, Stevens Institute of Technology, Hoboken, New Jersey 07030

Robert Guyer[c)]
Department of Physics, University of Massachussets, Amherst, Massachussets 4525

Maryline Talmant[d)] and Pascal Laugier[e)]
Laboratoire d'Imagerie Paramétrique, CNRS, Université Paris 6, 15 Rue de l'Ecole de Médecine, 75006 Paris, France

Paul A. Johnson[f)]
Geophysics, MS D443, Los Alamos National Laboratory of the University of California, Los Alamos, New Mexico 87545

(Received 25 May 2005; revised 23 September 2005; accepted 24 September 2005)

Nonlinear resonant ultrasound spectroscopy (NRUS) is a resonance-based technique exploiting the significant nonlinear behavior of damaged materials. In NRUS, the resonant frequency(ies) of an object is studied as a function of the excitation level. As the excitation level increases, the elastic nonlinearity is manifest by a shift in the resonance frequency. This study shows the feasibility of this technique for application to damage assessment in bone. Two samples of bovine cortical bone were subjected to progressive damage induced by application of mechanical cycling. Before cycling commenced, and at each step in the cycling process, NRUS was applied for damage assessment. For independent assessment of damage, high-energy x-ray computed tomography imaging was performed but was only useful in identifying the prominent cracks. As the integral quantity of damage increased, NRUS revealed a corresponding increase in the nonlinear response. The measured change in nonlinear response is much more sensitive than the change in linear modulus. The results suggest that NRUS could be a potential tool for micro-damage assessment in bone. Further work must be carried out for a better understanding of the physical nature of damaged bone and for the ultimate goal of the challenging *in vivo* implementation of the technique. © *2005 Acoustical Society of America.* [DOI: 10.1121/1.2126917]

PACS number(s): 43.80.Qf, 43.80.Ev, 43.25.Ba, 43.25.Gf [FD] Pages: 3946–3952

I. INTRODUCTION

The diagnosis of bone fragility is currently obtained through the measurement of bone mineral density (BMD) obtained from x-ray densitometric techniques.[1] BMD is well known as a good predictor of bone strength[2] and is considered to be the best clinical technique for fracture risk prediction.[1] Other structural or material bone characteristics have been recognized as independent predictors of bone strength. Microdamage in bone is such a factor and strength degradation due to damage accumulation is of major clinical importance. Several studies have revealed a strong correlation between micro-damage and bone fragility, suggesting the importance of micro-damage assessment.[3,4] However, *in vivo* micro-damage has remained relatively poorly documented due to the lack of noninvasive techniques for its assessment.

Micro-damage is induced *in vivo* in bone by daily cyclic loading. This fatigue damage is considered to be one of the factors controlling the local stimulus for bone turnover, and the resulting remodeling results in repair of the resulting fatigue damage.[3] When an imbalance takes place in the remodeling process, micro-damage accumulates as micro-cracks,[3,5] with typical dimension of 5 to 400 μm. Osteoporotic bones are more micro-damaged than healthy bones.[6] It has been shown that fracture risk and correspondingly micro-crack density increases exponentially with age, with a higher rate for women than for men.[7–9] Fatigue damage has consequences on bone mechanical properties. It has been demonstrated that micro-damage accumulation coincides with a decrease of bone toughness[4] or stiffness.[10] Moreover, some data suggest a negative exponential relationship between bone strength and micro-crack density.[5] These results suggest

[a)]Electronic mail: muller@lip.bhdc.jussieu.fr
[b)]Electronic mail: asutin@stevens-tech.edu
[c)]Electronic mail: guyer@physics.umass.edu
[d)]Electronic mail: talmant@lip.bhdc.jussieu.fr
[e)]Electronic mail: laugier@lip.bhdc.jussieu.fr
[f)]Electronic mail: paj@lanl.gov

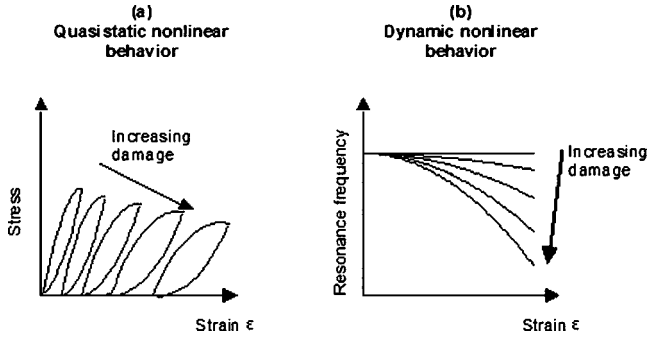

FIG. 1. (a) Stress-strain behavior of bone as a function of damage under quasitstatic conditions. (b) Resonance peak shift as function of strain amplitude, with increasing damage.

that micro-damage accumulation and bone fragility are related. *In vivo* micro-damage assessment could therefore provide important information regarding skeletal status and fracture risk. To date, two techniques are used for the assessment of fatigue damage in bone: histological measures of damage accumulation using staining techniques[11,12] and optical techniques such as micro-computed tomography. However, both are limited to the measurement of *in vitro* specimens. Indeed, dimensions of micro-cracks in bone (5 to 400 μm)[13,14] are such that the resolution needed for the imaging devices to detect them requires very high energy levels, difficult and dangerous to apply *in vivo*. It is therefore crucial to develop a damage assessment technique that could be used *in vivo*.

Accumulation of damage in bone leads to a stress-strain behavior that is correspondingly more nonlinear than in healthy bone.[15,16] In other words, as fatigue damage accumulates in bone, the stress-strain curve exhibits an increasingly pronounced bend and an increased hysteresis[17] [Fig. 1(a)], which may be a manifestation of a softening of the bone, due to a larger crack density. As damage level increases the corresponding nonlinear dynamical behavior manifests itself as a larger decrease in the resonance frequency for a given wave amplitude [Fig. 1(b)]. The decrease in resonance frequency corresponds to a decrease in modulus and wave speed. We hypothesize that the nonlinearity in the stress-strain relation may be exploited in the assessment of damage in bone as it has been elsewhere. Indeed, it is now well known that damaged materials, as well as consolidated and unconsolidated inhomogeneous materials, display a characteristic, elastic-nonlinear behavior, termed simultaneously "nonlinear mesoscopic," "nonclassical nonlinear," "nonequilibrium," and "anomalous" behavior.[18–20] From empirical evidence it is clear that micro-cracks in materials are responsible for the enhanced nonlinear response, acting as an ensemble of soft inclusions in a rigid matrix. This is referred to as the "hard/soft" paradigm of nonclassical nonlinear materials.[18,21,22] This is the reason why nonlinear elastic wave techniques are in development for nondestructive evaluation (NDE) and damage assessment in a very large group of materials. Nonlinear resonant ultrasound spectroscopy (NRUS) is one of those techniques and has proved to be valuable for damage detection because of its high sensitivity.[18,20,23,24] It is important to note that, while nonlinear methods are extremely sensitive to the presence of damage, we have no quantitative link between damage quantity and nonlinear response, although significant effort is being directed to this issue. Currently, empirical relations can be derived for specific materials providing the means to infer damage quantity from nonlinear response. The objective of this study was to explore for the first time the potential of nonlinear resonant ultrasound spectroscopy to assess progressively induced bone damage.

II. THEORY

Recent, careful studies carried out on rock under well-controlled conditions (constant temperature and in an atmosphere of nitrogen gas)[25] showed that, at low strains, "nonclassical" materials behave classically, exhibiting Duffing oscillator behavior (a perturbation expansion of the stress-strain describing nonlinear dynamics[26]). Above strains of roughly 10^{-6}, it is currently thought that macro- and micro-cracks, as soft mesoscopic structural features in a rigid matrix, are responsible for a characteristic nonlinear response related to the presence of strain memory and hysteresis in the stress-strain relation, the equation of state (EOS). Although the underlying physical mechanisms are not well understood, Guyer and McCall proposed a phenomenological description of these nonlinear effects,[21,27] considering the material as an ensemble of individual elastic units, some hysteretic and some not. In damaged bone, micro-cracks could play the role of these hysteretic units. The individual hysteretic units are recorded in the Preisach-Mayergoyz space (PM space), which provides the means to track the behavior of the ensemble of hysteretic units for a given stress history applied to the material. A one-dimensional EOS can be derived from the density of hysteretic units in PM space,[27]

$$\sigma = \int K(\varepsilon, \dot{\varepsilon}) d\varepsilon, \tag{1}$$

where σ is stress, ε is strain, $\dot{\varepsilon}$ is the strain rate, and K is the elastic modulus of the material,

$$K = K_0(1 + \beta\varepsilon + \delta\varepsilon^2) - \alpha(\varepsilon, \dot{\varepsilon}), \tag{2}$$

where K_0 is the linear modulus, ε is the strain and α is the hysteretic nonlinear parameter that depends on the strain derivative $\dot{\varepsilon}$ due to the hysteresis. The corresponding wave equation expresses the driving force for the local displacement as a function of the strain,

$$\ddot{u} = \frac{K_0}{\rho}\frac{\partial}{\partial x}(\Delta\varepsilon + \beta\Delta\varepsilon^2 + \delta\Delta\varepsilon^3 + \cdots) + \alpha(\Delta\varepsilon, \dot{\varepsilon}), \tag{3}$$

where $\ddot{u}$ is the particle acceleration, ρ is the material density, and $\Delta\varepsilon$ is the average strain over a wave cycle. The nonlinear parameters β and δ describe the classical nonlinear terms due to standard anharmonicity, although the material damage contributes to these terms in nonlinear mesoscopic materials. The hysteretic nonlinear parameter in the model, α, dominates the nonlinear behavior at large drive strains as noted above and it is relatively straightforward to track its behavior as the sample is progressively damaged and becomes more elastically nonlinear.[20,28] This phenomenon can be understood as a softening of the material when the excitation level

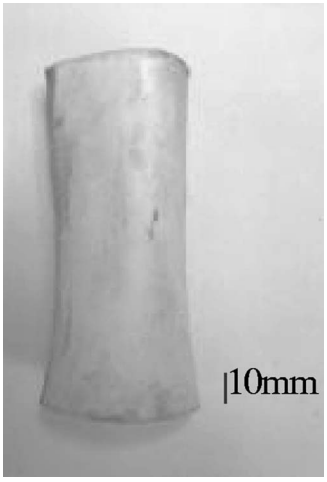

FIG. 2. Bone sample B1. The end surfaces are flat and parallel.

increases, which becomes more pronounced with accumulated damage. It can be shown from Eq. (3) that

$$\frac{\Delta f}{f_0} = \frac{f - f_0}{f_0} \approx \alpha \Delta \varepsilon, \tag{4}$$

where f is the linear resonance frequency and f_0 is the resonance frequency at the lowest (linear) drive level[23] for a given resonance mode. Thus from the frequency shift as a function of strain, we can extract α. As noted, there is no quantitative relationship between α and damage as yet; however, much empirical evidence shows a clear link.[18–23] The model is functional for our purposes here, but we note that, in its original formulation, it does not account for "slow dynamics," the recovery process that occurs in these materials after large amplitude wave excitation, nor for the process of "conditioning," strain-memory that takes place during application of NRUS.[21]

III. EXPERIMENTAL PROCEDURE

A. Samples

The study was carried out on two bovine femur specimens. After removing soft tissue and marrow, the samples were soaked in a 2% saline solution with a dish degreaser and wrapped in gauze in order to keep them hydrated during the experiment. The samples were machined frozen in a lathe in order to obtain flat and parallel surfaces at the sample ends for transducer placement. The two samples (termed B1 and B2) had a tubular shape, with an approximate wall thickness

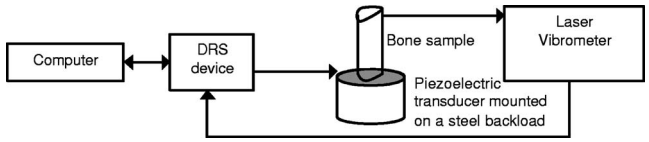

FIG. 4. Experimental setup for the NRUS experiment.

of 8 and 11 mm, respectively, and an approximate diameter of 49 and 46 mm, respectively. Both samples were 116 mm long. They were cut in the central part of the diaphyseal shaft and were approximately symmetrical compared to the mid-shaft line (see Fig. 2).

B. Fatigue

A progressive damage experiment was carried out in 11 steps (termed here steps 0 to 10, step 0 corresponding to the intact sample). The samples were progressively damaged by compressional fatigue cycling in an INSTRON 5569 press. For the first eight cycling sessions, the samples were cycled 60 times, to a maximum stress of 15 Mpa at a rate of 30 Mpa/min (about 1 h cycling). For the last two sessions, they were cycled 80 times to a maximum stress of 25 Mpa at a rate of 40 Mpa/min (about 1 h 40 min cycling, see Fig. 3).

C. Nonlinear resonant ultrasound spectroscopy (NRUS)

At each damage step, NRUS experiments were performed on the samples, using a resonant ultrasound spectroscopy device (Dynamic Resonance Systems, Inc., Powell, WY, USA). Each sample was probed using a step-sweep in frequency around a resonance mode of the sample. The modal peak frequency was determined, and the process was repeated at gradually increasing drive levels. The experimental setup used for the NRUS is shown in Fig. 4. To obtain large wave amplitudes, a resonator was constructed using a large piezoelectric transducer (77-mm diameter, 6-mm thickness) mounted with epoxy to a thick, 5180 steel backload (77-mm diameter, 51-mm thickness). The source was coupled to the specimens by application of phenyl salicylate. The source produced the desired large amplitudes; however, because of the coupled resonators (backload and bone sample), the measured resonance spectrum was complex. Therefore modeling was carried out in order to determine which resonance modes would provide information related to the bone sample rather than the backload, and thus be relevant for the NRUS experiment. The analytical model was

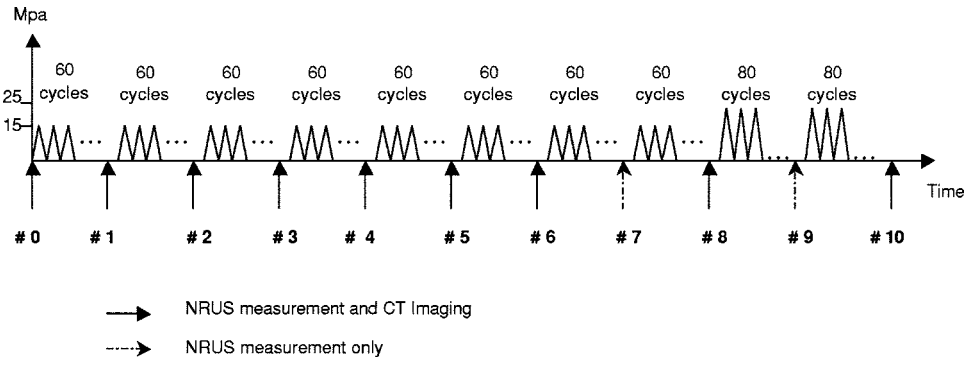

FIG. 3. Stress protocol for the progressive damage experiment.

for unidimensional propagation in two adjacent media (backload and bone), separated by a thin transducer generating forced oscillations at the interface between the two medias, mimicking the actual setup. Displacement at the bottom of the backload was fixed to zero (the backload was considered to be sitting on a rigid substrate) and the extremity of the bone was considered free. The simulation showed that the 42-kHz peak corresponded to a resonance mode of the bone sample and was well separated from adjacent modes. This resonance mode was selected for further study because the separation allows one to analyze the resonance frequency peak shift without overlap of adjacent peaks (which can influence the location and width of the peak).

Particle velocities related to the longitudinal displacement at the top, and the radial displacement on the side of the bone sample were measured using a laser vibrometer (Polytec OFV 3001 with the OFV 303 Sensor Head). Small pieces of aluminum foil were glued to the samples tops and sides in order to increase the reflectivity of the laser vibrometer and thereby increase the signal-to-noise ratio. Longitudinal dynamic strain amplitude ε_L is calculated from the measured particle velocity, $\varepsilon_L = \partial u/\partial x = \dot{u}/2\pi f L$, where f is the frequency and L is the length of the sample (116 mm). Radial strain is related by Poisson's ratio, meaning it is approximately $\varepsilon_L/4$.

Linear resonance has a long history of development and application for measurement of wave velocity and attenuation. For instance, Bolef and colleagues developed standing wave resonance techniques applying nonlinear (electronic) mixing to determine the wave velocity in materials.[29,30] Starting in the 1980s, the resonant ultrasound spectroscopy (RUS) technique was introduced to measure the full elastic tensor of solids.[31] The NRUS technique presented here is the extension of those two experimental methods to nonlinear elasticity, where the resonance (spectral) peak is used to extract the material nonlinear parameter and could potentially be used to extract the nonlinear parameter tensor.

D. Computed tomography (CT) imaging

High-energy x-ray, three-dimensional computed tomography (CT) was performed (x-ray cabinet model FCT-2252 with a 225 kV micro-focus source, Hytec Inc, Los Alamos, NM, USA), in order to have an independent assessment of damage in the samples. CT images were reconstructed with a pixel size of 127 μm. This resolution only allowed us to detect the larger cracks. CT imaging experiments were carried out for steps 0, 1, 2, 3, 4, 5, 6, 8, and 10.

IV. RESULTS

For each damage step, the resonance curves around 42 kHz were measured for increasing amplitudes of the drive level. Figure 5 shows an example of resonance curves, obtained by measuring the radial velocity close to the top of sample B1, and corresponding CT images, for damage steps 0 and 9.

As drive level increased, a shift in the resonance frequency could be observed at all damage steps. The resonant peak shift was, however, more significant in the progressively damaged stages [Fig. 5(b)] than in the undamaged sample [Fig. 5(a)]. α was then extracted according to Eq. (3).

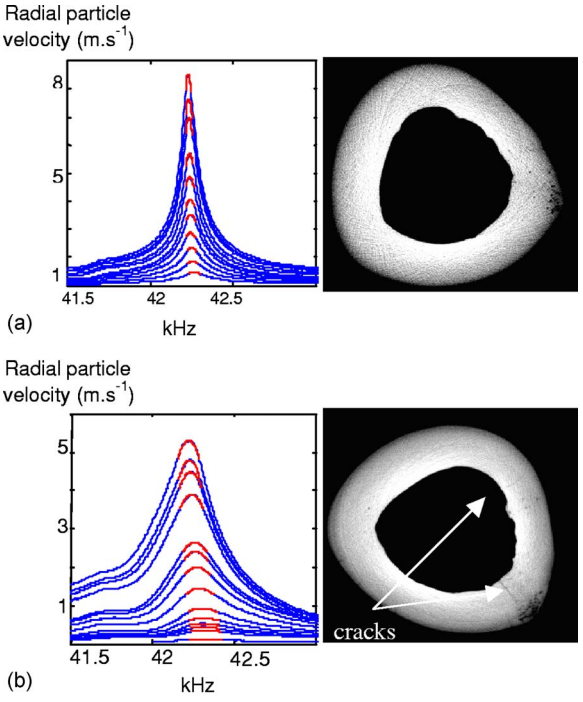

FIG. 5. (Color online) Example of resonance curves for damage steps 0 and 9. The radial velocity measured close to the top of sample B1 is plotted as a function of frequency. Top: damage step 0, Bottom: damage step 9.

Figure 6 illustrates the behavior of the frequency shift as a function of average strain for samples B1 [Fig. 6(a)] and B2 [Fig. 6(b)]. Each curve corresponds to a damage step. Some of the steps were eliminated due to poor experimental conditions (poor coupling primarily). The slope of the curves is very close to one for all steps and both samples, as the theory predicts (sample B1: mean=0.99, standard deviation =0.02, range=0.95–1; sample B2: mean=1.01, standard deviation=0.02, range=0.99–1.03).

As the amount of damage increases in the samples, the curves shift upward in the frequency-strain space, indicating an increased nonlinear signature meaning there is more frequency shift for the same strain interval.

Figure 7 shows the behavior of the speed of sound in the samples (derived from the linear resonance frequency f_0 at each step) and the nonlinear parameter α as a function of damage step for the two samples. As damage accumulates, the speed of sound c ($c=f_0\lambda$ where f_0 is the linear resonance frequency and λ is the wavelength) is almost constant (although a slight decrease can be observed in sample B2 when damage increases). On the other hand, α dramatically increases with the accumulated damage but its behavior is not the same for the two samples. In B1, the increase of α is almost linear ($\alpha \approx 1.17\#\text{step} + 0.86$) whereas the behavior in B2 is fit by a higher-order polynomial function ($\alpha \approx 0.05\#\text{step}^3 - 0.56\#\text{step}^2 + 2.13\#\text{step} - 0.96$). The different dependencies indicate that cumulative damage was not the same for the same quantity of cycling. The difference between linear and nonlinear measurements is remarkable.

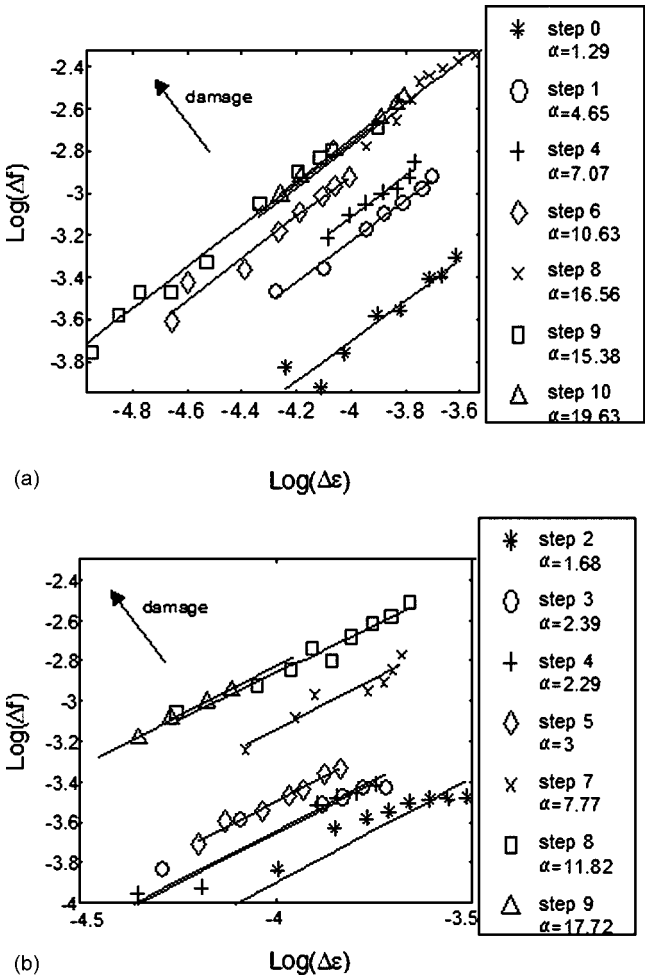

FIG. 6. Resonance frequency shift as a function of strain in log-log space. As damage increases, the curves are translated towards the top of the space, reflecting an increasing nonlinear parameter.

V. DISCUSSION

The primary purpose of this work was to demonstrate for the first time the feasibility of nonlinear resonant ultrasound spectroscopy techniques to detect progressive damage in bone. This was accomplished in a progressive damage experiment, in which the NRUS technique provided the means to characterize damage in bone via the nonlinear hysteretic parameter α.

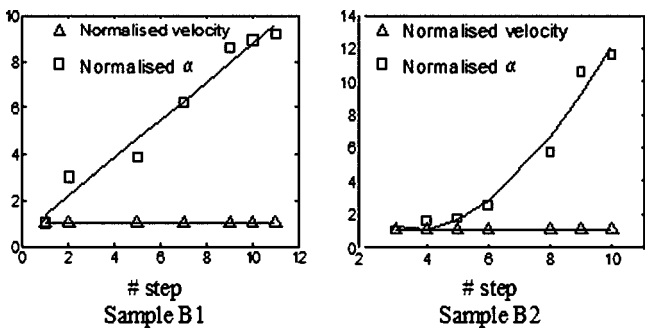

FIG. 7. Nonlinear parameter α (squares) and velocity (triangles) normalized to the nonlinear parameter and velocity for the "intact" sample, as a function of damage step in the two samples (left: sample B1, right: sample B2).

A. Resonance curves, hysteretic behavior

Figure 5 indicates that a small resonance frequency shift occurs in the "intact" sample. This result was expected, considering the fact that intact, healthy bone contains continually healing micro-cracks and remodeling as noted in the Introduction. Moreover, intact bone by itself could be classified as a nonlinear mesoscopic elastic material, because of its heterogeneous mesoscopic structure. As noted above, the α parameter measured in this study reflects damage accumulation, or relative damage, rather than an absolute quantity of damage. This has been demonstrated in numerous other materials as well.[23]

B. Imaging

In order to have an independent assessment of the damage mechanically induced in the samples, CT imaging was performed at different damage steps. Images of the same slice of sample B1 are shown in Fig. 5. Some cracks are visible in Fig. 5(b) (damage step 9 in sample B1) that are not present in the intact sample [Fig. 5(a), damage step #0 in sample B1]. The resolution of the images (the pixel size is 127 μm) does not allow for a quantification of microdamage since micro-cracks lengths in bone are in a range of 5 to 400 μm. Higher resolution imaging methods are required for comparative quantification.

C. Wave dissipation

Figure 5 shows a change in the wave dissipation, reflected by the fact that the curves obtained during progressive damage cycling are broader than the curves obtained from the "intact" state. A measure of the wave dissipation, given by the Q of the material, has been shown to be very useful for assessing nonclassical behavior, and thus the relative quantity of damage in a material.[22] Unfortunately, we were unable to exploit the Q observations because of inconsistent results. We suspect that the aluminium foil (glued on the sample to increase reflectivity for the laser vibrometer) was not always bonded properly to the sample, and that additional vibration of the foil could have influenced the width of some of the resonance curves (although not the frequency). It is also possible inconsistencies in the source bonding at each step influenced the Q.

D. Anisotropy

Changing the orientation of the laser vibrometer provided the means to measure two different velocities: the longitudinal particle velocity, measured on the top of the sample, and the radial particle velocity, measured on the side of the sample. The results presented in this paper only employed the radial velocity. Indeed, no consistent result could be found with the longitudinal particle velocity. Damage formed under compressive loads applied along the longitudinal bone axis has consistently been associated with the appearance of oblique shear cracks.[32] One possible interpretation to our results is that the effect of damage on mechanical properties is anisotropic and that the particle velocity in one direction (e.g., longitudinal) is less sensitive than in the other

direction (e.g., radial). An intensive modeling effort must be conducted, along with additional experiments, to understand this phenomenon.

E. Nonlinear hysteretic parameter

Figure 6 shows the behavior of the frequency shift as a function of the maximum amplitude strain for each damage step. The slopes of all the curves are about 1, for the two samples. This result is predicted by the theory. Indeed, Eq. (3) implies a linear relation between Δf and $\Delta\varepsilon$. As damage is induced in the samples, the curves move upward in $\Delta f/f_0$-strain-space, indicating an increasing nonlinear hysteretic parameter.

The behavior of α and the speed of sound as a function of damage is illustrated in Fig. 7. The result is impressive: clearly, the nonlinear parameter α measured by NRUS is much more sensitive to damage than the speed of sound, related to the Young's modulus of the material which stays nearly constant during the entire progressive damage experiment (only a very slight decrease is observable for sample B2). α begins to increase at the first damage step, even though damage is not yet discernable on the x-ray CT images. To date, quantitative ultrasound (QUS) techniques give access to parameters such as speed of sound (SOS) and attenuation in bone. These parameters being mainly related to bone mineral density (BMD) have already proved their efficacy in the assessment of fracture risk.[33,34] A recent experimental study reported the failure of SOS and attenuation to reflect mechanically induced damages in cancellous bone.[35] This observation is also supported by our results, showing that NRUS actually allows for micro-damage detection in bone with a sensitivity much higher than that of SOS.

For sample B1, the relation between α and the number of damage steps is almost linear whereas a third-order polynomial fits the data from sample B2. This may be related to the fact that damage did not occur in the same manner in the two samples, even though they were both cycled following an identical protocol. The two samples may not have been in the same damage state at step 0, or perhaps we are seeing an indication of the natural variability of how bone responds to induced damage. An independent quantitative evaluation of micro-damage (higher resolution imaging like micro-CT for example) would have been useful here to determine a semi-quantitative relation between the measured nonlinear parameter α and micro-damage. This will be done in future work. The other limitation of this study is the small number of data points. Indeed, the number of damage steps is not sufficient to correctly understand the shape of the curves shown in Fig. 7. In any case, the trend is clearly demonstrated in this work: there is a strong relation between micro-damage and the nonlinear hysteretic parameter α. We are currently conducting a study using a large number of human bone samples, with a larger number of damage steps.

A number of challenging difficulties have to be considered before the technique can be applied noninvasively, *in vivo*. Among them are bone excitation by means of an external mechanical vibration and recording the vibration by means of a remote sensor. Vibro-acoustic spectrography using the acoustic radiation force as an external source and a hydrophone as a remote sensor might be a tempting solution.[36] Other important factors to be considered will be the relation of bone to other organs (joint, tendons) and the influence of soft tissue surrounding bone that are likely to significantly change the resonance characteristics.

VI. CONCLUSIONS

This is the first study showing the feasibility of nonlinear resonant ultrasound spectroscopy to detect damage in bone. A progressive damage experiment has been conducted on two samples of bovine bone. The increasing amount of damage mechanically induced in the sample leads to an increased shift in the resonance frequency with wave amplitude, indicating a progressively more nonlinear behavior of the sample as the sample damage accumulates. This study allowed for the determination of a parameter relevant for bone damage assessment: the nonlinear hysteretic parameter, related to the resonance frequency shift. This work is a preliminary study and some aspects, such as the fact that only the radial displacement is sensitive to damage, are not well understood yet. For an accurate quantification of damage in human bone, the experiments must be repeated, with a larger number of data points. This work is in progress and will allow for the assessment of a quantitative relationship between bone micro-damage and the nonlinear hysteretic parameter. Further work will have to be carried on for the *in vivo* application of the technique to see if it may be viable as a diagnostic tool for skeletal status assessment.

ACKNOWLEDGMENTS

This work was supported by Institutional Support (LDRD) and by the Institute of Geophysics and Planetary Physics at Los Alamos, and the Centre National pour la Recherche Scientifique (CNRS, France). The authors would like to acknowledge J. Tencate, T. Darling, and P. Zysset for helpful discussions and comments.

[1]Consensus development conference: diagnosis, prophylaxis, and treatment of osteoporosis," Am. J. Med. **94**, 646–650 (1993).
[2]J. C. Rice, S. C. Cowin, and J. A. Bowman, "On the dependence of the elasticity and strength of cancellous bone on apparent density," J. Biomech. **21**, 155–168 (1988).
[3]R. Martin, "Fatigue Microdamage as an Essential Element of Bone Mechanics and Biology," Calcif. Tissue Int. **73**, 101–107 (2003).
[4]P. Zioupos, "Accumulation of in-vivo fatigue microdamage and its relation to biomechanical properties in ageing human cortical bone," J. Microsc. **201**, 270–278 (2001).
[5]D. B. Burr, M. R. Forwood, D. P. Fyhrie, R. B. Martin, M. B. Schaffler, and C. H. Turner, "Bone microdamage and skeletal fragility in osteoporotic and stress fractures," J. Bone Miner. Res. **12**, 6–15 (1997).
[6]A. M. Parfitt, "Bone age, mineral density, and fatigue damage," Calcif. Tissue Int. **53**(Suppl. 1), S82-5; discussion S85-6 (1993).
[7]M. B. Schaffler, K. Choi, and C. Milgrom, "Aging and matrix microdamage accumulation in human compact bone," Bone (N.Y.) **17**, 521–525 (1995).
[8]T. L. Norman and Z. Wang, "Microdamage of human cortical bone: incidence and morphology in long bones," Bone (N.Y.) **20**, 375–379 (1997).
[9]B. Martin, "Aging and strength of bone as a structural material," Calcif. Tissue Int. **53**(Suppl. 1), S34-9; discussion S39-40 (1993).
[10]M. B. Schaffler, E. L. Radin, and D. B. Burr, "Mechanical and morphological effects of strain rate on fatigue of compact bone," Bone (N.Y.) **10**, 207–214 (1989).

[11]D. B. Burr and T. Stafford, "Validity of the bulk-staining technique to separate artifactual from in vivo bone microdamage," Clin. Orthop. Relat. Res. **260**, 305–308 (1990).
[12]F. J. O'Brien, D. Taylor, and T. C. Lee, "An improved labelling technique for monitoring microcrack growth in compact bone," J. Biomech. **35**, 523–526 (2002).
[13]D. Taylor, "Microcrack growth parameters for compact bone deduced from stiffness variations," J. Biomech. **31**, 587–592 (1998).
[14]F. J. O'Brien, D. Taylor, and T. C. Lee, "Microcrack accumulation at different intervals during fatigue testing of compact bone," J. Biomech. **36**, 973–980 (2003).
[15]D. B. Burr and C. H. Turner", "Biomechanics of bone," Ame. Soc. Bone Min. Res., 58–64 (2003).
[16]D. Jepsen, Akkus, "Observation of Damage in Bone," in *Bone Mechanics Handbook* (CRC Press, 2001).
[17]D. R. Carter, W. E. Caler, D. M. Spengler, and V. H. Frankel, "Fatigue behavior of adult cortical bone: the influence of mean strain and strain range," Acta Orthop. Scand. **52**, 481–490 (1981).
[18]R. A. Guyer and P. A. Johnson, "Nonlinear Mesoscopic Elasticity: Evidence for a new class of materials," Phys. Today **52**, 30–35 (1999).
[19]L. Ostrovsky and P. Johnson, "Dynamic nonlinear elasticity in geomaterials," Riv. Nuovo Cimento **24**, (2001).
[20]K. V. D. Abeele, A. Sutin, J. Carmeliet, and P. A. Johnson, "Micro Damage diagnostics using nonlinear elastic wave spectroscopy (NEWS)," NDT & E Int. **34**, 239–248 (2001).
[21]R. A. Guyer and K. R. McCall, "Hysteresis, Discrete Memory, and Nonlinear Wave Propagation in Rock: A New Paradigm," Phys. Rev. Lett. **74**, 3491–3494 (1995).
[22]P. A. Johnson and A. Sutin, "Slow dynamics and anomalous nonlinear fast dynamics in diverse solids," J. Acoust. Soc. Am. **116**, 124–130 (2004).
[23]K. V. D. Abeele, J. Carmeliet, J. A. Tencate, and P. A. Johnson, "Nonlinear Elastic Wave Spectroscopy (NEWS) Techniques to Discern Material Damage, Part II: Single-Mode Nonlinear Resonance Acoustic Spectroscopy," Res. Nondestruct. Eval. **12**, 31–42 (2000).
[24]P. A. Johnson, B. Zinszner, P. Rasolofosaon, F. Cohen-Tenoudji, and K. V. D. Abeele, "Dynamic measurements of the nonlinear elastic parameter in rock under varying conditions," J. Geophys. Res. **109**, B02202 (2004).
[25]J. A. Tencate, D. Pasqualini, S. Habib, K. Heitmann, D. Higdon, and P. A. Johnson, "Nonlinear and nonequilibrium dynamics in geomaterials," Phys. Rev. Lett. **93**(6), 065501 (2004).
[26]J. J.Stoker, *Nonlinear Vibrations in Mechanical and Electrical Systems* (Intersciences, New York, 1950).
[27]K. R. McCall and R. A. Guyer, "Equation of state and wave propagation in hysteretic nonlinear elastic materials," J. Geophys. Res. **99**, 23887–23897 (1994).
[28]R. A. Guyer, K. R. McCall, and K. V. D. Abeele, "Slow elastic dynamics in a resonant bar of rock," Geophys. Res. Lett. **25**, 1585–1588 (1998).
[29]D. I. Bolef and J. G. Miller, "High Frequency Continuous Wave Ultrasonics," Phys. Acoust., 95–201 (1971).
[30]J. G. Miller and D. I. Bolef, "A 'sampled-continuous wave' ultrasonic technique and spectrometer," Rev. Sci. Instrum. **40**, 915–920 (1969).
[31]R. G. Leisure and F. A. Willis, "Resonant ultrasound spectroscopy," J. Phys.: Condens. Matter **9**, 6001–6029 (1997).
[32]W. T. Dempster and R. T. Liddicoat, "Compact bone as a non-isotropic material," Am. J. Anat. **91**, 331–362 (1952).
[33]D. Hans, L. Genton, S. Allaoua, C. Pichard, and D. O. Slosman, "Hip fracture discrimination study: QUS of the radius and the calcaneum," J. Clin. Densitom. **6**, 163–172 (2003).
[34]M. L. Frost, G. M. Blake, and I. Fogelman, "A comparison of fracture discrimination using calcaneal quantitative ultrasound and dual X-ray absorptiometry in women with a history of fracture at sites other than the spine and hip," Calcif. Tissue Int. **71**, 207–211 (2002).
[35]P. H. Nicholson and M. L. Bouxsein, "Quantitative ultrasound does not reflect mechanically induced damage in human cancellous bone," J. Bone Miner. Res. **15**, 2467–2472 (2000).
[36]M. Fatemi and J. F. Greenleaf, "Ultrasound-stimulated vibro-acoustic spectrography," Science **280**, 82–85 (1998).

Superresolution ultrasound imaging using back-projected reconstruction

G. T. Clement
Department of Radiology, Harvard Medical School, Brigham and Women's Hospital, Boston, Massachusetts 02115

J. Huttunen
University of Kuopio, P. O. Box 1627, Neulaniementie 2, FIN-70211, Finland

K. Hynynen
Department of Radiology, Harvard Medical School, Brigham and Women's Hospital, Boston, Massachusetts 02115

(Received 23 March 2005; revised 9 September 2005; accepted 10 September 2005)

An ultrasound technique for imaging objects significantly smaller than the source wavelength is investigated. Signals from a focused beam are recorded over an image plane in the acoustic farfield and backprojected in the wave-vector domain to the focal plane. A superresolution image recovery method is then used to analyze the Fourier spatial frequency spectrum of the signal in an attempt to deduce the location and size of objects in this plane. The physical foundation for the method is rooted in the fact that high spatial frequencies introduced by the object in fact affect the lower (nonevanescent) spatial frequencies of the overall signal. The technique achieves this by using *a priori* measurements of the ultrasound focus in water, which gives full spectral information about the image source. A guess is then made regarding the size and location of the object that distorted the field, and this is convolved with the *a priori* measurement, thus creating a candidate image. A large number of candidates are generated and the one whose spectrum best matches the uncorrected image is accepted. The method is demonstrated using 0.34- and 0.60-mm wires with a focused 1.05-MHz ultrasound signal and then a human hair (~0.03 mm) with a 4.7-MHz signal.
 [DOI: 10.1121/1.2109167]

PACS number(s): 43.80.Qf, 43.80.Vj [FD] Pages: 3953–3960

I. INTRODUCTION

Over the past decade, submillimeter imaging *in vivo* has been the goal of numerous imaging modalities. In medicine this is motivated by the considerable number of potential uses in diagnostics and in the study of biological models. Some of these uses include, but are not limited to, sensing tissue morphological changes, monitoring of disease progression, temperature monitoring, following mouse and chicken embryonic development for genomics and other areas, and monitoring of the vascular system. High-resolution optics, nuclear magnetic resonance (NMR), x-ray computed tomography (CT), and ultrasound have all been examined as methods for performing high-resolution imaging, each with their own unique advantages and disadvantages. Optical coherence tomography (OCT)[1] has been used to perform *in vivo* imaging of tissue interiors in a manner analogous to B-scan ultrasound by using infrared or near infrared light interferometry. Resolution of less than 1 μ has been achieved, but with a penetration depth of only a few millimeters. Magnetic resonance microscopy (μMRI)[2] and CT microscopy have both demonstrated significant progress in high-resolution imaging with deep penetration. However, the cost and large apparatus involved with these methods make them impractical for laboratory or small clinical use.

In ultrasound, high-resolution approaches[3,4] referred to as ultrasound microimaging (UMI) or ultrasound biomicroscopy (UBM) have been applied. Such methods use high-frequency backscattered ultrasound (50–200 MHz) to achieve resolution as low as 20 μ for imaging superficial tissues such as the skin and blood vessels. These techniques have been used for their ability to measure a number of tissue properties that are not readily obtainable with other imaging methods. These properties consist of ultrasound sound speed, attenuation, impedance, tissue stiffness, and temperature sensitivity.

On a practical level ultrasound has been considered an attractive alternative to other methods due to its potential for producing a compact, nonionizing, and very low cost imaging device that could be utilized in a clinical or laboratory setting. The traditional approach applied in both UMI and UBM has been to image at higher ultrasound frequencies. Using these methods, image resolution has been extended to about 10 μ, but with the tradeoff of significantly increased attenuation.

We propose, however, a method that could allow *in vivo* imaging at submillimeter resolution with frequencies up to one order of magnitude lower than previously reported methods. Lower frequencies would allow high-resolution imaging with significantly greater penetration depth. To achieve this, we introduce a new approach to high-resolution ultrasound, which employs a combination of phase-contrast imaging, angular spectral decomposition, and a superresolution reconstruction technique. With this approach, we examine the pos-

sibility of imaging objects located entirely within an ultrasound focus, over a field of view equal to the focal area. In contrast, traditional time-of-flight (TOF) ultrasound resolution is determined by the size of the focal region achieved within the tissue. Our approach could potentially have immediate application in detecting acoustic properties that are not visible optically. In particular, the method would be sensitive to dynamic changes that induce a change in sound speed and could have application in complementing the wide range of biological areas where very-high-frequency ultrasound is being investigated.[5–7]

Superresolution is a general term that describes a wide body of methods that seek to restore an image with spatial resolution greater than the classical diffraction limit.[8] Well-founded methods for imaging objects smaller than the imaging wavelength have been carried out in one of three ways: near-field imaging[9,10] records information within a distance of several wavelengths from the source, in order to collect information from evanescent wave components of the signal, whose magnitude decays exponentially with distance from an object. Time reversal[11] uses information from scattering centers in a highly inhomogeneous field to focus beyond that obtainable in a homogeneous medium.[12] Finally, spectral methods seek to reconstruct higher spatial frequencies beyond the cutoff frequency, using *a priori* information about the image.[8]

Image processing has benefitted significantly from the application of superresolution reconstruction techniques—both near field and, more recently, far field—to a variety of optical[13–20] and electromagnetic imaging applications ranging from array and astronomical data[21] to microscopic systems.[22] The concept and limits of the spectral far-field techniques (which will be exploited in this study) have been examined[17,23] and a superresolution algorithm developed for astronomical imagery at the University of California—San Diego has resulted in the founding of a private company (Pixon, Setauket, NY) dedicated to superresolution image enhancement. A significant amount of earlier work was performed in the areas of holographic superresolution by Sato,[24] including studies in ultrasound. However, this work was limited to reconstruction through correspondence techniques[25] or as an image-processing technique. Superresolution imaging has additionally been applied toward the reconstruction of ultrasonic impedance profiles.[26]

In contrast, we use the term superresolution exclusively in this paper to indicate the recovery of spatial frequencies above the bandwidth that would be propagated by a *single* source beam to an image plane. This reconstruction is restricted to cases of far-field imaging and does not rely on measurement of evanescent waves. The physical foundation for this definition of superresolution is rooted in the fact that propagated spatial information at spatial frequencies below the diffraction limit is not independent of the information above the frequency cutoff. Basic arguments, outlined in the next section, demonstrate that such reconstruction is possible, given certain *a priori* information about the localization of the object or—as we will demonstrate—the nature of the image source.

II. THEORETICAL FOUNDATION

The present problem considers a harmonic, localized, ultrasonic wave $p(\vec{r},t)$ that satisfies the linearized Stokes equation,[27]

$$\left(1+\tau\frac{\partial}{\partial t}\right)\nabla^2 p(\vec{r},t)=\frac{1}{c^2}\ddot{p}(\vec{r},t), \tag{1}$$

where c is the real sound speed and τ is the relaxation time for the medium. Both of these quantities are, in general, functions of frequency. The projection is considered in Cartesian coordinates, in order to relate the field between two planes at z_i and z_o, referred to as the image planes and the object planes, respectively. A Helmholtz equation

$$\left(\frac{\partial^2}{\partial z^2}+\tilde{k}^2\right)\tilde{p}(k_x,k_y,z,\omega)=0 \tag{2}$$

is obtained by the substitution of a Fourier integral with respect to the x and y coordinates into Eq. (1) where the Cartesian wave numbers are given by k_x and k_y and ω is the angular frequency.[28] To propagate the field from the image plane at z_i to the image plane z_o, the advanced solution of Eq. (2) is used:[29]

$$\tilde{p}(k_x,k_y,z_o)=\tilde{p}(k_x,k_y,z_i)\exp\left(i(z_o-z_i)\sqrt{\frac{\omega^2}{c^2}\frac{1}{1+i\tau\omega}-k_x^2-k_y^2}\right). \tag{3}$$

The exponential term in Eq. (3) serves as a transfer function for the case of a wave travelling in nondissipative homogeneous media. The use of this function for both transmission and backscattered data is well established.[30] However, this function may be readily modified to cover a wide range of situations including, for example, layered media,[31] dispersion,[31] and shear modes,[32] given sufficient information about the media. The generalized form of Eq. (3) for a given frequency is simply

$$\tilde{p}(k_x,k_y,z_i)=\tilde{p}(k_x,k_y,z_o)h(k_x,k_y,z_i-z_o), \tag{4}$$

where h is a generalized transfer function relating the object and image planes, which by the convolution theorem requires that

$$p(x,y,z_i)=p(x,y,z_o)\otimes_{x,y}h(x,y,z_i-z_o), \tag{5}$$

representing a two-dimensional convolution with respect to x and y. The insertion of an object $f(x,y,z_o)$ contained entirely within the beam is now considered, so that the field becomes $p(x,y,z_o)f(x,y,z_o)$ immediately after propagating through the object and the field at the image plane in the wave-vector domain becomes

$$\tilde{p}(k_x,k_y,z_i)=[\tilde{p}(k_x,k_y,z_o)\otimes_{x,y}\tilde{f}(k_x,k_y,z_o)]h(k_x,k_y,z_i-z_o)+n(k_x,k_y). \tag{6}$$

where n represents signal noise. Even in the absence of noise, the ability to reconstruct the object at z_o, given the image p at z_i, is limited by the cutoff spatial frequencies $k_x^2+k_y^2\leqslant\omega^2/c^2$, which serve as a low-pass filter. Following an

argument outlined by Hunt,[8] it is noted that the convolution integral in Eq. (6) signifies the high-frequency components ($k_x^2+k_y^2>\omega^2/c^2$) introduced by the object $\tilde{f}$ will affect the image $\tilde{p}(k_x,k_y,z_i)$ at spatial frequencies below the cutoff frequency. It is thus the task of the superresolution algorithm to infer the object shape, location, and intensity based on this partial amount of information.

It is assumed here that both the undisturbed beam $\tilde{p}(k_x,k_y,z_o)$ and the transfer function H are known for all k_x and k_y by *a priori* measurement of the field at z_o. As noted above, the ability to perform reconstruction with the information at the image plane is a result of the higher frequency information convolved into the signal. The success of reconstructing the object f is dependent on the ability to utilize this information. In the context of an inverse problem, the task becomes one of optimizing the likelihood of an estimated value for f over all k_x, k_y given $\tilde{p}(k_x,k_y,z_o)$ and a band limited $\tilde{p}(k_x,k_y,z_o)|_{k_x^2+k_y^2\leq\omega^2/c^2}$.

The reconstruction procedure starts by projecting the measured field from the image plane to the reconstruction plane, providing a band-limited representation of Eq. (6). The data are then analyzed using a simple optimization routine, which produces candidate values for the object function f as a function of object position, size, and intensity. The portion of each candidate image within $k_x^2+k_y^2\leq\omega^2/c^2$ is then compared to the actual projected image by calculating the sum of the difference between the two:

$$S(\alpha_1,\alpha_2,\ldots,\alpha_n) = \sum_{k_xk_y} |\,(\tilde{p}_{\alpha_1,\alpha_2,\ldots,\alpha_n}(k_x,k_y,z_o)-\tilde{p}(k_x,k_y,z_o))|_{k_x^2+k_y^2\leq\omega^2/c^2}|, \tag{7}$$

where S represents a single point on a multi-dimensional difference surface, and each dimension α_i represent a variable to be minimized (e.g., position of a single object, its intensity, and its location comprise three dimensions). The global minimum of this surface, if one exists, is selected as the reconstruction object f'.

Success of the algorithm centers on the ability to locate, at least to some desired precision, the position of this minimum on the mean difference surface. This requires particular attention to noise, as it relies on detecting subtle changes in the field. With this in mind, we examine below the effects of a simple numeric case with increasingly noisy data, paying particular attention to how it distorts the difference surface.

III. NUMERIC DATA

To initially demonstrate the approach under ideal conditions a simple two-dimensional simulation was set up, eliminating the y axis of Eq. (6), and seeking to resolve a 0.2 -mm scattering object imbedded in a medium with properties similar to that of a homogeneous tissue ($c=1560$ m/s) using a 1-MHz imaging beam. Two beams, one with a Gaussian-shaped amplitude profile (FWHM=2 mm) and the other with a step profile (width=4 mm), were separately considered, representing two significantly different spatial (angular) spectrums.

Simulations and data processing were implemented in Matlab 6.0 (Mathworks Inc, Natick, MA). The band-limited spectrum was calculated in the frequency domain by a discrete approximation to the Fourier integral,

$$\tilde{p}(k_x) = \frac{1}{\sqrt{2\pi}}\int p(x,z_o)f(x,z_o)e^{ikx}dx, \quad k_x<\omega/c, \tag{8}$$

simulating the measured signal at the object plane. This value was next compared with the known full spectrum of the beam profile, and the level of agreement between the two was determined. The two quantitative criteria for "agreement" used in the study are presented in Sec. V. Distortion was then added to the known beam profile corresponding to a guess in the object's size, location, and intensity, and the two signals were again compared. This was repeated in a loop for successively larger objects (increased at 0.04-mm increments) and with all possible positions using a spatial resolution of 0.04 mm.

The optimal reconstruction was first determined with the noise level set to zero. We then examined the effects of random white noise in the data and observed how it distorted the difference function. Complex broadband random noise of a controlled level was created with a pseudo-random number generator and added linearly to the measured field given by Eq. (6), causing both amplitude and phase distortion in the signal. Noise levels between 0% and 30% of the peak signal level were examined for the Gaussian signal. The field reconstruction was then performed and compared with the actual object size and location.

IV. LABORATORY MEASUREMENT

To demonstrate the algorithm in a controlled setting, we next attempted to image a series of successively thinner wires. The samples consisted of 0.6- and 0.3-mm nylon wires and finally a human hair ($\sim$0.03 mm). Success of the algorithm was determined by comparison of backprojection images with and without applying superresolution reconstruction. The apparent width of the wires was also measured from the reconstructed images and then compared with the actual wire diameter. We deliberately selected wires as the demonstration objects so that the reconstruction could be applied only along the y axis, similar to the numeric case. The algorithm was repeatedly applied along the direction perpendicular to the wire, so that the reconstruction of the two-dimensional image has superresolution applied only in one direction.

All measurements were made in a tank filled with degassed and deionized water. Inner walls of the tank were covered with rubber to prevent reflections. A multi-cycle sine waveform was generated by a 100-MHz synthesized arbitrary waveform generator (Wavetek, 395). The signal was sent to a rf power amplifier (ENI, A150) and then to a focused transducer. The waveform generator and the rf power amplifier remained the same during all of the measurements. Two different focused transducers were used: a single element transducer with driving frequency of 1.05 MHz

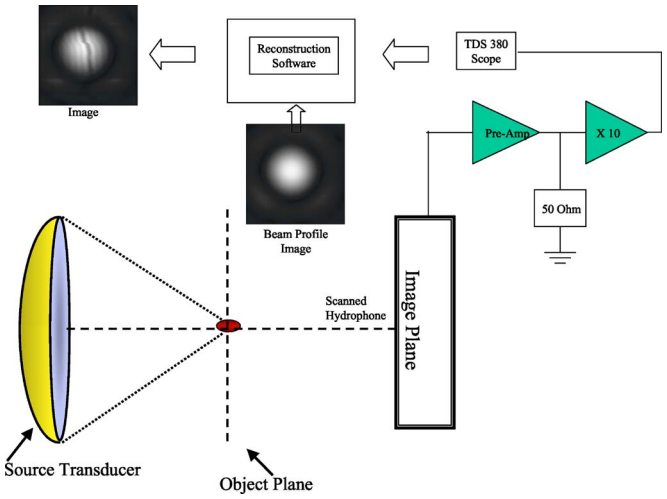

FIG. 1. (Color online) The experimental setup: A focused field is directed through the object plane and recorded at the image plane. This image is numerically back-projected to the object plane and reconstructed with a superresolution recovery method, using a stored beam profile image.

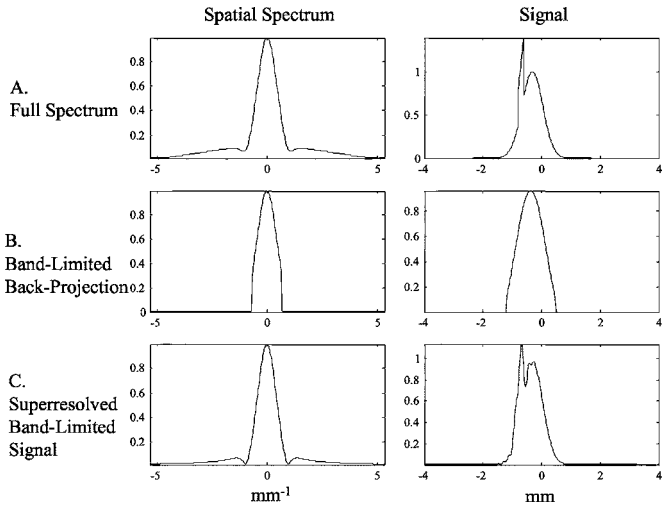

FIG. 2. A 2-mm object placed in a 1-MHz Gaussian-shaped beam. The true imaging signal and object (a) do not transmit sufficient spatial frequencies to reconstruct the object (b) unless superresolution recovery is used (c).

(diameter=25 mm radius=30 mm) and a 0.9 MHz driven at its fifth harmonic of 4.7 MHz (diameter=60 mm, radius =90 mm).

Signals were measured with a scanned hydrophone connected to a computer-controlled Parker 3D stepping motor-guided positioning system. An in-house manufactured 0.2 -mm hydrophone (ICBM01180102) was used for measurements at 1.05 MHz and a 0.075-mm polyvinylidene difluoride (PVDF) hydrophone (Precision Acoustics, SNS04) for measurements at 4.7 MHz. When using the PVDF hydrophone the signal was sent through a submersible preamplifier (Precision Acoustics, W210249). Both hydrophone signals were then amplified (Premeable Instruments, 1820 and LeCroy, DA1820A) before the time trace was recorded by a Tektronix (TDS 380, TDS 3012s) oscilloscope. A diagam of the setup is provided in Fig. 1.

Image reconstruction was implemented with a routine in Matlab. Before reconstruction, an autocorrelation function was applied between two images, one with and one without a wire. The autocorrelation was necessary to correct for slight motion of the field caused by thermally induced drifting or slight motions of the transducer. It is noted that this operation uses the same *a priori* field measurement that the superresolution method uses and does not require additional information. Object size was determined by measuring full width at half maximum (FWHM) from the backprojected image reconstruction.

V. RESULTS

A. Numeric study

The idealized (noiseless) simulated Gaussian-shaped field [Fig. 2(a)] was examined both with and without an object present, directly at the object plane. The image spectrum (left) and actual image (right) are both provided. For illustration, the object function is simulated as a net signal gain ("brightening" of the field), however the argument readily follows to cases where the object causes attenuation and/or phase shift. Specifically, phase gain is described in the next section. Figure 2(b) shows the reconstructed image without superresolution compensation, when the acoustic image plane is located more than a few wavelengths from the object. When the difference surface S was examined, a global minimum was found and selected as the object size and location. Figure 2(c) shows the data reconstructed using the superresolution algorithm. Partial reconstruction of the higher spatial components is evident in the spatial frequency plot (left). The object was next deconvolved from the source beam, resulting in the normalized object identifications shown in Fig. 3. It is clear that without superresolution, the object, shown in Fig. 3(b), simply produces an artifact, which is indiscernibly related to the actual object. However, the algorithm reconstruction, in Fig. 3(c), produces improvement in both object localization and spatial dimensions. Similarly, Fig. 4(a) shows the stepped field directly after passing through the object plane. Figure 4(b) shows the re-

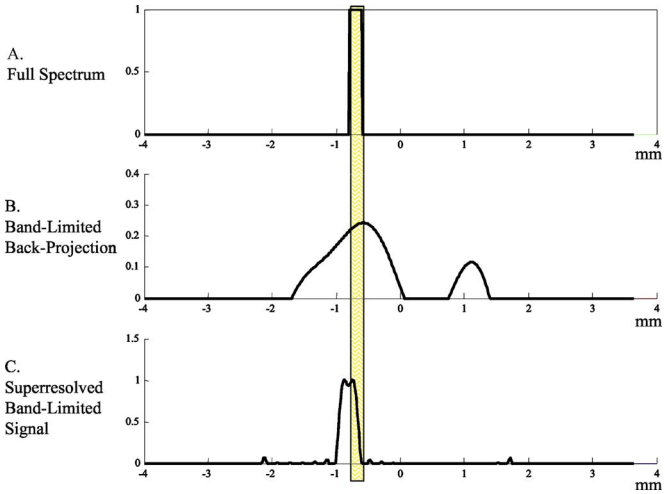

FIG. 3. (Color online) Simulation of a 2-mm object placed in a 1-MHz beam. The true imaging signal and object (a) do not transmit sufficient spatial frequencies to reconstruct the object (b) unless superresolution recovery is used (c).

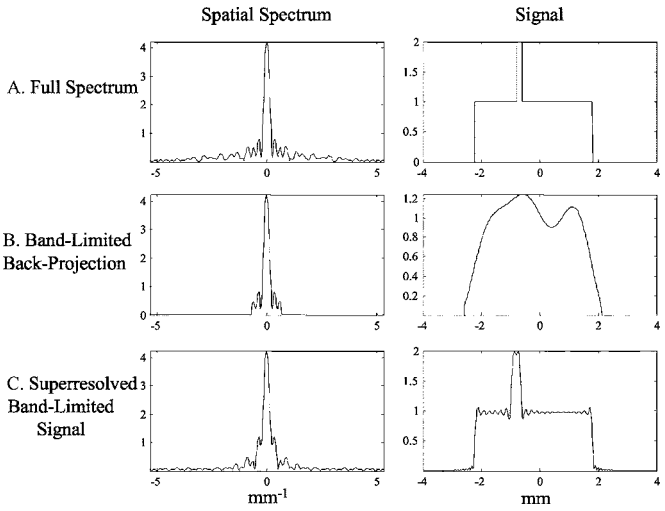

FIG. 4. Simulation of a 2-mm object placed in a 1-MHz step-shaped beam. The true imaging signal and object (a) do not transmit sufficient spatial frequencies to reconstruct the object (b) unless superresolution recovery is used (c).

constructed image without superresolution compensation, and Fig. 4(c) shows the same data reconstructed using the superresolution algorithm. As in the case with the Gaussian beam, the algorithm again successfully localized a stepped object, which contains a broadband spatial spectrum [Fig. 5(a)]. Figure 5(b) shows the reconstructed image without superresolution compensation, and Fig. 5(c) shows the same data using the superresolution algorithm.

The primary effect of noise on the difference surface was an overall gradient reduction or "flattening" of a region on the surface (Fig. 6), in many cases creating more than one global minimum. It is interesting to note that these reductions were both localized and centered around the minima present without noise suggesting that image recovery may be possible, even in the presence of a significant level of noise. In this preliminary study two possible recovery methods

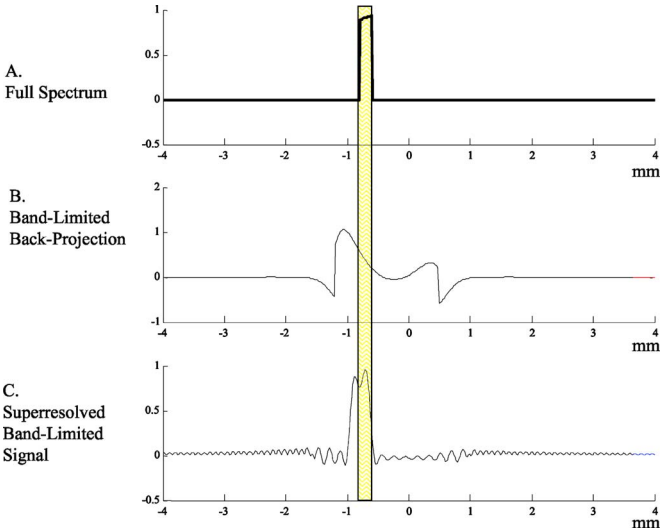

FIG. 5. (Color online) Simulation of a 2-mm object placed in a 1-MHz step-shaped beam. The true imaging signal and object (a) do not transmit sufficient spatial frequencies to reconstruct the object (b) unless superresolution recovery is used (c).

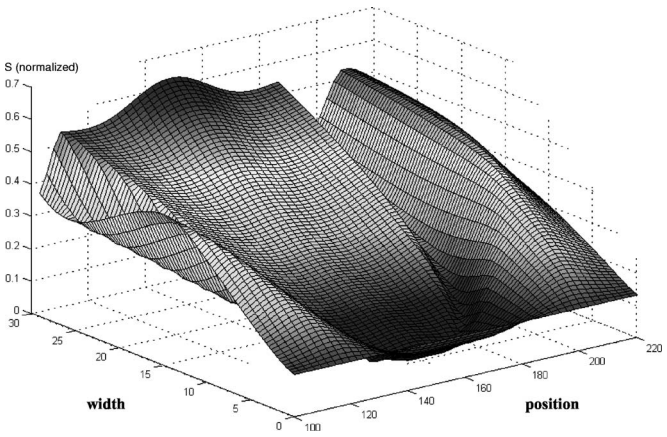

FIG. 6. Difference between the spectra produced by an image and candidate images containing different object positions and width. Introduction of a broadband noise was observed to flatten this surface about its global minimum.

were considered: The first method began by finding the 20 lowest values on the surface S. Next, the centermost position of these points was determined in a manner similar to a center-of-mass (COM) calculation:

$$\mathrm{COM} = \frac{\sum_{n=1}^{N} S_n r_n}{\sum_{n=1}^{N} S_n}, \tag{9}$$

where S_n is the value of the difference function at surface position r. In the present case, r represents a two-dimensional vector with dimensions expressing object width and location, respectively. This central point on the surface provided the width and position of the object in the image. It is noted that the calculation given by Eq. (9) readily generalizes to higher dimensions.

The second method first determined the minimum along each position line of the surface (see Fig. 6). The mean minimum then determined the object position. Next, the minimum width at this position was identified. Results using both methods are shown as a function of noise in Fig. 7.

B. Laboratory-acquired images

To investigate the feasibility of applying the method to authentic ultrasound signals, a total of six samples were reconstructed—four samples were examined with 0.34-

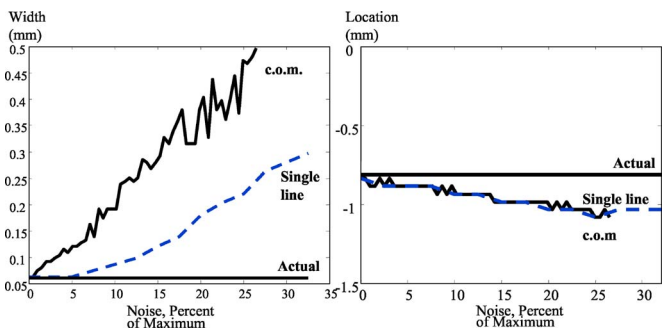

FIG. 7. (Color online) Graphs of actual width and location of an object compared with the predicted width and location as determined using two different techniques as a function of increasing noise.

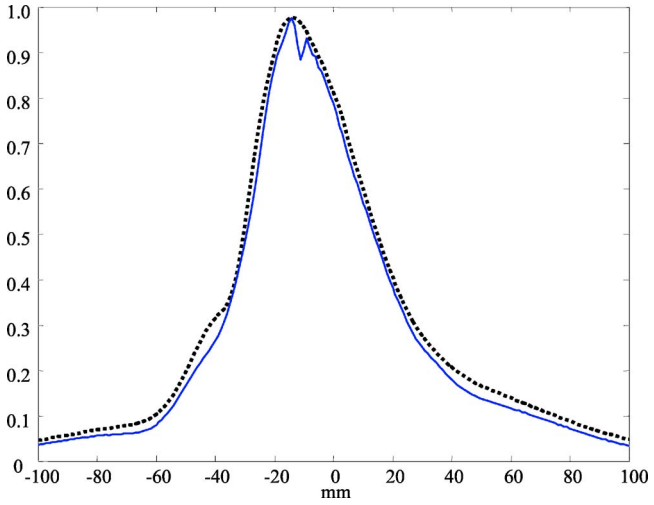

FIG. 8. (Color online) The on-axis backward-projected ultrasound signal before (dotted) and after (solid) a 0.34-mm nylon wire is placed in the focus of a 1.0-MHz field in water.

MHz nylon wire and a single sample each of 0.60-mm wire and 0.03-mm human hair. The 1.05-MHz transducer was used with the nylon wire and 4.70 MHz was used with the hair.

Initially, axial backprojections were performed to examine the evolution of the field along the axis of propagation. We discovered that these backprojections were highly sensitive to the presence of the wire, causing a reduction of image intensity near the object plane. As a result, we were able to use these images to identify the location of the object plane on the propagation axis. Figure 8 shows the on-axis projection before and after the 0.6-mm nylon wire was inserted. In this case there was a clearly visible reduction of the intensity at $z=-11$ mm. Using this information, high-resolution axial backprojections were performed in the x-z plane, perpendicular to the wire near $z=-11$, in order to identify the approximate location of the wire on the x axis, when compared to the same signal without a wire (Fig. 9, top). Similarly, high-resolution axial backprojections were performed in the y-z plane, perpendicular to the wire near the x-axis intersection of the wire in order to identify the approximate location of the wire along the y-axis (Fig. 9, bottom).

TABLE I. Summary of measurements.

Frequency (MHz)	Wire thickness (mm)	Measured thickness (mm)	% difference
1.05	0.60	0.44	15
	0.34	0.29	7.9
		0.35	1.5
		0.35	1.5
		None detected	N/A
4.70	0.03	0.03	0

Once the location of the image plane was identified, the image could be produced in the proper location. We back-projected the signal and constructed images both with and without the superresolution algorithm. This procedure was applied to the 0.60-mm wire, four cases with the 0.34-mm wire and one case with the 0.03-mm hair. The algorithm successfully identified the samples in five out of the six cases studied, the exception being one of the 0.34-mm measurements. The ability of the algorithm to identify the actual width of the object was considered after the reconstruction. A summary of the measurements is presented in Table I, showing that the wire (or hair) width was accurate to within an 15% difference in each of the cases where the sample was detected. However, in the case of the 0.60-mm wire, measurements were made on only 129 out of 220 image lines (59%), with failure to find the image in the remaining 91 lines. Comparison of images before [Fig. 10(a)1] and after a 0.34 mm wire was inserted [Fig. 10(a)2] indicated that the field experienced some distortion, but did not produce any sign of the wire. However, the same image with superresolution applied [Fig. 10(a)3] clearly shows an object through the focal area. Similarly, Figs. 10(b)1–3 illustrate the considerable image improvement experienced with superresolution applied to the human hair image.

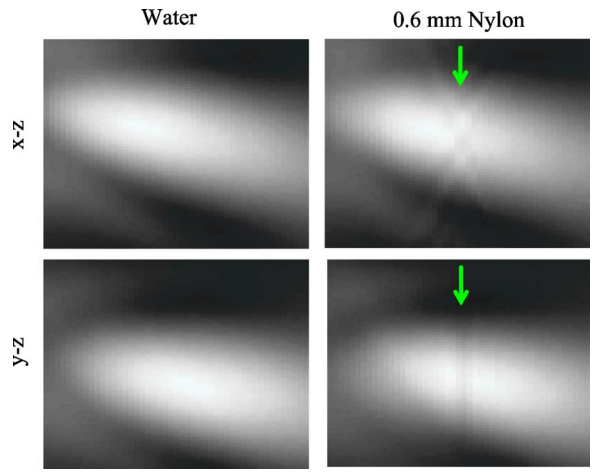

FIG. 9. (Color online) Axial back-projections of the signal before (left) and after (right) a 0.34-mm nylon wire is placed in the focus of a 1.0-MHz field in water.

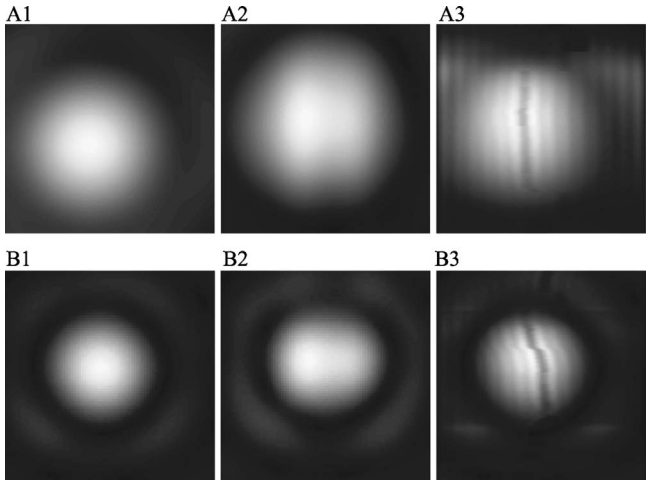

FIG. 10. Back-projected ultrasound field amplitude without 0.3 mm line (A1), with line (A2) and with line using superresolution. Series B shows the same but with a 0.03-mm human hair.

VI. DISCUSSION

This investigation proposes an approach to enhanced ultrasound imaging and microscopy while providing an assessment of the ability of superresolved backprojected ultrasound to recover the location and dimensions of objects smaller than the imaging wavelength. The ability to detect objects at relatively low frequencies could ultimately allow imaging at greater penetration depths. The approach is related to procedures which have been described in optics, but with several key differences. First, in the present approach, ultrasound is backprojected from the image to the object plane. Second, most optical methods only consider the localization of the object and not the source beam itself, i.e., $p(x,y,z_o)$ in Eq. (5) is simply a step function. In contrast, ultrasound allows this beam to be modified by different transducer geometries. Third, by adjusting the ultrasound beam shape a series of different source functions $p(x,y,z_o)$ can be formed, providing additional spatial information.

Although the ability to perform the method in a controlled setting is by itself interesting, the method's feasibility becomes greatly enhanced by the observation that the method is stable in the presence of noise. It is interesting to note that the reconstruction accuracy was lower for the larger sized (0.6 mm) wire and more accurate with the objects much smaller than a wavelength, which is the region where superresolution is designed to be applied. Our relatively simple algorithm searched for objects in the size range from zero to the size of the ultrasound beamwidth.

Future work will concentrate on implementing higher-dimensional optimization routines in order to image complex structures within the beams. We will investigate the use of global terrain methods[33] to find surface extrema in the presence of noise.[34] Additionally, by passing multiple beams through the region with differing beamwidths, shape, and direction, a more complete image of the *k*-space region may be possible to improve the reconstruction.

With our simple experimental demonstration, we were able to detect a human hair with a diameter equal to approximately 0.09 wavelengths. This result introduces the use of the full complex wavefront information for reconstruction of image, which has not been used before in superresolution imaging. The use of ultrasound is expected to allow even more advanced methods to be used for the imaging, such as use of multiple ultrasound beam shapes (both amplitude and phase spatial distribution can be controlled) to bring out a broader range of spatial frequencies, which are later combined to reconstruct images in the object plane. The approach could potentially have application in detecting acoustic properties that are not visible with present diagnostic methods. In particular, the method would be sensitive to dynamic changes that induce a change in sound speed. Practical examples of such changes may include breast tumor imaging, internal temperature monitoring, and blood flow measurement, as well as many *in vivo* laboratory applications.

[1] D. Huang, E. A. Swanson, C. P. Lin, J. S. Shuman, W. G. Stinson, W. Chang, M. R. Hee, T. Flotte, K. Gregory, C. A. Puliafito, and J. G. Fujimoto, "Optical coherence tomography," Science **254**(1178), 1181 (1991).

[2] E. T. Ahrens, P. T. Narasimhan, T. Nakada, and R. E. Jacobs, "Small animal neuroimaging using magnetic resonance microscopy," Prog. Nucl. Magn. Reson. Spectrosc. **40**, 275–306 (2002).

[3] D. A. Knapik, B. Starkoski, C. J. Pavlin, and F. S. Foster, "A 100–200 MHz ultrasound biomicroscope," IEEE Trans. Ultrason. Ferroelectr. Freq. Control **47**, 1540–1549 (2000).

[4] F. S. Foster, C. J. Pavlin, and K. A. Harasiewicz, "Advances in ultrasound biomicroscopy," Ultrasound Med. Biol. **26**(1), 1–27 (2000).

[5] C. Passmann and H. Ermert, "A 100 MHz ultrasound imaging system form dermatologic and ophthalmologic diagnostics," IEEE Trans. Ultrason. Ferroelectr. Freq. Control **23**, 545–552 (1996).

[6] F. S. Foster, G. Liu, J. Mehi, B. S. Starkoski, L. Adamson, Y. Zhou, K. A. Harasiewicz, and L. Zan, "High frequency ultrasound imaging: from man to mouse," *IEEE 2000 Ultrasonics Symposium*, Vol. **2**, pp. 1633–1638.

[7] D. H. Turnbull, T. S. Bloomfield, H. S. Baldwin, F. S. Foster, and A. L. Joyner, "Ultrasound backscatter microscope analysis of early mouse embryonic brain development," Proc. Natl. Acad. Sci. U.S.A. **92**, 2239–2243 (1995).

[8] B. R. Hunt, "Super-resolution of imagery: Understanding the theoretical basis for the recovery of spatial frequencies beyond the diffraction limit," *Proceedings of Information Decision and Control 99* (Institute of Electrical and Electronic Engineers, Inc., New York, 1999).

[9] M. Ueda and T. Sato "Superresolution by holography," J. Opt. Soc. Am. **61**(3), 418–419 (1971).

[10] E. G. Williams, and J. D. Maynard, "Holographic imaging without the wavelength resolution limit," Phys. Rev. Lett. **45**(7), 554 (1980).

[11] M. A. Fink, "Time-reversed acoustics," Phys. Today **50**, 34–40 (1997).

[12] P. Blomgren, G. Papanicolaou, and H. Zhao, "Super-resolution in time-reversal acoustics," J. Acoust. Soc. Am. **111**, 230–248 (2002).

[13] W. Lukosz, "Optical systems with resolving powers exceeding the classical limit," J. Opt. Soc. Am. **56**(11), 1463 (1966).

[14] D. O. Walsh and P. A. Nielsendelaney, "Direct method for superresolution," J. Opt. Soc. Am. A Opt. Image Sci. Vis **11**(2), 572–579 (1994).

[15] N. Miura and N. Baba, "Superresolution for a nonnegative band-limited image," Opt. Lett. **21**(15), 1174–1176 (1996).

[16] A. Manikas, T. Ratnarajah, and J. S. Lee, "Evaluation of superresolution array techniques applied to coherent sources," Int. J. Electron. **82**(1), 77–105 (1997).

[17] M. Elad and A. Feuer, "Restoration of a single superresolution image from several blurred, noisy and undersampled measured images," IEEE Trans. Image Process. **6**(12), 1646–1658 (1997).

[18] K. B. Wolf, D. Mendolvoic, and Z. Zalevsky, "Generalized Wigner function for the analysis of superresolution systems," Appl. Opt. **37**(20), 4374–4379 (1998).

[19] I. Leiserson, S. G. Lipson, and V. Sarafis, "Superresolution in far-field imaging," Opt. Lett. **25**(4), 209–211 (2000).

[20] I. Leizerson, S. G. Lipson, and V. Sarafis, "Superresolution in far-field imaging," J. Opt. Soc. Am. A Opt. Image Sci. Vis **19**(3), 436–443 (2002).

[21] W. X. Sheng and D. G. Fang, "Angular superresolution for phased antenna array by phase weighting," IEEE Trans. Aerosp. Electron. Syst. **37**(4), 1450–1458 (2001).

[22] E. A. Ash and G. Nicholls, "Super-resolution aperture scanning microscope," Nature (London) **237**(5357), 207 (1972).

[23] T. R. M. Sales and G. M. Morris, "Fundamental limits of optical superresolution," Opt. Lett. **22**(9), 582–584 (1997).

[24] S. Wadaka and T. Sato, "Superresolution in incoherent imaging system," J. Opt. Soc. Am. **65**(3), 354–355 (1975).

[25] M. Ueda and T. Sato, "Superresolution by holography," J. Opt. Soc. Am. **61**(3), 418 (1971).

[26] F. Boada, E. M. Haacke, W. Tobocman, K. Santosh, and Z.-P. Liang, "Superresolution imaging applied to ultrasonic scattering," Inverse Probl. **5**, L21–L25 (1989).

[27] A. D. Pierce, *Acoustics, An Introduction to its Physical Principles and Applications* (Acoustical Society of America, Woodbury, NY, 1989).

[28] P. R. Stepanishen and K. C. Benjamin, "Forward and backward projection of acoustic fields using FFT methods," J. Acoust. Soc. Am. **71**, 803–812 (1982).

[29]G. T. Clement and K. Hynynen, "Field characterization of therapeutic ultrasound phased arrays through forward and backward planar projection," J. Acoust. Soc. Am. **108**(1), 441–446 (2000).
[30]M. Kaveh, M. Soumekh, and J. F. Greenleaf, "Signal processing for diffraction tomography," IEEE Trans. Sonics Ultrason. **SU-31**(4), 230–239 (1984).
[31]G. T. Clement and K. Hynynen, "Forward planar projection through layered media," IEEE Trans. Ultrason. Ferroelectr. Freq. Control **50**, 1689–1698 (2003).
[32]G. T. Clement, P. J. White, and K. Hynynen, "Enhanced ultrasound transmission through the human skull using shear mode conversion," J. Acoust. Soc. Am. **115**, 1356–1364 (2004).
[33]A. Lucia and Y. Feng, "Global terrain methods," Comput. Chem. Eng. **26**, 529–546 (2002).
[34]H.-F. Cheng, "Optimization based on information containing uncertainties," Kybernetes **30**(9), 1177–1182 (2001).

Erratum: "The acoustical Klein-Gordon equation: The wave-mechanical step and a barrier potential functions" [J. Acoust. Soc. Am. 114(3), 1291–1302 (2003)]

Barbara J. Forbes[a)]
Phonologica, P. O. Box 43925, London NW2 1DJ, UK,

E. Roy Pike
Department of Physics, King's College London, Strand, London, WC2R 2LS, UK

David B. Sharp
Department of Environmental and Mechanical Engineering, The Open University, Walton Hall, Milton Keynes, MK7 6AA, UK

(Received 23 August 2005; revised 5 September 2005; accepted 7 October 2005)

[DOI: 10.1121/1.2130962]

PACS number(s): 43.20.Ks, 43.20.Mv, 43.70.Bk [ADP]

The first sentence above Eq. (16) should read: "For an initial value problem and setting $A_0=\sqrt{S(0)}$ and $\xi=[d\sqrt{S(x)}/dx]_{x=0}$ …"

Similarly, Eq. (40) should read

$$\alpha = \left.\frac{1}{2S(0)}\,\frac{dS(x)}{dx}\right|_{x=0}. \tag{1}$$

The sentence above Eq. (66) should begin: "For $\alpha=0$ and $U(0)=0$, corresponding to a strictly plane-wave source, the glottal volume velocity $u_g'(0,t)$ is …"

The area functions with $\alpha\neq 0$ (entailing $\xi\neq 0$) in Fig. (14) [see also Figs. (3) and (4)] are not described by the Green's function of Eq. (70) and thus do not correspond to the spectrum of Fig. (13), which is correct for $\alpha=0$.

The final sentence in the central paragraph above Fig. (12) on p. 1301 should read: "As noted in Sec. II, the dispersive properties of the set are identical; it has now been shown that any members with $\alpha=0$ also share a wave-mechanical Green's function and therefore have identical resonance characteristics, up to a frequency-independent normalization factor of $\rho_0 c/\sqrt{S(0)}$ [Eq. (70)].

[a)]Electronic mail: forbes@phonologica.com

Erratum: 4pAB4. Strategies for weighting exposure in the development of acoustic criteria for marine mammals [J. Acoust. Soc. Am. 118(3), 2019 (2005)]

James H. Miller
Dept. of Ocean Engineering, University of Rhode Island, Narragansett, Rhode Island 02882

Anne E. Bowles
Hubbs-Sea World Research Institute, 2595 Ingraham Street, San Diego, California 92109

Brandon L. Southall and Roger L. Gentry
NOAA Acoustics Program, National Marine Fisheries Service, Office of Protected Resources, Marine Mammal Division, 1315 East-West Highway, Silver Spring, Maryland 20910–6233

William T. Ellison
Marine Acoustics, Inc., P.O. Box 340, Litchfield, Connecticut 06759

James J. Finneran
Space and Naval Warfare Systems Center, 53560 Hull Street, San Diego, California 92152–5000

Charles R. Greene Jr.,
Greeneridge Sciences, Inc., 4512 Via Huerto, Santa Barbara, California 93110

David Kastak
Long Marine Laboratory, University of California at Santa Cruz, 100 Shaffer Road, Santa Cruz, California 95060

Darlene R. Ketten and Peter L. Tyack
Woods Hole Oceanographic Institution, Woods Hole, Massachusetts 02543

Paul E. Nachtigall
Hawaii Institute of Marine Biology, P.O. Box 1346, Kane'ohe, Hawai'i 96744

W. John Richardson
LGL Ltd. Environmental Research Associates, P.O. Box 280, 22 Fisher Street, King City, Ontario L7B 1A6, Canada

Jeanette A. Thomas
Western Illinois University Quad Cities, 3561 60th Street, Moline, Illinois 61265

(Received 2 November 2005; accepted 3 November 2005)
[DOI: 10.1121/1.2140581]

PACS number(s): 43.80.–n, 43.10.Vx

The correct authors and affiliations for this abstract are: James H. Miller (Dept. of Ocean Eng., Univ. of Rhode Island, Narragansett, RI 02882, miller@uri.edu), Anne E. Bowles (Hubbs-Sea World Res. Inst., San Diego, CA 92109), Brandon L. Southall, Roger L. Gentry (NOAA Acoustics Program, National Marine Fisheries Services, Silver Spring, MD 20910–6233), William T. Ellison (Marine Acoustics, Inc., Litchfield, CT 06759), James J. Finneran (Space and Naval Warfare Systems Center, San Diego, CA 92152–5000), Charles R. Greene, Jr. (Greeneridge Sciences, Inc., Santa Barbara, CA 93110), David Kastak (Univ. of California at Santa Cruz, Santa Cruz, CA 95060), Darlene R. Ketten, Peter L. Tyack (Woods Hole Oceanographic Inst., Woods Hole, MA 02543), Paul E. Nachtigall (Hawaii Inst. of Marine Biology, Kane'ohe, HI 96744), W. John Richardson (LGL Ltd. Environmental Research Assoc., King City, ON L7B 1A6, Canada), Jeanette A. Thomas, Western Illinois Univ., Moline, IL 61265)